Basic Sciences of Nuclear Medicine

Magdy M. Khalil

Editor

Second Edition

Springer

Basic Sciences of Nuclear Medicine

Magdy M. Khalil

Editor

Basic Sciences of Nuclear Medicine

Second Edition

Springer

Editor
Magdy M. Khalil
Department of Physics
Helwan University
Cairo
Egypt

(وَاللّٰهُ أَخْرَجَكُم مِّن بُطُونِ أُمَّهَاتِكُمْ لَا تَعْلَمُونَ شَيْئًا وَجَعَلَ لَكُمُ السَّمْعَ وَالْأَبْصَارَ وَالْأَفْئِدَةَ ۙ لَعَلَّكُمْ تَشْكُرُونَ)

"النحل -78"

(Allah has extracted you from the wombs of your mothers
not knowing a thing, and He made for you hearing and vision
and intellect that perhaps you would be grateful)
                                            "An-Nahl 78"

I dedicate this book to my Parents,

My Family,

My Colleagues,

And my Students

Preface

The parent book *Basic Sciences of Nuclear Medicine*, 2010, Springer, was initially designed to cover a wide spectrum of basic science disciplines as relevant and consistent with nuclear medicine and molecular imaging theory and practice. I believe the first edition was concomitant with a number of revolutions in nuclear medicine including wide spread of hybrid imaging, radionuclide therapy, new innovations in gamma camera and PET scanner technology, radiochemistry, radiation biology and dosimetry, computational algorithms and image reconstructions. The momentum of this second edition is also associated with new developments including extended axial of view PET scanners, radiomics and texture feature analysis, artificial intelligence including machine and deep learning and many others. This really reflects the dynamic nature of the field and how the scientific community rapidly cope with recent advances and their application for the benefit of patients. While the book deals with fundamental concepts and principles, there was a need to update some contents adding new ideas and approaches recently developed.

This second edition consists of six parts including physics and radiation protection, radiopharmacy and radiochemistry, internal dosimetry and radiobiology, SPECT and PET imaging instrumentation, image reconstruction and analysis as well as quantitative imaging analysis. A panel of expert scientists were carefully selected to document the theoretical and practical aspects of nuclear medicine and molecular imaging.

The day-to-day innovations observed in diagnostic imaging and particularly in nuclear medicine are due to better understanding and integration of key concepts and fundamental rules of physics, chemistry, biology, mathematics, engineering including computer science and electronics. This book was made to cover most of those disciplines and their direct applications in the field.

The audience of the book remain those who are interested in a one-stop-shop textbook that handles most of the important and relevant topics of nuclear medicine and molecular imaging. Potential targets are medical physicists, radiochemists, physicians, radiologists, medical students, clinical scientists and others. I wish the reader will find this new edition a valuable resource on their way towards deep understanding of the discipline and better practice for serving ill people.

Cairo, Egypt   Magdy M. Khalil
21 August 2020

Acknowledgements

Contents

Part IV   SPECT and PET Imaging Instrumentation

Part V   Image Reconstruction, Processing and Computation

Part VI   Quantitative Image Analysis

Contributors

Eman Al-Anezi, BSc Nuclear Medicine and Cyclotron Department, King Hamad University Hospital, Busaiteen, Bahrain

Simon M. Ametamey, PhD Animal Imaging Center-PET, Center for Radiopharmaceutical Sciences of ETH, PSI and USZ, ETH-Hönggerberg, D-CHAB IPW HCI H427, Zurich, Switzerland

James R. Ballinger, PhD School of Biomedical Engineering and Imaging Sciences, King's College London, London, UK

M'hamed Bentourkia, PhD Faculty of Medicine and Health Sciences, Department of Nuclear Medicine and Radiobiology, University of Sherbrooke, Sherbrooke, QC, Canada

C. David Cooke, MSEE Emory University School of Medicine, Atlanta, GA, USA

Adriano Duatti, PhD Department of Chemical and Pharmaceutical Sciences, University of Ferrara, Ferrara, Italy

Issam El Naqa, PhD Physics Division, Department of Radiation Oncology, University of Michigan, Ann Arbor, MI, USA

Kjell Erlandsson, PhD Institute of Nuclear Medicine, University College London, London, UK

Tracy L. Faber, PhD Emory University School of Medicine, Atlanta, GA, USA

James R. Galt, PhD Emory University School of Medicine, Atlanta, GA, USA

Taher Hosny, MSc Nuclear Medicine and Cyclotron Department, King Hamad University Hospital, Busaiteen, Bahrain

Magdy M. Khalil, PhD Medical Biophysics, Department of Physics, Faculty of Science, Helwan University, Cairo, Egypt

Michael Ljungberg, PhD Department of Medical Radiation Physics, Lund University, Lund, Sweden

Vivian Loveless, BS Pharmacy, Doctor of Pharmacy University of Tennessee Health Science Center College of Pharmacy, Memphis, TN, USA

Susan H. Morgan, BS, PharmD, MBA, BCNP University of Tennessee Health Science Center College of Pharmacy, Memphis, TN, USA

Tinsu Pan, PhD Department of Imaging Physics, University of Texas, M.D. Anderson Cancer Center, Houston, TX, USA

Anil Kumar Pandey, PhD Department of Nuclear Medicine, AIIMS, New Delhi, India

Gauri Shankar Pant, PhD Department of Nuclear Medicine, AIIMS, New Delhi, India

Gian Luca Poli, PhD ASST Papa Giovanni XXIII, Bergamo, Italy

Tobias L. Ross, PhD Radiopharmaceutical Chemistry, Department of Nuclear Medicine, Hannover Medical School, Hannover, Germany

Lise Wei, PhD Physics Division, Department of Radiation Oncology, University of Michigan, Ann Arbor, MI, USA

Pat Zanzonico, PhD Memorial Sloan Kettering Cancer Center, New York, NY, USA

Part I

Physics and Radiation Protection

Basic Radiation Physics as Relevant to Nuclear Medicine

1

Gauri Shankar Pant and Anil Kumar Pandey

Contents

G. S. Pant (✉)
Retried Professor, Department of Nuclear Medicine, All India Institute of Medical Sciences (AIIMS), New Delhi, India

A. K. Pandey
Department of Nuclear Medicine, All India Institute of Medical Sciences (AIIMS), New Delhi, India

The peaceful applications of atomic radiations have been well established, in many areas particularly in the field of medicine for diagnosis and treatment. The basic understanding of atomic radiations and their characteristics is therefore important for those working in nuclear medicine and other allied disciplines. A brief description on basic physics as relevant to nuclear medicine is given here.

1.1   Atom

It is well known that matter is comprised of atoms, and atom is the smallest unit of a chemical element. An atom rarely exists alone and often combines with other atoms to form the molecule, the component of a chemical compound.

1.2   Modern Atomic Theory

1.2.1   Wave–Particle Duality

According to classical physics, the particles cannot be wave and vice versa. However, Einstein, while explaining the photoelectric effect, postulated that electromagnetic radiation has wave–particle nature. He used the term photon for the packet of electromagnetic radiation and proposed a simple formula to relate the energy of the photon E to its frequency ν or the wavelength.

$$E = h\nu = h\frac{c}{\lambda} \qquad (1.1)$$

In this equation, h is the Planck's constant $(6.634 \times 10^{-34}\,\text{J s})$ and c is the velocity of light in vacuum.

De Broglie generalized the idea and postulated that all sub-atomic particles have wave–particle nature. In some phenomena, the particle behaves as a particle, and in others, it behaves as a wave but in none as both (wave–particle duality). He suggested the following equation to relate the momentum of the particle P to its wavelengths λ:

$$\lambda = \frac{h}{p} \qquad (1.2)$$

Only when the particles are with extremely small mass (subatomic particles), the associated wave is appreciable. Electron microscope is an instrument that proves the accuracy of the wave–particle duality. In macroscopic scale, De Broglie theory is not applicable. Erwin Schrodinger derived an equation in 1925, which describes not only the subatomic, atomic and molecular system but also the macroscopic systems. This discovery was a significant landmark in quantum mechanic for which he was awarded Nobel Prize in Physics in 1933. The detailed discussion on Schrodinger equation is beyond the scope of this chapter.

1.2.2   Electron Configuration

Electrons around a nucleus can be described with wave functions. Wave functions determine the location, energy and momentum of the particle. The square of a wave function gives probability distribution of the particle. At a given time, electrons can be anywhere around the nucleus, but different locations have different probabilities. The space around the nucleus in which the probability is highest is called an orbital. In quantum mechanics, orbital is a mathematical concept that suggests the average location of an electron around the nucleus. If the energy of the electron changes, this average location also changes. For the single electron of hydrogen atom, an infinite number of wave functions and therefore infinite number of orbitals exist.

Orbital can completely be described using the corresponding wave function, but the process is tedious and difficult. In simple terms, an orbital can be described by four quantum numbers.

- The principal quantum number n characterizes the energy and shell size in an atom. It is an integer and can have value from 1 to ∞, but practically n is always less than 8. Maximum number of electrons in the orbital n, is given as $2n^2$. The shells of electrons are labelled alphabetically as $K(n = 1)$, $L(n = 2)$, $M(n = 3)$, etc. based on the principal quantum number.
- The orbital quantum number l relates to the angular momentum of the electron; l can take integer values from 0 to $n - 1$. In a stable atom, its value does not go beyond 3. Orbital quantum number characterizes the configuration of the electron orbital. In the hydrogen atom, the value of l does not appreciably affect the total energy, but in atoms with more than one electron, the energy depends on both n and l. The sub-shells or orbitals of electrons are labelled as $s(l = 0)$, $p(l = 1)$, $d(l = 2)$ and $f(l = 3)$.
- The azimuthal or magnetic quantum number m_l relates to the direction of the electron's

angular momentum and takes on integer values from $-l$ to $+l$.

- The spin quantum number m_s relates to electron angular momentum and can have only two values $-\frac{1}{2}$ or $+\frac{1}{2}$.

In 1925 Wolfgang Pauli added a complementary rule for the arrangement of electrons around the nucleus. The postulation is now called **Pauli's exclusion principle** and states that no two electrons can have all quantum numbers same or exist in identical quantum states.

The filling of electrons in orbitals obeys the so-called Aufbau principle. The Aufbau principle assumes that electrons are added to an atom, one at a time, starting with the lowest energy orbital, until all of the electrons have been placed in an appropriate orbital. The sequence of energy states and electron filling in orbitals of a multi-electron atom can be represented as:

$$1s - 2s - 2p - 3s - 3p - 4s - 3d - 4p - 5s$$
$$-4d - 5p - 6s - 4f - 5d - 6p - 7s - 5f - 6d - 7p$$

1.3 Electron Binding Energies

The bound electrons need some external energy to make them free from the nucleus. It can be assumed that electrons around a nucleus have negative potential energy. The absolute value of the potential energy is called binding energy and is the minimum energy that is required to make an electron free of the atom.

1.3.1 Atomic Emissions

For stability, electrons are required to be in the minimum possible energy level or in the innermost orbitals. However, there is no restriction for an electron to transfer into outer orbitals if it gains sufficient energy. If an electron absorbs external energy that is more than or equal to the binding energy of its orbital, the electron is freed from the atom. A pair of ion, the electron and the atom with positive charge, is created. This process is termed as *ionization*. If the external energy

is more than the binding energy of the electron, the excess energy is divided between the two in such a way that conservation of momentum is preserved. The energy level of a free electron is not necessarily discrete.

If an electron absorbs energy and is either elevated to outer orbits or becomes free to move out of the atom, the original orbital does not remain vacant. Soon the vacancy will be filled by electron from outer layers. This is a random process, and occupier may be any electron from outer orbital. However, closer electron has more chance to occupy the vacancy. In each individual filling-up process, a quantum of energy equal to the difference between the binding energies $E_2 - E_1$ of the two involved orbitals is released, usually in the form of single photon. The frequency ν and wavelength λ of the emitted photon (radiation) are as follows:

$$E_2 - E_1 = \Delta E = h\nu = h\frac{c}{\lambda} \qquad (1.3)$$

When an atom has excess energy, it is in an unstable or *exited state*. The excess energy is released usually in the form of electromagnetic radiation until the atom is again in its natural *stable state*. The frequency spectrum of the radiation emitted from an exited atom can be used as the fingerprint of atom. Such radiation is called characteristic radiation.

1.3.2 Nucleus

In simple terms, the nucleus is made up of two fundamental particles, protons and neutrons. These particles together are called nucleons. The protons are positively charged, and neutrons are electrically neutral. Since electrons are light particles (with mass about 1/1840 times the mass of either neutron or protons), the entire mass of the atom is concentrated in the nucleus.

1.4 Nuclear Structure

There are several notations to summarize nuclear composition of an atom. The most commonly used is ${}_{Z}^{A}X_{N}$, where X represents the chemical

Table 1.1 Mass and charge of proton, neutron and electron

Particle	Symbol	Charge[a]	Mass[b]	Mass (kg)	Energy (MeV)	Relative mass
Proton	P	+1	1.007276	1.6726×10^{-27}	938.272	1836
Neutron	N	0	1.008665	1.6749×10^{-27}	939.573	1839
Electron	e^-	−1	0.000548	9.1093×10^{-31}	0.511	1

[a]Unit charge = 1.6×10^{-11} coulombs
[b]Mass expressed in Universal mass unit (mass of 1/12 of ^{12}C atom)
(Data from "Particles and nuclei 1999)

symbol of the element. Chemical symbol and atomic number carry the same information, and neutron number is the difference between A and Z. Hence, for the sake of simplicity, the notation is briefed to ^AX that is quite comprehensible and popular now. For example, in ^{137}Cs, where 137 is the mass number ($A + Z$), and the symbol Cs represents the 55th element in the periodic table. The neutron number can easily be calculated ($A - Z = 82$). Table 1.1 shows the mass, charge and energy of proton, neutron and electron.

1.5   Nuclear Forces

Protons in a nucleus are fairly at close distance ($\approx 10^{-15}$ m). This closeness results in an enormously strong repulsive force between them. They still remain within the nucleus due to the existence of a very strong (short range) nuclear force between nucleons that dominate the repulsive force and make the atom stable. The force is effective in a very short range, and neutrons must have an essential role in creating such force. Without neutrons, protons cannot stay in close distances.

In 1935, Yukawa proposed that the short-range *strong force* came about from the exchange of particles that he called *mesons*. The strong nuclear force is one of the four fundamental forces in nature that is created between nucleons by the exchange of mesons. This exchange can be compared to constantly hitting a tennis ball back and forth between two people. As long as this meson exchange is happening, the strong force holds the nucleons together. Neutrons also participate in the meson exchange and are even a bigger source of strong force. Neutrons have no

charge so they approach other nuclei without adding extra repulsive force, and meanwhile, they increase the average distance between protons and help to reduce the repulsion between them within a nucleus.

1.5.1   Nuclear Binding Energy and Mass Defect

Nuclear strong force is the resultant of the phenomenon known as *mass defect*. Direct measurements show that the mass of a nucleus is always less than the sum of the individual masses of the constituent protons and neutrons. Using the Einstein relationship, the deficient mass Δm is exactly equal to the energy required to separate the nucleons or *binding energy* E_b of the nucleus.

$E_b = \Delta m c^2$, c is the speed of the light in vacuum.

The **nuclear mass defect (Δm)** is the nuclear binding energy holding the nucleons together. The **average binding energy** per nucleon is a measure of nuclear stability. The higher the average binding energy, the more stable is the nucleus.

1.5.2   Radioactivity

Radioactivity is the spontaneous emission of particles and/or photons as a result of nuclear instability. The stability of a nucleus depends upon the arrangement of its nucleons particularly the ratio of the number of neutrons to the number of protons. Presence of adequate number of neutrons in relation to protons is essential for stability. Amongst the many possible combinations of protons and neutrons, only around 260 are stable, and
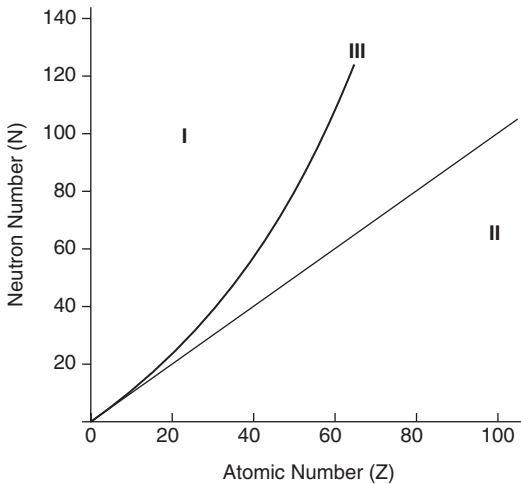
Fig. 1.1 The line of stability and different regions around it. (Reproduced from [2])

the rest all are unstable. It seems that there are favoured neutron-to-proton ratios amongst the stable nuclides. Figure 1.1 shows the function of the number of neutron (*N*) against the number of proton (*Z*) for all available nuclides. The stable nuclides gather around an imaginary line, called the line of stability. For light elements (*A* < 50), this line corresponds to *N* = *Z*, but with increasing atomic number, neutron-to-proton ratio increases up to 1.5 (*N* = 1.5*Z*). The line of stability ends at *A* = 209 (Bi), and all nuclides above that and those that are not close to this line are unstable. Nuclides that lie on the left of the line of stability (Area I) have excess of neutrons, those lying on the right of the line (Area II) are neutron deficient, and those above the line (Area III) are too heavy (excess of both neutrons and protons) to be stable.

An unstable nucleus sooner or later (nanoseconds to years) changes to a more stable proton–neutron combination by emitting particle(s) such as alpha, beta and gamma. As mentioned earlier, the phenomenon of spontaneous emission of such particles from the nucleus is called radioactivity, and nuclides involved in this phenomenon are called radionuclides. The change from the unstable nuclide (parent) to more stable nuclide (daughter) is called radioactive decay or disintegration. During disintegration, in addition to the emission of nuclear particle(s) energy is released. The process is spontaneous and remains unaf-

fected by external factors. It is also not possible to predict as to which radioactive atom will disintegrate first.

1.6 Modes of Decay

The radionuclide, which decays to another nuclide in order to attain stability, is called the 'parent' nuclide, and the nuclide so formed is called 'daughter'. The unstable nuclide may undergo transformation by any one of the following modes:

1.6.1 Nuclides Having an Excess Number of Neutrons

1.6.1.1 Beta Emission

Nuclides having excess number of neutrons attempt to acquire a stable form by the emission of beta particle (also called negatron). In this process, a neutron coverts to a proton. Along with an electron (negatron or beta minus), an antineutrino is also emitted. The nuclear equation may be given as follows:

$$n \rightarrow p + \beta^- + \bar{v} + \text{energy}$$
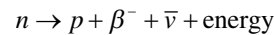
Here *n*, *p*, β^- and $\bar{v}$ represent the neutron, the proton, the negatron (beta minus) and the antineutrino, respectively. The proton stays in the nucleus, but the beta minus and the antineutrino are ejected out carrying the released energy as their kinetic energy. In this mode of decay, atomic number of the daughter nuclide is one more than that of the parent, but the mass number remains the same. The daughter may or may not be stable. The mass of the neutron is very slightly more than the masses of the proton, the beta and the antineutrino combined (the daughter is lighter than her parent). This difference in mass is converted into energy and randomly shared between beta particle and antineutrino. Hence, the beta particle may have energy between zero to a certain maximum level. The antineutrino has no mass and charge.

Radionuclides in which the daughter attains a ground or stable state by just emitting beta parti-

cles only are called pure beta emitters such as ^{3}H, ^{14}C, ^{32}P and ^{35}S. Those that cannot attain a stable state after beta emission and that still remain in one of the excited states of the daughter emit gamma photon(s) either in a single transition or through cascades to attain the ground state. In the latter situations, we get more than one gamma photon per beta emission. For example, ^{131}I, ^{132}Xe and ^{60}Co all of which emit beta particle followed by number of gamma emissions.

1.6.1.2 Nuclides Which Lack in Neutrons

In such cases, there are two alternatives for the nucleus to come to a stable state:

(a) **Positron emission and subsequent emission of annihilation photons**

In this mode of decay, a proton transforms to a neutron with the emission of a positron and a neutrino.

$$p \rightarrow n + \beta^+ + v + \text{energy}$$
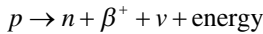
The neutron stays in the nucleus, but a positron and a neutrino are ejected out carrying the emitted energy as their kinetic energy. The positron is the antiparticle of the electron. They are very much alike but with opposite charge. In this mode of decay, the atomic number of the daughter is one less than that of the parent, but the mass number remains the same. The daughter may or may not be stable. The mass of the proton is slightly less than the combined mass of the neutron, the positron and the neutrino. Energy for the creation of this mass is supplied by the whole nucleus; hence, the difference between masses of parent and daughter elements must be sufficient to produce this energy ($E > 1.022$ MeV). Therefore, for positron emission to take place, the energy of parent nuclide must exceed that of the daughter by at least 1.022 MeV. The excess energy, if any, is randomly shared by positron and neutrino. Energy spectrum of the positron is like that of the beta minus (from zero up to a certain maximum). Some of the positron emitting radionuclides are ^{11}C, ^{13}N, ^{15}O and ^{18}F.

Just a few nanoseconds after its production, when its kinetic energy comes to zero, the positron combines with an electron at rest. Their masses are converted into energy in the form of two equal energy photons (0.511 MeV each) which leave the site of their creation in exactly opposite directions to conserve the momentum. This phenomenon is called annihilation reaction, and the photons so created are called annihilation photons.

(b) **Electron captures**

For a nucleus with excess protons has an alternative way to get a stable configuration by capturing one of its own orbital electrons (usually k electron). The electron combines with the proton producing a neutron and a neutrino in the process.

$$p + e \rightarrow n + v$$
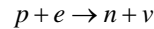
The electron capture is an important phenomenon because an electron from outer orbit fills the vacancy of the attracted electron. Photons (characteristic radiation) are emitted in the process, which may have a considerable amount of energy. These photons may knock out orbital electrons from outer orbits before leaving the atom creating the so-called Auger electrons. Auger electrons may be useful for therapeutic application (targeted therapy) due to their short range in the medium.

Electron capture is more likely to occur in heavy elements (electrons more close to the nucleus), whereas positron emission is more likely in lighter elements provided the energy of the parent exceeds that of the daughter by at least 1.022 MeV. Radionuclides such as ^{67}Ga, ^{111}In, ^{123}I and ^{125}I decay partially or fully by electron capture.

1.6.1.3 Nuclides Having an Excess of Protons and Neutrons

When the nuclides are too heavy (many nucleons) (region III in Fig. 1.1) and unstable, there are two ways for them to become stable, either by alpha emission or by fission process.

(a) **Alpha decay**

There are some nuclides, which have excess protons and neutrons and try to get rid of them by emitting an alpha particle (two neutrons and two protons). The atomic number of the daughter in such decay is reduced by 2, and the mass number is reduced by 4. The alpha particle emission may be sufficient to bring the daughter to the stable state or may follow with gamma emission. Naturally occurring radionuclides such as ^{238}U, ^{232}Th and ^{226}Ra not only decay by alpha emission but also form a chain of decay process as their daughter products are also radioactive.

(b) **Fission**

It is the spontaneous fragmentation of very heavy nuclei into two lighter nuclei usually with the emission of two to three neutrons. A large amount of energy (hundreds of MeVs) is also released in this process. Fissile nuclides themselves have no clinical application, but some of their fragments are found quite useful because of being carrier free. Thus, specific activity of fission-produced radionuclides is always higher than those produced by nuclear reactor.

1.7 Gamma Radiation and Internal Conversion

In some decay processes, the daughter nuclei are not in their ground state. This happens when all the energy associated with decay process is not carried away by the emitted particles. Such nuclei can be either in an excited state or in a metastable (isomeric) state. In both the situations, the excess energy is often released in the form of one or more gamma photons. Average life time of excited states is very short, and energy is released within a fraction of a nanosecond, but the average life time of metastable states is very much longer, and emission may vary from few milliseconds to few days or even more. During this period, the isomeric state behaves as an independent isotope that becomes a pure gamma emitter. Some of the metastable states have great clinical application in nuclear medicine. The decay scheme of ^{99}Mo–^{99m}Tc is an example of isomeric transition and shown in Fig. 1.2.

There are situations when the excited nuclei instead of emitting a gamma photon utilise the energy in knocking out one of the orbital electrons from their own atom. This process is called

Fig. 1.2 Decay scheme of ^{99}Mo. (Reproduced from [2])
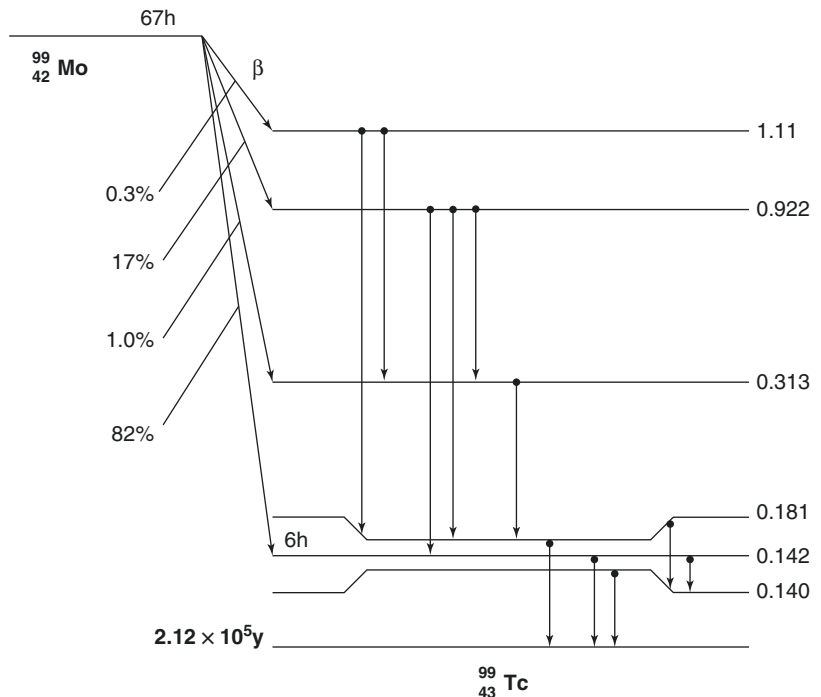
internal conversion, and the emitted electron is called a conversion electron. The probability of *K* conversion electron is more than *L* or *M* conversion electrons, and the phenomenon is more common in heavy atoms. The internal conversion is followed by emission of characteristic X-rays and Auger electrons as the outer shell electrons move in to fill the inner shell vacancies. It should be noted here that the X-ray emission is an atomic phenomenon even though there is no difference between an X-ray and a gamma photon of equal energy.

1.8 Laws of Radioactive Decay

There is no way to predict the time of disintegration of an atom nor should one be really interested about the fate of an individual atom. The number of atoms disintegrating within a given time interval can however be estimated which is of our interest. The radioactive decay has been found to be a spontaneous and random process independent of any environmental factor. In other words, nothing can influence the process of radioactive disintegration. Any random process just can be described in terms of probabilities and average constants.

In a sample containing a large number of identical radioactive atoms, during a short period of time (∂t) the number of decayed atoms ($-\partial N$) is proportional to the total number of atoms (N) present at that time. Mathematically, it can be expressed as:

$$-\partial N \propto N \partial t$$
$$-\partial N = \lambda N \partial t \qquad (1.4)$$
$$\text{or} \quad \frac{\partial N}{N} = -\lambda \partial t$$

In this equation, the constant λ (known as decay constant) has a characteristic value for each radionuclide. Decay constant is the fraction of atoms undergoing decay per unit time in a very large number of atoms. Its unit is inverse of time.

In simple terms, the decay constant can be defined as the probability of disintegration of a nucleus per unit time. Thus $\lambda = 0.01$ per second means that the probability of disintegration of each atom is 1% per second. It is important to note that this probability does not change with time.

The exact number of parent radionuclides in a sample at any time can be calculated by integrating Eq. (1.4), which takes the following form:

$$N = N_o * \exp(-\lambda t) \qquad (1.5)$$

where N_o is the initial number of atoms in the sample, and N is the number present at time t.

The term $\frac{\partial N}{\partial t}$ shows the number of disintegration per unit time and is known as activity. The SI unit of activity is Bq (one decay per second). The conventional unit of activity is Curie (Ci) which is equal to 3.7×10^{10} disintegrations per second (dps).

1.8.1 Half-Life

The time after which 50% of the atoms in a sample undergo disintegration is called the half-life. The half-life and decay constant are related to each other by the following equation:

$$T_{1/2} = \frac{0.693}{\lambda} \quad \text{or} \quad \lambda = \frac{0.693}{T_{1/2}} \qquad (1.6)$$

1.8.2 Average Life

The actual lifetimes of individual atoms in a sample are quite different. Some have very short and some have very long lifetime. The average lifetime, characteristics of the atoms, is related to the half-life by:

$$T_{av} = 1.44 * T_{1/2} \qquad (1.7)$$

The average life is a useful parameter for calculating the cumulated activity in source organ in internal dosimetry in nuclear medicine.

1.8.3 Radioactive Equilibrium

In many cases, the daughter element is also radioactive and immediately starts disintegrating after its formation. Although the daughter obeys the general rule of radioactive decay, its activity does not follow the exponential law of decay of its own while existing with the parent. The reason is that the daughter is produced (mono-exponentially) by disintegration of its parent, and at the same time, it disintegrates (mono-exponentially) as a radioactive element. So the activity of such elements changes bi-exponentially, first the activity increases, reaches a maximum value and then starts decreasing. The rate at which the activity changes in such a mixture of radionuclides depends on the decay constant of both the parent and the daughter.

If we start with a pure sample of a parent with a half-life of T_1 and decay constant λ_1 and contains $(N_1)_0$ atoms initially, the decay of this parent can be expressed by:

$$N_1 = (N_1)_0\, e^{-\lambda_1 t} \qquad (1.8)$$

The rate of decay of the parent is the rate of formation of the daughter. Let the daughter decays at the rate $\lambda_2 N_2$, where λ_2 is the decay constant of the daughter and N_2 is the number of atoms of the daughter present. The net rate of formation of the daughter can be given by:

$$\frac{\partial N_2}{\partial t} = \lambda_1 N_1 - \lambda_2 N_2 \qquad (1.9)$$

The solution of this equation in terms of activity can be given as:

$$A_2 = A_1 \frac{T_1}{T_1 - T_2}\left(1 - e^{-0.693\left(\frac{T_1 - T_2}{T_1 T_2}\right)t}\right) \qquad (1.10)$$

where A_1 and A_2 are the activity of the parent and the daughter, respectively, T_1 and T_2 are their physical half-lives and t is the elapsed time. This equation is for a simple parent–daughter mixture. In general, three different situations arise from Eq. (1.10).

(a) **Secular equilibrium**

When the half-life of the parent (T_1) is too long in comparison to that of the daughter (T_2), Eq. (1.10) may be expressed as:

$$A_2 = A_1\left(1 - e^{\frac{-0.693t}{T_2}}\right) \qquad (1.11)$$

After one half-life of the daughter ($t = T_2; A_2$) will become nearly $A_1/2$; after two half-lives, the daughter may grow up to 3/4 of the parent, and after four half-lives (of the daughter), it rises to about 94% of the parent activity. Thus, activity of the daughter gradually increases, and after few half-lives, the activity of the parent and the daughter become almost equal (Fig. 1.3). The parent and the daughter are said to be in secular equilibrium.

(b) **Transient equilibrium**

Half-life of the parent is few times (>10 times) longer than that of the daughter but not as much long as in secular equilibrium. In this case, the activity of daughter increases, eventually exceeds the activity of parent, reaches a maximum and then decays with the half-life of the parent, but the activity of the
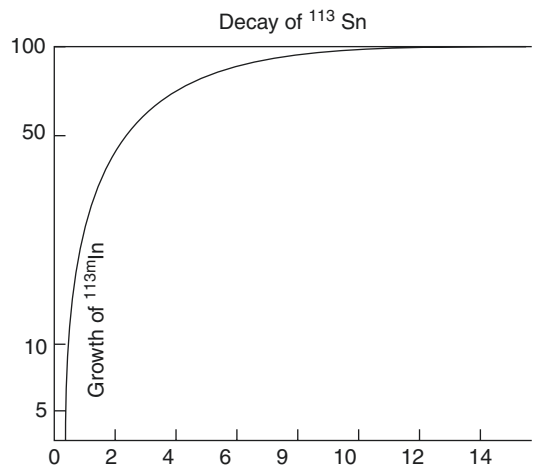
Fig. 1.3 Secular equilibrium
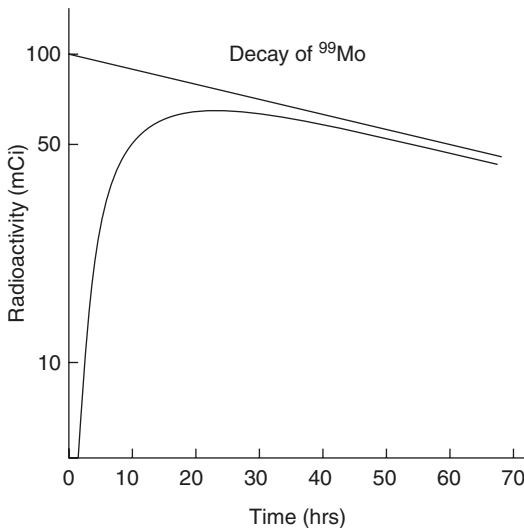
Fig. 1.4 Transient equilibrium. In case of 100% abundance of the daughter product and 100% extraction efficiency in elution, the growth curve of ^{99m}Tc will first cross over the decay curve of ^{99}Mo slightly then will decay in parallel to the parent. However, ^{99m}Tc has an abundance of 89% and extraction during elution is also less than 100%; therefore, the actual curve of transient equilibrium will look as given above

daughter slightly exceeds the parent activity after its maximum growth but practically the activity of daughter remains less than the parent because the extraction efficiency is normally less than 1 or 100%, as can be seen in Fig. 1.4a, b. Equation (1.10) in such a case can be written as:

$$A_2 = A_1 \frac{T_1}{T_1 - T_2} \quad \text{for} \quad t \gg T_2 \quad (1.12)$$

The growth of the daughter for multiples of $T_2(T_2, 2T_2, 3T_2, 4T_2,$ etc.) will be nearly 50%, 75%, 87.5% and 94%, respectively, of the activity of the parent. It is therefore advisable to elute the activity from technetium generator after every 24 h (Mo-99 with 67 h half-life and Tc-99m with 6 h half-life).

1.8.4   No Equilibrium

When the half-life of the daughter is longer than the half-life of the parent, there would be no equilibrium between them.

1.9   Interaction of Radiation with Matter

Ionizing radiations transfer their energy in full or part to the medium through which they pass by way of interactions. The significant types of interactions are excitation and ionization of atoms or molecules of the matter by both the charged particles and electromagnetic radiation (X- or gamma rays).

1.9.1   Interaction of Charged Particles with Matter

The charge particles lose some of their energy by way of the following interactions:

(a) Ejection of electrons from the target atoms (ionization)
(b) Excitation of electrons from lower to higher energy state
(c) Molecular vibrations along the path (elastic collision) and conversion of energy into heat
(d) Emission of electromagnetic radiation

For the charged particles in the energy range of 10 keV to 10 MeV, ionization predominates over excitation. The probability of absorption of charged particles is so high that even a small thickness of the material can stop them completely.

The nature of interaction of all charged particles in the energy range mentioned above is similar to each other. Light particles such as electrons deflect at larger angles than heavier particles, and there is a wide variation in their tortuous path. The path of a heavier particle is more or less a straight line. When electrons are deflected at large angles, they transfer more energy to the target atom and eject electrons from it. These electrons while passing through the medium produce secondary electrons along their track (delta rays). The charged particles undergo a large number of interactions before they come to rest. In each interaction, they lose a small amount of energy. These losses are called collision losses.

Energetic electrons can approach the nucleus where they get decelerated and produce brems-

strahlung radiation (X-rays). The chance of such an interaction increases with increase in electron energy and atomic number of the target material. Loss of electron energy by this mode is termed as radiative loss. The energy lost per unit path length along the track is known as the linear energy transfer (LET) and is generally expressed in keV/μm.

1.9.2 Range of a Charged Particle

After travelling through a distance in the medium, the charged particle loses all its kinetic energy and comes to rest. The average distance travelled in a given direction by a charged particle is known as its 'range' in that medium and is influenced by the following factors:

(a) Energy: Higher the energy of the particle more is the range
(b) Mass: Higher the mass of the charged particle smaller is the range
(c) Charge: The range is inversely proportional to square of the charge
(d) Density of the medium: Higher the density of the medium shorter is the range of charged particle

1.9.3 Interaction of Electromagnetic Radiation with Matter

When a beam of X- or gamma rays passes through an absorbing medium, some of the photons are completely absorbed, some are scattered, and the rest pass through the medium almost unchanged in energy and direction. The transferred energy results in excitation and ionization of atoms or molecules of the medium and also in the production of heat. The attenuation of the beam through a given medium may be summarized as follows:

– Greater the thickness of the absorbing material more is the attenuation.
– Greater the atomic number of the material more is the attenuation.

– Higher the photon energy lesser is the attenuation produced by a given thickness of material.

1.9.4 Linear Attenuation Coefficient

The linear attenuation coefficient (μ) is defined as the fractional reduction in the beam per unit thickness as determined by a thin layer of the material.

$$\mu = \frac{\text{Fractional reduction in a thin layer}}{\text{Thickness of the layers} (\text{cm})}$$

The unit of μ is cm^{-1}.

1.9.4.1 Exponential Attenuation

Exponential law can explain the attenuation of radiation beam intensity. The mathematical derivation is given below.

Let N_o be the initial number of photons in the beam, and N is the number recorded by the detector placed behind the absorber (Fig. 1.5).

The number δN, which gets attenuated, will be proportional to the thickness (δx) of the absorber and to the number of photons N present in the beam.

Mathematically:

$$\delta N \propto N \cdot \delta x$$
$$\text{or } \delta N = -\mu \cdot N \cdot \delta x \quad (1.13)$$

where μ is a constant called linear attenuation coefficient for the radiation. The negative sign indicates that as δx increases, the number of photons in the beam decreases. Equation 1.13 can be rearranged as:

$$\mu = -\frac{\delta N}{N \cdot \delta x} \quad (1.14)$$

The formal definition of attenuation coefficient is derived from Eq. 1.14, integration of which gives the following relationship:

$$N = N_o \cdot e^{-\mu x} \quad (1.15)$$

Fig. 1.5 Attenuation of
a radiation beam by an
absorber. The
transmitted beam is
measured by the detector
'*P*'. (Reproduced
from [3])
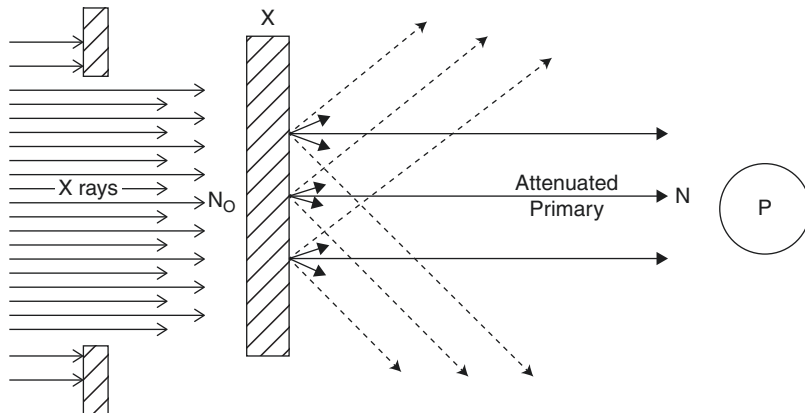
Table 1.2 Attenuation coefficients (cm^{-1}), mass attenuation coefficients (cm^2/g) and HVL (cm) in lead and concrete for 140 and 511 keV photons

Radiation type	HVL in cm lead (Pb 11.35 g/ cm^3)	HVL in cm concrete (2.35 g/cm^3)	Attenuation coefficient (μ cm^{-1}) in lead (11.35 g/cm^3)	Attenuation coefficient (μ cm^{-1} in concrete)	Mass attenuation coefficient (cm^2/g) in lead	Mass attenuation coefficient (cm^2/g) in concrete
Tc-99m 140 keV	0.027	1.99	25.67	0.348	2.26	0.148
PET annihilation photons 511 keV	0.4	3.4	1.7325	0.206	0.1526	0.0877

Equation 1.15 can also be expressed in terms of beam intensity as:

$$I = I_{\text{o}} \cdot e^{-\mu x} \qquad (1.16)$$

I and *I*$_{\text{o}}$ are the intensities of the beam as recorded by the detector with and without absorbing material, respectively. The attenuation coefficient may vary for a given material due to non-uniformity in its thickness. This is particularly so if the absorbing material is malleable. It is therefore better to express the **mass absorption coefficient**, which is independent of the thickness of the absorbing material. Mass absorption coefficient is obtained by dividing the linear attenuation coefficient with the density of the material. The unit of mass attenuation coefficient is cm^2/gm. Table 1.2 gives the values of attenuation coefficient, mass attenuation coefficient and HVL in lead and concrete for 140 keV photons and 511 keV photons. The electronic and atomic attenuation coefficients are also defined accordingly. The electronic attenuation coefficient is the

fractional reduction in X- or gamma ray intensity produced by a layer of thickness of 1 electron per cm^2, whereas the atomic attenuation coefficient is the fractional reduction by a layer of thickness of 1 atom per cm^2. Thus, the atomic attenuation coefficient will be *Z* times the electronic one.

1.9.5   Half-Value Layer (HVL)

From Eq. 1.16, it can be seen that for a certain thickness ($d_{1/2}$) of the absorbing material the intensity becomes half of its original value, i.e., $I = I_{\text{o}}/2$. Substituting these values, Eq. 1.4 can be rearranged as:

$$d_{1/2}\left(\text{HVL}\right) = \frac{0.693}{\mu} \qquad (1.17)$$

Half-value layer (thickness) can be defined as the thickness of an absorbing material, which reduces the beam intensity to half of its

original value. Depending upon the energy of radiation, various materials are used for the measurement of HVL such as aluminium, copper, lead, brick and concrete. Similarly tenth-value layer (TVL) can also be defined that reduces the intensity of the beam to 1/10th of its initial value.

1.9.6 Mechanism of Attenuation

There are many types of interactions between a photon and the matter, but only few are important for us as described below.

1.9.6.1 Photon Scattering

The scattering may or may not result in transfer of energy during interaction of photon with atom of the medium.

1.9.6.2 Elastic Scattering

In elastic scattering or unmodified scattering, the photons are scattered in different directions without any loss of energy. The process, thus, attenuates the beam without absorption. In this process, the photon interacts with a tightly bound electron in an atom. The electron later releases the photon in any direction without absorbing energy from it. The contribution of this mode of interaction is relatively insignificant in medical applications of radiation. However, it has tremendous application in X-ray crystallography.

1.9.6.3 Inelastic (Compton) Scattering

Compton elucidated the mechanism of this type of scattering. In this process, photon interacts with loosely bound (free) electrons. Part of the energy of the photon is used in ejecting out the electron and rest is scattered in different direction (Fig. 1.6).

In a so-called head on collision, the photon turns back along its original track (scattered through 180°), and energy is transferred to the recoil electron. The change in wavelength $\delta\lambda$ of the photon is given by:

$$\delta\lambda = 0.024\left(1-\cos\varphi\right)A^0 \qquad (1.18)$$
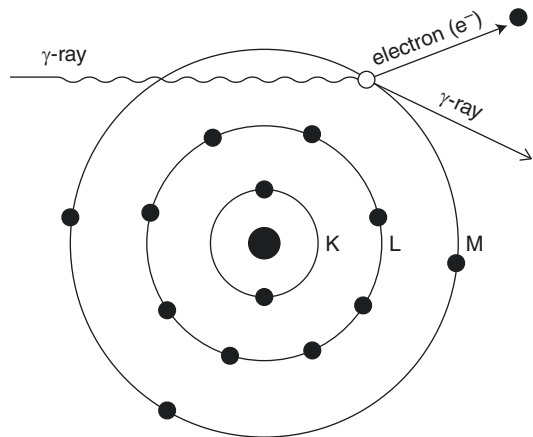
Fig. 1.6 Process of compton scattering. The incoming photon ejects the electron from outer orbit and gets scattered with reduced energy in a different direction. (Reproduced from [3])

where φ is the angle of scattering of gamma photon, and A^0 is angstrom unit for wave length. The energy of scattered photon is expressed as:

$$E_1 = E_0\Big/\left[1+\left(E_0/m_ec^2\right)\left\{1-\cos\varphi\right\}\right] \qquad (1.19)$$

where E_0 is the energy of incident photon and E_1 is that of the scattered photon, m_e is the mass of the electron, and c is the velocity of light in vacuum/space. Scattered photons at all angles therefore need appropriate shielding all around in X-ray rooms. The Compton scattering involves interaction between photons and electrons. The probability therefore depends upon the number of electrons present (electron density). With the exception of hydrogen, all elements contain nearly same number of electrons per gram (practically the same electron density). The Compton scattering thus depends upon the electron density and is the choice of interaction required in conventional radiation therapy, where the delivered dose is aimed to be homogeneous in spite of the tissue inhomogeneity within the body. The electron densities of some of the important elements are listed below:

Elements	Electron density
O_2	3.01×10^{23}
Ca	3.00×10^{23}
Pb	2.38×10^{23}
H_2	5.997×10^{23}

The total probability (σ) for Compton process is given by:

$$\sigma = \sigma_s + \sigma_a$$

where σ_s and σ_a are the probabilities for scattering and absorption, respectively.

1.9.7 Summary of Compton Scattering

- Involves interaction between a photon and a free electron.
- Is independent of Z (depends on electron density).
- Probability of occurrence decreases with increase in radiation energy.
- More the incident photon energy, more is the energy transferred as kinetic energy to the electron.
- Most common type of interaction in soft tissue in the energy ranges from 100 keV to 10 MeV.

1.9.8 Photoelectric Effect (PEE)

In this process, the photon disappears when it interacts with the bound electron. The photon energy has to be higher than the binding energy of the electron for this type of interaction to take place.

$$hv = BE + Kinetic\,energy$$

where hv is the energy of the photon, and BE is the binding energy of the electron in the shell (Fig. 1.7). If the photon energy is slightly higher than the binding energy (BE), then the chance of PEE is more. For example, a photon of energy 100 keV has high probability of undergoing PEE when it interacts with Pb atom for which the K shell binding energy is 88 keV. Rest of the (100–88) 12 keV energy will be carried away by the
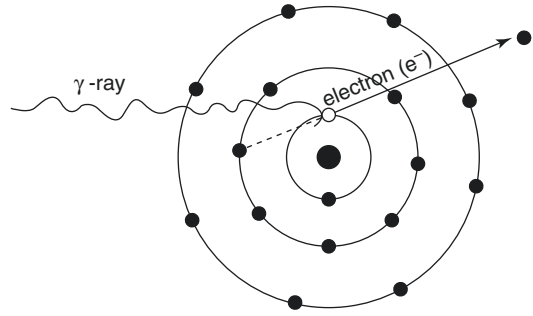
Fig. 1.7 Process of photoelectric absorption. The incoming photon disappears (absorbed) and orbital electron is knocked out. Electron from the outer shell falls (dotted line) into the inner shell to fill up the vacancy. (Reproduced from [3])

ejected electron as its kinetic energy. The ejection of electron creates a hole in the inner shell, which is filled by an electron from any one of the outer shells. Since the electron in outer shells possess higher energy than those in the inner shells, the difference in their energy is released as X-ray photon. Such photons are characteristic to the atom from which they are emitted. The *K*, *L*, *M*, etc. shells of a given atom have fixed energy so is the difference in their energies is also fixed. The radiation emitted are therefore termed as characteristic X-rays.

Three types of possibilities exist during photoelectric effect:

(i) **Radiative transitions**

As has been explained above, during the electron transition from the outer orbit to the inner one, a photon is emitted with energy equal to the difference of the binding energies of the orbits involved. The vacancy moves to a higher shell and consequently a characteristic photon of lower energy follows. The probability of emission of a photon is expressed as the fluorescent yield.

$$Fluorescent\ yield = \frac{Number\ of\ X-ray\ photons\ emitted}{Number\ of\ orbital\ vacancies\ created}$$

Mostly it is the *K* shell that is responsible for the fluorescent yield:

$$K\text{ shell fluorescent yield}(\omega_k) = \frac{\text{Number of } K \text{ X} - \text{ray photons emitted}}{\text{Number of } K \text{ shell vacancies}}$$

The yield increases with increase in the atomic number.

(ii) **Auger electrons**

The characteristic X-ray photon, instead of being emitted out, has a probability to eject another orbital electron from the atom. These electrons are called Auger electrons (Fig. 1.8). The energy of Auger electron is equal to the difference of the characteristic X-ray photon energy and the binding energy of the shell involved in the process. The Auger yield is expressed as the ratio of electrons emitted due to vacancies in subshell i and the total number of atoms with a vacancy in subshell i.

1.9.9 Coster–Kronig Electrons

The process is exactly like Auger transition except that the electron filling the vacancy comes from the subshell of the same principal shell in which the vacancy lies. The kinetic energy of the emitted electrons can be calculated exactly as for Auger electrons. The energy of Coster–Kronig electrons is so small that they are quickly absorbed in the medium.

1.9.10 Summary of the Photo Electric Effect

- The probability is very high when the photon has just enough energy to eject out electron from the shell.
- The process involves bound electrons.
- Effect is proportional to cube of the atomic number (Z^3) and is inversely proportional to the cube of the photon energy ($1/E^3$).
- Even though the PEE decreases with energy but suddenly increases near the *K* shell binding energy of the absorber. It is because of knocking out of *K* shell electron and emission of characteristic X-rays. The *K* edge depends upon the type of the absorber. In case of lead, the *K* edge is seen at 88 keV energy.

1.9.11 Pair Production

When a photon with energy in excess of 1.022 MeV passes close to the nucleus of an atom, it may disappear and in its place two anti-particles (negatron and positron) may be produced as shown in Fig. 1.9. In this process, energy is converted into mass in accordance with
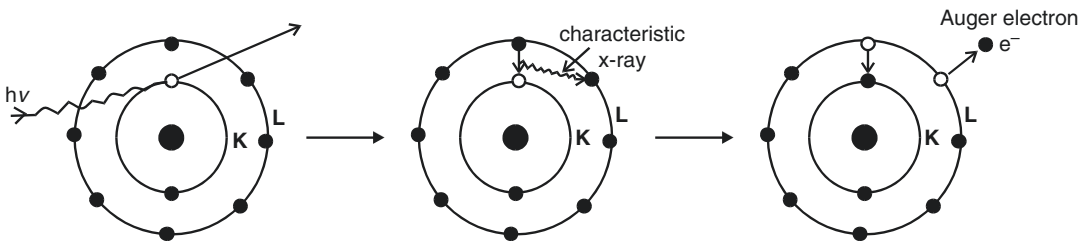
Fig. 1.8 Mechanism of Auger electron emission. (Reproduced from [3])
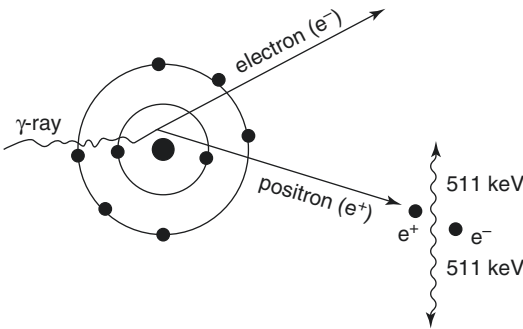
Fig. 1.9 Schematic representation of pair production. (Reproduced from [3])

Einstein mass energy equation ($E = mc^2$). After traversing some distance through the medium, the positron loses its energy and combines with an electron at rest and annihilates. During this process, both the antiparticles disappear (annihilate), and two photons of 0.511 MeV are emitted in opposite direction to obey the law of conservation of momentum.

1.9.12 Summary of Pair Production

- This involves interaction between photon and nucleus.
- Threshold energy for this process is 1.022 MeV, and the interaction is proportional to the energy in excess of 1.022 MeV.
- The probability of this type of interaction is proportional to the atomic number (Z) and density of the material.
- Two annihilated photons each of 0.511 MeV are produced per interaction and emitted from the site of interaction in the opposite directions.

1.9.13 Photo Nuclear Reaction

When photon energy is too high, either a neutron or proton may be knocked out (more likely the neutron) from the nucleus. For majority of atoms, the threshold energy for this effect is around 10 MeV, and the probability increases with increasing energy till a maximum is reached above which the probability falls rapidly.

1.10 Statistics in Radiation Measurements (Counting Statistics)

The purpose of counting statistics in nuclear medicine is to check the variability in the acquired data and to test the significance of observed variations. Let us first mention the types of error in the acquired data in nuclear medicine. There are three types of errors that are normally encountered:

1. Random error
2. Systematic error
3. Outliers or blunders

The random error is due to the random nature of physical processes involved in acquiring the data in nuclear medicine, such as radioactive disintegration, interaction of radiation with the detector material, etc. The nuclear medicine data usually suffers from random variation, resulting in imprecise results. Two measurements are from the same radiation source and, for exactly the same time period, are not identical. The data may however be accurate but not precise. The random nature of nuclear disintegration can be expressed in terms of Poisson statistics.

In systematic error, the result of several measurements may be same but not accurate. This error is mostly related to the instruments and may primarily be due to improper calibration of instruments or manufacturing defect.

The third type of error, not very common, is outlier or blunder, which results in grossly inaccurate results. Examples of blunders in radiation counting measurements result from:

- Incorrect energy window setting
- Counting heavily contaminated samples
- Using contaminated detectors
- High activities leading to excessive dead time effects
- Selecting wrong patient orientation during imaging

Blunders or outliers can be easily detected by experienced staff.

The measurement may be precise but inaccurate, or vice versa. Results of a radiation counting measurements may be imprecise (because of the random nature of emission) but still their (average) value may be accurate. Randomness is always present in counting measurements and during interactions of radiation with the scintillation detector. It is therefore necessary to know the statistical methods to analyse the data if so required. The statistical parameters and their application have been concisely described in the following text.

1.10.1 Measures of Central Tendency

It is convenient to summarize the results of a set of measurement with a single value in the form of **mean** or average value.

1.10.1.1 Mean

The mean of individual data points is simple to calculate. However, in grouped data, the central value of a group represents the class and the sum of their product with the respective frequency divided by the sum of frequencies results in the mean of the data.

Mathematically,

$$\text{Mean} = \sum X_i / N$$

where X_i is the ith data, and N is the total number of data points.

Simple mean cannot describe the data; therefore, two more terms, mode and median, are also defined.

1.10.1.2 Mode

Mode represents the most frequent value in the data distribution.

1.10.1.3 Median

Median divides the data into two equal parts. Each part can further be divided into two more parts. Thus, there are three data points which divide the distribution into four parts. The first data point is called first quartile or 25th(P25) percentile, the second is median or 50th percentile, and the third is 3rd quartile or 75th(P75) percentile. Twenty five percent values lie below P25 (first quartile).

1.10.1.4 Skewness

When distribution curve is exactly symmetrical, then mean, mode and median are equal. The same is not true, when there is asymmetry in the distribution curve (skewness) as shown in Fig. 1.10. For positive skewness in the distribution curve, the mode is greater than median, and the median is greater than mean. In case of negative skewness, the mean is greater than median, and the median is greater than mode. Skewness is defined in terms of its first and second coefficients.

- The first coefficient of skewness = (mean − mode)/standard deviation
- The second coefficient = 3(mean − median)/ standard deviation

1.10.1.5 Standard Deviation

One of the important statistical parameters which describes the variability in a set of data is the standard deviation. The standard deviation for a series of measurements determines the precision or reproducibility of the measured data. When data follows Poisson probability distribution, such as nuclear counting data, the standard deviation equals the square root of the mean. In some situations, where a single measurement is acquired as in digital imaging, the total pixel counts in the image is taken as mean for all practical purposes. This helps in estimating the noise in the image. For sample data, the standard deviation can be given by following equation:

$$\text{s.d.} = \sqrt{\left(\sum \left(x_i - \overline{x} \right)^2 / \left(N - 1 \right) \right)} \qquad (1.20)$$

where x_i is the ith data, $\overline{x}$ is the mean, and N is the total number of data points in the distribution.

Example The observed counts against each serial number and intermediate steps for the calculation of mean, standard deviation and coefficient of variation in a tabulated form is given below.
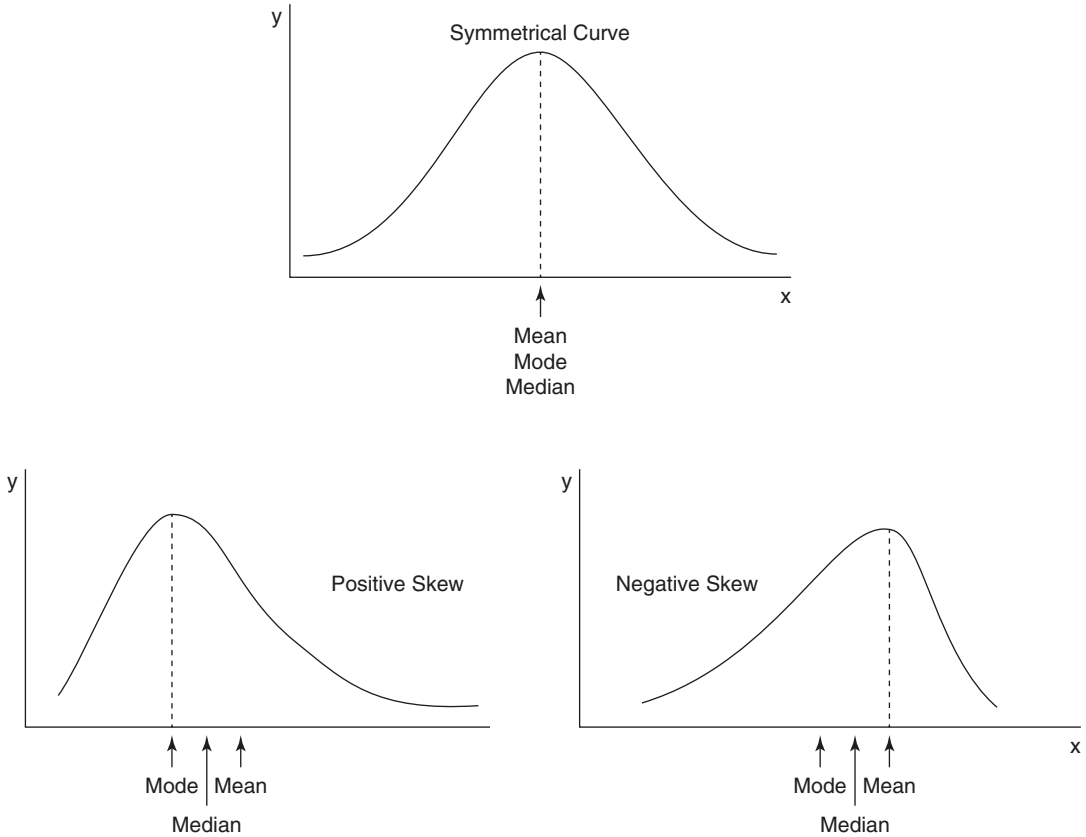
Fig. 1.10 Symmetrical distribution (top), asymmetrical distribution with positive skewness (bottom left) and asymmetric skewness (bottom right)

S.No.	Counts observed (x_i)	Deviation $\left(x_i - \bar{x}\right)$	$\left(x_i - \bar{x}\right)^2$
1.	1000	−50	2500
2.	1100	50	2500
3.	970	−80	6400
4.	980	−70	4900
5.	1150	100	10,000
6.	1060	10	100
7.	950	−100	10,000
8.	1200	150	22,500
9.	1000	−50	2500
10.	1090	40	1600
11.	Sum = 10,500		63,000

$$\text{Mean}\left(\bar{x}\right) = \sum x_i / n = 10,500 / 10 = 1050$$

$$\text{Standard deviation} \left(\text{s.d.}\right) = \sqrt{\left(\sum\left(x_i - \bar{x}\right)^2 / (n-1)\right)}$$
$$= \sqrt{\left(63,000 / 9\right)} = 83.6$$

Variance = (s. d.)^2 = 6989
Coefficient of variation (%) = (s.d./mean) × 100 = (83.6/1050) × 100% = 7.96%

1.10.2 Standard Error

The spread of observations in a given measurement is estimated by the standard deviation. If such measurements are repeated several times, a mean of all means can be estimated. The spread of means in such situations is measured in terms of standard error. Distribution of these means is usually normal.

$$\text{Standard error} = \text{standard deviation} / \sqrt{n}$$

where n is the number of individual measurements.

1.10.3 Confidence Interval

The confidence interval is the estimate of a parameter ±Margin of Error. The margin of error of a confidence level is determined by a couple of

factors. We can see this by examining the formula for margin of error. A margin of error is of the form:

$$\text{Margin of Error} = (\text{Statistic for Confidence Level}) * (\text{Standard Error})$$

The statistics for the confidence level depends upon what probability distribution is being used and what level of confidence has been chosen. For example, if C is our confidence level and we are working with a normal distribution, then C is the area under the curve between $-z^*$ and z^*. This number z^* is the number in the margin of error formula. The other term necessary in the margin of error is the standard error. In Fig. 1.11, a density plot of normal distribution data is given, the two vertical lines marking the 1.96 standard error above and below the mean. This is the z-score for two-tailed significance level of 0.05. In a normal distribution, there are 2.5% probability above and 2.5% probability below. It turns out that 94.4% of the confidence intervals captures the population mean. This is what confidence interval really means: *if we repeat the sampling procedures infinitely many times, about 95% of the confidence intervals will contain the population mean.* In other words, approximately 5% of the confidence intervals fail to capture the population mean. In normal distribution, the area under 1 (one) standard deviation on either side of the mean is about 68.3% of the total area as shown in Fig. 1.11c. Similarly, the lines drawn at 2σ and 3σ on either side will cover 95% and 99.7%, respectively, of the total area under the normal distribution curve. Other important characteristics of normal distribution curve are illustrated graphically in Fig. 1.11.

1.10.4 Normal Distribution

The normal distribution is also widely used in counting statistics. It should be emphasized that the binomial, Poisson and normal distribution become nearly identical for processes with a small probability for individual success and with a large enough number of trials.

In normal distribution, the area under 1 (one) standard deviation on either side of the mean is about 68.3% of the total area as shown in Fig. 1.11c. Similarly, the lines drawn at 2σ and 3σ on either side will cover 95% and 99.7%, respectively, of the total area under the normal distribution curve. Other important characteristics of normal distribution curve are illustrated graphically in Fig. 1.11.

The graphical representation shows the correct picture of the data distribution. It is not necessary that the two sets of data with the same mean and standard deviation will have the same graphical display. There are several methods of graphical representation of the data such as bar diagram, histogram and pie charts. Statistical parameters with the same mean and standard deviations can have different distribution (Fig. 1.12).

Generally the statistical properties of the data can be described by the frequency distribution, mean and variance (square of standard deviation). However, it is to understand the probability distribution function (pdf) to which the data belongs.

1.10.5 Probability Distribution Functions (pdf)

It describes the probability of each outcome from a measurement. There are three pdfs that are relevant to nuclear medicine:

1. Binomial
2. Poisson
3. Gaussian or normal

1.10.5.1   Binomial Distribution

In binomial distribution, a trial is an event that may have more than one outcome, and a measurement consists of counting the number of successes from a specified number of trials. Details of binomial distribution function are not described here as the following two probability distributions are more important in nuclear medicine.
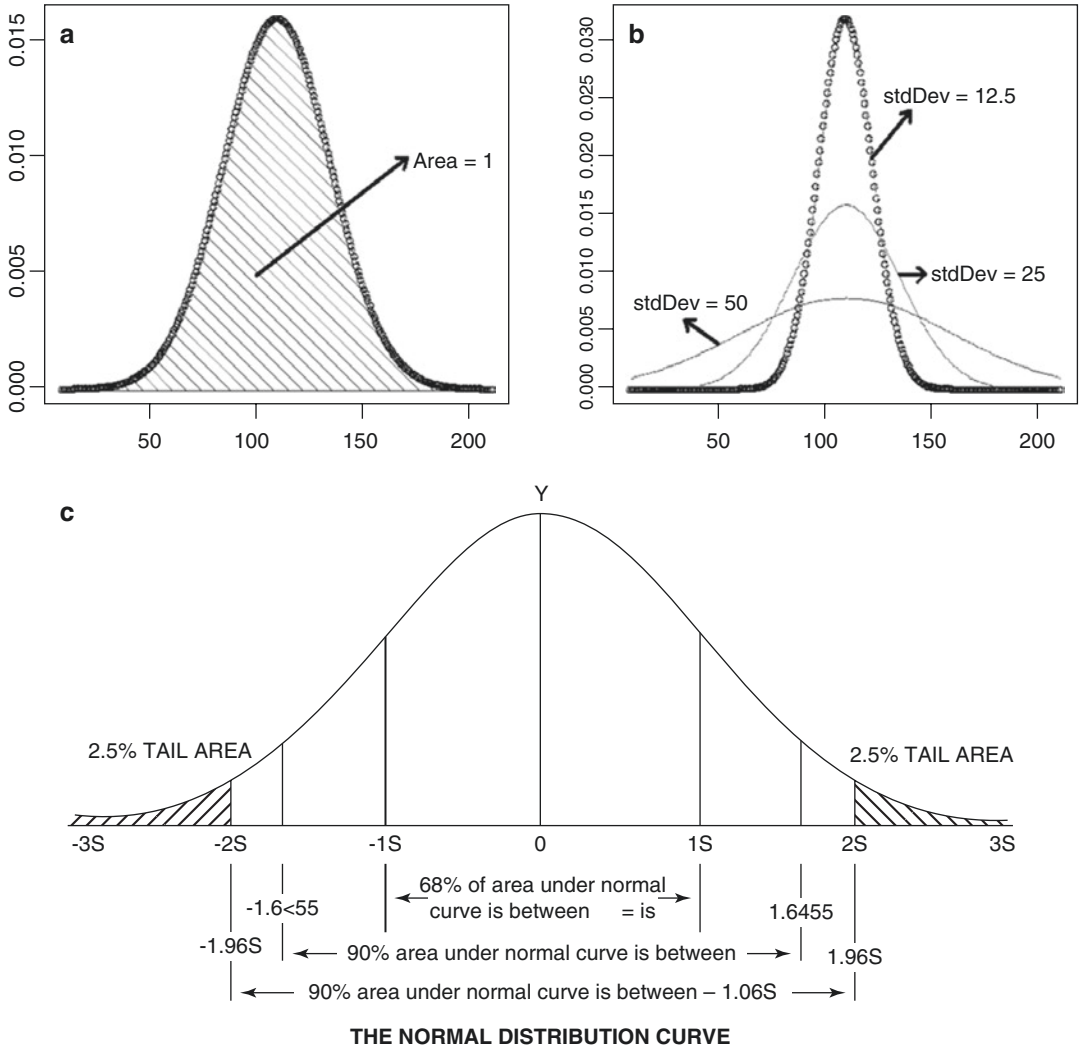
Fig. 1.11 Important characteristics of normal probability distribution. (**a**) Area under normal distribution is unity. (**b**) Standard deviation affects the shape of the normal dis-tribution. (**c**) The percentage of areas included under the various standard deviation

1.10.5.2 Poisson Distribution

The Poisson distribution is normally applied in the following conditions when:

1. The events are discrete or discontinuous.
2. The events are independent, i.e., the first event has no influence on the second event.
3. In a given interval, any number of events can occur.
4. The probability of a single occurrence of the event is very rare, but in a given interval of time, it is proportional to the length of the time interval.
5. In an infinitesimally small interval of time, the probability of an event to occur more than once is negligible.

The Poisson probability density function $p(x)$ at each value of x is given by

$$p(x,\mu) = \frac{\mu^x}{x!} e^{-\mu} \qquad (1.21)$$
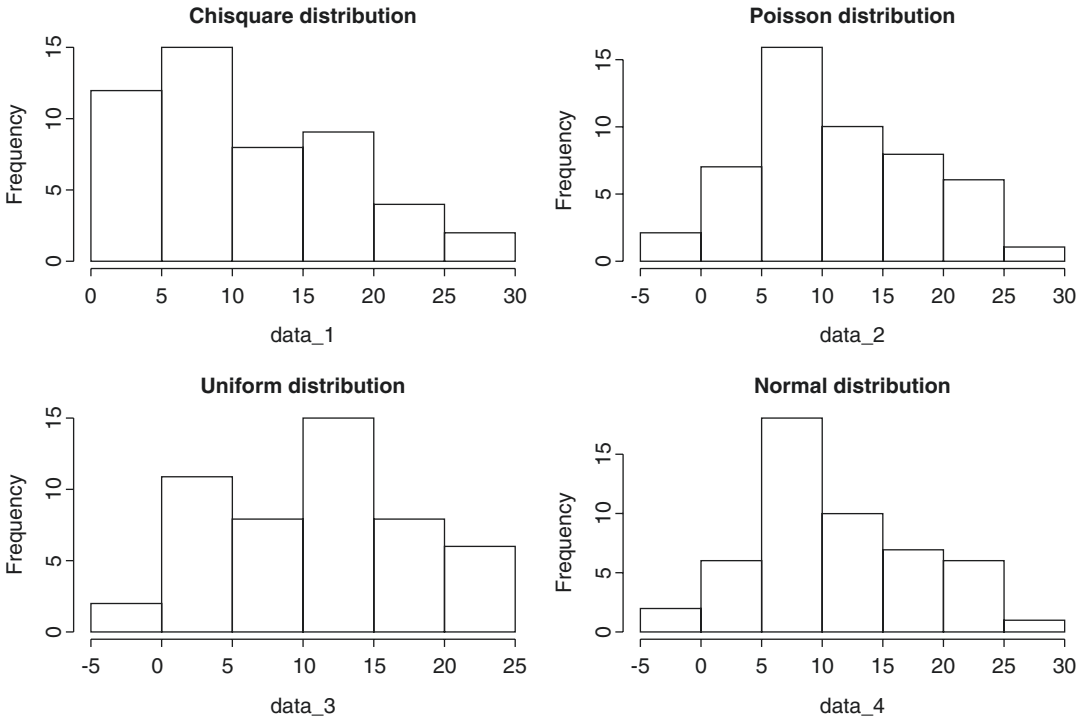
Fig. 1.12 The chi-square, Poisson, uniform and normal distribution of simulated data having mean = 11 and standard deviation = 7

where μ is the mean, and $p(x)$ is the probability of observing count x when the mean count is μ. In Poisson distribution, the mean is equal to the variance.

Example What is the probability of getting a count 15 in a measurement when the true or average count is 10.

Using Eq. 1.21

$$P(15,10) = \left(e^{-10}\ 10^{15}\right)/15! = \left(4.54 \cdot 10^{-5}\right)$$
$$\times \left(9.999 \cdot 10^{14}\right)/\left(1.3 \cdot 10^{12}\right)$$
$$= 3.49 \cdot 10^{-2} = 0.0349$$

The probability is 0.0349 or 3.49% that a count 15 will be obtained when the average count is 10.

In Poisson distribution, the variance is equal to the mean. Variance is a number that is equal to square of standard deviation.

$$\text{Varience}\left(\sigma^2\right) = \text{mean}\left(\mu\right)$$

Thus, as outlined above, the standard deviation $(\sigma) = \sqrt{\mu}$.

In counting measurements, the measured counts in a given time is always assumed as mean. This is very important and useful statements in nuclear medicine as the image data are acquired in one go, and the acquired counts are taken as a mean or variance. If 10,000 counts are acquired in a given length of time, the standard deviation will be ±100. The observer will have a confidence level of 68% that the data will lie between 9900 and 10,100 with an accuracy of ±1%. It is important to acquire more counts to reduce error in any counting measurement.

1.11   Propagation of Error in Counting Measurements

Any parameter that is estimated from counting measurement is associated with some degree of uncertainty. If the final result involves arithmetic operation of such parameters, as is usually

the case with nuclear medicine data, then the error gets propagated. The error introduced depends on the type of arithmetic operation performed and on the value of uncertainty in the original data.

For sum and difference of two terms N_1 and N_2, the error will be propagated as:

$$\left(N_1 \pm N_2\right) = \left(N_1 \pm N_2\right) \pm \sqrt{\left(N_1 + N_2\right)} \quad (1.22)$$

The error in case of multiplication and division is propagated as:

$$N_1 \times N_2 \text{ or } N_1 / N_2 = \left(N_1 \times N_2\right) \text{ or }$$
$$N_1 / N_2 \pm \sqrt{(1/N_1 + 1/N_2)} \quad (1.23)$$

Example for Addition or Subtraction of the Counts A radioactive sample is measured in a counter. The sample holder gives 10,000 and 100 counts in 10 s with and without sample. Find true counts in the sample.

- Background counts = 100
- Measured counts in the sample = 10,000
- True sample counts = (10,000 − 100) ± $\sqrt{(10,000 + 100)}$ = 9900 ± 100.5
- Percentage uncertainty = (100.5/9900) × 100 = 1.01%

To have better results in terms of accuracy and precision, it is always necessary to have measured counts many fold more than the background counts.

Example for Product or Quotient The integrated counts between two cursors in the rising portion of a renogram at 1 and 3 min for right and left kidney were found to be 3000 and 2800 counts, respectively. Calculate the relative function of the kidneys.

$$\text{Relative function of right kidney} = \text{Integrated counts for right kidney}(R) / \text{Iintegrated counts for}$$
$$\text{right and left kidney for the same time interval}(R + L)$$
$$= R / (R + L) \pm \text{error} = 3000 / 5800 \pm \sqrt{(1/3000 + 1/5800)}$$
$$= 3000 / 5800 \pm 0.024 = 0.517 \pm 0.024 = (51.7 \pm 2.4)\%$$

- Percentage right kidney function = 51.7 ± 2.4
- Similarly, percentage left kidney function = 48.3 ± 2.4%

While using count rate instead of counts, one can use the same formula (Eqs. 1.22 and 1.23), but the uncertainty will have to be estimated for the count rate 'R' instead of counts 'N'.

$$\text{Count rate}(C) = \frac{\text{Counts}(N)}{\text{Time interval}(t)}$$

$$\text{Uncertainty in count rate} = \frac{\text{Uncertainty in counts}(N)}{t}$$

$$\text{Uncertainty in count rate} = \frac{\sqrt{N}}{t} \quad (1.24)$$

$$\text{Uncertainty in count rate} = \frac{\sqrt{N}}{\left(\sqrt{t}\right)\left(\sqrt{t}\right)} = \frac{1}{\sqrt{t}} \times \sqrt{\frac{N}{t}} = \frac{1}{\sqrt{t}} \times \sqrt{C} = \sqrt{\frac{C}{t}}$$

$$\text{Uncertainty in count rate} = \sqrt{\frac{C}{t}}$$

Example In a measurement with 1500 counts in 10 s. Calculate the uncertainty in count rate?

Given $N = 1500$ counts and $t = 10\,\text{s}$

$$\text{Count rate} = \frac{1500\,\text{counts}}{10\text{s}} = 150\,\text{counts per second}$$

$$\text{Uncertainty in count rate} = \sqrt{\frac{150}{10}} = \sqrt{15} = 3.87$$

Thus, the count rate = 150 ± 3.87 counts/s.

1.12   Optimum Time of Measurement for Maximum Precision

For a given time of measurement $(t_g + t_b)$, the maximum precision can be obtained with the following condition:

$$t_g / t_b = \sqrt{\left(C_g / C_b\right)} \qquad (1.25)$$

Example In an experiment, the total time available for measurement is 5 min. Gross counts from the sample and background for 10 s are 5000 and 250, respectively. Calculate the optimum time for the sample and background for maximum precision.

Solution Gross sample count rate = 5000/10 = 500

Background count rate = 250/10 = 25

$$t_g / t_b = \sqrt{\left(C_g / C_b\right)} \quad (\text{see Eq.1.25})$$
$$= \sqrt{\left(500 / 25\right)}$$
$$= 4.47$$
$$t_g = 4.47 t_b$$

Given, $t_g + t_b = 5$ min

$$4.47 t_b + t_b = 5\text{min}$$
$$5.47 t_b = 5\text{min}$$
$$t_b = 0.91\text{min}$$

Therefore $t_g = 4.47 \times 0.91 = 4.09$ min

Example The total time allotted for measuring a sample and background is 5 min. Gross counts from the sample and background for 10 s were 50,000 and 30,000 respectively. Calculate the optimum time for the sample and background for maximum precision?

Solution Gross count rate = 50,000/10 = 5000

Background count rate = 30,000/10 = 3000

$$t_g / t_b = \sqrt{\left(C_g / C_b\right)}$$
$$= \sqrt{\left(5000 / 3000\right)}$$
$$= 1.29$$
$$t_g = 1.29 t_b$$

Given, $t_g + t_b = 5$

$$1.29 t_b + t_b = 5$$
$$2.29 t_b = 5$$
$$t_b = 2.18\text{min}$$

Therefore, $t_g = 2.82$ min

1.12.1 The Chi Square Test

The reliability of counting instruments in nuclear medicine can be evaluated by chi square (χ^2) statistics. For this test, a minimum of 20 measurements are recommended. The mean of the measurement is calculated and chi square is then estimated from the mean as follows:

$$\text{Mean}\left(\bar{x}\right) = \sum x_i / n$$
$$\chi^2 = \sum \left(x_i - \bar{x}\right)^2 / \bar{x}$$

From χ^2 table, p value is obtained for a given set of measurements. A p value of 0.02–0.98 is treated as acceptable. In fact p value of 0.5 would be ideal to indicate that observed chi square value is in the middle of the range expected for Poisson distribution. A low p value shows a small probability that a Poisson distribution would give the chi square value as large as actually observed and indicates the presence of additional sources of

random error. With a *p* value just smaller than acceptable, the experiment suggests repeat measurement, as the results are suspicious in such cases. Similarly a high *p* value between 0.98 and 0.99 is also considered to be suspicious, and the experiment needs to be repeated. For $p > 0.99$, the random variations are much smaller than expected for a Poisson distribution.

Example A radioactive sample was placed in a well counter and pre-set time for counting the sample was kept as 10 s. Without disturbing the geometrical condition, 20 measurements were recorded as given in Table 1.3:

Based on the chi square test, comment on the precision of the well counter performance.

Mean = 3239.75 and chi square value = 28,531.75/3239.75 = 8.806.

The degrees of freedom are equal to $n - 1$ where *n* equals the number of measurements made. Thus, the degree of freedom in this case is 19. The largest critical value for df = 19 is 36.1909. The obtained chi square value lies between the 7.63 (*p*-value = 0.99) and 9.59 (*p*-value = 0.97) as shown in Table 1.4. As mentioned earlier, the

value between 0.02 and 0.98 is considered acceptable. Thus, the precision of the well counter performance is within acceptable limit.

Table 1.3 Counts observed in 20 measurements of a radioactive sample

S.No.	Total counts (10 s)
1.	3242
2.	3201
3.	3283
4.	3198
5.	3286
6.	3291
7.	3249
8.	3189
9.	3295
10.	3160
11.	3324
12.	3169
13.	3333
14.	3170
15.	3134
16.	3172
17.	3312
18.	3345
19.	3290
20.	3152

Table 1.4 Chi square table; this table has been created with *R* statistical software

df	*p*-values							
	0.99	0.975	0.95	0.9	0.1	0.05	0.025	0.01
1	0.0002	0.001	0.0039	0.0158	2.7055	3.8415	5.0239	6.6349
2	0.0201	0.0506	0.1026	0.2107	4.6052	5.9915	7.3778	9.2103
3	0.1148	0.2158	0.3518	0.5844	6.2514	7.8147	9.3484	11.3449
4	0.2971	0.4844	0.7107	1.0636	7.7794	9.4877	11.1433	13.2767
5	0.5543	0.8312	1.1455	1.6103	9.2364	11.0705	12.8325	15.0863
6	0.8721	1.2373	1.6354	2.2041	10.6446	12.5916	14.4494	16.8119
7	1.239	1.6899	2.1673	2.8331	12.017	14.0671	16.0128	16.4753
8	1.6465	2.1797	2.7326	3.4895	13.3616	15.5073	17.5345	20.0902
9	2.0879	2.7004	3.3251	4.1682	14.6837	16.919	19.0228	21.666
10	2.5582	3.247	3.9403	4.8652	15.9872	18.307	20.4832	23.2093
11	3.0535	3.8157	4.5748	5.5778	17.275	19.6751	21.92	24.725
12	3.5706	4.4038	5.226	6.3038	18.5493	21.0261	23.3367	26.217
13	4.1069	5.0088	5.8919	7.0415	19.8119	22.362	24.7356	27.6882
14	4.6604	5.6287	6.5706	7.7895	21.0641	23.6848	26.1189	29.1412
15	5.2293	6.2621	7.2609	8.5468	22.3071	24.9958	27.4884	30.5779
16	5.8122	6.9077	7.9616	9.3122	23.5418	26.2962	28.8454	31.9999
17	6.4078	7.5642	8.6718	10.0852	24.769	27.5871	30.191	33.4087
18	7.0149	8.2307	9.3905	10.8649	25.9894	28.8693	31.5264	34.8053

Table 1.4   (continued)

df	p-values							
	0.99	0.975	0.95	0.9	0.1	0.05	0.025	0.01
19	7.6327	8.9065	10.117	11.6509	27.2036	30.1435	32.8523	36.1909
20	8.2604	9.5908	10.8508	12.4426	28.412	31.4104	34.1696	37.5662
21	8.8972	10.2829	11.5913	13.2396	29.6151	32.6706	35.4789	38.9322
22	9.5425	10.9823	12.338	14.0415	30.8133	33.9244	36.7807	40.2894
23	10.1957	11.6886	13.0905	14.848	32.0069	35.1725	38.0756	41.6384
24	10.8564	12.4012	13.8484	15.6587	33.1962	36.415	39.3641	42.9798
25	11.524	13.1197	14.6114	16.4734	34.3816	37.6525	40.6465	44.3141
26	12.1981	13.8439	15.3792	17.2919	35.5632	38.8851	41.9232	45.6417
27	12.8785	14.5734	16.1514	18.1139	36.7412	40.1133	43.1945	46.9629
28	13.5647	15.3079	16.9279	16.9392	37.9159	41.3371	44.4608	48.2782
29	14.2565	16.0471	17.7084	19.7677	39.0875	42.557	45.7223	49.5879
30	14.9535	16.7908	18.4927	20.5992	40.256	43.773	46.9792	50.8922
31	15.6555	17.5387	19.2806	21.4336	41.4217	44.9853	48.2319	52.1914
32	16.3622	18.2908	20.0719	22.2706	42.5847	46.1943	49.4804	53.4858
33	17.0735	19.0467	20.8665	23.1102	43.7452	47.3999	50.7251	54.7755
34	17.7891	19.8063	21.6643	23.9523	44.9032	48.6024	51.966	56.0609
35	18.5089	20.5694	22.465	24.7967	46.0588	49.8018	53.2033	57.3421
36	19.2327	21.3359	23.2686	25.6433	47.2122	50.9985	54.4373	58.6192
37	19.9602	22.1056	24.0749	26.4921	48.3634	52.1923	55.668	59.8925
38	20.6914	22.8785	24.8839	27.343	49.5126	53.3835	56.8955	61.1621
39	21.4262	23.6543	25.6954	26.1958	50.6598	54.5722	58.1201	62.4281
40	22.1643	24.433	26.5093	29.0505	51.8051	55.7585	59.3417	63.6907

Suggested Reading

1. Pant GS, Rajabi H. Basic atomic and nuclear physics. In: Basic physics and radiation safety in nuclear medicine. 2nd ed. Mumbai: Himalaya Publishing House; 2018.
2. Pant GS, Pandey AK. Radioactivity. In: Basic physics and radiation safety in nuclear medicine. 2nd ed. Mumbai: Himalaya Publishing House; 2018.
3. Pant GS. Basic interaction of radiation with matter. In: Basic physics and radiation safety in nuclear medicine. 2nd ed. Mumbai: Himalaya Publishing House; 2018.
4. Cherry SR, Sorenson JA, Phelps ME. Physics in nuclear medicine. 3rd ed. Philadelphia: Saunders; 2003.
5. Chandra R. Introductory physics of nuclear medicine. Philadelphia: Lea & Febiger, Publisher; 1992.
6. Meredith WJ, Massey JB. Fundamental physics of radiology. Bristol: John Wright & Sons Limited; 1974.
7. Johns HE, Cunningham JR. The physics of radiology. Springfield: Charles C Thomas Publisher; 1969.
8. Henkin R, editor. Nuclear medicine. St Louis: Mosby; 1996.
9. Brown PH. Mathematics and statistics. In: Bernier DR, Christian PE, Langan GK, editors. Nuclear medicine: technology and techniques. 4th ed. St. Louis: Mosby; 1997. p. 1–35.
10. Johnson TE, Birky BK. Health physics and radiological health. 4th ed. Philadelphia: Wolters Kluwer/Lippincott Williams and Wilkins; 2012.
11. Environmental health and safety. Radiological safety guidance. University of Michigan; 2018.

Radiation Safety in Nuclear Medicine

2

Gauri Shankar Pant

Contents

Most of the text in this chapter has been reproduced from my book 'Introduction to Basic Sciences of Nuclear Medicine', Himalaya Publishing House, Mumbai, India, 2020 (under printing).

G. S. Pant (✉)
Department of Nuclear Medicine, All India Institute of Medical Sciences (AIIMS), New Delhi, India

2.1   Introduction

The ionising radiations are either from natural radioactive sources or from manmade radiation sources. Natural radiations have been present on earth ever since its formation, and all of us are exposed to them continuously with an average annual dose ranging from 2 to 3 mSv all over the world. However, no ill effects have been observed so far in any part of the world from this level of natural background radiation. However, the hazards of ionising radiation became apparent with the higher exposure of individuals from manmade sources of radiation. The discovery of X-rays in 1895 and that of the radioactivity in 1896 found the use of X-rays and radioisotopes for the diagnosis and treatment of human diseases. Both these sources were used enthusiastically in medicine for the benefit of patients. Within a couple of years of these two great discoveries, a number of radiation injuries were observed in early workers. A need for radiation safety regulations was therefore realised and the three cardinal factors, namely (1) **time**, (2) **distance** and (3) **shielding**, were used to reduce the amount of radiation exposure. Shorter the time spent with or near the radiation source, the lesser is the exposure. Increasing the distance from the source of radiation reduces the exposure in accordance with the inverse square law. Third parameter is the shielding, which reduces the exposure to any extent depending upon the thickness of the absorbing material interposed between the radiation source and the individual. Among these three, the most economical way of reducing radiation exposure is to increase the distance from the radiation source.

The International X-ray and Radium Protection Commission (the forerunner of International commission on Radiological Protection (ICRP)) was established in 1928 during the Second International Congress of Radiology in USA [1]. The doses were initially expressed in Roentgen (R) that was the unit of radiation defined at that time for X and gamma radiation up to 3 MeV energy. The unit of absorbed dose was taken as rad (100 ergs/g). In 1934, the commission recommended a tolerance dose of 0.2 R day^{-1} (500 mSv year^{-1}). The tolerance dose was lowered to 0.1 R day^{-1} (250 mSv year^{-1}) in 1938 from exposure to X- and gamma rays in view of increasing the incidence of radiation-induced skin injuries and leukaemia. The name of the protection committee was changed to International commission on Radiological Protection (ICRP) in 1950 [2]. The recommendations of ICRP have been revised from time to time on the basis of available knowledge from radiobiological and epidemiological findings. Latest revision of general recommendation was published in 2007 (ICRP 103) [3].

A linear dose–response relationship was found between the dose of radiation and its effect at high dose levels. The biological effects to which we radiation workers are exposed are normally not observed. To estimate the risk at such low levels, the ICRP extrapolated the linear relationship at high doses to zero dose which is called the linear non-threshold (LNT) dose relationship. The nominal risk to small doses may thus be estimated using LNT model.

Radiation produces somatic (acute and chronic), hereditary and teratogenic effects. For radiation protection purpose, ICRP divided all

Fig. 2.1 **Lef**t: The probability of the effect is proportional to the radiation dose without any threshold. The known linear dose–response relationship of higher doses has been extrapolated (linear non-threshold (LNT)) to zero dose; **right**: the deterministic (non-stochastic) effect with a threshold dose below which the effects are not observed. In deterministic effect, severity of the effect is proportional to radiation dose
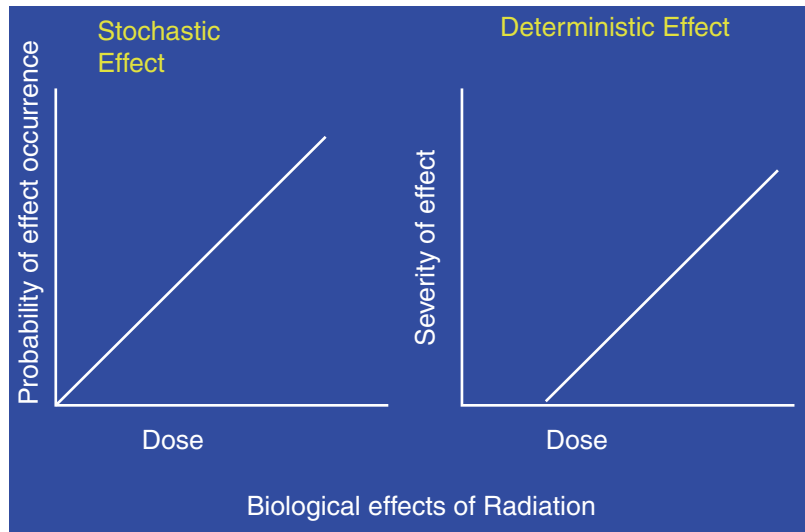
the biological effects produced by ionising radiations into two categories, namely the deterministic and stochastic effects (Fig. 2.1). The cell killing (large number) can result in deterministic effects, whereas cell modifications after radiation exposure may give rise to stochastic effects.

2.1.1 Deterministic Effects

Deterministic effects are observed if the exposure to the organ/individual exceeds a certain threshold dose. Radiation sickness, induction of sterility, leucopoenia, anaemia, reddening of skin, depilation, skin burns, cataract (opacity of eye lens), etc. are some examples of the deterministic effects. Different effects have different threshold doses.

2.1.2 Stochastic Effects

Occupational exposures generally result in small absorbed doses to the individuals. Such doses unlikely result in deterministic effects, but can modify few cells to lead to cell transformation or an alteration of genetic information. The two important stochastic effects of radiation, namely radiation carcinogenesis and genetic effects, originate from cell modifications. Somatic cell mutations can result in carcinogenesis, whereas the germ cell mutations have a potential to cause genetic disorders. There is no threshold dose for stochastic effects.

Objective of radiation protection is therefore to reduce the chance of stochastic effects to an acceptable level by reducing the exposure to as low as reasonably achievable (ALARA) and completely eliminate the chance of deterministic effects.

2.2 Unit of Radiation Dose Used in Radiation Safety

All radiations are not alike in their ability to produce ionisation in the matter through which they pass (ability to produce biological damage); therefore, each radiation type is assigned with a weighting factor. List of weighting factor for different type of radiation is given in Annexure 1 of this chapter. Once we multiply the radiation dose with its weighting factor (W_R), we get equivalent dose (H) in **Sievert (Sv)**.

$$\text{Equivalent dose}(H) = \text{Absorbed dose}(D) \times \text{Radiation weighting factor}(W_R)$$

1 Sv = 100 rem. This is the unit used in radiation protection. If part of the body is exposed, then the dose equivalent to that part or organ (H) is multiplied by the tissue weighting factor (W_T) for that organ. The result will be the effective dose (E) in Sv (to the whole body).

$$\text{Effective dose}(E) = H \times W_T$$

(The tissue weighting factors for various organs is given in Annexure 2.)

The ICRP further recommends the system for dose limitation as follows:

(a) No practice involving exposures to radiation should be adopted unless it produces sufficient benefit to the individual or to society to offset the radiation detriment it causes—the **justification of practice**.

(b) For any source, the magnitude of individual doses, the number of people exposed and the likelihood of incurring potential exposures should all be kept 'as low as reasonably achievable (**ALARA**), economic and social factors being taken into account'. The procedure should be constrained by restrictions on the doses to individuals (dose constraints) and risks to individuals from potential exposures (risk constraints)—the **optimisation of protection**.

(c) Individual exposure from all sources susceptible to control is subject to dose limits and some control of risk from potential exposures. These are aimed at ensuring that no individual is exposed to radiation risks that are judged to be unacceptable in any normal circumstances—**individual limits**.

These principles can be understood as follows:

- The Principle of **Justification**: Any decision that alters the radiation exposure situation should do more good than harm.
- The Principle of **Optimisation** of Protection: The likelihood of incurring exposure, the number of people exposed and the magnitude of their individual doses should be kept as low as reasonably achievable, taking into account economic and social factors.
- The Principle of Application of **Dose Limits**: The total dose to any individual from regulated sources in planned exposure situations other than medical exposure of the individual should not exceed the appropriate limits specified by the Commission.

Annual dose limits for staff and public as recommended by ICRP-103 (published in 2007) are given in Table 2.1.

Table 2.1 Dose limits recommended by ICRP-103 (2007)

Exposure condition	Dose limit (mSv per year)		
	Occupational	Apprentices (16–18 years)	Public
Whole body:	20 mSv per year, averaged over a period of 5 years with no more than 50 mSv in a single year	6 mSv in a year	1 mSv in a year (effective dose)
Parts of the body: (equivalent dose)			
Lens of the eye[a]	(*150 mSv*) * 20 mSv per year	50 mSv in a year	15 mSv in a year
Skin	500 mSv per year	50 mSv in a year	
Hands and feet	500 mSv per year	150 mSv in a year	50 mSv in a year

[a]ICRP [4] suggested a higher sensitivity of the eye lens and hence the recommended reduction in annual dose limit for the eye from 150 to 20 mSv/year for occupational workers

2.3   Radiation Safety in Nuclear Medicine

The applications of radiopharmaceuticals for medical diagnosis and therapy have been on rapid increase due to the development of favourable physical characteristics of artificially produced radionuclides, progress in instrumentation and computer technology and availability of desirable radiopharmaceuticals. Efforts are continuing to develop newer radiopharmaceuticals for providing better diagnostic information as well as therapeutic results. While such an enthusiasm is appreciable, adequate safeguards against radiation exposure are also necessary to minimise the radiation risk to the occupational workers, patients and the public. Fortunately, the necessity of radiological safety is well understood and practiced now in all the installations in hospitals world over, where radionuclides and radiations are handled for medical applications or research.

2.4   Categories of Exposure

Following three categories of people are likely to be involved in radiation exposure in the medical applications of ionising radiation:

1. Occupational staff
2. Patients
3. Public

Accordingly, the protection is aimed at achieving the objective of minimising the exposures to all these three categories of people to as low as reasonably achievable (ALARA).

For safe use of radionuclides in nuclear medicine, the following basic requirements should be met.

1. The Nuclear Medicine facility should be well planned with sufficient number of rooms for intended operations (including the storage and disposal of radioactive waste) duly approved by the competent authority.

2. All the equipment required for safe handling should be available for proposed operations in the facility.
3. The staff should be well trained and adequate in number for proposed operations with radioactive material.

2.5   Radiation Safety Considerations in Radiopharmacy Laboratory (Hot Lab)

Location and design of the radiopharmacy laboratory (hot lab) has to be given due consideration as entire radioactivity and radioactive sources are normally stored here. Further the storage of the generators, labelling of radiopharmaceuticals and their storage dispensing for clinical studies are done from the hot lab. When PET radiopharmaceuticals are hired from a distant cyclotron facility, they are also stored at a corner in this lab for manipulating the single dosage for administration to the patients. The laboratory should therefore be large enough to accommodate the necessary equipment/devices. Separate work areas should be designated for carrying out radioactive and non-radioactive work. Walls and ceilings of the radioisotope laboratory should be covered with a smooth, washable, non-porous and strippable paint. The floors should be of an impermeable and non-slippery material and that it is easily washable and resistant to chemical change and should be skirted to the walls, with all joints sealed.

All workbenches in the laboratory should be non-porous, non-reactive to chemicals and have impervious surfaces that can be decontaminated easily and should have sufficient weight bearing capacity to support the weight of any shielding material and radionuclide generator, etc. Sinks or washbasins should be preferably of stainless steel with a smooth finish, and the taps should be either elbow or foot operated. Plumbing lines carrying radioactive effluents should be of a non-corrosive material.

The effluent lines from the hot lab should go as directly as possible to the main sewers and should not be connected with other drains carrying non-active effluents within the building. The Fume-hood should be constructed of a material that is smooth, impervious, washable and resistant to chemicals. The ducts carrying the exhausted air activity from the fume-hood should be of a non-corrosive material and should be able to withstand harsh weather conditions. The exhaust fan of the fume-hood should be located at the rear end of the filtration duct assembly, i.e. after the filtration unit and just before the point of final exhaust into the atmosphere. The furniture and fixtures should be kept to the basic minimum in the laboratory.

The storage of radioisotopes and the preparation/labelling of radiopharmaceuticals are done in the hot laboratory. The radiopharmacy laboratory is a highly restricted area with limited access only to the authorised staff. Most of the ^{99m}Tc-labelled radiopharmaceuticals are in liquid form for intravenous injection to the patients, and they have to be sterile. The radiopharmacist/technologist who prepares the radiopharmaceutical has to use sterile equipment/materials and adheres to strict aseptic working techniques; this includes:

- Performing the preparation in a laminar air flow (LAF) cabinet.
- Wearing dust-free protective clothing.
- Wearing a mouth mask and a hat during the work at the LAF cabinet.
- The staff handling radioactive material should wear a ring dosimeter in addition to personal dosimeter such as thermoluminescent dosimeter (TLD) for whole body.
- Staff should wear disposable gloves during the manipulation of radioactive materials to protect themselves from radioactive contamination. The gloves should be checked frequently for a potential radioactive contamination and be immediately changed if found contaminated. A Geiger counter should be available in the laboratory.

- Eating, drinking or smoking in a hot lab is not allowed.
- Put on a special (dedicated) **lab coat**, **mouth mask** and **hat while working in the lab.**
- Put on **gloves and overshoes before entering the laboratory.**

2.6 Radiation Safety Considerations in PET Facilities

The PET radioisotopes give rise to two annihilation photons of 511 keV photons with each positron emission. In addition, there is also a possibility of emission of bremsstrahlung radiation particularly with high energy positron (such as ^{82}Rb) during their slowing down in the medium. ^{82}Rb (from the ^{82}Sr-^{82}Rb) has the positron energy of 3.15 MeV and also is the only isotope to have significant contamination from other gamma rays (approximately 9% at 777 keV). The ^{82}Sr-^{82}Rb generator therefore requires additional shielding.

2.7 Shielding Material for PET

Tungsten, lead and concrete are widely used as shielding materials in a PET facility. Lead is more commonly used than tungsten for being cost effective and readily available. Concrete (density 2.35 g/cm^3) is used for constructing the walls, floor and ceiling of the PET facilities for shielding the 511 keV photons. The thickness of concrete depends upon the room size and location of the PET system within the imaging room. Once shielding calculations are done for PET, there is no need for separate calculations for CT X-rays as the shielding requirement for them is less than that for PET annihilation photons. Under narrow beam conditions, lead has a mass attenuation coefficient of 0.153 cm^2/g and a half-value layer of around 4 mm at 511 keV [5]. The effective half-value layer of lead for shielding photons of this energy under broad beam conditions has been reported in the range 4.1–5.5 mm. Concrete has a

mass attenuation coefficient of 0.0877 cm^2/g and a half-value layer of 3.4 cm under narrow beam conditions at 511 keV. The shielding of the radiation rooms shall be in such a way that it is not weakened at the joints, openings for ducts, passing by of conduits, etc. that are embedded in the barriers. Doors (or other mean of access to the room) as well as observation windows also require special considerations to ensure adequate protection. By use of appropriate design and good operating practices, radiation doses to staff and the public can be kept below the prescribed limits.

2.8   Staff Exposure in PET/CT

The radiation exposure to the technologists has been reported to be slightly higher while working in PET/CT facility as compared to the conventional nuclear medicine facility. F. O. Roberts et al. [6] reported that the radiation exposure of PET technologists was higher than that of technologists performing general nuclear medicine studies, with doses averaging 771 ± 147 and 524 ± 123 μSv per quarter, respectively ($P = 0.01$). The preparations of single dosage in the hot lab may also add additional exposure to hands of the concerned staff. Some centres use auto-dispenser and auto-injector to further minimise the exposure. Using proper shielding devices, the doses to the staff in PET/CT can be minimised. Both the preparation of single dosages in the hot lab and injection of PET radiopharmaceuticals should be done cautiously to minimise the exposure. Dose manipulations should be done strictly under a thick L bench meant for PET isotopes. The loaded syringes should be kept in the lead shielded box for carrying to the injection site. The containers for sharps should be with extra lead shielding. The dose calibrator for measuring PET isotopes has additional lead thickness for attenuating annihilation photons. Further the injected patients become a source of radiation exposure as they have to wait for an hour (before their scanning) in specially designed waiting rooms with adequate shielding to minimise the exposure to the staff.

2.9   Protection of Staff in Nuclear Medicine

The nuclear medicine procedures demand preparation of radiopharmaceuticals, their internal movement within the facility and finally administration to the patient. At each step, there is a possibility of radiation exposure if safety guidelines are ignored. The radiation exposures in diagnostic nuclear medicine normally do not pose any alarming situation of exposure to the staff and public. However, the patients administered with large dose of radioactivity for therapeutic purposes become a source of radiation to the staff and after release from the hospital to their attendants/family members at home. Therapeutic radionuclides are usually beta emitters, and pure beta emitters do not pose much problem from radiation safety standpoint and can even be treated as outpatients. However, patients treated with radioiodine (^{131}I) need hospitalisation beyond a certain dose as per national regulatory requirement due to concurrent penetrating gamma radiation (364 keV). They are kept in a specifically designed isolation room/ward till the body burden comes down to an acceptable level for release from the hospital.

2.10   Classification of Work Areas

The relevant areas of practices can be classified as 'Controlled' and 'Supervised' areas in the facility as under:

- **Controlled area**: Areas in which there is a chance of receiving more than three-tenth of the annual effective dose limits (>6 mSv to <20 mSv) are designated as controlled areas.
- **Supervised area**: Workplaces are designated as supervised areas if the annual dose of the staff is likely to exceed one-twentieth but not likely to exceed three-tenths of the annual dose limits (i.e. should be within 1–6 mSv.
- Both in controlled and supervised areas, entry of the public or patient's attendants is restricted.
- **Unclassified area**: The unclassified area is the one in which the annual effective dose limits

are less than 1 mSv. This is the area where public entry or movement may be allowed. The facility may however put restriction of entry to public in some areas at even low doses by defining them as supervised or controlled areas for reasons other than radiation safety (e.g. control room of imaging system).

2.10.1 Work Practice

Good work practice is an essential component of radiation safety in nuclear medicine. This includes observation of all radiation protection rules as applicable to nuclear medicine, use of appropriate safety devices, remote handling tools/accessories and maintaining good house-keeping habits in the laboratory.

In addition to the external irradiation, there is chance of additional radiation from possible radioactive contamination and radioactive waste. These two aspects need to be addressed carefully. The practice should be such that the annual doses received by the occupational workers and the public is as low as reasonably achievable and in no circumstances exceed the limits prescribed by the national competent authority.

2.11 Protection of Patients

Every practice involving ionising radiation should be justified in terms of net positive benefit to the patient. It is particularly important for children for whom long-term risks of exposure to ionising radiation are larger (NRPB, 1999) [7]. Once clinically justified, each examination involving ionising radiation should be conducted such that the radiation dose to the patient is lowest necessary to achieve the clinical aim (optimisation). Reference and achievable doses for various radionuclide investigations have been proposed for this purpose (NRPB, 99). The concept of reference doses is recognised as a useful and practical tool for promoting the optimisation of patient protection. While reducing radiation dose to the patient, one should not compromise in image quality, which may otherwise lead to a

repeat investigation resulting in more dose to the patient and the staff involved.

Routine QC tests of imaging systems and radiopharmaceuticals have to be done to avoid repeat test because of equipment malfunctioning or inadequate radiopharmaceutical labelling.

Another consideration in reducing patient dose is to avoid misadministration and proper radiation counselling to patients and their relations.

2.12 What Is Misadministration?

Error in any part of the procedure starting from patient selection to the interpretation of final results may lead to repeat study. This in turn leads to increased radiation dose not only to the patient but also to the staff involved. One of the major contributors in increased radiation dose to the patient is misadministration. Misadministration has several components such as administration of wrong radiopharmaceutical, wrong dose, dose to a wrong patient or through a wrong route, which ultimately lead to unintentional exposure to patient.

The following points should be confirmed to avoid misadministration:

- **Identity of the patient**: The radiopharmaceutical should be administered to the patient for whom it is prepared. Name, age and parent's name should be checked before dose administration. At least two identifiers should be used for correct identification of the patient.
- **Radionuclide and its physical/chemical form**: The physical and chemical form of the radiopharmaceutical should be reconfirmed before administration. Radiopharmaceuticals should go through routine quality control procedures to avoid any repeat test due to inadequate preparation.
- **Dose/quantity of radioactivity/QC**: The radioactivity should be measured in a calibrated radionuclide dose calibrator before administration. The accuracy and precision of radionuclide dose calibrator need to be maintained at all time for accuracy in dose estima-

tion. Similarly imaging equipment should be maintained at its optimum level of performance. Variation in therapeutic dose by more than ±10% is treated as misadministration. For the diagnostic dose, a variation of more than 10% may be accepted. Different countries may have different levels of acceptance, but I feel that a variation in diagnostic dose by ±20% may be accepted.

- **Route**: Physician should confirm the route of administration (oral/intravenous/subcutaneous, etc.) of radiopharmaceutical.
- **Pregnancy and breastfeeding:** Ensure that patient notifies in case of pregnancy and breastfeeding. During pregnancy, radiopharmaceuticals are not administered except in clinical emergencies as recommended by the physician. However, radionuclide therapy is strictly prohibited during pregnancy. Some of

the radiopharmaceuticals are excreted in the breast milk, so the breastfeeding patient has to suspend the feeding for a given length of time or has to go for complete cessation as advised by the nuclear medicine physician or the radiation safety officer (RSO) of the facility. The IAEA has published a table recommending the interruption of breastfeeding as given in Table 2.2.

With PET radiopharmaceuticals (^{18}F–FDG) with injected dose of 370 MBq, 12 h interruption of breastfeeding is supposed to be adequate as per IAEA (RPOP). The lactating woman should be advised to express the milk and drain it through the sink. For other PET radiopharmaceuticals with shorter half-life than ^{18}F, 12 h interruption is more than adequate. Hicks et al. [9] feel that it is unlikely that the internal dose due to ingesting

Table 2.2 Activities of radiopharmaceuticals that require interruptions when administered to patients who are breastfeeding an infant (IAEA 2006) [8]

Radiopharmaceutical	Administered activity		Recommended interruption of breastfeeding
	(MBq)	(mCi)	
^{131}I ^{131}I NaI	120	3	Complete cessation
^{123}I NaI	50	1.5	9 h
^{123}I OIH	20	0.5	Nil
^{123}I MIBG	400	10	24 h
^{125}I OIH	2	0.05	Nil
^{125}I fibrinogen	Any	Any	Complete cessation
^{125}I HSA	Any	Any	Complete cessation
^{131}I OIH	2	0.05	Nil
^{32}P phosphate	Any	Any	Complete cessation
^{99m}Tc DTPA	800	20	Nil
^{99m}Tc MAA/microspheres	200	5	Nil
^{99m}Tc pertechnetate	800	20	40 h
^{99m}Tc DISIDA	300	8	Nil
^{99m}Tc glucoheptonate	800	20	Nil
^{99m}Tc human albumin microspheres	100	2.5	Nil
^{99m}Tc MIBI	800	20	Nil
^{99m}Tc-MDP	800	20	Nil
^{99m}Tc pyrophosphate	800	20	Nil
^{99m}Tc RBCs in vivo labelling	800	20	Nil
99mTc RBCs in vitro labelling	800	20	Nil
^{99m}Tc SC	400	10	5 h
^{99m}Tc DTPA aerosol	50	1.5	Nil
^{99m}Tc MAG3	400	10	Nil
^{111}In WBCs	40	1	48 h
^{67}Ga citrate	400	10	1 month (means cease)
^{201}Tl chloride	200	5	30 h

radioactive milk will exceed the 1 mSv limit, even without a temporary cessation of breast-feeding. However, they also conclude that the external dose due to being held in proximity to the mother could be more significant. Their advice is that mothers who choose not to temporarily suspend breastfeeding after FDG scan can minimise exposure to their infants by expressing the milk and allowing a third party to bottle-feed the infant during this period.

2.13 Protection of the Public/ Environment

To ensure that unnecessary exposure to the members of the public is avoided, the following guidelines shall be followed:

1. No member of the public shall be allowed to enter the controlled (hot laboratory and the injection room/area, imaging rooms) and supervised area (consoles).
2. Appropriate warning signs and symbols shall be posted on doors and at appropriate locations to restrict access to radiation areas.
3. Relatives or friends of the patients receiving therapeutic doses of radioactive iodine shall be allowed to visit the patient from a distance with the permission of RSO. The visitors shall not be young children or pregnant women.
4. A nursing mother who has been administered with radiopharmaceuticals shall be given instructions for avoiding close contacts with children for a period as suggested by RSO, after her release from the hospital.
5. An instruction sheet shall be given to the patient administered with therapeutic doses of radioiodine at the time of release from the hospital, which need to be followed at home for a specified period as suggested by RSO.
6. The storage of radioactive waste shall be done at a proper location within the hospital premises and near the facility, with adequate shielding to eliminate the public hazard.
7. Treated patients may carry a card of their radionuclide investigation/therapy (in particular) to show at the airport security, if flying to their destinations.

2.14 Radiation Emergencies and Incidents/Accidents

In a nuclear medicine facility, always there is a possibility of radiological emergency situation, which may cause a risk of potential exposure and contamination hazard to the staff, patients and the public. The IAEA in one of its publication has detailed the different types of emergency situations and their management [8]. The possible risk situations are described below.

2.14.1 Loss of Radioactive Sources

This poses greatest risk to the staff and possibly to the public if the radiation source enters the public domain. In the event of loss of any standard source with long half-life, the RSO should make a thorough survey of the facility to trace it. If not found after repeated attempts of survey, the matter has to be reported to the head of the institution and the police before informing to the regulatory body. To avoid such situation of loss of radioactive source to occur, the facility should maintain an up-to-date inventory of all the sources that are procured, used and disposed. The routine use and movement of each source can be traced with up-to-date inventory.

2.14.2 Damage to ^{99m}Tc Generators

The ^{99}Mo-^{99m}Tc generators contain relatively large amount of radioactivity. In the event of the generator being damaged, the following measures should be taken:

- Evacuate the area immediately.
- Inform the RSO, who should survey and confirm if there is any spillage. If spillage is found, then all the areas and surfaces, where the generator would have moved from its arrival till its final destination in the radiopharmacy room, should be surveyed. He/she should also supervise the monitoring and decontamination procedures.
- Monitor the personnel, who handled the damaged generator for any personnel contamination

and if contaminated undertake prompt decontamination.

- Record the event and report the incident according to the rules of the national regulatory body.

2.14.3 Management of Radioactive Spill

- Perform a radiation and contamination survey to determine the degree and extent of contamination.
- Isolate the contaminated area to avoid the spread of contamination. No person should be allowed to enter that area.
- Use gloves, shoe covers, lab coat and other appropriate personal protective equipment (PPE).
- Rapidly define the limits of the contaminated area and immediately confine the spill by covering the area with absorbent materials (with plastic backing if available).
- First remove the 'hot spots' and then scrub the area with absorbent materials, towards the centre of the contaminated area. Special decontamination chemicals (Radiac-wash) shall be used in the case of a severe spill.
- All personnel should be surveyed to determine contamination, including their shoes and clothing. If the radioactive material is relatively hazardous and appears to have become airborne, the nostrils and mouth of possible contaminated persons should be swabbed, and the samples shall be evaluated by the RSO.
- Shut off ventilation if airborne activity is likely to be present (rare situation).
- Heavily contaminated individual may take shower in the designated decontamination facility as directed by the RSO. Disposable footwear and gloves should be worn in transit.
- If significant concentration of radioiodine has been involved, administration of potassium iodide tablets and thyroid uptake measurements should be made on potentially exposed individuals after 24 h.
- Monitor the decontaminated area and all personnel leaving the area after the clean-up.

Particular attention should be paid to checking the hands and soles of shoes.

- All mops, rags, brushes and absorbent materials shall be placed in the designated waste container and stored in waste storage room after being surveyed by the RSO. Proper radioactive disposal should be observed.
- The RSO is supposed to provide the final radiation survey report with necessary recommendations/advice to avoid such an incidence in future.

2.15   Personnel Decontamination

2.15.1 Handling of Contaminated Eye

- Where eye contamination is found, the eye should be flushed profusely with isotonic saline or water by covering other parts with towel to prevent the spread of contamination. Ophthalmologist shall be consulted if there are signs of eye irritation.
- Stop the decontamination procedure when the level has reduced to acceptable level as suggested by the RSO.

2.15.2 Handling of Contaminated Hair

- If hair is contaminated, try up to three washings with liquid soap and rinse with water.
- Prevent water from running onto the face and shoulders by shielding the area with towels.
- Check the radiation level after each wash.
- Stop the decontamination procedure when the level has reduced to acceptable level as suggested by The RSO.

2.15.3 Handling of Contaminated Skin

- Remove any contaminated clothing before determining the level of skin contamination. Levels below 0.1 mR/h (1 µSv/h) are considered with minimal hazards.
- If there is gross skin contamination, it shall be given attention first. Wipe with cotton swab

moistened with water and liquid soap using long forceps. Place all used swabs in a plastic container for radiation level measurement and for storage before disposal.

- If large skin area is contaminated, the person should have a 10-min body wash/shower. Dry the body with a towel in the shower room and monitor the radiation level over the whole body. Do not allow any water to drip on to the floor outside the shower room to avoid the spread of contamination.
- Place all the towels and other contaminated clothing in a plastic bag for monitoring of radiation level then for storage and decay.
- Specific hot spots on the skin can be localised with a survey meter/appropriate contamination monitor.
- Clean the specific areas with mild soap and warm water. Avoid using detergents or vigorous scrubbing, for they might damage the skin. The use of a soft brush is adequate.
- For stubborn contamination, covering a contaminated area with plastic film or disposable cotton or latex gloves over a skin cream helps remove the contamination through sweating.

2.15.4 Internal Contamination

- Simple expedients such as oral and nasopharyngeal irrigation, gastric lavage, or an emetic and use of purgatives can reduce the uptake of a contaminant into the circulation.
- Blocking agents or isotopic dilution techniques can appreciably decrease the uptake of the radionuclides into relatively stable metabolic pools such as bone. These should be administered without delay.

When a contaminated person requires treatment (for wounds) by a physician, the emergency room (ER) should be informed. The following points must be remembered:

- Medical emergencies are the priority and must be attended first. Radiation injuries are rarely life threatening to the victim and the attending physician/staff.
- Clean the wound with mild detergent and flush with isotonic saline or water. If necessary, a topical anaesthetic, such as 4% lidocaine, can be used to allow a more vigorous cleansing. After a reasonable effort, there is no need to attempt to remove all contamination since it will probably be incorporated into the scab.
- Whenever radionuclides have entered the skin via a needle or sharps induce the wound to bleed by 'milking' it as a cleansing action, in addition to the use of running water.
- Perform radiation monitoring at the surface.

2.15.5 Power Failure

In case of power failure during the handling of unsealed radionuclides in the hood, the following steps shall be taken:

- Close the hood door if possible.
- Hold the breath, if possible, until you leave the laboratory area particularly if handling volatile radionuclide.
- Re-entry into the laboratory shall be approved by the RSO.

2.15.6 Management of Radioactive Waste

Radioactive waste is generated as a result of handling unsealed sources in the laboratory, leftover radioactive material from routine preparations, dose dispensing to patients, contaminated items in routine use, etc. The waste arises in a large variety of forms depending upon the physical, physiochemical and biological properties of the material. In radionuclide therapy, the waste may

also be in the form of effluent from the therapy isolation room.

2.15.7 Storage of Radioactive Waste

The solid waste generated in the working area should be collected in polythene bags and transferred to suitable containers in storage room. The liquid waste has to be collected preferably in plastic containers. The waste containing short-lived and long-lived radionuclides should be collected in separate bins for storage. If the laboratory is used for the preparation of ultra-short-lived radiopharmaceuticals (such as PET radiopharmaceuticals), then it is advisable not to collect the waste till next preparation (decay for 24 h). This will avoid unnecessary exposure to the staff handling radioactive waste. The storage room should have proper ventilation and exhaust system connected to a duct line. The shielding around the waste storage room should be adequate enough to prevent any leakage radiation. The waste shall be stored for at least 10 half-lives for decay or till such a time that the radiation level drops down to the acceptable level for disposal.

2.15.8 Disposal of Solid Waste

(a) **Low activity waste**

The solid waste comprising of paper tissues, swabs, glassware and similar materials which are of low activity (only a few Bq) can be disposed off with ordinary refuse provided that no single item contains concentrated activity, and the waste does not go through recycling procedure.

(b) **High activity wastes**

Contaminated clothing and those items, which need to be reused, are segregated and stored for physical decay of radioactivity. Derived working limits (DWL) 3.7 Bq/cm² is indicated for personal clothing and hospital bedding. Disposal methods for solid waste consist of decay and dispose, or by burial in the ground. The method chosen depends upon the quantity of radioactive materials present in the wastes. From each work area, the wastes are collected in suitable disposable containers. Extra care for radiation protection is necessary during the accumulation, collection and disposal of radioactive wastes. Containers should be marked with the radiation symbol and suitable designation for segregation [10].

Solid wastes like animal carcasses, animal excreta, and biologically toxic material can be conveniently dealt with by burial or incineration depending upon the national guidelines. Incineration of refuse containing non-volatile radionuclides concentrates the activity in the ash. If the ash does not contain undesirable high activity, then it can be diluted and disposed off without exceeding the specified limits. The design of the incinerator for handling the radioactive waste should be considered at the planning stage.

2.16 Management of Cadavers Containing Radionuclides

An unfortunate situation may arise if a patient dies after administration of high amount of radioactivity, and the radiation level exceeds the national limit of releasing the body from the hospital. If the activity is concentrated in few organs (as can be seen by scanning the cadaver under the gamma camera), then those organs should be removed, and the body may be handed over to the relatives after ensuring that the limits recommended by the competent authority are not exceeded. In case of widespread disease when organ removal may not bring down the radiation level to acceptable limit, the body may be put into a plastic bag and stored in a mortuary (cold room) for physical decay till the radiation exposure comes down to an acceptable level. In some countries, the national rules do not permit the removal of organs so the body (in plastic bag) has to be stored in a cold room of the mortuary. In any compelling social circumstances, the advice of the regulatory body may be sought. Autopsy,

management of removed organs/part of the body, handing over the body to the relations of the patient and cremation should be done under the direct supervision of the RSO.

2.17 Disposal of Liquid Waste

While disposing liquid wastes through sanitary sewage system, the limits of dilution and disposal should not exceed the prescribed limits recommended by the competent authority (monthly dilution limit of 22.2 MBq/m^3). If the activity in the waste is too low, then it may be disposed off with proper dilution (dilute and dispose). If the activity level is from moderate to high, and the half-life/lives of radionuclides is relatively short, then they should be stored for physical decays for a period of about 10 half-lives (delay and decay). This method is also applicable to solid waste.

Quantity of liquid radioactive waste generated due to nuclear medicine investigations hardly poses any problem of storage or disposal. However, it is not the same for therapeutic nuclear medicine where large amount of radioactive waste is generated in the form of effluent from the isolation room/ward of thyroid cancer patients treated with large dose of ^{131}I. The large doses of radioiodine used for the treatment of thyroid cancer calls for planned storage and release of waste by sewage disposal. Amounts of ^{131}I as high as 7.4–11.1 GBq (200–300 mCi) are being administered to patients with distant metastasis. Approximately 80–90% of administered radioactivity gets released through the patient's urine [11]. Therefore, management of radioactive urine poses a radiation safety problem. Various methods have been recommended for the disposal of high level radioactive liquid wastes. The widely used technique is the use of storage delay tank system with two tanks each of 5000–6000 L capacity. Tanks of larger capacity may also be used depending upon the situation. Storage of entire effluent from the isolation room/ward including urine in delay tank system is the recommended method and is more feasible in hospitals with tanks of appropriate volumes. The system allows collection of release from isolation room/ward in the first tank. The tank is closed after it is completely filled, and collection takes place in the second tank. By the time the second tank is completely filled, effluent in the first tank gets enough time to decay which makes its release possible to sewage system. It will even be better if effluent in each tank is allowed to decay for a given length of time and then released into a big dilution tank before its final release into the sewage line. Large number of small tanks are also used in some countries for allowing the decay of radioiodine for at least ten half-lives. Provision of access to dilution tank is useful to monitor the activity concentration at any time before final release to the main sewerage.

2.18 Disposal of Gaseous Waste

Gaseous wastes originate from exhausts of stores, fume cupboards, wards and emission from incinerators. Points of release into atmosphere should be carefully checked, and filters (including charcoal) may be used wherever possible. The concentration of radioactive materials in the air leaving the ventilation system should not exceed the maximum permissible concentrations for breathing unless regular and adequate monitoring or environmental surveys are carried out to prove the adequacy of the disposal system. When large quantities of radionuclides are routinely discharged to the environment, it is advisable to make environmental surveys in the vicinity since many radionuclides will be concentrated by absorption on surfaces.

In installations where large amounts of airborne activity are involved, it may be necessary to use suitable air filtration (HEPA with charcoal filter) systems and to discharge the filtered effluent through a tall stack. The height of the stack can be chosen to ensure that the radioactivity is sufficiently diluted before it reaches the ground level. Combustible low-level radioactive waste may be incinerated to reduce their bulk with adequate precautions.

Security: The waste has to be protected from fire, insects and extreme temperatures. The waste should not enter the public domain as it may cause unnecessary panic to the general public.

One of the major components of radiation safety in nuclear medicine arises because of radioiodine (^{131}I) therapy. It is used in large quantity for therapeutic use; it has long physical half-life of 8 days with penetrating gamma radiation (364 keV). It is volatile and human body has avidity for iodine. All these factors pose radiation hazards. Safety considerations in radioiodine therapy have therefore been described separately here.

2.18.1 Radionuclide Therapy

Radionuclide therapy other than with ^{131}I does not pose much problems from radiation safety view point. Most of these patients are treated with beta/alpha emitters and normally do not need hospitalisation because of low radiation exposure from the surface of their body. Patients are admitted in the hospital for reasons other than radiation safety issues. Those treated for bone pain palliation are treated with beta emitters with small components of low energy gamma radiation such as ^{153}Sm. Treatment of inoperable hepatocellular carcinoma (HCC) with ^{90}Y microspheres needs proper handling of energetic beta radiation. Personnel contamination has to be avoided and for shielding energetic betas, Perspex sheet of 5–10 mm thickness is used. Essential items should be arranged before the day of treatment.

2.18.2 Radioiodine Therapy: Safety Considerations

Radioiodine has been effectively used for many decades to ablate remnant thyroid tissue following thyroidectomy and for treating distant metastasis. Looking at the radiation hazard to staff and public, the national regulatory bodies have established the guidelines for hospitalisation of the patients and their subsequent release from the hospital. Critical groups among the public are fellow travellers during journey back home after release from the hospital, children and pregnant women at home. Therefore, a limit of body bur-

den with radioiodine has been recommended by the national regulatory bodies in all the countries at the time of release from the hospital. The limit at which these patients are released from the hospital varies from country to country.

The administered dose of radioiodine is avidly picked up by thyroidal tissue (thyroid remnant, differentiated thyroid cancer). It rapidly gets excreted via the kidney and urinary bladder and to a much smaller extent through perspiration, saliva, exhalation and the gut. The faster biological excretion of the activity in thyroid cancer patient reduces the radiation hazard from the patient to the environment. Counselling of patients and family members from radiation safety point of view is necessarily recommended before therapeutic administration.

2.18.3 Radiation Monitoring

Routine monitoring of all work surfaces, overcoats, exposed body parts, etc. of the staff involved in treatment is essential before leaving the therapy ward after dose administration. Both G.M.-type survey meters and ionisation chamber-type survey meters are required for the monitoring. The staff involved in radioiodine procedure should be covered by personnel radiation monitoring badges, and their neck counts should also be measured weekly. It is advisable to carry out periodic air monitoring in these areas to check for the presence of any air-borne activity.

2.18.4 Use of Fume Hood

Radioiodine in capsule form poses much less radiation safety problems than that in liquid form. When in liquid form, the vials containing ^{131}I should be opened only inside a fume hood using remote handling bottle openers. If these vials are opened outside the fume hood, there is every possibility that the staff involved in therapy may inhale a fraction of the vaporous activity. All operations using ^{131}I should be carried out wearing face masks, gloves, shoe cover and using remote handling tools. Contamination with ^{131}I results in

the accumulation of radioiodine in the thyroid gland. The radioactive iodine uptake measurement of the staff involved should therefore be done weekly to check for any internal contamination with radioiodine in the thyroid gland.

2.19 Specific Instructions to the Patient

It is the combined responsibility of the NM Physician and the RSO/Medical Physicists/technologist to administer the desired dose of radioiodine to the patient. Patient is normally advised to come empty stomach or with light breakfast and is advised after therapeutic dose administration not to eat or drink anything for about 2 h. On completion of such a restriction, they are advised to have as much fluids as possible for fast excretion of unbound radioiodine from the body. They are also advised to void the urinary bladder as frequently as they can and flush the toilet twice after each voiding. This practice not only reduces the radiation dose to kidneys, bladder and whole body of the patients but also helps in their fast release from the hospital.

In female patients of reproductive age group, two important aspects need to be considered:

1. Possibility of pregnancy: Radionuclide therapy is strictly prohibited during pregnancy.
2. Pregnancy after therapy should be avoided for at least 4 months (4–6 months).

2.20 Discharge of the Patient from the Hospital

The Regulatory Authority of each country decides the maximum limit of activity of ^{131}I at which the patient is discharged from the hospital. This can be roughly estimated by measuring the exposure rate from the patient at 1 m distance with a calibrated survey meter, which should read

Table 2.3 ^{131}I release criteria in some countries/organisations (IAEA) [12]

Countries or organisation	Release limit for I-131 (MBq)
European thyroid association	800
Japan	500 or (<30 μSv/h at 1 m)
Germany	259 (based on 3.5 μSv/h at 1 m)
Other EU member states	95–800; mostly 400–800
India	1100
BSS[a]	1100 (guidance level)

[a]The revised BSS is not expected to contain numerical values

50 μSv/h (5 mR/h) for a body burden of 30 mCi. Therefore, when the exposure rate at 1 m from the patient is less than 50 μSv/h, the patient may be released from the hospital in those countries where 1.11 GBq (30 mCi) is the limit for release from the hospital. Release criteria in some of the countries is given in Table 2.3 [12].

In the USA, therapies with ^{131}I for thyroid diseases can be performed within NRC regulations by evaluating the requirements for individual patients and giving advice on reducing radiation exposures through appropriate and patient-specific precautions. The limit is based on the assessment of individual circumstances [13]. If the patient can maintain the distance from the family members at home for a given length of time as suggested by the RSO, and fully satisfies other safety conditions, then large amount of radioiodine may be administered without hospitalisation.

2.20.1 Post Treatment

The patient must be provided with an instruction card detailing the type and duration of radiation protection restrictions they must follow at home. This should also contain details of therapy and necessary radiation protection procedures.

2.20.2 Contact with Spouse/Partner and Others at Home

The patient should make arrangements to sleep apart from spouse or children for a period as suggested by the RSO. The duration of such restriction actually depends upon the body burden of the patient at the time of release from the hospital [14–16]. Contact with family and friends at home should not be for prolonged period for initial few days after release from the hospital [17, 18]. Close contact with pregnant women and young children on a regular basis should be avoided for such a time as suggested by RSO. It would be ideal if arrangement could be made for young children to stay with relatives/friends, after the release of the patient from the hospital, for initial few days/weeks. If such an arrangement is not possible, then prolonged close contact with them should be avoided as per advice of RSO. These figures can only be estimated on individual basis depending upon the radioiodine burden and socio-economic status of the patient. Mathieu et al. [19] have estimated the radiation dose to the spouse and children at home and observed that dose to the spouse is more from radioiodine treatment of thyrotoxicosis patients than those from Ca-thyroid patients. Pant et al. [20] reported that the dose to family members of patients treated with radioiodine (^{131}I) for thyrotoxicosis and cancer thyroid is within 1 mSv in majority of the cases with proper counselling to the patient and their family members at the time of release from the hospital.

2.20.3 Returning to Work

If the work involves close contact with small children or pregnant women, then it should not be resumed for few weeks; otherwise, one can assume the routine work by avoiding close contact with fellow colleagues for prolonged period. European Thyroid Association Committee [18] on radioiodine has published a guideline on this in 1996.

2.20.4 Personal Hygiene and Laundering Instruction for the First Week After Therapy

The normal toilet should be used for voiding the urine. The sitting posture should be preferred to the standing one. Spilled urine should be wiped with a tissue paper and flushed. Hands should always be washed after using the toilet. Any linen or clothes, which become stained with urine, should be immediately washed but separately from other clothes.

2.20.5 Records

A proper logbook should be maintained in the treating facility with details of storage and disposal of radionuclides. The record of dose administration to the patients, their routine monitoring, transient storage of waste for physical decay, the level of activity at the time of disposal should be properly recorded. Decontamination procedures and routine survey should also be recorded in the radiation safety logbook. It should also include the name of the authorised person involved in the procedure.

Annexure 1: Radiation Weighting Factors

Radiation type	Radiation weighting factor, W_R (ICRP 60)	Radiation weighting factor, W_R (ICRP 103)
Photons	1	1
Electrons[a] and muons	1	1
Protons and charged pions	5	2
Alpha particles, fission fragments, heavy ions	20	20
Neutrons, energy <10 keV	5	A continuous function of neutron energy
10–100 keV	10	
>100 keV to 2 MeV	20	
> 2–20 MeV	10	
>20 MeV	5	

[a]Electrons excluding the Auger electrons

Annexure 2: Tissue Weighting Factors (W_T)

Organ/tissue	ICRP-60 (1991)	ICRP-103 (2007)
Bladder	0.05	0.04
Bone	0.01	0.01
Brain	–	0.01
Breasts	0.05	0.12
Colon	–	0.12
Oesophagus	0.05	0.04
Liver	0.05	0.04
Lower large intestine	0.12	–
Lungs	0.12	0.12
Ovaries/testes	0.20	0.08
Red marrow	0.12	0.12
Salivary glands	–	0.01
Skin	0.01	0.01
Stomach	0.12	0.12
Thyroid	0.05	0.04
Remainder tissues	0.05	0.12

Remainder tissues as per ICRP 103 are adipose tissue, adrenals, extrathoracic (ET) region, gallbladder, heart wall, lymphatic nodes, muscle, oral mucosa, pancreas, prostate, small intestine wall, spleen, thymus, uterus/cervix

References

1. International recommendations for X-ray and radium protection, Stockholm; 1929.
2. International recommendations on radiological protection: revised by the ICRP at the sixth international congress of radiology, London, July, 1950.
3. International commission on radiological protection Publication 103. Ann ICRP. 2007;37(2–4).
4. International commission on radiological protection. Statement on tissue reaction. Ann ICRP. 2011.
5. Courtney JC, Mendez P, Hidalgo-Salvatierra O, Bujenovic S. Photon shielding for a positron emission tomography suite. Health Phys. 2001;81(Suppl):S24–8.
6. Roberts FO, et al. Radiation dose to PET technologists and strategies to lower occupational exposure. J Nucl Med Technol. 2005;33:44–7.
7. National Radiological Protection Board (NRPB). Guidelines on patient dose to promote the optimisation of protection for diagnostic medical exposure (report of an advisory group on ionising radiation). 1999;10(2).
8. International Atomic Energy Agency. Nuclear medicine resource manual. Vienna: IAEA; 2006.
9. Hicks RJ, Binns D, Stabin MG. Pattern of uptake and excretion of 18F-FDG in the lactating breast. J Nucl Med. 2001;42(8):1238–42.
10. International Atomic Energy Agency (IAEA). Basic medical radiation safety package part a: principles of radiation safety; 2001.
11. International Atomic Energy Agency (IAEA) TECDOC-1183. Management of radioactive waste from the use of radionuclides in medicine; 2000.
12. Release of patients after radioiodine therapy. International Atomic Energy Agency with contributions from the ICRP, Safety report series 63. Vienna: IAEA; 2009.
13. Sisson JC, et al. Radiation safety in the treatment of patients with thyroid diseases by radioiodine [131]I: practice recommendations of the American Thyroid Association. Thyroid. 2011;21(4):335–46.
14. Barrington SF, Kettle AG, et al. Radiation dose rates from patients receiving iodine-131 therapy for carcinoma of the thyroid. Eur J Nucl Med. 1996;23:123–30.
15. Klerk John MH. [131]I therapy: inpatient or outpatient? J Nucl Med. 2000;41:1876–8.
16. Beierwalts WH, Widman J. How harmful to others are Iodine-131 treated patients. J Nucl Med. 1992;33:2116–7.
17. Erkan I, Charles R, Wison B, et al. Iodine-131 contamination from thyroid cancer patients. J Nucl Med. 1992;33:2110–5.
18. European Thyroid Association Committee on Radioiodine. Euro J Nucl Med. 1996;23:13–15.
19. Mathieu I, Caussin J, Beckers C. Regulations and policies on radioiodine ^{131}I therapy in Europe. Thyroid. 1997;7:221–4.
20. Pant GS, Sharma SK, Bal CS, Kumar R, Rath GK. Radiation dose to family members of hyperthyroidism and thyroid cancer patients treated with [131]I. Radiat Prot Dosim. 2006;118(1):22–7.

Further Reading

International Atomic Energy Agency. Applying radiation safety standards in nuclear medicine. Safety Reports Series No. 40. Jointly sponsored by the International Atomic Energy Agency, International Labour Office, International Organisation for Medical Physics, Pan American Health Organisation, World Federation of Nuclear Medicine and Biology and World Health Organisation. Vienna: IAEA; 2005.

Nagaratnam A. Radiological protection: a summary handbook of ICRP publications and recommendations. New Delhi: DRDO, Min of Defence; 1995.

Pant GS. Radiation safety for unsealed sources. 2nd ed. Mumbai: Himalaya Publishing House; 2000.

Radiological protection of patients in diagnostic and interventional radiology, nuclear medicine and radiotherapy. In: Proceedings of Int conf, Spain. Vienna: IAEA; 2001.

Non-imaging and Radiopharmacy Instrumentation in Nuclear Medicine

3

Eman Al-Anezi, Taher Hosny, and Magdy M. Khalil

Contents

3.1 Introduction

Non-imaging radiation detection and measurement instruments are of massive importance in nuclear medicine practice. This section illustrates a review on basic principle, performance, application, and the recent quality control recommendations for those of particular usage and daily applications. Three major categories are covered including non-imaging equipment, radioactive reference sources, and radiopharmacy equipment and tools. Non-imaging equipment category includes dose calibrator, well counter, thyroid uptake probe, intraoperative probes, survey meters, area monitors, and CT dosimetry toolkits. The second cate-

gory of tools used in nuclear medicine is an array of radioactive reference sources that are commonly used in calibration and daily quality control and assurance. The last category covered radiopharmacy laboratory equipment including laminar flow safety cabinet, high-performance liquid chromatography (HPLC), thin layer chromatography scanner, gas chromatography, gamma spectrometers, pH meter, and specialized tools for the determination of bacterial endotoxins. More details of these equipment could be found in other specialized references and textbooks.

3.2 Non-imaging Equipments

3.2.1 Dose Calibrator

In nuclear medicine departments, usage of a dose calibrator is a must. Prior to each radiopharmaceutical injection or administration, the radioactivity

E. Al-Anezi · T. Hosny
Nuclear Medicine and Cyclotron Department, King Hamad University Hospital, Busaiteen, Bahrain

M. M. Khalil (✉)
Medical Biophysics, Department of Physics, Faculty of Science, Helwan University, Cairo, Egypt

of such a prescribed radiopharmaceutical has to be well assayed and measured using the dose calibrator. It is a calibrated re-entrant ionization chamber filled with argon gas under pressure (typically 1–2 MPa or 10–20 atm), coupled to a high-voltage power supply and an electronic circuit that converts and displays chamber response.

The chamber is a well type (close to 4π geometry), and the wall of the chamber is a thin aluminum. It contains two electrodes having an electric potential between them. When a beam of ionizing radiation passes through the chamber, it produces electrical charges that are collected by positive (anode) and negative (cathode) electrodes forming total amount of current (time-averaged ionization current). Ionization current is measured using sensitive current-measuring devices called electrometers with a fixed time constant and converted to a voltage signal, which is amplified, processed, and displayed in digital form in units of radioactivity.

The dose calibrator chamber is usually provided with at least 6 mm lead to eliminate the background radiation that may be present in the working environment. This shielding also provides protection to the operator by minimizing the exposure rate resulting from the radioactivity being used and also prevents efficiency changes caused by scattering material in the vicinity. It is important to note that the shielding setup upon installation should remain the same after the calibration is carried out and any changes to that setup affect the calibration results.

A sample holder of low z material is provided into which a vial or syringe can be placed to ensure that it is positioned optimally within the chamber and to ensure reproducibility and consistency of the measurements if the same or different sample is inserted. The dose calibrator may include a printer to document the activity measurements or an RS-232 serial communications port or Universal Serial Bus (USB) port to interface the calibrator to radiopharmacy computerized management systems.

The dose calibrator can be calibrated by the manufacturer for the commonly used radionu-clides in medical facility. The calibration is being done through comparison with an appropriate standard activity that is directly traceable to a national primary standard. Using the primary or traceable standard sources, a calibration factor for the ionization chamber can be determined for each specific radionuclide. These calibration settings are then saved within the system for each specific radionuclide.

The use of dose calibrator in a medical facility should serve to provide reliable measurements of the radioactivity being assayed. However, some uncertainty within these measurements can be detected ($<0.0 \pm 5\%$) and dosage limit to the prescribed dose is ($<\pm10\%$). For such a reason, the dose calibrator has to be under quality system to ensure the reliability of the readings (see Table 3.1). Sources of such uncertainty can be caused by the fact that the calibration settings are made upon certain source geometry, volume, material type and thickness, and position in the chamber. The calibration factor can also be affected if a different container type (e.g., syringe) is used which affects the readings.

Also, the type of material of the container can contribute to uncertainty of the reading due to self-absorption that could occur on the surface of the container. This is significant in beta emitter radionuclide, and since the energy starts from 0 till the maximum transition, the sensitivity of the dose calibrator to beta emitter radionuclide is low. Further common sources of uncertainty are high activity and the increase of probability of ion pair recombination, chamber shielding, possible errors in calibration, and the differences between the standard calibration containers and other types [2, 3].

It is crucial for the operator to understand the importance of the correct choice of the radionu-clide before measurement as the dose calibrator itself would not be able to recognize the type of the radionuclide within the container. However, the reading will be done automatically in units of activity (Becquerel or curies). Table 3.2 compares between two different commercially available dose calibrators.

Table 3.1 Routine quality control tests for a dose calibrator

Routine test	Purpose	Acceptance	Daily	Monthly	Annually
Physical inspection	Check whole system including source holders, cables, and other accessories for damage	✓	✓	✓	✓
High voltage	Check system constancy and correct operating voltage	✓	✓	✓	✓
Clock accuracy	Check that the calibrator clock is the same as the time of day	✓	✓		
Zero adjustment	Check that the display is at zero when no radioactivity is present	✓	✓	✓	✓
Background counts	Check background response under operational conditions appropriate for a particular radionuclide; to detect contamination	✓	✓	✓	✓
Constancy (relative response)	Check the stability and reproducibility of the ionization chamber, electrometer, and calibrator nuclide settings. Using long lived source (e.g. Cs-137) absence of any radioactive impurities. Relative chamber response has to be monitored for any drift	✓	✓		
Stability	Check the short-term counting precision	✓			✓
Accuracy	Check the accuracy of the activity reading	✓			✓
Linearity	Confirm that the calibration setting for a particular radionuclide indicates the correct activity over the entire range of use	✓			✓
Subsidiary calibrations	For containers and volumes with no calibration factor provided by the manufacturer	✓			✓

Data are adapted from [1] with permission from Springer Publishing

3.2.2 Well Counter

Well counter is routinely used in nuclear medicine laboratories including research, clinical applications, as well as for radiation protection purposes. It is one of the most sensitive detectors for gamma rays. It consists of a single solid cylindrical crystal of thallium-doped sodium iodide-NaI (Tl) (at least 2×2 in., with a 3/4-in. diameter well about 1–1/4 in. deep) detector with a hole in the center for a sample to be placed. The crystal is surrounded by thick lead shielding around 5 cm or greater to minimize the background due to ambient radiation [6]. The sample can be collected for certain volume or shape in a tube, other kinds of sample could be blood, urine samples, or wipes from surveys of removable contamination.

The well counter consists of the cylindrical scintillation crystal (well type) coupled to photo-

multiplier tube (PMT) in connection with other electronics such as preamplifier, amplifier, pulse-height analyzer (PHA), and scalar timer. A well counter is an extremely sensitive detector. The counting results can be expressed on activity in the range of micro curies (~100 kBq). At higher activities, serious dead time problems do emerge, leading to count rate underestimation.

3.2.3 Thyroid Gamma Probe

Thyroid gamma probe is categorized under the well-known radiation measurements and counting detectors known as thyroid uptake probe. The thyroid uptake is measuring the fraction of an administered amount of radioactivity that accumulates in the thyroid at selected times following oral administration of ^{131}I-iodide,

Table 3.2 Specifications of two widely used dose calibrators[a]

Specifications	Capintec CRC	Atomlab 500
Ionization chamber dimensions	26 cm deep × 6 cm diameter	15.24 × 39.37 cm diameter
Measurement range	Auto-ranging from 0.001 MBq to 250 GBq	Auto-ranging from 0.0004 MBq to 3700 GBq
Nuclide selection	8 pre-set, 5 user-defined (80 radionuclide calibrations in memory)	12 pre-set, user-defined (98 radionuclide calibrations in manual)
Display units	Bq or Ci	Bq or Ci
Electrometer accuracy[b]	<±2%	±1% or 0.2 μCi, whichever is greater.
Response time[c]	Within 2 s	1–2 s for doses greater than 200 μCi; 3 s for doses greater than 20 μCi
Repeatability[d]	±1%	±0.3% above 1 mCi short term (24 h)

[a]Source: [4, 6]

[b]Electrometer accuracy: electrometer's measurement of current is traceable to primary standards

[c]Response time: time to convert and display the ionization current into an indication of the activity (MBq)

[d]Repeatability: the precision with which a single measurement is made

[123]I-iodide, or ^{99m}Tc-pertechnetate. Commercially available thyroid uptake probes are generally supplied as integrated, computerized systems with automated data acquisition and processing, capabilities, yielding results directly in terms of percent uptake (see Fig. 3.1). The thyroid probe shown typically consists of a wide aperture, diverging collimator, a 5-cm thick × 5-cm diameter sodium iodine NaI(Tl) crystal with an open cylindrically shaped, PMT, preamplifier, amplifier, an energy window, and a stand gantry. Figure 3.2 demonstrates the probe collimator and other connected components.

Determination of thyroid uptake includes measurement of counts collected for 1 min over the thyroid gland. Another measurement is then taken over the patient's mid-thigh for 1 min and at the same distance (e.g., 20–30 cm), taking care

to exclude the urinary bladder from the detector field. A source of the same radionuclide of identical activity to that given to the patient is placed in a standardized neck phantom, shown in Fig. 3.3, and again counted for 1 min using the same geometry. The room background is also counted for 1 min with the neck phantom with no radioactive material inside the room or the phantom. This approach is known as the two-capsule method, since one ^{131}I capsule is administered to the patient while a second, identical capsule serves as the standard and is counted with each uptake measurement [5, 7].

Alternatively, the radioiodine capsule can be counted in the neck phantom before oral administration, and the counts obtained can be corrected for decay at each patient counting session. This later approach is named one-capsule method [6]. The radioiodine uptake (RAIU) is then calculated using the following relationship:

$$RAIU = \frac{Neck\ counts - Thigh\ counts}{Phantom\ counts - Background\ counts} \times 100\%$$

The time of measurement is approximately 24 h after the radiopharmaceutical administration. An additional uptake measurement may also be performed at 4–6 h, particularly in cases of suspected rapid iodine turnover.

The routine quality tests that can be performed to implement quality assurance of thyroid uptake probe are many and can be summarized as follow. The operator must check all physical parts, collimator checks, probe mounting, and cable connections for any possible defect before using the equipment. Background count rate needs also to be checked. It is helpful to identify the count rate level in the absence of the sample and to detect any possible contamination in the area.

Operating voltage constancy and accuracy must also be performed before using the probe. Sensitivity and energy spectrum have to be inspected, and the energy window must be centered on the photopeak. System stability looks at short-term counting precision of the equipment and can be performed every 6 months [1]. The use of gamma camera method in measuring thy-

Fig. 3.1 A photograph of Atomlab™ Thyroid Uptake System, showing one example of thyroid uptake probe interfaced to computer system (PC) and printing facility. (Reproduced with permission)
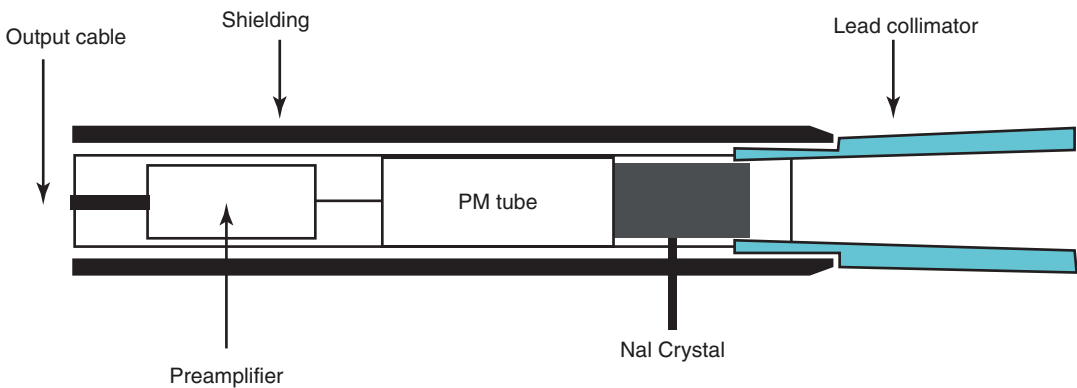
Fig. 3.2 Components of thyroid uptake probe

roid uptake using iodine-131 capsules has been proposed as an alternative providing measurements as accurate as the thyroid uptake probe [8]. However, gamma camera method requires validation versus known standards.

3.2.4 Intraoperative Probes

In early days of nuclear medicine practice, the intraoperative probe was a Geiger–Müller (GM) counter detecting phosphorus-32. In 1956, Harris
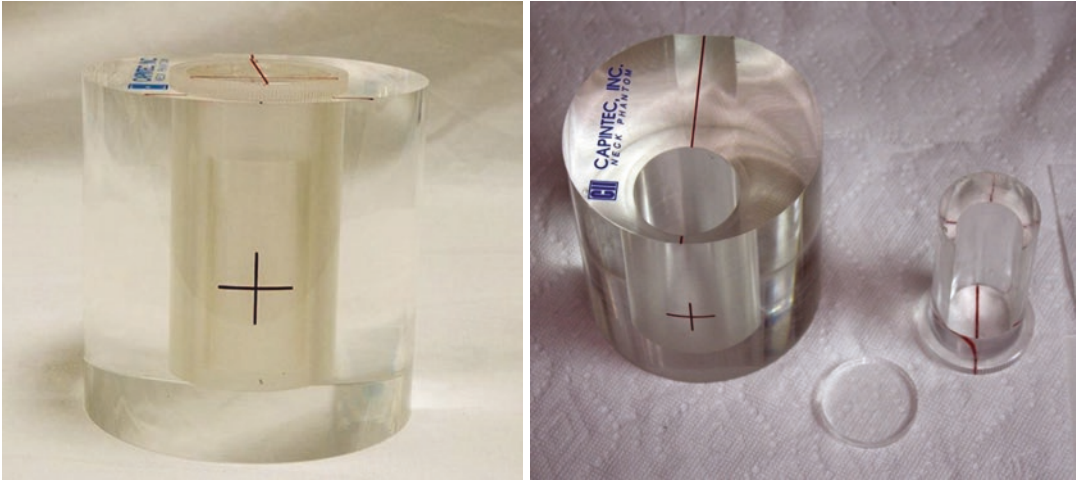
Fig. 3.3 The CAPTUS neck phantom is made of clear Lucite designed to represent a patient's neck (Mirion Technologies, Capintec, Inc., with permission). It has a two-part insert that allows counting from a bottle, vial, or capsule. A capsule holder is supplied to enable the user to count capsules directly, without having to dissolve them

et al., at the Oak Ridge Institute of Nuclear Studies Medical Hospital, reported the first radioguided surgery involving gamma detection probe systems [9]. They used a handheld scintillation detector device to detect gamma rays from ^{131}I that had been administered to a patient with differentiated thyroid cancer. Nowadays, intraoperative probes are widely used in the management of cancer and within the practice of surgery.

The intraoperative probe is a small handheld counting device for tumor localizations and removal in surgery. After the administration of a radiopharmaceutical that accumulates in the tumor of a patient, the surgeon detects the tumor with the intraoperative probe detection sensitivity (i.e., the probe provides the surgeon with an acoustic guide to locate the tumor over the large surgical field) and resects it during the surgery. However, it can be used either as radioguided sentinel lymph node biopsy (SLNB) or radioguided surgical resection of tumors [10].

Intraoperative detectors are categorized into two types: gamma probes that detect photons and beta probes for positron and beta-minus emitters. These detectors can be available as either scintillation detectors (both crystal and plastic types) or semiconductor detectors. A typical schematic diagram for intraoperative probes either scintillator or semiconductor is illustrated in Fig. 3.4. The crystals used in scintillator detector probes can be NaI(Tl), CsI(Tl), cerium-activated LSO, BGO, and cerium-doped GSO. Radionuclides that are of common use are ^{99m}Tc colloid for radioguided SLNB and the positron emitting radionuclide, e.g., (^{18}F) for resection of tumors. The choice of the appropriate detector depends on the surgeon needs and the surgery type. Table 3.3 compares between scintillation crystal and semiconductor-based intraoperative probes.

Recent developments of handheld self-contained gamma detection probes introduced the integrated Bluetooth wireless technology to eliminate the need for cables connecting the probe to the control unit, and to guarantee the comforts of the surgeon. Figure 3.5 shows a schematic drawing of the system.

Various quality control tests for intraoperative gamma probes (in accordance with Standard NEMA NU 3-2004) can be performed to ensure the high performance of this device; these tests include sensitivity test which can be done using pulse rate/activity (cps/MBq) carried out on different distances with selected nuclides and energy window. Measurements are to be carried out in air, in a scatter medium, and through side shielding in air. Also, short-term sensitivity stability can be done for a certain nuclide performing 20
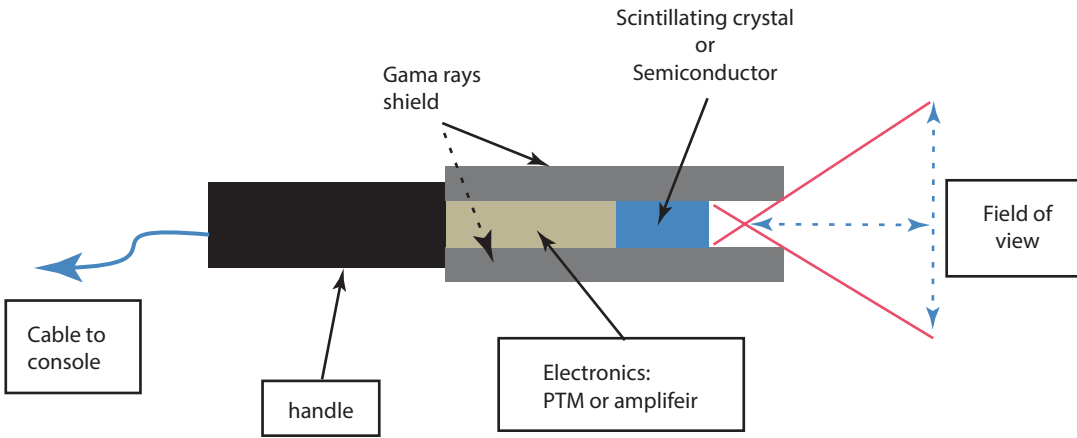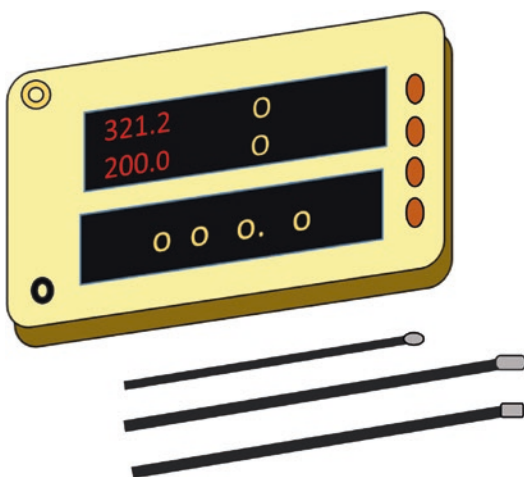
Fig. 3.4 A diagram for a typical design of intraoperative radiation detector

Table 3.3 Comparison between the advantages and disadvantages of scintillation and semiconductor detectors

Scintillator detector	Semiconductor detector
Higher sensitivity	Higher energy resolution
Scatter is relatively significant	Scatter rejection capability
Heavy	Has a very thin entrance window that enables counting of low energy β and γ rays
Poorer energy resolution and scatter rejection	Direct detectors with improved energy resolution
Much bulkier	Can be manufactured in very small sizes and it is expensive

Fig. 3.5 Schematic diagram of intraoperative gamma probe with different probe shapes and geometries

sequential measurements (pulses/selected time), observed, and expected standard deviance and chi-square value to be recorded. Spatial resolution test is carried out to determine the FWHM and FWTM at 30 mm source-detector-distance in water. Count rate capability in a scatter medium is tested by calculating the decay corrected count per time (cps) and comparing it to a reference count value to achieve a control reading within the acceptable range (less than 2 standard deviations from the reference value). Angular resolution in a scatter medium measures the FWHM and FWTM in degrees with 30 mm source–detector distance in water using a selected nuclide and an energy window. Both absolute and relative energy resolution can be performed. Side and back shielding efficiency are also to be tested.

3.2.5 Survey Meters and Area Monitors

In radiation safety practices, there are instruments routinely used to monitor and evaluate the radiation level (exposure rate or counts rate, e.g., contamination). Survey meter is a battery-operated, portable, handheld detector that can be either a gas-filled detector or solid-state detector (scintillator or semiconductor detectors).

Gas-filled detectors generally include ionization chamber, Geiger–Müller (GM) counter and
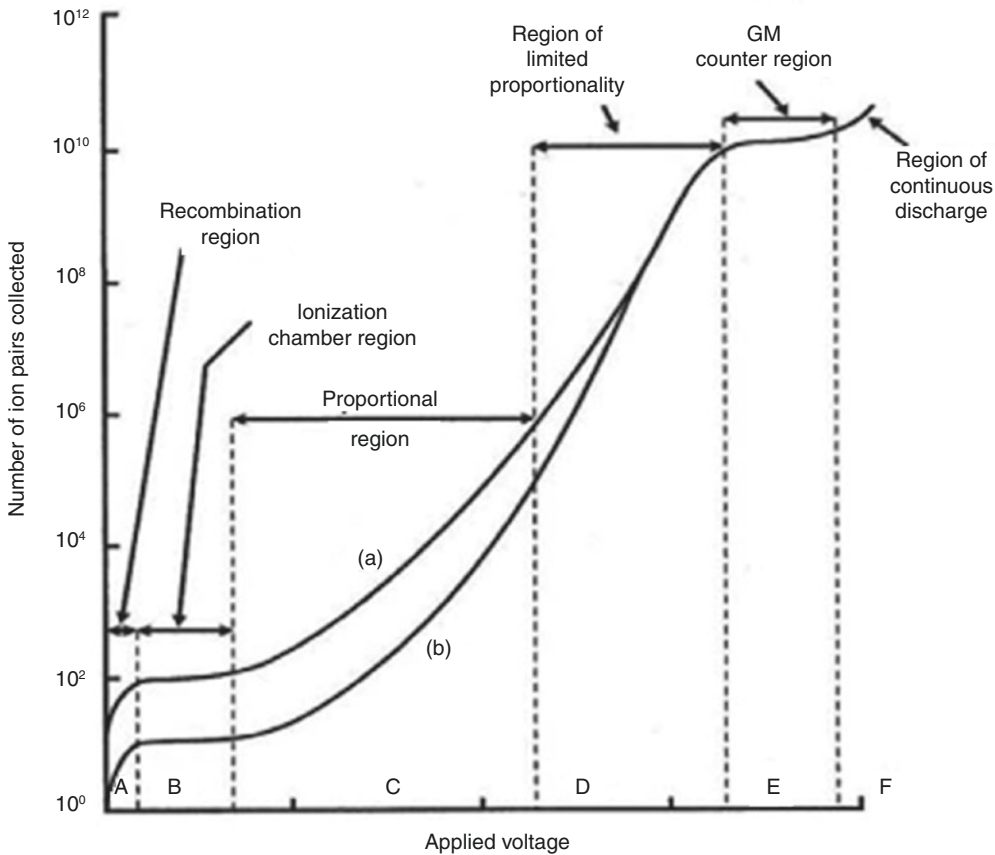
Fig. 3.6 Characteristic regions of gas-filled detectors

proportional counters. Nobel gases are generally used in these detectors. All respond to radiation by means of ionization-induced electrical currents generated in the ionization chamber, but depending on the different design and the voltage applied between the two electrodes, the detector operates in certain region specifying its own type (ionization region B, proportional region C, or Geiger–Müller (GM) region E), shown in Fig. 3.6.

Ionization current is being displayed on a monitor (digital type) or on a front-panel meter. The survey meter can be calibrated to illustrate the units of radiation level as exposure rate (e.g., sievert per hour) or air kerma (gray per hour). The survey meters may cover a range of radiation level measurement from nSv/h to Sv/h, but the typical range in use is μSv/h to mSv/h. Depending upon the electronics used, detectors can operate

in a "pulse" mode or in the "mean level" or current mode. Proportional and GM counters are normally operated in the pulse mode. Since ionization detector operates in the current mode, it is suitable for high-dose rate measurement, due to its relatively flat energy response and air kerma rate independence [11].

Geiger–Müller (GM) operates on pulse mode (which means that the signal pulses have the same amplitude regardless of the energy of the incoming radiation) and under high potential difference providing a high electron amplification factor, and thus, GM has a high sensitivity. Therefore, GM can be well suited for low-level surveys, for example, monitoring for radioactive contamination. Further, uncompensated GM detector can be used for evaluating the barrier thickness of a monoenergetic source. For energy discrimination, end window GM counters have a

removable buildup cap to discriminate β from γ rays. For β measurements the end cap must be removed to allow β particles to enter the sensitive volume.

Solid state scintillator detector (composed of organic and non-organic solid crystals, e.g., NaI(Tl)) converts the energy of the incoming gamma rays into light, these detectors use non-air-equivalent crystal as the detection medium, thus suitable for gamma rays (measure only the count rates). However, it is able to capture specific spectroscopic profiles and identify the measured radioactive materials. On the other hand, solid state semiconductor detectors can be intrinsic (very pure material) and extrinsic or doped. The most common semiconductor detector made of silicon (Si) or germanium (Ge) crystal suitable for both the gamma ray and the X-ray detections (operates similar to ion chamber, create electron-hole pairs instead) and convert the incoming energy into electrical pulses; their sensitivity is about 10^4 times higher than that of gas filled detectors [12].

The most common neutron survey meter gas-filled detector type are proportional counters, ionization chambers, and fission chambers. The detection of neutrons in theses detectors can be thermal through nuclear reaction, fast neutron via recoil interaction, and/or detection of neutrons that induce fissions in fissionable material (e.g., uranium) coated inside the inner wall of the chamber. Detectors filled with BF_3 and ^3He gases are thermal neutron detector type, which operate in the proportional mode, and have sufficiently large cross sections and high Q-values to convert slow neutrons with high probability into charged particles with enough kinetic energy to exceed detection thresholds. In case of ^4He- and CH_4-filled detector which called the fast neutrons detectors, neutrons produce light recoil nuclei (hydrogen) to ionize the gas in the tube. Moreover, detector lined with a boron (^{10}B) compound plated on the inside of the wall is considered as proportional counter where neutrons detection rely on boron coating compound causing an (n, α) reaction, and the α particles can easily then be counted or detected by their ionizing interactions current [13, 14]. All survey meters should be calibrated using a reference instrument that is traceable to a national standard laboratory.

Area monitors are importable instruments being fixed individually in a selected location for monitoring the radiation level within that specified area or facility. This instrument provides an audible and visible alarm types to warn the personnel within the area of the high radiation level if detected. The data of such monitors can be displayed on the monitor itself, and the data is integrated to master computer station, which is continuously monitoring the different areas through a special graphical/digital user interface that report the rooms reading in the selected unit (e.g., μSv/h). These devices may be known as gamma probes, ion chamber detector, or compensated GM counter detector type (see Fig. 3.7).

3.2.6 CT Dosimetry

The advent of X-ray computed tomography (CT) in hybrid nuclear imaging devices have received particular interest in the last two decades. CT scanner design with new features and capabilities have significantly been improved over the years, thanks to the amazing rapid developments in CT technology. This in turn contributes to the implementation of many new clinical applications based on CT which continues to grow, often by 10–15% per year [15]. However, the CT dose becomes a demanding concern in radiation protection and dose optimization to control radiation exposure within the CT applications.

The use of CT dose index (refereed as CTDI) is a useful tool for CT dose measurement and optimization protocols. By using CT pencil ionization chamber of sufficient length (100 mm is most commonly used) to cover the CT dose profile, one can estimate the delivered CT dose to phantoms of standard dimensions at several locations.

Phantoms adopted by the US Food and Drug Administration (FDA) were a 32-cm-diameter cylindrical acrylic phantom to represent an adult abdomen and a 16-cm-diameter version to represent an adult head or small pediatric bodies. Both of the phantoms are 15-cm thick (in the z-axis
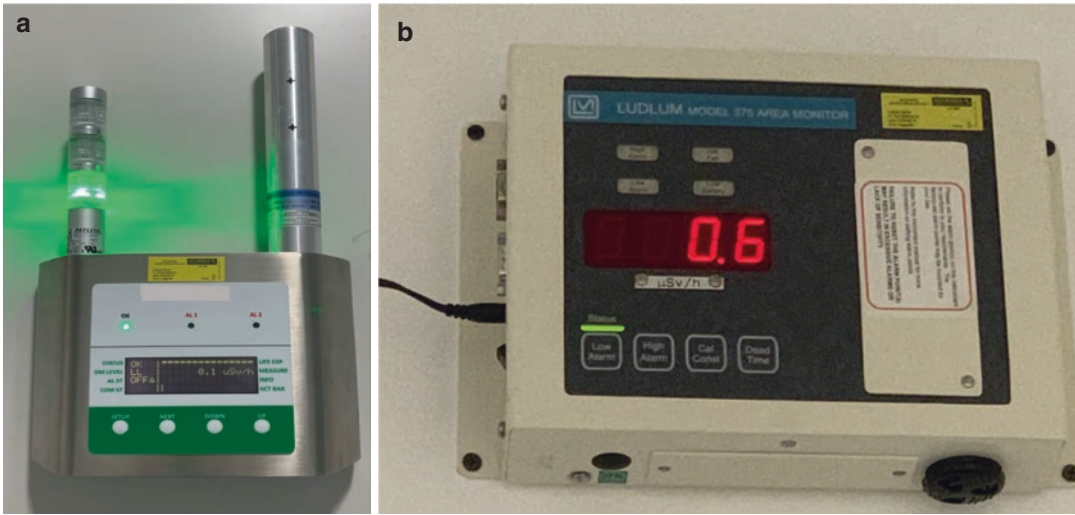
Fig. 3.7 Digital area monitor from different manufacturers. (**a**) Gas-filled detector type 2 energy compensated Geiger–Müller tubes for low and high dose rate measurements manufactured by a previous vendor named MecMurphil, Italy. (**b**) LUDLUM area monitors that incorporate an internally energy compensated GM. (LUDLUM measurements, Inc., with permission)
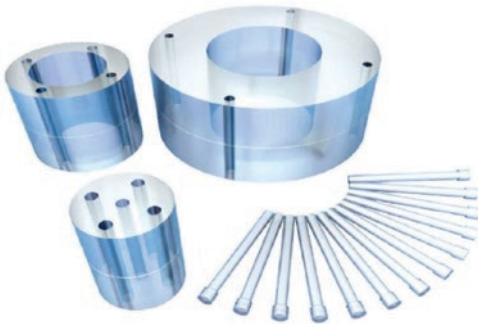
Fig. 3.8 CT scan test phantom/head/whole body/pediatric. RaySafe, CT Fluke Biomedical. (Image credit of RaySafe, Sweden, with permission)

direction) and contain several 1-cm-diameter holes for the insertion of the ionization chamber. The holes are at the center of the phantom and at a 1-cm depth at the 3-, 6-, 9-, and 12-o'clock positions (referred to as the peripheral sites). Figure 3.8 shows one commercial set used in CT dosimetry calibration.

CTDI can be defined as the z average dose (to the phantom location at which it is measured) from a complete series of slices (either axial or helical scan). The CTDI can be measured using calibrated electrometer and pencil ionization chamber of 100 mm length known as $CTDI_{100}$. The dose measurements differ from the center to the peripheral locations within the body phantom because of the scattering dose getting increased toward the center, further, the ionization chamber includes the tails of dose profile and therefore both the primary and the scatter radiation are being included. $CTDI_w$ quantity is that combines both the values measured at the center and the periphery locations within the standard phantom. The dose quantity $CTDI_{vol}$ takes into account the helical pitch or axial scan spacing and can be displayed by the CT system console in front of the operator. Table 3.4 displays important quantities and definitions used in CT dosimetry.

When irradiating patients during several examinations, the dose delivered is a major concern. Dose length product (DLP) is a term used to represent the amount of radiation delivered to the patient

Table 3.4 Terminology used in X-ray computed tomography (CT)

Quantity	The International Electro Technical Commission (IEC)
Measured free-in-air	
CT air kerma index	$\mathrm{CTDI_{air}} = \dfrac{1}{NT}\displaystyle\int_{-\infty}^{\infty} K_a(z)\,\mathrm{d}z$
Measured in standard phantom	
Weighted CT air kerma index	$\mathrm{CTDI_w} = \dfrac{1}{3}\mathrm{CTDI}_{100,c} + \dfrac{2}{3}\mathrm{CTDI}_{100,p}$
Normalized weighted CT air kerma index	$n\mathrm{CTDI_w}$
Volume CT air kerma index	$\mathrm{CTDI_{vol}} = \mathrm{CTDI_w}\,/\,\mathrm{pitch} \quad \mathrm{pitch} = \dfrac{1}{NT}$
CT air kerma—Length product	$\mathrm{DLP} = \mathrm{CTDI_{vol}} \times L$

N = actual number of data channels used during one axial acquisition, T = width of each channel ($N \times T$ = nominal radiation beam width), L = is the total z-direction length of the examination

by calculating the $\mathrm{CTDI_{vol}}$ multiplied by the whole examination length. However, the probable risk to the patient cannot be determined unless a radiosensitivity factors of the irradiated tissues/organs are taken into account to derive what is called effective dose, E [16] (see Chap. 9 for further details).

3.3 Standard Sources

To ensure a high level of performance of nuclear medicine instrumentations, reliability and accuracy of measurements need to be continuously verified and checked. Therefore, there are long-lived reference sources that are needed to support many periodical quality assurance procedures. Reference sources are often sealed, long-lived radionuclides, and can be ordered with various activities and geometries from commercial vendors. These sources must be traceable to a national standards dosimetry laboratory; traceability helps ensure the accuracy of the calibrated activity. National primary standards are maintained by the relevant National Metrology Institute (NMI), such as the National Physical Laboratory (NPL) in the UK, the National Institute of Standards and Technology in the USA, and the Australian Nuclear Science and Technology Organization (ANSTO) [2]. However, the world measurement standards authority, Bureau International des Poids et Mesures (BIPM), organizes the process

of standard comparison between the NMIs to confirm the accuracy of its standards. Another organization helping the cooperation between NMI within the European region is the European Association of National Metrology Institutes (EURAMET), who (beside other activities) also organizes comparative measurements. A number of standard sources that frequently used in quality assurance/quality control of nuclear medicine equipment will be discussed.

3.3.1 Reference Radioactive Sources

The National Institute of Standards and Technology (NIST) is the national metrology institute of the USA which provides physical measurements and standards in a variety of fields and industries with expansion developed to include the medical imaging. Particularly in radiation and radioactivity standards, radioactive standards reference material (SRMs) has been developed and produced and source calibrations are performed to guarantee the traceability for radiopharmaceuticals being used in medical imaging to ensure the accuracy and precision of the quantitative measurement within the medical modalities related to patients. NIST provides a framework for traceability through establishing primary standard, developing secondary standards, and disseminating those standards [17].

3.3.2 Gamma Camera Reference Sources

Standard radioactive sources are important accessories for performing daily quality control tests in nuclear medicine departments. As explained in Chap. 11, gamma camera and SPECT systems need a comprehensive quality assurance program that maintains clinical images of high quality and accurate diagnostic performance. Uniformity test of SPECT system describes the degree of uniformity of count density in the image when the detector is flooded with a spatially uniform flux of incident photons. Uniformity test can be performed using either fillable flood source or ^{57}Co flood sheet source. The flood source is a long-lived radionuclide in the form of an extended sheet of plastic, with photon energy (i.e., 122 keV) similar to the most commonly used in clinical practice, 140 keV.

Fillable flood source is a sheet of Perspex that is filled with water and ^{99m}Tc pertechnetate. The preparation of the phantom is advised to be carried out with radioactive range of 10–15 mCi at time of filling. The use of such source requires a preparation and care during the filling to ensure uniform/homogenous mixing and also to ensure that the phantom is free of air bubbles that may result due to shaking and filling. The solution should be refilled regularly after the phantom, wash with water and diluted sodium hypochlorite in order to avoid growth of algae, which can bind with ^{99m}Tc compounds, causing hot artifacts [18].

Some limitations of the fillable flood source usage are the exposure due to radiation during the preparation as well as the time consumed to make sure of the suitability of the phantom. Phantoms with thick walls and a large volume have shown an increase in counts in the center of the FOV, which is possibly due to scatter and septum penetration (depending on the collimator and radionuclide used).

The ^{57}Co flood source is a sealed sheet that is commercially available and comes at desired activity up to 15 mCi. It is very convenient for daily quality control tests due to handling simplicity and relatively long half-life (270 days). However, a caution needs to be taken while handing the source, especially newly purchased, due

to contamination of other isotopes including ^{56}Co, ^{58}Co, and ^{60}Co impurities. An operator may therefore experience some artifacts or failure of the routine daily uniformity test whenever a new ^{57}Co flood sheet source is used, that could disappear as time passes due to radioactive decay. Also, high count rates and pile-up effects from the scatter and septum penetration of the high energy photons may contribute to alternation of the test results. These problems can be avoided by using less count rate sources and maintain a distance between the source and the detectors at least 15 cm.

3.3.3 PET Scanners

In PET, primary sources and calibrated phantoms and methods have been introduced for improving image consistency and quantification accuracy. ^{18}F and ^{68}Ge are common radionuclides used in calibration of PET instrumentation. NIST developed primary activity standards for positron emitter radionuclides such as ^{18}F through various methods, but due to the short half-life of ^{18}F (109.8 min), it was not possible to be prepared for distribution [19]. As a result, ^{68}Ge/^{68}Ga source (half-life 270.9 days) was introduced as a reasonable surrogate of ^{18}F to be used for calibration by applying appropriate correction factors. Such correction factors would strongly depend on the instrument and the geometry in which the source is measured. Dose calibrator calibration methodology has been established using the ^{68}Ge-based calibration sources (syringe) for the calibration of dose calibrators for the measurement of ^{18}F [17].

Calibration methodology is developed for large ^{68}Ge solid PET phantoms, making traceable phantoms commercially available. NIST established a prototype of large volume (30 cm length × 20 cm diameter, approximately 9 L) of solid ^{68}Ge cylindrical phantom in epoxy as a surrogate for ^{18}F. This phantom has a calibrated value for the amount of ^{68}Ge that is directly traceable to a national standard. Similarly, NIST provides calibration of other epoxy ^{68}Ge phantoms of other manufacturers. These phantoms can be used for calibration and monitoring performance
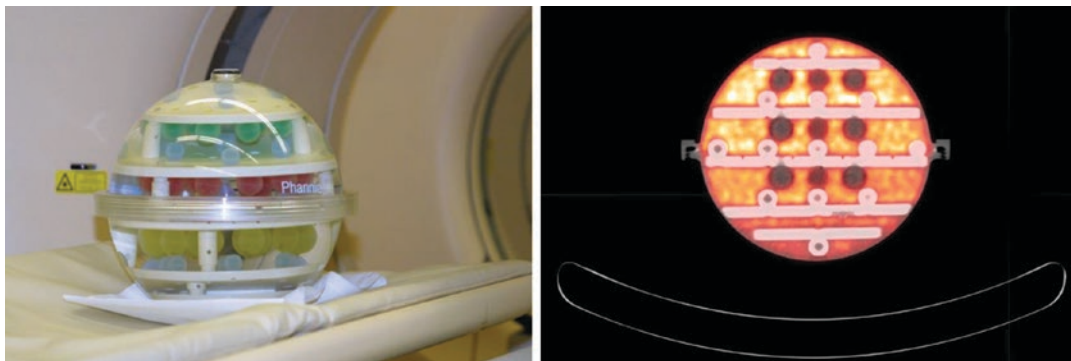
Fig. 3.9 NIST's first standard phantom for calibrating the PET-MR machines. This phantom consists of a plastic sphere about the size of a person's head filled with grids of smaller plastic spheres containing salt solutions that become magnetized in a magnetic field. Also includes a small, calibrated amount of fluorine-18 (^{18}F); a PET image shows the glowing of ^{18}F inside the phantom [20]

of the scanners during clinical trials in a way that is traceable to national standards.

Other efforts are still going on for PET/MR phantom design and calibration which includes future inserts of calibrated samples of solid, longer-lived radioactive sources such as solid ^{68}Ge hemispheres or discs, and an improved filling system that will make it easier and faster to introduce radioactive background solutions. Figure 3.9 shows NIST approach to tackle this issue.

3.4 Radiopharmacy Equipments

Radiopharmaceuticals require a well-designed quality program during production and preparation steps to assure the high quality of the final product. The quality program should specify and meet the acceptance limit set forth by national and/or international guidelines. The preparation procedures should be performed under certain conditions of microbial and particle contamination. Laminar flow and safety cabinet can verify these conditions of sterility for certain types of radiopharmaceuticals preparation. Further, quality control procedures are required to ensure that the final product is complying with standard specifications of this specific radiopharmaceutical. High-performance liquid chromatography (HPLC), thin layer chromatography (TLC), gas chromatography (GC), and gamma spectrometer are among the most important tools mainly required for radiopharmaceutical quality assurance purposes.

3.4.1 Laminar Flow Safety Cabinet

Most radiopharmaceutical administrations are injected through intravenous injection. To avoid microbiological contamination, particulate or pyrogens insertion into finished product, and to ensure radiation protection principles, radiopharmaceutical preparation should be carried out in a designated shielded area under aseptic condition or laminar flow cabinet (LAFC) [21, 22]. Laminar flow is defined as airflow in which the entire body of air within a confined area moves with uniform velocity along parallel lines with a minimum of eddies [21]. By design, laminar flow aims to maintain uniform velocity and direction of air flow at any cross section. Further, all air entering the system must be filtered by means of high-efficiency particulate air (HEPA) filter. Laminar flow safety cabinet provides three types of protection, namely personnel, environment, and product from airborne contamination or particles. Laminar flow safety cabinet should meet the classification criteria based on construction, airflow velocity, and pattern and exhaust system [23]. There are several international standards for bio-

logical safety cabinets, among these are the following major international standards [23].

1. American Standard (National Sanitation Foundation) NSF 49
2. European Standard EN 12469
3. Australian Standard AS 2252
4. Japanese Standard JIS K 3800

The main role of laminar flow is to protect personnel, product, and environment. Hence, air filtration and air flow patterns should be considered by design to avoid cross contamination. Therefore, safety cabinet provides a clean air into working area and prevents airborne particles from entering the semi-enclosed work space, i.e., the clean air chamber. The clean air environment is based on high-efficiency particulate air filtration and uniform parallel air flow. The HEPA filter consists of a boron silicate or fiberglass microfiber membranous filter that is folded back and forth across corrugated aluminum separators. The separators on both sides of the filter act as baffles to direct the air in a laminar air flow (i.e., a uniform parallel flow without turbulence) [24]. The filter efficiency is at least 99.97% for particles size 0.3 μm or larger. The efficiency should be 99.997% for strict sterile conditions. However, gases and vapors are not trapped, but particles and liquid droplets are removed. The HEPA filter cannot be cleaned and

must be replaced once it is loaded to its capacity as indicated by filter testing [24].

There are three major types of laminar flow: safety cabinets I, II, and III.

Class I safety cabinet is the basic design of safety cabinet, provides personnel and environment protection. The air filtration system consisting of per-filter and a HEPA filter. Class I safety cabinet is the most proper for biosafety levels 1, 2, and 3. As there is no product protection, it has limited applications.

Class II safety cabinet is a vertical laminar, providing descending downward unidirectional HEPA filtered air with continuous supply into the cabinet. Hence, it protects the product or sample from contamination. Class II safety cabinet is divided into two types: class II type A and type B.

The main difference among class II subcategories is the percentage of the extracted to circulating air (Fig. 3.10). Type A is recirculating air with a minimum exhaust 30% of HEPA filtered air into the laboratory. However, in type B, the percentage of recirculating air is reduced to 30% (Type B1) or totally removed (Type B2). Further, the route of discharge or exhaust; some cabinets may exhaust into the laboratory through HEPA filter, others (class II type B2) require designated duct to be connected to outside the building. The latter type is considered as a total exhaust system and does not recirculate air to the laboratory, which is more
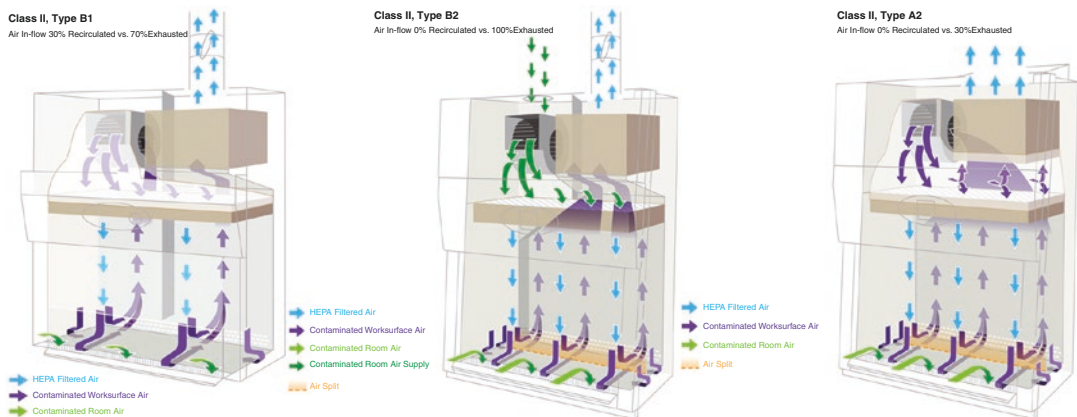
Fig. 3.10 Class II safety cabinet: Air directions and percentage of recirculating and exhausted air for type A2, B1, and B2. (NuAire, Inc., USA., with permission)

appropriate for volatile radionuclides such as radionuclide (I-131). Exhausted air will be discharged to external environment through HEPA filters. Nuclear medicine facilities should consider the total exhaust cabinets for installation [24]. As stated by IAEA, all radiopharmaceutical-labeling procedures, preparation, and elution of ^{99}Mo/^{99m}Tc generator should be executed in class II safety cabinet or isolator [23].

Class III safety cabinet/isolators is a totally enclosed cabinet usually designed to be metal-welded construction and gas tight. Manipulation of samples and work to be done through a gloves port installed at the cabinet front side. Materials are usually loaded from small airlock or pass through box to avoid cross contamination from external environment and to maintain particle count and microbial contamination within the recommended specifications. The cabinet is continuously under negative pressure relative to the ambient room pressure. The air supply is HEPA filtered and could exhaust into laboratory if no toxic chemicals are associated with microbiological process, otherwise it has to be connected to

the external environment through a dedicated duct, and the exhaust should be HEPA filtered [23]. This type of cabinets can be used for RBCs labeling.

3.4.2 High-Performance Liquid Chromatography (HPLC)

High-performance/pressure liquid chromatography (HPLC) is a specific form of chromatography for chemical compounds and molecule separation, identification, and quantification [25]. These processes can be performed using analytical HPLC; however, preparative HPLC has different approach for isolation and purification mechanism required for certain radiopharmaceuticals production setup. Analytical HPLC is the most widely used separation method applied to broad spectrum of organic and inorganic, polar and nonpolar, and ionic compounds but is not appropriate for volatile molecules. Figure 3.11 represents HPLC component [26]. It is being used in different fields including industrial, clini-
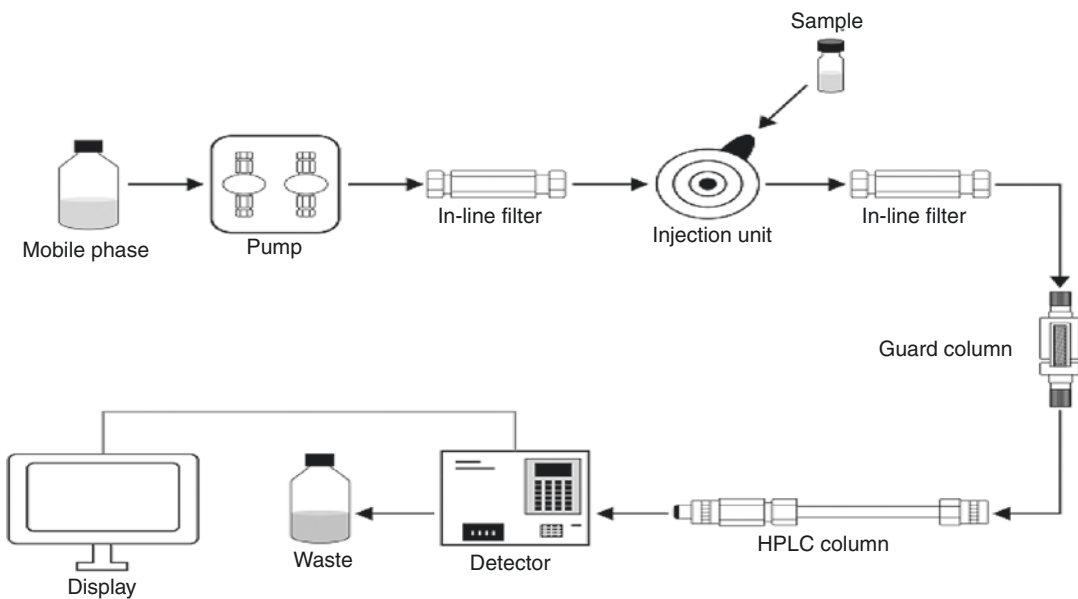
Fig. 3.11 HPLC system components. The pump that allows the flow of the mobile phase with a specified flow rate (mL/min). Injector or injection valve to load the sample into the stream of the mobile phase passing through guard column which acts as a protector of analytical col-umn. The column contains a packing material known as stationary phase which is required for the separation. The detector to identify the eluted compound, and the result is displayed as a chromatogram in PC connected to the HPLC system [26]

cal, environmental, and pharmaceutical applications, providing sensitive and accurate results.

The main concept of separation is based on the interaction between sample (analytes) with stationary phase (column) and mobile phase. The HPLC core component is the separation column that contains the stationary phase, usually it is 5–30 cm in length, loaded with different size of packing materials depending on the application of HPLC. Column length and diameter vary depending on chromatographic procedures [27]. Small size packing molecules require high operational pressure (back pressure) with enhanced system resolution. The packing material or stationary phase vary according to HPLC type.

Silica gel such as silica dioxide, polymer gel (polystyrene and poly methyl acrylate) and other gel including natural material cellulose and agarose are used as stationary phase [28]. The main function of the column is molecule separation depending on their retention time.

The retention time is molecule specific and defined as the time required for the sample to migrate from injection site (t_0) to end of column t_R (detector) or in other words is the time from sample injection to detection.

Several column packing designs are available to adapt various HPLC applications among these porous, non-porous, superficially porous, perfusion, and monoliths packings. HPLC pump is one of the essential HPLC components, and its main function is to push the mobile phase through the analytical column. The pump has to supply constant and pulse-free flow of mobile phase. The composition of mobile phase could be either constant composition (isocratic) or gradient, which means different compositions of mobile phase over time. The gradient compositions created by means of quaternary pump which provides different solvent composition percentage during the run time or analysis.

Furthermore, HPLC detector is a fundamental component of HPLC system. In early HPLC systems, an offline detector was the only method available for sample analysis by collecting fractions of sample under investigation for detection. In 1960s, the first ultraviolet detector was implemented in HPLC systems [29]. Further improve-

ments in detectors started to be developed and implemented such as variable wavelength and diode array detectors. Consequently, many HPLC detectors have been developed and shown potential improvement in a wide range of general and specific HPLC applications [29, 30].

HPLC detector reproducibility and predictability are potential specifications in detector selection. Recently, ultra-high-performance liquid chromatography (UHPLC) requires faster response of detector and contribution of flow cell as the particle size of packing material is sub 2 µm. Desired detector characteristics and specifications for proper HPLC column are listed herein [29, 31, 32]:

- High sensitivity, reproducibility, and predictable response
- Respond to all solutes or have predictable specificity
- Wide linear dynamic range; response that increases linearly with the amount of solute
- Response unaffected by changes in temperature and mobile phase flow
- Respond independently of the mobile phase
- Not contribute to extra-column band broadening
- Provide qualitative and quantitative information on the detected peak
- Chemical nature of analytes and potential interferences
- Limit of detection/quantitation required

There are several types of detectors that could be employed by HPLC system, among these which is widely used in radiopharmaceuticals quality control applications are UV, refractive index, and high-sensitivity radioactive detector [33, 34]. The main purpose of the detector is to measure the concentration of the solute in eluate (i.e., concentration of chemical identities) and concentration of radioactive tracers by chemical and radioactive detectors, respectively [34]. Radiometric detector installed in HPLC system for radiopharmaceuticals quality control is usually made of NaI(Tl) or BGO scintillators to quantify radiochemical purity [34, 35]. Comparing the retention time of the compound

under investigation with cold standard allows the radiochemical identification of the molecule. Other HPLC detector (UV, EC, RI, etc.) is connected in series with radiodetector to identify the radiochemical identity and identify the chemical impurities quantitatively.

Bearing in mind the compatibility of column and detector to HPLC application, HPLC is classified into several types based on the phase system (i.e., stationary phase). The main HPLC types commonly used in radiopharmaceuticals applications are [35]:

- Normal phase chromatography (NP-HPLC)
- Reversed phase chromatography (RP-HPLC)
- Ion-exchange chromatography

In normal phase chromatography or normal phase HPLC (NP-HPLC), the separation process is based on polarity. Polar stationary phase is mostly silica and nonpolar mobile phase such as hexane and diethyl ether [25, 33]. Nonpolar sample will be retained on the column and analyzed. Reverse phase HPLC (RP-HPLC) is another HPLC type where the stationary phase is nonpolar of hydrophobic and polar mobile phase. In this type, the analysis is based on the hydrophobic interactions between a polar mobile phase, the relatively nonpolar analyte, and the nonpolar stationary phase. The analyte retention is proportional to the contact surface area around the nonpolar part of the analyte molecule upon association with the ligand in the aqueous eluent [25].

Ion-exchange chromatography is among those HPLC types. The stationary phase has ionic properties opposite to mobile phase, and the retention is based on the attraction between solute ions and charged sites of the stationary phase. However, the mobile phase will be used in aqueous buffer to control pH and ionic strength [35]. The applications of this type are in ion-exchange chromatography of proteins, high-pH anion-exchange chromatography of carbohydrates, and oligosaccharides and others [25].

Radiochemical identity of radiopharmaceuticals depends on the selection of HPLC type. Analytical column and detector selection must be compatible with chemical properties of evaluated pharmaceutical for proper detection and quantification. The most widely used positron emitters and radiopharmaceuticals 2-[^{18}F]fluoro-deoxy-D-glucose ([^{18}F]FDG) require strongly basic anion-exchange column, pulsed amperometric detector, and radiometric detector [36, 37]. Sodium fluoride [^{18}F]NaF radiochemical purity and identity are evaluated by HPLC equipped by UV detector, radiometric detector, and anion exchange column [36, 38]. Other radiopharmaceuticals such as ^{68}Ga peptide requires reverse phase column, UV, and radiometer detector [39, 40].

HPLC system has a potential in radiopharmacy quality control procedures of finished product to evaluate and quantify the radiochemical and radionuclidic purities to assure the compliance of the final product with guidelines and recommendations.

3.4.3 TLC Scanners

Thin layer chromatography (TLC) and high-performance thin layer chromatography (HPTLC) are known as planer chromatography (Fig. 3.12). Like other chromatography techniques, TLC procedure is applied to separate a mixture of molecules based on their polarity. Polar stationary phase is silica packed as thin layer on glass plate, polyester or aluminum sheet, and proper solvent or solvent mixture as mobile phase. The sample is applied on the stationary phase before immersion in a mobile phase for migration. The movement of mobile phase through stationary phase is called development step [41]. Once the development is completed as the mobile phase reaches front sample point, the detection step will start on the stationary phase. The data are then recorded with TLC scanner equipped with a radiation detector, and the readout is plotted against separation time. The recorded plot is called densitogram [41] (see Chap. 6 for further details).

The main part of the scanner is to serve as radiation detector which could be NaI/PMT, plastic scintillator/PMT, well-type NaI/PMT, and pin diode detectors. To reduce background counts,
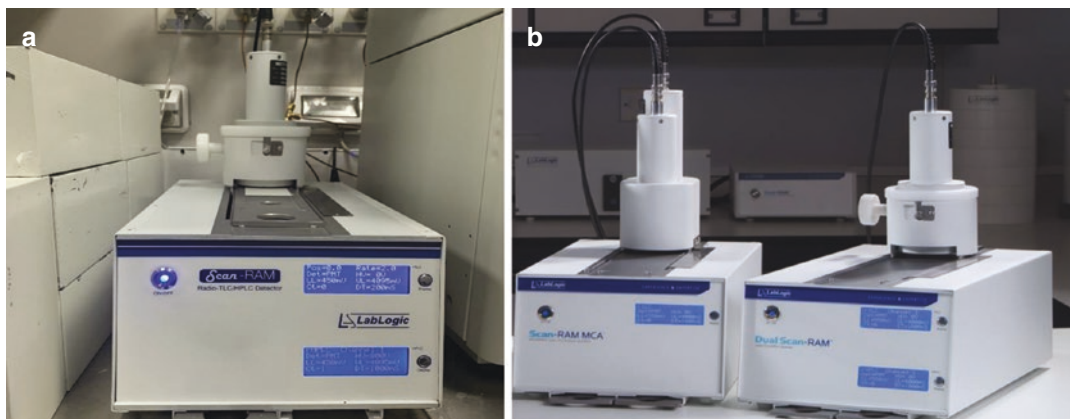
Fig. 3.12 TLC scanner. Commercially available TLC scanners to evaluate the radiochemical purity with thin-layer chromatography in most nuclear medicine laboratories and cyclotron facilities to meet GMP standards.

Advanced TLC is combined with MCA to execute basic gamma spectroscopy or radio-nuclidic identity. (**a**) Lateral view of *Lablogic* radio TLC scanner and (**b**) dual TLC and MCA. (LabLogic systems Ltd, UK, with permission)

the detector should be positioned in lead shield or collimator. Either movable detector or collimator set will move over TLC plate, or fixed detector and movable plate both can be seen according to the manufacturer design. The scan time range is normally 1–2 min according to the amount of radioactivity to be detected and user setting.

3.4.4 Gas Chromatography (GC)

Gas chromatography is used analytically to separate compounds that can be vaporized without dissociation. Gas chromatography is known as gas liquid chromatography in which the sample is injected into the column top at certain temperature to allow vaporization. The mobile phase (evaporated sample) is then passed through the stationary phase (column) by the flow of carrier gas, either inert gas such as helium and argon or nonreactive gas such as nitrogen. Column temperature is raised up, maintained, and controlled by oven where the column is located.

GC column is either packed or capillary column depending on the manufacture design. In packed column, the glass or metal tube of the column is filled with fine spherical support. The liquid stationary phase is adsorbed as a thin layer on the surface of these small particles. Capillary column walls are coated with thin layer of liquid stationary phase and referred as open tubular column [35].

The separation of molecules is affected by hold-up time and interaction of those molecules with stationary phase. Hold-up time is defined as the time required by solute to transfer through the column. The molecule functional group will control the interaction between stationary phase and the molecule. As the retention time is elapsed, sample concentration is determined by GC detector and represented in software for calculation from area under peak. Several GC detectors are available such as flame ionization detector (FID), nitrogen phosphors detectors (NPD), electron capture detector (ECD), thermal conductivity detector (TCD), and others [42].

FID is the widely used detector in GC applications. A schematic diagram is shown in Fig. 3.13. In radiopharmaceutical preparation, it is a must to quantify the residual solvents in the finished product as indicated in pharmaceuticals monograph of the European pharmacopeia and the United States pharmacopeia (USP). Quality control of the finished product applying GC analytical method is essential for residual solvent identification and quantification.

3.4.5 Gamma Spectrometers

Gamma spectrometer is a potential tool in radiopharmaceutical industry for radionuclide identification and generating a specific radionuclide

Flame Ionization Detector

Exhaust

(-)

(+)

Flame

Air Flow In

Helium Flow

Column input
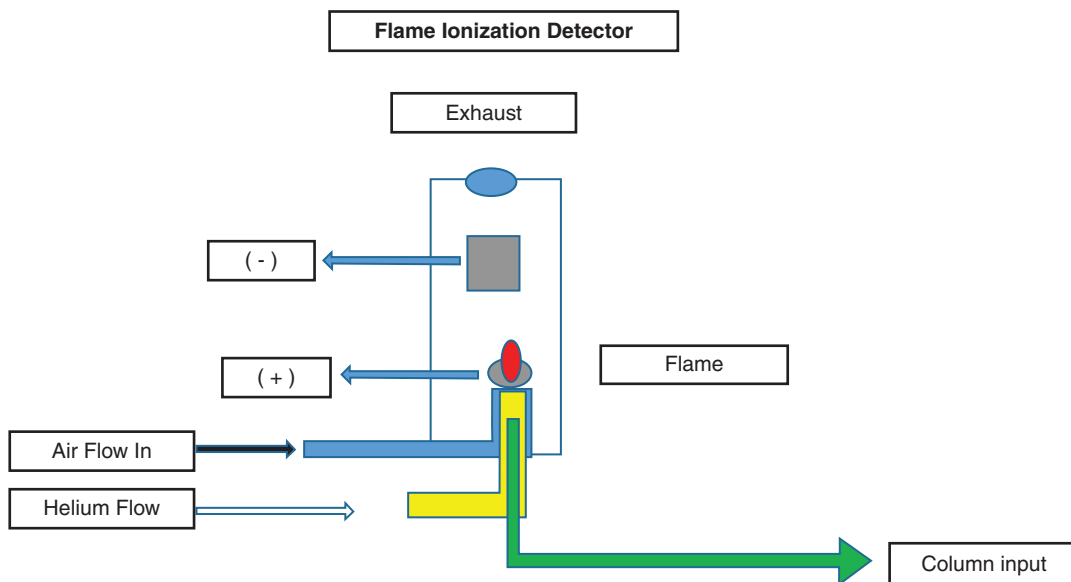
Fig. 3.13 Flame ionization detector (FID). The detector consists of small-volume chamber where the gas chromatograph column is fixed, the sample and carrier gas pass from the column through a hydrogen–air flame. The current produced from burned organic molecules is being measured by electrometer located near to the flame

spectrum. Furthermore, detection of radionuclide impurities is associated with the target radionuclide of the finished product. Moreover, it enables determining the percentage of those radionuclide impurities as well as the produced radionuclide [35]. In 1950s, the first gamma spectrometry was done by small and portable NaI(TI) spectrometer. Physical properties of NaI detectors such as good light yield and linearity response make it the most widely used gamma spectrometer [43]. However, other scintillator detectors could be used for this purpose. The semiconductor high-purity germanium (HPGe) detectors make a breakthrough in gamma spectrometry because of their high-energy resolution in the range of 0.5–2 keV [44]. Although HPGe provides the most accurate and precise method for radionuclide purity, the cooling required for the operation of HPGe to maintain the proper functionality is one of the drawbacks.

Gamma spectrometers are classified into two classes, single-channel analyzer (SCA) and multi-channel analyzer (MCA) in which energy deposited on the detector is proportional to the interacted gamma rays [13]. Detector size, shape, performance, packing configuration, and intended use of spectrometer are among the most important specifications to verify intended use requirements. The application of gamma spectrometer is a potential factor to define the tradeoff between detector efficiency and energy resolution.

Radionuclidic purity is an important measure to be evaluated in radiopharmaceutical quality control program to quantify radioactive impurities and particular isotopes. Radionuclide purity is defined as the ratio between the desired isotope and the total activity in the compound. In gamma ray spectrum, it is measured as the total count of desired peak in relative to other radioactive peaks. Figure 3.14 illustrates gamma spectrum of ^{18}F. Other equipment are also necessary in radiopharmacy laboratory to ensure other qualities of the finished product for intravenous injection including pH and endotoxins measurements.

3.4.6 pH Meter

A pH meter indicates hydrogen ion concentration of the solution which reflects the solution acidity or alkaline properties. The main part of pH meter is the probe or electrode which could be either
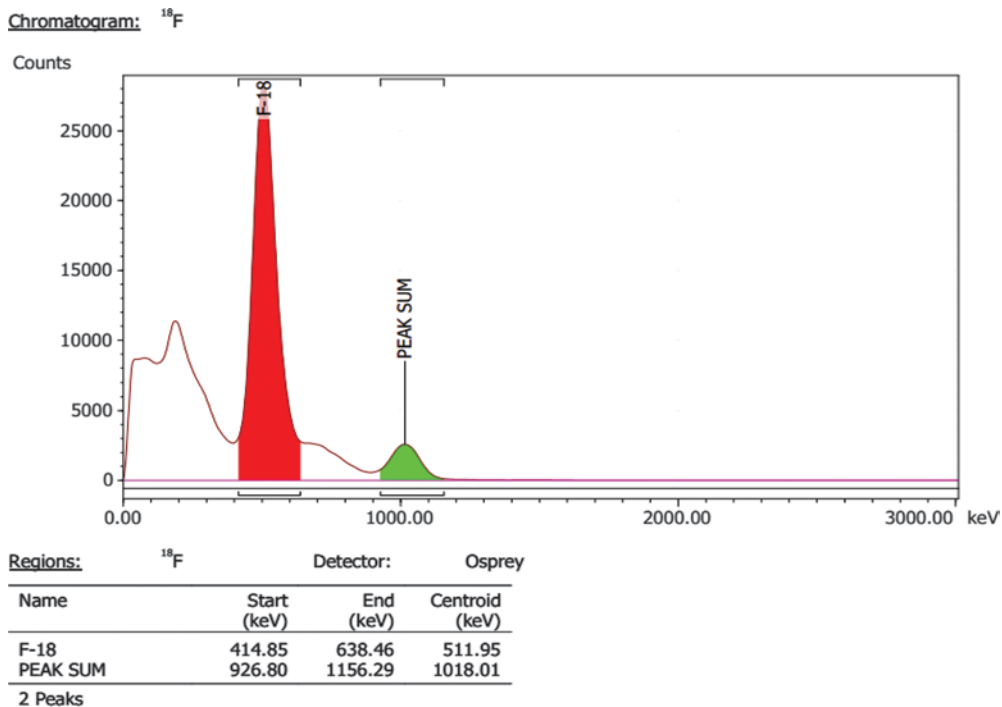
Fig. 3.14 Gamma spectrum of ^{18}F-FDG. The evaluation of radionuclidic purity during the quality control of FDG by multi-channel analyzer showing the ^{18}F peak at 511 keV and sum peak at 1022 keV

glass electrode or ion selective field effective transistor (ISFET) connected to electronic display for pH reading purposes [45]. The glass electrode is most widely used in pharmaceutical applications. The system consists of measuring electrode and reference electrode. The former provides voltage in mV proportional to hydrogen ion concentration while the latter provides a constant potential regardless the pH of the solution. The measuring electrode is usually immersed in a high-acidity reference solution such as the normally used 0.1 N HCl, and reference electrode is typically Ag/AgCl salt that surrounds the wire electrode [45]. The pH electrode components and configuration are shown in Fig. 3.15.

Daily calibration of pH meter with standard buffer solutions of known pH is required before measuring unknown samples. Radiopharmaceutical GMP require the daily calibration of pH meter with reference buffer of pH 4, 7, and 10. Microelectrode is commercially available to measure the sample of volume 10 μL [36].
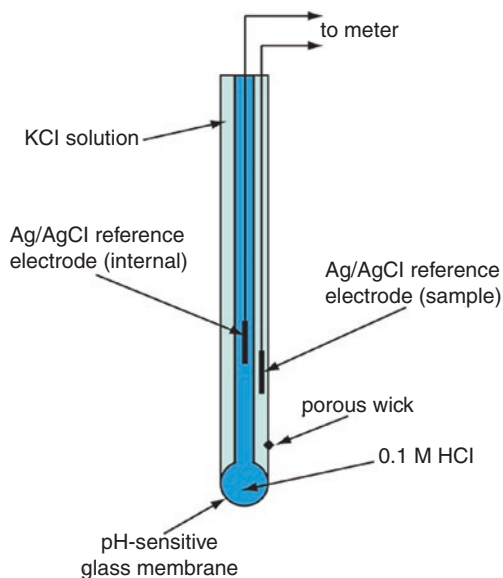
Fig. 3.15 pH meter basic components of glass electrode. The measuring electrode is bulb made of porous glass or preamble glass membrane coated with metal salts or silica and filled with high acidity solution. External reference electrode is surrounded by saturated KCl

Fig. 3.16 The Charles River Endosafe®-PTS™ System, an FDA-approved endotoxin system. A point-of-use and rapid portable system that provides quantitative LAL results in a quick fashion. It employs LAL reagents in a disposable test cartridge shown on the right. (Images credit of *Charles River Laboratories*, Inc., USA, with permission)

3.4.7 Endosafe PTS

Bacterial endotoxin should be assessed and evaluated before the product release for IV injection. Endotoxin is lipopolysaccharides found in the membrane of gram-negative bacteria. Endotoxin test is used to quantify the limulus ambocyte lysate (LAL). The test method could be gel clotting technique, turbidity approach, or chromogenic method. Gel clotting based on adding equal amount of sample and LAL reagent, and the mixture is incubated for 1 h at 37 °C. After incubation time, the tube will be inverted if any clot formation indicates that the presence of endotoxin. This approach cannot provide any quantification regarding the endotoxin amount. Turbid metric technique provides quantification of endotoxin determined by the change of sample color as a result of endotoxin reaction with LAL reagent. The amount of turbidity increases with time based on the endotoxin concentration in the solution. The standard curve is plotted, as time versus endotoxin concentration in endotoxin unit (EU) or international unit (IU) per milliliter. Endotoxin concentration is determined from the standard curve based on the reaction time of the sample. Chromogenic method is based on using substrate which releases chromophore as a result of interaction with endotoxin. The amount of chromophore is proportional with the endotoxin level existing in the sample. This method applies predefined end point. Charles River Laboratories has developed the Endosafe PTS™, shown in Fig. 3.16, which is a rapid portable device that determines quantitatively endotoxin concentration (EU) within 15 min through their unique cartridge technology.

3.5 Conclusion

Nuclear medicine procedures involve administration of radiopharmaceuticals into humans and thus quality of both imaging and non-imaging equipment as well as the injected compound must be properly evaluated and monitored. Equipment should be subjected to quality control program with calibrated standard sources. The availability of such radioactive sources for routine testing is important in order to maintain a medical standard of care on a daily basis. In normal radiopharmacy laboratory as well as in cyclotron production facility, a number of tests are requested to ensure com-

pliance with national or international regulations and safety of the injected compounds. Moreover, the quality assurance and control parameters should be well established and documented. This is to be maintained for all imaging, non-imaging, and radiopharmacy toolkits. Implementation of such quality measures using proper methodologies will ensure improvement of diagnostic accuracy and performance of nuclear medicine practices.

References

1. Committee EP, Busemann Sokole E, Plachcinska A, Britten A, et al. Routine quality control recommendations for nuclear medicine instrumentation. Eur J Nucl Med Mol Imaging. 2010;37(3):662–71.
2. Gadd R, Baker M, Nijran KS, Owens S, Thomson W, Woods MJ, Zananiri F. Measurement good practice guide no. 93: protocol for establishing and maintaining the calibration of medical radionuclide calibrators and their quality control prepared by a joint working party composed of representatives from the following: Institute of Physics and Engineering in Medicine, Ionising Radiation Metrology Consultants Ltd. and National Physical Laboratory; 2006. p. 1368–6550.
3. Carey JE, Byrne P, DeWerd L, Lieto R, Petry N. The selection, use, calibration, and quality assurance of radionuclide calibrators used in nuclear medicine. AAPM report no. 181; 2012.
4. https://m.biodex.com/nuclear-medicine/products/radiopharmacy/dose-calibration/atomlab-500-dose-calibrator. Accessed 23 Aug 2020.
5. ACR–SNM–SPR practice guidelines for the performance of thyroid scintigraphy and uptake measurements. American College of Radiology; 2009.
6. Bailey DL, Humm JL, Todd-Pokropek van Aswegen A, technical editors. Nuclear medicine physics: a handbook for teachers and students. Vienna: International Atomic Energy Agency; 2014.
7. Becker D, Charkes ND, Dworkin H, Hurley J, McDougall IR, Price D, et al. Procedure guideline for thyroid uptake measurement: 1.1. Society of Nuclear Medicine. J Nucl Med. 1996;37:1266–8.
8. Menon BK, Uday AS, Singh BN. γ-Camera-based method for measuring the γ-count from 131-I capsules: an alternative to the thyroid uptake probe. J Nucl Med Technol. 2018;46:45–8. https://doi.org/10.2967/jnmt.117.198077.
9. Harris CC, Bigelow RR, Francis JE, et al. A Csi(Ti)-crystal surgical scintillation probe. Nucleonics. 1956;14:102–8.
10. IAEA publications. Guided intraoperative scintigraphic tumour targeting (GOSTT): implementing advanced hybrid molecular imaging and non-imaging probes for advanced cancer management. IAEA human health series ISSN 2075–3772;29, Vienna; 2014.
11. NCRP Report No. 147—structural shielding design for medical X-ray imaging facilities; 2004.
12. Benedict SH. Review of radiation oncology physics: a handbook for teachers and students. J Appl Clin Med Phys. 2004;5:91–2.
13. Reilly D, Ensslin N, Smith H Jr, editors. Passive non-destructive assay of nuclear materials. No. NUREG/CR—5550. Nuclear Regulatory Commission; 1991.
14. Claus G, Irène B, editors. Handbook of particle detection and imaging. Berlin: Springer; 2011.
15. IAEA publications. Quality assurance programme for computed tomography: diagnostic and therapy applications. IAEA human health series ISSN 2075–4772;19, Vienna; 2012.
16. American Association of Physicists in Medicine. The measurement, reporting, and management of radiation dose in CT. AAPM report no. 96, ISSN: 0271-7344; 2008.
17. Zimmerman BE, Cessna JT. Development of a traceable calibration methodology for solid 68Ge/68Ga sources used as a calibration surrogate for 18F in radionuclide activity calibrators. J Nucl Med. 2010;51:448–53.
18. Busemann-Sokole E, editor. IAEA quality control atlas for scintillation camera systems. No. 1141. International Atomic Energy Agency; 2003.
19. Bergeron DE, Cessna JT, Coursey BM, Fitzgerald R, Zimmerman BE. A review of NIST primary activity standards for 18F: 1982 to 2013. J Res Natl Inst Stand Technol. 2014;119:371–96.
20. https://www.nist.gov/news-events/news/2015/01/prototype-first-traceable-pet-mr-phantom. Accessed 22 Aug 2020.
21. EANM. The radiopharmacy: a technologist' s guide; 2016. p. 22–3.
22. Operational guidance on hospital radiopharmacy: a safe and effective approach. Vienna: International Atomic Energy Agency; 2008.
23. Newsom S. Class II (laminar flow) biological safety cabinet. J Clin Pathol. 1979;32:505–13.
24. Chosewood L, Wilson D. Biosafety in microbiological and biomedical laboratories. US Department of Health and Human Services, Public Health Service, Centers for Disease Control and Prevention, National Institutes of Health; 2009.
25. Zabel P, Robichaud N, Hiltz A. Facilities and equipment for aseptic and safe handling of blood products. J Nucl Med Technol. 1992;20:236–41.
26. https://www.gelifesciences.com/en/us/solutions/lab-filtration/knowledge-center/hplc-pain-points-part-1. Accessed 22 Aug 2020.
27. Dahimiwal SM, Thorat DB, Jain NP, Jadhav VB, Patil PB. A review on high performance liquid chromatography. Int J Pharm Res. 2013;5:1–6.

28. Silva RGC, Bottoli CBG, Collins CH. New silica gel-based monolithic column for nano-liquid chromatography, used in the HILIC mode. J Chromatogr Sci. 2012;50:649–57. https://doi.org/10.1093/chromsci/bms081.

29. Swartz M. HPLC detectors: a brief review. J Liq Chromatogr Relat Technol. 2010;33:1130–50. https://doi.org/10.1080/10826076.2010.484356.

30. Zhang B, Li X, Yan B. Advances in HPLC detection-towards universal detection. Anal Bioanal Chem. 2008;390:299–301. https://doi.org/10.1007/s00216-007-1633-0.

31. Sunil A. HPLC detectors, their types and use: a review. Org Med Chem Int J. 2018;6:3–6. https://doi.org/10.19080/omcij.2018.06.555700.

32. Arti T, Ramni K, Navneet K, Ashutosh U, Suri OP. High performance liquid chromatography detectors—a review. Int Res J Pharm. 2011;2:1–7.

33. Vallabhajosula S. Molecular imaging: radiopharmaceuticals for PET and SPECT. New York: Springer; 2009. https://doi.org/10.1017/CBO9781107415324.004.

34. Saha GB. Fundamentals of nuclear pharmacy. 7th ed. Cham: Springer; 2018.

35. Khalil MM, editor. Basic science of PET imaging. Dordrecht: Springer; 2016. https://doi.org/10.1007/978-3-319-40070-9.

36. Kilian K, Chabecki B, Kiec J, Kunka A, Panas B, Wójcik M, et al. Synthesis, quality control and determination of metallic impurities in 18F-fludeoxyglucose production process. Rep Pract Oncol Radiother. 2014;19:22–31. https://doi.org/10.1016/j.rpor.2014.03.001.

37. Koziorowski J. A simple method for the quality control of [18F]FDG. Appl Radiat Isot. 2010;68:1740–2. https://doi.org/10.1016/j.apradiso.2010.03.006.

38. Mihon M, Tuța C, Lavric V, Niculae D, Drăgănescu D. Quality control and stability study of the sodium fluoride injection [18F]NaF. Farmacia. 2015;63:765–9.

39. Silveira MB, Soares MA, Valente ES, Waquil SS, Ferreira AV, dos Santos RG, et al. Synthesis, quality control and dosimetry of the radiopharmaceutical 18F-sodium fluoride produced at the center for development of nuclear technology-CDTN. Braz J Pharm Sci. 2010;46:563–9. https://doi.org/10.1590/S1984-82502010000300021.

40. Velikyan I. 68Ga-based radiopharmaceuticals: production and application relationship. Molecules. 2015;20(7):12913–43.

41. Spangenberg B, Poole CF, Weins C, editors. Quantitative thin-layer chromatography: a practical survey. Berlin: Springer; 2011.

42. Guiochon G, Guillemin CL. Quantitative gas chromatography for laboratory analyses and on-line progress control. Amsterdam: Elsevier; 1988.

43. Rahman MM, Abd El-Aty AM, Choi J-H, Shin H-C, Shin SC, Shim J-H. Basic overview on gas chromatography columns. Anal Sep Sci. 2015:823–34. https://doi.org/10.1002/9783527678129.assep024.

44. Knoll GF. Radiation detection and measurement. 3rd ed. New York: Wiley; 2000. https://doi.org/10.1002/hep.22108.

45. Karastogianni S, Girousi S, Sotiropoulos S. pH: principles and measurement. 1st ed. Elsevier Ltd; 2015. https://doi.org/10.1016/B978-0-12-384947-2.00538-9.

Part II

Chemistry of Nuclear Medicine

Fundamentals of Technetium-99m Radiopharmaceutical Chemistry

4

Adriano Duatti

Contents

4.1   Technetium

In the periodic table, the element technetium (Tc) belongs to group 7 of the transition metal series along with the congener elements manganese (Mn) and rhenium (Re). Its chemical properties are much similar to those of Re, but significantly

A. Duatti (✉)
Department of Chemical and Pharmaceutical Sciences, University of Ferrara, Ferrara, Italy
e-mail: dta@unife.it

different from Mn. For example, the atomic dimensions of Tc and Re, in their various oxidation states, are almost identical, but larger than those of Mn ions. The negligible increase of atomic size in passing from the second to the third transition metal series is a phenomenon known as "lanthanide contraction."

All Tc isotopes are unstable and, therefore, transform into other elements by radioactive decay. Since the most stable isotopes (^{97}Tc, ^{98}Tc, and ^{99g}Tc) have half-lives shorter than 5.0×10^6 years, no residual Tc has been left on the earth crust after its formation, and as a consequence, Tc was the first element artificially generated.

The γ-emitting metastable isomer ^{99m}Tc is produced by β-decay of the parent radionuclide ^{99}Mo, which in turn is obtained as a side product of ^{235}U fission in nuclear reactors. For medical applications, ^{99m}Tc is supplied under the form of a *generator*, which is a simple device constituted by a glass column filled with a tightly packaged alumina (Al_2O_3) powder (Fig. 4.1). A solution of highly purified ^{99}Mo oxide is then absorbed on the top of the column where ^{99}Mo is left to decay through the process ^{99}Mo $\rightarrow$ ^{99m}Tc + β$^-$ + $\bar{v}$, where $\bar{v}$ is an electron antineutrino. After decay, the radionuclide ^{99m}Tc is recovered under the chemical form of pertechnetate tetra-oxo anion $[^{99m}TcO_4]^-$ by passing a physiological solution through the column.
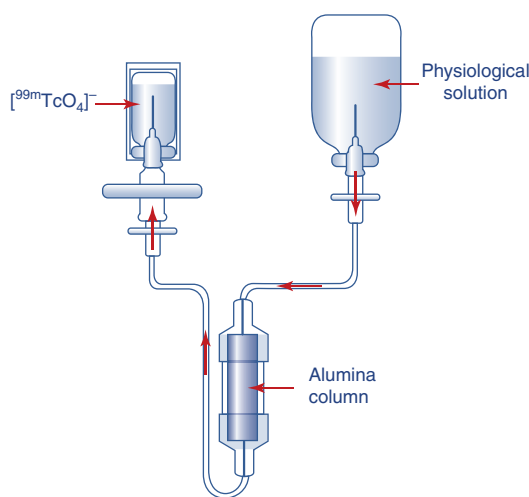
Fig. 4.1 Schematic representation of a ^{99}Mo/^{99m}Tc generator

4.2 Basic Concepts in Coordination Chemistry

In this section, some fundamental concepts of coordination chemistry that are required for a deeper understanding of the labeling chemistry of ^{99m}Tc are illustrated.

A chemical compound in which a metallic atom is bound to another molecule is called a *coordination compound* or *metal complex*. It is worthy to emphasize that the molecule that is chemically tethered to the metallic atom may also exist as a free and stable chemical entity not necessarily linked to the metal. However, other chemical species can exist only when attached to the metallic center and, thus, do not have an independent existence when separated from the metal.

In principle, every metal in the periodic table can form coordination compounds, the most relevant categories being the *transition elements*, the *lanthanides*, and the *actinides*. Yet, also metallic elements that belong to the classical groups (e.g., gallium, indium) are able to form coordination complexes.

The molecules or any chemical moiety that bind to a metal are called *ligands*. Usually, only a few specific atoms within the ligand are chemically bound to the metal, the remaining atoms being only involved in maintaining the original molecular scaffold of the ligand. The number of atoms of a single ligand molecule that are actually linked to the metallic atom determine the *denticity* of the ligand. A ligand binding a metal through only *one* of its atoms is called *monodentate*, whereas when there exist *n* atoms of the same ligand tethered to the metal, the ligand is called *n-dentate* or, alternatively, *chelating ligand*. Obviously, ligands that bind the metal with two atoms are dubbed *bidentate*, with three atoms *tridentate*, with four atoms *tetradentate*, and so on.

It is common to ascribe a so-called *oxidation state* to a metal in a coordination complex. This is a purely formal concept that is used for classification purposes. More precisely, the oxidation state is a positive or negative integer number assigned to an atom bound inside a molecule based on abstract rules. Therefore, it does not

have any real physical meaning except for a free isolated atomic ion for which it corresponds to the electric charge of the ion. For example, a free fluoride ion (F^-) has a −1 charge, and therefore, its oxidation state is −1. Similarly, a free cupric ion (Cu^{2+}) has a +2 charge, and an oxidation number +2 is assigned to it (for a free isolated neutral atom, the assigned oxidation state is zero). However, it should be noted that the element technetium cannot exist as a free ion, but it is always tethered to other atoms within some compound. For this reason, a set of formal rules should be specifically devised to allow conferring an oxidation state to the metal in a coordination complex. In a simplified version, these rules are as follows: (1) the *sum of oxidation states* of all atoms comprised in a single molecule should yield the *total charge* of the molecule, (2) by applying rule (1) to a *ligand*, it follows as a consequence that the *net charge* carried out by a ligand molecule should be taken as the overall *mean* oxidation state for all atoms in the ligand, (3) finally, the *sum of the oxidation state* of Tc and of *the total charge of the ligands* should yield the *net charge* of the coordination compound. From rule (3), it is possible to calculate the oxidation state of the Tc atom by *difference* between the *charge of the complex and the sum of the total charge of the ligands*.

The theoretical description of the origin of the coordination bond between the metal and the ligands is outside the scope of this chapter. However, a qualitative picture can be drawn by considering the simple concept of hard and soft Lewis acids and bases. Briefly, a Lewis acid is a chemical species that possesses empty orbitals in its external shell. Conversely, a Lewis base is a chemical species characterized by the presence of filled orbitals in its external shell (one orbital is fully filled when is occupied by two electrons). Usually, these orbitals lying at the edge of the electronic cloud surrounding an atom or a molecule are called *frontier orbitals* (FOs) In Lewis theory, a chemical bond is formed when two atoms share an electron pair. When a Lewis acid approaches a Lewis base, the latter can *donate* the electron pair in its filled FO to the empty FO of the former, thus leading to the formation of a
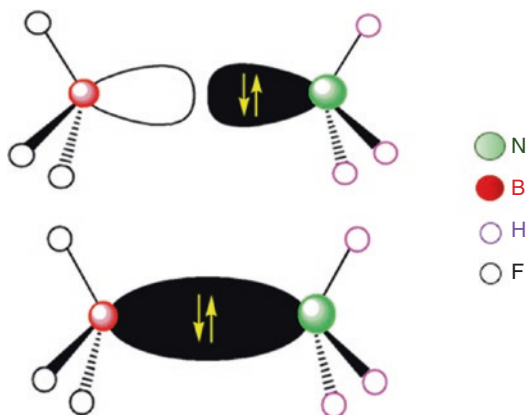
Fig. 4.2 Representation of the formation of a B–N bond through a Lewis acid-base interaction

chemical bond. A typical example of Lewis acid–base interaction is reported in Fig. 4.2 where the reaction of ammonia (NH_3) with boron trifluoride (BF_3) to yield the complex salt H_3NBF_3 is pictorially illustrated. In this reaction, the ammonia molecule behaves as a Lewis base and boron trifluoride as a Lewis acid. In NH_3, an FO located on the nitrogen atom is filled with two electrons, whereas an empty orbital is positioned on the boron atom in BF_3. The overlap of these two FOs leads to the formation of a chemical bond between boron and nitrogen.

The formation of a coordination bond between a metal and a ligand can be viewed as a Lewis acid–base interaction where the metal plays the role of Lewis acid and the ligand that of Lewis base. In another language, the Lewis base *donates* an electron pair to the Lewis metallic acid. When the electron pair is located on a single atom (and not spread over the entire molecule), this atom is dubbed as *donor* atom.

Depending on the energy of the FOs, soft and hard acids and bases can be defined. Specifically, *high-energy* FOs are associated with *soft* acids and bases. Conversely, *low-energy* FOs are characteristic of *hard* acids and bases. A general rule maintains that soft bases react preferentially with soft acids, and similarly, hard bases bind preferably to hard acids. To make this rule more practical, it is helpful to observe that, typically, hard acids and bases contain high-electronegative atoms, whereas soft acids and bases include low-

electronegative atoms. For example, ligands containing oxygen, neutral nitrogen, or halogens are hard bases, whereas ligands containing sulfur or negatively charged nitrogen are soft bases. Similarly, metals in high oxidation states are hard acids, whereas metals in low oxidation states are soft acids.

Another distinctive feature of a coordination complex is its *geometrical shape.* The most common spatial configuration of a Tc complex is where the metal atom lies at the center of an ideal solid and the ligands occupy the vertexes of this solid. Since the positions of the atoms inside a molecule can be precisely determined by crystallographic methods, the shape of these solids can be obtained by simply connecting these positions with ideal lines. This procedure is exemplified in Fig. 4.3 for the complex $[Zn(NH_3)_4]^{+2}$.

The complex $[Zn(NH_3)_4]^{+2}$ is composed of a zinc atom linked to four ammonia molecules. As explained above, the four coordination bonds originate from the Lewis acid–base interaction between the hard-acid Zn^{2+} with the four hard-base ammonia molecules. By drawing ideal lines (red) connecting the positions of the four nitrogen donor atoms, a tetrahedron emerges where the Zn atom occupies the center of the solid. Thus, following this abstract procedure, a *tetrahedral geometry* can be assigned to the complex $[Zn(NH_3)_4]^{+2}$. It turns out that, given the molecular structure of a coordination compound, as determined by crystallography, and using the proposed method, a geometrical solid can be always drawn for all coordination complexes.

The richness of technetium chemistry reflects in a variety of possible geometries of its coordination compounds. The number of ideal solids that have to be used to describe the molecular structure of a Tc complex is remarkable, and Fig. 4.4 illustrates the most important geometries.

Fig. 4.3 Drawing the geometry of the tetra-amino Zn(II) complex
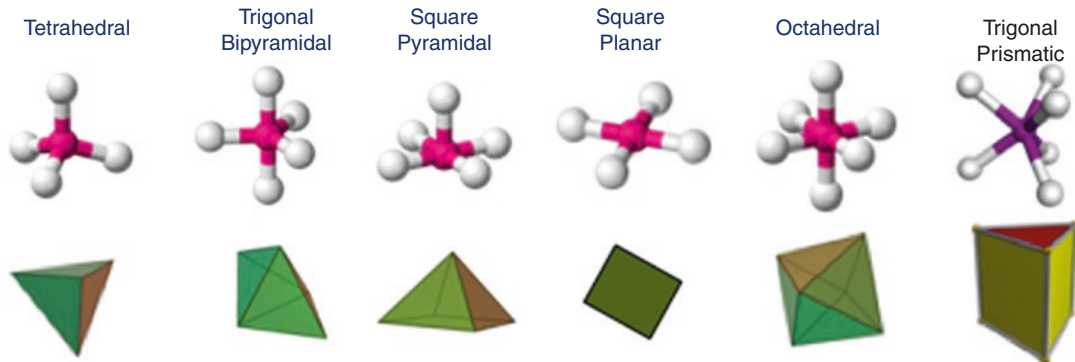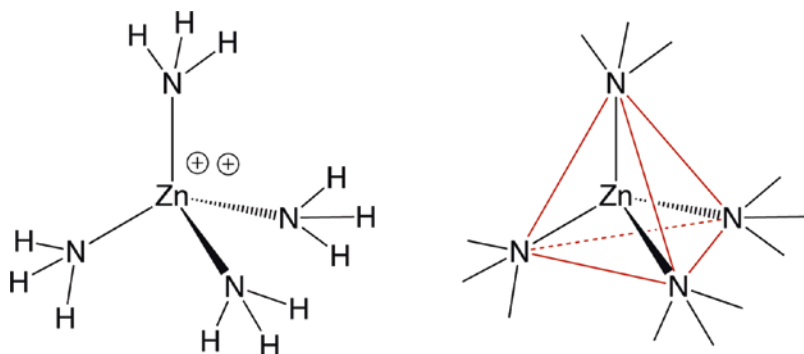
Fig. 4.4 The most important molecular geometries of technetium complexes

4.3 Characterization of the Chemical Structure of ^{99m}Tc Radiopharmaceuticals

The preparation of a radiopharmaceutical usually involves the reaction of a radionuclide, under some chemical form, with a reactive substrate (labeling reaction). The size of the chemical substrate can range from single molecules ($10^{-10}$ m) to nano- (10^{-9} m) or micro-particles (10^{-6} m). It is important to note that these labeling reactions are carried out using very low concentrations of the radionuclide that usually are of the order of 10^{-9} mol dm^{-3} (nanomolar concentrations, also called *tracer level*). Under these conditions, the sensitivity of conventional analytical and structural methods, commonly employed in synthetic chemistry to unearth the chemical composition and coordination geometry of a metallic complex, is not sufficiently high to detect these very tiny amounts of a radiocompound. Actually, conventional methods for structural determination (i.e., X-ray crystallography, magnetic resonance, and optical spectroscopy) can only be applied to macroscopic samples and at concentration levels higher than 10^{-6} mol dm^{-3}. Therefore, only highly sensitive analytical techniques, such as mass spectroscopy (MS) and high-performance liquid chromatography (HPLC), can afford effective approaches to get insights into the chemical composition of a radiopharmaceutical prepared at a nanomolar concentration scale. However, using MS and HPLC, only a partial insight into the true molecular arrangement of a ^{99m}Tc radiopharmaceutical can be achieved. More precisely, HPLC can be used only to determine whether the labeling reaction yields a single product or a mixture of radiolabeled compounds. Similarly, MS can shed light on the distribution of the molecular masses of the resulting radiolabeled products, but without offering details about its molecular structure. In short, there exists a mismatch between the group of analytical methods that are able to provide genuine structural information, but are affected by a low concentration sensitivity, and the group of highly sensitive analytical methods that are capable to detect a radiopharmaceutical at very low concentrations, but cannot provide a

precise picture of its true molecular architecture. Therefore, there was a need to develop an effective strategy for elucidating the molecular structure of a radiopharmaceutical, which could overcome the analytical barriers between the two different concentration scales. This strategy relies on the existence of stable isotopes of a particular radionuclide. Through this approach, the stable isotope can be conveniently used for attempting to synthesize, at the macroscopic concentration level, the same hypothetical chemical compound that is supposed to form at tracer level. If this synthesis were successful, the compound isolated at the macroscopic level could be fully characterized by structural analytical techniques and its molecular structure finally determined. Based on this result, strong evidence that also the radiocompound prepared at tracer level possesses the same molecular structure can be obtained by coinjection of a mixture containing the nonradioactive molecule and the radioactive counterpart, into a HPLC chromatograph equipped with both optical and radioactive detectors. If the two chromatographic profiles (optical and radioactive) exiting from the chromatographic column are almost superimposed (taking into account the delay always occurring because of the passage of the sample from one detector to the other), it is reasonable to assume that the two chemical species share the same molecular structure.

For most of the medical radionuclides, there exists at least one non-radioactive isotope that can be conveniently utilized for applying the above characterization strategy. However, owing to its artificial origin, all Tc isotopes are radioactive, and therefore, the synthesis of macroscopic amount of a particular Tc compound raises critical radiation safety concerns and, normally, should be carried out in a dedicated radiochemistry laboratory with shielded hot cells and glove boxes. In the past, the long-lived β-emitting radioisotope ^{99g}Tc (half-life = 2.11×10^5 years, $E_\beta = 297$ keV) has been employed as surrogate of a stable isotope for Tc, but its use has become sporadic mostly because of safety issues and poor availability. Luckily, the similarities between the chemical properties of the congener

Fig. 4.5 A pictorial representation of the overlapping of optical and radioactive chromatograms for a Tc/Re matched pair
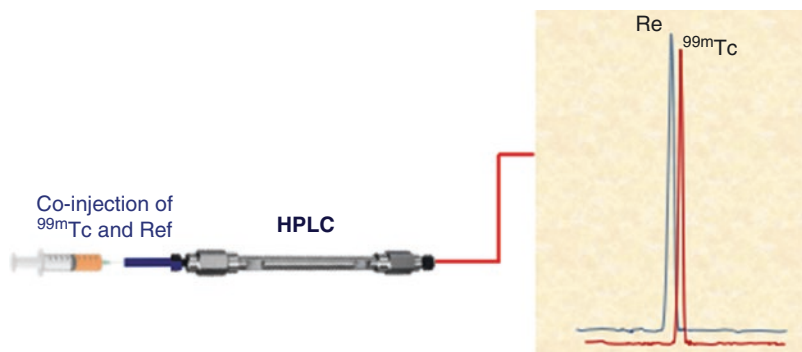

elements technetium and rhenium allow to devise a quite elegant solution. Actually, although the following rule does not hold for all categories of complexes, it is frequently observed that a pair of Tc and Re complexes containing the same type of ligands acquire the same molecular structure. This feature originates from the peculiar chemical properties of the two elements Tc and Re. In particular, despite they belong to different periods of the transition metal series, their atomic dimensions are almost identical (a phenomenon known as "lanthanide contraction"). As a result, when a Tc atom lies in the same chemical environment of the corresponding Re atom, the resulting pair of complexes possess exactly the same molecular structure and geometry. This distinctive feature has a fundamental impact on the biological properties of the pair of Tc and Re complexes because it is always found that they exhibit an identical biodistribution behavior (for this reason, they are called "a matched pair"). Another key advantage of the existence of the Tc/Re matched pair comes from the fact that the element rhenium possesses stable isotopes that can be used to prepare its complexes in macroscopic amounts (i.e., at millimolar concentrations). Thus, isolation and structural characterization of an Re complex may allow to unveil the structure of the corresponding matched pair ^{99m}Tc complex using the strategy outlined before in this section. Briefly, by applying the methods of synthetic chemistry, a labeling reaction carried out with the γ-emitting isomer ^{99m}Tc could be crudely mimicked using the stable Re isotope and, if the resulting metallic complex is sufficiently robust, it can be isolated and fully characterized by con-

ventional analytical methods, including X-ray crystallography, to determine its molecular structure. Finally, the Re product, obtained at the macroscopic level, and the radiolabeled ^{99m}Tc product, prepared at the nanomolar level, are *co-injected* in the same HPLC chromatograph equipped with both optical and radioactive detectors. As explained above, when the chromatographic profile of the radioactive ^{99m}Tc complex almost overlaps with the optical profile of the Re complex, it is reasonable to conclude that the radiolabeled product has the same molecular structure of the non-radioactive counterpart as pictured in Fig. 4.5.

A selected example may exemplify how the structural characterization of a novel ^{99m}Tc radiopharmaceutical can be achieved by merging analytical data collected at the macroscopic level with those collected at the tracer level. This procedure, as applied to the characterization of a novel ^{99m}Tc radiopharmaceutical for targeting amyloid plaques in Alzheimer's disease, is briefly outlined in Scheme 4.1 [for reference see Sagnou M, Mavroidi B, Shegani A, et al. *Journal of Medicinal Chemistry*. **2019**; 62, 2638–2650. https://doi.org/10.1021/acs.jmedchem.8b01949].

The starting point of this process is the discovery that the rhenium complex benzo[d]thiazole-2-(cyclopentadienyl)tricarbonylrhenium (**1** in Scheme 4.1) exhibit a remarkable in vitro inhibition power against Aβ fibril aggregation. This compound was synthesized through an exchange reaction between the precursor $[Re(CO)_3Br_3]$ $[NEt_4]_2$ and the iron derivative benzo[d]thiazole-2-ferrocene (**2** in Scheme 4.1). Complex **1** was isolated in macroscopic amounts and, then, fully
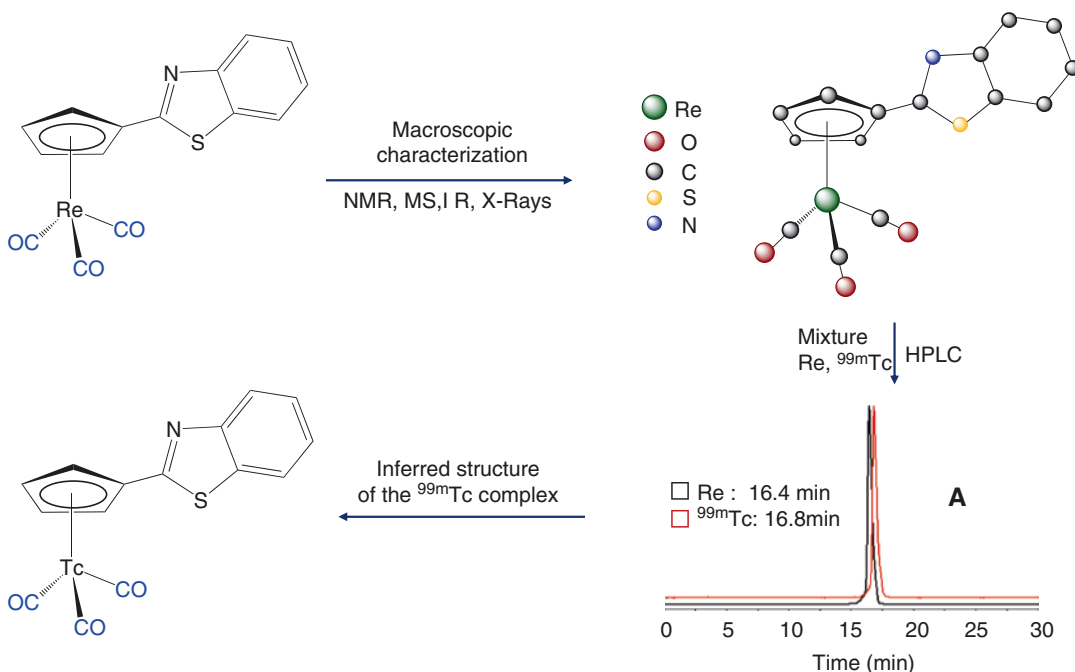
Scheme 4.1 Illustration of the procedure for establishing the chemical identity of a ^{99m}Tc complex in comparison with the properties of the analogous, and fully characterized, Re complex

characterized by high-resolution mass spectroscopy (HRMS), elemental analysis, infrared spectroscopy, high-performance liquid chromatography (HPLC), and X-ray crystallography. These results allowed to determine with high precision its molecular structure. Following a similar route, the preparation of the ^{99m}Tc analog was attempted using the *fac*-$[^{99m}$Tc(H$_2$O)$_3$(CO)$_3]^+$ precursor as starting substrate and this reaction yielded a radiolabeled product that was purified and isolated in solution. Obviously, the concentration of this product in the final solution was well below the lowest limit of sensitivity of the analytical methods used for the characterization of the Re complex, except HPLC and MS. Therefore, co-injection in HPLC of a mixture of the two Re and ^{99m}Tc complexes was employed as a method to establish the identity of the ^{99m}Tc compound. Figure (a) in Scheme 4.1 reports the resulting HPLC profile of this mixture composed of two HPLC peaks corresponding to the optical (Re) and radioactive (^{99m}Tc) signals, respectively. As discussed above, the close proximity of these two peaks is always taken as a strong evidence to infer that the Re and

^{99m}Tc complexes both share the same molecular structure and geometry.

4.4 The Reduction of the Pertechnetate Anion [^{99m}TcO$_4$]$^-$

The ubiquitous starting material for the preparation of ^{99m}Tc radiopharmaceuticals is the tetraoxo pertechnetate anion [^{99m}TcO$_4$]$^-$. This species is the most stable chemical form of ^{99m}Tc in aqueous solution and is composed of a Tc atom having an oxidation state of +7 bound to four oxygen atoms in a tetrahedral geometry. Since each oxygen atom carries a -2 oxidation state, the Tc atom is given a +7 oxidation state to yield a total charge of -1 for ^{99m}Tc pertechnetate.

The most common source of the ^{99m}Tc pertechnetate ion is the ^{99}Mo/^{99m}Tc generator. Basically, this system is composed of an alumina (Al$_2$O$_3$) column absorbed with reactor-produced ^{99}Mo oxide. The γ-emitting ^{99m}Tc originates from the β-decay of ^{99}Mo ($t_{1/2} = 65.94$ h) and is eluted as [^{99m}TcO$_4$]$^-$ by passing a physiological solution
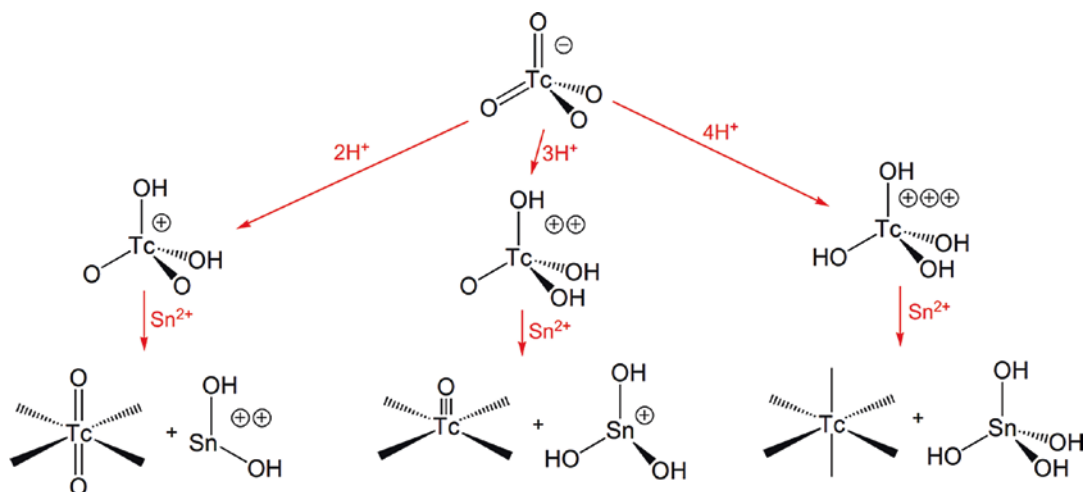
**Fig. 4.6** The stepwise oxygen-atom transfer occurring during the reduction of ^{99m}Tc pertechnetate

through the alumina column. The final solution of $[^{99m}TcO_4]^-$ is, then, employed for the preparation of all ^{99m}Tc radiopharmaceuticals.

Because of the high aqueous stability of $[^{99m}TcO_4]^-$, it is very difficult to replace the oxygen atoms by simple exchange with some suitable ligand. Thus, to prepare a new ^{99m}Tc radiocompound starting from ^{99m}Tc pertechnetate, the only practical strategy is to remove the oxygen through an oxidation-reduction (redox) process capable of lowering the oxidation state of the Tc metal.

In a more advanced representation, redox reactions are interpreted as "*atom transfer reactions*" where one atom (or group of atoms) is transferred from a donor to an acceptor. In this alternative picture, the donor corresponds to the oxidant, whereas the acceptor corresponds to the reductant. A broad class of atom transfer redox reactions involves the transfer of oxygen atoms, and the reduction of the $[^{99m}TcO_4]^-$ anion carried out by reaction with Sn^{2+} ions is one remarkable example. In this process, after the first protonation of the O atom, the electron pair involved in the bond between Tc and O migrates to the metal center. Subsequently, another electron pair is donated by Sn^{2+} to O, thus leading to the formation of a bond between Sn and O and completing the O atom transfer. At the end of this process, the O-donor atom Tc achieves two electrons causing
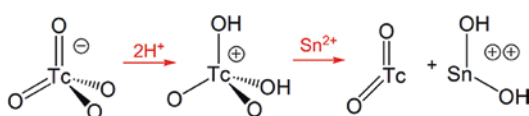
Fig. 4.7 Simplified mechanism of the formation of the dioxide $^{99m}TcO_2$

a decrease of its oxidation state, and the O-acceptor atom Sn loses two of its electrons corresponding to an increase of its oxidation state. Figure 4.6 illustrates the stepwise removal of the four O atoms during the overall reduction process of $[^{99m}TcO_4]^-$.

It is important to note that a parasitic reaction that may affect the scheme outlined in Fig. 4.6, is the formation of the neutral dioxide $^{99m}TcO_2$. This product could form when there is not any suitable ligand in solution able to coordinate the reduced Tc ion during the oxygen atom transfer (Fig. 4.7). The neutral $^{99m}TcO_2$ usually precipitates in aqueous solution as insoluble colloidal particles that may rise a biological risk when administered to a patient because of their trapping by spleen, lungs, and bone marrow. Therefore, it is essential to carry out the reduction process always in the presence of a ligand able to stabilize the Tc ion in its emergent oxidation state to prevent colloidal formation. Historically, colloidal $^{99m}TcO_2$ was also referred to as "hydrolyzed technetium," but

obviously this definition does not precisely disclose the chemical nature of ^{99m}Tc colloids.

Unfortunately, there exists another potential source of colloids during the reduction of ^{99m}Tc pertechnetate. This process is related to the production of the neutral tin tetra-hydroxide, $Sn(OH)_4$, that can precipitate in aqueous solution under the form of colloidal particles that, in turn, can absorb some ^{99m}Tc radioactivity on their surface. Obviously, these radioactive particles are indistinguishable from ^{99m}TcO$_2$ colloids by conventional chromatography. Usually, to prevent the formation of the neutral $Sn(OH)_4$, additional ingredients are added to the reagents required for the preparation of ^{99m}Tc radiopharmaceuticals, and the minimum amount of tin chloride ($SnCl_2$) necessary to achieve a satisfactory labeling yield is carefully determined.
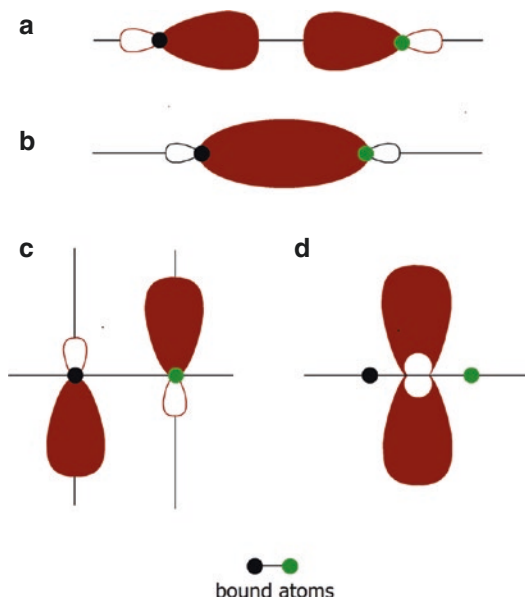
Despite these apparent difficulties, it is remarkable to notice that the preparation of ^{99m}Tc radiopharmaceuticals can be carried out using one-pot reactions involving the simple mixing of generator-eluted [^{99m}TcO$_4$]$^-$ with the appropriate reactants (reducing agent, ligands, and other ingredients) contained in a sterile vial under the form of a lyophilized powder (these vials are called *kit formulations* and are classified as pharmaceutical products). These procedures usually take a few minutes to generate the final ^{99m}Tc radiopharmaceutical in high yield (>95%) and with a total purity sufficient to permit its ready injection into patients immediately after preparation. Since the key reactions in the preparation of a ^{99m}Tc radiopharmaceutical are the reduction of the pertechnetate anion followed by the coordination of the ligands binding the Tc ion in the final product, a typical, ready-to-use kit formulation, normally comprises one (or multiple) sterile vial containing the reducing agent, the ligands, and a number of excipients. These latter substances are commonly added to prevent *radiolysis* (reaction with active radical species generated in situ by radiation) of the final product and to protect the reduced ^{99m}Tc ion from *hydrolysis* (reaction with water) that may cause re-oxidation of the metal back to oxo-containing species (namely ^{99m}TcO$_2$ and [^{99m}TcO$_4$]$^-$). The protective action of excipients is elicited through the forma-

tion of weak intermediate ^{99m}Tc complexes that are quickly converted into the final radiopharmaceutical by simple exchange reactions with the relevant ligands. In conclusion, the combination of a transportable source of the radionuclide ^{99m}Tc with sterile and pyrogen-free, freeze-dried kit formulations for the easy preparation of ready-to-use ^{99m}Tc agents, offers a key advantage in routine clinical practice that is hardly achieved with other radionuclides.

4.5 Ligand Classification

Ligands can be fundamentally categorized according to the properties of the set of atoms that are closely linked to the metallic core in the final coordination complex. This set of atoms is usually referred to as "chelating system." A simple classification scheme of atoms inside a chelating system can be derived from the basic Lewis acid–base interaction scheme depicted in Fig. 4.2. A key feature of this bonding interaction is the *symmetry* of the two overlapping orbitals (one from the donor and the other from the acceptor) with respect of the *bond axis* taken as a reference (i.e., the axis connecting the two bound atoms). Essentially, there exist two types of bonding interaction: (1) a *σ-interaction* where the donor and acceptor orbitals both envelope the bond axis and overlap along this line, and (2) a *π-interaction* where the donor and acceptor orbitals both lie above and below the bond axis and overlaps along a line perpendicular to this axis. Orbitals involved in a *σ*-interaction are called *σ-orbitals*. Similarly, orbitals involved in a *π*-interaction are called *π-orbitals*. Figure 4.8 shows a pictorial representation of these concepts.

A *σ-donor atom* (Lewis base) can donate bonding electrons to a *σ-acceptor atom* (Lewis acid) by overlapping its filled *σ*-orbitals with an empty *σ*-orbitals of the acceptor, thus forming *σ*-type chemical bonds. Similarly, a *π-donor atom* can donate bonding electrons to a *π-acceptor atom* by overlapping its filled *π*-orbitals, with empty *π*-orbitals of the acceptor, thus forming a *π*-type chemical bond. In the formation of a coordination compound, usually the ligand behaves

Fig. 4.8 Representation of (**a**) σ-orbitals, (**b**) σ-interaction, (**c**) π-orbitals, and (**d**) π-interaction

Fig. 4.9 The most common Tc functional groups: (**a**) nitrido, (**b**) oxo, (**c**) dioxo, (**d**) HYNIC, (**e**) trioxo, (**f**) tricarbonyl

as σ-/π-donor and the metal center as σ-/π-acceptor, although it may occur that for some electron-rich metallic fragments (see next paragraph) electron π-type back-donation from the metal to the ligand becomes also possible.

4.6   Technetium Cores

The chemistry of Tc-99m radiopharmaceuticals is dominated by the existence, in aqueous solution, of a number of "*inorganic functional groups*," which resemble the more familiar "organic functional groups" in organic chemistry. These groups, also called "*metallic fragments*" or "*cores*" are illustrated in Fig. 4.9.

Each functional moiety is characterized by peculiar electronic properties and, therefore, exhibits a selective reactivity toward specific classes of ligands. Interestingly, these electronic features impart distinctive coordination arrangements to the resulting complexes that, as a consequence, share common molecular geometries. Upon coordination, these metallic cores achieve a higher stability in water where they could not exist as isolated entities. The interpretation of

their selective reactivity toward different class of ligands is essential for the design of new ^{99m}Tc radiopharmaceutical having sufficient stability and inertness in a biological environment. Thus, the simple model of the coordination bond pictured above can be helpful to achieve at least a qualitative understanding of the most important chemical, structural, and biological features characterizing the various classes of ^{99m}Tc radiopharmaceuticals. In Fig. 4.10, the spatial distribution of empty σ-type frontier orbitals for each Tc core is illustrated. The nature of these orbitals determines the observed chemical reactivity of the corresponding metallic fragment and shapes their geometrical properties. As a consequence, analysis of the bonding properties of these orbitals may allow to identify the categories of ligands that are more appropriate for the production of robust radiopharmaceuticals with a selected ^{99m}Tc core.

4.7   The [Tc ≡ O]$^{3+}$ Oxo Core

A Tc atom bound to a single oxygen atom forms the *Tc-oxo* functional group. In this group, Tc has a +5 formal oxidation state, and a −2 oxidation state is conventionally assigned to O. As a consequence, the Tc-oxo moiety carries a +3 electric charge. The O atom is tightly bound to the Tc
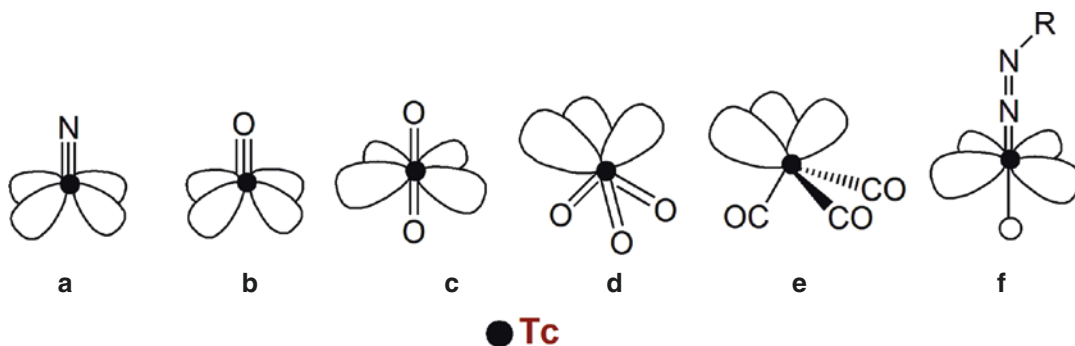
Fig. 4.10 Spatial distribution of frontier σ-orbitals for the most common Tc functional groups: (**a**) nitrido, (**b**) oxo, (**c**) dioxo, (**d**) trioxo, (**e**) tricarbonyl, (**f**) HYNIC

metal as revealed by a mean metal–oxygen bond distance closer to the value characteristic for a $Tc \equiv O$ triple bond.

The set of frontier orbitals of the $[Tc \equiv O]^{3+}$ metal fragment is composed of four empty σ-orbitals (σ-FOs) pointing toward the vertexes of the basal plane of a distorted square-pyramid, where the $Tc \equiv O$ multiple bond occupies an apical position. This spatial arrangement of σ-FOs imparts a characteristic square-pyramidal geometry to the resulting Tc-oxo complexes. In these complexes, the σ-donor atoms of the ligands span the four positions on the basal plane, and the Tc atom is displaced from this plane toward the O atom, thus yielding a typical distorted, umbrella-shaped molecular arrangement (Fig. 4.9). There exists a linear relationship between the length of the Tc-oxo bond and the degree of distortion of the square-pyramid: the more this bond shortens, the more the square-pyramid becomes distorted. When distortion is less pronounced, a sixth, weakly bound substituent can stick to the metal in a position opposite to the Tc-oxo triple bond (*trans* position).

Considered as a Lewis acid, the hardness or softness of the $[Tc \equiv O]^{3+}$ functional group is strongly dependent on the length of the $Tc \equiv O$ multiple bond, which in turn is determined by the hardness or softness of the donor atoms of the ligands. Basically, when coordinated with the $[Tc \equiv O]^{3+}$ group, hard Lewis bases shorten the Tc-oxo bond distance and the $[Tc \equiv O]^{3+}$ group more resembles a hard acid. Conversely, soft Lewis bases binding the $[Tc \equiv O]^{3+}$ core cause a

lengthening of the $Tc \equiv O$ bond distance, and the Tc-oxo group becomes softer. This phenomenon nicely explains the variety of ligands that can form complexes with the $[Tc \equiv O]^{3+}$ metallic fragment and was crucial to ensure the efficient preparation of a broad class of ^{99m}Tc radiopharmaceuticals showing high stability in aqueous solution.

In Fig. 4.11, some important examples of ligands bearing different chelating systems for the $[Tc \equiv O]^{3+}$ core are reported along with their coordination arrangement around the metallic moiety. These include the widely used tetradentate systems *NNNS* (N_3S), *SNNS* (N_2S_2), and *NNNN* (N_4), where *N* and *S* are nitrogen and sulfur donor atoms.

The preparation of ^{99m}Tc radiopharmaceuticals containing the $[Tc \equiv O]^{3+}$ core can be easily obtained through one-pot reactions by simple mixing of $[^{99m}TcO_4]^-$ with the appropriate kit formulation that commonly make use of $SnCl_2$ as reducing agent. It is important to note that the production of the $[Tc \equiv O]^{3+}$ moiety is crucially dependent on the nature of the coordinating ligands that should be able to firmly stabilize the Tc-oxo group soon after the removal of three of the four oxygen atoms from the tetra-oxo anion by the reducing agent.

4.8   The $[Tc \equiv N]^{2+}$ Nitrido Core

A *Tc-nitrido* core is composed of a Tc atom in the +5 oxidation state tightly bound to a nitrogen atom in the −3 oxidation state. Thus, the total

Fig. 4.11 Some relevant ligands for the Tc-oxo core: tetradentate (**a**) N_3S, (**b**) N_2S_2, and (**c**) N_4 ligands ($R^{1,2,3,4,5,6,7}$ = lateral substituents) and the corresponding coordination arrangements
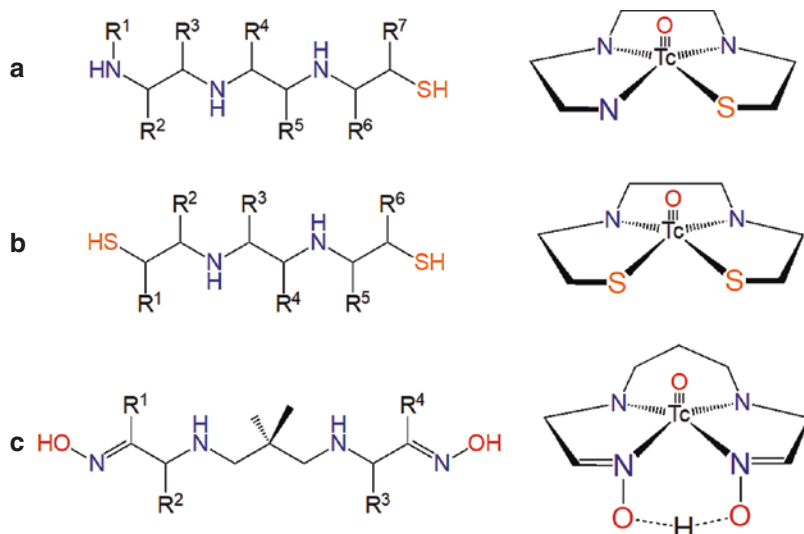
charge of this functional group is +2. The resulting metallic fragment is isoelectronic (i.e., it has the same number of valence electrons) with the $[Tc \equiv O]^{3+}$ core. As a consequence, the two groups share similar properties and types of σ-FOs, although there exist some fundamental differences. Since the nitrogen atom with a -3 oxidation number is the most efficient σ- and π-donor for metals, Tc and N atoms are tethered by a true triple bond that is stronger (hence shorter) than the $Tc \equiv O$ triple bond. This suggests that the $[Tc \equiv N]^{2+}$ fragment has a high electronic density and, therefore, is a soft Lewis acid. It turns out that it reacts preferentially with ligands that are soft σ- and π-donor Lewis bases. For example, ligands bearing $–S^-$ (sulfido-like) and $–HN^-$ (amido-like) groups are suitable coordinating systems for the $[Tc \equiv N]^{2+}$ fragment. In Fig. 4.12, drawings of the structures of some common ligands employed in the production of Tc-nitrido complexes are reported.

When bound by donor Lewis bases, complexes containing the $Tc \equiv N$ triple bond invariably acquire a distorted, umbrella-shaped, square-pyramidal geometry. However, an interesting effect arises when the electron-rich $[Tc \equiv N]^{2+}$ core also behaves as a π-donor by back-donating electron density to a π-acceptor ligand having empty π-orbitals. Typical
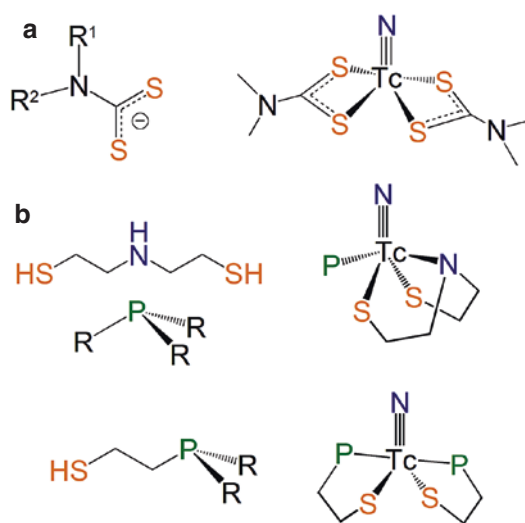
Fig. 4.12 Some relevant ligands for the Tc-nitrido core: (**a**) bidentate XS_2 (X = C, P), (**b**) tridentate NS_2 and NP_2 ligands (R = lateral substituents) and the corresponding coordination arrangements

π-acceptor ligands are monodentate and multi-dentate tertiary phosphines (Fig. 4.12). In this mixed-ligand coordination environment, the usual square-pyramidal geometry switches to trigonal-bipyramidal where two π-acceptor ligands occupy the *trans* axial positions, and $Tc \equiv N$ bond together with the π-donor ligands spans the three positions on the trigonal plane.
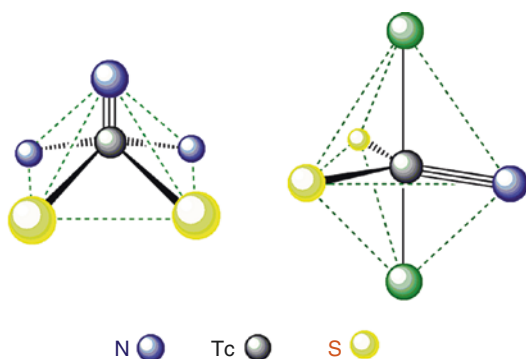
Fig. 4.13 Comparison between trigonal bipyramidal and square-pyramidal geometries in Tc-nitrido complexes

Figure 4.13 illustrates the comparison between square-pyramidal and trigonal bipyramidal geometries.

The procedure for the preparation of ^{99m}Tc radiopharmaceuticals incorporating a [Tc ≡ N]$^{2+}$ group is more elaborate than that used for the Tc-oxo core, although it can be similarly carried out using a lyophilized kit formulation. It is accomplished in two steps as sketched in Fig. 4.14. In the first step, [^{99m}TcO$_4$]$^-$ is reacted with a substance that has the property to transfer a nitrido nitrogen atom (N^{3-}) to the metal center in the presence of a reducing agent, thus yielding the Tc ≡ N multiple bond. The most common nitrido donor reagents are *succinic dihydrazide* and *S-methyl, N-methyl-dithiocarbazate* (Fig. 4.14). Then, the [Tc ≡ N]$^{2+}$ group is let to react with a suitable ligand to produce the final ^{99m}Tc radiopharmaceutical. Interestingly, when the reducing agent is SnCl$_2$, the labeling procedure has to be carried out in two separate steps, and the kit formulation includes two lyophilized vials. By contrast, when a tertiary phosphine (PR$_3$) is selected as both oxygen atom transfer and coordinating ligand, the preparation can be performed in a single step, and the molecular composition of the final ^{99m}Tc radiopharmaceutical necessarily comprises at least one phosphine ligand.

In Fig. 4.14 (bottom), two relevant examples of ^{99m}Tc nitrido radiopharmaceuticals, each prepared using one of the two routes outlined above, are illustrated. These two compounds were found to accumulate in normal myocardium and were,

therefore, utilized as myocardial perfusion imaging agents.
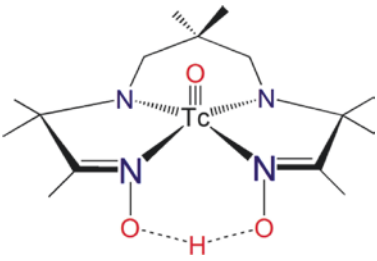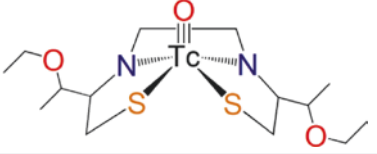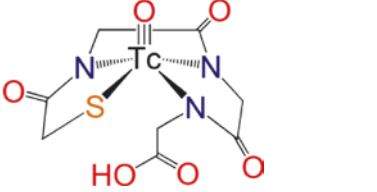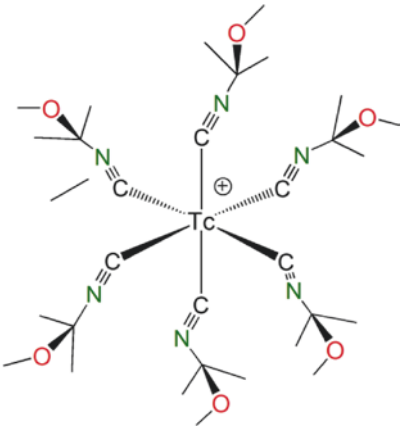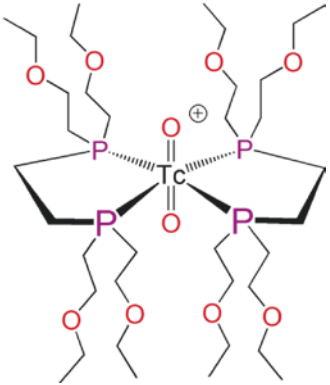
The tracer ^{99m}TcN-NOEt, (NOEt = *N*-ethyl, *N*-ethoxy-dithiocarbamato, [S$_2$CN(OEt)Et]$^{1-}$, Et = CH$_3$CH$_2$–) is a neutral ^{99m}Tc complex comprising two bidentate dithiocarbamato ligands bound to a [Tc ≡ N]$^{2+}$ core through the two sulfur atoms of the –C(=S)S$^-$ group. The resulting geometry is distorted square-pyramidal with the Tc ≡ N multiple bond occupying the apical position of the pyramid. This complex was prepared, at tracer level, through the two-step reaction shown in Fig. 4.14 where [^{99m}TcO$_4$]$^-$ is first mixed with a donor of N^{3-} groups (either *S*-methyl, *N*-methyl dithiocarbazate or succinic dihydrazide), in the presence of SnCl$_2$, to yield an intermediate ^{99m}Tc nitrido species. The chemical nature of this intermediate has not been elucidated yet, but it was found that it quickly reacts with the sodium salt of *N*-ethyl, *N*-ethoxy-dithiocarbamate {Na[NOEt] = Na[S$_2$CN(OEt)Et])} to produce the final neutral product ^{99m}Tc(N)(NOEt)$_2$. Surprisingly, despite its neutral character, ^{99m}Tc(N)(NOEt)$_2$ behaves as an almost ideal myocardial perfusion tracer and accumulates in cardiac cells through passive diffusion into the lipophilic membrane layer.

The monocationic compound [^{99m}Tc(N)(PNP)(DBODC)]$^+$, where PNP is a bidentate bis-phosphino-amine ligand and DBODC is a dithiocarbamato ligand [PNP = bis(dimethoxypropylphosphinoethyl)-ethoxyethylamine; DBODC = bis(*N*-ethoxyethyl)-dithiocarbamate] (Fig. 4.14), is an asymmetrical ^{99m}Tc nitrido complex comprising two different bidentate chelating agents coordinated to the same [^{99m}Tc ≡ N]$^{2+}$ core. The molecular geometry of this remarkable complex can be considered as either distorted trigonal bipyramidal or highly distorted square-pyramidal. At tracer level, [^{99m}Tc(N)(PNP)(DBODC)]$^+$ can be prepared through the one-step route (Fig. 4.14) by simple mixing of [^{99m}TcO$_4$]$^-$ with PNP and DBODC in the same physiological solution and in the presence of succinic dihydrazide as donor of N^{3-} groups. Because of the monocationic charge, this complex exhibits a biological behavior similar to that of the monocationic tracer ^{99m}Tc-MIBI (Table 4.1) widely used
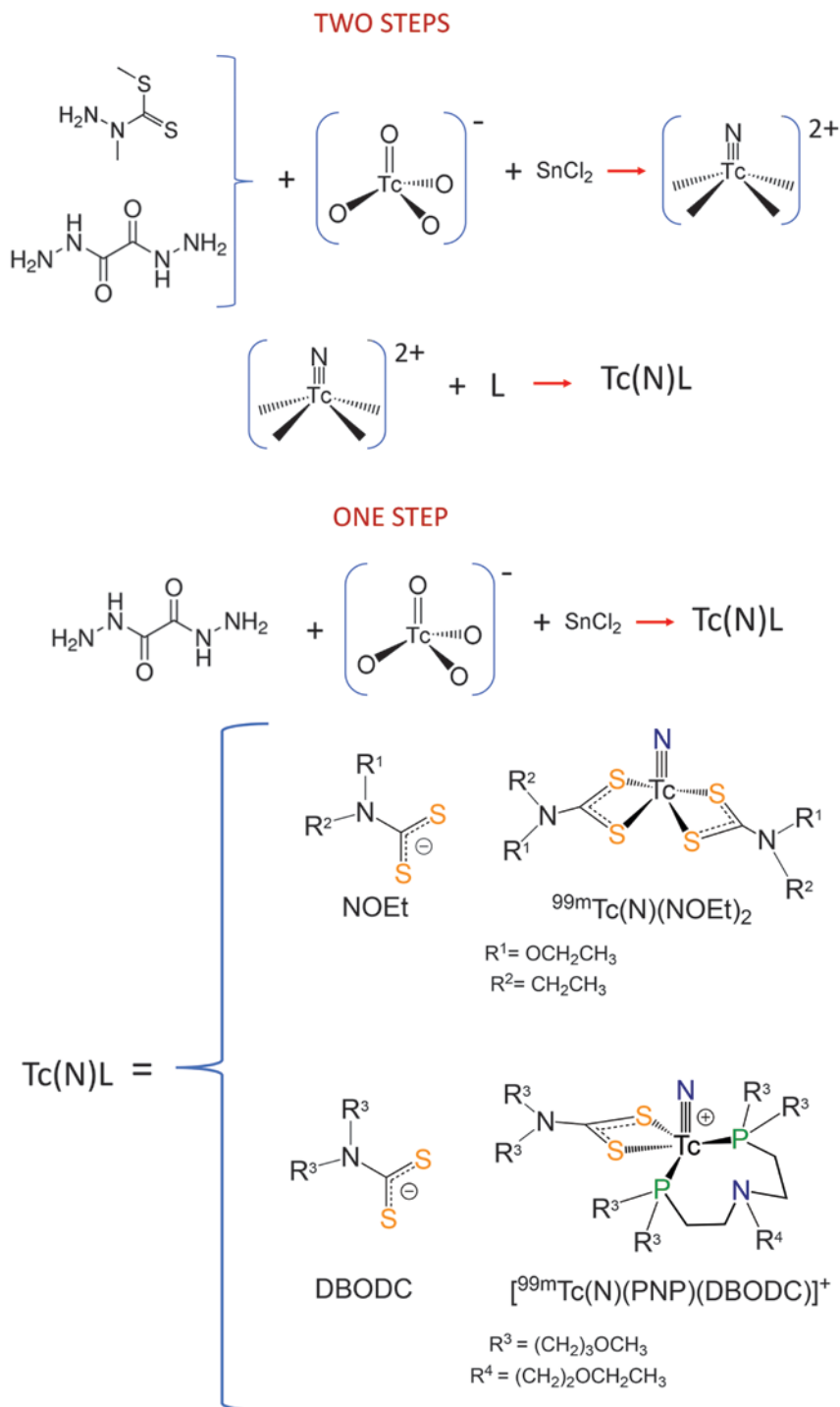
Fig. 4.14 The different routes for the production of ^{99m}Tc radiopharmaceuticals containing a Tc-nitrido group

Table 4.1 Small-molecule ^{99m}Tc radiopharmaceuticals

Structure	Acronym	Tc-core
	^{99m}Tc-HMPAO	$[Tc \equiv O]^{3+}$ (Tc-monoxo)
	^{99m}Tc-ECD	$[Tc \equiv O]^{3+}$ (Tc-monoxo)
	^{99m}Tc-MAG3	$[Tc \equiv O]^{3+}$ (Tc-monoxo)
	^{99m}Tc-MIBI	$[Tc]^+$ $[Tc(I)]$
	^{99m}Tc-Tetrofosmin	$[O = Tc = O]^+$ (Tc-dioxo)

as myocardial perfusion imaging agent in routine clinical practice. Clinical evaluation in human subjects revealed that a remarkable advantage of [^{99m}Tc(N)(PNP)(DBODC)]$^+$ over ^{99m}Tc-MIBI is its fast and quantitative liver clearance that allows to obtain high-quality imaging of the cardiac region without any significant interference from background activity.

4.9 The *trans*-[O = Tc = O]$^+$ Dioxo Core

A *trans*-[O = Tc = O]$^+$ dioxo core is made up of a Tc atom in the +5 oxidation state linked to two oxygen atoms. These three atoms are aligned along a straight line where the Tc atom is located at the central position and the two O atoms are opposite (*trans*) to each other. The value of the Tc-O bond distance indicates a double bond order between these two atoms. This group always exhibits an octahedral geometry, the O = Tc = O group being distributed along the main axis perpendicular to the square plane of the octahedron. The empty four σ-FOs of this fragment are all positioned along the diagonals of the octahedral square plane (Fig. 4.10).

Because of its high electron density, the t*rans*-[O = Tc = O]$^+$ group can be considered as both a hard Lewis σ-acid and a soft Lewis π-base. This indicates that it can bind σ-donor ligands, but also donate an electron pair to π-acceptor ligands. Typical σ-donor ligands for this fragment are polyamines and nitrogen-based macrocycles, whereas bidentate tertiary phosphines are excellent representative of a category of ligands able to behave as both σ-donors and π-acceptors. Invariably, complexes containing the *trans*-[O = Tc = O]$^+$ moiety attain an octahedral configuration, where the ligands usually span the four positions on the square plane perpendicular to the O = Tc = O bond axis. In Fig. 4.15, some typical examples of ligands employed for binding the [O = Tc = O]$^+$ metallic fragment, and the resulting molecular geometries are illustrated. From a mechanistic point of view, the *trans*-dioxo Tc group can be considered as an intermediate molecular arrangement for Tc complexes lying between the oxygen-rich pertechnetate precursor [TcO$_4$]$^-$ and the other oxygen-depleted Tc cores. For this reason, its preparation at tracer level with ^{99m}Tc always requires a fine tuning of the reaction conditions and in particular of the amount of reducing agent. Actually, an excess of the reducing agent might cause the complete removal of the oxo groups, whereas an exiguous amount of it could prevent the reduction of the ^{99m}Tc pertechnetate anion. The delicate equilibrium that should be achieved in the redox conditions for the preparation of *trans*-dioxo ^{99m}Tc radiopharmaceuticals has important practical implications in routine clinical practice because it always demands for a more careful and frequent control of the radiochemical purity of the final radiopharmaceutical before administration to patients.
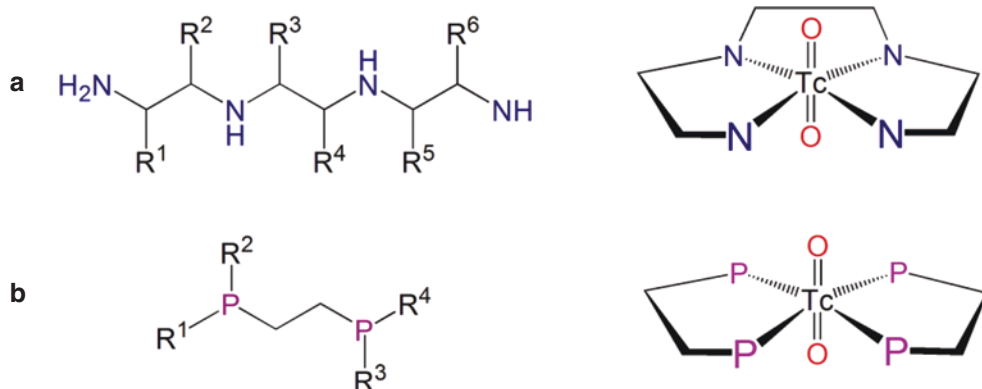
Fig. 4.15 Some relevant ligands for the Tc trans-dioxo core: (**a**) tetradentate N$_4$ ligands, (**b**) bidentate R$_3$P-PR$_3$ ligands (R = lateral substituents) and the corresponding coordination arrangements

4.10   The *fac*-[Tc(CO)₃]⁺ Tris-Carbonyl Core

The *fac*-[Tc(CO)₃]⁺ group is a complex metallic fragment where a Tc atom in one of its lowest oxidation states (+1) is linked to three carbonyl (CO) ligands. This metal–ligand combination is particularly stable as a consequence of the perfect matching between the donor–acceptor properties of the Tc^{+1} ion and of the carbonyl ligand. In particular, the Tc^{+1} ion is an electron-rich species, and thus, it can transfer electronic density to empty acceptor orbitals of the ligand. Conversely, the carbonyl group is a strong π-acceptor ligand and, therefore, avidly accepts the electron backdonation from the metal ion. The overall result is that the Tc-CO bond is built up on two opposite interactions, the first being the formation of a σ-bond between filled σ-FOs of CO and empty σ-FOs (Fig. 4.10) of the metal, followed by electron back-donation from filled π-FOs of the metal to empty π-FOs of the ligand. This concerted overlapping of σ- and π-FOs imparts a strong stabilization to the *fac*-[Tc(CO)₃]⁺ functional moiety. The prefix *fac* (facial) stems from the observation that the three CO ligands bind the metal in a characteristic trigonal-prismatic geometry (Fig. 4.4), thus spanning three adjacent vertexes on one face of the coordination polyhedron as shown in Fig. 4.16. It turns out that the remaining three facial positions of the trigonal prism opposite to those occupied by the three CO substituents are available to accept other suitable ligands able to complete the coordination arrangement. It is important to note that, in aqueous solution, these three positions are usually occupied by three weekly coordinated water molecules to yield the *fac*-[Tc(CO)₃(OH₂)₃]⁺ monocationic complex.
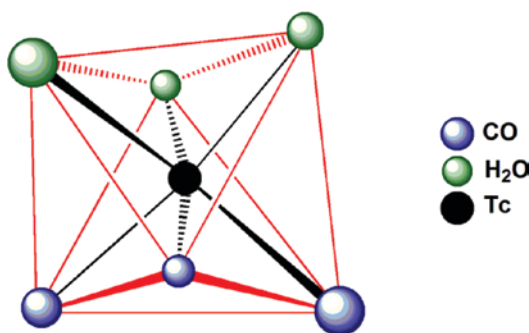
Given its peculiar characteristics, the production of the *fac*-[⁹⁹ᵐTc(CO)₃]⁺ core is not as simple as for the other Tc functional groups. More precisely, a specific class of reducing agents has been developed to allow the simultaneous reduction of ⁹⁹ᵐTc pertechnetate to Tc^{+1} and the formation of the Tc-CO bond. This reaction leads to the efficient formation of the *fac*-[⁹⁹ᵐTc(CO)₃(OH₂)₃]⁺ complex, which in turn is used as a precursor synthon for further reaction with any ligand appropriate to generate the final radiopharmaceutical. The compound potassium boranocarbonate, $K_2[BH_3CO_2]$, acts as both reducing agent and source of CO ligands. The most convenient procedure to prepare the *fac*-[⁹⁹ᵐTc(CO)₃(OH₂)₃]⁺ precursor complex is by heating a buffered aqueous solution of [⁹⁹ᵐTcO₄]⁻ and $K_2[BH_3CO_2]$ in a microwave oven, at 110 °C for approximately 5 min. Figure 4.17 reports the reagents and reaction diagram for the synthesis of the *fac*-[⁹⁹ᵐTc(CO)₃(OH₂)₃]⁺ complex.

Since all bonding electrons are shared between the metal and the three CO groups, the *fac*-[Tc(CO)₃]⁺ moiety has a remarkable kinetic inertness. Only three empty σ-acceptor FOs, pointing toward the remaining three coordination sites on the face of the trigonal prism opposite to the three CO ligands (Fig. 4.10), are left for the binding to

Fig. 4.16 The characteristic facial (fac), trigonal-prismatic arrangement of the fac-[Tc(CO)₃]⁺ metallic fragment. The three remaining positions on the opposite face of the trigonal prism can be utilized for the coordination of other suitable ligands
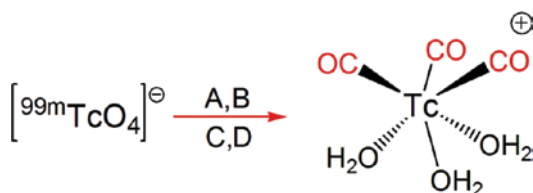
Fig. 4.17 Schematic drawing of the reaction for the preparation of the fac-[Tc(CO)₃]⁺ core. Reagents are: (A) potassium boranocarbonate ($K_2[BH_3CO_2]$), (B) sodium carbonate (Na_2CO_3), (C) sodium tetraborate decahydrate ($Na_2B_4O_7 \cdot 10H_2O$), and (D) potassium sodium tartrate $KOCO[CH(OH)]_2COONa \cdot 4H_2O$

other substituents. This orbital set confers to the *fac*-[Tc(CO)$_3$]$^+$ group a strong *σ*-acid character that allows this fragment to tether to a large variety of donor ligands. As mentioned above, in aqueous solution, these three empty orbitals commonly accommodate an electron pair coming from the oxygen atoms of three water molecules. Yet, these weakly bound OH$_2$ groups can be easily replaced by other incoming ligands to form a multitude of derivatives. In particular, the *fac*-[Tc(CO)$_3$]$^+$ moiety shows high affinity for aromatic amines such as imidazoles or pyridine. Typical ligands are histidine and cysteine, thioethers, and polyamino-carboxylates, but more complex derivatives such as cyclopentadienyl and scorpionate ligands can also efficiently bind this functional group. Figure 4.18 illustrates some examples of ligands employed in the production of ^{99m}Tc radiolabeled compounds containing the *fac*-[Tc(CO)$_3$]$^+$ core with their corresponding coordination arrangements.

4.11   The Tc-NNR (HYNIC) Core

When Tc reacts with the derivatives of 2-hydrazinonicotinic acid (HYNIC), a Tc = N multiple bond is established between the metal atom and the terminal hydrazine nitrogen atom (Fig. 4.19). The HYNIC ligand can bind the Tc atom essentially through two different coordination modes. As shown in Fig. 4.19, it can act as a monodentate, linear ligand through the terminal N donor atom or, alternatively, as a bidentate chelating ligand through both the terminal and the pyridyl N atoms. Although rather arbitrary, usually a +5 oxidation state is assigned to the Tc atom in these complexes. It is interesting to note that ^{99m}Tc radiopharmaceuticals containing the Tc-HYNIC group have not been unambiguously assigned to the two categories of coordination modes.

A key advantage of using the HYNIC moiety for the production of ^{99m}Tc radiopharmaceuticals is that the carboxylate group linked to the pyridine ring can be conveniently derivatized to append other functional groups or pharmacophores to the ligand. It turns out that, after coordination to the metal, the functionalized HYNIC
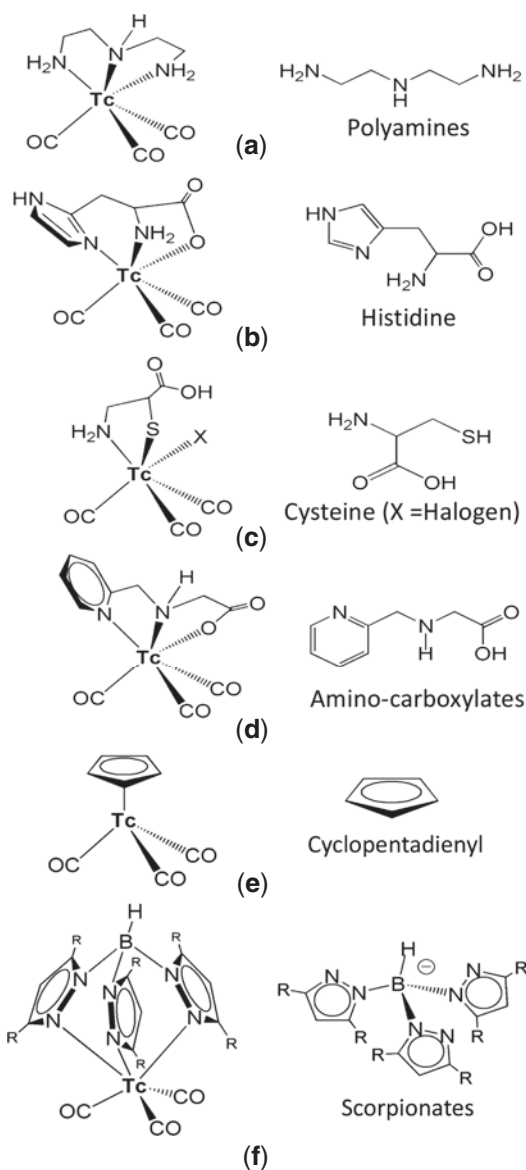
Fig. 4.18 Various classes of ligands for the fac-[Tc(CO)$_3$]$^+$ core and their relevant molecular geometries: (**a**) polyamines, (**b**) histidine, (**c**) cysteine (X = halogen), (**d**) amino-carboxylates, (**e**) cyclopentadienyl, and (**f**) scorpionates (R = lateral functional groups)

ligand will act as a bridging moiety between the appended chemical functionality and the metal.

Complexes containing the Tc-HYNIC group display invariably an octahedral geometry. However, since HYNIC can behave only as mono- or bidentate ligand, it cannot fill all the coordination positions of the octahedron. Therefore,

Fig. 4.19 The Tc-NNR (HYNIC) core and the possible coordination modes of the 2-hydrazinonicotinic acid ligand and its derivatives (R = lateral functional group): (**a**) bidentate chelating and (**b**) linear (• = ancillary ligands)
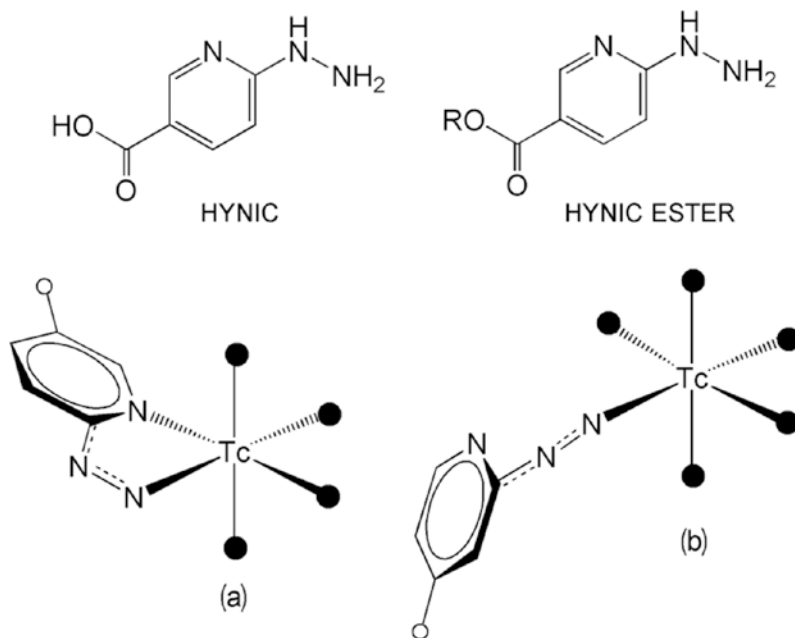
ancillary co-ligands are required to stabilize the coordination sphere. Various co-ligands and combinations of co-ligands have been proposed, including tricine, ethylenediamine diacetic acid (EDDA), mono-, di-, and tris(sulfonate) triphenylphosphine (TPPMS, TPPDS, and TPPTS), and pyridine-2,6-dicarboxylic acid (PDA). It has been hypothesized that the role of these co-ligands is not only in completing the octahedral coordination but also in favoring the formation of intermediate Tc-oxo complexes that are subsequently converted into Tc-HYNIC complexes. Tricine and EDDA proved particularly efficient as co-ligands and have been used extensively. Unfortunately, the labeled complexes are usually composed of multiple species in various isomeric forms, thus complicating the radiochemical characterization of the resulting mixture. In Fig. 4.20, the chemical structures of some of the most relevant co-ligands used in the production of ^{99m}Tc-HYNIC radiopharmaceuticals are reported.

Given the complexity of the chemistry of the HYNIC moiety when it reacts with Tc in the presence of ancillary co-ligands, it is arduous to find a ubiquitous reaction pathway for all possible preparations and ligand combinations. Certainly, the preliminary reduction of the $[^{99m}TcO_4]^-$ anion is always required to allow the binding of the HYNIC group to the metal atom, and this redox process is usually accomplished by reaction with $SnCl_2$. After reduction, the Tc ion should be promptly stabilized to avoid hydrolysis to colloidal Tc-oxo species, but this stabilization cannot be achieved by the action of the HYNIC ligand alone because this moiety can bind the metal only as either monodentate or bidentate chelating agent. To complete the residual positions of the octahedral coordination, addition of ancillary ligands is always necessary. It is assumed that these co-ligands may play two different roles. On the one side, they can form weakly bound intermediate complexes with the emerging reduced Tc ion, thus preventing hydrolysis or re-oxidation. Subsequently, the weakly bound co-ligand can be easily displaced by the coordination of the HYNIC group and of the other ancillary ligands to complete the octahedral arrangement and give rise to the final radiopharmaceutical. The compounds tricine and EDDA (Fig. 4.20) provide a widely used combination of co-ligands for the preparation of a variety of ^{99m}Tc-HYNIC radiopharmaceuticals. Some studies suggested that, in these reactions, the co-ligand tricine is able to form a first intermediate

Fig. 4.20 Some of the co-ligands most frequently used in the preparation of 99mTc-HYNIC radiopharmaceuticals: (**a**) tricine, (**b**) EDDA, (**c**) TPPTS, and (**d**) PDA
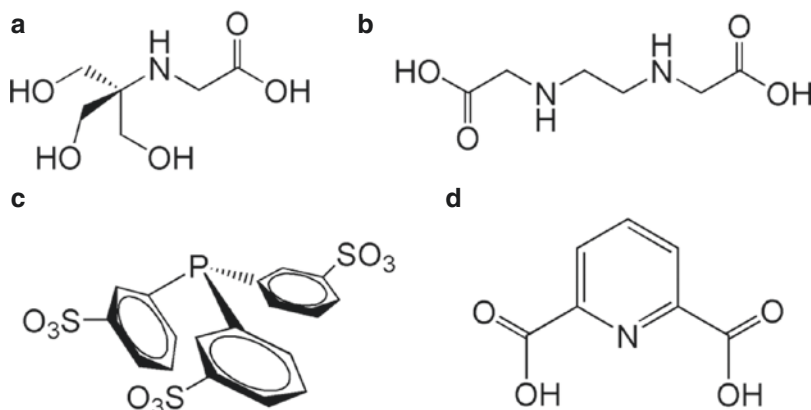
mixed 99mTc-HYNIC-tricine complex, which further reacts with the other co-ligand EDDA, thus causing the removal of tricine and the formation of the final 99mTc-HYNIC-EDDA complex. It should be noted, however, that it is commonly difficult to establish with certainty the true composition and molecular arrangement of 99mTc-HYNIC radiopharmaceuticals and that, in many reactions, a mixture of different isomeric forms is obtained. Despite these limitations, the HYNIC-based labeling procedure is among the most frequently used methods for tethering a bioactive pharmacophore to a Tc ion, and a number of peptide-derived 99mTc-HYNIC imaging agents have been successfully introduced into the clinical use (for further details, see Sects. 4.13 and 4.14 and Table 4.1).

4.12 Small-Molecule 99mTc Radiopharmaceuticals

The enormous success of 99mTc diagnostic agents can be traced back to fundamental studies of the chemistry of technetium, carried out decades ago by different research groups, that led to the development of a variety of complexes having diverse molecular structures and small dimensions. Among this multitude of compounds, a remarkable number of 99mTc complexes were demonstrated to possess biological properties suitable for diagnostic applications. It is worthy to note that the useful biodistribution characteristics of

these 99mTc complexes originated from their integral molecular structure and associated physical and chemical properties (e.g., charge, lipophilicity). In Table 4.1, a brief overview of the most important small-molecule 99mTc radiopharmaceuticals is reported.

4.13 Bifunctional Ligands

The discovery of novel 99mTc radiopharmaceuticals following the small-molecule approach fully relies on biologically useful structure–activity relationships that could emerge from the intrinsic molecular structure of a specific class of 99mTc complex. Obviously, these emerging biological properties are not totally predictable, and as a consequence, unearthing new clinically relevant diagnostic agents is largely based on a trial-and-error process and, ultimately, on *serendipity*. Most importantly, it is always dramatically arduous to identify the structural properties that a small-molecule 99mTc radiopharmaceutical should exhibit to specifically target a selected biomolecular cell population within a particular tissue. Although there are successful examples of the discovery of useful radiopharmaceuticals following this heuristic approach, yet attempts to concoct a more rational strategy have been actively pursued. The method that earned the highest consensus among the scientific community is known as *bifunctional approach*. Essentially, it conceives a radiopharmaceutical as
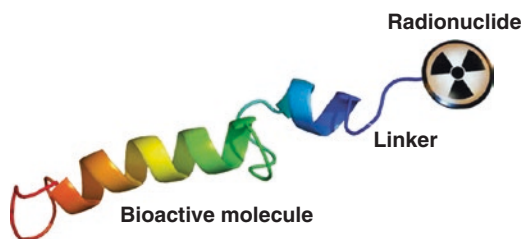
Fig. 4.21 Schematic representation of the structure of a conjugated complex

composed of three fundamental pieces: (a) a chemical moiety containing the radionuclide, (b) a chemical linker, and (c) a bioactive group imparting specific targeting properties to the final radiopharmaceuticals (Fig. 4.21). When assembled together to generate the final construct, the resulting radiopharmaceutical is called *conjugated complex*. This elegant design has some definite advantages, the most important being that various pieces can be selected, chemically manipulated independently, and then put together. In particular, the bioactive group can be picked from large libraries of biologically active molecules and active pharmaceutical compounds that demonstrated a selective affinity for some biological target or metabolic process.

Unfortunately, nature is not always sensitive to elegant concepts and looks more complex. Actually, the bifunctional approach suffers of many limitations, the most critical being that the biological behavior of the resulting conjugated complex does not exactly matches that of the bioactive moiety alone, but it is determined by the unique combination of the different pieces assembled inside the whole molecular architecture. In other words, the biological properties of a conjugated complex do not just arise from the sum of the constituent parts, but they are the result of the holistic combination of the whole molecular arrangement.

The structure of a bifunctional ligand should always be tailored to the particular type of ^{99m}Tc metallic fragment to which it has to be tied. In particular, a series of bifunctional ligands can bear the same bioactive group but differ in the chelating system that should adapt to the specific ^{99m}Tc core. Figure 4.22 illustrates three examples of bifunctional ligand designed to target the *pros-*

tate specific membrane antigen (PSMA), also known as glutamate carboxypeptidase II (GCPII) or *N*-acetyl-L-aspartyl-L-glutamate peptidase I (NAALADase I). PSMA is a zinc metalloenzyme that resides in membranes (a class II membrane glycoprotein) although most of the protein protrudes in the extracellular space. It catalyzes the hydrolysis of *N*-acetyl-aspartyl-glutamate (NAAG) to glutamate and N-acetyl-aspartate (NAA) and is highly expressed in the prostate. In some prostate cancers, PSMA is one the most upregulated gene product, with an 8–12-fold increase over levels in noncancerous prostate cells. Because of this elevated expression, PSMA is being developed as potential biomarker for therapy and imaging of prostate cancers. With the purpose of targeting PSMA, several PSMA inhibitors have been developed, and among them, the category of pharmacophores based on the lysine-urea-glutamate motif proved to be suitable tools for the synthesis of bifunctional ligands for imaging PSMA expression in prostate cancer patients. In Fig. 4.22, the structures of three of these bifunctional ligands are reported. These ligands were specifically designed to bind the ^{99m}Tc-oxo, ^{99m}Tc-*tris*-carbonyl, and ^{99m}Tc-HYNIC cores, respectively.

Another relevant class of bifunctional ligands for ^{99m}Tc are those developed to selectively target somatostatin receptors overexpressed by neuroendocrine tumors (NET) and other cancers. The ubiquitous bioactive group of this class of ligands is the octapeptide *octreotide* that mimics the pharmacological properties of the natural hormone *somatostatin*. This is a peptide hormone that regulates the endocrine system and affects neurotransmission and cell proliferation by interaction with G-protein-coupled somatostatin receptors. The structures of the bifunctional ligands for binding the ^{99m}Tc-oxo and ^{99m}Tc-HYNIC cores are illustrated in Fig. 4.23.

A more complex type of bifunctional chelator is represented by the ligand *tilmanocet* (Fig. 4.24). This compound is employed for the preparation of *^{99m}Tc-tilmanocet* a diagnostic agent for the detection of the first sentinel lymph node, which is the hypothetical first lymph node or group of nodes draining a cancerous lesion and postulated of being primarily reached by metastasizing can-

Fig. 4.22 Schematic drawing of the structures of bifunctional ligands for targeting PSMA expression and specifically designed to bind the following ^{99m}Tc cores: (**a**) [Tc ≡ O]$^{3+}$, (**b**) ^{99m}Tc-HYNIC, and (**c**) fac-[Tc(CO)$_3$]$^+$
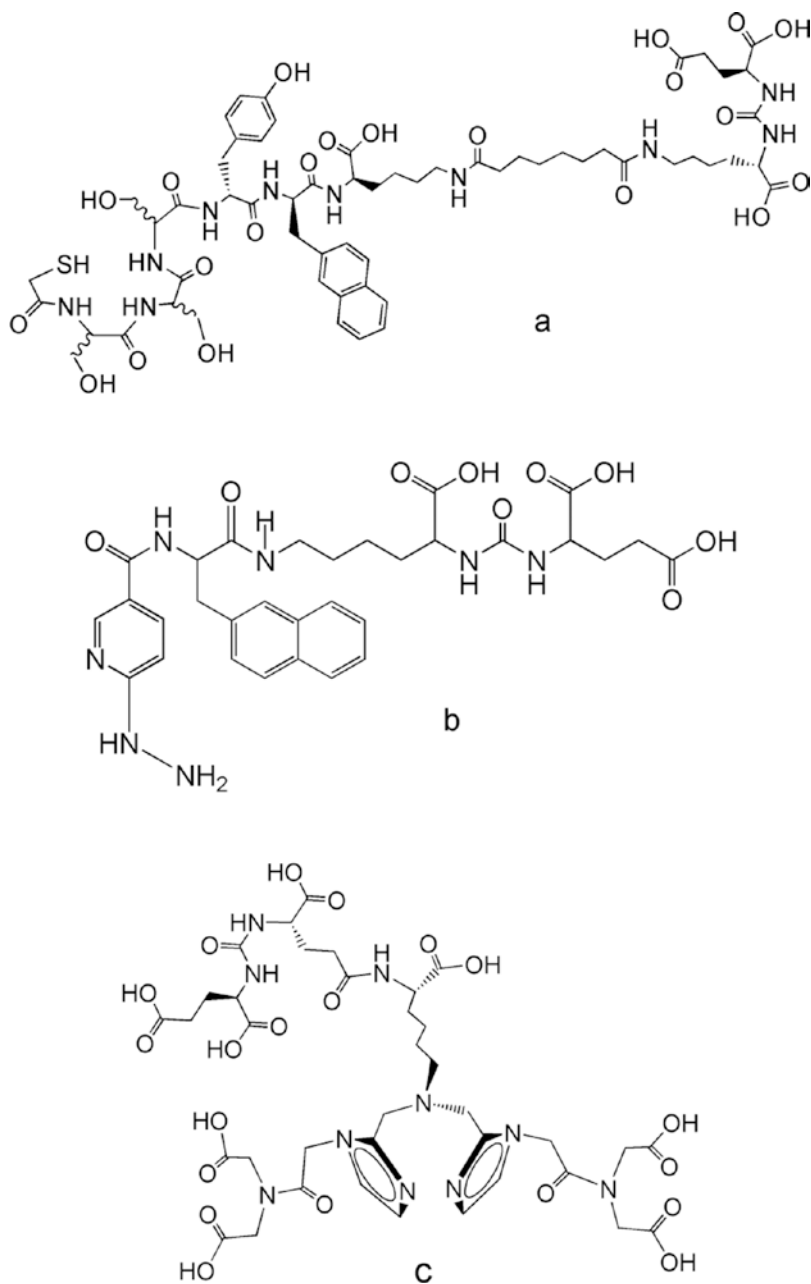
Fig. 4.23 Schematic drawing of the structures of bifunctional ligands for targeting somatostatin receptors and specifically designed to bind (**a**) $[Tc \equiv O]^{3+}$, (**b**) ^{99m}Tc-HYNIC, and (**c**) $[Tc \equiv N]^{2+}$
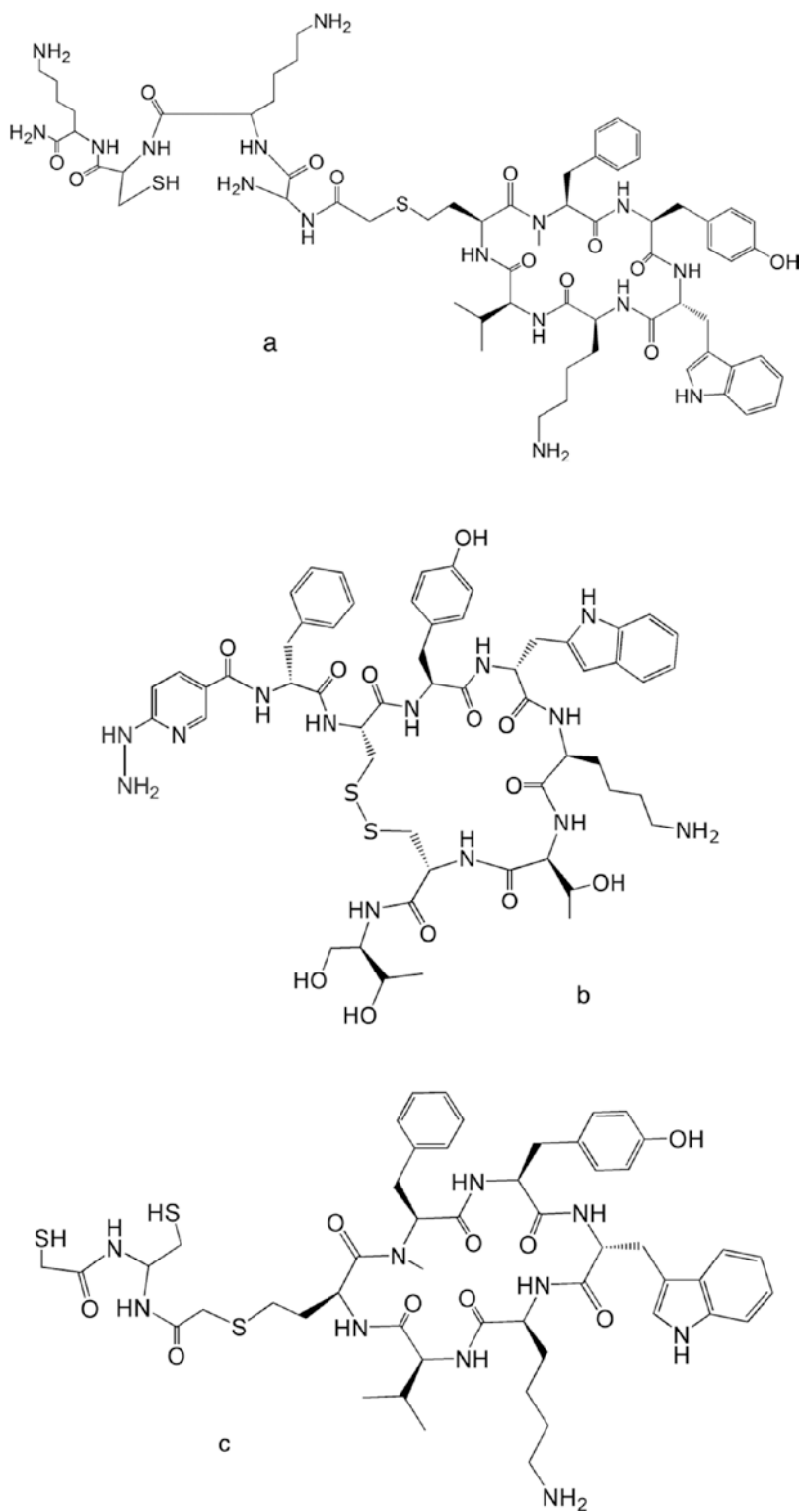
cer cells from the tumor. This ligand was constructed by appending a number of *mannose* residues to a dextran macromolecular scaffold. Since macrophages are commonly hosted in lymph nodes and specifically express mannose receptors on their surface, ^{99m}Tc-tilmanocet is selectively accumulated in lymph nodes by targeting these receptors through its pendant mannosyl groups. Beside mannose residues, the bifunctional ligand also bears a number of molecules of *diethylenetriaminepentaacetic acid* (DTPA) that play the role of chelating groups for the radiometal.

Although it is always arduous to develop a bifunctional ligand that, after coordination to ^{99m}Tc, is able to penetrate the blood–brain barrier (BBB) and to target receptors in the central nervous system, a relevant example is given in Fig. 4.25, where the chemical structure of the bifunctional ligand *trodat-1* is pictured. This ligand is formed by a chelating group specifically tailored to bind the $[Tc \equiv O]^{3+}$ core and a bioactive moiety derived from the pharmacologically active molecule *tropane* that has a selective affinity for *D2 dopamine transporters* (DAT) located in the hippocampus. Therefore, the resulting ^{99m}Tc complex has been used for imaging the distribution of DAT receptors in various brain disorders.

4.14 Conjugated ^{99m}Tc Radiopharmaceuticals
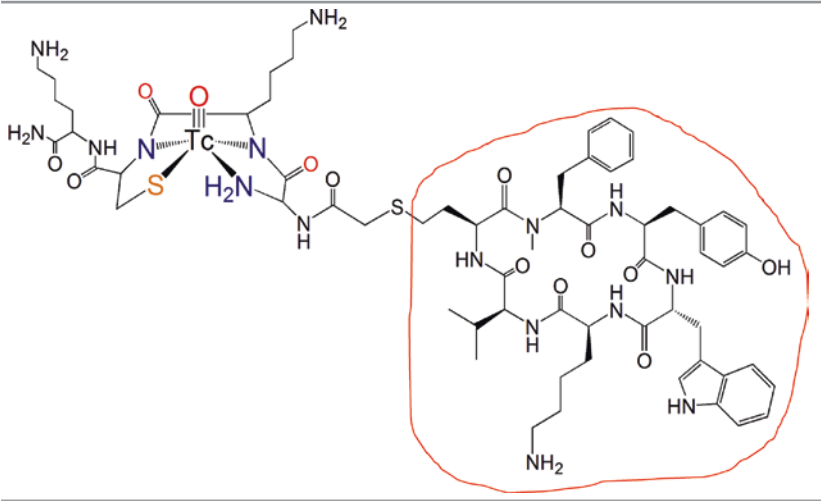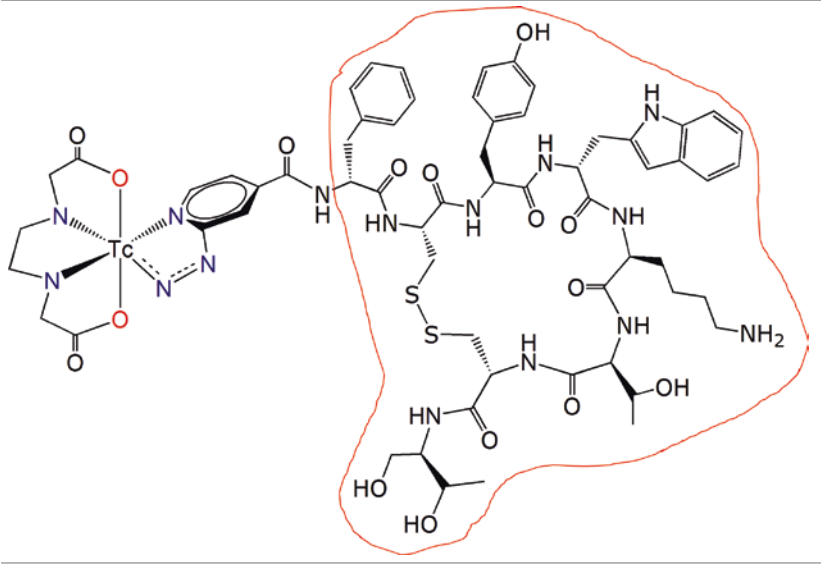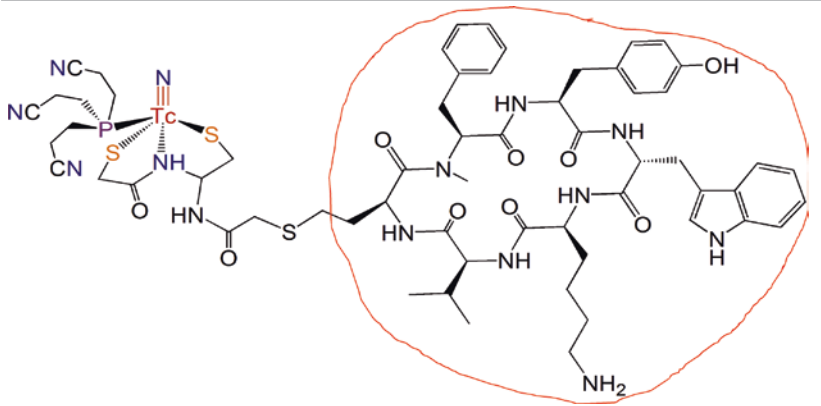
Despite its limitations, the bifunctional approach is proved highly effective particularly when applied to the design of radiopharmaceuticals for targeting receptors overexpressed by specific cell populations. A number of ^{99m}Tc agents have been produced by assembling various ^{99m}Tc cores with different types of bifunctional ligands. Table 4.2 summarizes the chemical structure and diagnostic application of these receptor-specific ^{99m}Tc radiopharmaceuticals (in the table, the pharmacophore is encircled).
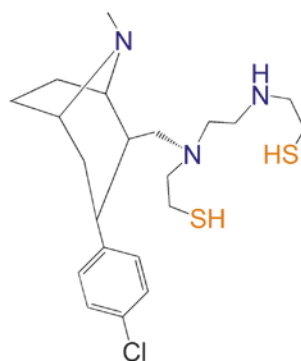
Fig. 4.25 Schematic drawing of the structures of the bifunctional ligand TRODAT-1

Fig. 4.24 Schematic drawing of the structures of the bifunctional ligand tilmanocet
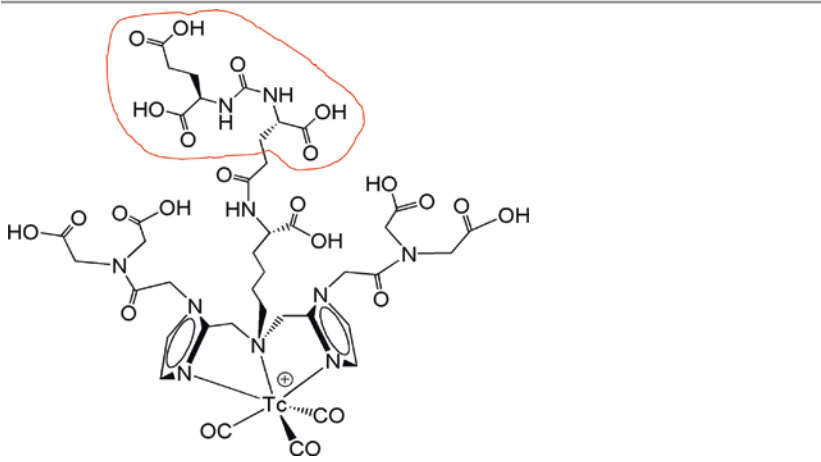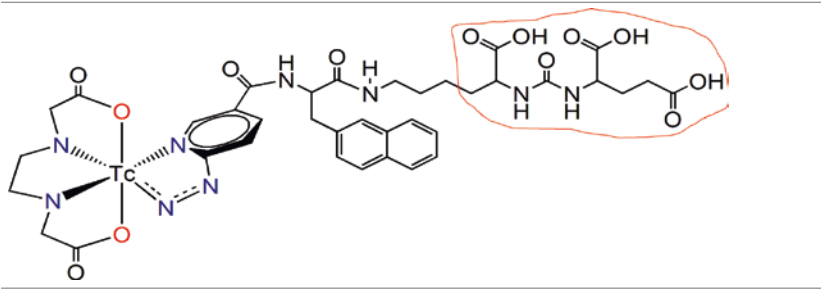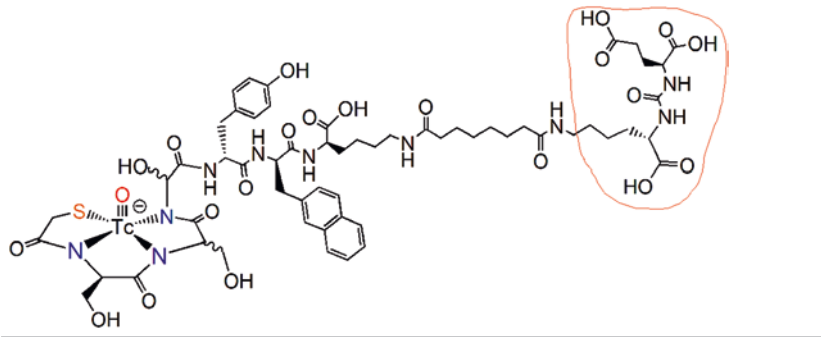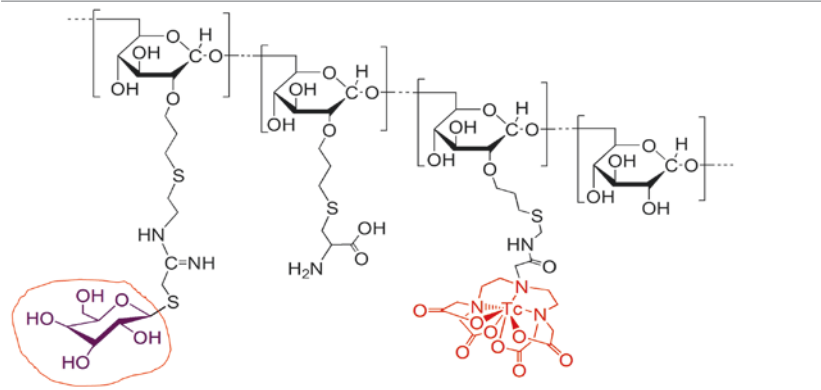
Table 4.2 Receptor-specific ^{99m}Tc radiopharmaceuticals
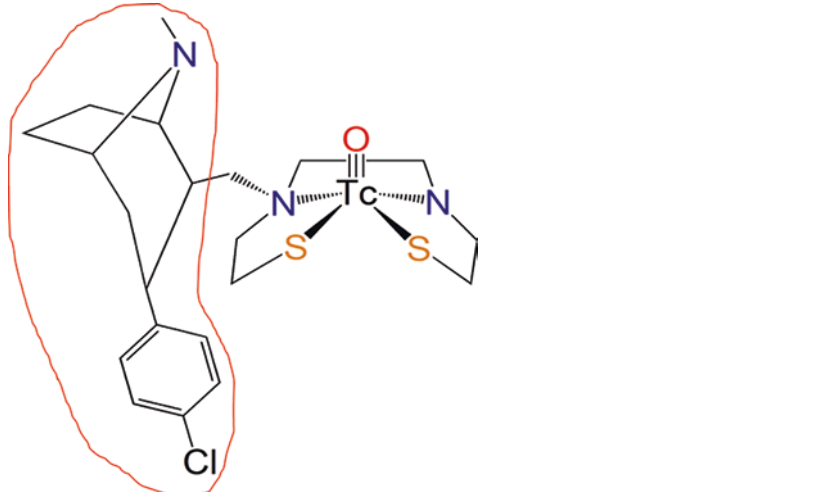
Structure	Acronym (application)[a]
	^{99m}Tc-Depreotide (SSTR imaging)
	^{99m}Tc-HYNIC-TOC (SSTR imaging)
	^{99m}TcN-3 + 1-TIDE (SSTR imaging)

Table 4.2 (continued)

Structure	Acronym (application)[a]
	99mTc-Trofolastat (PSMA imaging)
	99mTc-HYNIC-iPSMA (PSMA imaging)
	99mTc-PSMA-I&S (PSMA imaging)
	99mTc-Tilmanocet (SLND)

Table 4.2   (continued)

Structure	Acronym (application)[a]
	^{99m}Tc-TRODAT-1 (D2 receptors)

[a]*SSTR* somatostatin receptors, *PSMA* prostate-specific membrane antigen, *SLND* sentinel lymph node detection, *D2* type 2 dopamine receptors

Disclaimer The author hereby confirms that all figures used in this chapter are original and not from a published material.

Glossary

***π*-acid (*π*-acceptor)** A Lewis acid using empty *π*-orbitals to accept electron pairs.

***π*-base (*π*-donor)** A Lewis base using filled *π*-orbitals to donate electron pairs.

***π*-symmetry orbitals** A class of orbitals having inversion symmetry with respect to rotations around the main axis of a chemical bond (they change sign upon rotation of 180° around the bond axis).

***σ*-acid (*σ*-acceptor)** A Lewis acid using empty *σ*-orbitals to accept electron pairs.

***σ*-base (*σ*-donor)** A Lewis base using filled *σ*-orbitals to donate electron pairs.

***σ*-symmetry orbitals** A class of orbitals having cylindrical symmetry with respect to rotations around the main axis of a chemical bond (they do not change sign upon any rotation around the bond axis).

Bifunctional ligand A ligand composed of a chelating group for binding the radiometal linked to a biologically active molecule imparting a selective affinity for some biological target.

Bonding orbital The orbital obtained from the linear combination of two atomic orbitals (superposition), each belonging to one of the bound atoms.

Conjugated complex A coordination compound resulting from the combination of a bifunctional ligand and a radiometal.

Coordination geometry The geometrical solid that can be drawn by connecting with ideal lines the positions of the atoms bound to the metal center in the first coordination sphere.

Dopamine transporter An integral membrane protein (a symporter) that removes dopamine from the synaptic cleft and transfers it into surrounding cells, thus closing the neurotransmission cycle.

Hard Lewis acid A Lewis acid in which the empty acceptor orbitals are either atomic orbitals belonging to a *high-electronegative* atom or *low-energy* molecular orbitals of a single molecule.

Hard Lewis base A Lewis base in which the filled donor orbitals are either atomic orbitals belonging to a *high-electronegative* atom or *low-energy* molecular orbitals of a single molecule.

HPLC High-performance liquid chromatography is a technique for separating substances in a mixture after dissolution in a liquid. Separation is achieved by pumping the high-pressurized liquid through a capillary column containing a solid absorbent material that causes the various substances in the sample to flow at different rates.

Hydrolysis Side reaction with water molecules, occurring in physiological solution during the preparation of a ^{99m}Tc radiopharmaceutical, that may cause re-oxidation of the metallic ion to form oxo-species (e.g., ^{99m}TcO$_2$ or [^{99m}TcO$_4$]$^-$).

Kit formulation A sterile vial containing, under a lyophilized form, all the reagents and excipients required to produce a radiopharmaceutical after simple addition of a solution containing the radionuclide.

Lewis acid A single atom or molecule having empty orbitals able to *accept* electron pairs from a donor through the formation of a donor–acceptor chemical bond.

Lewis base A single atom or molecule having filled orbitals able to *donate* electron pairs to an acceptor through the formation of a donor–acceptor chemical bond.

Ligand A chemical species able to form a chemical bond with a metallic element.

Mass spectroscopy (MS) Analytical technique that allows the determination of the molecular mass of a ^{99m}Tc radiopharmaceutical when injected into a magnetic field. Before entering the magnetic field, the ^{99m}Tc compound is first isolated in a purified form by liquid chromatography and then sprayed into the mass spectrometric detector. The combination of liquid chromatography and mass spectroscopy is called LC-MS.

Octreotide A synthetic octapeptide mimicking the biological properties of the natural peptide somatostatin.

Orbital A region of space surrounding the atomic nucleus where there exists the highest probability of finding an electron.

PSMA A zinc metalloenzyme that belongs to class II membrane glycoproteins and catalyzes the hydrolysis of *N*-acetyl-aspartyl-glutamate (NAAG) to glutamate and N-acetyl-aspartate (NAA).

Radiolysis Side reaction of a ^{99m}Tc radiopharmaceutical with reactive radical species, generated in solution by the action of radioactivity, that may cause its decomposition and the concomitant formation of radioactive impurities.

Soft Lewis acid A Lewis acid in which the empty acceptor orbitals are either atomic orbitals belonging to a *low-electronegative* atom *or high-energy* molecular orbitals of a single molecule.

Soft Lewis base A Lewis base in which the filled donor orbitals are either atomic orbitals belonging to a *low-electronegative* atom or *high-energy* molecular orbitals of a single molecule.

Somatostatin A peptide hormone that regulates the endocrine system through the interaction with G-protein-coupled somatostatin receptors. This regulatory function also affects neurotransmission and cell proliferation.

Tc-core A characteristic chemical motif containing a Tc atom bound to another atom or group of atoms or molecules. Also called "metallic fragment" or "inorganic functional group." The presence of a particular Tc-core imparts characteristic chemical and geometrical properties to the resulting coordination complex.

The soft-soft hard-hard principle Soft acids react preferentially with soft bases, and conversely, hard acids react preferentially with hard bases.

TLC Thin-layer chromatography is a chromatographic technique for the separation of non-volatile substances contained in a mixture. Separation is accomplished by spotting a drop of the mixture, dissolved in some solvent, onto the surface of a plate coated with some appropriate material (stationary phase). After deposition of the sample, a solvent or solvent mixture (mobile phase) is flushed through the plate by capillary action. Because different substances are dragged through the surface at different rates, separation is achieved.

Tropane A nitrogenous bicyclic organic compound precursor of a group of alkaloids (tropane alkaloids), which includes atropine and cocaine.

Bibliography

1. Meszaros LK, Dose A, Biagini SCG, Blower PJ. Hydrazinonicotinic acid (HYNIC)—coordination chemistry and applications in radiopharmaceutical chemistry. Inorg Chim Acta. 2010;363:1059–69.

2. Abram U, Alberto R. Technetium and rhenium—coordination chemistry and nuclear medical applications. J Braz Chem Soc. 2006;17:1486–500.

3. Liu S, Chakraborty S. 99mTc-centered one-pot synthesis for preparation of [99mTc] radiotracers. Dalton Trans. 2011;40:6077–86.

4. Papagiannopoulou D. Technetium-99m radiochemistry for pharmaceutical applications. J Label Compd Radiopharm. 2017;60:502–20.

5. Duatti A. Fundamentals of technetium and rhenium chemistry. In: Theobald T, editor. Sampson's textbook in radiopharmacy. 4th ed. London: Pharmaceutical Press; 2011. p. 101–24.

6. Rathmann SM, Ahmad Z, Slikboer S, Bilton HA, Snider DP, Valliant JF. The radiopharmaceutical chemistry of technetium-99m. In: Lewis J, Windhorst A, Zeglis B, editors. Radiopharmaceutical chemistry. Cham: Springer; 2019. p. 311–33.

7. Sogbein OO, Pelletier-Galarneau M, Schindler TH, Wei L, Wells RG, Ruddy TD. New SPECT and PET radiopharmaceuticals for imaging cardiovascular disease. Biomed Res Int. 2014;2014:942960.

8. Duatti A, Liu S, Pasqualini S. The missed Tc-99m radiopharmaceuticals for cardiac imaging. Curr Radiopharm. 2009;2:268–76.

9. Méndez-Rojas MA, Kharisov BI, Tsivadze AY. Recent advances on technetium complexes: coordination chemistry and medical applications. J Coord Chem. 2006;59:1–63.

10. Morais GR, Paulo A, Santos I. Organometallic complexes for SPECT imaging and/or radionuclide therapy. Organometallics. 2012;31:5693–714.

11. Martini P, Pasquali M, Boschi A, Uccelli L, Giganti M, Duatti A. Technetium complexes and radiopharmaceuticals with scorpionate ligands. Molecules. 2018;23:2039.

12. Technetium-99m radiopharmaceuticals: manufacture of kits. International Atomic Energy Agency, Technical Reports, Report No. 466; 2008.

13. Banerjee SR, Foss CA, Castanares M, Mease RC, Byun Y, Fox JJ, Hilton J, Lupold SE, Kozikowski AP, Pomper MG. Synthesis and evaluation of technetium-99m- and rhenium-labeled inhibitors of the prostate-specific membrane antigen (PSMA). J Med Chem. 2008;51:4504–17.

14. Zolle I, editor. Technetium-99m pharmaceuticals: preparation and quality control in nuclear medicine. Berlin: Springer; 2007.

15. Bolzati C, Carta D, Salvarese N, Refosco F. Chelating systems for [99mTc]/[188Re] in the development of radio-labeled peptide pharmaceuticals. Anticancer Agents Med Chem. 2012;12:428–61.

16. Bolzati C, Refosco F, Marchiani A, Ruzza P. [99mTc]-radiolabelled peptides for tumour imaging: present and future. Curr Med Chem. 2010;17:2656–8.

17. Gonzàlez-Vàzquez A, Ferro-Flores G, Arteaga de Murphy C, Gutiérrez-Garcìa Z. Biokinetics and dosimetry in patients of [99mTc]-EDDA/ HYNIC-Tyr[3]-octreotide prepared from lyophilized kits. Appl Radiat Isot. 2006;64:792–7.

18. Plachcińska A, Mikolajczak R, Kozak J, Rzeszutek K, Kuśmierek J. Comparative analysis of [99mTc]-depreotide and [99mTc]-EDDA/HYNIC-TOC thorax scintigrams acquired for the purpose of differential diagnosis of solitary pulmonary nodules. Nucl Med Rev. 2006;9:24–9.

19. von Guggenberg E, Sarg B, Lindner H, Melendez-Alafort L, Mather SJ, Moncayo R, Decristoforo C. Preparation via coligand exchange and characterization of [[99mTc]-EDDA-HYNIC-D-Phe[1], Tyr[3]] octreotide ([99mTc]-EDDA/HYNIC-TOC). J Label Compd Radiopharm. 2003;46:307–18.

20. Meszaros LK, Dose A, Biagini SCG, Blower PJ. Hydrazinonicotinic acid (HYNIC)—coordination chemistry and applications in radiopharmaceutical chemistry. Inorg Chim Acta. 2010;363:1059–69. https://doi.org/10.1016/j.ica.2010.01.009.

21. Artiko V, Afgan A, Petrović J, Radović B, Petrović N, Vlajković M, Šobić-Šaranović D, Obradović V. Evaluation of neuroendocrine tumors with [99mTc]-EDDA/HYNIC TOC. Nucl Med Rev Cent East Eur. 2016;19:99–103.

22. Wester HJ, Schottelius M. PSMA-targeted radiopharmaceuticals for imaging and therapy. Semin Nucl Med. 2019;49:302–12.

23. Shih WJ, Samayoa L. Tc-99m depreotide detecting malignant pulmonary nodules: histopathologic correlation with semiquantitative tumor-to-normal lung ratio. Clin Nucl Med. 2004;29:171–6.

24. Hillier SM, Maresca KP, Lu G, Merkin RD, Marquis JC, Zimmerman CN, Eckelman WC, Joyal JL, Babich JW. [99mTc]-labeled small-molecule inhibitors of prostate-specific membrane antigen for molecular imaging of prostate cancer. J Nucl Med. 2013;54:1369–76.

25. Wester HJ, Schottelius M. PSMA-targeted radiopharmaceuticals for imaging and therapy. Semin Nucl Med. 2019;49:302–12.

26. Wüstemann T, Haberkorn U, Babich J, Mier W. Targeting prostate cancer: prostate-specific membrane antigen based diagnosis and therapy. Med Res Rev. 2019;39:40–69.

27. Surasi DS, O'Malley J, Bhambhvani P. [99mTc]-Tilmanocept: a novel molecular agent for lymphatic mapping and sentinel lymph node localization. J Nucl Med Technol. 2015;43:87–91.

Radiopharmaceuticals in Clinical Diagnosis and Therapy

5

James R. Ballinger

Contents

5.1 Diagnostic Radiopharmaceuticals

5.1.1 Skeletal System

The most commonly used radiopharmaceuticals for imaging the skeletal system are the ^{99m}Tc-labelled complexes of the diphosphonates medronate (methylene diphosphonate, MDP) and oxidronate (hydroxymethylene diphosphonate, HDP) (Fig. 5.1). In both the cases, the phosphonate groups perform the dual role of chelation of reduced ^{99m}Tc and binding to the biological target, hydroxyapatite crystals at the surface of bone. Even after more than four decades of use, the mechanism of localization of these agents is not fully understood, but the extent of accumulation of ^{99m}Tc-diphosphonate in a particular region of the skeleton is dependent upon two variables: delivery and affinity. Delivery occurs via blood
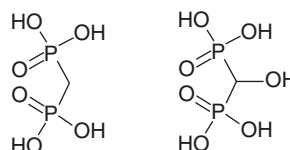
Fig. 5.1 Chemical structures of medronate (left) and oxidronate (right)

supply with passive diffusion into the bone extracellular fluid. ^{99m}Tc-diphosphonates appear to have greater affinity for immature or metabolically active bone, possibly due to the newly formed bone crystals being well hydrated and thus more accessible to diffusion of radiotracer. Whatever the mechanism, microautoradiography has demonstrated binding at sites of mineralization which is not correlated with the number of osteoblasts or amount of collagen.

Following intravenous injection, the tracer distributes throughout the body with about one-half of the activity localizing to bone while the remainder is excreted via glomerular filtration into the urine. Imaging is generally performed 2–3 h after injection to allow for clearance of unbound activ-

J. R. Ballinger (✉)

School of Biomedical Engineering and Imaging Sciences, King's College London, London, UK
e-mail: jim.ballinger@kcl.ac.uk

ity through the kidneys, providing a clearer image of the skeleton [1]. Whole-body planar images are usually obtained, ideally with a dual-headed gamma camera. This may be followed by SPECT images of the affected area. SPECT/CT may be useful for precise anatomical localization of the lesion. The information produced by a radionuclide bone scan is quite different from an X-ray which shows bone density. The bone scan reflects the rate of bone growth via osteoblastic activity, though vascularization also plays a role. The most common clinical indications for the bone scan are: detection of bone metastases (including selection of patients for radionuclide therapy), chronic inflammatory arthritis, osteomyelitis or loosening of replacement joints, sports injuries and metabolic bone disease [2].

5.1.2 Neuroimaging

5.1.2.1 Cerebral Blood Flow

Two ^{99m}Tc-labelled radiopharmaceuticals are used for imaging regional cerebral blood flow: exametazime (hexamethyl propyleneamine oxime, HMPAO, Ceretec®) and bicisate (ethyl cysteinate dimer, ECD, Neurolite®) (Fig. 5.2). Both are small, neutral, lipophilic complexes which are highly extracted by the brain on first pass by passive diffusion, then trapped in the brain following a chemical change which results in a charged moiety which cannot exit across the blood–brain barrier. With HMPAO, the change is believed to involve interaction with ubiquitous

compounds such as glutathione, whereas with ECD, it involves sequential enzymatic hydrolysis of the two ethyl ester groups, leaving free acids. After initial clearance of background activity, the regional distribution of tracer remains stable over time, allowing flexibility in imaging time. SPECT images are generally obtained. From a radiopharmaceutical point of view, the two products differ in their ease of preparation and use: HMPAO requires a fresh eluate of the generator and is stable for only 30 min after preparation (or 1 h after addition of a stabilizer), whereas ECD does not have these restrictions and is stable for 6 h [3]. The inherent instability of ^{99m}Tc-HMPAO is still not understood, and the identity of the alternative complexes, which do not enter the brain, has not been confirmed. The most common indications for use of cerebral blood flow imaging are cerebrovascular disease, presurgical localization of epileptogenic foci [4], early detection and differential diagnosis of dementia, evaluation of traumatic brain injury and assessment of brain death [5].

5.1.2.2 Dopamine Transporter

The dopamine transporter can be imaged with an ^{123}I-labelled analogue of cocaine, ioflupane (fluoropropyl carbomethoxy iodophenyl nortropane, FP-CIT, Datscan®) (Fig. 5.3). The function of the dopamine transporter is reuptake of dopamine released into the synapse into vesicles in the presynaptic nerve terminal. Ioflupane binds to the transporter to give an indication of the density of presynaptic nerve terminals. SPECT imaging is
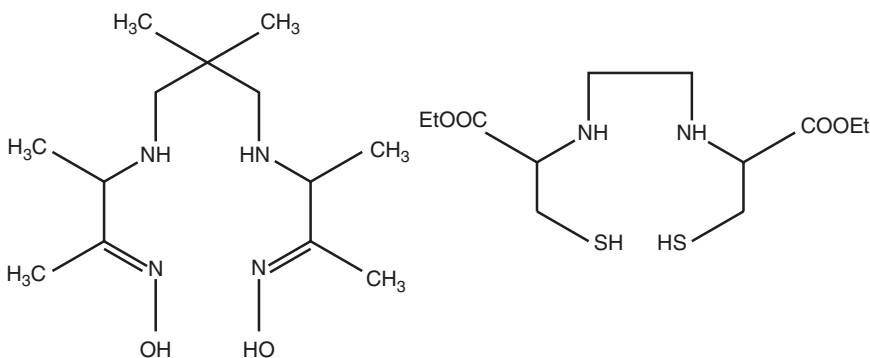
Fig. 5.2 Chemical structures of exametazime (left) and bicisate (right)

performed at a fixed time 3–6 h after injection [6]. Parkinson's disease involves degeneration of the nigrostriatal pathway with loss of dopaminergic nerve terminals. Thus, dopamine transporter imaging can be used to diagnose Parkinson's disease and to differentiate it from other causes of parkinsonian tremor such as essential tremor (i.e. non-degenerative) or that caused by certain neuroleptic drugs. It is also useful in the diagnosis of Lewy body disease [7].

5.1.3 Cardiovascular System

5.1.3.1 Myocardial Perfusion

Myocardial perfusion imaging (MPI) became established in the 1980s using the tracer ^{201}Tl-thallous chloride. ^{201}Tl is an analogue of potassium and is rapidly and efficiently transported into the myocardium by sodium-potassium ATPase. Thus, the distribution of ^{201}Tl in the myocardium reflects regional perfusion and when injected at rest allows assessment of infarcted areas (permanent defects). When injected at peak stress (exercise or pharmacological), areas of coronary artery disease will be evident with
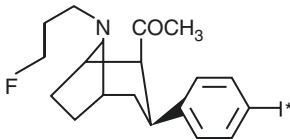
Fig. 5.3 Chemical structure of ioflupane

reduced delivery of tracer. Imaging must begin immediately after stress in order to map the full extent of ischaemia, because redistribution of tracer begins immediately, and ischemic defects will gradually fill in. Imaging 4 h after stress is the equivalent of a rest injection, and this dual time point imaging allows differential diagnosis to be made from a single radiation dose [8].

The physical limitations of ^{201}Tl as a tracer (poor emission energies, long half-life limiting administered activity, poor radiation dosimetry) led to the search for a ^{99m}Tc-labelled equivalent. Two such agents came into clinical use around 1990: sestamibi (methoxy isobutyl isonitrile, MIBI, Cardiolite®) and tetrofosmin (ethylene-bis[bis(2-ethoxyethyl)phosphine], TFOS, Myoview®) (Fig. 5.4). Both are lipophilic cations, designed to mimic the active transport of ^{201}Tl. However, it turns out that both enter cells by passive diffusion and are trapped in electronegative mitochondria due to their positive charge. Unlike ^{201}Tl, they do not undergo redistribution, so separate injections are required in order to image the rest and stress distributions. These are ideally performed on separate days, but sequential injections on the same day can be used, with a low activity first followed by a higher activity. Although planar imaging may be performed, SPECT provides better delineation of the affected territories of the coronary arteries. SPECT/CT allows attenuation correction and, with diagnostic quality CT detectors, coronary artery calcium scoring. Gating to the electrocardiogram may also be used [9].
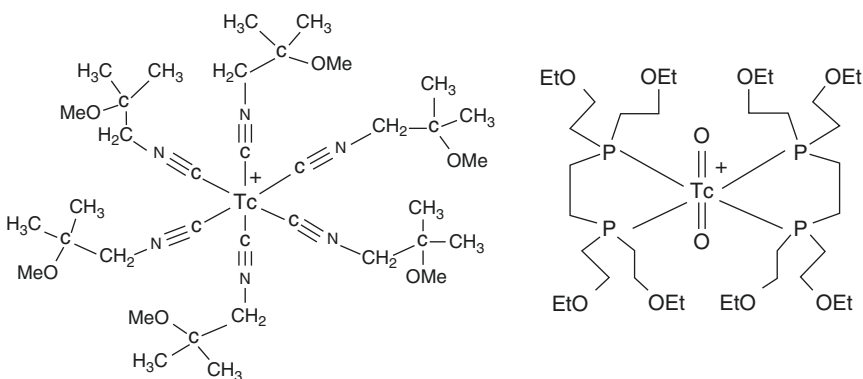
Fig. 5.4 Chemical structures of sestamibi (left) and tetrofosmin (right)

Sestamibi and tetrofosmin have generally similar properties, but there are significant differences in their biodistribution. The initial extraction of tracer into the myocardium is slightly higher and more linear with flow for sestamibi compared to tetrofosmin, though both are lower than [201]Tl. Sestamibi is excreted almost exclusively via the gall bladder into the intestinal tract, whereas tetrofosmin also undergoes a degree of urinary excretion. In general, imaging begins later for sestamibi, requiring more time for clearance from the liver. With both radiotracers, the high and changing activity in the intestine can create problems for reconstruction and interpretation of images.

The availability of sestamibi and tetrofosmin fuelled the expansion of MPI over the last 30 years to the extent that it comprises more than 50% of nuclear medicine patient volume in some countries. Its greatest value is the negative predictive value; a normal MPI study indicates a very low risk of cardiac events (<1% per year). Thus, it is used for risk stratification with asymptomatic airline pilots, truck drivers and other high-risk professions, as well as in symptomatic patients with chest pain or as part of workup for cardiovascular surgery [10].

5.1.3.2 Ventricular Function

Assessment of the efficiency of cardiac contraction is useful in a variety of cardiac conditions. Blood pool labelling followed by gated acquisition of images (multi-gated acquisition, MUGA) or equilibrium radionuclide ventriculography (ERNV) allows determination of the left ventricular ejection fraction (LVEF), the fraction of the blood ejected on average per beat of the heart. In vivo labelling of the blood pool with ^{99m}Tc is conveniently performed by sequential injection of a stannous agent followed by ^{99m}Tc-pertechnetate. The stannous agent distributes throughout the blood pool, and a fraction of it enters red blood cells (RBC). ^{99m}Tc-pertechnetate will also be widely distributed, but when it diffuses into RBC, it is reduced by stannous ions and binds to haemoglobin. About 80% of the injected ^{99m}Tc will be trapped in RBC, and the remainder will gradually clear from tissues. In most patients, this provides adequate image quality, although patients with low haematocrit and/or low haemoglobin, such as following chemotherapy, may require in vitro or modified in vivo labelling [11].

The left ventricle contains the largest pool of blood in the chest, so gamma camera imaging will allow definition of the size of the ventricle. Gating to the electrocardiogram allows acquisition of a series of 16–32 frames to construct a composite cardiac cycle. From this, the minimum and maximum sizes of the ventricle can be determined, and the LVEF is calculated.

ERNV is the method of choice for monitoring the cardiotoxicity of chemotherapeutic drugs. The test is performed before each cycle of chemotherapy in order to assess the cumulative damage [12]. Other indications include prognosis following acute myocardial infarction, assessment of patients with intermediate to high likelihood of coronary artery disease and diagnosis and prognosis in heart failure.

5.1.4 Pulmonary System

5.1.4.1 Perfusion

The integrity of the arterial system in the lungs can be assessed using ^{99m}Tc-labelled macroaggregated human serum albumin particles (MAA). The diameter of capillaries is ~7 μm, so particles larger than this diameter will be trapped in capillaries. MAA particles are engineered to be 10–90 μm in diameter (90% within this range, none >150 μm; median typically 20–40 μm). When ^{99m}Tc-MAA is injected intravenously, it will travel to the right ventricle, then to the pulmonary arterial system where it will encounter capillaries for the first time and be essentially completely trapped, outlining the pulmonary blood supply. This allows detection of pulmonary embolism as a cold spot. Lung perfusion imaging is routinely performed in conjunction with ventilation imaging to improve the differential diagnosis [13].

5.1.4.2 Ventilation

The airways can be visualized with an inhaled gas or aerosol droplets. Historically ^{133}Xe or [127]Xe gas was used, but this has been largely replaced. Generator produced [81m]Kr gas ($t\frac{1}{2}$ 13 s) is available in some countries. ^{99m}Tc-pertechnetate burnt at high temperature generates submicron graphite particles which behave like a gas (Technegas®). Most commonly, an aerosol of ^{99m}Tc-DTPA generated by wet nebulization is used. The disadvantage of an aerosol is that it only shows delivery not washout via the airways as a gas does [13].

Differential diagnosis is made by comparison of the ventilation and perfusion scans (V/Q) together with a recent chest X-ray to exclude other causes such as pneumothorax. Four abnormal patterns can be seen: (1) segmental perfusion defect with preserved ventilation = pulmonary embolism; (2) segmental matched perfusion and ventilation defect = pulmonary infarction or infection; (3) segmental or sub-segmental ventilation defect with preserved perfusion = infection; (4) non-segmental, patchy, matched perfusion and ventilation defect = chronic obstructive pulmonary disease (COPD). The use of SPECT or SPECT/CT imaging can reduce the incidence of indeterminate scans [14].

5.1.4.3 Permeability

Altered alveolar permeability is seen in a number of conditions. This can be assessed with ^{99m}Tc-DTPA delivered as an aerosol (as for lung ventilation imaging) followed by repeated imaging over 90 min to allow generation of clearance curves. This is particularly useful for rapid screening of *Pneumocystis carinii* infection (PCP) in patients with a normal chest X-ray. Clearance is accelerated in these patients and resolves with successful treatment. However, clearance is also accelerated in smokers, limiting the applicability of screening [15].

5.1.5 Renal System

5.1.5.1 Renal Function

Dynamic imaging of the kidneys with a tracer which is both passively filtered and actively secreted by the tubules allows assessment of the integrity of the kidney and collecting system, stenosis and the function of a transplanted kidney. Historically, [131]I- or ^{123}I-orthoiodohippurate was used, but currently ^{99m}Tc-mertiatide (mercaptoacetyl triglycine, MAG3®) and ^{99m}Tc-ethylenedicysteine (EDC or EC, Edicis®) are most popular (Fig. 5.5). Both are polar complexes which are negatively charged at physiological pH. A normal renogram shows rapid delivery of the tracer to both kidneys, peaking at ~1 min, followed by slower but continuous clearance over several minutes with a concomitant increase in activity in the bladder. The relative function of the two kidneys can be assessed. With stenosis of the pelviureteric junction, delivery is normal but clearance from the affected kidney is greatly prolonged. Similarly, decline in function of a transplanted kidney is reflected in reduced clearance [16].
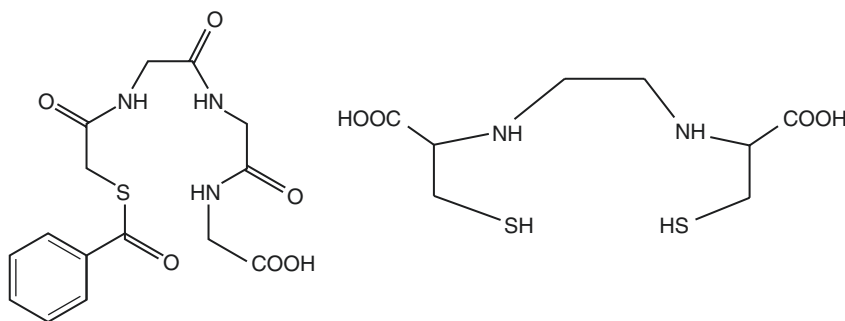
Fig. 5.5 Chemical structures of mertiatide (left) and ethylenedicysteine (right)

5.1.5.2 Renal Structure

Imaging the structure of the kidney is important in a number of conditions, particularly in children. The tracer used is ^{99m}Tc-succimer (dimercaptosuccinic acid, DMSA). Following IV injection, the tracer binds extensively but reversibly to plasma proteins. Over several hours, the tracer accumulates in the renal cortex. Imaging is generally performed 4 h after injection. This is useful for the assessment of congenital malformations, trauma or pyelonephritis following repeated urinary tract infections [17]. Quantification via regions of interest drawn around the kidneys gives an indication of relative function of the individual kidneys. There is no consensus on the utility of SPECT imaging, which involves a higher administered activity, and thus radiation dose and sedation may be required for children.

5.1.5.3 Glomerular Filtration Rate

A tracer that is cleared exclusively by glomerular filtration can be used to measure the glomerular filtration rate (GFR). Two such agents are ^{99m}Tc-pentetate (diethylenetriamine penta-acetic acid, DTPA) and ^{51}Cr-edetate (ethylenediamine tetra-acetic acid, EDTA), though the latter is becoming less widely available. With ^{99m}Tc-DTPA, dynamic imaging can be performed and GFR can be estimated with the use of an appropriate standard [18].

With either tracer, blood samples can be taken over several hours followed by counting of plasma samples and a standard based on the injected activity. A semi-log plot of activity vs time is prepared. This allows estimation of the volume of distribution (= total body water) and GFR, and this method is generally believed to be more accurate than camera-based methods [19].

Assessment of GFR is important prior to dosing of renotoxic drugs such as chemotherapeutics and ensuring adequate renal function in donors for renal transplant.

5.1.6 Gastrointestinal System

5.1.6.1 Gastric Emptying

Gastric emptying rates of solids and/or liquids can be determined by repeated imaging follow-ing ingestion of a radiolabelled meal. The solid phase is most often ^{99m}Tc-colloid-labelled scrambled egg or omelette served with bread or toast. The liquid phase can be ^{99m}Tc-DTPA; however, if solid and liquid emptying is performed at the same time, the liquid phase should be ^{111}In-DTPA, so that dual-energy imaging can be used. Regions of interest are placed around the stomach in the anterior and posterior views at each time point (after correction for cross-talk if dual-energy imaging is used) and the geometric mean activity in the stomach is calculated (geometric mean is used to eliminate errors due to depth within the abdomen). These values are plotted vs time, and a gastric clearance curve is generated. Gastric emptying may be faster or slower than normal in different conditions and repeated studies can be performed to monitor the effectiveness of drug therapies [20].

5.1.6.2 Transit Studies

Imaging can be used to investigate disorders in transit in various parts of the gastrointestinal system. Rapid dynamic imaging as the patient swallows a small amount of ^{99m}Tc-labelled liquid or solid can be used to measure the oesophageal transit time, which can be delayed in motility disorders, lower oesophageal sphincter dysfunction, scleroderma, spasm and achalasia. Gastroesophageal reflux with or without pulmonary aspiration can be particularly useful in children. Extension of a gastric emptying study can provide information about small bowel transit time. However, studies of colon transit cannot be performed with ^{99m}Tc due to its half-life being too short; in this case ^{111}In-DTPA is used [21].

5.1.6.3 Gastrointestinal Bleeding

In patients with suspected bleeding within the gastrointestinal tract, it is important to determine whether the bleeding is active, to localize the site of bleeding and to estimate the extent/rate/volume of bleeding. Two imaging approaches have been taken. If bleeding is active, it may be visualized using a ^{99m}Tc-labelled colloid (liver scan agent; see Sect. 5.1.6.4). The tracer is normally cleared quickly from the circulation and accumulates in the liver. Any hot spots in the abdomen

will represent an active bleed. However, the sensitivity of this test is relatively low. More commonly, an equilibrium study is used with ^{99m}Tc-labelled red blood cells (as in Sect. 5.1.3.2). This allows imaging over a number of hours and thus is not dependent upon the bleed being active at the time of injection [22].

5.1.6.4 Liver/Spleen

The liver scan was an important study in the early days of nuclear medicine but is less commonly used since the introduction of computed tomography and ultrasound. However, there are still some indications for the liver scan. The tracer is ^{99m}Tc-labelled colloidal particles that are cleared from the circulation by the Kupfer cells in the liver and spleen. ^{99m}Tc-sulphide colloid is prepared by heating ^{99m}Tc-pertechnetate with sodium thiosulphate at low pH; ^{99m}Tc is trapped in the particles as they grow. The reaction is terminated by cooling and addition of a buffer. Alternatively, there is a kit for the preparation of ^{99m}Tc-tin colloid. Clinical indications include functional morphology of the liver and/or spleen, detection of masses including haemangiomas, and evaluation of hepatic function in acute or chronic liver disease. Following an ^{111}In-leukocyte scan (see Sect. 5.1.8), liver/spleen imaging may be used to help identify abscesses and to differentiate infection from normal bone marrow activity [23].

5.1.6.5 Hepatobiliary System

Hepatobiliary scintigraphy is performed with a lipophilic compound which is taken up by the liver, then rapidly clears through the gall bladder and is excreted into the small intestine. The most widely used tracer is ^{99m}Tc-mebrofenin (bromo-2,4,6-trimethylacetanilido iminodiacetic acid, BrIDA, Cholecis®, Choletec®, Cholediam®), though ^{99m}Tc-disofenin (2,6-diisopropylacetanilido iminodiacetic acid, DISIDA, Hepatolite®) is still used in some countries. Dynamic imaging is used at 1 frame/min for up to 60 min to monitor the extraction from the blood into the liver (normally 100%) then concentration in the gall bladder followed by excretion. Delayed imaging may be required if the gall bladder is not visualized within 60 min, as in acute cholecystitis. Likewise, delayed imaging may aid in the detection of a bile leak [24].

5.1.7 Endocrine System

5.1.7.1 Thyroid Function

The role of the thyroid gland, located in the front of the neck, is to incorporate dietary iodine into the hormones triiodothyronine (T3) and thyroxine (T4) which, when secreted into the circulation, control a variety of metabolic, growth and development processes. One of the first radiopharmaceuticals was ^{131}I-iodide, which is a perfect probe of thyroid function as it is taken up by what we now know is the sodium iodide symporter (NIS) then organified as hormones. NIS is a transporter located in the basolateral membrane of thyroid epithelial cells which simultaneously transports Na$^+$ and I$^-$ ions from extracellular fluid into the thyroid epithelial cell via secondary active transport driven by the sodium gradient across the membrane. Because of the suboptimal radionuclidic properties of ^{131}I, ^{123}I is now the preferred radionuclide. ^{99m}Tc-pertechnetate is an alternative radiotracer which is also taken up by NIS but not organified [25]. ^{99m}Tc-pertechnetate is a substrate for NIS because it has some of the chemical properties of iodide (single negative charge, small size, hydrophilic), but it cannot be incorporated into thyroid hormones.

Hypothyroidism is diagnosed as reduced accumulation of ^{123}I-iodide and is associated with sensitivity to cold, little appetite, and low energy. In children, it can result in cretinism with abnormal bone formation and mental retardation. Hypothyroidism can be treated with thyroxine tablets. In contrast, hyperthyroidism (increased accumulation of ^{123}I-iodide) is associated with sensitivity to heat, excessive appetite and hyperactivity. It may be evident as a goitre or bulge in the neck. Hyperthyroidism can be treated with drugs, but radioiodine is also used (see Sect. 5.2.1.1). Hyperthyroidism can also result from thyroiditis, an inflammation which can eventually lead to hypothyroidism. The thyroid image in hypo- or hyperthyroidism is relatively uni-

form; however, in other conditions, focal hot or cold spots may be seen. Solitary thyroid nodules are generally benign but should be investigated with a fine needle aspiration (FNA) biopsy to determine if it is cancerous.

5.1.7.2 Thyroid Carcinoma

Papillary thyroid cancer is the most common form (~80%). It generally occurs in younger patients (peak 30–50 years) and predominantly in women. The prognosis is very good for small, well-differentiated tumours in younger patients. For radioiodine treatment, see Sect. 5.2.1.2. Follicular thyroid cancer is the second most common form. Peak onset is slightly later (40–60 years) but again predominantly female. Prognosis is slightly poorer than for the papillary form.

Imaging, as with benign thyroid diseases, uses ^{123}I-iodide, although ^{131}I-iodide is still used since radiation exposure is less of a concern in these patients and its longer half-life allows prolonged imaging of biodistribution. However, ^{99m}Tc-pertechnetate is not useful in the diagnosis of thyroid cancer due to inadequate retention in primary and metastatic tissue since it is not organified [26].

5.1.7.3 Parathyroid Imaging

The parathyroid glands are located adjacent to the thyroid, and they regulate the body's use of calcium. Parathyroid adenoma is a benign condition causing hyperparathyroidism, usually resulting in elevated blood calcium levels, which is best treated by minimally invasive surgery. Imaging plays an important role in guiding surgery. Most commonly used now is the myocardial perfusion agent, ^{99m}Tc-sestamibi, which accumulates in both the thyroid and parathyroid glands but is only retained in the parathyroid glands. The mechanism of accumulation of ^{99m}Tc-sestamibi is not fully understood but is believed to be related to high mitochondrial activity. Two imaging approaches are taken. One uses early and late imaging (15 min and 2 h) following injection of ^{99m}Tc-sestamibi. Relative focal increase in the parathyroid glands (as the tracer washes out of the thyroid) is indicative of adenoma. An alternative approach uses a second, thyroid-specific tracer such as ^{99m}Tc-pertechnetate

or ^{123}I-iodide to allow subtraction of thyroid activity for better definition of the parathyroid glands. In either case, SPECT or SPECT/CT imaging is useful to provide the surgeon with a roadmap [27].

5.1.7.4 Adrenal Medulla

Imaging the adrenal glands is difficult because they are so close to the kidneys. In the early 1980s, the tracer ^{123}I-iobenguane (metaiodobenzylguanidine, MIBG, Adreview®) was developed and remains the agent of choice. Iobenguane is an analogue of noradrenaline and is taken up by the noradrenaline transporter and stored in presynaptic vesicles. Whole-body and SPECT images are obtained 24 h after injection [28]. Adrenergic tumours include pheochromacytoma, carcinoid tumour and neuroblastoma (particularly paediatric). High activities of ^{131}I-iobenguane can be used to treat certain adrenergic tumours (see Sect. 5.2.1.3).

A secondary use of iobenguane is imaging of adrenergic innervation in the heart to determine prognosis in congestive heart failure. Early and delayed anterior planar images of the chest are obtained. On each set of images, regions of interest are placed around the heart (H) and the mediastinum (M). H/M ratios are calculated and also the fractional washout between time points. Low ratios and rapid washout are associated with poor prognosis in heart failure [29].

5.1.7.5 Neuroendocrine Tumours

Neuroendocrine tumours (NETs) arise from the neuroendocrine system and include gastrointestinal, lung and pancreatic NETs. NETs overexpress the somatostatin receptor, which can be imaged with tracers which are ligands for the receptor, including ^{111}In-pentetreotide (DTPA-octreotide, Octreoscan®) and ^{99m}Tc-hynic-TOC (EDDA/hynic-Tyr3-octreotide, Tektrotyd®) (Fig. 5.6). However, PET/CT imaging of ^{68}Ga-labelled analogues is becoming more widely used. Planar and/or SPECT/CT images are acquired at 24 h with ^{111}In and at 1–2 and 4 h with [99m]Tc [30, 31]. Analogues of pentetreotide coupled to beta-emitting radionuclides are used for therapy of NETs (see Sect. 5.2.1.4). Diagnostic scans are important

```
DTPA  D-Phe Cys Tyr
            |
            S            D-Trp
            S            Lys
            |
      Thr-ol Cys Thr


Hynic  D-Phe Cys Tyr
            |
            S            D-Trp
            S            Lys
            |
      Thr-ol Cys Thr


DOTA  D-Phe Cys Tyr
            |
            S            D-Trp
            S            Lys
            |
       Thr Cys Thr
```
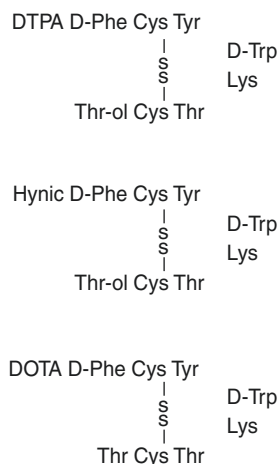
Fig. 5.6 Chemical structures of pentetreotide, Hynic-TOC and DOTATATE

for the selection of patients for therapy and for monitoring response to therapy. In particular, ^{68}Ga-DOTATATE (DOTA-Tyr$_3$-octreotate) is becoming widely used. ^{68}Ga ($t\frac{1}{2}$ 68 min) is obtained onsite from a generator loaded with ^{68}Ge ($t\frac{1}{2}$ 271 days). ^{68}Ga-DOTATATE was originally prepared with an automated synthesis device followed by purification but now a 'kit' formulation is available which requires only heating in a vial with no further purification.

5.1.8 Infection and Inflammation

Autologous leukocytes (white blood cells, WBC) labelled with ^{99m}Tc or ^{111}In are used to image sites of infection and inflammation. WBC cannot be labelled in whole blood and must first be separated by enhanced sedimentation, primarily to remove the ~1000-fold excess of RBC. The isolated WBC are then incubated for ~15 min with ^{99m}Tc-HMPAO or ^{111}In-oxine, then the excess labelling agent is washed off, and the cells are resuspended in plasma for reinjection into the patient. The entire process must be carried out in specialized, separate, aseptic facilities, both to protect the patient's blood from contamination and to protect the staff from blood-borne pathogens. The process is cumbersome, time-consuming (~2 h) and expensive but has been in routine use since ~1980 [32].

The normal biodistribution of radiolabelled WBC includes the liver, spleen and bone marrow on whole-body images 2–24 h after reinjection. There should be little retention of activity in the lungs unless the cells have been damaged during labelling. With ^{99m}Tc-labelled WBC, there is also excretion of activity into the GI tract which can interfere with interpretation of the image. Sites of infection or inflammation will be seen as hot spots. Among the most common indications for WBC imaging are osteomyelitis, prosthetic joints, inflammatory bowel disease, soft tissue infections and fever of unknown origin.

Because of the complexity of WBC labelling techniques, alternative tracers have been investigated, largely without success. There are two ^{99m}Tc-labelled anti-granulocyte antibodies which have some limited use: sulesomab (Leukoscan®) and besilesomab (Scintimun®) [32].

5.1.9 Lymphoscintigraphy

Lymphoscintigraphy with ^{99m}Tc-labelled radio-colloids was used in the earliest days of nuclear medicine. After a period of decline, the technique has become increasingly important in recent years to direct minimally invasive surgery based on the sentinel lymph node concept, which is the standard of care in an increasing range of solid tumours. The role of the radiocolloid is to act as a surrogate for cancer cells spreading from the tumour to adjacent lymph nodes. The radiocolloid is retained in lymph nodes due to phagocytosis by macrophages, a non-specific process. The radiocolloid thus allows identification of a lymph node but gives no information as to whether the node contains tumour cells; that can only be determined by histology of a biopsy specimen. The particular radiocolloid used depends on the geography and commercial availability rather than optimal properties: albumin nanocolloid (Nanocoll®, Nanotop®, NanoScan®) in most of Europe; rhenium sulphide colloid (Nanocis®) in France; sulphide colloid, filtered

or unfiltered, in North America; antimony trisulphide colloid in Australia and tin colloid in Japan. Indeed, there is a lack of agreement on optimal particle size: particles <5 nm in diameter are liable to penetrate capillaries and be carried away by blood, while particles >400 nm will not migrate in lymph and will remain at the injection depot. While it has been stated that a diameter of ~100 nm would be optimal, most of the available agents tend to be somewhat smaller than that (15–50 nm). Despite this, and the variety of agents used around the world, there are no glaring international differences in the sensitivity of the technique [33].

An alternative, non-colloidal agent was introduced in 2014. Tilmanocept (Lymphoseek®) targets the CD206 mannose receptor on macrophages. Its soluble nature and moderate size allow it to leave the depot efficiently and migrate along lymphatic channels to lymph nodes. Its high affinity for the mannose receptor causes it to be tightly bound in first echelon nodes [34].

The first widespread implementation of the sentinel node concept was in melanoma and breast cancer. It is now established in oropharyngeal and gynaecological cancers and is being applied in other solid tumours [35–38].

5.2 Therapeutic Radiopharmaceuticals

5.2.1 Endocrine System

5.2.1.1 Hyperthyroidism

^{131}I-iodide has been used for more than 70 years to treat benign thyroid conditions [39]. The main causes of hyperthyroidism which can be treated with radioiodine include Graves' disease (autoimmune hyperthyroidism, toxic diffuse goitre), solitary hyperfunctioning thyroid nodule and toxic multinodular goitre (Plummer's disease). Although there are drugs to treat these conditions, radioiodine is commonly used as it is inexpensive, well-tolerated and effective. The goal is to render the patient euthyroid or slightly hypothyroid, which can be treated with L-thyroxine. In preparation for treatment, a thyroid scan with

^{99m}Tc-pertechnetate is performed (see Sect. 5.1.7.1), sometimes combined with a 24-h ^{131}I uptake study. There should be blood tests for thyroid hormones. The thyroid target volume is assessed by ultrasound, and fine needle aspiration (FNA) biopsy may be required.

The administered activity of ^{131}I is determined empirically. The goal is to deliver a radiation dose of 100–150 Gy, which requires 3.7–5.5 MBq ^{131}I per g of thyroid tissue, corrected for the 24-h uptake. In practice, often fixed activities are used, based on an estimate of the size of the thyroid gland, with administered activities generally in the range 200–800 MBq. Sodium ^{131}I-iodide is usually given orally as capsules or liquid, though an injectable form is also available. Most patients can be treated on an outpatient basis, though some countries may require hospital admission for radiation protection purposes. The activity which is not trapped in the thyroid gland is excreted rapidly in the urine, and patients must be instructed how to minimize contamination and exposure to family members and the general public [40].

5.2.1.2 Thyroid Carcinoma

^{131}I-iodide has a well-established role in the treatment of differentiated thyroid cancer. Following surgical removal of the tumour, remnants and metastases are ablated by administration of a high activity of ^{131}I-iodide. Activities of 1–5 GBq have been used, though most commonly 3.7 or 5.5 GBq is administered [41]. However, two large recent studies have demonstrated that 1.1 GBq showed equivalent results to the standard 3.7 GBq in low-risk thyroid carcinoma [42, 43]. Because of the high quantity of activity administered, patients are generally admitted to hospital and kept isolated in shielded rooms for several days, although in some countries 1.1 GBq can be administered to outpatients. Oral administration is most convenient, although with appropriate shielding the IV route can be used.

5.2.1.3 Adrenergic Tumours

The indications for therapy with ^{131}I-iobenguane (MIBG) include inoperable pheochromacytoma, inoperable paraganglioma, inoperable carci-

noid tumours, stage III or IV neuroblastoma and metastatic or recurrent medullary thyroid cancer. A diagnostic scan with ^{123}I-iobenguane is used to determine whether there is sufficient accumulation of the tracer to permit treatment (i.e. to deliver a sufficient radiation dose). Prior to treatment, the patient receives cold sodium iodide/iodate to block the thyroid gland and reduce exposure due to free ^{131}I-iodide in the ^{131}I-iobenguane formulation or released by catabolism. There is an extensive list of medications which must be discontinued to avoid interactions with ^{131}I-iobenguane. Despite almost 40 years' experience with this therapy, selection of administered activity is largely empirical, with activities of 3.7–11.1 GBq being used and hospital admission to an isolation ward is required. The activity is administered by slow IV infusion with monitoring of blood pressure; the standard formulation is relatively low specific activity, and there is the risk of hypertensive response [44]. Recently, a no-carrier-added formulation of ^{131}I-iobenguane (Azedra®) has been licensed by the FDA. This reduces the risk of adverse reactions but also opens the door to higher administered activities which may result in improved response rates. This is particularly promising for paediatric neuroblastoma [45, 46].

5.2.1.4 Neuroendocrine Tumours

After a long gestation period, radionuclide therapy of neuroendocrine tumours which overexpress the somatostatin receptor became a reality in 2017 with the international licensing of ^{177}Lu-DOTATATE (Lutathera®) [47]. Adequate targeting must be demonstrated on a diagnostic scan with ^{111}In-pentreotide (Octreoscan®), ^{68}Ga-DOTATATE (NETSPOT®) or ^{68}Ga-DOTATOC (SomaKit-TOC®). A fixed activity of 7.4 GBq ^{177}Lu-DOTATATE is administered at 8-week intervals to a total of four doses. The drug is administered by IV infusion using a shielded syringe pump; the infusion must be monitored carefully to ensure that extravasation does not occur as this can lead to tissue necrosis. The patient also receives an infusion of amino acids (lysine and arginine) to minimize renal retention of [177]Lu. An antiemetic may also be given. The amino acid

infusion continues for 4 h, after which the patient may be discharged if there have been no adverse reactions [48].

5.2.2 Skeletal System and Bone Marrow

5.2.2.1 Palliation of Bone Metastases

Palliative treatment of painful bone metastases from prostate and breast cancer became more widely available in the 1990s with the commercial introduction of ^{89}Sr-strontium chloride (Metastron®), [153]Sm-lexidronam (EDTMP, Quadramet®) and [186]Re-etidronate (HEDP). Patient selection involves demonstration of sites of increased osteoblastic activity on a bone scan (see Sect. 5.1.1). The targeting of [153]Sm-lexidronam and [186]Re-etidronate is identical to the bisphosphonate bone scan agents binding to hydroxyapatite. ^{89}Sr-chloride, in contrast, is a calcium analogue. Standard activities are administered: 150 MBq ^{89}Sr-chloride, 37 MBq/kg body weight [153]Sm-lexidronam and 1.3 GBq [186]Re-etidronate (the vast differences in activity are inversely related to the radionuclide half-life). All are well tolerated and can be given on an outpatient basis. There may be a brief flare in bone pain a few days after administration which can be treated with analgesics. If the patient experiences pain relief (60–80% of patients respond), the duration of effect is 2–6 months, and treatment can be repeated after that time [49].

Although these three agents are effective, they were never as widely used as had been anticipated. However, the situation changed with the introduction in 2013 of [223]Ra-radium chloride (Xofigo®), the first alpha-particle-emitting therapeutic radiopharmaceutical to be licensed. [223]Ra-chloride is not only effective in pain relief with minimal side effects, but can also alter the course of disease. Indeed, the Phase III trial was terminated early due to the survival advantage of patients who received the active drug [50]. [223]Ra-chloride is currently licensed for use in patients with castration-resistant metastatic prostate cancer, though trials are underway in other cancers which tend to metastasize to bone.

^{233}Ra-chloride is administered at 55 kBq/kg body weight as a slow bolus at 4-week intervals to a total of six doses. Haematological evaluation must be performed at baseline and prior to every dose because of the bone marrow suppression which can result [51].

5.2.2.2 Radiosynovectomy

Radiation synovectomy involves the instillation of a beta-particle-emitting radiocolloid into a joint cavity to irradiate and destroy the inflamed synovial membranes in rheumatoid arthritis and other inflammatory joint diseases. Radionuclides of different energies are used for joints of different sizes. The knee is treated with ^{90}Y-citrate colloid, 185–222 MBq; this is the most common form of radiosynovectomy. Hip, shoulder, elbow, wrist, and ankle joints can be treated with ^{186}Re-sulphide colloid, 37–185 MBq, depending on the joint. Finger joints can be treated with ^{169}Er-citrate colloid, 10–40 MBq, depending on the joint.

Under local anaesthesia, a needle is inserted into the joint and fluid withdrawn to confirm proper placement. The radionuclide is then instilled into the joint along with a long-acting glucocorticoid. The joint is then immobilized for several days. Pain reduction typically occurs 1–3 weeks post injection [52].

5.2.2.3 Myeloproliferative Disease

Polycythaemia vera is a chronic progressive myeloproliferative disease characterized by an absolute increase in red cell mass due to overproduction of red blood cells by the bone marrow. This causes a thickening of the blood, slowing blood flow and risking thrombosis. ^{32}P-phosphate clears from the circulation to bone and irradiates the bone marrow, suppressing the hyperproliferative cells. The administered activity is 80–110 MBq/m^2 for the initial dose and 35–75 MBq for subsequent doses after 3–4 months [53].

5.2.3 Oncology

5.2.3.1 Non-Hodgkin's Lymphoma

Patients with CD20-positive follicular B-cell non-Hodgkin's lymphoma (NHL) which is refractory to or relapsed following standard treatment are candidates for radioimmunotherapy with ^{90}Y-ibritumomab tiuxetan (Zevalin®). Ibritumomab is a murine monoclonal antibody which binds to the CD20 antigen; it is derivatized with the chelator tiuxetan for labelling with ^{111}In (if required for a diagnostic scan) or the therapeutic beta-emitter ^{90}Y. ^{90}Y-ibritumomab is prepared onsite by adding ^{90}Y-chloride to a kit containing the antibody, incubating for 5 min, then quenching the reaction with a formulation buffer.

The administration protocol is complex. Six to eight days before the radioimmunotherapy is scheduled, the patient receives a loading dose of rituximab (MabThera®, Rituxan®) at 250 mg/m^2. On the day of radioimmunotherapy, the patient again receives a loading dose of rituximab followed by ^{90}Y-ibritumomab. The administered activity is 14.8 MBq/kg (to a maximum of 1184 MBq) if the patient's platelet count is >150,000/mm^3 or 11.1 MBq/kg if the platelets are lower but still above 100,000/mm^3 [54].

5.2.3.2 Prostate-Specific Membrane Antigen

The prostate-specific membrane antigen (PSMA) is overexpressed in prostate cancer, especially in advanced stage prostate carcinomas and little expression in normal tissue. This makes it a good target for imaging and ^{68}Ga-DKFZ-PSMA-11 and analogues have been rapidly adopted for PET/CT imaging [55]. These are small molecules with a peptide-urea recognition site linked to a chelator. The remarkable degree of targeting and high tissue contrast made this an ideal candidate for therapy, and a variety of ^{177}Lu-labelled analogues have been developed. Of these, ^{177}Lu-PSMA-617 seems to have the most commercial traction [56]. At the time of writing, there is a randomized clinical trial underway at 54 centres worldwide with the aim of recruiting 750 patients.

5.2.3.3 Selective Internal Radiation Therapy (SIRT)

Surgically unresectable liver tumours, whether primary hepatocellular carcinoma or metastatic, may be amenable to treatment by selective internal

radiation therapy (SIRT) in which ^{90}Y-containing microspheres are delivered through a catheter fed into the hepatic artery. The microspheres lodge in the capillaries of the hypervascular tumour and selectively irradiate the tumour tissue. Two agents with slightly different properties are available. ^{90}Y-resin microspheres (SIR-Spheres®) have a median diameter of 33 μm and specific activity of 75 Bq/sphere or 3 GBq per 40×10^6 microspheres. ^{90}Y-glass microspheres (TheraSphere®) have a diameter of 20–30 μm and a much higher specific activity of 2500 Bq/sphere or 3 GBq per 1.2×10^6 microspheres. Therapy must be scheduled relative to the availability and reference date of the product in order to deliver the required radiation dose. On the day of therapy, a catheter is fed into the hepatic artery under fluoroscopic guidance. The lung perfusion agent ^{99m}Tc-MAA is then injected via the catheter to determine the extent of arteriovenous shunting to the lungs (risk of radiation pneumonitis) and to confirm the absence of gastric and duodenal flow. If the distribution is satisfactory, the required quantity of ^{90}Y-microspheres can then be delivered [57].

References

1. Van den Wyngaert T, Strobel K, Kampen WU, Kuwert T, van der Bruggen W, Mohan HK, Gnanasegaran G, Delgado-Bolton R, Weber WA, Beheshti M, Langsteger W, Giammarile F, Mottaghy FM, Paycha F. The EANM practice guidelines for bone scintigraphy. Eur J Nucl Med Mol Imaging. 2016;43:1723–38. https://doi.org/10.1007/s00259-016-3415-4.

2. Agrawal K, Marafi F, Gnanasegaran G, Van der Wall H, Fogelman I. Pitfalls and limitations of radionuclide planar and hybrid bone imaging. Semin Nucl Med. 2015;45:347–72. https://doi.org/10.1053/j.semnuclmed.2015.02.002.

3. Kapucu OL, Nobili F, Varrone A, Booij J, Vander Borght T, Nagren K, Darcourt J, Tatsch K, Van Laere KJ. EANM procedure guideline for brain perfusion SPECT using ^{99m}Tc-labelled radiopharmaceuticals, version 2. Eur J Nucl Med Mol Imaging. 2009;36:2093–102. https://doi.org/10.1007/s00259-009-1266-y.

4. Van Paesschen W. Ictal SPECT. Epilepsia. 2004;45(Suppl 4):35–40. https://doi.org/10.1111/j.0013-9580.2004.04008.x.

5. Reid RH, Gulenchyn KY, Ballinger JR. Clinical use of technetium-99m HM-PAO for determination of brain death. J Nucl Med. 1989;30:1621–6.

6. Darcourt J, Booij J, Tatsch K, Varrone A, Vander Borght T, Kapucu OL, Nagren K, Nobili F, Walker Z, Van Laere K. EANM procedure guidelines for brain neurotransmission SPECT using ^{123}I-labelled dopamine transporter ligands, version 2. Eur J Nucl Med Mol Imaging. 2010;37:443–50. https://doi.org/10.1007/s00259-009-1267-x.

7. Cummings JL, Henchcliffe C, Schaier S, Simuni T, Waxman A, Kemp P. The role of dopaminergic imaging in patients with symptoms of dopaminergic system neurodegeneration. Brain. 2011;134:3146–66. https://doi.org/10.1093/brain/awr177.

8. Brown KA. The role of stress redistribution thallium-201 myocardial perfusion imaging in evaluating coronary artery disease and perioperative risk. J Nucl Med. 1994;35:703–6.

9. Verberne HJ, Acampa W, Anagnostopoulos C, Ballinger J, Bengel F, De Bondt P, Buechel RR, Cuocolo A, van Eck-Smit BLF, Flotats A, Hacker M, Hindorf C, Kaufmann PA, Lindner O, Ljungberg M, Lonsdale M, Manrique A, Minarik D, Scholte AJHA, Slart RHJA, Tragardh E, de Wit TC, Hesse B. EANM procedural guidelines for radionuclide myocardial perfusion imaging with SPECT and SPECT/CT: 2015 revision. Eur J Nucl Med Mol Imaging. 2015;42:1929–40. https://doi.org/10.1007/s00259-015-3139-x.

10. Beller GA, Heede RC. SPECT imaging for detecting coronary artery disease and determining prognosis by noninvasive assessment of myocardial perfusion and myocardial viability. J Cardiovasc Transl Res. 2011;4:416–24. https://doi.org/10.1007/s12265-011-9290-2.

11. Hesse B, Lindhardt TB, Acampa W, Anagnostopoulos C, Ballinger J, Bax JJ, Edenbrandt L, Flotats A, Germano G, Stopar TG, Franken P, Kelion A, Kjaer A, Le Guludec D, Ljungberg M, Maenhout AF, Marcassa C, Marving J, McKiddie F, Schaefer WM, Stegger L, Underwood R. EANM/ESC guidelines for radionuclide imaging of cardiac function. Eur J Nucl Med Mol Imaging. 2008;35:851–85. https://doi.org/10.1007/s00259-007-0694-9.

12. Alvarez JA, Russell RR. Cardio-oncology: the nuclear option. Curr Cardiol Rep. 2017;19:31. https://doi.org/10.1007/s11886-017-0844-z.

13. Bajc M, Neilly JB, Miniati M, Schuemichen C, Meignan M, Jonson B. EANM guidelines for ventilation/perfusion scintigraphy: part 1. Pulmonary imaging with ventilation/perfusion single photon emission tomography. Eur J Nucl Med Mol Imaging. 2009;36:1356–70. https://doi.org/10.1007/s00259-009-1170-5.

14. Mortensen J, Gutte H. SPECT/CT and pulmonary embolism. Eur J Nucl Med Mol Imaging. 2014;41(Suppl 1):S81–90. https://doi.org/10.1007/s00259-013-2614-5.

15. O'Doherty MJ, Peters AM. Pulmonary technetium-99m diethylene triamine penta-acetic acid aerosol clearance as an index of lung injury. Eur J Nucl Med. 1997;24:81–7.

16. Blaufox MD, De Palma D, Taylor A, Szabo Z, Prigent A, Samal M, Li Y, Santos A, Testanera G, Tulchinsky M. The SNMMI and EANM practice guideline for renal scintigraphy in adults. Eur J Nucl Med Mol Imaging. 2018;45:2218–28. https://doi.org/10.1007/s00259-018-4129-6.

17. Piepsz A, Colarinha P, Gordon I, Hahn K, Olivier P, Roca I, Sixt R, van Velzen J. Guidelines for ^{99m}Tc-DMSA scintigraphy in children. Eur J Nucl Med. 2001;28:BP37–41.

18. Taylor AT. Radionuclides in nephrourology, part 1: radiopharmaceuticals, quality control, and quantitative indices. J Nucl Med. 2014;55:608–15. https://doi.org/10.2967/jnumed.113.133447.

19. Fleming JS, Zivanovic MA, Blake GM, Burniston M, Cosgriff PS. Guidelines for the measurement of glomerular filtration rate using plasma sampling. Nucl Med Commun. 2004;25:759–69.

20. Abell TL, Camilleri M, Donohoe K, Hasler WL, Lin HC, Maurer AH, McCallum RW, Nowak T, Nusynowitz ML, Parkman HP, Shreve P, Szarka LA, Snape WJJ, Ziessman HA. Consensus recommendations for gastric emptying scintigraphy. Am J Gastroenterol. 2008;103:753–63. https://doi.org/10.1111/j.1572-0241.2007.01636.x.

21. Bonapace ES, Maurer AH, Davidoff S, Krevsky B, Fisher RS, Parkman HP. Whole gut transit scintigraphy in the clinical evaluation of patients with upper and lower gastrointestinal symptoms. Am J Gastroenterol. 2000;95:2838–47. https://doi.org/10.1111/j.1572-0241.2000.03195.x.

22. Dam HQ, Brandon DC, Grantham VV, Hilson AJ, Howarth DM, Maurer AH, Stabin MG, Tulchinsky M, Ziessman HA, Zuckier LS. The SNMMI procedure standard/EANM practice guideline for gastrointestinal bleeding scintigraphy 2.0. J Nucl Med Technol. 2014;42:308–17. https://doi.org/10.2967/jnmt.114.147959.

23. Middleton ML, Strober MD. Planar scintigraphic imaging of the gastrointestinal tract in clinical practice. Semin Nucl Med. 2012;42:33–40. https://doi.org/10.1053/j.semnuclmed.2011.07.006.

24. Tulchinsky M, Ciak BW, Delbeke D, Hilson A, Holes-Lewis KA, Stabin MG, Ziessman HA. SNM practice guideline for hepatobiliary scintigraphy 4.0. J Nucl Med Technol. 2010;38:210–8. https://doi.org/10.2967/jnmt.110.082289.

25. Sarkar SD. Benign thyroid disease: what is the role of nuclear medicine? Semin Nucl Med. 2006;36:185–93. https://doi.org/10.1053/j.semnuclmed.2006.03.006.

26. Heston TF, Wahl RL. Molecular imaging in thyroid cancer. Cancer Imaging. 2010;10:1–7. https://doi.org/10.1102/1470-7330.2010.0002.

27. Hindie E, Ugur O, Fuster D, O'Doherty M, Grassetto G, Urena P, Kettle A, Gulec SA, Pons F, Rubello D. 2009 EANM parathyroid guidelines. Eur J Nucl Med Mol Imaging. 2009;36:1201–16. https://doi.org/10.1007/s00259-009-1131-z.

28. Bombardieri E, Giammarile F, Aktolun C, Baum RP, Bischof Delaloye A, Maffioli L, Moncayo R, Mortelmans L, Pepe G, Reske SN, Castellani MR, Chiti A. [131]I/^{123}I-metaiodobenzylguanidine (mIBG) scintigraphy: procedure guidelines for tumour imaging. Eur J Nucl Med Mol Imaging. 2010;37:2436–46. https://doi.org/10.1007/s00259-010-1545-7.

29. Kasama S, Toyama T, Kurabayashi M. Usefulness of cardiac sympathetic nerve imaging using [123]Iodine-metaiodobenzylguanidine scintigraphy for predicting sudden cardiac death in patients with heart failure. Int Heart J. 2016;57:140–4. https://doi.org/10.1536/ihj.15-508.

30. Bombardieri E, Ambrosini V, Aktolun C, Baum RP, Bishof-Delaloye A, Del Vecchio S, Maffioli L, Mortelmans L, Oyen W, Pepe G, Chiti A. ^{111}In-pentetreotide scintigraphy: procedure guidelines for tumour imaging. Eur J Nucl Med Mol Imaging. 2010;37:1441–8. https://doi.org/10.1007/s00259-010-1473-6.

31. Garai I, Barna S, Nagy G, Forgacs A. Limitations and pitfalls of ^{99m}Tc-EDDA/HYNIC-TOC (Tektrotyd) scintigraphy. Nucl Med Rev. 2016;19:93–8. https://doi.org/10.5603/NMR.2016.0019.

32. Signore A, Jamar F, Israel O, Buscombe J, Martin-Comin J, Lazzeri E. Clinical indications, image acquisition and data interpretation for white blood cells and anti-granulocyte monoclonal antibody scintigraphy: an EANM procedural guideline. Eur J Nucl Med Mol Imaging. 2018;45:1816–31. https://doi.org/10.1007/s00259-018-4052-x.

33. Ballinger J. The use of protein based radiocolloids for sentinel node localisation. Clin Transl Imaging. 2015;3:179–86.

34. Surasi DS, O'Malley J, Bhambhvani P. ^{99m}Tc-Tilmanocept: a novel molecular agent for lymphatic mapping and sentinel lymph node localization. J Nucl Med Technol. 2015;43:87–91. https://doi.org/10.2967/jnmt.115.155960.

35. Giammarile F, Alazraki N, Aarsvold JN, Audisio RA, Glass E, Grant SF, Kunikowska J, Leidenius M, Moncayo VM, Uren RF, Oyen WJG, Valdes Olmos RA, Vidal Sicart S. The EANM and SNMMI practice guideline for lymphoscintigraphy and sentinel node localization in breast cancer. Eur J Nucl Med Mol Imaging. 2013;40:1932–47. https://doi.org/10.1007/s00259-013-2544-2.

36. Giammarile F, Bozkurt MF, Cibula D, Pahisa J, Oyen WJ, Paredes P, Olmos RV, Sicart SV. The EANM clinical and technical guidelines for lymphoscintigraphy and sentinel node localization in gynaecological cancers. Eur J Nucl Med Mol Imaging. 2014;41:1463–77. https://doi.org/10.1007/s00259-014-2732-8.

37. Chakera AH, Hesse B, Burak Z, Ballinger JR, Britten A, Caraco C, Cochran AJ, Cook MG, Drzewiecki KT, Essner R, Even-Sapir E, Eggermont AMM, Stopar TG, Ingvar C, Mihm MCJ, McCarthy SW, Mozzillo N, Nieweg OE, Scolyer RA, Starz H, Thompson JF, Trifiro G, Viale G, Vidal-Sicart S, Uren R, Waddington W, Chiti A, Spatz A, Testori A. EANM-EORTC general recommendations for sentinel node diagnostics in melanoma. Eur J Nucl Med Mol

Imaging. 2009;36:1713–42. https://doi.org/10.1007/s00259-009-1228-4.

38. Alkureishi LWT, Burak Z, Alvarez JA, Ballinger J, Bilde A, Britten AJ, Calabrese L, Chiesa C, Chiti A, de Bree R, Gray HW, Hunter K, Kovacs AF, Lassmann M, Leemans CR, Mamelle G, McGurk M, Mortensen J, Poli T, Shoaib T, Sloan P, Sorensen JA, Stoeckli SJ, Thomsen JB, Trifiro G, Werner J, Ross GL. Joint practice guidelines for radionuclide lymphoscintigraphy for sentinel node localization in oral/oropharyngeal squamous cell carcinoma. Eur J Nucl Med Mol Imaging. 2009;36:1915–36. https://doi.org/10.1007/s00259-009-1248-0.

39. Ballinger J. Theranostic radiopharmaceuticals: established agents in current use. Br J Radiol. 2018;91:20170969.

40. Stokkel MPM, Handkiewicz Junak D, Lassmann M, Dietlein M, Luster M. EANM procedure guidelines for therapy of benign thyroid disease. Eur J Nucl Med Mol Imaging. 2010;37:2218–28. https://doi.org/10.1007/s00259-010-1536-8.

41. Luster M, Clarke SE, Dietlein M, Lassmann M, Lind P, Oyen WJG, Tennvall J, Bombardieri E. Guidelines for radioiodine therapy of differentiated thyroid cancer. Eur J Nucl Med Mol Imaging. 2008;35:1941–59. https://doi.org/10.1007/s00259-008-0883-1.

42. Mallick U, Harmer C, Yap B, Wadsley J, Clarke S, Moss L, Nicol A, Clark PM, Farnell K, McCready R, Smellie J, Franklyn JA, John R, Nutting CM, Newbold K, Lemon C, Gerrard G, Abdel-Hamid A, Hardman J, Macias E, Roques T, Whitaker S, Vijayan R, Alvarez P, Beare S, Forsyth S, Kadalayil L, Hackshaw A. Ablation with low-dose radioiodine and thyrotropin alfa in thyroid cancer. N Engl J Med. 2012;366:1674–85. https://doi.org/10.1056/NEJMoa1109589.

43. Schlumberger M, Catargi B, Borget I, Deandreis D, Zerdoud S, Bridji B, Bardet S, Leenhardt L, Bastie D, Schvartz C, Vera P, Morel O, Benisvy D, Bournaud C, Bonichon F, Dejax C, Toubert M-E, Leboulleux S, Ricard M, Benhamou E. Strategies of radioiodine ablation in patients with low-risk thyroid cancer. N Engl J Med. 2012;366:1663–73. https://doi.org/10.1056/NEJMoa1108586.

44. Giammarile F, Chiti A, Lassmann M, Brans B, Flux G. EANM procedure guidelines for ^{131}I-meta-iodobenzylguanidine (^{131}I-mIBG) therapy. Eur J Nucl Med Mol Imaging. 2008;35:1039–47. https://doi.org/10.1007/s00259-008-0715-3.

45. Noto RB, Pryma DA, Jensen J, Lin T, Stambler N, Strack T, Wong V, Goldsmith SJ. Phase 1 study of high-specific-activity I-131 MIBG for metastatic and/or recurrent pheochromocytoma or paraganglioma. J Clin Endocrinol Metab. 2018;103:213–20. https://doi.org/10.1210/jc.2017-02030.

46. Pryma DA, Chin BB, Noto RB, Dillon JS, Perkins S, Solnes L, Kostakoglu L, Serafini AN, Pampaloni MH, Jensen J, Armor T, Lin T, White T, Stambler N, Apfel S, DiPippo V, Mahmood S, Wong V, Jimenez C. Efficacy and safety of high-specific-activity I-131 MIBG therapy in patients with advanced pheochromocytoma or paraganglioma. J Nucl Med. 2018;60(5):623–30. https://doi.org/10.2967/jnumed.118.217463.

47. Strosberg J, El-Haddad G, Wolin E, Hendifar A, Yao J, Chasen B, Mittra E, Kunz PL, Kulke MH, Jacene H, Bushnell D, O'Dorisio TM, Baum RP, Kulkarni HR, Caplin M, Lebtahi R, Hobday T, Delpassand E, Van Cutsem E, Benson A, Srirajaskanthan R, Pavel M, Mora J, Berlin J, Grande E, Reed N, Seregni E, Oberg K, Lopera Sierra M, Santoro P, Thevenet T, Erion JL, Ruszniewski P, Kwekkeboom D, Krenning E. Phase 3 trial of ^{177}Lu-Dotatate for midgut neuroendocrine tumors. N Engl J Med. 2017;376:125–35. https://doi.org/10.1056/NEJMoa1607427.

48. Bodei L, Mueller-Brand J, Baum RP, Pavel ME, Horsch D, O'Dorisio MS, O'Dorisio TM, Howe JR, Cremonesi M, Kwekkeboom DJ, Zaknun JJ. The joint IAEA, EANM, and SNMMI practical guidance on peptide receptor radionuclide therapy (PRRNT) in neuroendocrine tumours. Eur J Nucl Med Mol Imaging. 2013;40:800–16. https://doi.org/10.1007/s00259-012-2330-6.

49. Bodei L, Lam M, Chiesa C, Flux G, Brans B, Chiti A, Giammarile F. EANM procedure guideline for treatment of refractory metastatic bone pain. Eur J Nucl Med Mol Imaging. 2008;35:1934–40. https://doi.org/10.1007/s00259-008-0841-y.

50. Parker C, Nilsson S, Heinrich D, Helle SI, O'Sullivan JM, Fossa SD, Chodacki A, Wiechno P, Logue J, Seke M, Widmark A, Johannessen DC, Hoskin P, Bottomley D, James ND, Solberg A, Syndikus I, Kliment J, Wedel S, Boehmer S, Dall'Oglio M, Franzen L, Coleman R, Vogelzang NJ, O'Bryan-Tear CG, Staudacher K, Garcia-Vargas J, Shan M, Bruland OS, Sartor O. Alpha emitter radium-223 and survival in metastatic prostate cancer. N Engl J Med. 2013;369:213–23. https://doi.org/10.1056/NEJMoa1213755.

51. Du Y, Carrio I, De Vincentis G, Fanti S, Ilhan H, Mommsen C, Nitzsche E, Sundram F, Vogel W, Oyen W, Lewington V. Practical recommendations for radium-223 treatment of metastatic castration-resistant prostate cancer. Eur J Nucl Med Mol Imaging. 2017;44:1671–8. https://doi.org/10.1007/s00259-017-3756-7.

52. Clunie G, Fischer M. EANM procedure guidelines for radiosynovectomy. Eur J Nucl Med Mol Imaging. 2003;30:BP12–6.

53. Tennvall J, Brans B. EANM procedure guideline for ^{32}P phosphate treatment of myeloproliferative diseases. Eur J Nucl Med Mol Imaging. 2007;34:1324–7. https://doi.org/10.1007/s00259-007-0407-4.

54. Tennvall J, Fischer M, Bischof Delaloye A, Bombardieri E, Bodei L, Giammarile F, Lassmann M, Oyen W, Brans B. EANM procedure guideline for radio-immunotherapy for B-cell lymphoma with. Eur J Nucl Med Mol Imaging. 2007;34:616–22. https://doi.org/10.1007/s00259-007-0372-y.

55. Fendler WP, Eiber M, Beheshti M, Bomanji J, Ceci F, Cho S, Giesel F, Haberkorn U, Hope TA, Kopka K,

Krause BJ, Mottaghy FM, Schoder H, Sunderland J, Wan S, Wester H-J, Fanti S, Herrmann K. ^{68}Ga-PSMA PET/CT: joint EANM and SNMMI procedure guideline for prostate cancer imaging. Eur J Nucl Med Mol Imaging. 2017;44:1014–24. https://doi.org/10.1007/s00259-017-3670-z.

56. Violet JA, Jackson P, Ferdinandus J, Sandhu S, Akhurst T, Iravani A, Kong G, Ravi Kumar A, Thang SP, Eu P, Scalzo M, Murphy D, Williams SG, Hicks RJ, Hofman MS. Dosimetry of Lu-177 PSMA-617 in metastatic castration-resistant prostate cancer: correlations between pre-therapeutic imaging and "whole body" tumor dosimetry with treatment outcomes. J Nucl Med. 2018;60(4):517–23. https://doi.org/10.2967/jnumed.118.219352.

57. Giammarile F, Bodei L, Chiesa C, Flux G, Forrer F, Kraeber-Bodere F, Brans B, Lambert B, Konijnenberg M, Borson-Chazot F, Tennvall J, Luster M. EANM procedure guideline for the treatment of liver cancer and liver metastases with intra-arterial radioactive compounds. Eur J Nucl Med Mol Imaging. 2011;38:1393–406. https://doi.org/10.1007/s00259-011-1812-2.

Quality Assurance and Quality Control of Tc-99m Radiopharmaceuticals

6

Vivian Loveless and Susan H. Morgan

Contents

V. Loveless
Retired, University of Tennessee Health Science
Center College of Pharmacy, Memphis, TN, USA
e-mail: vloveles@uthsc.edu

S. H. Morgan (✉)
University of Tennessee Health Science Center
College of Pharmacy, Memphis, TN, USA
e-mail: smorgan@uthsc.edu

6.1 Introduction

Radiopharmaceuticals used in nuclear medicine studies provide valuable information for patient care; however, without strict adherence to standards of quality control, radiopharmaceutical studies may be rendered useless. Manufacturers as well as preparers of radiopharmaceuticals are charged with ensuring the standards found in package inserts, the Unites States Pharmacopeia

(USP), and Nuclear Regulatory Commission (NRC) regulations are met. The USP is a standard-setting body for pharmaceuticals, which establishes guidelines for quality and safety, while the NRC is a regulatory body overseeing radiation safety in the United States.

While ready-to-use products such as generators are tested for quality assurance by the manufacturer, further testing must be done during use, for example, molybdenum-99 breakthrough test (moly assay), radionuclidic purity, and aluminum ion testing. Products prepared in a nuclear pharmacy must undergo testing prior to release to a patient to determine radiochemical purity and a microscopic examination for those particulate-containing radiopharmaceuticals. Generators, such as ^{99}Mo/^{99m}Tc, are eluted and tested prior to shipment to ensure proper operation and provide quality assurance before release. Cold kits contain a lyophilized pellet with specified amounts of not only the ligand that binds the radionuclide but other components such as reducing agents, antioxidants, and those to adjust pH. Testing by the manufacturer ensures the adequacy of these components when prepared according to the instructions. Quality control procedures are discussed in this chapter, but it is also important to understand these procedures must be carried out by adequately trained personnel.

6.2 Radionuclidic Purity

USP defines radionuclidic purity of a radiopharmaceutical as the quantity of desired radionuclide expressed as a fraction of the total radioactivity assayed with the other fraction being radionuclidic impurities [1]. The ratio of the desired radionuclide to the total activity is dynamic over time with radioactive decay dictating the total of each radionuclide present. If the half-life of the desired radionuclide is shorter than that of the impurities, the ratio of the desired purity will continue to decline as time progresses. Radionuclidic impurities in administered radiopharmaceuticals increase the radiation dosimetry to the patient and negatively affect the image quality.

While radionuclidic purity is typically determined using a dose calibrator, a well counter connected to a multi-channel analyzer could be used to identify various impurities by their energy spectrum. This is useful for gamma emitting radionuclides; however, well counters are not acceptable for detecting beta emissions. Beta emissions can easily be detected using a beta spectrometer or liquid scintillation counter and thereby could be useful in determining radionuclidic purity.

Radionuclidic impurities in accelerator or reactor-produced radionuclides can arise from variations in production methods as well as impurities in the target material. Ensuring the radionuclidic purity of these radiopharmaceuticals is the responsibility of manufacturers. In the case of the ^{99}Mo/^{99m}Tc generator, ^{99}Mo breakthrough can be a source of radionuclidic impurity in the eluate. Minimal molybdenum contamination can occur during normal operation, but failure of the mechanics of the generator could result in significant breakthrough during elution. It is the responsibility of the nuclear pharmacist to ensure that the limit of ^{99}Mo is not exceeded. Radionuclidic purity testing must be performed on the first elution of the ^{99}Mo/^{99m}Tc generator per 10 CFR 35.204 [2]; however, package inserts of various manufacturers specify performing testing on all elutions [3–5]. The ratio of ^{99}Mo to ^{99m}Tc must not exceed 0.15 μCi ^{99}Mo/mCi of ^{99m}Tc at the time of administration [6], and testing can be completed using the dose calibrator lead shield method (Fig. 6.1).
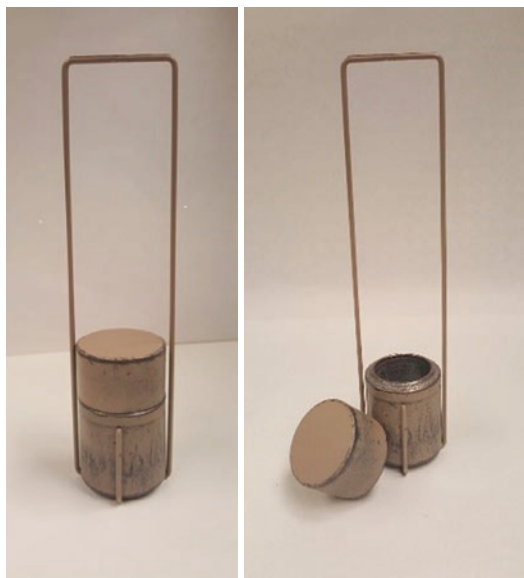
Fig. 6.1 Moly assay lead shield

By using this method, the thickness of the lead shield will block the 140 keV photons of ^{99m}Tc but will only attenuate the 740 and 780 keV photons of ^{99}Mo. Using a correction factor, the dose calibrator will display the correct activity of ^{99}Mo. Then, the ratio can be determined mathematically by dividing the total ^{99}Mo activity by the total activity of ^{99m}Tc. Modern dose calibrators automatically perform these calculations.

Another source of impurity is the buildup of ^{99}Tc from both the decay of ^{99}Mo as well as ^{99m}Tc. This is significant the older the eluate is as well as the longer the time between elutions. Even though ^{99}Tc cannot be easily detected, it can be calculated based on the radioactive decay of ^{99}Mo and ^{99m}Tc [7]. This impurity leads to ^{99}Tc competing with ^{99m}Tc for radiolabeling reactions, thus leading to the possibility of increased levels of free ^{99m}Tc-pertechnetate in a radiolabeled compound which could alter bio distribution of the radioactivity [8].

6.3   Radiochemical Purity

USP defines radiochemical purity of a radiopharmaceutical as the "fraction of the stated radionuclide present in the stated chemical form" [1]. Technetium-99m (^{99m}Tc) is the most commonly used radionuclide for preparing radiopharmaceuticals. Consideration must be given to quantifying the amount of both radiochemical impurities as well as the percent bound of the desired ligand. One radiochemical impurity, free pertechnetate with technetium in the +7 valence state, can bind to oxygen and localize in the stomach, thyroid, and choroid plexus. Hydrolyzed-reduced (H/R) technetium or colloidal ^{99m}TcO$_2$, another radiochemical impurity, is technetium in a lower valence state that binds to oxygen; this impurity can localize in the liver. The amount of bound radiopharmaceutical is critical to ensuring proper outcomes from the patient study and must meet minimum acceptable purity standards.

Impurities can arise from various sources, and they must be quantified since altered biodistribution can occur if they are present. Radiolytic decomposition can occur due to autoradiolysis or indirect radiolysis; both give rise to impurities. With autoradiolysis, emissions from the radionuclide break chemical bonds in the labeled compound in which the radionuclide is present. Indirect radiolysis refers to these same radionuclidic emissions creating free radicals in the compound's solvent, which also leads to the destruction of chemical bond of the radiolabeled product. Radioactivity in an aqueous solution can produce free radicals that can break chemical bonds resulting in the production of radiochemical impurities. This is especially problematic with high concentrations of radioactivity. Antioxidants, frequently added to cold kits by the manufacturer, enable higher concentrations of activity to be added. Other influences of radiochemical stability are pH, temperature, and light. For instance, environments that are cool and dark favor stability [8].

Thin layer chromatography is a method used to separate out different chemical species of a compound. This process can be used with radiopharmaceuticals as well but due to their time sensitivity, more efficient means are employed. Radiochemical purity is routinely determined in the nuclear pharmacy by performing paper chromatography, instant thin layer chromatography (ITLC), or solid phase extraction. In some cases, a combination of paper and ITLC are used to determine radiochemical purity. The stationary phase is media such as paper, ITLC impregnated media with silicic acid (ITLC SA) or silica gel (ITLC SG), glass microfiber chromatography paper (GMCP SA), and saturation pads. This list is not all inclusive of stationary media.

The solvent or mobile phase can be ethanol, water, acetone, saline, or other solvents. Choice of solvent is determined based on the solubility of the radiopharmaceutical; for example, those that are soluble in saline will not be soluble in organic solvents and thus not move with the solvent front. The different radiochemical species also travel at varying rates due to the electrostatic forces from the stationary phase as well as the differences in solubility with the solvents as mentioned [9]. After the solvent front has migrated to the top of the media, the strip can be cut according to the respective R_f values of the different radiochemical species. The different segments of the strips can

Fig. 6.2 Radiochemical purity testing for particulate radiopharmaceuticals
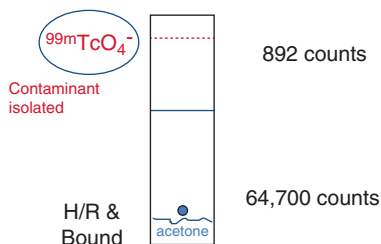
OVERALL DRUG COMPLEX

$$\frac{892}{64{,}700 + 892} \times 100 = 1.36\%$$

(free)

$$100\% - 1.36\% = 98.64\%$$

(free)   Drug Complex

be counted in a well counter connected to either a multi-channel analyzer or a single-channel analyzer. An important consideration when counting samples is to maintain the same sample distance from the detector and use the same counting geometry for each. If a well is not available, such as in a nuclear medicine department, a gamma camera may be used. Appropriate regions would be based on the radiochemical species of interest and then counts collected in each region. The calculations shown are performed on the counts obtained by either method.

6.4   Radiochemical Purity for Particulate Radiopharmaceuticals

^{99m}Tc macroaggregated albumin (MAA) or ^{99m}Tc sulfur colloid particulate radiopharmaceuticals do not dissolve in the solvent nor does the hydrolyzed-reduced component but pertechnetate does, thus allowing for limited separation and determination of radiochemical purity. When reporting percent bound for particulate radiopharmaceuticals, this includes both bound radiopharmaceutical and hydrolyzed-reduced. The pertechnetate component is the only directly measured species (Fig. 6.2).

6.5   Radiochemical Purity for True Solution Radiopharmaceuticals

Medronate, pentetate, pyrophosphate, and oxidronate are true solution radiopharmaceuticals due to each bound component's solubility in saline. These radiopharmaceuticals require two strips to separate various components (Fig. 6.3).

Fig. 6.3 Two-strip method for determining radiochemical purity for diphosphonates, pyrophosphate, and pentetate

Water soluble species will move with the solvent front in saline; species with a lipophilic tendency will move with the acetone or organic solvent front (Fig. 6.4). The strip, using acetone as the solvent, will separate out the free pertechnetate. The other strip using saline as the solvent will separate out hydrolyzed-reduced by moving the bound and free pertechnetate to the solvent front, thus allowing percent hydrolyzed-reduced to be determined from this strip. Since hydrolyzed-reduced is colloidal, it will not move with the solvent front (Fig. 6.5). Using an indirect method, subtract both of those percentages, percent free and percent hydrolyzed-reduced, from 100 to obtain percent bound (Fig. 6.6).

Solid phase separation is another method of determining radiochemical purity using a solid phase extraction (SPE) device, such as a Sep-Pak™ cartridge. The cartridge contains materials such as silica and alumina A which allows for the separation of various components by retaining one on the cartridge while other components are eluted off with various solvents [10]. This involves conditioning the cartridge prior to adding the radioactive sample. Then various solvents are passed through the cartridge, and each solvent is collected for counting. By using appropri-

Fig. 6.4 Determination of percent $^{99m}TcO_4^-$
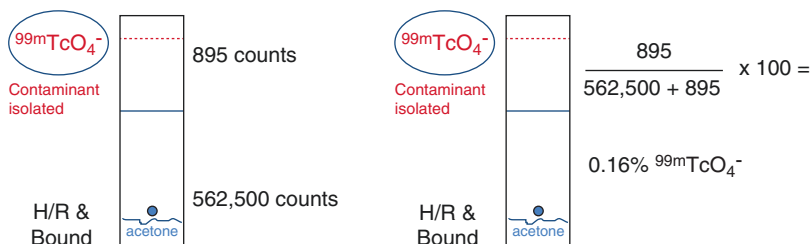
Fig. 6.5 Determination of percent hydrolyzed-reduced
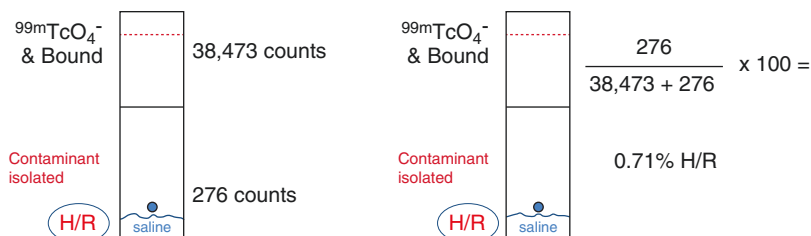
OVERALL DRUG COMPLEX

QC% = 100% − (Sum % of contaminants)

100% − (0.16% + 0.71%) = 99.13%

$^{99m}TcO_4^-$ ^{99m}Tc HR   Drug Complex

Fig. 6.6 Calculation to determine percent bound of radiopharmaceutical

ate solvents, the components separate out, and radiochemical purity can be determined via the activity in the collected solvents and cartridge. Due to the volume of solvents used as well as the quantity of radioactivity, samples must be assayed in the dose calibrator rather than counting the samples in a well detector. This method is a rather involved and lengthy procedure which can result in additional exposure to the user. This SPE method for the determination of radiochemical purity is referenced in the package insert of Technescan MAG3™ and Octreoscan™ [11, 12]. The Sep-Pak™ method is controversial as to whether the flow rate of the solutions through the cartridge can have an impact on quality control results [13–15]. Flow rate is specified in the Technescan™ package insert by directing the operator to push the solution slowly in a dropwise manner, and some authors have shown that faster flow rates impair the reliability of the quality control results [13]. However, Ponto reports that faster flow rates do not impact the results and may also reduce exposure to the operator [15].

This chapter describes some methods of determining radiochemical purity but is not to be considered all-inclusive. Not all package inserts describe the determination of radiochemical purity, and quality control methods in some package inserts are quite time consuming. Faster more efficient methods (paper chromatography) can be found in the literature; this method can be more suitable for use with radiopharmaceuticals in a commercial nuclear pharmacy setting versus a research environment. However, it is necessary to validate alternate methods against reference methods found in either the package insert or USP. Refer to Table 6.1 for examples of radiopharmaceutical quality control procedures and Table 6.2 for a sample of radiopharmaceutical's minimal acceptable radiochemical purity standards (MAP).

6.6 Pitfalls in Radiochemical Analysis

It is critical for the operator to be aware of pitfalls that could lead to erroneous results when performing radiochemical purity. Proper technique not only in preparation but also in radiochemical testing can ensure patients receive quality products, leading to an effective study outcome. Listed are many of the areas that may allow introduction of error into the quality control process and must be evaluated daily.

Table 6.1 Chromatography data for selected ^{99m}Tc radiopharmaceuticals

[99m]Tc radiopharmaceutical	Stationary phase	Mobile phase	Rf ^{99m}Tc-complex	[99m]TcO$_4^-$	Hydrolyzed [99m]Tc
Renal radiopharmaceuticals					
[99m]Tc pentetate	ITLC SG	Acetone	0.0	1.0	0.0
	ITLC SG	Saline	1.0	1.0	0.0
[99m]Tc mertiatide[a]	Waters Sep-Pak C18 Cartridge				
Cardiac radiopharmaceuticals					
[99m]Tc sestamibi	Baker-Flex aluminum oxide TLC	Ethanol	1.0	0.0	0.0
[99m]Tc tetrofosmin	Varian SA	Acetone/ dichloromethane (65:35% v/v)	0.5	1.0	0.0
Brain radiopharmaceuticals					
[99m]Tc exametazime	GMCP SA	MEK	1.0	1.0	0.0
	GMCP SA	Saline	0.0	1.0	0.0
[99m]Tc bicisate	Baker-Flex silica gel	Ethyl acetate	1.0	0.0	0.0
Miscellaneous					
[99m]Tc diphosphonates	ITLC SG	Acetone	0.0	1.0	0.0
	ITLC SG	Saline	1.0	1.0	0.0
[99m]Tc MAA	ITLC SG	Acetone	0.0	1.0	0.0
[99m]Tc sulfur colloid	ITLC SG	Acetone	0.0	1.0	0.0
[99m]Tc IDAs[b]	ITLC SA	20% sodium chloride	0.0	1.0	0.0
	ITLC SG	Water	1.0	1.0	0.0
[99m]Tc tilmanocept	Whatman 1	Acetone	0.0	1.0	0.0

Adapted from [16]

ITLC SG instant thin layer chromatography-silica gel, *ITLC SA* instant thin layer chromatography-silicic acid, *GMCP SA* glass microfiber chromatography paper-silicic acid

[a]Prep of Sep-Pak: flush 10 mL of ethanol through cartridge and discard eluate. Flush 10 mL of 0.001 N HCl through cartridge and discard eluate. Using a syringe, push 5 mL of air through cartridge to drain and then discard eluate. Sample Analysis: Add 0.1 mL of [99m]Tc Mertiatide to the head of cartridge through the long end. Push 10 mL of 0.001 N HCl slowly through the cartridge and collect eluate in tube for counting (contains hydrophilic impurities and H/R fraction of ^{99m}Tc). Push 10 mL of 1:1 ethanol/saline solution slowly through cartridge in a dropwise manner. Collect eluate in a separate tube for counting (contains ^{99m}Tc mertiatide complex). Place Sep-Pak in another tube for counting (contains H/R fraction of ^{99m}Tc and non-elutable impurities). Counting: Assay each tube in a dose calibrator. Calculations: % [99m]Tc mertiatide complex = (activity of the second tube/total activity of all three tubes) × 100; % H/R = (activity of the first tube/activity of all three tubes) × 100; % non-elutable impurities = (activity of the third tube / activity of all three tubes) × 100 [11]

[b]Squibb Diagnostic Product information. Feb 1987

Table 6.2 Sample of radiochemical purity standards

[99m] Tc radiopharmaceutical	MAP standards
[99m] Tc mertiatide	90% [11]
[99m] Tc sestamibi	90% [17]
[99m] Tc exametazime	>80% [18]
[99m] Tc tilmanocept	90% [19]
[99m] Tc bicisate	90% [20]

6.6.1 Instrumentation

- Exceeding dead time of well counter which will reduce the actual number of counts detected [21].
- Not using same geometry for the placement of each segment of the strip during counting in a well counter.

6.6.2   Spotting of the Radiopharmaceutical

- Too large of a radiopharmaceutical spot (too much radioactivity) will not only overwhelm your counting instrument but the increased size could fall below the solvent level and contaminate solvent [21].
- Allowing spot to air-dry when not indicated in package insert could result in falsely high level of radiochemical impurity [21].
- Splattering during application can cause contamination along the medium strip.

6.6.3   Solvent

- Too large/too small of a solvent volume [22].
- Contaminated solvent.
- Incorrect solvent or ratio of solvents [23].
- Organic solvent can absorb water when exposed to the air for excessive lengths of time. Hygroscopic solvent, like acetone, will absorb water from the atmosphere.

6.6.4   Media

- Do not handle stationary medium with ungloved hands as skin oils can be transferred to the medium negatively impacting accuracy.
- Incorrect medium.
- Contaminated absorbent pads used to protect work surface can contaminate stationary medium.
- Stationary medium that has not been stored properly—Keep stationary medium in a climate control environment (desiccator).
- Incorrectly marked stationary medium.
- Wicking of medium strip results in contaminated solvent.

6.6.5   Utensils

- Hot tweezers, test tubes, and scissors—it is critical to ensure utensils and work area are free from contamination before and during quality control testing.

6.7   Instrumentation

Radionuclide (dose) calibrators, well counters, gamma cameras, and radiochromatographic scanners are used in conducting quality control tests. In order to have confidence in the accuracy of test results, these instruments must undergo quality control testing on a consistent schedule. Potential sources of error with these instruments can be fluctuations in voltage, incorrect settings, and/or damage to the crystals in the case of scanners and well counters. Gas leakage could cause erroneous readings with the dose calibrator. For these reasons, it is important to follow manufacturer's guidelines as well as license commitments for quality control testing.

6.8   Physical

Part of the routine quality control of radiopharmaceuticals should include visual inspection using appropriate radiation safety techniques. Prior to preparation, inspection of cold vials will ensure presence of a lyophilized pellet, determination of foreign substances, and vial integrity. Once prepared, radiopharmaceuticals are typically clear and colorless with a few exceptions. ^{99m}Tc MAA and ^{99m}Tc sulfur colloid are cloudy in appearance and particulate in nature; thus, they must be checked for the size of particles to ensure proper localization and study quality. A hemocytometer is used to visually determine no ^{99m}Tc MAA particle present is greater than 150 µm, and the majority of the particles should be between 10 and 90 µm [16] (Fig. 6.7). This ensures that only capillaries and precapillary arterioles are blocked rather than larger vessels.

^{99m}Tc-sulfur colloid as well as filtered ^{99m}Tc-sulfur colloid should be checked with a hemocytometer, but in this case, to ensure no particles are visualized. Since the size of ^{99m}Tc-sulfur colloid particles are in the range of 0.1–1.5 µm, they cannot be visualized using a light microscope, thus ensuring particles will freely pass through the lungs to the liver.

Prior to dispensing, manufacturer prepared radiopharmaceuticals should be confirmed to be free of particulates and vial damage, as well as
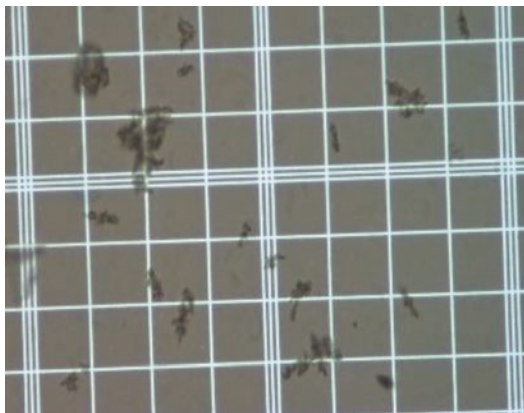
Fig. 6.7 Hemocytometer slide using light microscope: The smallest squares on the hemocytometer shown here represents 50 μm by 50 μm

Fig. 6.8 Aluminum ion testing material

have appropriate color and clarity. It is important to recognize that ^{131}I will develop an amber color over time, but this does not affect quality of the product.

6.9 pH Determination

The pH of eluate obtained from [99]Mo generators should range from 4.5 to 7.5 according to the manufacturers package inserts [3, 4]. While pH determination is not typically performed in nuclear pharmacies on [99]Mo/^{99m}Tc elutions from traditional generators, pH testing on each elution is recommended in the Radiogenix™ System package insert. The range should fall between 4.5 and 7.5 and is obtained using colorimetric pH paper and a drop of sodium pertechnetate [99m]Tc [5].

The pH of radiopharmaceuticals is an important consideration for stability; each product formulation has a limited range of acceptable values. Commercial radiopharmaceutical kits are formulated to maintain an acceptable pH. It is important to use the specified diluent from the package insert preparation instructions in order to be compatible with the manufactured formulation; this will ensure the quality of the product is not compromised.

6.10 Chemical Purity

Aluminum ion testing is performed on each elution from a [99]Mo/^{99m}Tc generator with the limit being 10 μg/mL [5, 6]. Aluminum ion can appear in the elutions due to leaching from the column. Commercial kits are available which allow for colorimetric testing of the elution using a reference solution and indicator paper (Fig. 6.8). If the intensity of the elution spot is less than the intensity of the reference spot, then there is less than 10 μg/mL of Al^{+3} in the eluate.

Aluminum ion in high concentrations can affect several radiopharmaceuticals such as sulfur colloid, diphosphonates, and pentetate. Positive aluminum ions can neutralize the negative zeta potential of the sulfur colloid particles. Since the plus three charge on aluminum ions brings the zeta potential closer to zero, the particles no longer repel one another with the result being flocculation.

Another possible issue with excessive amount of aluminum ions could occur with ^{99m}Tc diphosphonates in that the aluminum ions react with the diphosphonate radiopharmaceuticals to produce a radiocolloid impurity that localizes in the liver. With ^{99m}Tc pentetate, excessive aluminum ions can result in undesirable levels of free pertechnetate preventing the accurate determination of glomerular filtration rate [8].

6.11   Sterility and Apyrogenicity

Sterility and bacterial endotoxin testing (BET) of commercially available radiopharmaceuticals and radiopharmaceutical kits are the responsibility of the manufacturer. Since cold kits and generator elutions are sterile, ^{99m}Tc pertechnetate and ^{99m}Tc labeled preparations require aseptic handling to reduce the risk of sterility issues. Compounding with non-sterile components would necessitate a sterilization procedure and testing along with BET testing to validate apyrogenicity. Regardless of the original components, products can become contaminated during the labeling and/or dispensing process due to touch or improper technique.

6.12   Personnel Validation and Environmental Testing

Personnel validation testing is another quality control test to ensure delivery of sterile radiopharmaceuticals by assessing the preparer's aseptic technique. This must be done initially and annually using growth media and manipulations that simulate the most complex procedure. Environmental testing is also performed to validate that contamination risk is reduced as much as possible. This includes both surface and air sampling under dynamic conditions that are indicative of the environment and activities of the personnel present during radiolabeling procedures.

6.13   Development of New Radiopharmaceuticals

For radiopharmaceuticals to be dispensed to a patient, it is necessary to have a prescription from a physician who is an authorized user of radioactive materials for medical use. The Food and Drug Administration's Center for Drug Evaluation and Research (CDER) is charged with ensuring that drugs marketed in the United States are safe and effective.

The development of radiopharmaceuticals parallels the development of conventional pharmaceuticals; however, there are unique considerations and challenges associated with the development process of radiopharmaceuticals. Positron emission tomography (PET) drugs are short-lived and provide an excellent example of the issues faced with radiopharmaceutical development. The Food and Drug Administration (FDA) Modernization Act addressed the issues via the issuance of the new current good manufacturing practice (cGMP) regulations for PET drugs [24].

In the United States, it is law that a drug must be the subject of an approved marketing application prior to being distributed or transported across state boundaries. Since the sponsor (usually the drug manufacturer or potential marketer) will likely ship the investigational radiopharmaceutical to clinical investigators in multiple states, an exemption from this legal requirement must be acquired. The means to do this is by submitting an Investigational New Drug (IND) Application to the FDA. Once the FDA approves the application, clinical trials may begin [25].

6.13.1   Process of Drug Development

This process links discovery, development, FDA review and approval for marketing, and post marketing safety surveillance of an approved drug to guarantee its continued safety and efficacy. During the discovery phase, there is identification of lead drug candidates for additional assessment in human studies. Animal models are used in preclinical testing to demonstrate proof of concept. There must be establishment of safety, pharmacology, and toxicology profiles as well as determination of a safe starting dose for first-in-human studies. In order to support the IND drug's quality and suitability for human use, adequate chemistry, manufacturing, and control (CMC) information is collected on the investigational drug. Unique test attributes for a radiopharmaceutical must include the radionuclidic identity/purity, radiochemical purity, radiochemical impurities (unbound and/or free radioactivity), radiochemical identity, and specific activity. The IND application must include proposed clinical study protocols, criteria

for subject inclusion, and safety monitoring procedures. If no safety concerns are identified in the FDA review, the FDA allows investigational human studies to begin [24].

6.13.2 Traditional IND Applications

IND applications fall into two categories: commercial and research (non-commercial). Industry routinely submits commercial INDs while academic institutions submit research INDs. Both types of INDs are held to the same standards for review. There are three broad areas that an IND application must contain:

- Animal pharmacology and toxicology studies: These studies provide preclinical data for the assessment of whether the pharmaceutical is reasonably safe for initial human testing. This could also include previous drug experience in humans acquired from foreign use. This section for radiopharmaceuticals should provide sufficient data from animal or human studies to permit a reasonable radiation absorbed dose calculation to the whole body and critical organs from administration to a human subject.
- Manufacturing information: This includes composition, manufacturer, stability, and controls used for manufacturing the drug. This is necessary to prove that the manufacturer can adequately produce and supply consistent pharmaceutical batches.
- Clinical protocols and investigator information: This allows the FDA to determine if the initial-phase trials of the proposed clinical studies will expose research subjects to unnecessary risks. In addition, information regarding the clinical investigators must prove that they are qualified to successfully complete their clinical trial duties. This section also includes commitments for obtaining informed consent from research subjects, documentation of approval by an institutional review board, and the assurance of adherence to the IND regulations.

Once an IND has been submitted to the FDA, the sponsor is required to wait 30 calendar days prior to initiating any clinical studies. This provides the FDA an opportunity to review the IND application for safety to ensure subjects will not undergo unreasonable risk [24, 25].

6.13.2.1 Clinical Protocols
- Phase I: Phase I studies are the first time the investigational new drug is administered to humans. This phase is conducted in a small number of humans that may be patients or normal volunteer subjects. Studies include evaluation of safety, safe dosage range determination, and identification of side effects.
- Phase II: This phase routinely includes no more than several hundred research subjects and evaluates drug efficacy and safety.
- Phase III: Several hundred to several thousand research subjects are routinely enrolled. This phase also demonstrates safety and efficacy in adequate and well-controlled clinical studies [26, 27].

6.13.3 New Drug Application (NDA)

After all clinical investigational studies have been completed as required by the FDA and the manufacturer seeks approval for the radiopharmaceutical for clinical use, the drug manufacturer submits an NDA for radiopharmaceuticals that are small and well-characterized molecules. If the new radiopharmaceutical contains a biologic, such as monoclonal antibodies and other macromolecules, a Biologics License Application (BLA) is submitted to the FDA. The documentation for the application must include all pertinent history of the radiopharmaceutical. This includes the drug ingredients, results of animal studies, drug behavior in the body, results of clinical trials, and how it is manufactured, processed, and packaged. FDA approves the NDA/BLA for clinical use once it is convinced that the radiopharmaceutical's efficacy and safety are supported by the submitted data [24, 28].

6.14   Conclusion

Guidelines provided by professional organizations such as USP as well as those in package inserts are available to ensure proper preparation and quality control for radiopharmaceuticals. By following these methods, users can prepare quality radiopharmaceuticals, thereby maximizing benefits to the patients. Inferior quality diagnostic radiopharmaceuticals result in repeat studies that increase radiation exposure to the patients: however, inferior therapeutic radiopharmaceuticals could result in substatial harm to the patient [29].

References

1. https://online.uspnf.com/uspnf/document/GUID-ED624F74-B941-4145-829-BA3765CD3E80_2_en-US. Accessed Jan 2019.
2. https://www.nrc.gov/reading-rm/doc-collections/cfr/part035/part035-0204.html. Accessed Nov 2018.
3. Ultra-Technekow™ V4 [package insert]. Maryland Heights, MO: Mallinckrodt™ Pharmaceuticals; 2015.
4. TechneLite® [package insert]. N Bilerica, MA: Lantheus Medical Imaging; 2018.
5. Radiogenix® System [package insert]. Beloit, WI: NorthStar Medical Radioisotopes LLC; 2020.
6. USP Monograph for Sodium Pertechnetate Tc 99m Injection; 2018.
7. Lamson MIII, Hotte CE, Ice RD. Practical generator kinetics. J Nucl Med Technol. 1976;4(1):21–7.
8. Hung JC, et al. Radiopharmaceutical-related pitfalls and artifacts. Semin Nucl Med. 1996;26(4):208–55.
9. Robbins PJ. Chromatography of technetium-99m radiopharmaceuticals—a practical guide. New York: The Society of Nuclear Medicine; 1984.
10. Waters Corporation. Certified Sep-Pak cartridges: care and use manual. Milford, MA: Author; 2009.
11. Technescan MAG3™ [package insert]. Maryland Heights, MO: Mallinckrodt™ Pharmaceuticals; 2015.
12. Octreoscan™ [package insert]. Maryland Heights, MO: Mallinckrodt™ Pharmaceuticals; 2015.
13. Seetharaman S, Ballinger JR, Sosabowski MH. Simplified method for determining the radio-chemical purity of ^{99m}Tc-MAG$_3$. J Nucl Med Technol. 2006;34:179–83.
14. Ensing GJ, Knight HH. ^{99}TC^m-MAG$_3$: problems with radiochemical purity testing [Letter to the editor]. Nucl Med Commun. 2001;22:114–5.
15. Ponto JA. Effect of solvent flow rate in mini-column testing of ^{99m}Tc-mertiatide. J Nucl Med Technol. 2005;33:232–3.
16. Saha GB. Quality control of radiopharmaceuticals. In: Saha GB, editor. Fundamentals of nuclear pharmacy. 7th ed. Cham: Springer; 2018. p. 163–83.
17. Technetium Tc-99m Sestamibi injection [package insert]. New York: Drax Image®; 2009.
18. Ceretec™ [package insert]. Arlington Heights, IL: GE Healthcare Medi-Physics, Inc.; 2018.
19. Lymphoseek [package insert]. Dublin, OH: Cardinal Health 414, LLC; 2019.
20. Neurolite® [package insert]. N. Billerica, MA: Lantheus Medical Imaging; 2015.
21. Zimmer AM, Spies SM. Quality control procedures for newer radiopharmaceuticals. J Nucl Med Technol. 19, 4:210–4.
22. Métayé T, et al. Rapid quality control for testing the radiochemical purity of ^{99}Tc^m tetrofosmin. Nucl Med Commun. 2001;22:1139–44.
23. McKay BF, et al. Rapid miniaturized chromatography for tecnetium-99m-tetrofosmin. J Nucl Med Technol. 1997;25:52–4.
24. Harapanhalli R. Food and Drug Administration requirements for testing and approval of new radio-pharmaceuticals. Semin Nucl Med. 2010;40:364–84.
25. https://www.fda.gov/Drugs/DevelopmentApprovalProcess/HowDrugsareDevelopedandApproved/ApprovalApplications/InvestigationalNewDrugINDApplication/default.htm. Accessed Sep 18 2018.
26. https://www.ecfr.gov/cgi-bin/text-idx?SID=f640d0676f0a5f413cc184565e4724fc&mc=true&tpl=/ecfr-browse/Title21/21cfr312_main_02.tpl. Accessed 31 Dec 2018.
27. http://www.fda.gov/ForPatients/ClinicalTrials/Types/default.htm. Accessed Dec 2018.
28. Saha GB. Radiation regulations, protection, and uses. In: Saha GB, editor. Fundamentals of nuclear pharmacy. 7th ed. Cham: Springer; 2018. p. 221.
29. Loveless V. Quality control of compounded radiopharmaceuticals. University of New Mexico Health Science Center Pharmacy Continuing Education, vol. 15, Lesson 3; 2009.

PET Chemistry: An Introduction

7

Tobias L. Ross and Simon M. Ametamey

Contents

7.1   Introduction

One major advantage of radioactivity is its extremely high sensitivity of detection. Regarding the medical applicability of radioactivity, this permits non-invasive in vivo detection of radiolabelled compounds at nano- to picomolar levels. The use of substances at such low concentrations usually precludes a physiological, toxic or immunologic response of the investigated biological system. Consequently, the considered physiological process or system is examined in an unswayed situation. Furthermore, a wide range of substances, even those that are toxic at higher concentrations, become considerable for the development of radiopharmaceuticals and use in nuclear medicine. In contrast to the wide range of employable bioactive molecules, the range of suitable radioactive nuclides is much more restricted by their nuclear physical and chemical properties. In particular, radionuclides for diagnostic applications should provide appropriate (short) half-lives and radiation properties for detection and imaging, but at the same time, the radiation dose of patients and personnel have to be kept to a minimum. Nonetheless, to date, a couple of radionuclides have proven suitability for both the nuclear medical diagnostic applications, single-photon emission computed tomography (SPECT) and positron emission tomography (PET).

As indicated by their names, SPECT is based on photon- or γ-ray-emitting nuclides while PET derives from those nuclides that belong to the group of neutron-deficient nuclides and emit

T. L. Ross (✉)
Radiopharmaceutical Chemistry, Department of
Nuclear Medicine, Hannover Medical School,
Hannover, Germany
e-mail: ross.tobias@mh-hannover.de

S. M. Ametamey
Animal Imaging Center-PET, Center for
Radiopharmaceutical Sciences of ETH, PSI and USZ,
ETH-Hönggerberg, D-CHAB IPW HCI H427,
Zurich, Switzerland
e-mail: amsimon@ethz.ch

positrons (β⁺-decay). Large-scale production of positron-emitting radionuclides became available for the first time by the invention of the cyclotron by Ernest Orlando Lawrence in 1929 [1]. Since then, many (medical) cyclotrons have been built and have been in use at various nuclear medicine PET facilities. As a result, short-lived positron emitters such as most commonly employed fluorine-18 and carbon-11 are routinely produced at most nuclear medicine centres on a daily basis. In the last decades, the metallic positron emitters such as gallium-68, conveniently available from radionuclide generators, but recently also available from cyclotrons [2, 3], became highly important [4].

In the β⁺-decay of a neutron-deficient nucleus, a positron (β⁺) and a neutrino (ν) are synchronously emitted while in the nucleus a proton is converted into a neutron. Neutrinos show practically no interaction with matter, and thus, they are not detectable by PET cameras. In contrast, the emitted positron is able to interact with an electron, its anti-particle. As a result, both the particles annihilate and give two γ-rays with a total energy of 1.022 MeV, the sum of the masses of positron and electron, 511 keV each. Both the γ-rays show a nearly 180° distribution, and each carries the characteristic energy of 511 keV. Accordingly, the decay of positron emitters that are used as label for PET radiopharmaceuticals results in two γ-rays, and as these are body-penetrating photons, they can be detected by an appropriate PET camera. This physical phenomenon provides the base of PET imaging.

In PET scanners, a circular ring of detector pairs, which only record coincidence events, registers the in vivo generated pairs of γ-rays. An appropriate computer-aided data acquisition provides PET images with information about in vivo distribution and levels of accumulation of the radionuclide and the radiopharmaceutical, respectively. Consequently, biochemical processes can be visualised, and a dynamically data acquisition further allows for the registration of a temporal component such as pharmacokinetics of a certain drug. In combination with biomathematical models and individual corrections of attenuation, transmission and scatter effects, physiological and pharmacological processes can be precisely acquired and quantified [5].

The most important radionuclides for PET imaging are fluorine-18, gallium-68 and carbon-11. Particularly, the ¹⁸F-labelled glucose derivative 2-deoxy-2-[¹⁸F]fluoro-ᴅ-glucose ([¹⁸F]FDG) represents the most widely used PET radiopharmaceutical, which has contributed most to the worldwide success of clinical PET imaging. The combination of a highly efficient radiochemistry and a high-yielding $^{18}O(p,n)^{18}F$ nuclear reaction makes [¹⁸F]FDG in large amounts available and also enables shipment and distribution by commercial producers. Since its development in the 1970s [6] [¹⁸F]FDG has been employed in many PET studies in oncology, neuroscience and cardiology [7–10]. Very recently, ¹⁸F-labelled ligands targeting the prostate-specific membrane antigen (PSMA) became almost equally important [11]. However, further substances have followed [¹⁸F]FDG, and to date, several PET radiopharmaceuticals for specific targets have been developed and evaluated for a wide range of applications in clinical nuclear medicine as well as in preclinical research [12–15].

This chapter deals with the development and the use of PET radiopharmaceuticals. Here a comprehensive overview of basic considerations and possibilities in development of PET radiopharmaceuticals is given. An outline of commonly employed clinically established PET radiopharmaceuticals, their most important production routes and clinical applications follows in the next chapter, in which also aspects of routine production and quality control of PET radiopharmaceuticals as well as their use in drug development are introduced and briefly summarised.

7.2 Choice of the Radionuclide

There are a variety of basic functions and effects which can generally be followed and visualised by PET such as metabolism, pharmacokinetics, (patho)physiological and general biochemical functions; receptor-ligand biochemistry; enzyme functions and inhibition; immune reactions and response; pharmaceutical and toxicological effects. However, a close look into the designated processes and the related biochemistry is necessary to find a positron emitter with appropriate characteristics.

Although fluorine-18 is the most commonly preferred positron emitter for PET radiopharmaceuticals, monoclonal antibodies labelled with fluorine-18 for immuno-PET imaging are normally not useful because the physical half-life of 110 min does not fit to the slow accumulation (normally 1–3 days) of most monoclonal antibodies in solid tumours [16]. In such cases, longer-lived PET nuclides as iodine-124 ($T_{1/2}$ = 4.18 d) and zirconium-89 ($T_{1/2}$ = 3.27 d) are more suitable for this particular application. On the other hand, longer half-life increases radiation dose to patients, makes patient management and clinical routine more complex and thoughtful considerations towards a health/risk–benefit analysis are mandatory.

As a basic principle, short-lived radionuclides should preferably be used if their suitability is similarly good with respect to a certain application. In case of immuno-PET, pre-targeting approaches are available and combine benefits from both monoclonal antibody specificity and short-lived PET isotopes [17]. To go to the other extreme, blood flow tracers are a perfect example for the use of extremely short-lived radionuclides such as oxygen-15 ($T_{1/2}$ = 2 min), nitrogen-13 ($T_{1/2}$ = 10 min) and rubidium-82 ($T_{1/2}$ = 1.3 min). The scanning times of blood flow studies using PET are normally very short and not longer than 2–5 min. Hence, radiolabelled substances such as [^{15}O]water, [^{15}O]butanol, [^{13}N]ammonia and [^{82}Rb]RbCl are particularly suitable. However, the very short half-lives of these radionuclides place some constraints on imaging procedure and execution.

Beside half-lives, there are further physical aspects to be considered. One is the β^+-energy ($E_{\beta+}$) of the emitted positrons. The $E_{\beta+}$ also clearly affects the radiation dose to the patients and thus the lower the $E_{\beta+}$ the better it is for the patients. Since the $E_{\beta+}$ is also responsible for the positron range (travelling distance of the positron) and a short positron range enhances the spatial resolution in PET, a low $E_{\beta+}$ is favourable for high-resolution PET imaging. However, in human PET scanners, the distance of the detectors to the object is long, and the positron range is less significant for the absolute spatial resolution as demonstrated in comparable studies using

different positron emitters in imaging phantoms [18, 19]. In contrast, high-resolution small animal PET scanners show strongly affected image quality by the use of positron emitters with high $E_{\beta+}$ or complex decay schemes [20].

In comparison with most of the available positron emitters for PET, it is already quite evident from the nuclear properties that fluorine-18 is the most preferred radionuclide for PET. The optimal half-life of fluorine-18 offers multistep radiochemistry, extended PET studies of slower biochemistry as well as the shipment of the ^{18}F-labelled radiopharmaceuticals to clinics without an onsite cyclotron or a radiochemistry facility. Furthermore, it has one of the lowest $E_{\beta+}$ among the PET nuclides and provides high-resolution PET images. An overview of the nuclear data of important positron emitters for PET is given in Table 7.1.

In the same way as the radionuclide must fulfil the physical requirements of the PET imaging, it needs to exhibit suitable chemical properties with respect to available labelling techniques. Thereby the labelling strategy depends on the initial situation and attendant restrictions. If a certain radionuclide is given by reasons such as availability or imaging characteristics, the target structure often needs to be modified towards its suitability for corresponding labelling methods. In contrast, if the structure of a biomolecule is stipulated, a combination of a radionuclide with an appropriate and efficient labelling procedure needs to be found. However, a restricted number of PET radionuclides and a limited selection of reactions for their introduction into biomolecules generally necessitate the approach of tailored structures. Noteworthy, those structural modifications of the parent biomolecule are mostly accompanied by changes in the pharmacological behaviour and usually a compromise covering pharmacological performance, radiochemistry, dosimetry and PET imaging requirements must be found.

In general, the choice for the right positron emitter for a new PET radiopharmaceutical can be described as the best match between efficient radiochemistry, acceptable dosimetry and favourable pharmacological and PET imaging properties.

Table 7.1 Important positron emitters used for PET and their nuclear data (from [21–23])

Nuclide	Half-life	Decay mode (%)	$E_{\beta+,max}$ [keV]
Organic			
[11]C	20.4 min	β^+ (99.8) EC (0.2)	960
[13]N	9.96 min	β^+ (100)	1190
[15]O	2.03 min	β^+ (99.9) EC (0.1)	1720
[30]P	2.5 min	β^+ (99.8) EC (0.2)	3250
Analogue			
[18]F	109.6 min	β^+ (97) EC (3)	635
[73]Se	7.1 h	β^+ (65) EC (35)	1320
[75]Br	98 min	β^+ (75.5) EC (24.5)	1740
[76]Br	16.2 h	β^+ (57) EC (43)	3900
[77]Br	2.38 d	β^+ (0.7) EC (99.3)	343
[120]I	81.1 min	β^+ (64) EC (36)	4100
[124]I	4.18 d	β^+ (25) EC (75)	2140
Metallic			
[38]K	7.6 min	β^+ (100)	2680
[44]Sc	3.97 h	β^+ (94) EC (6)	1474
[45]Ti	3.09 h	β^+ (85) EC (15)	1040
[60]Cu	23.7 min	β^+ (93) EC (7)	3772
[61]Cu	3.33 h	β^+ (61) EC (39)	1215
[62]Cu	9.7 min	β^+ (98) EC (2)	2930
[64]Cu	12.7 h	β^+ (18) β^- (37) EC (45)	655
[68]Ga	67.7 min	β^+ (90) EC (10)	1900
[72]As	26 h	β^+ (88) EC (12)	2515
[82]Rb	1.3 min	β^+ (96) EC (4)	3350
[86]Y	14.7 h	β^+ (34) EC (66)	1300
[89]Zr	3.27 d	β^+ (33) EC (77)	902
[94m]Tc	52 min	β^+ (72) EC (28)	2470

7.3 Labelling Methods: Introduction of the Radionuclide

Organic positron emitters: The introduction of the radionuclide into a biomolecule or a structure of (patho)physiological interest obviously is one of the essential steps in the development of radiopharmaceuticals. Biomolecules and pharmaceuticals mainly consist of carbon, hydrogen, oxygen, nitrogen, sulphur and phosphorous. Due to that fact the so-called organic radionuclides (see Table 7.1), carbon-11, oxygen-15, ammonia-13 and phosphorous-30 allow the so-called authentic labelling without any changes in (bio) chemical and physiological behaviour of the radiolabelled molecule. However, these organic radionuclides are extremely short-lived isotopes with half-lives only from 2 min to 20 min and

that strongly limits their applicability. Only the half-life of 20 min of carbon-11 offers the possibility of radiosyntheses with more than one step and the detection of physiological processes with slower pharmacokinetics. Besides an unchanged pharmacology, the major advantage of such short half-lives is a low radiation dose to the patients and possible repeat studies within a short period.

Analogue positron emitters: Biomolecules and pharmaceuticals are generally relatively complex organic compounds and claim for multi-step radiosyntheses for their radiolabelled counterparts. In addition, many (patho) physiological processes are slower and thus not detectable with the extremely short-lived radionuclides. Alternatively, the so-called analogue radionuclides with longer half-lives from 80 min to 4 days are commonly introduced into biomolecules. The labelling with analogue radionuclides makes use of similarities in steric demand and/

or in electronic character of the substituted atom or functional group. The steric demand of an atom or a functional group refers to the amount of space occupied by an atom or a functional group. Accordingly, selenium-73 can be used in the manner of sulphur. Selenium as the next homologue to sulphur has very similar steric and chemical properties. The analogue radiopharmaceuticals L-[^{73}Se]selenomethionine [24] and L-homocysteine[^{73,75}Se]selenolactone [25] are examples for such a selenium–sulphur analogy. Similarly, ^{75,76,77}Br and ^{120,124}I can be regarded as structural analogues for methyl groups.

In the majority of cases, the analogue radionuclides evoke only small insignificant structural differences, but the arising electronic changes and those of chemical reactivity can be important. In each individual case, the pharmacological behaviour and properties of such analogue radiotracers have to be tested for changes in characteristics. In the last decades, the number of new pharmaceuticals has increased rapidly, and more and more compounds have been identified as pharmacologically relevant substances which are originally carrying fluorine, bromine or iodine [26, 27]. Consequently, the advantages of authentic labelling and longer half-lives accrue and simplify the development of a corresponding radiopharmaceutical.

Metallic positron emitters: In a third group, there are metallic positron emitters which are suitable for PET imaging (see Table 7.1). The half-lives vary from minutes to days and offer a broad range of applicability. In contrast to organic or analogue PET nuclides, some of the metallic radionuclides are achievable from generator systems (e.g. ^{62}Zn/^{62}Cu, ^{68}Ge/^{68}Ga and ^{82}Sr/^{82}Rb) which make them available in places without an onsite cyclotron. Metallic PET nuclides can be used either directly in their free cationic forms or as complexes. Rubidium-82 has been evaluated as a myocardial perfusion PET tracer [28, 29]. In the form of [^{82}Rb]RbCl, it is used as radiopharmaceutical for perfusion PET imaging on the market for almost 20 years (CardioGen-82©, approved by the FDA in 1989). The similarities of rubidium to the potassium cation lead to a rapid uptake of rubidium-82 into the myocardium and allow the identification of regions of insufficient perfusion by PET imaging [30, 31]. In complexes, the metallic radionuclides are usually incorporated into biomolecules which carry suitable chelators (i.e. DOTA for the somatostatin receptor ligand [^{68}Ga]Ga-DOTA-[Tyr^3]octreotide [32] or HBED for the prostate specific membrane antigen ligand [^{68}Ga]PSMA-11 [33]).

In addition to differences in chemical, physical and nuclear properties of the radionuclides, the production routes or processes can also influence the labelling approach. The production route as well as the work-up provides the radionuclide in a certain chemical form which requires suitable (radio)chemistry in the following synthetic steps. From the production process, PET radionuclides are obtained only in a nano- to picomolar range while they are still very well detectable by their radiation. As a result, the final PET radiopharmaceuticals are so attractive to medicinal purposes. In the body, they can be detected with non-invasive methods while the quantity of material is extremely small and generally toxic and pharmacological effects are negligible.

Specific Activity: Owing to the desired insignificant quantities, a fundamental criterion of the quality of a radionuclide and the final radiopharmaceutical is its specific (radio)activity (A_s) which depends on the amount of stable isotopes (carrier) present. Carrier can be divided into:

- **Isotopic carrier**: isotopes of the same element as the radionuclide.
- **Non-isotopic carrier**: isotopes of other elements mostly with very similar chemical and physical properties to the radionuclide.

On this account, A_s is defined as the mass related radioactivity:

$$A_s = A / m \left[\mathrm{Bq} / \mathrm{g} \right]$$

where A is the radioactivity in Becquerel and m is the mass of the radioactive material including all impurities and carrier, respectively. In (radio)chemistry, such a specification related to the mass is inconvenient, and thus A_s is generally expressed as molar activity (A_m) on the molar basis as radioactivity related to the amount of substance [34]:

$$A_m = A / n \, [\mathrm{Bq / mol}]$$

where m is replaced by n for the amount of substance in moles. In the absence of impurities or isotopic carrier, the theoretically attainable maximum A_m equals to:

$$A_m = N_A \left(\ln 2 / T_{\frac{1}{2}} \right) [\mathrm{Bq / mol}] \quad \text{or}$$
$$A_m = 1.16 \times 10^{20} / T_{\frac{1}{2}} [\mathrm{Bq / mol}]$$

where N_A is Avogadro's number (6.023×10^{23} in atoms/mol) and $T_{\frac{1}{2}}$ is the half-life of the radionuclide in hours. The general abundance of stable isotopes of the PET radionuclides smallers the theoretically attainable A_m and the quantity of material become higher by natural isotopic carrier, but it is normally still at a nano- to picomolar level (6.3×10^4 versus 300–600 GBq/µmol for theoretical and practical A_m, respectively, for fluoride-18 produced from $^{18}O(p,n)^{18}F$. Most applications in molecular imaging call for high A_m, and a lot of effort is put into this issue. Especially for brain receptor PET imaging, high specific activities are essential when receptor systems of low density can be saturated by radioligands with low A_m. Beside poor PET imaging results because of an unfavourable signal-to-noise ratio, pharmacological or toxic effects have also to be considered. In general, for radiochemical practise, the radionuclide situations can be classified as:

- Carrier-free (c.f.)
- No-carrier-added (n.c.a.)
- Carrier-added (c.a.)

Carrier-free (c.f): Ideally, carrier-free systems are not achievable with PET radionuclides as they all have naturally occurring stable isotopes. For example, carbon is the fourth most abundant element on earth, and it is present in almost every kind of material. Thus, especially for carbon-11, high specific activities are an exceptional challenge. However, in radiochemistry of PET radionuclides, traces of stable isotopes are omnipresent and act as isotopic carrier. Sources of isotopic carrier are the air, target and vessel materials, transport lines and tubes, chemicals and solvents.

No-carrier-added (n.c.a): Contaminations in chemicals and solvents are below normal chemical purification limits, but they are still in the quantity of the radionuclide. Those conditions are referred to as no-carrier-added (n.c.a.) conditions and correspond to a state of practically highest A_m attainable.

Carrier-added (c.a): On the contrary, some circumstances can require the addition of stable isotopes what is termed as carrier-added (c.a.). Predominantly, c.a. conditions are employed to achieve weighable quantities of a product for characterisation by non-radioactive analytical methods or to increase radiochemical yields. As a widely used c.a. procedure, the production of electrophilic fluorine-18 is well-known. The addition of the isotopic carrier fluorine-19 is necessary to mobilise n.c.a. $[^{18}F]F_2$ which is too reactive and adheres to the walls of targets and tubes.

Labelling reactions and radiosyntheses on the n.c.a. scale mean to work at a subnanomolar level regarding the amount of radioactive substance while all other reactants and solvents are still present at a macroscopic scale. Hence, the course of reaction may differ strongly from that of classical chemical reactions at balanced stoichiometric ratios, where all substrates and reagents are present in amounts in a similar or equal range. Such labelling reactions under non-equilibrium conditions generally proceed according to pseudo-first-order kinetics where the precursor amounts are in extreme excess to the radionuclide and can approximately be set as constant. On the other hand, the radionuclide and the labelled product exist on an n.c.a. scale, and thus, a consecutive labelling reaction or an interaction of two radioactive species can be statistically excluded.

In labelling procedures and radiosyntheses, obviously the decay has to be taken into account and thus the half-life of the employed radionuclide. With respect to the PET imaging, the final radiopharmaceutical must be obtained in reasonable amounts sufficient for the following PET procedures. As a rule of thumb, the radiosynthesis including purification, formulation and quality control of a PET radiopharmaceutical should not exceed three to four half-lives of the radionuclide. Consequently, the extremely short-lived

PET radionuclides call for very fast chemistry and preclude multi-step procedures.

The efficacy of radiolabelling reactions is generally quantified by the radiochemical yield (RCY) which corresponds to the decay-corrected yield related to the starting activity. In contrast, the activity yield reflects the amount of isolated radioactive material and important for the following applications, but is not functional as an appraisal factor of the labelling procedure.

7.3.1 Labelling Methods for Fluorine-18

The indisputable importance of fluorine-18 in PET makes ^{18}F-labelled radiopharmaceuticals be the most favoured ones; thus, especial procedures for the introduction of fluorine-18 are of great interest, and several methods and strategies have been developed [35–38]. There are many established nuclear production pathways for fluorine-18; the most commonly used are listed in Table 7.2 [39, 40].

The main difference between various nuclear reactions is the target material which is either gas or liquid (water) and determines the final chemical form of fluorine-18. From gas targets, fluorine-18 is achieved as electrophilic c.a. $[^{18}F]$fluorine gas ($[^{18}F]F_2$), and from the water targets, nucleophilic n.c.a. $[^{18}F]$fluoride in aqueous solution is obtained. As mentioned before, in case of the electrophilic $[^{18}F]F_2$, adsorption of the produced n.c.a. fluorine-18 on the walls of the target requires the addition of non-radioactive $^{19}F_2$ (isotopic carrier) for an isotopic exchange and removal of the n.c.a. fluorine-18 out of the target.

Due to this fact, the procedure dramatically lowers the obtainable specific activity which is one of the major disadvantages of these production routes.

Many compounds of (radio)pharmacological interest have called for electrophilic labelling methods and thus necessitated c.a. $[^{18}F]F_2$ or its derived secondary labelling agents. The most popular PET radiopharmaceutical which was routinely produced via an electrophilic c.a. ^{18}F-labelling (^{18}F-fluorodestannylation) is 6-$[^{18}F]$fluoro-L-DOPA ($[^{18}F]$F-DOPA) (see Fig. 7.3) [41, 42]. In the past decade, novel nucleophilic ^{18}F-labelling approaches became available for such molecules and have fundamentally changed the world ^{18}F-labelling [43]. Nowadays, commercial cassette-based automated nucleophilic syntheses n.c.a. $[^{18}F]$F-DOPA are available [44, 45].

However, the nucleophilic production route using ^{18}O-enriched water as target material is the most efficient procedure and also provides the n.c.a. $[^{18}F]$fluoride in high specific activities. As a result, the $^{18}O(p,n)^{18}F$ reaction is the most widely used method to produce fluorine-18. The required proton energy of 16 → 3 MeV for the nuclear reaction is achievable without problems from small cyclotron, so-called medical cyclotrons. Normal batches of 50–100 GBq for the production of ^{18}F-labelled clinically utilised PET radiopharmaceuticals can be obtained within 30–60 min depending on the target construction and the corresponding beam current, but even lager batches of up to several hundred GBq are conveniently producible.

Regarding the chemical concepts for the introduction of fluorine-18 into organic molecules, the methods of the macroscopic organic chem-

Table 7.2 Most common nuclear reactions for the production of fluorine-18

Reaction	$^{18}O(p,n)^{18}F$	$^{16}O(^3He,p)^{18}F$	$^{20}Ne(d,\alpha)^{18}F$	$^{18}O(p,n)^{18}F$
Target filling	$H_2^{18}O$	H_2O	Ne (200 µMol F_2)	$^{18}O_2$, Kr (50 µMol F_2)
Particle energy [MeV]	16 → 3	36 → 0	14 → 0	16 → 3
Chemical product form	$[^{18}F]$fluoride (aq)	$[^{18}F]$fluoride (aq)	$[^{18}F]F_2$	$[^{18}F]F_2$
Yield [GBq/µAh]	2.22	0.26	0.37–0.44	~0.35
Specific activity [GBq/µMol]	40×10^3	40×10^3	~0.04 – 0.40	~0.35–2.00

istry could be principally transferred. In general chemistry, the commonly used fluorination procedures are based on the Wallach reaction [46] and the Balz–Schiemann reaction [47]. However, in n.c.a. ^{18}F-radiosyntheses, these procedures let only to very low radiochemical yields [48, 49]. Effects of the unusual stoichiometric ratios under n.c.a. conditions as well as principle aspects of the reactions' mechanisms and reactants let to these results. Both the reaction types revealed inappropriate for fluorine-18 chemistry under n.c.a. conditions.

Generally, radiofluorination methods can be divided into electrophilic and nucleophilic reactions (substitutions) according to the chemical form of fluorine-18 and thus the production route. Both the methods represent direct ^{18}F-fluorinations and can be completed by two additionally indirect methods, the ^{18}F-fluorinations via prosthetic groups and the ^{18}F-fluorinations via built-up syntheses. In general, the indirect methods are based on direct methods for the ^{18}F-labelling of the required prosthetic group or synthon. Frequently, the nucleophilic ^{18}F-methods are employed here, due to higher specific activities, higher radiochemical yields and a better availability of n.c.a. [^{18}F]fluoride.

7.3.1.1 Electrophilic Substitutions

Fluorine-18 for electrophilic substitution reactions is available as c.a. [^{18}F]F$_2$ directly from targets. As target materials, ^{20}Ne and enriched [^{18}O] O$_2$ can be used (cf. Table 7.2). Both the alternatives come along with an adsorption of the fluorine-18 on the target walls and entail an addition of [^{19}F]F$_2$ to mobilise the produced fluorine-18 by isotopic exchange. In the ^{18}O(p,n)^{18}F reaction, the enriched ^{18}O-target filling is removed after bombardment, and the target is filled with 0.1% ^{19}F$_2$ in Kr and repeatedly irradiated for the [^{18}F]F$_2$ formation [50]. In comparison, the ^{20}Ne(d,α)^{18}F reaction is more practical as 0.1% [^{19}F]F$_2$ is directly added with the neon and an additional step for recovery of the enriched material and the consecutive irradiation is saved. Furthermore, the process does not require enriched material and is less expensive. Therefore, the ^{20}Ne(d,α)^{18}F reaction is the commonly employed process for

electrophilic fluorine-18, although its production rates are lower [39, 40]. As all production processes for electrophilic fluorine-18 require carrier addition, c.a. [^{18}F]F$_2$ or milder reagents derived from it cannot be used in the preparations of PET radiopharmaceuticals where high specific activities are mandatory [51, 52].

Generally, the methods of electrophilic fluorinations from organic chemistry can be directly transferred into c.a. fluorine-18 chemistry. Due to the fact that carrier is added, here the stoichiometric ratios are more balanced than under n.c.a. conditions and thus closer to macroscopic chemistry. In organic chemistry, elemental fluorine is known for its high reactivity and its poor selectivity. Therefore, c.a. [^{18}F]F$_2$ is often transferred into less reactive and more selective electrophilic fluorination agents such as [^{18}F]acetyl hypofluoride ([^{18}F]CH$_3$COOF) [53], [^{18}F]xenon difluoride ([^{18}F]XeF$_2$) [54, 55] or [^{18}F]fluorosulfonamides [56]. The maximum radiochemical yield in electrophilic radiofluorinations is limited to 50% as only one fluorine in [^{18}F]F$_2$ is substituted by a ^{18}F atom. Consequently, that is also the situation for all secondary electrophilic radiofluorination agents derived from c.a. [^{18}F]F$_2$.

The most popular example of electrophilic radiofluorinations using c.a. [^{18}F]F$_2$ is the first method to produce 2-deoxy-2-[^{18}F]fluoro-D-glucose ([^{18}F]FDG) by Ido et al. in 1978 (see Fig. 7.1) [6]. [^{18}F]F$_2$ was used in an electrophilic addition to the double bond of triacetoxyglucal and gave [^{18}F]FDG in a radiochemical yield of 8%. As a radioactive side product, 3% of the ^{18}F-labelled mannose derivative (2-deoxy-2-[^{18}F] fluoro-D-mannose, [^{18}F]FDM) was obtained. In 1982, a higher RCY of 20% and an improved product-to-byproduct ratio of 7:1 was achieved in the approach of Shiue et al. using the milder radiofluorination agent [^{18}F]acetyl hypofluoride [57]. Many other approaches were made to increase the radiochemical yields of [^{18}F]FDG in electrophilic procedures [58–60], including also attempts with [^{18}F]XeF$_2$ [61–63].

Another example for a direct electrophilic ^{18}F-fluorination is 5-[^{18}F]fluorouracil which is the ^{18}F-labelled analogue of 5-fluorouracil. 5-Fluorouracil is a chemotherapeutic, and thus,
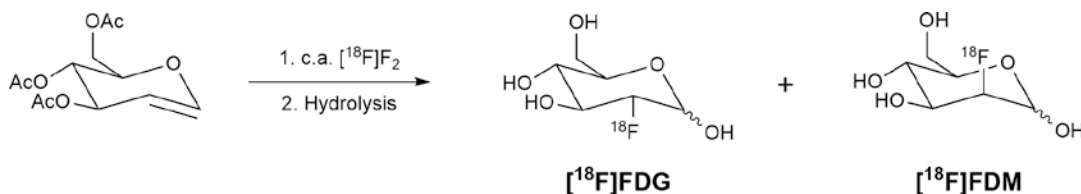
Fig. 7.1 Original radiosynthesis of [^{18}F]FDG (RCY = 8%) by Ido et al. using c.a. [^{18}F]F$_2$. As a side product, the ^{18}F-labelled mannose derivative ([^{18}F]FDM) was obtained in an RCY of 3%
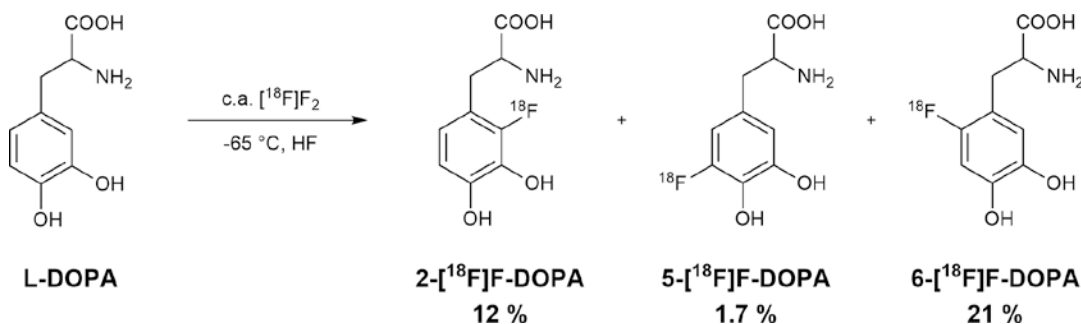
Fig. 7.2 Direct electrophilic radiofluorination of [^{18}F]F-DOPA using c.a. [^{18}F]F$_2$. The product mixture contains 21% of the desired ^{18}F-labelled regioisomer 6-[^{18}F]F-DOPA

its ^{18}F-labelled analogue can be used for therapy control, for visualisation of various tumours and for prediction of therapy response in liver metastases [64, 65]. 5-[^{18}F]fluorouracil can be prepared by direct ^{18}F-fluorination of uracil using c.a. [^{18}F]F$_2$ [66].

The most important PET radiopharmaceutical which was routinely produced via electrophilic ^{18}F-fluorination methods is 6-[^{18}F]fluoro-L-DOPA ([^{18}F]F-DOPA). After [^{18}F]FDG, [^{18}F]F-DOPA had ranked second in its frequency of clinical use, nowadays replaced by radiopharmaceuticals such as [^{18}F]FPSMA. The direct radiofluorination of 3,4-dihydroxyphenyl-L-alanine using [^{18}F]F$_2$ leads to three possible ^{18}F-labelled regioisomers, namely 2-[^{18}F]F-DOPA (12%), 5-[^{18}F]F-DOPA (1.7%) and 6-[^{18}F]F-DOPA (21%) (see Fig. 7.2), and requires a complex HPLC purification to obtain the desired 6-[^{18}F]F-DOPA in only 3% RCY [67].

Several attempts have been made to improve radiochemical yields and regioselectivity in the direct radiofluorination of L-DOPA [68, 69]. So far, the most efficient electrophilic procedure for 6-[^{18}F]F-DOPA which provides adequate RCY

of up to 33% for clinical PET imaging is based on an ^{18}F-fluorodemetallation reaction [70]. The ^{18}F-fluorodestannylation has been the most commonly used reaction for routinely produced 6-[^{18}F]F-DOPA (see Fig. 7.3) [71]. An automation of this radiosynthesis allowed reliable routine productions for clinical PET imaging using 6-[^{18}F]fluoro-L-DOPA [72].

For higher molar activities in electrophilic ^{18}F-fluorinations, [^{18}F]F$_2$ can be obtained from n.c.a. [^{18}F]CH$_3$F via an electric gaseous discharge reaction in the presence of [^{19}F]F$_2$ (150 nmol). This provides molar activities of up to 55 GBq/μmol in case of [^{18}F]F$_2$ which leads to A_m of ~15 GBq/μmol of final ^{18}F-labelled products [73].

However, electrophilic substitution reactions using [^{18}F]F$_2$ and secondary milder fluorination agents derived from it can be used in clinically routine production of PET radiopharmaceuticals where low molar activities and moderate radiochemical yields are not critical. PET imaging of receptor systems and other PET imaging investigations which require high molar activities still necessitate ^{18}F-radiopharmaceuticals produced under no-carrier-added conditions
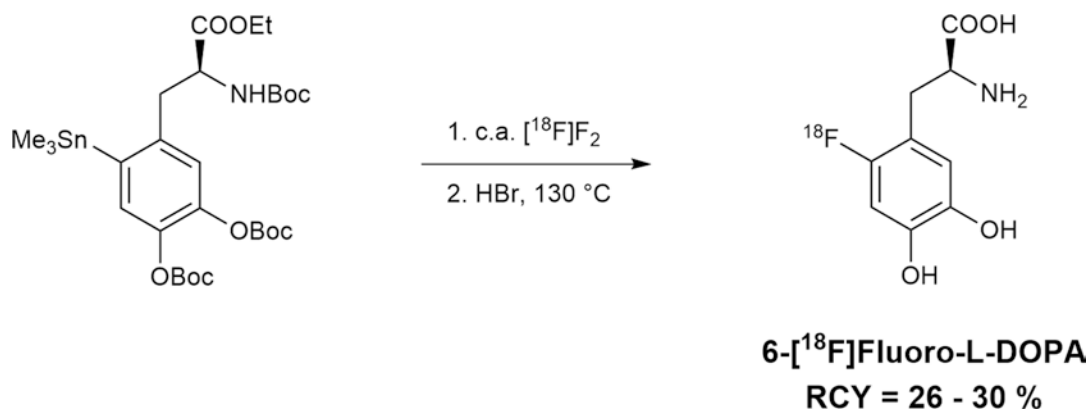
Fig. 7.3 Electrophilic radiofluorination of 6-[18F]F-DOPA by regioselective 18F-fluorodestannylation. After 45–50 min 6-[18F]F-DOPA is obtained in RCY of 26–33%
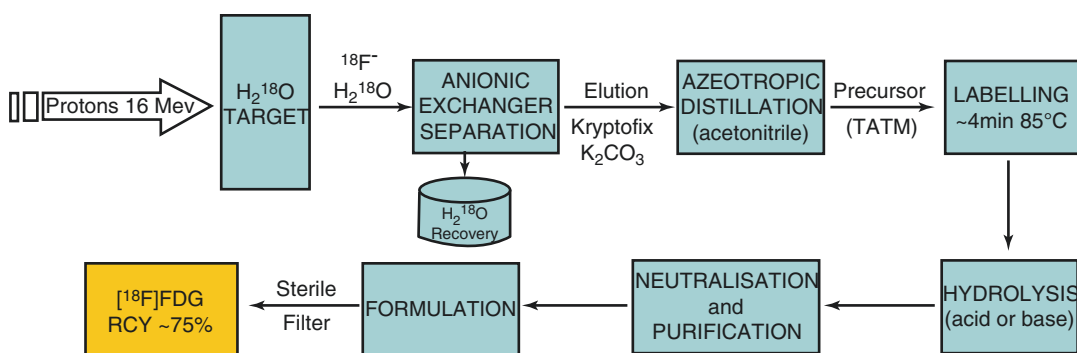
Fig. 7.4 Steps of routine production of [18F]FDG. TATM = 1,3,4,6-tetra-*O*-acetyl-2-*O*-trifluoro-methanesulfonyl-beta-D-mannopyranose

and thus derive from nucleophilic substitution using n.c.a. [18F]fluoride. To date, most electrophilic approaches have been replaced by modern direct nucleophilic (n.c.a.) 18F-fluorinations using various novel catalysts, allowing late stage 18F-fluorinations providing high yields and high molar activities [37].

7.3.1.2 Nucleophilic Substitutions

As mentioned before, the $^{18}O(p,n)^{18}F$ reaction using enriched [18O]water as target material is the most efficient and most widely used production route for (nucleophilic) fluorine-18. The required proton energy of 16 MeV can be easily generated by medial cyclotrons, and so 50–100 GBq of n.c.a. fluorine-18 can be produced within 30–60 min, and even higher amount of up to several hundred GBq can be produced conveniently.

Fluorine-18 is obtained directly from the target as nucleophilic n.c.a. [18F]fluoride in aqueous solution without any carrier addition.

The commonly appied synthesis route for [18F] FDG is depicted in Fig. 7.4. The first step after the irradiation is a separation of [18F]fluoride from [18O]water. Commonly, [18F]fluoride is trapped on an anionic exchange resin (solid phase extraction cartridge systems) while [18O]water is recovered. [18F]Fluoride in aqueous solution is strongly hydrated and inactivated for nucleophilic reactions. For an activation of [18F]fluoride, water is removed by azeotropic distillation with acetonitrile, and the remaining dry [18F]fluoride is available for nucleophilic substitution reaction as an activated nucleophile.

Due to the strong tendency of fluoride ions to form hydrogen fluoride, most 18F-labelling reac-
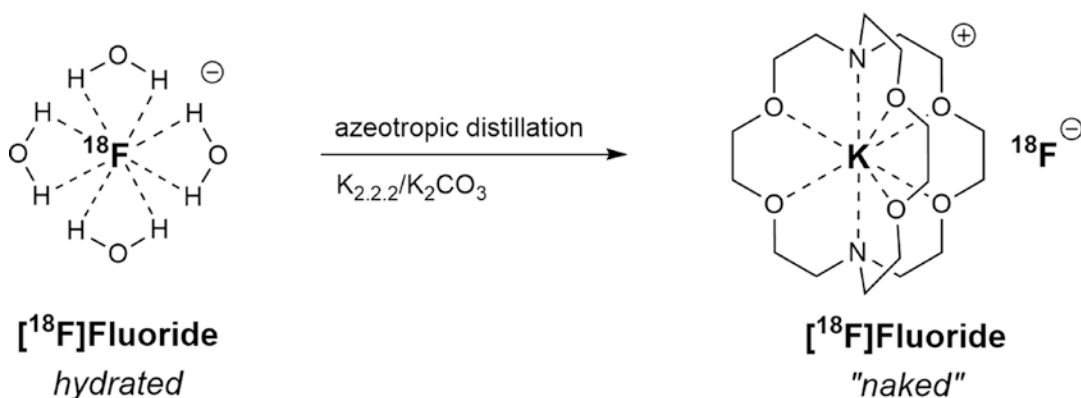
Fig. 7.5 Principle of [18F]fluoride activation by removal of water in combination with the Kryptofix©2.2.2/potassium carbonate system

tions must be carried out under dry and aprotic conditions. Hence, nucleophilic 18F-labelling is usually performed in dipolar aprotic organic solvents. For further activation and increased nucleophilicity of the [18F]fluoride, it is used in combination with weak and soft cations, those of caesium or rubidium. As a result, a so-called naked [18F]fluoride of high nucleophilicity is produced. Similarly, phase transfer catalyst such as tetraalkylammonium salts, mainly as their carbonates, hydroxides or hydrogen carbonates, can be used. One of the most efficient and commonly applied system in radiofluorinations is the combination of a cryptand, the aminopolyether Kryptofix©2.2.2, and potassium carbonate (see Fig. 7.5) [74].

In case of base-sensitive compounds, the carbonate can be exchanged by oxalate which provides less basic conditions. In another method, [18F]fluoride is separated from [18O]water by an electrochemical anodic adsorption [75]. For drying, the cell is flushed two times with acetonitrile or dimethylamide. A polarity change of the electrical field provides a subsequent desorption and release of the [18F]fluoride into a dipolar aprotic solvent containing a phase transfer catalyst system [76]. In other studies, the use of ionic liquids showed very high 18F-labelling efficiency of up to 90% RCY without previous drying procedures [77]. Small volumes of aqueous 18F-solution are directly added to the reaction mixture containing a base, precursor and ionic liquid. The best results

were obtained from the combination of caesium carbonate and the ionic liquid 1-butyl-3-methyl-imidazolium triflate ([bmim][OTf]). This method was also applied for [18F]FDG productions and showed good RCY of 50–60%, but so far it was tested just with small amounts of [18F]fluoride of less than 1 GBq [78].

In recent years, many new approaches have been developed to reduce the time-consuming step of azeotropic drying. One is the so-called minimalist approach, an on-cartridge approach in which aromatic onium salt precursors (iodonium or ammonium) are used [79]. Here, the precursor in aprotic solvent acts as soft cation and eluent, and so the counter anion of the onium is exchanged by [18F]fluoride and ready for 18F-fluorination after elution. In addition, the minimalist approach has successfully adapted to novel Cu-mediated 18F-fluorination [80]. In case of Cu-mediated 18F-fluorinations, the use of arylboronic acids, pinacol esters and trialkyl-stannanes as precursors in solvent mixtures with alcohols the direct radiolabelling of various aromatic systems in high radiochemical yields without an azeotropic drying [81].

Similarly, some efficient 18F-labelling systems just tolerate traces of water, such as the 18F-labelling of 1,2-ethylene ditosylate towards the prosthetic group 2-[18F]fluoroethyl tosylate. A minimal amount of water (2–3%) was sufficient for a rather standard elution of [18F]fluoride from the anion exchanger; subsequent 18F-fluorination

without azeotropic drying gave high yields of up to 96% [82]. A prominent example for water-tolerating ¹⁸F-fluorination reactions is the so-called SiFa approach, where ¹⁸F is bound to a silicone atom and the driving force is the very high binding energy of the F-Si-bound [83, 84].

Generally, the most important procedures to get ¹⁸F-labelled radiopharmaceuticals are based on the nucleophilic substitution using n.c.a. [¹⁸F] fluoride which is so far also the only way to get ¹⁸F-radiopharmaceuticals of high specific activities. Nucleophilic substitution reactions can be divided into aliphatic and aromatic substitutions.

Aliphatic substitution: In case of aliphatic nucleophilic substitutions, the reactions follow the S_N2 mechanism, and suitable leaving groups are required. The most efficient leaving groups are sulphonic acid esters such as the methane sulphonic acid ester (mesylate), the trifluoromethane sulphonic acid ester (triflate), the *para*-toluene sulphonic acid ester (tosylate) and the *para*-nitrobenzene sulphonic acid ester (nosylate). Further suitable leaving groups are halogens. The most important and prominent example of such an aliphatic nucleophilic substitution using n.c.a. [¹⁸F]fluoride is the synthesis of [¹⁸F]FDG using an acetyl-protected mannose precursor (1,3,4,6-tetra-*O*-acetyl-2-*O*-trifluoromethanesulfonyl-beta-ᴅ-mannopyranose, TATM) carrying a triflate leaving group which was developed by Hamacher et al. in 1986 (see Fig. 7.6) [74]. This procedure provides [¹⁸F] FDG after deprotection and purification in very high radiochemical yields of 50–70% with high specific activities of ~300–500 GBq/μmol. To date, this is the most widely used method for the production of [¹⁸F]FDG towards preclinical and clinical applications.
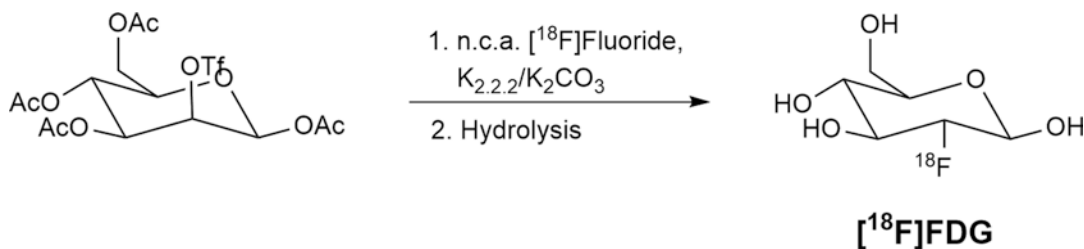
Regarding the reaction conditions for aliphatic nucleophilic substitutions using n.c.a. [¹⁸F]fluoride, the best results are typically obtained from acetonitrile as solvent and the Kryptofix©2.2.2/potassium carbonate system. Applied reaction temperatures vary from 80 to 110 °C and depend on the individual precursor molecule. Due to the low boiling point of acetonitrile of 82–84 °C, temperatures higher than 110 °C are not practical. Further suitable solvents are dimethylformamide, dimethylsulfoxide and dimethylacetamide which also allow higher temperatures up to 160–190 °C. In recent studies, Kim et al. found increased radiochemical yields in aliphatic nucleophilic ¹⁸F-labelling by the use of *tert*-alcohols (frequently *tert*-butanol) as co-solvents to acetonitrile. A beneficial effect was shown for a number of clinically important ¹⁸F-labelled PET radiopharmaceuticals [85].

Generally, the aliphatic nucleophilic substitution is high yielding and does not take much longer than 10–15 min for completion. Often a subsequent deprotection step is necessary, but can also be accomplished within short reaction times of 5–10 min. As a result, aliphatic nucleophilic substitution is widely applied in ¹⁸F-labelling chemistry and several routinely produced ¹⁸F-labelled PET radiopharmaceuticals are obtained from this reaction type. Besides [¹⁸F] FDG, the most popular examples are 3-deoxy-3′-[¹⁸F]fluoro-ʟ-thymidine ([¹⁸F]FLT) [86, 87], [¹⁸F]fluoromisonidazole ([¹⁸F]FMISO) [88], O-(2-[¹⁸F]fluoroethyl-ʟ-tyrosine ([¹⁸F]FET) [89, 90], [¹⁸F]florbetaben/−betapir [91], [¹⁸F]flutriciclamide ([¹⁸F]GE180) [92], and [¹⁸F]fluorocholine ([¹⁸F]FCH) [93].

Aromatic substitution: Generally, the "classic" nucleophilic aromatic n.c.a. ¹⁸F-fluorinations

Fig. 7.6 Most commonly used radiosynthesis of n.c.a. [¹⁸F]FDG (RCY = 60–80%) by Hamacher et al. [74]
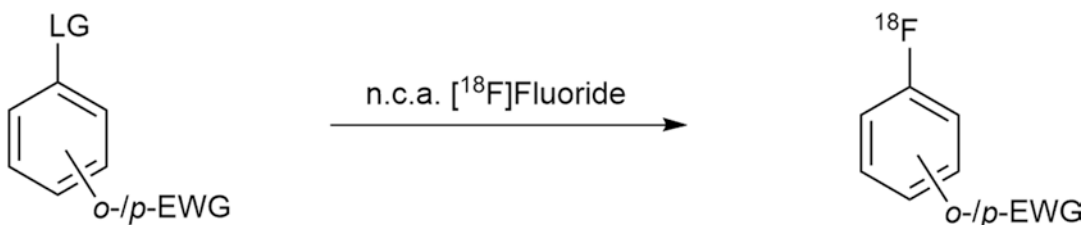
EWG = NO$_2$, CN, COR, CHO, COOR, Br, Cl
LG = NO$_2$, Alky$_3$N$^+$ (OTs$^-$, OTf$^-$,OCl$_4^-$ or I$^-$), Br, Cl, I

Fig. 7.7 Nucleophilic aromatic substitution using n.c.a. [18F]fluoride

N-methyl-[18F]fluorospiperone
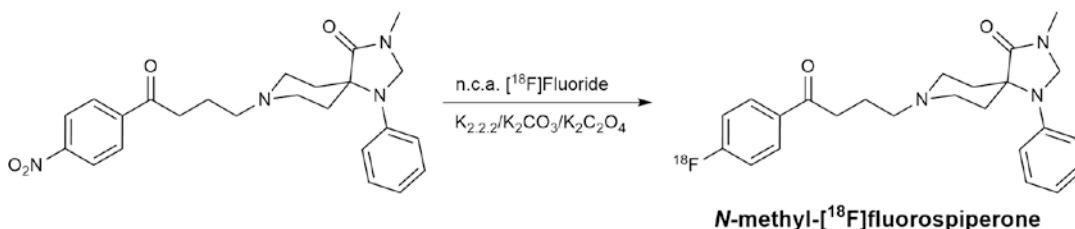
Fig. 7.8 Nucleophilic aromatic 18F-fluorination of n.c.a. N-methyl-[18F]fluorospiperone

require an activated aromatic system, an electron-deficient system. Otherwise, the desired target ring is not attractive for a nucleophilic attack by n.c.a. [18F]fluoride. Such activation can be reached by strong electron-withdrawing groups (EWG) such as nitro, cyano, carbonyl functionalities and halogens in *ortho*- or *para*-position to the substitution (see Fig. 7.7).

Suitable leaving groups (LG) are nitro, halogens and especially trimethylammonium salts as their triflate, tosylate, perchlorate or iodide [35, 36, 38]. Generally, dimethylsulfoxide is the solvent of choice for the nucleophilic aromatic substitution, but also dimethylamide and dimethylacetamide or solvent mixtures have been found beneficial. The nucleophilic aromatic substitution usually requires higher energy than its aliphatic variant, especially in case of the fluoro-for-nitro exchange. Therefore, the dipolar aprotic solvents with higher boiling points are preferred and the use of acetonitrile is rare.

An example of a nucleophilic aromatic substitution is the direct 18F-fluorination of the butyrophenone neuroleptic N-methyl-[18F]

fluorospiperone using the corresponding nitroprecursor which gave an RCY of ~20% (isolated product) after 70 min synthesis time (see Fig. 7.8) [94]. The aromatic system is activated by the electron-withdrawing effect of the *para*-ketone functionality. However, butyrophenones are base sensitive, and the direct 18F-labelling of N-methyl-[18F]fluorospiperone could only be realised with the less basic Kryptofix©2.2.2/potassium carbonate/oxalate buffer system. In the same manner, [18F]haloperidol [94, 95], [18F] altanserin [96, 97] and p-[18F]MPPF (4-[18F]fluoro-N-[2-[1-(2-methoxyphenyl)-1-piperazinyl] ethyl-N-2-pyridinyl-benzamide) [98, 99], have been successfully labelled with n.c.a. [18F]fluoride by the fluoro-for-nitro exchange.

Another possibility for nucleophilic aromatic substitutions is given by electron-deficient heteroaromatic systems such as pyridines which do not need further activating electron-withdrawing groups [100–102]. 18F-fluoroanalogues of epibatidine have been labelled via a nucleophilic (hetero)aromatic substitution in the *ortho*-position of the pyridinyl group (see Fig. 7.9) and gave radio-
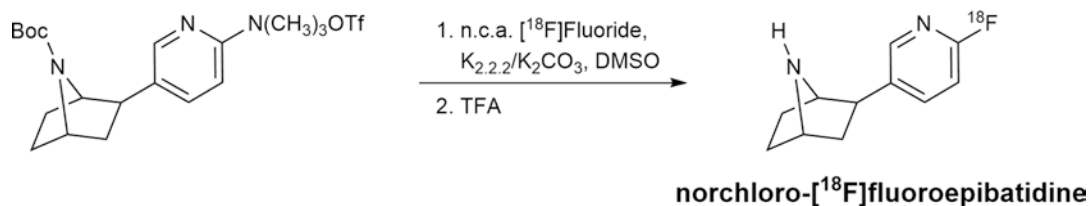
Fig. 7.9 ^{18}F-Fluoroanalogue of epibatidine. ^{18}F-labelling via nucleophilic (hetero)aromatic substitution
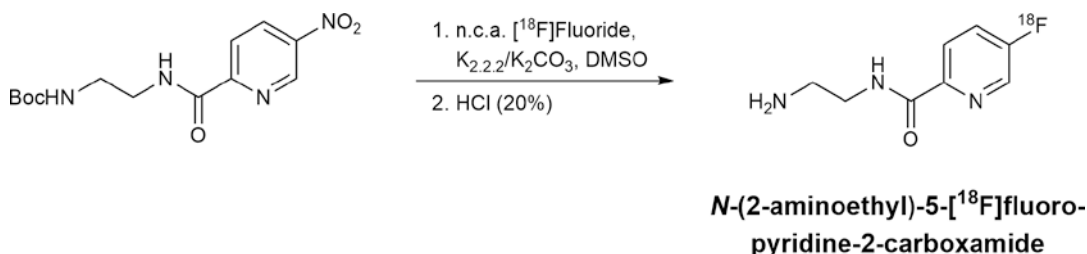
Fig. 7.10 ^{18}F-labelling of N-(2-aminoethyl)-5-[^{18}F]fluoropyridine-2-carboxamide, a MAO-B inhibitor, using nucleophilic (hetero)aromatic substitution in pyridine's *meta*-position

chemical yields of 55–65% using the trimethylammonium triflate leaving group [103–105]. However, the ^{18}F-labelled epibatidines revealed very toxic [104, 106] and further less toxic ^{18}F-labelled ligands for the nicotine acetylcholine receptor system have been developed, again via the nucleophilic (hetero)aromatic substitution on the *ortho*-position of a pyridinyl group [107, 108]. In case of *meta*-substitutions, the activation of the pyridine is normally not efficient enough and additional activating groups are necessary to obtain sufficient ^{18}F-incorporation [101] as shown by the ^{18}F-labelling of a MAO-B inhibitor in the *meta*-position of the pyridinyl moiety using the fluoro-for-nitro exchange (see Fig. 7.10); 10% RCY after 120 min total synthesis time [109].

Using the direct nucleophilic aromatic substitution, several ^{18}F-labelled PET radiopharmaceuticals have been successfully synthesised including [^{18}F]FPSMA-1007 [102], ^{18}F-labelled butyrophenone neuroleptics [94, 95], [^{18}F]altanserin [96, 97], [^{18}F]methylbenperidol [110], *p*-[^{18}F]MPPF [98, 99], [^{18}F]flumazenil [111], ^{18}F-labelled MAO-B inhibitor [109], ^{18}F-labelled epibatidine analogues [103–105] and further ligands for the nicotine acetylcholine receptor system (nAChR) [107, 108].

In general, radiolabelling chemistry benefits from microwave heating which usually dramatically enhances reaction (labelling) kinetics and provides products within minutes and often with higher (radiochemical)yields [112]. However, particularly the aromatic fluoro-for-nitro exchange usually profits from microwave heating and increased radiochemical yields within markedly reduced reaction times can be obtained [96, 113, 114].

If an aromatic system is somehow non-activated or even deactivated (electron-rich) for direct nucleophilic ^{18}F-fluorination, a possible strategy is the introduction of auxiliary activating groups transferring the deactivated arene into an activated system. Such supplementary groups or functions need to be removed or modified after the ^{18}F-labelling which implies a multi-step radiosynthesis. Aldehydes and ketone functions are particularly suitable as activating groups as they can be removed by reductive decarbonylation [115–117]. This method has been applied for the first nucleophilic ^{18}F-labelling approaches towards n.c.a. 6-[^{18}F]F-DOPA which resulted in only 3–5% RCY after a three-step radiosynthesis [118] and towards n.c.a. 2-[^{18}F]fluoroestradiol which could be achieved in 10–24% RCY [119].
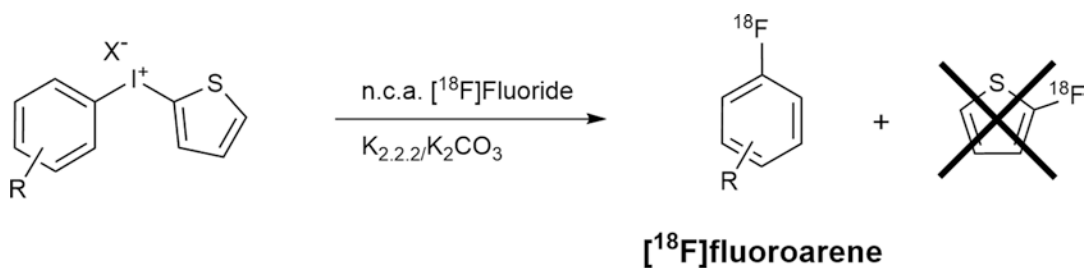
Fig. 7.11 Nucleophilic aromatic ^{18}F-labelling of various arenes including electron-rich systems using aryl(2-thienyl) iodonium salts as precursors
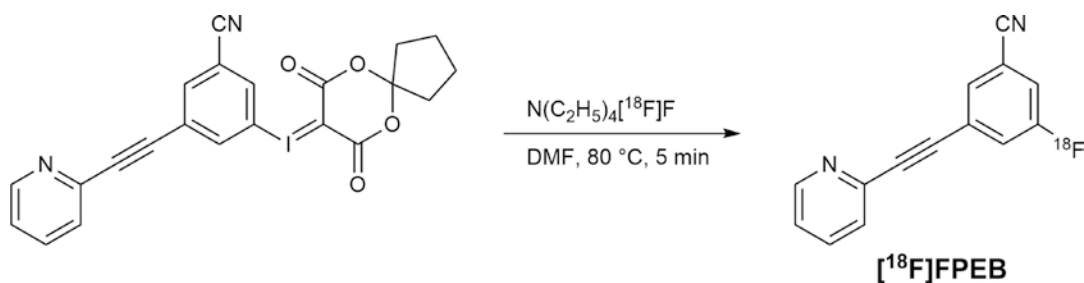
Fig. 7.12 Direct nucleophilic aromatic ^{18}F-labelling of 3-[^{18}F]fluoro-5-[(pyridin-3-yl)ethynyl]benzonitrile ([^{18}F]FPEB) in the deactivated 3-position using the corresponding spirocyclic iodonium ylide precursor

Further developments lead to automation of an approach using an isotopic exchange of ^{18}F-for-[19]F [44].

Another method that allows a direct nucleophilic aromatic ^{18}F-labelling of deactivated systems is the use of diaryliodonium or aryl(heteroaryl)iodonium salts (see Fig. 7.11) [120, 121]. The resulting product distribution after the nucleophilic attack of the n.c.a. [^{18}F] fluoride strongly depends on the electronic and steric character of each aryl ring and its substituents, respectively. Generally, the more electron-deficient ring of the iodonium salt is preferred for the ^{18}F-introduction. Thus, the use of electron-rich heteroaryl systems as one iodonium moiety such as the 2-thienyl group leads to a regioselective ^{18}F-labelling on the counter ring [121]. So far, some attempts of using diaryliodonium salts as precursors for complex structures towards ^{18}F-labelled radiopharmaceuticals have been made, but the ^{18}F-labelling of complex structures

via diaryliodonium salts still remains challenging [119, 122]. First successful examples are the PBR ligand [^{18}F]DAA1106 which was ^{18}F-labelled in radiochemical yields of 46% from a diaryliodonium precursor [123], [^{18}F]flumazenil [124], an ^{18}F-labelled ligand of the synaptic vesicle glycoprotein 2A ([^{18}F]UCB-H) [125] and *meta*-[^{18}F] fluorobenzylguanidine [126].

The challenging synthesis of diaryliodonium salt precursors and their limited shelf-life still give room for improvement. A quite successful optimisation was the use of iodonium ylides as precursors, which let to stable precursors and notable improved radiochemical yields [127–129]. The ^{18}F-labelling of the metabotropic glutamate receptor 5 (mGluR5) ligand 3-[^{18}F] fluoro-5-[(pyridin-3-yl)ethynyl]benzonitrile ([^{18}F]FPEB) was facilitated by the corresponding iodonium ylide precursor with radiochemical yields of 20% (isolated [^{18}F]FPEB) (see Fig. 7.12) and translated into human use [129].
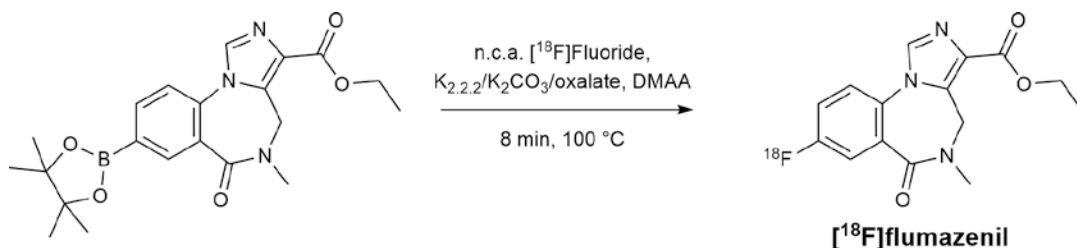
Fig. 7.13 [18F]-labelling of [18F]flumazenil using Cu-mediated nucleophilic substitution of a boron pinacole ester precursor

Recent developments of novel transition-metal catalysts enabled the direct nucleophilic [18F]-fluorination of deactivated systems in high yields and under mild conditions [43]. In first approaches, Pd(IV) complexes were applied to form a Pd-[18F]F complex, which undergo formation of the desired [18F]-labelled (electron-rich) aryl with another corresponding PD(II)-aryl-system [130]. The generated Pd-[18F]F complex revealed sensitive to moisture and the complex procedure with another Pd-aryl system have limited wider application. In a next step, Ni-catalysts were applied and offered direct and fast [18F]-fluorinations, even with aqueous [18F]fluoride [131, 132]. However, the Ni-complexes tend to degrade under high amounts of water or under basic conditions. Nonetheless, some electron-rich aromatic systems were successfully labelled by direct [18F]-fluorination [133] and the $5HT_{2a}$ receptor ligand [18F]MDL100907 was labelled with radiochemical yields of up to 35% in a one-step procedure and evaluated in non-human primates [134].

The real game-changers were introduction of the copper-mediated [18F]-fluorinations using arylboronic acids and boronic pinacol esters as precursors [135, 136] as well as arylstannanes [137]. Applying the Cu-mediated [18F]-fluorination to [18F]flumazenil, good radiochemical yields of 20–30% were obtained from the corresponding boron pinacole ester precursor (see Fig. 7.13) in an automated synthesis [138].

Several other [18F]-labelled PET radiopharmaceuticals have been successfully synthesised via Cu-mediated [18F]-fluorinatons, including [18F]DAA1106, [18F]MFBG, 6-[18F]fluoro-L-*meta*-tyrosine and [18F]fluorodopamine ([18F]FDA)

[139] as well as 6-[18F]F-DOPA [139, 140], [18F]atorvastatin [141], [18F]fluoro-L-tryptophan [142] and [18F]flumazenil [138].

In recent studies, the so-called minimalist approach was combined with iodonium ylide precursors as well as Cu-catalysts to enable high-yielding [18F]-fluorination of various electron-rich systems [143]. But also the combination of mesityl(aryl)iodonium salts and Cu-mediated [18F]-fluorinations turned out very beneficial, allowing efficient production of 4-[18F]fluorophenylalanine and 6-[18F]F-DOPA [144].

7.3.1.3 [18F]-Fluorinations Via Prosthetic Groups

[18F]-labelling via prosthetic groups is based on small molecules which are [18F]-labelled firstly and then introduced into appropriate biomolecules [36, 145–147]. As mentioned before, the direct nucleophilic [18F]-labelling methods which usually provide the [18F]-labelled PET radiopharmaceutical fast and in high RCY are generally inappropriate for multifunctionalised structures such as peptides, oligonucleotides or antibodies introduction. For that reason, small organic molecules are labelled with fluorine-18 using a direct method, and subsequently, they are conjugated to the target structure forming the final [18F]-labelled PET radiopharmaceutical. Principally, both electrophilic and nucleophilic [18F]-labelling are suitable for the [18F]-introduction into prosthetic groups, but due to high specific activities, higher RCY and better availability of n.c.a. [18F]fluoride, the nucleophilic methods clearly outperform the electrophilic procedures.

The prosthetic group: A variety of prosthetic groups have been developed so far, whereas only

prosthetic groups for acylation:
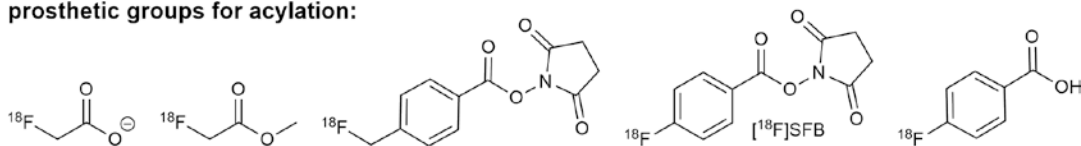
prosthetic groups for amidation: **photochemical conjugation**
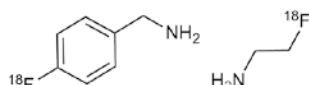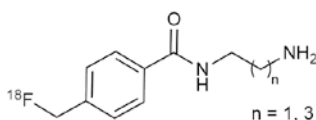
prosthetic groups for...

alkylation   **oxime-formation**   **thiol-coupling**   **imidation**
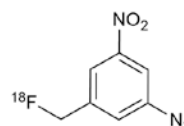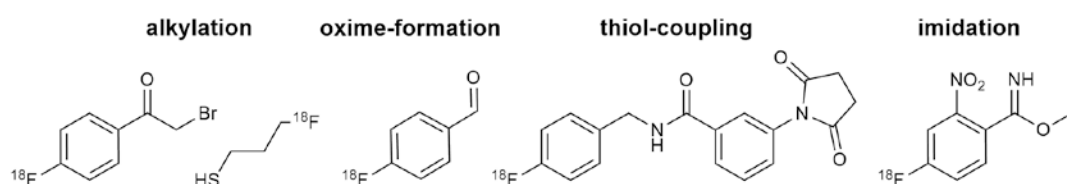
Fig. 7.14 Examples of prosthetic groups and their application in n.c.a. ^{18}F-labelling of biomolecules. References are given in brackets

limited methods for their introduction into biomolecules are available: acylation [148–159], alkylation [160–162], amidation [163–167], imidation [160], thiol-coupling [168, 169], oxime-formation [170, 171] and photochemical conjugation [158, 172] (see Fig. 7.14).

Most of the procedures for the preparation of prosthetic groups are multi-step radiosyntheses and with the final coupling step to bioactive molecules they end as 4–5 step radiosynthesis. Furthermore, the methods for the introduction of certain prosthetic groups require certain functionalities in the target structure and some suffer from low RCY or poor in vivo stability, but prosthetic groups are still indispensable, because of the limitations of direct nucleophilic ^{18}F-labelling.

[^{18}F]SFB: The most commonly applied ^{18}F-labelled prosthetic group is *N*-succinimidyl 4-[^{18}F]fluorobenzoate ([^{18}F]SFB) which cannot be obtained in a single step [153, 154]. Generally, [^{18}F]SFB derives from n.c.a. ^{18}F-labelling of the triflate salt of 4-trimethylammonium-ethylbenzoate yielding 4-[^{18}F]fluorobenzoic acid ([^{18}F]FBA)

after basic hydrolysis; in the next step, [^{18}F]FBA is converted into activated succinimidyl esters using activating agents like *N*-hydroxysuccinimidine/1,3-dicyclohexalcarbodiimide (NHS/DCC) [155], *N,N′*-disuccinimidyl carbonate (DSC) [156] or *O*-(*N*-succinimidyl)-*N*-N,N′,N′-tetramethyluronium tetrafluoroborate (TSTU) [158] to give [^{18}F]SFB. To date, the TSTU-mediated procedure is the fastest and the most convenient method to produce [^{18}F] SFB (see Fig. 7.15) [158]. [^{18}F]SFB can then be coupled to an amino function of the target structure.

Twenty years ago, the Cu(I)-catalysed 1,3-dipolar cycloaddition between alkynes and azides (CuAAC) which is the most prominent representative of the so-called click chemistry [173] has been applied to fluorine-18 chemistry [174–176]. Very mild reaction conditions accompanied by high efficiency, high selectivity and excellent yields make this click reaction particularly suitable for biological applications as well as for the synthesis of PET radiopharmaceuticals.

As an example, the hexapeptide neurotensin(8–13) was successfully n.c.a. ^{18}F-labelled
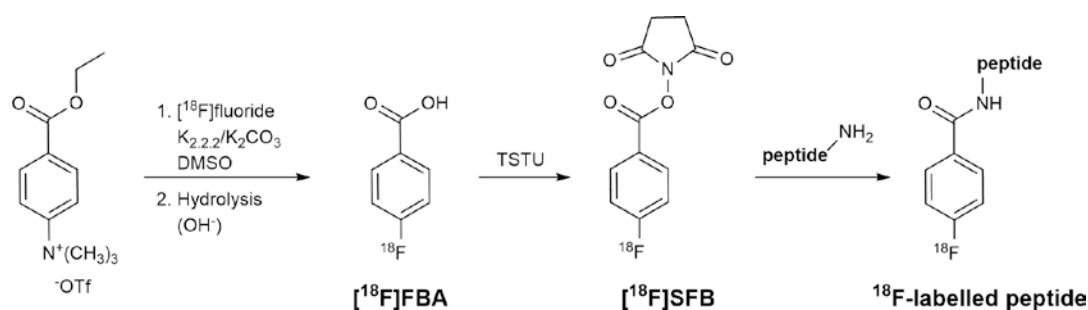
Fig. 7.15 Principle of prosthetic group ^{18}F-labelling of biomolecules using n.c.a. [^{18}F]SFB (TSTU mediated). TSTU: O-(N-succinimidyl)-N-N,N',N'-tetramethyluronium tetrafluoroborate
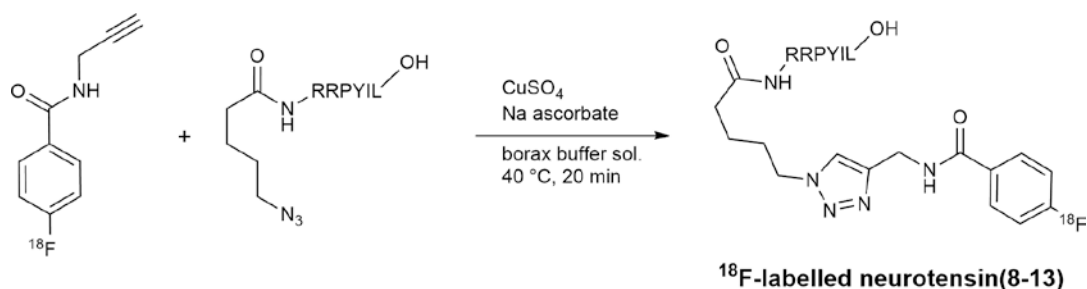
Fig. 7.16 N.c.a. ^{18}F-labelling of neurotensin(8–13) using click chemistry

using the click reaction of the ^{18}F-alkyne n.c.a. 4-[^{18}F]fluoro-N-(prop-2-ynyl)benzamide and the azide-functionalised N$_3$(CH$_2$)$_4$CO-neurotensin(8–13) (see Fig. 7.16) [177]. Under very mild conditions of only 40 °C reaction temperature and in borax buffer solution, radiochemical yields of 66% were achieved within 20 min. ^{18}F-Click chemistry has been further extended to strain-promoted Cu-free azide-alkyne cycloaddition (SPAAC) [178–181]. SPAAC calls for a strained alkyne, which is generally enabled through dibenzocyclooctyne (DBCO) derivatives. However, DBCO is quite lipophilic and tends to affect the pharmacological profile of the target molecule. The ^{18}F-SPAAC approach was applied to a folic acid derivative (see Fig. 7.17) and compared to an ^{18}F-folate derived from ^{18}F-CuAAC, where strong differences in lipophilicity and altered pharmacokinetics were found [182]. Another prominent click-reaction is the inverse electron demand Diels-Alder reaction (IEDDA), where tetrazines (Tz) and commonly *trans*-cyclooctene (TCO) as dienophile react [183]. Generally, the TCO is labelled with ^{18}F

[184, 185]. The major advantage of IEDDA is its extraordinary fast kinetics (10^4–10^5 M^{-1} s^{-1}), which even enables in vivo pre-targeting by IEDDA click [186].

In each individual case, the choice of the prosthetic group, and there with the method of conjugation is depending on the chemical and pharmacological properties of the target structure. Furthermore, the in vivo stability of the prosthetic group and the influence on the pharmacological behaviour of the ^{18}F-labelled compound has to be considered. In terms of the most important requirements for prosthetic group ^{18}F-labelling, to date, the [^{18}F]SFB group seems to be the most suitable prosthetic group. However, the wide scope and the very mild conditions of the ^{18}F-click cycloaddition have added a new and wide flexibility to the ^{18}F-labelling prosthetic groups.

7.3.1.4 Direct ^{18}F-Labelling of Multifunctional Molecules

As mentioned above, the method of choice to introduce the ^{18}F-label into structures like peptides is the use of small ^{18}F-labelled prosthetic
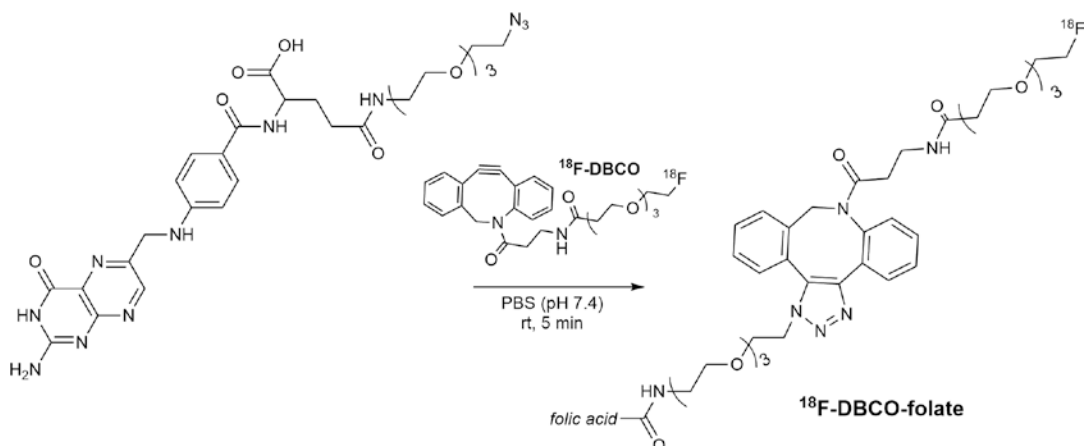
Fig. 7.17 ^{18}F-labelling of a folic acid derivative using ^{18}F-SPAAC click chemistry
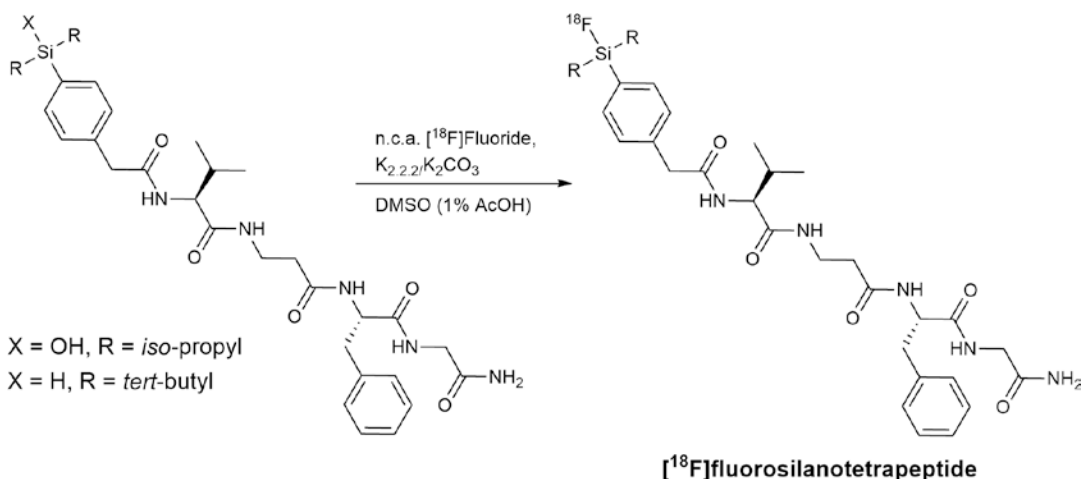
Fig. 7.18 Direct nucleophilic n.c.a. ^{18}F-labelling of a silicon tetrapeptide

groups which are coupled to the biomolecule (see previous paragraph). In the past decade, the first successful approaches of direct nucleophilic ^{18}F-labelling were reported. Peptides can be selectively functionalised with a highly activated aromatic system bearing a trimethylammonium leaving group which enables a direct one-step nucleophilic aromatic n.c.a. ^{18}F-labelling under very mild conditions [187]. Another strategy of direct ^{18}F-labelling is based on organoboron and organosilicon bioconjugates which can be labelled with n.c.a. [^{18}F]fluoride in one-step, even under aqueous conditions, with high RCY [84,

188–190]. In a similar approach, organosilicon building blocks were introduced into a peptide structure and facilitated direct nucleophilic n.c.a. ^{18}F-labelling of peptides in one step under very mild aqueous and even slightly acidic conditions without the need of protection group chemistry (see Fig. 7.18) [83]. Depending on the type of precursor, either 45% RCY or 53% RCY is achieved after 15 min ^{18}F-labelling of the silane precursor or the silanol precursor, respectively. The organosilicon concept has also been applied to develop a hybrid precursor for a PSMA ligand, which is easy and fast to label [191].

7.3.1.5 ^{18}F-Labelled Synthons for Built-up Radiosyntheses

The growing number of complex and multifunctional pharmaceuticals poses a particular challenge to radiolabelling methods. Frequently, the target structure is not suitable for direct ^{18}F-labelling, and only an indirect ^{18}F-labelling method can be applied. Besides the prosthetic group ^{18}F-labelling, the ^{18}F-labelling via built-up radiosynthesis offers another indirect alternative [38, 101, 192]. Both the methods are very similar as they are based on ^{18}F-labelled small organic molecules and indeed the lines between them are often blurred. Generally, the ^{18}F-labelling via built-up radiosyntheses using synthons is used in the direction of small monomeric radiotracers while the prosthetic groups are mostly applied towards ^{18}F-labelling of macromolecular structures such as peptides or antibody fragments. Obviously, the indirect ^{18}F-labelling methods imply multi-step radiosyntheses of minimum two steps.

The Synthons. The built-up radiosynthesis approach is based on small activated organic molecules which are subsequently to the ^{18}F-fluorination used for a built-up synthesis of the final target compound. Such ^{18}F-labelled synthons are generally derivatives of [^{18}F]fluorobenzene or similar ^{18}F-labelled aryls. Regarding the ^{18}F-introduction, they usually bear a leaving group and an activating group. In addition, they need to be functionalised towards further coupling or built-up reactions. Either the activation group is modified or the synthons bear additional substituents which provide further derivatisation and allow coupling reactions. Frequently, the activation group is modified for following coupling or built-up reaction steps.

[^{18}F]Fluorobenzaldehydes give several possibilities for built-up syntheses and represent the most versatile class of synthons. The aldehyde moiety can be easily transferred into other functionalities. Thus, [^{18}F]fluorobenzaldehydes can be reduced to their [^{18}F]fluorobenzamines or –amides and subsequently used in amination reactions towards N-[^{18}F]fluorobenzylamines [193–198]. Recently, the AChE inhibitor 5,7-dihydro-3-[2-[1-(2-[^{18}F]fluorobenzyl)-4-piperidinyl]ethyl]-6H-pyrrolo[3,2,f]-1,2-benzisoxazol-6-one (2-[^{18}F]fluoro-CP-118,954) has been labelled with fluorine-18 via reductive amination using 2-[^{18}F]fluorobenzaldehyde (see Fig. 7.19) [198].

Additional useful derivatives from [^{18}F]fluorobenzaldehydes are the [^{18}F]fluorobenzyl halides which can be used as alkylation agents for amino [199–201] hydroxyl [202] or thiol [201] functions. 2-[^{18}F]fluoro-4,5-dimethoxybenzaldehyde was prepared from its trimethylammonium triflate precursor and used as synthon in a five-step enantioselective radiosynthesis of n.c.a. 6-[^{18}F]fluoro-L-DOPA (see Fig. 7.20) [203, 204]. After reduction of the aldehyde group with sodium borhydride to the benzyl alcohol function, the treatment with the corresponding hydrogen halide leads to the 2-[^{18}F]fluoro-4,5-dimethoxy-benzyl halide. N.c.a. 6-[^{18}F]fluoro-L-DOPA was achieved from an enantioselective coupling with N-(diphenylmethylene)glycine *tert*-butyl ester, deprotection and semi-preparative HPLC in RCY of 25–30% with an enantiomeric excess of >95%.

Besides the conversion reactions of the aldehyde group, [^{18}F]fluorobenzaldehydes can also
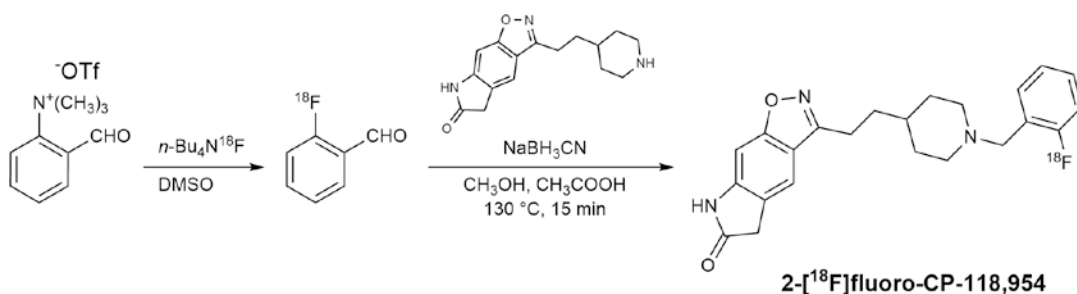
Fig. 7.19 Reductive amination with 2-[^{18}F]fluorobenzaldehyde forming the AChE inhibitor 2-[^{18}F]fluoro-CP-118,954
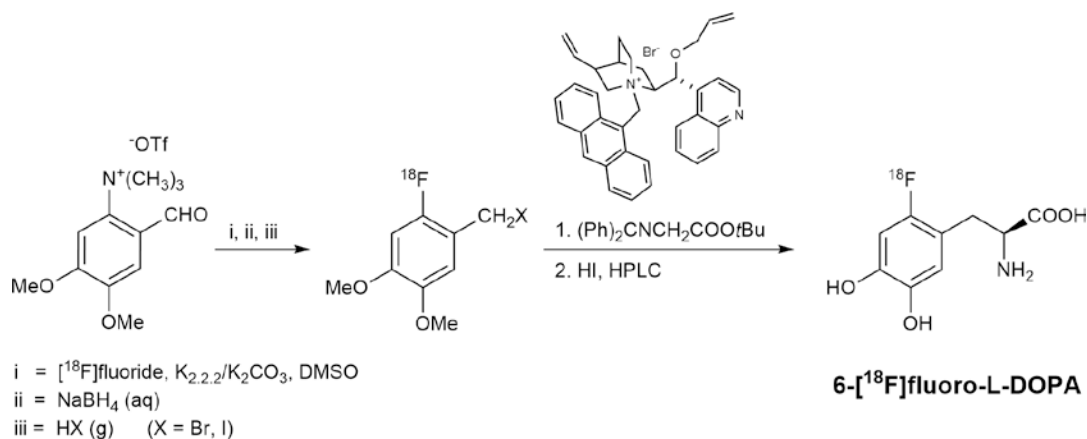
Fig. 7.20 2-[18F]fluoro-4,5-dimethoxybenzyl halides as synthons for n.c.a. radiosynthesis of 6-[18F]fluoro-ʟ-DOPA
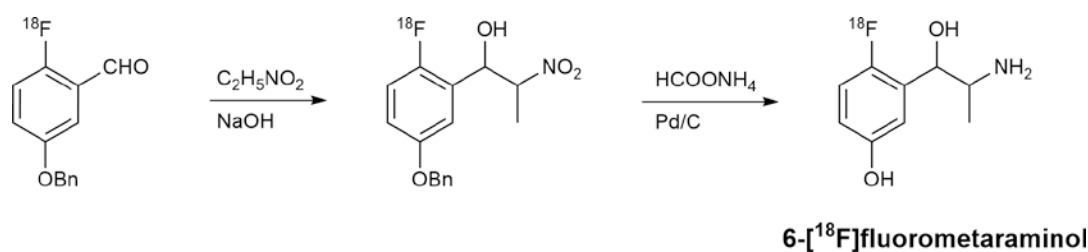
Fig. 7.21 N.c.a. radiosynthesis of 6-[18F]fluorometaraminol via nucleophilic addition of nitroethane to 3-benzyloxy-6-[18F]fluorobenzaldehyde

function as direct reaction partner according to organic carbonyl chemistry. Prominent representatives of such chemistry which have also been applied to 18F-radiochemistry are the Wittig reaction [205] the Horner–Wadsworth–Emmons reaction [206] and the Knoevenagel condensation [207].

In addition, the electrophilic character of aldehydes also offers the possibility of nucleophilic additions. [18F]Fluorobenzaldehydes have also been applied in nucleophilic additions [208, 209]. In this way, the nucleophilic addition of nitroethane to n.c.a 3-benzyloxy-6-[18F]fluorobenzaldehyde and following reductive deprotection led to n.c.a. 6-[18F]fluorometaraminol in a diastereomeric mixture from which the stereoisomers could be separately isolated by two subsequent semi-preparative HPLC purifications (see Fig. 7.21) [209]. In the same manner, also the n.c.a 4-[18F]fluorometaraminol was synthesised.

Similar to the carbonyl chemistry of [18F]fluorobenzaldehydes, [18F]fluoroacetophenones offer a broad range of synthetic possibilities [210, 211]. Moreover, secondary derived synthon/prosthetic group 4-[18F]fluorophenacylbromide can be conjugated to peptides and proteins via alkylation reaction or thiol-coupling reactions [160, 169].

Another group of versatile synthons derives from the [18F]fluoro-4-haloarenes which can be used in palladium(0)-catalysed C-C-bond formation reactions such as the Stille reaction [212–216], the Sonogashira reaction [217] and Suzuki cross-coupling reactions [218] (see Fig. 7.22). Furthermore, 4-bromo and 4-iodo-[18F]fluorobenzenes have been used in palladium-mediated *N*-arylation reactions, also referred to as Hartwig–Buchwald reactions [219, 220]. In addition, n.c.a. [18F]fluoro-4-haloarenes can also be easily transferred into reactive species such as
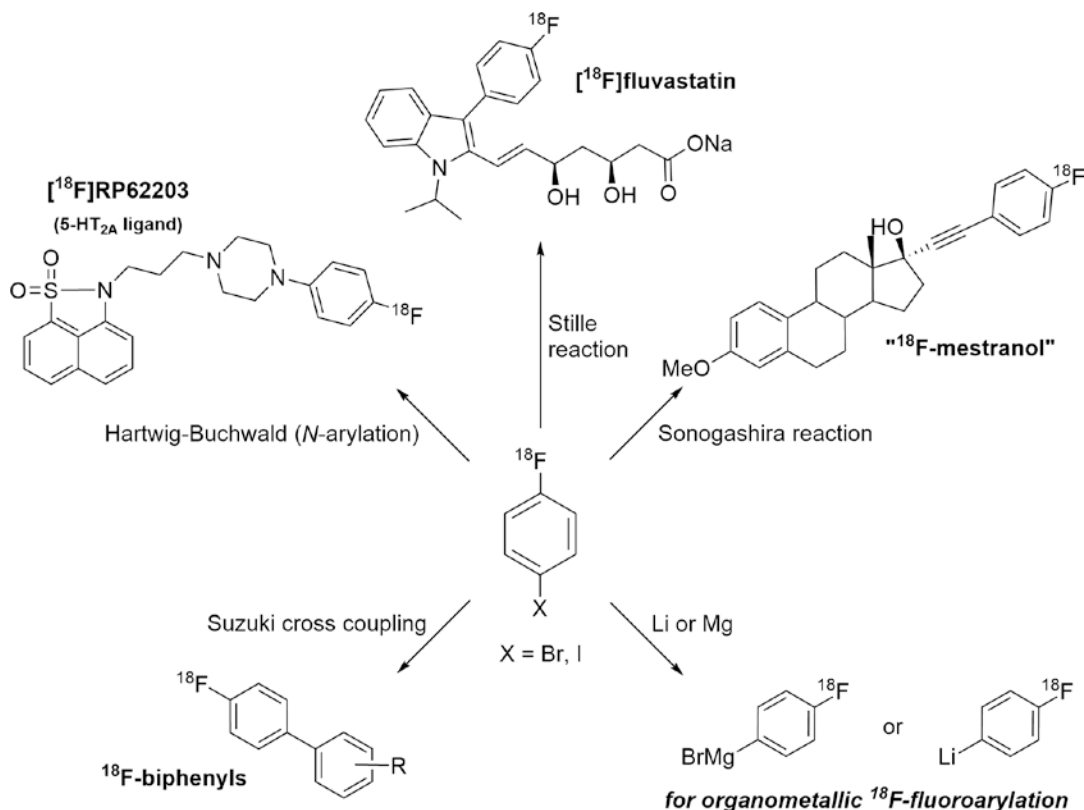
Fig. 7.22 N.c.a. 4-[¹⁸F]fluorohalobenzenes as versatile synthons for palladium(0)-catalysed coupling reactions and their transformation into metalorganic reagents for ¹⁸F-fluoroarylation reaction

Grignard reagents or into 4-[¹⁸F]fluorophenyl lithium which can be employed in various metalorganic coupling reactions [221].

Due to their broad applicability, [¹⁸F]fluorohalobenzenes and their secondary derived ¹⁸F-labelling synthons have become more and more attractive. In the past decade, several methods for an efficient preparation of [¹⁸F]fluorohaloarenes have been developed and make this class of ¹⁸F-labelled synthons readily available [121, 212, 222–225].

In addition to the most widely used ¹⁸F-labelling synthons [¹⁸F]fluorobenzaldehydes, [¹⁸F]fluorobenzyl halides and [¹⁸F]fluorohalobenzenes, further primary and secondary ¹⁸F-aryls have been developed and proven to be useful for ¹⁸F-labelling via built-up radiosynthesis. Accordingly, n.c.a. 4-cyano-1-[¹⁸F] fluorobenzene or 4-[¹⁸F]fluorobenzonitrile was employed for built-up radiosyntheses of several

¹⁸F-butyrophenone neuroleptics [226]. On the other hand, it can also be transferred into the secondary ¹⁸F-labelling synthon n.c.a. 4-[¹⁸F] fluorobenzyl amine which can be used as prosthetic group [165, 167] or further converted into N-4-[¹⁸F]fluorobenzyl-α-bromoacetamide as prosthetic group for the ¹⁸F-labelling of oligonucleotides [164]. More in a sense of a prosthetic group, n.c.a. 4-[¹⁸F]fluorobenzyl amine was used for the ¹⁸F-labelling of the first ¹⁸F-labelled folic acid derivatives [167].

N.c.a. [¹⁸F]fluoronitrobenzenes which are available from high-yielding ¹⁸F-labelling of the appropriate dinitrobenzene precursors can be easily reduced to the corresponding [¹⁸F]fluoroanilines by the use of common reducing agents such as $NaBH_4$, $SnCl_2$, N_2H_2/Pd, H_2/Pd-C, BH_3 or $LiAlH_4$ [227–229]. N.c.a. [¹⁸F]fluoroanilines have been employed for the ¹⁸F-labelling of several anilinoquinazolines as epidermal growth
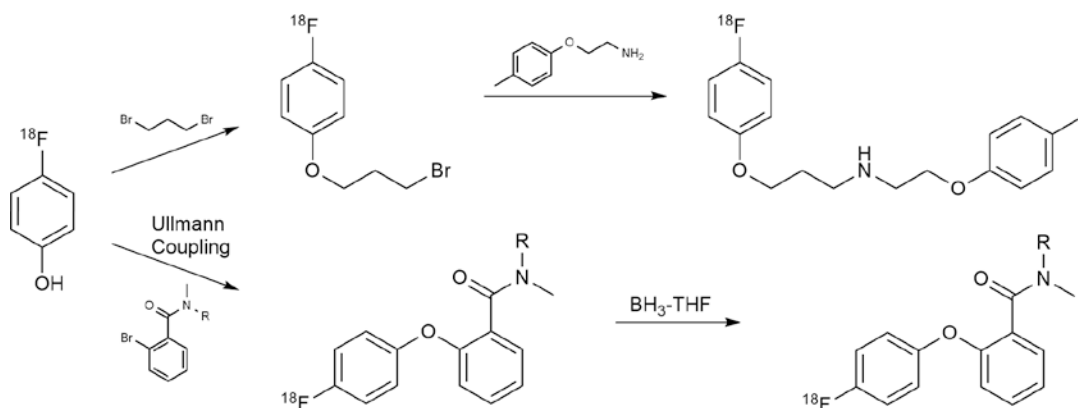
Fig. 7.23 N.c.a. 4-[^{18}F]fluorophenol as versatile synthon in built-up radiosyntheses

factor receptor (EGFR) ligands [228, 230, 231] as well as for fluorophenyl ureas [228]. A subsequent treatment of the 4-[^{18}F]fluoroaniline with nitrites leads to the 4-[^{18}F]fluorophenyldiazonium derivative which was used for the preparation of ^{18}F-labelled 5-HT$_2$ receptor ligands [227].

Since various biological active compounds bear a 4-fluorophenoxy moiety [232], the secondary synthon n.c.a. 4-[^{18}F]fluorophenol is of great interest. The first radiosynthesis of this versatile synthon was based on a hydrolysis of the 4-[^{18}F]fluorophenyldiazonium salt [233]. In recent years, new synthetic strategies towards 4-[^{18}F]fluorophenol and several improvements of the radiosyntheses have made 4-[^{18}F]fluorophenol readily available for built-up radiosyntheses [234, 235]. Thus, it was applied for the radiosynthesis of a highly selective dopamine D$_4$ receptor ligand [236] as well as in a catalysed variant of the Ullmann ether coupling to provide 2-(4-[^{18}F]fluorophenoxy)-benzylamines (see Fig. 7.23) [235].

Finding the right ^{18}F-labelling strategies for new radiopharmaceuticals is generally directed by the target structures themselves. Although a variety of ^{18}F-fluorination methods have been developed, many of them still do not provide the desirable broad applicability and call for specific conditions or molecular requirements. Thus, there is still room for improvement and new development of ^{18}F-labelling methods. However, many ^{18}F-labelled PET radiopharmaceuticals from various classes of compounds have been prepared, and many are routinely produced and employed in nuclear medicine practice.

7.3.2 Labelling Methods for Carbon-11

Carbon-11 is still one of the most commonly used organic positron emitters for PET radiopharmaceuticals. Although the short half-life of only 20.4 min of carbon-11 does not allow time-consuming radiosyntheses or the shipment of produced ^{11}C-labelled radiopharmaceuticals, several important ^{11}C-radiopharmaceuticals are routinely employed in the clinics.

Similar to the requirements for fluorine-18 productions, the production of carbon-11 can be facilitated with small medical cyclotrons using protons in an energy range of 15 → 7 MeV. As a general production method, the ^{14}N(p,α)^{11}C nuclear reaction is applied [237]. The reaction is carried out with ^{14}N-gas targets. Small portions of oxygen (≤ 2%) added to the target gas cause [^{11}C]CO$_2$ formation and in case of hydrogen (5–10%) addition, [^{11}C]CH$_4$ is the final product form [238, 239].

Several further production routes are known for carbon-11, but generally they are of much less importance than the ^{14}N(p,α)^{11}C reaction [22, 39, 240, 241]. Furthermore, using the ^{14}N(p,α)^{11}C nuclear reaction of carbon-11 can be obtained in high radiochemical yields with high specific/molar activities.
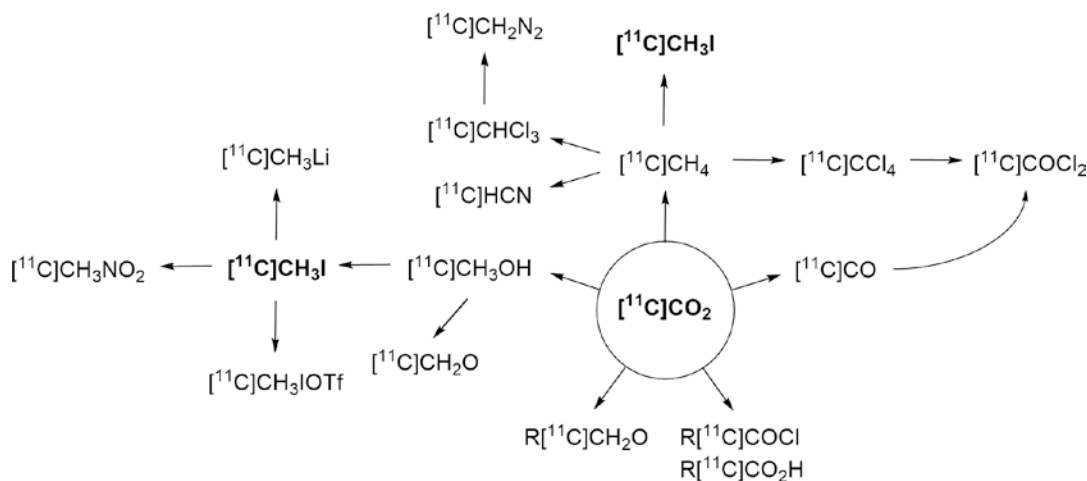
Fig. 7.24 Secondary and further ^{11}C-labelling synthons derived from the primary [^{11}C]CO$_2$
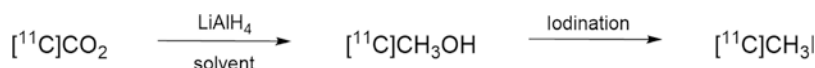
Fig. 7.25 Radiosynthesis of [^{11}C]CH$_3$I according to the 'wet' method starting from primary [^{11}C]CO$_2$

[11]C precursors: Regarding the two product forms and thus the two primary ^{11}C-labelling synthons [^{11}C]CH$_4$ and [^{11}C]CO$_2$, the latter is the most preferred labelling precursor. [^{11}C]carbon dioxide offers the possibility of direct ^{11}C-introductions into organic molecules. Accordingly, [^{11}C]CO$_2$ reacts with primary amino functions to form [^{11}C] ureas and [^{11}C]isocyanates [242]. Another direct ^{11}C-labelling possibility is given by the reaction with organometallic systems. Thus, the treatment of the Grignard reagents CH$_3$MgBr or CH$_3$MGCl with [^{11}C]CO$_2$ gives [1-^{11}C]acetate which is the most important ^{11}C-labelled radiopharmaceutical derived from direct ^{11}C-carboxylation [243, 244].

Even though the half-life of 20.4 min of carbon-11 allows only reactions and conversions with fast kinetics, most ^{11}C-labelling methods are based on secondary ^{11}C-labelling synthons derived from [^{11}C]CO$_2$ (see Fig. 7.24) [36, 245]. Along with all the possible pathways, the ones using [^{11}C] CH$_3$I are the preferred routes for ^{11}C-labelling. However, [^{11}C]HCN and [^{11}C]CO are also important ^{11}C-labelling synthons. Especially [^{11}C]CO has been proven its applicability in palladium- or selenium-catalysed reactions [245, 246].

'Wet Method': The first efficient radiosynthesis for [^{11}C]CH$_3$I was developed by Comar et al. in 1973 [247, 248]. This so-called wet method is based on the reduction of [^{11}C]CO$_2$ to [^{11}C] CH$_3$OH by means of lithium aluminium hydride (LiAlH$_4$) in solvents such as ethyleneglycol dimethylether, tetrahydrofuran or diethylether. [^{11}C]CH$_3$OH is then iodinated using hydroiodic acid or triphenylphosphite ethyliodide (see Fig. 7.25). As iodination agents, also diphosphorous tetraiodide [249] and triphenylphosphine diiodide [250] can be employed. Although the 'wet' method provides reliable and high radiochemical yields, it has one major drawback: the use of LiAlH$_4$. LiAlH$_4$ is a source of non-radioactive carbon dioxide which in turn brings in isotopic carrier carbon-12 and thus dramatically reduces the molar radioactivity of the [^{11}C]CH$_3$I and the following products.

Dry method: More recently, a new approach to [^{11}C]CH$_3$I, the so-called gas phase or dry method was developed [251, 252]. Starting from [^{11}C] CO$_2$, hydrogen reduction in the presence of a nickel catalyst provides [^{11}C]CH$_4$ which is passed through a heated glass tube (~720 °C) with iodine
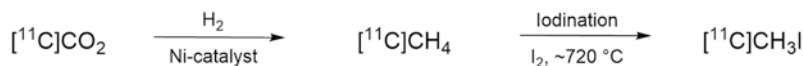
Fig. 7.26 Radiosynthesis of [^{11}C]CH$_3$I according to the 'dry' method starting from primary [^{11}C]CO$_2$

vapour for iodination (see Fig. 7.26). The product [^{11}C]CH$_3$I is trapped on a Porapak© column, and after completion of the iodination, [^{11}C]CH$_3$I is released by heating and a stream of helium. The iodination process can be performed in a single pass reaction where the [^{11}C]CH$_4$ slowly passes the heated glass tube for iodination only once [253] or in a circulation process where [^{11}C]CH$_4$ is circularly pumped though the iodination system until complete iodination [254].

Alternatively, the [^{11}C]CH$_4$ can be produced in situ in the target and used directly for the iodination process. This variant saves one reaction step and thus time. Furthermore, the in situ production of [^{11}C]CH$_4$ in the target generally provides higher molar radioactivity. To date, the highest reported specific radioactivity of [^{11}C] CH$_3$I was 4700 GBq/μmol and was obtained from the iodination of in situ produced [^{11}C]CH$_4$ in a single-pass reaction [255, 256]. Due to that fact and an easier automation of the process, and a more convenient ongoing maintenance of the synthesis system, the 'dry' method almost superseded the 'wet' alternative for [^{11}C]CH$_3$I productions. Particularly, when high molar radioactivity is required as for PET studies of receptor systems in the CNS, the 'dry' process is the method of choice for the [^{11}C]CH$_3$I production.

In some cases, [^{11}C]CH$_3$I is not reactive enough for sufficient ^{11}C-methylation, and a more reactive ^{11}C-methylation agent is needed [257]. Hence, [^{11}C]CH$_3$I can be converted to the more reactive [^{11}C]CH$_3$OTf by means of silver triflate at elevated temperatures. The ^{11}C-methylation with [^{11}C]CH$_3$OTf generally offers higher RCY in reduced reaction times and at lower temperatures in comparison to the [^{11}C]CH$_3$I methylation as it has already been demonstrated for several important ^{11}C-labelled PET radiopharmaceuticals [258–261].

Generally, ^{11}C-labelling via methylation is performed as N-, O- or S-heteroatom ^{11}C-methylation using the desmethyl precursors. Accordingly, the routinely used ^{11}C-labelled PET radiopharmaceuticals [^{11}C]PIB (Pittsburgh compound-B) [262], [N-methyl-^{11}C]flumazenil [255, 263, 264], [^{11}C]N-methylspiperone ([^{11}C]NMSP) [265], [O-methyl-^{11}C]raclopride [258, 266, 267] or L-[S-methyl-^{11}C]methionine [248, 268] are prepared via N-, O- or S-^{11}C-methylation, respectively (see Fig. 7.27).

Heteroatom ^{11}C-methylation reactions are usually carried out in solvents such as dimethylformamide, dimethylsulfoxide or acetonitrile. [^{11}C]CH$_3$I is transferred into the solution which contains the desmethyl precursor and mostly a base such as sodium hydroxide, sodium hydride, potassium carbonate or tetrabutylammonium hydroxide. ^{11}C-Methylations are normally completed within 10 min under elevated temperatures.

Solid phase: Over the years, the basic reaction conditions have not been changed so much, but several interesting and innovative technical improvements have been developed. As a consequence, most of the radiosyntheses of the routinely employed ^{11}C-labelled PET radiopharmaceuticals can be performed on solid-phase. As resin or solid phase material, commercially available C-18 solid-phase extraction (SPE) cartridges can be applied. The cartridges are loaded with precursor, base and small amounts of solvent, and the ^{11}C-methylation agent is passed through the cartridge by a gentle stream of nitrogen or helium. The reactions are normally efficient at ambient temperature and completed after short reaction times. The ^{11}C-labelled product is eluted from the cartridge with an appropriate solvent, and often, it is directly eluted into a loop of the HPLC system for the subsequent purification. For example, the 5-HT$_{1A}$ antagonist [^{11}C]WAY 100635 have been prepared and quickly isolated in good yields of ~40% (related to [^{11}C]CH$_3$I, not decay corrected) [269]. Several important ^{11}C-labelled PET radiopharmaceuticals have also
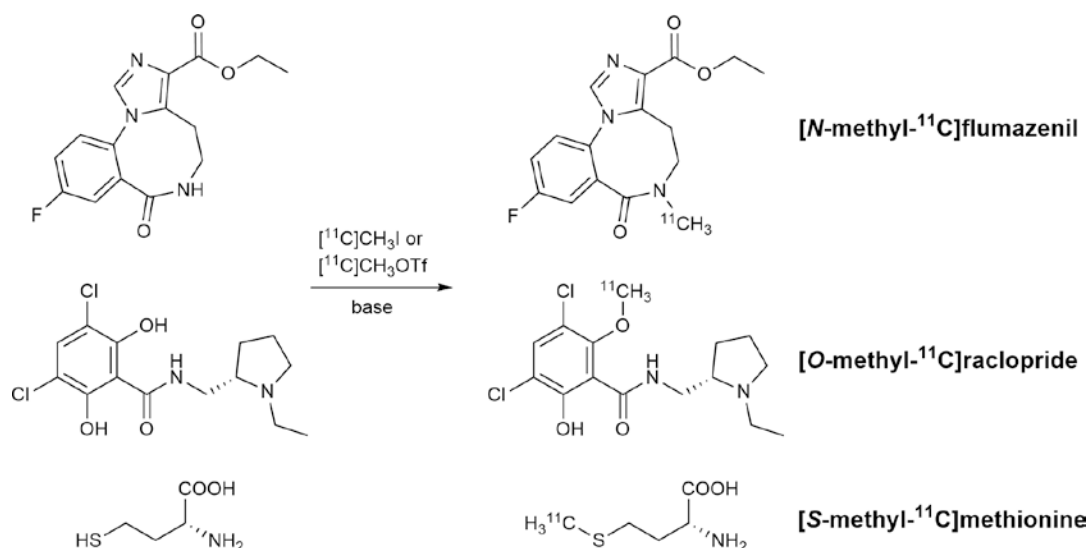
Fig. 7.27 N-, O- and S-heteroatom ^{11}C-methylation reactions based on [^{11}C]CH[3]I and/or [^{11}C]CH[3]OTf

shown applicability for solid-phase supported radiosynthesis [269, 270–272].

Loop method: A further development of the solid-phase supported radiosyntheses is the so-called loop method. A conventional HPLC loop is coated with a film of the precursor solution, and the ^{11}C-methylation agent is passed through by a gentle stream of nitrogen or helium. Subsequently, the loop content is washed out and simultaneously injected into the HPLC system. The method saves the reaction time and reduces the technical assembly to a bare minimum. A variety of ^{11}C-labelled radiopharmaceuticals can be prepared by this convenient and fast method [273–277].

Another technical advancement which has recently entered the PET radiochemistry field is the microfluidic radiosyntheses systems. The systems are based on continuous-flow microreactors and use only micro- or nanolitre volumes. Some systems have been developed so far and have been already successfully applied for ^{11}C-labelling of several carboxylic acid esters [278].

[11]C-C bond reactions: [^{11}C]CH[3]I can also be applied in ^{11}C-C bond formation reactions. Due to the short half-life, the most limiting factor is the reaction/synthesis time of such ^{11}C-C bond formations. Nonetheless, there are several examples of C-C bond formations applied in

[11]C-labelling using [^{11}C]CH[3]I. Some examples can be found for the use of [^{11}C]CH[3]I in Wittig reactions as its corresponding triphenylphosphorane [^{11}C]CH[2]PPh[3] [279] or triphenylarsonium [^{11}C]CH[2]ArPh[3] [280]. Most examples of various ^{11}C-C bond formation reactions can be found for ^{11}C-labelled amino acids using methods like enzymatic ^{11}C-C bond formations [281, 282] or enantioselective ^{11}C-C bond formations based on Schiff-base Ni-complexes as chiral auxiliaries [283, 284]. Furthermore, such multi-step radiosyntheses of ^{11}C-C bond formations towards ^{11}C-labelled amino acids have been shown to be transferable into automated synthesis systems [285]. However, besides amino acids also several other pharmacological relevant substances have been ^{11}C-labelled by C-C bond formations [286–291].

Other approaches for ^{11}C-C bond formations are palladium-supported cross-coupling reactions which have been developed for various ^{11}C-labelled radiopharmaceuticals [36, 245]. The most prominent representatives of these reaction types are the Stille reaction [292–295], the Suzuki cross coupling reaction [292, 294, 295] and the Sonogashira reaction [296, 297]. The Stille reaction is the most intensively employed variant of palladium-catalysed ^{11}C-C bond formations (see Fig. 7.28) and has proven its applicability for

Fig. 7.28 Radiosynthesis of the serotonin transporter ligand 5-[^{11}C]methyl-6-nitroquipazine ([^{11}C]MNQP) using [^{11}C]CH$_3$I in a palladium-catalysed Stille reaction

many ^{11}C-labelled PET radiopharmaceuticals [292–295, 298–302].

Most ^{11}C-labelling procedures are clearly based on [^{11}C]CH$_3$I as the most versatile ^{11}C-labelling synthon or precursor. The most convenient methods are the very fast N-, O- and S-heteroatom ^{11}C-methylation reactions which can be accomplished even with simple technical equipment such as a conventional HPLC loop in case of a [^{11}C]CH$_3$I loop reaction [36]. Furthermore, also multi-step radiosyntheses like ^{11}C-C bond formations have been proven as useful ^{11}C-labelling strategy. Particularly, the palladium-promoted ^{11}C-C bond formations have broadened the applicability of ^{11}C-labelling towards PET radiopharmaceuticals.

7.3.3   Fast Reactions for Oxygen-15 and Nitrogen-13

The half-lives 2 min and 10 min of the extremely short-lived positron emitter oxygen-15 and nitrogen-13, respectively, allow only very fast conversions without time-consuming labelling procedures. Moreover, in PET imaging using ^{15}O- or ^{13}N-labelled radiopharmaceuticals, only simple physiological processes with very fast kinetics such as perfusion or blood flow can be studied.

The extremely short half-life of oxygen-15 only allows very fast online reactions in terms of radiochemistry. A number of nuclear reactions exist for the production of oxygen-15, but the most commonly used method is the ^{14}N(d,n)^{15}O nuclear reaction [303]. The target material is aluminium, and the target content is a mixture of nitrogen and 0.2–1.0% of oxygen. An example for such an online reaction is the preparation of the perfusion tracer [^{15}O]water. The target release is mixed with hydrogen and passed over a palladium/activated charcoal catalyst at 200 °C to give [^{15}O]water [304, 305]. Another ^{15}O-labelled perfusion and blood flow tracer is n-[^{15}O]butanol [306]. In this case, a solid phase-supported (cartridge extraction) reaction of tri-n-butylborane and the target released c.a. [^{15}O]O$_2$ furnishes the n-[^{15}O]butanol. The radiosyntheses of ^{15}O-labelled PET radiopharmaceuticals are restricted to such fast online processes, and the application of ^{15}O-tracers in PET imaging is limited to perfusion or blood flow studies.

The general production route to nitrogen-13 is the ^{16}O(p,α)^{13}N nuclear reaction [307]. The nitrogen-13 is obtained in the form of ^{13}N-labelled nitrites and nitrates, which are subsequently reduced to [^{13}N]ammonia by titanium(III)chloride or Devarda's alloy in alkaline medium [308]. Another method uses additional ethanol in the target gas as radical scavenger to avoid nitrite and nitrate formation [309]. This method leads directly to [^{13}N]ammonia.

[^{13}N]ammonia is a perfusion tracer and the most commonly used ^{13}N-labelled PET radiopharmaceutical in PET imaging. In addition to the direct clinical applications of [^{13}N]NH$_3$, there are a few examples of ^{13}N-labelled compounds which derive from [^{13}N]NH$_3$, but generally without clinical relevance. The L-[^{13}N]amino acids, L-[^{13}N]LEU, L-[^{13}N]VAL and L-[^{13}N]GLU, were ^{13}N-labelled via an enzyme-supported amino acid synthesis and used for investigations of their pharmacokinetics in the myocardium [310]. Recently,

the ^{13}N-labelling of azo compounds were developed based on [^{13}N]NO$_3$ to enable imaging of β-amyloid plaques [311]. [^{13}N]NO$_3$ was reacted with primary aromatic amines and provides the desired azo compounds in good radiochemical yields of 20–50%. The novel ^{13}N-labelled azo compounds were evaluated in an Alzheimer's disease model [312]. The half-life of 10 min of nitrogen-13 offers a little bit more flexibility than oxygen-15 does, but its half-life remains still highly challenging for extensive radiosyntheses.

7.3.4 Chelating Chemistry for Gallium-68

In the last decades, gallium-68 has emerged to one of the most important radionuclides for PET radiopharmaceuticals due to its favourable nuclear characteristics. The prominent examples of clinically used ^{68}Ga-radiopharmaceuticals such as [^{68}Ga]HBED-PSMA (PSMA-11) [313] and [^{68}Ga]DOTA-TOC or -TATE [314] have mainly contributed to this success. Especially, the corresponding *theranostic* approaches have accelerated their applications [315]. Very recently, novel ^{68}Ga-radiopharmaceuticals targeting the fibroblast activation protein (FAP) have been devel-

oped and drawn further attention as (theranostic) ^{68}Ga-radiopharmaceuticals [316, 317].

Gallium-68 ($T_{½}$ = 67.7 min) is conveniently available from the ^{68}Ge/^{68}Ga generators [318, 319]. The generator is typically made up of a matrix of Sn(IV), Ti(IV), Ta(IV) and Zr(IV) oxides in a small glass column. The ^{68}Ga is eluted from the column with 0.05 M to 0.6 M HCl (depending on the generator type). Recently, cyclotron-produced gallium-68 became available for the production of radiopharmaceuticals. The nuclear reaction used is ^{68}Zn(p,n)^{68}Ga, on either solid targets [320–322] or liquid targets [323, 324].

In terms of radiochemistry, labelling with ^{68}Ga is based on chelatoring systems which are coupled to biomolecules or which have interesting biological properties themselves [325]. Prominent examples of chelating systems for gallium-68 are DOTA (1,4,7,10-tetraazacyclododecane-*N,N′,N″,N‴*-tetraacetic acid), NOTA (1,4,7-triazacyclononane-*N,N′,N″*-triacetic acid), HBED-CC (*N,N′*-bis[2-hydroxy-5-(carboxyethyl)benzyl]ethylenediamine-N,N′-diacetic acid) [326], TRAP (triazacyclononane phosphinate) [327], DATA (6-amino-1,4-diazepine-triacetic acid) [328, 329] and THP (tris(hydroxypyridinone)) [330] (see Fig. 7.29). The DOTA chelator is still the chelating system of choice for theranostic approaches as
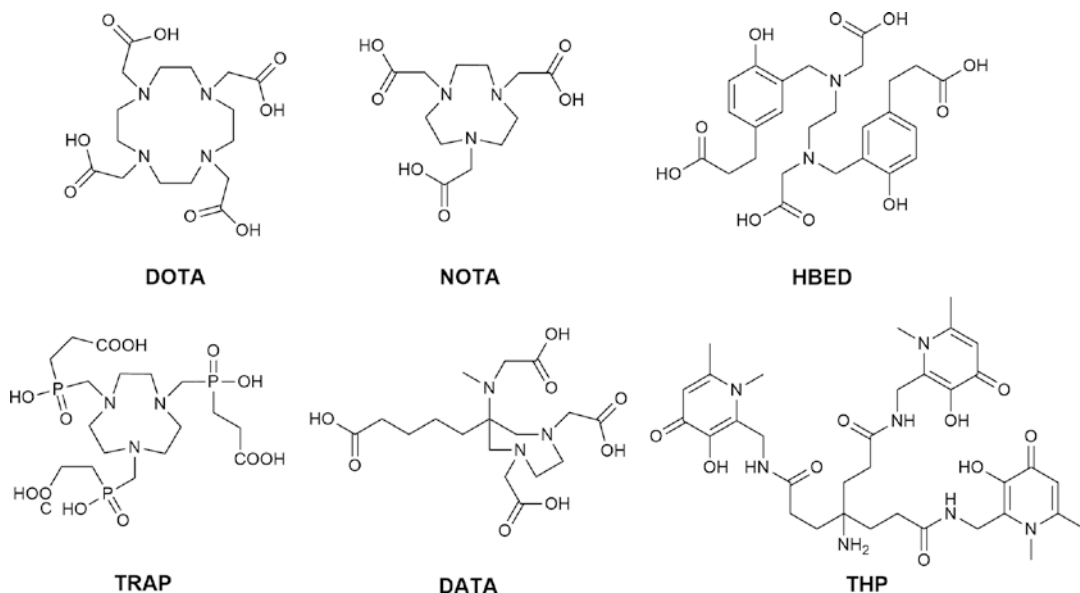
Fig. 7.29 Prominent chelating systems for gallium-68

it allows stable complexation of almost all clinically used radiometals. Chelating systems such as HBED-CC, TRAP, DATA and THP have been specialised for optimal chelating of gallium(III). As a result, they allow highly efficient radiolabelling of ^{68}Ga under very mild conditions and enable the development of kit-radiolabelling.

However, the importance and clinical need have even enabled a DOTA-based kit with market authorisation available for [^{68}Ga]DOTA-TOC (SomaKit TOC®, AAA/Novartis) [331]. As DOTA does not facilitate ^{68}Ga-labelling at room temperature nor at higher pH values, a heating step and additional buffering is required. The more Ga-specific kit preparations of [^{68}Ga]HBED-PSMA [332], [^{68}Ga]THP-PSMA [333, 334] or [^{68}Ga]Ga-DATA-TOC [335] offer rapid labelling kinetics at room temperature. All three kit preparations have already been translated and shown their clinical potential in patients.

7.3.5 Non-standard Positron Emitters

7.3.5.1 Labelling Using Radioiodine
From more than 30 radioactive isotopes of iodine, only iodine-120 and iodine-124 have suitable properties for use as PET radionuclides. However, the low abundance of positron emission (56% for ^{120}I and 22% for ^{124}I), their high positron energies (4.1 MeV for ^{120}I and 2.1 MeV for ^{124}I) and an extensive production route make them less attractive for routine PET imaging. Significantly more importance for nuclear medicine and general life science have iodine-123 (100% EC, 159 keV γ-line (main)) as SPECT nuclide, iodine-125 (100% EC, 35 keV γ-line (main)) for long-term in vitro studies and radioimmunoassays and the β$^-$-emitter iodine-131 as nuclide in radiotherapy of thyroid gland and tumours. Because of the convenient longer half-life ($T_{1/2}$ = 8.02 d), the well-detectable γ-line of 364 keV (85.5%) and the good availability, ^{131}I lends itself as model isotope for radiotracer development.

The main pathways for radioiodine labelling can be classified in four general procedures [14, 336, 337]:

- Direct electrophilic radioiodination.
- Electrophilic demetallation.
- Non-isotopic exchange (nucleophilic labelling).
- Prosthetic group labelling (indirect method).

7.3.5.2 Direct Electrophilic Radioiodination
The direct electrophilic substitution is the most commonly used radioiodination method. A lot of various techniques are available, which lead to high RCY in uncomplicated labelling reactions and which can be often carried out at room temperature. Due to its high volatility, low reactivity and the need of carrier addition, molecular iodine (I_2) is excluded for the n.c.a. scale. These problems to achieve reactive electrophilic species are easily circumvented by an in situ oxidation of iodide, which is obtained straight from the target. The generally used oxidants are Chloramine-T (CAT; *para*-tosylchloramide sodium), Iodogen™ (1,3,4,6-tetrachloro-3α,6α-diphenylglycouril) and *N*-halogensuccinimides.

The exact chemical nature and oxidation state of the iodinating species are not fully clarified so far. In case of aqueous solutions with strong acidic conditions a hypoiodite, and for neutral and alkaline conditions, an iodine-analogue of e.g. CAT are postulated [338]. Due to the insignificant differences in their redox potentials, the choice of the proper oxidant depends on the reaction conditions and the character of the iodine substrate. CAT allows oxidations in homogeneous aqueous solutions, whereas Iodogen™ is insoluble in water, and thus, it is the proper substance for a heterogenic reaction route, which is advantageous for oxidation-sensitive precursors. In the group of *N*-halogensuccinimides, *N*-chlorotetrafluorosuccinimide (NCTFS), *N*-chlorosuccinimide (NCS) and rarely *N*-bromosuccinimide (NBS) are applied for in situ oxidation [339, 340]. When using NCS in trifluoromethane sulphonic acid, even deactivated aromatic compounds can be labelled with radioiodine in acceptable RCY [341]. Besides these oxidants, conventional oxidising reagents are in use, such as hydrogen peroxide, respectively, peracids [342] and metal cations (Ag$^+$, Tl^{3+}, Pb^{4+} and Ce^{4+}) [343]. Rather unconventional, but also

useful are enzymatic [344] or electrochemical [345] methods for oxidation. As a disadvantage, the electrophilic radioiodination may raise the problem of a regio-unselective attack, as a result, isomeric derivatives may occur.

7.3.5.3 Electrophilic Demetallation

Contrary to the direct electrophilic procedure, the electrophilic demetallation provides an almost regiospecific radioiodination. Especially for automated syntheses, it offers simple purification and isolation of the radiotracer and is therefore the first choice. Nonetheless, the syntheses of the organometallic precursors may become complex and extensive [346]. Suitable precursors for demetallation radioiodine-labelling are organometallic compounds of thallium [347], boron [348], mercury [349] and particularly the organometallics of the elements of the group IVb. Of these, an exceptional position is taken by the organotins, which show, in many times, excellent RCY in very short reaction time (few minutes), generally the RCY increases with Si < Ge < Sn [350]. Presently, the radioiodo-destannylation is the most suitable radioiodination procedure, and thus, it is the most commonly employed method.

7.3.5.4 Non-isotopic Exchange (Nucleophilic Labelling)

Another labelling procedure for regiospecific radioiodine introduction is the non-isotopic exchange. Non-isotopic exchange is generally Cu(I)-catalysed and is suitable for electron-rich as well as for electron-deficient aromatic molecules [351]. In case of iodine-for-bromine exchange, high specific activities are available. In Cu(I)-promoted reactions, the readiness of the displacement follows the nucleofugality of the halogens ($I^- > Br^- > Cl^-$). In the Cu(I)-mediated substitution mechanism, a quadratic-planar complex was suggested, including Cu(I) as coordinated central atom, whereby the activation energy for the substitution process is reduced, and the iodine can be introduced [352]. In variations, the Cu(I) salts are in situ synthesised by a mild reduction of Cu(II)-salts (reducing agent: ascorbic acid, bisulphite or Sn(II)-compounds). Hereby Cu_2SO_4 is more applicable than the use of copper halides,

because the formation of halogenated side-products is excluded. One of the important advantages is the much easier precursor preparation and their high stability. Moreover, it is again a highly regiospecific labelling route for radioiodine. In comparison to the electrophilic radioiodination, disadvantages are relatively high reaction temperatures up to 180 °C and vastly longer reaction times up to hours. In the given cases, the separation and isolation of the radiotracer provoke difficulties due to its chemical and physical similarities to the bromine precursor.

7.3.5.5 Prosthetic Group Labelling

If molecules are sensitive to oxidative reagents or functional groups for iodination are lacking, the above-mentioned direct radioiodination methods fail. As alternative, small molecules can be radioiodinated as labelling synthons and subsequently coupled with the desired compound. This is principally the same procedure as for the ^{18}F-labelling via prosthetic groups (cf. Sect. 7.3.1).

The first approach on prosthetic groups for radioiodination was the so-called Bolton–Hunter reagent, *N*-succinimidyl-3-(4-hydroxyphenyl) propionate (SHPP), an activated ester as labelling synthon for proteins via coupling with a free amino function, normally of the amino acid lysine [353, 354]. It is still widely used for radioiodination of proteins and macromolecules, thus a [124]I-labelled VEGF antibody (VEGF = vascular endothelial growth factor) for measuring angiogenesis was recently radioiodinated via a derivative of the Bolton–Hunter reagent [355]. The Bolton–Hunter principle for the radioiodination of proteins led to further developments of prosthetic groups such as methyl-*p*-hydroxybenzimidate (Wood reagent) which is an activated imidate ester and also a versatile and convenient radioiodination synthon [356]. In addition, aldehydes, isothiocyanates [357] and activated α-carbonyl halides [358] are further prosthetic groups for labelling via free amino functions.

In case of aldehydes, radioiodo-tyramine-cellobiose is an important compound which, for example, was used for labelling monoclonal antibodies [359]. Several other coupling methods of prosthetic groups with functional groups of pro-

teins or complex molecules are known. Another common example for suitable functions is the thiol group of cysteine, where appropriate prosthetic groups are malimide derivatives [360].

7.3.5.6 Labelling Using Radiobromine

In case of positron emitting radioisotopes of bromine, three nuclides are suitable for PET imaging, ^{75}Br ($T_{1/2}$ = 98 min, 75% β$^+$), ^{76}Br ($T_{1/2}$ = 16.2 h, 57% β$^+$) and ^{77}Br ($T_{1/2}$ = 57 h, 0.7% β$^+$). Among these nuclides, the most preferred one is bromine-76. It has a longer and more convenient half-life than bromine-75 and a much higher β$^+$-abundance than bromine-77. Bromine-77 is more attractive for radiotherapy than for PET Imaging as it decays also by Auger electron emission [361–364]. It has been demonstrated that bromine-77 is highly lethal when it is incorporated into DNA of mammalian cells [361].

In small medical cyclotrons bromine-76 can be produced via the ^{76}Se(p,n)^{76}Br nuclear reaction using a Cu$_2$Se target. The bromine-76 is isolated from the target by a dry distillation process and usually trapped in alkaline solution [365]. In the same way as radioiodine, for electrophilic demetallation reactions (mostly destannylations), radiobromine can be easily oxidised in situ using oxidants such as CAT, NCS or simply hydrogen peroxide in combination with acetic acid. As an example, the proliferation marker [^{76}Br]bromofluorodeoxyuridine has been radiobrominated via in situ oxidation by CAT and electrophilic destannylation of the corresponding trimethyltin precursor [366–368]. An alternative radiobromination method is the nucleophilic non-isotopic exchange. Again the conditions of nucleophilic radioiodination reactions are transferable, thus Cu(II)-mediated exchange reactions are particularly suitable. According to this, a ^{76}Br-labelled derivative of epibatidine was synthesised for PET imaging studies of the nicotinic acetylcholine receptor system [369].

In general, radiobromine is less available than radioiodine, due to more complicated target work-up and isolation procedures. In the radiochemistry of radiobromine, methods from radioiodine labelling can often be directly adopted, and the radiochemistry is more convenient to accomplish than fluorine-18 labelling. Predominantly, the electrophilic destannylation reactions are employed for radiobromination chemistry. However, a few ^{76}Br-labelled radiopharmaceuticals have been developed to date [366, 370–374], but they have only little relevance clinical PET imaging.

7.3.5.7 Complexes for Labelling with Metallic PET Radionuclides

Among the metallic positron emitters which are suitable for PET imaging, the production routes can be divided into cyclotron-produced nuclides such as copper-64, titanium-45, scandium-44, yttrium-86 or zirconium-89 and generator-produced nuclides such as rubidium-82, scandium-44 or copper-62. The main advantage of the latter is clearly their availability which is not limited to facilities with an onsite cyclotron. Rubidium-82 ($T_{1/2}$ = 1.3 min) can be obtained from the ^{82}Sr/^{82}Rb generator, scandium-44 ($T_{1/2}$ = 3.97 h) from the ^{44}Ti/^{44}Sc generator and copper-62 ($T_{1/2}$ = 10 min) from the ^{62}Zn/^{62}Cu generator.

In terms of radiochemistry, labelling with metallic nuclides is based on chelatoring systems which are coupled to biomolecules or which have interesting biological properties themselves. Most prominent examples of chelating systems are DOTA and NOTA as well as DFO (desferrioxamine-B). The latter and its derivatives, i.e. DFO*, are particularly suitable for zirconim-89, and essential chelating systems in Immuno-PET [375, 376]. Scandium-44 exhibits almost identical complex chemistry as gallium-68, which makes Sc-44 highly interesting for following slower pharmacokinetics and investigating dosimetry in theranostic applications [377]. Radiocopper forms complexes such as Cu-PTSM (pyruvaldehyde-bis(N^4-methythiosemicarbazone)) or Cu-ATSM (diacetyl-bis(N^4-methylthiosemicarbazone)), which have interesting biological properties themselves (see Fig. 7.30) [378–381]. These Cu-complexes are both employed in the clinics. ^{62}Cu-labelled PTSM is used as perfusion and blood flow agent for heart and brain, whereas ^{62}Cu-labelled ATSM has been shown to accumulate in hypoxic tumour cells. Recent developments and an increased clinical use of copper-64 have stimulated research on Cu-specific chelators [382, 383].

Fig. 7.30 Chelator systems for (radio) copper

Cu-PTSM

Cu-ATSM
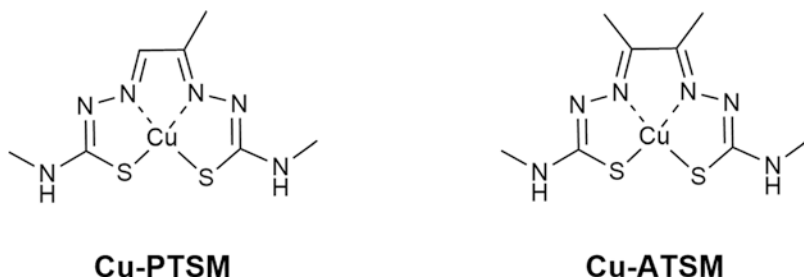
7.4 Conclusions

A variety of labelling methods has already been developed, and especially the latest developments in metal-catalysed ^{18}F-chemistry have made a huge impact in PET chemistry. But still some methods are only suitable for certain radionuclides and often limited in their applicability. On the other hand, more and more molecules of biological or pharmacological interest are discovered as well as more radionuclides established for medical applications, both pose new challenges to radiolabelling and radiochemistry. Consequently, the development and improvement of new labelling strategies and methods for PET radiopharmaceuticals are of paramount interest.

Then again, many PET radiopharmaceuticals have been developed and several of them found the way into clinical routine. PET chemistry forms the basis of PET radiopharmaceuticals and PET imaging and will always be a major contributor to the success of the growing field of this molecular imaging modality.

References

1. Lawrence EO, Livingston MS. The production of high speed light ions without the use of high voltages. Phys Rev. 1932;40:19–35.
2. Pandey MK, Byrne JF, Jiang H, Packard AB, DeGrado TR. Cyclotron production of ^{68}Ga via the ^{68}Zn(p,n)^{68}Ga reaction in aqueous solution. Am J Nucl Med Mol Imaging. 2014;4:303–10.
3. Talip Z, Favaretto C, Geistlich S, van der Meulen NP. A step-by-step guide for the novel radiometal production for medical applications: case studies with ^{68}Ga, ^{44}Sc, ^{177}Lu and ^{161}Tb. Molecules. 2020;25:966.
4. Velikyan I. Prospective of ^{68}Ga-radiopharmaceutical development. Theranostics. 2014;4:47–80.
5. Herzog H. In vivo functional imaging with SPECT and PET. Radiochim Acta. 2001;89:203–14.
6. Ido T, Wan C-N, Casella V, Fowler JS, Wolf AP, Reivich M, Kuhl DE. Labeled 2-deoxy-D-glucose analogs. ^{18}F-labeled 2-deoxy-2-fluoro-D-glucose, 2-deoxy-2-fluoro-D-mannose and ^{14}C-2-deoxy-2-fluoro-D-glucose. J Label Compd Radiopharm. 1978;14:175–82.
7. Coleman RE. FDG imaging. Nucl Med Biol. 2000;27:689–90.
8. Reske SN, Kotzerke J. FDG-PET for clinical use. Eur J Nucl Med. 2001;28:1707–23.
9. Gambhir SS, Czerni J, Schwimmer J, Silverman DHS, Coleman RE, Phelps ME. A tabulated summary of FDG PET literature. J Nucl Med. 2001;42:1S–93S.
10. Adam MJ. Radiohalogenated carbohydrates for use in PET and SPECT. J Label Compd Radiopharm. 2002;45:167–80.
11. Werner RA, Derlin T, Lapa C, Sheikbahaei S, Higuchi T, Giesel FL, Behr S, Drzezga A, Kimura H, Buck AK, Bengel FM, Pomper MG, Gorin MA, Rowe SP. ^{18}F-Labeled, PSMA-targeted radiotracers: leveraging the advantages of Radiofluorination for prostate cancer molecular imaging. Theranostics. 2020;10:1–16.
12. Shiue C-Y, Welch MJ. Update on PET radiopharmaceuticals: life beyond fluorodeoxyglucose. Radiol Clin North Am. 2004;42:1033–53.
13. Couturier O, Luxen A, Chatal J-F, Vuillez J-P, Rigo P, Hustinx R. Fluorinated tracers for imaging cancer with positron emission tomography. Eur J Nucl Med Mol Imaging. 2004;31:1182–206.
14. Adam MJ, Wilbur DS. Radiohalogens for imaging and therapy. Chem Soc Rev. 2005;34:153–63.
15. Schubiger PA, Lehmann L, Friebe M, editors. PET chemistry—the driving force in molecular imaging. Berlin: Springer; 2007.
16. Van Dongen GAMS, Visser GWM, Lub-De Hooge MN, Vries D, Perk LR. Immuno-PET: a navigator in monoclonal antibody development and applications. Oncologist. 2007;12:1279–390.
17. Van de Watering FCJ, Rijpkema M, Robillard M, Oyen WJG, Boerman OC. Pretargeted imaging and

radioimmunotherapy of cancer using antibodies and bioorthogonal chemistry. Front Med. 2014;1:44.

18. Dehdashti F, Mintun MA, Lewis JS, Bradley J, Govindan R, Laforest R, Welch MJ, Siegel BA. In vivo assessment of tumor hypoxia in lung cancer with 60Cu-ATSM. Eur J Nucl Med Mol Imaging. 2003;30:844–50.

19. Herzog H, Qaim SM, Tellmann L, Spellerberg S, Kruecker D, Coenen HH. Assessment of the short-lived non-pure positron-emitting nuclide 120I for PET imaging. Eur J Nucl Med Mol Imaging. 2006;33:1249–57.

20. Laforest R, Rowland DJ, Welch MJ. MicroPET imaging with nonconventional isotopes. IEEE Trans Nucl Sci. 2002;49:2119–26.

21. Qaim SM. Nuclear data for production and medical application of radionuclides: present status and future needs. Nucl Med Biol. 2017;44:31–49.

22. McQuade P, Rowland DJ, Lewis JS, Welch MJ. Positron-emitting isotopes produced on biomedical cyclotrons. Curr Med Chem. 2005;12:807–18.

23. Magill J, Pfennig G, Galy J. The Karlsruhe chart of the nuclides. 7th ed; 2006. ISBN 92-79-02175-3.

24. Plenevaux A, Guillaume M, Brihaye C, Lemaire C, Cantineau R. Chemical processing for production of no-carrier-added Selenium-73 from Germanium and Arsenic targets and synthesis of L-2-Amino-4-([73Se]Methylseleno) Butyric Acid (L-[73Se]Selenomethionine). Appl Radiat Isot. 1990;41:829–35.

25. Emert J, Blum T, Hamacher K, Coenen HH. Alternative syntheses of [73,75Se]selenoethers exemplified for homocysteine[73,75Se]selenolactone. Radiochim Acta. 2001;89:863–6.

26. Müller K, Faeh C, Diederich F. Fluorine in pharmaceuticals: looking beyond intuition. Science. 2007;317:1881–6.

27. Hagmann WK. The many roles for fluorine in medicinal chemistry. J Med Chem. 2008;51:4359–69.

28. Love WD, Romney RB, Burgh GE. A comparison of the distribution of potassium and exchangeable rubidium in the organs of dog using rubidium 86. Circ Res. 1954;2:112–22.

29. Selwyn AP, Allan RM, L'Abbate A, Horlock P, Camici P, Clark J, O'Brien HA, Grant PM. Relation between regional myocardial uptake of rubidium-82 and perfusion: absolute reduction of cation uptake in ischemia. Am J Cardiol. 1982;50:112–21.

30. Gould KL. PET perfusion imaging and nuclear cardiology. J Nucl Med. 1991;32:579–606.

31. Machac J, Bacharach SL, Bateman TM, Bax JJ, Beanlands R, Bengel F, Bergmann SR, Brunken RC, Case J, Delbeke D, DiCarli MF, Garcia EV, Goldstein RA, Gropler RJ, Travin M, Patterson R, Schelbert HR. Positron emission tomography myocardial perfusion and glucose metabolism imaging. J Nucl Cardiol. 2006;13:e121–51.

32. Hofmann M, Oei M, Boerner AR, Maecke H, Geworski L, Knapp WH, Krause T. Comparison of Ga-68-DOTATOC and Ga-68-DOTANOC for radiopeptide PET. Nuklearmedizin. 2005;44:A58.

33. Lutje S, Heskamp S, Cornelissen AS, Poeppel TD, van den Broek SA, Rosenbaum-Krumme S, Bockisch A, Gotthardt M, Rijpkema M, Boerman OC. PSMA ligands for radionuclide imaging and therapy of prostate cancer: clinical status. Theranostics. 2015;5:1388–401.

34. Coenen HH, Gee AD, Adam M, Antoni G, Cutler CS, Fujibayashi Y, Jeong JM, Mach RH, Mindt TL, Pike VW, Windhorst AD. Consensus nomenclature rules for radiopharmaceutical chemistry—setting the record straight. Nucl Med Biol. 2017;55:v–xi.

35. Ametamey SM, Honer M, Schubiber PA. Molecular imaging with PET. Chem Rev. 2008;108:1501–16.

36. Miller PW, Long NJ, Vilar R, Gee AD. Synthesis of 11C, 18F, 15O, and 13N radiolabels for positron emission tomography. Angew Chem Int Ed. 2008;47:8998–9033.

37. Cole EL, Stewart MN, Littich R, Hoareau R, Scott PJH. Radiosyntheses using Fluorine-18: the art and science of late stage fluorination. Curr Top Med Chem. 2014;14:875–900.

38. Coenen HH, Errmert J. 18F-labelling innovations and their potential for clinical application. Clin Trans Imaging. 2018;6:169–93.

39. Qaim SM, Clark JC, Crouzel C, Guillaume M, Helmeke HJ, Nebeling B, Pike VW, Stöcklin G. PET radionuclide production. In: Stöcklin G, Pike VW, editors. Radiopharmaceuticals for positron emission tomography—methodological aspects. Dordrecht: Kluwer; 1993. p. 1–43.

40. Guillaume M, Luxen A, Nebeling B, Argentini M, Clark JC, Pike VW. Recommendations for Fluorine-18 production. Appl Radiat Isot. 1991;42:749–62.

41. Namavari M, Bishop A, Satyamurthy N, Bida G, Barrio JR. Regioselective radiofluorodestannylation with [18F]F2, and [18F]CH3COOF: a high yield synthesis of 6-[18F]Fluoro-L-dopa. Appl Radiat Isot. 1992;43:989–96.

42. De Vries EFJ, Luurtsema G, Brüssermann M, Elsinga PH, Vaalburg W. Fully automated synthesis module for the high yield one-pot preparation of 6-[18F]fluoro-L-DOPA. Appl Radiat Isot. 1999;51:389–94.

43. Brook AF, Topczewski JJ, Ichiishi N, Sanford MS, Scott PJH. Late-stage [18F]fluorination: new solutions to old problems. Chem Sci. 2014;5:4545–53.

44. Wagner FM, Ermert J, Coenen HH. Three-step, "one-pot" radiosynthesis of 6-fluoro-3,4-dihydroxy-L-phenylalanine by isotopic exchange. J Nucl Med. 2009;50:1724–9.

45. Mossine AV, Tanzey SS, Brooks AF, Makaravage KJ, Ichiishi N, Miller JM, Henderson BD, Skaddan MB, Sanford MS, Scott PJH. One-pot synthesis of high molar activity 6-[18F]fluoro-l-DOPA by cu-mediated fluorination of a BP in precursor. Org Biomol Chem. 2019;17:8701–5.

46. Wallach O. Über das Verhalten einiger Diazo- und Diazoamidoverbindungen. Justus Liebigs Ann Chem. 1886;235:242–55.

47. Balz G, Schiemann G. Über aromatische Fluorverbindungen, I.: Ein neues Verfahren zu ihrer Darstellung. Chem Ber. 1927;60:1186–90.

48. Atkins HL, Christmann DR, Fowler JS, Hauser W, Hoyte RM, Kloper JF, Lin SS, Wolfe AP. Organic radiopharmaceuticals labelled with isotopes of short half-life. V. 18F-labeled 5- and 6-fluorotryptophan. J Nucl Med. 1972;13:713–9.

49. Tewson TJ, Welch MJ. Preparation of fluorine-18 aryl fluorides: piperidyl triazenes as a source of diazonium salts. J Chem Soc Chem Commun. 1979:1149–50.

50. Hess E, Blessing G, Coenen HH, Qaim SM. Improved target system for production of high purity [18F]fluorine via the 18O(p,n)18F reaction. Appl Radiat Isot. 2000;52:1431–40.

51. Bauer A, Zilles K, Matusch A, Holzmann C, Riess O, von Hörsten S. Regional and subtype selective changes of neurotransmitter receptor density in a rat transgenic for the Huntington's disease mutation. J Neurochem. 2005;94:639–50.

52. Ametamey SM, Honer M, Schubiger PA. Molecular imaging with PET. Chem Rev. 2008;108:1501–16.

53. Fowler JS, Shiue CY, Wolf AP, Salvador AP, MacGregor RR. Synthesis of 18F-labeled acetyl hypofluoride for radiotracer synthesis. J Label Compd Radiopharm. 1982;19:1634–5.

54. Chirakal R, Firnau G, Schrobigen GJ, MacKay J, Garnett ES. The synthesis of [18F]xenon difluoride from [18F]fluorine gas. Appl Radiat Isot. 1984;35:401–4.

55. Constantinou M, Aigbirhio FI, Smith RG, Ramsden CA, Pike VW. Xenon difluoride exchanges fluoride under mild conditions: a simple preparation of [18F] xenon difluoride for PET and mechanistic studies. J Am Chem Soc. 2001;123:1780–1.

56. Satyamurthy N, Bida GT, Phelps ME, Barrio J. N-[18F]Fluoro-N-alkylsulfonamides: novel reagents for mild and regioselective radiofluorination. Appl Radiat Isot. 1990;41:733–8.

57. Shiue CY, Salvadori AP, Wolf AP, Fowler JS, MacGregor RR. A new improved synthesis of 2-Deoxy-2-[18F]Fluoro-D-Glucose from 18F-labeled Acetyl Hypofluorite. J Nucl Med. 1982;23:899–903.

58. Ehrenkaufer RE, Potocki JF, Jewett DM. Simple synthesis of F-18-labeled 2-fluoro-2-deoxy-D-glu-cose. J Nucl Med. 1984;25:333–7.

59. Levy S, David RE, Livni E. A new method using anhydrous [18F]fluoride to radiolabel 2-[18F]fluoro-2-deoxy-D-glucose. J Nucl Med. 1982;23:918–22.

60. Bida TG, Satyamurthy N, Barrio JR. The synthesis of 2-[F-I8]fluoro-2-deoxy-D-glucose using glycals: a reexamination. J Nucl Med. 1984;25:1327–34.

61. Korytnyk W, Valentekovic-Horvat S. Reactions of glycals with xenon fluoride: an improved synthesis of 2-deoxy-2-fluoro-saccharides. Tetrahedron Lett. 1980;21:1493–6.

62. Shiue C-Y, To K-C, Wolf AP. A rapid synthesis of 2-deoxy-2-fluoro-D-glucose from xenon difluoride suitable for labelling with 18F. J Label Compd Radiopharm. 1983;20:157–62.

63. Sood S, Firnau G, Garnett ES. Radiofluorination with xenon difluoride: a new high yield synthesis of [18F]2-fluoro-2-deoxy-D-glucose. J Nucl Med. 1983;24:718–21.

64. Strauss LG, Conti PS. The application of PET in clinical oncology. J Nucl Med. 1991;32:623–48.

65. Dimitrakopoulou-Strauss A, Strauss LG, Schlag P, Hohenberger P, Mühler M, Oberdorfer F, van Kaick G. Fluorine-18-Fluorouracil to predict therapy response in liver metastases from colorectal carci-noma. J Nucl Med. 1998;39:1197–202.

66. Oberdorfer F, Hofmann E, Maier-Borst W. Preparation of 18F-labelled 5-Fluorouracil of very high purity. J Label Compd Radiopharm. 1989;27:137–45.

67. Firnau G, Chirakal R, Garnett ES. Aromatic radio-fluorination with [18F]fluorine gas: 6-[18F]Fluoro-L-Dopa. J Nucl Med. 1984;25:1228–33.

68. Coenen HH, Franken F, Kling P, Stöcklin G. Direct electrophilic radiofluorination of phenylalanine, tyro-sine and Dopa. Appl Radiat Isot. 1988;39:1243–50.

69. Chirakal R, Vasdev N, Schrobilgen GJ, Nahmias C. Radiochemical and NMR spectroscopic investigation of the solvent effect on the elec-trophilic elemental Fluorination of L-DOPA: syn-thesis of [18F]5-Fluoro-L-DOPA. J Fluorine Chem. 1999;99:87.

70. Szajek LP, Channing MA, Eckelman WC. Automated synthesis 6-[18F]fluoro-L-DOPA using polystyrene supports with 6-Mercuric of modified bound DOPA precursors. Appl Radiat Isot. 1998;49:795–804.

71. Dollé F, Demphel S, Hinnen F, Fournier D, Vaufrey F, Crouzel C. 6-[18F]Fluoro-L-DOPA by radio-fluorodestannylation: a short and simple synthe-sis of a new labelling precursor. J Label Compd Radiopharm. 1998;41:105–14.

72. Füchtner F, Angelberger P, Kvaternik H, Hammerschmidt F, Simovc P, Steinbach J. Aspects of 6-[18F]fluoro-L-DOPA preparation: precursor synthesis, preparative HPLC purification and deter-mination of radiochemical purity. Nucl Med Biol. 2002;29:477–81.

73. Bergman J, Solin O. Fluorine-18-labeled fluorine gas for synthesis of tracer molecules. Nucl Med Biol. 1997;24:677–83.

74. Hamacher K, Coenen HH, Stöcklin G. Efficient stereospecific synthesis of no-carrier-added 2-[18F]-fluoro-2-deoxy-D-glucose using aminop-olyether supported nucleophilic substitution. J Nucl Med. 1986;27:235–8.

75. Alexoff D, Schlyer DJ, Wolf AP. Recovery of [18F] Fluoride from [18O]water in an electrochemical cell. Appl Radiat Isot. 1989;40:1–6.

76. Hamacher K, Hirschfelder T, Coenen HH. Electrochemical cell for separation of [18F] Fluoride from irradiated O-18-water and subsequent no-carrier-added nucleophilic fluorination. Appl Radiat Isot. 2002;56:519–23.

77. Kim DW, Choe YS, Chi DY. A new nucleophilic fluorine-18 labeling method for aliphatic mesylates: reaction in ionic liquids shows tolerance for water. Nucl Med Biol. 2003;30:345–50.

78. Kim HW, Jeong JM, Lee YS, Chi DY, Chung KH, Lee DS, Chung JK, Lee MC. Rapid synthesis of [18F]FDG without an evaporation step using an ionic liquid. Appl Radiat Isot. 2004;61:1241–6.

79. Richarz R, Krapf P, Zarrad F, Urusova EA, Neumaier B, Zlatopolskiy BD. Neither azeotropic drying, nor base nor other additives: a minimalist approach to 18F-labeling. Org Biomol Chem. 2014;12:8094–9.

80. Zischler J, Krapf P, Richarz R, Zlatopolskiy BD, Neumaier B. Automated synthesis of 4-[18F]fluoroanisole, [18F]DAA1106 and 4-[18F]FPhe using cu-mediated radiofluorination under "minimalist" conditions. Appl Radiat Isot. 2016;115:133–7.

81. Zischler J, Kolks N, Modemann D, Neumaier B, Zlatopolskiy BD. Alcohol-enhanced cu-mediated radiofluorination. Chem A Eur J. 2017;23:3251–6.

82. Kniess T, Laube M, Steinbach J. "Hydrous 18F-fluoroethylation"—leaving off the azeotropic drying. Appl Radiat Isot. 2017;127:260–8.

83. Mu L, Höhne A, Schubiger PA, Ametamey SM, Graham K, Cyr JE, Dinkelborg L, Stellfeld T, Srinivasan A, Voigtmann U, Klar U. Silicon-based building blocks for one-step 18F-radiolabeling of peptides for PET imaging. Angew Chem Int Ed. 2008;47:4922–5.

84. Kostikov AP, Chin J, Orchowski K, Niedermoser S, Kovacevic MM, Aliaga A, Jurkschat K, Wängler B, Wängler C, Wester HJ, Schirrmacher R. Oxalic acid supported Si-18F-radiofluorination: one-step radiosynthesis of N-succinimidyl 3-(di-tert-buty[18F]fluorosilyl) benzoate ([18F]SiFB) for protein labeling. Bioconjug Chem. 2012;23:106–14.

85. Kim DW, Ahn D-S, Oh Y-H, Lee S, Kil HS, Oh SJ, Lee SJ, Kim JS, Ryu JS, Moon DH, Chi SY. A new class of SN2 reactions catalyzed by protic solvents: facile fluorination for isotopic labeling of diagnostic molecules. J Am Chem Soc. 2006;128:16394–7.

86. Martin SJ, Eisenbarth JA, Wagner-Utermann U, Mier W, Henze M, Pritzkow H, Haberkorn U, Eisenhut M. A new precursor for the radiosynthesis of [18F] FLT. Nucl Med Biol. 2002;29:263–73.

87. Oh SJ, Mosdzianowski C, Chi DY, Kim JY, Kang SH, Ryu JS, Yeo JS, Moon DH. Fully automated synthesis system of 3′-deoxy-3′-[18F]fluorothymidine. Nucl Med Biol. 2004;31:803–9.

88. Kämäräinen E-L, Kyllönen T, Nihtilä O, Björk H, Solin O. Preparation of fluorine-18-labelled fluoromisonidazole using two different synthesis methods. J Label Compd Radiopharm. 2004;47:37–45.

89. Hamacher K, Coenen HH. Efficient routine production of the 18F-labelled amino acid O-(2-

[18F]fluoroethyl)-L-tyrosine. Appl Radiat Isot. 2002;57:205–12.

90. Fedorova O, Kuznetsova O, Stepanova M, Maleev V, Belokon Y, Wester H-J, Krasikova R. A facile direct nucleophilic synthesis of O-(2-[18F]fluoroethyl)-l-tyrosine ([18F]FET) without HPLC purification. J Radioanal Nucl Chem. 2014;301:505–12.

91. Kung HF, Choi SR, Qu W, Zhang W, Skovronsky D. 18F stilbenes and styrylpyridines for PET imaging of a beta plaques in Alzheimer's disease: a miniperspective. J Med Chem. 2010;53:933–41.

92. Wadsworth H, Jones PA, Chau WF, Durrant C, Fouladi N, Passmore J, O'Shea D, Wynn D, Morisson-Iveson V, Ewan A, Thaning M, Mantzilas D, Gausemel I, Khan I, Black A, Avory M, Trigg W. [18F]GE-180: a novel fluorine-18 labelled PET tracer for imaging translocator protein 18 kDa (TSPO). Bioorg Med Chem Lett. 2012;22:1308–13.

93. DeGrado TR, Baldwin SW, Wang S, Orr MD, Liao RP, Friedman HS, Reiman R, Price DT, Coleman RE. Synthesis and evaluation of 18F-labeled choline analogs as oncologic PET tracers. J Nucl Med. 2001;42:1805–14.

94. Hamacher K, Hamkens W. Remote controlled one-step production of 18F-labeled butyrophenone neuroleptics exemplified by the synthesis of n.c.a. [18F]N-methylspiperone. Appl Radiat Isot. 1995;46:911–6.

95. Katsifis A, Hamacher K, Schnittler J, Stöcklin G. Optimization studies concerning the direct nucleophilic fluorination of butyrophenone neuroleptics. Appl Radiat Isot. 1993;44:1015–20.

96. Lemaire C, Cantineau R, Guillaume M, Plenevaux A, Christiaens L. Fluorine-18-Altanserin: a radioligand for the study of serotonin receptors with PET: radiolabeling and in vivo biologic behavior in rats. J Nucl Med. 1991;32:2266–72.

97. Hamacher K, Coenen HH. No-carrier-added nucleophilic 18F-labelling in an electrochemical cell exemplified by the routine production of [18F]altanserin. Appl Radiat Isot. 2006;64:989–94.

98. Shiue C-Y, Shiue GG, Mozley D, Kung M-P, Zhuang Z-P, Kim H-J, Kung HF. p-[18F]-MPPF: a potential radioligand for PET studies of 5-HT1A receptors in humans. Synapse. 1997;25:147–54.

99. Le Bars D, Lemaire C, Ginovart N, Plenevaux A, Aerts J, Brihaye C, Hassoun W, Leviel V, Mekhsian P, Weissmann D, Pujol JF, Luxen A, Comar D. High yield radiosynthesis and preliminary in vivo evaluation of p-[18F]MPPF, a Fluoro Analog of WAY-100635. Nucl Med Biol. 1998;25:343–50.

100. Knust EJ, Müller-Platz C, Schüller M. Synthesis, quality control and tissue distribution of 2-[18F]-nicotinic acid diethylamide, a potential agent for regional cerebral function studies. J Radioanal Chem. 1982;74:283–91.

101. Dollé F. Fluorine-18-labelled fluoropyridines: advances in radiopharmaceutical design. Curr Pharm Des. 2005;11:3221–35.

102. Cardinale J, Schäfer M, Benešová M, Bauder-Wüst U, Leotta K, Eder M, Neels OC, Haberkorn U, Giesel FL, Kopka K. Preclinical evaluation of 18F-PSMA-1007, a new prostate-specific membrane antigen ligand for prostate cancer imaging. J Nucl Med. 2017;58:425–31.

103. Horti A, Ravert HT, London ED, Dannals RF. Synthesis of a radiotracer for studying nicotinic acetylcholine receptors: (+/-)-exo-2-(2-[18F]fluoro-5-pyridyl)-7-azabicyclo[2.2.1]heptane. J Label Compd Radiopharm. 1996;38:355–65.

104. Ding Y-S, Liang F, Fowler JS, Kuhar MJ, Carroll FI. Synthesis of [18F]norchlorofluoroepibatidine and its N-methyl derivative: new PET ligands for mapping nicotinic acetylcholine receptors. J Label Compd Radiopharm. 1997;39:827–32.

105. Dolci L, Dollé F, Valette H, Vaufrey F, Fuseau C, Bottlaender M, Crouzel C. Synthesis of a fluorine-18 labeled derivative of epibatidine for in vivo nicotinic acetylcholine receptor PET imaging. Bioorg Med Chem. 1999;7:467–79.

106. Horti A, Scheffel U, Stathis M, Finley P, Ravert HT, London ED, Dannals RF. Fluorine-18-FPH for PET imaging of nicotinic acetylcholine receptors. J Nucl Med. 1997;38:1260–5.

107. Dolle F, Valette H, Bottlaender M, Hinnen F, Vaufrey F, Guenther I, Crouzel C. Synthesis of 2-[18F]fluoro-3-[2(S)-2-azetidinylmethoxy]pyridine, a highly potent radioligand for in vivo imaging central nicotinic acetylcholine receptors. J Label Compd Radiopharm. 1998;41:451–63.

108. Ding Y-S, Liu N, Wang T, Marecek J, Garza V, Ojima I, Fowler JS. Synthesis and evaluation of 6-[18F]fluoro-3-(2(S)-azetidinylmethoxy)pyridine as a PET tracer for nicotinic acetylcholine receptors. Nucl Med Biol. 2000;27:381–9.

109. Beer H-F, Haeberli M, Ametamey S, Schubiger PA. Comparison of two synthetic methods to obtain N-(2-aminoethyl)-5-[18F]fluoropyridine-2-carboxamide, a potential MAO-B imaging tracer for PET. J Label Compd Radiopharm. 1995;36:933–45.

110. Moerlein SM, Perlmutter JS, Markham J, Welch MJ. In vivo kinetics of [18F](N-Methyl)Benperidol: A Novel PET tracer for assessment of dopaminergic D2-like receptor binding. J Cereb Blood Flow Metab. 1997;17:833–45.

111. Ryzhikov NN, Seneca N, Krasikova RN, Gomzina NA, Shchukin E, Fedorova OS, Vassiliev DA, Gulyás B, Hall H, Savic I, Halldin C. Preparation of highly specific radioactivity [18F]flumazenil and its evaluation in cynomolgus monkey by positron emission tomography. Nucl Med Biol. 2005;32:109–16.

112. Stone-Elander S, Elander N. Microwave applications in radiolabelling with short-lived positron-emitting radionuclides. J Label Compd Radiopharm. 2002;45:715–46.

113. Hwang D-R, Moerlein SM, Lang L, Welch MJ. Application of microwave technology to the synthesis of short-lived radiopharmaceuticals. J Chem Soc Chem Commun. 1987;23:1799–801.

114. Stone-Elander S, Elander N. Fast chemistry in microwave fields: nucleophilic 18F-radiofluorinations of aromatic molecules. Appl Radiat Isot. 1993;44:889–93.

115. Ding Y-S, Shiue C-Y, Fowler JS, Wolf AP, Plenevaux A. No-carrier-added (NCA) aryl [18F]fluorides via the nucleophilic aromatic substitution of electron-rich aromatic rings. J Fluor Chem. 1990;48:189–206.

116. Chakraborty PK, Kilbourn MR. [18F]Fluorination/decarbonylation: new route to aryl [18F]fluorides. Appl Radiat Isot. 1991;42:1209–13.

117. Plenevaux A, Lemaire L, Palmer AJ, Damhaut P, Comar D. Synthesis of non-activated 18F-fluorinated aromatic compounds through nucleophilic substitution and decarboxylation reactions. Appl Radiat Isot. 1992;42:1035–40.

118. Reddy GN, Haeberli M, Beer H-F, Schubiger PA. An improved synthesis of no-carrier-added (NCA) 6-[18F]Fluoro-l-DOPA and its remote routine production for PET investigations of dopaminergic systems. Appl Radiat Isot. 1993;44:645–9.

119. Hostetler ED, Jonson SD, Welch MJ, Katzenellenbogen JA. Synthesis of 2-[18F] Fluoroestradiol, a potential diagnostic imaging agent for breast cancer: strategies to achieve nucleophilic substitution of an electron-rich aromatic ring with [18F]F. J Org Chem. 1999;64:178–85.

120. Pike VW, Aigbirhio FI. Reactions of cyclotron-produced [18F]fluoride with diaryliodonium salts—a novel single-step route to no-carrier-added [18F]fluoroarenes. J Chem Soc Chem Commun. 1995:2215–6.

121. Ross TL, Ermert J, Hocke C, Coenen HH. Nucleophilic 18F-fluorination of heteroaromatic iodonium salts with no-carrier-added [18F] fluoride. J Am Chem Soc. 2007;129:8018–25.

122. Wüst FR, Carlson KE, Katzenellenbogen JA. Synthesis of novel arylpyrazolo corticosteroids as potential ligands for imaging brain glucocorticoid receptors. Steroids. 2003;68:177–91.

123. Zhang MR, Kumata K, Suzuki K. A practical route for synthesizing a PET ligand containing [18F]fluorobenzene using reaction of diphenyliodonium salt with [18F]F−. Tetrahedron Lett. 2007;48:8632–5.

124. Moon B, Park J, Lee H, Lee B, Kim S. Routine production of [18F]flumazenil from iodonium tosylate using a sample pretreatment method: a 2.5-year production report. Mol Imaging Biol. 2014;16:619–25.

125. Warnier C, Lemaire C, Becker G, Zaragoza G, Giacomelli F, Aerts J, Otabashi M, Bahri MA, Mercier J, Plenevaux A, Luxen A. Enabling efficient positron emission tomography (PET) imaging of synaptic vesicle glycoprotein 2A (SV2A) with a robust and one-step radiosynthesis of a highly potent 18F-labeled ligand ([18F]UCB-H). J Med Chem. 2016;59:8955–66.

126. Hu B, Vavere AL, Neumann KD, Shulkin BL, Di Magno SG, Snyder SE. A practical, automated synthesis of meta-[18F]fluorobenzylguanidine for clinical use. ACS Chem Nerosci. 2015;6:1870–9.

127. Cardinale J, Ermert J, Humpert S, Coenen HH. Iodonium ylides for one-step, no-carrier-added radiofluorination of electron rich arenes, exemplified with 4-(([18F]fluorophenoxy)-phenylmethyl) piperidine NET and SERT ligands. RSC Adv. 2014;4:17293–9.

128. Rotstein BH, Wang L, Liu RY, Patteson J, Kwan EE, Vasdev N, Liang SH. Mechanistic studies and radiofluorination of structurally diverse pharmaceuticals with spirocyclic iodonium(III) ylides. Chem Sci. 2016;7:4407–17.

129. Stephenson NA, Holland JP, Kassenbrock A, Yokell DL, Livni E, Liang SH, Vasdev N. Iodonium ylide-mediated radiofluorination of 18F-FPEB and validation for human use. J Nucl Med. 2015;56:489–92.

130. Lee E, Kamlet AS, Powers DC, Neumann CN, Boursalian GB, Furuya T, Choi DC, Hooker JM, Ritter T. A fluoridederived electrophilic late-stage fluorination reagent for PET imaging. Science. 2011;334:639–42.

131. Lee E, Hooker JM, Ritter T. Nickel-mediated oxidative fluorination for PET with aqueous [18F]fluoride. J Am Chem Soc. 2012;134:17456–8.

132. Zlatopolskiy BD, Zischler J, Urusova EA, Endepols H, Kordys E, Frauendorf H, Mottaghy FM, Neumaier B. A practical one-pot synthesis of positron emission tomography (PET) tracers via nickel-mediated radiofluorination. Chem Open. 2015;4:457–62.

133. Hoover AJ, Lazari M, Ren H, Narayanam MK, Murphy JM, van Dam RM, Hooker JM, Ritter T. A transmetalation reaction enables the synthesis of [18F]5-fluorouracil from [18F]fluoride for human PET imaging. Organometallics. 2016;35:1008–14.

134. Ren H, Wey HY, Strebl M, Neelamegam R, Ritter T, Hooker JM. Synthesis and imaging validation of [18F]MDL100907 enabled by Ni-mediated fluorination. ACS Chem Nerosci. 2014;5:611–5.

135. Tredwell M, Preshlock SM, Taylor NJ, Gruber S, Huiban M, Passchier J, Mercier J, Génicot C, Gouverneur V. A general copper-mediated nucleophilic 18F fluorination of arenes. Angew Chem Int Ed. 2014;53:7751–5.

136. Mossine AV, Brooks AF, Makaravage KJ, Miller JM, Ichiishi N, Sanford MS, Scott PJH. Synthesis of [18F]arenes via the copper-mediated [18F]fluorination of boronic acids. Org Lett. 2015;17:5780–3.

137. Makaravage KJ, Brooks AF, Mossine AV, Sanford MS, Scott PJH. Copper-mediated radiofluorination of Arylstannanes with [18F]KF. Org Lett. 2016;18:5440–3.

138. Kessler M, Mamach M, Beutelmann R, Lukacevic M, Eilert S, Bascuñana P, Fasel A, Bengel FM, Bankstahl JP, Ross TL, Klump GM, Berding G. GABAA receptors in the Mongolian gerbil: a PET study using [18F]flumazenil to determine receptor binding in Young and old animals. Mol Imaging Biol. 2020;22:335–47.

139. Preshlock S, Calderwood S, Verhoog S, Tredwell M, Huiban M, Hienzsch A, Gruber S, Wilson TC, Taylor NJ, Cailly T, Schedler M, Collier TL, Passchier J, Smits R, Mollitor J, Hoepping A, Mueller M, Genicot C, Mercier J, Gouverneur V. Enhanced copper-mediated 18F-fluorination of aryl boronic esters provides eight radiotracers for PET applications. Chem Commun. 2016;52:8361–4.

140. Mossine AV, Tanzey SS, Brooks AF, Makaravage KJ, Ichiishi N, Miller JM, Henderson BD, Erhard T, Bruetting C, Skaddan MB, Sanford MS, Scott PJH. Synthesis of high-molar-activity [18F]6-fluoro-L-DOPA suitable for human use via cu-mediated fluorination of a BPin precursor. Nat Protoc. 2020;15:1742–59.

141. Clemente GS, Zarganes-Tzitzikas T, Dömling A, Elsinga PH. Late-stage copper-catalyzed radiofluorination of an Arylboronic Ester derivative of atorvastatin. Molecules. 2019;24:4210.

142. Zlatopolskiy BD, Zischler J, Schäfer D, Urusova EA, Guliyev M, Bannykh O, Endepols H, Neumaier B. Discovery of 7-[18F]fluorotryptophan as a novel positron emission tomography (PET) probe for the visualization of tryptophan metabolism in vivo. J Med Chem. 2018;61:189–206.

143. Zlatopolskiy BD, Zischler J, Krapf P, Zarrad F, Urusova EA, Kordys E, Endepols H, Neumaier B. Copper-mediated aromatic radiofluorination revisited: efficient production of PET tracers on a preparative scale. Chem A Eur J. 2015;21:5972–9.

144. Ichiishi N, Brooks AF, Topczewski JJ, Rodnick ME, Sanford MS, Scott PJH. Copper-catalyzed [18F]fluorination of (mesityl)(aryl)iodonium salts. Org Lett. 2014;16:3224–7.

145. Okarvi SM. Recent progress in fluorine-18 labelled peptide radiopharmaceuticals. Eur J Nucl Med. 2001;28:929–38.

146. Wester H-J, Schottelius M. Fluorine-18 labeling of peptides and proteins. In: Schubiger PA, Lehmann L, Friebe M, editors. PET chemistry—the driving force in molecular imaging. Berlin: Springer; 2007. p. 79–111.

147. Dollé F. [18F]Fluoropyridines: from conventional radiotracers to labeling of macromolecules such as proteins and oligonuclides. In: Schubiger PA, Lehmann L, Friebe M, editors. PET chemistry—the driving force in molecular imaging. Berlin: Springer; 2007. p. 113–57.

148. Müller-Platz CM, Kloster G, Legler G, Stöcklin G. [18F]Fluoroacetate: an agent for introduction no-carrier-added Fluorine-18 into Urokinase without loss of biological activity. J Label Compd Radiopharm. 1982;19:1645–6.

149. Block D, Coenen HH, Stöcklin G. N.c.a. 18F-Fluoroacylation via Fluorocarboxylic Acid Esters. J Label Compd Radiopharm. 1988;25:185–200.

150. Jacobson KA, Furlano DC, Kirk KL. A prosthetic group for the rapid introduction of fluorine into peptides and functionalized drugs. J Fluor Chem. 1988;39:339–47.

151. Guhlke S, Coenen HH, Stöcklin G. Fluoroacylation agents based on small n.c.a. [18F]Fluorocarboxylic acids. Appl Radiat Isot. 1994;45:715–27.

152. Guhlke S, Wester H-J, Burns C, Stöcklin G. (2-[18F] fluoropropionyl-(D)phe1)-octreotide, a potential radiopharmaceutical for quantitative somatostatin receptor imaging with PET: Synthesis, radiolabeling, in vitro validation and biodistribution in mice. Nucl Med Biol. 1994;21:819–25.

153. Garg PK, Garg S, Zalutsky MR. Fluorine-18 labeling of monoclonal antibodies and fragments with preservation of immunoreactivity. Bioconjug Chem. 1991;2:44–9.

154. Vaidyanathan G, Bigner DD, Zalutsky MR. Fluorine-18 labeled monoclonal antibody fragments: a potential approach for combining radioimmunoscintigraphy and positron emission tomography. J Nucl Med. 1992;33:1535–41.

155. Vaidyanathan G, Zalutsky MR. Labeling proteins with fluorine-18 using N-succinimidyl 4-[18F]fluorobenzoate. Nucl Med Biol. 1992;19:275–81.

156. Vaidyanathan G, Zalutsky MR. Improved synthesis of N-Succinimidyl-4-[18F]Fluorobenzoate and its application to the labeling of a monoclonal antibody fragment. Bioconjug Chem. 1994;5:352–6.

157. Lang L, Eckelman WC. One-step synthesis of 18F-labeled [18F]-N-succinimidyl-4-(fluoromethyl) benzoate for protein labelling. Appl Radiat Isot. 1994;45:1155–63.

158. Wester H-J, Hamacher K, Stöcklin G. A comparative study of n.c.a. Fluorine-18 labeling of proteins via acylation and photochemical conjugation. Nucl Med Biol. 1996;23:365–72.

159. Lang L, Eckelman WC. Labeling proteins at high specific activity using N-succinidyl 4-[18F](fluoromethyl) benzoate. Appl Radiat Isot. 1997;48:169–73.

160. Kilbourn MR, Dence CS, Welch MJ, Mathias CJ. Fluorine-18 labeling of proteins. J Nucl Med. 1987;28:462–70.

161. Block D, Coenen HH, Stöcklin G. N.c.a. 18F-fluoroalkylation of H-acidic compounds. J Label Compd Radiopharm. 1988;25:201–16.

162. Glaser M, Karlsen H, Solbakken M, Arukwe J, Brady F, Luthra SK, Cuthbertson A. 18F-Fluorothiols: a new approach to label peptides chemoselectively as potential tracers for positron emission tomography. Bioconjug Chem. 2004;15:1447–53.

163. Shai Y, Kirk KL, Channing MA, Dunn BB, Lesniak MA, Eastman RC, Finn RD, Roth J, Jacobson KA. Fluorine-18 labeled insulin: a prosthetic group methodology for incorporation of a positron emitter into peptides and proteins. Biochem. 1989;28:4801–6.

164. Dollé F, Hinnen F, Vaufrey F, Tavitian B, Crouzel C. A general method for labeling oligodeoxynucleotides with 18F for in vivo PET imaging. J Label Compd Radiopharm. 1997;39:319–30.

165. Haradahira T, Hasegawa Y, Furuta K, Suzuki M, Watanabe Y, Suzuki K. Synthesis of a F-18 labeled analog of antitumor prostaglandin delta 7-PGA1 methyl ester using p-[18F]fluorobenzylamine. Appl Radiat Isot. 1998;49:1551–6.

166. Jelinski M, Hamacher K, Coenen HH. C-Terminal 18F-fluoroethylamidation exemplified on [Gly-OH9] oxytocin. J Label Compd Radiopharm. 2002;45:217–29.

167. Bettio A, Honer M, Müller C, Brühlmeier M, Müller U, Schibli R, Groehn V, Schubiger PA, Ametamey SM. Synthesis and preclinical evaluation of a folic acid derivative labeled with 18F for PET imaging of folate receptor-positive Tumors. J Nucl Med. 2006;47:1153–60.

168. Shiue CY, Watanabe M, Wolf AP, Fowler JS, Salvadori P. Application of the nucleophilic substitution reaction to the synthesis of No-carrier-added [18F]fluorobenzene and other 18F-labeled aryl fluorides. J Label Compd Radiopharm. 1984;21:533–47.

169. Downer JB, McCarthy TJ, Edwards WB, Anderson CJ, Welch MJ. Reactivity of p-[18F]fluorophenacyl bromide for radiolabeling of proteins and peptides. Appl Radiat Isot. 1997;48:907–16.

170. Poethko T, Schottelius M, Thumshirn G, Hersel U, Herz M, Henriksen G, Kessler H, Schwaiger M, Wester H-J. Two-step methodology for high-yield routine radiohalogenation of peptides: 18F-labeled RGD and Octreotide analogs. J Nucl Med. 2004;45:892–902.

171. Poethko T, Schottelius M, Thumshirn G, Herz M, Haubner R, Henriksen G, Kessler H, Schwaiger M, Wester H-J. Chemoselective pre-conjugate radiohalogenation of unprotected mono- and multimeric peptides via oxime formation. Radiochim Acta. 2004;92:317–27.

172. Lange CW, VanBrocklin HF, Taylor SE. Photoconjugation of 3-azido-5-nitrobenzyl-[18F]fluoride to an oligonucleotide aptamer. J Label Compd Radiopharm. 2002;45:257–68.

173. Kolb HC, Finn MG, Sharpless KB. Click chemistry: diverse chemical function from a few good reactions. Angew Chem Int Ed. 2001;40:2004–21.

174. Marik J, Sutcliffe JL. Click for PET: rapid preparation of [18F]fluoropeptides using CuI catalyzed 1,3-dipolar cycloaddition. Tetrahedron Lett. 2006;47:6681–4.

175. Glaser M, Robins EG. 'Click labelling' in PET radiochemistry. J Label Compd Radiopharm. 52:407–14.

176. Ross TL. Recent advances in Fluorine-18 radiopharmaceuticals: the click chemistry approach applied to Fluorine-18. Curr Radiopharm. 2010;3:200–21.

177. Ramenda T, Bergmann R, Wüst FR. Synthesis of 18F-labelled Neurotensin(8-13) via copper-mediated 1,3-dipolar [3+2]cycloaddition reaction. Lett Drug Des Disc. 2007;4:279–85.

178. Campbell-Verduyn LS, Mirfeizi L, Schoonen AK, Dierckx RA, Elsinga PH, Feringa BL. Strain-promoted copper-free "click" chemistry for 18F Radiolabeling of Bombesin. Angew Chem Int Ed. 2011;50:11117–20.

179. Kettenbach K, Schieferstein H, Ross TL. 18F-labeling using click cycloadditions. Biomed Res Int. 2014;2014:361329.

180. Hausner SH, Carpenter RD, Bauer N, Sutcliffe JL. Evaluation of an integrin αVβ6-specific peptide labeled with [18F]fluorine by copper-free, strain-promoted click chemistry. Nucl Med Biol. 2013;40:233–9.

181. Kettenbach K, Ross TL. A 18F-labeled dibenzocyclooctyne (DBCO) derivative for copper-free click labelling of biomolecules. Med Chem Commun. 2016;7:654–7.

182. Kettenbach K, Reffert LM, Schieferstein H, Pektor S, Eckert R, Miederer M, Rösch F, Ross TL. Comparison study of two differently clicked 18F-folates—lipophilicity plays a key role. Pharmaceuticals. 2018;11:30.

183. Meyer JP, Adumeau P, Lewis JS, Zeglis BM. Click chemistry and radiochemistry: the first 10 years. Bioconjug Chem. 2016;27:2791–807.

184. Li Z, Cai H, Hassink M, Blackman ML, Brown RCD, Conti PS, Fox JM. Tetrazine-trans-cyclooctene ligation for the rapid construction of 18F labeled probes. Chem Commun. 2010;46:8043–5.

185. Liu S, Hassink M, Selvaraj R, Yap L-P, Park R, Wang H, Chen X, Fox JM, Li Z, Conti PS. Efficient 18F labeling of cysteine-containing peptides and proteins using tetrazine-transcyclooctene ligation. Mol Imaging. 2013;12:2121128.

186. Reiner T, Zeglis BM. The inverse electron demand Diels-Alder click reaction in radiochemistry. J Label Compd Radiopharm. 2014;57:285–90.

187. Becaud J, Karramkam M, Mu L, Schubiger PA, Ametamey SM, Smits R, Koksch B, Graham K, Cyr JE, Dinkelborg L, Suelzle D, Stellfeld T, Brumby T, Lehmann L, Srinivasan A. Development of new direct methods for 18F-labeling of peptides. J Label Compd Radiopharm. 2008;50:S215.

188. Ting R, Adam MJ, Ruth TJ, Perrin DM. Arylfluoroborates and Alkylfluorosilicates as potential PET imaging agents: high-yielding aqueous biomolecular 18F-labeling. J Am Chem Soc. 2005;127:13094–5.

189. Schirrmacher R, Bradtmöller G, Schirrmacher E, Thews O, Tillmanns J, Siessmeier T, Buchholz HG, Bartenstein P, Wängler B, Niemeyer CM, Jurkschat K. 18F-labeling of peptides by means of an Organosilicon-based fluoride acceptor. Angew Chem Int Ed. 2006;45:6047–50.

190. Schirrmacher E, Wängler B, Cypryk M, Bradtmöller G, Schäfer M, Eisenhut M, Jurkschat K, Schirrmacher R. Synthesis of p-(Di-tert-butyl[18F]fluorosilyl)benzaldehyde ([18F]SiFA-A) with high specific activity by isotopic exchange: a convenient labeling Synthon for the 18F-labeling of N-aminooxy derivatized peptides. Bioconjug Chem. 2007;18:2085–9.

191. Eiber M, Krönke M, Wurzer A, Ulbrich L, Jooß L, Maurer T, Horn T, Schiller K, Langbein T, Buschner G, Wester HJ, Weber WA. 18F-rhPSMA-7 positron emission tomography for the detection of biochemical recurrence of prostate cancer following radical prostatectomy. J Nucl Med. 2020;61:696–701.

192. Wüst FR. Fluorine-18 labelling of small molecules: the use of 18F-labeled aryl fluorides derived from no-carrier-added [18F]fluoride as Labeling precursors. In: Schubiger PA, Lehmann L, Friebe M, editors. PET chemistry—the driving force in molecular imaging. Berlin: Springer; 2007. p. 51–78.

193. Wilson AA, Dannals RF, Ravert HT, Wagner HN. Reductive amination of [18F]fluorobenzaldehydes: radiosynthesis of 2-[18F]- and 4-[18F]fluorodexetimides. J Label Compd Radiopharm. 1990;28:1189–99.

194. Negash K, Morton TE, VanBrocklin HF. [18F]Fluorobenzyltrozamicol: an efficient synthetic approach. J Label Compd Radiopharm. 1997;40:40–2.

195. Mishani E, McCarthy TJ, Brodbeck R, Dence DS, Krause JE, Welch MJ. Synthesis and evaluation of a fluorine-18 labeled NK-1 antagonist. J Label Compd Radiopharm. 1997;40:653–5.

196. Lee SY, Choe YS, Kim YR, Paik JY, Choi BW, Kim SE. Synthesis and evaluation of 5,7-dihydro-3[2-[1-(4-[18F]fluorobenzyl)-4-piperidinyl]ethyl]-6H-pyrrolo[3,2-f]-1,2-benzisoxazol-6-ome for in vivo mapping of acetylcholinesterase. Nucl Med Commun. 2004;25:591–6.

197. Mäding P, Füchtner F, Hilger CS, Halks-Miller M, Horuk R. 18F-labelling of a potent nonpeptide CCR1 antagonist for the diagnosis of the Alzheimer's disease. J Label Compd Radiopharm. 2004;47:1053–4.

198. Ryu EK, Choe YS, Park EY, Pail EY, Kim YR, Lee KH, Choi Y, Kim SE, Kim BT. Synthesis and evaluation of 2-[18F]fluoro-CP-118,954 for the in vivo mapping of acetylcholinesterase. Nucl Med Biol. 2005;32:185–91.

199. Hatano K, Ido T, Iwata R. The synthesis of o- and p-[18F]fluorobenzyl bromides asn their application to the preparation of labelled neuroleptics. J Label Compd Radiopharm. 1991;29:373–80.

200. Dence CS, John CS, Bowen WD, Welch MJ. Synthesis and evaluation of [18F] labelled benzamide: high affinity sigma receptor ligands for PET imaging. Nucl Med Biol. 1997;24:333–40.

201. Mach RH, Elder ST, Morton TE, Nowak PA, Evora PH, Scripko JG, Luedtke RR, Unsworth CD, Filtz T, Rao AV, Molinoff PB, Ehrenkaufer RLE. The use of 4[18F]fluorobenzyl iodide (FBI) in PET radiotracer synthesis: model alkylation studies and its application in the design of dopamine D1 and D2 receptor-based imaging agents. Nucl Med Biol. 1993;20:777–94.

202. Iwata R, Pascali C, Bogni A, Horvath G, Kovacs Z, Yanai K, Ido T. A new, convenient method for the preparation of 4-[18F]fluorobenzyl halides. Appl Radiat Isot. 2000;52:87–92.

203. Lemaire C, Damhaut P, Plenevaux A, Comar D. Enantioselective synthesis of 6-[Fluorine-18]-

Fluoro-L-Dopa from no-carrier-added Fluorine-18-Fluoride. J Nucl Med. 1994;35:1996–2002.

204. Lemaire C, Gillet S, Guillouet S, Plenevaux A, Aerts J, Luxen A. Highly enantioselective synthesis of no-carrier-added 6-[18F]Fluoro-L-dopa by chiral phase-transfer alkylation. Eur J Org Chem. 2004:2899–904.

205. Piarraud A, Lasne MC, Barrè L, Vaugois JM, Lancelot JC. Synthesis of no-carrier-added [18F] GBR 12936 via Wittig reaction for use in adopamine reuptake site study. J Label Compd Radiopharm. 1993;32:253–4.

206. Gerster S, Wüst FR, Pawelke B, Bergmann R, Pietzsch J. Synthesis and biodistribution of a 18F-labelled resveratrol derivative for small animal positron emission tomography (PET). Amino Acids. 2005;29:415–28.

207. Lemaire C, Guillaume M, Christiaens L, Palmer AJ, Cantineau R. A new route for the synthesis of [18F] fluoroaromatic substituted amino acids: no-carrier-added *L-p*-[18F]fluorophenylalanine. Appl Radiat Isot. 1987;38:1033–8.

208. Ding YS, Fowler JS, Gatley SJ, Dewey SL, Wolf AP. Synthesis of high specific activity (+)- and (-)-6-[18F]fluoronorepinephrine via the nucleophilic aromatic substitution reaction. J Med Chem. 1991;34:767–71.

209. Langer O, Dolle F, Valette H, Halldin C, Vaufrey F, Fuseau C, Coulon C, Ottaviani M, Någren K, Bottlaender M, Maziere B, Crouzel C. Synthesis of high-specific-radioactivity 4- and 6-[18F]fluorometaraminol-PET tracers for the adrenergic nervous system of the heart. Bioorg Med Chem. 2001;9:677–94.

210. Banks WR, Hwang DR, Borcher RD, Mantil JC. Production optimization of a bifunctional fluorine-18-labelled radiopharmaceutical intermediate: fluorine-18-fluoroacetophenone. J Label Compd Radiopharm. 1993;32:101–3.

211. Kochanny MJ, VanBrocklin HF, Kym PR, Carlson KE, O'Neil JP, Bonasera TA, Welch MJ, Katzenellenbogen JA. Fluorine-18-labeled progestin ketals: synthesis and target tissue uptake selectivity of potential imaging agents for receptor-positive breast tumors. J Med Chem. 1993;36:1120–7.

212. Allain-Barbier L, Lasne MC, Perrio-Huard C, Moreau B, Barrè L. Synthesis of 4-[18F] Fluorophenyl-alkenes and -arenes via palladium-catalyzed coupling of 4-[18F]Fluoroiodobenzene with vinyl and aryl tin reagents. Acta Chem Scand. 1998;52:480–9.

213. Forngren T, Andersson Y, Lamm B, Långström B. Synthesis of [4-18F]-1-bromo-4-fluorobenzene and its use in palladium-promoted cross-coupling reactions with organostannanes. Acta Chem Scand. 1998;52:475–9.

214. Marrière E, Rouden J, Tadino V, Lasne MC. Synthesis of analogues of (-)-cytisine for in vivo studies of nicotinic receptors using positron emission tomography. Org Lett. 2000;2:1121–4.

215. Wüst FR, Kniess T. Synthesis of 18F-labelled nucleosides using Stille cross-coupling reactions with [4-18F]fluoroiodobenzene. J Label Compd Radiopharm. 2004;47:457–68.

216. Wüst FR, Höhne A, Metz P. Synthesis of 18F-labelled COX-2 inhibitors via Stille reaction with 4-[18F]fluoroiodobenzene. Org Biomol Chem. 2005;3:503–7.

217. Wüst FR, Kniess T. Synthesis of 4-[18F]fluoroiodobenzene and its applicationin the Sonogashira cross-coupling reaction with terminal alkynes. J Label Compd Radiopharm. 2003;46:699–713.

218. Steiniger B, Wüst FR. Synthesis of 18F-labelled biphenyls via Suzuki cross-coupling with 4-[18F] fluoroiodobenzene. J Label Compd Radiopharm. 2006;49:817–27.

219. Marrière E, Chazalviel L, Dhilly M, Toutain J, Perrio C, Dauphin F, Lasne MC. Synthesis of [18F]RP 62203, a potent and selective serotonine 5-HT2A receptor antagonist and biological evaluation with ex-vivo autoradiography. J Label Compd Radiopharm. 1999;42:S69–71.

220. Wüst FR, Kniess T. Synthesis of 18F-labelled sigma-2 receptor ligands for positron emission tomograpy (PET) via *latN*-arylation with 4-[18F] fluoroiodobenzene. J Label Compd Radiopharm. 2005;48:31–43.

221. Ludwig T, Gail R, Coenen HH. New ways to n.c.a. radiofluorinated aromatic compounds. Isotop Lab Compds. 2001;7:358–61.

222. Gail R, Coenen HH. A one step preparation of the n.c.a. fluorine-18-labelled synthons: 4-fluorobromobenzene and 4-fluoroiodobenzene. Appl Radiat Isot. 1994;45:105–11.

223. Gail R, Hocke C, Coenen HH. Direct n.c.a. 18F-fluorination of halo- and alkylarenes via corresponding diphenyliodonium salts. J Label Compd Radiopharm. 1997;40:50–2.

224. Shah A, Pike VW, Widdowson DA. The synthesis of [18F]Fluoroarenes from the reaction of cyclotron-produced [18F]fluoride ion with diaryliodonium salts. J Chem Soc Perkin Trans. 1998;1:2043–6.

225. Ermert J, Hocke C, Ludwig T, Gail R, Coenen HH. Comparison of pathways to the versatile synthon of no-carrier-added 1-bromo-4-[18F]fluorobenzene. J Label Compd Radiopharm. 2004;47:429–41.

226. Shiue C-Y, Fowler JS, Wolf AP, Watanabe M, Arnett CD. Syntheses and specific activity determinations of no-carrier-added Fluorine-18-labeled neuroleptic drugs. J Nucl Med. 1985;26:181–6.

227. Collins M, Lasne MC, Barre L. Rapid synthesis of *N,N'*-disubstituted piperazines. Application to the preparation of no carrier added 1-(4-[18F]fluorophenyl)piperazine and of an [18F]-selective ligand of serotoninergic receptors (5HT2 antagonist). J Chem Soc Perkin Trans. 1992;1:3185–8.

228. VanBrocklin HF, O'Neil JP, Hom DL, Gibbs AR. Synthesis of [18F]fluoroanilines: precursors to [18F]fluoroanilinoquilazolines. J Label Compd Radiopharm. 2001;44:S880–2.

229. Olma S, Ermert J, Coenen HH. Preparation of n.c.a. [18F]fluorophenylureas. J Label Compd Radiopharm. 2005;48:S175.

230. Vasdev N, Dorff PN, Gibbs AR, Nandanan E, Reid LM, O'Neil JP, VanBrocklin HF. Synthesis of 6-acrylamido-4-(2-[18F]fluoroanilino)quinazoline: a prospective irreversible EGFR binding probe. J Label Compd Radiopharm. 2005;48:109–15.

231. Seimbille Y, Phelps ME, Czernin J, Silverman DHS. Fluorine-18 labeling of 6,7-disubstituted anilinoquinazoline derivatives for positron emission tomography (PET) imaging of tyrosine kinase receptors: synthesis of 18F-Iressa and related molecular probes. J Label Compd Radiopharm. 2005;48:829–43.

232. Kirk KL, Creveling CR. The chemistry and biology of ring-fluorinated biogenic amines. Med Res Rev. 1984;4:189–220.

233. Barrè L, Barbier L, Lasne MC. Investigation of possible routes to no-carrier-added 4-[18F]Fluorophenol. J Label Compd Radiopharm. 1993;35:167–8.

234. Ludwig T, Ermert J, Coenen HH. 4-[18F]fluoroarylalkylethers via an improved synthesis of n.c.a. 4-[18F]fluorophenol. Nucl Med Biol. 2002;29:255–62.

235. Stoll T, Ermert J, Oya S, Kung HF, Coenen HH. Application of n.c.a. 4-[18F]fluorophenol in diaryl ether syntheses of 2-(4-[18F]fluorophenoxy)-benzylamines. J Label Compd Radiopharm. 2004;47:443–55.

236. Ludwig T, Ermert J, Coenen HH. Synthesis of the dopamine-D4 receptor ligand 3-(4-[18F]fluorophenoxy)propyl-(2-(4-tolyloxy)ethyl)amine via optimised n.c.a. 4-[18F]fluorophenol. J Label Compd Radiopharm. 2001;44:S1–3.

237. Casella V, Christman DR, Ido T, Wolf AP. Excitation-function for N-14 (p, alpha) C-11 reaction up to 15-MeV. Radiochim Acta. 1978;25:17–20.

238. Buckley KR, Huser J, Jivan S, Chun KS, Ruth TJ. 11C-methane production in small volume, high pressure gas targets. Radiochim Acta. 2000;88:201–5.

239. Buckley KR, Jivan S, Ruth TJ. Improved yields for the in situ production of [11C]CH4 using a niobium target chamber. Nucl Med Biol. 2004;31:825–7.

240. Ferrieri RA, Wolf AP. The chemistry of positron emitting Nucleogenic (hot) atoms with regard to preparation of labelled compounds of practical utility. Radiochim Acta. 1983;34:69–83.

241. Wolf AP, Redvanly CS. Carbon-11 and radiopharmaceuticals. Appl Radiat Isot. 1977;28:29–48.

242. Schirbel A, Holschbach MH, Coenen HH. N.c.a. [11C]CO2 as a safe substitute for phosgene in the carbonylation of primary amines. J Label Compd Radiopharm. 1999;42:537–51.

243. Pike VW, Horlock PL, Brown C, Clarck JC. The remotely controlled preparation of a 11C-labelled radiopharmaceutical - [1-11C]acetate. Appl Radiat Isot. 1984;35:623–7.

244. Kruijer PS, Ter Linden T, Mooij R, Visser FC, Herscheid JDM. A practical method for the preparation of [11C]acetate. Appl Radiat Isot. 1995;46:317–21.

245. Taddei C, Gee AD. Recent progress in [11C]carbon dioxide ([11C]CO2) and [11C]carbon monoxide ([11C]CO) chemistry. J Label Compd Radiopharm. 2018;61:237–51.

246. Hosoya T, Sumi K, Doi H, Wakao M, Suzuki M. Rapid methylation on carbon frameworks useful for the synthesis of 11CH3-incorporated PET tracers: Pd(0)-mediated rapid coupling of methyl iodide with an alkenyltributylstannane leading to a 1-methylalkene. Org Biomol Chem. 2006;4:410–5.

247. Comar D, Maziere M, Crouzel M. Synthesis and metabolism of 11C-chlorpromazine methiodide. Radiopharm Label Compd. 1973;7:461–9.

248. Långström B, Lunquvist H. The preparation of [11C]methyl iodide and its use in the synthesis of [11C]methyl-L-methionine. Appl Radiat Isot. 1976;27:357–63.

249. Oberdorfer F, Hanisch M, Helus F, Maier-Borst W. A new procedure for the preparation of 11C-labelled methyl iodide. Appl Radiat Isot. 1985;36:435–8.

250. Holschbach MH, Schüller M. A new simple on-line method for the preparation of n.c.a. [11C]methyl iodide. Appl Radiat Isot. 1993;44:779–80.

251. Larsen P, Ulin J, Dahlstrom K. A new method for production of 11C-labelled methyl iodide from [11C]methane. J Label Compd Radiopharm. 1995;37:73–5.

252. Link JM, Clark JC, Larsen P, Krohn KA. Production of [11C]methyl iodide by reaction of [11C]CH4 with I2. J Label Compd Radiopharm. 1995;37:76–8.

253. Link JM, Krohn KA, Clark JC. Production of [11C]CH3I by single pass reaction of [11C]CH4 with I2. Nucl Med Biol. 1997;24:93–7.

254. Larsen P, Ulin J, Dahlstrom K, Jensen M. Synthesis of [11C]Iodomethane by iodination of [11C]methane. Appl Radiat Isot. 1997;48:153–7.

255. Noguchi J, Suzuki K. Automated synthesis of the ultra high specific activity of [11C]Ro15-4513 and its application in an extremely low concentration region to an ARG study. Nucl Med Biol. 2003;30:335–43.

256. Zhang MR, Suzuki K. Sources of carbon which decrease the specific activity of [11C]CH3I synthesized by the single pass I2 method. Appl Radiat Isot. 2005;62:447–50.

257. Jewett DM. A simple synthesis of [11C]methyl triflate. Appl Radiat Isot. 1992;43:1383–5.

258. Shao X, Schnau PL, Fawaz M, Scott PJH. Enhanced radiosyntheses of [11C]raclopride and [11C]DASB using ethanolic loop chemistry. Nucl Med Biol. 2013;40:109–16.

259. Någren K, Halldin C, Müller L, Swahn CG, Lehikoinen P. Comparison of [11C]methyl triflate and [11C]methyl iodide in the synthesis of PET radioligands such as [11C]beta-CIT and [11C]beta-CFT. Nucl Med Biol. 1995;22:965–79.

260. Lundkvist C, Sandell J, Någren K, Pike VW, Halldin C. Improved synthesis of the PET radioligands [11C]FLB 457, [11C]MDL 100907 and [11C]β-CIT-FE,

by the use of [11C]methyl triflate. J Label Compd Radiopharm. 1998;41:545–56.

261. Någren K, Halldin C. Methylation of amide and thiol functions with [11C]methyl triflate, as exemplified by [11C]NMSP, [11C]flumazenil and [11C]methionine. J Label Compd Radiopharm. 1998;41:831–41.

262. Klunk WE, Engler H, Nordberg A, Wang Y, Blomqvist G, Holt DP, Bergström M, Savitcheva I, Huang GF, Estrada G, Ausén B, Debnath ML, Barletta J, Price JC, Sandell J, Lopresti BJ, Wall A, Koivisto P, Antoni G, Mathis CA, Långström B. Imaging brain amyloid in Alzheimer's disease with Pittsburgh compound-B. Ann Neurol. 2004;55:306–19.

263. Maziere M, Hantraye P, Prenant C, Sastre J, Comar D. Synthesis of ethyl 8-fluoro-5,6-dihydro5- [11C]methyl-6-oxo-4H-imidazo[1,5-a] [1,4]benzodiazepine-3-carboxylate (RO 15.1788-11C): a specific radioligand for the in vivo study of central benzodiazepine receptors by positron emission tomography. Appl Radiat Isot. 1984;35:973–6.

264. Suzuki K, Inoue O, Hashimoto K, Yamasaki T, Kuchiki M, Tamate K. Computer-controlled large scale production of high specific activity [11C]RO 15-1788 for PET studies of benzodiazepine receptors. Appl Radiat Isot. 1985;36:971–6.

265. Suzuki K, Inoue O, Tamate K, Mikado F. Production of 3-N-[11C]methylspiperone with high specific activity and high radiochemical purity for PET studies: suppression of its radiolysis. Appl Radiat Isot. 1990;41:593–9.

266. Farde L, Ehrin E, Eriksson L, Greitz T, Hall H, Hedstrom C-G, Litton J-E, Sedvall G. Substituted benzamides as ligands for visualization of dopamine receptor binding in the human brain by positron emission tomography. Proc Natl Acad Sci U S A. 1985;82:3863–7.

267. Farde L, Hall H, Ehrin E, Sedvall G. Quantitative analysis of D2 dopamine receptor binding in the living human brain by PET. Science. 1986;231:258–61.

268. Långström B, Antoni G, Gullberg P, Halldin C, Malmborg P, Någren K, Rimland A, Svärd H. Synthesis of L- and D-[Methyl-11C]Methionine. J Nucl Med. 1987;28:1037–40.

269. Krasikova RN, Andersson J, Truong P, Nag S, Shchukin EV, Halldin C. A fully automated one-pot synthesis of [carbonyl-11C]WAY-100635 for clinical PET applications. Appl Radiat Isot. 2009;67:73–8.

270. Iwata R, Pascali C, Yuasa M, Yanai K, Takahashi T, Ido T. On-line [11C]methylation using [11C]methyl iodide for the automated preparation of 11C-radiopharmaceuticals. Appl Radiat Isot. 1992;43:1083–8.

271. Pascali C, Bogni A, Iwata R, Decise D, Crippa F, Bombardieri E. High effciency preparation of L-[S-methyl-11C]methionine by on-column [11C] methylation on C18 Sep-Pak. J Label Compd Radiopharm. 1999;42:715–24.

272. Pascali C, Bogni A, Iwata R, Cambie M, Bombardieri E. [11C]methylation on a C18 Sep-Pak cartridge: a convenient way to produce [N-methyl-11C]choline. J Label Compd Radiopharm. 2000;43:195–203.

273. Watkins GL, Jewett DM, Mulholland GK, Kilbourn MR, Toorongian SA. A captive solvent method for rapid N-[11C]methylation of secondary amides: application to the benzodiazepine, 4′-chlorodiazepam (RO5-4864). Appl Radiat Isot. 1988;39:441–4.

274. Wilson AA, Garcia A, Jin L, Houle S. Radiotracer synthesis from [11C]-iodomethane: a remarkable simple captive solvent method. Nucl Med Biol. 2000;27:529–32.

275. Iwata R, Pascali C, Bogni A, Miyake Y, Yanai K, Ido T. A simple loop method for the automated preparation of [11C]raclopride from [11C]methyl triflate. Appl Radiat Isot. 2001;55:17–22.

276. Iwata R, Pascali C, Bogni A, Yanai K, Kato M, Ido T, Ishiwata K. A combined loop-SPE method for the automated preparation of [11C]doxepin. J Label Compd Radiopharm. 2002;45:271–80.

277. Studenov AR, Jivan S, Adam MJ, Ruth TJ, Buckley KR. Studies of the mechanism of the in-loop synthesis of radiopharmaceuticals. Appl Radiat Isot. 2004;61:1195–201.

278. Lu S-Y, Watts P, Chin FT, Hong J, Musachio JL, Briard E, Pike VW. Syntheses of 11C- and 18F-labeled carboxylic esters within a hydrodynamically-driven micro-reactor. Lab Chip. 2004;4:523–5.

279. Kihlberg T, Gullberg P, Langström B. [11C] Methylenetriphenylphosphorane, a new 11C precursor, used in a one-pot Wittig synthesis of [Beta-11C]styrene. J Label Compd Radiopharm. 1990;28:1115–20.

280. Zessin J, Steinbach J, Johannsen B. Synthesis of triphenylarsonium [11C]methylide, a new 11C-precursor. Application in the preparation of [2-11C]indole. J Label Compd Radiopharm. 1999;42:725–36.

281. Bjurling P, Watanabe Y, Tokushige M, Oda T, Langström B. Syntheses of Beta-11C-Labeled L-tryptophan and 5-Hydroxy-L-tryptophan using a multi-enzymatic reaction route. J Chem Soc Perkin Trans. 1989;1:1331–4.

282. Ikemoto M, Sasaki M, Haradahira T, Yada T, Omura H, Furuya Y, Watanabe Y, Suzuki K. Synthesis of L-[beta-11C]amino acids using immobilized enzymes. Appl Radiat Isot. 1999;50:715–21.

283. Fasth KJ, Langström B. Asymmetric synthesis of L-[beta-11C]amino acids using a chiral nickel-complex of the Schiff-base of (S)-O-[(N-benzylprolyl)-amino]benzophenone and glycine. Acta Chem Scand. 1990;44:720–5.

284. Mosevich IK, Kuznetsova OF, Vasil'ev DA, Anichkov AA, Korsakov MV. Automated synthesis of [3-11C]-L-alanine involving asymmetric alkylation with (CH3I)-11C of the nickel complex of the Schiff base derived from glycine and (S)-2-N-(N-

benzylprolyl)aminobenzophenone. Radiochemistry. 1999;41:273–80.

285. Harada N, Nishiyama S, Sato K, Tsukada H. Development of an automated synthesis apparatus for L-[3-11C] labeled aromatic amino acids. Appl Radiat Isot. 2000;52:845–50.

286. Kihlberg T, Langström B. Cuprate-mediated 11C-C coupling reactions using Grignard-reagents and 11C alkyl iodides. Acta Chem Scand. 1994;48:570–7.

287. Hostetler ED, Fallis S, McCarthy TJ, Welch MJ, Katzenellenbogen JA. Improved methods for the synthesis of [omega-11C]palmitic acid. J Org Chem. 1998;63:1348–51.

288. Wuest F, Dence CS, McCarthy TJ, Welch MJ. A new approach for the synthesis of [11C]-labeled fatty acids. J Label Compd Radiopharm. 2000;43:1289–300.

289. Conti PS, Alauddin MM, Fissekis JR, Schmall B, Watanabe KA. Synthesis of 2′-fluoro-5-[11C]-methyl-1-beta-D-arabinofuranosyluracil ([11C]-FMAU)—a potential nucleoside analog for in-vivo study of cellular proliferation with PET. Nucl Med Biol. 1995;22:783–9.

290. De Vries EFJ, van Waarde A, Harmsen MC, Mulder NH, Vaalburg W, Hospers GAP. [11C]FMAU and [18F]FHPG as PET tracers for herpes simplex virus thymidine kinase enzyme activity and human cytomegalovirus infections. Nucl Med Biol. 2000;27:113–9.

291. Karramkam M, Demphel S, Hinnen F, Trognon C, Dolle F. Methylation of the thiophene ring using carbon-11-labelled methyl iodide: formation of 3-[11C] methylthiophene. J Label Compd Radiopharm. 2003;46:255–61.

292. Andersson Y, Cheng AP, Langström B. Palladium-promoted coupling reactions of [11C]methyl-iodide with organotin and organoboron compounds. Acta Chem Scand. 1995;49:683–8.

293. Samuelsson L, Langström B. Synthesis of 1-(2′-deoxy-2′-fluoro-beta-D-arabinofuranosyl)-[methyl-11C]thymine ([11C]FMAU) via a Stille cross-coupling reaction with [11C]methyl iodide. J Label Compd Radiopharm. 2003;46:263–72.

294. Madsen J, Merachtsaki P, Davoodpour P, Bergström M, Langström B, Andersen K, Thomsen C, Martiny L, Knudsen GM. Synthesis and biological evaluation of novel carbon-11-labelled analogues of citalopram as potential radioligands for the serotonin transporter. Bioorg Med Chem. 2003;11:3447–56.

295. Huang YY, Narendran R, Bischoff F, Guo NN, Zhu ZH, Bae SA, Lesage AS, Laruelle M. A positron emission tomography radioligand for the in vivo labeling of metabotropic glutamate 1 receptor: (3-ethyl-2-[11C]methyl-6-quinolinyl)   (cis-4-methoxycyclohexyl)methanone. J Med Chem. 2005;48:5096–9.

296. Wüst F, Zessin J, Johannsen B. A new approach for 11C-C bond formation: synthesis of 17 alpha-(3′-[11C]prop-1-yn-1-yl)-3-methoxy-3,17   beta-estradiol. J Label Compd Radiopharm. 2003;46:333–42.

297. Wuest FR, Berndt M. 11C-C bond formation by palladium-mediated cross-coupling of alkenylzirconocenes with [11C]methyl iodide. J Label Compd Radiopharm. 2006;49:91–100.

298. Bjorkman M, Doi H, Resul B, Suzuki M, Noyori R, Watanabe Y, Langström B. Synthesis of a 11C-labelled prostaglandin F-2 alpha analogue using an improved method for Stille reactions with [11C]methyl iodide. J Label Compd Radiopharm. 2000;43:1327–34.

299. Sandell J, Halldin C, Sovago J, Chou YH, Gulyas B, Yu MX, Emond P, Nagren K, Guilloteau D, Farde L. PET examination of [11C]5-methyl-6-nitroquipazine, a radioligand for visualization of the serotonin transporter. Nucl Med Biol. 2002;29:651–6.

300. Langer O, Forngren T, Sandell J, Dolle F, Langström B, Nagren K, Halldin C. Preparation of 4-[11C] methylmetaraminol, a potential PET tracer for assessment of myocardial sympathetic innervation. J Label Compd Radiopharm. 2003;46:55–65.

301. Hamill TG, Krause S, Ryan C, Bonnefous C, Govek S, Seiders TJ, Cosford NDP, Roppe J, Kamenecka T, Patel S, Gibson RE, Sanabria S, Riffel K, Eng WS, King C, Yang XQ, Green MD, O'Malley SS, Hargreaves R, Burns HD. Synthesis, characterization, and first successful monkey imaging studies of metabotropic glutamate receptor subtype 5 (mGluR5) PET radiotracers. Synapse. 2005;56:205–16.

302. Hosoya T, Sumi K, Doi H, Wakao M, Suzuki M. Rapid methylation on carbon frameworks useful for the synthesis of 11CH3-incorporated PET tracers: Pd(0)-mediated rapid coupling of methyl iodide with an alkenyltributylstannane leading to a 1-methylalkene. Org Biomol Chem. 2006;4:410–5.

303. Clark JC, Crouzel C, Meyer GJ, Strijckmans K. Current methodology for oxygen-15 production for clinical use. Appl Radiat Isot. 1987;38:597–600.

304. Welch MJ, Kilbourn MR. A remote system for routine production of oxygen-15 radiopharmaceuticals. J Label Compd Radiopharm. 1985;22:1193–200.

305. Meyer GJ, Osterholz A, Hundeshagen H. O-15-water constant infusion system for clinical routine application. J Label Compd Radiopharm. 1986;23:1209–10.

306. Kabalka GW, Lambrecht RM, Sajjad M, Fowler JS, Kunda SA, McCollum GW, MacGregor R. Synthesis of 15O-labeled butanol via organoborane chemistry. Appl Radiat Isot. 1985;36:853–5.

307. Sajjad M, Lambrecht RM, Wolf AP. Cyclotron isotopes and radiopharmaceuticals 37. Exitation-functions for the O-16(p,alpha)N-13 and N-14(p,pn) N-13 reactions. Radiochim Acta. 1986;39:165–8.

308. Vaalburg W, Kamphuis JA, Beerling-van der Molen HD, Reiffers S, Rijskamp A, Woldring MG. An improved method for the cyclotron production of 13N-ammonia. Appl Radiat Isot. 1975;26:316–8.

309. Wieland B, Bida G, Padgett H, Hendry G, Zippi E, Kabalka G, Morelle J-L, Verbruggen R, Ghyoot M. In target production of 13N-ammonia via proton

irradiation of aqueous ethanol and acetic acid mixtures. Appl Radiat Isot. 1991;42:1095–8.

310. Barrio JR, Baumgartner FJ, Henze E, Stauber MS, Egbert JE, MacDonald NS, Schelbert HR, Phelps ME, Liu F-T. Synthesis and myocardial kinetics of N-13 and C-11 labeled branched-chain L-amino acids. J Nucl Med. 1983;24:937–44.

311. Gómez-Vallejo V, Borrell JI, Llop J. A convenient synthesis of 13N-labelled azo compounds: a new route for the preparation of amyloid imaging PET probes. Eur J Med Chem. 2010;45:5318–23.

312. Gaja V, Gómez-Vallejo V, Puigivila M, Pérez-Campaña C, Martin A, García-Osta A, Calvo-Fernández T, Cuadrado-Tejedor M, Franco R, Llop J. Synthesis and evaluation of 13N-labelled azo compounds for β-amyloid imaging in mice. Mol Imaging Biol. 2014;16:538–49.

313. Eder M, Neels O, Müller M, Bauder-Wüst U, Remde Y, Schäfer M, Hennrich U, Eisenhut M, Afshar-Oromieh A, Haberkorn U, Kopka K. Novel preclinical and radiopharmaceutical aspects of [68Ga]Ga-PSMA-HBED-CC: a new PET tracer for imaging of prostate cancer. Pharmaceuticals. 2014;7:779–96.

314. Henze M, Dimitrakopoulou-Strauss A, Milker-Zabel S, Schuhmacher J, Strauss LG, Doll J, Maecke HR, Eisenhut M, Debus J, Haberkorn U. Characterization of 68Ga-DOTA-D-Phe1-Tyr3-octreotide kinetics in patients with meningiomas. J Nucl Med. 2005;46:763–9.

315. Notni J, Wester HJ. Re-thinking the role of radiometal isotopes: towards a future concept for theranostic radiopharmaceuticals. J Label Compd Radiopharm. 2018;61:141–53.

316. Lindner T, Loktev A, Altmann A, Giesel F, Kratochwil C, Debus J, Jäger D, Mier W, Haberkorn U. Development of Quinoline-based theranostic ligands for the targeting of fibroblast activation protein. J Nucl Med. 2018;59:1415–22.

317. Langer L, Hess A, Reffert LM, Bankstahl JP, Thackeray JT, Bengel FM, Ross TL. Visualisation of fibrosis after tissue damage with PET—a tracer for the fibroblast activation protein. J Label Compd Radiopharm. 2019;62:S535.

318. Rösch F. Past, present and future of 68Ge/68Ga generators. Appl Radiat Isot. 2013;76:24–30.

319. Kumar K. The current status of the production and supply of Gallium-68. Cancer Biother Radiopharm. 2020;35:163–6.

320. Lin M, Waligorski GJ, Lepera CG. Production of curie quantities of 68Ga with a medical cyclotron via the 68Zn(p,n)68Ga reaction. Appl Radiat Isot. 2018;133:1–3.

321. Tieu W, Hollis CA, Kuan KKW, Takhar P, Stuckings M, Spooner N, Malinconico M. Rapid and automated production of [68Ga]gallium chloride and [68Ga]Ga-DOTA-TATE on a medical cyclotron. Nucl Med Biol. 2019;74-75:12–8.

322. Nelson BJB, Wilson J, Richter S, Duke MJM, Wuest M, Wuest F. Taking cyclotron 68Ga production to the next level: expeditious solid target production of

68Ga for preparation of radiotracers. Nucl Med Biol. 2020;80-81:24–31.

323. Riga S, Cicoria G, Pancaldi D, Zagni F, Vichi S, Dassenno M, Mora L, Lodi F, Morigi MP, Marengo M. Production of Ga-68 with a General Electric PETtrace cyclotron by liquid target. Phys Med. 2018;55:116–26.

324. Pandey MK, Byrne JF, Schlasner KN, Schmit NR, DeGrado TR. Cyclotron production of 68Ga in a liquid target: effects of solution composition and irradiation parameters. Nucl Med Biol. 2019;74–75:49–55.

325. Spang P, Herrmann C, Roesch F. Bifunctional Gallium-68 chelators: past, present, and future. Semin Nucl Med. 2016;46:373–94.

326. Eder M, Wangler B, Knackmuss S, Legall F, Little M, Haberkorn U, Mier W, Eisenhut M. Tetrafluorophenolate of HBED-CC: a versatile conjugation agent for 68Ga-labeled small recombinant antibodies. Eur J Nucl Med Mol Imaging. 2008;35:1878–86.

327. Notni J, Šimeček J, Hermann P, Wester HJ. TRAP, a powerful and versatile framework for gallium-68 radiopharmaceuticals. Chemistry. 2011;17:14718–22.

328. Seemann J, Waldron BP, Roesch F, Parker D. Approaching "kit-type" labelling with 68Ga: the DATA chelators. ChemMedChem. 2015;10:1019–26.

329. Seemann J, Waldron B, Parker D, Roesch F. DATATOC: a novel conjugate for kit-type 68Ga labelling of TOC at ambient temperature. EJNMMI Radiopharm Chem. 2017;1:4.

330. Imberti C, Chen YL, Foley CA, Ma MT, Paterson BM, Wang Y, Young JD, Hider RC, Blower PJ. Tuning the properties of tris(hydroxypyridinone) ligands: efficient 68Ga chelators for PET imaging. Dalton Trans. 2019;48:4299–313.

331. Mukherjee A, Pandey U, Chakravarty R, Sarma H, Dash A. Single vial kit formulation for preparation of PET radiopharmaceutical: 68Ga-DOTA-TOC. J Radioanal Nucl Chem. 2014;302:1253–8.

332. Revy A, Hallouard F, Joyeux-Klamber S, Skanjeti A, Rioufol C, Fraysse M. Feasibility and evaluation of automated methods for radiolabeling of radiopharmaceutical kits with Gallium-68. Curr Radiopharm. 2019;12:229–37.

333. Hofman MS, Eu P, Jackson P, Hong E, Binns D, Iravani A, Murphy D, Mitchell C, Siva S, Hicks RJ, Young JD, Blower PJ, Mullen GE. Cold kit for prostate-specific membrane antigen (PSMA) PET imaging: phase 1 study of 68Ga-Tris(Hydroxypyridinone)-PSMA PET/CT in patients with prostate Cancer. J Nucl Med. 2018;59:625–31.

334. Derlin T, Schmuck S, Juhl C, Zörgiebel J, Schneefeld SM, Walte ACA, Hueper K, von Klot CA, Henkenberens C, Christiansen H, Thackeray JT, Ross TL, Bengel FM. PSA-stratified detection rates for [68Ga]THP-PSMA, a novel probe for rapid kit-based 68Ga-labeling and PET imaging, in patients

with biochemical recurrence after primary therapy for prostate cancer. Eur J Nucl Med Mol Imaging. 2018;45:913–22.

335. Sinnes JP, Nagel J, Waldron BP, Maina T, Nock BA, Bergmann RK, Ullrich M, Pietzsch J, Bachmann M, Baum RP, Rösch F. Instant kit preparation of 68Ga-radiopharmaceuticals via the hybrid chelator DATA: clinical translation of [68Ga]Ga-DATA-TOC. EJNMMI Res. 2019;9:48.

336. Seevers RH, Counsell RE. Radioiodination techniques for small organic molecules. Chem Rev. 1982;82:575–90.

337. Coenen HH, Mertens J, Mazière B. Radioiodination reactions for radiopharmaceuticals—compendium for effective synthesis strategies. Dordrecht: Springer; 2006.

338. Jirousek L. On the chemical nature of iodinating species. J Radioanal Chem. 1981;65:139–54.

339. Coenen HH, El-Wetery AS, Stöcklin G. Further studies on practically carrier-free 123I-iodination and 75,77Br-bromination of aromatic substrates. J Label Compd Radiopharm. 1981;18:114–5.

340. Youfeng H, Coenen HH, Petzold G, Stöcklin G. A comparative study of radioiodination of simple aromatic compounds via N-halosuccinimides and chloramine-t in TFAA. J Label Compd Radiopharm. 1982;19:807–19.

341. Mennicke E, Holschbach M, Coenen HH. Direct N.C.A. electrophilic radioiodination of deactivated arenes with N-chlorosuccinimide. J Label Compd Radiopharm. 2000;43:721–37.

342. Moerlein SM, Mathis CA, Yano Y. Comparative evaluation of electrophilic aromatic iododemetallation techniques for labeling radiopharmaceuticals with iodine-122. Appl Radiat Isot. 1987;38:85–90.

343. Mennicke E, Hennecken H, Holschbach M, Coenen HH. Thallium-tris(trifluoroacetate): a powerful reagent for the N.c.a: radioiodination of weakly activated arenes. Eur J Nucl Med. 1998;25:843–5.

344. Morrison M, Bayse GS. Catalysis of iodination by lactoperoxidase. Biochem. 1970;9:2995–3000.

345. Moore DH, Wolf W. Electrochemical radioiodination of estradiol. J Label Compd Radiopharm. 1978;15:443–50.

346. Moerlein SM, Beyer W, Stöcklin G. No-carrier-added radiobromination and radioiodination of aromatic rings using in situ generated peracetic acid. J Chem Soc Perkin Trans. 1988;1:779–86.

347. McKillop A, Taylor EC, Fowler JS, Zelesko MJ, Hunt JD, McGillivray G. Thallium in organic synthesis. X. A one-step synthesis of aryl iodides. Tetrahedron Lett. 1969;10:2427–30.

348. Kabalka GW, Varma RS. The synthesis of radiolabeled compounds via organometallic intermediates. Tetrahedron. 1989;45:6601–21.

349. Flanagan RJ. The synthesis of halogenated radiopharmaceuticals using organomercurials. In: Emran AM, editor. New trends in radiopharmaceutical synthesis quality assurance and regulatory control. New York: Plenum Press; 1991. p. 279–88.

350. Moerlein SM, Coenen HH. Regiospecific no-carrier-added radiobromination and radioiodination of aryl-trimethyl Group IVb organometallics. J Chem Soc Perkin Trans. 1985;1:1941–7.

351. Lindley J. Tetrahedron report number 163: copper assisted nucleophilic substitution of aryl halogen. Tetrahedron. 1984;40:1433–56.

352. Clark JH, Jones CW. Reverse halogenation using supported copper(I) iodide. J Chem Soc Chem Commun. 1987:1409–11.

353. Bolton AE, Hunter WM. The labelling of proteins to high specific radioactivities by conjugation to a 125I-containing acylating agent. Appl Radioimmun Assay Biochem J. 1973;133:529–33.

354. Rudinger J, Ruegg U. Appendix: preparation of N-succinimidyl 3-(4-hydroxyphenyl)propionate. Biochem J. 1973;133:538–9.

355. Glaser M, Carroll VA, Collinbridge DR, Aboagye EO, Price P, Bicknell R, Harris AL, Luthra SK, Brady F. Preparation of the iodine-124 derivative of the Bolton-Hunter reagent ([124I]I-SHPP) and its use for labelling a VEGF antibody as a PET tracer. J Label Compd Radiopharm. 2002;45:1077–90.

356. Wood FT, Wu MM, Gerhart JJ. The radioactive labeling of proteins with an iodinated amidination reagent. Anal Biochem. 1975;69:339–49.

357. Ram S, Fleming E, Buchsbaum DJ. Development of radioiodinated 3 Iodophenylisothiocyanate for coupling to monoclonal antibodies. J Nucl Med. 1992;33:1029.

358. Khawli LA, Chen FM, Alaudin MM, Stein AL. Radioiodinated monoclonal-antibody conjugates—synthesis and comparable-evaluation. Antibody Immunoconj Radiopharm. 1991;4:163–82.

359. Ali SA, Eary JF, Warren SD, Krohn KA. Synthesis and radioiodinationof tyramine cellobiose for labeling monoclonal antibodies. Nucl Med Biol. 1988;15:557–61.

360. Khawli LA, van de Abeele AD, Kassis AI. N-(m-[125I]iodophenyl)maleimide: an agent for high yield radiolabeling of antibodies. Nucl Med Biol. 1992;19:289–95.

361. Kassis AI, Adelstein SJ, Haydock S, Sastry KSR, McElvany KD, Welch MJ. Lethality of Auger electrons from the decay of bromine-77 in the DNA of mammalian cells. Radiat Res. 1982;90:362–73.

362. DeSombre ER, Hughes A, Mease RC, Harpet PV. Comparison of the distribution of bromine-77-bromovinyl steroidal and triphenylethylene estrogens in the immature rat. J Nucl Med. 1990;31:1534–42.

363. DeSombre ER, Hughes A, Gatley SJ, Schwartz JL, Harper PV. Receptordirected radiotherapy: a new approach to therapy of steroid receptor positive cancers. Prog Clin Biol Res. 1990;322:295–309.

364. Downer JB, Jones LA, Engelbach JA, Lich LL, Mao W, Carlson KE, Katzenellenbogen JA, Welch MJ. Comparison of animal models for the evaluation of radiolabeled androgens. Nucl Med Biol. 2001;28:613–26.

365. Tolmachev V, Lövqvist A, Einarsson L, Schultz J, Lundqvist H. Production of 76Br by a low-energy cyclotron. Appl Radiat Isot. 1998;49:1537–40.

366. Bergström M, Lu L, Fasth KJ, Wu F, Bergström-Pettermann E, Tolmachev V, Hedberg E, Cheng A, Langstrom B. In vitro and animal validation of bromine-76-bromodeoxyuridine as a proliferation marker. J Nucl Med. 1998;39:1273–9.

367. Ryser JE, Blauenstein P, Remy N, Weinreich R, Hasler PH, Novak-Hofer I, Schubiger PA. [76Br] Bromodeoxyuridine, a potential tracer for the measurement of cell proliferation by positron emission tomography, in vitro and in vivo studies in mice. Nucl Med Biol. 1999;26:673–9.

368. Lu L, Bergström M, Fasth K-J, Långström B. Synthesis of [76Br]Bromofluorodeoxyuridine and its validation with regard to uptake, DNA incorporation, and excretion modulation in rats. J Nucl Med. 2000;41:1746–52.

369. Kassiou M, Loc'h C, Dolle F, Musachio JL, Dolci L, Crouzel C, Dannals RF, Mazière B. Preparation of a bromine-76 labelled analogue of epibatidine: a potent ligand for nicotinic acetylcholine receptor studies. Appl Radiat Isot. 2002;57:713–7.

370. Foged C, Halldin C, Loc'h C, Maziere B, Pauli S, Maziere M, Hansen HC, Suhara T, Swahn CG, Karlsson P, Farde L. Bromine-76 and carbon-11 labeled NNC 13–8199, metabolically stable benzodiazepine receptor agonists as radioligands for positron emission tomography. Eur J Nucl Med. 1997;24:1261–7.

371. Lovqvist A, Sundin A, Ahlstrom H, Carlsson J, Lundqvist H. Pharmacokinetics and experimental PET imagingn of a bromine-76-labeled monoclonal anti-CEA antibody. J Nucl Med. 1997;38:395–401.

372. Loc'h C, Halldin C, Bottlaender M, Swahn CG, Moresco RM, Maziere M, Farde L, Maziere B. Preparation of [76Br]FLB 457 and [76Br]FLB 463 for examination of striatel and extrastriatal dopamine D-2 receptors with PET. Nucl Med Biol. 1996;23:813–9.

373. Wu F, Yngvu U, Hedberg E, Honda M, Lu L, Eriksson B, Watanabe Y, Bergstrom M, Langstrom B. Distribution of 76Br-labeled antisense oligonucleotides of different length determined ex vivo in rats. Eur J Pharm Sci. 2000;10:179–86.

374. Winberg KJ, Persson M, Malmstrom PU, Sjoberg S, Tolmachev V. Radiobromination of anti-HER2/neu/ErB-2 monoclonal antibody using the p-isothiocyanatobenzene derivative of the [76Br]undecahydrobromo-7,8-dicarba-nido-undecaborate(1-) ion. Nucl Med Biol. 2004;31:425–33.

375. Patra M, Bauman A, Mari C, Fischer CA, Blacque O, Haussinger D, Gasser G, Mindt TL. An octadentate bifunctional chelating agent for the development of stable zirconium-89 based molecular imaging probes. Chem Commun. 2014;50:11523–5.

376. Wei W, Rosenkrans ZT, Liu J, Huang G, Luo QY, Cai W. ImmunoPET: concept, design, and applications. Chem Rev. 2020;120:3787–851.

377. Eppard E, de la Fuente A, Benešová M, Khawar A, Bundschuh RA, Gärtner FC, Kreppel B, Kopka K, Essler M, Rösch F. Clinical translation and first in-human use of [44Sc]Sc-PSMA-617 for PET imaging of metastasized castrate-resistant prostate cancer. Theranostics. 2017;7:4359–69.

378. Green MA, Klippenstein DL, Tennison JR. Copper(II)bis(thiosemicarbazone) complexes as potential tracers for evaluation of cerebral and myocardial blood flow with PET. J Nucl Med. 1988;29:1549–57.

379. Takahashi N, Fujibayashi Y, Yonekura Y, Welch MJ, Waki A, Tsuchida T, Sadato N, Sugimoto K, Itoh H. Evaluation of 62Cu labeled diacetyl-bis(N4-methylthiosemicarbazone) in hypoxic tissue in patients with lung cancer. Ann Nucl Med. 2000;14:323–8.

380. Dehdashti F, Mintun MA, Lewis JS. *In vivo* assessment of tumour hypoxiy in lung cancer with 60Cu-ATSM. Eur J Nucl Med Mol Imaging. 2003;30:844–50.

381. Haynes NG, Lacy JL, Nayak N, Martin CS, Dai D, Mathias CJ, Green MA. Performance of a 62Zn/62Cu generator in clinical trials of PET perfusion agent 62Cu-PTSM. J Nucl Med. 2000;41:309–14.

382. Ikotun OF, Lapi SE. The rise of metal radionuclides in medical imaging: copper-64, zirconium-89 and yttrium-86. Future Med Chem. 2011;3:599–621.

383. Cai Z, Anderson CJ. Chelators for copper radionuclides in positron emission tomography radiopharmaceuticals. J Label Compd Radiopharm. 2014;57:224–30.

PET Chemistry: Radiopharmaceuticals

8

Tobias L. Ross and Simon M. Ametamey

Contents

8.1 PET Radiopharmaceuticals in the Clinics: Precursors

Although many radiolabelled compounds for PET imaging have been developed so far, only a few have reached the status of a clinically established and routinely used PET radiopharmaceutical. At the early stage of their development a reasonable medical indication obviously is fundamental for a PET radiopharmaceutical to be further considered as clinically relevant. However, besides a favourable in vivo behaviour and appropriate imaging characteristics, certain criteria have to be fulfilled such as a fast, straightforward and reliable radiosynthesis; an assured stability of the label as well as of the compound itself and a good availability of a suitable precursor. In particular, the ease and reliability of the radiochemistry is critical as the radiopharmaceutical needs to be available on demand in sufficient amounts. The precursors play the decisive role in the radiochemical approach as they specify the radiosynthetic route. Furthermore, the accessibility of the appropriate precursors is material for the applicability of the radiosynthesis. Today, most precursors of the commonly used PET radiopharmaceuticals are commercially available and provided as approved medical products by several different suppliers [1].

T. L. Ross (✉)
Radiopharmaceutical Chemistry, Department of Nuclear Medicine, Hannover Medical School, Hannover, Germany
e-mail: ross.tobias@mh-hannover.de

S. M. Ametamey
Animal Imaging Center-PET, Center for Radiopharmaceutical Sciences of ETH, PSI and USZ, ETH-Hönggerberg, D-CHAB IPW HCI H427, Zurich, Switzerland
e-mail: amsimon@ethz.ch

8.1.1 ¹⁸F-Labelled PET Radiopharmaceuticals and Their Precursors

Fluorine-18 is clearly the most important radionuclide employed in clinical PET imaging. While it is available at large scales, it also has further optimal physical and chemical properties for PET imaging. In its form of [¹⁸F]FDG, it probably contributed most to the success of PET imaging in clinical diagnostics. Since the development of [¹⁸F]FDG in the 1970s, it has become the most important and most commonly used PET radiopharmaceutical in nuclear medicine. However, during the past 30 years, several other useful ¹⁸F-labelled PET radiopharmaceuticals have been designed, and some have been further developed to routine PET radiopharmaceuticals in nuclear medicine clinics. Another famous and widely used PET radiopharmaceutical is [¹⁸F]FPSMA-1007 [2]. Following, some representative examples of clinically employed ¹⁸F-labelled PET radiopharmaceuticals are outlined. Furthermore, their general production routes and most commonly used precursors are described.

8.1.1.1 [¹⁸F]NaF

As mentioned before, ¹⁸F-labelled sodium fluoride is the simplest form of a ¹⁸F-labelled radiopharmaceutical, and it was shown already in 1940 in in vitro tests that [¹⁸F]NaF is uptaken by bone and dentine structures [3]. Since the 1960s, [¹⁸F]NaF has been used in the nuclear medicine clinics for skeletal scintigraphy to identify malignant and benign mass in bones [4, 5]. N.c.a. [¹⁸F]NaF can be achieved directly by elution of the trapped [¹⁸F]fluoride from the anionic exchange resin (solid phase extraction cartridge systems) using potassium carbonate solution. The obtained [¹⁸F]fluoride solution can be used directly for administration.

8.1.1.2 2-[¹⁸F]Fluorodeoxyglucose ([¹⁸F] FDG)

¹⁸FDG is the most important ¹⁸F-labelled PET radiopharmaceutical and its good availability, its broad applicability and an increasing use made PET imaging to a worldwide accepted diagnos-

TATM
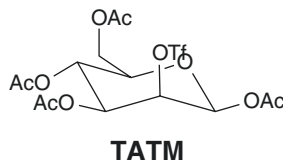
Fig. 8.1 Mannose triflate precursor for radiosynthesis of n.c.a. [¹⁸F]FDG

tic method. ¹⁸FDG is most widely used as diagnostic compound in oncology [6], but there are many more indications and applications for this versatile radiopharmaceutical [7–10]. The first approach towards 2-[¹⁸F]FDG was based on an electrophilic ¹⁸F-labelling with only low yields and in a mixture with the stereoisomer 2-[¹⁸F] fluorodeoxymannose [11]. In the 1980s, a new precursor, mannose triflate (1,3,4,6-tetra-*O*-acetyl-2-*O*-trifluoro-methanesulfonyl-beta-D-mannopyranose, TATM) (see Fig. 8.1) [12], for an efficient nucleophilic n.c.a. ¹⁸F-labelling of 2-[¹⁸F]FDG became available and is still the precursor of choice for routine productions of n.c.a. [¹⁸F]FDG with yields of up to 40–50 GBq per batch. Generally, TATM is n.c.a. ¹⁸F-fluorinated in the Kryptofix2.2.2©/K_2CO_3 system in acetonitrile. The subsequent hydrolysis using hydrochloric acid provides [¹⁸F]FDG in high radiochemical yields of ~50–70%. Recently, the deprotection procedure has been optimized by changing to an alkaline system [13–15]. The alkaline system sufficiently removes all acetyl protection groups already at 40 °C in 0.3 N NaOH in less than 5 min. The reaction conditions must be strictly kept to reduce an alkaline epimerization on the C-2 position towards 2-[¹⁸F]fluorodeoxymannose to a minimum [14].

8.1.1.3 [¹⁸F]FPSMA

After the ⁶⁸Ga-labelled PSMA ligands have proven their enormous potential in PET diagnostics of primarily metastatic castration-resistant prostate cancer (mCRPC) [16, 17], ¹⁸F-labelled PSMA ligands became more and more of interest [18]. Currently, the most widely used ¹⁸F-labelled PSMA ligand is [¹⁸F]FPSMA-1007 [2], which was developed as a second-generation ¹⁸F-labelled PSMA ligands after ligands such as

Fig. 8.2 Precursor for the ^{18}F-labelled PSMA ligand [^{18}F] FPSMA-1007
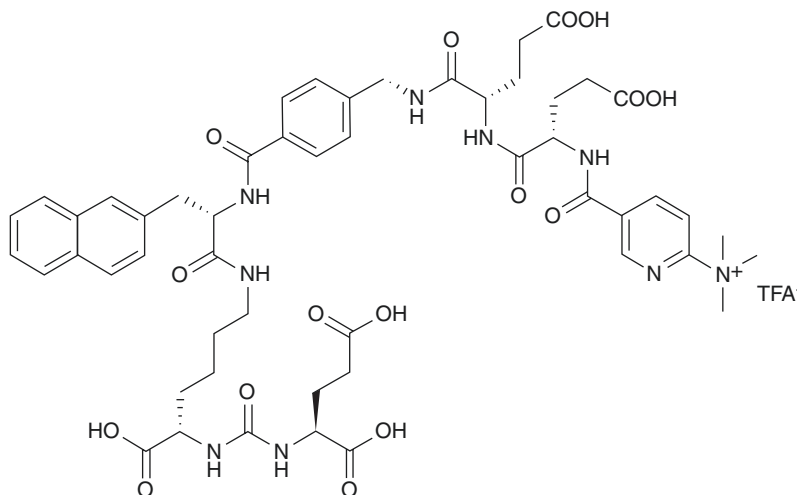
Precursor for [18F]FPSMA-1007

[^{18}F]DCFBC [19] and [^{18}F]DCFPyL [20]. [^{18}F] FPSMA-1007 is available by a standard one-step nucleophilic fluorination of the trimethylammonia triflate precursor (Fig. 8.2) [21]. [^{18}F]FPSMA-1007 can be easily produced under GMP, and GMP compliant synthesis kits are available for most of the commonly employed synthesis modules. The automated synthesis generally provides [^{18}F]FPSMA-1007 in high radiochemical yields of ~70–80%. Besides these, 18F-PSMA ligands, further 18F-labelled PSMA ligand, have been developed, including an [^{18}F]AlF and a hybrid approach [22–25].

8.1.1.4 6-[18F]Fluoro-ʟ-DOPA ([18F] F-DOPA)

Similar to 18FDG, the first 18F-labelling approaches to [^{18}F]F-DOPA were based on the direct electrophilic 18F-labelling using [^{18}F] F_2 and ʟ-DOPA as precursor. This method led to a mixture of the three possible regioisomers 2-, 5- and 6-[^{18}F]F-DOPA and gave only 21% RCY of the desired 6-[^{18}F]F-DOPA. The introduction of the 6-trimethyltin precursor for electrophilic 18F-fluorodemetallations offered enhanced 18F-labelling with regioselective 18F-introduction and higher RCY [26]. The electrophilic 18F-fluorodemetallation reaction for 6-[^{18}F]F-DOPA was further developed and opti-

mized and is still applicable as a fully automated version [27–29]. First attempts for a nucleophilic approach of n.c.a. 18F-labelling of 6-[^{18}F]F-DOPA focused on multi-step radiosyntheses using chiral auxiliaries and thus made automation difficult [30]. The first (automated) three-step (one-pot) approach was based on an isotopic exchange, followed by a Baeyer–Villiger oxidation and an acidic deprotection using HBr [31]. This nucleophilic approach to 6-[^{18}F]fluoro-ʟ-DOPA is available as GMP compliant kits for several synthesis modules and allowed for the first time a broad clinical production of 6-[^{18}F]fluoro-ʟ-DOPA at many sites. With the novel copper-catalysed fluorination methods using pinacol boronate (BPin) ester precursors, 6-[^{18}F]fluoro-ʟ-DOPA became available in good yields (RCY 6%) and high molar specific activities (up to 140 GBq/µmol) via a two-step, one-pot nucleophilic fluorination (Fig. 8.3) [32].

6-[^{18}F]fluoro-ʟ-DOPA is the PET tracer of choice for studies of the dopaminergic system [33], particularly for studies of changes in the presynaptic dopaminergic nerve terminals in Parkinson's disease [34, 35]. Furthermore, 6-[^{18}F]F-DOPA has also shown applicability in oncology for detecting neuroendocrine tumours where visualization using [^{18}F]FDG PET imaging is not feasible [36, 37].

Fig. 8.3 Precursors for electrophilic radiofluorination of 6-[18F]F-DOPA by regioselective 18F-fluorodestannylation (upper row). In the lower row, precursors for nucleophilic approaches via isotopic exchange and via copper-catalysed radiofluorination
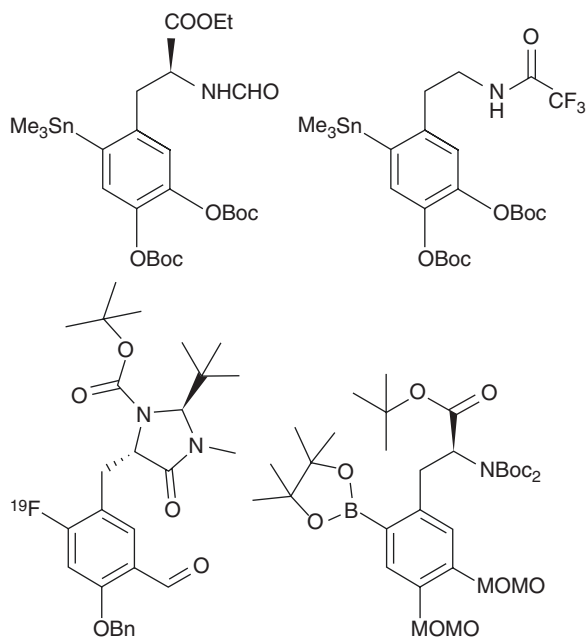
8.1.1.5 O-(2-[18F]Fluoroethyl)-L-tyrosine ([18F]FET)

[18F]FET is an 18F-labelled amino acid derivative and is routinely used for PET imaging of brain tumours as it has only minor uptake in normal brain and provides excellent tumour-to-background contrast [38]. Furthermore, it is not uptaken by inflammatory tissue like 18FDG and allows a more exact detection of tumour mass and size in general tumour imaging [39]. In combination with magnetic resonance imaging (MRI), PET imaging of cerebral gliomas using [18F]FET significantly enhanced the diagnostic assessment [40]. The first radiosynthesis was based on a two-step 18F-labelling using the primary precursor ethyleneglycol-1,2-ditosylate [41]. After 18F-labelling and a semi-preparative HPLC purification, 2-[18F]fluoroethyltosylate was coupled to the unprotected (S)-tyrosine to give [18F]FET. The two-step method could be circumvented by the advancement of a new precursor, (2S)-O-(2′-tosyloxyethyl)-N-trityl-tyrosine-*tert*-butyl ester (TET) for a direct 18F-labelling (Fig. 8.4) [42]. Although the precursor for direct 18F-labelling offers a shorter, more convenient and more efficient preparation of [18F]FET, both the methods are routinely used. A very recent developed pre-

TET
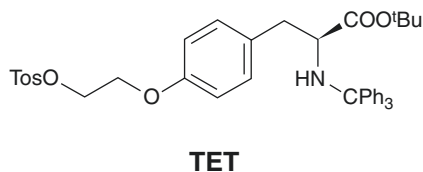
Fig. 8.4 Precursor TET for the direct 18F-labelling of [18F]FET

cursor is based on a chiral Ni(II) complex of a (S)-tyrosine Schiff base and led to an enantiomerically pure (S)-2-[18F]FET, and furthermore, this approach could avoid toxic TFA in the hydrolysis step [43].

8.1.1.6 3-Deoxy-3′-[18F]fluorothymidine ([18F]FLT)

This 18F-labelled thymidine derivative is a substrate of the thymidine kinase-1 (TK1) and thus phosphorylated and trapped in the cell [44]. The TK1 is correlated with cell proliferation as its designated substrate thymidine is essential for DNA and RNA synthesis. Hence, [18F]FLT can be used for PET imaging of cell proliferation and of tumours with increased TK1 levels [45]. [18F]FLT has proven clinical importance, even in comparison with [18F]FDG in several tumour imaging studies [46–52].
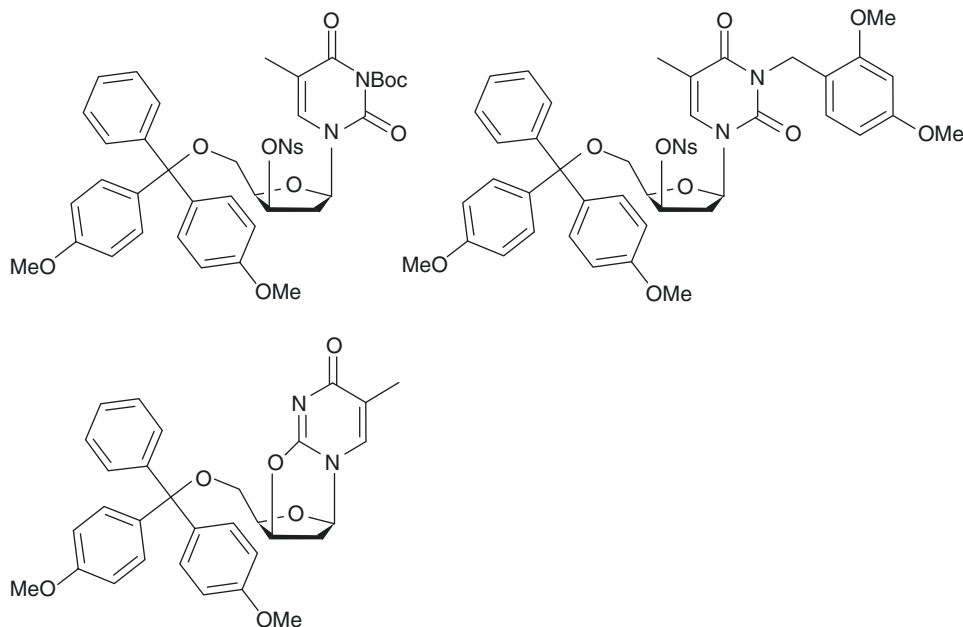
Fig. 8.5   Various precursors for the ¹⁸F-labelling of [¹⁸F]FLT

The first radiosynthesis of 3-deoxy-3′-[¹⁸F]fluoro-thymidine gave only low RCY of 7% [53]. Several improvements of the radiosynthesis, precursors and the HPLC systems for purifications have increased availability of [¹⁸F]FLT [54–59], but still the radiosynthesis remains tedious and causes difficulties in routine productions [59]. The most commonly used precursors for ¹⁸F-labeling of [¹⁸F] FLT are depicted in Fig. 8.5.

8.1.1.7   16α-[¹⁸F]Fluoro-17β-estradiol ([¹⁸F]FES)

¹⁸F-labelled oestrogens have been developed as PET radiopharmaceuticals for imaging the oestrogen hormone receptor [60]. The oestrogen receptor expression is a crucial factor in breast cancer development and critical for the response of endocrine therapies [61, 62]. The first ¹⁸F-labelled derivatives of oestrogen were the 4-[¹⁸F]fluoroestranone and the 4-[¹⁸F]Fluoroestradiol which were only achieved in low radiochemical yields of ~3% [63, 64]. Several other ¹⁸F-labelled oestrogen derivatives have been developed and evaluated preclinically [65–69]. However, the most promising candidate and today routinely used ¹⁸F-labelled oestrogen derivative is the 16α-[¹⁸F]Fluoro-17β-estradiol ([¹⁸F]FES)
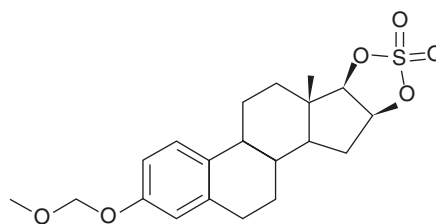
Fig. 8.6   Cyclic sulphate precursor for the ¹⁸F-labelling of [¹⁸F]FES

[66, 67]. The synthesis and preparation methods for [¹⁸F]FES have been improved and automated, and [¹⁸F]FES can be achieved in radiochemical yields of 70% within 60 min synthesis time [70–72]. As precursor, the cyclic sulphate 3-*O*-methoxymethyl-16β,17β-*O*-sulfuryl-estra-1,3,5(10)-triene-3,16β,17β-triol (Fig. 8.6) has prevailed and is commonly employed. After radio-fluorination, a hydrolysis step using 1 N HCl yields the 16α-[¹⁸F]fluoro-17β-estradiol. The product is then purified by semi-preparative HPLC and formulated.

8.1.1.8   [¹⁸F]Fluorocholine ([¹⁸F]FCH)

The ¹¹C-labelled derivative of choline, [¹¹C] choline, was found to be a suitable radiophar-

Fig. 8.7 Preparation of [¹⁸F]choline via the ¹⁸F-labelling synthon [¹⁸F]FBM
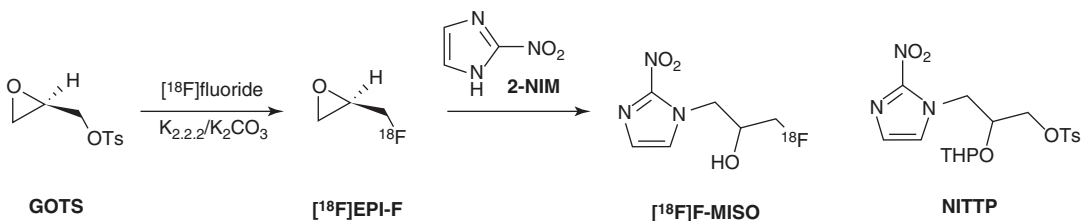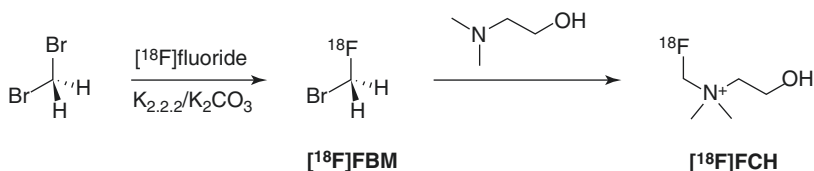
Fig. 8.8 Preparation of [¹⁸F]F-MISO using a two-pot radiosynthesis (left hand side) and the precursor NITTP for the one-step ¹⁸F-labelling procedure (right hand side)

maceutical for tumour imaging, especially for prostate cancer [73, 74]. As a consequence, also the ¹⁸F-labelled derivative [¹⁸F]fluorocholine was developed and showed similarly good imaging characteristics in PET tumour imaging [73, 75, 76]. Furthermore, [¹⁸F]FCH was also found to clearly visualize brain tumours [77], and in comparison with [¹⁸F]FDG, it gave better PET images for brain tumours, prostate cancer, lung cancer, head and neck cancer [76]. Generally, [¹⁸F]fluorocholine can be obtained in RCY of 20–40% from a coupling reaction of *N,N*-dimethylethanolamine with the ¹⁸F-labelling synthon [¹⁸F]fluorobromomethane ([¹⁸F]FBM) (see Fig. 8.7) [75]. The ¹⁸F-labelling of [¹⁸F]FBM is based on the precursor dibromomethane, and [¹⁸F]FBM is isolated by a subsequent gas chromatography purification [78, 79].

8.1.1.9 [¹⁸F]Fluoromisonidazole ([¹⁸F]F-MISO)
[¹⁸F]F-MISO   (1H-1-(3-[¹⁸F]fluoro-2-hydroxypropyl)-2-nitroimidazole) is used as an indicator for the oxygenation status of cells as is accumulated in hypoxic tissue. Particularly in oncologic radiotherapy and chemotherapy, hypoxia is of major interest for the therapy prognosis [80–82]. Although [¹⁸F]F-MISO shows some unfavourable pharmacological characteristics such as slow clearance from norm-oxygenated cells (background) and a relatively moderate uptake in hypoxic cells in general, it is the most widely used

PET radiopharmaceutical for imaging hypoxic tumours. Recently, other hypoxia PET tracers have been developed and showed very promising results, but they have not reached the clinics yet [83–85]. Generally, two variants of the radiosynthesis towards [¹⁸F]F-MISO are available [86–91]. The first successful attempts of an efficient radiolabelling of [¹⁸F]F-MISO were based on a two-pot reaction. The primary precursor (*2R*)-(−) glycidyl tosylate (GOTS) was labelled with [¹⁸F] fluoride to yield [¹⁸F]epifluorohydrin ([¹⁸F]EPI-F) which subsequently reacted with 2-nitroimidazole (2-NIM) in a nucleophilic ring opening to give [¹⁸F]F-MISO in RCY of 20–40% (Fig. 8.8) [87, 88]. The development of a direct ¹⁸F-labelling of [¹⁸F]F-MISO in one-pot has made radiosynthesis of this PET radiopharmaceutical more convenient and reliable [89, 90]. Starting from the precursor 1-(2′-nitro-1′-imidazolyl)-2-O-tetrahydropyranyl-3-O-toluenesulphonyl-propanediol   (NITTP) (Fig. 8.8), [¹⁸F]F-MISO can be obtained in a one-pot procedure within 70–90 min [89–91]. Both the approaches are capable for [¹⁸F]F-MISO preparation, while the one-pot method usually gives RCY of 35–40%, and it is much more suitable for automated routine productions [86]. Furthermore, the radiosynthesis based on the NITTP precursor is normally more reliable and more robust.

8.1.1.10 [¹⁸F]Altanserin
This ¹⁸F-labelled PET radiopharmaceutical is the most widely used PET tracer for studies
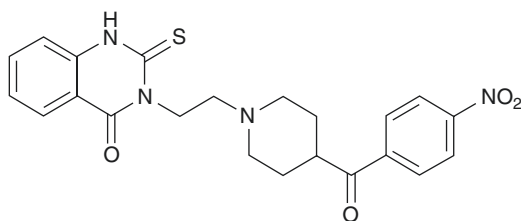
Nitro-Altanserin

Fig. 8.9 Nitro-precursor for the direct ^{18}F-labelling of [^{18}F]altanserin

Tosyl-Fallypride

Fig. 8.10 'Tosyl-fallypride' as a precursor for one-step ^{18}F-labelling of [^{18}F]fallypride
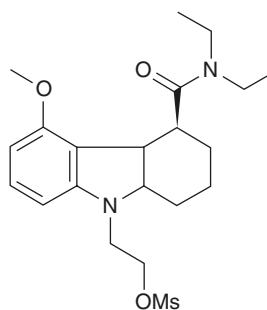
Fig. 8.11 Mesylate precursor for one-step ^{18}F-labelling of [^{18}F]GE180

of the 5-HT$_{2A}$ receptor system as it is so far the most suitable ^{18}F-labelled 5-HT$_{2A}$ receptor ligand. Among other ^{18}F-labelled ligands for this receptor system, [^{18}F]altanserin shows the highest affinity to 5-HT$_{2A}$ receptors and a good selectivity over the other receptor systems dopamine D$_2$, histamine H$_1$, adrenergic α_1 and α_2 and opiate receptor sites (μ-opiate) [92, 93]. [^{18}F]Altanserin can be obtained from direct ^{18}F-labelling of the appropriate nitro precursor (nitro-altanserin) (Fig. 8.9) with good RCY in a one-step procedure as no functional groups are present which need to be protected, the radiopharmaceutical is readily available after HPLC purification [94, 95].

8.1.1.11   [^{18}F]Fallypride
This ^{18}F-labelled derivative of benzamide neuroleptics has a high affinity (reversible binding) to dopamine D$_2$ receptors. [^{18}F]Fallypride is widely used as PET radiopharmaceutical for investigations of the dopamine D$_2$ receptor system and allows PET imaging of both striatal and extrastriatal dopamine D$_2$ receptors [96–100]. The ^{18}F-radiolabelling using the 'tosyl-fallypride' precursor (Fig. 8.10) is a one-step ^{18}F-labelling procedure and provides [^{18}F]fallypride in good RCY of 20–40% [101].

8.1.1.12   [^{18}F]GE180
Several ^{18}F-labelled TSPO ligands have been developed for PET imaging of neuroinflammation based on the TSPO expression on activated microglia and astrocytes [102–104]. Furthermore, TSPO is expressed on several different immune cells and even allows imag-

ing of peripheral inflammatory processes [105, 106]. One broadly applied TSPO ligand, [^{18}F] GE180, is available from a GMP-compliant synthesis kit for the GE FASTlab-Synthesizer (GE Healthcare) [107]. The radiolabelling is based on a mesylate precursor and a one-step nucleophilic ^{18}F-fluorination (Fig. 8.11). After an SPE cartridge purification, [^{18}F]GE180 is available in high radiochemical yields of 40–50%.

8.1.1.13   [^{18}F]Florbetaben, [^{18}F] Florbetapir and [^{18}F] Flutemetamol
Not only in Alzheimer's disease, amyloid deposits (Aβ plaques) are of great interest [108]. After [^{11}C]PIB proved to image amyloid burden in patients of Alzheimer's disease [109], ^{18}F-labelled β-amyloid plaque ligands have been developed. The most prominent ligands are [^{18}F]flutemetamol [110] as well as the stilbene derivatives [^{18}F]florbetaben and [^{18}F]florbetapir [111–113]. The latter are available from their corresponding tosylate or mesylate precursors
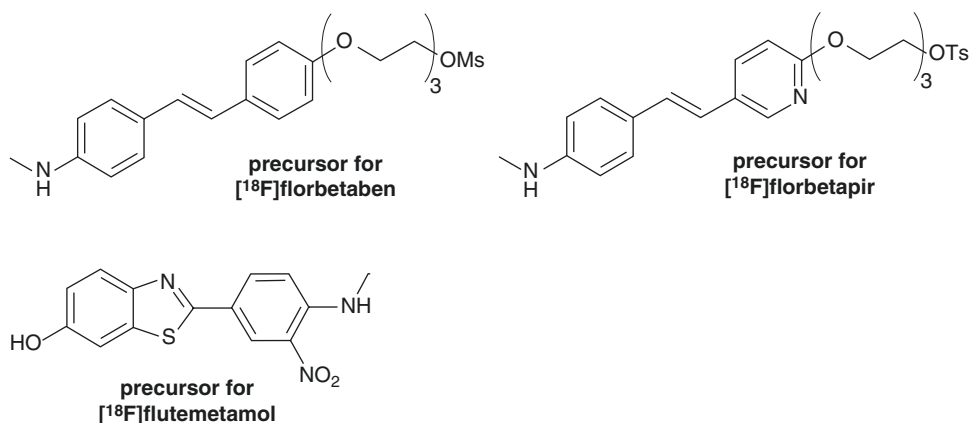
Fig. 8.12 Precursors for one-step ¹⁸F-labelling of the amyloid ligands [¹⁸F]florbetaben, [¹⁸F]florbetapir and [¹⁸F] flutemetamol

Fig. 8.13 Precursors for one-step ¹⁸F-labelling of the tau protein ligands [¹⁸F]T807 and [¹⁸F]PI-2620
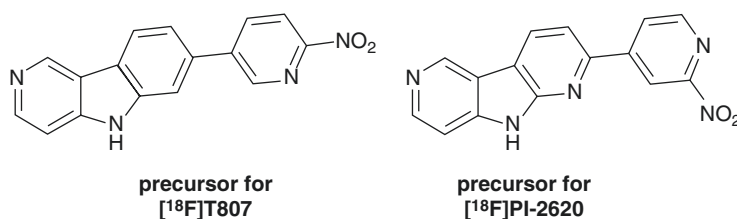
(Fig. 8.12) in one-step ¹⁸F-labelling reactions with high radiochemical yields ranging from 30% to 40%. [¹⁸F]Flutemetamol is labelled with ¹⁸F in a fluoro-for-nitro exchange on the aromatic system. The β-amyloid radioligands are either commercially available or can be produced from GMP compliant kits for most of the commercial radiosynthesizers.

8.1.1.14 [¹⁸F]THK5351, [¹⁸F]T807 and [¹⁸F]PI-2620

In research and diagnostics of Alzheimer's disease, a recent approach is called ATN (amyloid plaques–tau pathology (tangles)–neuronal loss) [114]. ATN describes the current understanding of the development of the different pathologies during the time course of the disease progress. Therefore, besides β-amyloid ligands, specific tau protein ligands are of particular interest. Examples of the first generation of ¹⁸F-labelled tau radioligands are the 2-arylquinoline [¹⁸F]THK-5351 [115] and the benzimidazole pyrimidine [¹⁸F]T807 (Fig. 8.13) [116]. However, the 2-arylquinoline series ([¹⁸F]

THK-5351 and derivatives thereof) revealed to be unspecific for tau protein, and [¹⁸F]THK-5351 is considered as MAO ligand, thus rather visualizing the present inflammation instead of the tau pathology [117]. In the second generation, tau radiotracers with higher specificity and reduced unspecific uptake in white matter have been developed [118]. One widely used and commercially available tau ligand is the [¹⁸F]PI-2620 (Fig. 8.13), which is available through nucleophilic ¹⁸F-substitution of a nitro leaving group [119]. Similar to amyloid radiotracers, ¹⁸F-labelled tau ligands have revealed tau pathologies being associated with various neurodegenerative processes and even with peripheral pathologies [108].

8.1.2 ¹¹C-Labelled PET Radiopharmaceuticals and Their Precursors

Carbon-11 is particularly suited for labelling compounds with short biological half-lives.
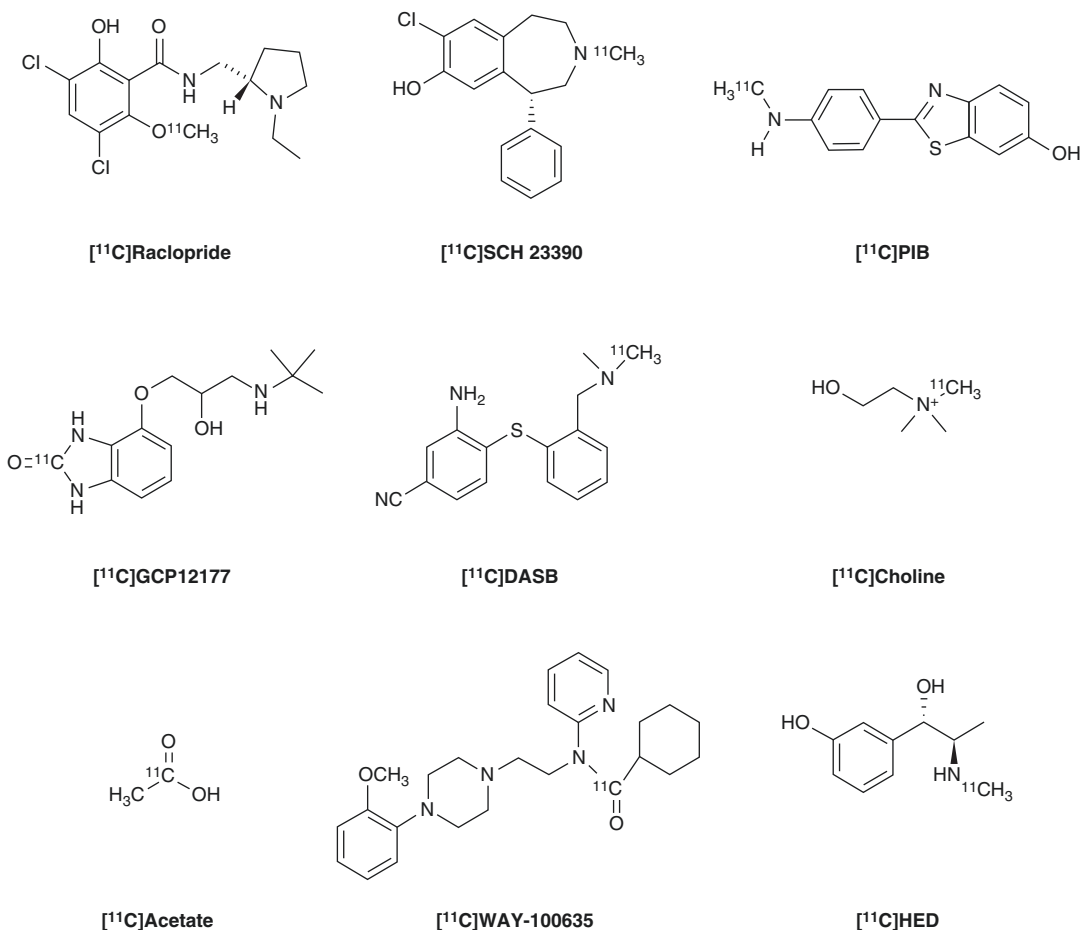
Fig. 8.14 Examples of commonly used and clinically established ^{11}C-labelled PET radiopharmaceuticals

Compared to fluorine-18, the short physical half-life of ^{11}C permits repeated investigations in the same subject and within short intervals. Labelling is mainly by isotopic substitution but unlike ^{18}F-labelled radiopharmaceuticals, carbon-11-labelled compounds can be prepared and used only in PET centres with a cyclotron and radiochemistry facility. As such carbon-11-labelled compounds are not commercially available. In Fig. 8.14, the structures of some established and commonly used carbon-11-labelled radiopharmaceuticals are shown, which have found routine application in clinical PET studies. All these compounds are prepared starting from the commercially available desmethyl or normethyl precursors. A large number of carbon-11-labelled radiopharmaceuticals have been reported

in the literature, but only a handful of these have been shown to have clinical utility (Table 8.1). Procedures for the preparation of some representative examples of these radiopharmaceuticals are described.

8.1.2.1 [^{11}C]Raclopride

Of all benzamide derivatives reported to date, ^{11}C-raclopride is the most widely used PET ligand for the investigation of postsynaptic striatal D2/D3 receptors in humans. It has been used to image D2/D3 receptors in patients with Parkinson's disease, Huntington's disease and schizophrenia, for determining receptor occupancy of antipsychotic drugs as well as for the indirect measurement of dopamine concentrations in the synaptic cleft. Raclopride can be

Table 8.1 Established ^{11}C-labelled PET radiopharmaceuticals and their clinical applications

[11]C-Radiopharmaceutical	Target	Reference
[^{11}C]Flumazenil	Central benzodiazepine receptors	[124]
[^{11}C]WAY-100635	5-HT$_{1A}$ receptors	[125]
[^{11}C]PIB	Amyloid deposits	[109]
[^{11}C]Raclopride	D2-receptor occupancy	[126]
[^{11}C]SCH23390	D1-receptor occupancy	[127]
[^{11}C]DASB	SERT	[128]
[^{11}C]Methionine	Amino acid uptake	[129–131]
[^{11}C]Choline	Cell membrane synthesis	[126]
[^{11}C]Acetate	Oxygen metabolism	[132]
[^{11}C]HED	Presynaptic uptake-1 and storage	[133, 134]
[^{11}C]GP 12177	β-Adrenoceptors	[133, 134]

labelled by *O*-methylation with ^{11}C-methyl iodide or ^{11}C-methyltriflate. Another approach involves *N*-ethylation with ^{11}C-ethyl iodide, however, due to the longer reaction time and a lower specific radioactivity, *O*-methylation is the preferred method for routine synthesis [120]. *O*-methylation was performed by using 5 M NaOH as the base in dimethylsulfoxide at 80 °C for 5 min. ^{11}C-raclopride is purified by reversed phase HPLC. The total synthesis time is around 40–45 min, and specific activities are in the range of 20–100 GBq/μmol depending on the synthesis method and the production route of ^{11}C-methyl iodide (i.e. 'wet' or 'dry' method).

8.1.2.2 [^{11}C]Flumazenil

[11]C-labelled flumazenil is routinely used in clinical PET studies for the visualization of benzodiazepine receptors. It has high affinity for the GABA$_A$ binding site and has been employed in PET studies mainly for the localization of epileptic foci. ^{11}C-flumazenil has been labelled with carbon-11 by *N*-methylation with ^{11}C-methyl iodide or esterification with ^{11}C-ethyl iodide. For routine synthesis, N-methylation with ^{11}C-methyl iodide is the method of choice. [^{11}C]flumazenil is purified by reversed phase HPLC [121]. The total synthesis time is around 40–45 min, and specific activities are in the range of 20–100 GBq/μmol.

8.1.2.3 L-[*S*-methyl-^{11}C]Methionine

Methionine, labelled in its methyl position and named L-[*S*-methyl-^{11}C]methionine, is a widely used amino acid for the detection of tumours using PET imaging. The uptake of L-[*S*-methyl-^{11}C] methionine reflects several processes including transport, protein synthesis and transmethylation. A number of synthetic pathways leading to L-[*S*-methyl-^{11}C]methionine have been reported [122, 123]. The most simple and commonly used synthetic approach utilizes the L-homocysteine thiolactone method. This method involves the in situ ring opening of L-homocysteine thiolactone by sodium hydroxide and the subsequent alkylation of the sulphide anion of L-homocysteine with ^{11}C-methyl iodide or ^{11}C-methyltriflate. The final product is purified by HPLC, formulated to give a sterile and pyrogen-free product. The total synthesis time is around 40–45 min. Although unlike brain receptors, high specific radioactivities are not required, and practical values obtained after the radiosynthesis are in the range of other ^{11}C-labelled compounds.

8.1.3 ^{68}Ga-Labelled PET Radiopharmaceuticals

Gallium-68 ($T_{1/2}$ = 68 min) is produced from the [68]Ge-^{68}Ga generator system. The generator is typically made up of a matrix of Sn(IV), Ti(IV), Ta(IV) and Zr(IV) oxides in a small glass column. The ^{68}Ga is eluted from the column with 0.05 M to 0.6 M HCl (depending on the generator type) [135]. The most prominent examples of clinically used ^{68}Ga-radiopharmaceuticals are [^{68}Ga] HBED-PSMA (PSMA-11) and [^{68}Ga]DOTA-
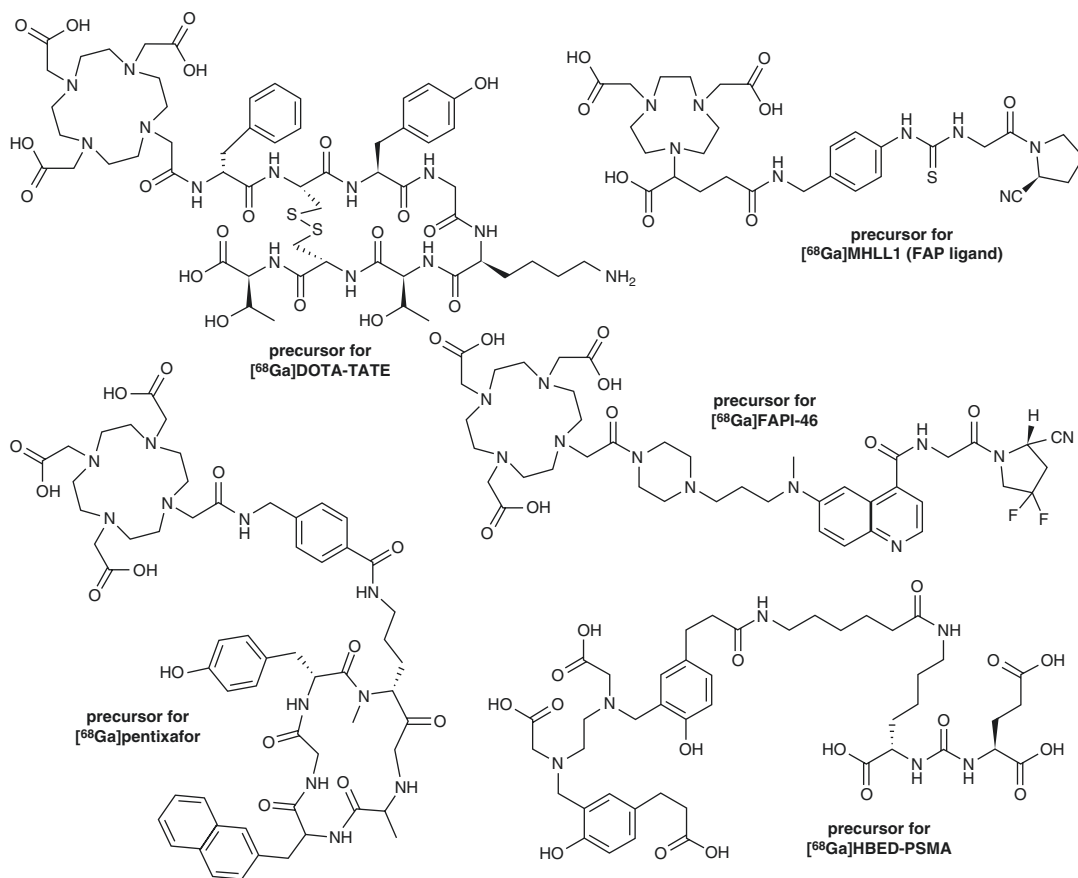
Fig. 8.15 Precursors for ^{68}Ga-labelling towards various clinically used ^{68}Ga-radiopharmaceuticals

TOC or -TATE which have found wide application as imaging agents for prostate-specific membrane antigen (PSMA) positive tumours and metastases [136, 137] and somatostatin receptor-positive tumours [138, 139], respectively. Very recently, novel ^{68}Ga-radiopharmaceuticals targeting the fibroblast activation protein (FAP) have been developed and gained great attention [140, 141]. ^{68}Ga-labelling in clinical routine is generally performed via module-based radiosynthesis following standard procedures, i.e. 5–10 min labelling at 95 °C in buffer (HEPES or acetate) at pH 3.5–4.0, subsequent purification on a C18 SPE cartridge delivers the desired product in high radiochemical yields of 80–90%. Figure 8.15 shows some important precursors for ^{68}Ga-labelling of the corresponding radiopharmaceuticals.

As mentioned above, the radiopharmaceuticals [^{68}Ga]HBED-PSMA (PSMA-11) and [^{68}Ga]DOTA-TOC or -TATE are established in clinical routine. Latest developments in ^{68}Ga-radiochemistry enable the first kit-based productions suitable for clinical use, i.e. SomaKit TOC® (AAA/Novartis) is a kit with market authorization available for [^{68}Ga]DOTA-TOC [142]. Similarly, the PSMA targeting motif has been connected to the THP (tris(hydroxypyridinone)) chelator for [^{68}Ga]THP-PSMA, which awaits market authorization as GalliProst® (ROTOP/ Theranostics). In the kit, [^{68}Ga]THP-PSMA is radiolabelled just by adding the generator eluate directly into the kit vial, the radiolabelling is completed at room temperature within 3–5 min and reaches almost quantitative radiochemical yields of 99% [143, 144]. ^{68}Ga-labelled PSMA-ligands

are of utmost importance for nuclear medicine, as they are the base of the theranostic concept for PSMA-targeted endoradiotherapy using the radionuclide pair ^{68}Ga and [177]Lu [145]. The latest developments in ^{68}Ga-radiopharmaceuticals are the ^{68}Ga-labelled FAP inhibitors, of which the most prominent radiotracers are the FAPI series [140, 146], but also other ^{68}Ga-labelled FAP inhibitors have shown already their high potential [141]. FAP is a highly interesting target in oncology, where it is expressed on cancer-associated fibroblasts in the tumour microenvironment of many human cancers [147] and enables theranostics approaches [148]. However, FAP is also expressed in many different diseases, and ^{68}Ga-labelled FAP inhibitors have already been used for fibroblast activity after myocardial infarction [141, 149].

8.1.4   [15]O- and ^{13}N-Labelled PET Radiopharmaceuticals

Oxygen-15 ($T_{1/2}$ = 2 min) has been used mainly for the labelling of oxygen, water and butanol. Of all these three compounds, ^{15}O-labelled water and butanol have found widespread application as myocardial and brain perfusion imaging agents.

8.1.4.1 [^{15}O]Water
A number of nuclear reactions exist for the production of oxygen-15, but the most commonly used method is the [14]N(d,n)[15]O nuclear reaction [150]. The target material is aluminium, and the target content is a mixture of nitrogen and 0.2–1.0% of oxygen. [^{15}O]water is then produced by reacting hydrogen with [^{15}O]O_2 (formed from the exchange reaction with carrier oxygen) over palladium-alumina catalyst at 200 °C. The [^{15}O] water vapour formed is trapped in sterile isotonic saline.

8.1.4.2 [^{15}O]Butanol
n-[^{15}O]Butanol is prepared by the reaction of tri-n-butyl borane with [^{15}O]O_2 produced via the [14]N(d,n)[15]O nuclear reaction. Alumina is used as a solid support for the tri-n-butyl borane. After the reaction, the labelled product is washed from the cartridge with water. Further purification is achieved by passing the product through a C-18

cartridge and eluting over a sterile filter with 10% ethanol/saline [151].

8.1.4.3 [^{13}N]Ammonia
Nitrogen-13 ($T_{1/2}$ = 10 min) is prepared via the [16]O(p,α)[13]N nuclear reaction [152]. The material is usually aluminium, but targets made of nickel or titanium are in use. Of all compounds labelled with nitrogen-13, [^{13}N]ammonia is the most commonly used for PET studies. Two general methods exist for its production. The first method involves the reduction of ^{13}N-labelled nitrites/nitrates, formed during the proton irradiation, with either titanium(III) chloride or hydroxide or Devarda's alloy in alkaline medium [153]. After distillation, trapping in acidic saline solution and sterile filtration, [^{13}N]ammonia is ready for human application. The second method prevents the in situ oxidation of ^{13}N to ^{13}N-labelled nitrites/nitrates through the addition of ethanol as a radical scavenger to the target content [153]. Thereafter, the target content is passed through a small cation exchanger. [^{13}N]Ammonium ions trapped on the cartridge are eluted with saline and the solution containing the product. [^{13}N] Ammonia is used mainly for myocardial perfusion studies.

8.1.5   Other PET Radiopharmaceuticals

As an alternative to carbon-11 and fluorine-18, the most commonly used PET radionuclides, metallic positron emitters have gained much attention as radionuclides for the labelling of biomolecules, especially for peptides and proteins. Apart from ^{64}Cu and [89]Zr, most of the metallic positron emitters including [82]Rb, ^{68}Ga, [62]Cu and [44]Sc are generator produced isotopes. An advantage of generators is the fact that PET studies can be performed without an onsite cyclotron or external sources.

Zirconium-89 ($T_{1/2}$ = 78.4 h) is generally produced in the [89]Y(p,n)[89]Zr reaction on a small cyclotron [154]. [89]Zr is well-known as the radionuclide for immuno-PET using [89]Zr-labelled antibodies [155]. With its longer half-life, shipping is even possible over longer distances. [89]Zr is

available from different suppliers in GMP quality [156]. Several different antibodies have been radiolabelled with ^{89}Zr and applied to humans, and quite a few have already been tested in clinical trials [155].

Rubidium-82 ($T_{1/2}$ = 1.3 min) is produced from the strontium-82 (^{82}Sr)-^{82}Rb generator system. The ^{82}Sr-^{82}Rb generator system (Cardiogen-82®) is commercially available from Bracco Diagnostics, Princeton, NJ. [^{82}Rb]RbCl is used in clinical routine for cardiac perfusion measurements.

Copper-64 ($T_{1/2}$ = 12.7 h) is produced via the ^{64}Ni(p,n)^{64}Cu reaction in no-carrier-added quality on a medium-sized cyclotron. Due to its longer half-life, ^{64}Cu can easily be shipped and is commercially available from different suppliers, even in GMP quality. The longer half-life fits ideally to larger biomolecules such as antibodies, nanobodies or nanoconstructs. So far, only [^{64}Cu]ATSM (diacetyl-bis(N^4-methylthiosemicarbazone)) for imaging tumour hypoxia has been approved by the FDA for routine use. Several peptides and further biomolecules have been radiolabelled with ^{64}Cu and used in preclinical research and clinical settings [157].

Copper-62 ($T_{1/2}$ = 10 min) is produced from the ^{62}Zn-^{62}Cu generator system. In this generator system, ^{62}Zn is loaded on a Dowex 1 × 10 anion exchange column, and ^{62}Cu is eluted with 2 M HCl. Two well-known copper-62 radiopharmaceuticals are [^{62}Cu]ATSM (diacetyl-bis(N^4-methylthiosemicarbazone)) and [^{62}Cu]PTSM (pyruvaldehyde-bis(N^4-methylthiosemicarbazone)). [^{62}Cu]ATSM is being used in the clinic as a hypoxia imaging agent [158–160]. [^{62}Cu]PTSM has found application as a myocardial and brain perfusion PET imaging agent [161].

8.2 Automated Radiosyntheses: Modules

Semi-automated and automated processes have always been part of radiochemical methods or syntheses. This is due to the fact that one major concern in radio- and nuclear chemistry is to keep the radiation dose to personnel at a minimum. Accordingly, automation is favourable and generally preferable as many of these automated operations process large amounts of radioactivity which are excluded for a direct manual handling. Particularly for short-lived radionuclides such as carbon-11, nitrogen-13, oxygen-15 and fluorine-18, the required amounts of radioactivity in routine productions are very high and call for fully remote-controlled operations. Furthermore, automated reaction steps or procedures generally are more reliable and thus more reproducible than manual radiosyntheses. In addition, automated processes save time and therefore enhance product yields and efficiency. Today, the radiosyntheses of almost all routine PET radiopharmaceuticals are fully automated and are performed in so-called modules.

The first radiosynthesis modules were self-constructed and made of several remote controlled valves, solvent reservoirs, radiation detectors and reactors or heating systems. The components were connected by tubes and lines from conventional HPLC systems. The radiosyntheses were carried out by manual switching of valves. Today, the modules are computer-controlled, and the reaction steps of a radiosyntheses are programmed while the basic concept of the hardware has not much changed [162–164].

After a module is equipped with precursor, solvents and reagents, the radionuclide is transferred directly from the target into the module, and the radiosynthesis is started. During the procedure, (radio)detectors and other probes in the module monitor the course of radioactivity, temperature, pressure and further reaction parameters which are usually all recorded by the computer.

Depending on the system, different radiosyntheses can be programmed. If they are all based on the same radiochemical principle (e.g. a two-step radiosynthesis consisting of a radiolabelling step and a subsequent deprotection step), only basic parameters such as temperature and time need to be re-programmed. For more complex radiosyntheses, more changes are required, and the radiosynthesis module has to be technically adapted to meet the demands of the new procedure. Consequently, in routine productions for

Table 8.2 Examples of vendors of automated radiosynthesis apparatuses and their systems suitable for [^{18}F]FDG

Company	Radiosynthesis module suitable for [^{18}F]FDG
GE Healthcare	FASTlab™ 2
ORA	Neptis Nx3, Neptis mosaic
Elysia-Raytest	F-18 Synthesis module, 'GAIA for F-18'
Eckert & Ziegler AG	Modular-Lab PharmTracer
IBA	Synthera®+
Trasis	All-in-one synthesizer

clinical use, on daily basis each PET radiopharmaceutical is produced in a specifically designed module.

Several commercial module-based synthesis systems have been marketed so far. The first systems were available for [^{18}F]FDG and have clearly contributed to the success and commercialization of [^{18}F]FDG [162–164]. Some examples of manufacturers and vendors of radiosynthesis modules and their corresponding synthesis modules for [^{18}F]FDG productions are outlined in Table 8.2.

Automated radiosynthesis devices are commercially available for almost every clinically relevant PET radiopharmaceutical such as [^{18}F]FDG, [^{18}F]FPSMA, [^{18}F]FET, [^{68}Ga]HBED-PSMA, [^{68}Ga]DOTA-TATE, [^{11}C]CH$_3$I, [^{13}N]NH$_3$ or [^{15}O]water. Furthermore, systems that are more flexible and adaptable for different radiosyntheses have been developed. The so-called modular systems offer a broad adaptability and high flexibility towards more complex radiosyntheses and individual method development. Various small components, generally designed for certain processes or reaction steps, are combined and assembled according to the desired radiosynthetic route. In contrast, the so-called black boxes allow only one or two types of radiosyntheses.

Recently, new approaches using microreactors and microfluidic systems have emerged in the field [165, 166]. Such microscale reactions benefit from very small amounts of precursors while they still give high yields after very short reaction times. The first systems have proven applicability and have shown satisfying results for the production of some ^{11}C-labelled [167,

168] and ^{18}F-labelled [167–169] PET radiopharmaceuticals. As [^{18}F]FDG is the most widely employed PET radiopharmaceutical in nuclear medicine, the radiosynthesis of [^{18}F]FDG is commonly used as a benchmark test for those microfluidic systems. The development of these systems is still ongoing, but the proof-of-principle has been made. New materials and production routes enable various novel approaches such as a 3D-printed radiosynthesis module [170].

8.3   Quality Control of PET Radiopharmaceuticals

As PET radiopharmaceuticals are administered to humans, they need to fulfil certain test criteria before they are authorized for administration. In comparison to normal drugs, some test results cannot be obtained before administration due to the short half-lives of the radionuclides used for PET radiopharmaceuticals. In such cases, the so-called dry runs for validation are performed. The full batch of a PET radiopharmaceutical production is used for tests, and thereby the method and procedure of production can be validated. In general, all productions, methods and test procedures have to be validated in accordance with GMP guidelines.

Quality control tests for PET radiopharmaceuticals can be divided into two subtypes: biological tests and physicochemical tests [171]. A list of required tests for PET radiopharmaceuticals is outlined in Table 8.3.

In general, the biological tests need prolonged time and cannot be analysed before the administration of the PET radiopharmaceutical. These tests are performed 'after the fact' (retrospectively) or for the validation of the production process.

The quality control tests for PET radiopharmaceuticals in clinical routine are regulated by the national law of the corresponding country and/or the pharmacopeia. Responsible authorities usually provide guidelines such as pharmacopeia with clear specifications of routine productions of PET radiopharmaceuticals in clinical use.

Table 8.3 Quality control tests for PET radiopharmaceuticals

Quality control test	Criteria or subject of test	Test method
Biological tests		
Sterility	Injected volume needs to be sterile	Incubation over 2 weeks (bacteria growth)
Pyrogenicity	Batch needs to be apyrogenic	Limulus Amebocyte Lysate (LAL) test[a]
Physicochemical tests		
Appearance	Colour/clarity—turbidity	Visual inspection
Isotonicity	Injected volume needs to be isotonic	Osmometry (cryoscopy)
pH	7.4 (ideal) and slightly lower or higher	pH meter
Radionuclidic purity	Radionuclides must be pure prior use	γ-Spectroscopy and further radioanalytics
Chemical purity	Impurities or solvent traces need to be removed or proved to be harmless	Chemical analytics, frequently HPLC or GC
Radiochemical purity	Individual limits[b]	Radiochromatography (HPLC and TLC)

[a]Quick test for pyrogens based on coagulation of the lysate of amebocytes from the blood of the horseshoe crab (*Limulus polyphemus*)

[b]Generally, for PET radiopharmaceuticals, there are individual limits/specifications set by the national pharmacopeia or the authorities of the corresponding country

8.4 PET Radiopharmaceuticals in Drug Development

During the development of new drugs, many questions and decisions have to be answered and made. Some of them are crucial and serve as knockout criteria for the drug candidates. In pharmaceutical industry and the drug development field, three main concepts are classified: 'proof of target (POT)', 'proof of mechanism (POM)' and 'proof of concept (POC)' [172]. The available methods to give such proofs are limited, and the field of PET imaging offers great opportunities for that. However, only a few examples can be found where PET radiopharmaceuticals have been employed as biomarkers in drug development.

Examples for the use of a PET tracer for the POT can be found in the development of therapeutics for neurodegenerative diseases. In the development of a new dopamine D2 receptor antagonist (ziprasidone, CP-88,059–01), the receptor occupancy of the dopamine D2 receptor antagonist, ziprasidone (CP-88,059–01), was determined using [11C]raclopride [173]. In the same manner, the dopamine D_2 and D_3 receptor occupancies were studied by PET imaging using [11C]raclopride during the development of a potential antipsychotic drug (aripiprazole, OPC 14597) [174]. In both studies, the displacement of the radiolabelled receptor ligand by the drug candidates gave the proof of target interaction. If, in a later stage, PET imaging results correlate with the clinical outcome, it could be further used as proof of concept.

In oncology, PET imaging is commonly used for the diagnosis and staging of cancers and has also shown potential in therapy monitoring. PET imaging using [18F]FDG can visualize changes in tumour metabolism and thus can show therapy effects at a very early stage. Consequently, [18F]FDG PET imaging can give the proof of mechanism as it can provide information of the tumour response to a new drug. This has been demonstrated in patients with gastrointestinal tumours treated with new kinase inhibitors as the [18F]FDG uptake into the tumours was significantly reduced already after one cycle of treatment [175, 176].

Most information can be obtained if the drug candidate itself is radiolabelled. This strategy is not always adaptable and limited to structures which allow a reasonable introduction of a radionuclide. However, a radiolabelled drug candidate

gives information about the full pharmacokinetics and can answer many crucial questions at once.

PET imaging is particularly suitable for several questions in drug development. However, PET imaging has been used in drug development only to a small extent until now, but it is gaining more and more acceptance. Besides neurosciences and oncology, the use of PET imaging in drug development can be expected to further grow and also to emerge in other fields of drug development [177].

8.5 Conclusions

[^{18}F]FDG is the best clinically known and the most successful PET radiopharmaceutical, so far. Due to the clinical utility of [^{18}F]FDG, PET imaging has grown rapidly, and PET has become a powerful imaging technique. Recently, the PSMA ligands and the theranostic concept have boosted PET imaging further and helped to gain more acceptance in various disciplines. Furthermore, pharma industry is stepping in and further accelerating developments and market authorization of PET radiopharmaceuticals. Currently, a number of novel PET radiopharmaceuticals have found application as routine imaging agents in the clinic. Latest developments in FAP-targeting radiotracers have gained greatest attention. Many commercially available automated synthesis modules from various vendors allow GMP-compliant and quick access to most of these novel radiopharmaceuticals. Moreover, several PET radiopharmaceuticals labelled with longer-lived nuclides are commercially available, enabling innovative PET imaging for those clinics lacking an onsite cyclotron or a radiochemistry facility. Nonetheless, still for a vast majority of new targets, there are currently no PET imaging probes available. Radiochemists are therefore constantly challenged to develop appropriate imaging probes for new targets. Hopefully, those PET radiopharmaceuticals currently under development and in preclinical evaluation will find their way very rapidly into clinical imaging routine.

References

1. Meyer GJ. Current availability of radiopharmaceuticals in Germany. Nuklearmedizin. 2018;41:386–92.
2. Cardinale J, Schäfer M, Benešová M, Bauder-Wüst U, Leotta K, Eder M, Neels OC, Haberkorn U, Giesel FL, Kopka K. Preclinical evaluation of 18F-PSMA-1007, a new prostate-specific membrane antigen ligand for prostate cancer imaging. J Nucl Med. 2017;58:425–31.
3. Volker JF, Hodge HC, Wilson HJ, Van Voorhis SN. The adsorpton of fluorides by enamel, dentin, bone and hydroxyapatite as shown by the radioactive isotope. J Biol Chem. 1940;134:543–8.
4. Blau M, Nagler W, Bender MA. Fluorine-18: a new isotope for bone scanning. J Nucl Med. 1962;3:332–4.
5. Grant FD, Fahey FH, Packard AB, Davis RT, Alavi A, Treves ST. Skeletal PET with ^{18}F-Fluoride: applying new technology to an old tracer. J Nucl Med. 2008;49:68–78.
6. Kumar R, Alavi A. Clinical applications of Fluorodeoxyglucose—positron emisson tomography in the management of malignant melanoma. Curr Opin Oncol. 2005;17:154–9.
7. Coleman RE. FDG imaging. Nucl Med Biol. 2000;27:689–90.
8. Reske SN, Kotzerke J. FDG-PET for clinical use. Eur J Nucl Med. 2001;28:1707–23.
9. Gambhir SS, Czerni J, Schwimmer J, Silverman DHS, Coleman RE, Phelps ME. A tabulated summary of FDG PET literature. J Nucl Med. 2001;42:1S–93S.
10. Adam MJ. Radiohalogenated carbohydrates for use in PET and SPECT. J Label Compd Radiopharm. 2002;45:167–80.
11. Ido T, Wan C-N, Casella V, Fowler JS, Wolf AP, Reivich M, Kuhl DE. Labeled 2-deoxy-D-glucose analogs. ^{18}F-labeled 2-deoxy-2-fluoro-D-glucose, 2-deoxy-2-fluoro-D-mannose and ^{14}C-2-deoxy-2-fluoro-D-glucose. J Label Compd Radiopharm. 1978;14:175–82.
12. Hamacher K, Coenen HH, Stöcklin G. Efficient stereospecific synthesis of no-carrier-added 2-[^{18}F]-fluoro-2-deoxy-D-glucose using aminopolyether supported nucleophilic substitution. J Nucl Med. 1986;27:235–8.
13. Füchtner FF, Steinbach J, Mäding P, Johannsen B. Basic hydrolysis of 2-[^{18}F]fluoro-1,3,4,6-tetra-O-acetyl-D-glucose in the preparation of 2-[^{18}F]fluoro-2-deoxy-D-glucose. Appl Radiat Isot. 1996;47:61–6.
14. Meyer G-J, Matzke KH, Hamacher K, Füchtner FF, Steinbach P, Notohamiprodjo G, Zijlstra S. Stability of 2-[18]f9fluoro-deoxy-D-glucose towards epimerisation under alkaline conditions. Appl Radiat Isot. 1999;51:37–41.
15. Beuthien-Baumann B, Hamacher K, Oberdorfer F, Steinbach J. Preparation of fluorine-18 labelled sug-

ars and derivatives and their application as tracer for positron-emission-tomography. Carbohydr Res. 2000;327:107–18.

16. Lutje S, Heskamp S, Cornelissen AS, Poeppel TD, van den Broek SA, Rosenbaum-Krumme S, Bockisch A, Gotthardt M, Rijpkema M, Boerman OC. PSMA ligands for radionuclide imaging and therapy of prostate cancer: clinical status. Theranostics. 2015;5:1388–401.

17. Schmuck S, Nordlohne S, von Klot CA, Henkenberens C, Sohns JM, Christiansen H, Wester HJ, Ross TL, Bengel FM, Derlin T. Comparison of standard and delayed imaging to improve the detection rate of [68Ga]PSMA I&T PET/CT in patients with biochemical recurrence or prostate-specific antigen persistence after primary therapy for prostate cancer. Eur J Nucl Med Mol Imaging. 2017;44:960–8.

18. Werner RA, Derlin T, Lapa C, Sheikbahaei S, Higuchi T, Giesel FL, Behr S, Drzezga A, Kimura H, Buck AK, Bengel FM, Pomper MG, Gorin MA, Rowe SP. 18F-labeled, PSMA-targeted radiotracers: leveraging the advantages of Radiofluorination for prostate cancer molecular imaging. Theranostics. 2020;10:1–16.

19. Mease RC, Dusich CL, Foss CA, Ravert HT, Dannals RF, Seidel J, Prideaux A, Fox JJ, Sgouros G, Kozikowski AP, Pomper MG. N-[N-[(S)-1,3-Dicarboxypropyl]carbamoyl]-4-[18F]fluorobenzyl-L-cysteine, [18F]DCFBC: a new imaging probe for prostate cancer. Clin Cancer Res. 2008;14:3036–43.

20. Chen Y, Pullambhatla M, Foss CA, Byun Y, Nimmagadda S, Senthamizhchelvan S, Sgouros G, Mease RC. Pomper MG (2011) 2-(3-{1-Carboxy-5-[(6-[18F]fluoro-pyridine-3-carbonyl)-amino]-pentyl}-ureido)-pentanedioic acid, [18F]DCFPyL, a PSMA-based PET imaging agent for prostate cancer. Clin Cancer Res. 17:7645–53.

21. Cardinale J, Martin R, Remde Y, Schäfer M, Hienzsch A, Hübner S, Zerges AM, Marx H, Hesse R, Weber K, Smits R, Hoepping A, Müller M, Neels OC, Kopka K. Procedures for the GMP-compliant production and quality control of [18F]PSMA-1007: a next generation radiofluorinated tracer for the detection of prostate cancer. Pharmaceuticals. 2017;10:E77.

22. Malik N, Zlatopolskiy B, Machulla HJ, Reske SN, Solbach C. One pot radiofluorination of a new potential PSMA ligand [Al18F]NOTA-DUPA-pep. J Label Compd Radiopharm. 2012;55:320–5.

23. Graham K, Lesche R, Gromov AV, Böhnke N, Schäfer M, Hassfeld J, Dinkelborg L, Kettschau G. Radiofluorinated derivatives of 2-(phosphono-methyl)pentanedioic acid as inhibitors of prostate specific membrane antigen (PSMA) for the imaging of prostate cancer. J Med Chem. 2012;55:9510–20.

24. Zlatopolskiy BD, Endepols H, Krapf P, Guliyev M, Urusova EA, Richarz R, Hohberg M, Dietlein M, Drzezga A, Neumaier B. Discovery of 18F-JK-PSMA-7, a PET Probe for the detection

of small PSMA-positive lesions. J Nucl Med. 2019;60:817–23.

25. Eiber M, Krönke M, Wurzer A, Ulbrich L, Jooß L, Maurer T, Horn T, Schiller K, Langbein T, Buschner G, Wester HJ, Weber WA. 18F-rhPSMA-7 positron emission tomography for the detection of biochemical recurrence of prostate cancer following radical prostatectomy. J Nucl Med. 2019;61(5):696–701.

26. Namavari M, Bishop A, Satyamurthy N, Bida G, Barrio JR. Regioselective Radiofluorodestannylation with [18F]F2, and [18F]CH3COOF: a high yield synthesis of 6-[18F]Fluoro-L-dopa. Appl Radiat Isot. 1992;43:989–96.

27. De Vries EFJ, Luurtsema G, Brüssermann M, Elsinga PH, Vaalburg W. Fully automated synthesis module for the high yield one-pot preparation of 6-[18F]fuoro-L-DOPA. Appl Radiat Isot. 1999;51:389–94.

28. Luxen A, Perlmutter M, Bida GT, Van Moffaert G, Cook JS, Satyamurthy N, Phelps ME, Barrio JR. Remote, semiautomated production of 6-[18F] Fluoro-L-dopa for human studies with PET. Appl Radiat Isot. 1990;41:275–81.

29. Szajek LP, Channing MA, Eckelman WC. Automated synthesis 6-[18F]fluoro-L-DOPA using polystyrene supports with 6-mercuric of modified bound DOPA precursors. Appl Radiat Isot. 1998;49:795–804.

30. Lemaire C, Gillet S, guillouet S, Plenevaux A, Aerts J, Luxen A. Highly enantioselective synthesis of no-carrier-added 6-[18F]Fluoro-L-dopa by chiral phase-transfer alkylation. Eur J Org Chem. 2004;2004:2899–904.

31. Wagner FM, Ermert J, Coenen HH. Three-step, "one-pot" radiosynthesis of 6-fluoro-3,4-dihydroxy-L-phenylalanine by isotopic exchange. J Nucl Med. 2009;50:1724–9.

32. Mossine AV, Tanzey SS, Brooks AF, Makaravage KJ, Ichiishi N, Miller JM, Henderson BD, Skaddan MB, Sanford MS, Scott PJH. One-pot synthesis of high molar activity 6-[18F]fluoro-l-DOPA by cu-mediated fluorination of a BPin precursor. Org Biomol Chem. 2019;17:8701–5.

33. Garnett ES, Firnau G, Nahmias C. Dopamine visualized in the basal ganglia of living man. Nature. 1983;305:137–8.

34. Volkow ND, Fowler JS, Gatley SJ, Logan J, Wang G-J, Ding Y-S, Dewey S. PET evaluation of the dopamine system of the human brain. J Nucl Med. 1996;37:1242–56.

35. Lee CS, Samii A, Sossi V, Ruth TJ, Schulzer M, Holden JE, Wudel J, Pal PK, De La Fuente-Fernandez R, Calne DB, Stoessl AJ. In vivo positron emission tomographic evidence for compensatory changes in presynaptic dopaminergic nerve terminals in Parkinson's disease. Ann Neurol. 2000;47:493–503.

36. Becherer A, Szabó M, Karanikas G, Wunderbaldinger P, Angelberger P, Raderer M, Kurtaran A, Dudczak R, Kletter K. Imaging of advanced neuroendocrine tumors with 18F-FDOPA PET. J Nucl Med. 2004;45:1161–7.

37. Lu MY, Liu YL, Chang HH, Jou ST, Yang YL. Characterization of neuroblastic tumors using ^{18}F-FDOPA PET. J Nucl Med. 2013;54:42–9.

38. Langen K-J, Hamacher K, Weckesser M, Floeth F, Stoffels G, Bauer D, Coenen HH, Pauleit D. O-(2-[18F]fluoroethyl)-L-tyrosine: uptake mechanisms and clinical applications. Nucl Med Biol. 2006;33:287–94.

39. Kaim AH, Weber B, Kurrer MO, Westera G, Schweitzer A, Gottschalk J, von Schulthess GK, Buck A. ^{18}F-FDG and ^{18}F-FET uptake in experimental soft tissue infection. Eur J Nucl Med Mol Imaging. 2002;29:648–54.

40. Pauleit D, Floeth F, Hamacher K, Riemenschneider MJ, Reifenberger G, Müller H-W, Zilles K, Coenen HH, Langen K-J. O-(2-[18F]fluoroethyl)-L-tyrosine PET combined with MRI improves the diagnostic assessment of cerebral gliomas. Brain. 2005;128:678–87.

41. Wester H-J, Herz M, Weber W, Heiss P, Senekowitsch-Schmidtke R, Schwaiger M, Stöcklin G. Synthesis and Radiopharmacology of O-(2-[18F] fluoroethyl)-L-tyrosine for tumor imaging. J Nucl Med. 1999;40:205–12.

42. Hamacher K, Coenen HH. Effcient routine production of the ^{18}F-labelled amino acid O-(2-[18F]fluoroethyl)-L-tyrosine. Appl Radiat Isot. 2002;57:205–12.

43. Krasikova RN, Kuznetsova OF, Fedorova OS, Maleev VI, Saveleva TF, Belokon YN. No carrier added synthesis of O-(2'-[18F]fluoroethyl)-l-tyrosine via a novel type of chiral enantiomerically pure precursor, Ni[II] complex of a (S)-tyrosine Schiff base. Bioorg Med Chem. 2008;16:4994–5003.

44. Kong XB, Zhu QY, Vidal PM, Watanabe KA, Polsky B, Armstrong D, Ostrander M, Lang SA Jr, Muchmore E, Chou TC. Comparisons of anti-human immunodeficiency virus activities, cellular transport, and plasma and intracellular pharmacokinetics of 3'-fluoro-3'-deoxythymidine and 3'-azido-3'-deoxythymidine. Antimicrob Agents Chemother. 1992;36:808–18.

45. Shields AF, Grierson JR, Dohmen BM, Machulla H-J, Stayanoff JC, Lawhorn-Crews JM, Obradovich JE, Muzik O, Mangner TJ. Imaging proliferation *in vivo* with [F-18]FLT and positron emission tomography. Nat Med. 1998;4:1334–6.

46. Mier W, Haberkorn U, Eisenhut M. [F-18]FLT; portrait of a proliferation marker. Eur J Nucl Med Mol Imaging. 2002;29:165–9.

47. Buck AK, Halter G, Schirrmeister H, Kotzerke J, Wurziger I, Glatting G, Mattfeldt T, Neumaier B, Reske SN, Hetzel M. Imaging proliferation in lung tumors with PET: ^{18}F-FLT versus ^{18}F-FDG. J Nucl Med. 2003;44:1426–31.

48. Francis DL, Visvikis D, Costa DC, Arulampalam THA, Townsend C, Luthra SK, Taylor I, Ell PJ. Potential impact of [18F]3'-deoxy-3'-fluorothymidine versus [18F]fluoro-2-deoxy-d-glucose in positron emission tomography for colorectal cancer. Eur J Nucl Med Mol Imaging. 2003;30:988–94.

49. Van Waarde A, Cobben DCP, Suurmeijer AJH, Maas B, Vaalburg W, de Vries EFJ, Jager PL, Hoekstra HJ, Elsinga PH. Selectivity of ^{18}F-FLT and ^{18}F-FDG for differentiating tumor from inflammation in a rodent model. J Nucl Med. 2004;45:695–700.

50. Chen W, Cloughesy T, Kamdar N, Satyamurthy N, Bergsneider M, Liau L, Mischel P, Czernin J, Phelps ME, Silverman DHS. Imaging proliferation in brain tumors with ^{18}F-FLT PET: comparison with ^{18}F-FDG. J Nucl Med. 2005;46:945–52.

51. Shields AF. Positron emission tomography measurement of tumor metabolism and growth: its expanding role in oncology. Mol Imaging Biol. 2006;8:141–50.

52. Yamamoto Y, Nishiyama Y, Kimura N, Ishikawa S, Okuda M, Bandoh S, Kanaji N, Asakura M, Ohkawa M. Comparison of ^{18}F-FLT PET and ^{18}F-FDG PET for preoperative staging in non-small cell lung cancer. Eur J Nucl Med Mol Imaging. 2008;35:236–45.

53. Wilson IK, Chatterjee S, Wolf W. Synthesis of 3'-fluoro-3'-deoxythymidine and studies of its ^{18}F-radiolabeling, as a tracer for the noninvasive monitoring of the biodistribution of drugs against AIDS. J Fluor Chem. 1991;55:283–9.

54. Kim DW, Ahn D-S, Oh Y-H, Lee S, Kil HS, Oh SJ, Lee SJ, Kim JS, Ryu JS, Moon DH, Chi SY. A new class of S$_N$2 reactions catalyzed by Protic solvents: facile fluorination for isotopic labeling of diagnostic molecules. J Am Chem Soc. 2006;128: 16394–7.

55. Martin SJ, Eisenbarth JA, Wagner-Utermann U, Mier W, Henze M, Pritzkow H, Haberkorn U, Eisenhut M. A new precursor for the radiosynthesis of [18F] FLT. Nucl Med Biol. 2002;29:263–73.

56. Grierson JR, Shields AF. Radiosynthesis of 3'-deoxy-3'-[18F]fluorothymidine: [18F]FLT for imaging of cellular proliferation *in vivo*. Nucl Med Biol. 2000;27:143–56.

57. Machulla H-J, Blocher A, Kuntzsch M, Piert M, Wei R, Grierson JR. Simplified labeling approach for synthesizing 3'-Deoxy-3'-[18F]fluorothymidine ([18F] FLT). J Radioanal Nucl Chem. 2000;243:843–6.

58. Yun M, Oh SJ, Ha H-J, Ryu JS, Moon DH. High radiochemical yield synthesis of 3'-deoxy-3'-[18F] fluorothymidine using (5'-O-dimethoxytrityl-2'-deoxy-3'-O-nosyl-β-D-threo pentofuranosyl)thymine and its 3-N-BOC-protected analogue as a labeling precursor. Nucl Med Biol. 2003;30:151–7.

59. Windhorst AD, Klein PJ, Eisenbarth J, Oeser T, Kruijer PS, Eisenhut M. 3'-Sulfonylesters of 2,5'-anhydro-1-(2-deoxy-β-D-*threo*-pentofuranosyl)thymine as precursors for the synthesis of [18F]FLT: syntheses and radiofluorination trials. Nucl Med Biol. 2008;35:413–23.

60. Mintun MA, Welch MJ, Siegel BA, Mathias CJ, Brodack JW, McGuire AH, Katzenellenbogen JA. Breast cancer: PET imaging of estrogen receptors. Radiology. 1988;169:45–8.

61. Dehdashti F, Mortimer JE, Siegel BA, Griffeth LK, Bonasera TJ, Fusselman MJ, Detert DD, Cutler PD, Katzenellenbogen JA, Welch MJ. Positron tomographic assessment of estrogen receptors in breast cancer: comparison with FDG-PET and in vitro receptor assays. J Nucl Med. 1995;36:1766–74.

62. Sundararajan L, Linden HM, Link JM, Krohn KA, Mankoff DA. 18F-Fluoroestradiol. Semin Nucl Med. 2007;37:470–6.

63. Palmer AJ, Widdowson DA. The preparation of ^{18}F-labelled 4-Fluoroestrone and 4-Fluoroestradiol. J Label Compd Radiopharm. 1979;16:14–6.

64. Eakins MN, Palmer AJ, Waters SL. Studies in the rat with ^{18}F-4-Fluoro-oestradiol and ^{18}F-4-Fluoro-oestrone as potential prostate scanning agents: comparison with ^{125}I-2-Iodo-oestradiol and ^{125}I-2,4-Di-iodo-oestradiol. Int J Appl Radiat Isot. 1979;30:695–700.

65. Heiman DF, Senderoff SG, Katzenellenbogen JA, Neeley RJ. Estrogen-receptor based imaging agents. 1. Synthesis and receptor-binding affinity of some aromatic and D-ring halogenated estrogens. J Nucl Med. 1980;23:994–1002.

66. Kiesewetter DO, Katzenellenbogen JA, Kilbourn MR, Welch MJ. Synthesis of 16-Fluoroestrogens by unusually facile fluoride ion displacement reactions: prospects for the preparation of fluorine-18 labeled estrogens. J Org Chem. 1984;49:4900–5.

67. Kiesewetter DO, Kilbourn MR, Landvatter SW, Heiman DF, Katzenellenbogen JA, Welch MJ. Preparation of four fluorine-18-labeled estrogens and their selective uptakes in target tissues of immature rats. J Nucl Med. 1984;25:1212–21.

68. Van Brocklin HF, Carlson KE, Katzenellenbogen JA, Welch MJ. 16β-([18F]Fluoro)estrogens: systematic investigation of a new series of fluorine-18-labeled estrogens as potential imaging agents for estrogen-receptor-positive breast tumors. J Med Chem. 1993;36:1619–29.

69. Benard F, Ahmed N, Beauregard JM, Rousseau J, Aliaga A, Dubuc C, Croteau E, van Lier JE. [F-18] fluorinated estradiol derivatives for oestrogen receptor imaging: impact of substituents, formulation and specific activity on the biodistribution in breast tumour-bearing mice. Eur J Nucl Med Mol Imaging. 2008;35:1473–9.

70. Römer J, Steinbach J, Kasch H. Studies on the synthesis of 16 alpha-[F-18]fluoroestradiol. Appl Radiat Isot. 1996;47:395–9.

71. Römer J, Füchtner F, Steinbach J, Johanssen B. Automated production of 16α-[F-18]fluoroestradiol for breast cancer imaging. Nucl Med Biol. 1999;26:473–9.

72. Mori T, Kasamatsu S, Mosdzianowski C, Welch MJ, Yonekura Y, Fujibayashi Y. Automatic synthesis of 16α-[F-18]fluoro-17β-estradiol using a cassette-type [F-18]fluorodeoxyglucose synthesizer. Nucl Med Biol. 2006;33:281–6.

73. DeGrado TR, Baldwin SW, Wang S, Orr MD, Liao RP, Friedman HS, Reiman R, Price DT, Coleman

RE. Synthesis and evaluation of ^{18}F-labeled choline analogs as oncologic PET tracers. J Nucl Med. 2001;42:1805–14.

74. Hara T, Kosaka N, Shinoura N, Kondo T. PET imaging of brain tumor with [methyl-^{11}C]choline. J Nucl Med. 1997;38:842–24.

75. DeGrado TR, Coleman RE, Wang S, Baldwin SW, Orr MD, Robertson CN, Polascik TJ, Price DT. Synthesis and evaluation of ^{18}F-labeled choline as an oncologic tracer for positron emission tomography: initial findings in prostate cancer. Cancer Res. 2000;61:110–7.

76. Hara T. ^{18}F-Fluorocholine: a new oncologic PET tracer. J Nucl Med. 2001;12:1815–7.

77. Kwee SA, Coel MN, Lim J, Ko JP. Combined use of F-18 fluorocholine positron emission tomography and magnetic resonance spectroscopy for brain tumour evaluation. J Neuroimaging. 2004;14:285–9.

78. Coenen HH, Colosimo M, Schüller M, Stöcklin G. Preparation of N. C. A. [18F]-CH2BrF via aminopolyether supported nucleophilic substitution. J Label Compd Radiopharm. 1985;23:587–95.

79. Eskola O, Bergman J, Lehikoinen P, Ögren M, Långström B, Solin O. Synthesis of ^{18}F-bromofluoromethane [18F]FCH2Br; fluoromethylation reagent with high specific radioactivity. J Label Compd Radiopharm. 1999;42:S543–5.

80. Rasey JS, Koh W-J, Evans ML, Peterson LM, Lewellen TK, Graham MM, Krohn KA. Quantifying regional hypoxia in human tumors with positron emission tomography of [18F]fluoromisonidazole: a pretherapy study of 37 patients. Int J Radiat Oncol Biol Phys. 1996;36:417–28.

81. Lui R-S, Chu L-S, Yen S-H, Chang C-P, Chou K-L, Wu L-C, Chang C-W, Lui M-T, Chen KY, Yeh S-H. Detection of anaerobic odontogenic infections by fluorine-18 fluoromisonidazole. Eur J Nucl Med Mol Imaging. 1996;23:1384–7.

82. Rajendran JG, Wilson DC, Conrad EU, Peterson LM, Bruckner JD, Rasey JS, Chin LK, Hofstrand PD, Grierson JR, Eary JF, Krohn KA. [18F]FMISO and [18F]FDG PET imaging in soft tissue sarcomas: correlation of hypoxia, metabolism and VEGF expression. Eur J Nucl Med Mol Imaging. 2003;30:695–704.

83. Lewis JS, Welch MJ. PET imaging of hypoxia. Q J Nucl Med. 2001;45:183–8.

84. Lehtiö K, Oikonen V, Nyman S, Grönroos T, Roivainen A, Eskola O, Minn H. Quantifying tumour hypoxia with fluorine-18 fluoroerythronitroimidazole ([18F]FETNIM) and PET using the tumour to plasma ratio. Eur J Nucl Med Mol Imaging. 2003;30:101–8.

85. Barthel H, Wilson H, Collingridge DR, Brown G, Osman S, Luthra SK, Brady F, Workman P, Price PM, Aboagye EO. In vivo evaluation of [18F]fluoroetanidazole as a new marker for imaging tumour hypoxia with positron emission tomography. Br J Cancer. 2004;90:2232–42.

86. Kämäräinen E-L, Kyllönen T, Nihtilä O, Björk H, Solin O. Preparation of fluorine-18-labelled fluoromisonidazole using two different synthesis methods. J Label Compd Radiopharm. 2004;47:37–45.

87. Grierson JR, Link JM, Mathis CA, Rasey JS, Krohn KA. A radiosynthesis of Fluorine-18 Fluoromisonidazole. J Nucl Med. 1989;30:343–50.

88. McCarthy TJ, Dence CS, Welch MJ. Application of microwave heating to the synthesis of [18F]fluoromisonidazole. Appl Radiat Isot. 1993;44:1129–32.

89. Lim J-L, Berridge MS. An efficient radiosynthesis of [18F]fluoromisonidazole. Appl Radiat Isot. 1993;44:1085–91.

90. Patt M, Kuntzsch M, Machulla HJ. Preparation of [18F]fluoromisonidazole by nucleophilic substitution on THP-protected precursor: yield dependence on reaction parameters. J Radioanal Nucl Chem. 1999;240:925–7.

91. Oh SJ, Chi DY, Mosdzianowski C, Kim JY, Gil HS, Kang SH, Ryu JS, Moon DH. Fully automated synthesis of [18F]fluoromisonidazole using a conventional [18F]FDG module. Nucl Med Biol. 2005;32:899–905.

92. Crouzel C, Guillaume M, Barré L, Lemaire C, Pike VW. Ligands and tracers for PET studies of the 5-HT system—current status. Nucl Med Biol. 1992;19:857–70.

93. Pike VW. Radioligands for PET studies of central 5-HT receptors and re-uptake sites—current status. Nucl Med Biol. 1995;22:1011–8.

94. Lemaire C, Cantineau R, Guillaume M, Plenevaux A, Christiaens L. Fluorine-18-Altanserin: a radioligand for the study of serotonin receptors with PET: radiolabeling and in vivo biologic behavior in rats. J Nucl Med. 1991;32:2266–72.

95. Lemaire C, Cantineau R, Christiaens L, Guillaume M. N.C.A. radiofluorination of altanserin: a potential serotonin receptor-binding radiopharamceutical for positron emission tomography. J Label Compd Radiopharm. 1989;26:336–7.

96. Mukherjee J, Yang Z-Y, Lew R, Brown T, Kronmal S, Cooper MD, Seiden LS. Evaluation of d-amphetamine effects on the binding of dopamine D-2 receptor radioligand, F-18-fallypride in nonhuman primates using positron emission tomography. Synapse. 1997;27:1–13.

97. Mukherjee J, Yang Z-Y, Brown T, Lew R, Wernick M, Ouyang X, Yasillo N, Chen C-T, Mintzer R, Cooper M. Preliminary assessment of extrastriatal dopamine d-2 receptor binding in the rodent and nonhuman primate brains using the high affinity radioligand, 18F-fallypride. Nucl Med Biol. 1999;26:519–27.

98. Christian BT, Narayanan TK, Shi BZ, Mukherjee J. Quantitation of striatal and extrastriatal D-2 dopamine receptors using PET imaging of [F-18] fallypride in nonhuman primates. Synapse. 2000;38:71–9.

99. Slifstein M, Narendran R, Hwang DR, Sudo Y, Talbot PS, Huang YY, Laruelle M. Effect of amphetamine on [F-18]fallypride in vivo binding to D-2 receptors in striatal and extrastriatal regions of the primate brain: single bolus and bolus plus constant infusion studies. Synapse. 2004;54:46–63.

100. Riccardi P, Baldwin R, Salomon R, Anderson S, Ansari MS, Li R, Dawant B, Bauernfeind A, Schmidt D, Kessler R. Estimation of baseline dopamine D-2 receptor occupancy in striatum and extrastriatal regions in humans with positron emission tomography with [F-18] fallypride. Biol Psychiatry. 2008;63:241–4.

101. Mukherjee J, Yang Z-Y, Das MK, Brown T. Fluorinated benzamide neuroleptics—III. Development of (S)-N-[(1-allyl-2-pyrrolidinyl)methyl]-5-(3-[18F] fluoropropyl)-2,3-dimethoxybenzamide as an improved dopamine D-2 receptor tracer. Nucl Med Biol. 1995;22:283–96.

102. Doorduin J, Klein HC, Dierckx RA, James M, Kassiou M, de Vries EF. [11C]-DPA-713 and [18F]-DPA-714 as new PET tracers for TSPO: a comparison with [11C]-(R)-PK11195 in a rat model of herpes encephalitis. Mol Imaging Biol. 2009;11:386–98.

103. Lartey FM, Ahn GO, Shen B, Cord KT, Smith T, Chua JY, Rosenblum S, Liu H, James ML, Chernikova S, Lee SW, Pisani LJ, Tirouvanziam R, Chen JW, Palmer TD, Chin FT, Guzman R, Graves EE, Loo BW Jr. PET imaging of stroke-induced neuroinflammation in mice using [18F]PBR06. Mol Imaging Biol. 2014;16:109–17.

104. Brackhan M, Bascuñana P, Postema JM, Ross TL, Bengel FM, Bankstahl M, Bankstahl JP. Serial quantitative TSPO-targeted PET reveals peak microglial activation up to 2 weeks after an epileptogenic brain insult. J Nucl Med. 2016;57:1302–8.

105. Thackeray JT, Hupe HC, Wang Y, Bankstahl JP, Berding G, Ross TL, Bauersachs J, Wollert KC, Bengel FM. Myocardial inflammation predicts remodeling and neuroinflammation after myocardial infarction. J Am Coll Cardiol. 2017;71:263–75.

106. Kapanadze T, Bankstahl JP, Wittneben A, Koestner W, Ballmaier M, Gamrekelashvili J, Krishnasamy K, Limbourg A, Ross TL, Meyer GJ, Haller H, Bengel FM, Limbourg FP. Multimodal and multiscale analysis reveals distinct vascular, metabolic and inflammatory components of the tissue response to limb ischemia. Theranostics. 2019;9:152–66.

107. Wadsworth H, Jones PA, Chau WF, Durrant C, Fouladi N, Passmore J, O'Shea D, Wynn D, Morisson-Iveson V, Ewan A, Thaning M, Mantzilas D, Gausemel I, Khan I, Black A, Avory M, Trigg W. [18F]GE-180: a novel fluorine-18 labelled PET tracer for imaging translocator protein 18 kDa (TSPO). Bioorg Med Chem Lett. 2012;22:1308–13.

108. Villemagne VL, Doré V, Burnham SC, Masters CL, Rowe CC. Imaging tau and amyloid-β proteinopathies in Alzheimer disease and other conditions. Nat Rev Neurol. 2018;14:225–36.

109. Klunk WE, Engler H, Nordberg A, Wang YM, Blomqvist G, Holt DP, Bergstrom M, Savitcheva I, Huang GF, Estrada S, Ausen B, Debnath ML,

Barletta J, Price JC, Sandell J, Lopresti BJ, Wall A, Koivisto P, Antoni G, Mathis CA, Langstrom B. Imaging brain amyloid in Alzheimer's disease with Pittsburgh compound-B. Ann Neurol. 2004;55:306–19.

110. Koole M, Lewis DM, Buckley C, Nelissen N, Vandenbulcke M, Brooks DJ, Vandenberghe R, Van Laere K. Whole-body biodistribution and radiation dosimetry of ^{18}F-GE067: a radioligand for in vivo brain amyloid imaging. J Nucl Med. 2009;50:818–22.

111. Kung HF, Choi SR, Qu W, Zhang W, Skovronsky D. ^{18}F stilbenes and styrylpyridines for PET imaging of A beta plaques in Alzheimer's disease: a miniperspective. J Med Chem. 2010;53:933–41.

112. Wong DF, Rosenberg PB, Zhou Y, Kumar A, Raymont V, Ravert HT, Dannals RF, Nandi A, Brašić JR, Ye W, Hilton J, Lyketsos C, Kung HF, Joshi AD, Skovronsky DM, Pontecorvo MJ. In vivo imaging of amyloid deposition in Alzheimer disease using the radioligand ^{18}F-AV-45 (florbetapir F-18). J Nucl Med. 2010;51:913–20.

113. Barthel H, Gertz HJ, Dresel S, Peters O, Bartenstein P, Buerger K, Hiemeyer F, Wittemer-Rump SM, Seibyl J, Reininger C, Sabri O. Cerebral amyloid-beta PET with florbetaben (^{18}F) in patients with Alzheimer's disease and healthy controls: a multicentre phase 2 diagnostic study. Lancet Neurol. 2011;10:424–35.

114. Jack CR Jr, Bennett DA, Blennow K, Carrillo MC, Dunn B, Haeberlein SB, Holtzman DM, Jagust W, Jessen F, Karlawish J, Liu E, Molinuevo JL, Montine T, Phelps C, Rankin KP, Rowe CC, Scheltens P, Siemers E, Snyder HM, Sperling R. NIA-AA research framework: toward a biological definition of Alzheimer's disease. Alzheimers Dement. 2018;14:535–62.

115. Lockhart SN, Baker SL, Okamura N, Furukawa K, Ishiki A, Furumoto S, Tashiro M, Yanai K, Arai H, Kudo Y, Harada R, Tomita N, Hiraoka K, Watanuki S, Jagust WJJ. Dynamic PET measures of tau accumulation in cognitively normal older adults and Alzheimer's disease patients measured using [^{18}F]THK-5351. PLoS One. 2016;11:e0158460.

116. Xia CF, Arteaga J, Chen G, Gangadharmath U, Gomez LF, Kasi D, Lam C, Liang Q, Liu C, Mocharla VP, Mu F, Sinha A, Su H, Szardenings AK, Walsh JC, Wang E, Yu C, Zhang W, Zhao T, Kolb HC. [^{18}F]T807, a novel tau positron emission tomography imaging agent for Alzheimer's disease. Alzheimers Dement. 2013;9:666–76.

117. Ng KP, Pascoal TA, Mathotaarachchi S, Therriault J, Kang MS, Shin M, Guiot MC, Guo Q, Harada R, Comley RA, Massarweh G, Soucy JP, Okamura N, Gauthier S, Rosa-Neto P. Monoamine oxidase B inhibitor, selegiline, reduces ^{18}F-THK5351 uptake in the human brain. Alzheimers Res Ther. 2017;9:25.

118. Leuzy A, Chiotis K, Lemoine L, Gillberg PG, Almkvist O, Rodriguez-Vieitez E, Nordberg A. Tau PET imaging in neurodegenerative tauopathies—still a challenge. Mol Psychiatry. 2019;24:1112–34.

119. Kroth H, Oden F, Molette J, Schieferstein H, Capotosti F, Mueller A, Berndt M, Schmitt-Willich H, Darmency V, Gabellieri E, Boudou C, Juergens T, Varisco Y, Vokali E, Hickman DT, Tamagnan G, Pfeifer A, Dinkelborg L, Muhs A, Stephens A. Discovery and preclinical characterization of [^{18}F]PI-2620, a next-generation tau PET tracer for the assessment of tau pathology in Alzheimer's disease and other tauopathies. Eur J Nucl Med Mol Imaging. 2019;46:2178–89.

120. Farde L, Pauli S, Hall A, Eriksson L, Halldin C, Hörgberg T, Nilsson L, Sjögren I, Stone-Elander S. Stereoselective binding of ^{11}C-raclopride in living human brain—a search for extrastriatal D2 receptors by PET. Psychopharmacology (Berl). 1988;94:471–8.

121. Halldin C, Stone-Elander S, Thorell J-O, Pearson A, Sedvall G. ^{11}C-labelling of Ro 15-1788 in two different positions, and also ^{11}C-labelling of its main metabolite Ro 153890 for PET studies of benzodiazepine receptors. Appl Radiat Isot. 1988;39:993–7.

122. Långström B, Lunqvist H. The preparation of [^{11}C]methyl iodide and its use in the synthesis of [^{11}C]methyl-L-methionine. Appl Radiat Isot. 1976;27:357–63.

123. Långström B, Antoni G, Gullberg P, Halldin C, Malmborg P, Någren K, Rimland A, Svärd H. Synthesis of L- and D-[Methyl-^{11}C]Methionine. J Nucl Med. 1987;28:1037–40.

124. Guadagno JV, Donnan GA, Markus R, Gillard JH, Baron JC. Imaging the ischaemic penumbra. Curr Opin Neurol. 2004;17:61–7.

125. Savic I, Lindström P, Gulyas B, Halldin C, Andree B, Farde L. Limbic reduction of 5-HT$_{1A}$ receptor binding in human temporal lobe epilepsy. Neurology. 2004;62:1343–51.

126. Tian M, Zhang H, Oriuchi N, Higuchi T, Endo K. Brain tumour imaging with comparison of ^{11}C-choline PET and FDG PET for the differential diagnosis of malignant tumors. Eur J Nucl Med. 2004;31:1064–72.

127. Farde L, Halldin C, Stone-Elander S, Sedvall G. PET Analysis of Human Dopamine Receptor Subtypes Using C-11 SCH 23390 and C-11 Raclopride. Psychopharmacology (Berl). 1987;92:278–84.

128. Houle S, Ginovart N, Hussey D, Meyer JH, Wilson AA. Imaging the serotonin transporter with positron emission tomography: initial human studies with [^{11}C]DAPP and [^{11}C]DASB. Eur J Nucl Med Mol Imaging. 2000;27:1719–22.

129. Strauss LG, Conti PS. The application of PET in clinical oncology. J Nucl Med. 1991;32:623–48.

130. Derlon JM. The in vivo metabolic investigation of brain gliomas with positron emission tomography. Adv Tech Stand Neurosurg. 1998;24:41–76.

131. Bombardieri E, Carriago I, Conzales P, Serafini A, Turner JH, Virgolini I, Maffioli L. Main diag-

nostic applications in oncology. Eur J Nucl Med. 1999;26:BP21–7.

132. Oyama N, Miller TR, Dehdashti F, Siegel BA, Fischer KC, Michalski JM, Kibel AS, Andriole GL, Picus J, Welch MJ. ^{11}C-acetate PET imaging of prostate cancer: detection of recurrent disease at PSA relapse. J Nucl Med. 2003;44:549–55.

133. Schäfers M, Dutka D, Rhodes CG, Lammertsma AA, Hermansen F, Schober O, Camici PG. Myocardial presynaptic and postsynaptic autonomic dysfunction in hypertropic cardiomyopathy. Circ Res. 1998;82:57–62.

134. Wichter T, Schäfers M, Rhodes CG, Borggrefe M, Lerch H, Lammertsma AA, Hermansen F, Schober O, Breithardt G, Camici PG. Abnormalities of cardiac sympathetic innervation in arrhythmogenic right ventricular cardiomyopathy: quantitative assessment of presynaptic norepinephrine reuptake and postsynaptic ß-adrenergic receptor density with positron emission tomography. Circulation. 2000;101:1552–8.

135. Rösch F. Past, present and future of ^{68}Ge/^{68}Ga generators. Appl Radiat Isot. 2013;76:24–30.

136. Eder M, Neels O, Müller M, Bauder-Wüst U, Remde Y, Schäfer M, Hennrich U, Eisenhut M, Afshar-Oromieh A, Haberkorn U, Kopka K. Novel preclinical and radiopharmaceutical aspects of [^{68}Ga]Ga-PSMA-HBED-CC: a new PET tracer for imaging of prostate cancer. Pharmaceuticals. 2014;7:779–96.

137. Wester HJ, Schottelius M. PSMA-targeted radiopharmaceuticals for imaging and therapy. Semin Nucl Med. 2019;49:302–12.

138. Hofmann M, Oei M, Boerner AR, Maecke H, Geworski L, Knapp WH, Krause T. Comparison of Ga-68-DOTATOC and Ga-68-DOTANOC for radiopeptide PET. Nuklearmedizin. 2005;44:A58.

139. Henze M, Dimitrakopoulou-Strauss A, Milker-Zabel S, Schuhmacher J, Strauss LG, Doll J, Maecke HR, Eisenhut M, Debus J, Haberkorn U. Characterization of ^{68}Ga-DOTA-D-Phe^1-Tyr^3-octreotide kinetics in patients with meningiomas. J Nucl Med. 2005;46:763–9.

140. Lindner T, Loktev A, Altmann A, Giesel F, Kratochwil C, Debus J, Jäger D, Mier W, Haberkorn U. Development of Quinoline-based theranostic ligands for the targeting of fibroblast activation protein. J Nucl Med. 2018;59:1415–22.

141. Langer L, Hess A, Reffert LM, Bankstahl JP, Thackeray JT, Bengel FM, Ross TL. Visualisation of fibrosis after tissue damage with PET—a tracer for the fibroblast activation protein. J Label Compd Radiopharm. 2019;62:S535.

142. Revy A, Hallouard F, Joyeux-Klamber S, Skanjeti A, Rioufol C, Fraysse M. Feasibility and evaluation of automated methods for radiolabeling of radiopharmaceutical kits with Gallium-68. Curr Radiopharm. 2019;12:229–37.

143. Hofman MS, Eu P, Jackson P, Hong E, Binns D, Iravani A, Murphy D, Mitchell C, Siva S, Hicks RJ, Young JD, Blower PJ, Mullen GE. Cold kit for prostate-specific membrane antigen (PSMA) PET imaging: phase 1 study of ^{68}Ga-Tris(Hydroxypyridinone)-PSMA PET/CT in patients with prostate cancer. J Nucl Med. 2018;59:625–31.

144. Derlin T, Schmuck S, Juhl C, Zörgiebel J, Schneefeld SM, Walte ACA, Hueper K, von Klot CA, Henkenberens C, Christiansen H, Thackeray JT, Ross TL, Bengel FM. PSA-stratified detection rates for [^{68}Ga]THP-PSMA, a novel probe for rapid kit-based ^{68}Ga-labeling and PET imaging, in patients with biochemical recurrence after primary therapy for prostate cancer. Eur J Nucl Med Mol Imaging. 2018;45:913–22.

145. Lenzo NP, Meyrick D, Turner JH. Review of Gallium-68 PSMA PET/CT imaging in the management of prostate cancer. Diagnostics. 2018;8:E16.

146. Loktev A, Lindner T, Burger EM, Altmann A, Giesel F, Kratochwil C, Debus J, Marmé F, Jäger D, Mier W, Haberkorn U. Development of fibroblast activation protein-targeted radiotracers with improved tumor retention. J Nucl Med. 2019;60:1421–9.

147. Kratochwil C, Flechsig P, Lindner T, Abderrahim L, Altmann A, Mier W, Adeberg S, Rathke H, Röhrich M, Winter H, Plinkert PK, Marme F, Lang M, Kauczor HU, Jäger D, Debus J, Haberkorn U, Giesel FL. ^{68}Ga-FAPI PET/CT: tracer uptake in 28 different kinds of cancer. J Nucl Med. 2019;60:801–5.

148. Lindner T, Loktev A, Giesel F, Kratochwil C, Altmann A, Haberkorn U. Targeting of activated fibroblasts for imaging and therapy. Eur J Nucl Med Mol Imaging Radiopharm Chem. 2019;4:16.

149. Varasteh Z, Mohanta S, Robu S, Braeuer M, Li Y, Omidvari N, Topping G, Sun T, Nekolla SG, Richter A, Weber C, Habenicht A, Haberkorn UA, Weber WA. Molecular imaging of fibroblast activity after myocardial infarction using a ^{68}Ga-labeled fibroblast activation protein inhibitor, FAPI-04. J Nucl Med. 2019;60:1743–9.

150. Clark JC, Crouzel C, Meyer GJ, Strijckmans K. Current methodology for oxygen-15 production for clinical use. Appl Radiat Isot. 1987;38:597–600.

151. Berridge MS, Cassidy EH, Terris AH. A routine, automated synthesis of oxygen-15 labelled butanol for positron emission tomography. J Nucl Med. 1990;31:1727–31.

152. Sajjad M, Lambrecht RM, Wolf AP. Cyclotron isotopes and radiopharmaceuticals 37. Exitation-functions for the O-16(p,alpha)N-13 and N-14(p,pn) N-13 reactions. Radiochim Acta. 1986;39:165–8.

153. Wieland B, Bida G, Padgett H, Hendry G, Zippi E, Kabalka G, Morelle J-L, Verbruggen R, Ghyoot M. In target production of ^{13}N-ammonia via proton irradiation of aqueous ethanol and acetic acid mixtures. Appl Radiat Isot. 1991;42:1095–8.

154. Holland JP, Sheh Y, Lewis JS. Standardized methods for the production of high specific-activity zirconium-89. Nucl Med Biol. 2009;36:729–39.

155. Jauw YW, Menke-van der Houven van Oordt CW, Hoekstra OS, Hendrikse NH, Vugts DJ, Zijlstra JM, Huisman MC, van Dongen GA. Immuno-positron emission tomography with Zirconium-89-labeled monoclonal antibodies in oncology: what can we learn from initial clinical trials? Front Pharmacol. 2016;7:131.

156. Poot AJ, Adamzek KWA, Windhorst AD, Vosjan MJWD, Kropf S, Wester HJ, van Dongen GAMS, Vugts DJ. Fully automated ^{89}Zr labeling and purification of antibodies. J Nucl Med. 2019;60:691–5.

157. Follacchio GA, De Feo MS, De Vincentis G, Monteleone F, Liberatore M. Radiopharmaceuticals labelled with copper radionuclides: clinical results in human beings. Curr Radiopharm. 2018;11:22–33.

158. Green MA, Klippenstein DL, Tennison JR. Copper(II)bis(thiosemicarbazone) complexes as potential tracers for evaluation of cerebral and myocardial blood flow with PET. J Nucl Med. 1988;29:1549–57.

159. Takahashi N, Fujibayashi Y, Yonekura Y, Welch MJ, Waki A, Tsuchida T, Sadato N, Sugimoto K, Itoh H. Evaluation of ^{62}Cu labeled diacetyl-bis(N^4-methylthiosemicarbazone) in hypoxic tissue in patients with lung cancer. Ann Nucl Med. 2000;14:323–8.

160. Dehdashti F, Mintun MA, Lewis JS. *In vivo* assessment of tumour hypoxiy in lung cancer with ^{60}Cu-ATSM. Eur J Nucl Med Mol Imaging. 2003;30:844–50.

161. Haynes NG, Lacy JL, Nayak N, Martin CS, Dai D, Mathias CJ, Green MA. Performance of a ^{62}Zn/^{62}Cu generator in clinical trials of PET perfusion agent ^{62}Cu-PTSM. J Nucl Med. 2000;41:309–14.

162. Satyamurthy N, Phelps ME, Barrio JR. Electronic generators for the production of positron-emitter labelled radiopharmaceuticals: where would PET be without them? Clin Posit Imag. 1999;2:233–53.

163. Alexoff DL. Automation for the synthesis and application of PET radiopharmaceuticals. In: Welch MJ, Redvanly CS, editors. Handbook of radiopharmaceuticals. Radiochemistry and application: Wiley; 2003. p. 283–305.

164. Krasikova R. Synthesis modules and automation in F-18 labeling. In: Schubiger PA, Lehmann L, Friebe M, editors. PET chemistry—the driving force in molecular imaging. Berlin: Springer; 2007. p. 289–316.

165. Lucignani G. Pivotal role of nanotechnologies and biotechnologies for molecular imaging and therapy. Eur J Nucl Med Mol Imaging. 2006;33:849–51.

166. Pike VW, Lu SY. Micro-reactors for pet tracer labeling. In: Schubiger PA, Lehmann L, Friebe M, editors. PET chemistry—the driving force in molecular imaging. Berlin: Springer; 2007. p. 271–87.

167. Brady F, Luthra SK, Gillies JM, Geffery NT. Use of microfabricated devices. PCT WO 03/078358 A2. 2003.

168. Lu SY, Watts P, Chin FT, Hong J, Musachio JL, Briard E, Pike VW. Syntheses of ^{11}C- and ^{18}F-labeled carboxylic esters within a hydrodynamically driven micro-reactor. Lab Chip. 2004;4:523–5.

169. Gillies JM, Prenant C, Chimon GN, Smethurst GJ, Perrie W, Hamblett I, Dekker B, Zweit J. Microfluidic reactor for the radiosynthesis of PET radiotracers. Appl Radiat Isot. 2006;64:325–32.

170. Amor-Coarasa A, Kelly JM, Babich JW. 3D-printed automation for optimized PET radiochemistry. Sci Adv. 2019;5:eaax4762.

171. Saha GB. Fundamentals of nuclear pharmacy. 5th ed. New York: Springer; 2004.

172. Littman BH, Williams SA. The ultimate model organism: progress in experimental medicine. Nat Rev Drug Discov. 2005;4:631–8.

173. Bench CJ, Lammertsma AA, Dolan RJ, Grasby PM, Warrington SJ, Gunn K, Cuddigan M, Turton DJ, Osman S, Frackowiak RSJ. Dose dependent occupancy of central dopamine D2 receptors by the novel neuroleptic CP-88,059–01: a study using positron emission tomography and ^{11}C-raclopride. Psychopharmacology (Berl). 1993;112:308–14.

174. Yokoi F, Gründer G, Biziere K, Stephane M, Dogan AS, Dannals RF, Ravert H, Suri A, Bramer S, Wong DF. Dopamine D-2 and D-3 receptor occupancy in normal humans treated with the antipsychotic drug aripiprazole (OPC 14597): a study using positron emission tomography and [C-11]raclopride. Neuropsychopharmacology. 2002;27:248–59.

175. Joensuu H, Roberts PJ, Sarlomo-Rikala M, Andersson LC, Tervahartiala P, Tuveson D, Silberman SL, Capdeville R, Dimitrijevic S, Druker B, Demetri GD. Effect of the tyrosine kinase inhibitor STI571 in a patient with a metastatic gastrointestinal stromal tumor. N Engl J Med. 2001;344:1052–6.

176. Demetri GD, George S, Heinrich MC, Fletcher JA, Fletcher CDM, Desai J, Cohen DP, Scigalla P, Cherrington JM, Van Den Abbeele AD. Clinical activity and tolerability of the multi-targeted tyrosine kinase inhibitor SU11248 in patients with metastatic gastrointestinal stromal tumor (GIST) refractory to imatinib mesylate. Proc Am Soc Clin Oncol. 2003;22:3273.

177. Bernard-Gauthier V, Collier TL, Liang SH, Vasdev N. Discovery of PET radiopharmaceuticals at the academia-industry interface. Drug Discov Today Technol. 2017;25:19–26.

Part III

Dosimetry and Radiation biology

Internal Radiation Dosimetry

9

Magdy M. Khalil

Contents

9.1　Introduction

Ionizing radiation has several beneficial applications to biomedical life sciences. The optimal use of ionizing radiation requires special understanding of quite important definitions, quantities, units and regulatory aspects. However, radiation risk cannot be ignored or marginalized when attempts are made to utilize ionizing radiation for human benefits. It is generally known that exposure to ionizing radiation can be classified into two categories including internal or external exposure. Nuclear medicine has the two ways of exposure. External exposure is commonly seen when medical, technical, or nursing staff become close to radioactive source or patients injected with radiopharmaceuticals while internal exposure is often seen when patients are administered by radioactive tracers or volatile radionuclides are inhaled or ingested. Patients can also get externally exposed during their presence in nuclear medicine clinic via some ways including patient to patient exposure (e.g., waiting area) or during injection.

Nuclear medicine imaging techniques rely on injecting a radiotracer of very small concentration (i.e., down to pico- or nanomolar levels) from pharmaceutical perspectives labeled with small amount of radioactivity. The aim is not to disturb the metabolic or molecular processes of human tissues but just to interrogate the underlying pathological disorder to come up with a diagnostic decision. What really positions nuclear medicine and molecular imaging among other modalities is its unique functional characterization

M. M. Khalil (✉)
Medical Biophysics, Department of Physics, Faculty of Science, Helwan University, Cairo, Egypt

of biological systems or subsystems when compared to other imaging procedures [1, 2].

There are several routes through which radioactivity can go through into humans such as inhalation, ingestion, and injection. When radioactivity is administered into the body, questions are raised of how much risks these radiotracers could cause to living tissues. Most of the radiopharmaceuticals used in nuclear medicine exhibit a wide range of target to non-target ratio. Moreover, health radiation risks associated with diagnostic doses are generally very low in contrast to high doses used in molecular radiotherapy that aim to damage biological tissues. The low risk–benefit ratio is greatly outweighing some inaccuracies of diagnostic dose estimates [3]. Nevertheless, the low doses should be well addressed and quantified in both target and non-target tissues and placed in proper perspectives. This enables to record doses that may cumulate over multiple sessions performed using the same or different diagnostic modalities [4]. However, therapeutic radiopharmaceuticals should follow a stricter control over dose estimates with optimal dosing scheme able to maximize therapeutic effectiveness.

The science of internal dose assessment or internal dosimetry in nuclear medicine deals with various technical, scientific methods, models, tools, and equipments to provide a reliable estimate of radiation dose received by a human body. The central term of this process is absorbed dose and is widely used to derive other physical and/or radiobiologically relevant definitions.

The development in the field of radionuclide therapy with high target specificity and capabilities to deliver a significantly large amount of radiation dose to specific tissues or organs has placed a need to move from population or average-based dosimetry to patient-specific dosimetry [5]. This topic has been increasing in the last few years in compliance with the notion of personalized or precision medicine. It will then care of individual body habitus and measured compound kinetics rather than relying on average phantom model and hypothetic kinetics [3].

The task of internal dosimetry in nuclear medicine may vary depending on the clinical question whether diagnostic or therapeutic or both (i.e., theranostic). For diagnosis, the rationale is to provide bases for stochastic risk quantification and procedure optimization [6]. In therapeutic nuclear medicine, radiotracer biokinetics is important to be accurately determined on an individual basis to target not only tissue of interest but also healthy organs at risk. In daily practice, however, a number of therapeutic procedures are carried out without accurate assessment or proper pretreatment dose planning [7].

9.1.1 Exposure

Exposure is an old term used to quantify ionizing radiations based on the amount of charge or ion pair produced in air. The unit roentgen (R) has been traditionally used to refer to radiation exposure. It is defined as the amount of gamma or X-rays that produce one electrostatic unit of charge of either sign per unit volume of air (1 cc of dry air equals 0.001293 g at 0 °C and 760 mmHg), and it takes the unit of charge/kg (C/kg) thus

$$1\,R = \frac{1\text{esu}}{0.001293\text{g}} \times \frac{1\text{C}}{2.998 \times 10^9\,\text{esu}} \times \frac{10^3\,\text{g}}{1\text{kg}} = 2.580 \times 10^{-4}\,\text{C}/\text{g}$$

There is no SI unit for exposure, and although it is still occasionally encountered, particularly in the older literature, the old special unit, roentgen, is no longer used [8].

The quantity exposure could probably be seen in some daily practice of area monitoring and survey measurements perhaps in the units of μR/h, mR/min, etc. Exposure is a measure of the photon fluence and is related to the amount of energy transferred from the X-ray field to a unit mass of *air*. It is a radiometric rather a dosimetrically useful term. However, if the amount of ex-

posure is known together with the energy of the X-rays and the composition of the irradiated medium, one can calculate the absorbed dose to any part of the irradiated medium [9]. Notice that exposure is a quantity restricted to gamma and X-rays as the source of radiation while the medium of interaction is only air. Using the appropriate units and conversion factors, one can obtain the dose to air as 0.00877 Gy (or 0.877 rad) as a result of exposure to 1 R. Further, the dose to tissue can be derived when correlating mass absorption coefficients of air and biological tissue since μ_m-tissue/μ_m-air $\approx$ 1.09 and thus 0.877 rad (air) $\times$ 1.09 = 0.95 rad (tissue). The terms μ_m-tissue and μ_m-air are the mass attenuation coefficient of tissue and air respectively [10].

9.1.2 Stochastic and Deterministic Effects

Exposure of biological systems to ionizing radiation vary considerably in terms of type and amount of radiation, energy, time of exposure, and other intrinsic and extrinsic factors. Therefore, radiation exposure can cause a multitude of reactions that could vary largely in response including cancer and other health adverse effects, leading to significant variation of what is called dose–response curve. For the purpose of dose limits, International Commission of Radiation Protection (ICRP) has defined and classified diverse radiation effects into stochastic effects and tissue reactions (or deterministic effects). The former effects have no threshold, whereas deterministic effects are threshold based. The probability of effects increases when we deal with stochastic effects (e.g., cancer, leukemia, hereditary effects) while the severity of the effects increase in proportion when tissues are deterministically exposed (hair loss, cataract, skin injury) [11].

Historically, there was a distinction between non-stochastic and stochastic effects that replaced the acute and late categories (ICRP, 1977) [12] and then the distinction between early and late effects for non-stochastic effects (ICRP, 1984) [13]. The term deterministic has then re-

placed the term "non-stochastic" [14], but recently "tissue reactions" was used to replace the term "deterministic" (or to use as a synonym) [4]. Tissue reactions were used due to the fact that some effects are not identified solely at the time of irradiation, and many types of tissue reactions can be modified after radiation exposure [15]. The objectives are to prevent the occurrence of deterministic effects, whereas risks associated with stochastic events are reduced to a reasonable achievable extent [4, 16].

9.1.3 Linear Energy Transfer (LET)

It is defined as the average energy deposited per unit length of radiation track [17]. As the ionizing radiation penetrate matter, it losses energy based on its type, energy, and density of the medium. Therefore, it was necessary to define a quantity that permits one to distinguish among various radiations in terms of their energy deposition when transverse biological systems. X-ray and gamma photons as well as electrons are identified as low LET radiations while alpha particles, protons, and neutrons are classified as high LET radiations. LET is usually expressed in units of kilo-electron volt per micrometer or keV/μm. Table 9.1 describes the LET values for different types of ionizing radiation.

Auger electrons. Emission of Auger electrons from an atom occurs due to filling of a vacancy in an inner shell of the same atom. During this process, a specific type of radiation called characteristic X-ray radiation is emitted during the

Table 9.1 Linear energy transfer for various types of radiation

Type of radiation	LET (keV/μm)
250 kVp X-ray	2.0
Cobalt-60	0.3
1 keV electrons	12.3
10 keV electrons	2.3
1 MeV electrons	0.25
10 MeV protons	4.7
150 MeV protons	0.5
14 MeV neutrons	12
2.5 MeV alpha particles	166

transition of electrons from higher to lower energy levels. This later emission might result in hitting one of the orbital electrons called auger electrons. Whether the characteristic radiation or Auger electrons are emitted is a matter of competition that is a function of the atomic number Z of the material.

Radionuclides that emit Auger electrons are widely used in nuclear medicine (^{111}In, ^{67}Ga, ^{99m}Tc, ^{201}Tl, and ^{123}I) and in biomedical research (^{51}Cr and ^{125}I) [18]. The majority of Auger electrons have low energy (<25 keV), which is deposited over short distances (nano- or micrometer range, ~2–500 nm) in tissues. This extremely short range yields high linear energy transfer (LET, 4–26 keV/μm), which makes these electrons of value in radiation treatment of cancer, especially if they are emitted in close proximity to cell sensitive targets such as DNA and cell membrane. It is therefore useful in radionuclide therapy, and preclinical results are encouraging [19]. Its subcellular range makes Auger electrons of particular interest especially when compared with DNA dimension (i.e., 2 nm) as well as cell membrane and other critically important structures within the cell.

9.1.4 Relative Biological Effectiveness

Relative biological effectiveness (RBE) is defined as the ratio of a dose of standard radiation to the dose of radiation in question that produces the same biological effect. Initially, X-ray produced from 250 kVp was the standard radiation dose to determine the RBE, but then ICRP recommended the use of gamma rays of ^{60}Co as reference radiation [20]. For a detailed definition of RBE, it is necessary to define the nature of the cells, radiosensitivity, and the biological end point. Moreover, several factors and experimental conditions should be taken into account including reference radiation, total dose, dose rate, acute versus chronic versus fractionated scheme, and whether internal or external irradiation [21].

The RBE depends on LET and of particular interest in radionuclide therapy as the use of targeting agents requires radionuclides of higher energy deposition in small volume. This permits to destroy tumor cells without compromising healthy tissues or organs at risks. Sparsely ionizing radiation such as gamma and X-rays have low LET and RBE while alpha particles, heavy ions, and Auger emitters are recognized by high LET and RBE values. As per ICRP recommendations, RBE is not a direct measure for radiation protection but has been utilized in constructing radiation weighting factors that replaced the original *Quality Factor* (Q) in characterizing different radiation qualities with respect to their biological effects [4, 14]. For the purpose of deterministic effects, the radiation weighting factors of alpha emitters range from 3 to 5.4 for cell killing based on a number of evidences derived from experimental investigations and MIRD Committee recommendations [21]. As will come later in this chapter, the radiation weighting factor of 20 was mainly derived to describe the stochastic effects and cancer induction related to alpha emitters. Notice that the values of the radiation weighting factors for a specified type and energy of radiation has been selected to be representative for values of the relative biological effectiveness (RBE) in inducing stochastic effects at low radiation doses [17].

9.2 Absorbed Dose

Absorbed dose is the amount of energy imparted by ionizing radiation in units of Joule per unit mass of tissue (kg) and expressed in gray (Gy). The gray is the SI (International System of Units) unit and was named after Louis Harold Gray (1905–1965), an English physicist who worked mainly on the effects of radiation on biological systems and one of the contributors to the science of radiobiology [22]. The mean dose to an organ or tissue (T) is written as:

$$\bar{D}_{\mathrm{T}} = \varepsilon_{\mathrm{T}} / m_{\mathrm{T}} \left(1 \mathrm{Joule} / 1 \mathrm{kg} \right) = 1 \mathrm{Gy}$$

The special old unit of absorbed dose is radiation absorbed dose (rad). In relation to the SI unit, it is defined as 1 Gy = 100 rad or 1 rad = 0.01 Gy.

One rad is equal to 100 ergs of energy absorbed per gram of tissue, or 1 rad = 100 ergs/g. There are two types of quantities defined for specific use in radiation protection, namely protection quantities and operational quantities. The former is defined by the ICRP and used for assessing the exposure limits while the later was defined by ICRU as instrumental in the determination of protection quantities. The conversion between the two quantities can be reviewed elsewhere [23].

9.2.1 Equivalent Dose

Not all ionizing radiations have the same quality in their damage to the biological system, and this has been accounted for using radiation weighting factors. The equivalent dose is the quantity that was coined to take into consideration different radiation qualities. It is defined as the sum of the absorbed dose (due to radiation i) times the radiation weighting factor and denoted by the letter H.

$$\text{Equivalent dose}(H) = \text{absorbed dose due to radiation type}(i) \times$$
$$\text{radiation weighting factor} = \bar{D}_{\mathrm{T},i} \times w_i \text{ and expressed in units of sievert}(\mathrm{Sv})$$

Rolf Maximilian Sievert (1896–1966) was a Swedish medical physicist who also made significant contribution on the biological effects of ionizing radiation [24]. It should be noted that when different types of radiations are encountered, the equivalent dose becomes

$$H_{\mathrm{T},i} = \sum_{\mathrm{T},i}^{n} D_{\mathrm{T},i}\, w_i$$

where the sum extends to cover the various types of radiation (i.e., n) and their respective radiation weighting factors, w_i. For example, when a tissue is exposed to mean absorbed dose of 0.05 mGy of alpha particles, 0.5 mGy of beta particle and 50 mGy of gamma rays (i.e., $D_{\mathrm{T},i}$), then the equivalent dose would be:

$$H_{\mathrm{T}} = 0.05 \times 20 + 0.5 \times 1 + 50 \times 1$$
$$= 1 + 0.5 + 5 = 51.5 \text{ mSv}$$

The question now is why we multiply the absorbed dose of alpha particles by 20, whereas the absorbed dose of beta particle and gamma rays are multiplied by 1? To explain, this dates back to the historical definition of quality factor (Q) which refers to the relative damage that caused by alpha particles in comparison to gamma and beta radiations. Therefore, the quality factor is related to two other definitions de-

scribed above, namely RBE and LET. The alpha particle has a large amount of energy loss per unit length or what is called high LET, whereas gamma and beta radiations transfer less energy as they pass through tissues and therefore considered low LET radiations. Both the types of LET are relevant to nuclear medicine applications as the former is consistent/ideal with radionuclide therapy (i.e., deterministic effects), and the later (i.e., gamma radiations) is commonly used for diagnostic purposes and its consideration in radiation protection practices (i.e., stochastic effects). As outlined earlier, the Q factor was initially defined to have a value of unity for 200 keV photons.

In 1990, ICRP introduced a modified concept. For radiological protection purposes, the absorbed dose is averaged over an organ or tissue which is then weighted for the radiation quality in terms of the radiation weighting factor, w_i, for the type and energy of radiation incident on the body. The resulting weighted dose is designated as the organ- or tissue-equivalent dose (H_{T}) [14]. The sum of the organ-equivalent doses weighted by the ICRP organ-weighting factors, w_{T}, is termed the effective dose (E).

The w_i for photons, electrons, positrons, beta-particles, alpha particles, and neutrons are described in Table 9.2. Although the ICRP

Table 9.2 Radiation weighting factors (w_i) recommended by the International Commission on Radiological Protection, Publication 103 (ICRP 2007)

Radiation	w_i
Photons	1
Electrons and muons	1
Protons and charged pions	2
Alpha particles, fission fragments, heavy ions	20
Neutrons	Continuous function of neutron energy

recommendations (ICRP 2007) accept the fact that in vitro experiments performed on cells are showing significant differences in radiation quality among radiation of different energies (e.g., X-rays versus Co-60), it continues to recommend a w_i of 1 for all low-LET radiation [4, 25]. Radiation weighting factors do not account for all known differences that exist among the types of radiation and their energies for different tissues and cancer types [4, 26, 27]. Radiation weighting factors (w_i) are used to represent the differences between radiation types in their ability to cause cancer per unit absorbed dose (Gy).

9.2.2 Effective Dose

Effective dose is a derived radiation protection term and not a physically measurable quantity [28]. It has been defined by ICRP to account for whole-body exposure and establishment of annual limits due to stochastic effects of radiation mainly for radiation workers and members of general public. The quantity takes into account external radiation fields and internal radionuclide sources [6, 28].

Effective dose is to be used for "prospective dose assessment for planning and optimization in radiological protection, and retrospective demonstration of compliance for regulatory purposes" as stated and according to ICRP Publication 103 [4]. It is not to be used for cancer risk assessment, prediction, or epidemiological studies. Epidemiological studies are conducted using subjects exposed to radiation from occupational exposures,

medical examinations, and military use and from exposure to man-made and naturally occurring radiation in the environment [25]. Effective dose was designed based on the reference models rather than the individual subjects. There is no solid radiobiological basis upon which effective dose or equivalent dose is related to biological response in tissues of organs [4, 28, 29].

ICRP has defined the effective dose in relation to the weighted equivalent dose being the sum of the individual tissues or organs multiplied by theoretical tissue weighting factors (w_T). The following formula was stated:

$$E = \sum_T w_T \left[\frac{H_T^M + H_T^M}{2} \right]$$

where H_T with superscript M and F are the equivalent doses obtained for organs and tissues of the reference male and the reference female, respectively. However, the widespread use of effective dose as a measure of risk goes beyond its intended applications [4]. Although there are some uncertainties associated with the application of the tissue weighting factors, the ICRP believes the appropriateness of its use in radiological protection purposes while adopting age- and sex-averaged tissue weighting factors and numerical risk estimates (ICRP, 2007) (Table 9.3) [4, 28].

Table 9.3 Recommended tissue weighting factors

Tissue	w_T	$\sum_T w_T$
Active bone marrow, colon, lung, stomach, breast, remainder tissues	0.12	0.72
Gonads	0.08	0.08
Bladder, esophagus, liver, thyroid	0.04	0.16
Endosteal tissues, brain, salivary glands, skin	0.01	0.04
Total		1.00

*Remainder tissues are adrenal glands, extrathoracic airways, gall bladder, heart, kidneys, lymphatic, nodes, skeletal muscle, oral mucosa, pancreas, prostate (male), small intestine, spleen, thymus, and uterus/cervix (female). Source (ICRP publication 103, 2007) [4]

9.3   Internal Dosimetry Frameworks

There are two major frameworks for internal radiation assessment, namely the internal dosimetry schema of the *Medical Internal Radiation Dose* (*MIRD*) Committee of the *Society of Nuclear Medicine* and the International Commission of Radiation Protection (ICRP) schema.

9.3.1   MIRD

The calculation of the internal absorbed dose to specific region or whole body when a radionuclide is localized in human tissues and organs requires some information regarding the physics of the radiotracer as well as its kinetics within

tissues and organs. Figure 9.1 shows a radiopharmaceutical that was only taken up by liver and spleen tissues for a given subject. When attempts are made to measure how much absorbed dose is received by liver or spleen or effective dose to the whole body of that subject, then a number of inputs and calculations are required. As described above, the absorbed dose is the mean energy imparted to target tissue (or region) per unit tissue mass [30]. The radiation dose delivered to the liver tissue is the amount of energy imparted by disintegrations that occurred in spleen as well as those disintegrations that came from liver itself provided that both the terms are normalized to the mass of the liver.

In mathematical form, the internal dose can be calculated based on schema developed by MIRD Committee as follows:
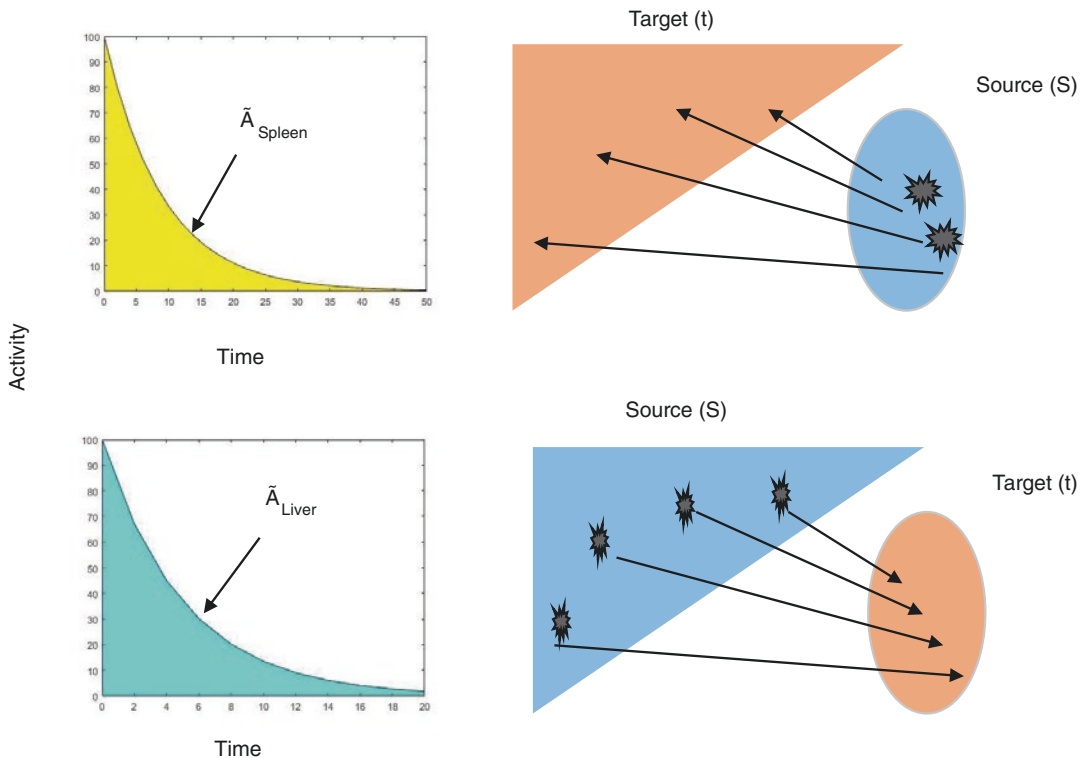
Fig. 9.1 Theory of internal dose calculations. The absorbed fraction needs to be determined for every configuration of source and target organs using Monte Carlo simulations provided an appropriate reference or standard phantom model. Physical radioactive decay information of the administered radionuclide needs also to be obtained. Tracer kinetics within source organs have to be calculated as accurate as possible

$$\bar{D}_{(T \leftarrow S)} = \frac{\tilde{A}_S \sum_i n_i E_i \cdot \phi_{T \leftarrow S}}{m_T} \quad (9.1)$$

where

$\bar{D}_{T \leftarrow S}$ is the mean absorbed dose in a target organ (T) (e.g., Gy).

$\tilde{A}_S$ is the cumulated activity assuming uniform distribution of the radiotracer within the source organ (S), it takes the unit of activity product time (e.g., MBq h).

The quantity $n_i E_i$ denoted by Δ_i is the mean energy emitted by the radiotracer per disintegration, it is the product of the mean (or individual) energy E_i of a nuclear transition and the number of nuclear transitions per disintegration, n_i [31]. In literature, a constant is added to the product (i.e., $k\, n_i\, E_i$) to account for the different quantities. It may take the units (Gy kg/Bq s).

$\phi_{T \leftarrow S}$ (Greek phi) is the absorbed fraction which represents the fraction of energy emitted from the source and absorbed within the target tissue due to radiotracer disintegration. Why the absorbed fraction was taken into account? This is because the gamma photons emitted from liver tissues, for example, will not deposit solely their energy in the liver. However, a percentage of photons will be internally absorbed, whereas the remaining portion will escape to irradiate other surrounding tissues. The absorbed fraction is a function of the radionuclide energy as well as geometry and source–target configuration [32]. Notice that the source and target can be the same tissue, and hence, the term self-irradiation would be used. The absorbed fraction is commonly calculated based on Monte Carlo simulation. A new term is defined when the absorbed fraction is divided by the mass of the target, which is the specific absorbed fraction $\Phi_{T \leftarrow S}$ that is represented by the relation $\Phi_{T \leftarrow S} = \phi_{T \leftarrow S}/m_T$.

Rewriting Eq. (9.1) in different forms provides

$$\bar{D}_{(T \leftarrow S)} = \frac{\tilde{A}_S \sum_i n_i . E_i . \phi_{T \leftarrow S}}{m_T} = \frac{\tilde{A}_S \sum_i \Delta_i . \phi_{(T \leftarrow S)i}}{m_T} = \tilde{A}_S \sum_i \Delta_i . \Phi_{(T \leftarrow S)i} \quad (9.2)$$

This simple formula can be used only when attempts are made to calculate the absorbed dose in one target using one source organ, which might be the same organ, for example, in Fig. 9.1 such as calculating the mean absorbed dose to the liver due to liver radioactivity (self-irradiation) or only due to spleen irradiation to the liver tissue. However, this is not the real case scenario as in order to accurately determine an organ mean absorbed dose, all "significant" sources that contribute to this given target must be considered for the analysis. Back to Fig. 9.1, now the absorbed dose to liver tissues is the sum of two components such that one part reflects the self-liver irradiation and the other is that related to irradiation from spleen. The same is also applicable to the spleen tissue.

Hence, Eq. (9.2) becomes

$$\bar{D}_{(T \leftarrow S)} = \sum_S \tilde{A}_S \sum_i \Delta_i . \Phi_{(T \leftarrow S)i} = \sum_S \tilde{A}_S . S_{(T \leftarrow S)} \quad (9.3)$$

The first summation term was added, so that all sources that received radioactivity and contributed to the absorbed dose of the target would be considered for calculation. A proper use of units and conversion factors must be considered in all terms in the equations above. Notice that in Eq. (9.3), a new term was introduced which is the S term. It can be represented using the information above as follows:

$$S_{(T \leftarrow S)} = \frac{\sum_i \Delta_i . \phi_{(T \leftarrow S)i}}{m_T} = \sum_i \Delta_i . \Phi_{(T \leftarrow S)i} \quad (9.4)$$

Now, we need to discuss some important points.

1. The cumulated activity $\tilde{A}_S$ is an integral quantity that is obtained by integrating the time–activity curve from sample data points obtained over time. These time points could be activity concentration of blood samples or image counts taken at specified time intervals based on tracer pharmacokinetics and reliability of data collection. It can be a particular tissue, organ, or one image voxel.

2. As shown in the graphical plot of Fig. 9.1, the clearance of the liver and spleen for the virtual radiotracer assumed here are different; however, it can simply be represented by the first-order kinetics using the famous mono-exponential function:

$$A_{(t,\text{Liver})} = A_o f_{\text{Liver}} e^{-\lambda_{\text{eff}1}t}$$

and

$$A_{(t,\text{Spleen})} = A_o f_{\text{Spleen}} e^{-\lambda_{\text{eff}2}t}$$

The $A_{(t,\text{tissue})}$ is the activity at time t while f is the fraction of the radiotracer taken up by the organ or tissue. $\lambda_{\text{eff}1}$ and $\lambda_{\text{eff}2}$ are the effective decay constant for liver and spleen, respectively. Integrating the time–activity curve from $t = 0$ to infinity provides the term

$$\tilde{A}_{(t-\infty)} = A_o\, f\, /\, \lambda_{\text{eff}} = 1.44.A_o\, f\, T_{1/2(\text{eff})}$$

Recall that the quantity 1.44 $T_{1/2(\text{eff})}$ is equivalent to the inverse of the effective decay constant $1/\lambda_{\text{eff}}$ (i.e. $T_{1/2} = 0.693/\lambda$).

The effective decay constant is the sum of the biological decay constant and physical decay constant ($\lambda_{\text{eff}} = \lambda_b + \lambda_p$) and t is the independent variable "time" plotted on the x-axis, through which the experiment was performed. Why then we used the effective decay constant and not the biological or physical decay constant. The explanation is that if a radionuclide is delivered to a biological environment, then its kinetics is not only depend on physical decay but also on its biochemical and pharmacokinetics profile. This means that the pattern or rate of tracer uptake into tissues including distribution, retention, and clearance are affected by the spontaneous radioactive decay (i.e., physical decay constant) as well as its pharmacokinetic characteristics (i.e., biological decay constant). In other radiotracers, the kinetic model could be bi- or tri-exponential function or even more complex.

3. If the radiotracer is beta or alpha emitter, then the absorbed fraction (ϕ) is 1 as the physics of these radionuclides mandates a short (e.g., beta particle) or even too short (e.g., alpha particles and Auger electrons) range in biological tissues. However, for gamma photons, the absorbed fraction is less than 1 due to the greater chance of gamma photons to escape source regions.

4. Equation (9.3) can simply be viewed as a product of two distinct terms: one related to source organ kinetics ($\tilde{A}_S$) and another term related to radionuclide physical decay scheme and other factors related to source–target configuration including size, shape, composition, distance, and material separating them (i.e., anatomy of standard phantom adopted). The mean dose of the target organ can be written in a further simplified form as this product [33]:

$$\bar{D}_{(T\leftarrow S)} = \tilde{A}s\, S_{(T\leftarrow S)}$$

5. The introduced S term or absorbed dose conversion factor in Eqs. (9.3) and (9.4) is the mean absorbed dose to target tissue per unit cumulated activity of the source organ, it may take the unit of mGy/MBq s or Gy/Bq s. Historically and for diagnostic examinations, S tables have been published by the MIRD Committee for several radionuclides and various source–target organ pairs from calculations performed for anthropomorphic phantoms.

6. As outlined, the S value is a characteristic of the radionuclide and anatomic model selected to represent the patient or tissue of interest. The value of S may be based on computational reference phantoms representing a given age, sex, total-body mass, and standing height [6, 34]. It can also be described at different levels of source–target configurations including organs,

cell clusters, as well as voxel level [35]. The tables of S factor provide a convenient and simple way to calculate mean organ doses within the MIRD Scheme [36]. This should not be a problem when internal dosimetry is used in diagnostic radiotracers where evaluation of possible toxicity is an important goal. This in principle relies on the presence of normal organs in their standard anatomical position.

The generalization of MIRD scheme has permitted researchers to extend the concept to the multi-regions within the same organ or neighboring structures [37, 38], or even down to cellular and subcellular levels [35] not only to account for non-uniform activity distribution but also to provide more detailed and accurate assessment of the absorbed dose in a selected target/region. However, in therapeutic applications and in the abnormal nature of tumor growth, clonal heterogeneity, as well as its probable abnormal locations within human tissues, determination of absorbed dose using the conventional MIRD approach would have some limitations to implement. It therefore requires some other ways to calculate the absorbed dose to the tumor itself or other tissues including organs at risk and whole body.

Because of the common use of beta particles in radionuclide therapy, a local energy deposition can be assumed. However, the contribution of gamma rays is not easy to account for, and its omission from the calculations scheme could cause some sort of underestimation especially if organs of higher uptake are close to the tumor volume [39]. Another potential solution for the determination of tumor dose assessment is the use of Monte Carlo techniques in three-dimensional or what is called patient-specific dosimetry. While the accuracy of Monte Carlo is very high, the associated computational power is very demanding for clinical practice [40].

9.3.2 International Commission of Radiation Protection (ICRP)

The role of ICRP is to develop, maintain, and elaborate the international system of radiation
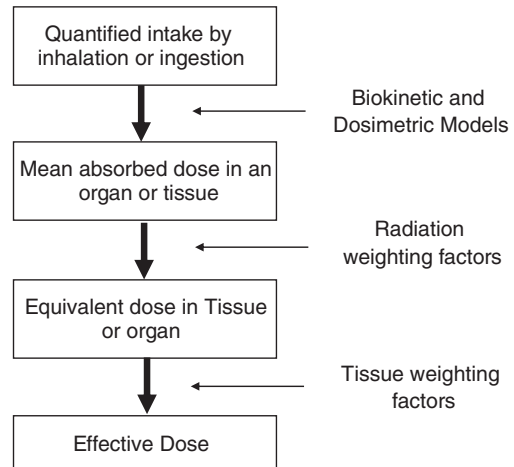
Fig. 9.2 Steps taken by ICRP to calculate absorbed dose, equivalent dose, and effective dose. Adapted from Harrison et al. [26]

protection, so that it can be used to derive the fundamental basis for radiological protection standards, guidelines, legislation, as well as practices on a global scale [41]. These roles cover but are not limited to internal dose coefficients and bioassay data for reference workers, member of the public, and reference patients in diagnostic nuclear medicine [41]. The ICRP does publish dose coefficients (e.g., Sv/Bq) for intakes of individual radionuclides, giving both equivalent doses to organs and tissues, and effective dose. Steps of calculations are depicted in Fig. 9.2 and summarized as follows [26, 27]:

1. The total number of disintegrations in the source organs or tissues are calculated through predefined biokinetic models that represent the distribution and retention of radionuclides.
2. The mean absorbed dose is calculated through dosimetric models making use of the decay data and emission energies that take place in the source region.
3. To account for the relative effectiveness of the different type of radiations in causing stochastic effects like hereditary effects or cancer, a radiation weighting factor is multiplied by the absorbed dose.
4. To account for the contribution of individual organs and tissues to overall detriment from hereditary effects or cancer, the equivalent

dose is then multiplied by the tissue weighting factor.

5. Equivalent and effective doses are commonly integrated over a 50- and 70-year period for adults and children, respectively, producing what is called committed doses.

The dose assigned to an exposed radiation worker is the computed effective dose received by a reference person when is assumed to be exposed to the same internal (e.g., radionuclide intake) or external radiation exposure as the worker [28]. The committed effective dose as described by ICRP is calculated using the formula

$$H_{(50,T)} = 1.6 \times 10^{-10} \frac{\text{Svg}}{\text{MeV}} U_S \cdot SEE$$

where

- $H_{50,\ T}$ is the 50-year committed dose equivalent.
- U_S is the number of disintegrations in the source organ over 50 years.
- SEE is the specific effective energy while the constant 1.6×10^{-10} is the product of conversion factors 1.610 J/MeV and 1000 g/kg, and its units include the definition that an Sv is equivalent to a J/kg [9]. The SEE term is defined using the following formula:

$$SEE(T \leftarrow S) = \sum_i \frac{n.E_{Ri}.w_i.AF_i(T \leftarrow S)}{m_T}$$

where

- n is the number of disintegrations that occur for energy E_i. The term w_i is the radiation weighting factor, $AF_i(T \leftarrow S)$ is the absorbed fraction, and m_T is the mass of the target tissue. For example, the fraction of energy for a 1 MeV photons emitted from liver tissues (male person) to left and right kidneys is 0.79% [42]. The specific absorbed fraction is therefore equal to (0.0079/0.422) kg^{-1} [42]. Note that 0.422 kg is the mass of the kidney in the reference person.

As shown from ICRP and MIRD scheme, both the methods have very similar fundamentals in internal dosimetry calculations. Harmonization between the two approaches was proposed in MIRD Pamphlet 21 [6]. Recently, ICRP publication 140 has been released dealing with radiological protection in therapy with radiopharmaceuticals [43]. A quite large number of radionuclides of 1252 of 97 elements are reported in ICRP publication 107 that can be used in dose coefficients for radioactive intake or exposure to radionuclides in workplace, environment, or nuclear medicine facilities [44]. However, the earlier source of this information was ICRP Publication 38 published in 1983 [45].

9.3.2.1 Biokinetic Models

Biokinetic models as employed by ICRP deals with the inhalation and ingestion of radionuclides including adults and children as well as doses to fetus following maternal intakes and infant doses due to radionuclides transferred to breastmilk. Models like alimentary and respiratory tracts are used to determine the movement of radionuclides within different compartments ending up as absorption to blood and/or loss from the body [27]. The later models handle also vapor and gases like radon and its radioactive progeny. Models that describe radionuclides release into the blood have also been provided ranging from very simple that assume uniform whole-body distribution to complex multi-compartment recycling models that consider radionuclide transport among different tissues and organs.

The application and reliability of these models and their associated uncertainties depend in large part on the quality of data used in model development as well as the robustness of the model itself [26, 27]. The results of using biokinetic models is greatly influenced by measuring the amount of intakes which are carried via a number of methods including bioassays (whole body retention and urinary excretion) or through environment-based methods such as air concentration or type of diets used [27].

9.3.2.2 Dosimetric Models

While biokinetic models are used for the calculation of the total amount and number of disintegrations that occur in source organs during a period of 50 or 70 years, the role of dosimetric models is to calculate the deposition of energy in target tissues due to the assigned number of source regions. The dosimetric models take into consideration the physics of decay, energy, and yield of all radioactive emissions, providing a measure of absorbed dose to target organs. Similar to what stated in MIRD assumptions, ICRP models assumes that the radioactivity is uniformly distributed in the source regions which might vary significantly in dimension and geometry when considering different tissues and organs within human body. This could be a limitation especially when dealing with short-range particulate radiations such as beta and alpha that deposit energy in a dispersion manner such as that seen for example in target cells and their nuclei.

9.4   Practical Internal Dosimetry

The MIRD scheme needs to go through a number of well-defined steps, so that dosimetric measurements are performed in a more simplistic but systematic manner. The three major steps required as outlined in MIRD 16 are data collection, analysis, and processing. However, data sources vary and may include external measurements using planar or tomographic SPECT or PET imaging, estimations through use of a compartmental model, extrapolation from animal data, measurement of excretory fluids and blood, tissue sampling, or direct measurement, for example, from thermoluminescent (TLD) radiation dosimeters [46].

The two fundamental modes of data acquisition in nuclear medicine are two and three dimensions (2D and 3D). The 2D imaging mode is fast and easy to acquire but lack the depth information about radiotracer distribution. It is a stacked compressed representation of the scanned patient volume. As described above, to calculate the absorbed dose to a particular target organ, measurements of $\sum_s \cdot \tilde{A}s$ which is the cumulated activity for each source organ is essential to be determined. Serial data acquisitions are thus required at several time points to generate the time–activity curve.

In the example shown in Fig. 9.1, the total absorbed dose to the liver is the sum of dose contributions from self-irradiation as well as from spleen tissue and can be detailed here as:

$$D_{\text{liver}} = \tilde{A}_{\text{liver}} \cdot S_{\text{liver} \leftarrow \text{liver}} + \tilde{A}_{\text{spleen}} \cdot S_{\text{liver} \leftarrow \text{spleen}}$$

where $\tilde{A}_{\text{liver}}$ and $\tilde{A}_{\text{spleen}}$ are the cumulated activity or the integrated time–activity curve of the source organs liver and spleen, respectively. The two terms $S_{\text{liver} \leftarrow \text{Liver}}$ and $S_{\text{liver} \leftarrow \text{spleen}}$ are the S-value for the pairs (liver ← liver) and (liver ← spleen), respectively. It is the mean dose delivered to the target (i.e., liver) tissue per unit cumulated activity in the source organs (i.e., liver and spleen, respectively). The problem can then simply be extended to include more source organs following the same method of calculation.

9.4.1   Dosimetry for Therapy

The conventional absorbed dose calculation that reveals averaged values to indicate risk to a model that represents a population is not appropriate for therapeutic purposes as the tumor dose distribution require more detailed information to cause tissue toxicity [47]. The conventional dose scheme might be adequate when the aim is only diagnostic. Tumor toxicity and tumor control probability that can be derived from radiobiological models require more detailed information of dose–volume histogram and also information about dose distribution to sensitive or dose-limiting regions of the tissue [48]. What really characterizes radionuclide therapy dosimetry from conventional diagnostic dosimetry is the accuracy of the input data and reliability of the radiobiological models [48].

9.4.2 The Radionuclide

Radionuclide is an important determinant in the calculations of the internal dosimetry. The decay scheme that includes energy and types of radiations emitted along with frequencies of occurrences or abundance of emission do influence the calculations of the absorbed fraction. The half-life of the radionuclide is also important and together with the biological half-life constitutes the ultimate rate through which the radionuclide reside in individual tissues (i.e., $T_{1/2(eff)}$). The most clinically used radionuclides are ^{89}Sr, ^{153}Sm, ^{186}Re, and ^{223}Ra for the treatment of bone metastasis in metastatic castration-resistant prostate cancer, ^{131}I-mIBG for the treatment of neuroblastoma and adult neuroendocrine tumors (NET). Another important compounds are ^{90}Y-labeled monoclonal antibodies for the treatment of non-Hodgkin's lymphoma and also ^{90}Y-labeled microspheres for intra-arterial treatments of tumors and metastases in the liver in addition to ^{177}Lu- or ^{90}Y-labeled peptides of NET [39]. Three radiopharmaceutical compounds have been recently approved by the FDA including radium-223 (223Ra)-dichloride (Xofigo®) for the treatment of metastatic castration-resistant prostate cancer, (177Lu)-DOTA-TATE (LUTATHERA®) for the treatment of somatostatin receptor-positive (SSTR) gastroenteropancreatic NETs, and (the high specific activity) Iodine-131-iobguane (AZEDRA®) for the treatment of patients with metastatic pheochromocytoma or paraganglioma [49].

For the purpose of imaging, the radionuclide should have gamma emission component that enables to visualize radiotracer uptake within different regions and tissues. In radiopharmaceutical therapy such as beta and alpha emitters, the gamma component provides an opportunity to investigate the biodistribution and tumor spatial extent in addition to the differential uptake in other neighboring structures.

Radionuclides used in therapy generally should have longer half-life and injected in relatively large amount when compared to diagnostic ones to provide an opportunity for cell death and tumor toxicity. The half-life of the radionuclide should carefully be selected, so that an appropriate time frame is given to the practitioners to perform data sampling strategy consistent with radiotracer uptake, retention, and washout. An adequate count collection and statistical certainty should be maintained along the time course of the dosimetric procedure.

Radioactive isotopes (elements with the same atomic number Z) are good examples when used in imaging and therapy such as ^{86}Y/^{90}Y, ^{68}Ga/^{67}Ga, ^{124}I/^{131}I, and ^{123}I/^{131}I to maintain no change would happen when the therapeutic agent is administered after performing dose planning using the diagnostic agent. Iodine-131 is used as imaging biomarker as well as therapeutic agent in thyroid cancer ablation and in patients with hyperthyroidism. However, when this option is not possible, then the diagnostic radionuclide should have chemical properties similar to the therapeutic radionuclide counterpart, and the final formulated therapeutic compounds share as closely as possible the same pharmacokinetic characteristics [50]. While Lu-177 has beta and gamma components in the decay scheme and hence can be used as theranostic agent [51], indium-111 and Y-90 are two couples that used in imaging and therapy for examples in neuroendocrine tumors or radiolabeled antibody [51]. Table 9.4 describes the physical properties of some clinically useful radionuclides.

Emitters of both gamma and beta need one to understand the two different contributions to the target tissues and how the gamma emissions can be accounted for in the tumor mass as well as to organs at risk. Beta particle dose contribution to tumor has been dealt with using a number of approaches including point dose kernel, voxel-based dosimetry, and Monte Carlo simulation [52, 53].

Electrons/beta have a range in tissue around few millimeter or less, alpha have usually a range of 100 μL or even less. Low energy Auger electrons deposit their energy in the range of nanometer. Note that the high LET of alpha particle emitters such as ^{223}Ra lead to greater relative biological effectiveness than gamma or beta radiations with more toxicity that is independent of dose rate, cell cycle, and oxygenation level [21].

Table 9.4 Physical properties of some clinically useful radionuclides

Radionuclide	Particulate decay mode	Physical half-life	Beta particle energy (E_{max}), keV	Maximal range, mm
Iodine-131, I-131	β^{-1}	8.0 d	610	2.0
Lutetium-177, Lu-177	β^{-1}	6.7 d	496	1.6
Yttrium-90, Y-90	β^{-1}	2.7 d	2290	11.9
Strontium-89, Sr-89	β^{-1}	50.53 d	1496	8.0
Samarium-153, Sm-153	β^{-1}	46.5 h	808.2	3.1
Radium-223, R-223	α	11.44 d	5979.2	<10 μ

9.4.3 Kinetic Data

Pharmacokinetics of a radiopharmaceutical compound has a significant role on the fate of energy deposition in different organs and their relative absorbed dose. Understanding the biokinetics of a given compound permits us to estimate the tumor absorbed dose more accurately and reduce the exposure of dose-limiting organ to lower levels [48]. Dosimetry of radionuclide therapy is different from chemotherapy as it quantifies in advance the absorbed dose to a specific tissue per unit administered radioactivity, providing more precision in dose delivery to the target. Chemotherapy on the other hand is largely based on weight or body surface area-based prescription regimen [54].

The integral of TAC represents the total number of disintegrations that occurred in the source organ (e.g., shaded curves in Fig. 9.1). A number of different ways were proposed to integrate the TAC including direct integration such as the trapezoidal method or fitting function that can adequately describe the data (e.g., mono- or bi-exponential functions) [55]. Alternatively, compartmental modeling can be used as described in Chap. 20 where the target tissues or organs of interest can be seen as separate physical spaces (i.e., compartment) interconnected through what is called transfer rate constant that determine the rate of radiotracer transportation among compartments.

The imaging protocol should follow an appropriate data sampling scheme, so that integral of the time–activity curve is accurate with less impact from missing important temporal data points. In mono-exponential data kinetics perhaps a minimum of three points is required at first approximation. For example, in In-111 Zevalin, an imaging scheme of five whole-body scans was recommended: 0.5–1; 4; 24; 72–96; 120–144 h post administration. As most of the time the tail part is exponentially decreasing and prolonged data collection is not practically feasible, it might be important to extend the sampling period as far as possible, so that estimation uncertainty of the remaining portion is reduced [46].

9.4.4 Quantitative Planar and SPECT Imaging

The most commonly used method for data sampling is through planar anterior-posterior imaging. To determine the radiotracer activity with acceptable accuracy, then a number of corrections are required. As described in Chap. 18, attenuation, scatter, resolution effects, noise, and background are among the most influential image degrading confounder in image quantitation including planar and tomographic imaging. The conjugate view method is one of the common strategies to reduce the effect of source depth on photon attenuation calculations. Scatter correction using effective

scatter source estimation (ESSE) and double or triple energy window with down scatter correction are reported in internal dose data collection [39, 56, 57]. Resolution recovery is very necessary to be implemented especially in small structures that undergo partial volume effect [58, 59].

A strict quality assurance should be in place to ensure that measurements of internal dosimetry would be accurate with high acceptable precision. The gamma camera should be under strict quality control program (e.g., Chap. 11). Other equipment perhaps well counter, gamma probe, and dose calibrator must also be properly checked and working in standard conditions (Chap. 3). A number of corrections and preparatory measures are requested to come up with reliable estimate of absorbed dose. It can be summarized here as follows:

1. Calibration of gamma camera.
2. Dead time (only during therapy with 131-I labeled agents and seldom with 177Lu).
3. Correction for scattered photons.
4. Correction for photon attenuation.
5. Background from overlapping structures.
6. Self-absorption of source object.
7. Partial volume effect for small objects.

Planar conjugate view is often used to mitigate the effect of depth due to photon attenuation. It has a number of pitfalls that discussed in some details in Chap. 18. However, it is often used when organ activity is required for internal dose calculations. The collected data points are then plotted versus the time of measurements to create the corresponding source time–activity curve. In a given ROI, the activity concentration estimate can be derived using the formula:

$$A_t = \text{CF} \cdot e^{(\mu_e d/2)} \cdot \sqrt{C_{\text{ant}} \cdot C_{\text{post}}} \qquad (9.5)$$

$$\mu_e = \frac{1}{T} \sum_{i=1}^{n} \mu_i T_i$$

where

- C_{ant} and C_{post} are the measured count of the ROIs drawn on anterior and posterior images, respectively.

- μ_e is the effective attenuation coefficient.
- T is the patient body thickness.
- CF is the calibration factor and i is the pixel index.

Photon attenuation has been an issue along with other corrections required to attain images of high diagnostic quality as well as improved quantitative accuracy. Transmission imaging using X-ray computed tomography is used to account for photon attenuation with reliable results. However, the conjugate views methods described above provides an alternative means despite some approximations are required. It assumes constant attenuation coefficients along the beam path, but it works independent on organ depth inside patient body, whereas dependent on patient body thickness [60–62]. Therefore, when the source is not significantly small, self-attenuation will then need to be considered adding some modifications to Eq. (9.5) as follows:

$$A_t = \text{CF} \cdot e^{(\mu_e d/2)} \cdot \sqrt{C_{\text{ant}} \cdot C_{\text{post}}} \cdot \frac{\mu b/2}{\sinh(\mu b/2)}$$

where b is a measure of the object thickness.

Photon scatter correction is also one of the main degrading factors in image quantitation resulting in reduced image contrast and elevated noise. The most common correction methods are dual and triple energy windows. Both rely on using additional energy windows placed below or adjacent to the main radionuclide photopeak(s), respectively, to obtain relevant information about the scattered events in a given acquisition. Both have been used in planar and tomographic SPECT imaging with some caveats that must be understood [60–62].

During whole-body imaging, a reference source with small activity (e.g., 2–5 MBq) of the same administrated radionuclide (but could be different like Ba-133 instead of I-131) is normally used as standard to ensure consistency of sensitivity measurement across scans and also to account for any variation that may rise due to energy photopeak and system instability as well as physical decay.

9.4.5　Organ Region of Interest

Organ region of interest (ROI) should be defined precisely, so that an accurate estimate of time–activity curve integration can be realized. Due to its two-dimensional nature, planar imaging has some limitations in providing clear-cut distinction of tissue boarders, and hence, organs overlap do occur in the acquired scintigraphic images. The advent of anatomical imaging has made organ delineation better than Scintigraphic-based contouring. In case of absence of anatomical images to use, an overestimation of organ activity might be preferred than underestimation, so that we conservatively ensure absorbed dose estimate is not underestimated. Background correction may result in over- or underestimation of the source organ activity, and thus, proper selection of the background location is a good practice of internal dosimetry calculations [63, 64].

Once all necessary source organs are determined for their time activity curve, the MIRD formalism come into operation to provide an estimate of organ dose and whole body effective dose. MIRDOSE3.1 was developed for this purpose as source for the S values. The software has initially included 223 radionuclides and 10 different anatomical phantoms covering adult male and female and pediatric geometries (i.e., 6 phantoms for adult and children at various ages and 4 representing adult female that is non-pregnant or pregnant at different stages). It also included isolated spherical model with uniform activity distributions and models for prostate gland, peritoneal cavity, kidney, head, and brain. Afterwards, the MIRDOSE3 was replaced by OLINDA/EXM (Organ Level INternal Dose Assessment/EXponential Modeling) package in 2004 with an agreement of 1%–2% in most cases (with few exceptions) [33]. The number of radionuclides was significantly increased for more than 800 including decay data for some alpha particles. Radiation weighting factors were covered along with the possibility of accounting for patient organ mass.

OLINDA/EXM software calculates radiation doses to different organs of the body from systemically administered radiotracers and also able to perform regression analysis on biokinetic data through a Java (Sun Microsystems)-based GUI interface [33]. The code was also modified to provide an opportunity to perform exponential mono-, bi-, or tri-exponential fitting for the biokinetic data in question. Recently, OLINDS/EXM versions 2 has been released with new features including more than 1000 radionuclides (including alpha emitters), next-generation voxel-based realistic phantoms for adults, children, and pregnant women. It has capabilities to modify organ masses to patient-specific values and assign activity to the walls of hollow organ. For research objectives, the new version has voxel-based realistic phantoms for three mouse, five rat, and two dog models [65, 66].

9.4.6　Human Phantoms

As explained above, derivation of the absorbed fraction requires detailed information about different human organs and their relative geometric relationship. This provides an opportunity for the Monte Carlo simulation to produce the absorbed fraction for organ self-irradiation as well as cross irradiation among different tissues and organs. Anatomical variation including organ size, geometry, and distance from other organs could contribute to remarkable differences in dose estimates exceeding more than 50%. There are quite different models that have been proposed to simulate human anatomy that can be classified as follows [66–68]:

1. Stylized phantoms that consist of primitive geometries and surface equations such as cylindrical, conical, and ellipsoidal shapes. These phantoms were common before 1990s but can be traced back to 1940s, although the first anthropomorphic phantom was not reported until 1960s. These phantoms had undergone a number of modifications, changes, and update in terms of a number of organs, geometry, tissue heterogeneity and detailed anatomical features, gender, and pediatric age groups. Advances were made in 1970s and 1980s when special emphases were

placed on single organ mass and the use of simple shapes to simulate organs or the entire body of an adult human [67]. Among those developed based on stylized approach is "Reference Man" which was adopted by ICRP in their publication 23 [69].

In 1969, the first heterogeneous phantom was reported, namely "MIRD-5 Phantom," due to the adoption made by MIRD Committee for the phantom in MIRD pamphlet 5 [70]. This phantom was composed of a skeleton, a pair of lungs, and soft tissue remainder. The representation of internal organs in this mathematical phantom was crude as the simple equations had generally described position and geometry of each organ. ADAM and EVA phantoms were modified version of the MIRD-5 phantom by developing two separate sex-specific phantoms [71]. They were originally developed in the German National Research Center for Environment and Health (GSF) based on reference male and female organ masses provided by ICRP publication 23. A family of phantoms were also introduced that consisted of an adult male, a newborn, and individuals of ages 1, 5, 10, and 15 years (also representing an adult female with additional anatomical features). A model for pregnant female at the end of each trimester of pregnancy was also developed [72]. While the stylized phantoms are not realistic due to its crude mathematical origin, they can be easily manipulated to model anatomical variations and patient motion [73].

2. Voxelized phantoms are derived from anatomical images taken from real individuals. The organs are well defined, segmented, and labeled. These phantoms appeared in late 1980s and applied by many in 1990s. It is not like stylized phantoms, the voxelized phantoms consist of large number of small volumetric picture elements called voxels that grouped into distinct anatomical structures forming human organs. These phantoms are very realistic but lack the anatomical variations and patient motion. They are essentially fixed to the source data that were used in model design [68]. In publication 110 released

by ICRP in 2009, attempts were made to employ ICRP computational phantoms of the Reference Male and Reference Female in consistency with data provided in publications 89 describing the reference anatomical and physiological parameters for both male and female subjects [74, 75].

3. Hybrid phantoms (or boundary representation) started in mid-2000s and are based on non-uniform rational B-splines (NURBS) or polygon meshes to define individual objects and structures [76]. It combines the features of reality associated with voxelized phantom with the flexibility of stylized phantoms incorporating shapes, motion, and variations. While the cardiac-torso phantom (NCAT) was developed from the CT images of the visible human project, the phantom dynamics were obtained from 4D tagged MRI data set [77]. The XCAT version offers great opportunities in modeling whole-body anatomies for adult male and female in addition to population of phantoms at several age groups. There are also several remarkable features including change of pixel and matrix size, organ dimension, and cardiac and respiratory motion. The phantom has versatile applications and has been extensively used in the last two decades. A number of modifications were made from collaborations and independent research groups that produced a wide range of NURBS-based phantoms able to address several tasks of dosimetry and imaging in nuclear medicine, radiology, and external beam radiotherapy [67, 78–82].

9.4.7 Uncertainty in Internal Dose Estimates

There are numerous sources of data uncertainty in internal dose estimate including data collection which cover sampling, measuring devices or imaging equipment and other issues related to statistical counting [83]. The gamma camera has performance limitations in terms of spatial resolution, system sensitivity, count rate performance in planar and tomographic imaging. There are

also some potential image degrading factors including photon attenuation and scatter and resolutions effects that reduce the performance of the gamma camera to provide an accurate measure of tracer concentration. Other additional factors that contribute to variable degrees to the overall accuracy are image acquisition, reconstruction, processing methods, and data analysis. Those parameters may be tuned variably to address the detection task to improve the estimate of tracer concentration rather than improving image quality [59, 84].

The process of converting the acquired total counts or count rate into units of radioactivity require proper handling of the interfering parameters and standardization of the imaging protocol provided a particular setting of gamma camera and collimation characteristics. This calibration process along with partial volume correction was investigated to contribute significantly to measurement uncertainty [59]. All the above-mentioned sources could impact the calculations of the tracer kinetics leading to significant inaccuracies in the calculation of the integral of the time–activity curve. Moreover, the individual variation of organ kinetics and normal physiology that exist among subjects could add more variability to dose coefficient determination (e.g., mSv/MBq) [66].

As the stochastic nature of radiopharmaceuticals in causing sever- or radiation-related illness is generally very low (except few instances of misadministration or improper handling), individual calculation of the absorbed dose is not considered a matter of routine practice. However, dose assessment in therapeutic applications should be properly planned [85]. The strategy of "one size fits all" might not be the optimal approach to follow and even the use of patient weight or body surface area as normalizing factor might bear significant uncertainty [5, 86]. Patient personalized dosimetry is of particular interest as it could revise the current standards, adding beneficial outcome to patient management through improvement of tumor control probability and reduction or avoidance of normal tissue toxicity.

9.5 Radiobiology of Radionuclide Therapy

Radiobiology and dosimetry are so connected and of particular relevance to be emphasized especially in the new era of radiopharmaceutical therapy and precision medicine [5, 86]. The absorbed dose in its pure physical definition cannot be used to understand or predict a biological response or survival outcome. However, low doses are generally linked to stochastic effects of radiation and process of cancer induction or inheritable disease is a matter of low probability that increases with absorbed dose. High absorbed dose as normally seen in therapeutic applications requires robust measures that enable a derivation of dose–response relationship. This is important to achieve as accurate absorbed dose assessment provides a means for successful treatment without over or underdosing and also without compromising healthy or organs at risk. High doses to non-target tissues may increase the probability of stochastic effects and could also cause side effects such as, hematologic toxicity, renal failure, gastrointestinal tract toxicity, or lung fibrosis [6]. The aim is to predict the level of radioactivity required for administration in an individual patient. This permits physician to prescribe an optimal dosing in terms of adequate tumor control while minimizing potential side effects to normal tissues [87].

Absorbed dose therefore needs some modifications to account for the variation that may arise from the nature of radiation and perhaps all its related physical parameters as well as the biological medium under investigation. The radiation and tissue weighting factors described above to modify the absorbed dose to be equivalent and effective dose, respectively, along with the definition of RBE were not sufficient to address dose–response relationship since they consider average age and gender for a selected population with main focus on stochastic effects. However, tumor damage and treatment using radiopharmaceutical therapy require different scale of quantities (more appropriate modifications) as practical tools to support dose prescription regimens.

9.5.1 Radiation Therapy Vs. Radionuclide Therapy

Radiobiology was developed significantly in concomitance with radiation therapy that has well-established dose planning techniques along with a wide range of experimental and clinical results [88]. A number of inherent technical differences exist between external beam radiotherapy and radionuclide therapy including geometry of the delivered beam to target tissues, and radiation beam is well controlled in terms of time of irradiation and conformance with the irradiated volume in addition to dose rate and total period of treatment cycles/fractions [87]. Radionuclide therapy, however, is affected by radiotracer biodistribution, tissue retention function, homogeneity of the administrated compound within tissues, non-isotropic nature of charged particles emitted including spatial distribution and energy spectrum and their fate of interactions. Dose rate is significantly lower than external beam radiotherapy, and length of irradiation is much longer and often decreasing in an exponential fashion [86].

The average dose rate for radionuclide therapy is typically of the order of 2–8 Gy/day being maximum of 50 Gy delivered over a period of many days. In contrast, a fraction of 1–2 Gy may be delivered in a couple of minutes or even shorter in external beam radiotherapy (i.e., 1–5 Gy/min). While the mechanism of cell damage using low-dose radiation is via apoptosis, the high dose rate tends to cause cell necrosis as the main mechanism of cytotoxicity [89]. The underlying radiobiology of fractionated radiotherapy rely on the 5 R's principle, namely repair of DNA damage, repopulation of tissues, redistribution, reoxygenation of tumor cells, and redistribution in the cell cycle [86].

The fractionated radiotherapy relies on the fact that the DNA repair should be efficient in normal tissues while the genetic instability of the tumor cells makes them less efficient in repair. This concept permits us to deliver radiation doses in fractions providing spare opportunities for normal tissue while maximizing the rate of tumor cell death.

Extrapolation of the radiobiology of external beam therapy to that of radionuclide therapy does not seem to be straightforward as both treatments can induce variable biological signaling leading to different cellular pathway activation [90, 91]. However, there is an ongoing interest and formal calls being conducted to strength the relationship and deepen the radiobiological basis of radionuclide therapy [91].

Radionuclide therapy is featured by the fact that the dose rate is not constant over the course of treatment. There is an initial uptake phase in which the dose rate of the radionuclide is increasing and then a plateau region of maximum dose rate then a decline phase characterized by gradual reduction of the dose rate. The biochemical targeting of radiopharmaceuticals used in radionuclide therapy serves to improve dose delivery to the target with differential toxicity and potential lethality determined by the type of particulate radiations including beta or alpha emitters. The alpha emitters tend to deposit local doses within 100–150 μm from the site of emission with two to three order of magnitude damage relative to those caused by photons or beta particles [92].

Tissues vary in their radiosensitivity into two major classes including early and late responding tissues. The former class has relatively fast proliferating capacity, and thus, clinical manifestations appear sooner within days or weeks after irradiation. The late responding tissue has a relatively slower growing rate, and manifestations on the other hand appear on late stages within months or years. The latter is of particular interest in radiation oncology and dose-limiting organ in radionuclide therapy. Bone marrow is an early while kidney are late tissue-limiting organs, and several investigations have solely focused on figuring out radiation toxicities, dose limitations, and organ tolerances associated with radionuclide therapies [47, 93, 94].

9.5.2 Types of Damage

There are two major effects when ionizing radiation interacts with biological cells and living tissues: called direct and indirect effects. The

former occurs when the ionizing radiation interacts with the DNA molecules while the latter occurs when the ionization radiation interacts with water molecules producing free radicals that migrate to attack the DNA causing several modes of damage. When the damage of the DNA is at one single strand, then the chance for repair is very high. However, when the damage of the DNA occurs on both sides of the DNA strands, then the chance to repair becomes less likely to occur. The former damage is called single-strand break, whereas the second damage is called double-strand break. Therefore, the double-strand break is more lethal to the cell than single-strand break.

Fig. 9.3 Cell survival curve due to exposure to low and high LET ionizing radiations. It demonstrates how the α/β is calculated

9.5.3 Linear Quadratic Model

One of the most often radiobiological models used over the decades in radiotherapy treatment strategies is the linear quadratic model or LQ model. The linear quadratic model provides an explanation of fractionation and dose rate effects observed at the macroscopic (i.e., clinical) level and may be applied to both tumor and normal tissues [88]. In 1930s, it has been discovered that splitting radiation dose into a number of small fractions reveled better outcomes than a single exposure [95]. It can also be instrumental in estimating the therapeutic index for a given therapeutic regimen weighing the balance between tumor control probability and normal tissue complication probability.

Cell survival fraction "SF" after irradiation is expressed according to the LQ model using the formula:

$$\text{SF} = N / No = \exp-\left(\alpha D + \beta D^2\right)$$

The term α/β has the units of dose (Gy) and is a measure of the shape of the survival curve (see Fig. 9.3). The parameter α defines the initial slope of the survival curve, whereas β describes the curvature of the survival curve. α is proportional to dose (one single event is lethal) and β is proportional to squared dose (two sublethal events are required for lethal damage). Early

molecular understanding of the damage caused by the two-track β lethal damage is largely due to dicentric chromosome aberration, whereas alpha damage is due to point mutations in vital genes, small deletions, chromosome breaks, or induced apoptosis [96].

Higher values of α indicate more steepness of the initial portion of the survival curve while larger values of β imply more curvature of the survival curve (see Fig. 9.4). The shoulder part of the curve refers to the repair capacity of the cells such that lower values are consistent with greater repair capacity while higher values of the shoulder curve indicate lower repair capacity [17, 97]. LQ model is used to calculate effectiveness of various dose schedule regimens in radiation therapy.

The LQ model is based on two modes of cell death namely a single hit and double hit cell kill. The former is due to a lethal single-ionization event and dose rate independent while the latter is due to two closely spaced ionizations occurring in a short time interval and hence dose rate dependent. At low doses, single-strand breaks will dominate, and hence, likelihood of repair is common. However, at high doses, double-strand breaks will dominate with less chance for DNA to repair, and hence, the survival curve will become steeper. High rates of repair make the survival curve more curva-

Fig. 9.4 Different cellular radiosensitivity with their relative alpha and beta values
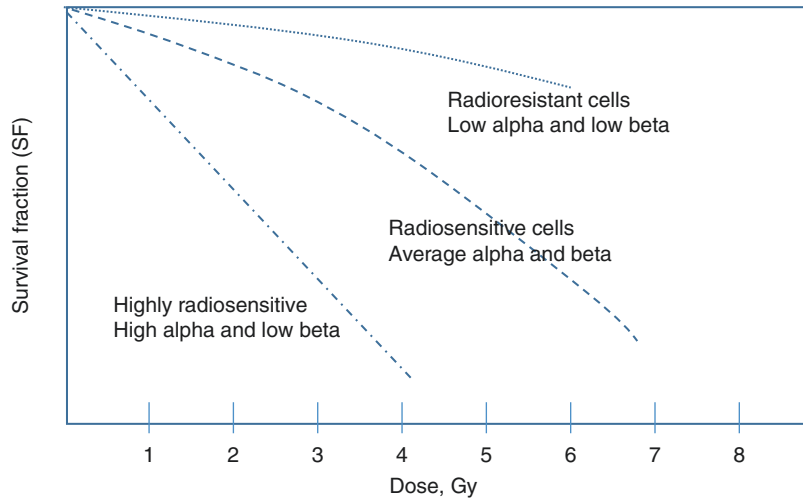
ture. As dose rate increases, the repair decreases and cell lethality increases [98]. The repair also decreases as time between fractions decreases. Repair is of particular importance for normal cells, and hence, enough time is required to let the normal cells get back to normal. However, the low dose rate that accompany radionuclide therapy permits normal cells to repair than tumor cells.

9.5.4 Biological Effective Dose (BED)

A central feature of LQ methodology is the quantity known as the biologically effective dose (BED) which may be used to quantify the radiobiological impact of a treatment on both tumors and normal tissues.

BED is a radiobiological quantity widely used in conventional radiotherapy and also has been used to quantify various forms of targeted radiotherapy [6, 86]. It may also permit designing of targeted treatments which are therapeutically equivalent to external beam treatments quantifying effects on both tumors and normal tissues [99]. Biological effective dose may be defined as the total physical dose required for a specified biologic effect when it is delivered at a very low dose rate or in many small-dose fractions [99].

If the absorbed dose D is delivered over a time T, the lethal double hit events must be corrected for repair due to sublethal damage. The LQ model is then need to be rewritten as

$$\text{SF} = N / No = \exp-\left(\alpha D + G(T).\beta D^2\right)$$

The function G, called the "Lea-Catcheside factor," acts as a modifier of the second term and takes into account the temporal occurrence of cell repair and induction of a second cell lesion. It is therefore proportional to the absorbed dose rate and takes values between 0 and unity [43]. BED can be mathematically defined as

$$\text{BED} = D \times RE = D\left(1 + \frac{G(T).D}{\alpha / \beta}\right)$$
$$= D\left(1 + \frac{D\lambda}{(\alpha / \beta)(\mu + \lambda)}\right)$$

where

- D is the absorbed dose expressed in Gy.
- Alpha and beta are tissue specific and related to cell radiosensitivity and expressed in Gy^{-1} and G^{-2}, respectively.
- μ is the exponential repair rate constant that quantifies the rate of sublethal damage repair, it is equivalent to the term $\ln [2]/T_{1/2}$ in units of h^{-1} defined as the repair half-time of sublethal damage.

- λ is the effective clearance rate constant (given by the sum of the physical decay and the biological clearance rate constants).

It tells us that the BED is a product of the physical absorbed dose and modifying parameter that relates dose rate to cellular radiosensitivity and cellular repair. It is called relative effectiveness per unit dose [89]. An interesting work showed a dose–response relationship between renal toxicity measured by creatinine clearance (CLR) loss per year and measurements of BED. The study revealed a strong correlation with CLR loss per year ($r = 0.93$; $p = 0.0001$) in patients with somatostatin receptor–positive neuroendocrine tumors treated with ^{90}Y peptide receptor radionuclide therapy. It was also shown that the relationship between BED and the incidence of renal complications was comparable with that obtained for external-beam radiotherapy [98]. There was also a relationship between BED and the normal tissue complication probability of liver [99]. Moreover, prospective dosimetry using a 37 Gy BED as the threshold for kidney toxicity was found to be a good guide for ^{90}Y-DOTATOC PRRT and was associated with a low risk of rapid renal function deterioration (expressed as annual glomerular filtration rate loss) and evolution to severe nephrotoxicity [100].

9.6 Conclusion

Internal radiation dosimetry as applied to diagnostic and therapeutic radiopharmaceuticals is an indispensable tool to get information about absorbed doses to organs and tissues. Efforts are to be exercised when attempts are made to measure and calculate effective dose to administered subjects. There are some factors that if not taken cautiously, they would result in erroneous or large uncertainties in the measured data. Due to the large evidence that effective doses received by nuclear medicine patients are significantly small, it is of no potential value to carry out daily dosimetric measurements on those patients. Special cases might need proper assessment of the internal doses including accidents and misadministra-

tion as well in pregnant ladies and young age groups and infants. However, when therapeutic radiopharmaceuticals come into play, specific measures and procedures must be in place to ensure accurate delivery of the radionuclide into the target site with minimal dose received by non-target tissues. Radiobiological models of radionuclide therapy provide several benefits in terms of tumor control probability, normal tissue complication probability, toxicity, and treatment efficacy. Further research work is highly requested to establish those models in individual treatments.

References

1. Khalil MM, Tremoleda JL, Bayomy TB, Gsell W. Molecular SPECT imaging: an overview. Int J Mol Imaging. 2011;2011:796025.
2. Phelps ME. PET: The merging of biology and imaging into molecular imaging. J Nucl Med. 2000;41(4):661–81.
3. Zanzonico PB. Internal radionuclide radiation dosimetry: a review of basic concepts and recent developments. J Nucl Med. 2000;41(2):297–308.
4. ICRP publication 103. The 2007 Recommendations of the International Commission on Radiological Protection. Ann ICRP 2007;37(2–4):1–332.
5. Lassmann M, Eberlein U. The relevance of dosimetry in precision medicine. J Nucl Med. 2018;59(10):1494–9.
6. Bolch WE, Eckerman KF, Sgouros G, Thomas SR. MIRD pamphlet no. 21: a generalized schema for radiopharmaceutical dosimetry--standardization of nomenclature. J Nucl Med. 2009;50(3): 477–84.
7. Mattsson S. Patient dosimetry in nuclear medicine. Radiat Prot Dosimetry. 2015;165(1–4):416–23.
8. Niemann EG. Radiation biophysics. In: Hoppe WLW, Markl H, Ziegler H, editors. Biophysics. Berlin, Heidelberg: Springer; 1983.
9. Thomas EJ. Introduction to health physics. 5th ed. New York: McGraw-Hill Professional; 2017.
10. Stabin MG. Radiation protection and dosimetry. New York: Springer-Verlag; 2007.
11. Hamada N, Fujimichi Y. Classification of radiation effects for dose limitation purposes: history, current situation and future prospects. J Radiat Res. 2014;55(4):629–40.
12. ICRP publication 26. Recommendations of the ICRP. Ann ICRP. 1977;1(3).
13. ICRP1984. Nonstochastic effects of ionizing radiation. Ann ICRP. 1984;14(3):1–33.
14. 1990 Recommendations of the International Commission on Radiological Protection. Ann ICRP. 1991;21(1–3):1–201.

15. Stewart FA, Akleyev AV, Hauer-Jensen M, Hendry JH, Kleiman NJ, Macvittie TJ, et al. ICRP publication 118: ICRP statement on tissue reactions and early and late effects of radiation in normal tissues and organs--threshold doses for tissue reactions in a radiation protection context. Ann ICRP. 2012;41(1–2):1–322.

16. Authors on behalf of I, Stewart FA, Akleyev AV, Hauer-Jensen M, Hendry JH, Kleiman NJ, et al. ICRP publication 118: ICRP statement on tissue reactions and early and late effects of radiation in normal tissues and organs—threshold doses for tissue reactions in a radiation protection context. Ann ICRP. 2012;41(1–2):1–322.

17. IAEA. Radiation biology: a handbook for teachers and students, training course series. Vienna: IAEA; 2010.

18. Persson L. The auger electron effect in radiation dosimetry. Health Phys. 1994;67(5):471–6.

19. Ku A, Facca VJ, Cai Z, Reilly RM. Auger electrons for cancer therapy—a review. EJNMMI Radiopharm Chem. 2019;4(1):27.

20. Relative biological effectiveness (RBE), quality factor (Q), and radiation weighting factor (w(R)). A report of the international commission on radiological protection. Ann ICRP. 2003;33(4):1–117.

21. Sgouros G, Roeske JC, McDevitt MR, Palm S, Allen BJ, Fisher DR, et al. MIRD pamphlet no. 22 (abridged): radiobiology and dosimetry of alpha-particle emitters for targeted radionuclide therapy. J Nucl Med. 51(2):311–28.

22. Sekiya M, Yamasaki M. Louis Harold gray (November 10, 1905-July 9, 1965): a pioneer in radiobiology. Radiol Phys Technol. 2016;10(1):2–7.

23. A. Endo on behalf of ICRU Report Committee 26 on Operational Radiation Protection Quantities for External Radiation. Operational quantities and new approach by ICRU. Ann ICRP. 2016;45(1 Suppl):178–87. https://doi.org/10.1177/0146645315624341.

24. Sekiya M, Yamasaki M. Rolf Maximilian Sievert (1896–1966): father of radiation protection. Radiol Phys Technol. 2015;9(1):1–5.

25. Hunter N, Muirhead CR. Review of relative biological effectiveness dependence on linear energy transfer for low-LET radiations. J Radiol Prot. 2009;29(1):5–21.

26. Harrison J, Day P. Radiation doses and risks from internal emitters. J Radiol Prot. 2008;28(2):137–59.

27. Harrison J. Biokinetic and dosimetric modelling in the estimation of radiation risks from internal emitters. J Radiol Prot. 2009;29(2A):A81–A105.

28. Fisher DR, Fahey FH. Appropriate use of effective dose in radiation protection and risk assessment. Health Phys. 2017;113(2):102–9.

29. Paquet F, Bailey MR, Leggett RW, Harrison JD. Assessment and interpretation of internal doses: uncertainty and variability. Ann ICRP. 45(1 Suppl):202–14.

30. Allisy A, Jennings WA, Kellerer AM, Müller JW, Rossi HH, Seltzer SM. Report 60. ICRU. 1998;os31(1):NP. https://doi.org/10.1093/jicru/os31.1.Report60.

31. Eckerman K, Endo A. MIRD: radionuclide data and decay schemes. 1st ed. Reston, VA: Society of Nuclear Medicine; 2008.

32. Snyder WSFM, Warner GG. Estimates of specific absorbed fractions for photon sources uniformly distributed in various organs of a heterogeneous phantom. MIRD pamphlet no. 5, revised. New York, NY: Society of Nuclear Medicine; 1978.

33. Stabin MG. Sparks RB, Crowe E. OLINDA/EXM: the second-generation personal computer software for internal dose assessment in nuclear medicine. J Nucl Med. 2005;46(6):1023–7.

34. Snyder W, Ford M, Warner G, Watson S. "S" absorbed dose per unit cumulated activity for selected radionuclides and organs. MIRD pamphlet no 11. New York: Society of nuclear Medicine; 1975.

35. Vaziri B, Wu H, Dhawan AP, Du P, Howell RW. MIRD pamphlet no. 25: MIRDcell V2.0 software tool for dosimetric analysis of biologic response of multicellular populations. J Nucl Med. 2014;55(9):1557–64.

36. Howell RW, Wessels BW, Loevinger R, Watson EE, Bolch WE, Brill AB, et al. The MIRD perspective 1999. Medical Internal Radiation Dose Committee. J Nucl Med. 1999;40(1):3S–10S.

37. Bouchet LG, Bolch WE, Blanco HP, Wessels BW, Siegel JA, Rajon DA, et al. MIRD pamphlet no 19: absorbed fractions and radionuclide S values for six age-dependent multiregion models of the kidney. J Nucl Med. 2003;44(7):1113–47.

38. Bouchet LG, Bolch WE, Weber DA, Atkins HL, Poston JW Sr. MIRD pamphlet no. 15: radionuclide S values in a revised dosimetric model of the adult head and brain. Medical Internal Radiation Dose Committee. J Nucl Med. 1999;40(3):62S–101S.

39. Ljungberg M, Gleisner KS. 3-D image-based dosimetry in radionuclide therapy. IEEE Trans Radiat Plasma Med Sci. 2018;2(6):527–40.

40. Hippelainen E, Tenhunen M, Sohlberg A. Fast voxel-level dosimetry for (177)Lu labelled peptide treatments. Phys Med Biol. 2015;60(17):6685–700.

41. Funk T, Despres P, Barber WC, Shah KS, Hasegawa BH. A multipinhole small animal SPECT system with submillimeter spatial resolution. Med Phys. 2006;33(5):1259–68.

42. Bolch WE, Jokisch D, Zankl M, Eckerman KF, Fell T, Manger R, et al. ICRP publication 133: the ICRP computational framework for internal dose assessment for reference adults: specific absorbed fractions. Ann ICRP. 2016;45(2):5–73.

43. Yonekura Y, Mattsson S, Flux G, Bolch WE, Dauer LT, Fisher DR, et al. ICRP publication 140: radiological protection in therapy with radiopharmaceuticals. Ann ICRP. 2019;48(1):5–95.

44. Andersson M, Johansson L, Eckerman K, Mattsson S. IDAC-dose 2.1, an internal dosimetry program for diagnostic nuclear medicine based on the ICRP adult reference voxel phantoms. EJNMMI Res. 2017;7(1):88.

45. Radionuclide transformations. Energy and intensity of emissions. Report of a Task Group of Committee 2 of the International Commission on Radiological Protection on data used in ICRP Publication 30. Ann ICRP. 1983;11–13:1–1250.

46. Wessels BW, Syh JH, Meredith RF. Overview of dosimetry for systemic targeted radionuclide therapy (STaRT). Int J Radiat Oncol Biol Phys. 2006;66(2 Suppl):S39–45.

47. Barone R, Borson-Chazot F, Valkema R, Walrand S, Chauvin F, Gogou L, et al. Patient-specific dosimetry in predicting renal toxicity with (90)Y-DOTATOC: relevance of kidney volume and dose rate in finding a dose-effect relationship. J Nucl Med. 2005;46(Suppl 1):99S–106S.

48. Sgouros G, Hobbs RF. Dosimetry for radiopharmaceutical therapy. Semin Nucl Med. 2014;44(3):172–8.

49. Malcolm J, Falzone N, Lee BQ, Vallis KA. Targeted radionuclide therapy: new advances for improvement of patient management and response. Cancers (Basel). 2019;11(2).

50. Geworski L, Schaefer A, Knoop BO, Pinkert J, Plotkin M, Kirsch CM. Physical aspects of scintigraphy-based dosimetry for nuclear medicine therapy. Nuklearmedizin. 2010;49(3):85–95.

51. Leichner PK, Akabani G, Colcher D, Harrison KA, Hawkins WG, Eckblade M, et al. Patient-specific dosimetry of indium-111- and yttrium-90-labeled monoclonal antibody CC49. J Nucl Med. 1997;38(4):512–6.

52. Lee MS, Kim JH, Paeng JC, Kang KW, Jeong JM, Lee DS, et al. Whole-body voxel-based personalized dosimetry: the multiple voxel S-value approach for heterogeneous media with nonuniform activity distributions. J Nucl Med. 2017;59(7):1133–9.

53. Strigari L, Menghi E, D'Andrea M, Benassi M. Monte Carlo dose voxel kernel calculations of beta-emitting and Auger-emitting radionuclides for internal dosimetry: a comparison between EGSnrcMP and EGS4. Med Phys. 2006;33(9):3383–9.

54. Gurney H. Developing a new framework for dose calculation. J Clin Oncol. 2006;24(10):1489–90.

55. Siegel JA, Thomas SR, Stubbs JB, Stabin MG, Hays MT, Koral KF, et al. MIRD pamphlet no. 16: techniques for quantitative radiopharmaceutical biodistribution data acquisition and analysis for use in human radiation dose estimates. J Nucl Med. 1999;40(2):37S–61S.

56. King M, Farncombe T. An overview of attenuation and scatter correction of planar and SPECT data for dosimetry studies. Cancer Biother Radiopharm. 2003;18(2):181–90.

57. de Nijs R, Lagerburg V, Klausen TL, Holm S. Improving quantitative dosimetry in (177)Lu-DOTATATE SPECT by energy window-based scatter corrections. Nucl Med Commun. 2014;35(5):522–33.

58. Dewaraja YK, Frey EC, Sgouros G, Brill AB, Roberson P, Zanzonico PB, et al. MIRD pamphlet no. 23: quantitative SPECT for patient-specific 3-dimensional dosimetry in internal radionuclide therapy. J Nucl Med. 2012;53(8):1310–25.

59. Gustafsson J, Brolin G, Cox M, Ljungberg M, Johansson L, Gleisner KS. Uncertainty propagation for SPECT/CT-based renal dosimetry in (177) Lu peptide receptor radionuclide therapy. Phys Med Biol. 2015;60(21):8329–46.

60. Berker Y, Goedicke A, Kemerink GJ, Aach T, Schweizer B. Activity quantification combining conjugate-view planar scintigraphies and SPECT/CT data for patient-specific 3-D dosimetry in radionuclide therapy. Eur J Nucl Med Mol Imaging. 2011;38(12):2173–85.

61. Koral KF, Dewaraja Y, Li J, Barrett CL, Regan DD, Zasadny KR, et al. Initial results for hybrid SPECT-conjugate-view tumor dosimetry in 131I-anti-B1 antibody therapy of previously untreated patients with lymphoma. J Nucl Med. 2000;41(9): 1579–86.

62. Koral KF, Dewaraja Y, Li J, Lin Q, Regan DD, Zasadny KR, et al. Update on hybrid conjugate-view SPECT tumor dosimetry and response in 131I-tositumomab therapy of previously untreated lymphoma patients. J Nucl Med. 2003;44(3):457–64.

63. Buijs WC, Siegel JA, Boerman OC, Corstens FH. Absolute organ activity estimated by five different methods of background correction. J Nucl Med. 1998;39(12):2167–72.

64. Shanei A, Afshin M, Moslehi M, Rastaghi S. Estimation of Organ Activity using Four Different Methods of Background Correction in Conjugate View Method. J Med Signals Sens. 2015 Oct-Dec;5(4):253–8. PMID: 26955568; PMCID: PMC4759842.

65. Stabin MG, Siegel JA. RADAR dose estimate report: a compendium of radiopharmaceutical dose estimates based on OLINDA/EXM version 2.0. J Nucl Med. 2018;59(1):154–60.

66. Stabin M, Xu XG. Basic principles in the radiation dosimetry of nuclear medicine. Semin Nucl Med. 2014;44(3):162–71.

67. George Xu X, Eckerman KF. Handbook of anatomical models for radiation dosimetry. 1st ed. Boca Raton, FL: CRC; 2009.

68. Segars WP, Tsui BMW, Jing C, Fang-Fang Y, Fung GSK, Samei E. Application of the 4-D XCAT phantoms in biomedical imaging and beyond. IEEE Trans Med Imaging. 2017;37(3):680–92.

69. ICRP. Report of the task group on reference man. ICRP Publication 23. Ann ICRP. 1979;3(1–4):iii.

70. Snyder WS, Fisher HL Jr, Ford MR, Warner GG. Estimates of absorbed fractions for monoenergetic photon sources uniformly distributed in various organs of a heterogeneous phantom. J Nucl Med. 1969;Suppl 3:7–52.

71. Kramer R, Zankl M, Williams G, et al. The calculation of dose from external photon exposures using reference human phantoms and Monte Carlo methods: part I. the male (ADAM) and female (EVA) adult mathematical phantoms. GSF-Report S-885. 1982.

72. Stabin M, Watson E, Cristy M, et al. Mathematical models and specific absorbed fractions of photon energy in the nonpregnant adult female and at the end of each trimester of pregnancy. ORNL Report ORNL/TM-12907. 1995.

73. Paul Segars W, Tsui BM. MCAT to XCAT: the evolution of 4-D computerized phantoms for imaging research: computer models that take account of body movements promise to provide evaluation and improvement of medical imaging devices and technology. Proc IEEE Inst Electr Electron Eng. 2009;97(12):1954–68.

74. Menzel HG, Clement C, DeLuca P. ICRP publication 110. Realistic reference phantoms: an ICRP/ICRU joint effort. A report of adult reference computational phantoms. Ann ICRP. 2009;39(2):1–164.

75. ICRP Publication 89. Basic anatomical and physiological data for use in radiological protection: reference values. A report of age- and gender-related differences in the anatomical and physiological characteristics of reference individuals. Ann ICRP. 2002;32(3–4):5–265.

76. Segars JP. Development and application of the new dynamic NURBSbased cardiac-torso (NCAT) phantom. PhD dissertation. The University of North Carolina; 2001.

77. Segars WP, Lalush DS, Frey EC, Manocha D, King MA, Tsui BM. Improved dynamic cardiac phantom based on 4D NURBS and tagged MRI. IEEE Trans Nucl Sci. 2009;56(5):2728–38.

78. Veress AI, Segars WP, Weiss JA, Tsui BM, Gullberg GT. Normal and pathological NCAT image and phantom data based on physiologically realistic left ventricle finite-element models. IEEE Trans Med Imaging. 2006;25(12):1604–16.

79. Segars WP, Mahesh M, Beck TJ, Frey EC, Tsui BM. Realistic CT simulation using the 4D XCAT phantom. Med Phys. 2008;35(8):3800–8.

80. Segars WP, Sturgeon G, Mendonca S, Grimes J, Tsui BM. 4D XCAT phantom for multimodality imaging research. Med Phys. 2010;37(9):4902–15.

81. Williams CL, Mishra P, Seco J, St James S, Mak RH, Berbeco RI, et al. A mass-conserving 4D XCAT phantom for dose calculation and accumulation. Med Phys. 40(7):071728.

82. Fung GS, Segars WP, Gullberg GT, Tsui BM. Development of a model of the coronary arterial tree for the 4D XCAT phantom. Phys Med Biol. 2011;56(17):5651–63.

83. Gear JI, Cox MG, Gustafsson J, Gleisner KS, Murray I, Glatting G, et al. EANM practical guidance on uncertainty analysis for molecular radiotherapy absorbed dose calculations. Eur J Nucl Med Mol Imaging. 2018;45(13):2456–74.

84. Stabin MG. Uncertainties in internal dose calculations for radiopharmaceuticals. J Nucl Med. 2008;49(5):853–60.

85. Flux GD, Verburg FA, Chiesa C, Bardies M, Gleisner KS, Hertz B, et al. Comparison of empiric versus dosimetry-guided radioiodine therapy: the devil is in the details. J Nucl Med. 2017;58(5):862.

86. Strigari L, Konijnenberg M, Chiesa C, Bardies M, Du Y, Gleisner KS, et al. The evidence base for the use of internal dosimetry in the clinical practice of molecular radiotherapy. Eur J Nucl Med Mol Imaging. 2014;41(10):1976–88.

87. Ljungberg M, Sjogreen Gleisner K. Personalized dosimetry for radionuclide therapy using molecular imaging tools. Biomedicine. 2017;4(4):25.

88. Bleehen NM. Radiobiology in radiotherapy. 1st ed. Berlin: Springer-Verlag; 1988.

89. Strauss HW, Mariani G, Volterrani D, Larson SM, editors. Nuclear oncology: from pathophysiology to clinical applications. Berlin: Springer International; 2007.

90. Pouget JP, Lozza C, Deshayes E, Boudousq V, Navarro-Teulon I. Introduction to radiobiology of targeted radionuclide therapy. Front Med (Lausanne). 2015;2:12.

91. Terry SYA, Nonnekens J, Aerts A, Baatout S, de Jong M, Cornelissen B, et al. Call to arms: need for radiobiology in molecular radionuclide therapy. Eur J Nucl Med Mol Imaging. 2019;46(8):1588–90.

92. Sgouros G. Dosimetry, radiobiology and synthetic lethality: radiopharmaceutical therapy (RPT) with alpha-particle-emitters. Semin Nucl Med. 2020;50(2):124–32.

93. Forrer F, Krenning EP, Kooij PP, Bernard BF, Konijnenberg M, Bakker WH, et al. Bone marrow dosimetry in peptide receptor radionuclide therapy with [177Lu-DOTA(0),Tyr(3)]octreotate. Eur J Nucl Med Mol Imaging. 2009;36(7):1138–46.

94. Prinsen HT, Klein Hesselink EN, Brouwers AH, Plukker JT, Sluiter WJ, Van der Horst-Schrivers AN, et al. Bone marrow function after (131)I therapy in patients with differentiated thyroid carcinoma. J Clin Endocrinol Metab. 2015;100(10):3911–7.

95. Nahum AE. The radiobiology of hypofractionation. Clin Oncol (R Coll Radiol). 2015;27(5):260–9.

96. Sachs RK, Hahnfeld P, Brenner DJ. The link between low-LET dose-response relations and the underlying kinetics of damage production/repair/misrepair. Int J Radiat Biol. 1997;72(4):351–74.

97. Kuperman VY. Effect of dose rate in hypofractionated radiotherapy. Phys Med. 2019;65:191–9.

98. Wessels BW, Konijnenberg MW, Dale RG, Breitz HB, Cremonesi M, Meredith RF, et al. MIRD pamphlet no. 20: the effect of model assumptions on kidney dosimetry and response—implications for radionuclide therapy. J Nucl Med. 2008;49(11):1884–99.

99. Strigari L, Sciuto R, Rea S, Carpanese L, Pizzi G, Soriani A, et al. Efficacy and toxicity related to treat-

ment of hepatocellular carcinoma with 90Y-SIR spheres: radiobiologic considerations. J Nucl Med. 2010;51(9):1377–85.

100. Van Binnebeek S, Baete K, Vanbilloen B, Terwinghe C, Koole M, Mottaghy FM, et al. Individualized dosimetry-based activity reduction of (9)(0) Y-DOTATOC prevents severe and rapid kidney function deterioration from peptide receptor radio-nuclide therapy. Eur J Nucl Med Mol Imaging. 2014;41(6):1141–57.

SPECT and PET Imaging Instrumentation

Elements of Gamma Camera and SPECT Systems

10

Magdy M. Khalil

Contents

10.1 Introduction

Nuclear medicine provides noninvasive imaging tools to detect a variety of human diseases. The tracer principle discovered by George De Hevesy has made invaluable impact on how disease can be observed and detected [1]. The two major components of nuclear medicine procedures are radiopharmaceuticals and gamma-ray imaging systems. The latter is a position-sensitive radiation detector that relies on detecting gamma photons emitted from the administered radionuclide. Many single-photon and positron emitters are used in nuclear medicine clinical regime. The radiopharmaceuticals are designed for specific purpose of detecting pathophysiologic, meta-bolic, cellular, subcellular, or molecular process. The gamma photons emitted from the localized tracer are then used to functionally map the distribution of the administered compound within different biological compartments. The imaging systems used for the detection of radionuclide-labeled compounds are special devices called scintillation cameras or positron emission tomographic (PET) scanners. These devices have passed through a number of developments since their introduction in the 1950s–1960s and have had a significant impact on the practice and diagnostic quality and/or accuracy of nuclear medicine examinations.

10.1.1 History

The birth of nuclear medicine instrumentation dates to 1925; Blumgert and his coworker Otto C. Yens had modified the cloud chamber to mea-

M. M. Khalil (✉)

Medical Biophysics, Department of Physics, Faculty of Science, Helwan University, Cairo, Egypt

sure the circulation time using an arm-to-arm method [2]. They used a mixture of radium decay products that emit beta and gamma rays. Blumgert postulated some assumptions for designing a detector or measurement technique that still hold true when compared with today's requirements: The technique must be objective and noninvasive and have the capability to measure the arrival of the substance automatically [1, 2]. In 1951, Benedict Cassen introduced the rectilinear scanner to register a distribution of radioactivity accumulated in a human body [3]. To scan a given area of interest, the scanner moves along a straight line collecting activity point by point. The scanner then moves over a predetermined distance and moves back in the opposite direction to span an equivalent length. This process is continued until the device scans the desired area of interest. Images are formed by a mechanical relay printer that prints the acquired events in a dot style. Initially, the scanner was used to scan iodine-131 in thyroid patients [4, 5]. A major drawback of the rectilinear scanner was the long acquisition time since radiation events are registered point by point in a sequential manner, taking 60–90 min to determine the outline of the thyroid gland [2, 4]. Low contrast and spatial resolution of the formed images were also disadvantages of the rectilinear scanner.

In 1953, Hal Anger (at the Donner Laboratory of the Lawrence Berkeley Laboratory, USA) developed the first camera in which a photographic X-ray film was in contact with an NaI(Tl) intensifying screen. He used a pinhole collimation and small detector size to project the distribution of gamma rays onto the scintillation screen [6]. Initially, the camera was used to scan patients administered therapeutic doses of ^{131}I. A disadvantage of this prototype was the small field of view of the imaging system (i.e., 4-in. diameter). Moreover, good image quality was difficult to obtain unless high doses were administered along with long exposure times. In 1958, Anger succeeded in developing the first efficient scintillation camera, which was then called by his name, the Anger camera. Marked progress in detection efficiency was realized as he used an NaI(Tl)

crystal, photomultiplier tubes (PMTs), and a larger field of view [7, 8].

Recent years have witnessed remarkable advances in the design of the gamma camera and single-photon emission computed tomographic (SPECT) systems. These were concerned with not only clinical scanners but also small-animal SPECT in addition to new hybrid-multimodal imaging system, providing a new era of molecular and imaging innovations. Unlike PET, SPECT physics can permit in theory images with high spatial resolution besides the capability of following tracer uptake over extended time intervals including hours and days. PET imaging lacks such a property due to the short half-lives of most tracers. In contrast to PET scanners, dual tracer imaging capability can be easily achieved using SPECT compounds and a gamma camera system equipped with a multichannel analyzer.

While most of the present and commercially available gamma cameras are based largely on the original design made by Anger using sodium iodide crystal, successful new imaging systems that suit either specific imaging requirements or improved image quality and enhanced diagnostic accuracy are emerging [9, 10]. One of these changes is the trend toward manufacturing a semiconductor gamma camera with performance characteristics superior to those achieved by the conventional design. Organ-specific or dedicated designs are now well recognized in cardiac as well as breast imaging (i.e., scintimammography). Both the imaging procedures were shown to overcome some current limitations of low system sensitivity and/or spatial resolution as well as reduction of the injected dose or acquisition time.

For breast imaging, a miniaturized version of the gamma camera based on either semiconductor technology or scintillation detectors has been commercially available. On the other hand, a number of dedicated cardiac systems have been developed (some of them are combined with X-ray computed tomography (CT) to improve the diagnostic performance. Not only the developments in this area are concerned with hardware components, but also some successful approaches were devised to improve diagnostic images using resolution recovery with significant reduction of

imaging time or administered dose [11, 12]. It has become possible that some imaging systems can perform cardiac imaging in a significantly shorter scanning time than conventionally used.

The utility of SPECT systems is increasing with the addition of anatomical imaging devices such as CT and magnetic resonance imaging (MRI) increasing the array of technical and clinical applications.

Now, there is also interest in using semiconductor photodetectors to replace the historical PMTs to provide compactness, portability, and reduction of space requirements along with features that allow incorporation in multimodality imaging systems. The current and next generation of SPECT and PET devices will exploit these characteristics to overcome the current performance limitations of both the imaging modalities.

10.2   The Gamma Camera

10.2.1   Theory

The gamma camera is a highly specialized medical radiation detection system of various hardware components such that each component has a specific role in the photon detection process. It is outside the scope of the chapter to describe all these elements and their detailed functions. However, the principal components of the imaging system are described in addition to their relative contribution to image formation. The major components of typical gamma camera are hardware collimator, scintillation crystal, PMTs, preamplifier, amplifier, pulse height analyzer (PHA), position circuitry, computer system for data acquisition including signal processing and correction, and ultimately a monitor for image display and analysis.

Once the patient has been injected and prepared for imaging, the first hardware component that is met by the incident photons is the collimator. The collimator determines the directionality of the incident photons and accordingly forms the hardware role in outlining the activity distribution within different organs. The accepted photons then interact with the detector crystal to produce scintillation light photons. The photomultiplier converts the light pulse into an electronic signal. Through a number of steps that involve an identification of the photon energy and event positioning, the scintillation site is determined, which in turn reflects the spatial position of the emitted photons.

The heart of the scintillation camera is a position-sensitive detector that can localize the interaction sites where incident photons imparted their energy. The conventional design of the gamma camera consists of a continuous structure of a scintillation crystal mapped by an array of PMTs. The later component is not a point or pencil-like photodetector. However, the size, shape, and number of PMTs vary among manufacturers. Upon interaction of the incident photon with the scintillation crystal, the light diverges in a cone-shaped pattern until it reaches the backside of the crystal which is viewed by an array of PMTs.

Most often, one PMT receives the maximum amount of light produced by the scintillation event; therefore, the site of interaction could be determined based on a single PMT signal [13]. The original design that was proposed by Anger is shown in Fig. 10.1.

To spatially determine a distribution of radioactivity inside a human organ, an electronic circuit that is able to localize the position of the emitted gamma radiations must exist in the detection system. The inclusion of all PMT signals should theoretically yield better precision in positioning measurements. However, as the distant PMTs receive little light, they contribute with less certainty to the identification process, leading to increased noise. This can be treated by a thresholding process, by which the tube signals below a set value are either ignored or the tubes are adjusted by a threshold value [14, 15].

The output of the PMTs is mapped by a network of electric resistors. The resistors are weighted according to the spatial position of the PMTs in the *x*- and *y*-axes of the coordinate system of the array. This helps to identify the spatial position of an event based on the relative amount of current received by each resistor. The classical method of event positioning determination is the
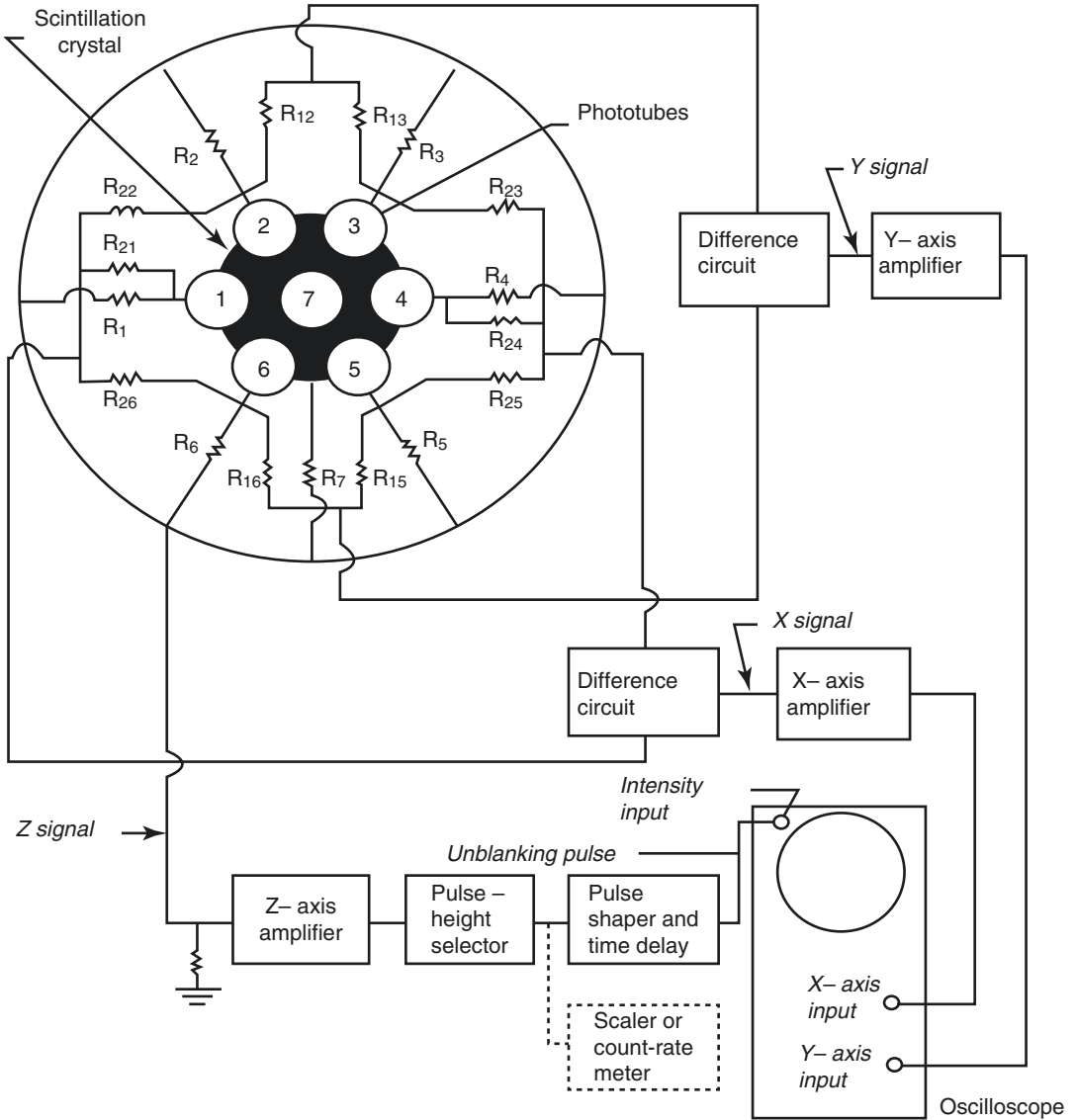
Fig. 10.1 A diagram showing the original scheme of the anger logic circuit. (From [6] with permission from AIP publishing)

Anger logic centroid approach, by which each event results in four signals *X−*, *X+*, *Y−*, and *Y+*, and then applying a simple formula per coordinate to obtain the spatial position within the two-dimensional (2D) matrix [2].

10.2.1.1 Analog Design

In the analog design of the gamma camera, three signals are detected. Two signals indicate the spatial position (*X*, *Y*), and one signal indicates the energy of the incident photon, *Z*-signal, or pulse height. The three signals are a mathematical analysis of the PMT output identified according to the positive and negative directions of the *x* (*x+* and *x−*) and *y* (*y+* and *y−*) coordinates. The energy is proportional to the amount of light produced in the crystal and with the energy deposited by the gamma radiation and computed by summing all the output signals of the involved PMTs. The position signal is divided by the energy signal, so

that the spatial coordinate signals become more independent of the energy signal. However, this simple process for event localization suffers from nonuniform spatial behavior, differences in PMT gain, and edge packing problems, which occurs when the scintillation event becomes close to the crystal edge [16]. In the last situation, the positioning algorithm fails to accurately position the scintillation event as the light distribution from the scintillation site is asymmetric or truncated, leading to improper PMT position weighting and loss of spatial resolution. Furthermore, these problems associated with the detector peripheral regions cause loss of detection efficiency and a reduction of the imaging field of view. In gamma camera-based coincidence systems, this phenomenon could result in malfunctioning detector areas corrupting the reconstruction process.

10.2.1.2 Digital Design

In the digital gamma camera, the signal of the PMT is digitized by what is called an analog-to-digital converter (ADC). Further detector development has resulted in a process of digitizing the signal directly at the preamplifier output to couple each PMT to a single ADC. In this situation, position information is no longer established using resistors and a summation circuit, but the localization circuitry has been totally replaced by a dedicated onboard computer [17].

After signal digitization, the determination of pulse position on the crystal is achieved by using the "normalized position-weighted sum" circuit, in a fashion similar to the analog camera "Anger logic circuit," or by picking up a correction factor from lookup tables constructed previously in a calibration test. This process is implemented through a software program using mathematical algorithms. Other event-positioning methods were developed, such as detailed crystal mapping, Gaussian fitting, neural networks, maximum likelihood estimation, and distance-weighted algorithms applied in an iterative manner [14, 18]. The lookup correction tables contain information regarding the spatial distortion or camera nonlinearity for accurate determination of event position during routine patient acquisition. In the calibration process, the PMT response is cali-brated to a spatial activity distributing with a well-defined pattern on the crystal surface [16]. Quality assurance procedures as related to gamma camera and SPECT/CT systems are described in Chap. 11.

10.2.2 Collimators

Gamma radiation emitted from a radioactive source are uniformly distributed over a spherical geometry (i.e., 4π). They are not like light waves, which can be focused into a certain point using optical lenses. Gamma radiation emitted from an administered radionuclide distributed within patient body is detected by allowing only those photons that pass through a certain direction to interact with the crystal. Therefore, we can collect and outline the radioactivity distributed within different tissues by a multihole aperture or what is called a collimator.

The collimator is an array of holes and septa designed with a specific geometric pattern on a slab of lead. The geometric design of the holes and septa determines the collimator type and function, and collectively called collimator characteristics. Unfortunately, most gamma radiation emitted from an injected radionuclide cannot be detected by the gamma camera since many gamma rays do not travel in the directions provided by collimator holes. This is in great part due to the small solid angle provided by the collimator area in addition to the area occupied by the septal thickness. In the detection process for gamma rays, approximately 1 of every 100,000 photons is recorded by the detector system, which is relatively inefficient process for gamma ray detection, leading to poor count statistics [19]. While the collimator material could be tungsten, gold, or tantalum, the collimator material is often made of lead due to its attenuation and absorption properties and relatively low cost. Lead has a high atomic number ($Z = 82$) and high density (11.3 g/cm^3), providing a mass absorption coefficient of 2.2 cm^2/g at 140 keV gamma line associated with Tc-99m radioactive decay.

To obtain a better count rate performance, a reduction of collimator resolution usually cannot

Fig. 10.2 A collection and varieties of collimator shapes, sizes, and geometries. (Images are reprinted with permission from Nuclear Fields International B.V.)

be avoided. On the other hand, collimators with better spatial resolution tend to reduce sensitivity at the cost of improving image details. Therefore, there is often a trade-off that should be made to the geometric dimensions of the holes and septa. The collimation system has an important role in spatial resolution, sensitivity, and count rate of acquired data; it affects the spatial properties and signal-to-noise ratio of the acquired scintigraphic images. A collection and varieties of collimator shapes, sizes, and geometries are shown in Fig. 10.2.

10.2.2.1 Types of Collimators

Different types and designs were proposed and operating in nuclear medicine laboratories. However, the general types of collimators used in nuclear medicine imaging are parallel-hole, converging, diverging, and a special type known as a pinhole collimator, which has valuable utility in scanning small organs, joints, extremities, and some applications in pediatric population. It has also demonstrated several applications in small animal imaging with superb intrinsic spatial resolution. The main differences among collimators, as mentioned, are their geometric dimensions, including shape, size, and width of the collimator holes. Collimator holes can take different shapes including round, square, or hexagonal and others. The hexagonal configuration is illustrated in Fig. 10.3 along with geometric drawing showing hole diameter (H), hole length (l), and hole septa (S).

Figure 10.4 shows three distinct types of collimators, namely parallel-hole, pinhole, and divergent collimator designs that are used in a variety of nuclear medicine applications.

Parallel-hole collimators: The holes and septa of parallel-hole collimators are parallel to each other, providing a chance for those photons that fall perpendicular to the crystal surface to be accepted (Fig. 10.4a). The image size projected by the parallel-hole collimator onto the crystal is 1:1 since it does not offer any geometric magnification to the acquired images. Table 10.1 describes the approximate relation of parallel-hole collimator efficiency and spatial resolution to collimator design parameters including hole diameter, hole length, and septal thickness.

The most common types of parallel-hole collimator are
- Low-energy all-purpose (LEAP) (or low-energy general- purpose, LEGP) collimator.
- Low-energy high-resolution (LEHR) collimator.
- Low-energy high-sensitivity (LEHS) collimator.
- Medium- and high-energy (ME and HE, respectively) collimators.

LEHR collimators provide a small acceptance angle by the aid of their narrow and longer holes. This helps to resolve fine details and improves the spatial resolution of the acquired images. Moreover, it tends to keep resolution at a distance and hence is recommended in cardiac SPECT imaging due to the varying distance of the heart from the surface of the detector.

In *LEGP collimators*, the hole diameter is relatively larger, and the acceptance angle is wider

Fig. 10.3 Example of hexagonal collimator design. (Images are Courtesy of Nuclear Fields International B.V. with permission)

l: Hole length
H: Hole diameter
S: Septal thickness
b: Source distance
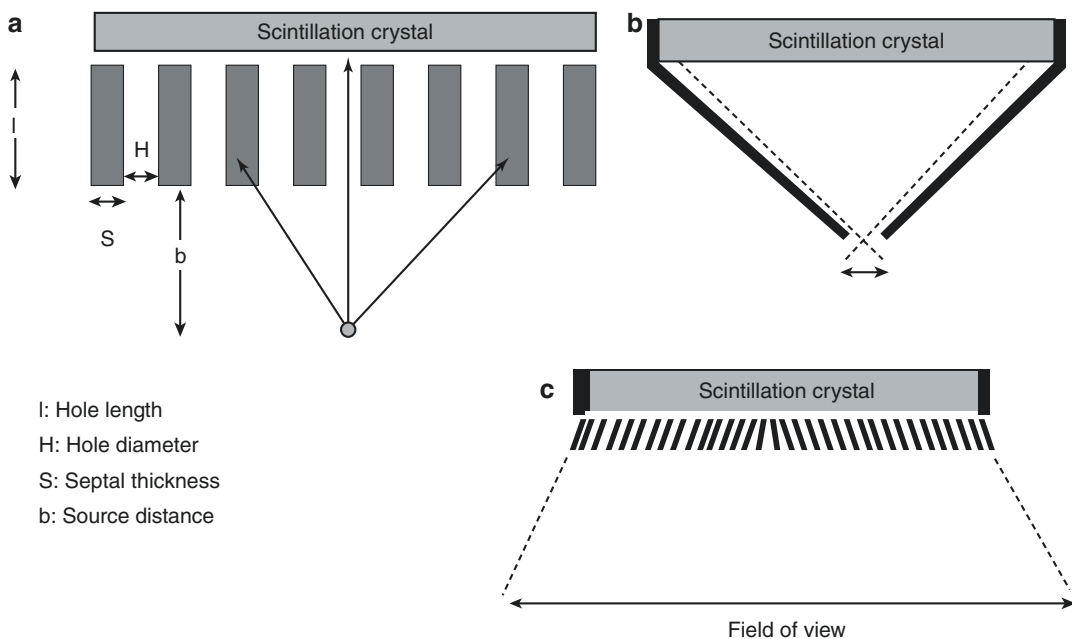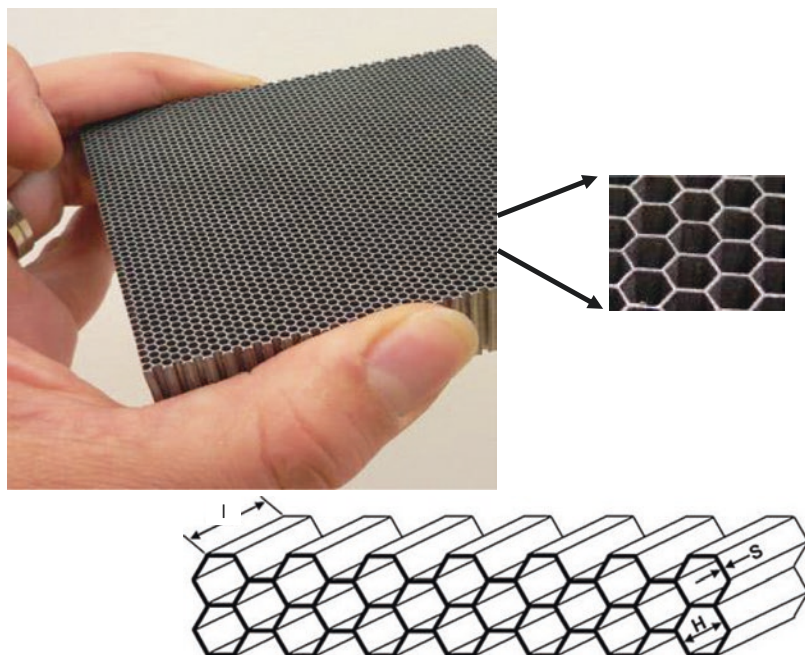
Fig. 10.4 Three different types of collimator. (**a**) Parallel-hole geometry along with definition of collimator holes and septa. (**b**) Pinhole geometry. (**c**) Divergent collimator

than that for the high-resolution (HR) collimator. It provides greater sensitivity and lower spatial resolution characteristics as opposed to the LEHR collimator. LEGP collimators are useful in exami-nations that require a high count rate (e.g., dynamic studies) to improve sensitivity while spatial reso-lution is not so influential to the interpretation of the images. Table 10.2 compares the general pur-

pose (GP) and HR collimators for a commercially available gamma camera system [20].

The difference in geometric dimensions of the hole diameter and length in addition to the septal thickness of both collimators results in a significant improvement of the sensitivity of the GP collimator over the HR collimator with minimal loss in resolution measurements. In Table 10.2, notice that the GP collimator provides a count rate efficiency about 50% greater than that of the HR collimator. It should be pointed out that manufacturers have their own special designs and label them differently. Collimator specifications given, for example, to a GP collimator might be completely different from those given by another manufacturer to the same type of collimator [21].

LEHS collimators: This type of collimators provides good count rate capabilities and pro-duces images with low statistical noise if compared with other collimators given the same acquisition time. However, this is achieved by trading off the resolution properties of the acquired images. In other words, the improvement in sensitivity is obtained at the cost of compromising the detectability of fine structures. Figure 10.5 shows the trade-off between spatial resolution and sensitivity in collimator design.

HE and ME collimators: Medium-energy radionuclides in nuclear medicine such as gallium-67 and In-111 and high-energy radionuclides such as I-131 and fluorodeoxyglucose-F18 (FDG) have high penetrating power and thus could penetrate collimator septa, causing higher background images and could adversely affect spatial contrast. ME and HE collimators have increased septal thickness and provide a lower transparency to high-energy gamma photons than lower-energy collimators. However, radionuclide studies that use ME and HE collimators manifest lower spatial resolution by degrading small-size lesions. As a result, lower quantitative accuracy is achieved by partial volume averaging [22]. Nevertheless, ME collimators were recommended over LE collimators in studies that required low-energy photons (e.g., iodine-123) if there were other emissions of higher-energy gamma rays to lessen septal penetration artifacts and improve quantitative accuracy. Some manufacturers overcame the problem by introducing new collimators with a special design that were able to maintain resolution and sensitivity of the examination while providing lower septal penetration [22].

Converging and diverging collimators have a field of view different from parallel-hole collimators with the same exit plane size. The converging collimators have a smaller field of view, whereas the diverging ones offer a larger field of

Table 10.1 Analytical approximation of efficiency and spatial resolution of parallel-hole collimators

Parameter	Efficiency	Resolution
	$\left(\dfrac{Kd^2}{L(d+t)}\right)^2$	$\dfrac{d(L+s)}{L}$
L	Effective length of collimator hole and is measured in terms of the hole physical length (l) and the linear attenuation coefficient of the collimator material ($L = l - 2\,\mu^{-1}$)	
d	Hole diameter	
t	Septal thickness	–
s	–	Object distance from collimator surface
K	Constant and function of hole shape and geometry (e.g., hexagonal, square, circular)	–

Refer to Figs. 10.3 and 10.4 for the illustration of collimator parameters

Table 10.2 Characteristics of two different collimators: low-energy general-purpose (GP) and high-resolution (HR) collimators[a]

Collimator	Hole diameter (mm)	Septal thickness (mm)	Hole length (mm)	Resolution at 15 cm (mm)	Relative efficiency
GP	1.40	0.18	25.4	11.5	1.0
HR	2.03	0.13	54.0	9.5	0.52

[a]Taken from [20]
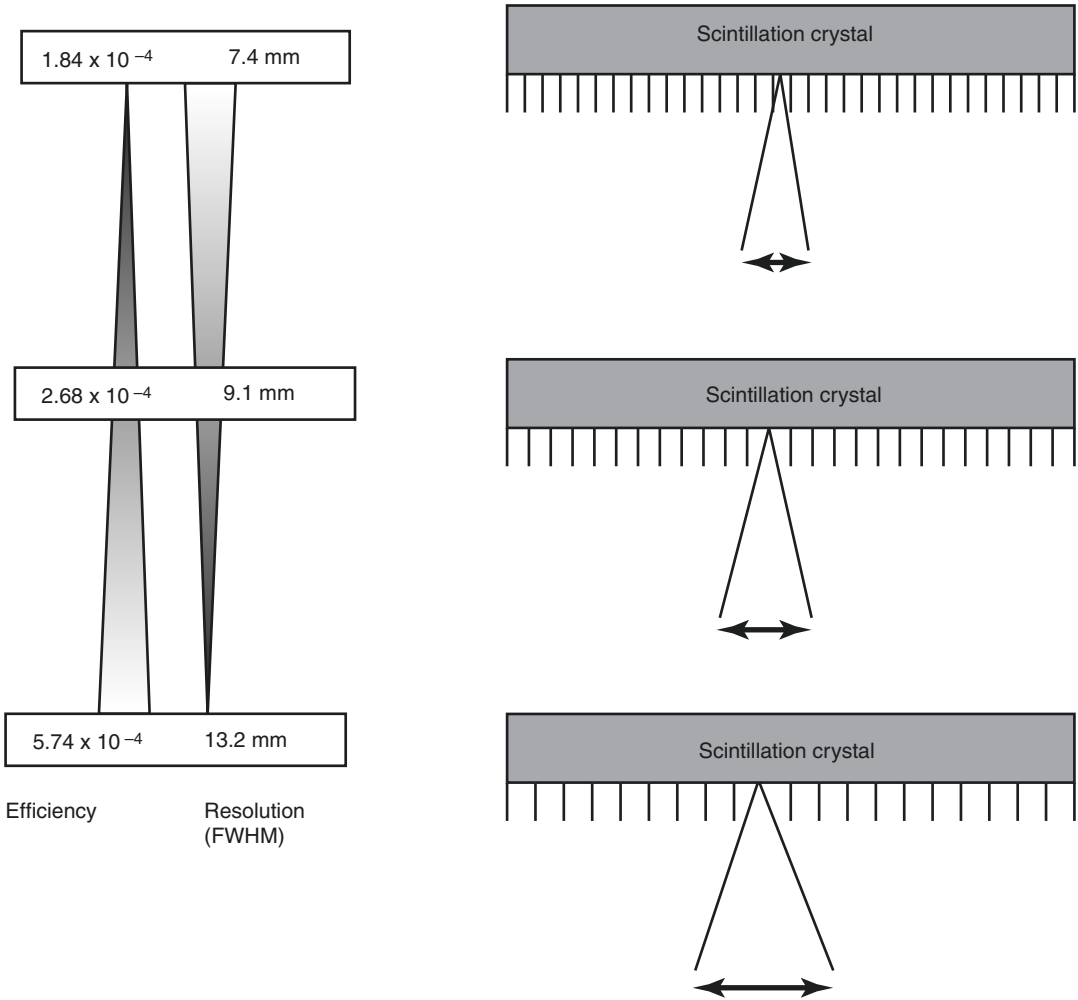
Fig. 10.5 Three different types of parallel-hole collimators organized from top to bottom: low-energy high-resolution, low-energy general-purpose, and low-energy high-sensitivity collimators. The respective spatial resolution and geometric efficiency are indicated. *FWHM* full width at half maximum

view than that provided by parallel-hole collimators. In diverging collimators, the direction of the holes diverges from the point of view of the back surface of the collimator (the face opposing the crystal). They are used in cameras with a small field of view so that they can lessen large organs to be projected onto the camera crystal (Fig. 10.4c).

In *converging collimators*, the holes are converging from the perspective of the back surface of the collimator. Cone beam and fan beam are special types of gamma camera converging collimators; the former has one focal point for all

collimator holes that lies at a certain distance away from the collimator surface and is called the focal point. The focal length is minimal at the center of the collimator and increases gradually as it goes to the periphery. However, in fan beam collimator, each row of collimator holes has its own focal point, and all the focal points form a focal line for the entire collimator. As such, it has parallel collimation along the axial direction of the subject and converging collimation within each slice, providing independent and nonoverlapping projection profiles. This geometry allows for a simplified slice-by-slice image reconstruc-
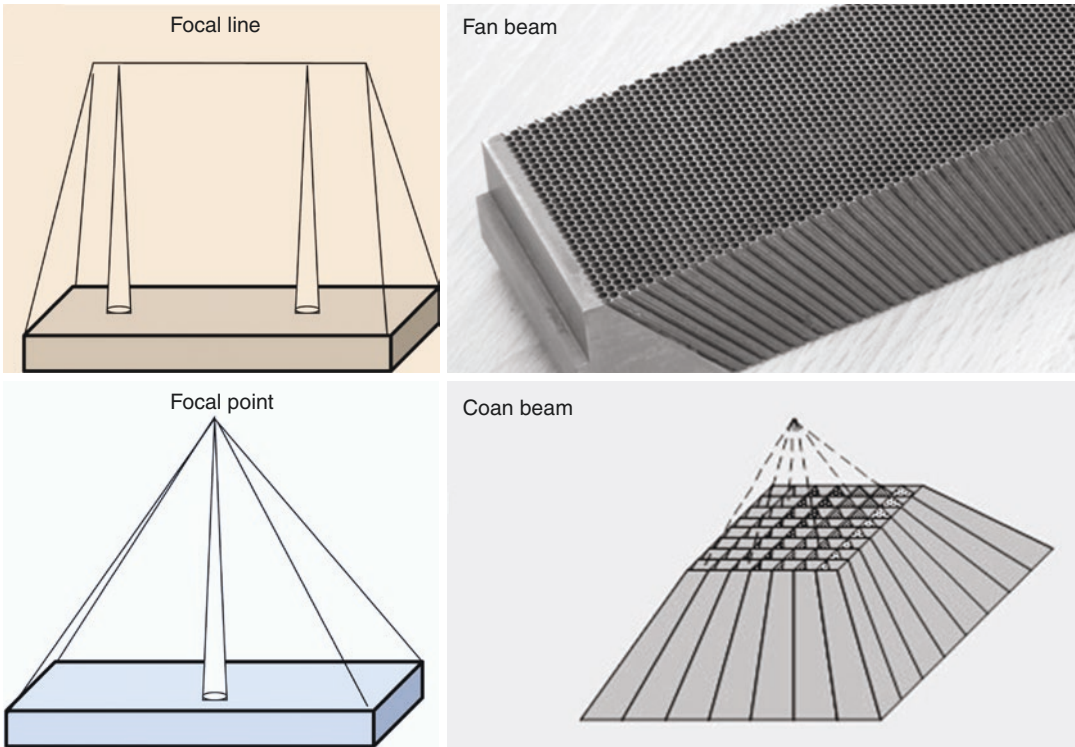
Fig. 10.6 Diagrams of cone beam (bottom) and fan beam (top) collimators. In the former, all holes focus at a single point while in the later all holes at the same transaxial

slice look at the same focal point. The focal points can be collectively connected to form a virtual focal line

tion to be applied. Cone beam geometry, however, complicates image reconstruction by involving the holes axially and transaxially. Both collimators are shown in Fig. 10.6.

A converging collimator provides a magnified view of small objects found at locations between the collimator surface and the focal point/line with relative improvement in count sensitivity, which is maximum at the focal site. They are of particular interest in brain tomographic imaging and in small organ applications. Resolution of the converging collimator is maximum at the surface and decreases with an increase in source distance, while the sensitivity increases gradually from the collimator surface until the source reaches the focal point. This is because the fraction of holes that can see the object at a near distance increases with an increase in object distance; therefore, the object at larger distances is seen by more holes, resulting in improved sensitivity. Magnification

takes place only in one direction, typically the transverse direction, and the cone beam collimator magnifies along the axial direction as well [23]. The drawbacks of converging collimators are reduced field of view and data insufficiency for 3D (three-dimensional) reconstruction.

Pinhole collimator: The pinhole collimator is an important type that is used frequently in nuclear medicine laboratories, especially in small-organ imaging, such as thyroid and parathyroid scanning (Fig. 10.4b). Also, it has useful applications in skeletal extremities, bone joints, and the pediatric population. It is a cone-shaped structure made of lead, tungsten, and platinum and has an aperture of a few millimeters in diameter (2–6 mm). In the small-animal pinhole collimator, the aperture size goes down to 1–2 mm or even less to meet the resolution requirements imposed by small structures and minute tracer uptake [24]. The collimator length that extends

from the back surface to the point of the aperture is 20–25 cm. Image formation can be described using lens equations in the sense that the acquired data reveal an inverted and magnified image. The pinhole collimator provides a magnified image of small objects, yielding an appearance that reflects an improvement in spatial resolution.

Nuclear imaging technology never stopped at those aforementioned conventional collimator designs and new approaches were devised so as to improve system detection characteristics. A cardiofocal or multifocal collimator design was introduced by one commercial vendor into the market with the trade name IQ SPECT [25]. The collimator holes are specially arranged such that the central holes are focusing on the heart region while they gradually get parallel as we move to collimator edges. It therefore permits heart magnification (fourfold than parallel hole) without truncation. In essence, the IQ SPECT system includes SMARTZOOM collimators, cardiocentric image acquisition, and an ordered subset conjugate-gradient minimizer (OSCGM) that provide a significant reduction in imaging time and/or injected radioactivity [26, 27]. However, heart positioning within the region of highest magnification of the multifocal collimators are recommended. A mispositioning of greater than 2.5 cm of the heart can adversely impact diagnostic accuracy [28]. Also, tracer distribution within different cardiac segments has to be identified with and without attenuation and scatter correction and also when attempts are made to create normal databases [29].

10.2.3 Scintillation Crystal

Scintillation crystal is the second component that encounters the incident photons after passing the collimator holes. There are some favorable properties based on which the crystal needs to be selected before implementation in gamma camera design. Scintillators of high density, high atomic number, short decay time, high light output, and low cost are desired and allow better imaging performance. However, there is no ideal detector material in the field of diagnostic radiol-

Table 10.3 Properties of scintillation crystals used in gamma camera

	Na(Tl)	CsI(Tl)	CsI(Na)
Z_{eff}	3.67	54	54
Density (g/cm³)	50	4.51	4.51
Decay time (ns)	230	1000	630
Photon yield (keV)	38	45–52[a]	39
Refraction index	1.85	1.8	1.84
Hygroscopic	Yes	Slightly	Yes
Peak emission (nm)	415	540	420

[a]CsI(Tl) is poorly matched to the response of photomultiplier tube (PMT). However, the scintillation yield is much higher when measured by photodiodes with extended response into the red region of the spectrum [30]

ogy; most often, the selected material has some desired features that make it preferred over alternatives. Table 10.3 lists the most common crystals used in gamma camera design.

The most commonly used detector material for the gamma camera is the thallium-activated sodium iodide [NaI(Tl)] crystal. It utilizes the scintillation phenomenon to convert gamma rays into light quanta that can be amplified by a PMT to produce a detectable electronic signal. Scintillation occurs when the incident photon interacts with the crystal material to produce photoelectrons or Compton scattering. The resulting electrons from photoelectric or Compton interactions travel short distances within the crystal to produce more interactions in the form of excitations or ionizations of the crystal atoms and molecules. These excited products are deexcited by converting to the ground state by releasing scintillation light.

A continuous large slab of sodium iodide crystal is the conventional structure that is used in most gamma camera designs. The crystal thickness can be 3/8 in., 5/8 in., or even larger for high detection efficiency [31]. A pixilated or segmented version of scintillation crystals has also been utilized in small SPECT systems using photosensitive PMTs as photodetectors and parallel or pinhole imaging geometry, yielding high-resolution tomographic images. Segmentation of the scintillation crystal allows the spatial resolution of the imaging system to be improved to an extent determined mainly by the segmentation size. Nevertheless, this comes with a reduction of

count sensitivity, increased costs, and degraded energy resolution [32]. It is often used in small field-of-view, organ-specific systems or in small-animal scanners. Another option that can be considered as an intermediate solution between continuous and segmented or pixilated crystals is partially slotted crystals, which have been investigated to produce better energy resolution than fully pixilated crystals and improved detection sensitivity while maintaining the spatial resolution at better levels with an appropriate data analysis [33, 34]. Additional features provided by such systems are their relative ease and cheap manufacturing costs.

10.2.3.1 NaI(Tl)

The NaI(Tl) crystal is formed by adding a controlled amount of thallium to a pure sodium iodide crystal during growth. The addition of thallium makes the NaI crystal scintillate at room temperature since pure NaI crystal works at a low temperature under nitrogen cooling [16, 30]. Some precautions are taken into account during the design of the NaI(Tl) crystal. It must be sealed in an airtight enclosure, usually aluminum, to avoid exposure to air owing to its hygroscopic properties. Exposing the crystal to air can cause yellow spots, which can develop heterogeneous light transmission.

10.2.3.2 CsI(Tl)

Thallium-activated cesium iodide, CsI(Tl), is slightly denser than sodium iodide crystal and better suited if coupled to photodiodes as the emission wavelength is shifted to higher values, at which the response of PMTs is relatively weaker. It therefore does not properly fit the requirements imposed by PMTs, which need light quanta of shorter wavelengths. A pixilated CsI(Tl) crystal has been tested in a miniaturized gamma camera with the collimator matching the detector array and size suitable for breast imaging. The system showed good performance characterisics, such as an improved spatial resolution, high detection efficiency, and better scatter rejection (~8% full width at half maximum [FWHM] at 140 keV) [35]. The CsI(Tl) crystal has also been utilized in a pixilated fashion and coupled

with silicon photodiode in a commercial design developed as a dedicated cardiac tomograph. Cardius 3 XPO is manufactured by Digirad and consists of 768 pixilated Cs(Tl) crystals coupled to individual silicon photodiodes and digital Anger electronics for signal readout [36].

A portable scanner based on CsI(Tl) called Ergo from the same company was also technically evaluated [37]. The system consists of 11,520 elements of 3×3 mm^2 CsI(Tl) crystals with 6 mm thickness and couped to silicon photodiodes. The detector element has a size of 3.31×3.24 mm^2. The suitability of the system for clinical routine is demonstrated with recommendations for further improvement.

10.2.3.3 CsI(Na)

Sodium-activated cesium iodide, CsI(Na), has an emission spectrum similar to NaI(Tl) that suits PMT response, with comparable light yield and relatively slow decay time. It has been utilized in small-animal SPECT scanners in pixilated 5 mm thickness (21×52 pixels of 2.5×2.5 mm) coupled to photosensitive PMTs [38]. The system provided an intrinsic spatial resolution of 2.5 mm, intrinsic energy resolution of 35% (at 140 keV), and intrinsic sensitivity of 42% using an energy width of 35% at 140 keV. Comparison of partially slotted CsI(Na) and CsI(Tl) crystals revealed the superior performance of the latter in terms of detection efficiency and spatial and energy resolution [34].

10.2.3.4 YALO₃:Ce

Yttrium aluminum perovskite (YALO$_3$:Ce) is a non-hygroscopic scintillation crystal with the structure of the perovskite and is called YAP. It has a density of 5.37 g/cm^3, an effective atomic number of 34–39, and light output of 40% relative to NaI(Tl) and is used for gamma as well as annihilation coincidence detection [39].

10.2.3.5 LaBr:Ce

Lanthanum bromide (LaBr:Ce) is a fast scintillator (short decay time, 16 ns) with high light output. These characteristics are suitable for time-of-flight applications in PET scanners (see Chap. 12). High light yield is an important

parameter that improves the certainty of photon statistics and serves to improve system spatial and energy resolution. The crystal has been evaluated using a flat-panel, photosensitive PMT; it has shown good imaging performance for single-photon applications with superior energy resolution (6–7.5%) and spatial resolution of 0.9 mm. The detection efficiency was also high, yielding 95% at 140-keV photon energy [40].

10.2.3.6 Crystal Thickness
SPECT and PET scanners were combined into one imaging device known as hybrid SPECT/PET camera. Therefore, there were some modifications that had to be implemented in electronic circuitry and crystal thickness. The latter should be adapted to improve photon detection efficiency. The NaI(Tl) crystal is an efficient scintillator for low-energy photons; it is greater than 95% for 140 keV. However, its response against 511 keV is significantly poorer as it shows a coincidence detection efficiency of about 10%.

Some manufacturers have used the traditional scintillation crystal by increasing the thickness up to 25 mm, while others have modified the crystal so that the back surface of the crystal is grooved, allowing detection of single-photon emitters to be maintained. Meanwhile, the system is efficiently able to image patients injected with medium- and high-energy radiotracers. However, all the major suppliers are currently providing PET scanners with a more efficient performance, which have a cylindrical-type design.

StarBrite crystal, developed by Bicron Corporation (Newbury, OH), is a dual-function 1-in.-thick crystal that serves to improve the detection efficiency of medium- and high-energy photons and has been incorporated in some commercial designs [31, 41]. The slots at the back surface of the NaI(Tl) crystal are machined to prevent light diffusion, reducing the impact of wide-angle reflected light. This also maintains a uniform light collection as a function of position, achieving better intrinsic spatial resolution (4 mm) [42, 43]. In performance evaluation with other systems, this design provided a good compromise in terms of spatial resolution and sensitivity for [111]In ProstaScint® SPECT imaging. However, the collimator–crystal pair combined with system electronics work together to determine the overall system spatial resolution and sensitivity given a particular detection task.

In humans, visual perception is the ability to interpret information and surroundings from visible light reaching the eye. In a similar way, the light released from the scintillator after the interaction of the incident radiation with the detector system needs an interpretation process. This process in the gamma camera is implemented by the readout component or photodetectors that lie in close proximity to the back surface of the scintillation crystal. A remarkable feature of the design made by Anger is the photomultiplier mapping of the detector crystal together with the mathematical logic he used in event identification [7].

10.2.4 Photomultiplier Tube

The PMT is an important hardware component in the detection system of the gamma camera. Its main function is to convert the scintillation photons to a detectable electronic signal. The PMT as shown in Fig. 10.7 is a vacuum tube consisting of an entrance window, a photocathode, focusing electrodes, electron multiplier (dynodes), and anode. The PMT has a long history in many applications, including medical as well as other fields such as high-energy physics, spectrophotometry, and is widely used in many SPECT and PET imaging systems.

10.2.4.1 Photocathode
The photocathode is a photo-emissive surface usually consisting of bialkali metals with low work functions and weakly bound valence electrons. The photocathode receives the scintillation light from the crystal, such as an NaI(Tl), by a wavelength of 415 nm at maximum. The material for the photocathode that emits photoelectrons (on an incidence of light quanta) equivalent to that wavelength will be the material of choice as it will allow increasing the amount of electrons emitted and hence be able to improve the certainty of the output signal [44].
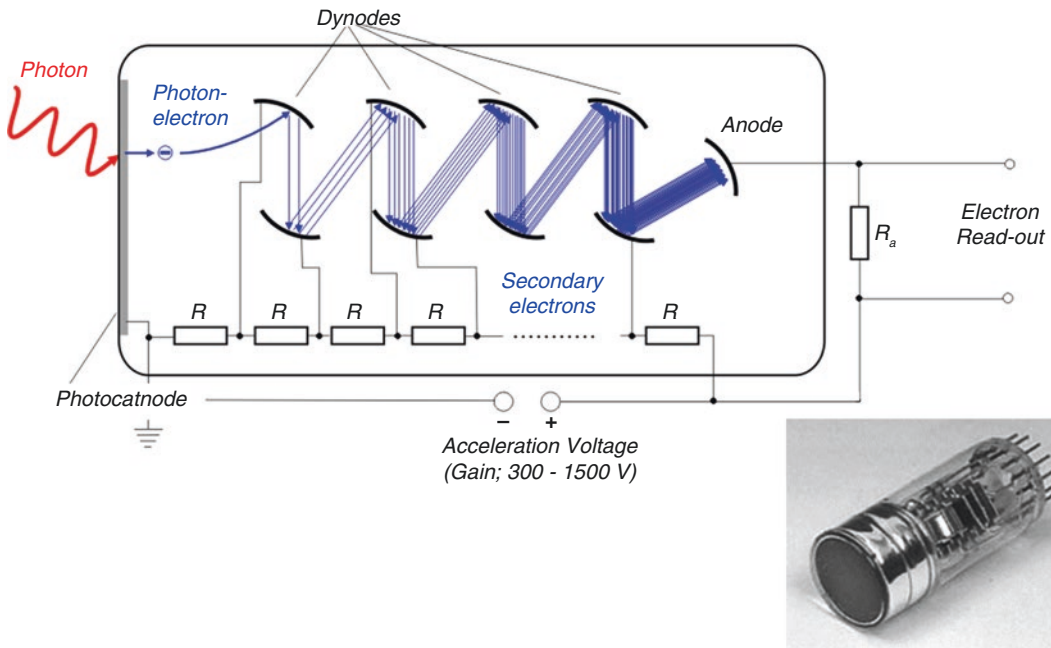
Fig. 10.7 Schematic diagram showing the photomultiplier tube (PMT) and its internal structures that include photocathode, several dynodes connected under cascade of increasing potential difference and positively charged anode. (Image taken from www.physicsopenlab.org under the license of Creative Commons Attribution 4.0 International)

The photons emitted from the NaI(Tl) crystal fall on the photocathode of the PMT to eject photoelectrons by the physical phenomenon of photoelectric effect. The emitted electrons are amplified through a series of dynodes placed in a special geometric pattern with high potential difference so that each dynode has greater voltage (100–300 keV) than the preceding one. In some details, when scintillation light strikes the photocathode, it releases electrons, which are accelerated by the effect of the high voltage on the first dynode to collide with it. Electrons emitted from the first dynode are accelerated to the second dynode to eject more electrons on collision. The third dynode accelerates the electrons from the second dynode toward its face; this multistage electron amplification continues until the electrons reach the last dynode. At the back end of the PMT, the anode of the PMT collects all the electrons that result from this cascade process.

10.2.4.2 Anode

The anode of the PMT is an electrode that collects the amplified electrons through the multistage dynodes and outputs the electron current to an external circuit. An adequate potential difference between the anode and the last dynodes can be applied to prevent space charge effects and obtain a large output current [45]. PMTs have a large electronic gain that can reach 10^6–10^8 in addition to low electric noise. However, the *quantum conversion efficiency* of PMT is low since, on average, for every ten scintillation photons that fall on the photocathode, there is approximately a release of two electrons, resulting in an efficiency of about 20–25% [42]. This in turn has an impact on intrinsic spatial resolution and energy resolution. The PMT is susceptible to variations in high-voltage power supply, and its performance is influenced by temperature, humidity, gravity, and magnetic field because of the high voltage applied on the dynodes (i.e., limitation in design of PET/MRI scanners).

10.2.5 Preamplifier

The shape of the output signal from the PMT is a rapid rising peak with a slow decaying tail. The rapid peak denotes the decay time of the scintillation event within the crystal, and the decaying tail denotes the time taken by the electrons to traverse the PMT. The output signal of the PMT cannot be fed directly into the amplifier because of the impedance difference between the PMT and the amplifier. The preamplifier plays an important role in this regard. It matches the impedance between the PMT and the main amplifier, so that it could be handled by the amplifier and other subsequent electronics. The function of the preamplifier is matching, shaping, and sometimes amplification of the signal [16, 46].

Matching: The signal produced from the PMT has a high impedance value, and this requires matching with the other electronic circuit components (i.e., amplifier).

Shaping: The signal that is to be fed into a main amplifier needs to have a certain pulse decrease time to allow proper pole-zero and baseline correction. The preamplifier works to shape the PMT signal using an resistor-capacitor circuit (RC) by increasing the time constant, which is then handled by the amplifier.

Amplification: The amplification element of the preamplifier varies in the amount of amplification according to the type of detector and the magnitude of the signal. In PMT electronic assembly, the preamplifier sometimes has no significant amplification gain since the PMT itself provides a considerable amplification through the multistage process of the dynodes. The output

signal from the preamplifier is a slow decaying pulse that causes pulse pileup. However, it conveys information regarding the signal amplitude and timing of the scintillation event. This information requires more additional manipulation by an amplifier without introducing any type of distortion. The newly developed SiPM (silicon photomultiplier) photodetectors (see Chap. 12) provide similar amplification gain as that of PMTs; hence, preamplification requirements are less demanding in comparison to photodetectors with low gain properties [16, 46].

10.2.6 Amplifier

The amplifier plays a major role in signal amplification and shaping; it is therefore called a shaping amplifier. Signal amplification is required to permit further processing by the rest of the detector electronics. However, the amplification factor varies greatly with application and typically is a factor of 100–5000 [30]. Shaping of the signal is accomplished by eliminating the tail from the output signal and giving each signal its separate width and amplitude without overlapping with other signals. In summary, the functions of the amplifier are shaping the pulse and decreasing the resolving time and providing higher gain to drive PHAs, scalars, and so on. It also provides stability to maintain proportionality between pulse height and photon energy deposition in the crystal. The amplifier serves to increase the signal-to-noise ratio and maintain proper polarity of the output signal [47]. Figure 10.8 depicts the signal shape

Fig. 10.8 The signal shape characteristics released from PMT and fed into preamplifier and amplifier circuitry. (From www.physicsopenlab.org under the license of Creative Commons Attribution 4.0 International)
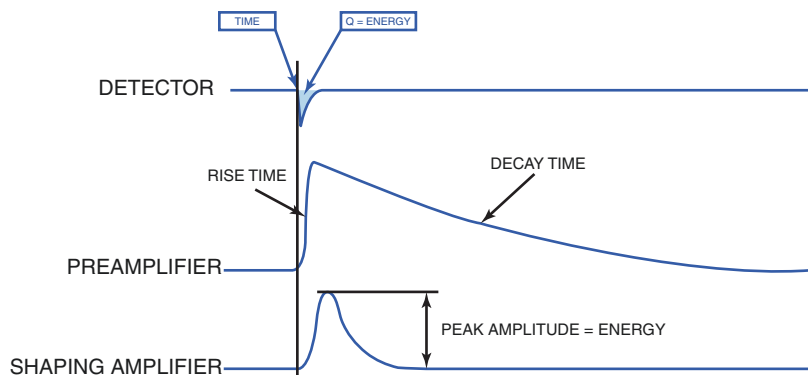
released from the PMT and subsequent processing using the preamplifier and amplifier circuitry.

10.2.7 Pulse Height Analyzer

There are different probabilities for the interaction of the incident gamma radiations with the crystal. Some photons impart a fraction or all of their energy into the crystal, whereas other photons impart some of their energy and escape the crystal without further interactions. Another fraction of photons undergo more than one interaction, dissipating all their energies. Therefore, there are two general forms of scatter that serve to reduce the capability of the system to accurately determine the position and the energy of the incident gamma radiations. One part results from scattering that takes place inside the patient body, and the other part results from scattering that occurs in the camera crystal. The latter is not significant and does not contribute to a great extent to the total fraction of scattered radiation and the shape of the pulse height spectrum. It is important in medium- and high-energy gamma photons (e.g., In-111 and ^{131}I) and in thick crystals. The former type of scattering dominates the spectrum and results in degraded image quality and contrast resolution. As a result and for other instrumental reasons (e.g., detector energy resolution), the output signal is not a sharp peak line on the spectrum; it is a distribution of pulse heights with one or more photo peaks representing the energies of the administered radionuclides. The output signal is measured in terms of voltage or "pulse height," and every pulse has amplitude proportional to the amount of energy deposited by the gamma ray interactions [48]. A pulse height analyzer (PHA), as the name implies, is a device that is able to measure the amplitude pulse heights and compare them to preset values stored within it. There are two types of PHA: single channel and multichannel.

10.2.7.1 Single-Channel Analyzer

The single-channel analyzer records events within a specified range of pulse amplitude using one channel at a time, applying lower and upper voltage discriminators. The output signal of the amplifier has a range of heights (voltages), and selection of the desired signals for counting is achieved by setting the lower discriminator to a level that diminishes all lower amplitudes, thereby allowing the upper values to be recorded [30].

10.2.7.2 Multichannel Analyzer

Acquisition studies that require more energies to be detected, as in dual-radionuclide acquisitions (e.g., parathyroid Tl-201–Tc-99m subtraction, meta-iodobenzylguanidine [MIBG]-131–Tc-99m DTPA [diethylenetriaminepentaacetate], and others) and radionuclides with more than one energy photo peak (e.g., Ga-67, In-111, and Tl-201), the proper choice for recording these energies separately and simultaneously is to use a multichannel analyzer (MCA). An MCA provides a means of rejecting the scatter region from the spectrum, allowing the acquired image to be less contaminated by scattered photons. However, the photo peak region will still contain a significant fraction of photons that have undergone small-angle scattering. The MCA allows an energy window to be set over the photo peak centerline to confine the accepted photons to a certain energy range. This range is chosen by lower and upper voltage discriminators. The former determines the threshold below which all pulse heights are rejected, and the latter determines the value at which no higher values are accepted. Values that fall between the lower and upper discriminator are adjusted by a window width and often are a percentage of the photo peak energy. For example, a 20% energy window is usually selected over the 140-keV photons emitted by Tc-99m. A 15% window is also used with an improvement in contrast and minimal loss in primary photons. Moreover, a 10% window is used at the expense of reducing sensitivity [49]. An asymmetric window is another way to reduce the effect of scattered photons as it can improve image contrast, spatial resolution, and clinical impression [50, 51].

A variety of scatter correction techniques have been devised to reduce the adverse effects of scattered radiation. For proper quantitation and absolute measures of tracer concentrations,

images must be corrected for scatter and other image-degrading factors. A gamma camera with an MCA is necessary when energy-based scatter corrections are applied to the acquired data. Advances in semiconductor technology have motivated the development of gamma camera systems with significant improvement in energy resolution. This in turn improves the spatial contrast and signal-to-noise ratio, resulting in improved image quality. Chapter 18 has more details on scatter correction techniques.

10.3   Other Photodetectors

10.3.1   Position-Sensitive PMT

The position-sensitive PMT (PSPMT) is a modified version of the conventional PMT but with compact size and position determination capabilities, allowing for an improvement in image spatial resolution [52]. The PSPMT-based gamma camera shows the same advantages of a standard gamma camera with the additional possibility of utilizing scintillation arrays with a pixel dimension less than 1 mm, thus giving the ability to achieve submillimeter spatial resolution [53]. Several models have been developed since its introduction in 1985 [53]. Three different types can be found [54, 55].

Proximity mesh dynode: This is the first generation and is based on the proximity mesh dynode, by which the charge is multiplied around the position of the light photon striking the photocathode. The charge shower has a wide intrinsic spread. This model can provide a large active area (e.g., 5 in.) and large number of dynodes (e.g., 256) but with large dead space.

Multichannel dynode: This is a multianode structure that minimizes cross talk between anodes and provides better localization measurements. This type has the following drawbacks: large dead zone, limited effective area, and limited number of dynodes.

Metal channel dynode: Combined with multichannel or crossed-plate anode techniques, this dynode can provide low cross talk and well-focused charge distribution, reducing the intrin-

sic spread to 0.5 mm FWHM [54]. For SPECT imaging, the use of a crossed-wired anode PSPMT is more suitable when coupled with a flat crystal because of continuous position linearity requirements. However, this configurations may not allow the best performance of the PSPMT; thus, to utilize the full potential of its intrinsic characteristics, a multicrystal array is needed to attain high detection efficiency, narrow light spread function, and reasonable light output [56].

A PSPMT is relatively more expensive than the conventional type, and most of its use is in preclinical small-animal SPECT and PET scanners and portable and compact miniaturized gamma cameras, and it is of interest in producing high-resolution breast scanners [57, 58]. This type of diagnostic examination requires compact and flexible systems to fit geometric requirements imposed by the female breast. The technologic advances in the development of a compact flat-panel PSPMT with less dead space allowed manufacture of a portable gamma camera with a large detection area and high imaging performance with better spatial resolution [59]. It has become possible that an array of 256 crystal elements can be coupled directly to one PMT, and the crystals can be read out individually [60]. The Hamamatsu different channel flat-panel PSPMTs are shown in Fig. 10.9.

10.4   Semiconductor Gamma Camera

Instead of detecting the scintillation light on multiple stages, semiconductor detectors provide a detection means by which the incident radiation is converted to an electronic signal once it interacts with the detector material. As described above, the standard gamma camera relies on converting the incident photon to a scintillation light, which is converted to electronic signal via the PMT for subsequent processing and analysis.

The use of semiconductor material in the field of radiation detection and measurements has been established for many years in different areas of science and engineering. The most commonly used are silicon (Si) and germanium (Ge). The

64 Channel   256 Channel
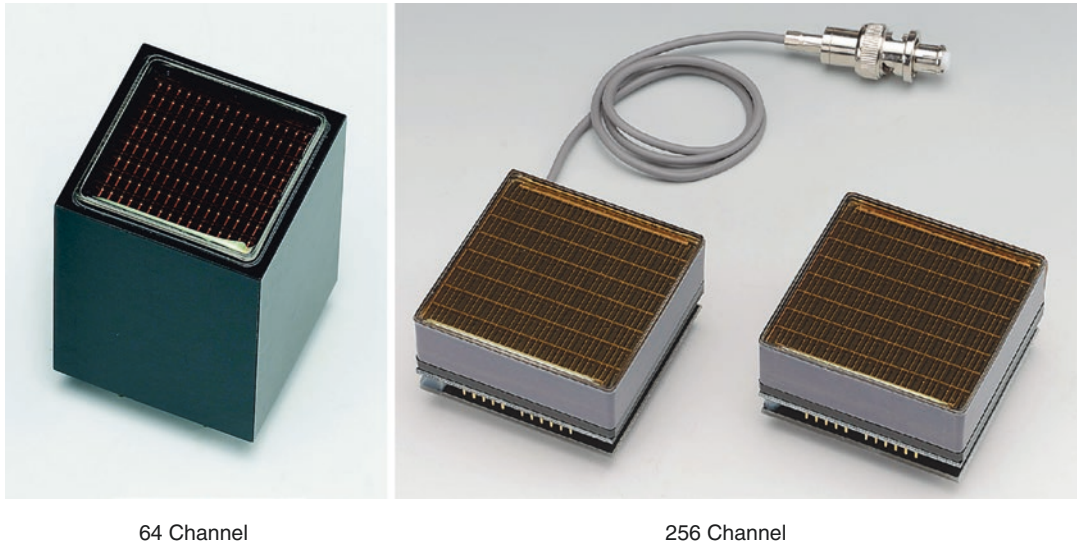
Fig. 10.9 Different shape, size, and number of channels of position-sensitive photomultiplier tubes. (Images are Courtesy of Hamamatsu Photonics)

atomic number of the former is 14, while that of the latter is 32; incorporating them in a radiation detector necessitates cooling to liquid nitrogen temperatures to avoid electronic noise generated from excessive thermal effects [61]. To fabricate a gamma camera based on a semiconductor detector, there have been efforts to search for other materials of high detection efficiency and amenable for operation in a room temperature environment.

Better alternatives of interest in the design of gamma ray detection systems are cadmium telluride (CdTe) and cadmium zinc telluride (CdZnTe), which can be considered promising materials for radiation detectors with good energy resolution, high detection efficiency, and room temperature operation. The physical density for the two materials are 6.0 g/cm^3 and 5.78 g/cm^3, whereas the effective Z are 50 and 49.1, respectively. Several advantages can be obtained when designing a gamma camera based on semiconductor detectors. One is system portability as they enable construction of a compact structure free from the PMT and its bulky volume. A semiconductor camera also provides improved image contrast due to its better energy resolution compared to a sodium iodide crystal. Besides this last feature, high spatial resolution images can be

obtained owing to the pixilated structure that can be implemented in the detector design [62].

CZT camera serves to convert the incident gamma photons directly into electronic signal through the generation of electron and hole pairs with number proportional to the incident photons. The generated electron–hole pair carries information about event position and energy. As energy conversion is efficient process and large amount of charge are created upon photon interaction with the detector, the energy resolution is much better than the standard gamma camera [63]. The charges are collected through negative and positive electrodes, and the resulting signal is preamplified and processed subsequently. The CZT can handle large amount of photons per unit area (i.e., 10^6 photons/s mm^2). The superior system sensitivity do help in significantly reducing the imaging time without loss of image quality or diagnostic performance but meta-analyses showed a lower diagnostic specificity of CZT-based myocardial perfusion imaging [64, 65].

10.4.1 CZT Systems

More than one commercial SPECT system has been released to the market making use of semi-
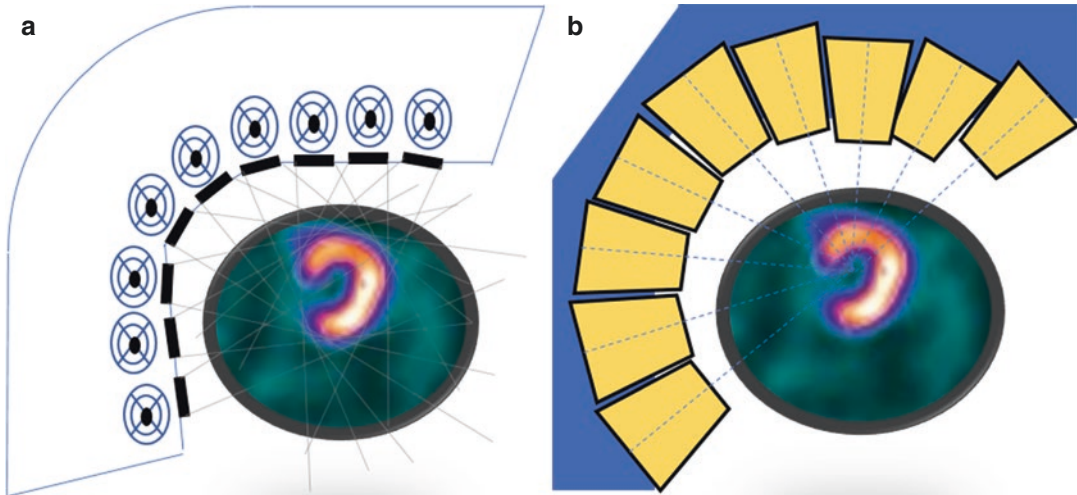
Fig. 10.10 Gamma camera imaging systems based on CZT detectors. (**a**) A diagram showing the rotating collimator configuration in D-SPECT model (Spectrum Dynamics) and (**b**) Discovery NM 530c showing the stationary collimator design (GE Healthcare)

conductor technology for improving count efficiency and reduction of acquisition time or injected radioactivity and hence lower effective dose [12, 66, 67]. D-SPECT (Spectrum Dynamics) is a CZT-based semiconductor camera commercialized for imaging cardiac patients (Fig. 10.10a). The system consists of nine collimated detector columns arranged in a curved configuration to conform to the shape of the left side of a patient's chest. Each individual detector is allowed to translate and rotate independently, so that a large number of viewing angles can be achieved for the region of interest. It was also configured in a position toward the heart leading to high detection efficiency. Each individual detector is 40 × 160 mm in dimension and made of large number of CZT pixel elements (16 × 64, or 1024), each has a size of 2.26 × 2.26 mm. The collimator is made of tungsten with relatively wide square hole and shorter length in comparison to conventional parallel-hole collimator. These characteristics serve to improve count efficiency with some resolution loss that is compensated by modeling the system response in iterative reconstruction [66, 68]. The improved energy

resolution (5.5% at 140 keV) also allows simultaneous application of a dual-isotope protocol with better identification of lesion defect and reduction of photon cross talk [68, 69]. There are also some shortcomings associated with D-SPECT reported in the literature and highlighted in recent reviews such as mechanical faults, patient- as well as operator-related artifacts, including motion, attenuation, and extra-cardiac uptake [70]. While this type of detector exhibits a superior energy resolution, a dual isotope imaging requires scatter cross-talk corrections as well as treatment for the long tail of the low energy side of the energy photopeak [68].

Another design has been introduced by GE Healthcare (Discovery NM 530c) that utilizes an array of pixilated (CZT) semiconductor detectors in fixed positions (without motion) that allow acquisition of cardiac projections in a simultaneous manner (Fig. 10.10b). Evaluations of the system demonstrated an improvement in image spatial resolution, energy resolution, and sensitivity as opposed to a conventional gamma camera design [71, 72]. An additional feature was brought about by combining this system with CT

in an integrated SPECT/CT (Discovery NM 530c with the LightSpeed VCT or Discovery NM/CT 570c, GE Healthcare) [73]. This hybrid system enables clinical institutions of performing a one-stop-shop scan for cardiac patients. A myocardial perfusion SPECT, attenuation correction, calcium scoring, and CT coronary angiography can be carried out in a relatively short time. The system has 19 detector modules such that each with a pinhole collimator of tungsten material. The individual detector in this design is configured in 2×2 array rather than 4×1 as in the D-SPECT design. Unlike D-SPECT, the detector remains stationary during data acquisition. The field of view is approximately 19 cm, and this along with pinhole collimation geometry comprises a critical problem to position patients with high body mass index (BMI) especially those >40 kg/m^2 who are recommended to be performed on a conventional gamma camera [74].

A semiconductor camera made of CZT is relatively expensive; thus, most of the current commercial versions are confined to handheld, miniaturized imaging systems, or intraoperative small probes. Scintimammography is one of the diagnostic procedures that requires a dedicated device able to match the position and geometry of the breast. Small and deep lesions are a challenging task and require characteristics better than provided by a standard gamma camera. The sensitivity of the test is limited by the lesion size, particularly for those less than 10 mm [75].

The difficulty in detecting small and deep pathologic breast lesions by conventional imaging systems lies in their limited detection efficiency and relatively poor spatial resolution. However, earlier detection of a breast lesion has better diagnostic and prognostic implications. This in turn should be met by instruments with high-performance characteristics that provide better lesion detectability. A breast imager based on semiconductor materials such as CZT can provide better spatial and energy resolution, leading to improved lesion contrast. This can be achieved using a narrow energy window, reducing the adverse effects of scattered photons on image quality. Other properties of the semiconductor camera are its compactness, portability, and smaller dimensions, which fit well with breast imaging [76–78].

Apart from organ-specific systems, Discovery NM/CT670 CZT SPECT (GE Healthcare) was recently designed for whole-body examination. It is based on GE Discovery NM/CT 670 Pro system having the same gantry while replacing the conventional NaI(Tl) detector by the semiconductor CZT detector [79]. The camera has 130 CZT modules, and each detector contains 32×32 pixelated (2.46×2.46 mm^2) CZT elements [80]. The collimator holes are square in shape, made of lead, and specifically designed for that particular configuration. The pixilated nature and the mechanism of converting photon energy into electronic signal permit for proper determination of energy deposition and precise event localization. The detector area is smaller but effectively larger than the conventional design due to the absence of the edge packing phenomenon discussed earlier. System spatial resolution as reported by vendor is 2.8 mm nearly equivalent to detector pixel size 2.46 mm^2 while better than 4.3 mm measured on conventional systems. The system energy resolution is 6.3% FWHM at 140-keV photons. The third-generation NM/CT 870 CZT has also been reported by the same manufacturer [81].

10.5 Hybrid SPECT Imaging

Nuclear imaging using SPECT or PET techniques has well-known capabilities in extracting functional and metabolic information for many human diseases. The anatomical details provided by CT and MRI enjoy better structural description for human organs by resolving capabilities that are significantly higher than that provided by nuclear SPECT and PET machines. They have the advantages of providing a resolution in the milli- or submillimeter range, precise statistical characteristics, and better tissue contrast, especially in the presence and use of contrast media [82]. However, it lacks the property of describing the functional status of a disease. This is important in following up cancer patients postsurgically and in the presence of fibrotic or necrotic lesions after chemo- or radiotherapy [83].

The early work of Hasegawa and colleagues opened a gate to many applications in the field of diagnostic radiology and nuclear medicine by coupling two imaging techniques into one operating device. This has been translated in merging SPECT camera with X-ray computed tomography (CT) scanner in one device providing superb inherent anatomolecular information in one imaging session. While this process of image coregistration can be accomplished by fusing images obtained from two separate modalities, it has been demonstrated that inline SPECT or PET and CT image acquisition would be more advantageous.

The advantages provided by CT to functional imaging are not singular. It enables the reading physicians to precisely localize pathological lesions detected on functional images with great confidence. The other advantage is the improvement in performing attenuation correction. Again, although this can be performed by radionuclide transmission sources, the CT-based attenuation correction has been shown to outperform radionuclide-based transmission scanning by providing fast and significantly less-noisy attenuation maps.

Another benefit provided by CT is the capability of deriving dosimetric measurements from the fused images due to accurate outlining of the region of interest and thus better volumetric assessment. In the field of nuclear cardiology, SPECT/CT systems are of particular importance due to utilization of CT in attenuation correction [84, 85] and other degrading factors that reduce diagnostic quality and quantitative accuracy, such as partial volume effects [86]. Apart from attenuation correction, calculation of calcium scoring is also possible with the CT portion of the machine in addition to performing noninvasive coronary angiography. Figure 10.11 shows two SPECT/CT systms produced by two major vendors in nuclear medicine.

In some instances, the addition of CT data to the functional images provides a guiding tool for image-based biopsy and thus can play a role in patient management; it can also be of synergistic effect in radiotherapy treatment planning, targeted treatment with brachytherapy, or intensity-modulated radiation therapy [87]. However, this has become more attractive with PET imaging than SPECT derived data.

The image of the year for 2006 was a SPECT/CT image showing both the coronary arteries and blood flow to the heart. This took place at the 53rd annual meeting of the Society of Nuclear Medicine in San Diego, California. The images clearly depicted the anatomical correlation of the blood flow defects to the corresponding artery. SPECT/CT devices also are of interest in preclinical and molecular imaging research with similar
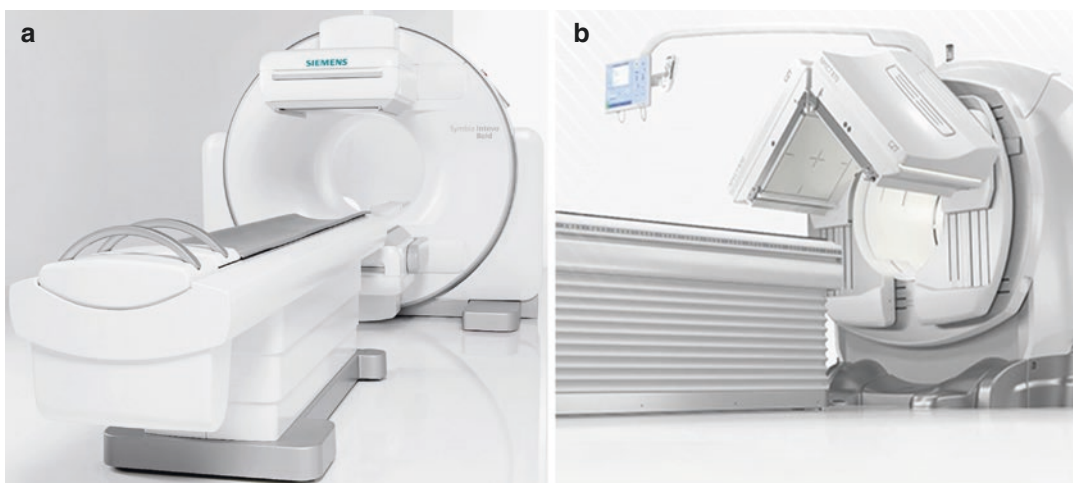
Fig. 10.11 State-of-the-art SPECT/CT systems: (**a**) Symbia Intevo bold and (**b**) NM/CT 870 DR SPECT/CT. (Images are courtesy of Siemens Healthcare and GE Healthcare, respectively)

benefits as those provided to the clinical arena in addition to increased flexibility in performing longitudinal research studies.

On the research level, a tremendous improvement in the spatial resolution of micro-CT systems has enabled the investigators to look at minute structural changes that were not possible to see with conventional systems. Advances in micro-CT systems has revealed images of 10 μm and far better, permitting subcellular dimensions to be imaged [88].

10.5.1 Levels of Integration

Transmission scanning has been defined as "a useful adjunct to conventional emission scanning for accurately keying isotope deposition to radiographic anatomy" [89]. This article was published by Edward and coworkers in the mid-1960s when they realized the importance of combining functional data with their anatomical templates, although they used a simple approach to obtain the transmission scanning. Investigators assigned this as the first demonstration of the feasibility of hybrid imaging [90]. They used an Am-241 source located at the center hole of a collimated detector; the other detector was adjusted to acquire the emission and transmission data. This early functional/anatomical study is a clear sign of the early recognition of combining the two types of images to strengthen each other and to overcome their inherent weaknesses. However, despite this interesting beginning, it was not pursued, and both imaging modalities were almost developed independently until the early 1990s. Before this time, there was some interest and research efforts to use radioactive transmission sources for attenuation correction [91, 92]. The approaches and different levels of integrating structural imaging with the functional data were as follows:

1. The *primitive level* of integrating functional and structural images is evidenced by the human brain. This is the traditional way that diagnosticians used to correlate two images acquired from separate imaging modalities.

However, human spatial perception and differences in image textures acquired from two different modalities represent a challenge for the reading physicians to mentally correlate the two data sets. This can be more problematic in small-size lesions and in identifying the spatial extent and spread of a disease.

2. The second level of image coregistration was brought to the clinic by software algorithms. They are relatively simple to apply to rigid structures such as the brain, where images acquired by CT or MRI can be merged to functional images acquired and processed on a separate SPECT or PET machine. This successful implementation is due to brain rigidity, and variations in the position of internal structures are less likely to occur compared to lung or abdominal image fusion. In a review [93], localization of brain structures was less challenging compared to whole-body applications, and image fusion may be required for only a subgroup of patients. Moreover, in a wide comparison of various available software tools for retrospective registration of PET/MRI and PET/CT, an accuracy of 2–3 mm was consistently achieved, which was below the voxel dimension of PET [94] and SPECT as well.

3. Use of intrinsic landmarks or extrinsic markers to accurately fuse the two data sets has been implemented with some impractical drawbacks placed on its feasibility in the clinical routine, added technical complexity to the diagnostic procedures, or inaccurate image correlation. This could arise from variations that may exist between imaging sessions, fixation strategy, or perhaps inability to correlate internal organs with external markers [83]. Furthermore, automatic registration for internal landmarks could also be affected by the limited spatial resolution of nuclear images with precise selection of anatomical landmarks; therefore, accurate alignment is not guaranteed. These apparent shortcomings of image coregistration, particularly in nonrigid body structures, have motivated the development of nonlinear 3D image fusion algorithms able to improve the accuracy of alignment.

4. Ideally, one would like to acquire the structural as well as the functional data in a simultaneous manner in the same spatial and temporal domain. This can be achieved when the detector systems can be incorporated into each other, achieving concurrent image acquisition. This multimodality design has been realized in hybrid PET/MRI systems with substantial modification to the PET detector system using APDs instead of the conventional PMTs, as mentioned in this chapter (see [95]).

5. The other alternative is to modify the detector technology so that a single detector system can record the two signals with adequate distinction for each individual electronic pulse. However, X-ray detector systems are energy integrators and do not allow individual events to be discriminated according to their energies. This is in great part due to the high fluence of the X-ray source compared to nuclear photon emission and owing to beam polychromaticity [96]. In other words, the significant differences in photon rates pose challenges to implement multimodality imaging using a "conventional" detector for both X-ray and radionuclide processes; this requires a detector that can switch between pulse-mode SPECT/PET acquisition and charge integration mode [97]. Nevertheless, it has been proposed to simultaneously acquire trimodality images, namely SPECT/PET/CT, with great complexities placed on detector design [84].

6. The other strategy is to place the two detector systems side by side such that images can be acquired in a sequential manner. This is the way all clinical SPECT/CT and PET/CT scanners are presently manufactured and operated. Therefore, one can simply deduce that the higher the level of integration, the more demands placed on the technologic complexity. The range of multimodality imaging has been extended to include functional only, structural only, or a combination of functional and structural imaging modalities to yield a variety of integrated or hybrid diagnostic options [98]. SPECT/CT is among the best dual-modality approaches that drew the attention of many researchers in the field, and its

technical value has been proven in a significant number of clinical conditions, leading to a change in patient management. Although other multimodality imaging approaches have been or are being developed, they are aimed most of the time toward preclinical imaging, and their clinical counterparts are yet to be determined.

10.5.2 Applications of Hybrid SPECT Imaging

The utility of SPECT/CT systems is expanding in many areas of research and clinical practice. In addition to attenuation correction, other image degrading factors can also be accounted for from the use of the CT images. A model-based approach to derive Compton probabilities or transmission-based scatter correction can be applied using CT images to correct for scattered photons, as shown by Willowson et al. [99]. In the same report, the effect of partial volume was also accounted for using the CT data, and all corrections revealed an accurate tracer estimate of 1% with a precision of ±7%. In brain studies, correction for partial volume is critical, and reliable and quantitative outcome cannot be obtained without considerations placed on the phenomenon. The binding potential of the striatum can be underestimated by 50% in the absence of partial volume correction. However, in the presence of anatomically guided partial volume correction, substantial improvement can be obtained [100, 101]. In a porcine model, Da Silva et al. showed that an attenuation correction alone for myocardial perfusion Tc-99m-labeled sestamibi cannot yield higher quantitative accuracy without proper correction for partial volume [86]. The combined corrections, however, resulted in higher absolute activity concentrations within a range of 10%. CT data provided an accurate template for modeling the subject anatomy and for accurate definition of the myocardial boundaries.

SPECT/CT systems are also helpful in absorbed dose estimation since the CT images are able to provide a highly accurate assessment of tumor volume. This is an important step in

dose calculation schemes required in radioimmunotherapy and other dose estimation disciplines. As SPECT data can provide important functional information about drug distribution, residence time, and patient follow-up, the additive value of CT can enhance the quantitative accuracy of the measurements for subsequent accurate dose estimates. In the case of pure beta emitters and attempts to image radiotracer distribution based on bremsstrahlung radiation, X-ray CT provides a good anatomical template to delineate and distinguish various tissue uptakes [102].

The current era is witnessing an increasing interest in theranostics, those compounds of combined diagnostic and therapeutic utility, and therefore the gamma camera should be able to meet these requirements and challenges imposed by imaging beta and alpha emitters provided the low abundance of the gamma photons and difficulties associated with detection of bremsstrahlung signal. Efforts are being taken to find out new avenues to address the limitation of the current design or capabilities of the gamma camera rendering it qualified for the emerging new tasks [103].

10.6   Conclusions

The gamma camera has been a cornerstone in the world of nuclear medicine. The original concept made by Hal Anger still remain in many commercial systems. However, significant developments were made in detector electronics, computer systems, and other interfaces that handled the signal in a more efficient and accurate manner. The gamma camera is a highly specific position sensitive radiation detector with multi-compartments. Each of these elements plays a role in photon detection process and determination of tracer biodistribution. Digital technology and multi-head systems were also key factors that enhanced and motivated the performance of the gamma camera. Implementations of new camera design with different geometry, fast acquisition protocols, and reconstruction algorithms are relatively new features for the current and future generations of the gamma camera. Semiconductor systems with room temperature materials and good perfor-

mance characteristics are of interest among some manufacturers and nuclear medicine practitioners. The use of new photodetectors would help to enhance the diagnostic quality of nuclear medicine images. They also provide compactness, portability, and better imaging features. The addition of CT as a structural imaging modality to SPECT systems has found numerous applications in many areas of diagnostic and therapeutic nuclear medicine as well as in clinical research setting.

References

1. Myers WG. Georg Charles de Hevesy: the father of nuclear medicine. J Nucl Med. 1979;20(6):590–4.
2. Patton DD. The birth of nuclear medicine instrumentation: Blumgart and Yens, 1925. J Nucl Med. 2003;44(8):1362–5.
3. Cassen B, Curtis L, Reed C. A sensitive directional gamma-ray detector. Nucleonics. 1950;6:78–80.
4. Graham LS, Kereiakes JG, Harris C, Cohen MB. Nuclear medicine from Becquerel to the present. Radiographics. 1989;9(6):1189–202.
5. Cassen B, Curtis L, Reed C, et al. Instrumentation for 1-131 use in medical studies. Nucleonics. 1951;9:46–50.
6. Anger H. Scintillation camera. Rev Sci Instrum. 1985;29:27–33.
7. Anger HO. Scintillation camera with 11-inch crystal. Ucrl-11184. UCRL US At Energy Comm. 1963;72:69–85.
8. Anger HO. Scintillation camera with multichannel collimators. J Nucl Med. 1964;5:515–31.
9. Slomka PJ, Pan T, Berman DS, Germano G. Advances in SPECT and PET hardware. Prog Cardiovasc Dis. 2015;57(6):566–78.
10. Slomka PJ, Patton JA, Berman DS, Germano G. Advances in technical aspects of myocardial perfusion SPECT imaging. J Nucl Cardiol. 2009;16(2):255–76.
11. Borges-Neto S, Pagnanelli RA, Shaw LK, Honeycutt E, Shwartz SC, Adams GL, et al. Clinical results of a novel wide beam reconstruction method for shortening scan time of Tc-99m cardiac SPECT perfusion studies. J Nucl Cardiol. 2007;14(4):555–65.
12. Buechel RR, Herzog BA, Husmann L, Burger IA, Pazhenkottil AP, Treyer V, et al. Ultrafast nuclear myocardial perfusion imaging on a new gamma camera with semiconductor detector technique: first clinical validation. Eur J Nucl Med Mol Imaging. 2010;37(4):773–8.
13. Chandra R. Nuclear medicine physics: the basics. 5th ed. London: Williams &Wilkins; 1998.
14. Vesel J, Petrillo M. Improved gamma camera performance using event positioning method based on

distance dependent weighting. IEEE Nucl Sci Symp Conf Rec. 2005;5:2445–8.

15. Kulberg GH, Muehllehner G, van Dijk N. Improved resolution of the Anger scintillation camera through the use of threshold preamplifiers. J Nucl Med. 1972;13(2):169–71.

16. Cherry S, Sorenson J, Phelps M. Physics in nuclear medicine. 4th ed. Amsterdam: Elsevier Health Sciences; 2012.

17. Ricard M. Imaging of gamma emitters using scintillation cameras. Nucl Instrum Meth Phys Res A. 527(12):124–129. In: Proceedings of the 2nd International Conference on Imaging Technologies in Biomedical Sciences. 2004.

18. Joung J, Miyaoka RS, Kohlmyer S, Lewellen TK. Implementation of ML based positioning algorithms for scintillation cameras. IEEE Trans Nucl Sci. 2000;47(3):1104–11.

19. Moore SC, Kouris K, Cullum I. Collimator design for single photon emission tomography. Eur J Nucl Med. 1992;19(2):138–50.

20. Lau YH, Hutton BF, Beekman FJ. Choice of collimator for cardiac SPET when resolution compensation is included in iterative reconstruction. Eur J Nucl Med. 2001;28(1):39–47.

21. Murphy PH. Acceptance testing and quality control of gamma cameras, including SPECT. J Nucl Med. 1987;28(7):1221–7.

22. Inoue Y, Shirouzu I, Machida T, Yoshizawa Y, Akita F, Doi I, et al. Physical characteristics of low and medium energy collimators for 123I imaging and simultaneous dual-isotope imaging. Nucl Med Commun. 2003;24(11):1195–202.

23. Accorsi R. Brain single-photon emission CT physics principles. AJNR Am J Neuroradiol. 2008;29(7):1247–56.

24. Peremans K, Cornelissen B, Van Den Bossche B, Audenaert K, Van de Wiele C. A review of small animal imaging planar and pinhole spect gamma camera imaging. Vet Radiol Ultrasound. 2005;46(2):162–70.

25. Vija A, Malmin R, Yahil A, Zeintl J, Bhattacharya M, Rempel T, et al. A method for improving the efficiency of myocardial perfusion imaging using conventional SPECT and SPECT/CT imaging systems. In: Nuclear Science Symposium Conference Record (NSS/MIC) IEEE; 2010. p. 3433–7.

26. Caobelli F, Kaiser SR, Thackeray JT, Bengel FM, Chieregato M, Soffientini A, et al. IQ SPECT allows a significant reduction in administered dose and acquisition time for myocardial perfusion imaging: evidence from a phantom study. J Nucl Med. 2014;55(12):2064–70.

27. Zeintl J, Rempel T, Bhattacharya M, Malmin R. Performance characteristics of the SMARTZOOM collimator. In: Nuclear Science Symposium and Medical Imaging Conference. Nuclear Science Symposium and Medical Imaging Conference (NSS/MIC) IEEE; 2011. p. 2426–9.

28. Caobelli F, Ren Kaiser S, Thackeray JT, Bengel FM, Chieregato M, Soffientini A, et al. The importance of a correct positioning of the heart using IQ-SPECT system with multifocal collimators in myocardial perfusion imaging: a phantom study. J Nucl Cardiol. 2015;22(1):57–65.

29. Okuda K, Nakajima K, Matsuo S, Kondo C, Sarai M, Horiguchi Y, et al. Creation and characterization of normal myocardial perfusion imaging databases using the IQ.SPECT system. J Nucl Cardiol. 2017;25(4):1328–37.

30. Knoll GF. Radiation detection and measurements. 3rd ed. New York: Wiley; 2000.

31. Wong TZ, Turkington TG, Polascik TJ, Coleman RE. ProstaScint (capromab pendetide) imaging using hybrid gamma camera-CT technology. AJR Am J Roentgenol. 2005;184(2):676–80.

32. Kupinski MA, Barrett HH, editors. Small animal SPECT imaging. New York: Springer Science and Business Media; 2005.

33. Giokaris N, Loudos G, Maintas D, Karabarbounis A, Lembesi M, Spanoudaki V, et al. Partially slotted crystals for a high resolution camera based on a position sensitive photomultiplier. Nucl Instrum Meth Phys Res A. 2005;550:305–12.

34. Giokaris N, Loudo G, Maintas D, et al. Comparison of CsI(Tl) and CsI(Na) partially slotted crystals for high resolution SPECT imaging. Nucl Instrum Meth Phys Res A. 2006;569:185–7.

35. Patt BE, Wanczyk JS, Rossington TC, Wang NW, Tornai MP, Hoffman EJ. High resolution CsI(Tl)/Si PIN detector development for breast imaging. IEEE Trans Nucl Sci. 1998;45(4):2126–31.

36. Garcia EV, Faber TL. Advances in nuclear cardiology instrumentation: clinical potential of SPECT and PET. Curr Cardiovasc Imaging Rep. 2009;2(3):230–7.

37. Siman W, Kappadath SC. Performance characteristics of a new pixelated portable gamma camera. Med Phys. 2012;39(6):3435–44.

38. Walrand S, Jamar F, de Jong M, Pauwels S. Evaluation of novel whole-body high-resolution rodent SPECT (Linoview) based on direct acquisition of linogram projections. J Nucl Med. 2005;46(11):1872–80.

39. Pani R, Cinti MN, De Notaristefani F, Pellegrini R, Bennati P, Betti M, et al. Imaging performances of LaCl3:Ce scintillation crystals in SPECT. IEEE Nucl Sci Symp Conf Rec. 2004;4:2283–7.

40. Pani R, Pellegrini R, Cinti M, Bennati P, Betti M, Vittorini F. LaBr3(Ce) crystal: the latest advance for scintillation cameras. Nucl Instrum Meth A. 2007;572(1):268–9.

41. Groch MW, Erwin WD. Single-photon emission computed tomography in the year 2001: instrumentation and quality control. J Nucl Med Technol. 2001;29(1):12–8.

42. Madsen MT. Recent advances in SPECT imaging. J Nucl Med. 2007;48(4):661–73.

43. Sayeram S, Tsui B, De Zhao X, Frey E. Performance evaluation of three different SPECT systems used in in 111 ProstaScint1 SPECT imaging. IEEE Nucl Sci Symp Conf Rec. 2003;5:3129–33.

44. Harbert J, Eckelman W, Neumann R. Nuclear medicine: diagnosis and therapy. New York: Thieme Medical; 1996.

45. https://www.hamamatsu.com/resources/pdf/etd/PMT_handbook_v3aE.pdf. Accessed 21 Aug 2020.

46. Syed A. Physics and engineering of radiation detection. 1st ed. Amsterdam: Elsevier; 2007.

47. Boyd C, Dalrymple G. Basic science principles of nuclear medicine. London: Mosby; 1974.

48. Harris CC. The use of a nuclear medicine computer as a multichannel pulse-height analyzer. Design of an interface. Radiology. 1983;148(3):857–9.

49. Buvat I, De Sousa MC, Di Paola M, Ricard M, Lumbroso J, Aubert B. Impact of scatter correction in planar scintimammography: a phantom study. J Nucl Med. 1998;39(9):1590–6.

50. Graham LS, LaFontaine RL, Stein MA. Effects of asymmetric photopeak windows on flood field uniformity and spatial resolution of scintillation cameras. J Nucl Med. 1986;27(5):706–13.

51. Collier BD, Palmer DW, Knobel J, Isitman AT, Hellman RS, Zielonka JS. Gamma camera energy windows for Tc-99m bone scintigraphy: effect of asymmetry on contrast resolution. Work in progress. Radiology. 1984;151(2):495–7.

52. Yamamoto S, Watabe H, Kato K, Hatazawa J. Performance comparison of high quantum efficiency and normal quantum efficiency photomultiplier tubes and position sensitive photomultiplier tubes for high resolution PET and SPECT detectors. Med Phys. 2012;39(11):6900–7.

53. Kume H, Suzuki S, Takeuchi J, Oba K. Newly developed photomultiplier tubes with position sensitivity capability. IEEE Trans Nucl Sci. 1985;NS-32(1):448.

54. Pichler BJ, Ziegler SI. Photodetectors. In: Wernick M, Aarsvold J, editors. Emission tomography: the fundamentals of PET and SPECT. San Diego: Elsevier Academic Press; 2004.

55. Del Guerra A, Belcari N, Bisogni MG, Llosá G, Marcatili S, Moehrs S. Advances in position-sensitive photodetectors for PET applications. Nucl Instrum Meth Phys Res A. 2009;604(1–2):319–22.

56. Dornebos P, van Eijk CW, Dornebos P, van Eijk CW. Proceedings of the international conference on inorganic scintillators and their applications. Delft University of Technology, Delft, The Netherlands, 28 August–1 September 1995; 1995.

57. Loudos GK, Nikita KS, Uzunoglu NK, Giokaris ND, Papanicolas CN, Archimandritis SC, et al. SCINT95, proceedings of the international conference on inorganic scintillators and their applications. Improving spatial resolution in SPECT with the combination of PSPMT based detector and iterative reconstruction algorithms. Comput Med Imaging Graph. 2003;27(4):307–13.

58. Del Guerra A, Di Domenico G, Scandola M, Zavattini G. High spatial resolution small animal YAPPET. Nucl Instrum Meth Phys Res A. 1998;409:537–41.

59. Pani R, Pellegrini R, Cinti MN, Trotta C, Trotta G, Scafe R, et al. A novel compact gamma camera based on flat panel PMT. Nucl Instrum Meth Phys Res A. 2003;513:36–41.

60. Renker D. New trends on photodetectors. Nucl Instrum Meth Phys Res A. 2007;571:1–6.

61. Wagennar DJ. CdTe and CdZnTe semiconductor detectors for nuclear medicine imaging. In: Wernick MN, Aarsvold JN, editors. Emission tomography. The fundamentals of PET and SPECT. San Diego: Elsevier; 2004.

62. Mori I, Takayama T, Motomura N. The CdTe detector module and its imaging performance. Ann Nucl Med. 2001;15(6):487–94.

63. Herzog BA, Buechel RR, Katz R, Brueckner M, Husmann L, Burger IA, et al. Nuclear myocardial perfusion imaging with a cadmium-zinc-telluride detector technique: optimized protocol for scan time reduction. J Nucl Med. 2010;51(1):46–51.

64. Zhang YQ, Jiang YF, Hong L, Chen M, Zhang NN, Yang HJ, et al. Diagnostic value of cadmium-zinc-telluride myocardial perfusion imaging versus coronary angiography in coronary artery disease: a PRISMA-compliant meta-analysis. Medicine (Baltimore). 2019;98(9):e14716.

65. Nudi F, Iskandrian AE, Schillaci O, Peruzzi M, Frati G, Biondi-Zoccai G. Diagnostic accuracy of myocardial perfusion imaging with CZT technology: systemic review and meta-analysis of comparison with invasive coronary angiography. JACC Cardiovasc Imaging. 2017;10(7):787–94.

66. Gambhir SS, Berman DS, Ziffer J, Nagler M, Sandler M, Patton J, et al. A novel high-sensitivity rapid-acquisition single-photon cardiac imaging camera. J Nucl Med. 2009;50(4):635–43.

67. Slomka PJ, Miller RJH, Hu LH, Germano G, Berman DS. Solid-state detector SPECT myocardial perfusion imaging. J Nucl Med. 2019;60(9):1194–204.

68. Erlandsson K, Kacperski K, van Gramberg D, Hutton BF. Performance evaluation of D-SPECT: a novel SPECT system for nuclear cardiology. Phys Med Biol. 2009;54(9):2635–49.

69. Berman DS, Kang X, Tamarappoo B, Wolak A, Hayes SW, Nakazato R, et al. Stress thallium-201/rest technetium-99m sequential dual isotope high-speed myocardial perfusion imaging. JACC Cardiovasc Imaging. 2009;2(3):273–82.

70. Allie R, Hutton BF, Prvulovich E, Bomanji J, Michopoulou S, Ben-Haim S. Pitfalls and artifacts using the D-SPECT dedicated cardiac camera. J Nucl Cardiol. 2016;23(2):301–10.

71. Keidar Z, Kagna O, Frenkel A, Israel O. A novel ultrafast cardiac scanner for myocardial perfusion imaging (MPI): comparison with a standard dual head camera. J Nucl Med. 2009;50(Suppl 2):478.

72. Verger A, Djaballah W, Fourquet N, Rouzet F, Koehl G, Imbert L, et al. Comparison between stress myocardial perfusion SPECT recorded with cadmium-zinc-telluride and Anger cameras in vari-

ous study protocols. Eur J Nucl Med Mol Imaging. 2012;40(3):331–40.

73. Bocher M, Blevis IM, Tsukerman L, Shrem Y, Kovalski G, Volokh L. A fast cardiac gamma camera with dynamic SPECT capabilities: design, system validation and future potential. Eur J Nucl Med Mol Imaging. 2010;37(10):1887–902.

74. Fiechter M, Gebhard C, Fuchs TA, Ghadri JR, Stehli J, Kazakauskaite E, et al. Cadmium-zinc-telluride myocardial perfusion imaging in obese patients. J Nucl Med. 2012;53(9):1401–6.

75. Taillefer R. Clinical applications of 99mTc-sestamibi scintimammography. Semin Nucl Med. 2005;35(2):100–15.

76. Mueller B, O'Connor MK, Blevis I, Rhodes DJ, Smith R, Collins DA, et al. Evaluation of a small cadmium zinc telluride detector for scintimammography. J Nucl Med. 2003;44(4):602–9.

77. Blevis IM, O'Connor MK, Keidar Z, Pansky A, Altman H, Hugg JW. CZT gamma camera for scintimammography. Phys Med. 2006;21(Suppl 1):56–9.

78. Pani R, Pellegrini R, Cinti MN, Bennati P, Betti M, Casali V, et al. Recent advances and future perspectives of gamma imagers for scintimammography. Nucl Instrum Meth A. 2006;569:296–300.

79. Ljungberg M, Pretorius PH. SPECT/CT: an update on technological developments and clinical applications. Br J Radiol. 2018;91(1081):20160402.

80. Gimelli A, Liga R, Bertasi M, Kusch A, Marzullo P. Head-to-head comparison of a CZT-based all-purpose SPECT camera and a dedicated CZT cardiac device for myocardial perfusion and functional analysis. J Nucl Cardiol. 2019.

81. https://www.gehealthcare.com. Accessed 21 Aug 2020.

82. Stout DB, Zaidi H. Preclinical multimodality imaging in vivo. PET Clin. 2008;3(3):251–73.

83. Keidar Z, Israel O, Krausz Y. SPECT/CT in tumor imaging: technical aspects and clinical applications. Semin Nucl Med. 2003;33(3):205–18.

84. Garcia EV. SPECT attenuation correction: an essential tool to realize nuclear cardiology's manifest destiny. J Nucl Cardiol. 2007;14(1):16–24.

85. Germano G, Slomka PJ, Berman DS. Attenuation correction in cardiac SPECT: the boy who cried wolf? J Nucl Cardiol. 2007;14(1):25–35.

86. Da Silva AJ, Tang HR, Wong KH, Wu MC, Dae MW, Hasegawa BH. Absolute quantification of regional myocardial uptake of 99mTc-sestamibi with SPECT: experimental validation in a porcine model. J Nucl Med. 2001;42(5):772–9.

87. Ellis RJ, Kim EY, Conant R, Sodee DB, Spirnak JP, Dinchman KH, et al. Radioimmunoguided imaging of prostate cancer foci with histopathological correlation. Int J Radiat Oncol Biol Phys. 2001;49(5):1281–6.

88. Ritman EL, Small-animal CT. Its difference from, and impact on, clinical CT. Nucl Instrum Meth Phys Res A. 2007;580(2):968–70.

89. Kuhl DE, Hale J, Eaton WL. Transmission scanning: a useful adjunct to conventional emission scanning for accurately keying isotope deposition to radiographic anatomy. Radiology. 1966;87(2):278–84.

90. Patton JA, Townsend DW, Hutton BF. Hybrid imaging technology: from dreams and vision to clinical devices. Semin Nucl Med. 2009;39(4):247–63.

91. Bailey DL, Hutton BF, Walker PJ. Improved SPECT using simultaneous emission and transmission tomography. J Nucl Med. 1987;28(5):844–51.

92. Tsui BM, Gullberg GT, Edgerton ER, Ballard JG, Perry JR, McCartney WH, et al. Correction of non-uniform attenuation in cardiac SPECT imaging. J Nucl Med. 1989;30(4):497–507.

93. Slomka PJ, Baum RP. Multimodality image registration with software: state-of-the-art. Eur J Nucl Med Mol Imaging. 2009;36(Suppl 1):S44–55.

94. West J, Fitzpatrick JM, Wang MY, Dawant BM, Maurer CR Jr, Kessler RM, et al. Comparison and evaluation of retrospective intermodality brain image registration techniques. J Comput Assist Tomogr. 1997;21(4):554–66.

95. Beyer T, Pichler B. A decade of combined imaging: from a PET attached to a CT to a PET inside an MR. Eur J Nucl Med Mol Imaging. 2009;36(Suppl 1):S1–2.

96. Seibert JA, Boone JM. X-ray imaging physics for nuclear medicine technologists. Part 2: X-ray interactions and image formation. J Nucl Med Technol. 2005;33(1):3–18.

97. Darambara DG. State of the art radiation detectors for medical imaging: demands and trends. Nucl Instrum Meth Phys Res A. 2006;569(2):153–8.

98. Cherry SR. Multimodality imaging: beyond PET/CT and SPECT/CT. Semin Nucl Med. 2009;39(5):348–53.

99. Willowson K, Bailey DL, Baldock C. Quantitative SPECT reconstruction using CT-derived corrections. Phys Med Biol. 2008;53(12):3099–112.

100. Soret M, Koulibaly PM, Darcourt J, Hapdey S, Buvat I. Quantitative accuracy of dopaminergic neurotransmission imaging with (123)I SPECT. J Nucl Med. 2003;44(7):1184–93.

101. Vanzi E, De Cristofaro MT, Ramat S, Sotgia B, Mascalchi M, Formiconi AR. A direct ROI quantification method for inherent PVE correction: accuracy assessment in striatal SPECT measurements. Eur J Nucl Med Mol Imaging. 2007;34(9):1480–9.

102. D'Asseler Y. Advances in SPECT imaging with respect to radionuclide therapy. Q J Nucl Med Mol Imaging. 2009;53(3):343–7.

103. Zubal IG. Time for a next-generation nuclear medicine gamma camera? [NEWSLINE]. J Nucl Med. 2020;61:16N.

Quality Control of Planar and SPECT Imaging Systems

11

Gian Luca Poli and Pat Zanzonico

Contents

G. L. Poli (✉)
ASST Papa Giovanni XXIII, Bergamo, Italy
e-mail: glpoli@asst-pg23.it

P. Zanzonico
Memorial Sloan Kettering Cancer Center,
New York, NY, USA
e-mail: zanzonip@mskcc.org

11.1   Introduction

Diagnostic imaging plays a vital role on patient management. Therefore, it is extremely important that all imaging equipment used in nuclear medicine facilities operate at optimal system performance. This allows the acquisition of images of reliable diagnostic quality while optimizing radiation dose to patients. Moreover, the high cost and increasing complexity of diagnostic procedures demand optimized performance of imaging equipment. A Quality Assurance (QA) programme should be established and followed as part of the routine and essential work of a nuclear medicine department, to assure the safe and effective use of all imaging equipment and to comply with applicable regulations. This applies to planar gamma cameras, SPECT systems and hybrid systems such as SPECT/CT, PET/CT and PET/MR. This chapter describes the main aspects of a QA programme for planar gamma cameras, SPECT and SPECT/CT systems, and the reader is referred to other documents [1–3] for other imaging modalities.

11.2   Quality Assurance and Quality Control

QA in nuclear medicine imaging can be considered as the set of planned and systematic actions necessary to ensure that the scintigraphic images produced are consistently of sufficiently high quality to provide reliable diagnostic information, with consideration for optimization of the radiation exposures to patients and of the costs of imaging procedures. Quality Control (QC) is one aspect of QA and can be considered as the process by which the performance level of an imaging system is measured and then compared against standards or tolerance values established by the user and/or the system manufacturer.

QC tests on a gamma camera consist of a set of measurements of performance parameters or characteristics of the imaging system. These tests must be performed at the time of acceptance and commissioning of the equipment prior to its clinical use on patients and periodically thereafter. QC tests are designed to identify a compromised, inadequate or even potentially hazardous performance of the gamma camera.

QA of an imaging instrument starts with establishing the specifications for the procurement of the equipment. All relevant health professionals should be involved in the preparation of the specifications according to the needs of the nuclear medicine facility and participate in the tender evaluation and purchase recommendation of the equipment. It is advisable to include radioactive sources, phantoms and other test devices, and software needed for QC tests in the tender document in order to ensure that these are available at the time of installation. In the context of leasing (rather than actually purchase) equipment, return and replacement of expired QA radioactive sources and upgrades of software should be incorporated into the tender specifications.

Acceptance tests should be performed immediately after installation to ensure that the system is fully operational and conforms to the manufacturer's specifications. The National Electrical Manufacturers' Association (NEMA) has developed standardized tests that allow for an objective comparison of the performance of different systems [4], and these are the tests that should be performed for the acceptance of a newly installed system. In the context of acceptance testing based on the applicable NEMA specifications, the distinction should be noted between "performance

standards" and "class standards." A performance standard is a parameter that each unit of a particular make and model of an imaging system must meet or exceed. A class standard is a representative value of a performance parameter and not every unit of a particular make and model may necessarily meet the class-standard value.

Commissioning an imaging equipment consists of a number of actions necessary to ensure that the system is actually ready for clinical use. As part of commissioning, **reference tests** are performed immediately after the acceptance test, when the gamma camera is presumably functioning optimally and within specifications. These establish the baseline QC values against which future performance can be compared and provide reference results for the following routine tests. The QC tests performed for the acceptance testing can, of course, be incorporated into the reference tests.

Routine tests should be performed once the system is operational to assure consistent results over the instrument's lifetime. These tests verify that the technical parameters of the imaging system remain within an acceptable range of variation with respect to some reference values (or "tolerance values"). These values are typically those obtained during the acceptance and commissioning of the system and provide baseline data against which its subsequent performance can be compared. Routine tests should be reasonably straightforward, so that they can be conducted in a practically acceptable timeframe.

Several documents provide guidance on QA/QC programmes of gamma cameras and SPECT systems [5–9], with specification of the tests to be performed and suggested frequencies. Even though recommendations in the literature of the tests to be performed and their frequencies are reasonably similar, there is no unanimity among relevant reference documents. Normally, the best approach is to develop a QA/QC programme tailored to the specific system and its use, prioritizing those tests that are more likely to detect malfunctions or degradation of system performance that may adversely affect the interpretation of clinical studies. The frequency of the test should take into account the potential variation

with time of the characteristic under consideration and the time required to perform the test and can be adjusted as appropriate based on the history of the instrument's stability.

Different routine tests can therefore have different frequencies and be repeated weekly, monthly, quarterly or yearly. A special case of routine tests are the **daily tests** (or operational checks) that need to be performed each day the instrument is used. Daily tests are usually simple and can be completed in a short time, while capable of detecting with high sensitivity the most likely technical problems that may occur.

QC procedures do not replace the need for preventive maintenance procedures performed by the vendor's service engineers. These should be performed on a regular basis and a maintenance contract with the vendor should therefore always be in place.

A QC programme requires the definition of the performance parameters that need to be measured, the preparation of written procedures on how to perform each such measurement, including frequencies, tolerances, action levels, and corrective measures. Adequate documentation of the results of tests is a fundamental component of the QC programme. The results of acceptance, reference and routine tests should be recorded, together with preventive or corrective maintenance reports from the vendor's system engineers and reports of out-of-tolerance results or unusual findings (e.g., artefacts). Trend analysis of the results with control charts and graphs can help ascertain the long-term stability of a physical parameter or document a progressive degradation or a repeated failure, thus identifying emerging problems that could be solved with preventive actions before the system would need to be removed from clinical use. In case the results of QC tests reveal unsatisfactory performance, appropriate corrective action should follow.

QC reports need to specify the type of test and the date of execution of the test. They should be easy to complete and understand, with specified acceptable limits for the results. These are normally the responsibility of a medical physicist.

In this chapter, only the most common and/or clinically relevant QC tests that should be

Table 11.1 Gamma camera, SPECT and SPECT/CT system tests described in the present chapter with frequencies recommended by the IAEA, AAPM and EANM

	IAEA	AAPM Task Group 177	EANM
Peaking	D		D
Uniformity	D	D	D
Energy resolution		A + Y	A
Intrinsic spatial resolution	A + ½Y	A + Y	A + ½Y
System spatial resolution and linearity	A + W	A + W	A
WB spatial resolution		A + Y[a]	A + Y
System planar sensitivity	A + ½Y	A + Y	
Count rate performance	A + ½Y	A + Y	Y
Multiple window spatial registration	A + ½Y	A + Y[a]	A + ½Y/Y
Pixel size	A + ½Y		A + ½Y
Inter-detector sensitivity variation			A
Centre of rotation	A + W/M	M	W/M
SPECT performance	A + ½Y	A + Q	½Y
Tomographic uniformity	A + ½Y	A + Y	
Tomographic spatial resolution	A + ½Y	A + Y	A + ½Y
SPECT/CT alignment		A + Y[b]	M
CT number accuracy		D	A + M
CT dose assessment		A + Y	
CT image quality assessment		D	D

A at acceptance, *D* daily, *W* weekly, *M* monthly, *Q* quarterly, *½Y* semi-annually, *Y* yearly
[a]Optional, [b]As recommended by the manufacturer

performed on a planar gamma camera or SPECT(/CT) system will be described. The reader is referred to international guidance documents [5–9] for a more detailed description of the execution and analysis of the tests and for additional tests which are not reported here. The frequencies suggested by American Association of Physicist in Medicine (AAPM), the International Atomic Energy Agency (IAEA) and the European Association of Nuclear Medicine (EANM) for the QC tests described in this chapter are reported in Table 11.1.

11.3 Test Conditions

QC tests need to be performed under specific test conditions. The following describes the different conditions that are normally recommended by international guidelines and that need to be considered when performing the respective tests. It is beyond the scope of this chapter to be prescriptive about acquisition and reconstruction parameters. However, the rea-

sons underlying the choice of these parameters and of the applicable source activities will be provided in this section. The reader is referred to other documents for more detailed and prescriptive QC procedures.

11.3.1 Intrinsic and Extrinsic (System) Measurements

Some of the QC tests on gamma cameras and SPECT systems can be performed both without and with the collimator mounted on the system head. When the collimator is removed, the **intrinsic** value of the physical parameter under study is evaluated. Certain QC test can be performed intrinsically, such as intrinsic uniformity and intrinsic spatial resolution. When the collimator is mounted on the system head, the physical parameter under study is evaluated under conditions which are those used in the clinical practice. Conventionally, this is called the **extrinsic** or **system** value of the parameter.

11.3.2 UFOV and CFOV Measurements

Because of the distribution of photomultiplier tubes (PMTs) coupled with the scintillation crystal, the performance of a gamma camera in terms of, for example, uniformity and linearity can be superior in the central part compared to the borders of the image. At the periphery of the scintillation detector, a smaller number of PMTs contribute to the signal, thus making it more difficult to accurately determine the position and energy of the scintillation event. For this reason, the results of specific QC tests are reported both for the Useful Field of View (**UFOV**), the physical area of the detector as defined by the manufacturer, and for the Central Field of View (**CFOV**), which is derived by scaling all linear dimensions to 75% of the respective dimensions of the UFOV.

11.3.3 Count Rate

The performance of a gamma camera varies depending on the rate at which photons strike the detector and therefore on the activity that is used for the test. The results of specific QC tests can worsen with increasing count rate because of dead-time-related issues; the dead time of a detector is the interval of time it requires to process and record each event. For this reason, the recommendation of the international guidance documents is to perform QC tests at count rates not exceeding 20,000 counts per second (i.e., 20 kcps). Source activities should therefore be chosen to avoid exceeding this count rate value. An exception is during acceptance testing, for which some parameters should be evaluated by design at higher count rates (e.g., 75 kcps).

11.3.4 Measurements With or Without Scatter

QC tests need to be performed under conditions which are as simple and reproducible as possible. Often parameters under study are evaluated with test sources positioned in air. However, in some cases, it is useful to perform the measurements with the sources surrounded by a scattering medium, simulating conditions that are closer to those encountered in clinical practice. For example, tomographic spatial resolution can be measured by using line sources both in air or positioned in a cylindrical phantom filled with water. The scattering medium is normally a soft tissue-equivalent material such as water or plastic, for example, polymethyl methacrylate (PMMA).

11.3.5 Directions

Many of the QC tests involve measurements of quantities that need to be evaluated in different directions relative to the detector. In planar imaging, x- is referred to as the direction perpendicular to the patient's bed (usually the longest of the two dimensions of rectangular detectors), while direction y- is the one parallel to the bed. In SPECT imaging, z- is referred to as the direction along the patient's bed (i.e., the one parallel to the axis of rotation or, equivalently, to the longitudinal axis of the patient).

11.3.6 Matrix and Pixel Size

The matrix size of a nuclear medicine image and the detector size, in addition to any zoom or magnification factor applied, determine the pixel dimension. It is important for some QC tests to acquire images with a specific pixel size. Larger pixel sizes provide better count statistics, while smaller pixel sizes are more compatible with fine spatial resolution and may be required to achieve adequate spatial sampling for certain resolution measurements. An example is given by the spatial resolution test, where the pixel size should be small enough to adequately define the line spread function (LSF), but large enough to acquire sufficiently high numbers of counts per pixel to minimize statistical uncertainty (i.e., "noise") (see Sect. 11.8). Here a good compromise is to use a pixel size as close as possible to 0.2 times

the expected value of the FWHM spatial resolution. In the case of uniformity tests, images should be acquired with large matrix sizes (512 × 512 or even 1024 × 1024) to allow a better visual assessment of uniformity. However, the quantitative evaluation of uniformity will actually be performed on an image with a rescaled matrix size to reduce the effect of statistical noise (see Sect. 11.6). There are also tests for which the pixel size is irrelevant, for example, sensitivity and energy resolution.

11.3.7 Source Activity

The choice of the source activity depends on different factors and criteria. To avoid dead-time-related issues, the recommendation of guidelines is to avoid exceeding a count rate of 20 kcps. On the other hand, a higher source activity allows the user to perform QC measurements in a shorter time or, for the same duration, to improve count statistics. Therefore, the source activity is, in fact, a compromise between these two factors.

11.4 Detector and System Calibrations

System calibrations and corrections should be part of the QA programme of the imaging system and should be done by a qualified medical physicist or a service engineer to ensure that the sys-

tem is performing adequately. These include, for example, energy, linearity and uniformity corrections and, additionally for SPECT systems, the centre-of-rotation (COR) calibration. In the case of SPECT/CT, assessment of the accuracy of the alignment, or co-registration, of the SPECT and CT image sets should also be performed.

Calibrations and corrections of the imaging system should be current at the time QC tests are performed to avoid the possibility of out-of-tolerance results and the need to repeat these tests after the acquisition of updated calibrations and corrections.

Even gamma cameras performing optimally exhibit some non-uniformity of response. This non-uniformity requires several different corrections: the linearity, energy and sensitivity corrections (or "maps") [10, 11]. With the position of a scintillation event in the gamma camera crystal determined by the relative amount of light collected by the array of discrete PMTs backing the crystal, the "raw" position of each such event is actually incorrect, that is, skewed towards the centres of the respective PMTs. This is because light from a scintillation directly beneath a PMT is collected more efficiently than that from a scintillation between PMTs, resulting in position non-linearity. Creation of the linearity correction is performed by acquiring a high-count transmission image through a "mask" with hundreds of narrow apertures each with a well-defined position (x,y). The uncorrected image will appear as shown in the left-hand image in Fig. 11.1. The
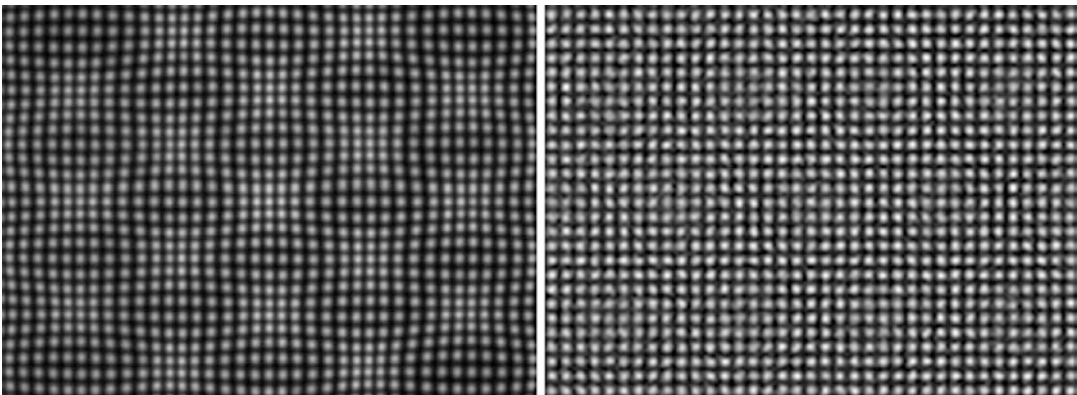
Fig. 11.1 Transmission image of the linearity mask without (left-hand figure) and with (right-hand figure) the linearity correction applied

apparent, but incorrect, position (x',y') of the focus of counts (or dot) corresponding to the aperture at position (x,y) is then translated a distance Δx in the x-direction and Δy in the y-direction to re-position to its correct position (x,y), that is, the actual position of the corresponding aperture. The linearity correction is then comprised of the table of aperture position (x,y)-dependent translations $(\Delta x, \Delta y)$; for positions between those of the apertures, the respective corrections (i.e., translations) are determined by interpolation. Once the linearity correction is applied, the distorted left-hand transmission image will now appear as the undistorted right-hand image in Fig. 11.1. Usually the mask is provided by the vendor, and the linearity correction is created by the service engineer rather than by the end-user. Because the geometric configuration of the crystal and PMTs within the gamma camera detector is fixed, linearity corrections generally do not have to be updated, unless a major servicing of the detector itself is performed. Additionally, the energy spectra (i.e., the position of the isotope's photopeak relative to the energy, or channel, settings for that photopeak) may vary to some extent from position to position over a gamma camera detector. The correction for this variation is generally acquired by the service engineer, rather than the end user.

Finally, among the thousands of pixels comprising an image, slight variations in detector thickness, crystal light emission or crystal-PMT coupling properties, electronics performance, etc. result in slightly different measured count rates for the same photon flux even with the linearity and energy corrections applied. In principle, the residual non-uniformity can be corrected by acquiring data from a uniform flux of gamma rays and normalizing each pixel's counts to the *mean* counts among all the pixels. In practice, a correction table may be acquired using either a uniform flood source placed on the detector or a point source placed sufficiently far (typically ≥ 3 m) from the uncollimated detector to deliver a uniform photon flux. This sensitivity map corrects for the non-uniform count rate detected among individual pixels based on the resulting pixel-by-pixel scaling factors. Pixels having a count value lower (or higher) than average will have an associated multiplicative scaling factor higher (or lower) than 1. Such sensitivity corrections are generally isotope- (i.e., photon-energy) dependent and may need to be updated periodically by the end-user for one or more isotopes.

11.5 Peaking

In planar and SPECT imaging, only those events that have a detected photon energy within the pre-set energy window centred on the photopeak energy will yield counts in the acquired image. Rejection of events having an energy outside (below) the energy window allows for a reduction of scattered photons. These, in fact, do not provide useful information on the position where the decay took place. The energy window should be checked prior to every patient study to ensure that the correct one has been selected and that the photopeak is centred within the energy window.

Instability of the PMTs or variation (drift) in the high voltages applies to the PMTs can result in both poorer energy resolution and/or a shift in the position of the photopeak. Energy resolution is discussed in Sect. 11.7. Energy peaking should be checked daily for all radionuclides that are used clinically. For isotopes that emit low-energy photons such as ^{99m}Tc and ^{57}Co, the centroid position of the photopeak should correspond within $\pm 3\%$ to the nominal photon energy for that isotope (140.5 keV for ^{99m}Tc and 122 keV for ^{57}Co).

Figure 11.2 shows the possible effect of selecting a wrong energy window (e.g., for ^{57}Co instead of ^{99m}Tc) or of a shift of the energy window relative to the actual photopeak. In both the cases, many of the events lying within the energy window will actually be scattered photons, resulting in degradation of diagnostic information.

Ideally, the peaking QC test should be performed without the collimator to avoid the contribution of scattered photons in the collimator using a setup similar to that depicted in Fig. 11.4. However, for practical reasons, this test can also be performed with the collimator attached and
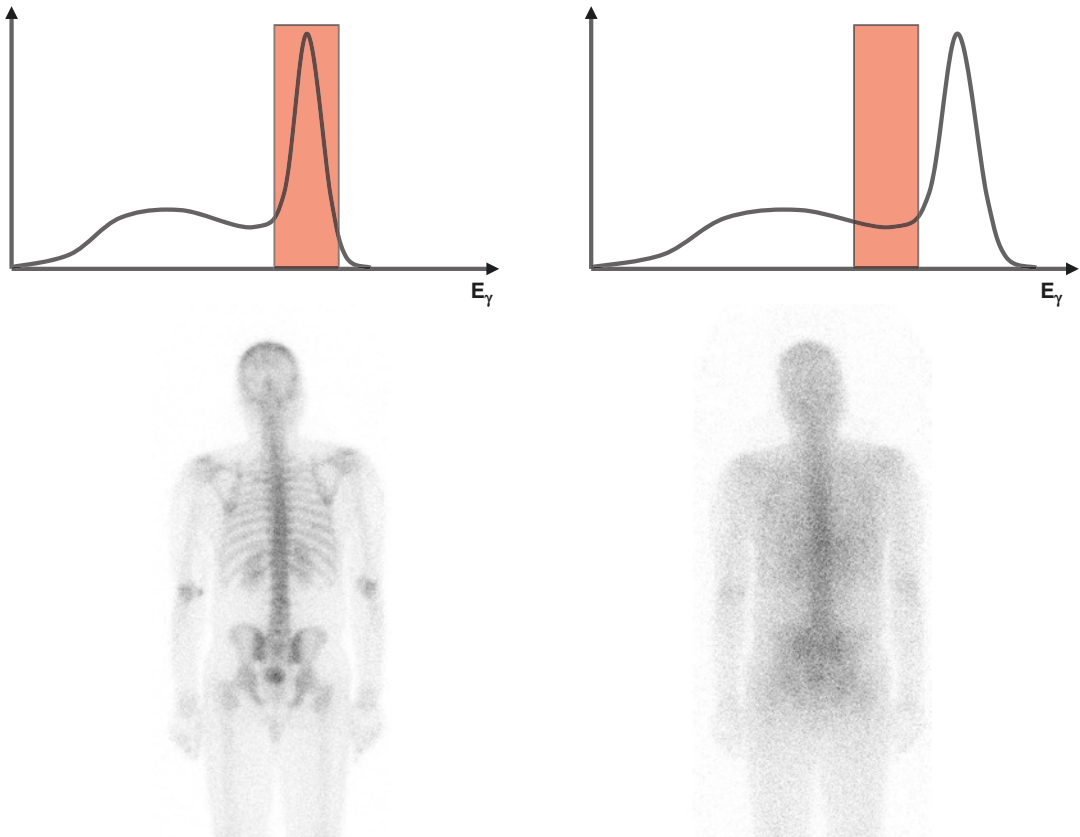
Fig. 11.2 Correct energy (E_γ) peaking (left-hand figures) and the effect of incorrect peaking (right-hand images)

using a flood source of ^{57}Co or ^{99m}Tc. Modern gamma cameras usually include peaking as an automated daily QC test.

11.6 Uniformity

An image acquired with a gamma camera should reflect the actual activity distribution within the patient or other source. The aim of the uniformity test is to assess the position-dependent variation of the observed count distribution within the image when the detector is exposed to a uniform flux of photons. This test can be performed without the collimator (*intrinsic uniformity*) or with the collimator attached to the gamma camera head (*system uniformity*). Both the tests can help to identify non-uniform detection sensitivity over the detector caused, for example, by unbalanced PMT outputs, outdated or corrupted corrections,

imperfections in the NaI(Tl) crystal or problems with the optical coupling between the PMTs and the crystal. Because system uniformity is performed with the collimator attached to the detector, this test can additionally detect other causes of non-uniformity, such as collimator defects due to, for example, damaged septa or variable sizes and/or angulation of the apertures.

Either intrinsic or system uniformity of the gamma camera should be tested daily, before its clinical use. The choice will depend on the particular gamma camera make and model. Additionally, both the tests should be performed with high-count statistics on a regular basis, for example, monthly.

When acquiring the image for a uniformity test, the matrix size should be large (e.g., 512×512). This allows a qualitative, visual assessment of image uniformity. However, for a quantitative evaluation of uniformity, the statisti-

cal error associated with each pixel count needs to be minimized. For this reason, the image is first re-binned to a coarser matrix size. The final matrix size on which calculations are performed is such that the pixel size has a dimension of approximately 6.4 mm. This will significantly increase the number of counts in each pixel and therefore reduce the associated statistical error. To further reduce the noise level, a smoothing of the image by convolution with the following 9-point filter function is performed:

$$\begin{bmatrix} 1 & 2 & 1 \\ 2 & 4 & 2 \\ 1 & 2 & 1 \end{bmatrix} \tag{11.1}$$

Integral uniformity (IU) is a measure of the global variation of pixel counts over the image. It is calculated on the UFOV and CFOV from the maximum and minimum pixel values (C_{max} and C_{min}, respectively) anywhere within these respective FOVs, according to the following equation:

$$\text{IU}(\%) = \frac{C_{max} - C_{min}}{C_{max} + C_{min}} \times 100(\%) \tag{11.2}$$

While integral uniformity reflects global non-uniformities in the image, differential uniformity (DU) is a measure of local variations of pixel counts. To measure differential uniformity, all possible combinations of five consecutive pixels (i.e., 5 × 1 pixel ROIs), both in the x- and y-directions of the image, are considered within the UFOV or CFOV (see Fig. 11.3). For each one of these combinations, differential uniformity is calculated as

$$\text{DU}(\%) = \frac{C_{high} - C_{low}}{C_{high} + C_{low}} \times 100(\%) \tag{11.3}$$

where C_{high} and C_{low} are the highest and lowest pixel values for all 5 × 1 pixels ROIs over the entire UFOV or CFOV. The highest of the values obtained for all the combinations of five consecutive pixels will be reported as the differential uniformity in the UFOV or CFOV. These calculations can be easily performed with software usually supplied by the vendor on gamma camera workstations.

Because of the statistical error (noise) associated with each pixel count in the image, an IU or DU of 0% can never be achieved in practice.

11.6.1 Intrinsic Uniformity

Intrinsic uniformity is measured by removing the collimator from the gamma camera head and acquiring an image of a point source (typically ^{99m}Tc or ^{57}Co) placed in front of the centre of the detector. When the source-to-detector distance is
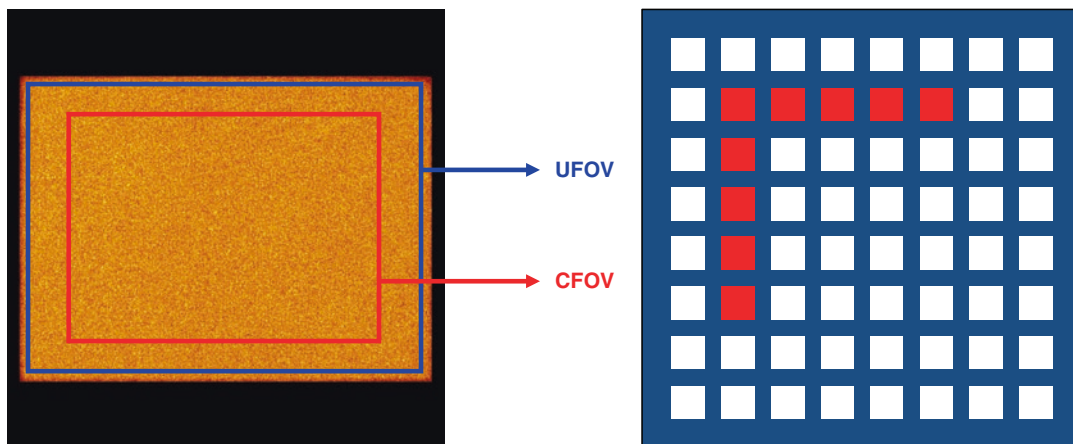
Fig. 11.3 A uniformity, or 'flood', image illustrating the UFOV and CFOV (left-hand figure) and sample 5 × 1 pixel ROIs used to calculate the differential uniformity (right-hand image)

at least five times the larger dimension of the crystal UFOV, the detector is irradiated with a sufficiently uniform photon flux (within less than 1%). Because of the absence of the collimator, relatively low-activity sources—of the order of a few tens of MBq—would result in count rates that are high enough to obtain the desired count statistics (e.g., 5–10 Mcounts) within a reasonable acquisition time. Attention must be paid to the count rate, which should not exceed 20 kcps. Sources can be shielded with copper plates to eliminate lower-energy scattered photons impinging on the detector, as shown in Fig. 11.4.

Imaging rooms are sometimes not large enough to allow the setup depicted in Fig. 11.4, and the source can only be placed closer to the detector. In this case, the flux of photons on the detector surface will no longer be uniform. Because of the inverse-square law, the flux of photons and therefore the counts in the acquired

image will be higher in the centre and decrease towards the peripheral of the image. Such an image can still be used to evaluate the intrinsic uniformity of the system according to Eqs. (11.2) and (11.3), but only with software correction for the inverse-square-related variation of the counts in the image (Fig. 11.5).

11.6.2 System Uniformity

The measurement of intrinsic uniformity is more sensitive than measurement of extrinsic uniformity in detecting non-uniformities, but it is unable to detect non-uniformities caused by the collimator. For this reason, it is important to assess also system uniformity, measured with the collimator attached to the detector. Because of the presence of the collimator, it is not possible to use a point source for this test. Instead, a flood
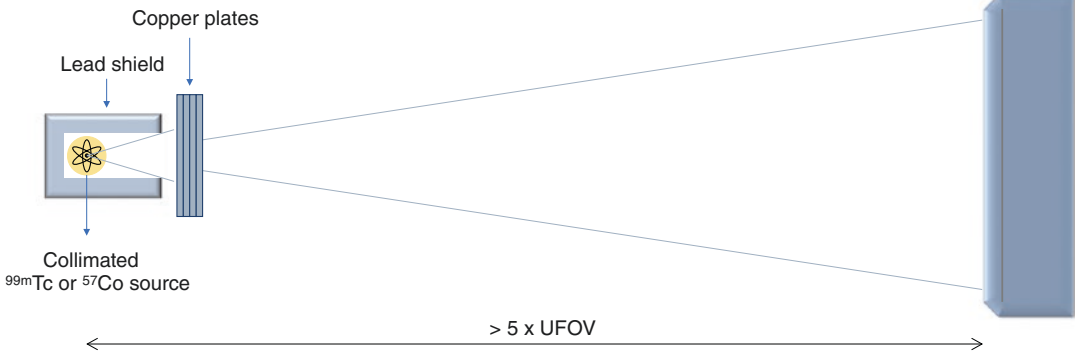
Fig. 11.4 Source–detector configuration for the evaluation of gamma camera intrinsic uniformity
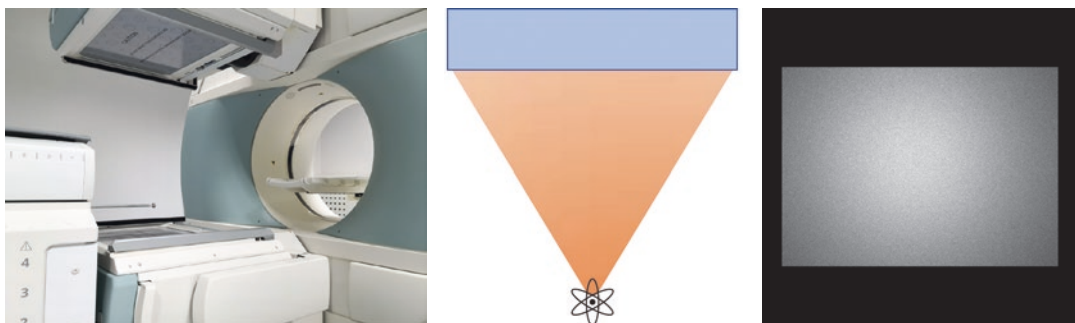
Fig. 11.5 Evaluation of gamma camera uniformity with a short source–detector distance and corresponding inverse-square-related effects
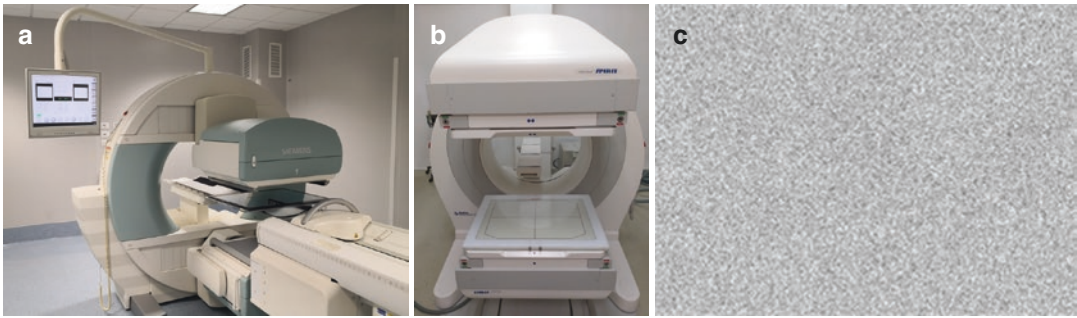
Fig. 11.6 (**a**) ^{57}Co and (**b**) fillable flood sources in position for the evaluation of gamma camera uniformity and (**c**) sample flood-source image. [(**b**) courtesy of L. Torres Aroche (CENTIS, Cuba)]

source containing a uniform distribution of activity and having an active area larger than the detector is required. One option is to use a fillable flood phantom (Fig. 11.6). This can be filled, for example, with uniform solution of ^{99m}Tc. The activity used can be about 400 MBq, keeping in mind that the count rate should not exceed 20 kcps.

The advantage of using a fillable flood phantom is that the gamma camera can be tested with ^{99m}Tc, which is the most widely used isotope in nuclear medicine. However, obtaining a homogeneous distribution of activity within the phantom is not simple and at the same time can raise radiation protection concerns due to its preparation. A well-accepted alternative is to use a commercially available ^{57}Co flood source, where ^{57}Co is bound to a resin and distributed uniformly. These are produced by manufacturers with a certified uniform distribution of activity (usually within 3%) and an initial activity of 370 or 740 MBq (10 or 20 mCi). The gamma photopeak of ^{57}Co is at 122 keV, which is similar to that of ^{99m}Tc at 140.5 keV, making this isotope a good surrogate of ^{99m}Tc.

Uniformity is an essential daily test of system performance, and a ^{57}Co flood source allows to perform this test quickly and safely prior to patients' examinations. The only real disadvantage of ^{57}Co is its relatively short half-life of 272 days, thus requiring a replacement of the source after 1–2 years and its associated cost.

11.6.3 Whole-Body Scanning Uniformity

Whole-body scanning involves continuous translation of the patient relative to the gamma camera system to acquire a single image of the distribution of a radiopharmaceutical over the patient's entire body. This may be achieved by translating the patient through the stationary gantry or translating the gantry over the stationary patient. In either approach, the relative motion of the patient's bed and gantry conceivably may degrade image quality with respect to that of a static, or spot, image. Uniformity of response may be evaluated by acquiring a whole-body scan of, for example, a ^{57}Co flood source, placing the source on the patient palette at the beginning position of the scan, quickly moving it to the middle position of the scan (immediately after the entire source at the beginning position has been imaged), and then moving it to the ending position of the scan (immediately after the entire source at the middle position has been imaged) (see Fig. 11.7). Equal-size ROIs (dashed red rectangles in Fig. 11.7) are then placed over the three resulting images of the flood source and the whole-body scanning uniformity calculated according to Eq. (11.2), where C_{max} and C_{min} are the maximum and minimum total counts among the three equal-size ROIs shown in Fig. 11.7.
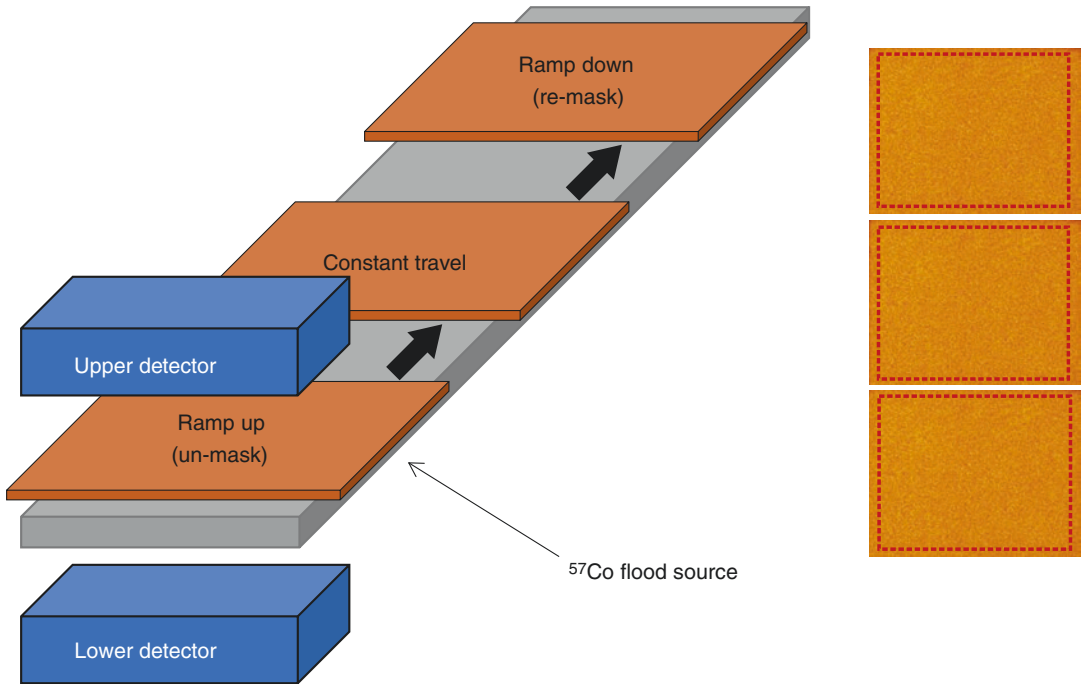
Fig. 11.7 Evaluation of whole-body scanning uniformity using a ^{57}Co flood source

11.7 Energy Resolution

Events that are scattered before being detected by the gamma camera do not provide accurate information in the image, as the positions of such events do not reflect the actual distribution of activity in the patient. The strategy that is used to reduce the presence of scattered radiation in a gamma camera image is to reject all the events having an energy lying outside a predefined energy window (see Sect. 11.5). Figure 11.8 represents a typical energy spectrum of a gamma camera from a ^{99m}Tc source and an energy window of ±10%. Better energy resolution (corresponding to a narrower photopeak) allows for a reduction of the energy window width without loss in detection efficiency for unscattered radiation, thus improving discrimination of scatter and unscattered events (further details on scatter correction can be found in Chap. 18).

Energy resolution is a measure of the ability of a detector to distinguish gamma rays of different energies. It is quantitatively expressed in terms of the full-width half-maximum (FWHM) of the photopeak in the energy spectrum and is typically expressed as a percentage of the photopeak energy. Energy resolution depends on the energy of the photopeak, and, when expressed in terms of a percentage of the photopeak energy, it is inversely proportional to the square root of energy. For the photopeak energy of ^{99m}Tc (140.5 keV) or ^{57}Co (122 keV), energy resolution is typically 10% or slightly better (lower) for NaI(Tl) scintillation detectors. This parameter is mainly determined by the physical characteristics of the detector and should not rapidly change with time. The worsening of energy resolution may indicate sub-optimal tuning of PMTs or a degradation of the detector.

The setup used to measure energy resolution is the same as for the intrinsic uniformity test described in Sect. 11.6.1. Modern systems can display the energy spectrum acquired and may include a software for the evaluation of the FWHM energy resolution. When such a feature is not available, the spectrum data should be saved and analysed offline by fitting the photopeak with a Gaussian function, as shown in Fig. 11.8.

Fig. 11.8 Gamma camera energy spectrum with the photopeak fit to a Gaussian function. The fitted function can be used to evaluate the FWHM energy resolution
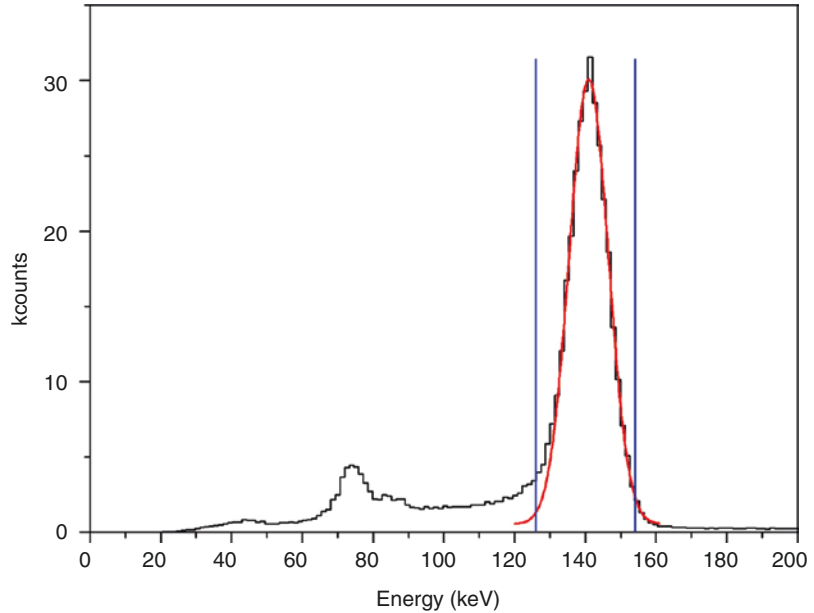
11.8   Spatial Resolution

Spatial resolution reflects the ability of a gamma camera to visually distinguish spatially separated radioactive sources. Coarse spatial resolution would result in poor visualization or reduced contrast between radioactive sources, compromising image quality and the diagnostic capability of the imaging system. The level of detail present in a clinical image is dependent on both intrinsic and collimator spatial resolution. These two components sum in quadrature, resulting in the system spatial resolution.

11.8.1   Intrinsic Spatial Resolution

Intrinsic spatial resolution is a measure of the capability of the detector to correctly assign the position of an event within the scintillation crystal, which is limited by the statistical fluctuation of light photon distribution among the PMT photocathodes and of PMT amplification, as well as by multiple scattering of gamma photons within the detector. It can be improved, for example, by using a thinner crystal (which would cause less light dispersion among the PMTs) or a larger number of smaller-area PMTs.

Intrinsic spatial resolution is measured by using a lead mask with parallel slits as shown in Fig. 11.9. The slits are 3 cm apart from each other, and their width is small compared to the expected FWHM intrinsic spatial resolution. Intrinsic spatial resolution should be evaluated in both *x*- and *y*-directions. The source used is a ^{99m}Tc point source placed at a distance from the detector at least five times the larger dimension of the UFOV.

Because the lead mask needs to be mounted on the gamma camera head, it is make and model specific and not always available in a typical nuclear medicine department. This test is therefore not always routinely performed, but should be performed during acceptance of a newly installed system.

Typical FWHM values of intrinsic spatial resolution of modern gamma cameras are less than 3 mm. The collimator further degrades spatial resolution with a contribution that increases with increasing source-to-collimator distance. Since the FWHM collimator resolution is considerably larger than 3 mm at a distance of 10 cm, the resulting system spatial resolution at practical imaging distances (i.e., for source regions at any significant depth in patients) is dominated by the blurring effect of the collimator.
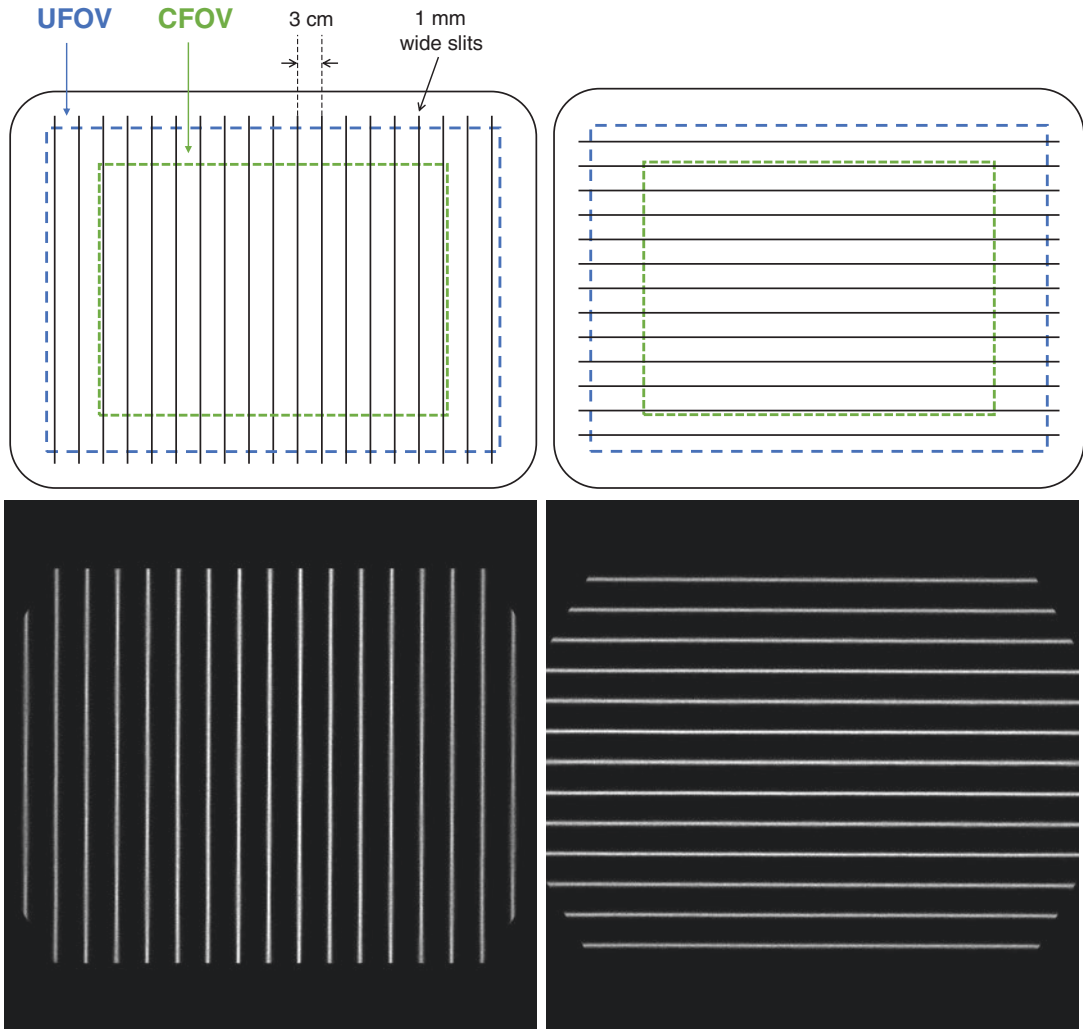
Fig. 11.9 Slit phantom (upper panels) for the measurement of gamma camera intrinsic spatial resolution in the *x*-direction (left-hand images) and in the *y*-direction (right-hand images) and slit-phantom transmission images (lower panels)

11.8.2 Four-Quadrant Bar Phantom

A quantitative assessment of intrinsic spatial resolution from an image obtained with a four-quadrant bar phantom (Fig. 11.10), with radiopaque lead bars and intervening radiolucent plastic strips 2, 2.5, 3 and 4 mm in width, can be performed with the method proposed by Handler [12]. Briefly, a 'point' source of ^{99m}Tc is placed at distance from the detector equal to five times the larger UFOV dimension and centred over the uncollimated detector, with the phantom placed directly over the detector. A 5- to ten-million-count transmission image is then acquired and visually inspected. The lead bars should be visually resolvable at least in the two coarsest quadrants (i.e., with the 3- and 4-mm-wide bars). For modern gamma cameras, the lead bars in the third coarsest quadrant (i.e., with the 2.5-mm-wide bars) should be visible as well. This approach also allows an estimation of the Modulation Transfer Function (MTF) for the spatial frequencies corresponding to the different bar thicknesses in the four sectors of the phantom.
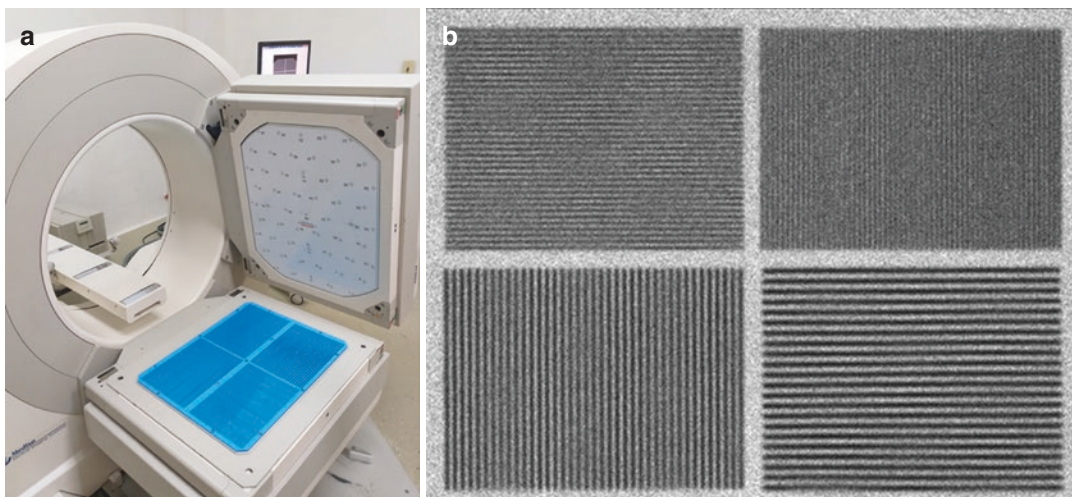
Fig. 11.10 (**a**) Four-quadrant bar phantom in position for imaging and (**b**) the resulting transmission image of the phantom. [(**a**) Courtesy of L. Torres Aroche (CENTIS, Cuba)]

11.8.3 System Spatial Resolution

System spatial resolution characterizes the overall capability of the gamma camera to detect the details and identify the features of interest in an image under conditions that are similar to those encountered in the clinical practice. This should be measured for different isotopes and collimators.

System spatial resolution can be easily estimated quantitatively using line sources and subsequent analysis of the resulting line spread function (LSF). The system spatial resolution R_s of a gamma camera depends on the intrinsic spatial resolution R_i, and the collimator spatial resolution R_c according to the equation $R_s = \sqrt{R_i^2 + R_c^2}$. R_i has values that are typically in the range of 2.5–3 mm, as noted, while the contribution to spatial resolution given by the collimator varies significantly with the source-to-collimator distance. For this reason, this test needs to be performed with the source carefully positioned at a specified distance from the collimator. International guidance documents [5] recommend a source-to-collimator distance of 10 cm, which is a realistic value in a clinical setting. Under these conditions, the contribution to spatial resolution of the collimator dominates and will depend on the geometric characteristics of the collimator.

The line source used for this test can be a capillary or a tube with internal diameter smaller than 1 mm, a dimension which is small enough compared to the expected values of R_s (in the range of 7–13 mm depending on the collimator), and thus not resulting in an overestimate of R_s. The line source is usually filled with a solution of ^{99m}Tc having an activity concentration high enough to yield an adequate count rate (e.g., ~ 400 MBq/mL) to collect a statistically reliable number of counts in a reasonable acquisition time (i.e., no longer than several minutes). A profile of the measured counts per pixel as a function of position across a line source can be obtained from the image either with software tools usually available on the gamma camera workstation or with third-party image-processing software [13, 14]. This profile represents the LSF of the source and can be fitted with a Gaussian function, as shown in Fig. 11.11. The system spatial resolution can be then easily derived from the fitting parameters obtained.

The matrix size should be chosen, so that the pixel size is small enough compared to the expected system spatial resolution to allow adequate spatial sampling and accurately define the LSF. Normally, a pixel size of ~1 mm is adequate.

The system spatial resolution test can also be performed with two parallel line sources (left image
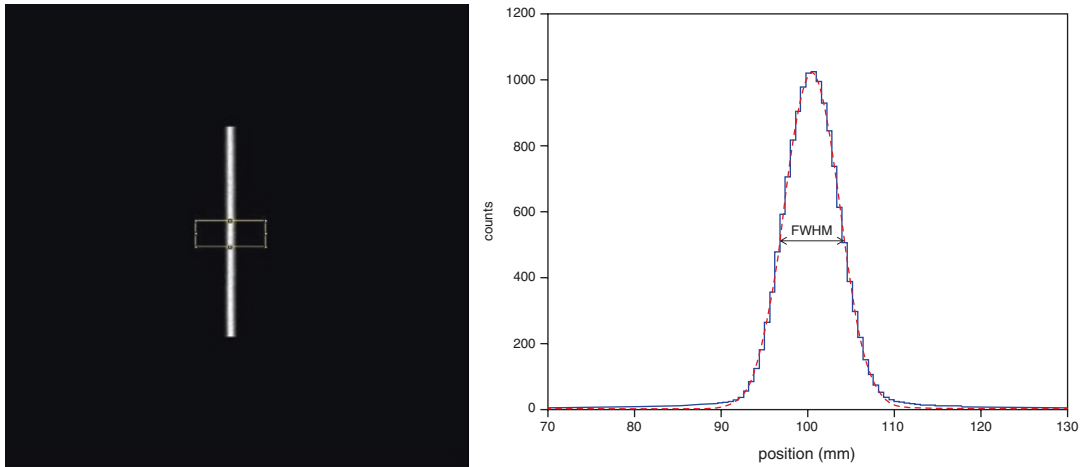
Fig. 11.11 A line source and its corresponding count profile (LSF) and FWHM system spatial resolution
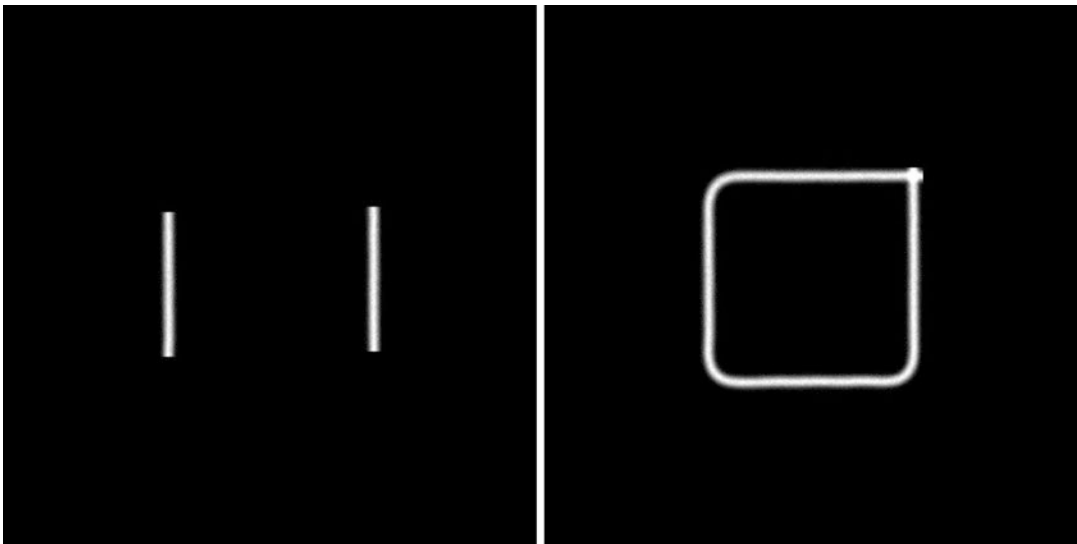
Fig. 11.12 Configurations of two parallel line sources for simultaneous measurement of spatial resolution and pixel size in the *x*-direction (left-hand image) and of four line sources (i.e., two pairs of parallel lines sources) for simultaneous measurement of spatial resolution and pixel size in the *x*- and *y*-directions

in Fig. 11.12). When the two sources are positioned at a known distance, this setup allows at the same time the measurement of the pixel size in one direction (see Sect. 11.12). System spatial resolution and pixel size must, of course, be measured in both the *x*- and *y*-directions. Therefore, two pairs of parallel line sources with the two sources in each pair placed a known distance apart can be used to perform these measurements for both directions with a single acquisition (right image in Fig. 11.12).

System spatial resolution can be estimated also with scattering medium surrounding the line source(s). The presence of scatter will degrade system spatial resolution (i.e., yield higher values of the FWHM). In fact, photons that are scattered at small angles lose only a small portion of their energy and may result in detected events with an energy that can still fall within the pre-set photopeak energy window. The difference in the measured system spatial resolution with and without

scatter is only due to the different interaction of photons with the medium surrounding the source and the composition and position, and the thickness of such a medium is highly variable in practice. The measurement with scatter does not add significant information to the performance of the gamma camera compared to the same test performed in air. For this reason, system spatial resolution measurements are normally performed without scatter, with the line source(s) in air.

11.8.4 Whole-Body Spatial Resolution

Spatial resolution for whole-body (WB) scanning can be worse than for static, or spot, imaging both in the *x*- and *y*-directions. Among other considerations, WB imaging relies on a mechanical movement at constant speed of translation of the patient bed (or, alternatively, of the gantry). Any deviation of the table speed from the specified value or mechanical misalignment would result in blurring, thus degrading WB spatial resolution.

WB spatial resolution can be tested by using line sources in the same configurations described in Sect. 11.8.3 for the system spatial resolution test, with the only difference that these sources have to be positioned on the patient palette as shown in Fig. 11.13. The analysis and reporting of the test data are also similar to those for spatial resolution generally.

11.9   System Planar Sensitivity

The statistical uncertainty (or 'noise') in a planar nuclear medicine image depends on the number of counts N in each pixel, with percent standard deviation (% SD) per pixel equal to $100\% / \sqrt{N}$. It is therefore important to have a high detection sensitivity to decrease noise in the image and thereby improve overall image quality and lesion detectability.

Sensitivity of a gamma camera is defined as the count rate per unit activity and is usually expressed in units such as counts per second (cps)/MBq or counts per minute (cpm)/µCi. It
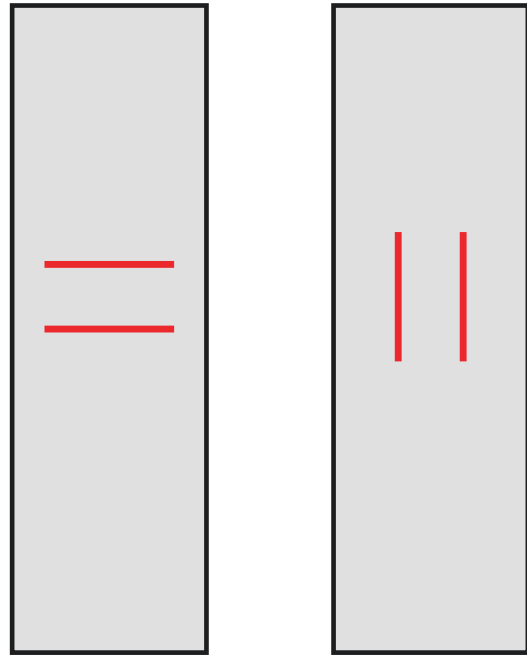
Fig. 11.13 Line source configurations (red lines) for the evaluation of WB scanning spatial resolution

increases with the detection efficiency, and therefore thickness, of the crystal and decreases with increasing photon energy. Sensitivity also depends on the width of the acceptance energy window, which should therefore be chosen to achieve the optimum compromise between sensitivity and scatter rejection capability. The collimator of a gamma camera is the major source of event losses in the final image. Sensitivity is thus highly dependent on the type of collimator used and its geometric efficiency, and the choice of the collimator has to be a compromise between good spatial resolution and high efficiency.

Sensitivity should be measured at acceptance for each isotope with the appropriate collimator and energy window. It is important to measure sensitivity regularly to make sure that the detection efficiency of the system is not degrading with time. However, this physical parameter should not vary rapidly with time and a half-yearly or yearly frequency is adequate for routine testing of sensitivity.

Sensitivity is usually measured by using a flat plastic dish (petri dish) having a diameter of

15 cm. This is placed at a 10 cm distance from the collimator and filled with a known activity of the isotope under consideration. The depth of the radioactive solution filling the dish should be several millimetres (2–3 mm), enough to ensure a homogeneous activity distribution, but shallow enough to minimize gamma rays self-absorption within the source (Fig. 11.14).

It is important to know accurately the activity of the solution in the dish at the time of acquisition. The size and shape of such a dish source are incompatible with the measurement of its activity in a standard activity meter (or dose calibrator). Therefore, the initial activity in the syringe used to fill the dish should be measured with a properly calibrated activity meter. Moreover, residual activity in the syringe after filling should also be measured and all measured activities decay-corrected to the time of acquisition.

The activity used should be high enough to be accurately measured with the activity meter, but low enough to give a count rate not exceeding 20 kcps. It can, for example, be of the order of tens of MBq, thus requiring only a few seconds to obtain sufficient count statistics. For such durations, considering the typical half-lives of the isotopes used in clinical practice, decay correction during acquisition is therefore not necessary.

The number of counts in the whole image (or in a circular ROI big enough to include most of the count events) is divided by the acquisition time to obtain the total count rate, R_{tot}. This count rate can be corrected for background, by sub-tracting the background count rate, R_{bkg}, measured by acquiring an image with no radioactive sources near the gamma camera that may affect its value. The background-corrected count rate is finally divided by the source activity A at start of acquisition time to obtain sensitivity in cps/MBq or cpm/µCi:

$$\text{Sensitivity} = \frac{R_{tot} - R_{bkg}}{A} \qquad (11.4)$$

11.10 Count Rate Performance

After each event detected by the gamma camera, the system cannot register subsequent events for an ensuing time interval τ referred to as the 'dead-time'. In a typical gamma camera, any subsequent event detected during the dead-time interval τ is not recorded and will also extend the duration of the non-responsiveness of the system further by a time τ. Gamma cameras, like most radiation detectors, are thus paralysable systems. When such systems are exposed to an increasing flux of photons, the measured count rate initially increases in proportion to the photon flux (i.e., the true count rate), reaching a maximum count rate and subsequently decreasing as the true count rate continues to increase.

Figure 11.15 graphically displays the non-linearity in the relationship between the measured and true count rates; the latter reflects the intensity
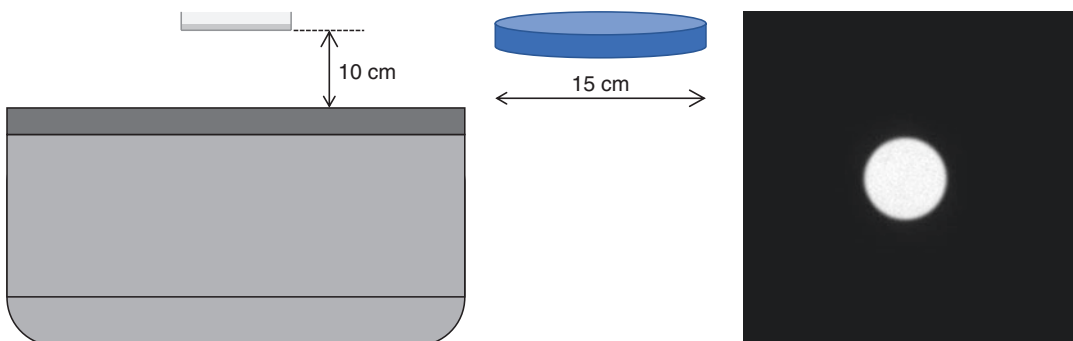
Fig. 11.14 Source configuration (left-hand and middle figures) and source image (right-hand figure) for the measurement of gamma camera sensitivity

Fig. 11.15 The measured count rate R_{meas} as a function of the true count rate R_{true} for a paralysable detector such as a gamma camera. The maximum measured count rate, R_{max}, and the measured count rate corresponding to a 20% loss relative to the true count rate, $R_{-20\%}$, are indicated
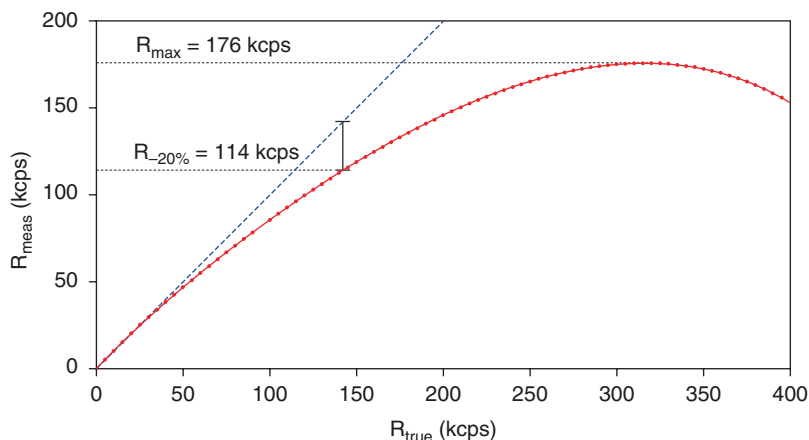
of incident gamma radiation on the crystal surface. The purpose of the count rate QC test is to measure the maximum observed count rate, R_{max}, and the measured count rate corresponding to a 20% loss relative to the true count rate, $R_{20\%}$. The true count rate can be obtained by extrapolating the measured count rate for low count-rate values, for which dead-time count losses can be considered negligible. Different methods can be used to obtain the curve shown in Fig. 11.15.

The decay method consists of using a point source of ^{99m}Tc at a sufficiently long distance to uniformly irradiate the uncollimated detector, with a configuration similar to that in Fig. 11.4. The activity of the source should be high enough to yield a true count rate higher than that corresponding to the maximum observed count rate in Fig. 11.15. A series of acquisitions is performed over 2 days to allow decay of the source activity over the course of the acquisitions. After reaching its maximum value, the observed count rate starts decreasing with decreasing activity. Data collection should be stopped when the observed count rate reaches several kcps. The duration of the acquisitions should be adjusted and increased as the source decays to acquire a statistically reliable number of counts (>1 and preferably ~10 kcounts). Assuming the gamma camera is available (perhaps over the weekend), a dynamic acquisition, with an appropriate starting time and frames durations chosen, is useful, as the test can last for 2 days.

An alternative method makes use of copper absorber sheets 0.25 cm in thickness interposed between the source and the detector but the configuration otherwise similar to that used for the decay method. The curve in Fig. 11.15 is in this case obtained by adding one copper sheet at a time, thus reducing the photon flux reaching the detector. This method is obviously faster than the decay method but requires an accurate calibration of the attenuation factors of each copper sheet.

The maximum value of the observed count rate can also be determined by slowly moving the source towards the detector. With decreasing source-to-detector distance, the photon flux impinging on the detector increases, and the observed count rate will change in a manner similar to that in Fig. 11.15. This method, however, can be used to measure only the maximum count rate observed, R_{max}, but not the 20% loss count rate, $R_{-20\%}$.

11.11   Multiple Window Spatial Registration

Some of the radionuclides used in nuclear medicine have more than one photopeak in their energy spectrum. When the relative intensities (branching ratios) of these gamma emissions is significant, it can be convenient, in order to increase image count statistics, to accept all events corresponding to more than one photopeak. In this case, acquisitions will be performed by accepting counts from multiple energy win-

dows, each one being centred on the corresponding photon energy in the energy spectrum. Two acceptance energy windows are also used for dual-isotope imaging.

Examples of radionuclides that can be acquired with multiple energy windows with their corresponding photopeaks are [67]Ga (93, 184.5, 300 keV), [111]In (171, 245 keV) and [201]Tl. [201]Tl has a complicated decay scheme with five photopeaks close to each other in the range 69–82 keV and one photopeak at 167 keV. Different protocols can be adopted for ^{201}Tl, but all have in common the use of two acceptance energy windows, one at 167 keV and a second one set at a lower energy to capture the photons in the 69–82 keV energy range.

During the acquisition of a clinical image with multiple energy windows, all the events detected with an energy within one of the energy windows will be added as counts to the image. This is predicated on the ability of the gamma camera to accurately register the position of photons regardless of their energy. The multiple window spatial registration QC test verifies the accuracy of this by acquiring separate images for each energy window of point sources at different positions on the detector. The test can be performed both intrinsically, by using a vial source in a lead shield having a small (e.g., 3 mm) circular aperture that is moved on the detector surface, or extrinsically, by using point sources placed in different positions on the collimator. The difference of the *x*- and *y*-centroid position of a source as measured in the respective images acquired with different energy windows should not exceed 1 mm.

11.12 Pixel Size

The accuracy of the pixel size values in both the *x*- and *y*-directions should be tested for different matrices and zoom factors. This test can be easily performed by using two or four point sources placed at a known distance apart in the *x*- and *y*-directions (Fig. 11.16). The distance between the point sources should be greater than 10 cm and measured with an accuracy of 1 mm or better. The centroid positions of the point-source count profiles in the image can be used to compute the percentage difference between the measured (i.e., image-derived) distance and the actual distance between the point sources. This is equal to the percentage difference between the actual pixel size and the pixel size value stored in the DICOM header. The accuracy of the pixel size is important in extracting the dimensions of organs and tumours from images and in correcting SPECT images for the effects of attenuation.

The QC test of pixel size can also be performed simultaneously with the system spatial resolution test as described in Sect. 11.8.3.

11.13 Inter-Detector Sensitivity Variation

A tomographic reconstruction of a SPECT acquisition performed with a dual-head system and 180-degree gantry rotation relies on the fact that the sensitivity of the two detectors is identical. If the sensitivities of the two detectors are different, the projection images from the detector having
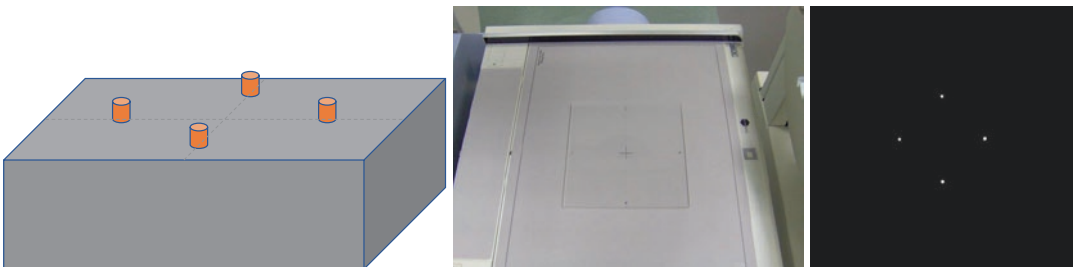
Fig. 11.16 Source configuration for measurement of pixel size (left-hand and middle figures) and the resulting four-source image (right-hand figure)

lower sensitivity will yield an underestimation of activity for those projections. This will ultimately result in poorer image quality and image artefacts. For this reason, it is important to routinely check dual-head systems for the inter-detector sensitivity difference.

One method to assess this difference is simply to use the results of the QC test of sensitivity described in Sect. 11.9. Alternatively, a flood source can be used to assess the inter-detector sensitivity difference over the UFOVs of the two detectors. The difference in sensitivity between the detectors of a dual-head system should not exceed 5%.

11.14   Centre of Rotation (COR)

The image reconstruction algorithms used in SPECT assume that the axis of rotation of the gamma camera is always centred in the image for each projection angle. However, because of the weight of the detectors and collimators and the mechanics of rotation, the gantry undergoes severe mechanical stress. These can create at certain projection angles a mismatch between the 'electronic' centre of rotation as seen by the detector and the actual 'mechanical' centre of rotation. For this reason, it is important that the centre-of-rotation (COR) alignment is routinely checked for each collimator set and for different detector configurations and the COR calibration updated as needed. COR alignment should be checked weekly or monthly.

The COR calibration is usually performed by using a point source of ^{99m}Tc positioned in the FOV with an offset of 2–3 cm from the axis of rotation, and a tomographic acquisition with a total gantry rotation of 360°. As the detector rotates, the position of the point source in the x-direction varies among the projection images. The trace of the lateral position (x-coordinate) of the source as a function of the projection angle can be fit with a sinusoidal function (Fig. 11.17). At the same time, the position of the source in the y-direction should be approximately constant, and deviations in the trace of the vertical position (y-coordinate) of the source as a function of the projection angle from a horizontal are a sign of detector tilt. Deviations of the source position in the x-direction from the fitted sinusoidal function and in the y-direction from the horizontal line yield a table of x- and y-direction offsets, Δx and Δy, respectively, as a function of angle which are used to shift the projection images in subsequently acquired SPECT studies. The COR calibration thus consists of a small shift adjustment of the projection image at each angle. A misalignment as small as 3 mm can produce perceptible blurring in reconstructed SPECT images. Therefore, if the mean value of the centre of rotation offset exceeds 2 mm, the newly measured offsets should be stored in an updated COR calibration file. With software available on modern SPECT system workstations, the measurement of COR alignment (i.e., of the Δx and Δy offsets) and, as necessary, the updating of the COR calibration file is straightforward and relatively quick.

The actual COR calibration procedure is vendor- and model-specific and may differ from the foregoing general procedure. Some SPECT systems require the use of more than one source

Fig. 11.17 Trace of the lateral position (x-coordinate) of the source (data points) versus the projection angle fit to a sinusoidal function (curve). Also shown are the best-fit parameters and the correlation coefficient for the fit

Sine Fit
y = a+b * sin(c*x + d)
a = 264.37059
b = 4.94916
c = −0.98810
d = 0.70249
R^2 = 0.9996
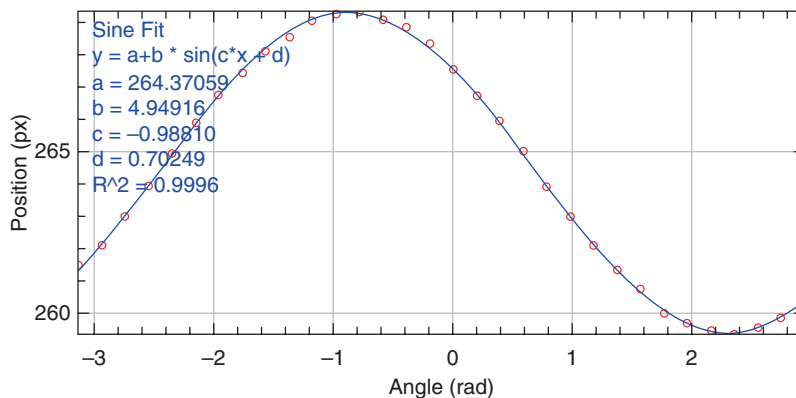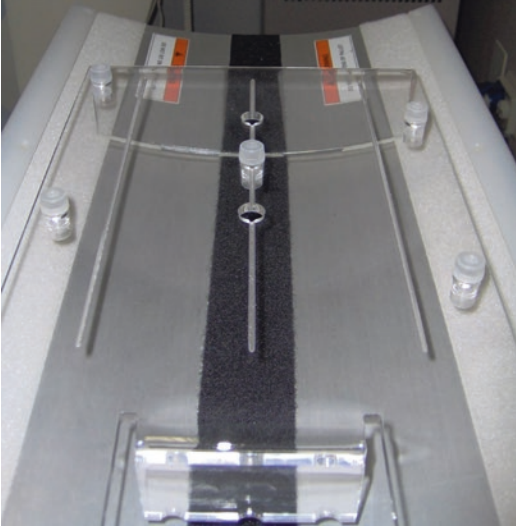
Fig. 11.18 Source and source-holder configuration for a proprietary method for the measurement and calibration of COR alignment

(see, for example, Fig. 11.18). A source holder is usually part of the system, and as noted, the software for COR measurement and calibration is provided on SPECT systems.

11.15 SPECT Performance

Different phantoms exist that can be used to assess the overall performance of a SPECT system. The most widely used of these is the 'Jaszczak' phantom (also known now as the American College of Radiology (ACR) phantom), shown in Fig. 11.19. This can be used to assess the quality of tomographic images, to identify COR calibration errors, to evaluate the accuracy of attenuation correction and to disclose the presence of artefacts in the reconstructed image.

The phantom can be filled, for example, with aqueous solution containing an activity of approximately 400 MBq of ^{99m}Tc. Care must be taken to obtain a homogeneous activity distribution within the phantom and to avoid air bubbles in the solution. The tomographic acquisition should be performed with a 128×128 matrix size and 3-degree angular steps, with a time per projection that should be adjusted to achieve good

count statistics (several hundred kcounts per projection). Auto-contouring should be used to allow for the smallest possible radius of rotation at each projection image. It is important to always use the same acquisition conditions and reconstruction parameters to compare the tomographic images and results with reference values.

The 'cold-rod' section of the Jaszczak phantom can be useful to assess tomographic spatial resolution (see Sect. 11.17). This can be done qualitatively by identifying the section with the narrowest rods in which the rods can be visually distinguished.

The solid spheres of a Jaszczak phantom can be used to evaluate contrast levels for cold lesions having different dimensions. The contrast can be calculated for each cold sphere as:

$$\mathrm{Contrast} = \frac{C_{\mathrm{bkg}} - C_{\min}}{C_{\mathrm{bkg}} + C_{\min}} \qquad (11.5)$$

where C_{bkg} is the average count level in the homogeneous section of the phantom and $C_{\min}$ is the minimum count within each of the cold spheres.

The homogeneous section of the Jaszczak phantom can be useful to assess tomographic uniformity and accuracy of attenuation correction, as described in Sect. 11.16.

11.16 Tomographic Uniformity

Tomographic uniformity reflects the variations in the observed count distribution (i.e., count per pixel) in the reconstructed image of a source with a uniform activity concentration. In general, when an accurate attenuation correction is applied, good planar uniformity should translate into good tomographic uniformity. However, because of the reconstruction process and attenuation correction, tomographic uniformity is usually worse than planar uniformity. Moreover, a planar non-uniformity artefact is amplified during the reconstruction process and can result in prominent image artefacts [15].

Tomographic uniformity can be assessed using a cylindrical phantom filled with a homogeneous solution of ^{99m}Tc or another isotope. The
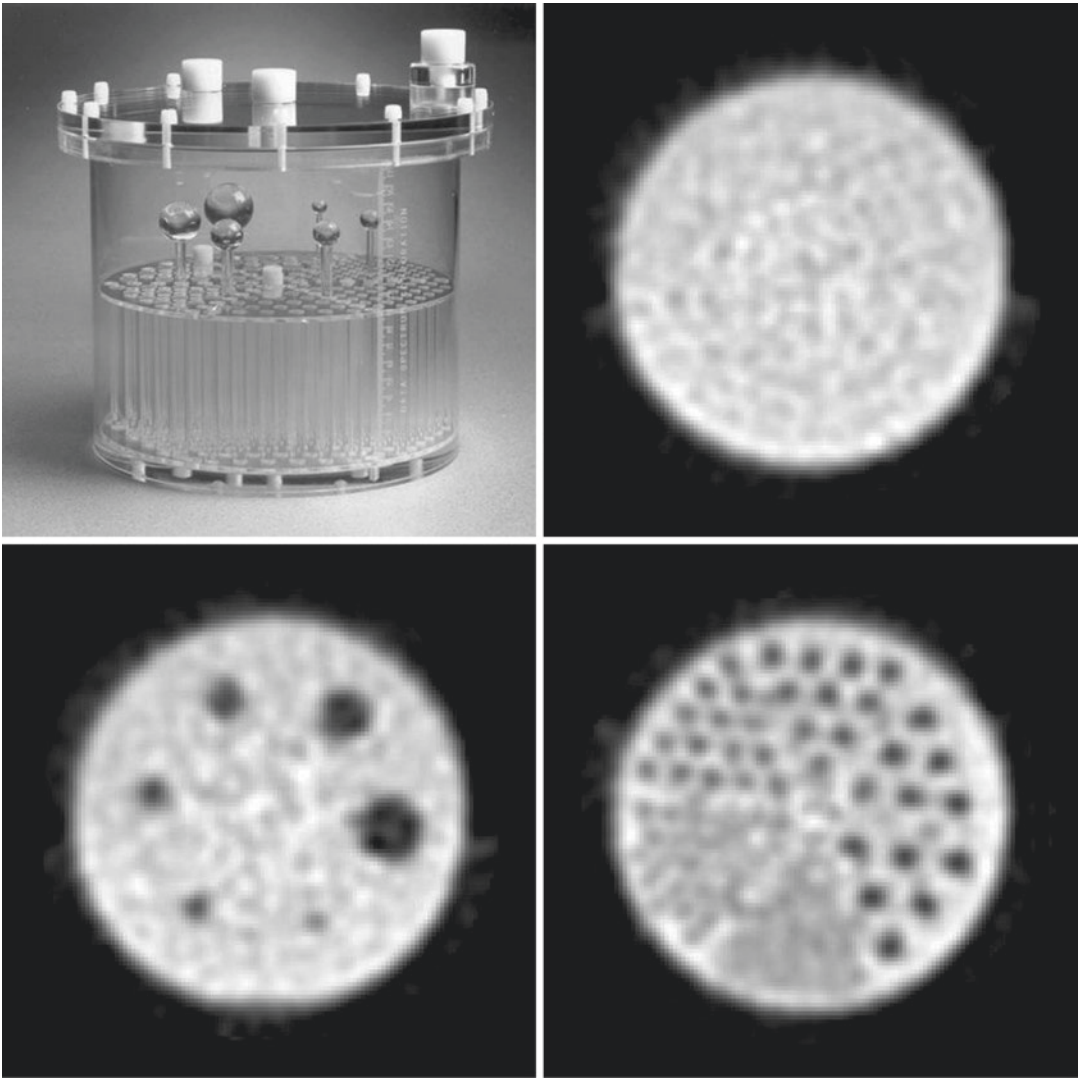
Fig. 11.19 Photographs of the assembled 'Jaszczak' (ACR) phantom (upper left-hand figure), with 'cold' (i.e., non-radioactive) spheres, and a cold rods insert. This fillable PMMA phantom is 22 cm in diameter by 19 cm in length and includes a plain section for the evaluation of tomographic uniformity (upper right-hand image), a section containing solid (cold) spheres ranging from 9.5 to 31.8 mm in diameter for the evaluation of 'cold-sphere' contrast (lower left-hand figure) and a section containing solid (cold) rods ranging from 3.2 to 11.1 mm in diameter for the evaluation of reconstructed spatial resolution (lower right-hand figure). The tomographic images shown have been corrected for attenuation

Jaszczak phantom, for example, has a portion without inserts that is filled with a homogeneous radioactive solution and can be used for this purpose. The reconstructed attenuation-corrected image should be a circle with a uniform distribution of pixel counts as shown in Fig. 11.20. Tomographic uniformity is usually assessed qualitatively, but different approaches for a quantitative evaluation of tomographic uniformity are also available [16].

The tomographic uniformity test allows the user to assess the accuracy of attenuation correction. When attenuation correction is applied adequately, the mean count level in the centre of the
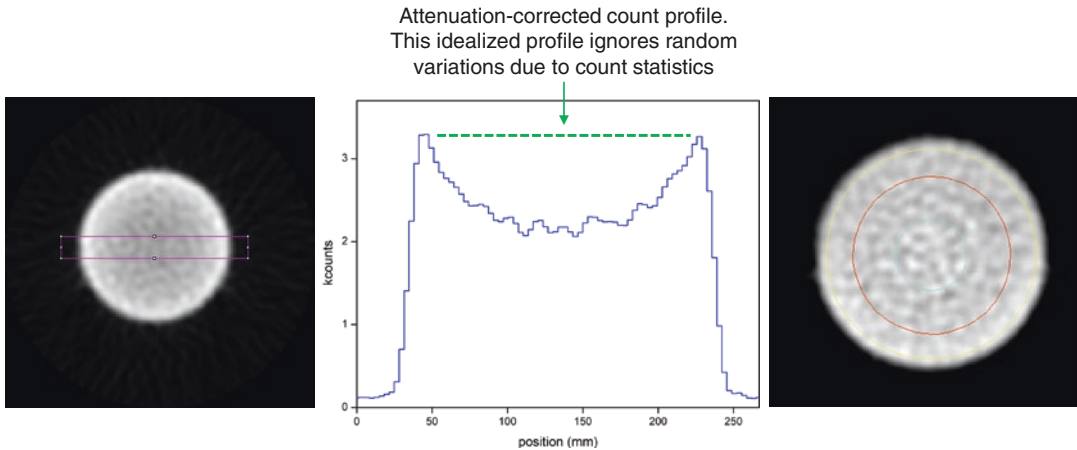
Fig. 11.20 A reconstructed transverse image through the homogeneous section of the Jaszczak phantom without attenuation correction (left-hand image). The image is noticeably less intense towards the centre than towards the periphery of the cylindrical phantom due to greater thickness of material that photons emitted from the centre of the phantom must traverse. Correspondingly, the count profile across the red rectangle superimposed on this image shows progressively fewer count per voxel from the periphery to the centre of the cylinder (middle image). With appropriate attenuation correction, this image appears uniform (right-hand image). Superimposed on this image are three concentric ROIs, a central circular ROI and two annuli. Without attenuation, the mean counts per voxel in the central circular ROI would be less than that in the inner-most annular ROI and the mean counts per voxel in that ROI would be less than that in the outer-most annular ROI. With attenuation correction, the mean counts per voxel in these three ROIs would be comparable

phantom image should be close to the mean count level towards the periphery of the phantom image. A profile along a line or within a thin rectangular ROI passing through the centre of the image should be approximately flat (apart from some random variations due to count statistics). Alternatively, one could consider the mean counts per voxel in concentric-rings (or annuli) ROIs, which should be approximately the same when attenuation correction is correctly applied. Any deviation from this ideal situation would be a sign of under- or over-correction for attenuation.

11.17 Tomographic Spatial Resolution

Tomographic spatial resolution reflects the ability of a SPECT system to resolve spatially separated radioactive sources in the reconstructed images. This depends on the planar spatial resolution, the radius (or radii) of rotation during the SPECT acquisition, the accuracy of the COR calibration, and the reconstruction process.

Tomographic spatial resolution for a given radius of rotation r is therefore usually worse than planar spatial resolution at a source-to-collimator distance $d = r$.

Tomographic spatial resolution can be measured with a point source having linear dimensions smaller than 1 mm. This allows the measurement of the in-plane (i.e., x- and y-directions) as well as axial (z-direction) spatial resolution. The voxel dimensions should be small compared to the expected FWHM spatial resolution.

Alternatively, one or more line sources can be used. Figure 11.21 shows a triple-line phantom where three line sources are inserted in a cylindrical phantom that can be filled with water as scattering material. Obviously, the use of such line sources (i.e., line source parallel to the axis of rotation) does not allow the measurement of tomographic spatial resolution in the z-direction. To measure z-direction resolution, one or more line sources perpendicular to the axis of rotation are needed, with the FWHM spatial resolution measured in the reconstructed coronal or sagittal images.

As noted, tomographic spatial resolution can also be evaluated qualitatively by identifying the smallest diameter rods in the rod section of a Jaszczak phantom that can be distinguished visually (see Fig. 11.19).

11.18 SPECT/CT Alignment

In multi-modality imaging such as SPECT/CT, it is important to ensure that there is an accurate alignment between the SPECT and CT image sets. An inaccurate co-registration of SPECT and CT images would affect not only the correct localization of SPECT and CT features but also
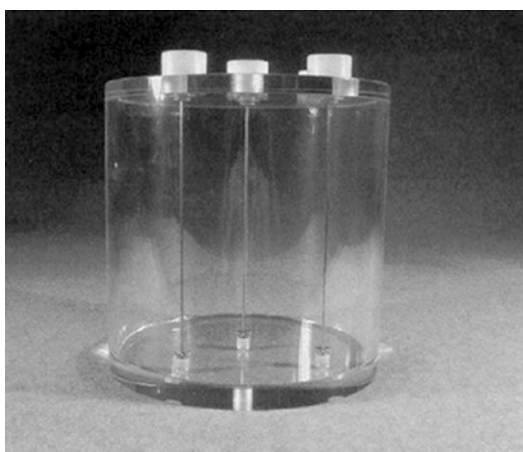
Fig. 11.21 Configuration of triple-line sources in a fillable phantom for evaluation of in-plane (i.e., *x*- and *y*-directions) tomographic spatial resolution

the accuracy of CT-based attenuation correction of SPECT images. At installation, the two systems are positioned at a known distance, and residual alignment differences are measured and software-corrected using co-registration calibration (i.e., rigid transform). Alignment of SPECT and CT images should be regularly checked as part of the QC programme.

Both the calibration and QC test of SPECT and CT alignment are usually performed using a procedure defined by the vendor as well as a vendor-provided specific phantom and analysis tool. The procedure and phantom can differ among vendors, but all of them have in common the use of radioactive plus radiopaque fiducial markers. The radioactivity in the fiducial marker is detected by the SPECT part of the system, while the radiopacity is clearly seen by the CT, and the two images can be used to assess any residual difference in the position of the marker.

Figure 11.22 shows three examples of setup used for the co-registration calibration and test, using either point sources or syringes.

Alternatively, the alignment of SPECT and CT images can be also assessed by using fillable spheres inserted into a Jaszczak phantom. These spheres can again be filled with a mixture of both radioactive and radiopaque solutions. The distance between the centre of mass of a radioactive sphere and the corresponding sphere centre as seen by the CT component can be used to quantitatively assess the accuracy of alignment of the SPECT and CT sub-systems. This test can
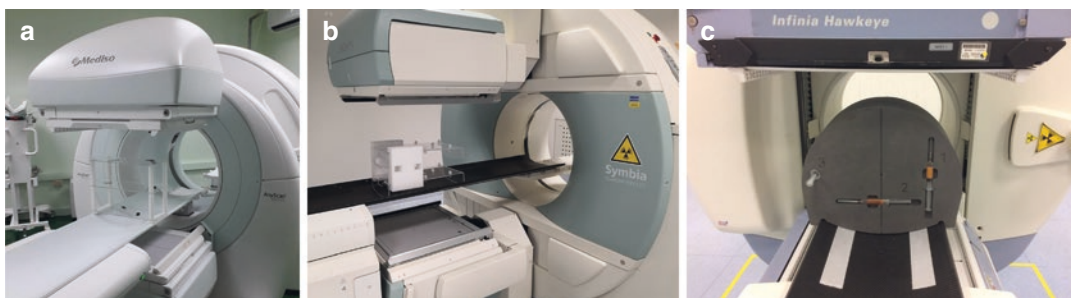
Fig. 11.22 Phantom configurations for the evaluation of SPECT/CT alignment using point fiduciary markers (**a** and **b**) and syringe fiduciary markers (**c**). (**a**) Mediso Spirit (courtesy of L. Torres Aroche (CENTIS, Cuba)). (**b**) Siemens Symbia T (courtesy of P. Colleoni (ASST Papa Giovanni XXIII, Italy)). (**c**) GE Infinia Hawkeye (courtesy of E. De Ponti (ASST Monza, Italy))

Fig. 11.23 CT transverse image of a water-filled phantom used for daily QC of a CT scanner (left-hand figure). The absence of visually perceptible ring, streak or other artefacts confirms that the uniformity is satisfactory. ROIs used for daily evaluation of CT number accuracy and noise (right-hand figure)
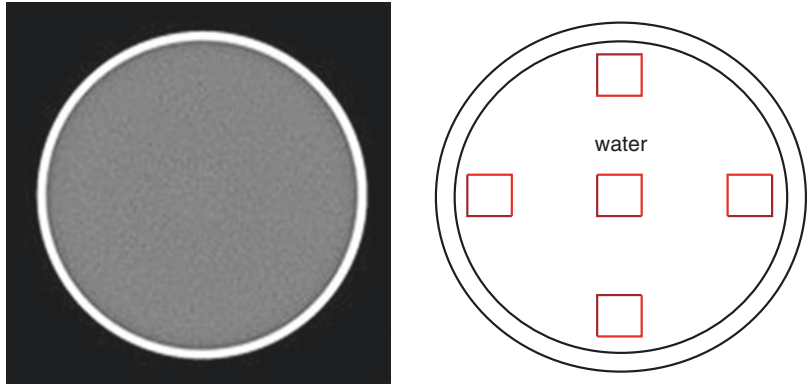
be performed with and without a weight on the bed to simulate a patient and assess if and how such a weight affects accuracy of image co-registration.

11.19 CT Testing

CT scanners have, of course, been in widespread clinical use long before their incorporation into multi-modality devices (such as SPECT/CT scanners), and detailed protocols for acceptance testing and evaluation of numerous performance parameters are well established [17]. However, less rigorous and less extensive procedures are generally performed for routine QC of the CT component of SPECT/CT scanners.

11.19.1 Tube Warmup

Daily testing of a CT scanner begins with the manufacturer-prescribed X-ray tube warmup procedure and automatic monitoring, perhaps at various tube voltages (in kilovoltage peak, kV_p) and/or current (milliampere, mA) settings, of the tube output and detector response.

11.19.2 Uniformity and Artefacts, CT Number Accuracy and Noise

Assuming the operator has received the appropriate 'system-ready' message, the daily QC procedures are then performed. These include, at

minimum, evaluation of tomographic uniformity, the accuracy of the CT number of water and image noise, based on scanning a water-filled cylinder phantom (typically ~20 cm in diameter by ~20 cm in length). These parameters should be evaluated using a clinically routine set of scan parameters (i.e., X-ray tube voltage (kV_p), tube current-exposure time (in mAs), pitch, etc.). Acceptable image uniformity is confirmed by visual inspection (i.e., by verifying the absence of perceptible ring, streak or other artefacts) of reconstructed transverse images of the water-filled cylinder phantom (Fig. 11.23). CT number accuracy and noise may be evaluated quantitatively by ROI analysis of the reconstructed images of the water-filled phantom. A set of 5×5-cm^2 ROIs (one at the centre and four at the periphery, at approximately the 12, 3, 6, and 9 o'clock positions) is superimposed on a transverse image and the mean CT numbers (in Hounsfield units,[1] HU) compared between the central and each of the peripheral ROIs; the maximum difference should not exceed 5 HU. The accuracy of the CT number of water and image noise can also be evaluated using the same ROIs. The accuracy of the CT number for water is checked by comparing the mean CT number for each ROI to the CT number expected for water (0 HU). All of the mean CT

---

[1]The Hounsfield unit (HU) scale is based on a linear transformation of the linear attenuation coefficient as measured by CT in which the radiodensity of water is assigned a value of 0 HU and that of air at STP a value of 1000 HU. For a material X with linear attenuation coefficient μ_X, the corresponding HU value is therefore $\{(\mu_X - \mu_{water})/(\mu_{water} - \mu_{air})\} \times 1000$, where μ_{water} and μ_{air} are the linear attenuation coefficients of water and air, respectively.

numbers thus derived should be within 5 HU of that of water, that is, 0 ± 5 HU. The image noise is evaluated by comparing the standard deviation (SD) of the CT number in each of the ROIs to the scanner's reference SD established at the time of its installation: for each ROI, the SD should be no greater than twice the benchmark standard deviation.

11.19.3   Laser Alignment, Slice Thickness, Spatial Resolution, Linearity and High- and Low-Contrast Resolution

In addition to the foregoing daily checks of CT performance, laser alignment, image slice thickness, spatial resolution, linearity (i.e., CT number accuracy) and high- and low-contrast resolution should be evaluated monthly or at least quarterly. At the same time, image uniformity and noise, as discussed above, should also be evaluated for different tube voltages (i.e., kV_p) which bracket the range of values used clinically. Evaluation of these parameters require appropriate phantoms.

Figure 11.24 shows a schematic of one of such phantoms. It is a water fillable PMMA cylinder with multiple sections (i.e., inserts) for the measurement of these CT performance parameters.

- *Laser alignment.* The laser lights should lie precisely on the circumferential surface groove of the phantom. If the lasers are properly aligned, the two laser alignment cavities in the reconstructed transverse image will be horizontal and at precisely the same *y*-position coordinate.
- *Slice thickness.* Since the line cavities in each of the two 'slice-thickness measurement' components of the insert are staggered (offset) 1 mm apart in the longitudinal direction, the number of black lines (using a high-contrast display) appearing on a transverse reconstructed image corresponds to the slice thickness in millimetres. However, if one of the lines appears as grey rather than black, the slice thickness in millimetres equals the number of black lines plus one-half, with 0.5 mm

of slice thickness 'contributed' by the cavity appearing as the grey line.
- *Spatial resolution.* Spatial resolution is assessed by identifying the narrowest set of line cavities in which the separate cavities can be visualized.
- *Linearity.* Linearity (i.e., CT number accuracy) is checked by verifying that the mean CT number (in HU) in a 10×10 mm ROI in air, water and PMMA matches the expected CT numbers, 1000, 0 and 100 HU, respectively.
- *High-contrast resolution.* High-contrast resolution is expressed as the SD of the CT number (in HU) in a 10×10 mm ROI centred over the coarsest set of line cavities (i.e., the set in which the lines are 1.6 mm in width). The higher the image contrast, the larger the difference between the water and the PMMA CT numbers within this ROI and the higher the SD of the CT number. According to reference [18], the acceptable value of the SD of the CT number in this ROI is 37 ± 4 HU (i.e., 33–41 HU).
- *Low-contrast resolution.* Low-contrast resolution is evaluated using the insert and the ROIs (red boxes), ~ 400 mm^2 in area, shown in the lower left-hand image in Figure 11.24 and is expressed as the percent difference between the CT numbers (in HU) in the water and the polystyrene membrane ROIs. According to reference [18], this difference should agree within 0.1% (1 HU) with the scanner's reference low-contrast resolution established at the time of its installation. Optionally, low-contrast resolution can also be evaluated as a function of object size by calculating the foregoing parameter for each of the circular holes in the polystyrene membrane.

11.19.4   CT Dose Index (CTDI)

On at least an annual basis, radiation dose should be evaluated by measuring the CT dose index (CTDI) for various scan parameters (i.e., kV_p and mA) which bracket the range of values used clinically. The CTDI is the basic radiation dose parameter in CT and is defined as the integral under the exposure or absorbed dose profile along
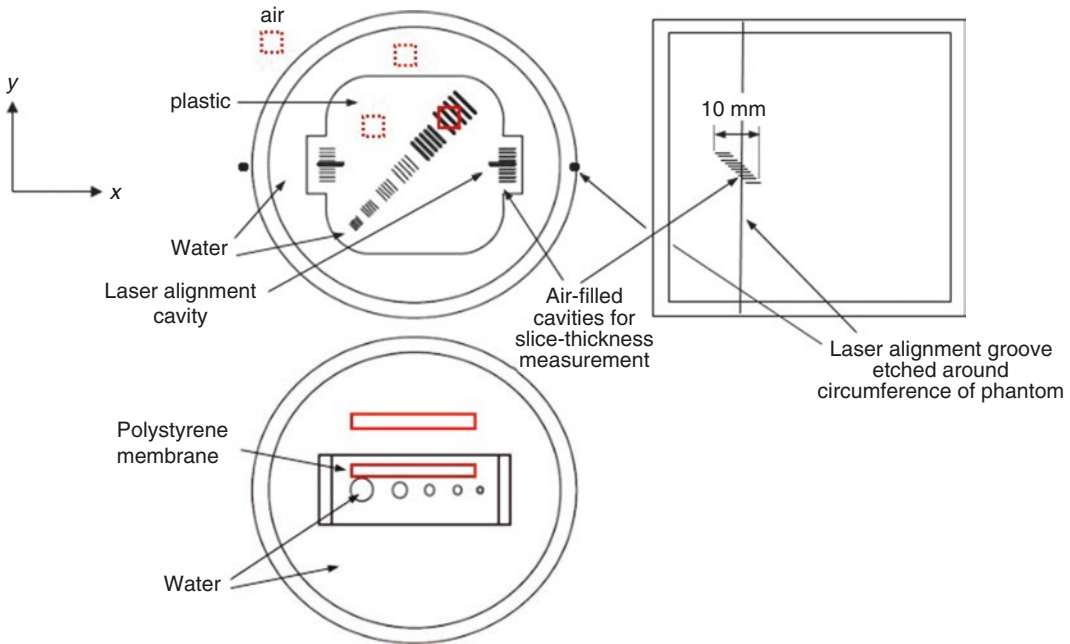
Fig. 11.24 Cross-sectional diagrams of a Quality Assurance Phantom [18] illustrating the respective sections (inserts) for evaluation of laser-light alignment, image slice thickness, spatial resolution, linearity and high-contrast resolution (upper left-hand figure); low-contrast uniformity (lower left-hand figure). The various short black lines in the PMMA insert in the section shown in upper left-hand figure are cavities which fill with water when the phantom is filled, providing high contrast between the cavities and the Plexiglas™; the portion of this section outside this insert is also water-filled. The diagonally arranged sets of line cavities range are 1.6 (upper right), 1.3, 1.0, 0.8, 0.6 and 0.5 mm in line width and are used to evaluate spatial resolution. The section shown in the lower left-hand figure includes a polystyrene membrane with a series of holes (10, 7.5, 5, 3 and 1 mm in diameter) which also fill with water when the phantom is filled, providing low contrast between the holes and the polystyrene. The right-hand figure shows a side-view diagram (not to scale) of the section of the phantom in upper left-hand figure showing only one of the 'slice-thickness measurement' components of the insert; these line cavities are air-, not water-, filled. Note that they are staggered (offset) 1 mm apart in the longitudinal direction. Also shown in the right-hand as well as the upper left-hand figure is the laser alignment groove around the circumference of the phantom and the two corresponding laser alignment cavities

the patient's longitudinal axis for a single tomographic image. The volume CTDI ($CTDI_{vol}$) is derived from the CTDI and is the average dose delivered to a scan volume (vol) for a specific examination. The 100-mm CTDI ($CTDI_{100}$) is the integral under the exposure or absorbed dose profile along a 100-mm length of the phantom's longitudinal axis. The weighted 100-mm CTDI ($CTDI_w$) is the weighted average of the $CTDI_{100}$ measurements at the centre and periphery of a dose-measurement phantom:

$$CTDI_w = \left[\frac{2}{3} \cdot CTDI_{100}(p) + \frac{1}{3} \cdot CTDI_{100}(c) \right] \cdot f$$

(11.6)

where $CTDI_{100}(p)$ is the $CTDI_{100}$ at the periphery (p) of a cylindrical phantom, $CTDI_{100}(c)$ the $CTDI_{100}$ at the centre (c) of a cylindrical phantom, and f, the exposure-to-absorbed dose conversion factor, 33.7 Gy/C/kg, or 0.87 rad/R, for water or soft tissue.

The $CTDI_w$ thus reflects the mean absorbed dose over the transverse (x- and y-) dimensions of such a phantom and is an approximation of the average radiation dose to the cross-section of a patient. Measurements of the $CTDI_{100}(p)$ and $CTDI_{100}(c)$ are typically performed using ionization chambers or thermoluminescent dosimeters (TLDs) positioned in a commercially available soft tissue-equivalent PMMA phantom

Ionization chamber in a peripheral measurement position
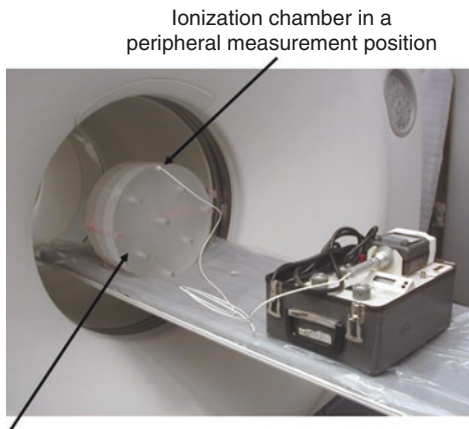
A 32-cm "body" acrylic phantom

Fig. 11.25 Setup for the measurement of CT radiaton exposures using an ionization chamber and a 32-cm diameter PMMA torso (body) phantom. (Courtesy of Dr. Sadek Nehmeh, Weill-Cornell Medical Centre, New York, NY)

cylindrical in shape and either 16 or 32 cm in diameter, approximating an adult head or torso (body), respectively (Fig. 11.25). Ionization chambers actually measure exposure, which is then converted to absorbed dose using the aforementioned *f* factor. TLDs, on the other hand, yield absorbed dose directly.

11.20 Concluding Remarks

An essential element of a successful QC programme is that the leadership of the nuclear medicine department recognizes its importance and supports its implementation. QC must be an integral component of the routine work of the department, and the time and effort required for its implementation must be considered in scheduling patient studies and allocating departmental resources.

References

1. NEMA. NEMA standards publication NU 2–2018: performance measurements of positron emission tomographs. Rosslyn, VA: National Electrical Manufacturers Association; 2018.
2. Khalil MM. Basic science of PET imaging. Berlin: Springer International; 2016.
3. Boellaard R, et al. Quality control for quantitative multicenter whole-body PET/MR studies: a NEMA image quality phantom study with three current PET/MR systems. Med Phys. 2015;42(10):5961–9.
4. NEMA. NEMA Standards Publication NU 1–2012: performance measurements of gamma cameras, in NEMA Standard NU 1–2012. Rosslyn, VA: National Electrical Manufacturers Association; 2012.
5. International Atomic Energy Agency. Quality assurance for SPECT systems. In: IAEA Human Health Series. Vienna: IAEA; 2009.
6. Busemann Sokole E, Plachcinska A, Britten A. Acceptance testing for nuclear medicine instrumentation. Eur J Nucl Med Mol Imaging. 2010;37(3):672–81.
7. Busemann Sokole E, et al. Routine quality control recommendations for nuclear medicine instrumentation. Eur J Nucl Med Mol Imaging. 2010;37(3):662–71.
8. International Atomic Energy Agency. Quality control of nuclear medicine instruments 1991. In: IAEA-TECDOC-602. Vienna: IAEA; 1991.
9. AAPM. Report No. 177—acceptance testing and annual physics survey recommendations for gamma camera, SPECT, and SPECT/CT systems. 2019.
10. Zanzonico P. Technical requirements for SPECT: equipment and quality control. In: Kramer EL, Sanger JJ, editors. Clinical applications in SPECT. New York: Raven Press; 1995. p. 7–41.
11. Zanzonico P. Routine quality control of clinical nuclear medicine instrumentation: a brief review. J Nucl Med. 2008;49(7):1114–31.
12. Hander TA, et al. Rapid objective measurement of gamma camera resolution using statistical moments. Med Phys. 1997;24(2):327–34.
13. Rueden CT, et al. ImageJ2: ImageJ for the next generation of scientific image data. BMC Bioinform. 2017;18(1):529.
14. Schindelin J, et al. Fiji: an open-source platform for biological-image analysis. Nat Methods. 2012;9(7):676–82.
15. International Atomic Energy Agency. IAEA quality control atlas for scintillation camera systems. Vienna: IAEA; 2003.
16. IAEA-NMQC Toolkit. [cited 1 Aug 2019]. https://humanhealth.iaea.org/HHW/MedicalPhysics/NuclearMedicine/QualityAssurance/NMQC-Plugins/index.html.
17. International Atomic Energy Agency. Quality assurance programme for computed tomography: diagnostic and therapy applications. In: IAEA Human Health Series. Vienna: IAEA; 2012.
18. GE Healthcare. LightSpeed 4.X Lightspeed 16 technical reference manual (CE 0459). Waukesha, WI: General Electric Company; 2005.

Positron Emission Tomography (PET): Physics and Instrumentation

12

Magdy M. Khalil

Contents

12.1 Introduction

Single-photon emission computed tomography (SPECT) and positron emission tomography (PET) are three-dimensional (3D) techniques used by nuclear imaging to functionally map radiotracer uptake distributed in human body. SPECT systems have been described previously; PET imaging is the main topic of the present chapter. The radiopharmaceuticals of PET provide more insights into the metabolic and molecular processes of the disease. This in turn has made PET a molecular imaging technique that examines biochemical processes that take place at the molecular level [1].

PET has become a potential "multipurpose" imaging technique in biomedical, clinical, and research arenas. Clinical indications for PET are numerous and include many diseases where cancer imaging occupies the most important and abundant category. Thus, it has a well-defined and established role in oncology and diagnosing many types of malignancies besides staging and assessment of response to therapy. Another important role of PET lies in its ability to diagnose some neurologic and psychiatric disorders in addition to noninvasive quantitation of cerebral blood flow, metabolism, and receptor binding [2]. Further, PET has a significant role in evaluating patients with coronary artery disease and detection of tissue viability, together with its ability to provide an absolute measure of myocardial blood flow. PET by nature is "molecular" since its radioligands are acceptable and familiar to living tissues; therefore, it is considered an indispensible tool in molecular imaging research. It has several quantitative features with acceptable accuracy in determination of the amount of

M. M. Khalil (✉)
Medical Biophysics, Department of Physics, Faculty of Science, Helwan University, Cairo, Egypt

tracer transported to or deposited in tissues. In comparison to other imaging modalities, PET has significantly higher detection sensitivity such that tracers with low concentrations, in the nano or pico-molar range, can be detected.

PET imaging has moved from a useful research tool mainly in neurology (and cardiology) to more specific tasks in oncology and has become a potential clinical diagnostic modality. The instrumental aspects were a cornerstone in the development of PET imaging and its introduction into the clinic. Furthermore, advances in PET technology are moving forward and are not only confined to clinical whole-body scanners but also are expanding to include organ-dedicated instruments such as positron emission mammography and dedicated brain and prostate scanners in addition to small-animal imaging systems [3]. Now, more attention is paid to the hybrid PET/CT (computed tomographic) systems, by which the functional information obtained by PET imaging and morphologic data obtained from diagnostic CT are merged into a fused image to reveal a more accurate and confident anatomolecular diagnosis [4]. This instrumental marriage has resulted in a significant improvement of patient diagnosis, disease staging, and therapy monitoring. Moreover, it has had a positive impact on patient comfort, throughput, and more importantly clinical outcome that has been proven to outperform both techniques used separately [5]. The growth and spread of PET/MR was relatively slower than PET/CT but a number of clinical applications are emerging with interest to standardize protocols. Technical challenges are also continuously being tackled and resolved.

12.1.1 History

In 1928, Paul Dirac predicted the existence of the positron, and he shared the Nobel Prize with Erwin Schrödinger in 1933. In 1932, Carl Anderson observed positrons in cosmic rays and shared the Nobel Prize in 1936 with Victor Hess. From the beginning, one could expect that the electron antiparticle known as a positron would receive much interest or at least provide impor-

tant applications as those who discovered it were awarded well-ranked and recognized scientific prizes. The positron is one of the antimatter physical particles that has a short lifetime and decays quickly by combining with a surrounding electron to release two 511-keV photons in a back-to-back collision process. These two photons are the two arms by which the physics of PET imaging is rotating.

12.1.2 Positron Emitters

There are several positron emitters that are of particular clinical interest. Fluorine-18 is the most widely used positron emitter for many reasons. It has well-defined radiochemistry, and labeling with various biomolecules is continuously advancing to suit specific target tissues. It has a half-life (109.8 min) that allows radiochemists to synthesize labeled compounds in a reasonable time and permits other imaging logistics, such as injection, patient preparation, and imaging over several time points on either a static or dynamic basis, to be carried out. The physical characteristics of fluorine are also desirable for production of high-resolution PET images. The maximum energy of the decay of F-18 is 0.634 MeV with a small positron range. Other positron emitters, such as oxygen-15 (2.03 min), nitrogen-13 (9.97 min), carbon-11 (20.3 min), and others, have documented clinical utility in PET imaging (see Table 12.1).

The physics of PET imaging is based on positron emission, in which nuclei of an excess amount of protons exhibit nuclear transition by emitting a positron particle whose half-life is short. The positron travels a short distance based on its kinetic energy and then annihilates by combining with an electron present in the surrounding medium to give two opposing 511-keV photons with an angular distribution of 0.5° full width at half maximum (FWHM) at 180°. Before annihilation takes place, the positron forms a new configuration with an electron called positronium, which is a hydrogen-like atom with a short lifetime of about 10^{-7} s [6]. Because of this unique emission process, a single detector system

Table 12.1 Physical properties of clinically useful PET radionuclides

Radionuclide	$T_{1/2}$	Mode of decay	Decay product	Energy (MeV)	Average range in water (mm)
^{18}F	109.8 min	β^+ (97%)	^{18}O	0.634 (E_{max})	0.6
^{11}C	20.4 min	β^+ (100%)	^{11}B	0.960 (E_{max})	1.2
^{13}N	10.0 min	β^+ (100%)	^{13}C	1.199 (E_{max})	1.8
^{15}O	2.0 min	β^+ (100%)	^{15}N	1.732 (E_{max})	3.0
^{64}Cu	12.7 h	β^+ EC(61%) β^- (39%)	^{64}Ni ^{64}Zn	0.653 (E_{max}) 0.329–1.675 0.579	0.7
^{68}Ga	67.6 min	$\beta+$ (89%) EC (11%)	^{68}Zn	1.899 (E_{max}) 0.227–2.821	3.5
^{76}Br	16.0 h	$\beta+$ (55%) EC (45%)	^{76}Se	3.382 (E_{max}) 0.599	7.1
^{82}Rb	1.3 min	$\beta+$ (100%)	^{82}Kr	3.378 (E_{max})	7.1
^{86}Y	14.7 h	$\beta+$ (32%)	^{86}Sr	1.221, 1.545, 1.988 (E_{max})	1.9, 2.8, 3.7
^{89}Zr	3.3 days	IT (68%) $\beta+$ (23%) EC (77%)	^{89m}Y	0.433–1.920 0.902 (E_{max})	1.3
^{124}I	4.2 days	$\beta+$ (26%) EC (74%)	^{124}Te	2.183, 1.535 (E_{max}) 602	4.4, 2.4

does not provide appropriate geometry for detection of the two photons as in SPECT imaging; hence, two detectors in coincidence are the most convenient way to detect the two events concurrently. Therefore, any two photons that will reach two opposing detectors (in coincidence) will be recorded as long as their incidences on the detector fall within a predefined timing window (2τ). The line that connects the two detectors in space is called the *tube* or *line of response* (LOR). The LOR does not necessarily indicate the path along which annihilation took place since one or both photons may have undergone a scattering interaction before reaching the detectors or both may have originated from different annihilating sites. Accordingly, there are different types of events that can describe the coincidence events detected by a PET scanner. These are true, scatter, and random coincidences and are discussed further in this chapter.

Positron Range. A physical phenomenon that reduces the resolution capability of the scanner to record events exactly as emitted from their true original locations (Fig. 12.1). Once the positron is emitted from the nucleus, it undergoes an annihilation with an electron to produce the clinically useful 511-keV photons. However, before this interaction takes place, the positron travels a distance before collision occurs. This distance is a function of the kinetic energy of the emitted positrons being higher in positron emitters with high maximum β^+ energy, such as O-15, Ga-68, and Rb-82 nuclei (maximum energy 1.73, 1.89, and 3.37 MeV, respectively) [7] (Table 12.1). Besides the kinetic energy of the released positron, the surrounding medium contributes to the spatial blurring caused by the positron range. In tissues with low density (e.g., lung tissue), the resolution degradation is more pronounced than in tissues with high density (e.g., compact bone) (see Fig. 12.2). Together with the radionuclide maximum energy and the density of the medium, the relative influence of the positron range on the final resolution of the reconstructed image depends on the spatial resolution of the system [8–10].

The distribution of the positron trajectories was found not to follow a normal Gaussian-like distribution and the cusp-shaped pattern was found in a number of simulation studies [7, 8]. The effect of positron range on resolution loss is thus recommended to be measured using the positron root mean square range in the medium of interest or the full width at 20% of maximum [8]. The characteristic shape of the positron distribution preserves some high frequencies, and

Fig. 12.1 (**a**) Positron range as determined by the *two-headed arrow* is the perpendicular distance from the transformed nuclei to the recorded line of response. In (**b**), the recorded line of response has an angular distribution of full width at half maximum (FWHM) of 0.25° adding uncertainty to spatial resolution
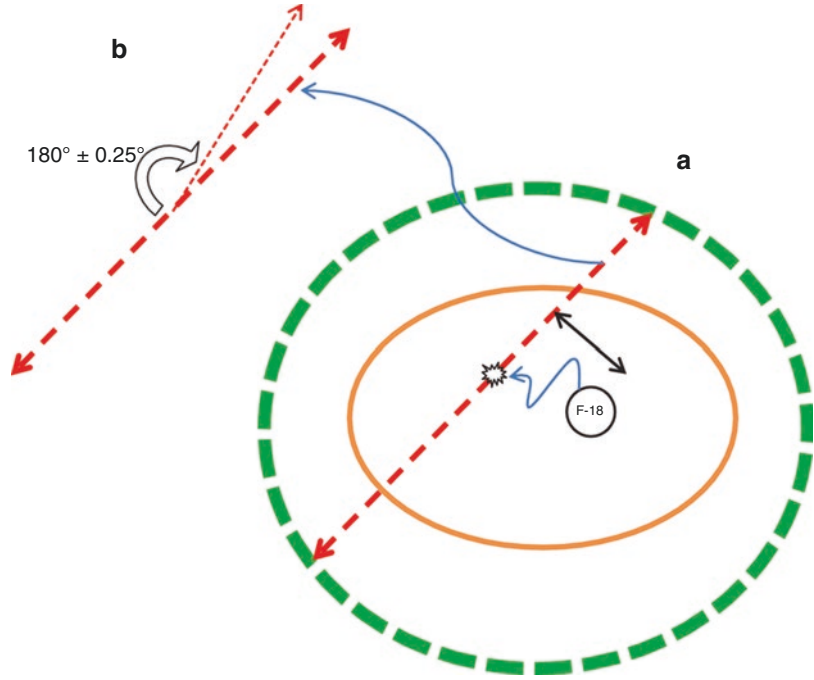
Fig. 12.2 Monte Carlo-calculated distribution of annihilation events around a positron source inserted in different human tissues (compact bone, soft tissue, and lung tissue). The spread of the distribution is larger for positron emitters of high maximum kinetic energy in tissues with low density. (From [8] with permission from Springer + Business media)
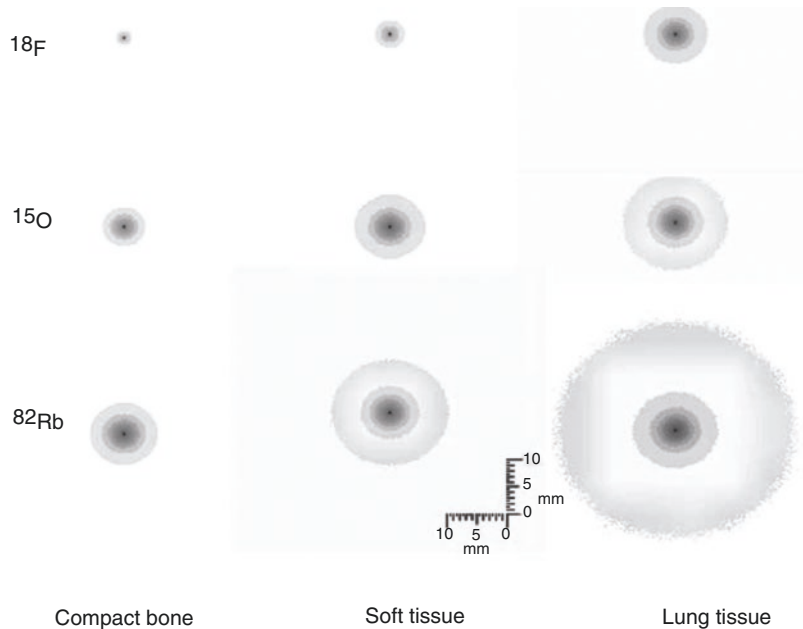
the long tail estimated by full width at tenth maximum (FWTM) causes severe resolution degradation [7]. In another simulation study using Phits software package, a number of positron emitters were simulated within Digimouse as well as in Dorenzo small-animal phantom [11]. The simulated and measured images using Mn-57, F-18, Zr-89, Y-86, Ga-68, and As-74 are shown in Fig. 12.3. Their respective E_{max} of the emitted positrons are 242, 250, 396, 660, 830, 1170 keV. The image quality and degree of blurness is in proportion to the E_{max} of the radionuclide being higher in the reconstructed images of As-74 and Ga-68 [11].
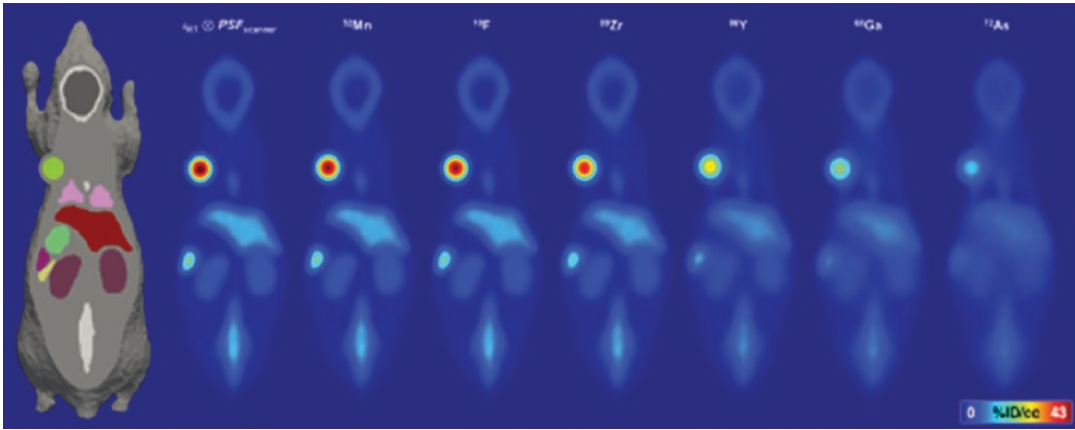
Fig. 12.3 Impact of use of different PET emitters (Mn-57, F-18, Zr-89, Y-86, Ga-68, and As-74) in simulated preclinical PET Digimouse on resolution degradation. It is clear that as the positron range increases the degrada-tion in spatial resolution becomes greater, Ga-68 and AS-74. Notice the degradation of the tumor and spleen tissues. (From [11] with permission from Springer)

Acollinearity. This is another physical phenom-enon that is related to the conservation of momen-tum of the annihilated positron-electron pair. The conservation of mass and energy requires that the two photons are released in 180°; however, some residual kinetic energy remains to reduce this angular measure, on average, by ±0.25° FWHM as shown in Fig. 12.1b. This in turn leads to a LOR that does not exactly pass through the annihilation site, resulting in event mispositioning and spatial resolution loss. Unlike the positron range, the acol-linearity resolution effects are a function of the detector diameter; thus, a PET scanner with an 80-cm diameter would suffer a resolution degrada-tion of $0.0022 \times D$ or 0.0022×800 mm = 1.76 mm. The constant 0.0022 is derived from the geometry of the ray and can be calculated as 0.5 tan 0.25°. For a 15-cm detector diameter, resolution loss would be 0.33 mm, approximately 5–6 times less than a clinical whole-body scanner. Corrections for acollinearity and positron range are discussed in the spatial resolution section.

12.2   PET Scanners: Geometry and Components

A number of different geometries have been implemented in the design of PET scanners. Starting from the simple geometry of 2 oppos-ing detectors as in the conventional dual-head gamma camera to more sophisticated full-ring scanners, performance characteristics varied widely from one system to another. Figures 12.4 and 12.5 illustrate different geometries used in clinical PET systems.

Hybrid PET/SPECT Camera. As mentioned, the process of positron-electron annihilation and the release of two antiparallel photons impose geometric constraints on PET detector design. This requires that the detector pair must be in an opposite direction to determine the path traversed by annihilation photons to reach the detectors. Anger proposed the use of two opposing gamma cameras at 180° and electronic collimation of the 511-keV photons to record coincident events [12]. This has been employed in longitudinal tomogra-phy using a dual camera without a rotating system. Further developments resulted in the design of two large field-of-view gamma cameras with a thicker crystals mounted on a rotating gantry [13].

Several limitations faced the early dual oppos-ing detector design in providing a convenient measure of activity distribution inside human subjects, such as low sensitivity, poor count rate capability, and lack of a radionuclide to provide sufficient count statistics over the time course of the study. These limitations were attrib-uted mainly to the use of NaI(Tl) crystal, old-fashioned system electronics, and the inherent open design. NaI(Tl) crystals have a low stop-ping power against 511-keV photons and a slow
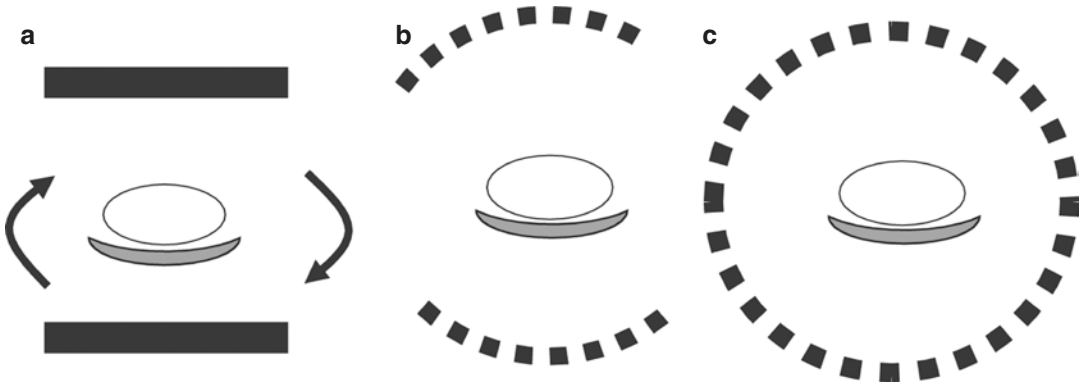
Fig. 12.4 Different geometries used in positron emission tomographic (PET) scanners. (**a**) A dual-head gamma camera with coincidence circuitry and sufficient crystal thickness of about 2.5 cm. (**b**) Partial-ring detector geometry that requires rotation around the patient for data sampling. (**c**) Full-ring detector geometry
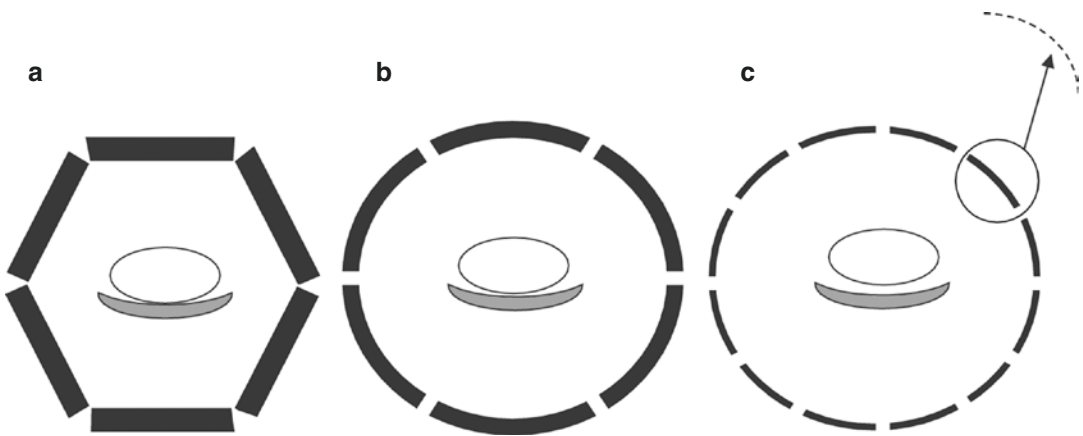
Fig. 12.5 Another set of positron emission tomographic (PET) scanners that was proposed in the literature and implemented in practice. (**a**, **b**) Hexagonal designs using flat- or curved-plate detector arrays, respectively. (**c**) Discrete crystals arranged in modular style in which modules are adjoined side-to-side

decay time. The open design, however, allows for more single events and random coincidences to be accepted, especially from regions outside the field of view, resulting in a low signal-to-noise ratio and reduced image contrast.

This system was named SPECT/PET camera and was able to provide dual functionality in imaging single-photon radiopharmaceuticals and positron-labeled compounds by switching between SPECT and coincidence detection mode (Fig. 12.4a). Using appropriate collimators for 511 keV, this type of imaging system was also used to image patients injected with dual tracers to look at two different metabolic or functional processes that happen simultaneously [14–16].

Modifications must be made on the conventional gamma camera to operate in the coincidence mode [17]. Coincidence triggering is the basic electronic element that needs to be incorporated in the detector electronics. The count rate capability must be high enough since collimators are unmounted and the system sensitivity is larger. Crystal thickness (e.g., 16–25 mm) should be larger than that normally used in SPECT systems to provide a sufficient interaction depth to stop a significant portion of the incident photons, thus improving the detection efficiency. Dual- and triple-coincidence gamma cameras have been manufactured, and owing to some performance limitations, such as spatial resolution, sensitivity,

and count rate performance, they were no longer attractive PET design when compared to the full-ring systems [18–20].

Partial Ring. In PET systems with partial detector rings, the detectors are packed in two opposing detector banks arranged in a circular system that continuously rotates to capture a complete data set necessary for image reconstruction [21] (Fig. 12.4b). For example, the ECAT ART (Siemens/CTI, Inc., Knoxville, TN) consists of 2 opposing detectors, each of 3 × 11 crystal blocks arranged in axial and tangential direction. The banks are slightly asymmetrically opposed to increase the effective transaxial field of view. The block material is bismuth germanate (BGO) and is segmented into $6.75 \times 6.75 \times 20$ mm^3 and coupled to 4 photomultiplier tubes (PMTs). There are three blocks in the axial dimension, giving a 16.2-cm axial field of view and 24 crystal rings with 242 possible planes of response [21]. The partial ring design was used in prototyping the first PET/CT scanner in which the PET electronics were placed at the rear portion of the CT gantry housing but with different operation consoles [22].

Hexagonal geometry. Other systems were also implemented that were based on arrays of six- or eight-sided geometry. The former design is shown in Fig. 12.5a, b and has more than one variant, such that the detector assembly can be a single continuous scintillation detector or curved-plate design. However, the number of detectors can be larger, with flat modules and discrete crystal structure (Fig. 12.5c).

The hexagonal design has some good features as it is relatively simple and uses fewer PMTs than used in a full-ring block design. The number of PMTs may vary from 180 or 288 as in NaI(Tl)-based detector to a larger number (e.g., 420) as in discrete GSO (gadolinium oxyorthosilicate) or LYSO (Cerium-doped lutetium yttrium orthosilicate) modular detectors [23–27]. Further, it has a relatively large axial field of view that can reach 25 cm, such as that found, for example, in the curved-plate NaI(Tl) design [25].

The use of a large continuous crystal allows only 3D data acquisitions; to some extent, the large axial field of view can compensate for the lower sensitivity of the NaI(Tl) crystal. However,

such a detector design and the use of Anger logic position circuitry led to an increase in the system dead time. Limiting the light signal to a finite number of PMTs and optimizing the light guide for light spread were proposed to mitigate these effects [28]. One of the disadvantages of hexagonal geometry is the intercrystal dead space left by adjoining the detector modules, a reason that could cause some reduction of the system sensitivity and confound the reconstruction process.

A hectagonal or eight-sided detector system can be found in the HRRT system (High Resolution Research Tomograph, Siemens Medical Solutions), a dedicated brain PET scanner that uses two types of scintillation crystals to identify the depth of interaction (DOI) of the 511-keV photons. The system achieves a spatial resolution of 2.3–3.2 mm in the transaxial direction and a resolution of 2.5–3.4 mm in the axial direction, together with a point source system sensitivity of 6% and National Electrical Manufacturers Association (NEMA) NU-2001 line source sensitivity of 3%. The transaxial and axial extents are 31 and 25 cm, respectively [29].

12.2.1 Cylindrical Design

The most efficient geometries that found wide acceptance among manufacturers and PET users are those that depend on circular or ring design. The advantage provided by full-ring scanners is their detection efficiency and count rate capabilities. This in turn provides better system spatial resolution by realizing the statistical requirements imposed by image reconstruction [30]. The ring design is the most widely used system geometry and is preferred among manufacturers in clinical and preclinical PET scanners. Clinical PET systems have somewhat variable axial extent that may range from 15 to 26 cm.

12.2.2 Long Axial FOV

PET scanners with extended axial field of view dates back to 1990s [31]. The time period 2000–2010 was concomitant with prototypes but with

no successful operating system released into the clinical environment. Recently, there was a potential interest to develop and introduce PET scanners with a significant long axial extent. The goal was many folds including but not limited to full coverage and observation of organs physiology in a simultaneous real time, increased system sensitivity and reduction of the injected radioactive and effective dose, in addition to depicting tracer dynamics and disease extent in an integrated manner.

The recent introduction of the uEXPLORER (Extreme performance Long REsearch scanneR) system that developed by investigators of University of California, Davis in partnership with United Imaging Healthcare, has made a tremendous change in system sensitivity [32]. The system photo is shown in Fig. 12.6. The system axial extent is 194 cm exploiting the full potential of positron emission with significant improvement of solid angle coverage resulting in great elevation of count efficiency. This improvement also has made a substantial increase in signal to noise ratio translated into about six times reduction of noise standard deviation when compared to conventional scanners [33]. A similar approach named PennPET Explorer was also recently developed at the University of Pennsylvania in collaboration with KAGE Medical and Philips Healthcare [34, 35]. The system is a 3-ring configuration operating with a 64-cm axial FOV with

plans to be expanded to 140 cm, see Fig. 12.7. The reported sensitivity is 55 kcps/MBq and spatial resolution of 4.0 mm. The photodetector employed is SiPM developed by Philips digital silicon photon counting connected via 1:1 coupling to LYSO scintillation crystal. The NECR is 1000 at 40 kBq/cm^3, timing resolution of 250 ps and energy resolution of 12% [34]. Clinical evaluation of the uEXPLORER and PennPET Explorer were recently reported [32, 35]. Table 12.2 summarizes the specification of the two systems [31].

12.2.3 PET/CT

The introduction of PET/CT in the early years of this century was attractive for many practitioners as well as manufacturers; now, almost all PET scanners are purchased as hybrid PET/CT systems. The current generation of hybrid PET/CT systems is the side-by-side configuration such that the CT component is placed in the front portion of the scanner while the PET component is placed at the back end mounted using the same housing over the two gantries or gantries with separate covers and in all cases using the same imaging table. The axial length traversed by the imaging table varies among manufacturers, and as the bed travels axially there is more chance for bed deflection, resulting in misalignment errors. A number of approaches were therefore

Fig. 12.6 A photograph of the long axial field of view uEXPLORER developed and installed in UC Davis, California, USA, in partnership with United Imaging Healthcare. Many thanks to Prof Ramsey Badawy and Dr. Yasser Gaber, UC Davis, California, USA, for providing the images

Fig. 12.7 Photographs of the PennPET Explorer showing the (**a**) axial extent, (**b**) table of the patient couch along with (**c**) general view of internal anatomy demonstrating the 3 ring design of the scanner. Many thanks to Prof Joel Karp and Dr. Suleman Surti, University of Pennsylvania, Department of Radiology, for providing the images

undertaken by scanner manufacturers to take into account this deflection of the imaging bed. It is worth noting that the latest guidelines NEMA NU-2018 has added the accuracy of the PET/CT coregistration among other tests to be considered in the acceptance testing of newly installed PET/CT systems [36].

Moving from a single to more CT slices (e.g., 4, 6, 8, 16, 64, and beyond) offered a great opportunity to enhance the diagnostic speed and possibility of performing cardiac CT as well as angiography. The addition of spiral CT technology was remarkable and significantly reduced the acquisition times by manyfold together with the advantage of acquiring a large number of thin slices. In this type of data acquisition, the imaging table moves forward in a simultaneous motion with rotation of the X-ray source in a

Table 12.2 Comparison between two recently developed long axial field of view PET/CT scanners namely Penn PET Explorer and uEXPLORER

	Penn PET Explorer	uEXPLORER
Axial length, cm	70/140	194
Scintillator	LYSO	LYSO
Crystal dimension, mm^3	$3.86 \times 3.86 \times 19$	$2.76 \times 2.76 \times 2.76$
Photodetectors	SiPM (digital)	SiPM
Bore/detector diameter, cm	70/81	68.6/78.6
Resolution (FWHM), mm		
Transaxial	4.0	3.0
Axial	4.0	3.0–3.5
Energy resolution (%)	10	11.7
Energy window, keV	440–660	430–645
Scatter fraction[a] (%)	32	35.8
Sensitivity,[a] kcps/MBq	55	191.5 at 9 cm
Coincidence window, ns	5	4.5–6.9[b] ns
TOF resolution, ps	250	505
Peak NEC[a] (kcps)		
70 cm phantom	>1200 kcps[c]	1435 kcps @ 16.8 kBq/cc
175-cm phantom		1718 kcps @ 8.0 kBq/cc

Ref. [31]

[a]Performed using NEMA NU 22012

[b]Ring difference dependent

[c]This is for incomplete 70-cm system

spiral path. The delay that occurs interscans can thus be eliminated (a feature of older CT generations), while the *z*-axis is kept variable across projections. Data interpolation is then used to account for these angular inconsistencies. These fully diagnostic CT systems, when combined with state-of-the art PET machines, have made a "one-stop-shop" diagnosis a clinical reality. The radiation dose delivered to the patient using multislice CT systems has been considered, and solutions such as beam modulations and optimized acquisition protocols have been used. Low-dose attenuation correction using low tube current is another way to reduce patient dose as long as diagnostic CT is not required. The two major advantages provided by the CT are attenuation correction and anatomical localization of the PET images; both features have significantly improved the diagnostic performance of the nuclear scans. State-of-the-art PET/CT systems are shown in Fig. 12.8.

There have been several attempts to improve the performance characteristics of PET scanners in terms of spatial resolution, system sensitivity, coincidence timing resolution, and energy resolution while keeping the cost of the device reasonably affordable. These requirements are as follows [37].

1. High detection sensitivity for the 511-keV photons to improve the detection or areas of low tracer concentration, enhance the statistical quality of dynamic images, and to reduce the injected dose.
2. High resolving capabilities to achieve the maximal spatial resolution for volume elements.
3. High-energy resolution to minimize the contribution of scattered events.
4. Low dead time to improve count rate performance and high timing resolution to improve random rejections and for time-of-flight (TOF) applications.
5. Low cost.

Achieving such requirements in one practical tomograph is difficult from physical and engineering perspectives as well as associated costs. Some performance parameters are traded off while maintaining the quality of others. For

Philips PET/CT

Vereos Digital

Ingenuity ToF

Siemens PET/CT

Biograph Vision

Biograph Horizon

GE PET/CT

Discovery MI

Discovery 710
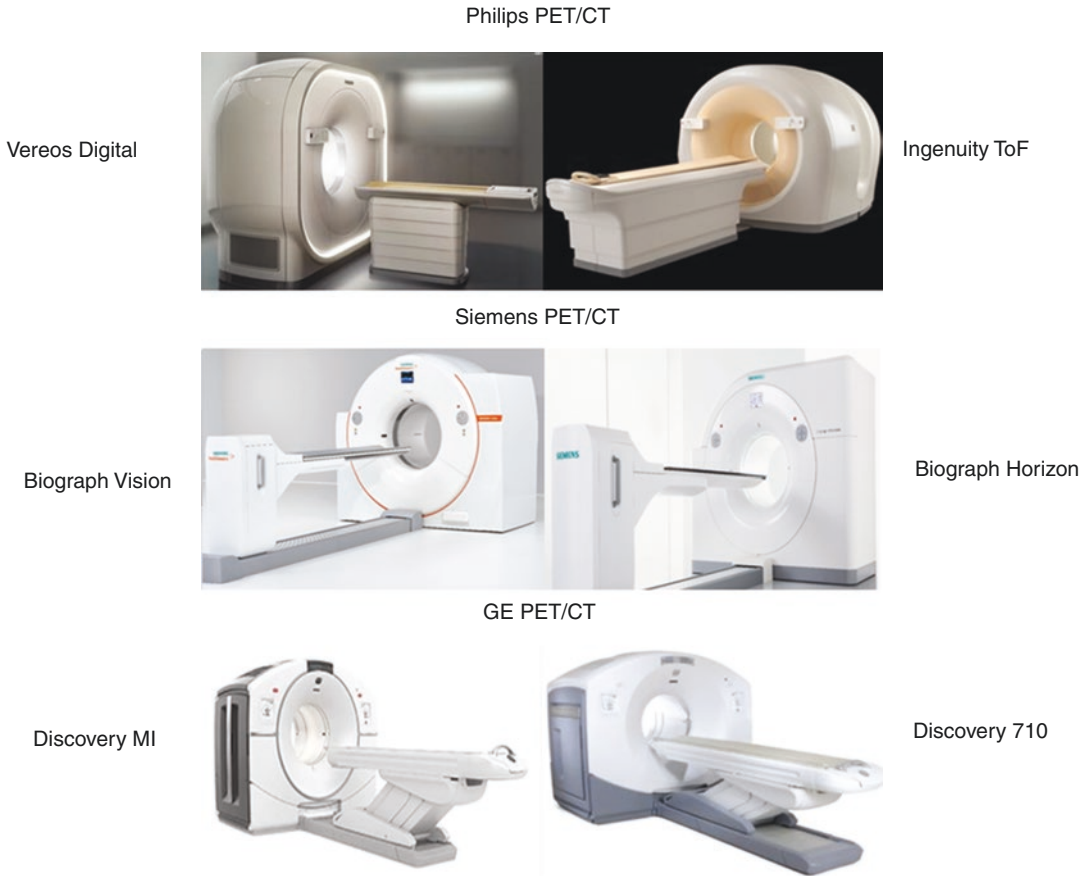
Fig. 12.8 A subset of commercial (PET/CT) scanners developed by the major vendors. The left side panel is the recent digital version provided by each manufac- turer while the right side is the conventional PMT-based design. (Images courtesy of Philips Healthcare, Siemens Healthcare, and GE Healthcare)

instance, reducing the detector diameter is advantageous for improving count sensitivity, while it is not in favor of spatial resolution due to the DOI errors. Small-animal scanners have better angular coverage owing to smaller ring diameter but suffer from depth of interaction. Another factor that is affected by ring diameter is photon acollinearity, which increases and decreases in a linear fashion with the ring diameter. Extension of the axial extent of the PET scanner can be used to improve scanner sensitivity, but this comes with increased cost and degradation of spatial resolution in the axial direction. However, the recent introduction of the previously described uEXPLORER as well as PennPET systems was a significant step toward full exploitation of the PET signal.

12.2.4 PET/MR

The birth of PET/CT and its successful implementation in routine practice was so motivating in introducing the PET/MR systems in clinical arena adding more options to the molecular/anatomical toolkit. Magnetic resonance imaging is featured with high spatial resolution, increased soft tissue contrast and absence of ionizing radiation [38]. Drawbacks of PET/MR systems are poor bone signal and difficulties associated with photon attenuation corrections.

In terms of electronics, one of the earliest limitation of integrating PET and MR was the sensitivity of the PMT to the magnetic field. The PET detector should also be shielded to avoid interference effects from rapidly chang-

ing magnetic field that can cause vibrations and heating effects. On the MR side, however, the field homogeneity needs to be maintained with minimum noise during operation, which can be caused by insertion of the PET detector. The logic but less practical solution was to separate the PMTs array and position it at a distance from the MR magnetic coils [39]. Further development to realize the integration was the introduction of avalanche photodiode (APD) due to its minimal sensitivity to the magnetic field but this came at the expense of the system timing resolution. However, the advent of the SiPM was successful in tacking the timing issues related to APD providing opportunities for time of flight application in addition to other qualities including system sensitivity and count rate performance.

The interest in combining PET with MR was initially given to preclinical systems in 1990s but real clinical model was introduced in 2006 (BrainPET, Siemens Healthcare.) with subsequent commercialization in 2010. As of mid-2020, there is an approximately 250 PET/MR systems distributed worldwide from the same large manufacturers of PET/CT. There are two current approaches that are devised to have an operational PET/MR system in clinical practice including simultaneous (or concurrent) data acquisition as well as sequentially (or axially) aligned PET/MR systems. The former model has been implemented in the Biograph mMR (Siemens Healthcare) and Signa PET/MR (GE Healthcare) whereas the later strategy was carried out and executed in the Ingenuity TF (Philips Healthcare, OH) or the two separate PET/CT and MR scanners [40].

The Triple system PET/CT and MR was initially proposed by GE Healthcare such that the two imaging systems PET/CT and MR are located in two adjacent rooms. A one common bed shuttle is then used to move the patient from one room to another. This method while being less concurrent and requires relatively large space and likelihood of patient motion, it has some merits in terms of independent operation of the two systems (PET vs. MR) as well as independent operation and hardware update [41, 42].

Another modified model of the concurrent acquisition was that implemented by Philips Healthcare, called Ingenuity TF, in which the PET and MR are axially aligned but physically separated while sharing the same imaging bed. Advantage of this system is minimal interference between the two scanners without major modification of detector design or electronics. However, patient motion and total acquisition time is relatively compromised similar to the triple PET/CT-MR system. The Philips design also places additional requirements on room dimensions approximately 4.5×13 m. The PET detector ring is surrounded by laminated steel shield and each PMT is inserted in a mu-metal case [43].

The first integrated PET/MR design was introduced by Siemens in 2010 (Biograph mMR) providing simultaneous acquisition of PET emission as well as MR signal [44]. The MR component was the 3-T Siemens Verio while the PET detector was avalanche photodiode-based coupled to LSO. The bore size was reduced to 60 cm due to increased system components and integration having the PET detector behind the radiofrequency coil.

A similar integrated PET/MR was then released into the market named GE Signa with TOF capabilities [10, 45]. The GE 3-T Discovery 750w MRI was combined with PET detector that consists of lutetium based crystal ($3.95 \times 5.3 \times 25$ mm^3) coupled to SiPM photodetector (1×3 arrays) with custom made ASIC readout. The transverse and axial dimension of the PET was 60 and 25 cm respectively accommodating 5 rings of 112 detector blocks. In the GE Signa, the PET detector was inserted close to the inner surface of the shielding assembly in a central dip between the body coil and gradient coil. This configuration maintains the same field of view of the standalone GE clinical MR system of bore 60 cm [46]. Specification and physical parameters of the currently available PET/MR systems are provided in Table 12.3 and systems photographs are demonstrated in Fig. 12.9.

Integrated systems that provide simultaneous data acquisition have benefits in terms of improved temporal correlation as well as high spatial registration in addition to reduced

Table 12.3 PET/MR systems provided by the three major vendors in the clinical market

PET/MR system	Biograph mMR Siemens	Ingenuity TF Philips	Signa TF GE Healthcare
Crystal material	LSO	LYSO	Lutetium-based scintillator
Crystal dimension, mm	$4 \times 4 \times 20$	$4 \times 4 \times 22$	$4.0 \times 5.3 \times 25$
Photodetector	APD (no. 4032)	PMT (420)	SiPM
Transaxial FoV, cm	59.4	67.6	60.0
Axial FoV, cm	25.8	18.0	25.0
Energy window, keV	430–610	460–665	425–650
Energy resolution, FWHM, %	11.5	12	10.3
Coincidence window, ns	5.9	6.0	4.57 (±2.29 ns)
Time of flight	No	Yes	Yes
FWHM @ 1 cm off center, mm	4.3	4.7	4.2
FWHM @ 10 cm off center, mm	5.5	5.1	5.1
Timing resolution, ps	2930	525	385
Sensitivity (avg of 0 and 10 cm), cps/kBq	14.4	7.1	22.9
Max NECR (kcps) @ kBq/mL	184 @ 23.1	88.5 @ 13.7	218 @ 17.7
Scatter fraction at NECR peak (%)	37.9	26.0	43.6
MR system			
Magnet	Superconductor	Superconductor	Superconductor
Field strength, T	3	3	3
Bore diameter, cm	60	60	60
Max FoV, cm	$50 \times 50 \times 45$	$50 \times 50 \times 45$	$50 \times 50 \times 50$

Data adapted from [38, 46, 49]

LSO lutetium oxyorthosilicate, *LYSO* lutetium–yttrium oxyorthosilicate, *NECR* noise equivalent count rate, *FWHM* full width at half-maximum, *FoV* field of view

scan time in comparison to sequential systems. Applications of PET/MR systems are increasing and include but not limited to neurology, cardiology, and oncology with potential in targeted radionuclide therapy and precision medicine [47]. Standardization of the imaging workflow as well as imaging parameters are deemed necessary for more and widespread of this hybrid imaging modality. A recent consensus recommendations stated by HYBRD consortium for PET/MR was recently reported proposing a minimum set of quality control recommendations that include daily testing, cross-calibration tests as well as assessment of image quality for PET together with coil checks and image quality procedures for MRI part of the hybrid system [48].

12.2.5 Scintillation Crystals

The type and composition of the scintillation crystal are of considerable importance in the detection efficiency of 511-keV photons. The function of the crystal is to convert the energy received by the incident photons into light quanta that are proportional to the imparted energy. Two major interactions occur when the photon deposits its energy in the crystal: photoelectric and Compton scattering. The electrons released from either photoelectric or Compton processes undergo several interactions within the scintillator material and excite other electrons, which in turn decay to emanate the scintillation light [50].

Crystal with a high probability of photoelectric effect, or photofraction, is preferred since all energy is imparted on the crystal and at one site. However, Compton interactions reveal more than one interaction site and hence degrade the spatial resolution as well as the energy spectrum by broadening the photo peak width. Figure 12.10 shows the dependence of the photoelectric effect on the atomic number of various types of scintillation crystals.

The light emitted by the crystal is viewed and detected by photodetectors, where light photons are converted into an electronic signal for deter-
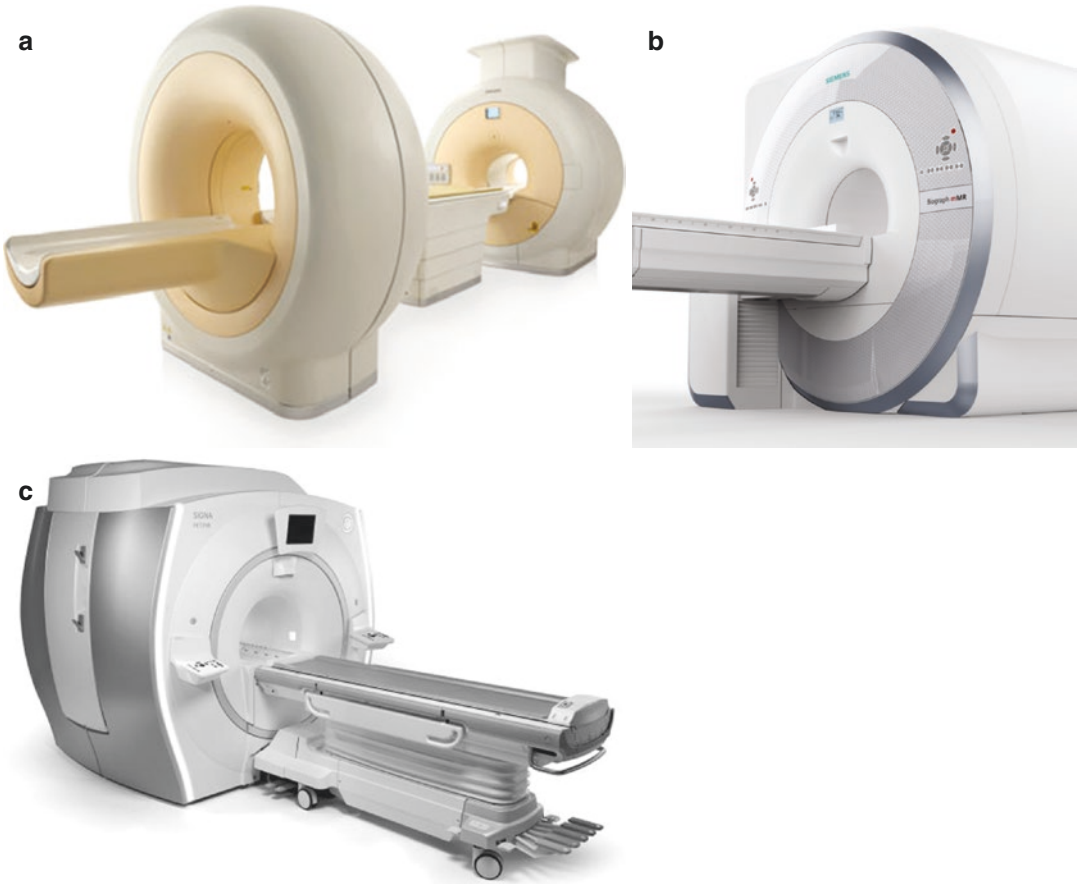
Fig. 12.9 Commercially available PET/MR scanners including (**a**) Ingenuity TF, (**b**) Biograph mMR and (**c**) SIGNA™ PET/MR. (Images courtesy of Philips, Siemens, and GE healthcare systems, respectively)
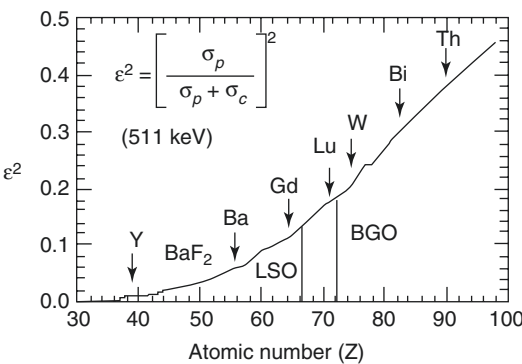
Fig. 12.10 The probability that both 511-keV photons interact via the photoelectric effect as a function of Z_{eff}. There is an increasing trend in the photofraction probability with the effective atomic number. (From [51] with permission from William Moses, Lawrence Berkeley Lab, USA)

mination of event attributes such as energy and position. Many types of the scintillator material have been proposed and implemented to improve the detection performance of PET scanners. Crystals that are able to provide high photon detection efficiency, short decay time, and better energy resolution are highly preferred. Other optical properties, such as an emission wavelength that matches the photocathode of the PMT, transparency, and good refractive index, are also important factors to ensure maximum transfer of the scintillation light to the PMT. Other manufacturing requirements, such as mechanical flexibility, hygroscopic properties, ease of handling, and fabrication into small crystal elements, cost, and availability, are all of concern in the selection of the scintillator material [52, 53]. The following is

a list of the major properties of the scintillation crystals that can significantly improve the scanner performance:

1. Crystals with *high density and high effective atomic number* Z_{eff} have good intrinsic efficiency. Photoelectric effect is strongly related but Compton scattering is linearly related to the atomic number of the material for photons (>100 keV). Crystals with high ρZ_{eff}^4 have good stopping capabilities for 511-keV photons [54]. The density and effective atomic number also determine the attenuation length. Scintillation crystals of smaller attenuation length are desired as they serve to reduce resolution degradation caused by parallax errors.

2. Crystals should have high *light output* since event positioning and energy resolution are related to the amount of light quanta released from the crystal. A sufficient amount of scintillation light can release a significant number of photoelectrons from the photocathode and thus provide better accuracy in signal measurements and improve energy resolution. The small size of the crystal elements in the block detector design requires a scintillator that can produce high light output so that position encoding can be done with good precision. There are a number of factors responsible for the statistics of light emanating from the scintillator, such as homogeneous distribution of the activation centers, nonproportional response of the crystal, and variation in crystal luminosity [52].

3. Crystals with *short decay constants* or "fast scintillators" serve to improve the timing of the coincidence detection and thus reduce the dead time and random fractions. Scintillators with a short decay constant help to improve the count rate performance, especially for scanners operating in 3D mode and for clinical studies in which short-lived radionuclides with high activities are used [55]. Another advantage gained by such crystals is their recent introduc-

tion in TOF applications, which require high efficiency and fast scintillators, leading to an improvement in the signal-to-noise ratio and improved lesion detectability, reduction of scan time or injected dose, and more accurate lesion quantitation [56].

4. Although the selection of the scintillator material is important and can potentially affect the performance of the scanner, one should realize that the overall system performance is a function of many components of the imaging system, such as electronic circuitry, acquisition and reconstruction parameters, together with the correction and computational algorithms [57]. This has been noted in PET scanners upgraded using better electronic circuitry or when new scintillation crystals were introduced in scanners not equipped with appropriate electronic components [58, 59].

12.2.5.1   NaI(Tl)

NaI(Tl) has been extensively used in many nuclear medicine devices, especially in the design of the gamma camera. In the early 1970s, it was the most commonly used crystal in PET scanners even though it was an inefficient scintillator for 511-keV photons. The detection efficiency of NaI(Tl) crystal to Tc-99m energy and other relatively low-energy gamma emitters is reasonably good, and it remains the scintillator of choice in many SPECT cameras. In comparison to other types of scintillation crystals, it has better energy resolution, poor timing resolution, high dead time, and low stopping power. The low density and moderately low atomic number are responsible for the poor detection efficiency of NaI(Tl) crystal for 511-keV photons. Another limitation of NaI(Tl) crystal is its hygroscopic properties and careful handling to avoid humidity effects must be taken into account; hermetic sealing is required. This in turn led to difficulty in producing small-size elements suitable for block detector design.

12.2.5.2 BGO

The BGO type of crystals has a better detection efficiency and high probability of photoelectric interaction (i.e., 40%) for 511-keV photons. It contains the bismuth element (Bi), which has a large atomic number ($Z = 83$) and its ionic form (Bi^{3+}) is the intrinsic luminescence center in the crystal [52]. The density of the crystal is approximately two times greater than for NaI(Tl), and the attenuation coefficient is three times larger (Table 12.4). These properties have allowed BGO to replace NaI(Tl) crystal, and it was the scintillator of choice for many years, until the end of 1990s. However, the low light yield [~15–20% relative to NaI(Tl)] and poor energy resolution and response time have made it inferior to the other new scintillators, which showed a better response time and better light output, such as Gadolinium Oxyorthosilicate (GSO), Lutetium Orthosilicate (LSO) or its yttrium doped version (LYSO). As mentioned, better response time allows a significant reduction of system dead time and works to minimize the amount of random coincidences that contaminate the prompt events. Moreover, it allows a reduction of pulse pileup in 3D mode, in which system sensitivity is high, thereby resulting in better count rate performance. The first small-animal PET scanner designed specifically to image rodents was made of BGO-based block detectors and was developed in the mid-1990s

[60]. When compared to NaI(Tl), both the non-hygroscopic nature of BGO and its high detection efficiency have permitted manufacturing of a more compact detector assembly and narrower crystals that improved significantly the system resolution and sensitivity.

12.2.5.3 GSO

Cerium-doped Gadolinium Oxyorthosilicate (GSO) has good properties that have made it applicable in some PET scanners (Allegro and Gemini-GXL, Philips Company). Also, it founds some applications in small-animal scanners and in combination with LSO in systems equipped with parallax error correction. The density of this scintillator is comparable to BGO and LSO crystals, and it is roughly twice as dense as NaI(Tl). The effective Z is intermediate between NaI(Tl) and both BGO and LSO. The decay constant (60 ns) is slightly higher than LSO but significantly lower than BGO and NaI(Tl) crystals. An evaluation of a pixilated GSO Anger logic-based scanner using NEMA NU 2-2001 procedures revealed acceptable results in terms of energy resolution, sensitivity, and better image quality provided that a patient study can be performed in a time course of half an hour, including transmission measurements [24]. That system also demonstrated a better count rate capability in 3D mode served by the fast decay constant of

Table 12.4 Properties of scintillation crystals used in positron emission tomographic (PET) scanners

	NaI(Tl)	BGO	GSO:Ce	LSO:Ce	LYSO:Ce	LaBr₃	BaF₂
Density (gm/cm³)	3.67	7.13	6.7	7.4	7.1	5.3	4.89
Effective atomic number (Z)	51	74	59	66	64	47	54
Linear attenuation coefficient (1/cm)	0.34	0.92	0.62	0.87	0.86	0.47	0.44
Light yield (% NaI[Tl])	100	15	30	75	75	160	5
Decay time (ns)	230	300	65–60	40	41	16	0.8
Emission maximum (nm)	410	480	440	420	420	370	220
Hygroscopic	Yes	No	No	No	No	Yes	Slightly
Photoelectric effect (%)	17	40	25	32	33	13	12
Refractive index	1.85	2.15	1.85	1.82	1.81	1.88	1.56

NaI(Tl) thallium-activated sodium iodide crystal
BGO bismuth germanate oxyorthosilicate
GSO:Ce cerium-doped gadolinium oxyorthosilicate
LSO:Ce cerium-doped lutetium orthosilicate
LYSO:Ce cerium-doped lutetium yttrium orthosilicate
LaBr3:Ce cerium-doped lanthanum bromide
BaF2 barium fluoride

the GSO crystal and optimizing the light spread detected by PMTs [28]. GSO is not hygroscopic, absent of intrinsic radioactivity, has good stability versus temperature, and has a good uniform light output but is not simple to manufacture, and a special fabrication procedure is followed to avoid cracking during crystal design. Another disadvantage is its susceptibility to magnetic field effects, rendering it an unsuitable scintillator for PET/MR hybrid systems [61].

12.2.5.4   LSO/LYSO

Unlike BGO, which has no activator, LSO is a cerium-activated scintillator and has a large ρZ_{eff}^4, but this is lower than BGO. It has good character-istics for dealing with 511-keV photons: The effective Z is 66, density (7.4), and $\mu = 0.87$ cm^{-1}; thus, it is an efficient scintillator for stopping the annihilation coincidence photons. LYSO is similar to LSO and is produced such that some lutetium is replaced by yttrium atoms.

LSO scintillators are characterized by their fast response, represented by short decay time, achieving excellent timing resolution. These properties have made LSO/LYSO an attractive scintillator for PET scanners, in particular for TOF applications, and with its high light output, there is no compromise in detector efficiency [62] (see Fig. 12.11). The light output is approximately three or five times higher than BGO when
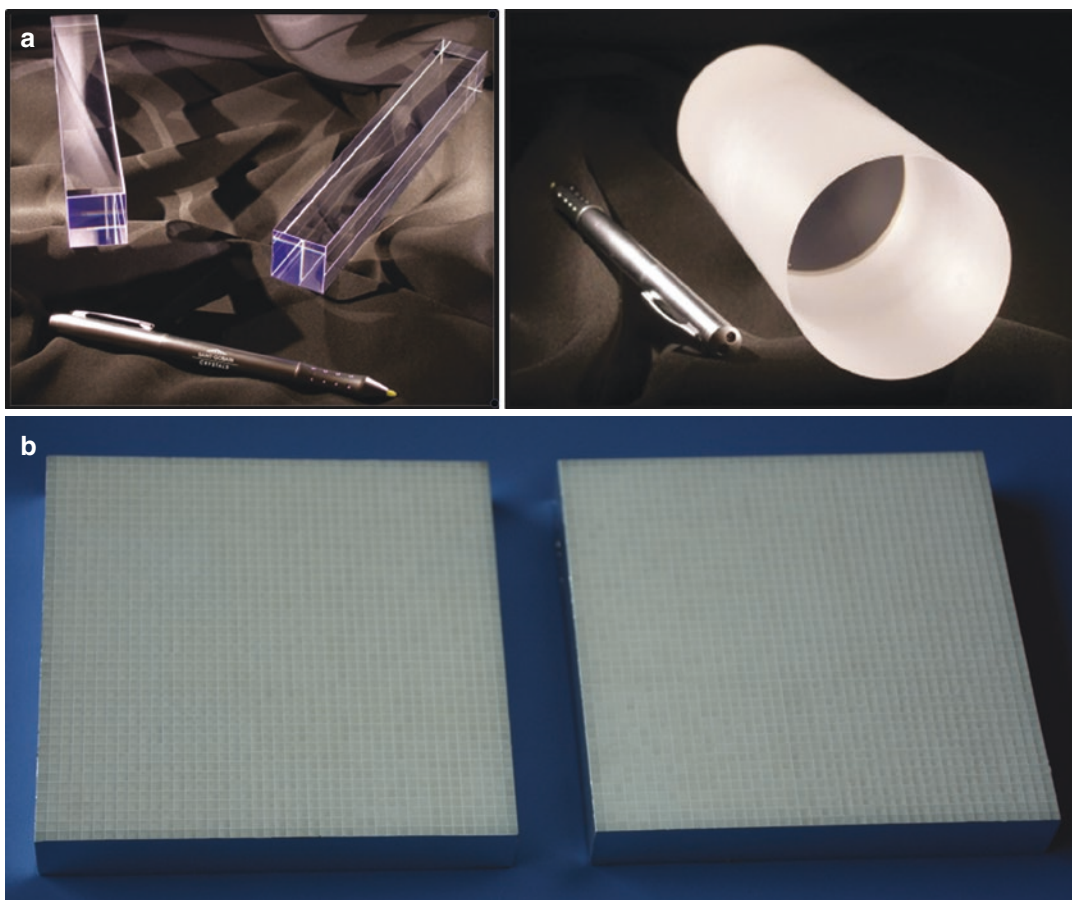
Fig. 12.11 (**a**) LYSO (Lu$^{1.8}$Y^{2}SiO^5:Ce) is a cerium-doped lutetium based scintillation crystal. It has several attractive features for PET imaging including high density, high light output and fast response making it suitable for time of flight applications, Image credit of Saint Gobain (www.crystals.saint-gobain.com). (**b**) Segmented LYSO crystal (LYSO 43 × 43 pixel: 2 × 2 × 10 mm^3) produced by Kinheng crystal material (Shanghai, China) Co., Ltd. http://www.kinheng-crystal.com/

using an avalanche photodiode (APD) or PMT, respectively. Because of the statistical nature of the detection process, an LSO-based PET scanner should enjoy better energy resolution, better event positioning, and a short coincidence timing window. The last is instrumental in establishing the noise level resulting from random events [63].

LSO is nonhygroscopic and mechanically rugged, and simple fabrication is relatively possible to produce small and discrete versions of the crystal [53]. However, it has a number of limitations, such as inhomogeneity of light production, high melting point (>2000 °C), and cost higher than other crystal types [GSO, BGO, and NaI(Tl)]. Another limitation of LSO scintillation crystals is their Lu-176 content, which emits low-level radioactivity; yet, this has been found not to affect the extrinsic 511-keV coincidence detection but can affect precise measurements of system sensitivity and scatter fraction using low-level radiation.

LSO crystals are found in many PET systems, such as high-resolution dedicated brain scanners [64] and hybrid multimodality imaging, such as PET/CT, PET/SPECT, and PET/MRI systems. Other special-purpose systems have also been designed using LSO crystals, such as breast PET scanners and small-animal imaging systems [65, 66].

12.2.6 Crystal Photodetector: Light Readout

In the conventional gamma camera, the scintillation crystal is a continuous large slab of NaI(Tl) viewed from its back surface by an array of PMTs that collect the scintillation light produced from interaction of the emitted photons with the detector material (Fig. 12.12). In one of the earliest PET detector designs, the PMT is coupled to a single crystal; thus, the cross section of the crystal defines the LOR and intrinsic spatial resolution [67]. Following this procedure in building up a full multiring scanner is neither efficient nor

cost-effective as one needs a significantly large number of PMTs and crystal material along with electronic channels to implement such a design. Earlier efforts in coupling the scintillation detector to PMTs included four crystals per one or two PMTs. However, this strategy was advanced by using more crystal elements per PMTs. It was a turning point when the block detector concept was introduced in the design of the PET scanners, which is a cost-effective technique in coupling the PMT to the scintillation detectors and has also led to an improvement in spatial resolution [68].

12.2.6.1   Avalanche Photodiode

An interesting approach was the development of semiconductor photodetectors to replace the bulky and significantly large volumetric shape of the PMT. One of the major drawbacks of PMT is sensitivity to magnetic fields. As the electrons are accelerated within the PMT by the effect of high potential applied between photocathode and dynodes and between successive dynodes, any source that influences this process would be an undesired component of noise leading to tube performance degradation. A magnetic field more than 10 mT is able to alter the gain and energy resolution of a PMT [69]. One of the earliest solutions was to use long cables of fiber optics. The better alternative was to use semiconductor photodetectors.

Efforts have then been made to develop semiconductor detectors with better detection efficiency and intrinsic spatial resolution, providing a reliable and robust performance compared to PMTs or PSPMTs. Among these developments are the avalanche photodiodes (APDs), which can be produced in small dimensions, providing an improvement of spatial resolution in addition to reduced detector volume, and thereby fit space requirements imposed by multimodality imaging scanners as well as small-animal imaging [70]. In comparison to the PMT, the APD is sensitive to temperature variations, suited for pixilated detectors, operated in a lower voltage and is stable in the presence of high magnetic fields, like that

hv   *hv*

SEGMENTED BLOCK OF BGO
OR LSO SCINTILLATOR

REFLECTOR MATERIAL

D

B

C

A
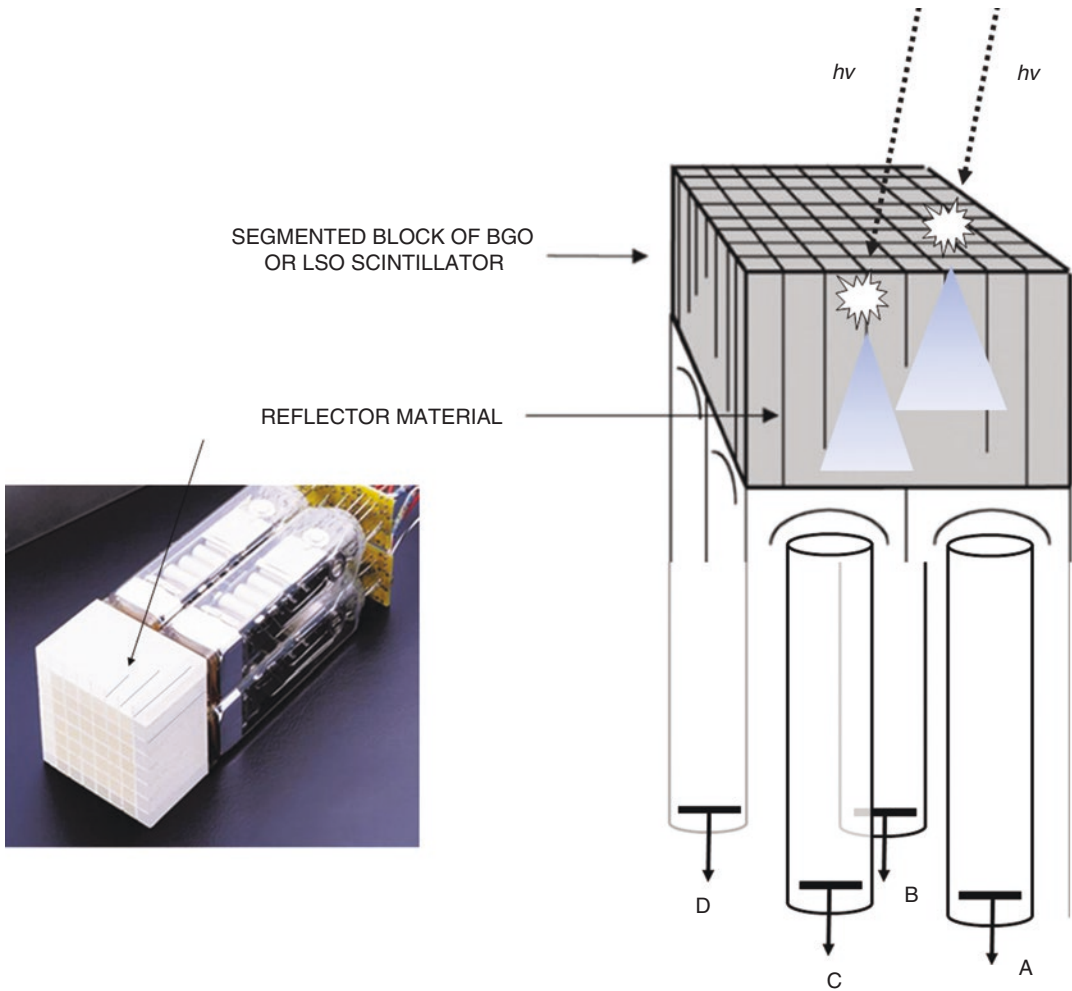
Fig. 12.12 Crystal segmentation and light readout by block detector coupled to four photomultiplier tubes (PMTs). The crystal block is carefully cut into an array of smaller detector elements. A very thin reflective material is used in the saw cuts to optically isolate elements. The depth of the cuts determines the spread of scintillation light onto the four PMTs

encountered in MRI [71]. Thus, the APD was suitable in PET inserts incorporated into MRI machines, providing compact and simultaneous hybrid PET/MRI imaging systems. The semiconductor junction is operated at a high reverse bias, and the output signal is proportional to the initial number of light photons. They are characterized by low gain and relatively higher quantum efficiency. See Fig. 12.13.

Position-sensitive APD (PSAPD) is similar to the APD but with fewer readout requirements. The back surface is connected to a resistive layer that allows for multiple contacts to be fabricated. Position information can then be obtained by the charge sharing among electrodes that enables the determination of position of interaction [72, 73]. Consequently, this structure allows for simple and compact detector assembly and enables use
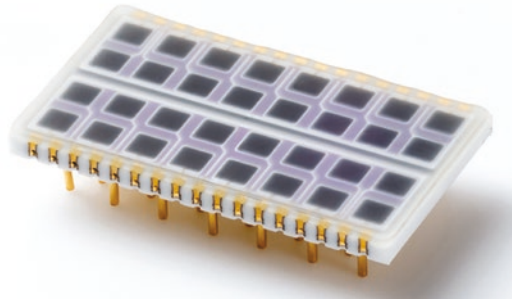
Fig. 12.13 A 4 × 8 element Si APD array. (Courtesy of Hamamatsu Photonics, Japan)

of significantly fewer readout channels, resulting in lower manufacturing costs. The alignment of the detector with the crystal array in this design is not as important as is the case in the individual APD array. This type of photodetector has an attractive interest in small-animal scanners, including depth of interaction encoding that serves in improving scanner spatial resolution and sensitivity [74, 75].

12.2.6.2 Silicon Photomultiplier (SiPM)

The Geiger mode APD or silicon photomultiplier (SiPM) is a densely packed matrix of small APDs (20×20 to 100×100 μm^2) joint together on common silicon substrate and work in limited Geiger discharge mode. Each cell is an independent Geiger mode detector, voltage biased, and discharges when it interacts with an incident photon. The scintillation light causes a breakdown discharge for triggering a cell resulting in a fast single photoelectron pulse of very high gain 10^5–10^7. SiPM produces a standard signal when any of the cells goes to breakdown. When many cells are fired at the same time, the output is the sum of the standard pulses [76]. See Fig. 12.14.

Characteristics of SiPM are low noise factor, photon detection efficiency equivalent to the standard PMT, and low bias voltage. The higher gain feature provided by SiPM detector marginalizes the electronic noise in contrast to the standard
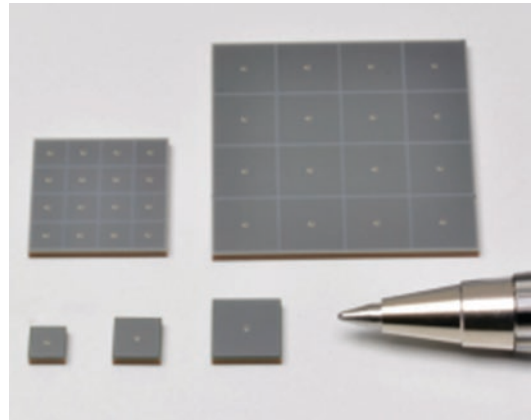
Fig. 12.14 Multiple-pixel photon counters from Hamamatsu Photonics with higher photon detection efficiency, lower operating voltage and small dead space in the photosensitive area. (Courtesy of Hamamatsu Photonics, Japan)

APDs, which generally have a gain of 100–200. However, the dead space around each pixel and the finite probability of photons to produce avalanche breakdown reduce the detection efficiency of the SiPM, making it significantly lower than for the APD [77]. SiPM is an interesting alternative to the conventional PMT in terms of compactness, same level of electronic gain, suitability for PET inserts in magnetic resonance systems and in detector design based on depth encoding information [78, 79]. Figure 12.15 shows the differences that exist between the conventional PMT and SiPM in crystal coupling.

The introduction of digital PET in the clinical arena was mainly due to the utilization of the silicon photomultiplier in the detector system without the use of Anger logic positioning circuitry. This new light readout element has several properties that made it a better alternative to the conventional PMTs which has limited photon-electron conversion quantum efficiency. Moreover, the lower magnetic susceptibility in addition to compact size were very attracting features in incorporating SiPM in PET/MR systems tackling technical issues related to the use of PMT. A coupling of 1:1 for the crystal and SiPM was also a technical advantage that simplified crystal identification

Fig. 12.15 Light sharing among more than PMT in the conventional design of PET/CT has been advanced by the new 1:1 coupling of the SiPM to the scintillation crystal. The opportunity for improved spatial resolution in addition to reduced detector volume offered by the compact size of the solid state detector has therefore been increased. (Images courtesy of Philips healthcare)
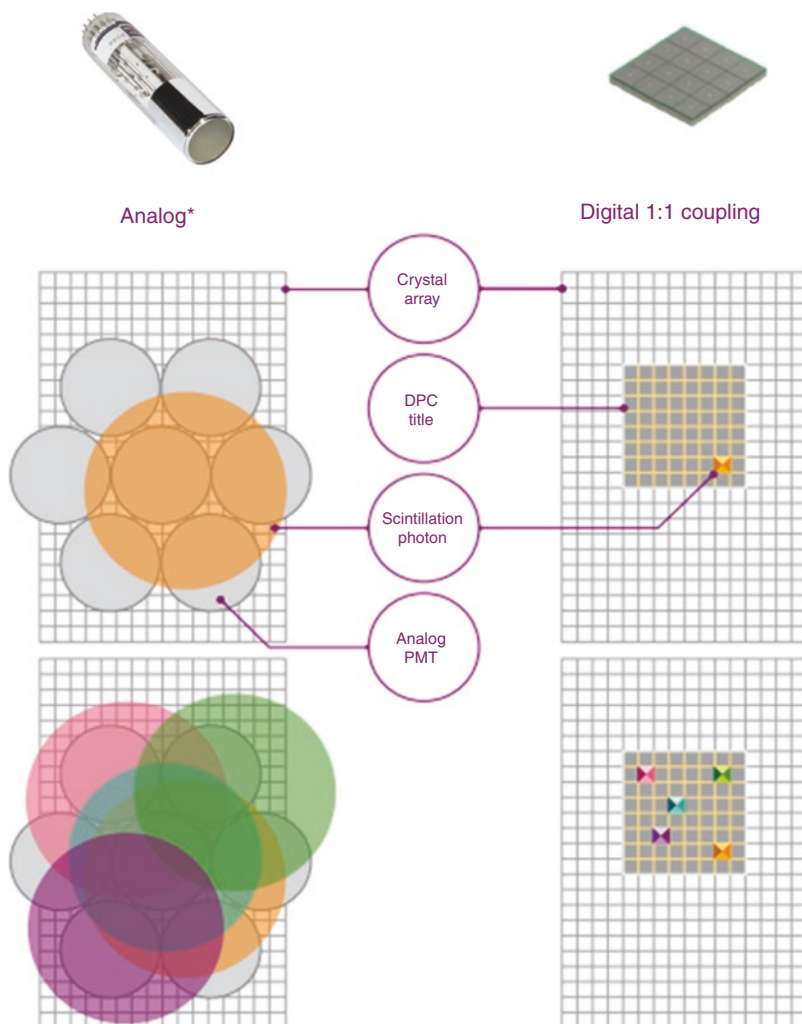
and improved spatial resolution. Another important feature provided by SiPM is fast response that permitted its incorporation in time of flight-based commercial scanners. Clinical evaluations of the digital PET/CT showed better system sensitivity, spatial resolution with better diagnostic performance than analog counterparts. Lesion morphology, sharpness, and diagnostic confidence have also been reported for digital PET in addition to more positive lesions in comparison to analog counterpart [80, 81]. Analog SiPMs require dedicated circuitry and application specific integrated circuits (ASIC), however, scaling of such elements to large detector design serve

to degrade performance. As of mid-2020, the current clinical systems that are designed with SiPM as photodetectors are Philips Vereos PET/CT; Discovery MI PET/CT and Signa PET/MR by GE Healthcare, and Biograph Vision PET/CT by Siemens Healthcare [46, 82–85]. Figure 12.16 compares the technical differences between analog and digital SiPM in signal processing.

12.2.6.3   Block Design
In block detector design, as shown in Fig. 12.8b, c, the scintillation block is segmented into an array of small crystals by cutting into precise and well-defined dimensions in the transaxial
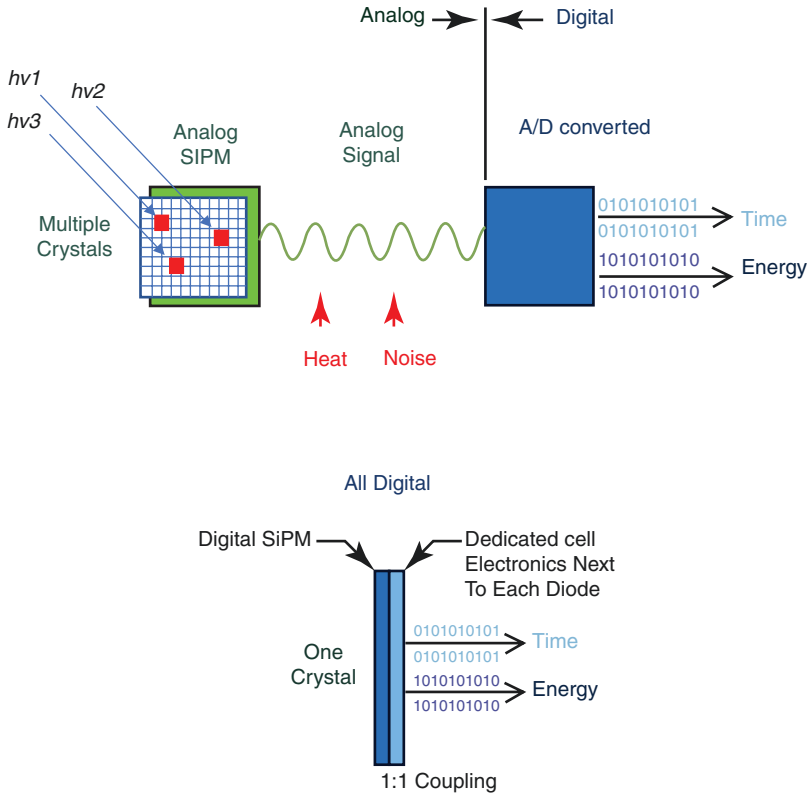
Fig. 12.16 Signal processing in PET detectors assembled with analog versus digital SiPM. In the former, an electrical analog signal that is proportional to the number of scintillation photons is recorded. The signal is constructed by building up the contributions of each individual photodiode avalanche triggered by incident photons. Analog SiPMs use single photon avalanche diode (SPAD) arrays. However, when used in conventional analog SiPMs, the pulses generated by multiple photon detections (avalanche diode breakdowns) are combined into an analog output signal that requires extensive off-chip processing to produce a photon count and time of arrival for the photon. In digital SiPM counters, however, each individual signal from each photodiode is taken as integer increment. The total count of individual contributions becomes then a digital number that is proportional to the number of photons reaching the detector, which also relates to the energy of the gamma photons that released the scintillation light quanta. (Images courtesy of Philips Healthcare)

and axial directions. The cutting process leaves a space between the small crystals; therefore, a reflective material is used to optically separate between the neighboring crystals, defining a path for the light to travel to the PMTs and to maximize light collection efficiency (Fig. 12.17a). The depth of cutting is empirically implemented so that the light is distributed in a spatially linear fashion among the exposed array of PMTs [67]. In this pseudodiscrete design, a greater depth of cutting is found at the block periphery rather than at the center. The advantage of the block detector design is improved spatial resolution by segment-ing the scintillation crystal into smaller elements viewed by a finite number of PMTs (usually 4), thus minimizing the high cost required if each crystal element is coupled to a single PMT.

In the original design developed by Casey and Nutt, the block was cut into a 4×8 crystal array, each $5.6 \times 13.5 \times 30$ mm^3, using BGO detector material. The crystal block was glued to 4 square PMTs, each 25 mm, through a Lucite light guide [68]. Now, the crystal dimensions vary among PET scanners using different types of scintillation materials. In commercial clinical PET/CT scanners, the crystal dimension varies from one
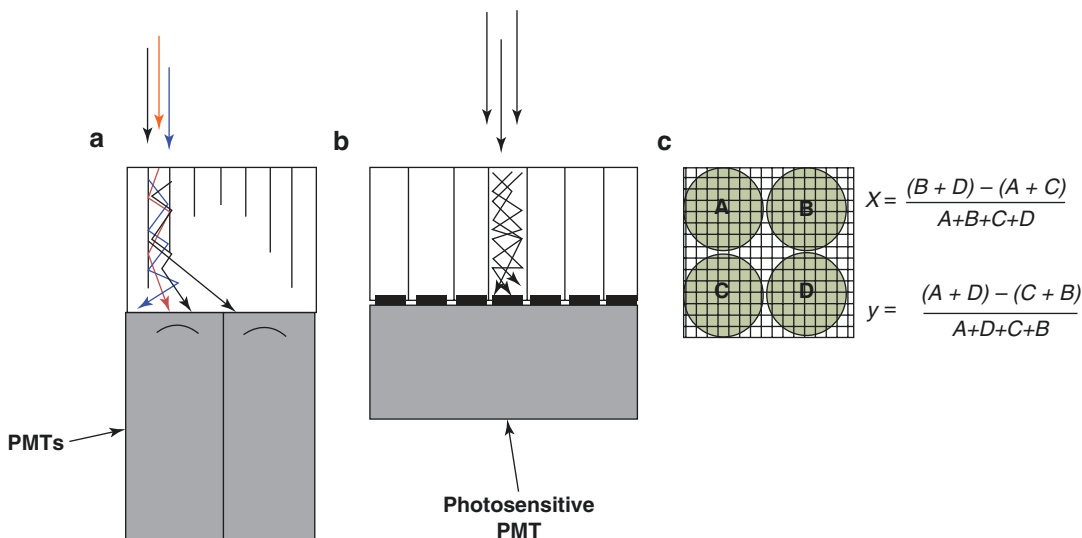
Fig. 12.17 (**a**) Crystal segmentation in block detector design. It allows defining a path for incident photons and improved collection efficiency. (**b**) Discrete crystal design,

a useful approach in high-resolution PET but with some limitations (see the text). (**c**) Anger logic positioning

system to another (e.g., 4×4, 6.4×6.4, 3.2×3.2, etc.), while the crystal thickness ranges from 20 to 30 mm. Crystal size can be reduced to 1–2 mm in an array of larger elements, such as 20×20 or 13×13, based on design specifications. However, this later arrangement is most common in small-animal micro-PET scanners.

Another choice is an assembly of *discrete individual* scintillation crystals that are packed together yet optically separated by reflective material to confine the light spread to those crystals that receive the scintillation light (Fig. 12.17b). This finger-like array of discrete crystals provides an improvement in spatial resolution. It can be read out by a position-sensitive or multichannel photodetector or individual and separate readout channels [86]. Use of semiconductor readout devices has also been implemented in the last design, in which discrete crystals are read out by an array of elements of APD [87]. APDs can be produced in dimensions (individual elements or array) similar to discrete crystal dimensions and therefore can overcome size limitations encountered in fabricating small PMTs (smaller than 10 mm) [88, 89]. They have been successfully introduced as light photodetectors in encoding the position of the light signal

and offer a compact volume that is useful in PET/MRI systems and small-animal scanners, including SPECT and PET imagers.

Discrete detector design has a number of limitations, especially when an individual crystal is read out by a single readout channel. Crystal fraction and packing must match with the size of the available photodetectors [86]. Further, it requires extensive use of electronic readout channels and thus is an expensive and cost-ineffective approach. PET systems based on discrete crystal design are more common in research and small-animal scanners [86, 88]. Alternatively, discrete crystal design can be used in a modular structure in which the crystal sets are mapped by an array of PMTs with a continuous light guide adjoining the detector modules, as can be found, for example, in the Allegro system (Philips Healthcare).

In the block detector, four PMTs are often used to read out the light emitted from the scintillation material. The centroid Anger logic is used to identify the individual crystals from which light photons were emitted (Fig. 12.17c). Another approach that improved the encoding ratio but suffers from increased dead time is the quadrant-sharing approach, in which the PMT is

Fig. 12.18 Quadrant light sharing (**a**) Frontal view. (**b**) Lateral view
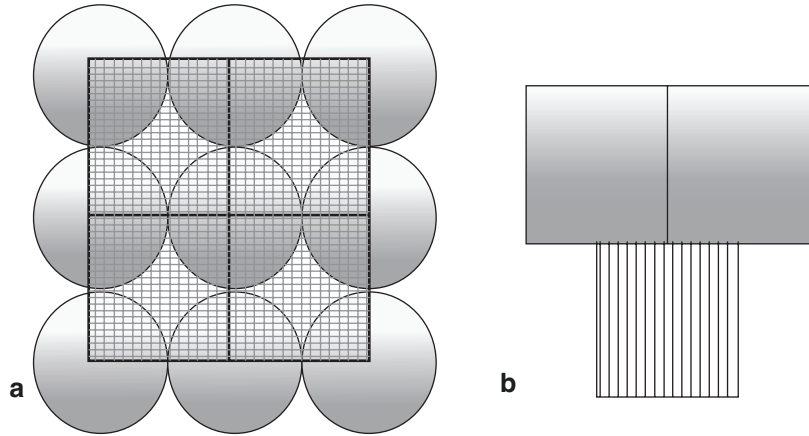
shared among four block detectors; the encoding ratio of 16:1 in the conventional block detector design is increased by three to four times based on the PMT size and the crystal dimensions [90] (Fig. 12.18). This design was initially proposed to improve the spatial resolution of the PET scanner without increasing the cost and to reduce the high price of the scanner by lowering the number of PMTs decoding the scintillation detector [91]. However, dead time effects and pulse pileup can be treated using advanced signal-processing electronics with event recovery methods [91, 92].

12.3 Type of Coincidence Events

Singles. PET detectors receive a large amount of events. A small fraction of these events are detected as in coincidence, while the remaining are singles that constitute a large fraction of the detected count rate. Singles can be detected from the coincidence field of view as well as from activity lying outside the field of view. They are a problem in 3D data acquisition, for which the axial extent of data acquisition is larger and extends over the area examined [93].

12.3.1 True Coincidences

True coincidences are those photons emitted from a single nuclei and detected by the detectors without interactions in the surrounding medium

(Fig. 12.19a). They are the most preferred type of events not actually achievable in practice without contamination with other events (scatter and randoms).

12.3.2 Random Coincidences

Random or accidental coincidences are undesired types of events that occur as a result of detecting two coincident events from two different locations while their timing falls within the coincidence timing window of the system (Fig. 12.19b). Because these two photons are unrelated, they have nearly equal probability to occur between most decaying nuclei in the field of view, resulting in a high background image. True coincidences increase in linear proportion to the object activity; however, random coincidences are estimated to equal the product of count rates of the two detectors multiplied by the timing window (2τ):

$$R_{ij} = 2\tau S_a S_b$$

where S_a and S_b are the single-photon event rate of detectors a and b, respectively. Thus, they are approximately proportional to the square of the singles count rate. Random coincidences add false information regarding position and serve to reduce image contrast and quantitative accuracy as well. They are large in areas with high count rates, such as the abdomen and pelvis, especially if bladder activity is high. A lon-
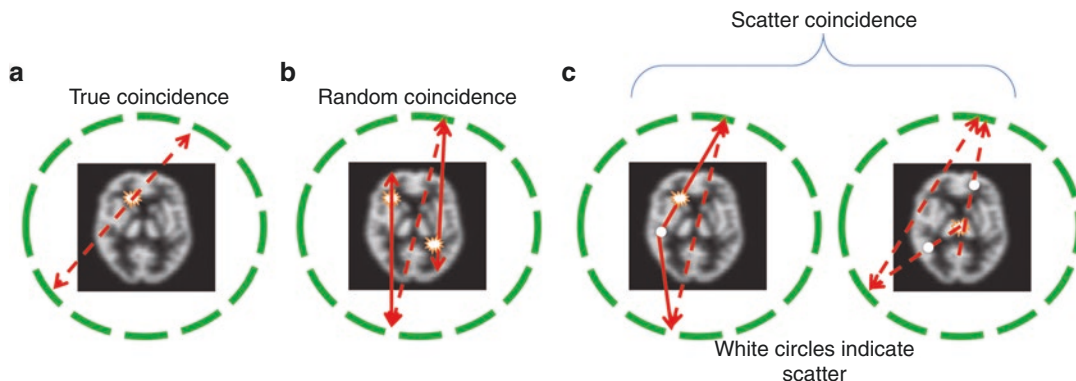
Fig. 12.19 Three different types of coincidences that take place during PET imaging. (**a**) True coincidence occurs due to decay of a single nuclei and emission of 2 antiparallel 511-keV photons and without undergoing any further interactions. (**b**) Random coincidence occurs due to decay of two unrelated nuclei such that their detection by two opposing detector pairs is within the acceptance timing window. (**c**) Scatter events take place when 1 or 2 of the 511-keV photons undergo Compton interaction during their travel to the detector pair and again with detection time within the specified limit; however, single-photon scattering is more abundant than two-photon scattering

ger coincidence timing window increases the chance of accepting more random events, but a shorter timing window reduces the number of true events. Consequently, selection of coincidence time is a trade-off between sensitivity of the scanner and reduction of undesired events such as randoms [94]. In fully 3D acquisition mode, the random events are greater than for 2D acquisition (with use of septa) since the former provides a larger axial field of view relative to the field of the true events.

The formula can be used in estimating the random events in the acquired images if the activity in the field of view remains constant during the time course of the study. However, in some situations in which the tracer undergoes some dynamic or fast metabolic processes, this method may not be precise enough. Another approach that is frequently applied is the delayed window subtraction method. This method is based on measuring the random coincidences in a delayed acceptance window; then, data are corrected on the fly by subtraction or saved for further analysis [95]. The variance estimate in data collected by the delayed window is high, and applying it directly on the prompts window will add noise to the reconstructed images. A variance reduction technique can be used to suppress such a problem to yield a better signal estimate [96].

12.3.3 Scatter Coincidences

Another undesired type of events is scattered coincidence, which results from deflection of one or both annihilation photons from their true LOR, resulting in a false recorded event regarding position of the annihilated nuclei and energy of the 511-keV photons (Fig. 12.19c). Further, scatter coincidences are a function of the activity distribution, source size, and composition of the surrounding media. Scatter events cause a loss of image contrast and degrade the quantitative accuracy of the measurements. Energy resolution plays an important role in controlling the amount of scattered photons in the acquired data. PET systems with better energy resolution have a greater capability to reject scattered photons. For a scanner with good energy resolution, such as those with LSO/LYSO or GSO detector material, the lower energy bound can be set at a threshold greater than 400 keV, and a significant amount of photons with large-angle scattering can be rejected. For a scanner with less energy resolution (e.g., BGO), the energy width is set wider, and the lower bound may go to 300 keV, which results in projection data contaminated by large proportion of scattered events. Table 12.5 shows the scatter fraction for a number of com-

Table 12.5 Scatter fractions as measured for commercial digital and conventional PET/CT scanners. All measurements were taken in 3D mode

System	Manufacturer	Crystal	Photodetectors	Energy window (keV)	Scatter fraction @ peak NECR (%)	Reference
Vereos	Philips	LYSO	SiPM	449.6–613.2	30.8–33.2	[97, 98]
Ingenuity TF	Philips	LYSO	PMT	460–665	36.7	[43, 99]
mCT flow	Siemens	LSO	PMT	435–650	33.4	[100]
Biograph vision	Siemens	LSO	SiPM	435–585	38.7	[85, 101]
Discovery MI	GE	LYSO	SiPM	425–650	40.5	[83, 84]
Discovery MI-DR	GE	LYSO	PMT	425–650	36.6	[83]
Discovery STE/VCT	GE	BGO	PMT	425–650	33.9	[58]
Discovery ST	GE	BGO	PMT	375–650	45.0	[102]

mercial PET/CT scanner designs with different scintillation crystals, photodetectors and energy window setting.

The contribution of multiple coincidences is also another possible type of events that result from three or more photons detected in the coincidence timing window, leading to detector confusion regarding where the annihilation photons are located. The detection system does not discriminate between the various types of the coincidences, and they are automatically recorded as long as their detection time falls within the specified timing limits of the scanner. These events (true, random, and scatter coincidences) are collectively called *prompts*, bearing in mind that the most useful type is the true coincidence.

12.4   2D Versus 3D

In SPECT imaging, photon detection is performed by collimator holes, which define the path along which emitted photons are collected. In a similar manner, PET scanners are able to limit the emitted photons to be accepted through one or more planes using interplane septa or the 2D acquisition mode. To increase the sensitivity of the PET scanner, the interplane septa are removed (retracted) so that the coincidence field of view can be larger than that when septa are extended. Radiation shielding provided by septa was mandatory in early PET scanners to avoid many problems arising from high count rates,

scatter, and random events. Brain studies were the first to exploit volumetric imaging provided by 3D acquisition [103]. However, the count rate arising from outside the field of view was problematic; this has been tackled by appropriate shielding at the axial end of the scanner [104]. In whole-body PET scanning, 3D acquisition has become the common mode of data acquisition implemented by all system suppliers.

Advantages of 3D imaging are an increase in sensitivity by four to five times when compared to 2D imaging, and fast scanning can be performed, avoiding patient discomfort and minimizing the likelihood of patient motion. An increase in patient throughput is an important outcome of 3D imaging and is demanded in busy and high-workload nuclear medicine departments. However, this increase in system sensitivity comes at the expense of increasing the accidental random coincidences, scatter events, and singles from activity outside the field of view. This increase in the singles count rate also leads to an increase in the system dead time and count losses.

3D PET imaging requires an improvement in scatter and random correction techniques and detectors with high count rate performance. Part of the problem can be solved by selecting an appropriate scintillation crystal coupled to high performance electronic circuits. As mentioned, the emergence of fast scintillators such as LSO or LYSO has motivated the successful use of 3D imaging in the clinical setting with a significant reduction of imaging time [105]. Fast scintilla-

tors also provide a means of reducing system dead time and serve to improve the coincidence timing window, which are critical requirements imposed by 3D data acquisition.

12.5   Conclusions

Positron emission tomography is an invaluable piece of medical technology that has demonstrated successful results in patient diagnosis and biomedical research. Scanner performance has changed significantly in the last two decades due to the incorporation of new scintillators with better detection capabilities. Digital-processing technology, including fast electronics and high computation power, introduction of solid state photodetectors along with robust correction algorithms were milestones in the development of a new generation of PET scanners showing better performance characteristics. The new advances in these technologies have resulted in a reduction of the acquisition time, reduction of the injected dose, and an increase in scanner throughput. Diagnostic confidence and better clinical outcome were also remarkable. PET/CT scanners with long axial field of view recently developed will enrich the diagnostic world of PET imaging with anticipation of novel medical applications in disease detection and management.

References

1. Phelps ME. PET: the merging of biology and imaging into molecular imaging. J Nucl Med. 2000;41(4):661–81.
2. Tai YF, Piccini P. Applications of positron emission tomography (PET) in neurology. J Neurol Neurosurg Psychiatry. 2004;75(5):669–76.
3. Pichler BJ, Wehrl HF, Judenhofer MS. Latest advances in molecular imaging instrumentation. J Nucl Med. 2008;49(Suppl 2):5S–23S.
4. Blodgett TM, Meltzer CC, Townsend DW. PET/CT: form and function. Radiology. 2007;242(2):360–85.
5. Hany TF, Steinert HC, Goerres GW, Buck A, von Schulthess GK. PET diagnostic accuracy: improvement with in-line PET-CT system: initial results. Radiology. 2002;225(2):575–81.
6. Podgorsak EB. Radiation physics for medical physicists. Berlin: Springer; 2005.
7. Levin CS, Hoffman EJ. Calculation of positron range and its effect on the fundamental limit of positron emission tomography system spatial resolution. Phys Med Biol. 1999;44(3):781–99.
8. Sanchez-Crespo A, Andreo P, Larsson SA. Positron flight in human tissues and its influence on PET image spatial resolution. Eur J Nucl Med Mol Imaging. 2004;31(1):44–51.
9. Cherry S, Sorenson J, Phelps M. Physics in nuclear medicine. 4th ed. Philadelphia: Saunders; 2012.
10. Caribe P, Koole M, D'Asseler Y, Deller TW, Van Laere K, Vandenberghe S. NEMA NU 2-2007 performance characteristics of GE Signa integrated PET/MR for different PET isotopes. EJNMMI Phys. 2019;6(1):11.
11. Carter LM, Kesner AL, Pratt EC, Sanders VA, Massicano AVF, Cutler CS, et al. The impact of positron range on PET resolution, evaluated with phantoms and PHITS Monte Carlo simulations for conventional and non-conventional radionuclides. Mol Imaging Biol. 2020;22(1):73–84.
12. Anger HO. Scintillation camera. Rev Sci Instrum. 1958;29:27–33.
13. Budinger TF. PET instrumentation: what are the limits? Semin Nucl Med. 1998;28(3):247–67.
14. Peschina W, Conca A, Konig P, Fritzsche H, Beraus W. Low frequency rTMS as an add-on antidepressive strategy: heterogeneous impact on 99mTc-HMPAO and 18 F-FDG uptake as measured simultaneously with the double isotope SPECT technique. Pilot study. Nucl Med Commun. 2001;22(8):867–73.
15. Sandler MP, Videlefsky S, Delbeke D, Patton JA, Meyerowitz C, Martin WH, et al. Evaluation of myocardial ischemia using a rest metabolism/stress perfusion protocol with fluorine-18 deoxyglucose/technetium-99m MIBI and dual-isotope simultaneous-acquisition single-photon emission computed tomography. J Am Coll Cardiol. 1995;26(4):870–8.
16. Laymon CM, Turkington TG. Characterization of septal penetration in 511 keV SPECT. Nucl Med Commun. 2006;27(11):901–9.
17. Turkington TG. Introduction to PET instrumentation. J Nucl Med Technol. 2001;29(1):4–11.
18. Lonneux M, Delval D, Bausart R, Moens R, Willockx R, Van Mael P, et al. Can dual-headed 18F-FDG SPET imaging reliably supersede PET in clinical oncology? A comparative study in lung and gastrointestinal tract cancer. Nucl Med Commun. 1998;19(11):1047–54.
19. Bergmann H, Dobrozemsky G, Minear G, Nicoletti R, Samal M. An inter-laboratory comparison study of image quality of PET scanners using the NEMA NU 2-2001 procedure for assessment of image quality. Phys Med Biol. 2005;50(10):2193–207.
20. Kadrmas DJ, Christian PE. Comparative evaluation of lesion detectability for 6 PET imaging platforms using a highly reproducible whole-body phantom with (22)Na lesions and localization ROC analysis. J Nucl Med. 2002;43(11):1545–54.
21. Bailey DL, Young H, Bloomfield PM, Meikle SR, Glass D, Myers MJ, et al. ECAT ART - a continuously rotating PET camera: performance characteristics,

initial clinical studies, and installation considerations in a nuclear medicine department. Eur J Nucl Med. 1997;24(1):6–15.

22. Beyer T, Townsend DW, Brun T, Kinahan PE, Charron M, Roddy R, et al. A combined PET/CT scanner for clinical oncology. J Nucl Med. 2000;41(8):1369–79.

23. Karp JS, Muehllehner G, Mankof FD, Ordonez CE, Ollinger JM, Daube-Witherspoon ME, et al. Continuous-slice PENN-PET: a positron tomograph with volume imaging capability. J Nucl Med. 1990;31(5):617–27.

24. Surti S, Karp JS. Imaging characteristics of a 3-dimensional GSO whole-body PET camera. J Nucl Med. 2004;45(6):1040–9.

25. Adam LE, Karp JS, Daube-Witherspoon ME, Smith RJ. Performance of a whole-body PET scanner using curve-plate NaI(Tl) detectors. J Nucl Med. 2001;42(12):1821–30.

26. Karp JS, Surti S, Daube-Witherspoon ME, Freifelder R, Cardi CA, Adam LE, et al. Performance of a brain PET camera based on anger-logic gadolinium oxyorthosilicate detectors. J Nucl Med. 2003;44(8): 1340–9.

27. Surti S, Kuhn A, Werner ME, Perkins AE, Kolthammer J, Karp JS. Performance of Philips Gemini TF PET/CT scanner with special consideration for its time-of-flight imaging capabilities. J Nucl Med. 2007;48(3):471–80.

28. Surti S, Karp JS, Freifelder R, Liu F. Optimizing the performance of a PET detector using discrete GSO crystals on a continuous lightguide. IEEE Trans Nucl Sci. 2000;47:1030–6.

29. de Jong HW, van Velden FH, Kloet RW, Buijs FL, Boellaard R, Lammertsma AA. Performance evaluation of the ECAT HRRT: an LSO-LYSO double layer high resolution, high sensitivity scanner. Phys Med Biol. 2007;52(5):1505–26.

30. Phelps ME. Molecular imaging with positron emission tomography. Annu Rev Nucl Part Sci. 2002;52:303–38.

31. Vandenberghe S, Moskal P, Karp JS. State of the art in total body PET. EJNMMI Phys. 2020;7(1):35.

32. Badawi RD, Shi H, Hu P, Chen S, Xu T, Price PM, et al. First human imaging studies with the EXPLORER total-body PET scanner. J Nucl Med. 2019;60(3):299–303.

33. Zhang X, Zhou J, Cherry SR, Badawi RD, Qi J. Quantitative image reconstruction for total-body PET imaging using the 2-meter long EXPLORER scanner. Phys Med Biol. 2017;62(6):2465–85.

34. Karp JS, Viswanath V, Geagan MJ, Muehllehner G, Pantel AR, Parma MJ, et al. PennPET Explorer: design and preliminary performance of a whole-body imager. J Nucl Med. 2020;61(1):136–43.

35. Pantel AR, Viswanath V, Daube-Witherspoon ME, Dubroff JG, Muehllehner G, Parma MJ, et al. PennPET Explorer: human imaging on a whole-body imager. J Nucl Med. 2020;61(1):144–51.

36. National Electrical Manufacturers Association. Performance measurements of positron emission tomographs (PET). NEMA Standards Publication NU 2-2018. Rosslyn: National Electrical Manufacturers Association; 2018.

37. Lewellen TK. Recent developments in PET detector technology. Phys Med Biol. 2008;53(17):R287–317.

38. Khalil MM. PET/MR: basics and new developments. In: Khalil M, editor. Basic science of PET imaging. 1st ed. Cham: Springer; 2016.

39. Shao Y, Cherry SR, Farahani K, Meadors K, Siegel S, Silverman RW, et al. Simultaneous PET and MR imaging. Phys Med Biol. 1997;42(10):1965–70.

40. Veit-Haibach P, Kuhn FP, Wiesinger F, Delso G, von Schulthess G. PET-MR imaging using a tri-modality PET/CT-MR system with a dedicated shuttle in clinical routine. MAGMA. 2013;26(1):25–35.

41. von Schulthess GK, Schlemmer HP. A look ahead: PET/MR versus PET/CT. Eur J Nucl Med Mol Imaging. 2009;36(Suppl 1):S3–9.

42. Spick C, Herrmann K, Czernin J. 18F-FDG PET/CT and PET/MRI perform equally well in cancer: evidence from studies on more than 2,300 patients. J Nucl Med. 2016;57(3):420–30.

43. Zaidi H, Ojha N, Morich M, Griesmer J, Hu Z, Maniawski P, et al. Design and performance evaluation of a whole-body ingenuity TF PET-MRI system. Phys Med Biol. 2011;56(10):3091–106.

44. Delso G, Furst S, Jakoby B, Ladebeck R, Ganter C, Nekolla SG, et al. Performance measurements of the Siemens mMR integrated whole-body PET/MR scanner. J Nucl Med. 2011;52(12):1914–22.

45. Levin CG, Deller T, McDaniel D, Peterson W, Maramraju S. Prototype time-of-flight PET ring integrated with a 3T MRI system for simultaneous whole-body PET/MR imaging. J Nucl Med. 2013;54(Suppl 2):148.

46. Grant AM, Deller TW, Khalighi MM, Maramraju SH, Delso G, Levin CS. NEMA NU 2-2012 performance studies for the SiPM-based ToF-PET component of the GE SIGNA PET/MR system. Med Phys. 2016;43(5):2334.

47. Huo E, Wilson DM, Eisenmenger L, Hope TA. The role of PET/MR imaging in precision medicine. PET Clin. 2017;12(4):489–501.

48. Valladares A, Ahangari S, Beyer T, Boellaard R, Chalampalakis Z, et al. Clinically valuable quality control for PET/MRI systems: consensus recommendation from the HYBRID consortium. Front Phys. 2019;7:136. https://doi.org/10.3389/fphy.2019.00136.

49. Boellaard R, Quick HH. Current image acquisition options in PET/MR. Semin Nucl Med. 2015;45(3):192–200.

50. Knoll GF (Editor). Radiation detection and measurement, 4th Edition, ISBN: 978-0-470-13148-0, Wiley; 2010.

51. Moses WW, Derenzo SE. In: Dorenbos P, Eijk CWEv, editors. Proceedings of SCINT'95, Delft, The Netherlands (LBNL 37720), 1996. p. 9–16.

52. Humm JL, Rosenfeld A, Del Guerra A. From PET detectors to PET scanners. Eur J Nucl Med Mol Imaging. 2003;30(11):1574–97.

53. Melcher CL. Scintillation crystals for PET. J Nucl Med. 2000;41(6):1051–5.

54. van Eijk CW. Inorganic scintillators in medical imaging. Phys Med Biol. 2002;47(8):R85–106.

55. Surti S, Karp JS. A count-rate model for PET scanners using pixelated Anger-logic detectors with different scintillators. Phys Med Biol. 2005;50(23):5697–715.

56. Surti S. Update on time-of-flight PET imaging. J Nucl Med. 2015;56(1):98–105.

57. Karp JS. Against: is LSO the future of PET? Eur J Nucl Med Mol Imaging. 2002;29(11):1525–8.

58. Teras M, Tolvanen T, Johansson JJ, Williams JJ, Knuuti J. Performance of the new generation of whole-body PET/CT scanners: discovery STE and discovery VCT. Eur J Nucl Med Mol Imaging. 2007;34(10):1683–92.

59. Martinez MJ, Bercier Y, Schwaiger M, Ziegler SI. PET/CT biograph sensation 16. Performance improvement using faster electronics. Nuklearmedizin. 2006;45(3):126–33.

60. Bloomfield PM, Rajeswaran S, Spinks TJ, Hume SP, Myers R, Ashworth S, et al. The design and physical characteristics of a small animal positron emission tomograph. Phys Med Biol. 1995;40(6):1105–26.

61. Yamamoto S, Kuroda K, Senda M. Scintillator selection for MR-compatible gamma detectors. IEEE Trans Nucl Sci. 2003;50(5):1683–5.

62. Cherry SR. The 2006 Henry N. Wagner Lecture: of mice and men (and positrons)—advances in PET imaging technology. J Nucl Med. 2006;47(11):1735–45.

63. Nutt R. For: is LSO the future of PET? Eur J Nucl Med Mol Imaging. 2002;29(11):1523–5.

64. Wienhard K, Schmand M, Casey ME, et al. The ECAT HRRT: performance and first clinical application of the new high resolution research tomograph. IEEE Trans Nucl Sci. 2002;49:104–10.

65. Doshi NK, Shao Y, Silverman RW, Cherry SR. Design and evaluation of an LSO PET detector for breast cancer imaging. Med Phys. 2000;27(7):1535–43.

66. Cherry SR, et al. MicroPET: a high resolution PET scanner for imaging small animals. IEEE Trans Nucl Sci. 1997;1161:44–6.

67. Zanzonico P. Positron emission tomography: a review of basic principles, scanner design and performance, and current systems. Semin Nucl Med. 2004;34(2):87–111.

68. Casey ME, Nutt R. A multicrystal two dimensional BGO detector system for positron emission tomography. IEEE Trans Nucl Sci. 1986;33(1):460–3.

69. Lecomte R. Novel detector technology for clinical PET. Eur J Nucl Med Mol Imaging. 2009;36(Suppl 1):S69–85.

70. Bergeron M, Thibaudeau C, Cadorette J, Tétrault M, Pepin CM, Clerk-Lamalice J, et al. LabPET II, an APD-based detector module with PET and counting CT imaging capabilities. IEEE Trans Nucl Sci. 2015;62(3):756–65.

71. Pichler BJ, Judenhofer MS, Catana C, Walton JH, Kneilling M, Nutt RE, et al. Performance test of an LSO-APD detector in a 7-T MRI scanner for simultaneous PET/MRI. J Nucl Med. 2006;47(4):639–47.

72. Shah KS, Grazioso R, Farrell R, Glodo J, Mcclish MA, Entine G, et al. Position sensitive APDs for small animal PET imaging. In: IEEE nuclear science symposium conference record, Norfolk, VA, USA, vol 3, 2002. p. 1411–5.

73. Shah KS, Farrell R, Grazioso R, Harmon ES, Karplus E. Position sensitive avalanche photodiodes for gamma ray imaging. IEEE Trans Nucl Sci. 2002;49(4):1687–92.

74. Yang Y, Dokhale PA, Silverman RW, Shah KS, McClish MA, Farrell R, et al. Depth of interaction resolution measurements for a high resolution PET detector using position sensitive avalanche photodiodes. Phys Med Biol. 2006;51(9):2131–42.

75. Yang Y, Wu Y, Qi J, St James S, Du H, Dokhale PA, et al. A prototype PET scanner with DOI-encoding detectors. J Nucl Med. 2008;49(7):1132–40.

76. Renker D. Geiger mode avalanche photodiodes, history, properties and problems. Nucl Instrum Meth Phys Res A. 2006;48(56):567.

77. Otte N, Dolgoshein B, Hose J, Klemin S, Lorenz E, Mirzoyan R, et al. The SiPM a new photon detector for PET, nuclear physics B. In: Proceedings of the 9th topical seminar on innovative particle and radiation detectors, vol 150, 2006. p. 417–20.

78. Schaart DR, van Dam HT, Seifert S, Vinke R, Dendooven P, Lohner H, et al. A novel, SiPM-array-based, monolithic scintillator detector for PET. Phys Med Biol. 2009;54(11):3501–12.

79. Maas MC, Schaart DR, van der Laan DJ, Bruyndonckx P, Lemaitre C, Beekman FJ, et al. Monolithic scintillator PET detectors with intrinsic depth-of-interaction correction. Phys Med Biol. 2009;54(7):1893–908.

80. Nguyen NC, Vercher-Conejero JL, Sattar A, Miller MA, Maniawski PJ, Jordan DW, et al. Image quality and diagnostic performance of a digital PET prototype in patients with oncologic diseases: initial experience and comparison with analog PET. J Nucl Med. 2015;56(9):1378–85.

81. Lopez-Mora DA, Flotats A, Fuentes-Ocampo F, Camacho V, Fernandez A, Ruiz A, et al. Comparison of image quality and lesion detection between digital and analog PET/CT. Eur J Nucl Med Mol Imaging. 2019;46(6):1383–90.

82. Rausch I, Ruiz A, Valverde-Pascual I, Cal-Gonzalez J, Beyer T, Carrio I. Performance evaluation of the Vereos PET/CT system according to the NEMA NU2-2012 Standard. J Nucl Med. 2019;60(4):561–7.

83. Chicheportiche A, Marciano R, Orevi M. Comparison of NEMA characterizations for discovery MI and discovery MI-DR TOF PET/CT systems at different sites and with other commercial PET/CT systems. EJNMMI Phys. 2020;7(1):4.

84. Hsu DFC, Ilan E, Peterson WT, Uribe J, Lubberink M, Levin CS. Studies of a next-generation silicon-photomultiplier-based time-of-flight PET/CT system. J Nucl Med. 2017;58(9):1511–8.

85. van Sluis J, de Jong J, Schaar J, Noordzij W, van Snick P, Dierckx R, et al. Performance characteristics of the digital biograph vision PET/CT system. J Nucl Med. 2019;60(7):1031–6.

86. Tai YC, Laforest R. Instrumentation aspects of animal PET. Annu Rev Biomed Eng. 2005;7:255–85.

87. Pichler BJ, Swann BK, Rochelle J, Nutt RE, Cherry SR, Siegel SB. Lutetium oxyorthosilicate block detector readout by avalanche photodiode arrays for high resolution animal PET. Phys Med Biol. 2004;49(18):4305–19.

88. Surti S, Karp JS, Kinahan PE. PET instrumentation. Radiol Clin N Am. 2004;42(6):1003–16, vii.

89. Ziegler SI, Pichler BJ, Boening G, Rafecas M, Pimpl W, Lorenz E, et al. A prototype high-resolution animal positron tomograph with avalanche photodiode arrays and LSO crystals. Eur J Nucl Med. 2001;28(2):136–43.

90. Muehllehner G, Karp JS. Positron emission tomography. Phys Med Biol. 2006;51(13):R117–37.

91. Wong W, Uribe J, Hicks K, Hu G. An analog decoding BGO block detector using circular photomultipliers. IEEE Trans Nucl Sci. 1995;42:1095–101.

92. Liu J, Li H, Wang Y, Kim S, et al. Real time digital implementation of the high yield pileup event recover (HYPER) method. In: IEEE nuclear science symposium conference record, 2007. p. 4230–2.

93. Bailey DL. Data acquisition and performance characterization in PET. In: Bailey DL, Townsend DW, Valk PE, Maisey MN, editors. Positron emission tomography: basic sciences. London: Springer; 2006.

94. Meikle SR, Badawi RD. Quantitative techniques in PET. In: Bailey DL, Townsend DW, Valk PE, Maisey MN, editors. Positron emission tomography: basic sciences. London: Springer; 2006.

95. Lewellen T, Karp J. PET systems. In: Wernick M, Aarsvold J, editors. Emission tomography: the fundamentals of PET and SPECT. San Diego: Elsevier Academic; 2004.

96. Badawi RD, Miller MP, Bailey DL, Marsden PK. Randoms variance reduction in 3D PET. Phys Med Biol. 1999;44(4):941–54.

97. Salvadori J, Labour J, Odille F, Marie PY, Badel JN, Imbert L, et al. Monte Carlo simulation of digital photon counting PET. EJNMMI Phys. 2020;7(1):23.

98. Zhang J, Maniawski P, Knopp MV. Performance evaluation of the next generation solid-state digital photon counting PET/CT system. EJNMMI Res. 2018;8(1):97.

99. Kolthammer JA, Su KH, Grover A, Narayanan M, Jordan DW, Muzic RF. Performance evaluation of the ingenuity TF PET/CT scanner with a focus on high count-rate conditions. Phys Med Biol. 2014;59(14):3843–59.

100. Rausch I, Cal-Gonzalez J, Dapra D, Gallowitsch HJ, Lind P, Beyer T, et al. Performance evaluation of the biograph mCT flow PET/CT system according to the NEMA NU2-2012 standard. EJNMMI Phys. 2015;2(1):26.

101. Kunnen B, Beijst C, Lam M, Viergever MA, de Jong H. Comparison of the biograph vision and biograph mCT for quantitative (90)Y PET/CT imaging for radioembolisation. EJNMMI Phys. 2020;7(1):14.

102. Mawlawi O, Podoloff DA, Kohlmyer S, Williams JJ, Stearns CW, Culp RF, et al. Performance characteristics of a newly developed PET/CT scanner using NEMA standards in 2D and 3D modes. J Nucl Med. 2004;45(10):1734–42.

103. Dhawan V, Kazumata K, Robeson W, Belakhlef A, Margouleff C, Chaly T, et al. Quantitative brain PET. Comparison of 2D and 3D acquisitions on the GE advance scanner. Clin Positron Imaging. 1998;1(2):135–44.

104. Bailey DL, Miller MP, Spinks TJ, Bloomfield PM, Livieratos L, Young HE, et al. Experience with fully 3D PET and implications for future high-resolution 3D tomographs. Phys Med Biol. 1998;43(4):777–86.

105. Everaert H, Vanhove C, Lahoutte T, Muylle K, Caveliers V, Bossuyt A, et al. Optimal dose of 18F-FDG required for whole-body PET using an LSO PET camera. Eur J Nucl Med Mol Imaging. 2003;30(12):1615–9.

Positron Emission Tomography (PET): Characteristics and Performance

Magdy M. Khalil

Contents

13.1 Introduction

Positron emission tomography (PET) scanning systems convey valuable metabolic and physiologic information about human diseases. Their technical and physical performance should therefore meet certain qualification standards to reliably use this information in patient diagnosis and subsequent utilization in treatment strategies. There are several operating parameters that monitor and/or control the stability, reproducibility and reliability of the scanning PET systems. This chapter was designed to highlight those parameters that need special attention and of particular importance for daily practice of PET imaging systems. NEMA offers uniform and consistent method for measuring and reporting performance parameters. NEMA acceptance testing is the first-line procedure recorded for scanner performance, and its measurements can be used as reference values for subsequent operations or calibrations needed for the scanner. NEMA-94 and NEMA NU 2-2001, NEMA NU 2-2007, NEMA NU 2-2012, and the recently released NEMA NU 2-2018 and the International Electrotechnical Commission (IEC) provide guidelines to those who are involved in accepting the machines as well those who are assigned to keep the device in a uniform mode of performance. Performance measures required by NEMA are spatial resolution, sensitivity, scatter fraction, count losses and random

M. M. Khalil (✉)

Medical Biophysics, Department of Physics, Faculty of Science, Helwan University, Cairo, Egypt

generation, image quality, accuracy of correction for scatter, dead time, randoms, and attenuation. The revised standards (i.e. NEMA NU 2-2018) have added two new tests including measurement of TOF resolution for TOF-PET scanners and coregistration accuracy between CT and PET components of the imaging system.

Daily performance tests are essential to check the stability of the system and to ensure day-to-day performance consistency.

13.2 System Sensitivity

For a given activity distribution inside a human body and fixed acquisition time, the signal-to-noise ratio and image quality are substantially influenced by the sensitivity of the PET scanner. This can be noted in dynamic studies in which short time intervals require a detection system with high sensitivity to collect the maximum amount of information. This is particularly important in areas of poor count uptake or in short half-life positron emitters (e.g., Rb-82 or O-15). PET systems with high detection efficiency allow for better counting statistics that impact positively on image quality in terms of improved signal-to-noise ratio, spatial resolution and contrast resolution, and also any subsequent quantitative analysis.

The sensitivity of PET scanners can be classified into two major components: geometric and intrinsic efficiency. The former is related to the detector geometric design and how its elements are packed closely together so that fewer photons can escape without undergoing an interaction [1]. In other words, the angular coverage obtained by the detector surface area should be large enough when exposed to the emitted radiations. The ring-packing fraction can be defined as the ratio of the true detection area to the total circumferential ring area [2]. For example, the packing fraction of the Advance GE scanner was calculated to be 0.844 in comparison to a nonsegmented solid annulus detector based on simulation results

obtained from the SimSET software package [3]. The other component is the intrinsic efficiency of the detector, which is related to the type and composition of the scintillation material and is determined by scintillator density and its effective atomic number Z_{eff}. Other factors that influence the overall system sensitivity are energy and time window settings.

Geometric efficiency can be increased by reducing the diameter of the detector ring or extending the field of view in the axial direction. Reducing the system diameter will expose the detector more efficiently to the annihilation photons by increasing the solid angle, but this comes at the cost of spatial resolution loss caused by parallax depth of interaction (DOI) error. This phenomenon is of importance when attempts are made to improve the spatial resolution of small-animal scanners in which the scanner diameter is significantly small (10–15 cm) when compared to a clinical whole-body PET scanner (70–90 cm).

Dedicated PET scanners for brain imaging enjoy also better solid-angle coverage for the emitted 511-keV photons, and hence an improvement in system sensitivity but again this is accomplished at the cost of increased radial resolution loss. This last limitation has been treated by designing dedicated brain scanners that include DOI correction utilizing two scintillation layers or what is called a "phoswich" design, in which LSO crystals are stacked to GSO or LYSO and differences in light decay are exploited to discriminate between events based on pulse shape discrimination [4]. The other way is to increase the axial extent of the scanner, an issue that is more related to the cost of the scanner as one needs to add more detector material, including scintillation crystals, readout channels, and additional electronic circuitry. In 3D acquisition, an increase in the axial extent by 30% can lead to an increase in the volume sensitivity by approximately 80% [5, 6]. A point source and 200-cm-long line source geometric coverage with a 1-m axial extent scanner would result in solid-angle fraction of about 0.8 and 0.2, respectively (notice

the great reduction of geometric efficiency for the 200 cm line source). However, the gain in sensitivity with respect to 20-cm-long axial configuration can therefore go up to a factor of 3 and 40 respectively in a PET system with 200 cm axial extent [7].

As described in the previous chapter, the newly developed Penn Explorer and the total-body uEXPLORER have achieved a half and full length coverage of patients undergoing PET imaging. The superb counting efficiency provided by the long-axial field of view has resulted in several merits including reduced injected radioactivity, lower effective dose, reduced imaging time, low likelihood of patient motion, increased signal to noise ratio satisfying statistical requirements for improved spatial resolution [8]. Sensitivity can be effectively increased by a factor of about 40 for total-body scanning while a factor of about 4–5 for single organs such as cardiac and brain-based examinations [9].

Moreover, tracer dynamics and kinetics of biodistribution can be acquired and visualized within all organs at a time and thus kinetic modeling can be carried out deciphering many pathophysiological disorders [10]. The ultra-sensitivity of the system as well as adding a fast dynamic image reconstruction enabled data acquisition on a subsecond timing level. This would substantially impact tracer kinetics and motion-dependent organs as well as eliminating or minimizing temporal associated artifacts [11]. An example F18-FDG PET/CT images acquired using the Penn Explorer and uEXPLORER are shown in Figs. 13.1, 13.2, and 13.3. In Fig. 13.1, a male patient was injected with a radioactive dose of 0.56 mCi and scanned at 40-, 90- and 180-min after injection for a period of 20 min each. Figures 13.2 and 13.3 show F18-FDG images for female patients injected with 15 mCi and acquisition started 1.5 h post administration.

The *intrinsic efficiency*, however, is a matter of crystal type and thickness. The crystal den-

sity and effective atomic number determine the linear attenuation coefficient, that is, the ability of the detector material to attenuate incident radiations. One can therefore estimate the coincidence detector intrinsic efficiency using the formula $(1 - e^{-ul})^2$. A 3-cm thick BGO crystal can stop approximately 87% of the incident photon and thereby is considered an efficient scintillator material, whereas the same crystal thickness for NaI(Tl) can stop about 40% of incident 511-keV photons. Increasing the LSO crystal thickness from 2 to 3 cm would lead to an increase by 40% of the detector intrinsic efficiency [6]. However, these values are altered when an energy threshold is varied or the timing window of the system is changed. Increasing the crystal thickness is also not an advantage as it enhances DOI errors. Increasing the crystal thickness could lead to more crystal penetration, especially for photons that are radially shifted from the center field of view; this results in event mispositioning and spatial resolution errors. For example, BaF_3 crystal is a fast scintillator, but unfortunately it has lower detection efficiency; thus, the crystal needs to be thicker (e.g., 45 mm) than normally used for BGO or other crystals of high detection efficiency. This was found to degrade the spatial resolution of the system especially as one moves to radial positions [2]. For comparison, Fig. 13.4a shows the sensitivity of clinical PET and SPECT scanners together with their preclinical counterparts.

13.3 Spatial Resolution

Spatial resolution is a crucial performance parameter of the PET imaging systems. Attempts are continuously carried out to improve the spatial resolution of PET images. Functional images acquired with poor spatial resolution have several drawbacks, such as the likelihood of missing small metabolically active lesions, inaccurate quantitative measurements, and finally higher

Fig. 13.1 Clinical 18FDG images acquired with Penn Explorer for female patient, 62 years old, BMI of 26.5, administered with radioactivity of 15 mCi. Images were acquired at 1.5 h post injection for a duration of (**a**) 16 min and (**b**) 2 min. Many thanks to Profs Joel Karp and Suleman Surti, University of Pennsylvania, Department of Radiology, USA, for providing the images

a

16 min scan

b

2 min scan
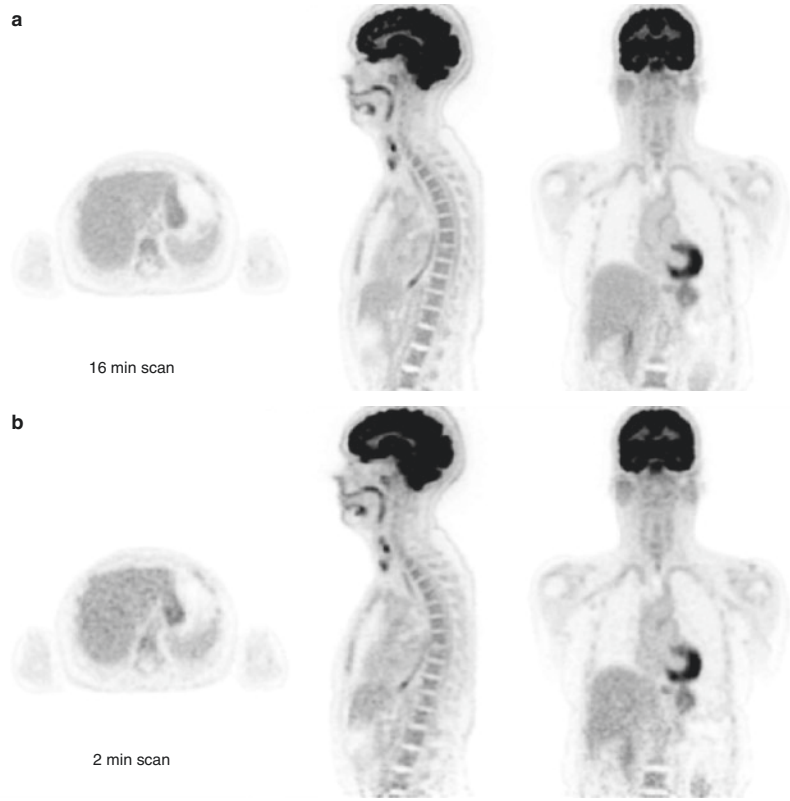
likelihood of misdiagnosis. Factors affecting the resolution limits are detector size, positron range, and photon acollinearity in addition to other physical and engineering parameters.

The spatial resolution of PET scanners is evaluated by measuring the FWHM of the point spread function. The FWHM can be approximated and parameterized as

$$\text{FWHM} = \left(\sum_i^n R_i^2 \right)^{1/2}$$

where R_i is the resolution element and can be as many parameters (i.e., n) as far as they affect image spatial resolution. An empirical mathematical form of the spatial resolution has been formulated:

$$\text{FWHM} \approx 1.25 \sqrt{\left(\frac{d}{2} \right)^2 + b^2 + \left(0.0022 \right)^2 + r^2}$$

where d is the detector width, b accounts for secondary components that contribute to spatial resolution loss in the photon detection process or spatial resolution loss due to block detector effect, the factor ($0.0022D$) is the acollinearity associated with angular deviations from 180° and D is the detector ring diameter, and r^2 is a parameter related to positron range blurring effects. The constant 1.25 is related to the applied image reconstruction algorithm [12].

The NEMA guidelines measure the spatial resolution of the PET scanner at different locations within the field of view using a small point source of ^{18}F (or ^{22}Na source based on NEMA NU 2-2018 recommendations) and the spatial resolution is determined by measuring the FWHM and FWTM of the resulting images. Image reconstruction is performed by filtered backprojection (FBP) with a ramp filter [13]. Figure 13.4b shows the spatial resolution of clinical and preclinical

Fig. 13.2 Clinical 18FDG images acquired with Penn Explorer for female patient, 56 years old, BMI of 21.6, administered with radioactivity of 15 mCi. Images were acquired at 1.5 h post injection for a duration of 10 min. One can appreciate the quality of the images with a significant coverage of the body length in one imaging bed. Many thanks to Prof Ramsey Badawy and Dr. Yasser Gaber, UC Davis, California, USA, for providing the images
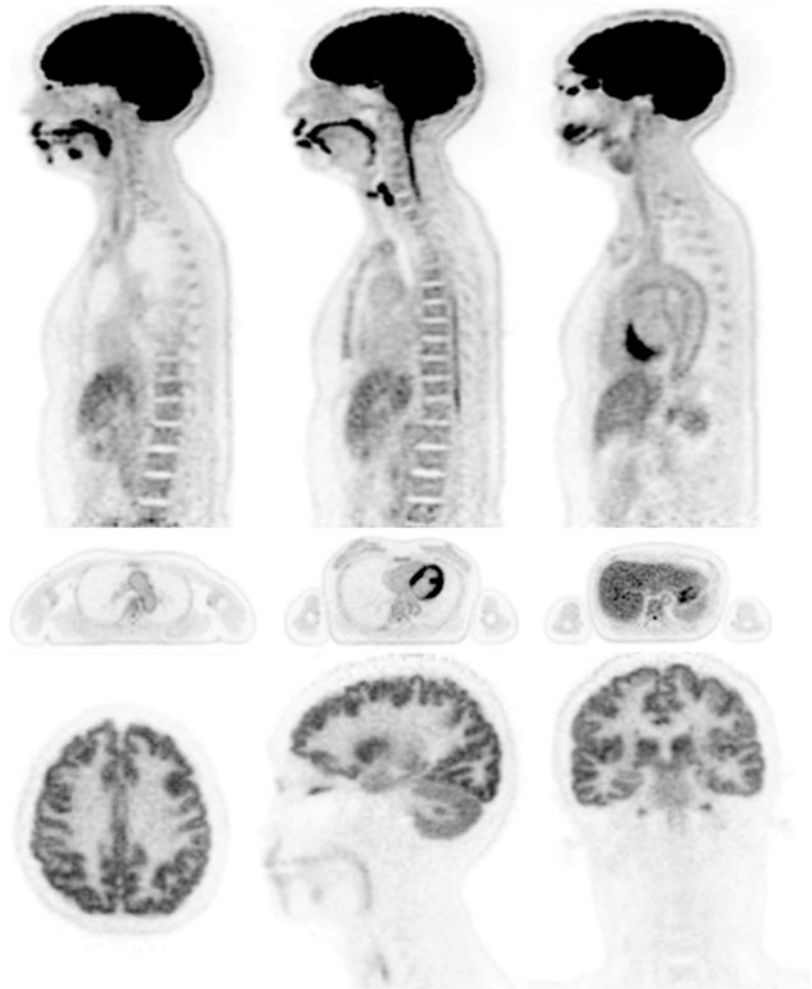
PET scanners in comparison to their SPECT counterparts.

Positron range is an unavoidable physical phenomenon, and some investigators suggested the use of a high magnetic field to reduce its impact on the resolution of the reconstructed images. However, this is might be an impractical approach due to the fact that PET/MRI is still not widely available and a limited magnetic field strength is currently applied in clinical systems [14]. While some reports showed the improvement of spatial resolution in the in-plane axis, there is some deterioration in the plane axis, there is some deterioration in the

axial plane and also in presence of different tissue interface as well as being higher in isotopes of large E_{max} [15, 16].

Fortunately, the most usable positron emitter, F-18, has a minimal positron range effect on the resolution of the reconstructed images. While efforts are often performed to improve scanner resolving capabilities, particularly for those of preclinical imaging and dedicated PET systems, an appropriate correction for the positron blurring effects would be essential to realize the full potential of the scanner spatial resolution. An intrinsic spatial resolution of 600 μm (0.6 mm, FWHM)

40-60 min   90-110 min   180-200 min
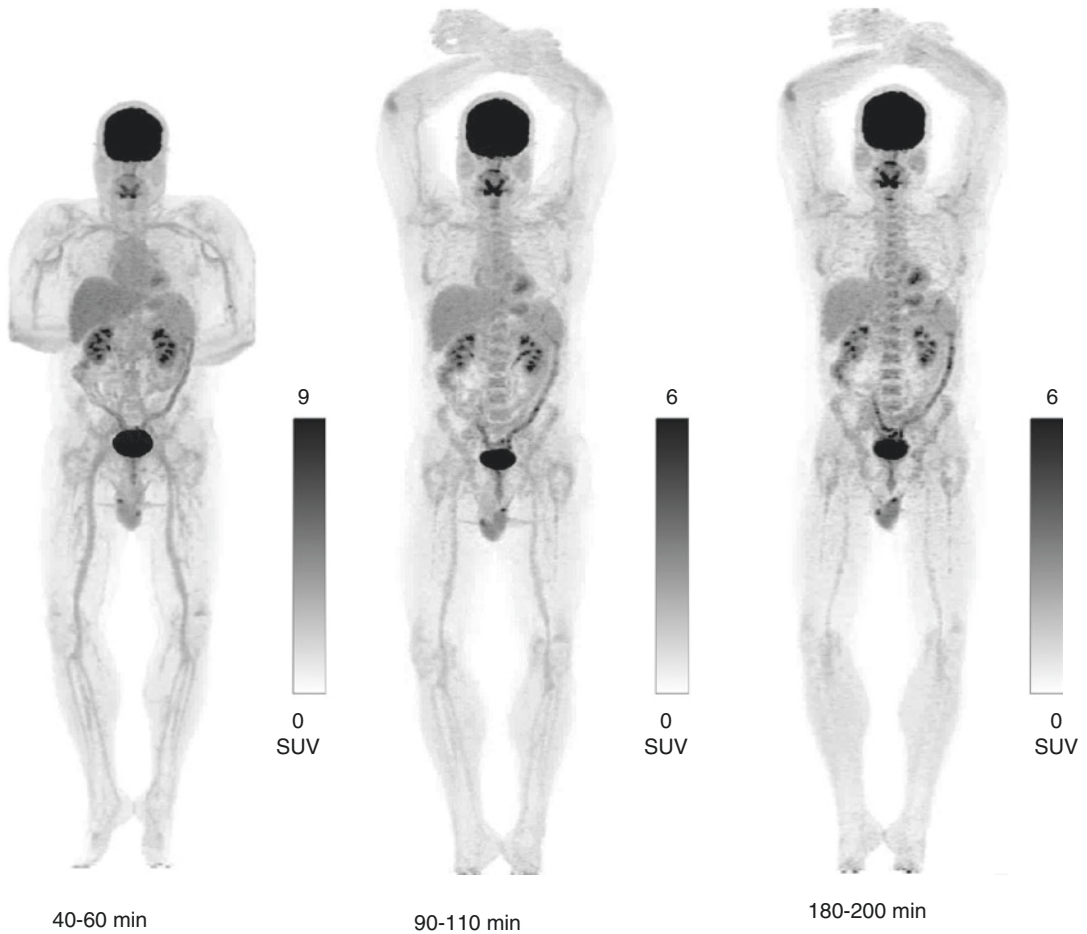
Fig. 13.3 Healthy white male, 49-year-old, 175 cm, 99 kg (BMI = 32.2). Amount of F18-FDG injected was 0.56 mCi, left antecubital. The position of the hands is different for the first image (left) because dynamic acquisition was obtained for the first hour. MIP images were acquired for 20-min acquisitions at 40-, 90-, and 180-min after injection. Reconstruction parameters: manufacturer-provided 3D iterative TOF, 4 iterations, 20 subsets. All corrections on with PSF modeling. Voxel size was 4 mm isotropic. Many thanks to Prof Ramsey Badawy and Dr. Yasser Gaber, UC Davis, California, USA, for providing the images

has been achieved after successful fabrication of small-size LSO crystals (0.43×0.43 mm^2) for the purpose of developing high-resolution small-animal imaging systems [17, 18].

The incorporation of positron range effects in the system matrix of iterative reconstruction has been suggested and implemented to restore images degraded due to positron range [19, 20]. In radionuclides with high positron range, it was found that the inclusion of positron range in the reconstruction process (i.e., maximum a posteriori (MAP)) was successful in restoring the spatial resolution of the images; however, long computation time was placed on data processing. The utility of iterative reconstruction in this regard lies in its ability to control the amount of noise in the Bayesian framework of MAP [20]. Recent work on positron range effect has been conducted to correct for positron range using tissue-specific kernels in the forward projection operation dur-
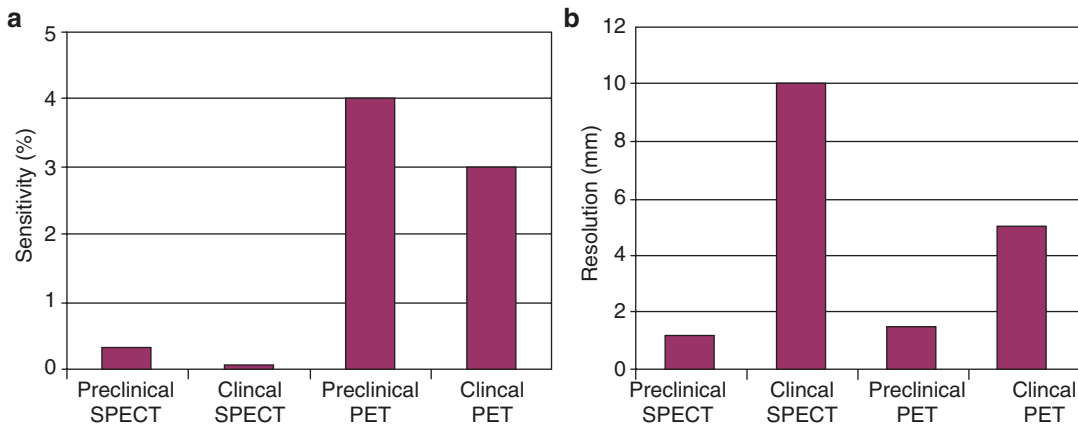
Fig. 13.4 (**a**) Sensitivity and (**b**) Spatial resolution of clinical as well as preclinical scanners in single-photon emission computed tomographic (SPECT) and positron emission tomographic (PET) imaging. (Adapted from Jansen FP, Vanderheyden J-L (2007). Nucl Med Biol. 34:733–735).

Notice that some new scanners especially those with extended axial FOV (i.e., uEXPLORER and PennPET Explorer) can achieve sensitivity values significantly better than shown in the graph

ing iterative reconstruction. Furthermore, it has been validated in material-variant as well as material-invariant positron range corrections and can be implemented in presence or absence of magnetic field [21].

Deconvolution using the Fourier transform of the positron blurring effect was also proposed and was found useful in restoring the degraded images and improved activity quantitation, especially for positrons with high range, but this occurs at the cost of increased projection count uncertainty due to amplification of noise [22]. A residual correction method using a dual-matrix approach has been introduced to deal with the effects of positron range through the use of Monte Carlo simulation and a simplified system matrix. The method showed a trade-off between a complex system model and a simplified system matrix in terms of efficiency and model accuracy [23].

Acollinearity effects, as mentioned previously, are dependent on the detector diameter and hence are influential in PET systems with large transaxial dimension. Acollinearity resulting from positron-electron annihilation can also be included in the iterative scheme, and corrections can be

obtained to reduce its effect. A reduction of ring diameter is necessary to geometrically control the phenomenon, and this will also improve the detection efficiency of the scanner; however, resolution measurements will be confounded by DOI errors. As a result, a correction for the later would serve to improve the resolution measurements and system sensitivity.

Detector size. A key instrumental factor that determines the intrinsic spatial resolution of the PET scanner is the crystal dimension *d*. For a point source located at mid-distance between two detectors in coincidence, the resultant FWHM is a convolution of the point spread function (PSF) of the two detectors and is equal to *d*/2. The geometrical response of these two opposing detectors is triangular at the center and worsens as the source moves closer to either of the detectors, yielding a trapezoidal shape as the object approaches the surface of the detector. This is in contrast with the gamma camera, for which distant objects exhibit lower spatial resolution than objects in close proximity to the detector surface.

Manufacturing small-size crystal arrays is technically challenging and costly. Small-crystal

dimensions may also limit the amount of light that is received by the photodetector, thereby reducing energy and spatial resolution of the detected photons. However, the advent of new scintillators that showed better light output and improvements in cutting techniques have made the production of small-size crystals a successful process in improving detector resolution.

Most of the state-of-the-art PET/CT scanners use crystal sizes of 3–5 mm; however, in some dedicated brain scanners the crystal size is approximately 2 mm wide, such as in HRRT. Moreover, in small-animal imagers, the crystal dimension is typically 1–2 mm, with a recent development of a submillimeter version of LSO crystals as mentioned earlier.

Detector size, positron range, and acollinearity are major factors that convolve to determine the fundamental resolution limit of the scanner. Another important resolution element that plays a significant role in the uniformity of the spatial resolution across the field of view is the DOI error or parallax error.

Parallax error. The geometric design of the block detectors and their arrangement in a circular fashion to form a closed ring has introduced another resolution-limiting element, parallax error. It results from the uncertainty of the depth of the interaction of the 511-keV photons within the crystal. This factor was described in the sensitivity section in the discussion about how PET scanners with small diameters can improve system sensitivity and how this will enhance image blurring, especially for events detected at the periphery. This degrading factor is also a concern in detector design with larger crystal thickness.

As the rays arising from the patient move away from the center field of view, there is a greater chance that rays detected in coincidence will produce a blurring error, affecting the resolution of the scanner. This blurring effect is shown in Fig. 13.5, in which photons arising from the center of the field of view do reach the detector pair in a direction normal to the crystal surface, while those photons shifted radially from the center fall on the detector pair with oblique angles, causing false determina-

Fig. 13.5 Demonstration of the depth-of-interaction (DOI) error. Notice that the intrinsic point spread function is broader and asymmetric when compared to a similar one from the center field of view
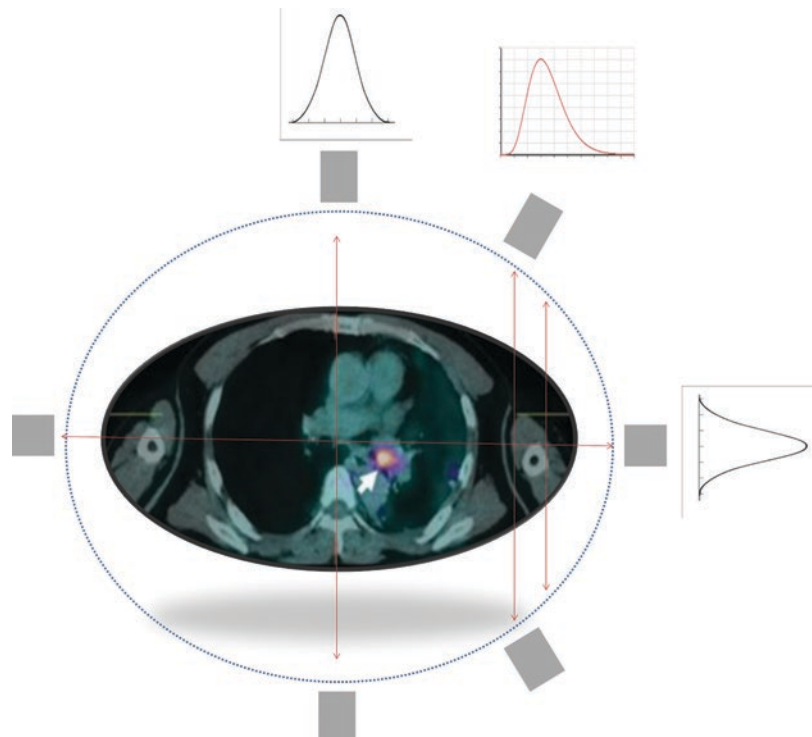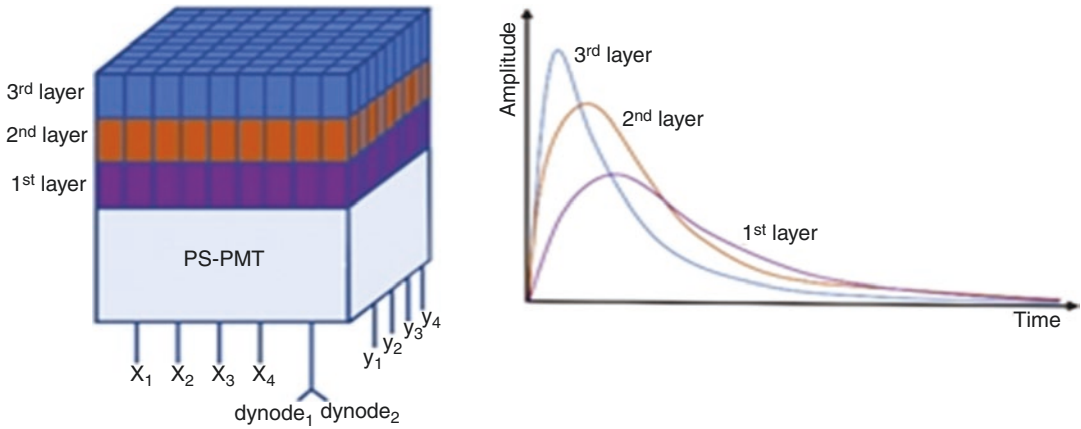
Fig. 13.6 Phoswich detector module for DOI error correction comprised of three layers of individual crystals each with a different shape in output pulse. (Taken from [27] under terms of the Creative Commons Attribution 3.0 license)

tion of event position. As a result, data acquired without DOI correction suffer from an additional component of resolution degradation. It can reach 40% of the FWHM for a clinical system at 10 cm from the radius and increases linearly with further increase in the radial position of the annihilation site [24]. DOI errors also influence the spatial resolution of 3D imaging and thus place physical limits on increasing the axial extent of the PET scanner.

Approaches for depth encoding and parallax error correction are various and can be implemented using a bilayer or more (see Fig. 13.6) of different scintillation crystals, applying two photodetectors, one at the entrance and one at the back side, or measuring the scintillation light distribution on position-sensitive photodetector array; or using a dual-ended photosensitive APD readout Scheme [25]. The former is implemented by using two scintillation crystals of different decay constants. Examples of commercial scanners that use DOI correction are HRRT (Siemens Healthcare) or the small-animal scanner eXplore (GE Healthcare), which uses LYSO/GSO stacked together, and the difference in their scintillation decay time is used to identify the DOI by analyzing the energy signal using pulse shape discrimination [26]. Proper correction for the phenomenon allows an opportunity for producing scanners with greater crystal thick-

ness; hence, an improvement in system sensitivity can be achieved. A recent review of methods and approaches to correct for DOI can be found in [27]. Simulation studies, however, showed that the benefits of DOI predominates in the radial than axial direction provided modern iterative reconstruction is applied [28]. This is particularly important due to the recent interest and successful development of long-axial FOV PET/CT scanners [9, 29].

13.3.1 Data Sampling

Although PET scanners designed in cylindrical geometry provide better detection efficiency than other proposed geometries, they possess two fundamental problems regarding data sampling and spatial resolution. Events collected at the center of the field of view have the chance to fall perpendicularly on the detector pairs, with equal sampling intervals determined basically by the detector width. However, as the sampling moves radially toward the patient's periphery, the LORs are no longer equally spaced in comparison to rays arising from the center. The reconstruction algorithm, however, assumes a uniform sampling across the scanner field of view; therefore, a correction for such a problem is necessary. This cor-

rection is called *arc correction* and is of particular importance in objects with large dimensions for which the periphery is located a distance away from the center and in dedicated brain PET systems and small-animal scanners [30].

The discrete nature of the crystals in block detectors places physical limitations on the data-sampling regime and hence restricts the realization of the full potential of the resolving capabilities of the scanner. Linear and angular samplings are the two parameters that define the spatial resolution of the acquired images. The former is defined by the detector width, while the latter is determined by the number of detectors in the ring. Data undersampling is a reported resolution problem in the literature, and several data-sampling schemes were proposed to solve it. Wobbling motion of the detector array was implemented in some systems to compensate for information lost or the sampling inconsistency that occurs between the unevenly spaced LORs. Data interleaving between adjacent projection angles does help to reduce the effect of undersampling, and this occurs by interleaving the LORs of a given projection to the neighboring angle so that the resolution of the sampled data can reach the $d/2$ limits equivalent to the resolution of a detector pair in coincidence (Fig. 13.7). This interpolation process leads to an increased linear sampling and reduction of angular sampling by a factor of 2 [31].

13.3.2 Reconstruction

The two major reconstruction methods in emission tomography are filtered backprojection and iterative reconstructions. As discussed in Chap. 16, FBP is an analytic approach that does not allow for modeling the noise in the backprojection step during image reconstruction. However, iterative reconstructions outperform FBP in handling noise such that regions of low-activity concentrations can be reconstructed with better noise properties.

Smoothing filters in FBP are essential to eliminate the drawbacks of the ramp filter and result in data with lower spatial resolu-
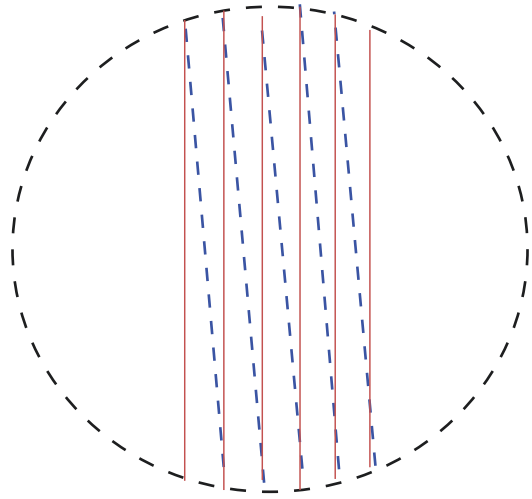
Fig. 13.7 Lines of response (*red lines*) for a given projection are interleaved to the adjacent projection angle (*blue lines*) so that linear sampling can reach the detector response $d/2$. This process yields an increment in the linear sampling by a factor of 2, while it reduces the angular intervals into half. For the purpose of reconstruction, the increased number of LORs mimic an additional detector inserted between the detector arrays

tion. In OSEM (Ordered Subset-Expectation Maximization), MLEM (Maximum Likelihood-Expectation Maximization) or iterative reconstructions, however, convergence depends on the size of the structure; thus, small lesions converge slower than other structures with large or different dimensions. This in turn produces metabolic information with variable resolution properties. At a high number of iterations, a postsmoothing filter is required to reduce the noise amplification during the iterative process and to improve visual quality. Consequently, the reconstruction algorithm and its parameters are influential in controlling the final spatial resolution of the reconstructed images. In FBP, a trade-off between noise and resolution should be maintained in selecting the cutoff frequency. However, the noise is signal dependent, and achieving a bias variance trade-off using this type of filtering is not particularly effective [32]. The number of subsets, number of iterations, and smoothing kernel in iterative reconstruction should also be optimized for a given detection task. Image restoration using Fourier filtering has been used to improve image spatial reso-

lution; however, these filters produce different noise texture, require calculations of the system modulation transfer function, and their performance are based on the system resolution [33].

The most promising but technically challenging is to model the resolution elements in the system matrix of iterative reconstruction. Modeling the response function by measuring the system response for a large number of points across the transaxial and axial fields of view and incorporating this information in the system matrix can lead to an improvement of spatial resolution and noise properties of the reconstructed image [34]. The importance of improving the spatial resolution of the reconstructed images has several benefits, among which it serves to improve tracer quantitative accuracy, lesion contrast recovery, and reduction of partial volume effects (PVEs) [35, 36].

Another analytical approach modeling the individual effects of positron range, photon acollinearity, intercrystal scattering, and intercrystal penetration for Rb-82 myocardial perfusion images has been employed in the reconstruction algorithm. An improvement in contrast, noise, and spatial resolution could be realized but with an increase in the reconstruction time [37].

Partial volume. One of the practical consequences of the relatively low spatial resolution of PET scanners versus small structures is the PVE. This phenomenon has caught the attention of many researchers to develop correction techniques able to overcome bias in data measurements and to improve quantitative accuracy. As stated, the spatial resolution of a given scanner is determined by the FWHM of the point spread function. Tracer uptake or small structures that occupy an area smaller than the measured PSF would suffer from PVE provided that the measured value is less than thrice or twice the FWHM. This effect is a 3D problem and not only related to the size of the structures being measured but also involves those voxels of the structure that contain signals from surrounding tissues or what is called the "spillover" effect. Count spillover from one tissue to another results from the fact that data are sampled by a discrete number of cells or "voxels," each of finite dimen-

sion, which causes imprecise distinction between tissue borders. The tissue fraction effect, on the other hand, reflects the underlying tissue heterogeneity (e.g., gray and white matter in the brain); therefore, coregistered anatomical information is particularly important in the correction procedure [38]. However, both effects sometimes are thought of as one phenomenon instead of two different faces for the same coin. Data sampling is a digitized process and does not allow image voxels to realistically outline the actual activity distribution within different structures. As a result, the intensity of a particular voxel could be a mixture of counts measured from different and neighboring tissues. This process becomes more complicated if these tissues have different tracer uptake or different metabolic activities. An ideal correction method for PVE must therefore compensate for both effects together [39].

The PVE in PET imaging can be seen in a number of clinical situations, such as brain studies in which many cerebral structures are small in size and accurate quantitation requires a reliable correction of PVE. This is also important in oncologic FDG studies, in which small-size lesions suffer from biased quantitative accuracy demonstrated by altered standardized uptake value (SUV). In sequential studies in which response to therapy is assessed on a quantitative basis and tumor size is pursued with respect to its physical size, SUV values should be carefully interpreted unless an accurate technique has been applied to correct for PVE [40]. Another problem that is encountered in dealing with partial volume is when the lesion is located in or adjacent to a moving organ, such as the lung/heart or lung–liver interface.

In dynamic cardiac PET studies, the determination of myocardial blood flow necessitates correction for PVEs, which are represented by underestimation of myocardial wall thickness, inclusion of arterial or blood counts with the measurements of myocardial walls, and spillover that comes from neighboring walls or blood pool counts within the chamber. The inclusion of partial volume correction terms in the kinetic model has been implemented in many studies and was found successful in reducing the bias

introduced in the measurements. Furthermore, a reconstruction-based partial volume correction using normalization and attenuation-weighted OSEM was found to improve the spatial resolution and tracer kinetics outcome, leading to improved quantitative accuracy for brain PET imaging [41].

13.4 Noise-Equivalent Count Rate

Count rate response is an important intrinsic performance measure of the PET scanner. From the statistical viewpoint and image quality requirements, higher counting rates are desired. It serves to reduce patient motion and discomfort, and increases scanner throughput. High count rates can be achieved by increasing the injected radioactivity or using high sensitive PET scanners. The former solution is regulated by radiation protection rules while the latter is not easily accomplished as discussed above in the sensitivity section. However, if no restrictions are placed on the radioactivity to be injected, another problem would arise, which is the nonlinear system response represented by count rate saturation and

dead time losses. At high count rates, the random rate increases in a quadratic fashion with the injected activity. Scatter fraction, as mentioned, is also non-negligible, particularly in 3D imaging mode or in large patients. As a result, the response of the PET scanner versus a wide range of clinically relevant activity concentrations should be properly outlined to determine the most operable range that allows for optimizing the injected dose.

A metric that allows accounting for factors that alter the observed count rate will be more likely an appropriate measure of the system count rate performance [42]. The noise-equivalent count rate (NECR) is the metric that reflects the ability of the scanner to measure true events while accounting for other interfering factors, such as dead time, scatter, and random events [43]. By plotting the NECR curve (see Fig. 13.8) the peak that maximizes the ratio of true events with respect to other undesired events can be determined through the relation:

$$\mathrm{NEC} = \frac{T^2}{S + T + kR}$$

Fig. 13.8 Measurement of count rates as a function of activity concentration in the Discovery MI 3-ring PET/CT (GE Healthcare). Prompts, trues, randoms, scatters and NECR are displayed as a function of F18 activity concentration. The peak NECR is 102.3 kcps at activity concentration of 23.0 kBq/cc. The peak true counting rate is 463.1 kcps at 36.9 kBq/mL. (From [44] under the terms of the Creative Commons CC BY license)
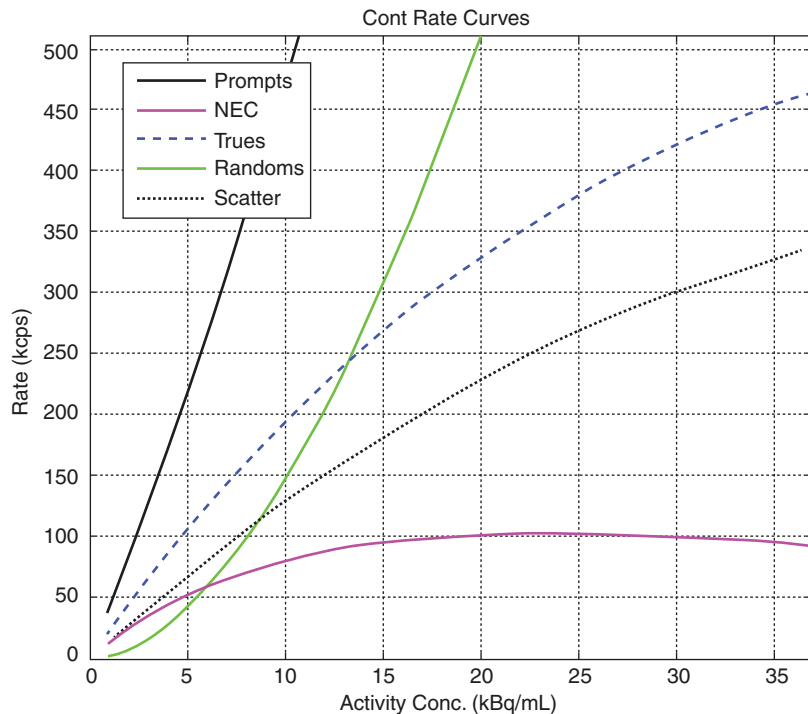
Table 13.1 The peak noise-equivalent count rate (NECR, kcps) and the corresponding radioactivity concentration as measured for a number of commercial PET designs including conventional PMT, SiPM, and APD-based systems as well as analog and digital configurations

	GE Healthcare					Siemens Healthcare		Philips Healthcare	
	DI-MI 3	DI-MI 4	DI-MI 5	Signa PET/MR	Discovery 690/710	Biograph mCT / Flow mCT	Biograph mMR / PET/MR	Vereos	Ingenuity TF 128 PET/CT
Peak NECR, kcps	102.3	193.4	266	214.8	139.1	185	184	171	124.1
Peak NEC activity, kBq/mL	23	21.9	20.8	17.6	29	29	23.1	50	20.3
Timing resolution, ps	375.6	375.4	381.7	390	544.3	555	2930	316	502

Values are summarized from [44, 49]

where *T*, *S*, and *R* are the trues, scatter, and random rates, respectively; *k* is a constant that depends on the random estimate technique. It has a value of 2 when random correction is performed using online random subtraction (the estimate is noisy as in the delayed window subtraction method); otherwise, the value is 1 for the noise free estimate [13]. The NEC is a global measure of signal-to-noise ratio and does not reflect the regional count variation for a particular activity distribution can be used in acceptance testing procedures, comparing different protocols, imaging techniques, or acquisition modes (2D, 3D, or partial collimation) and as a figure of merit to optimize patient dose, but not as a direct or sole measure of lesion detectability, image quality, or overall system performance [45, 46]

To accommodate realistic conditions of clinical count rate measurements, the updated NEMA guidelines have replaced the 20 × 20 (diameter × length) phantom by a different one measuring 20 × 70 cm to account for the activity contributions arising from outside the field of view [13, 47, 48]. A line source is inserted axially into the cylinder at a radial distance of 4.5 cm from the center. At start of data acquisition the line source is filled with an activity beyond the expected peak of the NECR or as recommended by system manufacturer and the acquisition is extended for a prolonged time (e.g., 10 h or even longer) to cover a wide range of activity concentration utilizing the spontaneous radioactive decay.

After calculating the trues, scatter, randoms, and NECRs and plotting them versus the activity concentrations, the peaks of true counting and NECRs are determined along with their corresponding activity concentrations. The peak NEC is the best estimate of the activity concentration that if met with an injected activity should reveal the best counting rate performance, better signal-to-noise ratio, and improved detectability. Table 13.1 summarizes the peak NECR for a number of commercial PET/CT scanners and their respective activity concentrations.

13.5 Coincidence Timing Window

In the conventional gamma camera, the geometric angle of the collimator holes and septa determine the direction along which emitted photons are accepted. However, in PET imaging, an electronic timing window is used to determine the acceptance of the coincident events. The timing coincidence circuitry plays a significant role in the inclusion of coincidence events and in the rejection of other undesired events, such as randoms. The random rate is a function of the timing coincidence window; thus, a window width with a lower value allows a reduction of the random contribution to the total collected coincidences. This directly affects the count rate performance of the scanner such that the peak NECR can be increased by shortening the coincidence timing window. As stated, the fast new scintillators were

key elements in designating scanners with a narrow timing window. An obvious application of these advances has been the production of TOF scanners [50, 51].

The timing coincidence window can be a few nanoseconds (2–12 ns), as in many commercial PET scanners, to hundreds of picoseconds, as in systems equipped with TOF.

13.5.1 Time of Flight

TOF is a time-distance relationship through which the site of annihilation can be determined if the time difference of the arrival of the two coincident events can be accurately measured. Incorporating the TOF information in the reconstruction process allows for precise localization of the emitted photons. It is simply demonstrated in Fig. 13.9. Without TOF, the annihilation site is equally likely to emanate from any point that lies along the LOR. In other words, TOF constrains this large distance (i.e., LOR) to a smaller value determined primarily by the time resolution capability of the scanner (see the previous discussion). The simple formula $\Delta x = (1/2)c \cdot \Delta t$ is used to define the distance that most probably confines the length along which annihilation took place. Δx is the error in position (positioning uncertainty), Δt is the error in the timing measurement, and c is the speed of light (3×10^8 m/s).

With an accurate measurement of the coincidence timing of the two 511-keV photons, the probability of the annihilation site could be assigned to a single point; thus, a 3D image can be obtained without reconstruction. In a PET scanner with timing resolution of $\Delta t = 6$ ns, the measurements of position error will extend along the whole diameter of the scanner because the calculated Δx would be 90 cm. Reducing the timing resolution, for instance, to 500 ps would allow reduction of the positioning uncertainty to 7.5 cm, a value that still cannot provide the full potential of using TOF in image reconstruction yet is able to reduce the statistical noise in the reconstructed image by limiting the propagation of noise to an area of smaller diameter represented by fewer reconstruction pixels in the image space

[52, 53]. As a result, the gain obtained in image quality using TOF is therefore proportional to the object size and inversely proportional to the timing resolution of the system. Systems with TOF capability have the chance to improve the signal-to-noise ratio, reduce significantly the accidental random events as well as effective handling of high count rates [53].

BaF_2 and CsF were used in the early generation of TOF systems, achieving a system timing resolution of 470–750 ps; however, their use was mainly in research laboratories without commercial release of any practical tomograph [54]. Even though these scintillators are fast and provide excellent timing properties, they suffer from low photofraction and low light output, produce images with low spatial resolution, and have poor sensitivity compared to BGO-based scanners.

Lanthanum bromide (LaBr:Ce) is a fast scintillator (short decay time, 16 ns) with high light output providing excellent energy resolution. These characteristics are suitable for time-of-flight applications in PET scanners. High light yield is an important parameter that improves the certainty of photon statistics and serves to improve system spatial and energy resolution. A prototype based LaBr3 has achieved a timing resolution of 460 ps with further improvement to 375 ps in a TOF based system [55, 56].

Moving from the research setting to the clinical arena with great effort made in detector technology, including new fast scintillators and data acquisition and reconstruction techniques, the first commercial TOF system was introduced in 2006 by Philips healthcare and had a timing resolution of 585 ps [57].

Experimental and patient evaluation studies reported fast convergence for high-contrast recovery coefficients with considerable benefits to small lesions and large patients [27]. Another feature of systems working with TOF is that it permits an injection of lower tracer activity into patients or reduces the imaging time while keeping the image properties fairly acceptable in comparison to non-TOF operating scanners [14]. In Fig. 13.9, one can appreciate the gain in TOF SNR due to improvement in system timing resolution [51].

Time Resolution (ns)	Δx (cm)z	TOF NEC gain	TOF SNR gain
0.1	1.5	26.7	5.2
0.3	4.5	8.9	3.0
0.6	9.0	4.4	2.1
1.2	18.0	2.2	1.5
2.7	40.0	1.0	1.0

Fig. 13.9 Time of flight (TOF) can enhance the precision of localizing the positron emission along the line of response as a result of improving the timing resolution of the scanner. Scanners with relatively large coincidence window width have lower precision in event position determination (*blue* and *red bars*), while other systems manifested with better timing resolution serve to improve the probability of event localization, being best for systems with the lowest coincidence timing window (*black* and *green*). The table on the left demonstrate numerically the spatial uncertainty and estimated TOF gain as a function of system time resolution in a patient whose effective diameter is 40 cm [51]. Remember 1 ns = 1000 ps
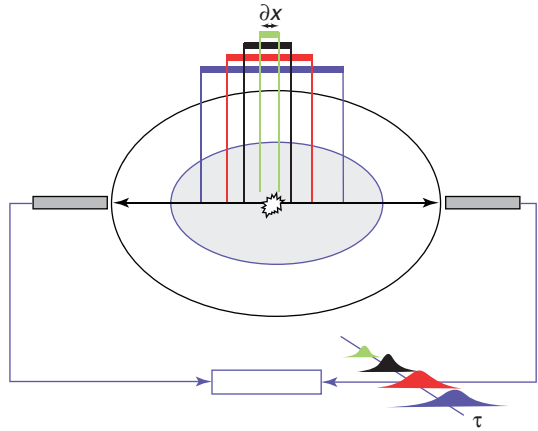
13.6   Data Corrections

PET images provide metabolic information about the tissue under investigation, and data obtained have several qualitative and quantitative features. The qualitative information is represented by images that reflect the spatial activity distribution within different biological tissues. The quantitative outcome, however, is numerical values through which one can reach more straightforward results reducing interobserver variability and increasing reader confidence. As a result and because of the importance of these measures, system calibration and correction techniques are essential to satisfy the qualitative and quantitative tasks placed on the scanner.

13.6.1 Normalization

In the gamma camera, a number of corrections are needed to verify that all PMTs have equal or nearly equal signal output when exposed to a uniform source of radiation. In a similar manner and to accurately measure the LORs in PET scanning with minimal electronic and geometric effects, a normalization test must be performed to account for variation in detector efficiency. This variability of detector sensitivity could arise from a number of sources, such as variations in solid angle and distance between detector pairs, electronic PMT drifts, and crystals with unequal efficiencies. Accurate normalization is essential to perform accurate quantification of data measurements, and improper normalization may result in artifacts, poor uniformity, and increased image noise.

One of the earliest methods devised to account for normalization was implemented by generating a normalization factor for each detector pair with respect to the averaged acquired counts across all LORs. This is a direct method, and its implementation is straightforward. However, it requires extended acquisition times to achieve adequate statistical accuracy. Also, it may produce biased results if the source does not have a uniform activity distribution or the scatter coincidences are dissimilar to real patient acquisition [58]. The situation is further complicated in 3D, for which the calibration procedure requires a low amount of activity to reduce dead time effects and normalization techniques able to account for scatter events as normalization factors are different for true and scatter coincidences. A number

of source distributions have been used in detector normalization, such as uniform cylinder, planar source, and rotating line source. Iterative approaches have been proposed to treat the problem of normalization and methods based on scanner self-normalization [59, 60].

Other approaches that account for system geometry and individual detector pair efficiency have been employed. One method is component-based normalization. Initially, it was suggested by dividing normalization factors into two major components, detector efficiency and spatial distortion [61]. This approach has resulted in a reduction of the total acquired counts and has been extended to normalize data acquired in fully 3D [62] and use of geometric means rather arithmetic means to calculate geometric factors. Further modifications have been made by including crystal intrinsic efficiency as well as geometric factors such as the detector geometric profile and block detector interference [63, 64]. Other developments resulted in the inclusion of the time alignment factor and count-rate-dependent block profile [65, 66]. Systems operating in 2D and 3D modes are preferred to have separate normalization tests to account for geometric and different sensitivities that arise when septa are retracted or extended.

13.6.2 Dead Time

While a detector is busy handling and processing one event, it would not be able to process any further successive events during this time period. This phenomenon is called *dead time*. With the increased activity concentrations inside the object being investigated, particularly in 3D imaging mode, the probability of emitting a significant number of consecutive or simultaneous photons is relatively high when viewed and compared to lower-activity concentrations and when compared to 2D imaging. At high rates, the likelihood of pulse pileup is therefore increased because there is a higher chance that events that reach the detector are so close in time and thus the output signal would be their sum rather than an individual signal for each event. This process might lead

to events whose amplitudes are greater than the upper energy threshold or signal amplitudes that fall within the energy window. The former events will be rejected while the latter will be accepted with false determination of position and energy [67]. As a result, the count rate performance of PET scanners toward increased activity concentrations is not a linear relation, especially at high activities, for which count losses and pulse pileup start to dominate. Ignoring dead time as a degrading factor of the acquired data results in loss of spatial resolution and signal-to-noise ratio and reduced quantitative accuracy.

The loss in effective sensitivity of the scanner (a quantitative performance parameter that combines between absolute sensitivity and NECR) showed the necessity of employing fast scintillators with high-performance electronics to realize the full potential of using septaless-volumetric 3D imaging over a wide dynamic range [68]. Hardware components that contribute to dead time in the event detection chain are front-end electronics, coincidence processing stage, and coincidence data transfer with more burden placed on the front-end electronics component due to the increased signal multiplexing [67].

Because of these significant count rate increases, saturation in 3D imaging occurs at a lower-activity level than if the scanner is operated in 2D mode. Fast scintillators coupled to electronics of high-speed signal processing serve to handle a large amount of data and are able to reduce dead time effects. Notice the decay constant of BGO and NaI(Tl) versus GSO and LSO in Table 12.4 (Chap. 12). However, the specific tomograph construction and the associated electronic assembly together with the administered dose are the factors that determine the overall system count rate performance [69]. For instance, a significant improvement of the peak NECR was not realized when the LSO crystal was used in PET scanners originally designed with electronics that match the BGO crystal until additional modifications were carried out on the coincidence timing window and other electronic circuitry [70].

Mathematical models for dead time have been proposed and classified mainly into paralyzable

and nonparalyzable. The count rate response of the PET scanner can be modeled using these two different models, and determination of model parameters could then help to correct for count losses observed on the measured count rates.

13.6.3 Attenuation Correction

Attenuation correction is an important issue in SPECT and PET imaging. X-ray CT provide several advantages over those given by radionuclide transmission imaging, which has been used for many years in clinical practice and research arena. The former technique is able to improve the statistical noise of the attenuation map to a significant level, reducing noise propagation from the transmission data to the radionuclide activity distribution. The CT attenuation map is performed in a short time course as compared to radionuclide transmission scanning and thus provides an efficient mechanism for attenuation correction. This allows minimization of patient movement during the imaging session and leads to higher patient throughput. However, radionuclide transmission scanning has the same temporal characteristic of the emission acquisition; therefore, problems associated with high-speed CT scanning are absent. On the other hand, problems of source decay, maintenance, and replacement are not applicable to the X-ray transmission source, which is an additional advantage provided by CT transmission scanning. In PET imaging, radionuclide transmission using positron emitters (e.g., Ga68/Ge68) or single-photon emitters (Cs-137) were used to provide an attenuation map for the 511-keV emission images.

Because of the kinetic properties of the chest region due to respiration, it is the most frequent area where image fusion fails to register the two data sets. Respiratory motion is a problem in PET scanning based on CT attenuation correction, and several approaches were devised to account for such a temporal mismatch. Different breathing protocols, respiratory gating (4D PET/CT), correlated dynamic PET techniques, list mode data-based techniques, modeling of the respiratory motion in iterative reconstruction, cine or aver-

aged CT scanning, and other methods were proposed to resolve or mitigate respiratory motion artifacts [71].

Respiratory motion serves to blur the emission images and degrade the quantitative accuracy of radiotracer uptake. The degree of degradation depends on lesion size, location, and patient breathing pattern. This problem is more critical in pathological lesions that lie in a region that is near to a tissue interface, more specifically in the lower base of the right lung. In this particular site, diaphragmatic motion may develop cold artifacts in patients scheduled for PET/CT scanning. Further, a metastatic liver lesion might be misinterpreted and localized in lung tissue, misleading the diagnostic process. In cardiac PET studies, it has also been found that fast CT scanning may result in significantly altered FDG uptake within the myocardium being higher in myocardial segments located in close proximity to the lung–heart interface (i.e., anterior and lateral wall).

CT-based attenuation correction has another drawback that should be discussed. The X-ray beam is polychromatic, meaning that it has a range of energies released from the tube, and the resulting spectrum depends on the tube voltage. This heterogeneity of the energy spectrum produces what is called a *beam-hardening effect*. As the rays pass through the different tissues toward the detector, there is a preferential occurrence for the low-energy photons to be absorbed in a greater amount than high-energy photons. This phenomenon is due to the fact that the probability of the photoelectric effect at low photon energies is higher, leading to an increase of the mean photon energy of the radiation beam. In turn, this causes some kind of heterogeneity for determination of the Hounsfield numbers of the same tissue. Therefore, attempts to correct beam hardening have been implemented in commercial CT scanners.

The fact that the CT numbers are derived from the effective X-ray energy requires a conversion step so that the calculated attenuation coefficients reflect the attenuation properties of the emission SPECT or PET radionuclides [72]. Methods developed to solve this problem have

been segmentation, scaling, bilinear transformation, hybrid methods [73, 74]. Initial efforts have used single- or dual-energy CT to generate a transmission data set. Scaling techniques are used to convert the attenuation coefficients into the corresponding values of the radionuclide energy using a global attenuation coefficient ratio. An essential problem with this approach is the differences of photoelectric and Compton probabilities that occur as a result of energy differences, in particular for μ values generated by CT in bone structures, which are dominated by the photoelectric effect, while at higher energies the Compton effect dominates, resulting in large errors of the estimated attenuation coefficients for bone structures.

Segmentation is a process of classifying patient tissues based on their anatomical borders and outline from neighboring regions and hence provides a chance to separate and assign each individual segment its corresponding attenuation coefficient. These areas of the human body are typically air, bone, and soft tissue. The assumption that each anatomical region is homogeneous and has one *μ* value may be invalid in some anatomical regions, such as lung tissues, where investigators found a variability of tissue density that may reach 30% [75].

Bilinear transformation is a common method used in many commercial hybrid scanners and is based on experimental phantom measurements containing different concentrations of tissue-equivalent materials that could mimic biological tissue. These are air, water, and K_2HPO_4 bone-equivalent solutions prepared in clinically relevant concentrations. The linear attenuation coefficient of these materials, which are known, are plotted versus the CT numbers obtained from phantom studies acquired using the CT machine. The resulting plot is used as a calibration curve in estimating the attenuation map from the CT information obtained from a patient scan. The calibration curve has generally two distinct zones such that CT numbers below zero are combinations of air and soft tissue, while values greater than zero are combinations of bone and soft tissue [76, 77] (Fig. 13.10). However, the piecewise linear conversion method can be confounded by beam-hardening effects and in the presence of metallic implants or contrast agents, for which tissues of contrast uptake must be identified and properly corrected.

The CT images are characterized by high-resolution properties, and to use the same image as an attenuation map for images acquired with larger pixel dimensions (i.e., emission images), a pixel-matching procedure is performed by downsampling the CT images into larger pixel sizes. The pixel size of the CT images is commonly built on a matrix of 512×512 whereas being relatively smaller matrix size in PET. The attenuation correction factors can then be
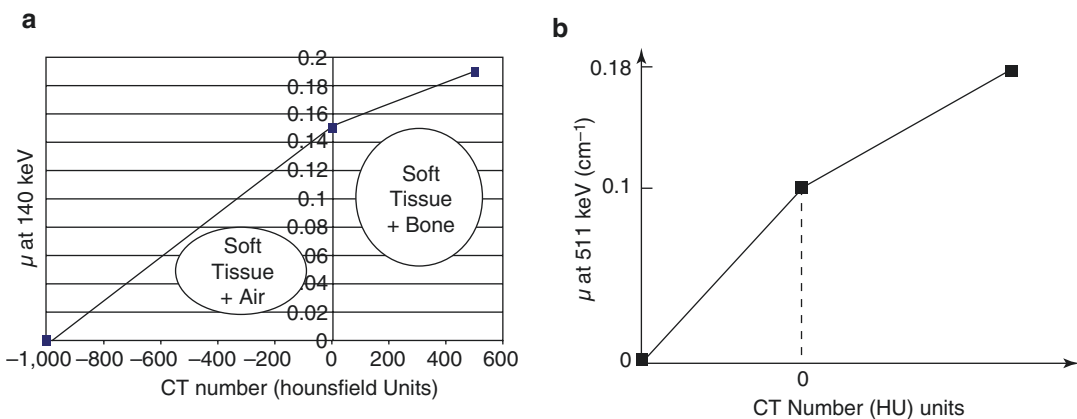
Fig. 13.10 Bilinear transformation curve used in computed tomographic (CT)-based attenuation correction in (**a**) single-photon emission computed tomography (SPECT) and in (**b**) positron emission tomography (PET)

included in the forward step of iterative reconstructions, as can be seen in attenuation-weighted OSEM reconstruction, yielding emission data of superior signal-to-noise ratio. Further, the CT images must be aligned with the emission image before correction to verify that an accurate attenuation correction and image correlation would be implemented. As outlined before, a new test for PET/CT image coregistration was added to the NEMA NU-2018 release [48].

For the purpose of reducing dose levels delivered to the patient, a low-current CT scan can be performed for the sake of attenuation correction without compromising the accuracy of the attenuation factors.

13.6.4 Scatter Correction

As described in this chapter, one of the undesired effects that contaminate the total coincidence counts is scattered radiation. Many factors contribute to determine the proportion of scatter in clinical studies, such as the distribution of activity within a given patient, composition and shape of the attenuating structures, as well as detector characteristics such as geometry of the imaging system, system energy resolution, and the pulse height window setting [78–81].

In 3D PET, the absence of septal collimation results in the acceptance of a large amount of scattered events, which can reach 50% or even more. Scattered events could arise from areas that lie out of plane and from regions located outside the field of view; both are important to account for in the correction scheme. Consequences of scattered events are increased image noise, reduced lesion contrast, and reduced quantitative accuracy. Accurate measures of SUV and reliable estimates of tracer kinetic parameters necessitate proper scatter correction. Many scatter correction approaches have been suggested and implemented in PET imaging, and some are similar to those used in SPECT imaging. The use of two, three, or more energy windows was proposed and implemented such that more than an energy window is used to record scattered and unscattered coincidences. The following are some correc-

tion methods used in research and clinical PET studies.

1. The dual-energy window (DEW) method is one of the simplest energy-based techniques that found application in both SPECT and PET scatter correction. One approach in the dual-energy method is to use two contiguous energy windows, one photo peak and another for scatter; both are assumed to have scattered as well as unscattered coincidences. Phantom measurements are used to generate scaling parameters of ratio measures of scattered and unscattered events in both energy windows. A scaled subtraction of the two energy windows is then performed to yield an estimate of the scatter distribution in the acquired patient data, which is then smoothed and subtracted from the data of the photo peak window [82].

2. An alternative approach to DEW is to use two overlapping energy windows, namely, a higher and a standard window, such that both have the same upper energy level, which is greater than 511 keV. The lower discriminator level for the higher-energy window is set at 511 keV, whereas the corresponding one for the standard window is positioned at energy below 511 keV. Since this method seeks to measure the true unscattered events and utilize them in the estimation task, it is therefore called the estimation of trues method [83].

3. Another type of scatter correction is carried out by deconvolution or convolution subtraction. This type of correction technique has a number of variants in terms of whether the correction is applied on projection data or image space, the scatter response function (srf) used in the correction, and whether it is modeled as stationary or nonstationary [84–86].

4. One approach that integrates the information of the reconstructed radioactivity distribution and transmission measurements into the scatter correction process has been implemented. It is called the model-based technique and relies on the physics of Compton scattering, such as photon energy, probability of the scattering angle, and attenuation properties of the scatter-

ing medium. Monte Carlo simulation demonstrated that most scattered photons that are detected in the photo peak window are single-scatter photons, and their percentage is within a range of 75–80%. This has made some investigators think of correcting the scatter based on single-scattered photons, and the distribution of multiple scatter can then be obtained by integral transformation of the single-scatter estimate [87]. For a given LOR, photon scatter is simulated through selected points distributed over the emission image and determined by the attenuation coefficients obtained from the transmission map. Using the emission image in the estimation procedure may produce a bias scatter estimate; however, this can be mitigated by incorporating the scatter estimate in the iterative reconstruction [87].

5. The single-scatter simulation approach has been pursued, and faster implementation was applied with advances in using the iterative reconstruction for the simulation images, as well as the iteration of the scatter calculation [88]. Further, extension of the algorithm was used in the TOF application, for which it can explicitly model the TOF of the annihilation photon pair along their individual scattered paths to produce an estimate of the scatter distribution for each time offset bin of the measured TOF. However, this takes place with increased computation times [89].

Monte Carlo simulation has several features and capabilities in elucidating and characterizing the scattered versus unscattered photons in terms of magnitude and spatial distribution. Monte Carlo simulation is an efficient procedure to follow the history of photons from birth to death (i.e., emission of the positron, annihilation process, traveling distance before scattering, scattering interaction with the detector, or escaping from the gantry, etc.) and is able to account for other physical interactions as well as detector characteristics. This large numerical capability must be met by computers with high computation performance and fast processors to make its application feasible in practice. It is considered a gold standard for evaluating scatter correction techniques and can be used as a tool in the correction algorithm [80, 81]. More challenging is the development of Monte Carlo-based scatter correction techniques in 3D PET imaging that might be available in the near future in clinical workstations. However, the emerging convolutional networks and deep learning could potentially assist in attenuation and scatter correction in PET Imaging [90, 91].

13.7 Conclusion

PET scanner performance has been changed significantly in the last two decades due to a number of reasons including new scintillation crystals, high computation power, new reconstruction approaches and dedicated electronic circuits. There are several performance metrics that must be maintained on a daily as well frequent basis to ensure system stability and reproducibility. A well-defined quality assurance system can achieve these goals with minimal failure. Records-keeping throughout the scanner life time is an essential part of system quality assurance. Acceptance and commissioning data must be used as reference when new modifications, significant corrective actions or routine repairs are made to the scanning system. Time of flight has become available by most if not all of the PET/CT manufacturers and its utility has been shown in clinical practice. New digital PET/CT scanners would play a significant role in the current and future practice of clinical PET. Recently developed PET scanners with long-axial field of view would be a game changer in many of our understanding of human physiology and novel applications are expected with interesting findings. Deep and machine learning would also add a new signature to many of the PET scanner corrections, image analysis and data reconstructions.

References

1. Humm JL, Rosenfeld A, Del Guerra A. From PET detectors to PET scanners. Eur J Nucl Med Mol Imaging. 2003;30(11):1574–97.

2. Wong WH. PET camera performance design evaluation for BGO and BaF2 scintillators (non-time-of-flight). J Nucl Med. 1988;29(3):338–47.

3. Schmitz RE, Kinahan PE, Harrison RL, Stearns CW, Lewellen TK. Simulation of count rate performance for a PET scanner with different degrees of partial collimation. In: IEEE nuclear science symposium conference record, October 23–29, 2005. p. 2506–9.

4. Schmand M, et al. Performance results of a new DOI detector block for a high resolution PET LSO research tomograph HRRT. IEEE Trans Nucl Sci. 1998;45:3000–6.

5. Townsend DW. Positron emission tomography/computed tomography. Semin Nucl Med. 2008;38(3):152–66.

6. Townsend DW. Multimodality imaging of structure and function. Phys Med Biol. 2008;53(4):R1–R39.

7. Vandenberghe S, Moskal P, Karp JS. State of the art in total body PET. EJNMMI Phys. 2020;7(1):35.

8. Badawi RD, Shi H, Hu P, Chen S, Xu T, Price PM, et al. First human imaging studies with the EXPLORER total-body PET scanner. J Nucl Med. 2019;60(3):299–303.

9. Cherry SR, Jones T, Karp JS, Qi J, Moses WW, Badawi RD. Total-body PET: maximizing sensitivity to create new opportunities for clinical research and patient care. J Nucl Med. 2018;59(1):3–12.

10. Cherry SR, Badawi RD, Karp JS, Moses WW, Price P, Jones T. Total-body imaging: transforming the role of positron emission tomography. Sci Transl Med. 2017;9(381):eaaf6169.

11. Zhang X, Cherry SR, Xie Z, Shi H, Badawi RD, Qi J. Subsecond total-body imaging using ultrasensitive positron emission tomography. Proc Natl Acad Sci U S A. 2020;117(5):2265–7.

12. Moses WW, Derenzo SE. Empirical observation of resolution degra-dation in positron emission tomographs utilizing block detectors. J Nucl Med. 1993;34:101P.

13. Daube-Witherspoon ME, Karp JS, Casey ME, DiFilippo FP, Hines H, Muehllehner G, et al. PET performance measurements using the NEMA NU 2-2001 standard. J Nucl Med. 2002;43(10):1398–409.

14. Rahmim A, Zaidi H. PET versus SPECT: strengths, limitations and challenges. Nucl Med Commun. 2008;29(3):193–207.

15. Kolb A, Sauter AW, Eriksson L, Vandenbrouke A, Liu CC, Levin C, et al. Shine-through in PET/MR imaging: effects of the magnetic field on positron range and subsequent image artifacts. J Nucl Med. 2015;56(6):951–4.

16. Caribe P, Koole M, D'Asseler Y, Deller TW, Van Laere K, Vandenberghe S. NEMA NU 2-2007 performance characteristics of GE Signa integrated PET/MR for different PET isotopes. EJNMMI Phys. 2019;6(1):11.

17. Stickel JR, Cherry SR. High-resolution PET detector design: modelling components of intrinsic spatial resolution. Phys Med Biol. 2005;50(2):179–95.

18. Stickel JR, Qi J, Cherry SR. Fabrication and characterization of a 0.5-mm lutetium oxyorthosilicate detector array for high-resolution PET applications. J Nucl Med. 2007;48(1):115–21.

19. Palmer MR, Zhu X, Parker JA. Modeling and simulation of positron range effects for high resolution PET imaging. IEEE Trans Nucl Sci. 2005;52:1391.

20. Ruangma A, Bai B, Lewis JS, Sun X, Welch MJ, Leahy R, et al. Three-dimensional maximum a posteriori (MAP) imaging with radiopharmaceuticals labeled with three Cu radionuclides. Nucl Med Biol. 2006;33(2):217–26.

21. Bertolli O, Eleftheriou A, Cecchetti M, Camarlinghi N, Belcari N, Tsoumpas C. PET iterative reconstruction incorporating an efficient positron range correction method. Phys Med. 2016;32(2):323–30.

22. Derenzo SE. Mathematical removal of positron range blurring in high resolution tomography. IEEE Trans Nucl Sci. 1986;33(1):565–9.

23. Fu L, Qi J. A residual correction method for high-resolution PET reconstruction with application to on-the-fly Monte Carlo based model of positron range. Med Phys. 2010;37(2):704–13.

24. Levin CS, Zaidi H. Current trends in preclinical PET system design. PET Clin. 2007;2(2):125–60.

25. Yang Y, Wu Y, Qi J, St James S, Du H, Dokhale PA, et al. A prototype PET scanner with DOI-encoding detectors. J Nucl Med. 2008;49(7):1132–40.

26. Wang Y, Seidel J, Tsui BM, Vaquero JJ, Pomper MG. Performance evaluation of the GE healthcare eXplore VISTA dual-ring small-animal PET scanner. J Nucl Med. 2006;47(11):1891–900.

27. Mohammadi I, Castro IFC, Correia PMM, Silva ALM, Veloso JFCA. Minimization of parallax error in positron emission tomography using depth of interaction capable detectors: methods and apparatus. Biomed Phys Eng Exp. 2019;5(6):062001.

28. Schmall JP, Karp JS, Werner M, Surti S. Parallax error in long-axial field-of-view PET scanners-a simulation study. Phys Med Biol. 2016;61(14):5443–55.

29. Karp JS, Viswanath V, Geagan MJ, Muehllehner G, Pantel AR, Parma MJ, et al. PennPET explorer: design and preliminary performance of a whole-body imager. J Nucl Med. 2020;61(1):136–43.

30. Fahey FH. Data acquisition in PET imaging. J Nucl Med Technol. 2002;30(2):39–49.

31. Cherry S, Sorenson J, Phelps M. Physics in nuclear medicine. 4th ed. Philadelphia: Saunders; 2012.

32. Qi J, Leahy RM. Iterative reconstruction techniques in emission computed tomography. Phys Med Biol. 2006;51(15):R541–78.

33. Links JM, Leal JP, Mueller-Gaertner HW, Wagner HN Jr. Improved positron emission tomography quantification by Fourier-based restoration filtering. Eur J Nucl Med. 1992;19(11):925–32.

34. Panin VY, Kehren F, Michel C, Casey M. Fully 3-D PET reconstruction with system matrix derived from point source measurements. IEEE Trans Med Imaging. 2006;25(7):907–21.

35. Varrone A, Sjoholm N, Eriksson L, Gulyas B, Halldin C, Farde L. Advancement in PET quantification using 3D-OP-OSEM point spread function reconstruction with the HRRT. Eur J Nucl Med Mol Imaging. 2009;36(10):1639–50.

36. Sureau FC, Reader AJ, Comtat C, Leroy C, Ribeiro MJ, Buvat I, et al. Impact of image-space resolution modeling for studies with the high-resolution research tomograph. J Nucl Med. 2008;49(6):1000–8.

37. Rahmim A, Tang J, Lodge MA, Lashkari S, Ay MR, Lautamaki R, et al. Analytic system matrix resolution modeling in PET: an application to Rb-82 cardiac imaging. Phys Med Biol. 2008;53(21):5947–65.

38. Aston JA, Cunningham VJ, Asselin MC, Hammers A, Evans AC, Gunn RN. Positron emission tomography partial volume correction: estimation and algorithms. J Cereb Blood Flow Metab. 2002;22(8):1019–34.

39. Soret M, Bacharach SL, Buvat I. Partial-volume effect in PET tumor imaging. J Nucl Med. 2007;48(6):932–45.

40. Boellaard R, Krak NC, Hoekstra OS, Lammertsma AA. Effects of noise, image resolution, and ROI definition on the accuracy of standard uptake values: a simulation study. J Nucl Med. 2004;45(9):1519–27.

41. Mourik JE, Lubberink M, van Velden FH, Kloet RW, van Berckel BN, Lammertsma AA, et al. In vivo validation of reconstruction-based resolution recovery for human brain studies. J Cereb Blood Flow Metab. 2010;30(2):381–9.

42. Lewellen T, Karp J. PET systems. In: Wernick M, Aarsvold J, editors. Emission tomography: the fundamentals of PET and SPECT. San Diego: Elsevier Academic; 2004.

43. Strother SC, Casey ME, Hoffman EJ. Measuring PET scanner sensitivity: relating count rates to image signal to noise ratios using noise equivalent counts. IEEE Trans Nucl Sci. 1990;37:783–8.

44. Vandendriessche D, Uribe J, Bertin H, De Geeter F. Performance characteristics of silicon photomultiplier based 15-cm AFOV TOF PET/CT. EJNMMI Phys. 2019;6(1):8.

45. Badawi RD, Dahlbom M. NEC: some coincidences are more equivalent than others. J Nucl Med. 2005;46(11):1767–8.

46. Lartizien C, Comtat C, Kinahan PE, Ferreira N, Bendriem B, Trebossen R. Optimization of injected dose based on noise equivalent count rates for 2- and 3-dimensional whole-body PET. J Nucl Med. 2002;43(9):1268–78.

47. National Electrical Manufacturers Association. Performance measurements of positron emission tomographs (PET). NEMA Standards Publication NU 2-2012. Rosslyn: National Electrical Manufacturers Association; 2012.

48. National Electrical Manufacturers Association. Performance measurements of positron emission tomographs (PET). NEMA Standards Publication NU 2-2018. Rosslyn: National Electrical Manufacturers Association; 2018.

49. Pan T, Einstein SA, Kappadath SC, Grogg KS, Lois Gomez C, Alessio AM, et al. Performance evaluation of the 5-ring GE discovery MI PET/CT system using the national electrical manufacturers association NU 2-2012 standard. Med Phys. 2019;46(7):3025–33.

50. Moses WW. Advantages of improved timing accuracy in PET cameras using LSO scintillator. In: IEEE nuclear science symposium conference record, vol. 3, 2002. p. 1670–5.

51. Conti M. Focus on time-of-flight PET: the benefits of improved time resolution. Eur J Nucl Med Mol Imaging. 2011;38(6):1147–57.

52. Budinger TF. Time-of-flight positron emission tomography: status relative to conventional PET. J Nucl Med. 1983;24(1):73–8.

53. Moses WW. Time of flight in PET revisited. IEEE Trans Nucl Sci. 2003;50:1325–30.

54. Conti M. State of the art and challenges of time-of-flight PET. Phys Med. 2009;25(1):1–11.

55. Kyba CM, Wiener RI, Newcomer FM, Perkins AE, et al. Evaluation of local PMT triggering electronics for a TOF PET scanner. In: Sellin P, editor. IEEE nuclear science symposium and medical imaging conf record (Dresden, Germany), 2008.

56. Daube-Witherspoon ME, Surti S, Perkins A, Kyba CC, Wiener R, Werner ME, et al. The imaging performance of a LaBr3-based PET scanner. Phys Med Biol. 2010;55(1):45–64.

57. Surti S, Kuhn A, Werner ME, Perkins AE, Kolthammer J, Karp JS. Performance of Philips Gemini TF PET/CT scanner with special consideration for its time-of-flight imaging capabilities. J Nucl Med. 2007;48(3):471–80.

58. Ollinger JM. Detector efficiency and compton scatter in fully 3D PET. IEEE Trans Nucl Sci. 1995;42:1168–73.

59. Badawi RD, Marsden PK. Self normalization of emission data in 3D PET. IEEE Trans Nucl Sci. 1999;46:709.

60. Ishikawa A, Kitamura K, Mizuta T, Tanaka K, Amano M. Self normalization for continuous 3D whole body emission data in 3D PET. IEEE Trans Nucl Sci. 2004;6:3634–7.

61. Hoffman EJ, Guerrero TM, Germano G, Digby WM, Dahlbom M. PET system calibrations and corrections for quantitative and spatially accurate images. IEEE Trans Nucl Sci. 1989;36:1108–12.

62. Defrise M, Townsend DW, Bailey D, Geissbuhler A, Michel C, Jones T. A normalization technique for 3D PET data. Phys Med Biol. 1991;36(7):939–52.

63. Casey ME, Gadagkar H, Newport D. A component based method for normalization in volume PET. In: Proceedings of the 3rd international meeting fully three dimensional image reconstruction in radiology and nuclear medicine. Aix les Bains, France, 1995. p. 67–71.

64. Kinahan PE, Townsend DW, Bailey DL, Sashin D, et al. Efficiency normalization technique for 3D PET data. In: Proceeding of the IEEE nuclear science symposium and medical imaging conference recording, vol. 2, 1995. p. 21–8.

65. Badawi RD, Marsden PK. Developments in component-based normalization for 3D PET. Phys Med Biol. 1999;44(2):571–94.

66. Badawi RD, Ferreira NC, Kohlmyer SG, Dahlbom M, Marsden PK, Lewellen TK. A comparison of normalization effects on three whole-body cylindrical 3D PET systems. Phys Med Biol. 2000;45(11):3253–66.

67. Germano G, Hoffman EJ. A study of data loss and mispositioning due to pileup in 2D detectors in PET. IEEE Trans Nucl Sci. 1990;37(2):671–5.

68. Bailey DL, Meikle SR, Jones T. Effective sensitivity in 3D PET: the impact of detector dead time on 3D system performance. IEEE Trans Nucl Sci. 1997;44:1180–5.

69. Spinks TJ, Bloomfield PM. A comparison of count rate performance for 15O water blood flow studies in the CTI HR + and Accel tomographs in 3D model. In: Nuclear science symposium conference record, vol 3, 2002. p. 1457–60.

70. Moisan C, Rogers JG, Douglas JL. A count rate model for PET and its application to an LSO HR plus scanner. IEEE Trans Nucl Sci. 1997;44:1219–24.

71. Guerra L, Ponti E, Morzenti S, Spadavecchia C, Crivellaro C. Respiratory motion management in PET/CT: applications and clinical usefulness. Curr Radiopharm. 2017;10(2):85–92.

72. Blankespoor SC, Xu X, Kaiki B, Tang HR, Cann CE, et al. Attenuation correction of SPECT using x ray CT on an emission transmission CT system: myocardial perfusion assessment. IEEE Trans Nucl Sci. 1996;43:2263–74.

73. Kinahan PE, Townsend DW, Beyer T, Sashin D. Attenuation correction for a combined 3D PET/CT scanner. Med Phys. 1998;25(10):2046–53.

74. Burger C, Goerres G, Schoenes S, Buck A, Lonn AH, Von Schulthess GK. PET attenuation coefficients from CT images: experimental evaluation of the transformation of CT into PET 511-keV attenuation coefficients. Eur J Nucl Med Mol Imaging. 2002;29(7):922–7.

75. Benard F, Smith RJ, Hustinx R, Karp JS, Alavi A. Clinical evaluation of processing techniques for attenuation correction with 137Cs in whole-body PET imaging. J Nucl Med. 1999;40(8):1257–63.

76. Bai C, Shao L, Da Silva AJ, et al. A generalized model for the conversion from CT numbers to linear attenuation coefficients. IEEE Trans Nucl Sci. 2003;50:1510–5.

77. Seo Y, Mari C, Hasegawa BH. Technological development and advances in single-photon emission computed tomography/computed tomography. Semin Nucl Med. 2008;38(3):177–98.

78. Thompson CJ. The problem of scatter correction in positron volume imaging. IEEE Trans Med Imaging. 1993;MI-12:124–32.

79. Lercher MJ, Wienhard K. Scatter correction in 3D PET. IEEE Trans Med Imaging. 1994;13:649–57.

80. Adam LE, Bellemann ME, Brix G, Lorenz WJ. Monte Carlo-based analysis of PET scatter components. J Nucl Med. 1996;37(12):2024–9.

81. Zaidi H, Koral KF. Scatter modelling and compensation in emission tomography. Eur J Nucl Med Mol Imaging. 2004;31(5):761–82.

82. Grootoonk S, Spinks TJ, Sashin D, Spyrou NM, Jones T. Correction for scatter in 3D brain PET using a dual energy window method. Phys Med Biol. 1996;41(12):2757–74.

83. Bailey DL. Quantitative procedures in 3D PET. In: Bendriem B, Townsend DW, editors. The theory and practice of 3D PET. Dordrecht: Kluwer Academic; 1998. p. 55–109.

84. Bentourkia M, Lecomte R. Energy dependence of nonstationary scatter subtraction restoration in high resolution PET. IEEE Trans Med Imaging. 1999;18:66–73.

85. Bailey DL, Meikle SR. A convolution-subtraction scatter correction method for 3D PET. Phys Med Biol. 1994;39(3):411–24.

86. McKee B, Gurvey AT, Harvey PJ, Howse DC. A deconvolution scatter correction for a 3D PET system. IEEE Trans Med Imaging. 1992;11(4):560–9.

87. Ollinger JM. Model-based scatter correction for fully 3D PET. Phys Med Biol. 1996;41(1):153–76.

88. Watson CC, Casey ME, Michel C, Bendriem B. Advances in scatter correction for 3D PET/CT. In: IEEE nuclear science symposium conference record, vol. 5, 2004. p. 3008–12.

89. Watson C. Extension of single scatter simulation to scatter correction of time of flight PET. IEEE Trans Nucl Sci. 2007;54(5):1679–86.

90. Shiri I, Arabi H, Geramifar P, Hajianfar G, Ghafarian P, Rahmim A, et al. Deep-JASC: joint attenuation and scatter correction in whole-body (18)F-FDG PET using a deep residual network. Eur J Nucl Med Mol Imaging. 2020;47:2533.

91. Yang J, Park D, Gullberg GT, Seo Y. Joint correction of attenuation and scatter in image space using deep convolutional neural networks for dedicated brain (18)F-FDG PET. Phys Med Biol. 2019;64(7):075019.

CT in Hybrid SPECT/CT and PET/CT

14

Tinsu Pan

Contents

14.1　Introduction

Hybrid imaging modalities of SPECT/CT and PET/CT are becoming standard of care in diagnosis and treatment response assessment for both oncology and cardiology. First SPECT/CT and PET/CT prototypes were developed in the University of California at San Francisco by Dr. Hasegawa [1] and the University of Pittsburgh by Dr. Townsend [2, 3], respectively. It was not until

1999 for SPECT/CT and 2001 for PET/CT to be commercialized for clinical use [4, 5]. Except for the first GE Healthcare Infinia Hawkeye SPECT/CT, which was equipped with a dental CT of limited X-ray capability (<2 mSv per scan) and slow gantry rotation (2.6 revolutions/min) [6], all the SPECT/CT and PET/CT scanners are equipped with the diagnostic CT scanner of high spatial (<1 mm) and high temporal resolution (≥1 revolution/s) imaging capabilities.

CT is an important diagnostic imaging modality capable of producing detailed anatomic information that is complementary to functional imaging of SPECT and PET, which have low spa-

T. Pan (✉)

Department of Imaging Physics, University of Texas, M.D. Anderson Cancer Center, Houston, TX, USA
e-mail: tpan@mdanderson.org

tial resolution ($\geq$5 mm for PET and $\geq$10 mm for SPECT) and low temporal resolution (~average breath cycle of 4–5 s). Attenuation correction of the functional imaging and spatial localization of the radiopharmaceutical uptake are the two major applications of CT in SPECT/CT and PET/CT.

Majority of PET/CT scans are performed for oncologic applications, and the most used radiopharmaceutical in PET/CT is ^{18}F-FDG, which has been approved for diagnosis and staging of many cancer types. Two major applications of SPECT/CT are myocardial perfusion imaging based on ^{99m}Tc-Sestamibi [7], which mainly uses CT for attenuation correction, and bone SPECT/CT imaging based on ^{99m}Tc-MDP [8, 9], which uses CT for localization. In this chapter, we will discuss the unique aspects of CT for assisting SPECT and PET imaging.

14.2   Introduction of CT Scanner

Majority of the commercial CT scanners are of the third generation CT, which has a single X-ray tube and a fan-shape detector assembly spanning about 60° to the X-ray source. The major components of a third generation CT scanner are shown in Fig. 14.1, and it includes (1) an X-ray tube, where the X-ray source is produced; (2) collimator and filters, which collimate the X-ray beams, remove the lower energy X-rays not capable of penetrating the body, as well as attenuate the X-rays via a bow-tie filter to uniformly irradiate the cross-section of the body (see Fig. 14.2); (3) detector assembly, which converts the attenuated X-rays into light signals; (4) data acquisition system (DAS), which converts light signals into electronic signals; and (5) slip ring, which houses the mechanical and electrical infrastructure for channeling the electrical signals out for image reconstruction at a high gantry rotation speed (<1 s per gantry rotation). The other supporting components are the high voltage inverter, anode and cathode high voltage tanks for the X-ray tube, and the gantry control computer for controlling the gantry rotation speed and coordinating the subsystems, whose weights are balanced around the gantry.

A CT scanner is a high-precision instrument. Any subtle mechanical misalignment will create artifacts and malfunction the CT scanner. The fourth generation CT was equipped with a complete ring of detectors around the gentry so that CT image quality will not be dependent on the center few detector elements of the fan-shape
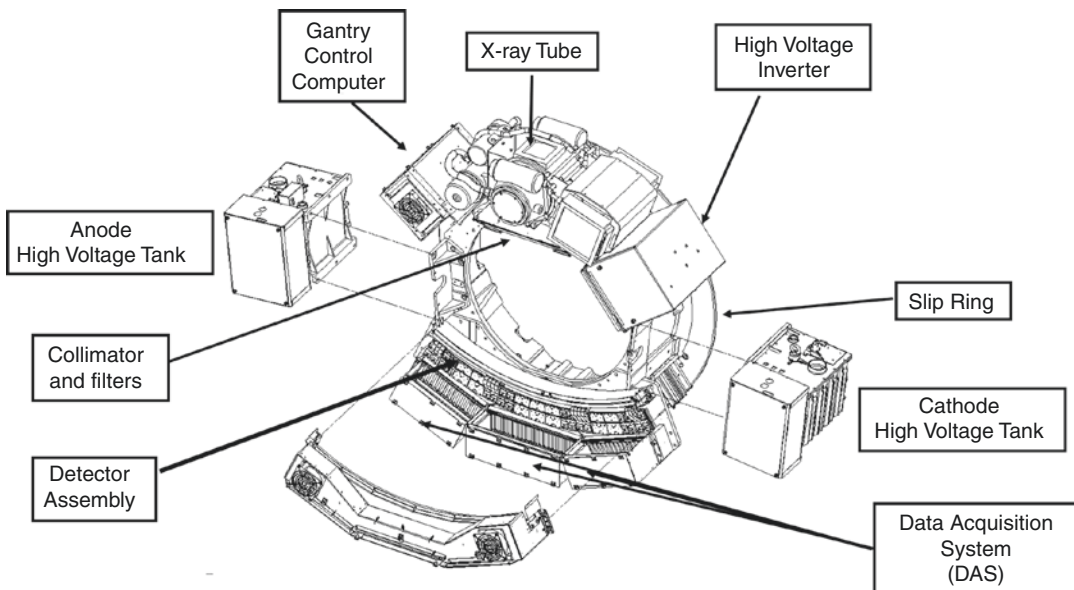
Fig. 14.1 CT scanner subsystem components
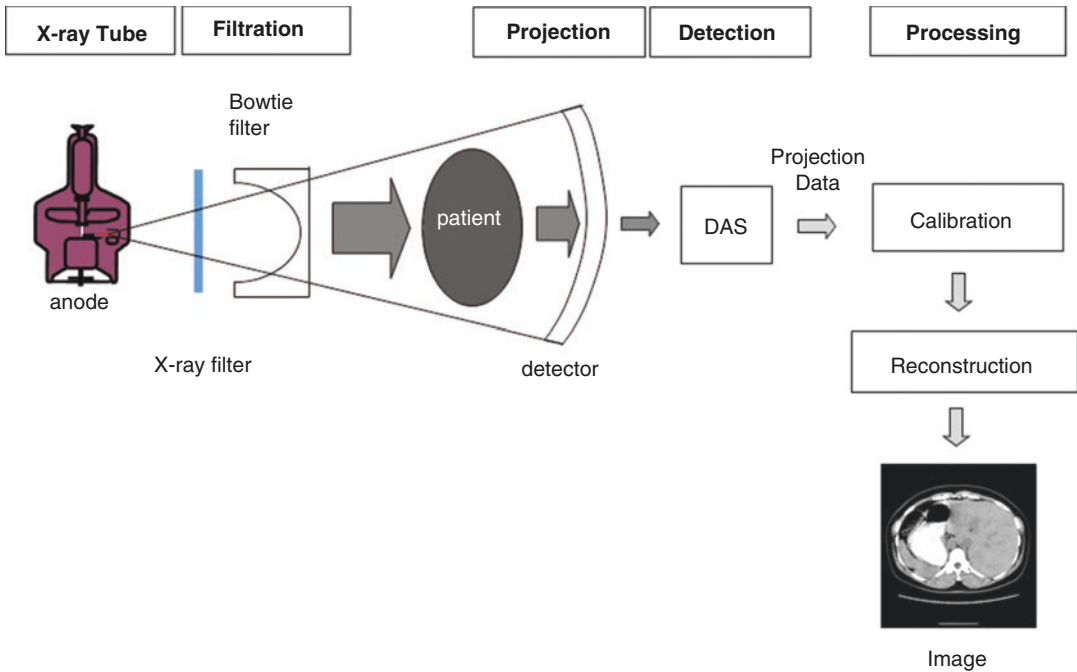
Fig. 14.2 Image generation in CT

detector of the third generation CT. However, the evolution of single-slice CT to multi-slice CT in the late 1990s made the cost of the fourth generation CT prohibited for practical use, thus there is only the third generation CT available for hybrid imaging.

Figure 14.2 shows the data path of the CT image reconstruction. Calibration is a very important step which processes the raw data to the projection data in the form of line integrals for image reconstruction. Beam hardening correction, which corrects the effect of hardening of the X-ray beam as it travels through the body, is included in the calibration. Any imperfect detector fluctuation between side-by-side detector elements is also included. The calibration step is very specific to each scanner and is proprietary to each vendor, and is normally not available in the public domain. This is why the raw CT data can be archived but cannot be processed without the help of the CT vendor. Since CT is a much larger market than Nuclear Medicine, it is normally the case that a hybrid scanner will get a CT scanner that is already commercialized rather than a CT scanner designed for a specific hybrid imaging device.

14.3 Selection of a CT Scanner

All the modern SPECT/CT (e.g., Siemens Symbia T16) and PET/CT (e.g., GE Discovery 710) scanners are equipped with either a 16- or 64-slice diagnostic CT. The main difference between the 16- and 64-slice CT is the CT detector arrangement in the direction of the imaging table. On GE, it is 2 cm for the 16-slice or 4 cm for the 64-slice. The width of X-ray collimation (2–4 cm, typically the same as the detector size), gantry rotation cycle time (0.5–1 s) and pitch factor (0.5:1 to 1.75:1), defined as the ratio of imaging table translation distance per rotation to the width of the X-ray collimation—all of which determine the CT scanning speed (i.e., CT scan coverage per unit time). The configurations of 64-slice and 16-slice allow a CT scan to acquire 64 channels of 0.625 mm and 16 channels of 0.625 or 1.25 mm data simultaneously. The advantages of 64-slice over 16-slice are twice the scanning coverage (4-cm vs. 2-cm) per unit time, twice smaller the slice thickness at full detector coverage (0.625 mm vs. 1.25 mm), and reduced

radiation exposures to the patient by 12–20% (see Table 14.1).

It is important to consider the collimation choices of a CT scanner and their radiation exposure ramifications. In general, we would choose the collimation as large as possible to cover the whole detector such as 16 × 1.25 and 64 × 0.625 mm for the GE 16-slice and 64-slice CT scanners, respectively. The larger the collimation configured in imaging, the higher the dose efficiency (see Table 14.1) in scanning because the penumbra of the X-ray beam, which is not a

Table 14.1 The radiation exposures of the 16-slice and 64-slice CT on the GE PET/CT. The first column is X-ray collimation. The 16-slice can be 16 × 0.625 or 16 × 1.25 mm. The 64-slice is almost exclusively 64 × 0.625 mm. There are two focal spot sizes; however, the small focal spot changes to a large focal spot at 210 mA for 16-slice and at 340 mA for 64-slice. The third column is the radiation exposure per 100 effective mAs, which is the multiplication of X-ray tube current and gantry rotation time per revolution divided by the pitch factor. The 64-slice CT is more dose efficient than the 16-slice CT is

120 kV	mA	mGy/100mAs
16 × 0.625 mm	<210	10.66
	≥210	11.58
16 × 1.25 mm	<210	8.90
	≥210	9.48
64 × 0.625 mm	<340	7.92
	≥340	7.91

flat exposure to the detector, would lead to image artifacts if the penumbra is on the edge detector elements. As such, the X-ray collimation is dynamically controlled at any angle to maintain a uniform exposure of the umbra region on the detector regardless the heat load on the X-ray rotor. As the X-ray tube heats up from CT scans, the focal spot will shift in space due to the expansion of the heated rotor. A small umbra extending outside the X-ray collimation is necessary so that the X-ray beams on the imaging detectors will not see any portion of the penumbra. Therefore, there are always some X-ray beams reaching the detector assembly to be thrown away for image quality. Figure 14.3 shows the different configurations and their associated dose efficiencies. There is 13% of the X-rays going through the patient not used in the image reconstruction for a dose efficiency of 87% for the collimation of either 16 × 1.25 or 8 × 2.50 mm. For image quality, it is better to use 16 × 1.25 mm than 8 × 2.50 mm because the data are twice sampled in 16 × 1.25 than in 8 × 2.50 mm and it allows the reconstruction of a thicker slice with more data points for a better image quality.

Some SPECT/CT scanners come with 2-, 4-, or 6-slice CT such as the 2-slice CT on Siemens Symbia T2, 4-slice CT on GE Infinia Hawkeye 4- and 6-slice CT on Siemens Symbia T6. These CT scanners are not strictly qualified as a diag-

Fig. 14.3 Options of X-ray collimation in the table direction on the GE 16 and 64-slice CT scanners. The radiation beam in the umbra is flat on the detector for image quality, but the one in the penumbra is not and could lead to artifacts in image reconstruction. This extra dose from the penumbra is about the same for all collimations. As a result, the dose efficiency was at 77% for 16 × 0.625 or 8 × 1.25 mm, at 87% for 16 × 1.25 or 8 × 2.50 mm, and at 93% for 64 × 0.625 mm

nostic CT as their scan speeds are significantly slower than the diagnostic CT scanners of at least 16-slice or typical 64-slice. Most diagnostic CT scans are performed in a single breath-hold. Fast CT scan speed can improve patient comfort. SPECT/CT tends to have a lower wattage X-ray tube than PET/CT because it only needs to scan a limited area of about 40 cm on SPECT/CT rather than over 100 cm for the whole-body PET/CT. The X-ray tube wattage on the new Siemens Intevo Bold T16 is 33 kilo-watt (kW); the one on the GE Discovery STE 16-slice is 52.8 kW; and the one on the GE Discovery MI 64-slice is 67.2 kW. It is important to evaluate the capacity of the X-ray tube if the CT of SPECT/CT or PET/CT will be used for diagnostic imaging.

Some PET/CT scanners with 64-slice CT (e.g., Siemens mCT 64-slice) may not have 64 physical channels. Siemens mCT 64-slice has only 32 physical channels of 0.6 mm detector coverage (1.92 cm); however, Siemens claims to have 64 channels of 0.3 mm as a result of applying the technology of flying focal spot, which doubles the sampling in the table direction on the detector by fast switching two focal spot positions to achieve 0.3 mm spatial resolution for imaging the inner ear. Although Siemens mCT 64-slice can image the inner ear at a higher spatial resolution than GE Discovery PET/CT of 64-slice, it has less than 50% scan speed and 12–20% higher dose penalty than GE. If the inner ear imaging is not of interest in PET/CT imaging, then Siemens mCT 64-slice becomes Siemens mCT 20-slice, which has at most 16 channels of 1.2 mm (1.92 cm), and is smaller than the detector coverage of the GE Discovery PET/CT 16-slice, which has 16 channels of 1.25 mm (2 cm). This tradeoff should be taken into consideration when purchasing a PET/CT scanner because the price difference can be substantial between Siemens mCT 20 and mCT 64-slice whether the inner ear application, which is a CT rather than PET/CT application, is needed. In general, PET/CT with the 64-slice CT of a 4-cm detector is preferred if the CT component of PET/CT is to be used in diagnostic CT. Otherwise, 16-slice CT with 2-cm detector should be sufficient for the routine whole-body PET/CT.

Other than GE NM/CT 570c which has a 64-slice CT attached to the GE NM 530c, the most advanced CT option for SPECT/CT is 16-slice CT. In the GE NM/CT 570c configuration, the 64-slice CT can be used for coronary artery CT imaging and the NM 530c SPECT camera with the solid-state CZT detector is used for myocardial perfusion imaging. It is not possible to use a 16-slice CT for coronary artery CT because it will be very difficult for a patient to hold breath for over 20 s to complete a coronary artery CT imaging, which requires a thin slice imaging of ≤1 mm. In addition, coronary artery CT needs to be taken at the deep inspiration breath-hold, and myocardial perfusion nuclear imaging of SPECT or PET is taken at free-breathing. Care should be taken when both sets of images are to be fused as they are likely be taken at two different breathing conditions.

14.4 Importance of Calcium Scoring to Myocardial Perfusion Imaging

Calcium deposits in the coronary arteries are an important biomarker to assist the diagnosis of myocardial perfusion imaging of SPECT or PET. The transformation from a soft plaque to a hardened plaque, such as calcification, has been associated with the disease process of atherosclerosis, which may take years to develop. Calcification is an excellent negative predictive biomarker for coronary artery disease, because a chest pain patient presented to the emergency room without coronary calcification is not likely to have the coronary artery disease.

CT can be used to estimate the burden of coronary calcification in the major coronary arteries. Standard coronary calcification is measured when the patient is at deep breath-hold to avoid smearing of the calcified plaque during a short snapshot CT imaging of less than 1 s for calcium scoring. A faster gantry rotation translates into a better temporal resolution and fewer motion artifacts thus more accurate calcium scoring. Calcium scores are typically derived from the Agatston method [10], which is based on the
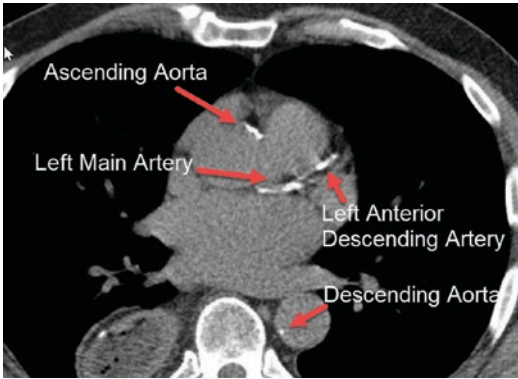
Fig. 14.4 Assessment of calcium deposits with CT of no ECG gating is feasible, and can be done with the radiation exposure of 3.3 mGy of 120 kVp, 100 mA, 0.5 s gantry rotation, 2.5 mm slice thickness, and 16 × 1.25 mm X-ray collimation on the GE 16-slice CT

areas of at least 3 voxels of greater than 130 Hounsfield units weighted by a factor related to maximum plaque attenuation: 130–199 HU, factor 1; 200–299 HU, factor 2; 300–399 HU, factor 3; and ≥400 HU, factor 4. The risk of major heart attacks has been extensively studied to be 4.3, 7.2, and 10.8% for the scores of 100–400, 401–999, and >1000, respectively [11].

Since the risk is associated with a range of HU, it may be possible to use the non-gated CT for attenuation correction of the myocardial perfusion imaging for calcium scoring. Knowing that the non-gated CT images are more blurred due to motion than the gated CT images, the scores derived from the non-gated CT images may be different and likely lower than the ones from the gated CT images. Nonetheless, it is still beneficial to have an estimate of the calcium scores from the non-gated CT images if a separate calcium scoring CT with ECG gating is not available (Fig. 14.4).

14.5 Tube Current Modulation (TCM) for Reduction of Radiation Exposure

CT in PET/CT typically covers the anatomy from the skull base to mid-thigh, or the head to toe for the diagnosis of melanoma with ^{18}F-FDG, or bone metastases with ^{18}F-NaF for PET; and a limited area of about 40 cm for SPECT. The oval shape of the chest or the position of the arms on the sides of the patient can result in more tissues for the X-ray to traverse in the lateral than in the anterior-to-posterior (AP) or posterior-to-anterior (PA) direction to cause some streaking artifacts (Fig. 14.5). If the object is entirely inside the scan field of view, the total attenuation will be the same for all CT projection angles, but the distribution of tissue attenuation in the fan-beam projection CT data is more compact in space in the lateral than in the AP or PA direction. Less signal on the detector in the lateral direction makes it more susceptible to the noise resulting from the streaking artifacts in the lateral direction.

All modern CT scanners come with TCM, which allows radiation exposure to change or modulate according to the anatomy or the size of cross-section anatomy, in the X-ray beam. For example, if both the lungs and the abdomen are to be scanned at the same time, TCM renders less radiation to the lungs than to the abdomen, and less radiation in the AP or PA direction than in the lateral direction. TCM was first designed to take into account the anatomy change in the imaging table or Z direction, and was later modified to take into account the variation between the lateral and the AP or PA directions (see Fig. 14.6) rendering a higher exposure in the lateral views and a lower exposure in the AP or PA views.

The desired image quality can be translated into a metric of noise index on GE or quality reference mAs on Siemens for TCM. A low dose survey scan (called scout in GE or topogram in Siemens), typically in the AP direction, provides the anatomy information to guide CT radiation exposure during the CT scan. TCM assumes the anatomy of interest is centered in the CT gantry, which is possible in the organ-based diagnostic imaging and is not feasible in the whole body.

PET/CT imaging. Centering the chest does not mean centering the abdomen and vice versa. Patient positioning should also be considered in setting up the CT scan protocol. If the AP survey scan data are used, the patient positioned farther away from the X-ray source is projected smaller
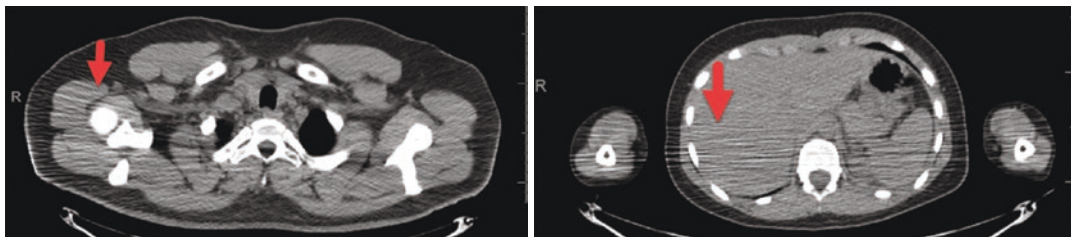
Fig. 14.5 Streaking artifacts in the lateral direction can be caused by the oval shape cross-section on the shoulder (left) and the arms positioned on the sides of the patient (right)
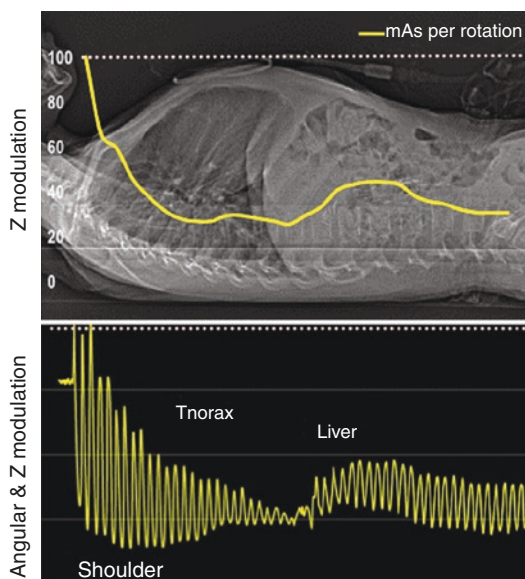
Fig. 14.6 Tube current modulation of a CT scan from the shoulder, the thorax, and to the liver. The upper panel shows the modulation along the Z or table direction; whereas the lower panel shows the modulation along the Z and angular plane, which accounts for the higher exposure in the lateral views and lower exposure in the AP or PA views. (Courtesy of Siemens)

on the survey scan (Fig. 14.7), and thus receives less radiation.

14.6   Breath-Hold or Free-Breathing CT Scan

Diagnostic CT procedures are typically performed during breath-hold with iodine contrast injection. However, most of the CT scans on PET/CT or SPECT/CT are taken at free-breathing due to the long scan time of PET/SPECT over

several minutes to form an image. Without loss of generality, we will discuss mainly the misregistration issue between PET and CT in PET/CT, which is similar to the same issue between SPECT and CT in SPECT/CT.

Migration from stand-alone PET and stand-alone CT in two separate imaging sessions to PET/CT in a single imaging session has improved registration between PET and CT due to sharing of the same imaging table without patient repositioning. However, due to the different scan speeds of CT and PET, there is still registration issue between the CT and PET data of PET/CT, in particular, in the thorax or the abdomen due to patient respiration. Osman et al. observed that curve-linear cold artifacts paralleling the dome of the diaphragm at the lung bases were frequently noted in PET/CT images [12]. However, clinically, they reported that this type of artifact resulted in significant inaccurate localization of lesions for only 2% of the 300 patients investigated. Gould et al. reported from a cohort of 259 patients for cardiac PET/CT imaging, 40% of the patient data exhibited false-positive defects due to misalignment [13]. It is evident from these two studies that the severity of misalignment depends on the area of interest. Misalignment between PET and CT may not be a significant issue in a whole-body PET/CT scan if the lesions are not near the diaphragm. However, it may become a significant issue in cardiac PET/CT imaging, where the heart is right above the diaphragm.

Coaching the patient to breath-hold at midexpiration to mitigate the artifact from misalignment was not very successful. In a study of 100 patients undergoing PET/CT with breath-hold at mid-expiration CT by Pan et al. [14], 50% of the

Fig. 14.7 Patient radiation exposure is determined by the survey scan if TCM is used. The left panel shows the patient was positioned farther away from the X-ray source than in the right panel. As a result, the same patient positioned closer to the X-ray source (the right panel) will be exposed to more radiation with TCM
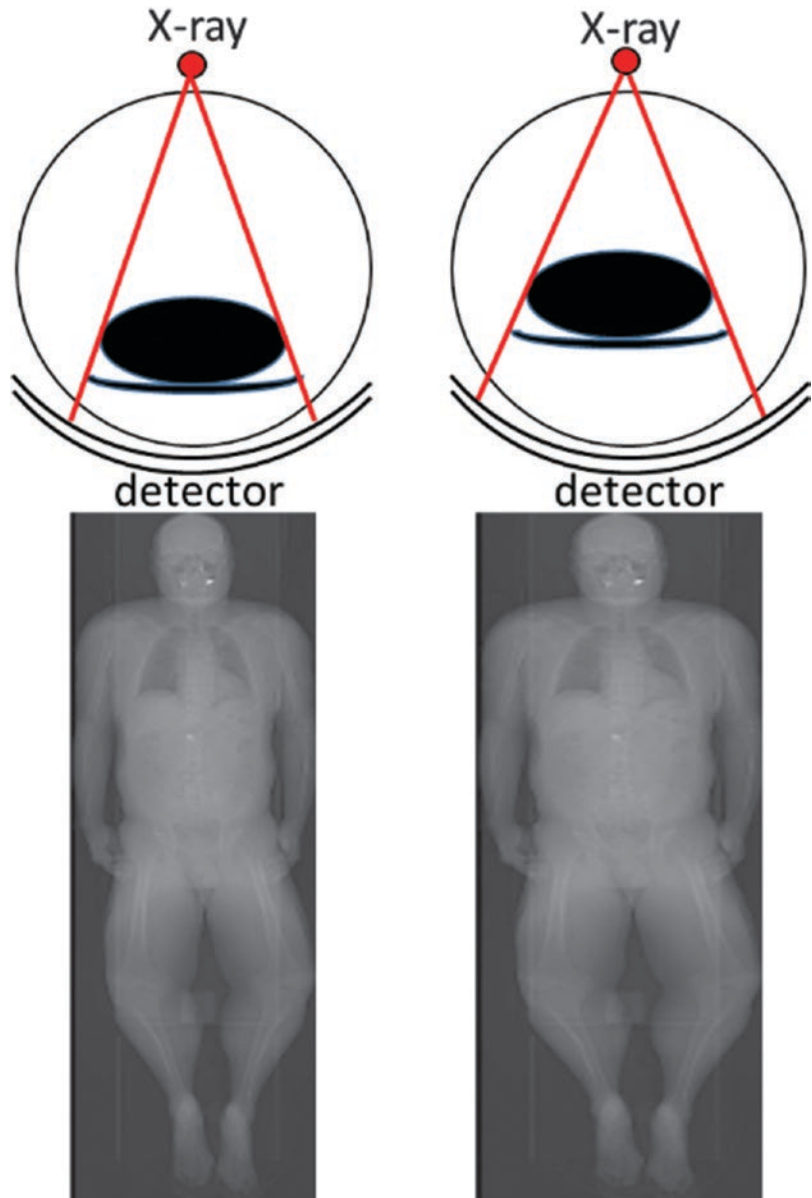
patients exhibited the curve-linear cold artifacts in the PET images caused by the respiratory motion. In a study of 216 patients undergoing free-breathing CT in PET/CT by Chi et al. [15], 68% of the patient data exhibited either the curve-linear cold artifacts or tumor misalignment. Misalignment due to breathing has been shown to cause variation in standardized uptake value (SUV) [14], critical to delineation of the gross tumor volume with the PET data.

14.7 Causes of Mis-Registration Artifacts

CT is mostly a 2D whereas PET is a 3D imaging device. A CT scanner is composed of an X-ray source and a bank of detector modules arranged in a fan-beam geometry, which needs to rotate at least 180 plus the 60° of fan-beam angle to produce a tomographic image. The detector coverage along the cranio-caudal or table direction at the isocenter is

2 cm for a 16-slice or 4 cm for a 64-slice GE CT scanner. A helical CT scan of 100 cm from the skull base to mid-thigh in a PET/CT scan can be performed in less than 20 s on a 16-slice or less than 10 s on a 64-slice PET/CT. The speed of helical CT is determined by the gantry rotation cycle time, the width of X-ray collimation, and the pitch factor. A faster CT scan can be accomplished with a fast gantry rotation cycle time of 0.5 s, use of maximum X-ray collimation of 2 cm on a 16-slice or 4 cm on a 64-slice CT, and a high pitch factor of 1.375:1 for the scan speeds of 5.5 and 11 cm/s for a 16-slice and 64-slice CT, respectively. On the other hand, combination of a slow gantry rotation cycle time of 1 s, a smaller X-ray collimation of 1 cm for a 16-slice or 2 cm for a 64-slice, and a pitch factor of 1 would make the scan speeds of 1 and 2 cm/s for a 16-slice and 64-slice CT, respectively. Note that the pitch factor of 1 on the GE CT scanner is 0.9375 (=15/16 on a 16-slice), or 0.984 (=63/64 on a 64-slice).

The 3D volume of a CT scan is composed of a stack of 2D CT images acquired in the craniocaudal direction. Fast CT gantry rotation time of sub-second improves the temporal resolution of the CT image to sub-second, making each CT image almost free of respiratory motion artifacts. However, these 2D CT images, cannot represent a consistent 3D CT anatomy because each CT image is a snap shot of the anatomy at a particular phase of a respiratory cycle when the patient free-breaths during the CT data acquisition of a PET/CT scan. An example of the inconsistency in free-breathing CT scans is in Fig. 14.8, where
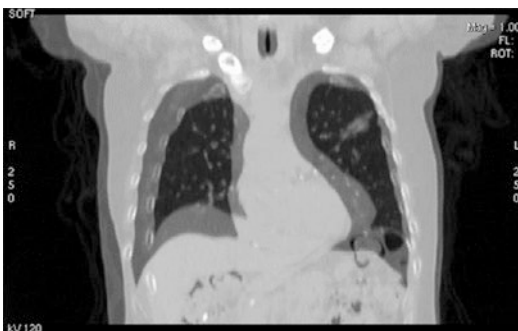
Fig. 14.8 Superposition of two consecutive free-breathing CT scans of a patient shows a significant difference between the two scans

the difference in CT anatomy can be quite different between two consecutive free-breathing CT scans.

A respiratory phase can be quantified as a percentage in a breath cycle between two consecutive end-inspirations, which typically correspond to a local maximum in amplitude. On the other hand, end-expiration phases correspond to a local minimum in amplitude (see Fig. 14.9). The respiratory signal can be detected by the optical sensing device of the Real-time Position Management (RPM) respiratory gating system (Varian Medical Systems, Palo Alto, CA), the pressure sensor device AZ-733V (Anzai Medical Corporation, Tokyo, Japan) or the air bellows (Philips Medical Systems, Andover, MA). However, at this time, it is still cumbersome from the operational standpoint for either PET or CT gating during acquisition.

Most of the PET acquisitions today are in 3D acquisition mode without the septa between slices to improve the sensitivity of detecting annihilation photons of 511 keV. The scan coverage of a GE PET detector module in the craniocaudal direction is 15.4 cm, which is much larger than the CT detector module of 2 cm for the 16-slice or 4 cm for the 64-slice. The PET detectors are arranged in a ring geometry without a space or gap to improve its sensitivity. The duration of a PET scan at each bed position is typically 2–3 min and it can be shortened by utilizing a larger axial field of view such as the 21.6 cm detector on the Siemens mCT scanner or 25 cm detector on the GE Discovery MI to further improve the sensitivity of PET imaging. There is no guarantee that the CT images from a fast scan CT at the temporal resolution of sub-second would match temporally with the PET images of a slow PET scan. It is this mismatch in temporal resolution between the CT and PET data acquisitions that causes mis-registration between the CT and PET images in PET/CT imaging of a patient at free-breathing.

The current design of PET/CT only matches the spatial resolution of the CT and PET data by blurring the CT images so that the spatial resolution of the CT images matches with the spatial resolution of the PET images. There has been no

Fig. 14.9 Conventional demarcation of a respiratory cycle with 0% end-inspiration and 100% between two consecutive end inspirations. In this case, end-expiration occurs at about 60%
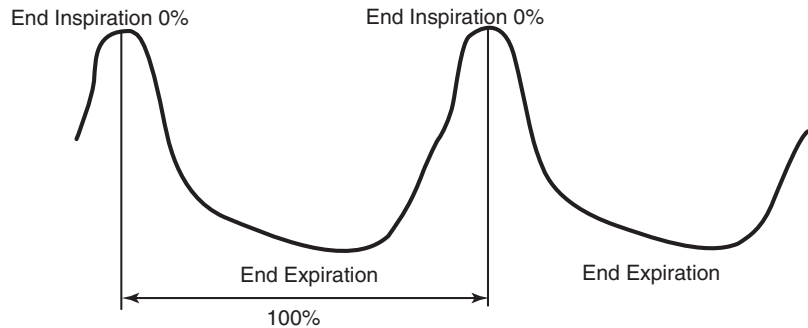
attempt from manufacturers to match the temporal resolutions of CT and PET for a routine whole-body PET/CT scan. For any measure to match the temporal resolution of the PET and CT data, additional acquisition time cannot be too long and post-processing steps cannot be too cumbersome. The patient is normally asked to position his/her arms over the head during data acquisition of the CT and PET data in order to improve the image quality of the thorax and the abdomen. In this position, an average person can maintain stationary for about 15–20 min and not more than 30 min at maximum. Any scan over 30 min is susceptible to patient motion due to discomfort to keep at the still location for a prolonged period of time.

14.8 Average CT to Reduce Mis-Registration

One approach to improve registration between the CT and PET data is to bring the temporal resolution of the CT images to that of the PET data [14]. Recognizing that a PET image is averaged over many breath cycles, a CT image averaged over one breath cycle could approach the temporal resolution of the PET image and register better with the PET image. Figure 14.10 shows an example of mis-registration between the CT and PET data, and correction of the mis-

registration by average CT. This concept of average CT is very similar to the one on a stand-alone PET scanner whereby two to three rotating transmission rod sources of ^{68}Ge were used to obtain the transmission map for attenuation correction of the PET data. The transmission map from transmission rod sources has been shown to register well with the emission PET data [16]. Since most PET/CT scanners are not equipped with a transmission rod source, average CT can serve as an alternative for the transmission rod sources. The advantages of average CT over transmission rod sources are (1) short acquisition time: 1 min for average CT, and several min per bed for transmission imaging and (2) high photon flux and less noisy attenuation maps. The disadvantages are (1) radiation dose of about 1 mSv from average CT than about 0.13 mSv from the transmission rod sources. Average CT has been shown to be effective in attenuation correction of the PET data not only in oncological imaging with ^{18}F-FDG but also in cardiac imaging [17], and confirmed by others [18, 19].

Acquiring cine CT images for average CT can be accomplished by scanning at the same location with a fast gantry rotation of sub-second over a breath cycle of 3–5 s. Average CT can also be implemented with a low-pitch (<0.1) helical CT. The conventional approach of using a slow-scan CT of several seconds per gantry rotation to generate a slow CT to mimic average
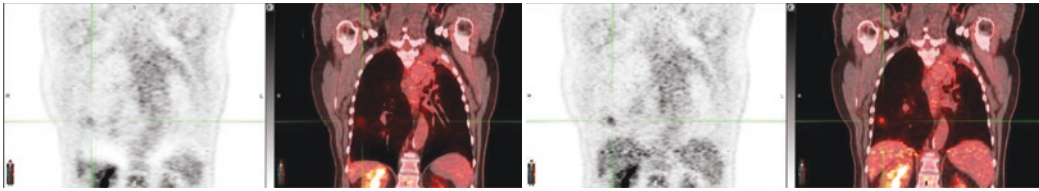
Fig. 14.10 (Left panel) The CT data had a lower (inferior) diaphragm position than the PET average data of free-breathing, resulting a photo-penic region with an underestimation of ^{18}F-FDG uptake. (Right panel) After correction with the average CT data, the photo-penic region disappeared and the SUV_{max} of the tumor (above the diaphragm) increased by 57% from 2.3 to 3.6

CT is not correct and should be discouraged [17, 20]. The slow-scan CT acquires data over one CT gantry rotation of several seconds, typically 2 or 4 s on the GE CT scanner. This scan technique can cause severe reconstruction artifacts because the projection data of the slow 4-s CT are not consistent over one revolution of the CT scan due to respiratory motion, in violation of the basic tomographic image reconstruction principle which requires the imaged object to be stationary during data acquisition. The average CT and PET data are similar in temporal resolution and have a better chance of registration between CT and PET.

Scan of either cine CT on the GE scanner or low-pitch helical CT (pitch <0.1) on the scanners of the other vendors can be adopted to obtain average CT, and has been available in 4D-CT imaging [21–23]. However, it is not clear whether the setup of 4D-CT imaging primarily for the assessment of tumor motion in radiation therapy with a respiratory monitoring device is ideal for obtaining average CT when the majority of PET/CT scanners are in diagnostic imaging. The approach that average CT can only be generated after 4D-CT may not be a practical solution.

The radiation exposure with average CT is about 4.4 mGy for the technique of 120 kV, 10 mA, 0.5 s gantry rotation, 8×2.5 mm collimation, and 5 s cine duration or 0.86 mSv for the coverage of 14 cm on the GE CT scanner (sufficient to cover the heart). In comparison, the low dose lung screening CT has a higher effective dose of 1.4 mSv [24]. The scan time of the cine CT for average CT is less than 1 min. Processing for average CT can be automated. Once the cine CT scan is completed after a cardiac stress perfusion PET scan, the technologist enters the scanner room to unload the patient from the imaging table. By the time, the technologist is back to the scanner console in a couple of minutes, the task of computation for average CT is already finished, which will not impact the overall scan time of a PET/CT procedure [25].

In a whole-body PET/CT scan, the CT images are typically acquired before PET. The technologist can determine if a cine or average CT scan is needed for attenuation correction of the PET images in the thorax or the abdomen before completion of the PET scan. Therefore, only the patient data with mis-registration may need average CT for an improvement of alignment and attenuation correction. The coverage of 14 cm can be further reduced for the consideration of radiation dose if the target tumor area is small.

There was an approach of interpolated average CT to reduce radiation dose of average CT by only acquiring the end-inspiration and end-expiration phases and interpolating the between phases from the two acquired phases. This interpolated average CT approach requires gating, patient coaching and deformable image registration. Its application can be limited due to the

additional requirements even though it may save some radiation dose [26].

14.9 Benefits of Average CT for Radiation Therapy

Radiation therapy has embraced the use of average CT for radiation treatment dose calculation in conventional radiation therapy [27] and proton beam therapy [28] when simulation CT may be impacted by respiratory motion altering the treatment dose calculation. Average CT has also been shown to be the CT images for alignment with the cone beam CT images before radiation treatment in image-guided radiation therapy [29]. Average CT can be generated from the cine CT scan by averaging the cine CT images without a respiratory gating device [15, 30, 31], which means that it can be derived on all GE PET/CT scanners for attenuation correction of the PET data, dose calculation for radiation therapy with photon and proton in particular, and alignment with cone beam CT for image-guided radiation therapy.

From the same scan data for average CT, the maximum-intensity-projection (MIP) CT images can be derived by computation for the maximum pixel value at each pixel location from all the images of cine CT or 4D-CT [22, 30]. It has been shown that MIP CT images are effective in depicting the extent of tumor motion [32, 33]. For peripheral lung tumors (surrounded by the lower density air in the lungs), MIP CT images

can be used to assist the delineation of tumor target volume and to avoid ambiguity of thresholding the biological target volume with SUV in PET. Any ^{18}F-FDG uptake in the lungs should be supported by the soft tissues depicted in the MIP images. Any PET gross tumor volume (GTV) determined by an SUV threshold should not exceed the soft-tissue boundary in the MIP images. Their application for treatment planning for stereotactic body radiation therapy has been demonstrated [34]. The MIP CT images can help determine the tumor volume in the thorax. Figure 14.11 shows an example of determining the extent of PET GTV with MIP CT to avoid the uncertainty of thresholding a functional tumor with SUV. A similar concept has been attempted with the regular helical CT data for peripheral non-small cell lung cancer (NSCLC) by Biehl et al. [35], in which the boarder of the tumor is identified by the CT data.

Figure 14.12 shows an example of mis-registration that caused a false-negative diagnosis and a change of the gross target volume for radiation therapy when the mis-registration was removed with average CT. In the era of image-guided radiation therapy to deliver a high dose of radiation at a great precision, it is very important to pay attention to any mis-registration between the CT and PET images in tumor delineation when PET/CT images are used in the treatment planning. The most ideal approach is to conduct PET/CT and 4D-CT in the same simulation session. However, insurance providers may only pay for one PET/CT before cancer treatment, and

Fig. 14.11 The fusion of (left to right) axial, sagittal, and coronal MIP CT and PET images of a patient. The tumor contour from the MIP CT is superimposed on the PET image with a contour of 40% SUV_{max} to demonstrate that the size of the functional tumor should not exceed the maximum supporting tissues in the MIP CT
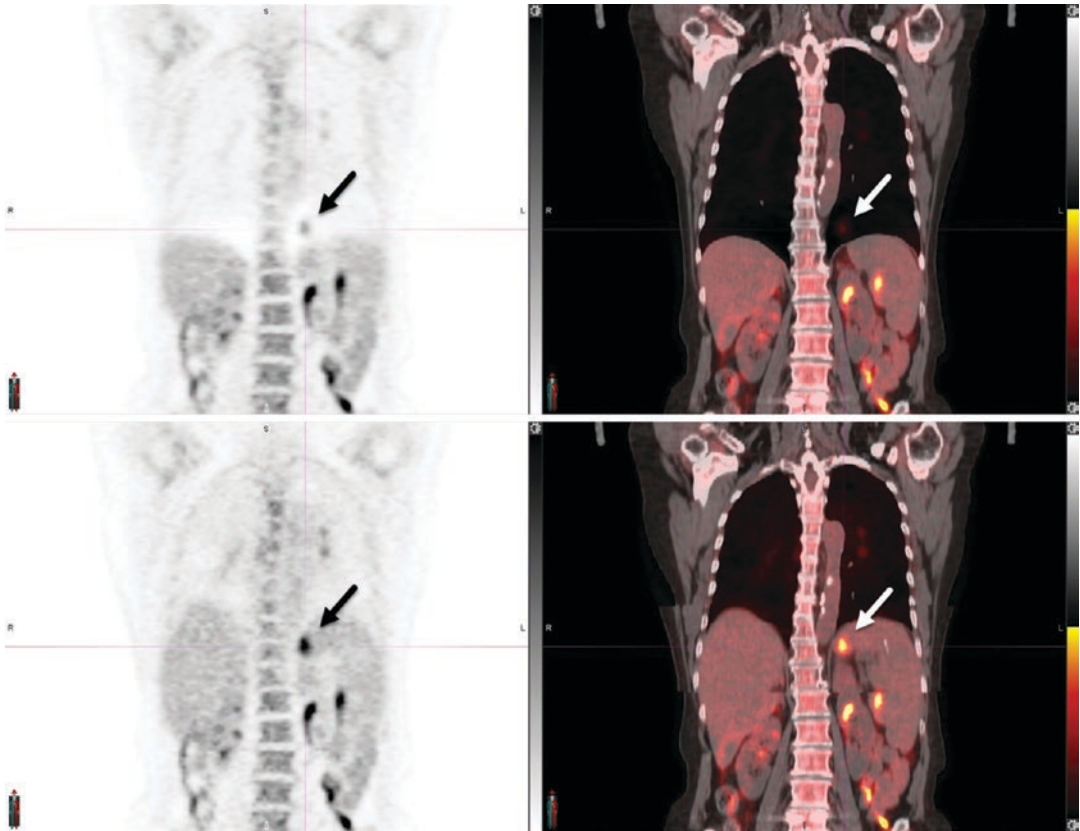
Fig. 14.12 The PET/CT images of a 69-year-old female patient with an esophageal tumor after induction chemotherapy. The top panel shows a coronal slice of the PET (left) and fused CT and PET (right). The initial report indicated the patient had a positive response to the chemotherapy. After removal of misalignment by average CT, the tumor reappeared in the PET and fused CT and PET in the bottom panel. The arrows point to the tumor location

this issue has resulted in a decline of interest in the application of PET/CT for radiation therapy simulation.

14.10 Summary

CT is an integral part of the hybrid imaging of SPECT/CT and PET/CT. It provides the important functions of lesion localization and attenuation correction. As the sensitivity of PET imaging improves over the years, the procedure requires less contrast agent and renders a shorter scan time, the proper use of CT becomes more important from the radiation exposure standpoint. It is imperative to use TCM technology to reduce the radiation exposure to the patient. It is also important to know the orientation of the survey scan to avoid unintended radiation exposure to the patient. It is very effective to use CT for detection of calcified plaque in the coronary arteries to help diagnosis with myocardial perfusion imaging of SPECT or PET. Average CT can help registration of the CT and PET data and does not have the disadvantage of long scan time as the transmission rod sources do. It is only acquired in the region of mis-registration between the CT and PET data. Average CT can also be used for radiation therapy treatment dose calculation and image-guided radiation therapy alignment with cone beam CT. The same CT image data for average CT can also be used for derivation of the MIP CT data for tumor delineation and can help guide delineation of a functional tumor. It is advisable to use average CT in PET/CT and radiation therapy.

References

1. Lang TF, et al. Description of a prototype emission-transmission computed tomography imaging system. J Nucl Med. 1992;33(10):1881–7.

2. Beyer T, et al. A combined PET/CT scanner for clinical oncology. J Nucl Med. 2000;41(8):1369–79.

3. Kinahan PE, et al. Attenuation correction for a combined 3D PET/CT scanner. Med Phys. 1998;25(10):2046–53.

4. Townsend DW, Beyer T. A combined PET/CT scanner: the path to true image fusion. Br J Radiol. 2002;75 Spec No:S24–30.

5. Seo Y, Mari C, Hasegawa BH. Technological development and advances in single-photon emission computed tomography/computed tomography. Semin Nucl Med. 2008;38(3):177–98.

6. Sawyer LJ, et al. Effective doses to patients from CT acquisitions on the GE Infinia Hawkeye: a comparison of calculation methods. Nucl Med Commun. 2008;29(2):144–9.

7. Dvorak RA, Brown RK, Corbett JR. Interpretation of SPECT/CT myocardial perfusion images: common artifacts and quality control techniques. Radiographics. 2011;31(7):2041–57.

8. Matesan M, et al. SPECT/CT bone scintigraphy to evaluate low back pain in young athletes: common and uncommon etiologies. J Orthop Surg Res. 2016;11(1):76.

9. Van den Wyngaert T, et al. The EANM practice guidelines for bone scintigraphy. Eur J Nucl Med Mol Imaging. 2016;43(9):1723–38.

10. Rumberger JA, Kaufman L. A Rosetta stone for coronary calcium risk stratification: agatston, volume, and mass scores in 11,490 individuals. AJR Am J Roentgenol. 2003;181(3):743–8.

11. Neves PO, Andrade J, Moncao H. Coronary artery calcium score: current status. Radiol Bras. 2017;50(3):182–9.

12. Osman MM, et al. Clinically significant inaccurate localization of lesions with PET/CT: frequency in 300 patients. J Nucl Med. 2003;44(2):240–3.

13. Gould KL, et al. Frequent diagnostic errors in cardiac PET/CT due to misregistration of CT attenuation and emission PET images: a definitive analysis of causes, consequences, and corrections. J Nucl Med. 2007;48(7):1112–21.

14. Pan T, et al. Attenuation correction of PET images with respiration-averaged CT images in PET/CT. J Nucl Med. 2005;46(9):1481–7.

15. Chi P-CM, et al. Effects of respiration-averaged computed tomography on positron emission tomography/computed tomography quantification and its potential impact on gross tumor volume delineation. Int J Radiat Oncol Biol Phys. 2008;71(3):890–9.

16. Carson RE, Daube-Witherspoon ME, Green MV. A method for postinjection PET transmission measurements with a rotating source. J Nucl Med. 1988;29(9):1558–67.

17. Pan T, et al. Attenuation correction of PET cardiac data with low-dose average CT in PET/CT. Med Phys. 2006;33(10):3931–8.

18. Cook RA, et al. Respiration-averaged CT for attenuation correction in canine cardiac PET/CT. J Nucl Med. 2007;48(5):811–8.

19. Alessio AM, et al. Cine CT for attenuation correction in cardiac PET/CT. J Nucl Med. 2007;48(5):794–801.

20. Keall PJ, et al. The management of respiratory motion in radiation oncology report of AAPM Task Group 76. Med Phys. 2006;33(10):3874–900.

21. Low DA, et al. A method for the reconstruction of four-dimensional synchronized CT scans acquired during free breathing. Med Phys. 2003;30(6):1254–63.

22. Pan T, et al. 4D-CT imaging of a volume influenced by respiratory motion on multi-slice CT. Med Phys. 2004;31(2):333–40.

23. Keall PJ, et al. Acquiring 4D thoracic CT scans using a multislice helical method. Phys Med Biol. 2004;49(10):2053–67.

24. Larke FJ, et al. Estimated radiation dose associated with low-dose chest CT of average-size participants in the National Lung Screening Trial. AJR Am J Roentgenol. 2011;197(5):1165–9.

25. Gould KL, et al. Reducing radiation dose in rest-stress cardiac PET/CT by single poststress cine CT for attenuation correction: quantitative validation. J Nucl Med. 2008;49(5):738–45.

26. Mok GSP, et al. Interpolated average CT for cardiac PET/CT attenuation correction. J Nucl Cardiol. 2016;23(5):1072–9.

27. Riegel AC, et al. Dose calculation with respiration-averaged CT processed from cine CT without a respiratory surrogate. Med Phys. 2008;35(12):5738–47.

28. Cai J, et al. Estimation of error in maximal intensity projection-based internal target volume of lung tumors: a simulation and comparison study using dynamic magnetic resonance imaging. Int J Radiat Oncol Biol Phys. 2007;69(3):895–902.

29. Shirai K, et al. Phantom and clinical study of differences in cone beam computed tomographic registration when aligned to maximum and average intensity projection. Int J Radiat Oncol Biol Phys. 2014;88(1):189–94.

30. Pan T, Sun X, Luo D. Improvement of the cine-CT based 4D-CT imaging. Med Phys. 2007;34(11):4499–503.

31. Riegel AC, et al. Cine computed tomography without respiratory surrogate in planning stereotactic radiotherapy for non-small-cell lung cancer. Int J Radiat Oncol Biol Phys. 2009;73(2):433–41.

32. Underberg RW, et al. Use of maximum intensity projections (MIP) for target volume generation in 4DCT scans for lung cancer. Int J Radiat Oncol Biol Phys. 2005;63(1):253–60.

33. Bradley JD, et al. Comparison of helical, maximum intensity projection (MIP), and averaged intensity

(AI) 4D CT imaging for stereotactic body radiation therapy (SBRT) planning in lung cancer. Radiother Oncol. 2006;81(3):264–8.

34. Riegel AC, et al. Cine CT without a respiratory surrogate in planning of stereotactic radiotherapy for non-small cell lung cancer. Int J Radiat Oncol Biol Phys. 2009;73(2):433–41.

35. Biehl KJ, et al. 18F-FDG PET definition of gross tumor volume for radiotherapy of non-small cell lung cancer: is a single standardized uptake value threshold approach appropriate? J Nucl Med. 2006;47(11): 1808–12.

Part V

Image Reconstruction, Processing and Computation

Fundamentals of Image Processing in Nuclear Medicine

15

C. David Cooke, Tracy L. Faber, and James R. Galt

Contents

Learning Objectives

The purpose of this chapter is to introduce the reader to the fundamentals of image processing in Nuclear Medicine. It is not meant as a comprehensive guide, but more as an overview and introduction to those topics important to understanding the various forms of image processing.

At the conclusion of this chapter, it is hoped that the reader will be able to:

1. Briefly describe the history of imaging in Nuclear Medicine.
2. Briefly describe the components and processes necessary for generating an image.
3. Briefly describe spatial resolution and how to calculate it.
4. Briefly describe image interpolation.
5. Briefly describe how images are converted to color and displayed.

C. D. Cooke (✉) · T. L. Faber (Deceased) · J. R. Galt
Emory University School of Medicine,
Atlanta, GA, USA
e-mail: ccooke@emory.edu; jgalt@emory.edu

6. Briefly describe image filtering and its effect on images, as well as having a working knowledge of the two most common filters in Nuclear Medicine.
7. Briefly describe the Fourier Transform and its use in Nuclear Medicine.
8. Briefly describe the process of analyzing regions of interest.
9. Briefly describe different ways of segmenting images to extract useful information.
10. Briefly describe different ways of generating and displaying three-dimensional images.
11. Briefly describe the principles of image registration.
12. Briefly describe the importance of image normalization.

15.1 Introduction

Most Nuclear Medicine procedures are, by their very nature, image-oriented. As early as 1950, printed images of the Thyroid, using I-131, could be obtained using the rectilinear scanner developed by Benedict Cassen [1] (see Fig. 15.1). In 1958, the Anger scintillation camera [2], developed by Hal Anger, could be used to image an entire organ at one time; and by 1963, Kuhl and Edwards were using the Anger camera to produce tomographic images [3]. It has been over 60 years since Hal Anger's initial developments, and the traditional gamma camera remains largely unchanged, though most now have better electronics resulting in increased sensitivity, spatial resolution, energy resolution, and stability. Recently, cameras have been developed that replace the original Anger electronics and detectors with solid state detectors; however, the image processing techniques presented in this chapter remain much the same. Space will not permit for a detailed history of the gamma camera; however, those who are interested might enjoy the article by Ronald Jaszczak [4].

Today, Nuclear Medicine images are acquired and stored on computers, making the data easily accessible and readily available for further processing and quantification. The goal of this chapter is to familiarize the reader with the basic fundamental techniques of image processing, and specifically, those techniques most useful in Nuclear Medicine.

15.2 Image Presentation

15.2.1 Analog and Digital Images

The scintillation camera was first developed by Hal Anger of the University of California at Berkley in the late 1950s and early 1960s [5] long before computers were in common use and even longer before computer displays that could adequately display a diagnostic image were invented. A major component of these early cameras was circuitry that could convert the output of the photomultiplier array into three voltages representing the x and y locations and the energy (z, the brightness of a scintillation is proportional to the incident photon's energy) of the scintillation photon. If the z voltage matched the voltages calibrated to define the energy window, the x and y locations were sent to an oscilloscope and a momentary flash would appear at a corresponding point on the screen. By placing a focusing lens between the oscilloscope screen and a piece of X-ray film the film was exposed one flash of light (corresponding to one scintillation event) at a time. This type of image is called an analog image because the x and y locations of the oscilloscope flashes that exposed the film are continuous; they can occur anywhere on the screen. Very nice images could be created with these systems but they also had some drawbacks. Like all film based systems, they were subject to under and over exposure if the technologist cut the exposure time too short or let it go too long. If the clinician wanted to monitor the activity over time, several pieces of film had to be exposed or a system for making several images on one piece of film had to be used.

The progress of computers over the years brought about the development of digital scintillation cameras where a computer is an integral part of the system that processes a scintillation event. Digital cameras provide images in the form of a computer matrix, or a digital image. Each cell of
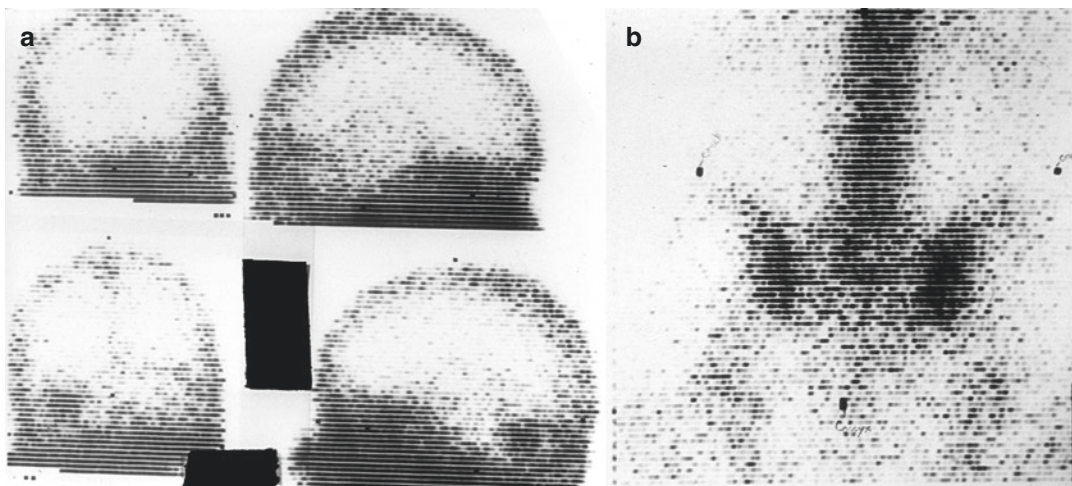
Fig. 15.1 Early rectilinear scans. (**a**) Brain perfusion scan (note defect in bottom left and bottom right images). (**b**) Bone scan (three markers can be seen delineating the left and right Iliac crests and the coccyx). (Images courtesy of Naomi Alazraki, MD, Emory University and VA Medical Center, Atlanta, GA)

this computer matrix is called a picture element, or pixel, and represents the counts collected at a corresponding point on the camera face. The values of the pixels are often called pixel counts because they represent the count of the number of scintillation events detected. The great benefit of a digital image is that it is available for computer processing and display. The exposure time is not a problem because the brightness of the image can be controlled when it is displayed. The pixel counts are also available for computerized analysis instead of being limited to the strictly visual interpretation common with analog images.

The image, or scintigram, is built over time by calculating the *x* and *y* location of each scintillation event and, if the energy is determined to be within the desired energy window, incrementing the corresponding pixel. If this is done in real time, the acquisition is said to be in frame mode. If, instead, a list of events and locations is kept it is said to be in list mode. An image is produced from a list mode acquisition after the acquisition is completed. List mode acquisition requires significantly more memory and disk space than frame mode because all scintillation events (regardless of energy) are recorded and more information is kept per event. Regardless of how the image is formed it still needs to be displayed. Scintigram formation is illustrated in

Fig. 15.2 and scintigram display is illustrated in Fig. 15.3.

Images are displayed by coding the pixel values to the brightness, or color, of the pixels in the image displays. Usually scintigrams are displayed in a grayscale format where black is equal to zero counts and white is equal to the brightest pixel in the image. At times this is inadequate to capture the dynamic range of an image. It is possible to rescale the image so that a pixel count well below the image maximum but better matching the area of clinical interest is scaled to white. An example of this would be a bone scan that includes the bladder as shown in Fig. 15.4.

Another benefit of digital imaging in nuclear medicine is the ability to acquire images in different formats (Fig. 15.5). Static scintigrams are formed when the scintillation camera acquires a single image from a single location. Dynamic scintigrams are a sequence of static images acquired by defining phases where each image is acquired for a specific period of time. Gated scintigrams of the heart (often called multigated or MUGA scans but officially known as equilibrium radionuclide angiography or ERNA) are formed as a sequence of static images that each represent a segment of the heart's EKG R-to-R interval. These images are built up over many heart beats. Whole body images are made by using the scin-

a

b

| Time | 00:00:01 | 00:00:04 | 00:00:07… |
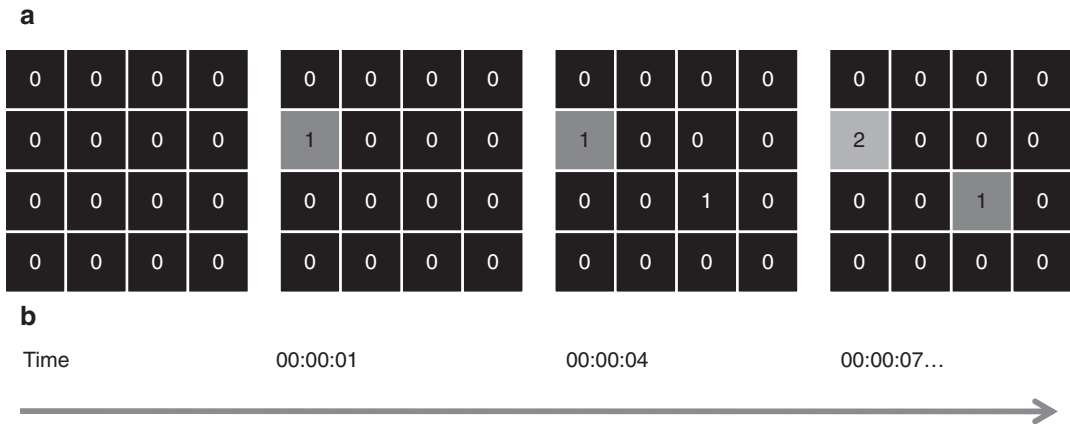
Time	X	Y	Energy
00:00:01	1.1	3.4	136
00:00:02	3.8	3.4	100
00:00:04	3.5	2.2	145
00:00:07	1.4	3.1	142
…			

Fig. 15.2 (**a**) In frame mode acquisition each pixel in the image is incremented as scintillations are counted at a particular point on the camera face. This panel shows how pixels are incremented as photons with the desired energy are detected and localized by the camera. (**b**) In list mode the same scintillation events are placed into a list and the image is formed from the list after acquisition. Note that if this is a ^{99m}Tc image the second entry may be excluded from the image because of its energy

tillation camera to scan the patient from head to foot (or vice versa) and building an image that appears to be one long image made with a very large camera.

Tomograms represent slices through the body and are reconstructed from projection data. SPECT images are traditionally made by acquiring static images in an arc around the patient of at least 180° and reconstructing tomograms from these projections. While it is possible to construct projections from a PET acquisition, such a display has little value and is not needed for reconstruction.

15.2.2 Image Math

At times it may be desirable to perform basic mathematical functions on scintigrams and tomograms. Since these images are made up of pixels and those pixels define a pixel count at a specific location in space it is possible to add, subtract, multiply, or divide images by a constant or to perform the operation between two images. Addition of images may be used to reduce the number of images in a dynamic image set by summing frames within a phase, a process known as reframing. This is used in

Scintigram

Individual Pixels

Pixel Counts

99	80	40	10	0	1	0	0
70	90	44	20	7	0	0	0
50	80	90	90	20	5	1	0
45	60	70	95	90	20	2	0
35	52	65	80	92	25	0	0
30	41	53	65	93	64	10	0
32	45	55	64	92	67	11	0
33	47	67	85	91	59	9	0
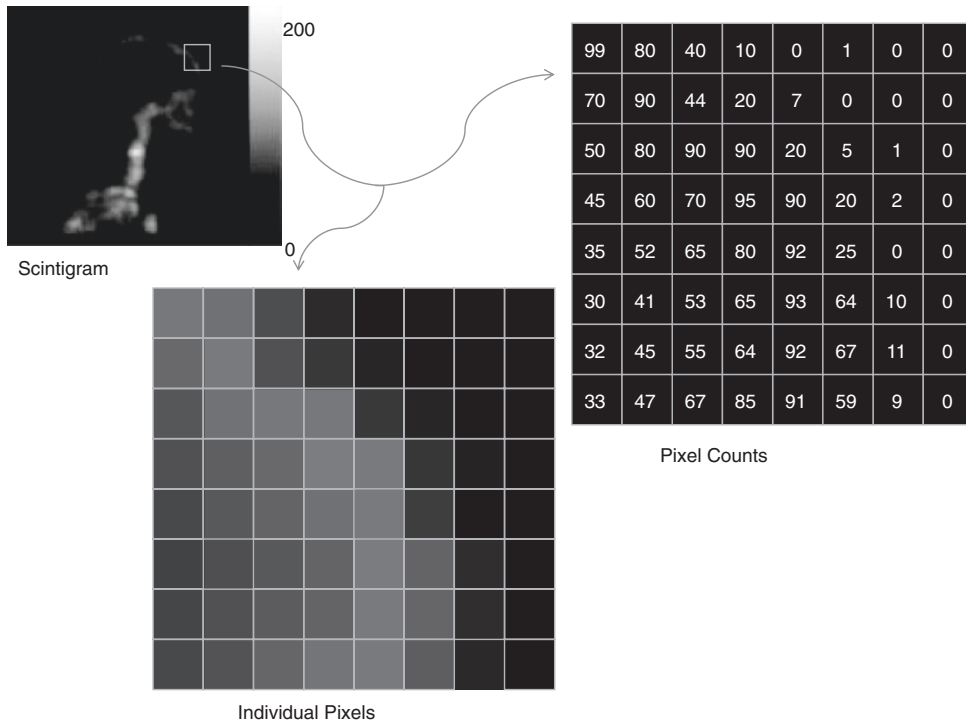
Fig. 15.3 A scintigram is a matrix or array of individual pixels where each pixel has a numeric value related to the number of scintillation events detected in that location. The image is displayed by coding the brightness, or color, of each pixel of the display to the pixel counts
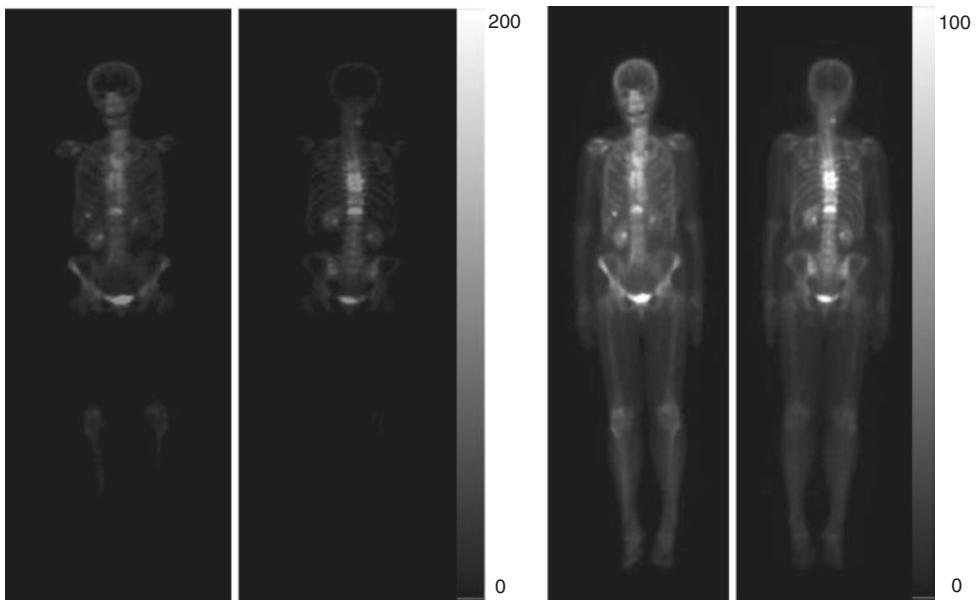
Fig. 15.4 Some scintigrams, such as the bone scan shown here may contain areas of dynamic range well outside of the range of pixel counts in the area of clinical interest. This may be due to high organ uptake in an different organ or, as is the case here, the extraction and excretion of the tracer into the bladder. If the image is displayed scaled from zero to the image maximum, the organ of clinical interest (for example, the bones in the left-hand panel) may have too little contrast to be read. By reducing the maximum pixel of the display it is possible to increase the displayed contrast in the area of clinical interest as shown by the right-hand panel. The process of adjusting the displayed brightness and range to suit the scintigram is called windowing
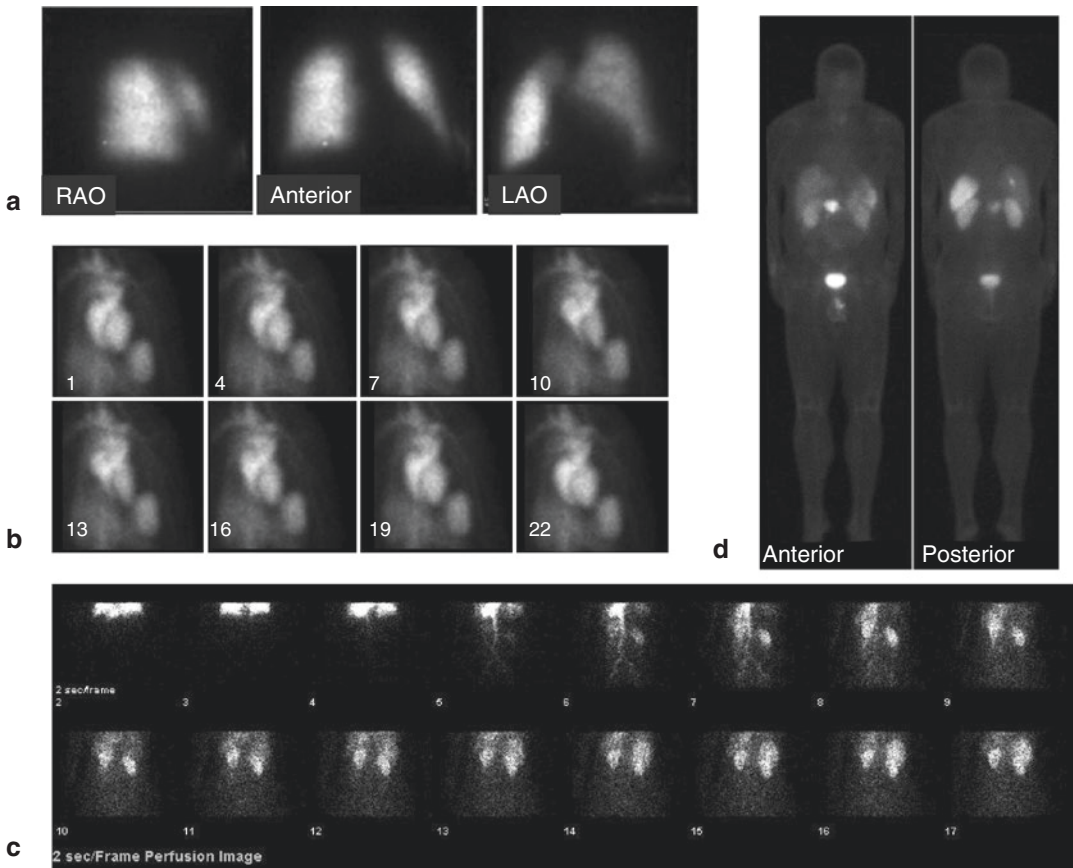
Fig. 15.5 Planar scintigrams may be acquired in different formats. (**a**) Static scintigrams are formed when the scintillation camera acquires a single image from a single location. The technologist manually moves and positions the camera at each desired position. Three views were taken in the 99mTc MAA perfusion lung scan shown here. (**b**) Gated scintigrams of the heart are acquired over several minutes and show the beating of the heart over an "average" cycle. Each frame of the image represents one segment of the hearts R to R interval. In this example, 8 of the 24 frames that were acquired are shown. The sequence shows the cardiac blood pool starting at diastole, proceeding and to systole, and ending back at diastole. (**c**) Dynamic scintigrams allow the clinician to follow a process over time. The example shows the uptake phase of a 99mTc renogram. Beginning immediately after injection, each of the images in the sequence represents 2 s. The progress of the tracer can be followed as it appears in the blood stream and begins to appear in the kidneys. (**d**) Whole body scans are acquired by scanning the length of a patient's body with a large field-of-view scintillation camera. An image is formed that appears to have been made with a single very large scintillation camera. This example shows the uptake of **111**In OctreoScan in a patient with an islet cell tumor in the pancreas and metastasis in the liver. (The authors would like to acknowledge Raghuveer K. Halkar, MD, Emory University, Atlanta, GA, for his assistance with this figure)

renal imaging, for example, to reduce the number and improve the displayed quality of the frames of the dynamic image, where the original images appear to be very noisy on display but are preferable for extraction of the renogram curves. Subtraction of two images may be used to highlight the difference between two images as in 99mTc sestamibi—123I subtraction scintigraphy for hyperparathyroidism where subtraction of the 123I scintigram removes the thyroid gland from the images, making it easier to locate abnormal parathyroid tissue [6] (Fig. 15.6). Prior to subtraction the two images must be carefully normalized so that the thyroid glands have the same pixel count values in both scintigrams. This is done by determining a constant
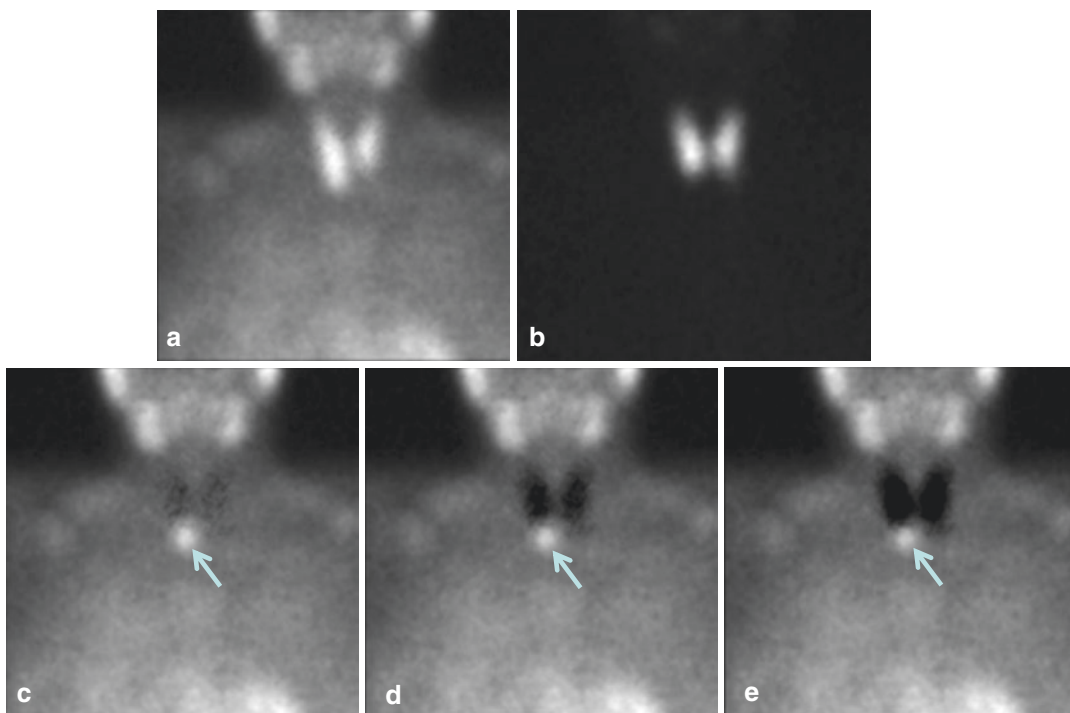
Fig. 15.6 ^{99m}Tc sestamibi–^{123}I scintigraphy illustrates how one image may be subtracted from the other. While ^{99m}Tc sestamibi (**a**) localizes in both thyroid and parathyroid tissue, ^{123}I (**b**) only localizes in the thyroid tissue. The ^{123}I scintigram is normalized to have the same counts over the thyroid gland as the ^{99m}Tc sestamibi scintigram and subtracted from that image resulting in subtraction scintigram (**c**, **d**, **e**), making abnormal parathyroid tissue more conspicuous (arrow). In the subtrac-tion scintigram labeled (**c**), the ^{123}I scintigram, which has many times fewer counts in the thyroid than the ^{99m}Tc sestamibi scintigram, has been normalized to match the pixel count level of the ^{99m}Tc sestamibi image. In (**d**, **e**) it has been normalized to have progressively more counts. (The authors would like to acknowledge Raghuveer K. Halkar, MD, Emory University, Atlanta, GA, for his assistance with this figure)

that is multiplied by each pixel in the ^{123}I scintigram to give the same pixel counts (on average) as in the ^{99m}Tc sestamibi scintigram. Thus when the images are subtracted only the areas that represent different activity levels are left.

15.2.3 Matrix Size and Spatial Resolution

Digital images are, as the name implies, discrete representations of the objects that were imaged. This discrete nature can be quantified in terms of Matrix Size and Spatial Resolution. The spatial resolution can actually be broken down into two separate categories: (1) the inherent resolution of the actual imaging device (both with and with-out a collimator) and (2) the resolution or size of each individual pixel in the image.

15.2.3.1 Matrix Size

Before we delve into calculating Spatial Resolution, we need to briefly cover image matrices. As mentioned above, an image is made up of a collection of discrete picture elements or pixels. These images (collections of pixels) are most often arranged in a square grid or pattern whose size is given as the number of pixels across the face of the image (columns) by the number of pixels down the face of the image (rows); this is also referred to as the images matrix size. For instance, an image that has 64 rows by 64 columns (4096 total pixels), would be said to have a matrix size of 64×64 pixels. Knowing the matrix

size of an image is important when calculating the spatial resolution of an imaging system.

15.2.3.2 Spatial Resolution

The spatial resolution of an imaging system can be measured with (extrinsic) and/or without (intrinsic) a collimator, by placing a point source on the face of the camera and acquiring an image. The spatial resolution is then calculated by extracting the counts and location of a row of pixels (called a profile) in this image that go through the point source and measuring the width of the point source profile at half the height of the point source profile (see Fig. 15.7). This number is called the Full Width at Half Maximum (FWHM) and is a direct measure of the spatial resolution of the imaging system. As an example, Fig. 15.7 shows a profile drawn through a point source whose maximum count is 2908. At half this height (1454) the width of the profile is 3.5

pixels, so the spatial resolution of this imaging device is 3.5 pixels. To convert this to mm, we need to know the matrix size of the image, and the field-of-view of the camera. For this example, the point source was acquired on a camera with a field-of-view of 532 mm, and the acquired image has a matrix size of 256 × 256 pixels. Putting all of this together, the resultant spatial resolution is:

$$\text{Spatial Resolution} = 3.5\,\text{pixels} \times \left(532\,\text{mm}/256\,\text{pixels}\right)$$
$$= 7.27\,\text{mm}$$

The second part of the above equation (532 mm/256 pixels), is the answer to the second category of the resolution question, the resolution or size of each individual pixel in an image. In the above case, each pixel in this image is 2.08 mm, and is specific for this camera size and this image matrix size. If we had acquired the image in a 128 × 128 pixel matrix, instead of a 256 × 256 pixel matrix then the pixel size would have been
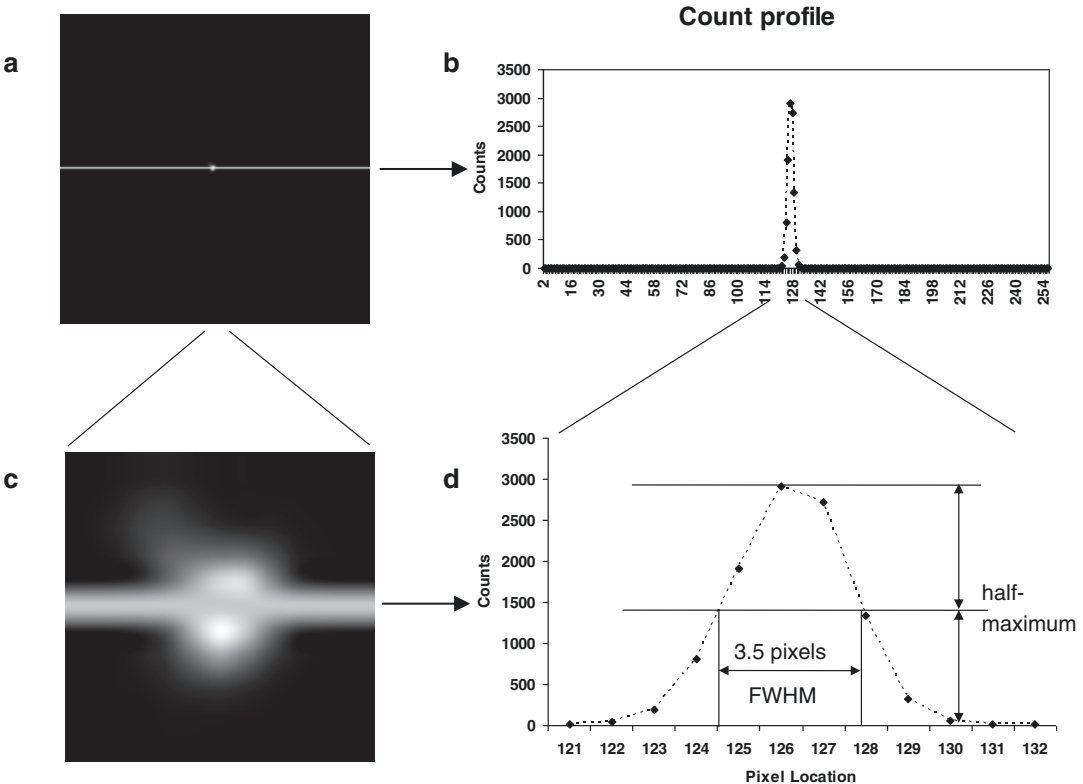
Fig. 15.7 Measuring the FWHM. (**a**) Original point source acquired in a 256 × 256 matrix, (**b**) plot of counts vs. pixel location for the original image, (**c**) 12 × 12 pixel zoom of original point source image, and (**d**) plot of counts vs. pixel location for the 12 center pixels showing how the FWHM is calculated

4.16 mm (532 mm/128 pixels). Likewise, if we had used a different camera, with a different field-of-view, this would have also affected the pixel size.

Before we leave this topic, let's explore, briefly, why the FWHM is a measure of the resolution of the imaging system. Another way to refer to the resolution of the imaging system would be to indicate its "resolving" power, or its ability to resolve two different point sources. In other words, how close can two point sources be and the system can still be able to distinguish the two point sources. If you look at Fig. 15.8, you will see an example of two point sources spaced generously apart (10 pixels, panel a). As the point sources are moved closer together, the counts begin to overlap (5 pixels, panel b). At the point where half of each profile overlaps each other, we can no longer resolve the two different point sources; for all practical purposes, it looks like one big point source (3 pixels, panel c). You will notice that this happens when the two point sources are spaced exactly 1 FWHM apart (FWHM = 3.5 pixels for this par-

ticular camera), which is why this number is often used as the resolution of the imaging system (the point at which two point sources can no longer be resolved) [7, 8].

15.3   Image Interpolation

Another aspect of images and matrix size is changing the size of the image; for instance, you might want to make an image smaller or larger for display purposes. This is usually accomplished by interpolating the original image pixels and making them smaller or larger; in most instances we are generally interested in making the images larger. As an example, if you were to display a 64×64 pixel image on a typical 19″ computer screen whose resolution is 1280×1024, the image would only take up 1/320th of the screen and would measure approximately 3/4 in. square. To make the image easier to see we could zoom or interpolate the image to a larger matrix size, say 256×256, which would result in an image
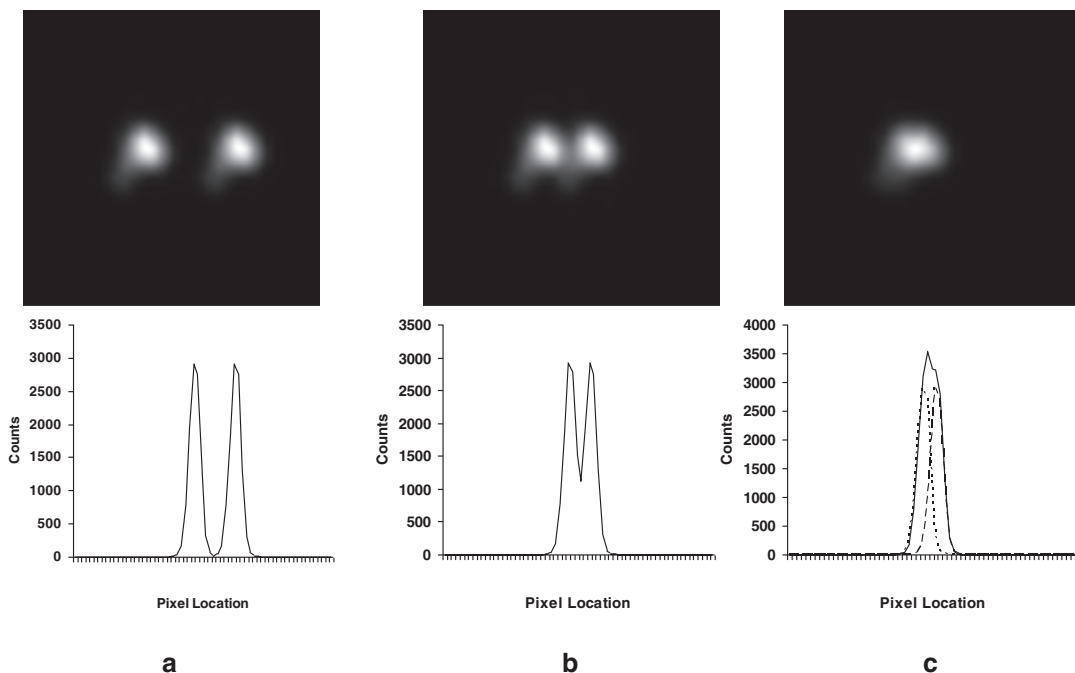
Fig. 15.8 Explanation of FWHM as resolution or resolving power. (**a**) Two point sources spaced 10 pixels apart. (**b**) Same two point sources spaced five pixels apart. (**c**) Same two point sources spaced three pixels apart, the original profiles of the two separate point sources are seen as dashed lines

size 1/20th of the screen or approximately 3 in. square. There are many ways to interpolate an image; we will take a look at three of the more popular methods: Nearest Neighbor (or Pixel Replication), Bilinear Interpolation and Bicubic Interpolation. An important point to remember is that regardless of the interpolation method used, you can never add more detail or information to an image than what was there to begin with.

15.3.1 Nearest Neighbor

Nearest neighbor interpolation is the process of copying pixels to make an image larger, and is only useful when your final image size is an integer multiple of the original image size. In our previous example, we could have used the nearest neighbor method to interpolate our 64×64 image into a 256×256 image by replicating each original image pixel 4 times in the new image. Let's illustrate this with a much simpler example. Suppose we have a 2×2 image that we want to interpolate to a 4×4 image (effectively doubling its size). Figure 15.9a shows our original 2×2 image with 4 pixels whose values range from 3 to 13, and Fig. 15.9b shows our resultant 4×4 image with the nearest neighbor interpolation. The advantage of this technique is that it can be done very quickly on any computer and all of the original image data is preserved; however, the results are not always visually pleasing (typi-
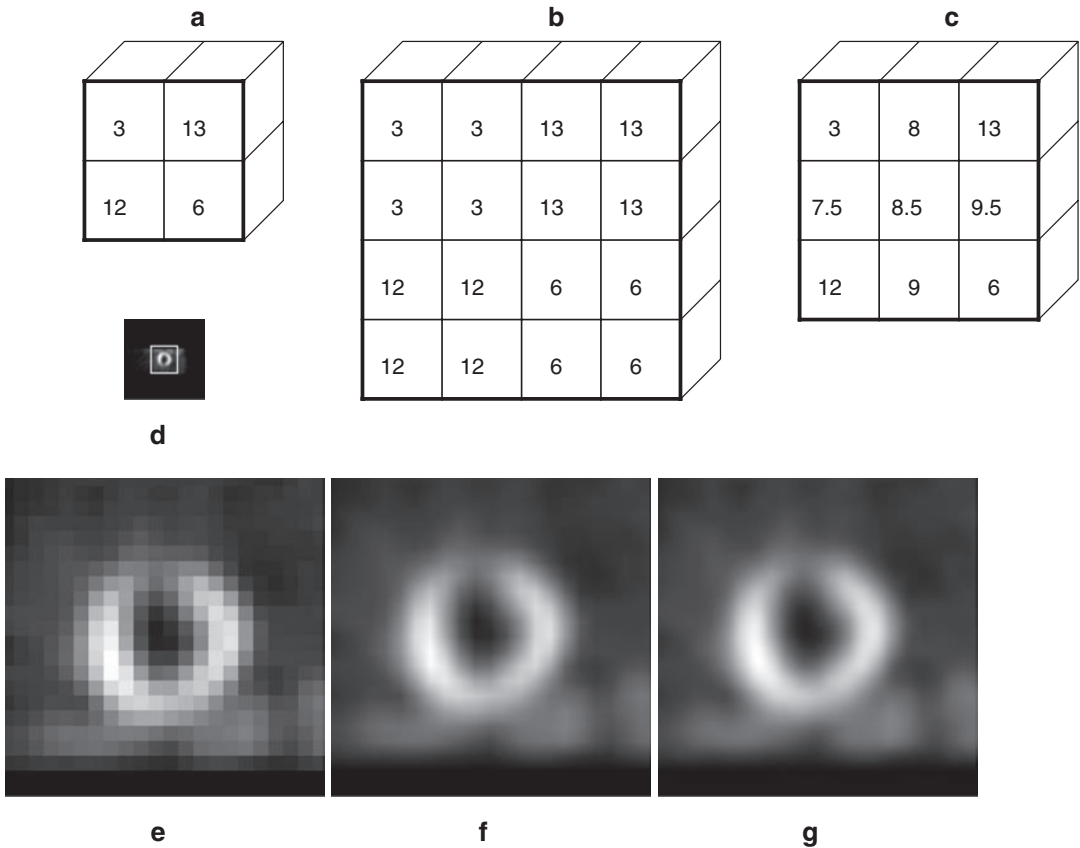
Fig. 15.9 Example of image interpolation. (**a**) Original 2×2 image with 4 pixels, (**b**) nearest neighbor interpolation to 4×4 image, (**c**) bilinear interpolation to 3×3 image, (**d**) original 64×64 central short-axis slice from a SPECT myocardial perfusion scan, (**e**) nearest neighbor interpolation of central 21×21 pixels of original image (shown as white box in **d**) to 256×256, (**f**) bilinear interpolation of same area as (**e**), and (**f**) bicubic interpolation of same area as (**e**)

cally the resultant images will look blocky). The main disadvantage of this technique is that you can only interpolate images by integer multiples of the original image size. Figure 15.9d shows a central 64 × 64 pixel short-axis slice from a myocardial perfusion scan, with a white box around the central 21 × 21 pixels. Figure 15.9e shows a nearest neighbor interpolation of this central 21 × 21 pixel region zoomed to a 252 × 252 pixel region (12× the original size), notice how blocky the resultant image is.

15.3.2 Bilinear Interpolation

Bilinear interpolation fills in the missing pixels by linearly interpolating between the 4 neighboring pixels (the closest 2 × 2 neighborhood). As an example, we can use linear interpolation to zoom the original 2 × 2 pixel image shown in Fig. 15.9a to a 3 × 3 pixel image. Using bilinear interpolation (linear interpolation applied separately in the *x* and then the *y* directions), the resultant image is shown in Fig. 15.9c. Notice how each edge pixel value is half-way between the pixel values on either side (both in the *x* and *y* directions—this is a special case for the pixels on the edge of the image), and the very center pixel (8.5) is the average of the 4 corner or neighbor pixels ((3 + 13 + 12 + 6)/4 = 8.5). The main advantage of this method over the nearest neighbor method is that the resultant image does not need to be an integer multiple of the original image and it produces an image that is more visually pleasing (not as blocky); however, it does take more computing power. Figure 15.9f shows a bilinear interpolation of the same central 21 × 21 pixel region zoomed to a 252 × 252 pixel region. Note that this image still contains some slight blockiness.

15.3.3 Bicubic Interpolation

Bicubic interpolation improves upon bilinear interpolation by considering the nearest 4 × 4 neighborhood of pixels (instead of the nearest 2 × 2 neighborhood) and uses a weighted average of these 16 pixels to calculate the value of

the new pixel. In this technique, closer pixels are weighted higher than further pixels and the result is a sharper image then can be achieved with bilinear interpolation. The disadvantage is that it takes even more computing power to calculate. Figure 15.9g shows a bicubic interpolation of the same central 21 × 21 pixel region zoomed to a 252 × 252 pixel region. Note how smooth this interpolation is (there is no apparent blockiness).

15.4   Image Display and Lookup Tables

15.4.1 Pseudocolor Displays

In medical imaging, images are usually displayed by assigning a color to each pixel value consisting of red, green, and blue (R, G, and B) intensities. This type of display is called a pseudocolor display. The mapping from pixel value to color is called a lookup table (LUT) or video lookup table (VLT). The number of entries in the lookup table; that is, its length, determines the number of colors that can be displayed, and while historically this has been limited to 256, in theory it may be much larger. In fact, the number of entries in the lookup table should be equal to the maximum value in the image, so that entries exist for every possible pixel value. However, it is always possible to scale the image prior to display, so that the lookup table size is more a matter of hardware considerations.

The depth of the lookup table is split into three portions, one each for the red, green, and blue values of the color to be assigned. In most cases, each of these portions is one byte, so the total depth of the lookup table is three bytes. Again, this is more a consideration of the hardware and software used for display and may not be user selectable. Note, however, that the size of the R, G, and B entries determines the range of possible values for those colors. That is, if each entry is one byte long, then only the values of 0–255 can be used. Note that this allows 2^{24} possible colors to be placed in the lookup table (256^3); however, as noted above, the number that can be placed there at one time is a function of the length of the
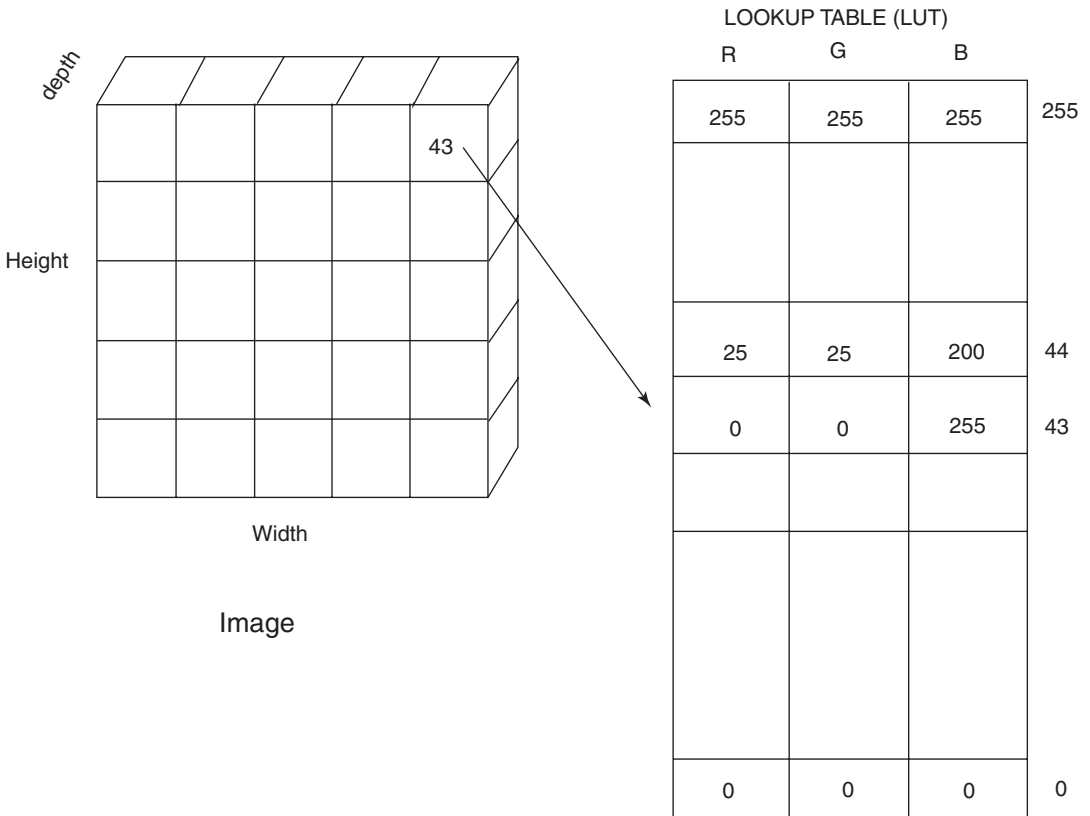
Fig. 15.10 Graphic explanation of pseudocolor displays. Each pixel value in the image is used as an index into the video lookup table (LUT). Red (R), green (G), and blue (B) color values are obtained from the LUT at that index entry. These values are then used to display that pixel

lookup table rather than its width. Figure 15.10 shows how the LUT works to define a color that will be used to display each pixel.

Pseudocolor displays are very flexible, because the color mapping associated with the LUT can be interactively changed. A completely new LUT can be loaded almost instantaneously so that the image may be viewed in color, or using a gray scale, without modifying the image data itself. The most common operation for changing a LUT is that of modifying the lower bound or upper bound. The lower and upper bounds are the pixel values at which the LUT changes from its first to its second color, or from its next-to-maximum to maximum color. Generally, if the LUT has 256 entries, then the default lower bound is 0, and the upper bound is 255. (The lower bound is also called the level, and the difference between the upper and lower bounds may be called the window.) However, if

the lower bound is changed to 10, then the LUT will be compressed so that the value that originally was at 0 will be placed at all values between 0 and 10, the value at 255 will remain the same, and the other colors that originally ranged from 0 to 255 will be compressed, using interpolation, between those values. Raising the lower bound acts as a type of background subtraction, because low values are now displayed using the same color as "0," so that these low intensity regions seem to disappear. Lowering the upper bound tends to enhance lower values, because smaller pixel values are now displayed using the portions of the color map that used to be assigned to the higher intensity pixel values. Figure 15.11 shows how modifying the color tables changes the display of a bone scan.

Some particular lookup tables are important to understand. The gray scale contains the same R,
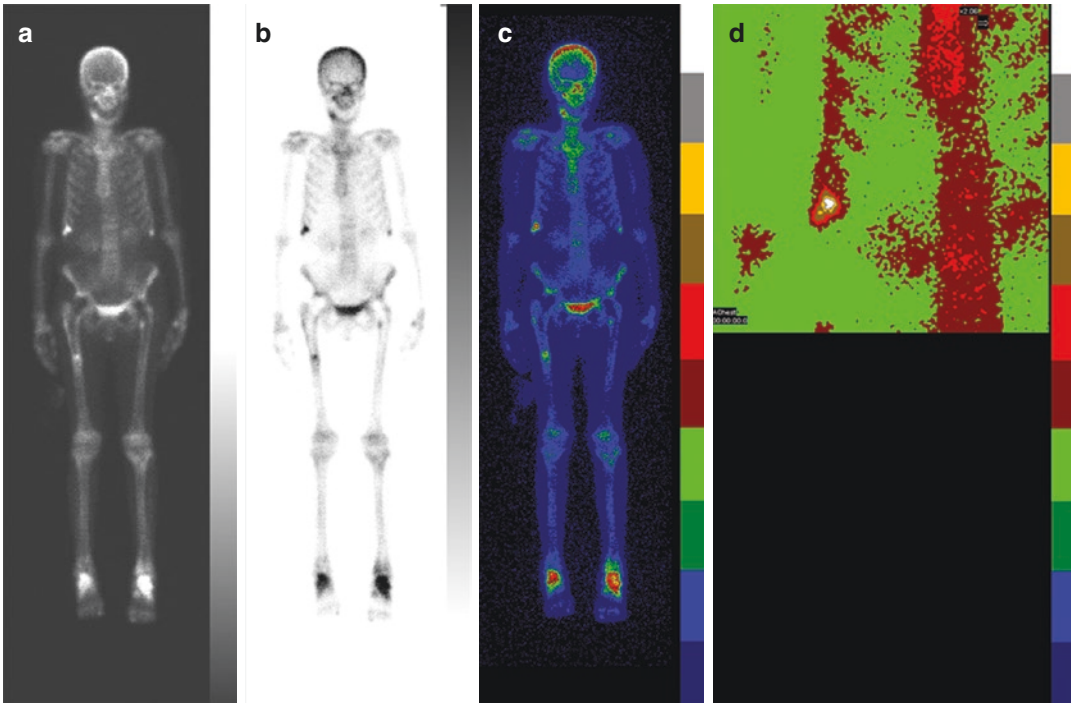
Fig. 15.11 Bone scan displayed using different lookup tables (LUT). (**a**) Gray scale mapping, with bright shades of gray (white) indicating large counts. (**b**) Reverse gray scale, where dark shades of gray indicate large counts. This LUT has been modified so that its lower bound is greater than 0, giving the image the appearance of having fewer counts in the background. (**c**) Ten-step color scale, so that at every 10% of maximum counts, the color changes dramatically. When a portion of the image is zoomed (**d**), the rapid changes from about 50 to 100% of maximum counts in the hot region of the right rib cage can be appreciated

G, and B values for each entry, so the "colors" are all gray. They range from black (R, G, B = 0) at the first entry, to white (R, G, B = 255) at the top entry, so that background colors are dim and high pixel values are near white. The reverse gray scale ranges from 255 at the first entry to 0 at the top entry, so that background colors are white, while high pixel values are black. Discrete lookup tables change to different colors in the space of a single entry, and are often scaled so that these color changes occur every 10%. In this way, a quantitative assessment of the pixel values can be obtained—a green value may be associated with pixel values equal to 50–60% of the maximum in the image, for example. However, discrete lookup tables, and indeed, any color table that changes hue in the space of a few pixel values can result in what are called false contours. Two pixel values that are very similar in value may end up being assigned very different colors. This leads the eye to believe there are hard boundaries between the two pixel values when in fact there is very little difference between them.

15.4.2 True Color Displays

A second type of display requires that each pixel value in the image contain values for red, green, and blue colors. This is typically not the case for any medical image; however, such displays can be generated and are frequently used for 3D graphics. In these images, the data has three "planes", each associated with the red, green, and blue values used for display. Again, these planes are usually one byte in width, so that the R, G, and B values can range from 0 to 255. No lookup table needs to be used to translate the image into a display; rather, the three planes already encode the colors. Note that in true color displays with

byte-sized planes, 2^{24} colors can be displayed at one time all in the same image. This color resolution is necessary in three-dimensional graphics, since many more colors are necessary to give the display realism. However, given that nuclear medicine images really only have one value per pixel, true color displays are not generally needed for displaying slices.

15.5   Image Filtering

Image filtering can be thought of as a mathematical process applied to an image for various reasons, such as removing noise or enhancing features. This process can occur before, during or after the image reconstruction process, and in most Nuclear Medicine procedures it is employed to remove noise. It is a very necessary process for SPECT reconstruction, as shown in Fig. 15.12.

Because filtering is a mathematical process, it is much easier to convert images into the math "world" (better known as frequency space) for filtering, rather than converting the filters into the image world. This process of converting images into the math world, or frequency space, is accomplished using the Fourier Transform, and will be covered in the next section. However, it would be good to take a step back and examine how image objects and properties relate to this new math world called frequency space.
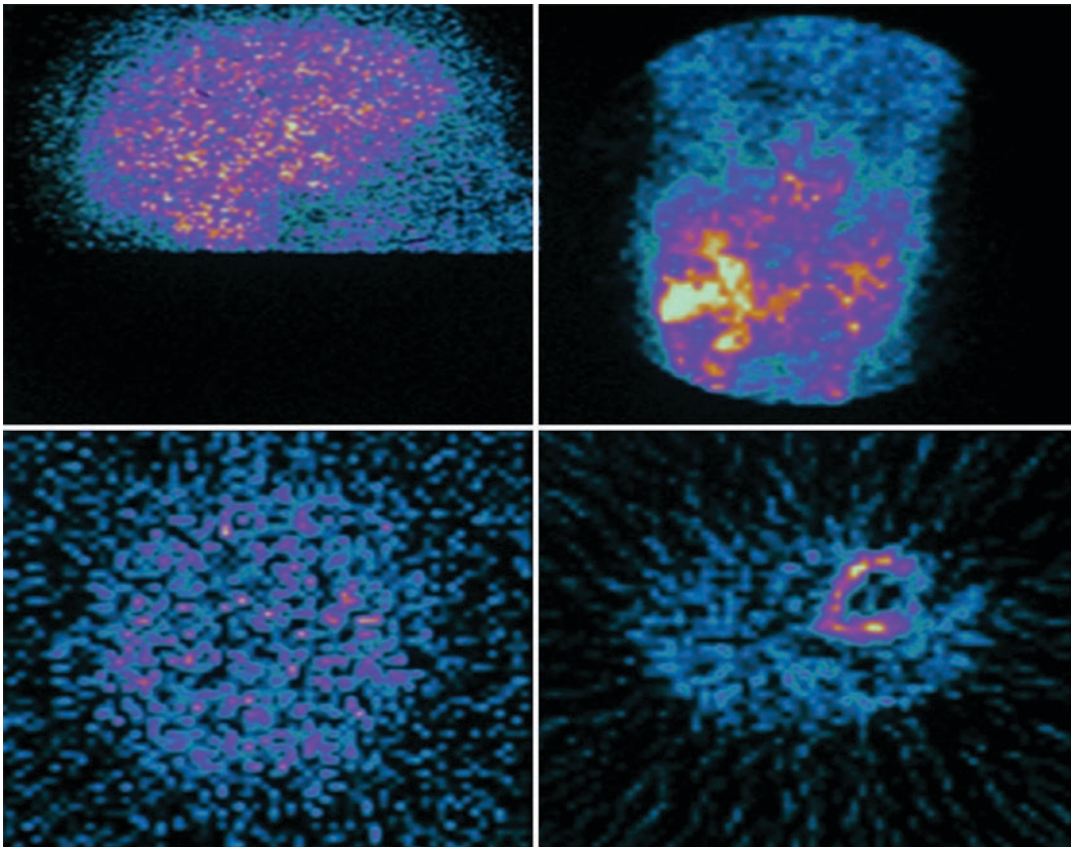
Fig. 15.12 Top left panel shows one frame from a Brain Perfusion SPECT acquisition, bottom left shows the same SPECT acquisition reconstructed with no filtering applied.

Top right shows one frame from a Myocardial Perfusion SPECT acquisition, bottom right shows the same SPECT acquisition reconstructed with no filtering applied

15.5.1 Frequency Space

From Collins Essential English Dictionary [9], frequency is defined as the number of times that an event occurs within a given period. For instance, a clock pendulum that swings back and forth every second would have a frequency of one cycle (one back and forth swing) per second, or 1 cycle/s. Similarly (though overly simplified), since a digital image is made up of pixels, there are a finite number of these elements that can be turned on and off. Let's take the example of an image that has 64 pixels across the image. If we turn half of the pixels (32 pixels) on and then the remaining half of the pixels off, this would translate into a frequency of 1 cycle (pixels on, then off) per 64 pixels or 0.015625 cycles/pixel (Fig. 15.13a). If this process were halved such that 16 pixels were on, then off, then on, then off, this would translate into a frequency of 2 cycles/64 pixels or 1 cycle/32 pixels or 0.03125 cycles/pixel (Fig. 15.13b). If we continue this process of halving the number of pixels that are on or off (Fig. 15.13c–e), we eventually get to the point where every other pixel is on and off, which translates into a frequency of 1 cycle/2 pixels or 0.5 cycles/pixel (Fig. 15.13f). This special case represents the maximum frequency (on/off cycles) that can be represented in a digital image, and is called the Nyquist Frequency (named after the Swedish-American engineer Harry Nyquist).
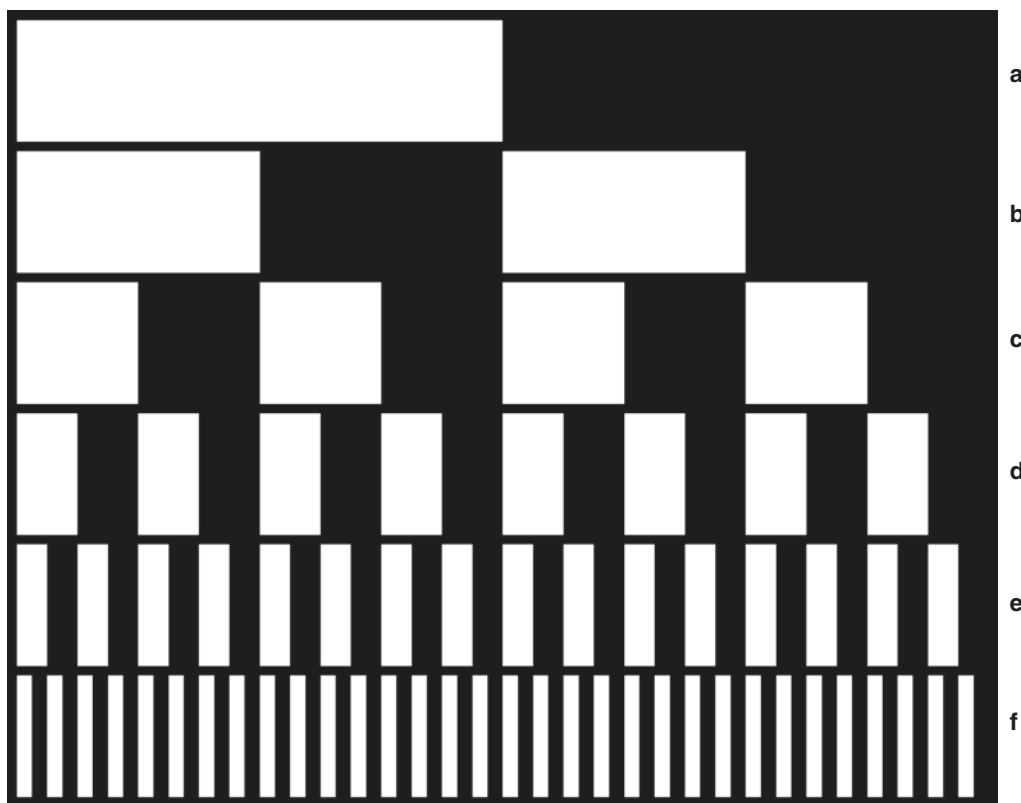
Fig. 15.13 Panels **a–f** show increasing numbers of cycles/pixel for a 64 pixel image (image was zoomed for display purposes). (**a**) 0.015625 cycles/pixel (1 cycle/64 pixels), (**b**) 0.03125 cycles/pixel (2 cycles/64 pixels), (**c**) 0.0625 cycles/pixel (4 cycles/64 pixels), (**d**) 0.125 cycles/pixel (8 cycles/64 pixels), (**e**) 0.25 cycles/pixel (16 cycles/64 pixels) and (**f**) 0.5 cycles/pixel (32 cycles/64 pixels)

Up to this point, we have been using cycles/pixel as the unit of measure for frequency, but other units may also be used. As just noted, the maximum frequency that can be displayed in a digital image is 0.5 cycles/pixel, which can also be represented as a percentage or fraction of the Nyquist frequency. Thus 0.5 cycles/pixel = 1 × Nyquist frequency = 100% of the Nyquist frequency (note that when using units of percent or fraction of the Nyquist frequency, that the maximum frequency is now greater than 0.5). In addition, if the physical size of the detector is taken into consideration, then the units of frequency can be converted into cycles/cm using the following formulas:

$$\text{freq}(\text{cycles / cm}) = \text{freq}(\text{cycles / pixel}) * (\#\text{pixels}) / \\ (\text{size of detector in cm})$$

or

$$\text{freq}(\text{cycles/cm}) = \text{freq}(\%\text{of Nyquist}) * 0.5\,\text{cycles} \\ /\text{pixel} * (\#\text{pixels}) \\ /(\text{size of detector in cm})$$

For instance, in our above example, if the field-of-view was 40 cm, then the Nyquist frequency would be 0.5 cycles/pixel × 64 pixels/40 cm = 0.8 cycles/cm (note that when using units of cycles/cm, the maximum frequency can again be greater than 0.5).

Now that we know what a frequency is, the next obvious question is how do frequencies relate to image objects?

15.5.2 Spatial Domain Versus Frequency Domain

If we look again at Fig. 15.13, we notice that as more pixels are turned on and off (more cycles), the corresponding frequency also increases (from 0.015625 to 0.5 cycles/pixel). Following this line of reasoning, low frequencies correspond to the slowly varying portions of images, while high frequencies correspond to quickly varying portions of images. This means that "edges" (points in an image with an abrupt change in intensity such as going from black to white, or white to black) contain numerous high-frequency components. In addition, image noise (spurious bright and dark pixels scattered randomly throughout the image) also contains numerous high frequencies; this makes sense if you stop and think about it. Randomly distributed bright and dark pixels will have very abrupt edges when compared with their neighbors, and as mentioned before, it's these edges that contribute to the high-frequency components. However, real edges in images (such as boundaries between myocardium and background) also contribute high-frequency components. So filtering is always a balance between removing as much noise as possible while preserving as much resolution and detail as possible.

15.5.3 Fourier Transform

15.5.3.1 Types of Filters

Generally speaking, all filters fall into one of three classes: (1) Low-Pass filters (filters that pass low frequencies), (2) High-Pass filters (filters that pass high frequencies) and (3) Band-Pass filters (filters that pass a narrow range of frequencies). From the previous section we learned that noise in Nuclear Medicine images is almost always a high-frequency component, therefore, the goal of most of the filtering we do in Nuclear Medicine is to reduce this noise, which means we mostly employ Low-pass filters. The one exception to this is the ramp back-projection filter, a High-Pass filter used in the Filtered Back-Projection process (this topic is covered in a later chapter in this book). Band-Pass filters are a special class of filters, and since they are not generally used in Nuclear Medicine, we will not discuss them here.

There are many Low-Pass filters that we could discuss, including: Metz, Weiner, Hanning (or Hann), and Butterworth. Because of space constraints, we will focus on two of the more popular filters, Hanning and Butterworth.

Hanning Filters

In years past, the most common filter in Nuclear Medicine was the Hanning filter. It is a relatively simple filter with one parameter defining its char-

acteristics, the cutoff frequency. The mathematical definition of the Hanning Filter is as follows:

$$w(f) = 0.5 + 0.5\cos\left(\frac{\pi f}{f_m}\right) \quad \text{if } |f| < f_m$$

Where:

f = spatial frequencies of the image
f_m = cutoff frequency

By definition, this filter is defined to be 0 at all frequencies greater than the cutoff frequency, completely removing them from the image. Figure 15.14 shows 3 different Hanning filters with cutoff frequencies of 0.4, 0.6 and 0.822 cycles/cm. Note how the filter rolls quickly toward the cutoff frequency and is 0 for all frequencies above the cutoff frequency. This figure also shows a typical brain SPECT study filtered with these three filters. Because the Hanning filter rolls-off to 0 so quickly, it is a very good smoothing filter (it very effectively removes high-frequency components, including noise and edge detail); however, it tends not to preserve image resolution.

Butterworth Filters

Sometime in the 90s the popularity of the Butterworth filter started gaining momentum. Today, it seems to be the filter of choice in Nuclear Medicine. Perhaps it is because the Butterworth Filter is so versatile, it can be constructed in such a way that mimics the properties of a Hanning filter, but it can also do a lot more.

There are two parameters that define the Butterworth filter, they are (1) Critical Frequency
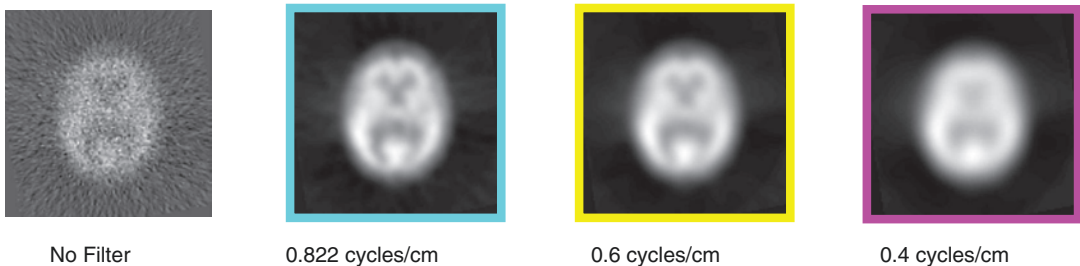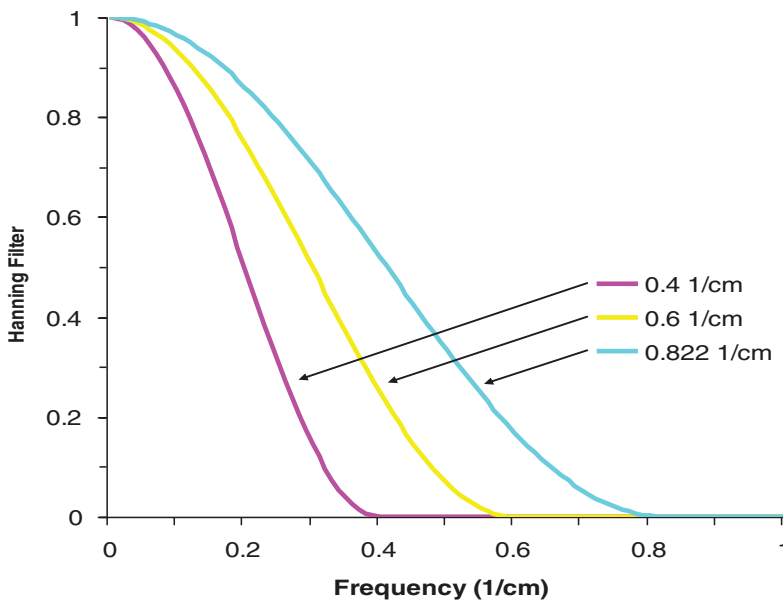
Fig. 15.14 Hanning filter with 3 different cutoff frequencies shown, 0.4, 0.6 and 0.822 cycles/cm. Note how changing the critical frequency effectively shifts the Hanning filter up and down the Frequency axis of the plot

and (2) Power Factor (sometimes called Order). Notice that the first parameter is called the "critical frequency" instead of the "cutoff frequency" as it was for the Hanning filter. This is because the critical frequency is the point at which the Butterworth filter start's it's roll-off toward 0, rather than being defined as 0, as in the Hanning filter. In fact, mathematically, the Butterworth filter never reaches 0, it merely approaches 0. Unfortunately, there is some confusion as to the correct name of the second parameter (what I have called power factor). Mathematically, the power factor = 2 × order, though there are some manufacturers that do not follow this rule. The only real way to determine if the Butterworth filter, as implemented in your particular equipment, is using the power factor or order is to examine the equation that was actually implemented. Here is the equation for the Butterworth filter using power factor:

$$w(f) = \frac{1}{\sqrt{1 + \left(\dfrac{f}{f_c}\right)^p}}$$

Where:

f = spatial frequencies of the image
f_c = critical frequency
p = power factor

In the case where a manufacturer has implemented the Butterworth filter using order instead of power factor, then the equation would look like this (note that p has been replaced with $2n$, where n is the order):

$$w(f) = \frac{1}{\sqrt{1 + \left(\dfrac{f}{f_c}\right)^{2n}}}$$

In practice, the critical frequency of the Butterworth filter behaves much like the cutoff frequency of the Hanning filter, in that as the critical frequency is changed the effect is to shift the resultant Butterworth filter up and down the Frequency axis, as shown in Fig. 15.15. The power factor effectually changes the steepness of the Butterworth filter's roll-off toward 0, as shown in Fig. 15.16. Because of this versatility (the ability to change not only the frequency of the roll-off, but also the steepness of the roll-off), the Butterworth filter can be used to more effectively remove noise while still preserving resolution. Note how the noise in the Brain images at the bottom of Fig. 15.16 is affected by the change in power factor (increasing the power factor effectively reduces the higher frequency components, such as noise), but the detail in the interior structures is preserved.

15.5.3.2 Fourier Transform in Filter Application

In this section we will examine the process of actually applying a filter to an image. As mentioned in the previous section, filtering usually takes place in the mathematical world of frequency space, because filter implementation and application is easier. The complete filtering process is shown in Fig. 15.17 and goes something like this: an image is converted to frequency space, the filter is applied and the resulting image is converted back to image space. The process of converting an image into frequency space is accomplished using the Fourier transform [10–14]. This mathematical operator is non-destructive, completely reversible and can be computed fairly quickly for images whose dimensions are a power of 2 (using the FFT or Fast Fourier Transform). The frequency information that is returned by the Fourier Transform can also be viewed as a series of sine or cosine waves. For instance, the square wave shown in Fig. 15.18, panel a has frequency components that are shown in panel b. These components can also be shown as a series of sine waves, as seen in panel c. If one were to do a point-by-point addition of all of the sine waves, the resultant wave-form would be equal to the square wave shown in panel a. Another term for each of these individual sine waves, or fre-
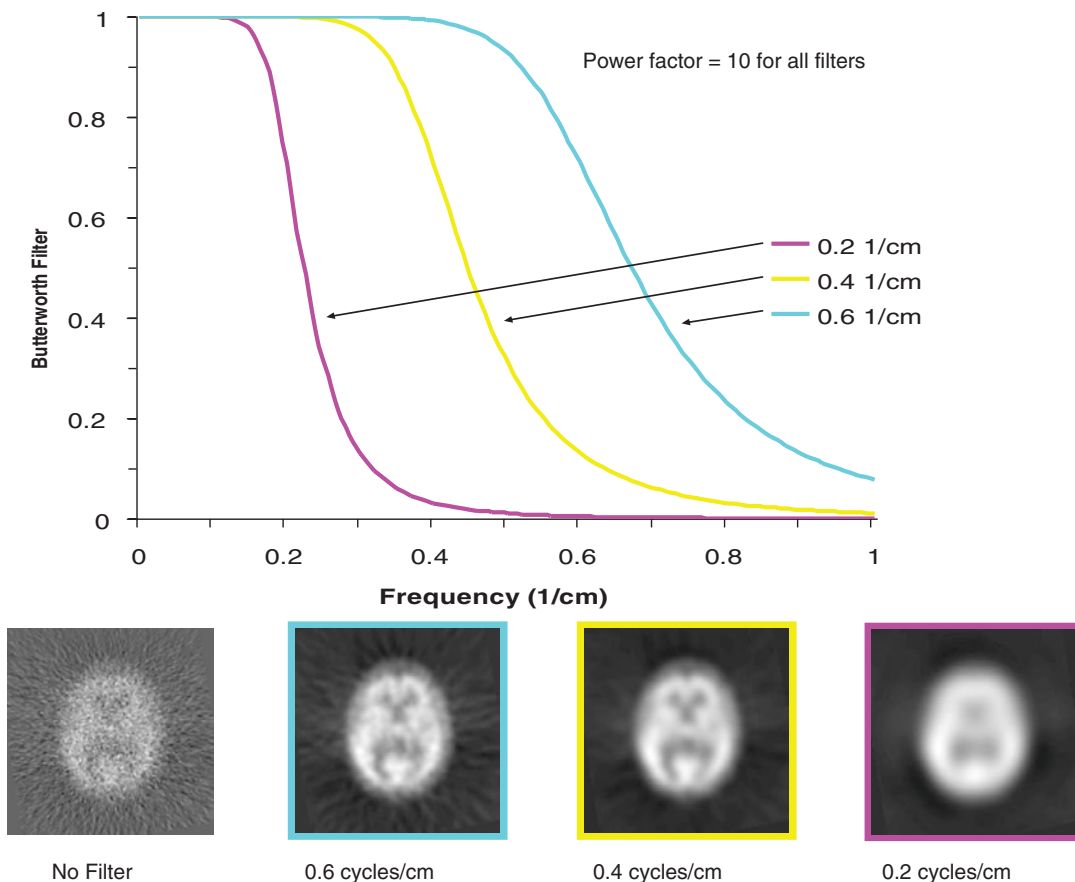
Fig. 15.15 Butterworth filter with 3 different critical frequencies and a constant power factor of 10: 0.6, 0.4 and 0.2 cycles/cm. Note how changing the critical frequency (like changing the cutoff frequency of the Hanning filter) effectually shifts the filter up and down the Frequency axis of the plot

quencies, is harmonics. The lowest frequency is referred to as the first harmonic, the second lowest frequency as the second harmonic, and so on. In reality, the first harmonic is the best "fit" of a sine wave to the original data. As one adds more harmonics, the "fit" becomes more and more like the original curve. There are several different ways to display this frequency information to the user, we will be showing the information in graph style, where each point on the *x*-axis represents a specific frequency, and the height of each point represents how much of that frequency is in the image (as in Fig. 15.18b). Let's illustrate this with several examples.

Figure 15.19a shows an image consisting of 8 increasing frequencies, ranging from 0.0039 cycles/pixel to 0.5 cycles/pixel. Panel b shows the corresponding graph of these eight frequencies (also referred to as the input frequency spectrum or just input spectrum). Panel c shows a graphical representation of a uniform filter, note that this graph uses the same units as the input frequency spectrum. In frequency space, filtering is simply the multiplication of the input frequency spectrum, point-by-point, with the filter. In other words, every frequency point in the input spectrum is multiplied by its corresponding point in the filter graph. For this example, since the uni-
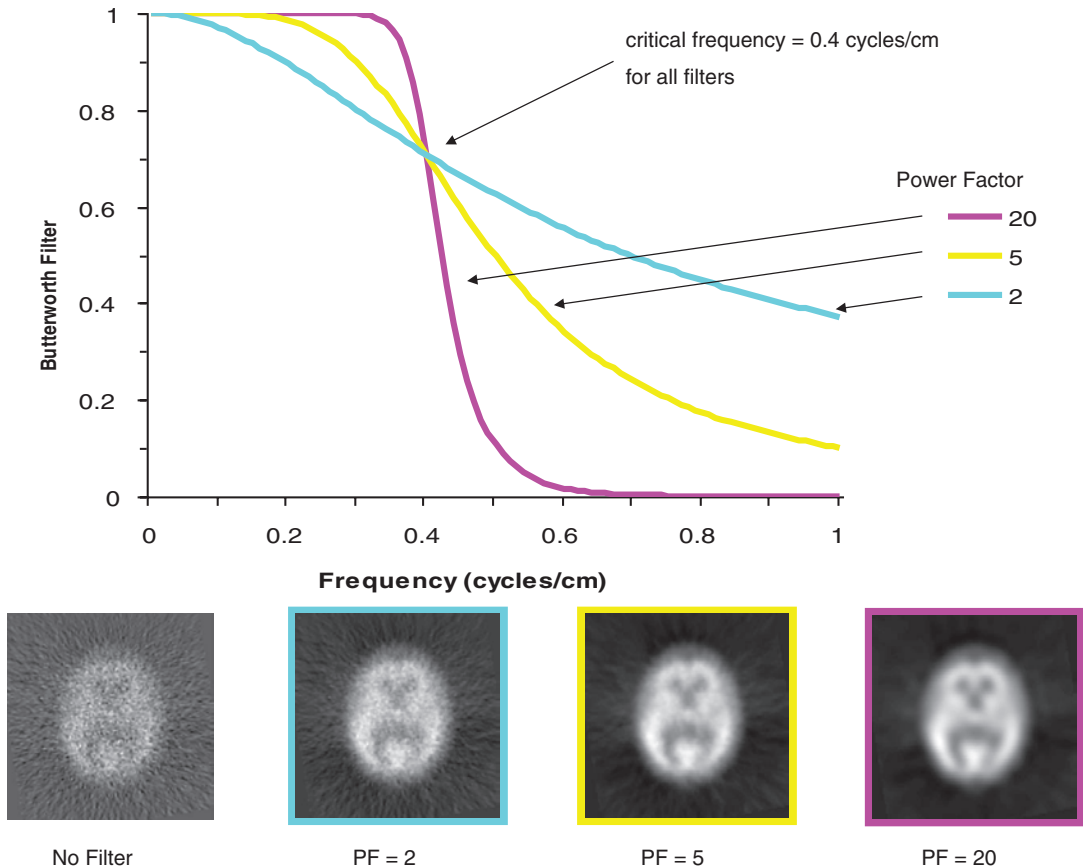
Fig. 15.16 Butterworth filter with 3 different power factors and a constant critical frequency of 0.4 cycles/cm: PF = 20, PF = 5 and PF = 2. Note how increasing the power factor increases the steepness of the filters roll-off toward 0

form filter has a value of "1" for each frequency, each input frequency is multiplied by 1 and copied to the output frequency spectrum graph (see Panel d). We can now convert this filtered output frequency spectrum into an image by running the inverse of the Fourier transform, the resultant image is seen in Panel e. Since the output spectrum is identical to the input spectrum, it is not surprising that the filtered image (output image) is identical to the input image.

We can now add what we learned about different filters in the previous section to the filtering process. Figure 15.20, panels a and b show the same input image and spectrum as Fig. 15.19. However, the filter in Fig. 15.20c is now that of a Hanning filter with a cutoff value of 0.5 Nyquist. The output spectrum in Panel d shows the results

of multiplying the input spectrum by this filter, and the corresponding image is shown in panel e. Note that because of this filters sharp roll-off, the frequency at 0.5 Nyquist is completely removed from the image, and the other frequencies have been somewhat reduced. Figure 15.21 shows an additional example using a Butterworth filter with a critical frequency of 0.03125 Nyquist and an order of 5. Note that this filter has completely removed the frequency at 0.5 Nyquist, and has all but completely removed the frequencies at 0.125 and 0.25 Nyquist as seen in the output spectrum and the resultant filtered image.

As a final example of filtering, let's look at a real case involving a Planar Bone Scan (Fig. 15.22). In Panel a you can see the original image, Panel b shows the input spectrum of the
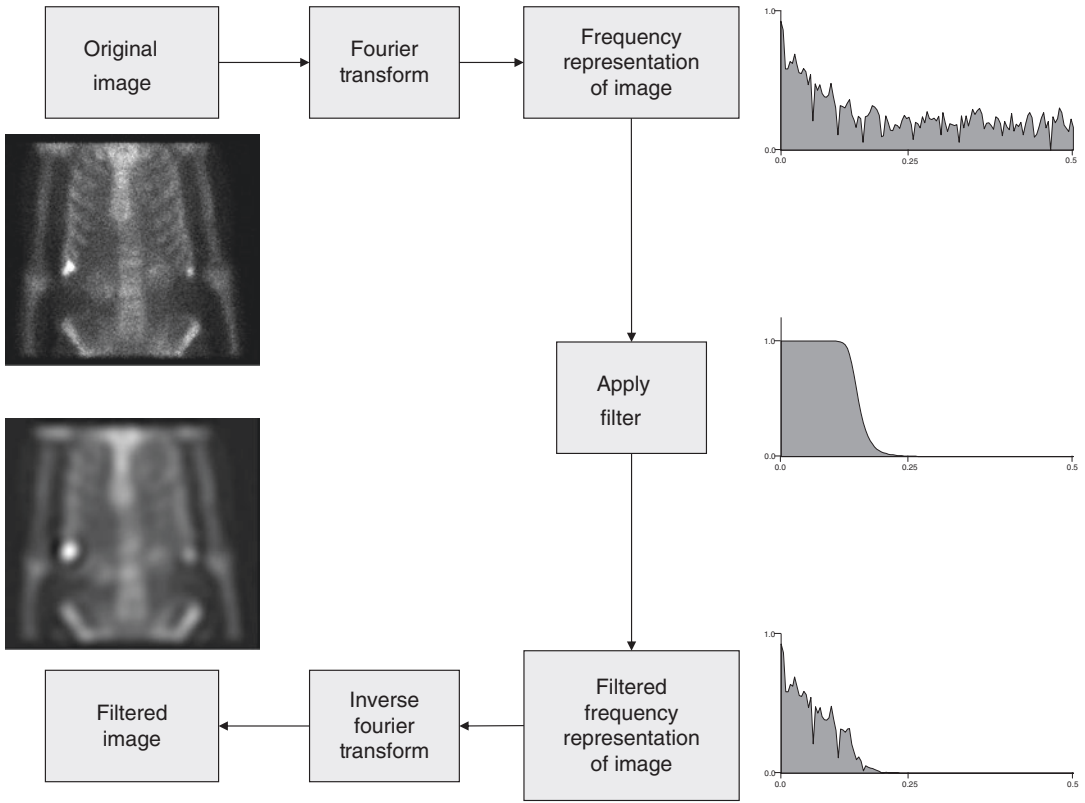
Fig. 15.17 Diagram of the filtering process. The original image is converted to frequency space using the Fourier transform, where an image filter is applied. The resultant frequency spectrum is converted back to image space using the inverse Fourier Transform

Bone scan (note the rather continuous nature of the input spectrum, indicating that frequencies of all values are present). Panel c shows a Butterworth filter with a critical frequency of 0.125 Nyquist and a Power Factor of 20. The resultant spectrum (Panel d) and image (Panel e) show the results of this filter.

15.5.3.3 Fourier Transform in Curve Fitting

We can use the "fitting" property of the Fourier Transform to our advantage when looking at various physiologic phenomena. For instance, when calculating an ejection fraction, the time-volume curve generally looks much like a time-shifted sine wave (see Fig. 15.23). We can use the first harmonic of the Fourier Transform of the time-volume curve to actually "fit" this time-volume curve to a sine wave. This is of particular interest when there are few time points or where the data is particularly noisy [15]. As you can see in Fig. 15.23, the first harmonic of the Fourier Transform is much smoother than the curve of the original eight points. In addition, recent research has shown that the temporal resolution of an 8 or 16-frame study is equivalent to a 64-frame study, when the original study has been "fitted" to the first, second or third harmonics of a Fourier Transform [16].

There are at least two exciting Cardiology applications of fitting time-volume curves using the Fourier Transform: (1) Determination of Wall Thickening and (2) Phase Analysis. Though space will not permit a detailed treatment of these two applications, we will describe them briefly below.
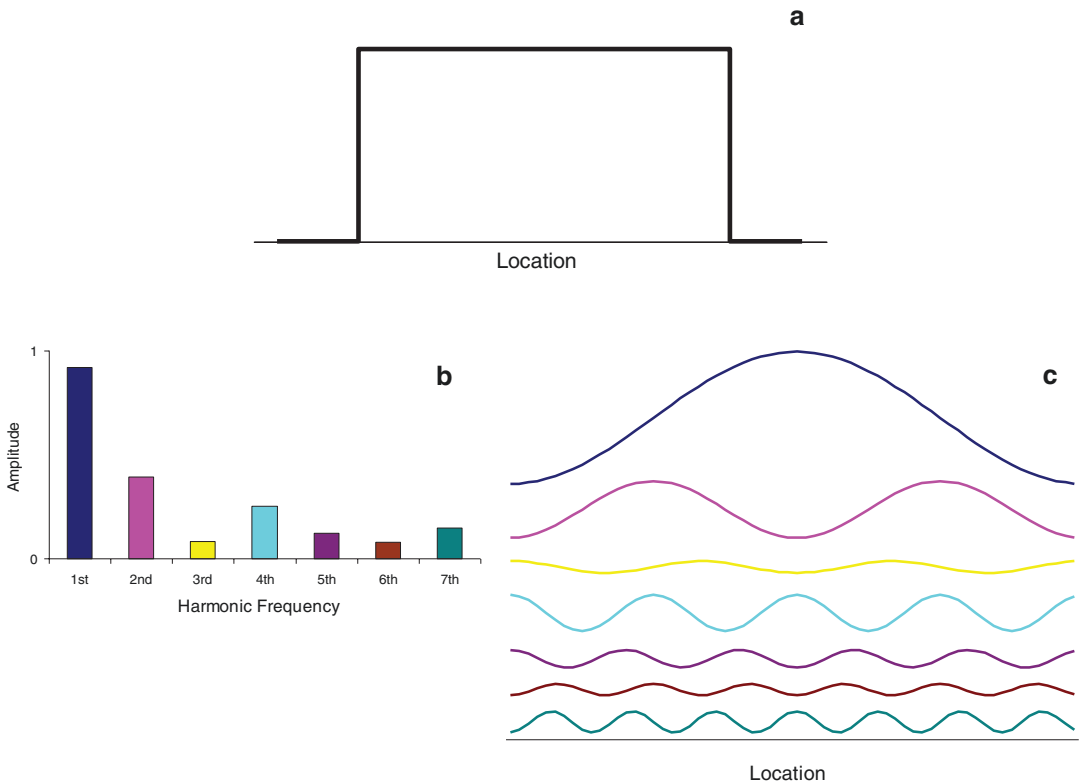
Fig. 15.18 Decomposition of square wave into frequency components using the Fourier Transform. (**a**) Original square wave. (**b**) Fourier Transform frequency spectrum of the square wave shown in (**a**). (**c**) Another way of showing the Fourier Transform spectrum as sine waves

15.5.3.4 Fourier Transform in the Determination of Wall Thickening

It has been shown that if the size of an object being measured is less than or equal to twice the resolution of the imaging equipment (twice the FWHM), then the counts in the object increase linearly with its thickness [17]. This property of linear count increases can be used to measure the "thickening" of the myocardial wall in myocardial perfusion gated SPECT studies [18]. A typical SPECT system has an intrinsic resolution of about 10 mm, and the average end-diastolic width of the walls of the left ventricle are about 1 cm [19]; this falls into the category of the object size being less than twice the FWHM of the imaging system. If we extract the counts of

the left ventricular myocardium from a myocardial perfusion gated SPECT study, and look at the counts of each point in the myocardium as it goes through the cardiac cycle, we will get a series of time-count curves similar to the curve shown in Fig. 15.23. If we fit each of these curves using the first harmonic of the Fourier Transform (also shown in Fig. 15.23), then we can estimate the percentage of thickening of the myocardium between end-systole and end-diastole. Assuming that the counts are linearly proportional to thickness, then the percentage of increase of counts from end-diastole to end-systole should be linearly proportional to the increase in wall thickness. For example, if the amplitude of the sine wave is 13, and the DC component is 135, then the % thickening could be calculated as
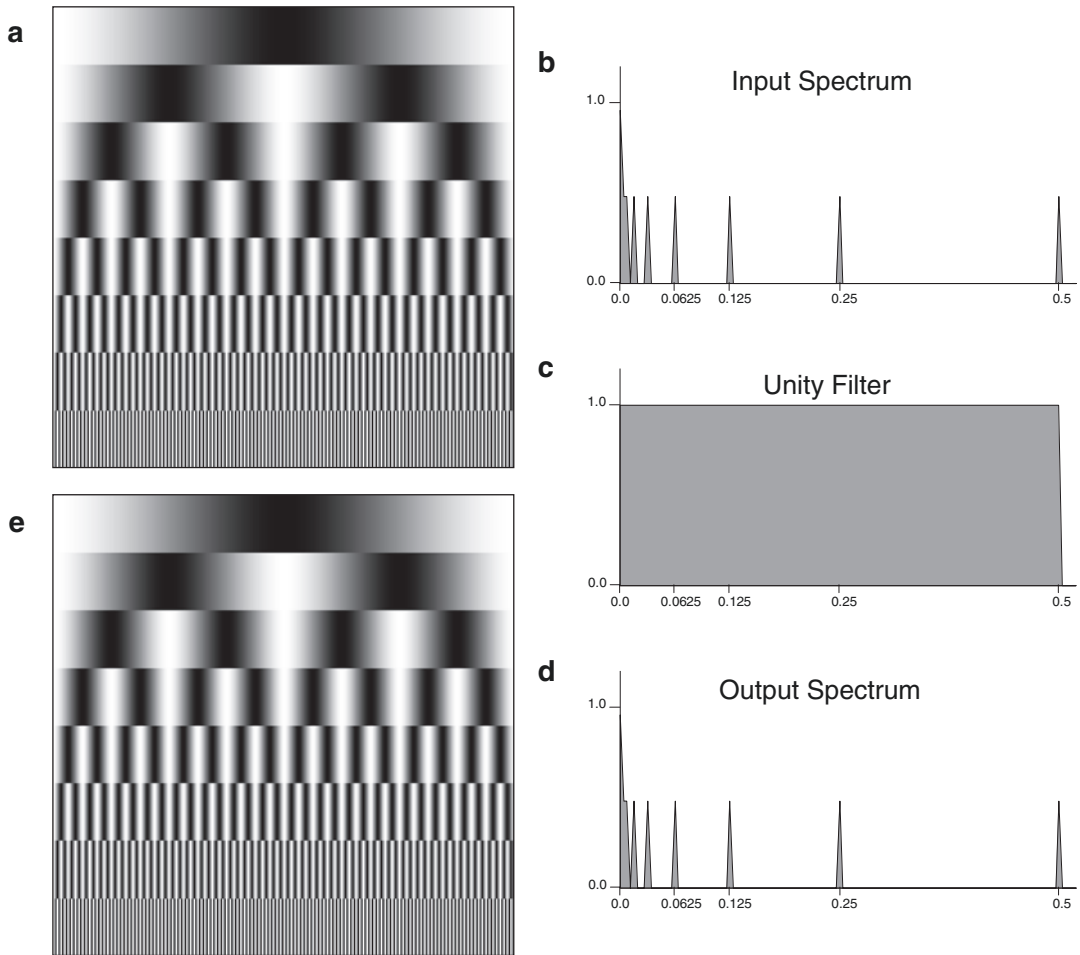
Fig. 15.19 Filtering Example. (**a**) Original image with eight frequencies. (**b**) FFT spectrum of original image. (**c**) Unity filter (one everywhere). (**d**) FFT spectrum after application of filter. (**e**) Filtered image

$(2 \times Amplitude)/(DC - Amplitude)$ and would be 21%. Though this number could be calculated directly from the counts extracted from the myocardium, it is less affected by noise or number of acquired frames/cardiac cycle if the Fourier Transform is used. By calculating this % thickening for every point in the myocardium we can come up with a global assessment of how the myocardium is thickening throughout the cardiac cycle. This assessment can be important, as areas that are not thickening (which implies impaired function) may be an independent indi-cator of dead or dying myocardial tissue. It can also be used to rule-out false positives. For instance an area of the myocardium that does not exhibit many counts at stress and at rest (compared to the surrounding tissue) would normally be viewed as dead myocardial tissue. However, if this same area is seen to "thicken", i.e., there are count changes between end-diastole and end-systole, then the count reductions are probably due to some kind of artifact (Breast or Diaphragm attenuation), and the tissue is more than likely alive and well [20].
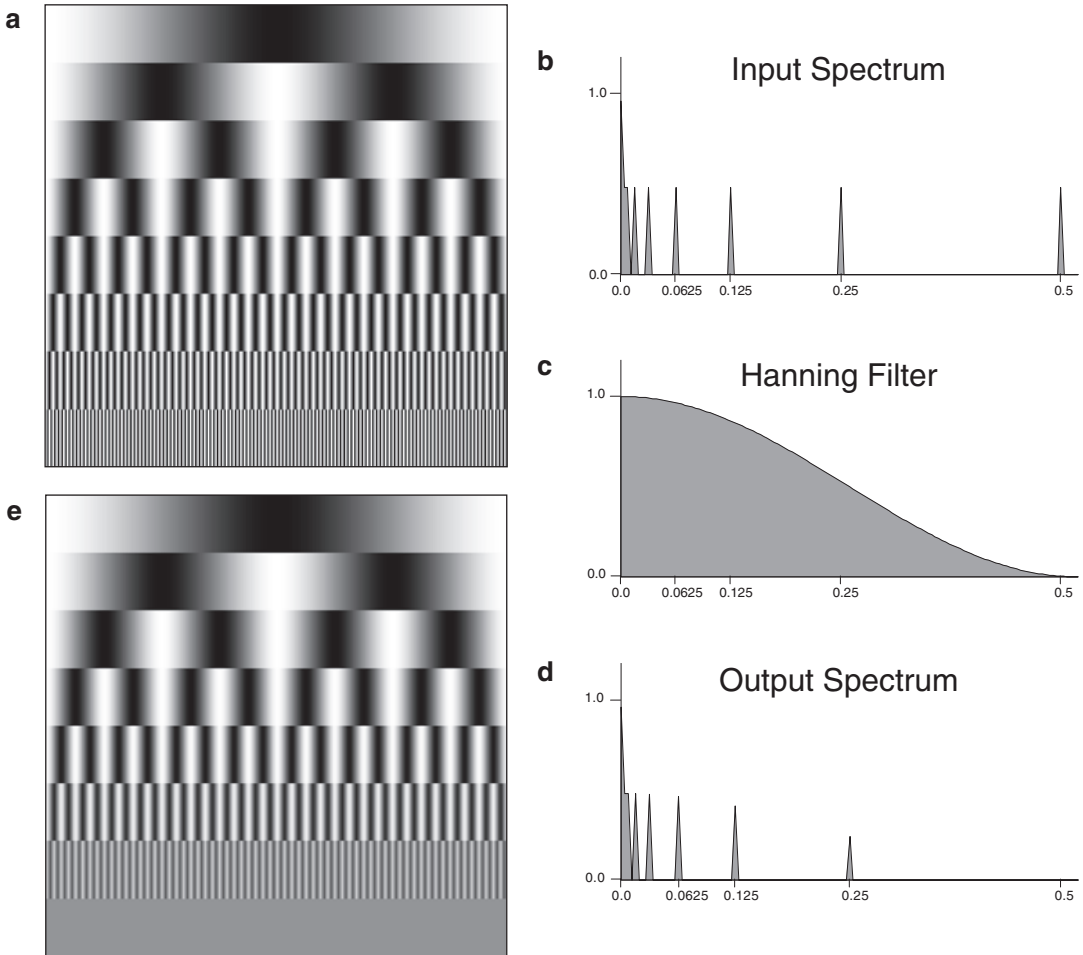
Fig. 15.20 Hanning Filter Example. (**a**) Original image with eight frequencies. (**b**) FFT spectrum of original image. (**c**) Hanning Filter, cutoff frequency = 0.5 Nyquist. (**d**) FFT spectrum after application of filter. (**e**) Filtered image

15.5.3.5 Fourier Transform in the Calculation of Phase Analysis

Another benefit of using the Fourier Transform is that we can also measure the onset of thickening (or onset of mechanical contraction); this is sometimes referred to as Phase Analysis. If we again look at Fig. 15.23, the point at which the thickening curve crosses the DC component of the Fourier Transform is known as the phase shift or just phase of the curve. A sine wave with no phase shift would have started at the DC crossing point, which would be a phase of 0. As the sine wave is shifted to the right, the phase increases indicating a delay in the contraction of the ventricle. If we calculate this phase shift
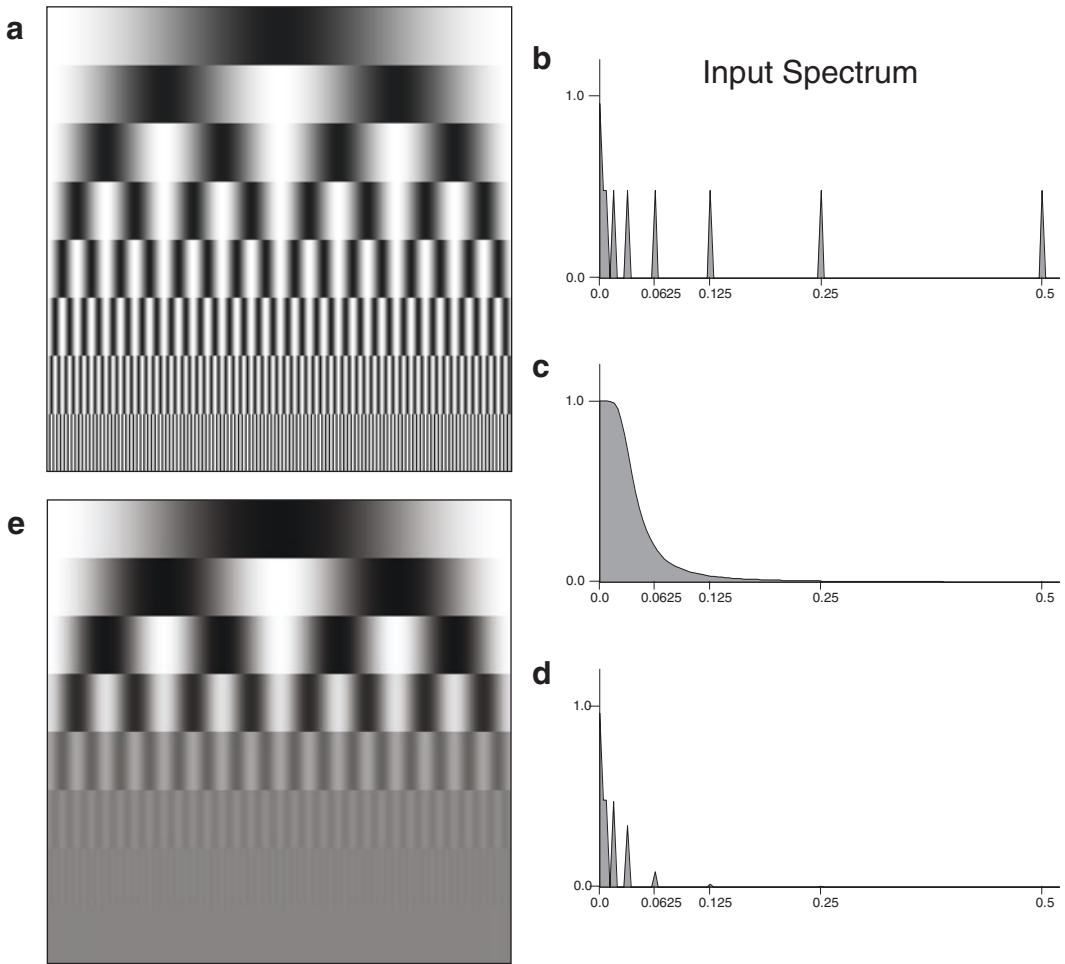
Fig. 15.21 Butterworth Filter Example. (**a**) Original image with eight frequencies. (**b**) FFT spectrum of original image. (**c**) Butterworth Filter, critical frequency = 0.03125 Nyquist, power factor = 5. (**d**) FFT spectrum after application of filter. (**e**) Filtered image

for every point in the myocardium (much like we calculate the % thickening for every point in the myocardium) we can use this distribution of phases to diagnose various cardiac conditions. There are several ways to look at this distribution of phases, two of which are most common: (1) as a histogram and (2) as an image. Figure 15.24 shows the output screen of a normal Multiple Gated Acquisition (MUGA) study. Notice that the phase image is all one color and the histogram is very narrow, both indicating that all sections of the ventricle are essentially contracting at the same time. Figure 15.25 shows the output screen of a MUGA for a patient with an api-
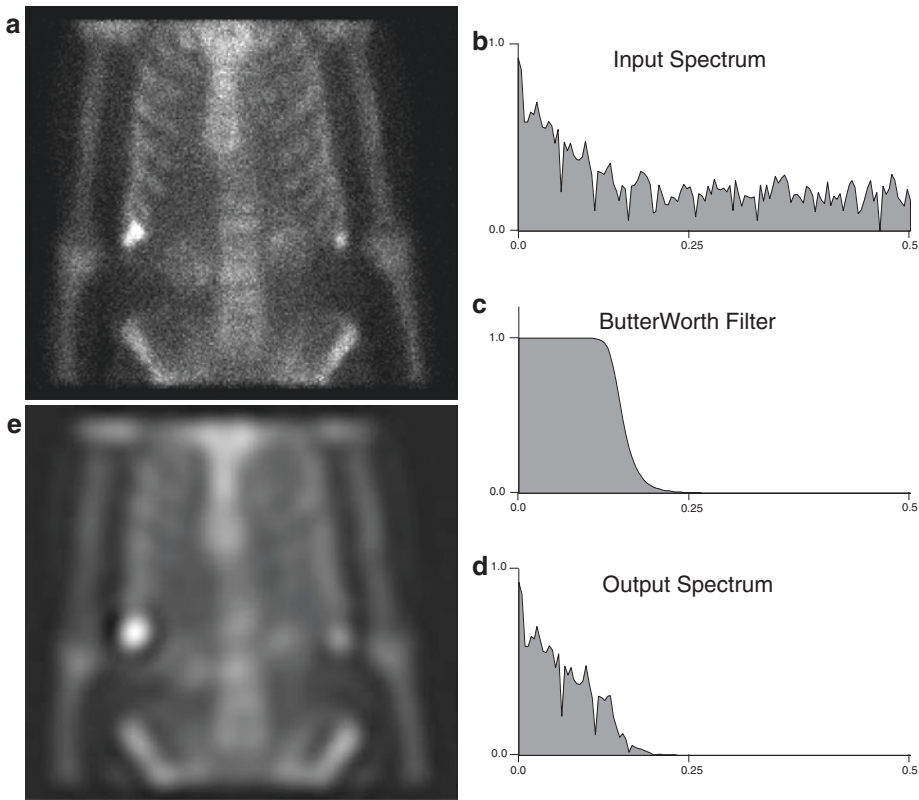
Fig. 15.22 Butterworth Filter Example with Planar Bone Scan. (**a**) Original Planar Bone Scan. (**b**) FFT spectrum of original image. (**c**) Butterworth Filter 0.125 Nyquist, power factor = 20. (**d**) FFT spectrum after application of filter. (**e**) Filtered image
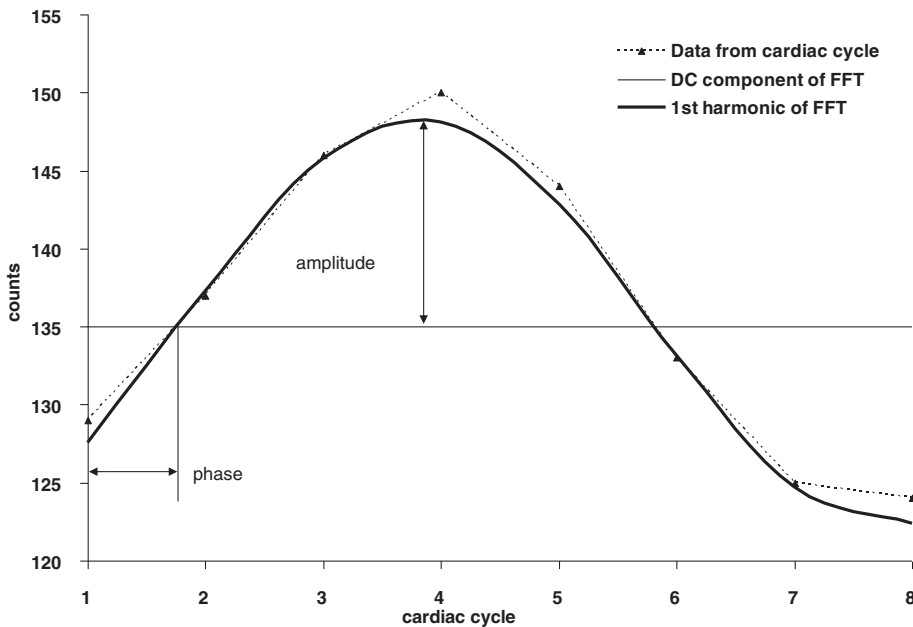
Fig. 15.23 Example of Fourier curve fitting. Eight time points from a mid-ventricular gated short-axis slice are shown in the dotted lines. The result of fitting these eight points to the first harmonic of the FFT are shown in the dark solid line. The light solid line shows the DC component (or average) of the FFT
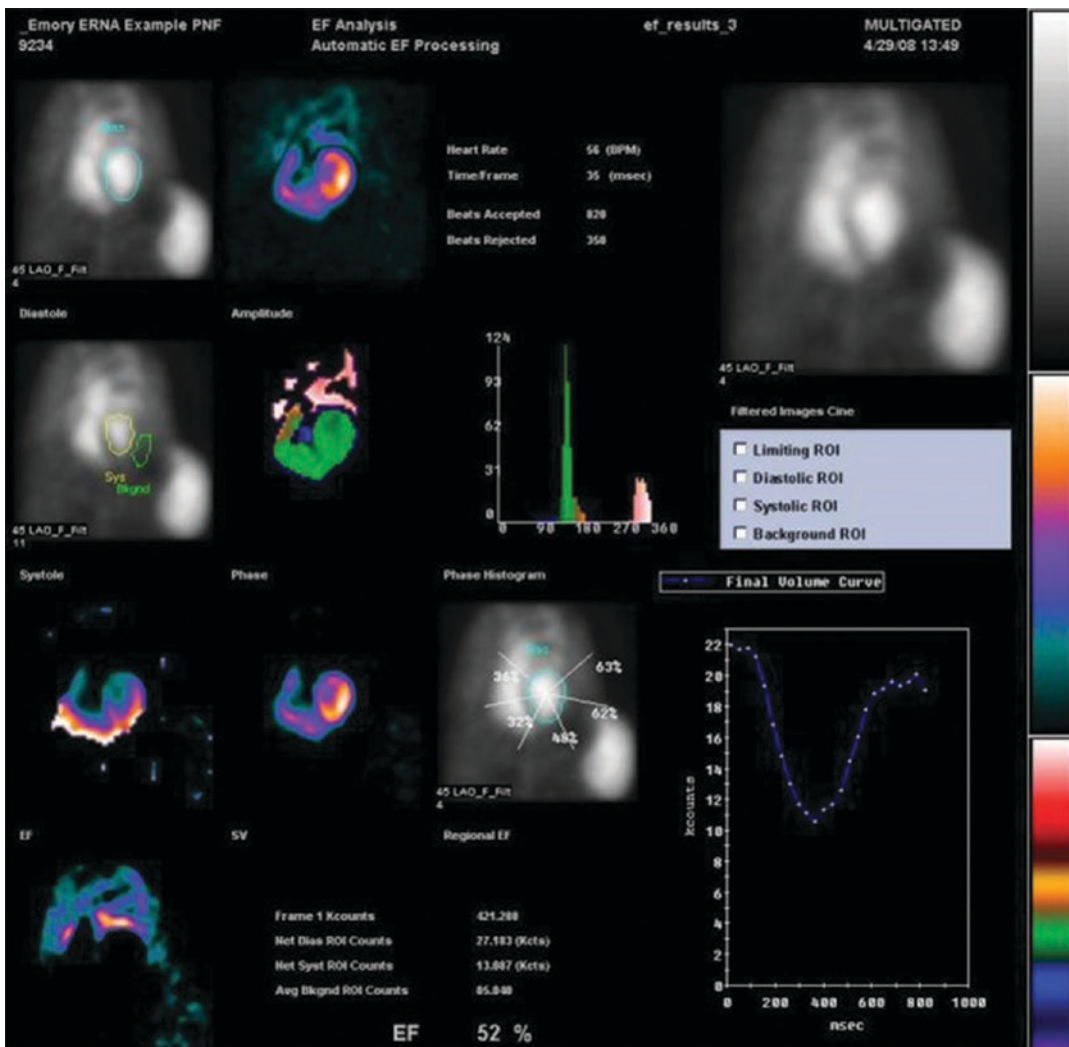
Fig. 15.24   Normal MUGA example

cal aneurysm. Notice that the phase image is no longer a single color and the histogram has broadened a little. More recently, phase analysis information extracted from gated SPECT or PET studies [15, 21, 22] has proven useful in evaluating patients being considered for Cardiac Resynchronization Therapy (CRT) [23–28]. Figure 15.26 shows the normalized phase polar-

maps and histograms from two different studies, a normal study (top) and an abnormal study (bottom). Note how the normal study has a tall, narrow, well-defined peak, indicating that the left ventricle is very synchronous. In contrast, notice how the abnormal study has a very broad diffuse distribution, indicating that the left ventricle is severely dyssynchronous.
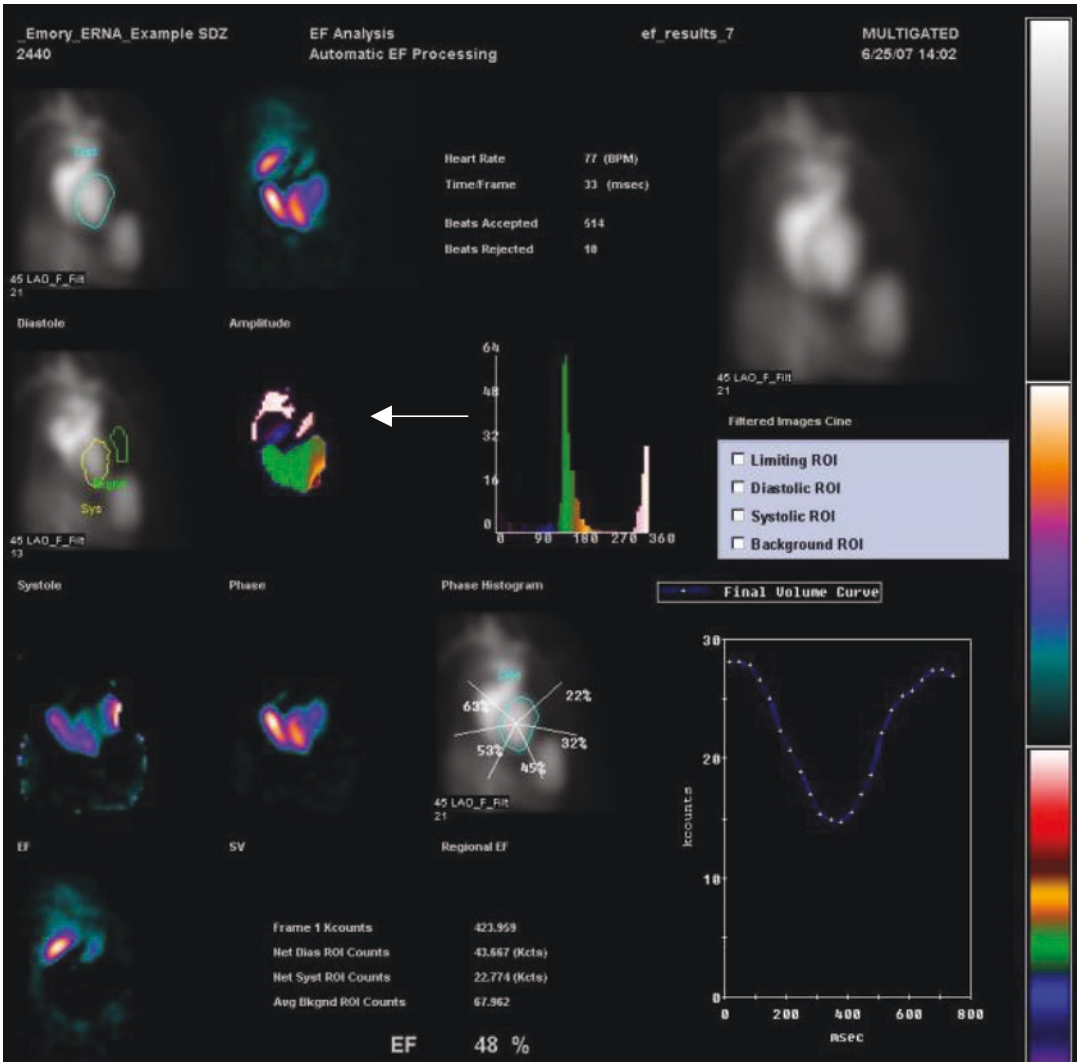
Fig. 15.25 MUGA example showing an apical aneurysm (arrow)

15.6 Region of Interest Analysis

Generally, quantitative measures from nuclear medicine images are obtained only from certain important regions; these are called regions of interest (ROIs). If the region is three-dimensional (3D), the term "volume of interest" is sometimes used (VOI). A ROI can be, for example, a tumor in an oncologic image, the kidney in a renal image, or the myocardium in a cardiac image. Measurements may be taken from the count val-

ues within the region; for example, the mean and maximum count values can be computed. They may also be taken from the shape of the boundary of the ROI; for example, the number of pixels within it, or its size may be determined. Obtaining an appropriate, or accurate, ROI is one of the most basic steps in image quantitation. In some cases, geometric ROIs, such as an oval or circle, may be appropriate. It is always possible to interactively trace the region of interest, and this is still probably the most common approach. An expert
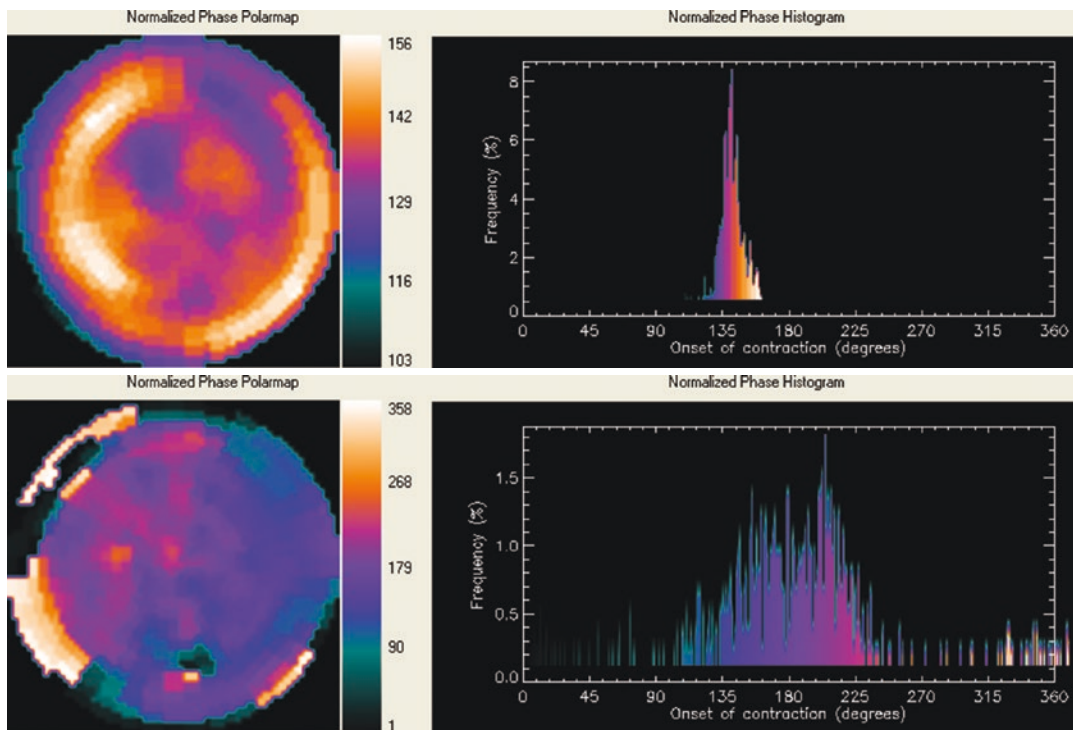
Fig. 15.26 Examples of phase analysis from gated myocardial perfusion SPECT studies. Top: normalized phase polarmap and histogram from a normal study, note how tall and narrow the histogram is, indicating that the ventricle is very synchronous. Bottom: normalized phase polarmap and histogram from an abnormal study, note how spread out the histogram is, indicating severe myocardial dyssynchrony

user can use his or her knowledge of the expected shape of the organ along with the appearance of the image to obtain a good boundary. These two approaches are shown in Fig. 15.27. However, interactive processes are associated with significant inter and intraobserver variability, they are time-consuming, and there are not always experts available to perform the task. For that reason, automatic methods may be helpful, if only to aid the user in performing the interactive tracing.

15.6.1 Background Subtraction

In planar images, counts through the entire body are acquired, from soft tissue both in front of and behind the organ of interest. Accurate quantification of the counts within the organ may only be obtained if these counts can be eliminated from the organ ROI; this is called background subtrac-

tion. The most common approach for background subtraction is to find a region in the image that is near to, but not in the organ ROI, with no obvious additional high-count structures. A background region can be drawn interactively or automatically in this area. The mean counts per pixel are determined, and this value is subtracted from every value in the image. More complicated background regions can be drawn as well; for example, an oval shell, or doughnut, can be used to surround the kidney in renal images. In this case, when the background region extends from one side of the organ ROI to the other, values within the background may be interpolated from the edge values to account for a varying background. The resulting 2D map of background values is then subtracted pixel by pixel from the organ ROI. An example of this is shown in Fig. 15.28; there, the background was automatically generated in a renal processing program.
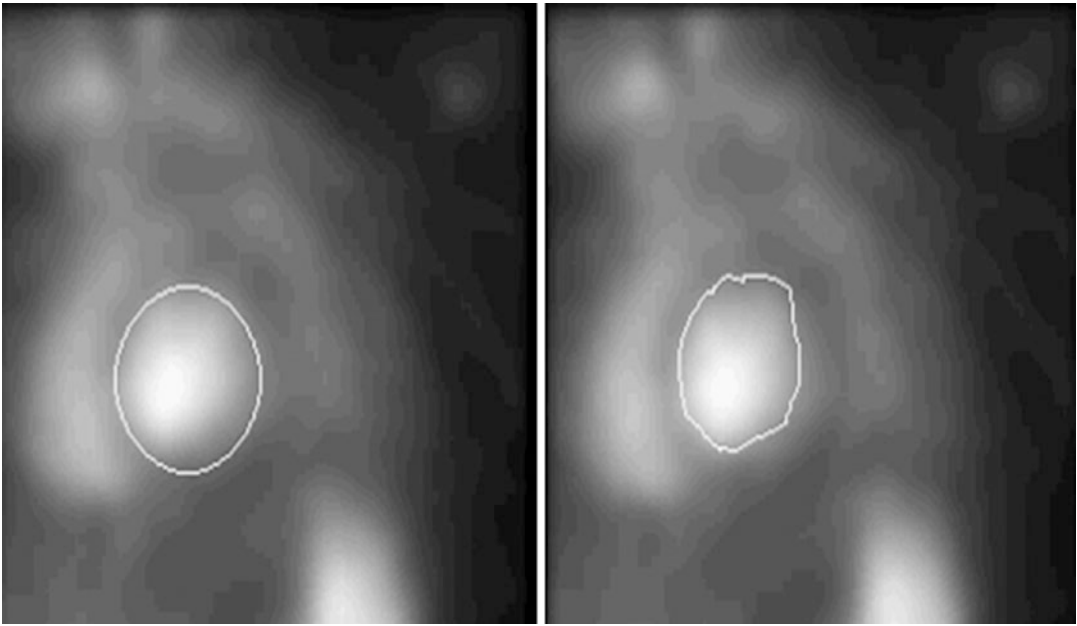
Fig. 15.27 Examples of a geometric region of interest (left) and a free-hand drawn region of interest (right) placed around the left ventricle in a radionuclide ventriculogram, or MUGA study
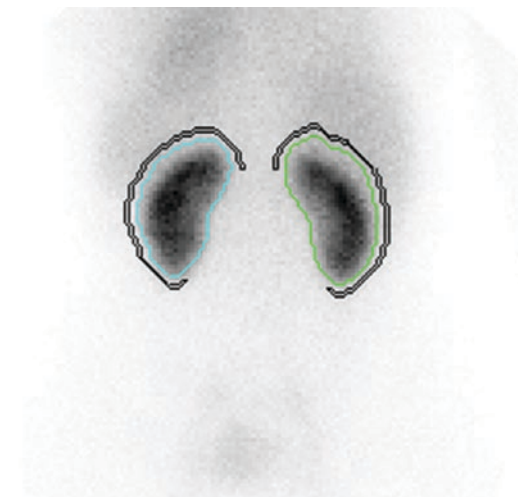
Fig. 15.28 An example of automatic ROIs placed on a renal image. The kidney ROIs are determined by a complex algorithm using expected location, image intensities, and edge detection in polar coordinates. Note the rather crescent-shaped background regions placed at the lateral edge of each kidney. Their shapes are based on the detected kidney ROIs, and are a single pixel thick

15.6.2 Time–Activity Curves

In much of nuclear imaging the changes in radiotracer concentration over time due to mechanical or physiological processes can be more important than visualization of anatomy. The primary tool for analyzing these changes are Time Activity Curves (sometimes abbreviated as TACs) which represent the counts in a region of interest of a dynamic image graphed over time. Examples of widely used time activity curve analysis include estimation of filling and clearance of radiotracer from the kidneys in renograms, left ventricular volume changes of gated blood pool studies of the heart and calculation of myocardial blood flow from dynamic PET studies.

Renogram curves are time activity curves of a radiopharmaceutical as it transits the kidney. Used for the diagnoses of renovascular disease, the curves are used to evaluate the kidney uptake and washout of radiopharmaceuticals with key factors being the time to the peak height of the
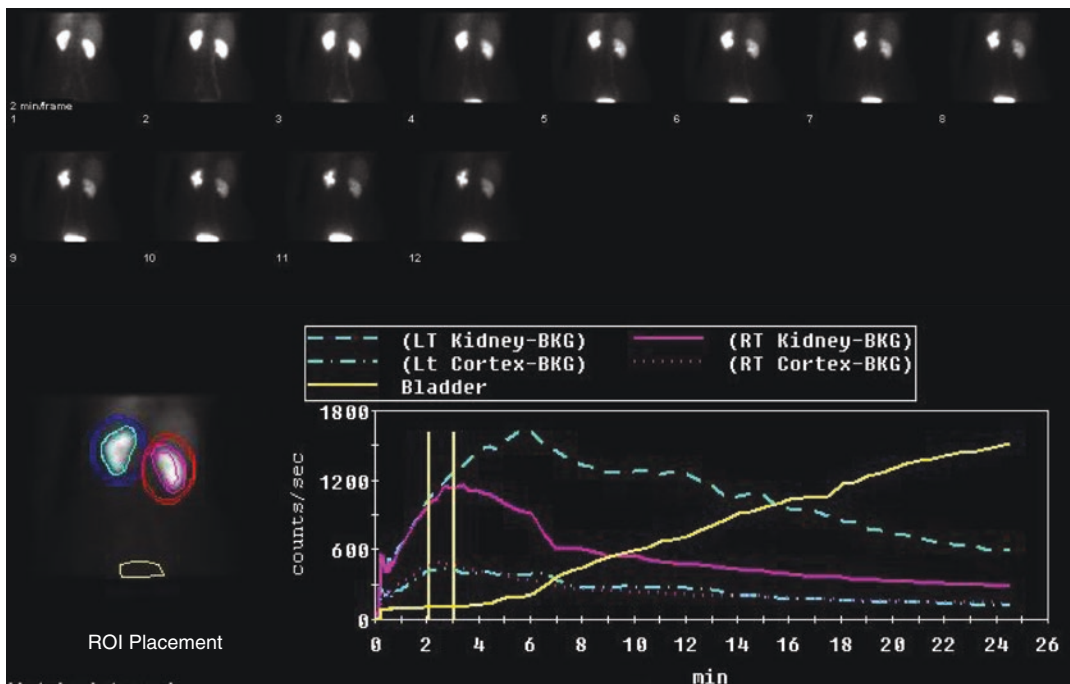
Fig. 15.29 ^{99m}Tc MAG3 renogram curves for each kidney are extracted from ROIs placed over the kidney, the renal cortex (along the outside rim of the kidney), and background. An ROI is also placed over the bladder. This image shows the clearance phase of the renogram, and each frame represents a 2 min interval. The uptake phase of this renogram is shown in Fig. 15.5. With 2 s per frame, counts from the uptake phase are shown in the first 30 s of the curve in this figure. Counts extracted from the kidney ROIs are background corrected before plotting. Counts extracted from the bladder ROI increase throughout the study as the tracer is cleared from the blood by the kidneys. (The authors would like to acknowledge Raghuveer K. Halkar, MD, Emory University, Atlanta, GA, for his assistance with this figure)

curve after injection (T_{max}), the time it takes for the activity in the kidney to fall to 50% of its peak value and the relative uptake values between the left and right kidneys ($T_{1/2}$) [29]. Since T_{max} is much shorter than $T_{1/2}$, the dynamic renogram is usually acquired in two phases with 1–3 s frames from the first 60 s and 1–3 min intervals for the remainder of the study. The rapid frame rate of the first phase allows the evaluation of the rapid uptake of the radiopharmaceutical as the kidney clears it from the blood. The second phase uses longer frames to evaluate the washout of the radiopharmaceutical from the kidney. The key ROIs are those placed over the kidneys and background (which may be elliptical around the whole kidney or crescent shaped as described earlier) but ROIs over the bladder and aorta may also provide useful information [30, 31]. The generation and analysis of renogram curves is shown in Fig. 15.29.

Gated blood pool studies (equilibrium radionuclide angiography) of the heart provide a great deal of information about regional heart motion and other factors, but the single most important calculation is that of the ejection fraction calculated from a time activity curve of the left ventricle [29]. The EKG R-to-R interval is usually divided into 24 time segments, each with a corresponding scintigram representing the distribution of blood (which has been labeled with a radiopharmaceutical) at that time in the cardiac cycle. ROIs are drawn over the left ventricle of the heart at
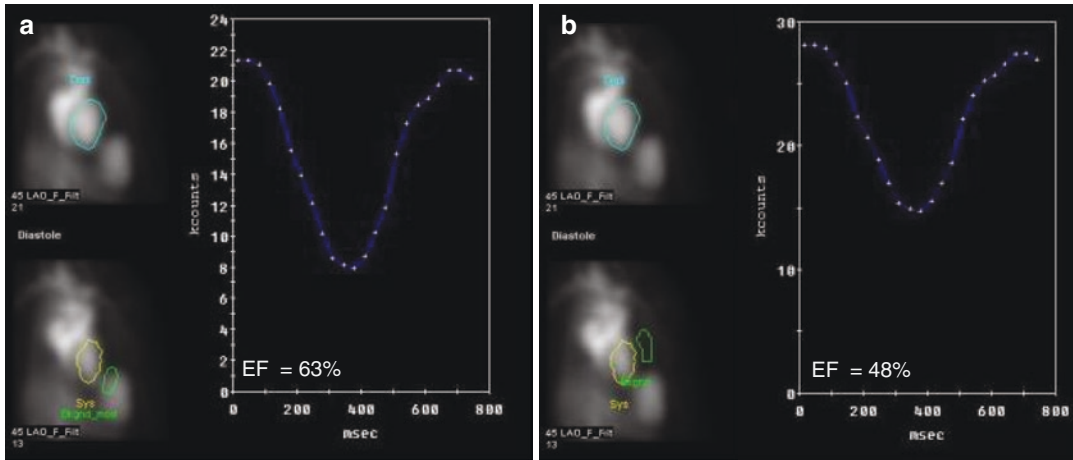
Fig. 15.30 Gated blood pool volume curves are extracted from ROIs drawn over the blood pool of the left ventricle of the ERNA study shown in Fig. 15.5. The volume curve represents background corrected counts at each of the 24 frames or segments of the cardiac cycle. Care must be taken in the placement of the background ROI, since the counts from this region are used to estimate the non-blood pool counts in ventricular ROI. In panel (**a**), the background ROI is placed in a standard location but overlaps the spleen which has an unusually high concentration of activity. The resulting over-subtraction of background gives an artifactually high estimate of the ejection fraction (EF). In panel (**b**), the background ROI is placed in a more appropriate location for this patient and a much lower EF is calculated. (The authors would like to acknowledge Raghuveer K. Halkar, MD, Emory University, Atlanta, GA, for his assistance with this figure)

end-diastole (and preferably at each of the intervals) [32] and counts are extracted. Displayed as a curve, the graph represents the change in volume of the left ventricle at that time in the heart's cycle. The assumption is made that the counts extracted from the ROI are proportional to the volume of blood in the ventricle. To improve the accuracy of this assumption counts from the ROI that may originate in front of or behind the heart are estimated using a background ROI drawn over an area near the heart but not over areas of significant blood pool. The counts per pixel in the background ROI are calculated, and subtracted from the counts in the volume curve. Selection of a proper background ROI is critical to the calculation as over-subtracting background can falsely elevate the ejection fraction as shown in Fig. 15.30.

Myocardial blood flow studies of the heart use kinetic modeling to estimate the flow of blood from the coronary arteries into the myocardial tissue [33]. The kinetic modeling makes use of several time activity curves extracted from volumes of interest in the dynamic PET studies. These volumes of interest are generally divided into two distinct regions: (a) a small arterial input region (~10 mm sphere) placed near the left atria at the level or just above the mitral valve and (b) a tissue region encompassing the myocardial tissue of the left ventricular walls. An example of these TACs and the resultant myocardial blood flow is shown in Fig. 15.31; the actual math behind these calculations can be found in Chaps. 20 and 21.

Regardless of how time activity curves are generated there are a number of techniques that maybe used to analyze the data they contain. If the frames are acquired very quickly or there is little activity in the ROI, it may be necessary to use curve smoothing algorithms to reduce the noise in the curve. If the underlying processes behind the changes in activity represented by the time activity curve are understood, curve fitting techniques may be used to glean further information from the curve.
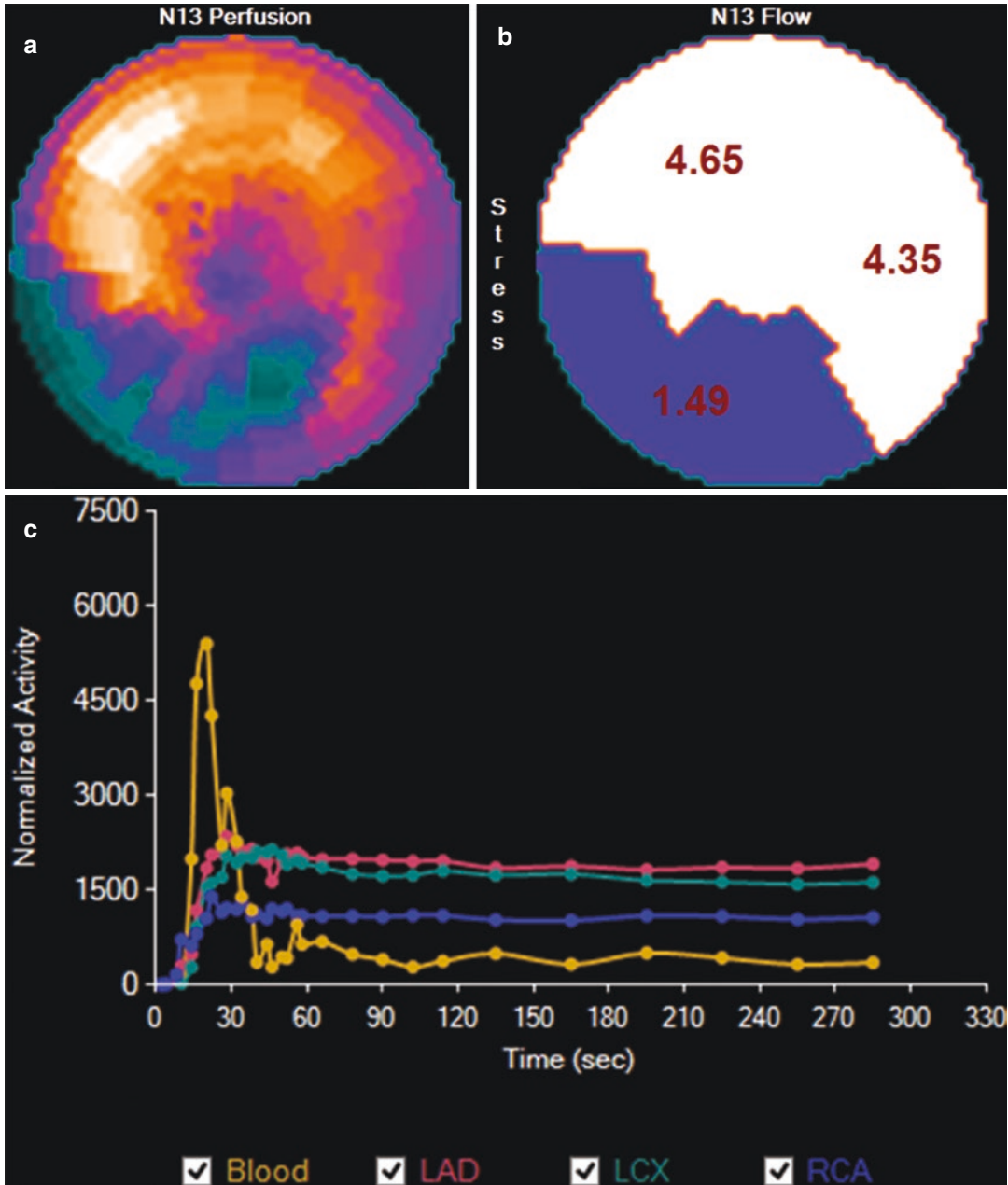
Fig. 15.31 Absolute myocardial blood flow from a myocardial perfusion PET scan of a patient with a large inferior wall perfusion defect. (**a**) Polar map of stress NH3 perfusion. (**b**) Polarmap of stress LAD, LCX and RCA coronary territory flow, note the greatly reduced stress flow in the RCA territory (inferior wall, flow = 1.49 mL/min/g). (**c**) Time activity curves for the arterial input function (gold), the LAD tissue (red), the LCX tissue (green) and the RCA tissue (blue)

15.7 Image Segmentation

15.7.1 Thresholding

It may be possible to find a pixel value above which everything is in the region of interest, and below which everything is background. Such a pixel value is called a threshold. Thresholds can be set interactively, but a few methods for obtaining them automatically have been proposed. In some cases, setting a single threshold at a known percentage of the maximum pixel intensity may suffice. Multiple thresholds, for example, one every 10%, can be used to create isocontours; this may give the user an idea of which threshold is the correct one to define the ROI. These approaches are shown in Fig. 15.32.

Another simple approach is to use a histogram of pixel values, so that a graph of number of pixels vs. pixel value is obtained. In some images, for example, brain images, the histogram will be bimodal. A high peak will exist at low pixel values, indicating background pixels; a second peak will occur at higher pixel values, indicating brain pixels. The valley between the two peaks can be used as a threshold to separate brain from background. In other images, where more than one structure is higher in intensity, it may be possible for the user to select which structure is most important. The result of thresholding is an image where all areas above the threshold are set to 1, and all areas below are set to 0. An example of this type of approach on a single slice of a brain perfusion image is shown in Fig. 15.33. Finding the boundary of the region containing 1's can be performed using the edge tracking method described below, for example.

While most thresholding operations are too simplistic to be widely applicable in defining ROIs,
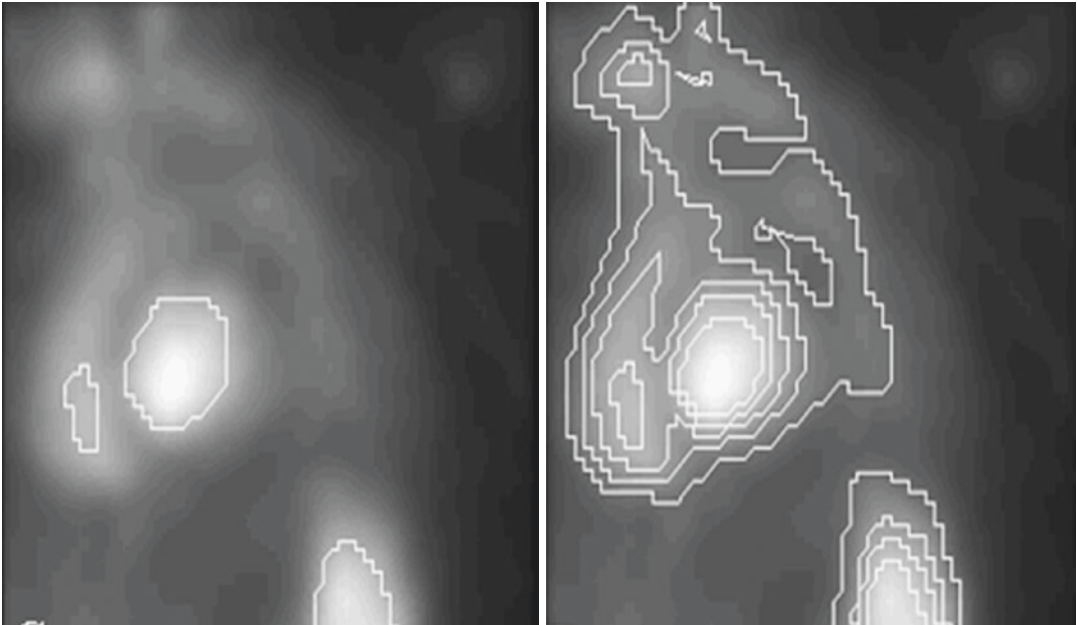
Fig. 15.32 Example of threshold-based regions of interest placed in the same study as Fig. 15.1. A single threshold of 50% (left) creates multiple regions of interest; however the user can indicate which is important. Use of multiple thresholds (right) provides isocontours that allow the user to choose more accurately the correct threshold to outline the heart
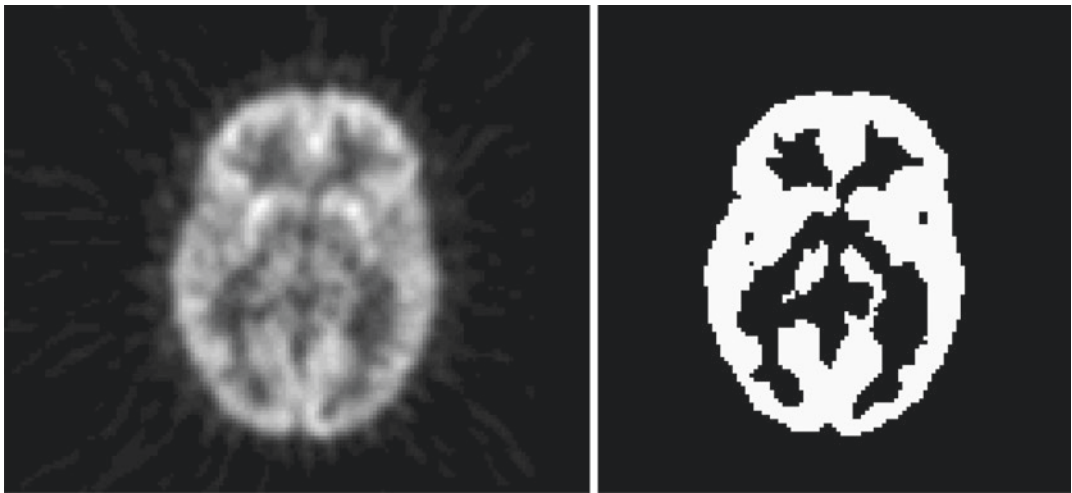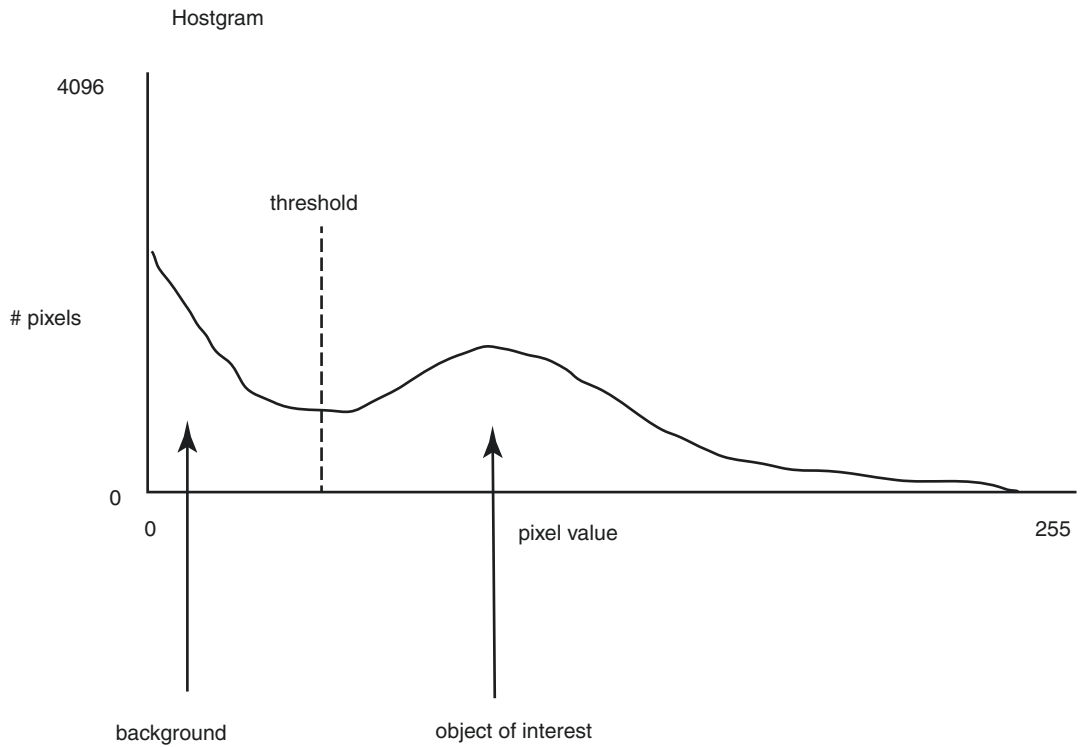
Fig. 15.33 A histogram of image intensities in a slice of a PET FDG brain image (top) shows a bimodal distribution. One peak occurs in the background pixel intensities, and another is seen in the gray matter pixel intensities. Choosing a pixel intensity between these two peaks allows the background to be separated from the object of interest, in this case, the gray matter. The original image and the result of the thresholding are seen at the bottom of the figure

they often are used as an important step in a more complicated processing algorithm. One application where thresholding is particularly important is tumor delineation [34–36]. Again, additional processing is usually applied; however, given that there is rarely any a priori information about tumor shape or location, image intensity is often the most important factor in defining its boundaries.

15.7.2 Edge Detection

Edges of structures in images are generally defined points of quick intensity changes, or high intensity gradients. A portion of the image that falls rapidly from a high value to a low value is often taken to be the edge of a structure. High-pass filtering, or image sharpening, brings out these regions of changing intensity. However, in a complete image slice, there are usually many edges not associated with the region of interest. Conversely, some edges of the ROI may not actually have strong intensity changes associated with them, particularly if there are low pixel values associated with some physiological process or abnormality. Some method of following the correct boundary is necessary. The problem is, given a potential point on the boundary, or seed, to successively follow the contour and create a closed boundary. This is generally posed as a search algorithm; that is, finding the best contour given some specific constraints that act as a cost function that is to be optimized. Moving from the seed pixel onward, a boundary "cost" is accumulated associated with the possible neighboring pixels that may be chosen as the next boundary point. Typical cost functions might include edge magnitude and direction, curvature of a segment, or closeness to a known average contour. One sophisticated approach is described generally for 2D medical image boundary detection [37]; however, note that edge following in 3D becomes much more complicated, and is infrequently used.

15.7.3 Model-Based Approaches

If the expected shape of the region of interest is known, then it may be possible to locate the ROI by fitting a model of the object to the image. This model may be obtained for example by hand tracing numerous training images and finding the average shape of the ROI. The model may be as simple as a new image containing nothing but this average shape with its values set to the average values obtained from the training set. In one simple approach, registration techniques may be used to fit the model to the new image containing the object. The model is shifted, rotated, and scaled over all possible locations in the new image, and a measure of the match is computed at each. It may even be nonlinearly warped to match the new image. A common metric for evaluating the goodness of the match is the sum of the squared differences between the template and the image. This difference should be small when the model matches well with the image. In a second more complicated approach, the boundaries of the model may be iteratively adapted so that it better fits the object of interest. Constraints on the boundary may be used so that they do not stretch too far beyond the original model and that they maintain a smooth surface. In fact, fitting of the model may also be posed as a registration problem. At any rate, the goal of fitting the model to the image in this manner is to be able to use the boundaries of the transformed model as the boundaries of the ROI in the new image. This approach is becoming more and more common in 3D, as it is able to encode complicated 3D shapes as well as variances in image intensities. When shape is included, the model may be called an active shape model; when it includes image intensity, it may be called an active appearance model.

Most model-based approaches have focused on the brain and heart [38–42]. Often, they were developed as part of a first step in finding abnormal regions of perfusion or metabolism. The model is used to segment a set of normal studies, and then normal ranges within the model ROIs are determined. When a test subject is segmented with the model, the values within the model ROIs can be compared to the normal values in order to automatically determine any regions of hypometabolism or hypoperfusion. Figure 15.34 shows how this approach has been used in quantitation of brain FDG images.
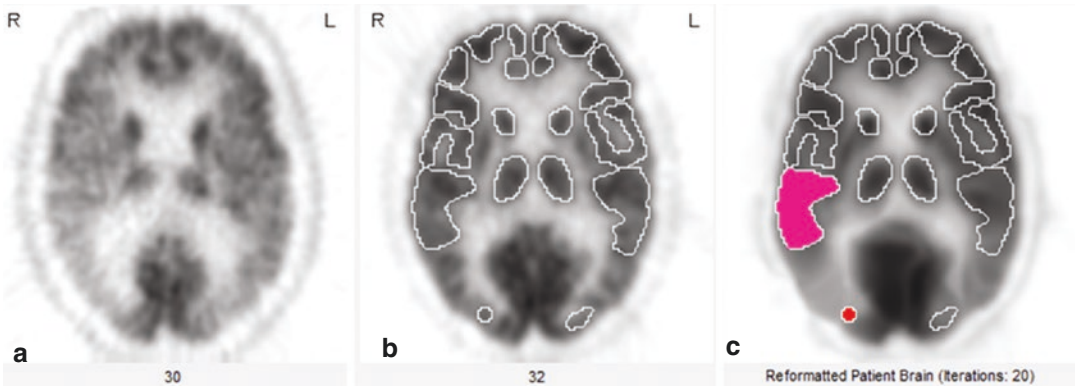
Fig. 15.34 An example of a model-based approach for defining ROIs on a PET FDG image of the brain. (**a**) One slice of a patient's FDG brain image. (**b**) One slice of the "standard", or model, normal FDG image. Regions of interest have already been defined on this standard. (**c**) The patient's image is aligned to the standard, and the ROIs from the standard can then be placed over the patient's brain

15.7.4 Application-Specific Approaches

Most automatic quantitative programs use very application-specific techniques to isolate the region of interest. This is simply because encoding more specific information into the boundary detection algorithm tends to make it more accurate and more robust. One very common method for automated boundary detection in cardiac imaging, for example, is to perform the operation in polar (for 2D), spherical, or cylindrical (for 3D) coordinates. In this approach, the origin of the coordinate system is placed inside the region of interest. This may be done interactively or automatically. Searching along rays that extend from this origin at set angles, points of high intensity or of high gradient are determined. High intensity points might be used when searching for the mid myocardium in perfusion images, while high gradient points might be used when searching for the edge of the ventricular chamber in blood pool images. Because the radius of the boundary should not change greatly between neighboring rays, the search can be constrained, and the boundary can be forced to be smooth. Searches can be limited by placing constraints on how far the ray can extend, and filtering the radii after the boundary detection can further enforce smoothness constraints. This sort of approach is used frequently in organs that are primarily con-

vex, such as the kidney, the brain surface, and the heart [43, 44]. In addition, note that this approach provides a simple way to find the boundary of a thresholded object, given that the object is mostly convex. Figure 15.28 shows an example of how this approach has been applied to find kidney ROIs as a first step in quantitation of renal function [45].

15.8 Three-Dimensional Displays

15.8.1 Surface Rendering

Three-dimensional graphics techniques can be used to display both the structure and function of organs visualized in nuclear medicine. If the organ of interest has been accurately segmented using edge detection techniques, then the resulting boundaries can be used to create a 3D surface onto which information about detected counts can be overlaid. The 3D surface may be generated by connecting points of the detected boundaries into triangles, or in some cases quadrilaterals. Various algorithms exist to perform such triangulations. If the result of edge detection is a set of points, the theoretically most efficient triangularization is called a "Delauney" triangularization [46]. If the result of the edge detection is a binary image, perhaps obtained by thresholding, then an efficient algorithm for generating the triangles of the sur-

face, such as the marching cubes algorithm, can be used [47]. However, if a systematic approach has been used for the edge detection, often a standard triangularization will be sufficient. For example, if the boundary can be divided into the same number of points in each slice of the organ, then connecting the points into triangles is simple. Color can be assigned to each vertex of the triangles in numerous ways. In brain imaging, perfusion or metabolism may be estimated by sampling perpendicularly to the detected surface at each triangle vertex and determining the count value just inside of it. The LV epicardial surface can be color coded with the maximum values obtained at the middle of the myocardium; this is straightforward if both epicardial surface detection and mid-myocardial maximum count determination are done using the same spherical coordinate system, for example. Once a set of triangles with vertex colors has been generated, standard software programs are used to display them. Such displays can routinely be rotated in real time and viewed from any angle with current computer power. Sophisticated effects, including highlights, reflection, and transparency may be easily applied. The mathematics behind these effects, as well as a much more detailed discussion of surface rendering can be found in the book by Foley and Van Dam [48]. Such displays have the advantage of showing the actual size and shape of the organ, and the extent and location of any defect. Some studies have shown that the 3D models displaying left ventricular perfusion are more accurate for evaluating the size and location of perfusion defects than polar maps [49] or slice-by-slice displays [50]. Figure 15.35 shows a typical surface rendering of the left ventricle, color coded for myocardial perfusion.

15.8.2 Maximum Intensity Projection

A second approach to creating 3D displays from cardiac images generates the myocardial boundaries directly from image voxels without explicit boundary detection. The most useful technique employed in nuclear medicine is maximum intensity projection (MIP) developed by Wallis et al. [51]. Maximum intensity projection
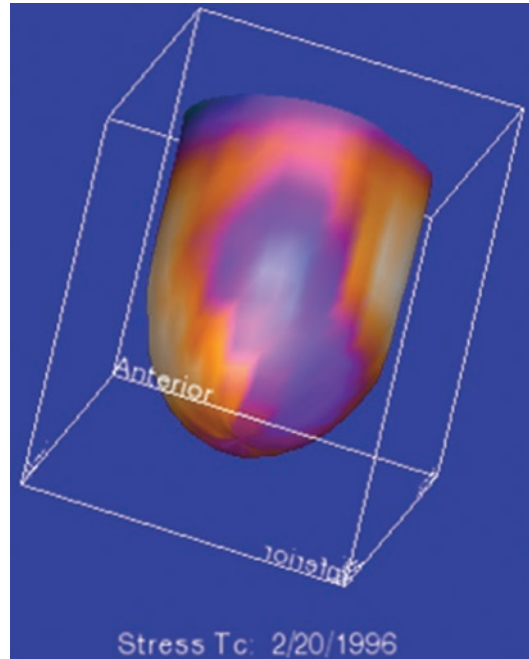
Fig. 15.35 A surface-rendered 3D display created from a SPECT myocardial perfusion study. Once the epicardial and endocardial surfaces have been detected (i.e., a myocardial ROI has been defined), the x, y, and z values of the epicardial surface can be connected into a triangle mesh. The colors used to shade each triangle are based on the maximum values of the perfusion image between the epicardial and endocardial surface at each epicardial point

involves rotating the 3D tomographic volume into a desired viewing angle and extracting the maximum pixel along each row and column of the rotated volume onto a 2D image plane. To enhance the 3D effect of the image, the volume can be depth-weighted so that pixels extracted from the front of the volume are scaled more highly than those extracted from the rear of the volume, even if their original intensities were equal. This emphasizes structures in the front of the volume. Since the maximum pixel is always extracted, this type of volume rendering is very useful in blood pool imaging [52] as well as other hot-spot imaging procedures. Although not directly applicable to cold-spot imaging, a variation of this technique has been successfully applied to liver-spleen imaging and brain perfusion imaging [53]. This variation consists of blurring the original image using a 3D filter

and subtracting the blurred image from the original image. The resultant dataset is then rendered using MIP as described above.

15.8.3 Volume Rendering

While maximum intensity projection techniques may be considered a simple type of volume rendering, generally the term implies a much more complicated algorithm. Like maximum intensity projection, however, volume rendering techniques do not need explicit boundary detection or creation of geometric surfaces. While volume rendering techniques are more useful when used with MRI or CT data, it is useful to understand the methods given the current interest in combined PET/MR, PET/CT and SPECT/CT scanners. Volume rendering is a 3D graphics technique first described by Drebin et al. [54] which provides very realistic appearing visualizations. For a volume of data, such as a stack of 2D tomographic slices, one assigns to every pixel value a transparency, a color, and a reflectivity. The visual process is then simulated by recreating the physical process of light traveling through or bouncing off the pixels that it encounters as it travels through the volume. For any given volume of data, the main problems involve the correct assignment of the pixel properties. Selecting a pixel intensity threshold above which everything is opaque, and below which everything is transparent, for example, will provide a 3D image with hard surfaces at that threshold. In nuclear medicine, the use of such a threshold often results in normal pixels being assigned a value of 1, and abnormal pixels being assigned a value of 0, so that the 3D display depicts a "hole" in the surface. Such techniques have been used primarily in brain images; however, they have also been applied to cardiac images. Unfortunately, very few medical images are accurately segmented with such simplistic threshold techniques, and note that the size of the abnormality, or hole, is completely dependent on choosing the right threshold. CT images are in fact probably the best adapted to this simple method of assigning pixel properties, since Hounsfield units are related to the electron density of particular tissues, and thus, bone can be made opaque and white, while muscle tissue can be made translucent and red, for example. In fact, a basic 3D display method similar to volume rendering was described quite early for use in CT images by Hoehne et al. [55]. While volume rendering of bone in CT images is generally quite robust, most 3D displays of soft tissue generated from CT require large amounts of preprocessing to remove unwanted structures or improve the segmentation. The accuracy of this preprocessing is generally related to the quality of the images, and user intervention may be required to produce a useable 3D display. In addition, large amounts of memory and processing power are required for volume rendering of large datasets. Nevertheless, the realism, high resolution, and flexibility of volume renderings give them an advantage over surface renderings in many cases; this can be appreciated in Fig. 15.36.
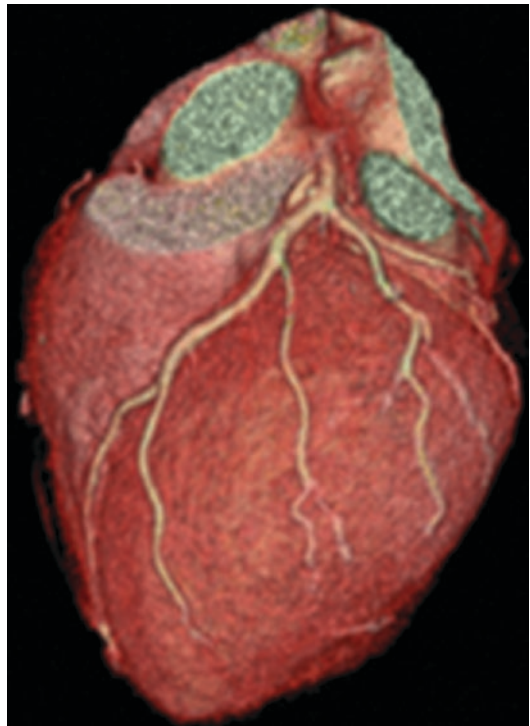
Fig. 15.36 A cardiac CT study may be volume rendered by assigning colors and transparencies to the Hounsfield units within it, and then reproducing the effect of light being transmitted and reflected from it. In this case, sophisticated segmentation and additional user interaction must be used to eliminate non-cardiac structures from the CT prior to 3D rendering

15.9   Principles of Image Registration

As mentioned above in the model-based approach for segmentation, alignment of a pre-segmented model with a specific patient's image can be used to find regions or volumes of interest in the new image. In addition, alignment (also called registration or fusion) is often used with nuclear medicine for other important purposes. Low resolution nuclear medicine images are aligned with higher resolution anatomic images of the same patient to help identify the exact location of a hot- or cold-spot in the nuclear image. In this application, it may be sufficient to transform the test image using only linear transformations. Also, in order to use many quantitative programs, the patient's specific nuclear image must be put into a standard space. More and more, this standardization implies that the test image is being aligned to a standard, or atlas, image. In this application, frequently a nonlinear warping transformation is needed.

Registration is generally posed as an iterative optimization problem. The differences between two images are to be minimized over some transformation. Thus, two separate pieces of software are needed: one to measure the difference, or cost function, and a second to determine how to change the image with respect to the standard to reduce this difference function at each iteration.

While there are many options for computing the cost function, a very popular approach is called the mutual information criterion [56, 57]. Mutual information can be described as the joint histogram between the two images. When two images are perfectly aligned, the joint histogram should ideally only exist along the line of identity. As the images are moved away from each other, the joint histogram also spreads out. Mutual information is a measure of the spread of the joint histogram. An example of this can be seen in Fig. 15.37.

For linear registration, that is, registration that includes only translation, scale, and rotation, generally closed form optimization methods are used to iteratively find the transformation that optimizes mutual information between two images. One such method is the Newton–Raphson method, which finds the roots of the
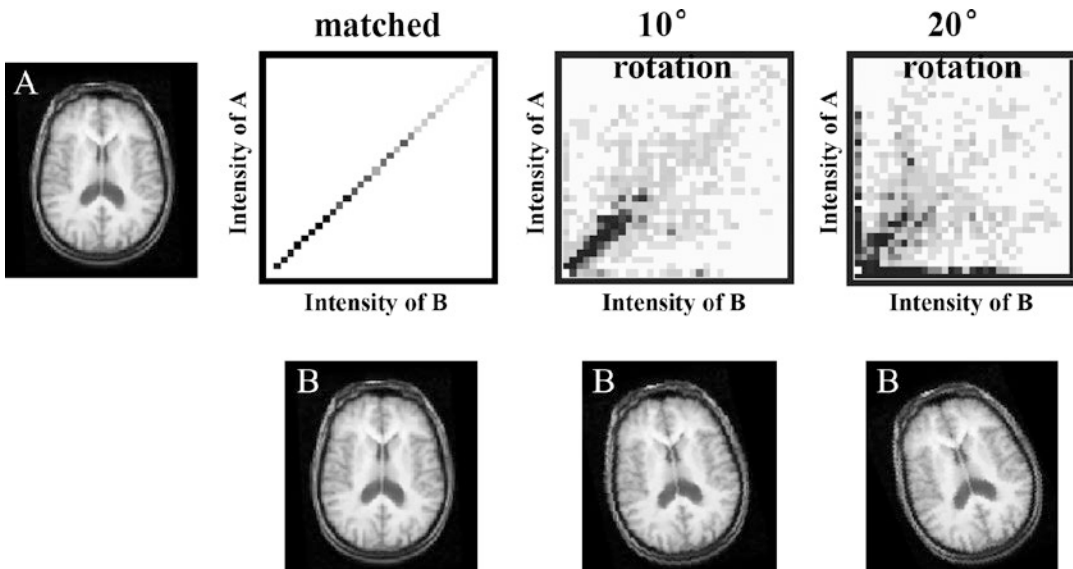
Fig. 15.37 Mutual information criteria for image registration. Image (**b**) is to be aligned with Image (**a**). At each rotation of (**b**), the joint histogram is created. When the images are in exact alignment, the joint histogram only has values on the line of identity. As the images are rotated more and more out of alignment, the joint histogram becomes more diffuse. Mutual information is a measure of the spread of the joint histogram
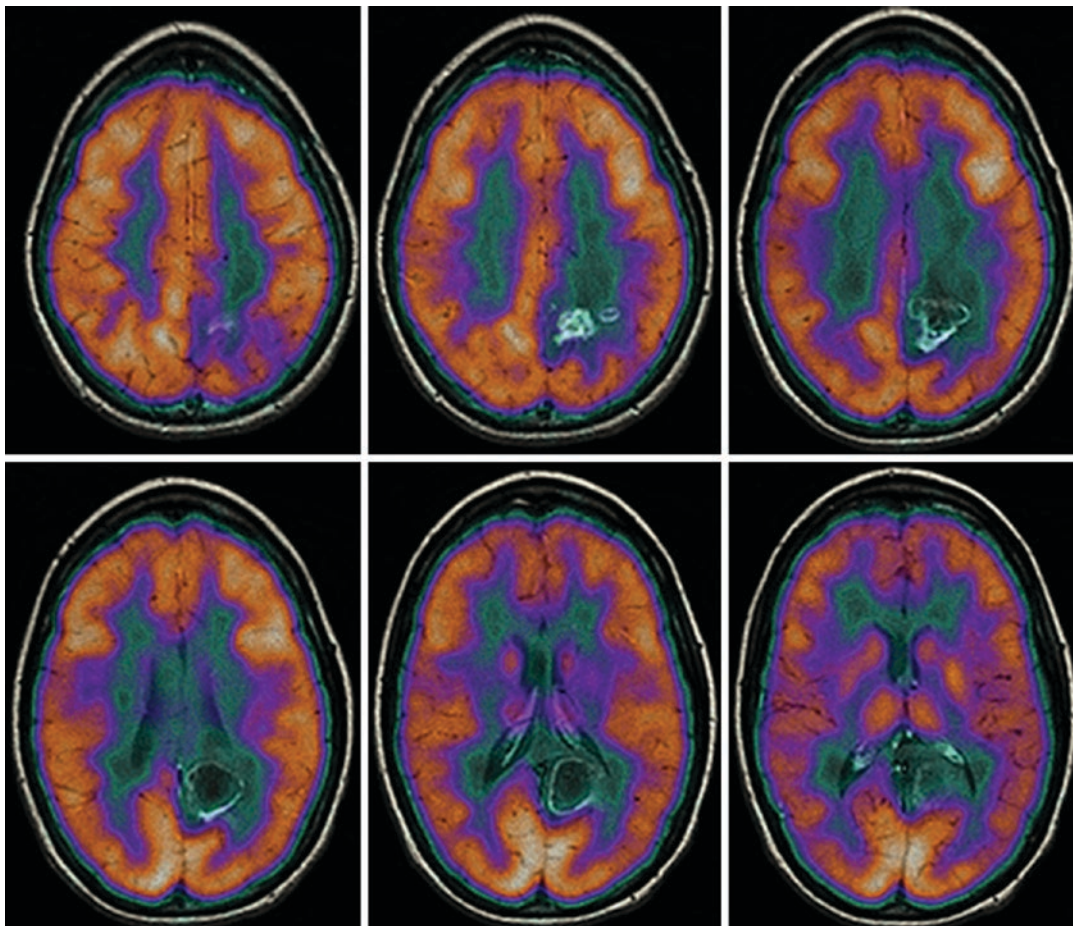
Fig. 15.38 An example of using linear registration to align a PET brain image to an MRI of the same patient. A function based on the ratio of the image pixel values was used as the difference measure, and this was minimized using a Newton-Raphson method. In this image, the PET is overlaid in color over the gray scale MRI

derivative of the cost function, which occur at function minima. Woods et al., used this method in early work aligning PET brain images to MRI, and an example is shown in Fig. 15.38.

For nonlinear registration, or warping, the challenge is to find a good match between the images while making sure that the warping is smooth. This can be achieved by adding a regularizer, or smoothness constraint. For example, the warping can be constrained to be elastic, so that small deformations are easily achieved, but larger movements are "penalized", as they require more "force", similar to any elastic deformation. This is the approach taken by Bajcsy et al., in early work aligning MR brain images

[58]. Other constraints based on the known physical properties of the objects being aligned may be used to help find a good solution to the warping problem. For example, it is possible to constrain all deformations to be volume preserving, so that pixels can change shape but must keep their original volumes, as suggested by Haber et al. [59]. Minimization of these more complicated functions may be attained by posing them as Euler-Lagrange equations, whose solution is a local optimum. An example of warping a brain image to match an atlas was shown in Fig. 15.34.

However, nonlinear warping has some major drawbacks. First, it can be quite time-consuming, especially for large images. One additional

source of computational complexity is the non-linear interpolation required. For example, a method such as thin plate splines may be required to interpolate multiple unevenly spaced points to new, unevenly spaced pixel locations [60]. Another problem is that if the proper constraints are not used in the warping algorithm, physically impossible deformations may occur. Parts of the image may "fold" onto one another, or more than one point may be mapped into a single location. Finally, it is very difficult to evaluate the results of a warping algorithm. What may look like a reasonable deformation may not be accurate, as there is often no "ground truth". The user should be sure to accept nonlinear alignments only after careful assessment.

15.10 Image Normalization

As mentioned in the above section on Image Presentation, images that are acquired in Nuclear Medicine are generally constructed from the counts that are received at each individual pixel. This means that the counts in each pixel are relative (or related) to each other and the actual activity being measured in the object; however without additional processing these counts are not absolute in nature. Furthermore, there may be some physiologic phenomena that occurs that obscures the object of interest.

15.10.1 Extra-Object Activity

In Cardiac SPECT, it is not uncommon for the gall-bladder or a loop of bowel to have more activity than the heart, thereby causing the heart to appear reduced in the images. Figure 15.39 shows a cardiac SPECT study where a loop of bowel (seen in the bottom of the image) is much brighter than any of the pixels in the heart, thereby causing the counts in the heart to seem very low. To correct this problem, the study needs to be "normalized" to the counts in the myocardium, and not the counts in the entire image. This normalization (or scaling) process simply rescales the image such that the maximum displayed value is now equal to the maximum in the heart, instead of the maximum in the image or volume. In this example the maximum activity in the bowel was 839 counts and the maximum activity in the heart was 530 counts. Figure 15.40 shows the same image scaled to the maximum of the myocardium, instead of the maximum of the volume. Notice how the loop of bowel is now very bright but the myocardium looks much more normal. This phenomenon can be seen in many different imaging scenarios, such as the bone scan shown previously (Fig. 15.4). Notice how hot the bladder is compared to the rest of the image in the left-hand image. There are several ways to correct for this: (a) masking out the hot bladder and renormalizing to the maximum count in the image, (b) drawing a region of interest around most of the image (but excluding the bladder) and renormalizing to the maximum count in the ROI and (c) using the color table to renormalize the image by setting a new maximum value for display. In this case the display maximum was reset to 100 in the right-hand image, thereby allowing the clinical details in the image to be seen.

15.10.2 Absolute Normalization/ Quantification

Another area of interest and research over the years has been in the area of absolute quantification, or converting the relative counts from the image into absolute measures of activity. Briefly, this involves correcting the image for attenuation, scatter and resolution as well as measuring the counts in the arterial blood supply and then some form of modeling to predict the activity in the target organ. As you can see, this can be a complicated problem, but it can have big rewards. For instance, in Cardiac SPECT, if a
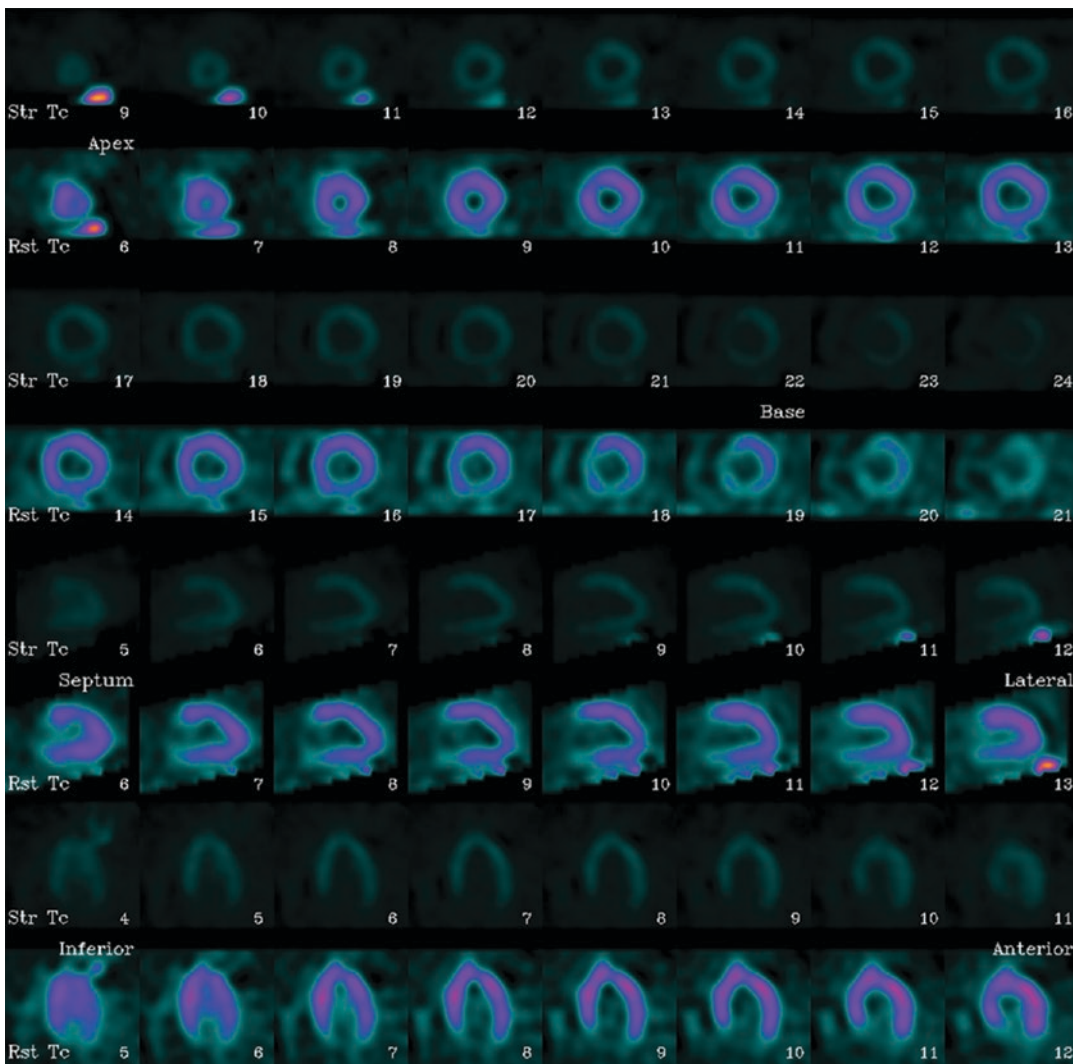
Fig. 15.39 Normalization example, scaled to the maximum pixel in the volume

patient has balanced disease (equal disease in all of the coronary territories), then all of the heart will look "relatively" the same which could easily be interpreted as a normal scan. However, if we could get an absolute measure of the activity in the heart, then we would be able to tell that the activity was below normal and that the scan was actually abnormal, though in "relative" terms it looked normal [61–63].

15.10.3 Normalization for Database Quantification

Because of the "relative" nature of the counts acquired in Nuclear Medicine, one of the approaches to overcome this is to compare a patient's scan to a database of normal volunteers. This technique is used in many imaging scenarios such as Cardiac, Renal, Neuro, and
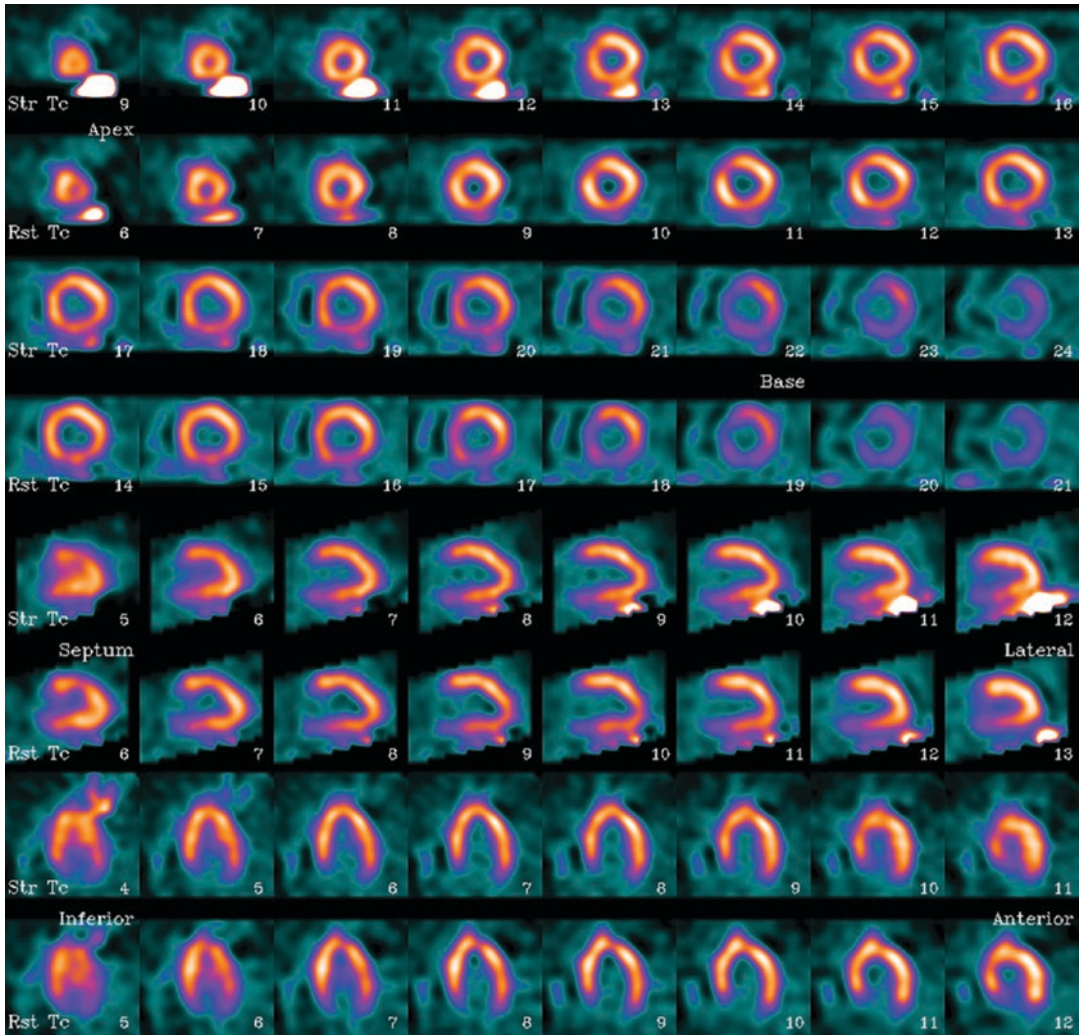
Fig. 15.40 Normalization example, scaled to the maximum activity in the myocardium

others. In order for this technique to work correctly the patient's scan needs to be normalized or scaled to the same range as the data in the normal database. For instance, Fig. 15.41a shows the average or mean counts for the male and female normal files for a typical 1 day ^{99m}Tc Sestamibi myocardial SPECT scan. In order to compare a patient's scan to this normal file, it must first be scaled into the same range as the normal file, using the same region of activity.

For instance, if the normal file had a maximum count of 1000, which occurred in the anterior wall, and the anterior wall of the patient's scan had a maximum count of 1200, then the patient's scan would need to be multiplied by 0.83 before comparison to the normal file. Figure 15.41 shows an abnormal patient after comparison to the normal file, in which abnormal areas have been turned black (note the large anterior and inferior wall defects) [64–66].

Stress

a   **b**   **c**   **d**

Rest

a   **b**   **c**   **d**
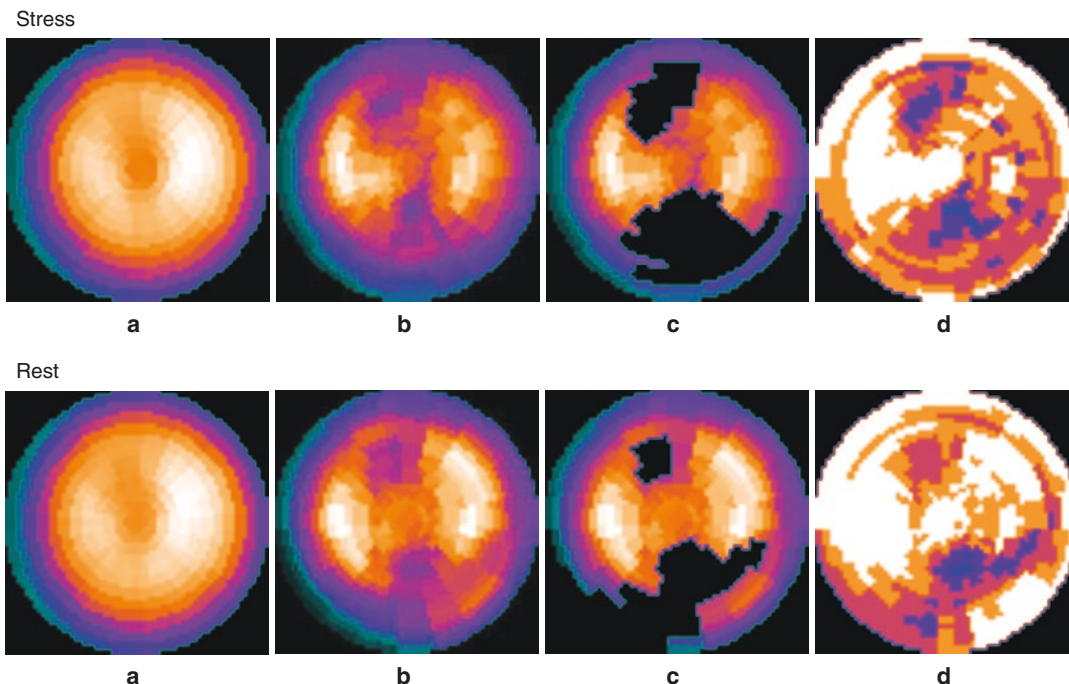
Fig. 15.41 SPECT Database comparison example. (**a**) Stress and rest female normal file for Tc-99m 1 day sesta-mibi. (**b**) Stress and rest raw polar maps (counts extracted from the stress and rest short-axis datasets). (**c**) Stress and rest blackout polar maps after comparison to the normal database, blacked-out areas show regions of significant hypoperfusion. (**d**) Stress and rest standard deviation polar maps, darker areas show regions that are more standard deviations from the normal file then lighter areas

15.11   Conclusion

Image processing is an integral part of the daily nuclear medicine routine and many physiological as well as functional parameters can be extracted from the different nuclear medicine procedures by various processing tools. Not only is image processing able to convey this desired information but also a variety of display tools exist to assist in image interpretation and patient diagnosis. Hopefully this overview has given you an appreciation for how difficult it would be to work with any kind of imaging modality without the use of computers. In fact, computers are a very necessary part of any imaging modality and will only become more important as we continue to push the envelope of imaging.

References

1. Cassen B, Curtis L, Reed C. A sensitive directional gamma ray detector. UCLA report 49. Los Angeles: University of California; 1949.
2. Anger HO. A new instrument for mapping gamma-ray emitters, Biol Med Quart Rep UCRL-3653:38:1957
3. Kuhl DE, Edwards RQ. Image separation radioisotope scanning. Radiology. 1963;80(4):653–62, (in English).
4. Jaszczak RJ. The early years of single photon emission computed tomography (SPECT): an anthol-

ogy of selected reminiscences. Phys Med Biol. 2006;51(13):R99–115.

5. Anger HO. Scintillation camera with multichannel collimators. J Nucl Med. 1964;5:515–31.

6. Gotway MB, et al. Hyperfunctioning parathyroid tissue: spectrum of appearances on noninvasive imaging. AJR Am J Roentgenol. 2002;179(2):495–502.

7. Hoffman EJ, Huang SC, Phelps ME. Quantitation in positron emission computed tomography: 1. Effect of object size. J Comput Assist Tomogr. 1979;3(3):299–308.

8. Demirkaya O, Al Mazrou R. Performance test data analysis of scintillation cameras. IEEE Trans Nucl Sci. 2007;54(5):1506–15, (in English).

9. Anderson S. Collins English dictionary. 7th ed. Glasgow: HarperCollins; 2005. p. xiii, 1872 p.

10. Galt JR, Garcia EV, Nowak DJ. Filtering in frequency space. J Nucl Med Technol. 1986;14(3):152–60.

11. Hansen CL. Digital image processing for clinicians, part I: basics of image formation. J Nucl Cardiol. 2002;9(3):343–9.

12. Hansen CL. Digital image processing for clinicians, part II: filtering. J Nucl Cardiol. 2002;9(4):429–37.

13. Hansen CL. Digital image processing for clinicians, part III: SPECT reconstruction. J Nucl Cardiol. 2002;9(5):542–9.

14. Zubal IG, Wisniewski G. Understanding Fourier space and filter selection. J Nucl Cardiol. 1997;4(3):234–43.

15. Cooke CD, Garcia EV, Cullom SJ, Faber TL, Pettigrew RI. Determining the accuracy of calculating systolic wall thickening using a fast Fourier transform approximation: a simulation study based on canine and patient data. J Nucl Med. 1994;35(7):1185–92.

16. Chen J, Faber TL, Cooke CD, Garcia EV. Temporal resolution of multiharmonic phase analysis of ECG-gated myocardial perfusion SPECT studies. J Nucl Cardiol. 2008;15(3):383–91.

17. Galt JR, Garcia EV, Robbins WL. Effects of myocardial wall thickness on spect quantification. IEEE Trans Med Imaging. 1990;9(2):144–50, (in English).

18. Faber TL, et al. Left ventricular function and perfusion from gated SPECT perfusion images: an integrated method. J Nucl Med. 1999;40(4):650–9.

19. Pflugfelder PW, Sechtem UP, White RD, Higgins CB. Quantification of regional myocardial function by rapid cine MR imaging. Am J Roentgenol. 1988;150(3):523–9.

20. DePuey EG, Rozanski A. Using gated technetium-99m-sestamibi SPECT to characterize fixed myocardial defects as infarct or artifact. J Nucl Med. 1995;36(6):952–5, (in English).

21. Chen J, et al. Onset of left ventricular mechanical contraction as determined by phase analysis of ECG-gated myocardial perfusion SPECT imaging: development of a diagnostic tool for assessment of cardiac mechanical dyssynchrony. J Nucl Cardiol. 2005;12(6):687–95, (in English).

22. Chen J, et al. Assessment of left ventricular mechanical dyssynchrony by phase analysis of ECG-gated SPECT myocardial perfusion imaging. J Nucl Cardiol. 2008;15(1):127–36, (in English).

23. Henneman MM, et al. Can LV dyssynchrony as assessed with phase analysis on gated myocardial perfusion SPECT predict response to CRT? J Nucl Med. 2007;48(7):1104–11, (in English).

24. Marsan NA, et al. Left ventricular dyssynchrony assessed by two three-dimensional imaging modalities: phase analysis of gated myocardial perfusion SPECT and tri-plane tissue Doppler imaging. Eur J Nucl Med Mol Imaging. 2008;35(1):166–73, (in English).

25. Henneman MM, et al. Phase analysis of gated myocardial perfusion single-photon emission computed tomography compared with tissue Doppler imaging for the assessment of left ventricular dyssynchrony. J Am Coll Cardiol. 2007;49(16):1708–14, (in English).

26. Trimble MA, et al. Evaluation of mechanical dyssynchrony and myocardial perfusion using phase analysis of gated SPECT imaging in patients with left ventricular dysfunction. J Nucl Cardiol. 2008;15(5):663–70, (in English).

27. Peix A, et al., Value of intraventricular dyssynchrony assessment by gated-SPECT myocardial perfusion imaging in the management of heart failure patients undergoing cardiac resynchronization therapy (VISION-CRT). J Nucl Cardiol; 2019. https://doi.org/10.1007/s12350-018-01589-5.

28. Zhou W, Garcia EV. Nuclear image-guided approaches for cardiac resynchronization therapy (CRT). Curr Cardiol Rep. 2016;18(1):7.

29. Taylor A, Schuster DM, Alazraki NP. A clinician's guide to nuclear medicine. 2nd ed. Reston: Society of Nuclear Medicine; 2006.

30. Taylor A Jr, et al. Measuring technetium-99m-MAG3 clearance with an improved camera-based method. J Nucl Med. 1995;36(9):1689–95, (in English).

31. Taylor AT Jr, et al. Procedure guideline for diagnosis of renovascular hypertension. Society of Nuclear Medicine. J Nucl Med. 1998;39(7):1297–302, (in English).

32. Corbett JR, et al. Equilibrium radionuclide. J Nucl Cardiol. 2006;13(6):e56–79, (in English).

33. Murthy VL, et al. Clinical quantification of myocardial blood flow using PET: joint position paper of the SNMMI Cardiovascular Council and the ASNC. J Nucl Cardiol. 2018;25(1):269–97.

34. Erdi YE, et al. Segmentation of lung lesion volume by adaptive positron emission tomography image thresholding. Cancer. 1997;80(12 Suppl):2505–9.

35. Jentzen W, Freudenberg L, Eising EG, Heinze M, Brandau W, Bockisch A. Segmentation of PET volumes by iterative image thresholding. J Nucl Med. 2007;48(1):108–14.

36. Brambilla M, Matheoud R, Secco C, Loi G, Krengli M, Inglese E. Threshold segmentation for PET target volume delineation in radiation treatment planning: the role of target-to-background ratio and target size. Med Phys. 2008;35(4):1207–13.

37. Mortensen E, Morse B, Barrett W, Udupa J. Adaptive boundary detection using live-wire 2-dimensional dynamic-programming. In: Computers in cardiology 1992: Proceedings, 1992. p. 635–8., (in English).

38. Declerck J, Feldmar J, Goris ML, Betting F. Automatic registration and alignment on a template of cardiac stress and rest reoriented SPECT images. IEEE Trans Med Imaging. 1997;16(6):727–37.

39. Slomka PJ, Hurwitz GA, Stephenson J, Cradduck T. Automated alignment and sizing of myocardial stress and rest scans to three-dimensional normal templates using an image registration algorithm [see comment]. J Nucl Med. 1995;36(6):1115–22.

40. Mykkanen J, Tohka J, Luoma J, Ruotsalainen U. Automatic extraction of brain surface and mid-sagittal plane from PET images applying deformable models. Comput Methods Prog Biomed. 2005;79(1):1–17.

41. Minoshima S, Koeppe RA, Frey KA, Kuhl DE. Anatomic standardization: linear scaling and nonlinear warping of functional brain images. J Nucl Med. 1994;35(9):1528–37.

42. Minoshima S, Frey KA, Koeppe RA, Foster NL, Kuhl DE. A diagnostic approach in Alzheimer's disease using three-dimensional stereotactic surface projections of fluorine-18-FDG PET. J Nucl Med. 1995;36(7):1238–48.

43. Garcia EV, et al. Technical aspects of myocardial SPECT imaging with technetium-99m sestamibi. Am J Cardiol. 1990;66(13):23E–31E.

44. Germano G, et al. A new algorithm for the quantitation of myocardial perfusion SPECT. I: technical principles and reproducibility [see comment]. J Nucl Med. 2000;41(4):712–9.

45. Garcia E, Folks R, Pak S, Taylor A. Automatic definition of renal regions-of-interests (ROIs) from MAG3 renograms in patients with suspected renal obstruction. J Nucl Med (Meeting Abstracts). 2008;49:386P.

46. Delaunay B. Sur la sphere vide. A memoire de Georges Voronoi. Izv. Akad. Nauk SSSR, Otdelenie Matematicheskih i Estestvennyh Nauk. 1934;7: 793–800.

47. Lorensen WE, Cline HE. Marching cubes: a high resolution 3D surface construction algorithm. SIGGRAPH Comput Graph. 1987;21(4):163–9.

48. Foley JD, Phillips RL, Hughes JF, van Dam A, Feiner SK. Introduction to computer graphics. Boston: Addison-Wesley Longman Publishing; 1994. p. 557.

49. Cooke CD, Vansant JP, Krawczynska EG, Faber TL, Garcia EV. Clinical validation of three-dimensional color-modulated displays of myocardial perfusion. J Nucl Cardiol. 1997;4(2):108–16.

50. Santana CA, et al. Three-dimensional color-modulated display of myocardial SPECT perfusion distributions accurately assesses coronary artery disease. J Nucl Med. 2000;41(12):1941–6.

51. Wallis JW, Miller TR. Volume rendering in three-dimensional display of SPECT images [see comments]. J Nucl Med. 1990;31(8):1421–8.

52. Miller TR, Wallis JW, Sampathkumaran KS. Three-dimensional display of gated cardiac blood-pool studies [see comments]. J Nucl Med. 1989;30(12):2036–41.

53. Wallis JW, Miller TR. Display of cold lesions in volume rendering of SPECT studies. J Nucl Med. 1991;32(5):985.

54. Drebin RA, Carpenter L, Hanrahan P. "Volume rendering," presented at the Proceedings of the 15th annual conference on computer graphics and interactive techniques, 1988.

55. Hoehne KH, Delapaz RL, Bernstein R, Taylor RC. Combined surface display and reformatting for the three-dimensional analysis of tomographic data. Invest Radiol. 1987;22(8):658–64, (in English).

56. Viola P, Wells WM. Alignment by maximization of mutual information. In: Fifth international conference on computer vision, proceedings, 1995. p. 16–23. , (in English).

57. Collignon A, Maes F, Delaere D, Vandermeulen D, Suetens P, Marchal G. Automated multi-modality image registration based on information theory. Inf Process Med Imaging. 1995;3:263–74, (in English).

58. Bajcsy R, Kovacic S. Multiresolution elastic matching. Comput Vision Graphics Image Process. 1989;46(1):1–21, (in English).

59. Haber E, Modersitzki J. Numerical methods for volume preserving image registration. Inverse Problems. 2004;20(5):1621–38, (in English).

60. Bookstein FL. Principal warps—thin-plate splines and the decomposition of deformations. IEEE Trans Pattern Analysis Mach Intell. 1989;11(6):567–85, (in English).

61. Kuhle WG, et al. Quantification of regional myocardial blood flow using 13N-ammonia and reoriented dynamic positron emission tomographic imaging. Circulation. 1992;86(3):1004–17.

62. Hutchins GD, Schwaiger M, Rosenspire KC, Krivokapich J, Schelbert H, Kuhl DE. Noninvasive quantification of regional blood flow in the human heart using N-13 ammonia and dynamic positron emission tomographic imaging. J Am Coll Cardiol. 1990;15(5):1032–42.

63. Kaufmann PA, Camici PG. Myocardial blood flow measurement by PET: technical aspects and clinical applications [erratum appears in J Nucl Med. 2005 Feb;46(2):291]. J Nucl Med. 2005;46(1):75–88.

64. Van Train KF, et al. Quantitative same-day rest-stress technetium-99m-sestamibi SPECT: definition and validation of stress normal limits and criteria for abnormality. J Nucl Med. 1993;34(9):1494–502.

65. Van Train KF, et al. Multicenter trial validation for quantitative analysis of same-day rest- stress technetium-99m-sestamibi myocardial tomograms. J Nucl Med. 1994;35(4):609–18.

66. Santana CA, et al. Quantitative (82)Rb PET/CT: development and validation of myocardial perfusion database. J Nucl Med. 2007;48(7):1122–8.

Emission Tomography and Image Reconstruction

16

Magdy M. Khalil

Contents

16.1   Introduction

In the early days of nuclear medicine, measurement of radioactivity administered into a human body was simply acquired by placing a Geiger counter over the desired region of interest. Further progress was undertaken using a rectilinear scanner. The breakthrough, as mentioned in Chap. 10, came from the development of the gamma camera and the use of the scintillation crystal coupled to photomultiplier tubes (PMTs). To this end, there was no available tool to measure the spatial extent of tracer distribution in three-dimensional (3D) fashion, and all measurements were confined to two-dimensional (2D) planar imaging. The third dimension is important to fully depict radiopharmaceutical uptake, hence enabling the interpreting physician to make a confident decision. Another feature of 3D imaging is the ability to quantify tracer concentrations more accurately than with 2D imaging. Tracer uptake, residence time, and clearance rates are important dynamics of tracer biodistribution in diseased and healthy tissues, in which temporal sampling is particularly useful for studying tracer or organ kinetics. Adding the time dimension to 2D planar imaging is important in some scintigraphic studies, such as renal scintigraphy and planar equilibrium radionuclide angiocardiography (ERNA). In the former case, kidney function is studied through a time course of about half an hour, dividing the examination time into two phases (perfusion and function) such that the first minute is assigned to depict organ perfusion while the rest of the study is used to assess renal function. In planar ERNA, the time dimension is essential to make snapshots of different phases of the heart cycle through identification of the R-R signal during heart contraction. This helps to obtain valuable information about heart motion and to assessment of functional parameters.

M. M. Khalil (✉)
Medical Biophysics, Department of Physics, Faculty of Science, Helwan University, Cairo, Egypt

Many nuclear medicine procedures are performed by acquiring planar views of the area under investigation. However, planar images are manifested by poor image contrast and lack of quantitative accuracy. Nuclear examinations such as bone scintigraphy and thyroid, parathyroid, and lung scanning are among those studies for which planar imaging is commonly used; however, under many circumstances the 2D nature of the acquired data have shortcomings in their yield of accurate diagnostic results, especially when dense overlying structures obscure the inspection of tracer spread and accumulation. This directly influences the interpretation results and may lead to an inconclusive diagnosis.

Many nuclear medicine procedures have been revolutionized by use of 3D imaging in terms of the amount of information that can be extracted and incorporated into the decision-making process. Among those are myocardial perfusions, brain, and bone imaging, for which tomographic acquisition provides a greater opportunity to visualize organs from different angular perspectives. This allows reading physicians to thoroughly investigate pathological lesions from many directions, especially when appropriate visualization tools are available on the viewing workstation. This in turn has had a positive impact on the diagnostic accuracy of many nuclear medicine examinations. For example, a tomographic bone scan is more sensitive than planar imaging and has been reported to improve the diagnostic accuracy for detecting malignant bone involvement [1].

16.1.1 History

Emission and transmission CT rely on the fact that to obtain a 3D picture of the human body a set of multiple 2D projections is required for image reconstruction. This necessitates collection of a sufficient amount of information about the object under examination. Johann Radon (1887–1956) introduced the principles of data formation through what is called the radon transform, which describes an object in 3D space as a sum of line integrals. In 1917, Radon developed a

solution for image reconstruction utilizing projection data sets and applied his technique to nonmedical applications, namely, gravitational problems. In 1956, the reconstruction technique developed by Radon found another application by Bracewell in the field of radioastronomy [2]. Allan Cormack, a few years later after Bracewell, independently and without knowledge about Radon's work, developed a method for calculating radiation absorption distributions in the human body based on transmission scanning. Kuhl and Edwards were the first to introduce the concept of emission tomography using backprojection in 1963, and about 10 years later, Godfrey Hounsfield, the inventor of CT, succeeded to practically implement the theory of image reconstruction in his first CT scanner. Shortly after the invention, Hounsfield and Cormack were recognized by sharing the Noble Prize in Medicine and Physiology in 1979. By analogy to PET imaging, CT scanning was focused on brain imaging; however, body examinations were introduced a few years later, and the first body images taken in the body prototype machine were of Hounsfield himself on December 20, 1974 [3].

One of the earlier works on tomography was to move the object while keeping the imaging system stationary. This was in the late 1960s and early 1970s, when investigators used transaxial tomography to image a patient setting on a rotatable chair placed in front of a stationary gamma camera. After the mid-1970s, a gamma camera detector was mounted on a rotated gantry to take multiple images around the patient under investigation [4].

16.1.2 SPECT and PET

There are two 3D techniques provided by nuclear imaging namely single-photon emission computed tomography (SPECT) and positron emission tomography (PET). Both are noninvasive diagnostic modalities that are able to provide valuable metabolic and physiologic information about many pathophysiologic and functional disorders. A remarkable feature of SPECT and PET is their ability to improve contrast resolution

manyfold compared to planar scintigraphic imaging. The two imaging modalities have proved useful as applications in molecular imaging research and translational medicine. In addition, attempts to derive quantitative parameters are more accurate than planar imaging. Furthermore, when the timing factor is added to the 3D imaging, the amount of information that can be obtained from analyzing the data is significantly high. Two examples are worth mentioning when SPECT or PET is used to collect tracer spatial distribution and its associated temporal component. One of these is gated myocardial perfusion tomographic imaging, in which the tracer distribution and heart function can be captured in one imaging session, providing an assessment of myocardial perfusion (or metabolic) parameters, such as defect extent and severity or tissue viability, in addition to calculations of regional and global left ventricular function and ejection fraction. Another important area of application is the study of tracer distribution during the time course of tracer uptake and clearance from biological tissues. In these acquisition protocols, dynamic frames are collected over predefined timing intervals (or reframed in case of list-mode acquisition) to record tracer flow, extraction, retention, and clearance from the tissue of interest. The recorded data are then presented to an appropriate mathematical model to obtain physiologically important parameters, such as transport rate constants and calculation of tissue metabolic activity or receptor density (see Chaps. 20 and 21).

The addition of temporal sampling to tomographic imaging has other utilities, such as recording the respiratory cycle to correct for lung motion on myocardial perfusion imaging and to correct for spatial coregistration errors arising from temporal mismatch between computed tomography (CT) and PET in lung bed positions during whole-body fluorodeoxyglucose-F18 (FDG) PET/CT examinations. The time information required for motion characterization in four-dimensional (4D) imaging can be obtained either prospectively or retrospectively using respiratory-gating or motion-tracking techniques [5].

The advances in hybrid imaging and introduction of PET/CT and SPECT/CT to the clinic have added another dimension to the diagnostic investigations; currently, hybrid modalities provide greater opportunity to study functional as well as morphological changes that occur at different stages of disease progression or regression. The characterizing aspects that distinguish these imaging methods from other imaging modalities are the underlying physical principles, the way data are acquired, image reconstruction and correction techniques, and finally image visualization, quantitation and display.

16.1.3 Resolution and Sensitivity

SPECT and PET imaging modalities have common and different characteristics in terms of spatial resolution and sensitivity. In general, clinical PET systems have better spatial resolution than SPECT; the former can provide an intrinsic spatial resolution of about 4–6 mm, and the latter can hardly achieve 10 mm full width at half-maximum (FWHM) using the conventional NaI(Tl) designs. The resolution of PET images is determined by many factors, which differ from those that affect SPECT resolution. Detector size, positron range, photon acollinearity, and some instrumental factors contribute by different degrees to the spatial resolution of PET images, as discussed in Chap. 12. On the other hand, SPECT imaging uses multihole collimation to identify structures and to determine directionality of the emitted radiation. This type of data collection imposes constraints on the overall system sensitivity and spatial resolution. There is often a trade-off between sensitivity and spatial resolution in collimator design. For instance, collimators with high spatial resolution have reduced count efficiency and vice versa. Another aspect of this trade-off is realized in some other (divergent) collimator geometry, in which the spatial resolution is improved while keeping the sensitivity at the same level, but this comes with a reduced imaging field of view.

In PET imaging, there is also a trade-off of these performance parameters but not in a similar manner as the principles of photon detection in PET imaging obviate the need for such photon collimation, leading to increased system
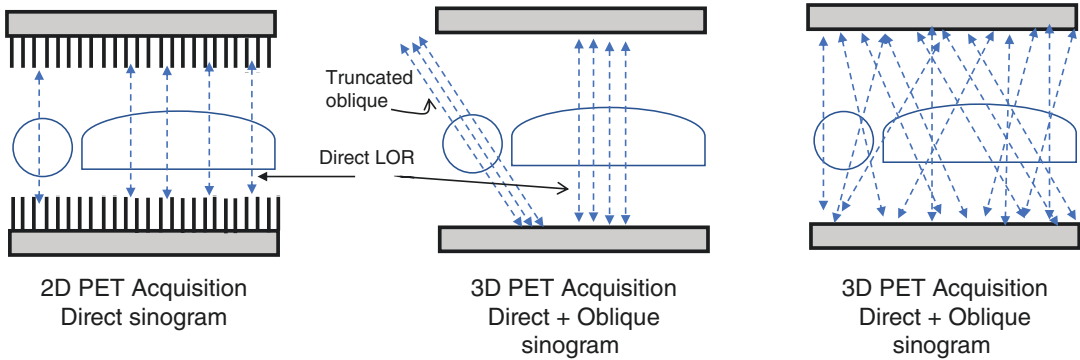
Fig. 16.1 Acquisition modes in positron emission tomographic (PET) scanning

sensitivity. However, collimation also exists in PET imaging in a form of 2D acquisition modes by using collimating septa between scanner rings. In 3D scanner configuration where the interplane septa are removed, a significant increase in detection efficiency is obtained (four- to sixfold) than that when the scanner is operated in 2D mode. In the later mode, collimator septa are placed between detector rings to confine the acquired projections to a set of 2D projection arrays. This facilitates image reconstruction so that any 2D reconstruction algorithms can be used similar to 2D SPECT data reconstruction. In this way, image reconstruction is implemented in an independent slice-by-slice manner. Image reconstruction in 2D is a straightforward procedure, while in 3D some kind of data manipulation is required to utilize the increased system sensitivity in improving image quality. In septaless or 3D acquisition mode, however, the scanner sensitivity is not uniform across the axial field of view, and approaches to reconstruct images are either to use fully 3D reconstruction techniques or to rebin the data into a 2D projection array. Figure 16.1 shows the two acquisition modes offered by PET scanning.

16.1.4 Image Acquisition

Data sampling by gamma camera detector is implemented by computer digitization for the events detected on the scintillation crystal. The computer matrix varies according to system sen-

sitivity, resolution, and data storage capacity. A lower matrix size, such as 64×64 and 128×128, is commonly used in SPECT while being higher in PET due to the improved spatial resolution. The matrix size in X-ray CT is even higher than nuclear techniques due to the submillimeter resolution capabilities and superior photon statistics. However, in nuclear PET and SPECT imaging, the relatively lower photon flux due to radioactive decay properties, restrictions on the injected dose, lower detection efficiency, acquisition time, and the expected spatial resolution are among the factors for reducing the matrix size.

In planar imaging, the patient is positioned in front of the detection system, and adequate time is given to form an image. The resulting image is a depiction of tracer distribution in two dimensions, x and y. The third dimension cannot be realized as the collected counts over a particular point of the detector matrix are a superimposition of tracer activities that lie along the accepted beam path. This manner of data acquisition does not allow for extracting valuable information about source depth. However, to solve such a problem additional information must be provided to obtain further details about tracer spatial distribution. Moving the detector to another position can produce another image for the given tracer distribution, and another angular view would again reveal information that was not present in the previous two views. This process can be repeated several times to complete an acquisition arc of at least 180°, which is the smallest angular arc that can be applied to reliably reconstruct an

image [6]. Let us go though some basic geometric and mathematical principles of this type of data acquisition.

In SPECT imaging, data acquisition is performed by a one-, two-, or three-head camera that is adjusted to rotate around the patient over small angular intervals to acquire an adequate set of 2D projections. The increased number of detector heads serves to improve study sensitivity and reduces the acquisition time. This is dissimilar to PET scanning, in which the circular ring design circumvents the patient in a 2π fashion; thus, detector rotation is not necessary. However, in the old dual-detector coincidence gamma camera and partial-ring design, detector motion is required to satisfy angular requirements imposed by reconstruction algorithms. The detection process relies on annihilation photons (~180° apart) and coincidence circuitry to record events in an emission path, called the tube or line of response (LOR).

Fig. 16.2 shows one projection view for SPECT and PET cameras such that the former is positioned to acquire a cardiac study while the latter was chosen to scan a brain patient. Suppose that we select one-detector row (i.e., 1D) of the detector 2D matrix, and in 2D PET this corresponds to one projection angle acquired using a single ring. The activity distribution within a patient injected by myocardial tracer or FDG is defined by $f(x,y)$, where x and y are the coordinates of the tracer uptake inside the patient boundaries. The counts collected over the elements of the projection row at an angle θ is denoted by the function $p(s,\theta)$, where θ is the angle subtended by the SPECT camera and the cartesian x and y coordinates as shown in Fig. 16.2. This is also the same angle at which the PET scanner was chosen to look at the brain study.

According to Radon, every projection bin of the 1D image is a result of count accumulation along the path traversed by the emitting radiations and falling perpendicular on the detector plane. However, in PET it is the line that connects a detector pair in coincidence. One can therefore consider the acquired counts at a given angle as a compressed version of the slice under investigation. At the end of data acquisition, we obtain a multiple number of projection angles; each is a compressed version of the object distribution viewed from different angles. In PET imaging, data format is mostly represented by rebinning the coincidence data in a sinogram. Another format of data acquisition and event storage is list mode, in which events are individually recorded for their timing, position, and possibly any other relevant attributes, such as energy.

The problem now is how to reconstruct or get a solution for the tracer concentration given the information provided by the set of projections. It is easy to understand that once we are able to reconstruct or find a solution for one transverse image, then it becomes possible to obtain the contiguous slices following the same pathway. In the given examples, the function of the reconstruction algorithm is to find the best estimate of the tracer spatial distribution within the slices taken across the myocardium or the brain tissues. Apart from considering the effect of photon scatter and detector response, one can write the measured projection data as

$$p(s,\theta) = \int f(x,y) e^{-\int \mu(x,y) dt'} dt \qquad (16.1)$$

This is the attenuated radon transform, and solving the equation for $f(x, y)$ is the way to find estimates of tracer activity within the patient and hence image reconstruction. Here, t and s are elements of a coordinate system such that t is passing along the direction of the rays and perpendicular on the detector plane while s is the axis parallel to the detector. In terms of x and y directions, s and t are defined as follows:

$$s = x \cos\theta + y \sin\theta$$
$$t = -x \sin\theta + y \cos\theta$$

By neglecting the exponential term, the resulting formula will be the Radon transform equation, which states that the acquired count over a particular projection bin $p(s, \theta)$ is the integration of tracer activity along the line that passes through the object studied and, in SPECT, falling perpendicular on the detector plane, while in PET it is the line that connects a coincident detector pair.
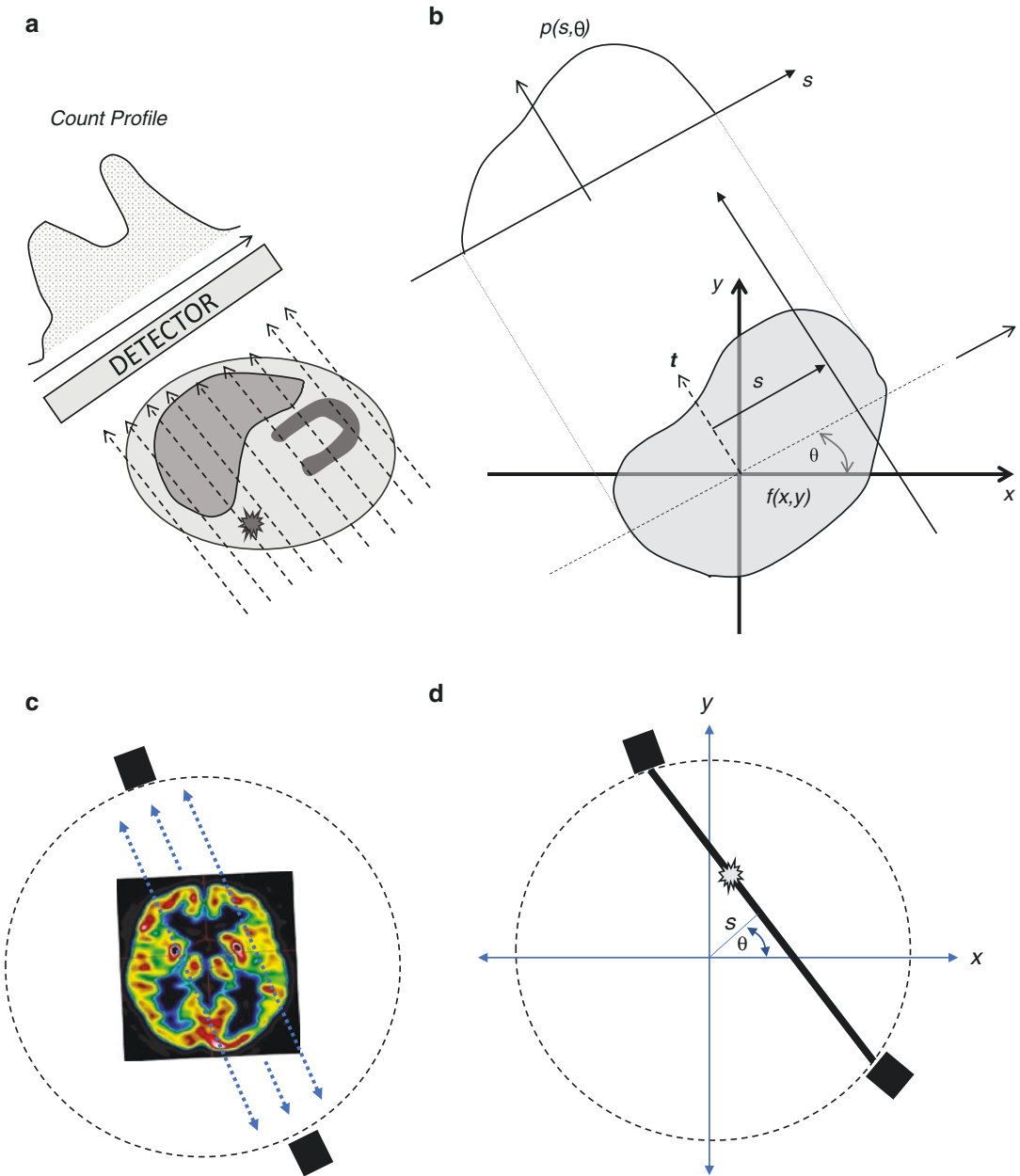
Fig. 16.2 (**a**) Projection profile for a one-dimensional (1D) row of the detector is displayed; a varying count intensity is evident. Any point on the profile is the line integral of all activity concentrations lying along the path of the ray. (**b**) The coordinate system (*t, s*) is defined so that *s* is parallel to the detector plane, while *t* is perpen-dicular on it. This coordinate system is used to define the projection profile *p*(*s, θ*) in relation to the stationary coordinate system (*x, y*). In (**c**, **d**) positron emission tomographic (PET) acquisition setting, similar projections are defined by sinogram variables *s* and *θ*, where both determine the location of the annihilation site on the sinogram

The process that maps the tracer activity $f(x, y)$ onto the projection image $p(s, \theta)$ is defined as the X-ray transform.

In the case of SPECT, the exponential term of the formula denotes the amount of photon attenuation that extends from the site of emission $f(x, y)$

to the detector plane, demonstrated in Fig. 16.3, whereas in PET it refers to the amount of attenuation experienced by annihilation photons while traversing the corresponding patient thickness. Figure 16.4 shows how an attenuation correction in PET imaging can be solved by calculating the probability of detecting two coincident photons by a detector pair.

It is noted that the attenuation correction factor is a function of the patient thickness and independent of the emission site given a recorded LOR. By moving the exponential term to outside the integra-

$$p = \sum_{i=1}^{a} f_i e^{-\mu_i l}$$
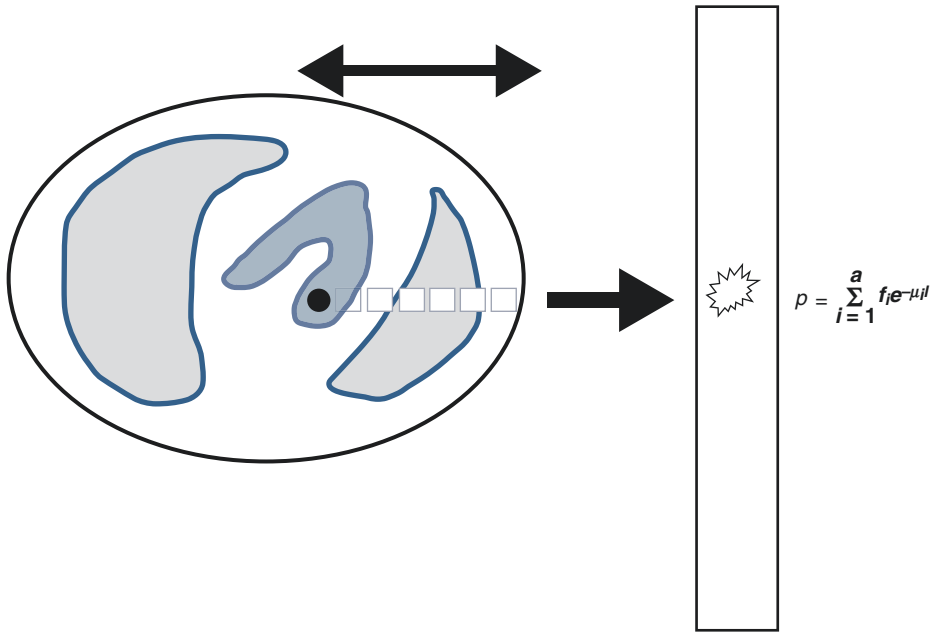
Fig. 16.3   Photon attenuation in single-photon emission computed tomography (SPECT)

Fig. 16.4   Photon attenuation in positron emission tomography (PET)

$C_1 = f(x,y) * e^{-\mu(d-x)}$

$P_1 = C_1 / f(x,y) = e^{-\mu(d-x)}$

d

$d - x$

x

$C_2 = f(x,y) * e^{-\mu x}$

$P_2 = C_2 / f(x,y) = e^{-\mu x}$

Attenuation is the probability of detecting the photon pair:

$P_1 P_2 = e^{-\mu x} * e^{-\mu(d-x)} = e^{-\mu d}$

$C = P_1 P_2 \cdot f(x,y) \Rightarrow C = f(x,y) e^{-\mu d}$
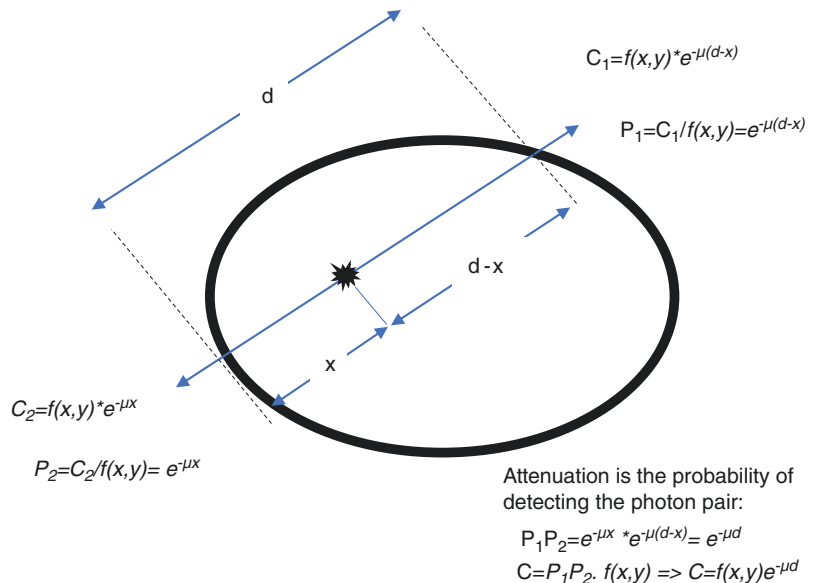
tion, denoting the measured projection as I and the integration term as I_o, and rearranging the formula, we can obtain the attenuation correction factors (ACF) required to correct a measured LOR:

$$\text{ACF} = I_o / I$$

This is simply achievable in practice using a transmission source where I_o is the measurements performed while the patient is outside the field of view (i.e., blank scan), and I corresponds to the data taken when the patient is positioned inside the field of view (i.e., transmission scan).

Each LOR can be corrected for attenuation by multiplication with the corresponding correction factors, or the latter data can be reconstructed to obtain a spatial distribution of attenuation coefficients. In SPECT attenuation correction, the direct multiplication of the emission data by the correction factors is not applicable due to dependence of photon attenuation on the emission site, which is unknown. Instead, the logarithmic ratios of the initial and transmitted projections are reconstructed to obtain a spatial distribution of attenuation coefficients or what is known as an attenuation map.

The introduction of hybrid imaging such as SPECT/CT and PET/CT has allowed the use of CT images to correct the radionuclide emission data for photon attenuation. CT images provide low noise correction factors and faster scanning times, but corrected data may suffer from quantitative bias and correction artifacts. A CT scan also provides high-resolution anatomical images and with image coregistration serves to strength the confidence of lesion localization detected in radionuclide images. Radioactive sources provide more noise, less bias, and increased imaging time. Different methodologies have been devised to correct for the bias introduced by CT-based attenuation correction and methods to reduce noise propagation into radionuclide emission images when radioactive transmission scanning is used.

16.1.5 X-Ray CT

For a monoenergetic X-ray beam passing through an object of thickness L and linear attenuation

coefficient μ, the transmitted radiation can be calculated from

$$I = I_o e^{-\mu L}$$

where I and I_o are the transmitted and initial beam intensity, respectively. For an X-ray beam in CT, the rays traverse various body tissues of different attenuation properties due to their various compositions and effective Z number. Thus, the amount of attenuation that the beam encounters is equal to the total sum of all μ values that lie along the beam path.

Therefore, the measured transmission data for an X-ray beam of initial intensity I_o passing through a human body can be written as

$$p(s,\theta) = I_o e^{-\int \mu(x,y)\mathrm{d}t}$$

Rearranging the formula and renaming the measured projection $p(s,\theta)$ as described, we obtain

$$\ln \frac{I_o}{I} = \int \mu(x,y)\mathrm{d}t$$

where $\mu(x, y)$ is the linear attenuation coefficient for a pixel located at position (x, y), and the integration is the line integral of attenuation coefficients along the transmission beam (see Fig. 16.5).

The reconstruction algorithm here does not try to find the activity distribution of the tracer, but it estimates the spatial distribution of attenuation coefficients using two pieces of information, the initial beam intensity I_o and the transmitted projection data. Note that this is the same equation used to derive the correction factors for PET emission data since it accounts for the total amount of photon attenuation experienced by the initial X-ray beam I_o while moving through the object. Actually, in real practice and data analysis of X-ray CT, determination of the distribution of attenuation coefficients is not simply performed by solving the equation stated here; several pre- and postprocessing steps are taken to correct for many variables and confounders that deviate the practical measurements from being consistent with the theoretical ideal conditions; for further details, see [7].
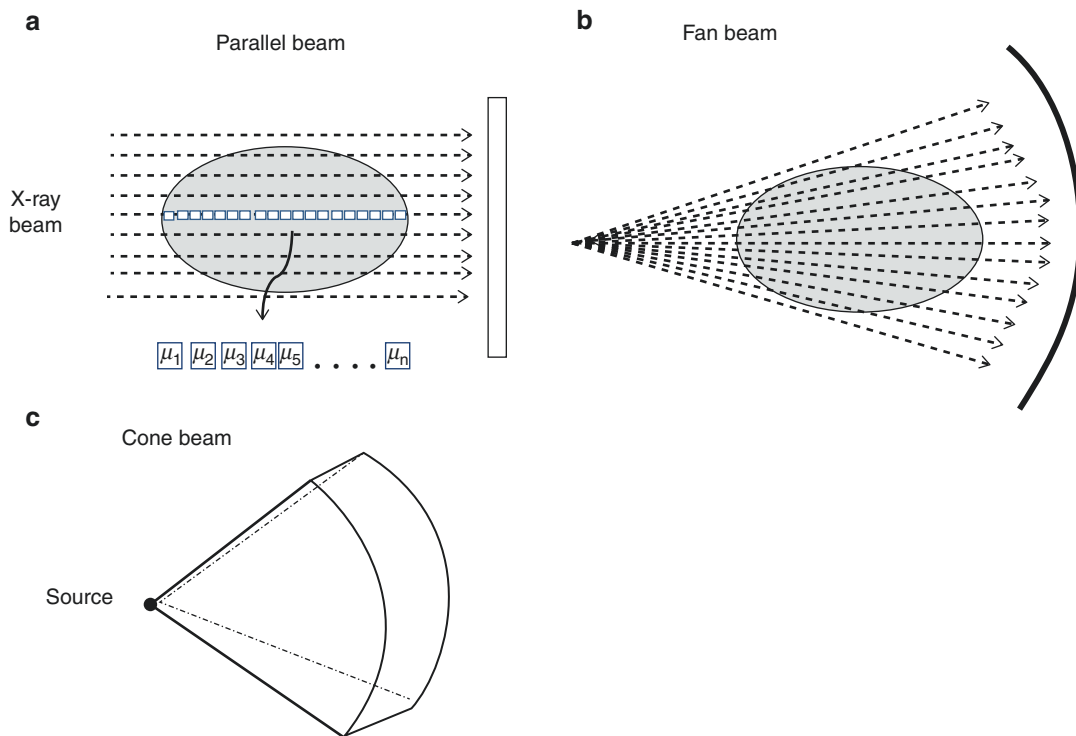
Fig. 16.5 In X-ray CT, different geometries have been used in image acquisition which in turn posed different requirements on image reconstructions. (**a**) Image reconstruction is straightforwardly implemented using direct filtered backprojection (FBP). The other geometry is shown in (**b**) where image can be either reconstructed using rebinning or direct FBP algorithm. (**c**) Cone beam: another design currently used in commercial CT scanners where image reconstruction is modified to adapt and account for beam geometry

16.1.6 Sinogram

Rebinning the acquired data in a single diagram such that the projection bin represents the horizontal axis while the projection angle is placed on the vertical direction produces a sine wavelike pattern called a *sinogram*. Representing the acquired data in a sinogram has several benefits in terms of data processing, image reconstruction, and correction techniques. Also, it is useful in inspecting detector failure, in which a diagonal black line in a PET sinogram indicates an artifact in a single detector element, while a diagonal band could indicate a malfunction of a detector block [8]. It can also be used to correct for patient motion and for other correction techniques. Note that one selected pixel on the sinogram should indicate the total counts collected for a particular LOR regardless of any contamination from any other events. In SPECT, it is the integral of counts that lie along the emission path and falling perpendicular on the detector surface (i.e., line-integral model).

For a point source located at the center of the field of view, the resulting sinogram is just a vertical line that extends from the top to the bottom of the sinogram. Further, a horizontal line passing through the sinogram indicates a particular projection angle taken for a transverse slice. Figure 16.6 shows sinograms for an object having one and two hot spots on the transverse section. The figure clearly represents location (angle and position) and intensity of "two lesions" and also real complex emission similar to clinical studies (i.e. brain) where the object consists of a large number of points taken at multiple projection angles. Figure 16.7 shows also how sinogram formation relies on number of disintegrations collected from positron emission as opposed to
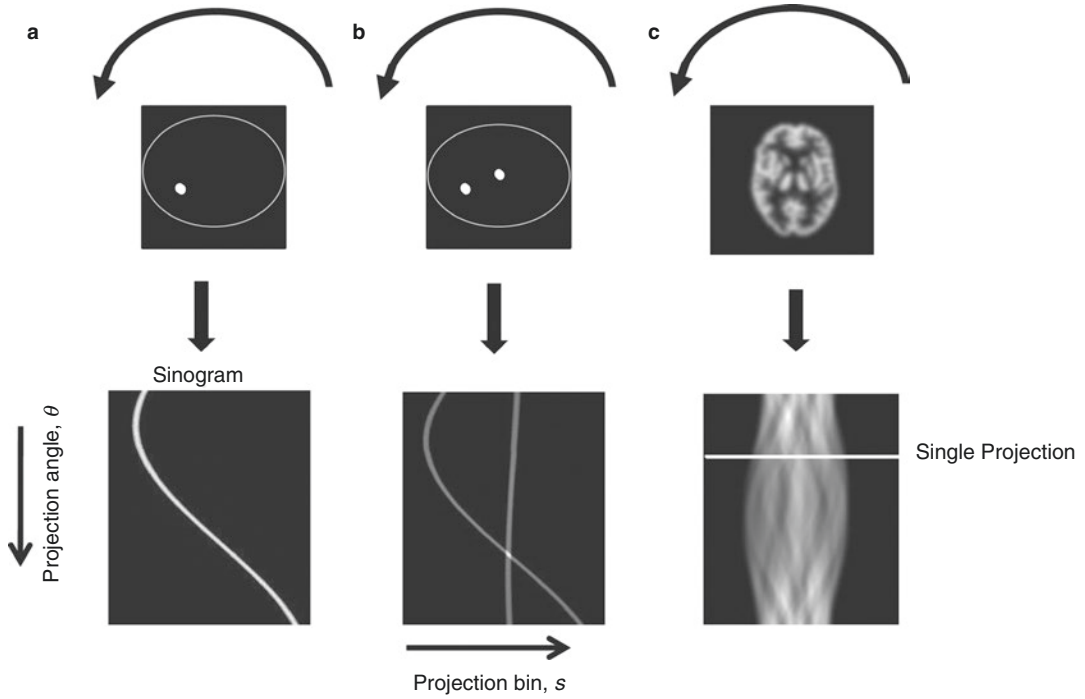
Fig. 16.6 Sinograms for different activity distributions. The sine wave pattern can be seen for a single hot lesion (**a**) and two hot lesions (**b**). The third sinogram (**c**) is more complicated due to its representation for many points in the projection profile, including all the angular views
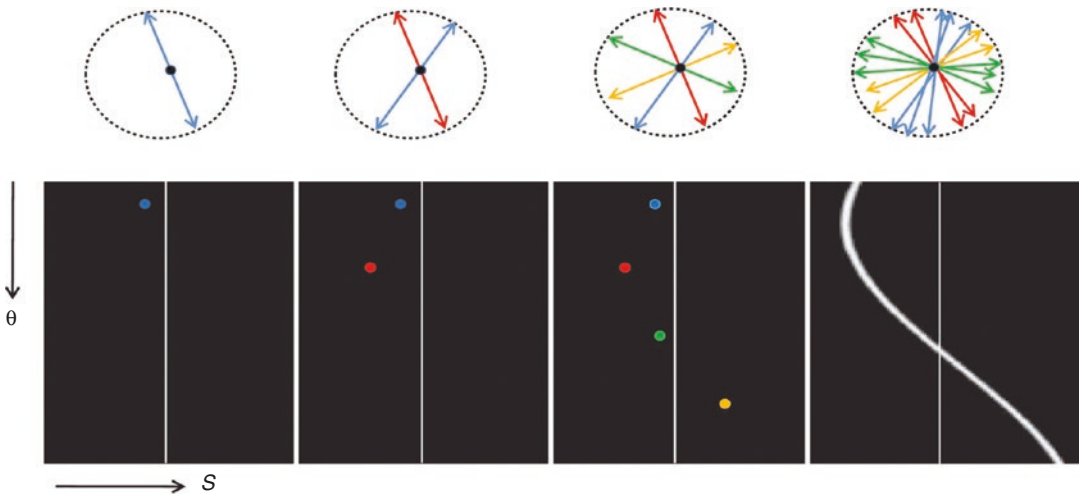
Fig. 16.7 The rebinning of the acquired events as the source decays into a sinogram that represents the projection bin on the horizontal axis, while the vertical axis denotes the projection angle. Note that each colored line of response (LOR) refers to a particular projection view; in other words, it points to a certain set of parallel LORs taken at a given angle

conventional SPECT systems, in which detector rotation is necessary to build up a complete sinogram. This is one of the advantages provided by PET scanners based on circular design since all projections are acquired simultaneously and also possibly in 3D fashion. This characteristic is absent in most conventional designs of the gamma camera, for which detector rotation is essential to accomplish the task.

16.2   Image Reconstruction

16.2.1 Analytic Methods

16.2.1.1   Simple Backprojection

As described, a collected count from a projection element according to the Radon transform is a line integral of tracer concentration along the emission path length. The task placed on the reconstruction algorithms is to find the spatial distribution of tracer activity within the body segment in question. One way to reconstruct an image from the raw data is to redistribute the collected counts (i.e., backproject) over the contributing individual pixels that lie along the path of the rays in the reconstruction matrix. Repeating this process for each projection element and for each acquired angle, one can obtain a picture of the tracer concentration as shown in Fig. 16.8. It can be seen that this method of image reconstruction cannot reveal useful information about tracer

distribution due to the blurry appearance and substantially degraded signal-to-noise ratio.

Backprojection operation at point b can be represented as

$$f_{BP} = \int_0^\pi p\big(x\cos\theta + y\sin\theta, \theta\big)\mathrm{d}\theta$$

The backprojected image f_{BP} at a particular point b is the result of summing all the corresponding projection bin values across all angular views taken during data acquisition. Here, s is the location of the projection bin on the detector. In PET geometry, the backprojection operation is performed for those LORs that connect detector pairs in coincidence. For obvious reasons, this process of count redistribution cannot determine the exact site where photon annihilation took place. Therefore, all pixels along the ray path are equally likely to get the same amount of counts. In PET systems with time of flight, calculation of the arrival of the two photons allows reduction of this LOR to a significantly smaller distance (based on system timing resolution) that, if included in image reconstruction, would result in an improvement of signal-to-noise ratio.

This is actually not the exact description of the backprojection operation since it is implemented on a grid of finite elements or computer matrix (and acquisition geometry), and thus it is possible that, for a given pixel, the backprojected ray can pass through a small part or intersect the pixel at
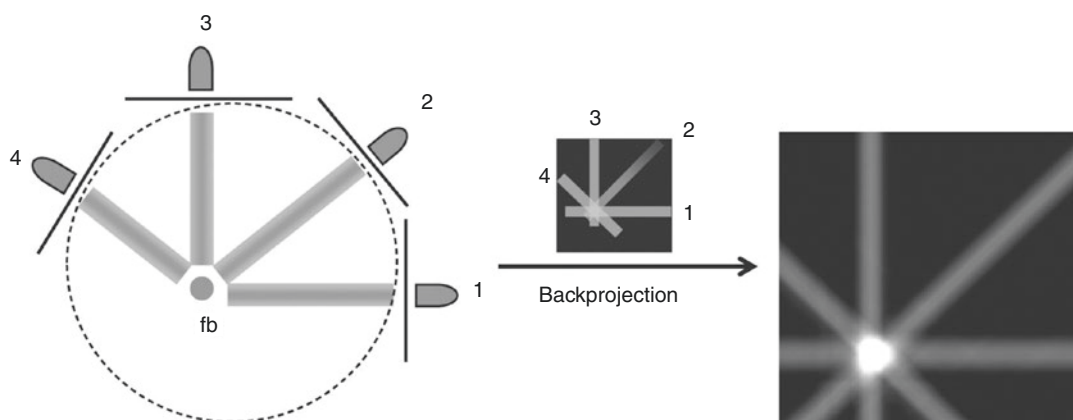
Fig. 16.8 Image reconstruction using simple backprojection

its full length. Therefore, a number of backprojection methods have been developed to deal with this point. Methods used in forward- and backprojection are pixel driven, ray driven, distance driven, distance weighted, matrix rotation, and others. Also, a combination of these methods, such as ray driven and pixel driven, can be used [9]. However, these methods differ in their computational efficiency, interpolation, and estimation accuracy. In iterative reconstruction, they should be carefully selected since several iterations may accumulate interpolation errors, introducing reconstruction artifacts.

Two clinical examples are shown in Fig. 16.9, one slice from a myocardial perfusion SPECT study and another one from brain-FDG PET study. The characteristic blurring appearance of simple backprojection is clear in both studies, with most low-frequency components overexpressed with a remarkable reduction of high frequencies. This significant artifact is attributed to the fact that the sampling criteria do not match the model assumptions; hence, the reconstructed image is far from an accurate estimate of the tracer distribution. Simple backprojection assumes that data are collected with infinite linear and angular sampling, and the data collected are free from attenuation and scattered radiation in addition to shift-invariant and perfect system response (Fig. 16.10). These assumptions are violated in practice due to image digitization and the discrete angular intervals undertaken in image
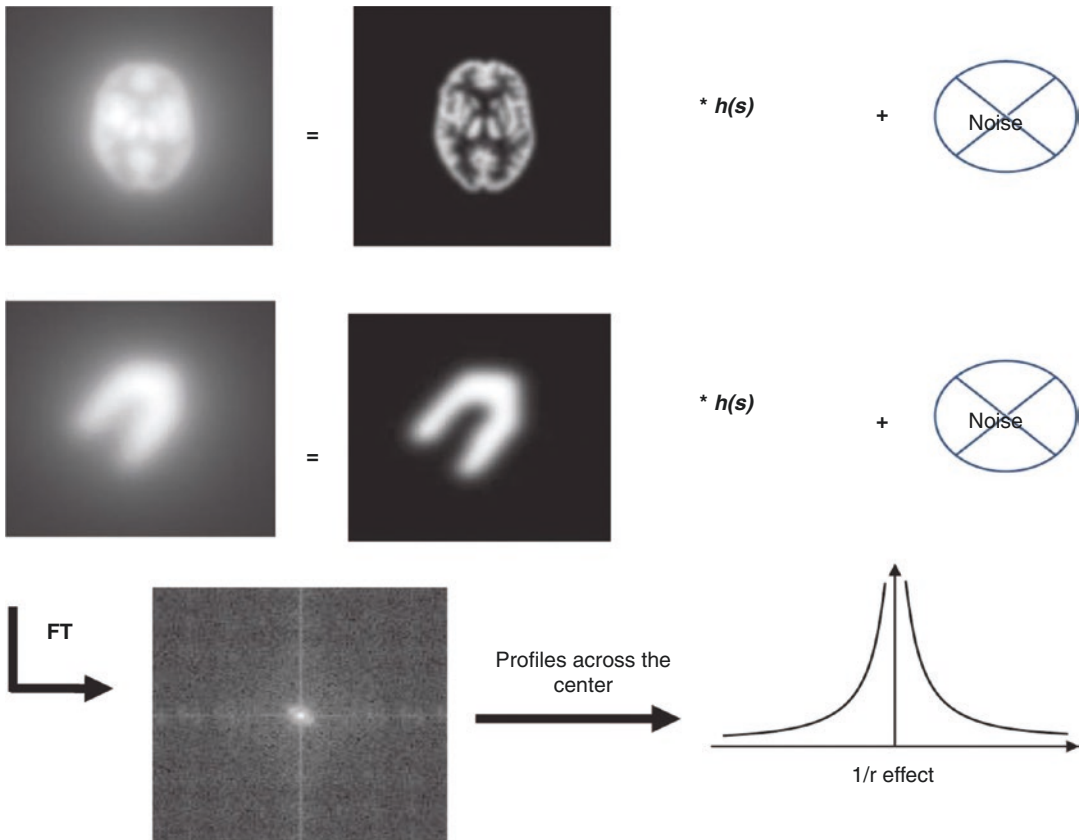
Fig. 16.9 When the backprojection images are Fourier transformed the low frequencies are overemphasized while the low frequencies are reduced showing a pattern called 1/r effect. This backprojected blurry images are therefore corresponds to a convolution of the underlying true activity distribution with the h(s) function. Analytic approaches remove this effect by deconvolving the acquired data with the blurring function, neglecting the noise component and leading to a tremendous increase in image noise. As a result, regularization using a smoothing function is required
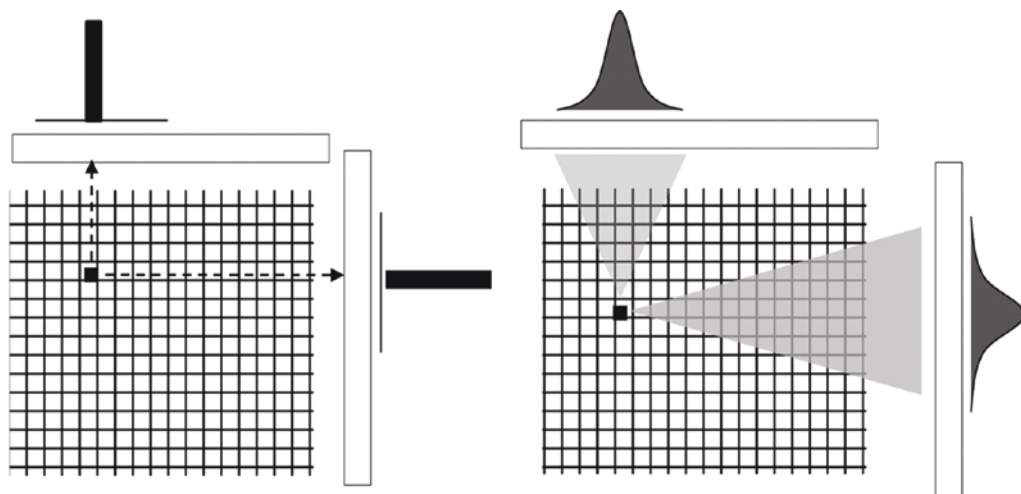
Analytic Approach
❑ Perfect system response
❑ No attenuation
❑ No scatter or randoms
❑ No Noise Model
❑ Infinite Sampling

Realistic Approach
❑ Beam divergence
❑ Photon attenuation
❑ Photon scatter
❑ Noise
❑ Finite Sampling

Fig. 16.10 Ideal versus realistic model of analytic image reconstruction

acquisition. Furthermore, the emitted photons undergo different types of interactions, resulting in photon loss or recoiling from the original path, and hence invalidate the absence of photon attenuation and scatter assumption in data acquisition. The measured projections are noisy due to the Poisson statistics of the radioactive decay process, and ignoring the noise component serves to alter the statistical properties of the reconstructed images and degrades image quality.

A profile drawn over the Fourier transform (FT) of the backprojected image shows a damping function that extends from the center of the spectrum (low-frequency region) toward the periphery (high-frequency region). This is referred to as the $1/r$ effect, in which the reconstructed image can be described as a convolution of the underlying activity distribution and a $1/r$ blurring function (Fig. 16.9). This situation can be written in the frequency domain as

$$F_{\mathrm{BP}} = \frac{1}{\sqrt{v_x^2 + v_y^2}} F\left(v_x, v_y\right) = \frac{1}{v} F\left(v_x, v_y\right)$$

where the backprojected image F_{BP} is equal, in theory, to the original image $F(v_x, v_y)$ multiplied by the inverse of the function $h(s)$ in the frequency space. The latter function is defined as the system output to an ideal point source object and describes the system blurring effects on image formation. It is usually called the system spread function or point spread function (PSF). It is the key to solving the problem of backprojection by removing the blurring effect shown in Fig. 16.9 by either convolving the measured projections with the function $h(s)$ or multiplication in the frequency domain as described by the equation. Similarly, in 3D image reconstruction without data truncation, the backprojected image can be convolved with an appropriate 3D filter function to get an estimate of the original object distribution; alternatively, the measured projections are convolved with the 3D filter function. Before proceeding further to use this approach in image reconstruction, an important theorem that is central to many analytic reconstruction techniques should be discussed.

16.2.1.2 Fourier Reconstruction Theorem

Fourier analysis has a wide range of applications in many disciplines of science and engineering. This includes image and signal processing, filtering, image reconstruction, and many other biomedical applications. It has also been used in radioastronomy, electron microscopy, optical holography, magnetic resonance imaging (MRI), CT, and radionuclide SPECT and PET imaging [10]. Refer to Chap. 15, in which the FT is applied to a number of useful applications in nuclear medicine. In short, projection data and reconstructed slices can be represented in two different domains: spatial and frequency. The FT for a given input function can be represented by the sum of the sine and cosine waves with different amplitudes and phases.

Image reconstruction based on the FT is different from simple backprojection, and both can be combined to yield a variety of reconstruction approaches, as will be discussed further. The concept can easily be understood if we reversely assumed that we already have a transverse section of a patient thorax in which we can see the myocardium, and the 2D FT of this section has been calculated. The reconstruction theorem based on Fourier analysis states that a profile taken at a certain angle (θ) from the 2D FT of the transaxial section is equal to the 1D FT of the projection profile computed at the same angle. This is the underlying assumption of Fourier reconstruction theorem or the *central section* theorem, which relates the acquired projection

data to the reconstructed image by the aid of Fourier transformation (Fig. 16.11).

Suppose the Fourier coefficients (intensity values in the frequency domain) are defined by the function $F(u, v)$, which is the 2D FT of the activity distribution $f(x, y)$ for a given cross-sectional slice; then, it can be proven that

$$F\left(v_x, v_y\right) = P\left(v, \theta\right)$$

where $P(v, \theta)$ is the FT of the projection $p(s, \theta)$, which is the function we have used to describe the counts collected over a 1D detector row.

Figure 16.12 summarizes the steps involved in Fourier reconstruction for a myocardial perfusion study, where the 1D FT of projection data is first calculated for all angular views, then data are collected in a 2D format and interpolated to account for gaps between views. Finally, inverse 2D FT is computed to yield a reconstructed myocardial image. Here, u and v are the spatial frequencies in the Fourier space and are defined in a square matrix; however, the polar sampling regime taken by the detector does not match the rectangular requirements, and therefore interpolation is required. Such a problem could be dealt with using standard interpolation methods or interpolation by gridding, taking into account that the accuracy of the results depends strongly on the interpolation method [11].

By analogy to 2D Fourier image reconstruction, a central plane through the FT of the 3D activity distribution is equal to the 2D FT of the 2D parallel projection data taken at the same ori-
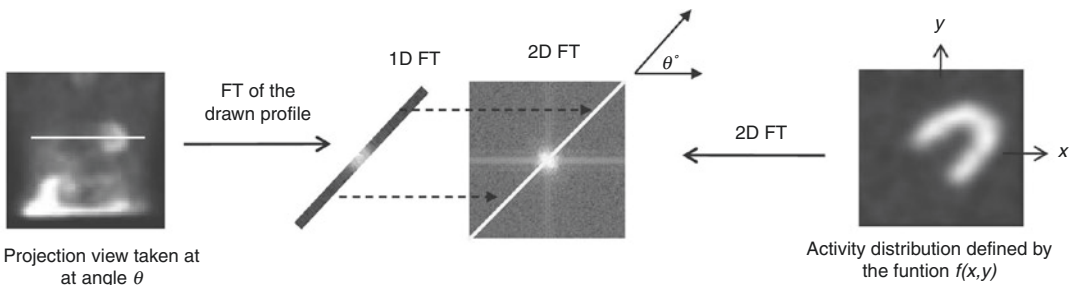
Fig. 16.11 The principle of two-dimensional (2D) Fourier reconstruction. The one-dimensional Fourier transform (1D-FT) of a horizontal profile drawn over a projection image at angle $\theta°$ is equal to the 2D-FT of the reconstructed image taken at the same angle
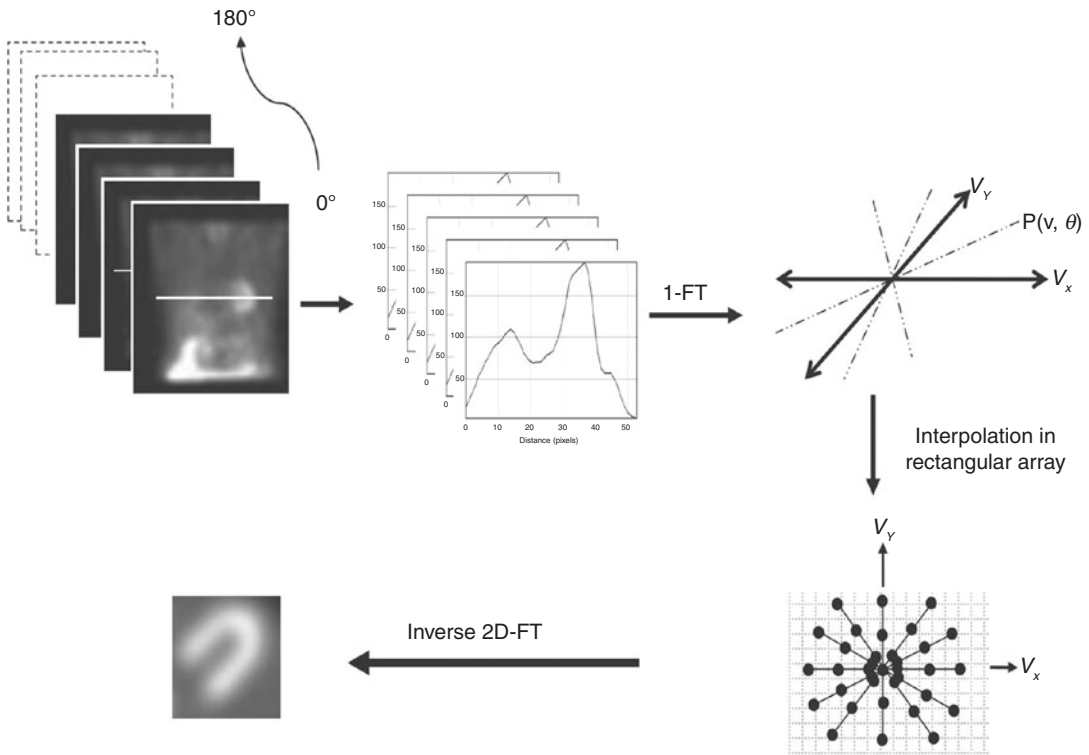
Fig. 16.12 Fourier transform reconstruction theorem states that the Fourier transform of a one-dimensional (1D) projection profile is equal to the two-dimensional (2D) Fourier transform of the corresponding activity distribution imaged at the same angle. This example shows a 1D profile taken across the patient's heart for all angles; then, the FT was calculated and interpolated in a rectangular array to obtain a 2D data set. Finally, the inverse Fourier transform is computed to generate the corresponding activity distribution represented here by the transaxial myocardial slice

entation. However, the 3D transform of the object has different and more complex structure manifested by local sampling density when compared to 2D and thus requires special interpolation and weighting approaches [12].

The central section theorem and simple backprojection can be combined in different forms of image reconstruction utilizing the mathematical properties of FT and convolution theorem, which states that convolution in the spatial domain is equivalent to multiplication in the frequency domain. However, these methods differ in the order of reconstruction steps regarding whether convolution or backprojection is accomplished first and if convolution is implemented in the spatial or frequency domain, together with their computational efficiency.

Backprojection filtering (BPF) or filtering of the backprojection is one of these reconstruction approaches that combines Fourier reconstruction and backprojection in one procedure. BPF starts first by backprojecting the image into a reconstruction matrix, 2D FT is then computed, the result is multiplied by 2D ramp filter, and finally image reconstruction is performed by taking the inverse 2D FT. Image reconstruction can also be implemented by convolving the projection data with a convolution kernel, and then the product is simply backprojected to produce an image of the object activity distribution. However, the most computationally efficient and easy to implement is filtered backprojection, which has been extensively used in the routine practice of image reconstruction.

16.2.1.3 Filtered Backprojection

The most analytic approach that is used in SPECT and PET reconstruction is filtered backprojection. It has a historical dominance in many applications due to its speed and easy implementation in software reconstruction programs. It relies on filtering the projection data after Fourier transformation of all the acquired angular views; then, backprojection is carried out to give an estimate of the activity distribution. Data filtering is performed to eliminate the $1/r$ effect that works to blur the reconstructed images and is implemented in the Fourier space. Backprojection alone yields an image dominated by low-frequency components. By looking at the reconstructed brain and cardiac slices in Fig. 16.9, one can perceive the smoothing appearance of the images due to the prevalence of low frequencies with difficulty in identifying small details, a situation that results in a significant loss of signal-to-noise ratio. This problem can be tackled by using a ramp filter, which serves to suppress low frequencies and enhance high-frequency components of the projection data.

The ramp filter function $|v|$, as can be seen in Fig. 16.13, is a diagonal line that extends from the center in the frequency space to a sharp cutoff value. This significantly reduces the drawbacks of the backprojection step in image reconstruction. However, the sharp cutoff value has a disadvantage of producing count oscillations over regions of sharp contrast [13]. Further, it increases the image noise due to the enhancement of the high-frequency components. To overcome this problem, an additional filter function is often used with the ramp filter to roll off this sharp cutoff value and to suppress high frequencies to a certain level.

The steps involved in reconstructing one slice using filtered backprojection (FBP) are demonstrated in Fig. 16.14 and summarized as follows:

1. 1D FT is calculated for each projection profile.
2. The Fourier transformed projections are multiplied with the ramp filter (plus a smoothing filter) in the frequency domain.
3. The inverse FT of the product is computed.
4. The filtered data are backprojected to give an estimate of the activity distribution.

These steps can be written mathematically as

$$f\left(x,y\right) = \int_0^\pi p^F\left(s,\theta\right)\mathrm{d}\theta = \int_0^\pi p^F\left(x\cos\theta + y\sin\theta,\theta\right)\mathrm{d}\theta$$

The reconstructed image $f(x,y)$ is obtained by filtering the projection data in the frequency space (by multiplication with the ramp-smoothing function); then, the filtered data p^F are backprojected in the spatial domain to obtain the object activity distribution. 2D FBP is used in the
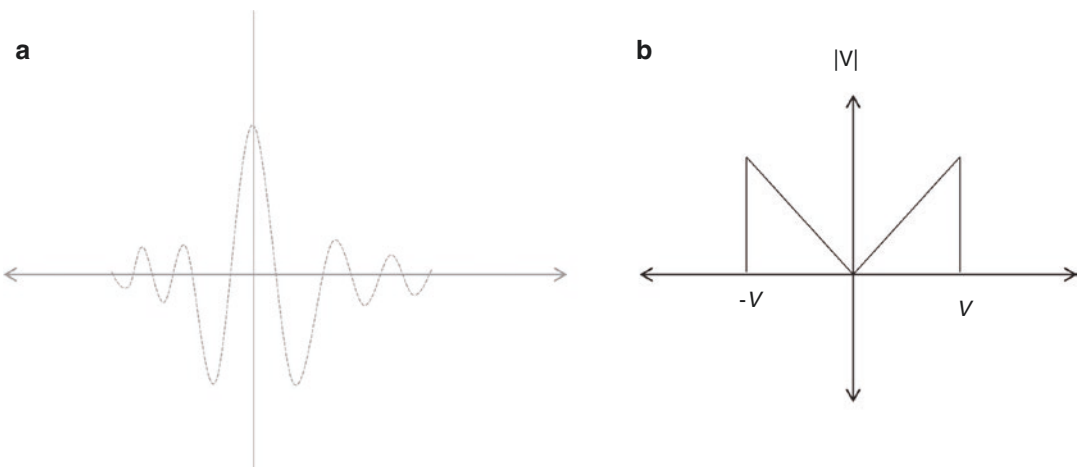
Fig. 16.13 Ramp filter in (**a**) spatial and (**b**) frequency domain
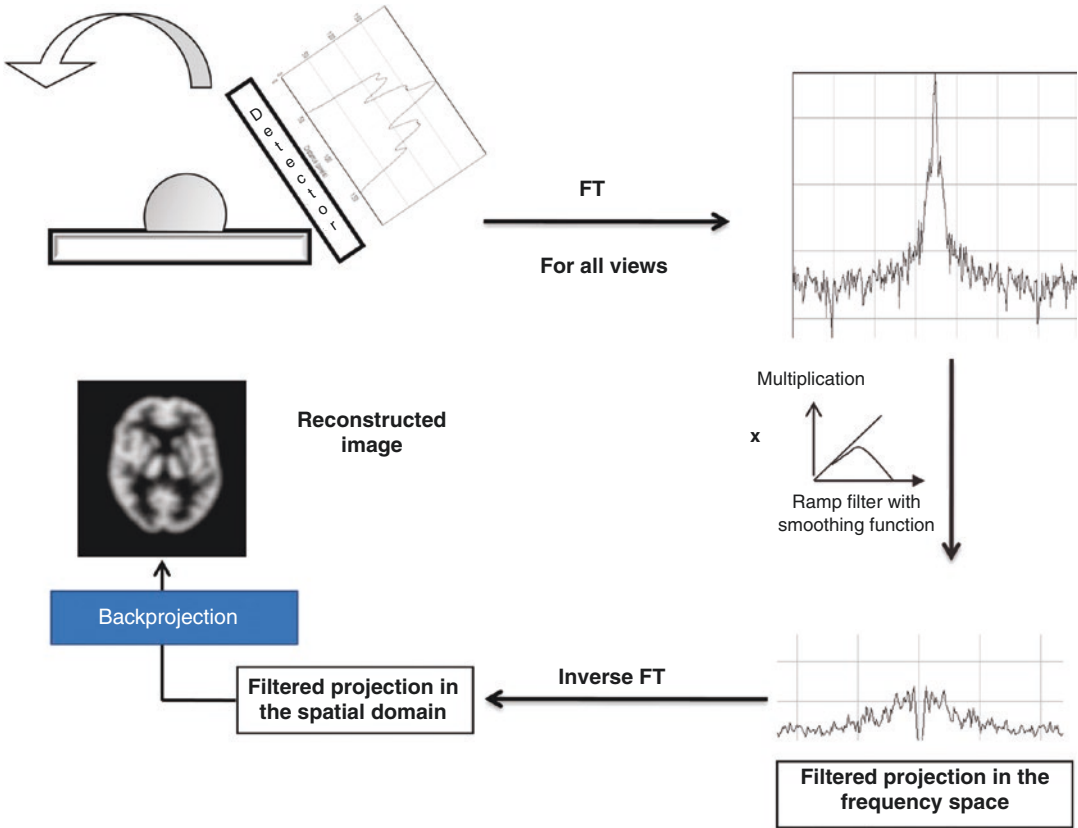
Fig. 16.14 [14] Steps involved in filtered backprojection (FBP) image reconstruction. The projection profiles are Fourier transformed and are then multiplied by the ramp function to yield filtered data in the frequency domain. The inverse Fourier transform is then computed for the filtered data to move back to the spatial domain, and then backprojection is implemented. The filtration step can be performed prior to or after backprojection

reconstructions of the 2D PET (septa extended) and SPECT images acquired with parallel hole or fan beam collimators. An image reconstructed with FBP is demonstrated in Fig. 16.15 using different projection angles.

16.2.1.4 Filtering

As shown in Fig. 16.13, a ramp is a high-pass filter that does not permit low frequencies to appear in the image; therefore, it is used to overcome the problem of simple backprojection in image reconstruction. However, this filter has positive coefficients near the center and negative values at the periphery, as can be seen in Fig. 16.13a, in which the filter is plotted in the spatial domain. These characteristics of a ramp filter can introduce artifacts at regions that lie close to areas of high activity concentrations. This can be noted in the clinic in patients with full bladder activity undergoing bone SPECT imaging over the pelvic region. A severe cold artifact could be seen on the femoral head due to multiplying the ramp negative values with the projection counts. This could adversely affect the interpretation process and might be resolved by emptying the bladder and repeating the scan or reconstructing the image using iterative techniques [15]. Another example can be seen in patients scheduled for whole-body FDG scanning and who have full bladder activity. This negative lobe effect introduced by a ramp filter can also cause a reduction of the inferior wall counts in myocardial perfusion SPECT studies if there are increased extracardiac activity concentrations in close proximity to the heart
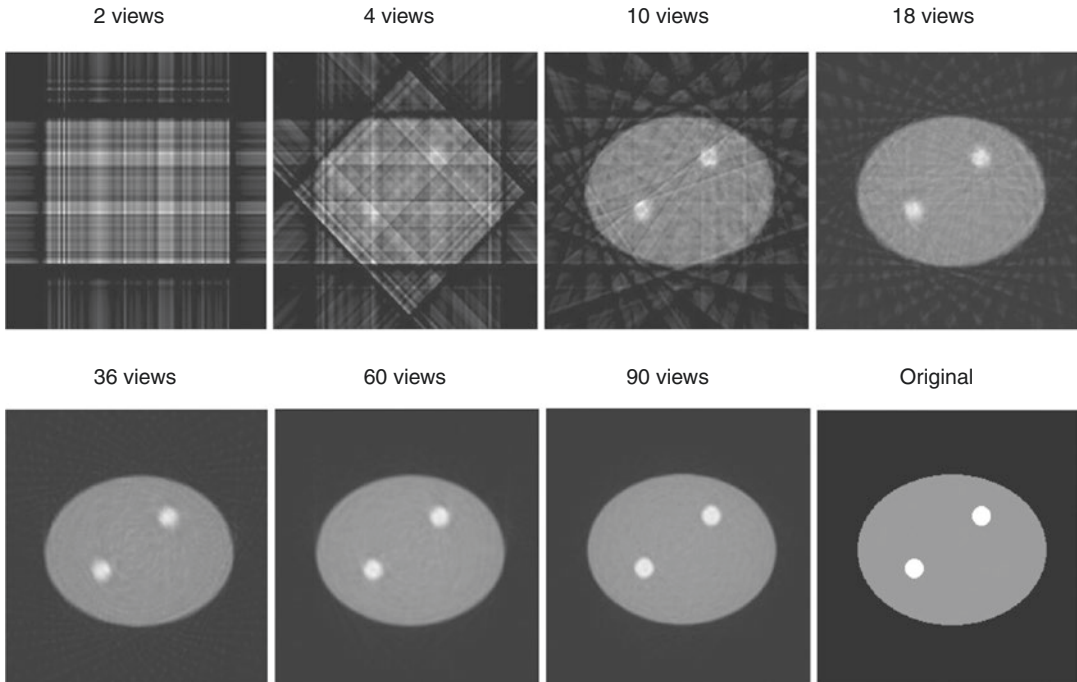
Fig. 16.15 Filtered backprojection (FBP) using different viewing angles

boundaries. This could result in an impression of diseased myocardial segments, causing false-positive results.

Another drawback of a ramp filer is its property of elevating the high-frequency components, thus increasing the noise level of the reconstructed images. An analytic solution for data acquired with noise is an ill-posed problem in which small perturbations (noise) in the input data cause a significant impact on the solution. Thus, a smoothing filter (regularization) is commonly used with a ramp filter to eliminate the noisy appearance of the ramp-filtered data and to improve image quality. Many filter functions were used with a ramp filter in several applications of nuclear medicine, such as Shep-Logan, parzen, hann, Hamming, and the commonly used Butterworth filter. Another class of filters has been proposed to correct for detector response function in image reconstruction, such as Metz and Wiener. Both filters rely on a system modulation transfer function taken at a certain depth and thus do not match the requirement of the shift-variant response imposed by the detector system. The inclusion of the detector response function in iterative reconstruction showed superior performance over other methods of image restoration.

A low cutoff value may smooth the image to a degree that does not permit perceiving small structures in the image, leading to blurred details and resolution loss. On the other hand, higher cutoff values serve to sharpen the image, but this occurs at the expense of increasing the amount of noise in the reconstructed images. The optimum cutoff value is therefore the value at which a fair suppression of noise is achieved while maintaining the resolution properties of the image. This trade-off task of the cutoff frequency is important to properly use a given filter function and to improve the image quality as much as possible. The cutoff value depends on factors such as the detector response function, spatial frequencies of the object, and count density of the image [16]. Better isotropic resolution properties are produced with 3D smoothing, and therefore it is preferred over 1D filters applied for individual slices.

However, a 2D filter for the projection data may produce almost equal smoothing effects and is also computationally less intensive.

16.2.2 Summary of Analytic Image Reconstructions

Analytic approaches for image reconstruction in emission tomography seek to find an exact solution for tracer activity distribution. There are a number of assumptions that are invalid under the imaging conditions encountered in practice. Thus, the results provided by FBP are suboptimal to restore the true activity concentrations accumulated in target tissues. Images reconstructed with FBP need a number of corrections to improve the reconstruction results. As mentioned, effects of attenuation, scatter, and detector response are potential degrading factors that FBP does not account for in the reconstruction process. Nevertheless, this reconstruction method has the advantages of being fast and easy to implement, and nuclear physicians have long-term experience working with its outcome. Most image reconstruction in SPECT is implemented on a 2D slice-by-slice basis, so that at the end of image reconstruction one can obtain a complete set of transverse slices that, if stacked together, would represent the tracer distribution within the reconstructed volume. In PET image reconstruction, however, the same situation exists when data are acquired using 2D acquisition mode or the 3D data set are sorted into 2D projection arrays. Analytic image reconstruction can be summarized as follows:

1. Analytic reconstruction using FBP does not account for the inherent statistical variability associated with radioactive decay, and data collected are assumed to follow Radon transform, for which the object measured is approximated by line integrals. Regularization using linear filtering is necessary to control the propagation of noise into the reconstructed images. However, the noise is signal dependent, and filtering to achieve an optimal noise resolution trade-off is not an appropriate solu-

tion. Therefore, to solve the problem as accurately as possible, iterative refinement can be a better alternative.

2. Images reconstructed by FBP show streak artifacts as a result of the backprojection step along with the possibility of generating negative reconstruction values in regions of low count or poor tracer uptake. Both artifacts can be treated using iterative reconstruction techniques.

3. While many factors affect the PET LORs and serve to deviate the data to be approximated as line integrals when reconstructed by analytic image reconstruction, it remains an approximate reasonable approach in PET rather than SPECT [17]. Photon attenuation is an exact and straightforward procedure to implement in PET scanning, and the detector response function is not substantially degraded with source depth. In contrast, SPECT images suffer from photon attenuation in a more complicated way in addition to significant resolution loss as the source position increases.

4. The assumption of line integrals does not hold true for some imaging geometries, such as SPECT systems equipped with coded apertures and PET scanners based on hexagonal or octagonal detectors. In the former, analytical inversion of the acquired data is not a simple task and constitutes a considerable challenge, while for the latter the gaps between detector modules (e.g., C-PET and HRRT) need to be filled before applying the analytic approach. Methods to account for the missed data were therefore developed, such as linear and bilinear interpolation or constraint Fourier space gap filling [18, 19].

5. In 3D data acquisition, coincidence events are allowed to be recorded among all scanner rings; accordingly, the collected data result in direct as well as oblique sinograms. For a point source located in a scanner operating in 2D mode, the in-plane system sensitivity does not depend on source location when compared to 3D imaging. In the latter scenario, the solid angle subtended by the scanner detectors differs from one position to another, especially when the source moves in the axial direction.

6. Another point that must be discussed is data truncation due to the fact that the axial extent of the PET scanner is limited. However, in the 3D situation, the oblique LORs are redundant in the sense that their statistical contribution to data reconstruction is unexploited. Direct 2D reconstruction uses LORs that arise from the direct planes to form an image, but this leads to compromising a lot of useful coincident events recorded as oblique LORs. The incorporation of these events into image reconstruction serves to improve the statistical quality of the scan by increasing count sensitivity. Analytic FBP with using a Colsher filter can reconstruct the oblique projection if data are not truncated [20]. In the case of data truncation, however, the missed information due to the limited axial extent of the scanner can be estimated by reconstructing the direct planes of the 2D projections (they are adequate for data reconstruction) and then reprojecting the resulting images to get an estimate of the truncated oblique projections. This method is called 3D reconstruction by reprojection (3DRP) [11]. In other words, 3DRP estimates the missed information of the oblique sinogram in the forward projection step, assuming the scanner axis is extended beyond the practical limit of data acquisition. This step is important to satisfy the requirements of (axial) data shift invariance. Image reconstruction is then carried out using 3D FBP with a 2D Colsher filter. 3DRP is computationally demanding and was extensively used as a standard analytic 3D method of choice for volumetric PET imaging.

7. The other alternative to make use of the oblique LORs is to rebin the data so that the 3D data set is reduced to a 2D problem. A number of rebinning approaches have been developed to overcome the increased reconstruction times and to utilize the count sensitivity of the scanner, yet this occurs with some drawbacks placed on spatial resolution and image noise.

16.2.3 Rebinning Methods

For many reasons, 3D PET imaging was not the acquisition mode of choice; an important one is the lack of an acceptable algorithm suited to provide clinically feasible reconstruction times. Another problem is the large amount of data that need to be processed along with extensive computational demands. An alternative way to handle this problem is to rearrange the oblique LORs into a direct array of parallel projections or a 2D data set. The latter allows for reconstruction times that are practically acceptable when compared to 3D reconstruction as the data can be reconstructed by any available 2D reconstruction algorithm. As mentioned, rebinning methods have been developed to benefit from the increased system sensitivity and to reduce computational speed requirements imposed by 3D reconstruction. Some of these rebinning approaches are summarized as follows:

1. Single-slice rebinning (SSRB) is a simple geometric approach to reduce the 3D PET data into 2D parallel sinograms [21] (Fig. 16.16a). The method is implemented by rebinning an oblique sinogram that connects a two-detector pair into a parallel sinogram that lies midway between the two detectors. Although this method can simply be applied to rearrange the 3D information into direct planes consisting of parallel sinograms, it is valid when the oblique lines are close to the center of the field of view and in systems with small aperture size.

2. The geometric simplification provided by SSRB has been refined by the multislice rebinning (MSRB) method, in which the sinograms that lie across two detectors that connect an oblique LOR are incremented as shown in Fig. 16.16b. Stated another way, for each oblique LOR, the transverse slices intersected are identified, and the corresponding sinogram is incremented. Thus, it can be viewed as a backprojection on the z-direction [22]. This process depends on the number of

Fig. 16.16 (**a**) Single-slice rebinning and (**b**) multislice rebinning
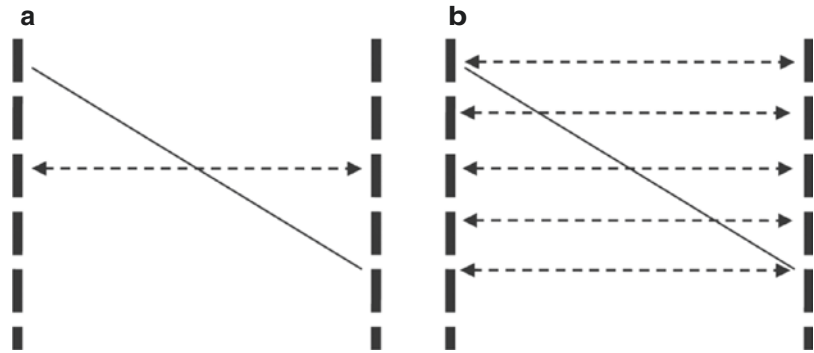
sinograms to be incremented, and the increment varies with different oblique lines. However, axial blurring and amplification of noise are the drawbacks of MSRB.

3. By utilizing the properties of FT, the estimate of the FT of direct sinograms can be exactly and approximately derived in the frequency domain from the FT of the oblique sinograms using the frequency–distance relationship [23]. It is based on an acceptable equivalence between the Fourier transformed sinograms arising from direct and oblique LORs. This is called Fourier rebinning or FORE. It has significantly improved the computation time required to rearrange the 3D data sets into 2D direct sinograms with an order of magnitude gain in reconstruction times when compared to the 3DRP. FORE showed little differences compared to 3DRP, with good accuracy and stability in a noisy environment, but was less accurate in scanners with a large aperture [24, 25].

4. Besides the reconstruction time gained from FORE, it can be combined with statistical iterative 2D image reconstruction techniques [26] to improve image quality when compared to FORE plus FBP or 3DRP and to exploit the incorporation of the imaging physics into the reconstruction model.

5. Several studies have shown that iterative techniques have the capabilities to improve image quality and quantitative accuracy when compared to analytic techniques or hybrid approaches (rebinning + 2D reconstruction) with the drawback of increased computational

burdens. However, this has been tackled using accelerating reconstruction algorithms implemented on fast computer systems.

16.2.4 Iterative Reconstructions

The task of the reconstruction algorithm is to solve $p = Af$ to find the best estimate of f. Here, p is the measured projection data, and A is a matrix that maps the tracer activity to the projection space. The presence of image noise does not allow finding a unique solution for the problem, or the solution might not exist or might not depend continuously on the data.

The better alternative to find a solution is to perform the task in an iterative manner. In this way, an initial estimate is assumed for the reconstructed image (solution), and the image is forward projected, simulating and accounting for all possible factors that work together to form the projection data. This initial estimate or guess can be a uniform image or FBP image and can be a zero image for additive-type algorithms. Many physical factors can be handled in the projection step to produce a projection image that is a close match to the acquired projections. Then, the measured and estimated projections are compared in such a way that allows derivation of a correction term. This last step allows the algorithm to modify the reconstructed slice through what is known as image update, and the process is controlled by the cost function or the objective likelihood function, as in the maximum likelihood (ML) algorithm. It is clear that the initial estimate will be

far from the solution; thus, the process is continued by repeating the same steps to reach the best estimate of the solution: convergence. This means that the algorithm will alternate through several steps of forward- and backprojection, in contrast to direct analytic methods, for which the estimated solution is obtained through a few predefined steps.

Most iterative techniques share the aforementioned idea and generally differ in the objective function, the optimization algorithm, and the computation cost [17]. The combined selection of the cost function and the optimization algorithm, as underlined above, is important in optimizing the iterative reconstruction technique. Both should not be confused and are distinguished in terms of their functionality as the first denotes the governing principle or the statistical basis on which the best estimate of the solution is determined, while the latter is the "driving" tool to achieve that estimate through a number of defined steps [27].

Iterative reconstructions have the advantages of incorporating corrections for image-degrading factors in the system matrix to handle an incomplete, noisy, and dynamic data set more efficiently than analytic reconstruction techniques. An important outcome of these advantages is that the final results enjoy better qualitative features in addition to more accurate estimation of tracer concentration, improved image contrast, spatial resolution and better noise properties.

Iterative reconstruction can be statistical, such as ML or ordered subset (OS) expectation maximization (EM) algorithms, or nonstatistical, as in conventional algebraic reconstruction methods like algebraic reconstruction techniques (ARTs), steepest descent, simultaneous iterative reconstruction, and others. Another group of iterative methods based on FBP image reconstruction has also been proposed. Statistical methods can further be categorized into Gaussian or Poisson based on the noise model assumed. In Gaussian methods, the objective function can be weighted or nonweighted least square, while in Poisson-based models the objective function is the log likelihood function. The latter guarantees positivity constraint so that the pixel value is always in

the positive direction, while in the Gaussian least square model, additional requirements are needed to maintain positivity.

Another possible classification for the statistical techniques is whether they consider prior information. The inclusion of prior information in image reconstruction allows driving the reconstructed images to the desired solution using penalty terms or prior function. This can be applied when Bayes's theorem is used in defining the objective function so that information regarding image distribution can be included in the reconstruction formula in advance. Morphological or patient anatomy, pixel smoothness, or nonnegativity constraints are different types of prior that can be used in Bayesian-based image reconstruction. The increased variance as the number of iterations increases is one of the noticeable but undesired features of statistical reconstruction techniques such as ML. Regularization using a smoothness penalty function can thus be applied to reduce image noise and to improve detectability of the reconstructed images.

16.2.4.1 System Matrix

A projection or system matrix (and also a transition matrix) is a key component in iterative techniques. It is based on the fact that the projection data are constructed by differential contributions of the object voxels being imaged. This transition from the image space to the projection space (Fig. 16.17) is the forward projection and is described in a matrix form as

$$P = Af$$

Unlike FBP, a system matrix in iterative reconstruction takes into account that each image voxel has a probability to contribute to a particular projection bin or sinogram. The system matrix A is the information reservoir that describes how the projection image is formed. It contains the coefficients a_{ij} that denote the probabilities of detecting a photon (or LOR) emitted from a particular site and detected in a particular bin.

Many physical phenomena can therefore be incorporated as far as they significantly contribute to data formation. In other words, the image space is mapped to the projection space by the

Projection space P
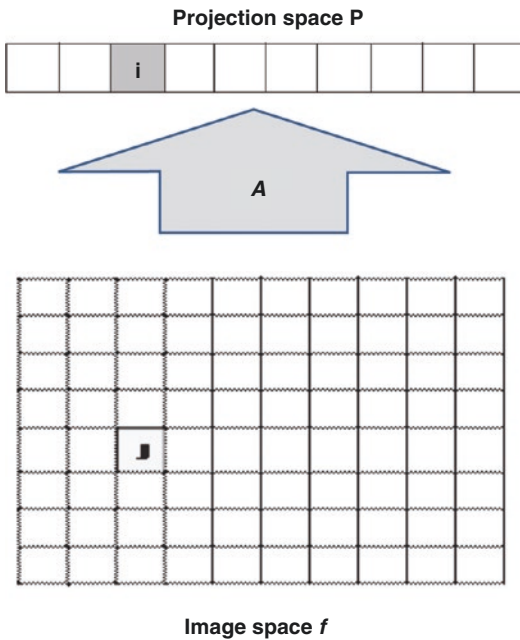
Image space *f*

Fig. 16.17 The system matrix maps the data from the image space to the projection space

aid of the transition matrix that describes the probability of detecting a photon emitted from pixel *j* and measured in projection bin *i* such that

$$p_i = \sum_j a_{ij} f_j$$

where *f* is the image vector representing the activity distribution indexed by pixel *j*, and *p* is the measured projection and indexed by pixel *i*. *A* is the transition matrix of elements and is equal to *i* × *j*.

However, this is not only for a one-detector row at one angle but also for all the acquired views, including all the detector elements. The situation becomes more problematic in building up a transition matrix for 3D image reconstruction when the interslice plane (3D SPECT) or oblique LOR (3D PET) is considered. Overall, the size of the system matrix is a function of the type and dimension of the data acquisition, number of detectors, number of projection angles, and size of the reconstructed image [28].

The system matrix can be structured so that it can account for the imaging physics and detector characteristics. In the context of SPECT imaging, attenuation, scatter, and detector response are major degrading factors that can be incorporated in the iterative scheme. An accurate correction for these image-degrading elements can lead to a significant improvement in image quality and quantitative accuracy. In PET imaging, the system matrix can also be built to handle geometric components and many physical parameters of positron emission and detection. It can be decomposed into individual matrices so that each matrix can account for particular or combined physical effects [29]. The accuracy of the system matrix is essential to ensure that the sources of degrading effects are well addressed and to realize the benefits underlying the modeling procedure. Otherwise, oversimplification or inaccuracies of the system matrix would transfer the signal into noise due to inconsistencies that would arise as the estimated projection will no longer match the measured data [30, 31].

It can be calculated on the fly using efficient geometric operators, or it can be computed and stored prior to image reconstruction. Analytical derivation, Monte Carlo simulation, experimental measurements, or a combination of these techniques can be used to compute the system matrix. However, these estimation approaches vary in terms of their complexity, computational burdens, accuracy, and validity. To reduce storage capacity, the sparseness and intrinsic symmetry of the scanner is utilized to generate a compressed version of the probability matrix. Also, for efficient use of the 3D-PET matrix, it can be decomposed into individual matrices, such as geometric, attenuation, sensitivity, detector blurring, and physics of positron emission.

The inclusion of many effects that degrade image quality and contribute to image formation has expensive computational requirements. Attempts made to overcome these computational demands have been the development of accelerated image reconstruction approaches such as OSEM (ordered subset expectation maximization), the rescaled block iterative expectation maximization (RBI-EM) method [32], and the row action ML algorithm (RAMLA). Other approaches were to use an unmatched pair of projection–backprojection in the iterative scheme to accelerate the reconstruction process by not

taking into account the effect of all degrading factors in both operations [33, 34]. Efficient algorithms that include dual-matrix and variance reduction techniques have significantly reduced the processing times of Monte-Carlo-based statistical reconstructions to clinically feasible limits [34].

16.2.4.2 Maximum Likelihood Expectation Maximization

Maximum likelihood expectation maximization (MLEM) is a popular iterative reconstruction technique that gained wide acceptance in many SPECT and PET applications. The technique comprises two major steps:

1. Expectation
2. Maximization

The algorithm works to maximize the probability of the estimated slice activity given the measured projection data with the inclusion of count statistics. Stated another way, the ML algorithm seeks to find the best estimate of the reconstructed image f that with the highest likelihood can produce the acquired projection counts p. The probability function is derived from the Poisson statistics and is called the likelihood objective function:

$$L\left(p|f\right) = \text{prob}\left[p|f\right] = \prod_i e^{-q_i^k} \frac{\left(q_i^k\right)^{p_i}}{p_i!} \quad (16.2)$$

where q_i^k is the estimated forward projection data and equal to $\sum_j a_{ij} f_j^k$, while the measured projection data are represented by p_i. The ML estimate can be calculated by Eq. 16.2 but it is more convenient and easier to work with the log of the likelihood function. The selection of Poisson function is appropriate since it maintains positivity of the pixel values and agrees with the statistics of photon detection. As a result, ML reconstruction has good noise properties and is superior to FBP, especially in areas of poor count statistics. One important issue in implementing the ML algorithm is that the input data (projections/sinograms) should be matched with the

noise hypothesis of the ML model, and prior treatments or corrections for the acquired data would serve to alter the noise properties assumed by the algorithm. This can be solved by either modifying the noise model (e.g., shifted Poisson) or feeding the data directly into the iterative process without a prior correction for any of the noise-disturbing elements.

Expectation maximization is the algorithm of choice to solve the likelihood function and works to estimate the projection data from knowledge of the system matrix and the current estimate of the image. The estimated and measured projection data are then compared by taking the ratio, which in turn is used to modify the current estimate of the slice. An image update takes place by multiplying that ratio with the current estimate to get a new image estimate "update." This process continues for several iterations until convergence is obtained and can be summarized as follows for iteration numbers k and $k + 1$:

1. The slice activity in the kth iteration is forward projected using the proposed imaging model to form a new projection image.
2. The ratio of the measured and estimated projection is calculated for each bin.
3. The result of the previous step is backprojected and normalized by dividing over the coefficients a_{ij} (see Eq. 16.3).

The new image f^{k+1} is produced by the multiplying the image in the kth iteration with the normalized backprojected data.

The equation used to define the MLEM reconstruction algorithm is [36]

$$f_j^{k+1} = \frac{f_j^k}{\sum_j a_{ij}} \left[\sum_i a_{ij} \frac{p_i}{q_i^k} \right] \quad (16.3)$$

It tells us that the $(k + 1)$th iteration is equal to the immediate previous iteration k multiplied by a correction term. The correction term is a normalized backprojection of the ratio of the measured projection p_i and the estimated projection of the slice activity resulting from iteration k, or q_i^k.

The drawback of using the Poisson formula is that it makes the algorithm reach a solution (reconstructed image) that is statistically consistent with the proposed activity distribution of the acquired projections. The reconstructed images therefore tend to be noisy, especially at a high number of iterations. As the number of iterations increases and the algorithm approaches the solution, the log-likelihood of the function also increases but with image deterioration due to high variance estimate. This is one of the major drawbacks of the ML algorithm, which can be overcome using stopping criteria, postreconstruction smoothing filters, or regularization by Gaussian kernels: "the method of sieves" [35, 36]. This last approach is implemented by restricting the range of the optimization in least squares or ML to a subset of smooth functions on the parameter space.

Penalized likelihood and Bayesian algorithms are also applied to regularize the solution and reduce noise artifacts. In practice, however, noise reduction is accomplished mostly using postreconstruction smoothing filters. However, in analytic image reconstruction, regularization is implemented using linear filtering, compromising spatial resolution.

Convergence of the MLEM is slow, but guaranteed, and depends on the spatial frequency (object dependent) such that low-frequency regions converge faster than high-frequency regions. At a large number of iterations, however, resolution tends to be uniform across the reconstructed slice.

The second limitation of ML is the computation requirements since it converges slowly, and high-speed computer devices are needed to make it feasible in practice. However, new computer technology is continuously advancing to resolve this issue (Moore's law). The other alternative to ML estimation is the OS algorithm, which has gained wide acceptance in many areas of research and clinical practice as it provides a significant improvement in computation time by accelerating the reconstruction process.

16.2.4.3 Ordered Subset Expectation Maximization (OSEM)

The accelerated version of the ML algorithm is the OS. This type of algorithm is also called block iterative or row action as it relies on using a single datum or subset of data at each iteration. OSEM was derived by Hudson and Larkin to speed up the iteration process [37].

The underlying concept of OSEM reconstruction is that instead of using the whole data set to obtain an update for the reconstructed image, all projection data are divided into smaller groups of projections, or subsets, and thus the image update is implemented when one subset is used; this is called *subiteration*. However, full iteration takes place when the algorithm uses all the available subsets in the image reconstruction.

The number of projections is divided equally into subsets. For example, in SPECT acquisition of 72 projections, the data set can be divided into 8 subsets, each with 9 projections. The projections in each subset are not contiguous but are spread over the whole set of angular views such that the first subset includes the projection numbers 1, 9, 18, and so on, and the second subset would have the projection numbers 2, 10, 19, and so on, and the same holds for the remaining subsets. The standard EM reconstruction of projection/backprojection is applied to each subset, one by one, so that the resulting reconstruction from subset 1 is the starting value for subset 2 and so on. In that example, a reduction of the reconstruction time by a factor of 8 can be achieved when using the OSEM technique as the rate of convergence is accelerated by a factor proportional to the number of subsets [37].

The properties of OSEM are similar to MLEM. Low-frequency regions converge faster than high-frequency regions. Thus, stopping iterations at an early stage may result in suboptimal results represented in a biased contrast; however, running a large number of iterations produces noisy images. Therefore, a trade-off between the number of iterations and detail recovery should be considered [38]. In regions of low tracer con-

centration, OSEM reconstruction might underestimate tracer activity concentration. This has been shown in a number of reports, including myocardial FDG studies and brain DatScan SPECT imaging [38, 39]. The spatially variant and object dependency convergence of iterative reconstruction is a limitation in determining the optimal number of iterations particularly with the increased noise as the iteration progresses. It is therefore of importance to optimize the reconstruction parameters, including the filtration step, given a particular detection task to exploit the full potential of the iterative technique in improving the observer performance or quantitative measurements [40].

Both 2D- and 3D-OSEM have found a number of successful applications in the reconstruction of SPECT and PET images, including corrections for many potentially degrading factors in addition to noise handling. These results have been exploited and commercialized in different software packages provided by scanner manufacturers. Attenuation-weighted OSEM reconstruction has been implemented in commercial PET scanners. Instead of precorrecting for photon attenuation before image reconstruction and presenting the data to the iterative technique in a Poisson-corrupted form, attenuation correction factors can be included in the system matrix to yield images with less noise and superior quality than data precorrected for attenuation. Not only attenuation but also other degrading factors, such as system response, has been incorporated into iterative OSEM and resulted in remarkable improvement of PET image quality and spatial resolution [41]. Also, it has become evident that including all corrections starting from random, dead time, normalization, geometric scatter, attenuation, and arc correction (the problem of unevenly spaced acquired projections) in the system matrix of iterative reconstruction allows preservation of the statistical nature of the raw data and satisfies the Poisson likelihood function of OSEM or MLEM, yielding an image with superior noise properties [42, 43].

16.2.4.4 Maximum A Posteriori

Maximum a posteriori (MAP) is a Bayesian reconstruction method that found several applications in SPECT and PET imaging [44]. It has a superior performance over analytic image reconstruction, especially when image-degrading factors are taken into account [45, 46]. However, in contrast to the ML mentioned here, MAP reconstruction uses prior knowledge to force the solution in the preferred or desired direction. According to Bayes's theorem, the probability of estimating an image provided the measured projection data is given by the posterior density function

$$\mathrm{prob}\big[f\,|\,p\big] = \frac{\mathrm{prob}\big[P\,|\,f\big]\,\mathrm{prob}\big[f\big]}{\mathrm{prob}\big[p\big]}$$

The first term of the nominator refers to the likelihood, while the second term denotes the distribution of the prior. The denominator is a constant (not a function of f) and can be dropped [40]. Note that in ML no preferences are placed on the reconstructed image; therefore, the objective function returns to the ML form once no information about the prior is assumed. The property given by MAP reconstruction to incorporate prior knowledge in the iterative procedure allows the associated noise elevation to be overcome as the number of iterations increases, as mentioned. This is implemented by penalizing the likelihood function by a prior term, driving the log-likelihood to the favored solution. The prior function is often selected to smooth the reconstructed images; however, this occurs with drawbacks of blurring sharp edges. Functions designed to smooth the image while being able to preserve edges have also been suggested. Another type of prior attempts to utilize morphological information provided by anatomical imaging modalities such as CT and MRI and based on the assumption that tracer uptake within a given structure or organ is uniformly distributed. However, using MAP reconstruction with anatomical priors has a number of limitations that, if

properly addressed, could significantly improve lesion detectability and image quality.

One of the commonly used is Gibbs distribution prior, which penalizes a given pixel based on differences with the neighboring pixels. It has the following mathematical representation:

$$P(x) = \frac{1}{Z} e^{-\beta U(x)}$$

$$U(x) = \frac{1}{2} \sum_{j=1}^{N} \sum_{k \in N_j} \psi(x_j - x_k)$$

where Z is a normalization constant, and β is a weighting parameter that determines the strength of the prior. $U(x)$ is the energy function and often contains potentials, $U(\cdot)$, defined on a pairwise cliques of neighboring pixels [46]. Prior functions based on absolute pixel differences have been devised as well as functions that use relative pixel differences. It is the selection and design of the potential function that allows penalization of the reconstructed images in favor of smoothing the images or preserving sharp edges, and this is implemented by increasing or decreasing the probability of the desired solution [47]. In the same vein, MAP-based reconstruction techniques produce an image with complex and object-dependent spatial resolution; this again can be controlled by the prior function. A nonuniform spatial resolution is obtained if a shift-invariant prior is used, whereas a uniform resolution comparable to postsmoothed ML (with a sufficient number of iterations) can be achieved with appropriate tuning of the prior [48, 49].

The availability of multimodality imaging devices such as SPECT/CT, PET/CT, and PET/MRI allows the introduction of morphological information in the iterative algorithm and thus has the potential to improve the quality of the diagnostic images. However, some problems could arise, such as image coregistration errors, identification of lesion location within the anatomical structures or segmentation errors, addition of lesion or organ boundaries or both, and selection of the penalty function and optimal prior strength [50]; ultimately, research efforts need to optimize the technique and prove an improved diagnostic confidence over other methods that do not rely on prior information. Furthermore, an underutilized application of MAP-type reconstruction is the unexploited feature of incorporating an anatomical prior to correct for the partial volume effect. There is an interest in improving the spatial resolution of PET images using resolution recovery approaches; however, investigations could also be directed to make use of the anatomical data provided by CT or MRI images to formulate feasible correction schemes in multimodality imaging practice [50–52].

16.2.5 Time of Flight Reconstruction

Time of flight as explained in Chap. 13 has received a renewed interest after its initial inception in 1980s. Initial results presented due to TOF image reconstruction in commercial LSO scanner have shown measurable gain in signal-to-noise ratio despite the use of relatively poor timing resolution of 1.2 ns [53]. Once the timing resolution of the PET scanner is very short such that the time arrival of the individual photons of the coincidences can be precisely measured, the theory of image reconstruction of the PET data is no longer required as photons "point" of annihilation can be determined. The current clinical PET systems still have not reached that goal and hence image reconstruction is required while having TOF data as additional piece of information to the reconstruction algorithm. PET data acquired with 3D mode are four dimensional and the additional TOF information increases data sparsity (a matrix with many zero elements) [54]. A Gaussian distribution function, the kernel, is then given instead of using the whole line of response in estimating the location of positron annihilation. The Gaussian is determined primarily by the system timing resolution (denoted by full width at half-maximum, FWHM) using the time-distance relationship $\Delta x = c \Delta \tau / 2$ where c is the speed of light.

List-mode data format is an efficient method for storing uncompressed PET containing TOF information. While being very slow in image

reconstruction due to handling the coincidences on an event-by-event basis, some advantages are obtained for the sake of image quality. Full utilization of the 3D PET data including TOF information and plugging into reconstruction without data reduction or rebinning could provide an improved image characteristics including uniform spatial resolution and noise-contrast trade-off [55, 56]. However, this process is computationally intensive and computer clusters are used in commercial TOF systems. A factor that may enhance the computation time and speed up the process is kernel truncation but inaccurate assignment of the TOF kernel could result in image quality deterioration [57]. In Philips GEMINI TOF, for example, the optimal kernel width was found less critical for the recovered contrast but influential on the background uniformity. Moreover, a smaller or wider kernels yielded less uniform background and reduced contrast recovery [58].

The 3D TOF data can also be transformed into different format including TOF as well as non-TOF in the 2D and 3D domains. This comes at the expense of increased image noise in the direction of going from 3D to 2D and also from TOF to non-TOF [59]. However, data rebinning via optimal weightings may have better variance and contrast recovery assessments in contrast to data without optimal weightings [60]. Furthermore, data rebinning into non-TOF sinograms retains significant signal to noise ratio over sinograms collected in absence of TOF information [61].

SSRE can also be implemented for TOF data in a similar fashion described for data acquired without TOF information [21, 62]. Fourier rebinning mapping in frequency space or native coordinate were also devised to reduce the size and dimensionality of the 3D TOF data into 2D data set [56, 63]. Fast accelerating methods employing graphics processing units (GPUs) using the compute unified device architecture (CUDA) framework was also presented to reconstruct TOF list-mode data set [54].

Earlier methods of TOF data reconstruction was the analytic methods [53, 64]. As described above, the analytic TOF reconstruction is carried out through backprojection of the sinogram data using confidence weighting function that utilize the uncertainty of the time resolution window of the system and then an inverse filter is employed to reconstruct the activity distribution in the image space. Various TOF reconstruction filters were proposed such as the most likely position (MLP), confidence weighting (CW), transverse ramp (TR), convolved ramp and Gaussian and others. The confidence weighting was shown to have minimal noise variance when having Poisson data derived from infinite uniform source distribution [64].

While analytic methods can be utilized to reconstruct the TOF PET data providing more speed and consistent quantification, model based statistical methods such as ML (or OSEM) are the most commonly used [65]. Direct reconstruction of the list-mode data is computationally demanding and used in some clinical systems but rebinning or transverse mashing methods could serve in data reduction and time saving.

16.2.6 Machine Learning

The topic of machine learning has been discussed in more than on instance in this textbook. There are several reasons behind this interest among which is the successful implementation of machine and deep learning in several aspects of radiology and nuclear medicine including image processing, classification, segmentation, super-resolution, and denoising, and many other disciplines related to disease detection, characterization and monitoring [66–68]. However, there are continued interests in improving network performance and more applications are emerging. Image reconstruction using convolutional neural networks or deep learning has been reported in several reports. DeepPET is a convolutional network devised as end-to-end encoder-decoder PET image reconstruction technique [69]. The method reconstructs the PET image from the sinogram data with high quality and quantitative accuracy. Initial results showed better relative error, peak signal to noise ratio, structural similarity index, and faster performance than iterative and analytic image reconstruction. On the SPECT side, a specialized method called SPECTNet was developed such that it split the

deep network into two subsystems and trained them separately; thus, avoiding training difficulty [70]. The projection space was mapped and compressed to a low-dimensional space in the image domain and then the compressed image was upscaled to the original dimension. More accurate images were obtained with less sensitivity to noise. Another approach was used to utilize the convolutional neural network in deriving SPECT images with quality comparable to Monte-Carlo-based image reconstruction but in a faster rate of processing [71]. In a similar manner, it was also demonstrated that deep learning reconstruction of scattered data in Y90 studies could provide comparable performance to Monte-Carlo based scatter estimates in the context of patient dosimetry and safety [72]. The merits achieved are accelerated image reconstruction by orders of magnitude faster than Monte-Carlo approach while able to maintain high accuracy.

Image noise in tomographic PET and SPECT is one of the most annoying factors in image reconstruction. Neural network may be trained on a predetermined noise level but this prior may lose generalizability due to noise sparsity in training or testing data and introduce additional bias if not properly treated. An approach to incorporate a local linear fitting function with denoising convolutional network was reported to robust versus noise level disparities while the network was trained with a predetermined noise level. A better quantitative and qualitative results were obtained in comparison to conventional methods [73]. The future of machine and deep learning in tomographic image reconstruction looks promising and would be able to overcome many of the current limitations providing a significant improvement in image quality, quantitative accuracy, and diagnostic performance.

16.3   Conclusions

Image reconstruction is a key element in conveying the diagnostic information given an activity distribution within different tissues. Analytic approaches are simple, fast, and easy to imple-

ment in research and clinical practice. However, they have some drawbacks that can be eliminated using iterative techniques. These provide improved image quality and quantitative accuracy, with some efforts to be done on optimizing the reconstruction parameters given a particular detection task. The system matrix of iterative reconstruction can be considered an information reservoir that allows the technique to reach the most accurate solution and thus should be optimally constructed. The future of machine and deep learning in tomographic image reconstruction looks promising and would be able to overcome many of the current limitations providing a significant improvement in image quality, quantitative accuracy, and diagnostic performance.

References

1. Even-Sapir E. Imaging of malignant bone involvement by morphologic, scintigraphic, and hybrid modalities. J Nucl Med. 2005;46(8):1356–67.
2. Bracewell RN. Strip integration in radio astronomy. Aust J Phys. 1956;9:198–217.
3. Beckmann EC. CT scanning the early days. Br J Radiol. 2006;79(937):5–8.
4. Jaszczak RJ. The early years of single photon emission computed tomography (SPECT): an anthology of selected reminiscences. Phys Med Biol. 2006;51(13):R99–115.
5. Li G, Citrin D, Camphausen K, Mueller B, Burman C, Mychalczak B, Miller RW, Song Y. Advances in 4D medical imaging and 4D radiation therapy. Technol Cancer Res Treat. 2008;7(1):67–81.
6. Noo F, Wagner JM. Image reconstruction in 2D SPECT with 180° acquisition. Inverse Probl. 2001;17:1357–71.
7. Hsieh J. Computed tomography: principles, design, artifacts, and recent advances. In: SPIE. International society for optical engineering, Bellingham; 2003.
8. Zanzonico P. Routine quality control of clinical nuclear medicine instrumentation: a brief review. J Nucl Med. 2008;49(7):1114–31.
9. Zeng GL, Gullberg GT. Unmatched projector/back-projector pairs in an iterative reconstruction algorithm. IEEE Trans Med Imaging. 2000;19(5):548–55.
10. Brooks RA, Di Chiro G. Principles of computer assisted tomography (CAT) in radiographic and radioisotopic imaging. Phys Med Biol. 1976;21(5):689–732.
11. Kinahan PE, Defrise M, Clackdoyle R. Analytic image reconstruction methods. In: Wernick M, Aarsvold J, editors. Emission tomography: the funda-

mentals of PET and SPECT. San Diego: Academic; 2004.

12. Matej S, Kazantsev IG. Fourier-based reconstruction for fully 3-D PET: optimization of interpolation parameters. IEEE Trans Med Imaging. 2006;25(7):845–54.

13. Madsen MT, Park CH. Enhancement of SPECT images by Fourier filtering the projection image set. J Nucl Med. 1985;26(4):395–402.

14. National Electrical Manufacturers Association. Performance measurements of positron emission tomographs (PET). Rosslyn: NEMA Standards Publication NU 2-2012; 2012.

15. Wells RG, Farncombe T, Chang E, Nicholson RL. Reducing bladder artifacts in clinical pelvic SPECT images. J Nucl Med. 2004;45(8):1309–14.

16. Gilland DR, Tsui BMW, McCartney WH, Perry JR, Berg J. Determination of the optimum filter function for SPECT imaging. J Nucl Med. 1988;29(5):643–50.

17. Qi J, Leahy RM. Iterative reconstruction techniques in emission computed tomography. Phys Med Biol. 2006;51(15):R541–78.

18. van Velden FH, Kloet RW, van Berckel BN, Molthoff CF, Lammertsma AA, Boellaard R. Gap filling strategies for 3-D-FBP reconstructions of high-resolution research tomography scans. IEEE Trans Med Imaging. 2008;27(7):934–42.

19. Karp JSMG, Lewitt RM. Constrained Fourier space method for compensation of missing data in emission computed tomography. IEEE Trans Med Imaging. 1988;7(1):21–5.

20. Colsher JG. Fully three-dimensional positron emission tomography. Phys Med Biol. 1980;25:103.

21. Daube-Witherspoon ME, Muehllehner G. Treatment of axial data in three-dimensional PET. J Nucl Med. 1987;28(11):1717–24.

22. Lewitt RM, Muehllehner G, Karp JS. Three-dimensional reconstruction for PET by multi-slice rebinning and axial image filtering. Phys Med Biol. 1994;39:321–40.

23. Defrise M, Kinahan PE, Townsend DW, Michel C, Sibomana M, Newport DF. Exact and approximate rebinning algorithms for 3D PET data. IEEE Trans Med Imaging. 1997;MI-16:145–58.

24. Matej S, Karp JS, Lewitt RM, Becher AJ. Performance of the Fourier rebinning algorithm for 3D PET with large acceptance angles. Phys Med Biol. 1998;43:787–97.

25. Krzywinski M, Sossi V, Ruth TJ, Nuclear Science Symposium CRI. Comparison of FORE, OSEM and SAGE algorithms to 3DRP in 3D PET using phantom and human subject data. In: IEEE nuclear science symposium, conference record, 1998, vol. 3, 1998. p. 1546–51.

26. Kinahan PE, Michel C, Defrise M, Townsend DW, Sibomana M, Lonneux M, Newport DF, Luketich JD. Fast iterative image reconstruction of 3D PET data. In: IEEE nuclear science and medical imaging conference, Anaheim, 1996. p. 1918–22.

27. Lalush DS, Wernick MN. Iterative image reconstruction. In: Wernick M, Aarsvold J, editors. Emission tomography: the fundamentals of PET and SPECT. San Diego: Academic Press; 2004.

28. Loudos GK. An efficient analytical calculation of probability matrix in 2D SPECT. Comput Med Imaging Graph. 2008;32:83.

29. Qi J, Leahy R, Cherry S, Chatziioannou A, Farquhar T. High-resolution 3-D Bayesian image reconstruction using the microPET small-animal scanner. Phys Med Biol. 1998;43:1001–13.

30. Qi J, Huesman RH. Effect of errors in the system matrix on maximum a posteriori image reconstruction. Phys Med Biol. 2005;50(14):3297–312.

31. Ortuno J, Pedro Guerra-Gutierrez P, Rubio J, Kontaxakis G, Santos A. 3D-OSEM iterative image reconstruction for high-resolution PET using precalculated system matrix. Nucl Instrum Meth Phys Res A. 2006;569:440–4.

32. Byrne CL. Block-iterative methods for image reconstruction from projections. IEEE Trans Imaging Process. 1996;5:792.

33. Kamphuis C, Beekman F, Van Rijk PP, Viergever MA. Dual matrix ordered subsets reconstruction for accelerated 3D scatter compensation in single-photon emission tomography. Eur J Nucl Med. 1998;25:8–18.

34. De Wit TC, Xiao J, Beekman FJ. Monte Carlo-based statistical SPECT reconstruction: influence of number of photon tracks. IEEE Trans Nucl Sci. 2005;52:1365–9.

35. Snyder DL, Miller MI. The use of sieves to stabilize images produced with the EM algorithm for emission tomography. IEEE Trans Nucl Sci. 1985;NS-32:3864–72.

36. Snyder DL, Miller MI, Thomas LJ, Politte DG. Noise and edge artifacts in maximum-likelihood reconstructions for emission tomography. IEEE Trans Med Imaging. 1987;6(3):228–38.

37. Hudson H, Larkin R. Accelerated image reconstruction using ordered subsets of projection data. IEEE Trans Med Imaging. 1994;13:601.

38. Seret A, Boellaard R, van der Weerdt A. Number of iterations when comparing MLEM/OSEM with FBP. J Nucl Med. 2004;45(12):2125–6.

39. Dickson JC, Tossici-Bolt L, Sera T, Erlnadsson K, Tatsch K, Hutton B. The impact of reconstruction method on the quantification of DaTSCAN images. Eur J Nucl Med Mol Imaging. 2010;37(1):23–35.

40. Hutton B, Nuyts J, Zaidi H. Iterative image reconstruction methods. In: Zaidi H, editor. Quantitative analysis in nuclear medicine imaging. New York: Kluwer/Plenum; 2004.

41. Panin VY, Kehren F, Michel C, Casey M. Fully 3-D PET reconstruction with system matrix derived from point source measurements. IEEE Trans Med Imaging. 2006;25:907–21.

42. Kadrmas DJ. LOR-OSEM: statistical PET reconstruction from raw line-of-response histograms. Phys Med Biol. 2004;49:4731.

43. Comtat C, Kinahan PE, Defrise M, Michel C, Townsend DW. Fast reconstruction of 3D PET data with accurate statistical modeling. IEEE Trans Nucl Sci. 1998;45:1083–9.

44. Levitan E, Herman GT. A maximum a posteriori probability expectation maximization algorithm for image reconstruction in emission tomography. IEEE Trans Med Imaging. 1987;6(3):185–92.

45. Frese T, Rouze NC, Bouman CA, Sauer K, Hutchins GD. Quantitative comparison of FBP, EM, and Bayesian reconstruction algorithms for the IndyPET scanner. IEEE Trans Med Imaging. 2003;22(2):258–76.

46. Qi J. Theoretical evaluation of the detectability of random lesions in Bayesian emission reconstruction. Inf Process Med Imaging. 2003;2732:354–65.

47. Qi J. Analysis of lesion detectability in Bayesian emission reconstruction with nonstationary object variability. IEEE Trans Med Imaging. 2004;23:321.

48. Fessler JA. Penalized weighted least squares image reconstruction for PET. IEEE Trans Med Imaging. 1994;13:290.

49. Fessler JA, Rogers WL. Spatial resolution properties of penalized-likelihood image reconstruction: spatialinvariant tomographs. IEEE Trans Image Process. 1996;5(9):1346–58.

50. Lehovich A, Gifford HC, Schneider PB, King MA. Choosing anatomical-prior strength for MAP SPECT reconstruction to maximize lesion detectability. IEEE Nucl Sci Symp Conf Rec. 2007;6(1):4222–5.

51. Baete KNJ, Van Laere K, Van Paesschen W, Ceyssens S, De Ceuninck L, Gheysens O, Kelles A, Van den Eynden J, Suetens P, Dupont P. Evaluation of anatomy based reconstruction for partial volume correction in brain FDG-PET. NeuroImage. 2004;23(1):3.

52. Alessio AM, Kinahan PE. Improved quantitation for PET/CT image reconstruction with system modeling and anatomical priors. Med Phys. 2006;33(11):4095–103.

53. Conti M, Bendriem B, Casey M, Chen M, Kehren F, Michel C, et al. First experimental results of time-of-flight reconstruction on an LSO PET scanner. Phys Med Biol. 2005;50(19):4507–26.

54. Pratx G, Surti S, Levin C. Fast list-mode reconstruction for time-of-flight PET using graphics hardware. IEEE Trans Nucl Sci. 2011;58(1):105–9.

55. Defrise M, Panin V, Michel C, Casey ME. Continuous and discrete data rebinning in time-of-flight PET. IEEE Trans Med Imaging. 2008;27(9):1310–22.

56. Vandenberghe S, Daube-Witherspoon ME, Lewitt RM, Karp JS. Fast reconstruction of 3D time-of-flight PET data by axial rebinning and transverse mashing. Phys Med Biol. 2006;51(6):1603–21.

57. Daube-Witherspoon ME, Surti S, Matej M, Werner S, et al. Influence of time-of-flight kernel accuracy in TOF-PET reconstruction. In: IEEE nuclear science symposium conference record, San Diego, CA, 2006. p. 1723–7.

58. Vandenberghe S, van Elmbt L, Guerchaft M, Clementel E, Verhaeghe J, Bol A, et al. Optimization of time-of-flight reconstruction on Philips GEMINI TF. Eur J Nucl Med Mol Imaging. 2009;36(12):1994–2001.

59. Bai B, Asma E. PET image reconstruction: methodology and quantitative accuracy. In: Khalil MM, editor. Basic science of PET imaging. Berlin: Springer; 2016. p. 259–84.

60. Ahn S, Cho S, Li Q, Lin Y, Leahy RM. Optimal rebinning of time-of-flight PET data. IEEE Trans Med Imaging. 2011;30(10):1808–18.

61. Cho S, Ahn S, Li Q, Leahy RM. Exact and approximate Fourier rebinning of PET data from time-of-flight to non time-of-flight. Phys Med Biol. 2009;54(3):467–84.

62. Mullani N, Wong W, Hartz P, et al. Sensitivity improvement of TOFPET by the utilization of the inter-slice coincidences. IEEE Trans Nucl Sci. 1982;29:479–83.

63. Defrise M, Casey ME, Michel C, Conti M. Fourier rebinning of time-of-flight PET data. Phys Med Biol. 2005;50:2749–63.

64. Tomitani T. Image reconstruction and noise evaluation in photon time-of-flight assisted positron emission tomography. IEEE Trans Nucl Sci. 1981;NS-28(6):4582–8.

65. Vandenberghe S, Mikhaylova E, D'Hoe E, Mollet P, Karp JS. Recent developments in time-of-flight PET. EJNMMI Phys. 2016;3(1):3.

66. Hosny A, Parmar C, Quackenbush J, Schwartz LH, Aerts H. Artificial intelligence in radiology. Nat Rev Cancer. 2018;18(8):500–10.

67. Choi H. Deep learning in nuclear medicine and molecular imaging: current perspectives and future directions. Nucl Med Mol Imaging. 2018;52(2):109–18.

68. Veit-Haibach P, Buvat I, Herrmann K. EJNMMI supplement: bringing AI and radiomics to nuclear medicine. Eur J Nucl Med Mol Imaging. 2019;46(13):2627–9.

69. Haggstrom I, Schmidtlein CR, Campanella G, Fuchs TJ. DeepPET: a deep encoder-decoder network for directly solving the PET image reconstruction inverse problem. Med Image Anal. 2019;54:253–62.

70. Shao W, Du Y. SPECT image reconstruction by deep learning using a two-step training method. Med Image Anal. 2019;60(Suppl 1):1353.

71. Dietze MMA, Branderhorst W, Kunnen B, Viergever MA, de Jong H. Accelerated SPECT image reconstruction with FBP and an image enhancement convolutional neural network. EJNMMI Phys. 2019;6(1):14.

72. Xiang H, Lim H, Fessler JA, Dewaraja YK. A deep neural network for fast and accurate scatter estimation in quantitative SPECT/CT under challenging scatter conditions. Eur J Nucl Med Mol Imaging. 2020;47(13):2956–67.

73. Kim K, Wu D, Gong K, Dutta J, Kim JH, Son YD, et al. Penalized PET reconstruction using deep learning prior and local linear fitting. IEEE Trans Med Imaging. 2018;37(6):1478–87.

Fundamentals of Radiomics in Nuclear Medicine and Hybrid Imaging

17

Lise Wei and Issam El Naqa

Contents

17.1 Introduction

Recent years have witnessed exponential growth in the use of imaging for diagnostic and therapeutic radiological purposes. In particular, positron emission tomography (PET) has been widely used in oncology for the purposes of diagnosis, grading, staging, and assessment of response. For instance, PET imaging with ^{18}F-FDG (fluoro-2-deoxy-D-glucose), a glucose metabolism analog, has been applied for diagnosis, staging, and treatment planning of lung cancer [1–10], head and neck cancer [11, 12], prostate cancer [13], cervical cancer [14, 15], colorectal cancer [16], lymphoma [17, 18], melanoma [19], and breast cancer [20–22]. Moreover, accumulating evi-

dence supports that pretreatment or posttreatment FDG-PET uptake could be used as a prognostic factor for predicting outcomes [23–27]. A review of recent advances in PET imaging for oncology is presented in our recent work [28].

Beside FDG-PET, other PET tracers have been also shown to be useful in interrogating tumor properties such as hypoxia by FMISO or Cu-ATSM and DNA synthesis and cell proliferation by FLT [29]. Interestingly, Denecke et al. compared CT, MRI and FDG-PET in the prediction of outcomes to neoadjuvant radiochemotherapy in patients with locally advanced primary rectal cancer, demonstrating sensitivities of 100% for FDG-PET, 54% for CT, and 71% for MRI and specificities of 60% for FDG-PET, 80% for CT, 67% for MRI [30]. In prostate cancer, Gallium-68 labeled ligand to the prostate specific membrane antigen (^{68}Ga-PSMA) has been demonstrated as promising marker for prostate cancer diagnosis [31–34]. Benz et al. showed that combined

L. Wei · I. El Naqa (✉)
Physics Division, Department of Radiation Oncology, University of Michigan, Ann Arbor, MI, USA
e-mail: liswei@umich.edu; ielnaqa@med.umich.edu, issam.elnaqa@moffitt.org

assessment of metabolic and volumetric changes predicts tumor response in patients with soft tissue sarcoma [35]. Similarly, Yang et al. showed that the combined evaluation of contrast-enhanced CT and FDG-PET/CT predicts the clinical outcomes in patients with aggressive non-Hodgkin's lymphoma [36].

Indeed, quantitative imaging information from hybrid-imaging modalities could be related to biological and clinical endpoints, a new emerging field referred to as "radiomics" [37, 38]. We were among the leading groups to demonstrate the potential of this new field to monitor and predict response to radiotherapy in head and neck [39, 40], cervix [39, 41], sarcoma [42], and lung [43] cancers, in turn allowing for adapting and individualizing treatment regimens. More recently, with the development of deep neural networks as well as the enhanced graphics processing unit (GPU) computing power, featureless deep learning-based image analyses showed promising results in several applications, including segmentation, reconstruction, and outcome modeling. These algorithms allow for learning the image representation directly from the raw images in opposite to conventional approaches that would require manual extraction of these features [44]. For instance, Sharif et al. presented an artificial neural networks in the wavelet domain for PET volume segmentation [45]. Zhao et al. proposed a multimodality segmentation method based on a 3D fully convolutional neural network (FCNN), which is capable of taking into account both PET and CT information simultaneously for tumor segmentation [46]. Ypsilantis et al. showed that one CNN based PET imaging representation are highly predictive of response to neoadjuvant chemotherapy [47].

On the other hand, SPECT remains a major modality for nuclear myocardial perfusion imaging (MPI) due to its lower cost and reliability [48]. Arsanjani et al. built an support vector machine (SVM) model using quantitative perfusion and functional variables showing an improvement in the diagnostic accuracy of automated analysis in predicting severe stenosis [49]. Betancur et al. used 28 clinical variables, 17 stress test variables, and 25 imaging variables

(including total perfusion deficit [TPD]) to build machine learning models for the prediction of major adverse cardiac events (MACE) [50]. Information gain ranking was applied for variable selection and a boosted ensemble algorithm was used for the model building. An AUC of 0.81 was achieved by their model. The same group recently applied deep learning for the analysis of SPECT MPI for prediction of obstructive coronary artery disease using multicenter data, which showed improved interpretation compared with other methods [51]. Aside from MPI application, imaging gene expression in vivo is another application of SPECT that is very helpful for cancer research [52, 53]. SPECT is also extensively used for the diagnosis of bone metastases in clinical practice [54, 55]. In addition, Ma et al. employed a DenseNet structure of CNN for the diagnosis of thyroid diseases with SPECT images [56]. Studies also showed that SPECT imaging increases the number and improves the localization of displayed lymph nodes in breast cancer patients [57–59].

In this chapter, we will discuss the application of advanced machine/deep learning techniques in nuclear medicine and hybrid imaging with specific focus on two major areas of improving image quality and image-based prediction of treatment outcomes.

17.2 Quantitative Image Features from PET and SPECT

A necessary prerequisite of image processing application in PET and SPECT is the robust extraction of relevant imaging features, which could be used in varying applications. Usually, preprocessing is required before radiomic feature extraction in order to enhance image quality, determine regions of interest (ROI), and obtain comparable features, especially for multimodality situations. Some general procedures, like up- or down- sampling to get isotropic voxel size and gray levels quantization, are commonly applied prior to textural feature extraction. Polynomial and spline interpolation are typical ways for resampling of the images [60]. Fixed bin number and

fixed bin width are two methods described in the Image Biomarker Standardization Initiative (IBSI) that can be used for quantization [61]. Fixed bin number method is recommended when the modality is not well calibrated [62, 63]. Though no consensus has been reached for quantization in PET/SPECT, 64 equally divided bins has been a common approach [64]. Comparing with CT, PET and SPECT require more preprocessing efforts due to lower contrast and signal-to-noise ratio. In addition to the steps mentioned above, functional imaging has poorer anatomical structures, thus, delineation of ROIs (e.g., tumors) is one of the most problematic part in their radiomics analysis workflow [65]. Manually drawing the ROIs suffers from inter- and intraobserver variability. Moreover, using a fixed percentage threshold of the SUVmax might underestimate the true tumor volume but is highly reproducible. More complex method, such as the fuzzy locally adaptive Bayesian method fits better for heterogeneous volumes with low resolution and variable noise and contrast [66, 67]. In addition to delineation of ROIs using PET/SPECT alone, the widely usage of PET/CT or SPECT/CT enables co-registration relying on rigid and/or deformable algorithms or inherent hardware, which would be an efficient and reproducible way to obtain the ROIs [68]. Furthermore, a conversion into a standardized scale, such as standardized uptake values (SUV) that takes into account the injected amount of radiotracer and the patient's weight is required as well [69]. Although varieties of preprocessing procedures are implemented to assure the robustness of extracted radiomic features, repeatability is still very variable among the radiomics features in nuclear imaging [70]. A lot of features are sensitive to acquisition and reconstruction settings, respiratory motion, segmentation methods, etc. Thus, except for the standardization discussed above, phantom study and test-retest analysis are recommended prior to radiomics signature construction.

The features extracted from PET/SPECT images could be divided into static (time invariant) and dynamic (time variant) features according to the acquisition protocol at the time of scanning, and into pre- or during-treatment features according to the scanning time point [71].

17.2.1 Static PET Features

(a) *Standard uptake value (SUV) descriptors:* SUV is a standard method in PET image quantitative analysis [72]. In this case, raw intensity values are converted into SUVs and statistical descriptors such as maximum, minimum, mean, standard deviation (SD), and coefficient of variation (CV) are extracted.

(b) *Total lesion glycolysis (TLG)*: This is defined as the product of volume and mean SUV [5, 35, 73].

(c) *Intensity-volume histogram (IVH)***:** This is analogous to the dose volume histogram widely used in radiotherapy treatment planning in reducing complicated 3D data into a single easier to interpret curve. Each point on the IVH defines the absolute or relative volume of the structure that exceeds a variable intensity threshold as a percentage of the maximum intensity [39]. This method would allow for extracting several metrics from PET images for outcome analysis such as I_x (minimum intensity to x% highest intensity volume), V_x (percentage volume having at least x% intensity value), and descriptive statistics (mean, minimum, maximum, standard deviation, etc.). We have reported the use of the IVH for predicting local control in lung cancer [43], where a combined metric from PET and CT image-based model provided a superior prediction power compared to commonly used dosimetric-based models of local treatment response.

(d) *Morphological features:* These are generally geometrical shape attributes such as eccentricity (a measure of noncircularity), which is useful for describing tumor growth directionality; Euler number (the number of connected objects in a region minus the solidity (this is a measurement of convexity), which may be a characteristics of benign lesions [74, 75]. An interesting demonstration of this

principle is that a shape-based metric based on the deviation from an idealized ellipsoid structure (i.e., eccentricity), was found to have strong association with survival in patients with sarcoma, and also shown in Fig. 17.1 [75, 76].

(e) *Texture features*: Texture in imaging refers to the relative distribution of intensity values within a given neighborhood. It integrates intensity with spatial information resulting in higher-order histograms when compared to common first-order intensity histograms. It should be emphasized that texture metrics are independent of tumor position, orientation, size, and brightness, and take into account the local intensity-spatial distribution [77, 78].

This is a crucial advantage over direct (first-order) histogram metrics (e.g., mean and standard deviation), which only measures intensity variability independent of the spatial distribution in the tumor microenvironment. Texture methods are broadly divided into three categories: statistical methods (e.g., high-order statistics, co-occurrence matrices, moment invariants), model-based methods (e.g., Markov random fields, Gabor filter, wavelet transform), and structural methods (e.g., topological descriptors, fractals) [79, 80]. Among these methods, statistical approaches based on the co-occurrence matrix and its variants such as the gray level co-occurrence matrix (GLCM), neighborhood gray tone difference matrix (NGTDM), run-length
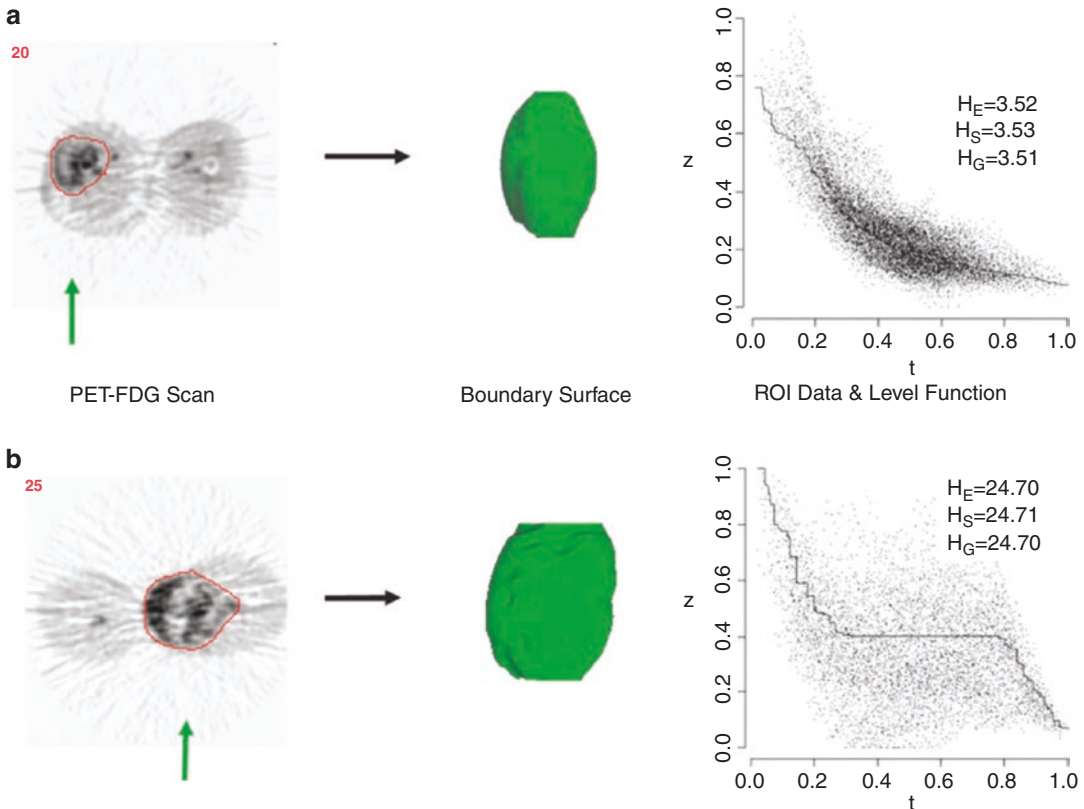
Fig. 17.1 Illustrations of heterogeneity computations for a relatively homogeneous tumor (**a**) and a more heterogeneous example (**b**). The graphics show (left) transverse FDG-PET scans through the tumor volumes; (middle) frontal view of the fitted boundary surface—the illumination point is shown with the green arrow on the scans (where the heterogeneity computations were conducted), the location of the transverse scan is shown with the black arrow. The glucose utilization within the tumor plotted against the fitted generalized contour coordinate function. The line shows the monotone level function estimate corresponding to the generalized heterogeneity computation

matrix (RLM), and gray level size-zone matrix (GLSZM) have been widely applied for characterizing FDG-PET heterogeneity [81].

The GLCM matrix characterizes the texture of an image by computing how often pairs of pixels with specific values and in a specified spatial relationship occur in an image. GLCM is an image-based description of the spatial relationships and is directional and step size dependent. The matrix is Ng × Ng size, where Ng stands for the discretized gray level number. Four commonly used features from the GLCM include: energy, entropy, contrast, and homogeneity [78]. GLRLM is also a two-dimensional matrix that each element is the number of elements with specific intensity along a predefined direction. The rows of GLRLM are the number of discretized gray levels, and the number of columns are defined by maximum run length along specified direction. Galloway recommended 5 texture features extracted from GLRLM matrix: short runs emphasis (SRE), long runs emphasis (LRE), grey level nonuniformity (GLN), run length nonuniformity (RLN), and run percentage (RP) [82]. The GLSZM is defined by Thibault et al. to classify cell nuclei for diagnosis of patients with Progeria disease [83]. GLSZM counts the number of zones of linked voxels, where the rows are the number of discretized gray levels, the number of columns is the maximum zone size of any region of connected voxels. It is quite similar with the GLRLM matrix, but with zone size instead of run lengths for the columns. And it is not directional. Typical features include large zone emphasis (LZE), low gray level zone emphasis (LGLZE), gray level nonuniformity (GLN), zone size nonuniformity (ZSN), etc. RLM and GLSZM emphasize regional effects. NGTDM contains the sum of gray level differences of pixels with discretized gray level and the average discretized gray level of neighboring pixels within a Chebyshev distance. It is a one column matrix with one value for each intensity. The value is the difference between the intensity and the average value of the neighborhood around that intensity. The NGTDM is thought to provide more human-like perception of texture such as: coarseness, contrast, busyness, and complexity.

These features were shown to predict response in cancers of the cervix [39], esophagus [84], head and neck [85], and lung cancer [86].

17.2.2 Dynamic PET Features

These features are based on kinetic analysis using tissue compartment models and parameters related to transport and binding rates [87]. In the case of FDG, a 3-compartment model could be used to depict the trapping of FDG-6-Phosphate (FDG6P) in tumor [88, 89]. Using estimates from compartmental modeling, glucose metabolic uptake rate could be evaluated. The uptake rate and other compartment estimates themselves could form "parameter-map" images, which previously described static features, could be derived from as well.

Glucose metabolic rate was correlated with pathologic tumor control probability in lung cancer [90]. Thorwarth et al. published interesting data on the scatter of voxel-based measures of local perfusion and hypoxia in head and neck cancer [91, 92]. Tumors showing a wide spread in both showed less reoxygenation during a course of radiotherapy and had lower local control. A rather interesting approach to improve the robustness of such features is the use of advanced 4D iterative techniques. Further improvement could be achieved by utilizing multi-resolution transformations (e.g., wavelet transform) to stabilize kinetic parameter estimates spatially [93].

Once the radiomic features are extracted, machine learning methods, both handcrafted based conventional methods and machine-engineered deep learning methods could be utilized for the outcome modeling, or other endpoints that is needed.

17.2.3 Handcrafted Radiomics Methods

With hundreds or even more radiomics features available, feature selection and/or feature extraction is a necessary step that aims to obtain the optimal subset or combination of features to

achieve better performance and also to reduce the risk of overfitting. Three categories filter, wrapper and embedded methods are commonly used for feature selection. Filter method is a ranking-based method that ranks the importance of features based on a score that measures how relevant the feature is to the data or the outcome. Some example filter methods are correlation based (e.g., Spearman, Pearson), relief, and classical test statistics. Wrapper methods select features based on a single classifier performance of certain feature. LASSO (least absolute shrinkage and selection operator) is an example of embedded method, which implements feature selection and model building simultaneously [94]. Principle component analysis (PCA) [95], clustering, and t-Distributed Stochastic Neighbor Embedding (t-SNE) [96] are some examples of the feature extraction methods. PCA compresses the high-dimensional data into a new low-dimensional space by maintaining the large variances. Clustering, such as K-means and hierarchical clustering, is able to explore the feature relationship and obtain a representation using the cluster centroid. T-SNE is a nonlinear dimension reduction method that is suitable for data visualization, since it is capable of retaining the local structure (pairwise similarity) of data, while revealing some important global structure.

Based on the endpoints, either time dependent (survival) or independent (classification) machine learning algorithms could be applied for the feature selection [97]. Typical classification algorithms include logistic regression, support vector machines (SVM), random forests (RF), and neural networks [98–100]. Specifically, various kernel functions (e.g., radial basis function) enabled SVM to perform nonlinear classification by mapping to higher dimensional feature space. Decision trees are popular in medical application due to sequential reasoning similar to human thinking, while suffered from the high variance [101, 102]. Random forests solved this issue by applying bootstrap aggregation [102]. Cox regression [103], random survival forests [104], and support vector survival [105] methods, as well as recently proposed deep learning-based survival models [106, 107] are available methods

for survival analysis. For these popular machine learning methods, we will not go into details. More information could be found from the references. In addition to these supervised algorithms, various clustering methods, such as those mentioned for feature extraction are also available to reveal the subgroups for certain diseases. Another challenge in the medical field is the lack of labeled data, semi-supervised method could make use of small labeled data and the large size of unlabeled data for the model training. Transductive SVM (TSVM) is an example for semi-supervised conventional machine learning method that tries to keep the unlabeled data as far away from the margin as possible to classify new samples with better accuracy [108].

17.2.4 Machine-Engineered Radiomics Methods

Though handcrafted features introduced above can provide prior knowledge, they also suffer from the tedious designing process and may not faithfully capture the underlying imaging information for the task at hand. Alternatively, with the development of deep learning technologies, as a branch of machine learning, the extraction of machine learnt features is becoming widely applicable recently. These deep learning methods are generally based on multilayer neural networks, especially the convolutional neural networks (CNN). In deep learning, the processes of data representation and prediction (e.g., classification or regression) are performed jointly. In such a case, multi-stack neural layers of varying modules (e.g., convolution or pooling) with linear/nonlinear activation functions perform the task of learning the representations of data with multiple levels of abstraction and subsequent fully connected layers are tasked with classification/regression, for instance [44].

A typical scenario to get such features is to use the data representation CNN layers as feature extractor. Each hidden layer module within the network transforms the representation at one level. For example, the first level may represent edges in an image oriented in a particular direc-

tion, the second may detect motifs in the observed edges, the third could recognize objects from ensembles of motifs [109]. Patch−/pixel-based machine learning (PML) methods use pixel/voxel values in images directly instead of features calculated from segmented objects as in other approaches [110]. Thus, PML removes the need for segmentation, one of the major sources of variability of radiomic features. Moreover, the data representation removes the feature selection portion eliminating associated statistical bias in the process.

For the CNN network, either self-designed (from scratch) or existing structures (e.g., VGG [111], Resnet [112], two CNN network structure that performed well for ImageNet classification task) can be used. Depending on the data size, we can choose to fix the parameters or fine tune the network using our data, also called transfer learning. Instead of using deep networks as feature extractors, we can use them directly for the whole modeling process. Similar to the conventional machine learning methods, there are also supervised, unsupervised, and semi-supervised methods. CNN are similar to regular neural networks, but the architecture is modified to fit to the specific input of large-scale images.

Inspired by the Hubel and Wiesel's work on the animal visual cortex [113], local filters are used to slide over the input space in CNNs, which not only exploit the strong local correlation in natural images, but also reduce the number of weights significantly by sharing weights for each filter. Recurrent neural networks (RNN) can use their internal memory to process sequence inputs (e.g., dynamic PET acquisition) and take the previous output as inputs. There are two popular types of RNN—Long short-term memory (LSTM) and Gated recurrent units (GRU) [114, 115]. They were invented to solve the problem of vanishing gradients for long sequences by internal gates that are able to learn which data in the sequence is important to keep or discard.

Deep autoencoders (AE), which are unsupervised learning algorithms (no labels are needed for the input data), have been applied to medical imaging for latent representative feature extraction. There are variations to the AEs, such as

variational autoencoders that resemble the original AE and variational Bayesian methods to learn a probability distribution that represents the data [116], convolutional autoencoders that preserve spatial locality [117], etc. Another unsupervised method is the restricted Boltzmann machine (RBM), which consists of visible and hidden layers [118]. The forward pass learns the probability of activations given the inputs, while the backward pass tries to estimate the probability of inputs given activations. Thus, the RBMs lead to the joint probability distribution of inputs and activations.

Deep belief networks can be regarded as a stack of RBMs, where each RBM communicates with previous and subsequent layers. RBMs are quite similar with AEs, however, instead of using deterministic units, like RELU, RBMs use stochastic units with certain distribution. As mentioned above, labeled data is limited, especially in the medical field. Neural network-based semi-supervised approaches that combine unsupervised and supervised learning by training the supervised network with an additional loss component from the unsupervised generative models (e.g., AEs, RBMs) [119]. More details on the machine learning aspect is provided here [120, 121].

Comparing with feature-based methods, deep learning methods are more flexible and can be used with some modifications in various tasks. In addition to classification, segmentation, registration, and lesion detection are widely explored by deep learning techniques. Fully CNN (FCN), trained end-to-end, merge features learnt from different stages in the encoders and then upsampling low resolution feature maps by deconvolutions [122]. Unet, built upon FCN, with the pooling layers being replaced by upsampling layers, resulted in a nearly symmetric U-shaped network [123]. Skipping structures combines the context information with the unsampled feature maps to achieve higher resolution. In order to identify Alzheimer's disease or mild cognitive impairment, Suk et al. exploited deep Boltzmann machine (DBM) to obtain a latent hierarchical feature representation from a 3D patch, and then devised a systematic method for a joint feature
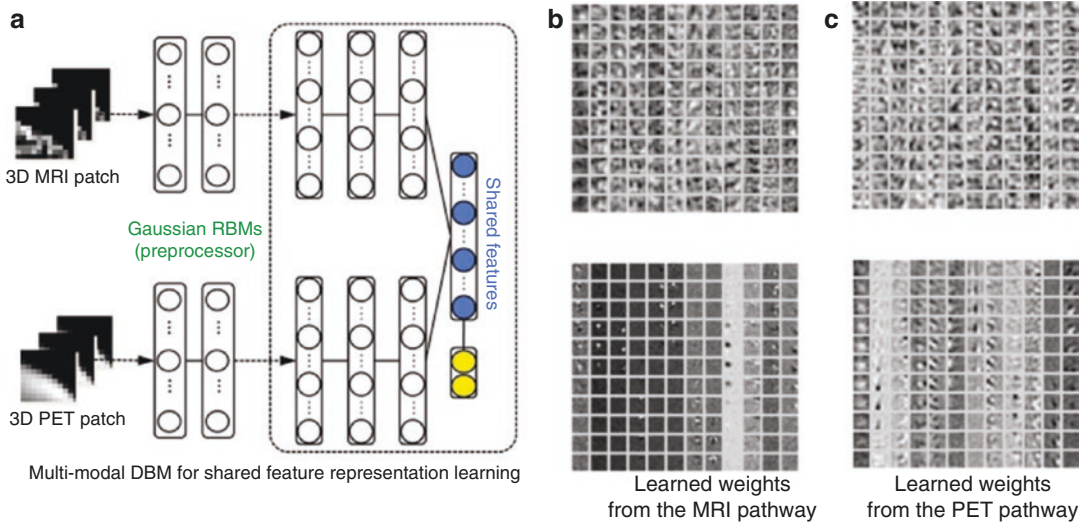
representation, as shown in Fig. 17.2a, from the paired patches of MRI and PET with a multimodal DBM by fusing neuroimaging and biological features. Figure 17.2b, c visualize, respectively, the learned connection weights from the MRI pathway and the PET pathway [124].

Once the model is built using the algorithms introduced above, the final step is the model evaluation. Ideally, the model should be tested on a large independent patient cohort. Alternatively, resampling methods were developed to evaluate the model performance in the situation of limited sample sizes. Two commonly applied methods are bootstrapping and cross-validation. The basic idea of bootstrapping is to make inference about a population using the sample data by resampling with replacement methods. It was first introduced by Bradley Efron in 1979 [125], and the more commonly used bias-corrected and accelerated (BCa) bootstrap was developed by Efron as well [126]. Cross-validation is used to measure (evaluate) the goodness of fit for a prediction model. Models will be developed on the training folds and tested on the validation fold. Typically used frames are fivefold or tenfold cross-validation. Cross-validation is commonly used for model hyper-parameter tuning as well. In terms of the metrics that measure the goodness of fit, the receiver operating characteristic (ROC) curve, or the area under the ROC curve (AUC) quantifies the sensitivity and specificity of the model and represents the probability that a randomly selected case is correctly distinguished with a larger probability than a randomly selected case is incorrectly distinguished for the classification task, and c-index is similar to AUC and is used as a measure for survival models, which is the probability of concordance between predicted and observed survival. The instruction of using these techniques can be found in the TRIPOD guidelines [127].

One thing to point out is that the training data used for feature selection and model construction should not be used for the evaluation of the model, which will lead to overoptimistic results and worse generalization for new data. Careful design of training, validation, and test sets within any resampling technique is vital for reducing the selection or optimization bias [102, 128, 129], where a balance between fitting and generalization can be achieved. The size of the training data is an intractable problem that depends on the dataset, the complexity of the problem, and the learning algorithm. Ideally, more data is desired to train complex models (e.g., deep learning models) and estimate the generalizability of the developed models. However, in reality, especially in the
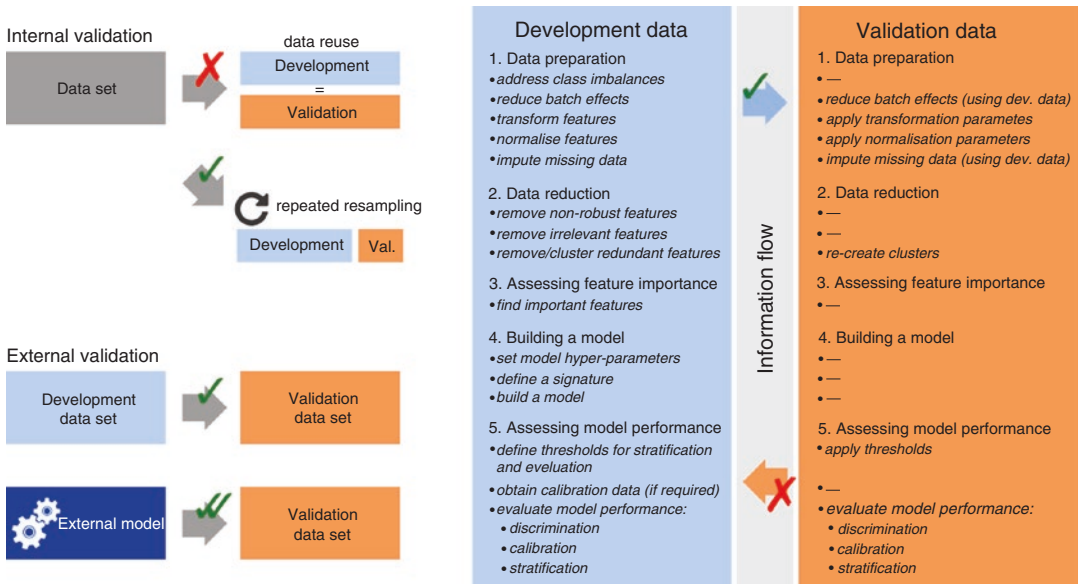
Fig. 17.3 (**a**) Data analysis strategies and typical analysis workflow. Generalizability of a radiomics model is assessed through internal and external validation (**a**). Internal validation should be reported by repeatedly dividing the data into development and validation datasets instead of reusing the development data for validation to avoid optimistic biases. (**b**). Many steps are only fully performed on the development dataset, and the resulting parameters and results are applied to the validation dataset

medical field, data scarcity is a challenge hard to be resolved. To deal with this issue, synthetic data methods were applied, such as generative adversarial networks, or simply using slices or patches of images. Theoretically, power analysis is used to estimate the sample size needed to detect an effect. The definition of power is the probability of rejecting the null hypothesis when it is true.

In a review by Zwanenburg, the radiomics workflow as shown in Fig. 17.3 was summarized. Meanwhile several pitfalls during radiomics analysis was pointed out as well, such as the split of training, validation and testing data, class imbalance and incomplete reporting, which should be paid attention to when conducting radiomics study [130].

17.3 Application of PET and SPECT

In the following, we discuss application of PET and SPECT to radiotherapy with focus on two cases: PET image reconstruction at low dose,

outcome prediction for clinical decision-making using radiomics and deep learning for both PET and SPECT.

17.3.1 Acquisition of High-Quality PET and SPECT Images Using Deep Learning

Though having better sensitivity compared with other modalities, PET/SPECT images suffered from low resolution and signal-to-noise ratio (SNR). Usually, a full-dose radioactive tracer is needed to obtain high-quality PET images. However, this raises concerns about the potential health influence. On the other hand, dose reduction will lead to even worse image quality. Wang et al. adopted a mapping based sparse representation method for full-dose PET prediction, utilizing both low-dose PET and multimodal MRI [131]. They further proposed a semi-supervised triple dictionary learning method for full-dose PET image prediction to take advantage of the large number of missing-modality samples [132].

The same group further developed a method based on 3D conditional generative adversarial networks (3D c-GANs) to estimate the full-dose PET images from low-dose ones [133].

The previous methods were based on small patches, which are time-consuming when testing on new samples and will lead to over-smoothed images that lack the texture information within typical full-dose PET images. Figure 17.4a shows the training procedure of 3D c-GANs network, with the generator network taking low-dose PET image and the discriminator network taking a pair of images—both the low-dose PET and the corresponding real/estimated full-dose PET images, which tries to differentiate between the real and estimated pairs. A 3D U-net-like deep architecture was used as the generator with the skip connections. The results are shown in Fig. 17.4b. The proposed c-GANs can reduce the noise in low-dose PET images and enhance the image quality toward the real full-dose PET images. Several other methods were compared with the 3D c-GAN. The proposed 3D c-GANs produce better visual quality that is close to the real full-dose image in all three views, the results obtained by 2D c-GANs only show good performance in the corresponding trained view.

Instead of generating full-dose images from low-dose ones, Gong et al. trained a deep residual CNN to improve PET image quality by using the existing inter-patient information. They embedded the neural network in the iterative reconstruction framework for image representation, rather than using it as a postprocessing tool. The objective function was formulated as a constraint optimization problem and solved by the alternating direction method of multipliers (ADMM) algorithm [134]. Interestingly, later they came up with a novel method for PET image reconstruction using deep image prior to bypass the requirement of large amounts of prior training pairs for deep learning applications [135, 136]. The essence of deep image prior is that the only information required to solve the reconstruction (as well as other tasks, e.g., denoising, super-resolution) is contained in the single degraded image and the handcrafted structure of the network [135].

As early as 1991, an artificial neural network with one hidden layer was developed to reconstruct SPECT images by Floyd [137]. SPECT images at 64 spatial positions at 60 angles (3840 projection elements) were used as the input and the output was 1976 pixels in a circular reconstruction region. The optimization was conducted by minimizing the mean squared loss using shift invariance trick to reduce the weight number.

17.3.2 PET and SPECT Radiomics (Feature-Based and Featureless Neural Network-Based)

The extraction of quantitative information from imaging modalities and relating information to biological and clinical endpoints is a new emerging field referred to as "radiomics" [37, 38]. Traditionally, quantitative analysis of FDG-PET or other PET tracers' uptake is conducted based on observed changes in the standardized uptake value (SUV). For instance, decrease in SUV post-irradiation has been associated with better outcomes in lung cancer [138, 139]. However, SUV measurements themselves are potentially pruned to errors due to the initial FDG uptake kinetics and radiotracer distribution, which are dependent on the initial dose and the elapsing time between injection and image acquisition. In addition, some commonly reported SUV measurements might be sensitive to changes in tumor volume definition (e.g., mean SUV). These factors and others might make such approach subject to significant intra- and interobserver variability [25, 26, 39].

Radiomics consist of two main steps extraction of static and dynamic and outcomes modeling as presented in the Sect. 17.3. Outcomes in oncology and particularly in radiation oncology are characterized by tumor control probability (TCP) and the surrounding normal tissues complications (NTCP) [140, 141]. A detailed review of outcome modeling in radiotherapy is presented in our previous work [142]. DREES is a dedicated software tool for modeling of radiotherapy response [143]. In the context of image-based
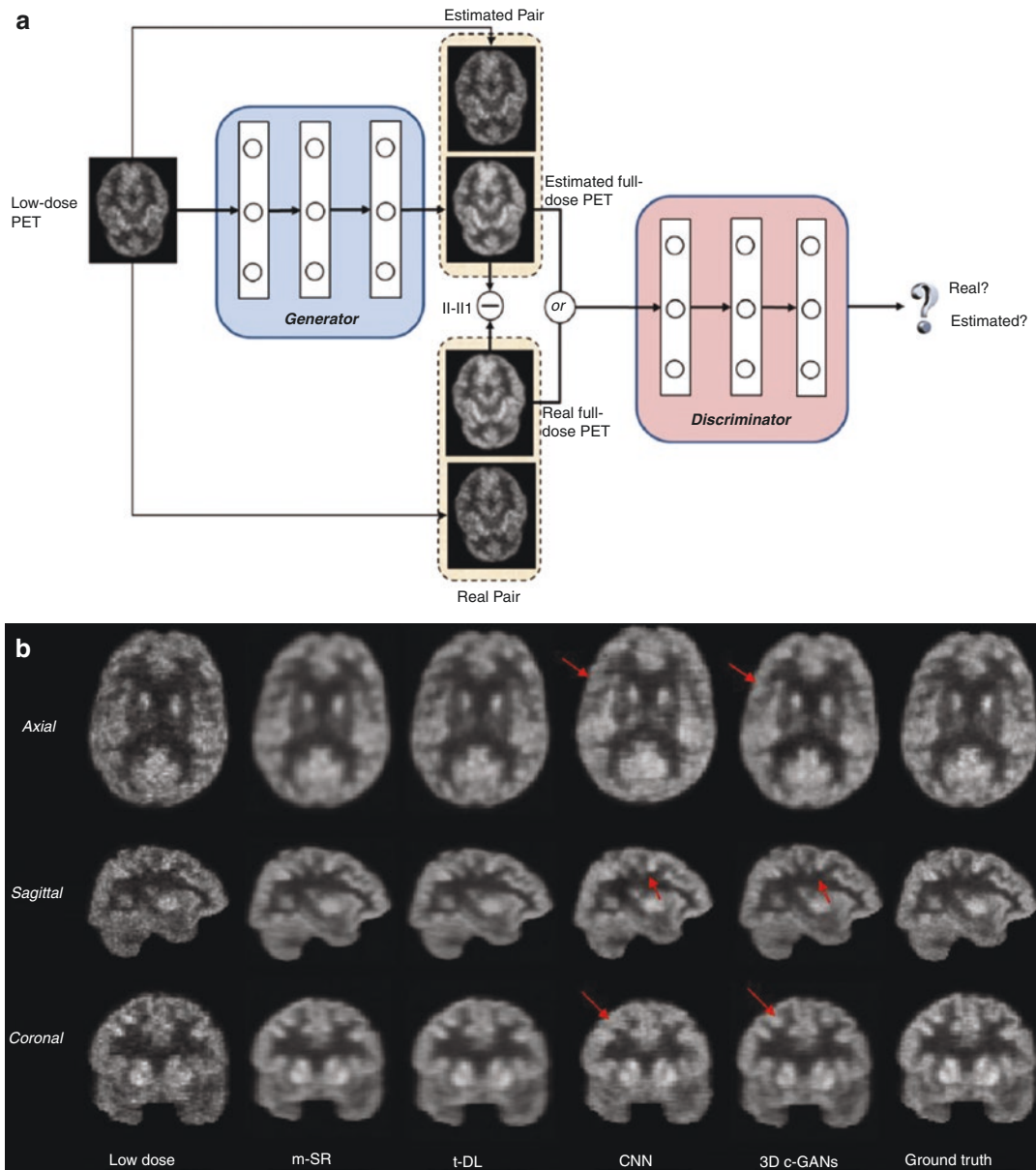
Fig. 17.4 (**a**) Framework of training a 3D c-GANs to estimate the full-dose PET image from low-dose counterpart; (**b**) Qualitative comparison of low-dose PET images, estimated by the mapping based sparse presentation method (m-SR), by semi-supervised tripled dictionary learning method (t-DL), by convolutional neural networks (CNN), and by the proposed concatenated 3D c-GANs method (3D c-GANs), as well as the real full-dose PET images (Ground truth). In the axial and coronal images, the left side of the image is the right side of the brain, and the right side of the image is the left side of the brain (From Wang et al. 2018)

treatment outcomes modeling, the observed outcome (e.g., TCP or NTCP) is considered to be adequately captured by extracted image features [39, 144].

El Naqa et al. investigated intensity-volume histogram metrics and shape and texture features extracted from PET images to predict patient's response to treatment. Logistic regression was

applied on two datasets for cervix and head and neck cancers were used and showed good preliminary discriminant power for utilizing functional imaging in clinical prognosis [39]. Cook et al. conducted research on 53 patients with non–small cell lung cancer (NSCLC) treated with chemoradiotherapy underwent pretreatment 18F-FDG PET/CT scans. They found that baseline 18F-FDG PET scan uptake showing abnormal texture as measured by coarseness, contrast, and busyness is associated with nonresponse to chemoradiotherapy by RECIST and with poorer prognosis [86]. In another study, maximum and mean standard uptake value (SUVmax and SUVmean), metabolic tumoral volume (MTV), total lesion glycolysis (TLG), as well as 13 global, local and regional textural features were extracted for 63 patients with NSCLC treated by Stereotactic body radiotherapy (SBRT) who underwent an 18F-FDG PET/CT before treatment. Logistic regression and Kaplan–Meier analysis were applied using these along with clinical features for overall survival (OS), disease specific survival (DSS) and disease-free survival (DFS) [145]. They found that the textural feature dissimilarity measured on the baseline 18F-FDG PET/CT appears to be a strong independent predictor of the outcome. Yip et al. assessed the association of and predictive power of FDG-PET-based radiomic features for somatic mutation in NSCLC patients [146]. Twenty-one imaging features were extracted form 348 patients and the association between imaging features and mutation status was assessed using the Wilcoxon rank-sum test. They found that eight radiomic features and two conventional features were significantly associated with EGFR mutation status (FDR Wilcoxon = 0.01–0.10).

Figure 17.5 showed the PET images for different mutation groups and the predictive power for each feature. Hsu et al. introduced a FDG-PET radiomics tissue classifier for differentiating FDG-avid-normal tissues from tumor [147]. Thirty-three scans from 15 patients with Hodgkin lymphoma and 68 scans from 23 patients with Ewing sarcoma treated on two prospective clinical trials were retrospectively analyzed. Standard-uptake-value (SUV) derived shape and first-order radiomics features were computed to build a random forest classifier. Classifier performance was varied across normal tissue types (brain, left kidney and bladder, heart and right kidney were 100%, 96%, 97%, 83% and 87% respectively). This work showed that the radiomics features from PET images are able to correctly capture the characteristics of normal tissues and tumor. Figure 17.6 showed one of the decision tree, the threshold for the random forests and the t-SNE visualization for better understanding of the role of different features.

Comparing with PET radiomics, there are fewer studies for SPECT. Buda'n et al. developed a novel multimodal radiomics evaluation method, utilizing X-ray computed tomography (CT) and (SPECT) with Tc-99 m methyl diphosphonate (Tc-99 m-MDP) tracer [148]. The properties of bone formation process within poly (methyl methacrylate)-based bone cement graft (PMMA) was compared to that of albumin coated, sterilized, antigen-extracted freeze-dried human bone grafts (HLBC), in caudal vertebrae (C5) of rats. Linear regression analysis of PMMA-treated group variables (mean opacity increase; mean Tc-99 m-MDP activity decrease), revealed a negative correlation with the medium strength ($r = 0.395$, $p = 0.605$) and strong positive correlation when HLBC group variables were analyzed ($r = 0.772$, $p = 0.012$), which indicates that HLBC grafts is advantageous in terms of the osteoblast activity and bone vascularization over PMMA cement. Figure 17.7 shows the raw activity for the vertebrae of rats in this study.

Another study of SPECT texture analysis is the dopamine transporter (DAT) SPECT imaging for diagnostic purposes in suspected Parkinsonian syndromes by Rahmim et al. [149]. SPECT images were registered onto corresponding MRI images to obtain region-of-interest (ROI), followed by computation of Haralick texture features. Univariate and multivariate regression analyses were performed between the quantitative metrics and different clinical measures, including (1) the unified Parkinson's disease rating scale (UPDRS) (part III–motor) score, disease duration as measured from (2)) Disease duration (DD), taken with respect to time of diag-
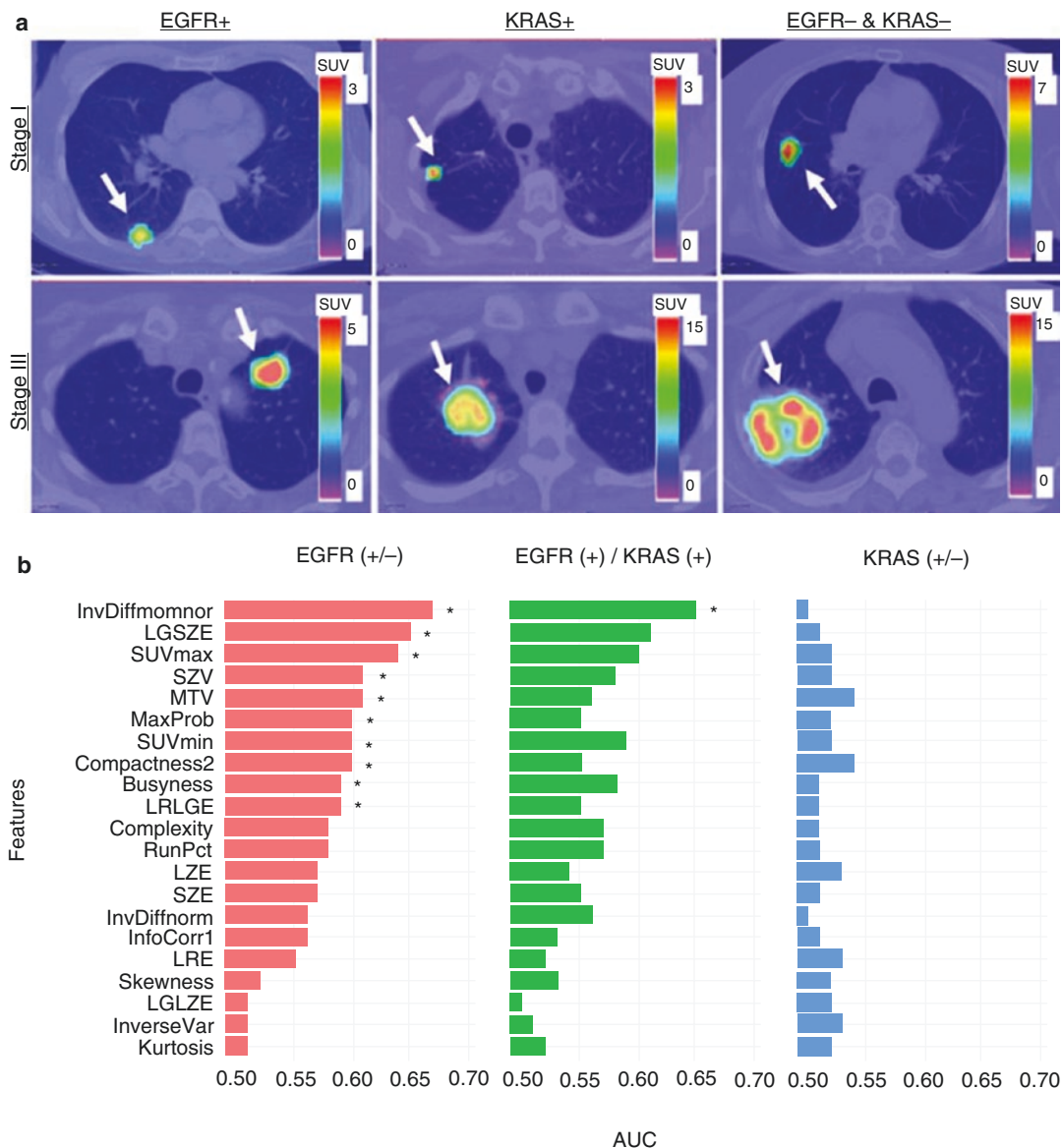
Fig. 17.5 (**a**) From left to right are patients with EGFR mutation, KRAS mutation, and EGFR—and KRAS—tumors. Stage I and III tumors are shown in top and bottom rows, respectively. Arrows indicate locations of lung tumors; (**b**) AUC. * indicates that AUC is significantly >0.50 (random guessing) assessed with Noether test (FDR$_{Noether}$ ≤ 0.10). Many of the features significantly predict EGFR+ tumors; however, they are not able to predict KRAS+ tumors

nosis (DD-diag.) and (3) time of appearance of symptoms (DD-sympt.) as well as (4) the Montreal Cognitive Assessment (MoCA) score on 141 subjects from the Parkinson's Progressive Marker Initiative (PPMI) database. For the Parkinson's disease (PD) subjects, significant correlations were observed in the caudate when including texture metrics, with (1) UPDRS (*p*-values <0.01), (2) DD-diag. (*p*-values <0.001), (3) DD-sympt (*p*-values <0.05), and (4) MoCA (*p*-values <0.01), which demonstrated the ability to capture valuable information using advanced

a

b   **c**

| Bladder | Brain | Heart | Kidney L | Kidney R | Tumor |
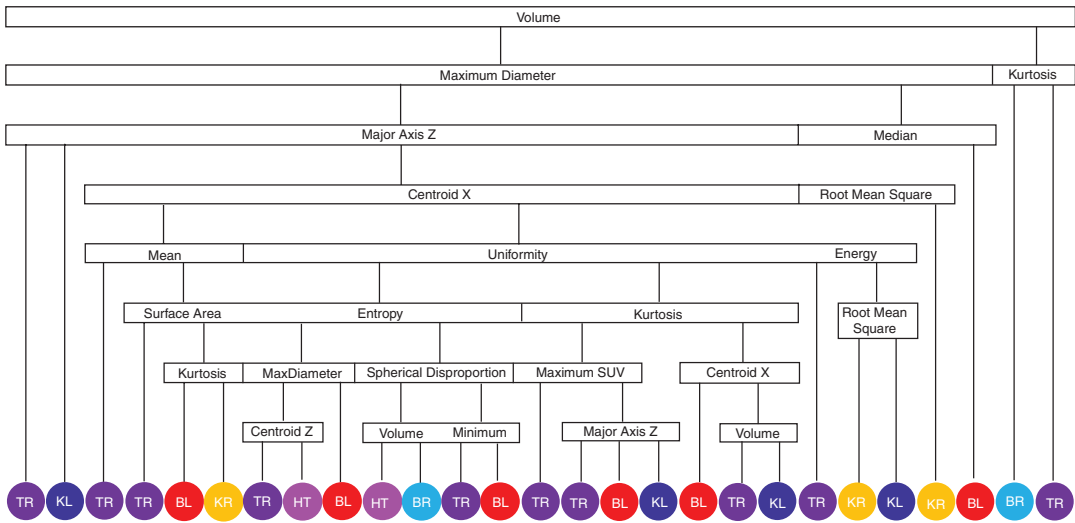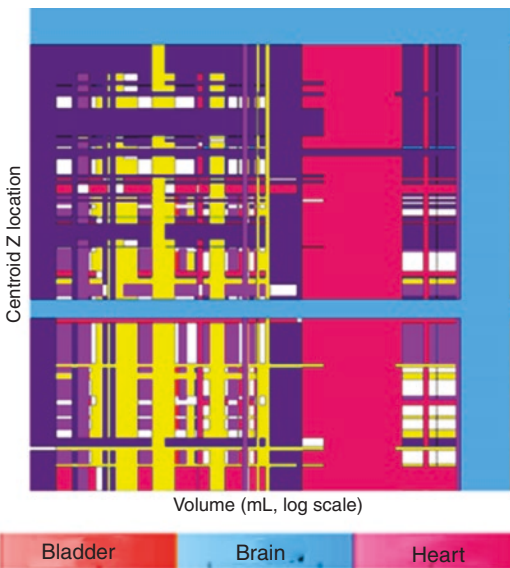
Fig. 17.6 Visualization of random forest classifier. (**a**) Binary decision tree for classifying FDG-avid tissues and tumor. Fifty binary decision trees were trained with the random forest classifier. (*TR* tumor, *KL* kidney left, *BL* bladder, *KR* kidney right, *HT* heart, *BR* brain). (**b**) Display of threshold values for volume and maximum SUV in all 50 trees. The color coding (red: bladder, green: brain, blue: heart, purple: kidney left, gold: kidney right, teal: tumor, white: undecided) shows the tissue classification made on two features: volume and centroid Z. (**c**) t-SNE plot illustrating the classification results for all segmented volumes and features using dimension reduction

texture metrics from striatal DAT SPECT and serve as biomarkers of PD severity and progression. Figure 17.8 shows example images and Fig. 17.9 shows the corresponding correlation patterns against UPDRS for a number of metrics in the caudate (more affected side).

A study using SPECT radiomics to predict Coronary Artery Calcification (CAC) was con-
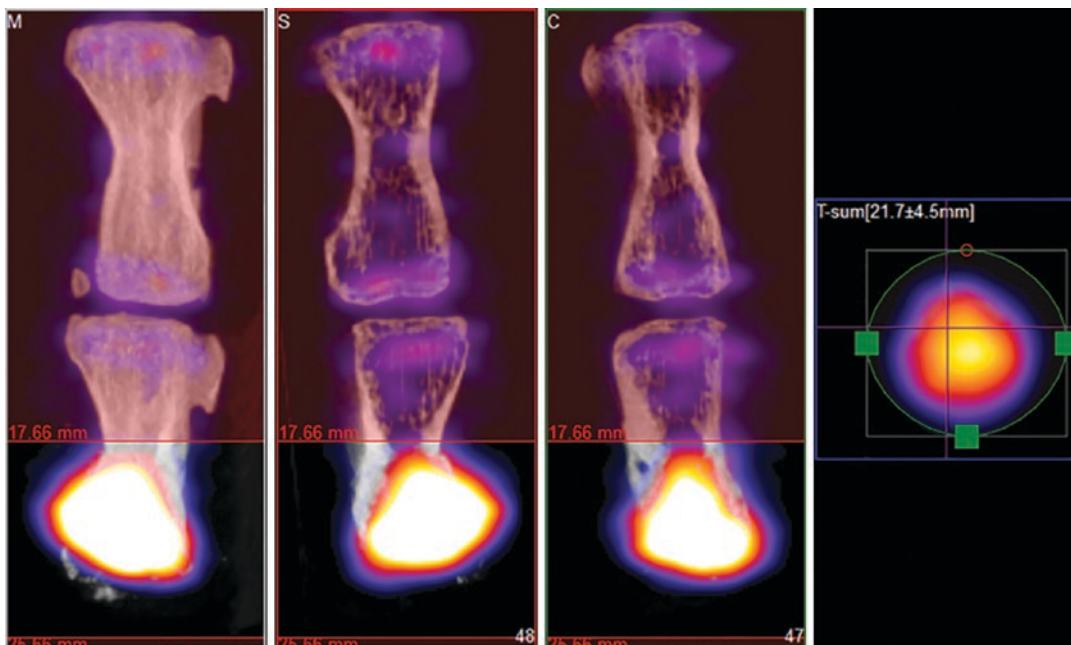
Fig. 17.7 Tc-99 m-MDP activity in caudal vertebrae of treated rats after 8 weeks. The C5 vertebrae (down) were treated and filled with a bone graft which was selected as VOI in SPECT at 8 weeks after surgery. The color intensity shows the activity of Tc-99 m-MDP in the last region of vertebra. The upper bones are C4 control vertebrae
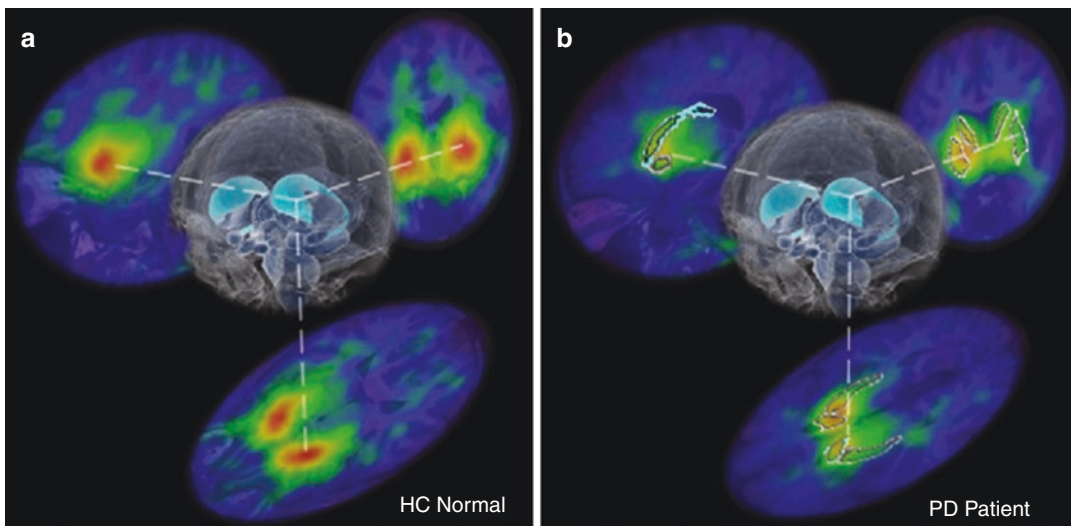
Fig. 17.8 Examples of transaxial, coronal, and sagittal slices through the DaT SPECT images for a HC subject (**a**) and a PD subject (**b**), also showing segmentation for caudate and putamen (**b**)

ducted by Ashrafinia et al. [150]. A number of 188 3D radiomics features were evaluated for 7 ROIs of the heart using Myocardial Perfusion SPECT (MPS), along with cardiac risk factors, including BMI, smoking, diabetes, hypertension, hyperlipidemia and family history of CAD for 372 patients selected with normal (non-ischemic) stress MPS scans (injected with 8–30 mCi 99mTc-Sestamibi, consensus reading). The consistently significant features (FDR p-value <0.05)
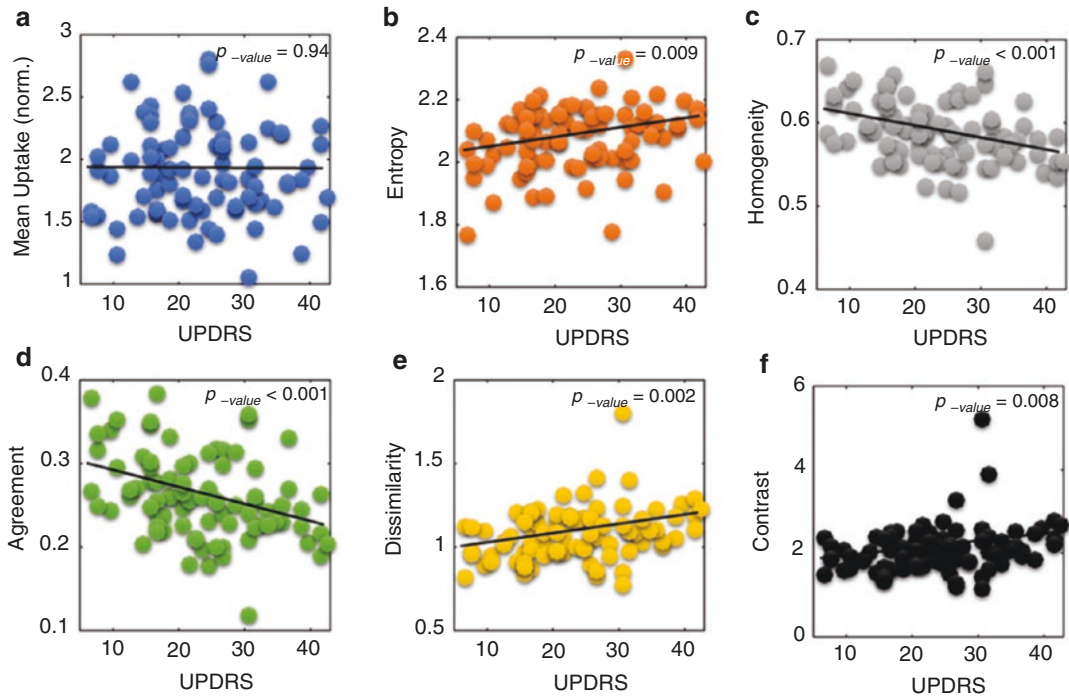
Fig. 17.9 Plots of metric values vs. UPDRS, for conventional mean uptake (**a**), as well as five Haralick texture metrics (**b**–**f**). The correlation values were −0.008, 0.28, −0.36, −0.37, 0.33 and 0.28. The more affected caudate side is shown, for PD subjects ($n = 85$)

in univariate analysis were intensity skewness and GLCM cluster shade for right coronary artery (RCA), and intensity at 90% volume histogram for left circumflex artery (LCX). Multivariate analysis was performed without and with patient risk factors data. In both cases, CAC in different ROIs of heart was predicted significantly well (p-value <0.001) by texture features, which suggested the ability of radiomics analysis to capture valuable information from MPS scans, enabling significant correlation of perfusion heterogeneity to CAC scores.

Ypsilantis et al. compared the performance of two competing radiomics strategies: an approach using state-of-the-art statistical classifiers based on radiomics features; and a CNN trained directly from the PET scans. For radiomics feature-based approach, 103 radiomics features including texture and model-based features were extracted and four statistical classifiers (logistic regression, gradient boosting, random forests and support

vector machines) were adopted for the discrimination of responders/non-responders for 107 patients treated with neoadjuvant chemotherapy. For the featureless approach, in order to capture patterns of FDG uptake across multiple adjacent slices that might be important for predicting chemotherapy response, all possible sets of three adjacent slices were constructed as input to a three-channel CNN network (3S-CNN). The input and network structures were shown in Fig. 17.10. They showed that the CNN based PET imaging representation are highly predictive of response to therapy and outperformed the feature-based approach [47].

Kawauchi et al. conducted a retrospective study included 6462 patients who underwent whole body FDG PET-CT. The CNN network was able to predict the sex, as well as age and body weight to prevent patient misidentification in clinical settings [151]. Schwyzer et al. studied the performance of artificial neural network dis-
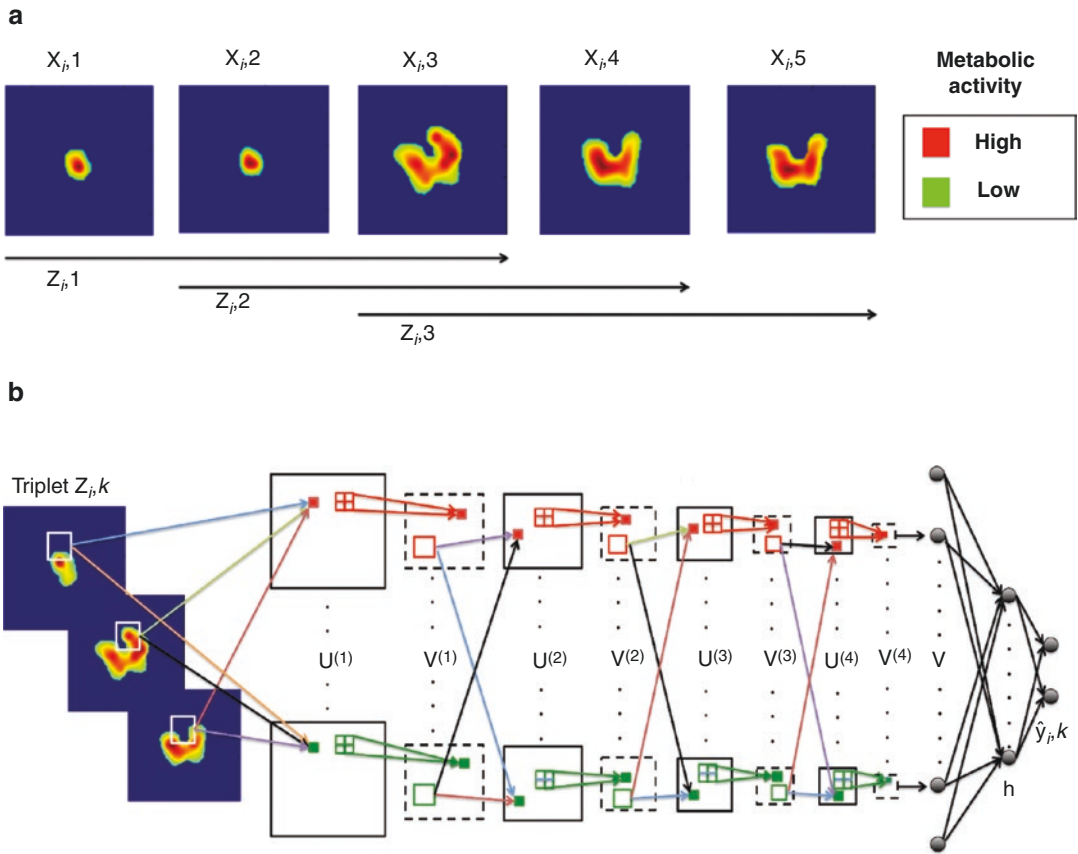
Fig. 17.10 (**a**) ^{18}F-FDG PET ROIs of a specific tumor i after segmentation embedded into larger square background of standard size of 100×100 pixels. Each enlarged slice is denoted by $x_{i,j}$ and each set of three spatially adjacent enlarged slides is denoted by $x_{i,k}$, where j and k represent the slices and triplets of the specific tumor i. In this example only 3 triplets, from the 5 available slices can be formed, so $k = 1,2,3$; (**b**) CNN architecture for fusion of 3 adjacent ^{18}F-FDG PET intra slices into a vector v. The CNN architecture is composed from 4 convolutional and 4 max-pooling layers denoted by $\left[U^{(i)}\right]_{i=1}^{4}$ and $\left[V^{(i)}\right]_{i=1}^{4}$ (From Ypsilantis et al. 2015)

criminating lung cancer patients based on clinical standard dose, tenfold and 30-fold reduced radiation dose FDG-PET images. They found that machine learning algorithms may aid fully automated lung cancer detection even at very low dose [152].

Betancur et al. evaluated the prediction of obstructive disease from combined analysis of semiupright and supine stress SPECT myocardial perfusion imaging (MPI) by deep learning (DL) as compared with standard combined total perfusion deficit (TPD) on 1160 patients imaged at 4 centers [51]. DL was trained using polar distribu-tions of normalized radiotracer counts, hypoperfusion defects, and hypoperfusion severities and was evaluated for prediction of obstructive disease in a leave-one-center-out cross-validation procedure equivalent to external validation. The DL model structure is shown in Fig. 17.11, which estimates the obstructive per-vessel CAD probability—left anterior descending (LAD), left circumflex (LCx), and right coronary arteries (RCA). The area under the receiver operating characteristics curve for prediction of disease on a per-patient and per-vessel basis by DL was higher than for combined TPD (per-patient, 0.81
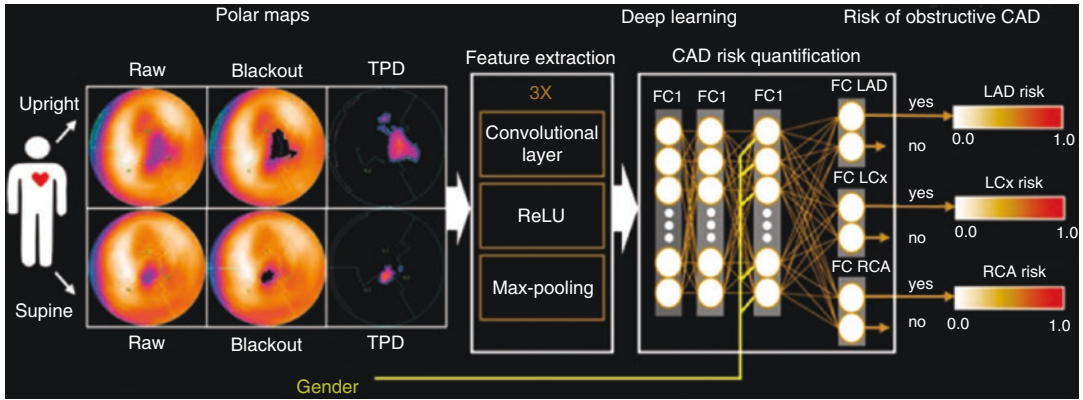
Fig. 17.11 DL prediction of obstructive CAD from upright and supine MPI. A deep convolutional neural network trained from obstructive stenosis correlations by correlating invasive coronary angiography (ICA) was used to simultaneously estimate probability of obstructive CAD for the left anterior descending (LAD), LCx, and RCA territories from upright and supine polar MPI maps. Maximum probability was retained as probability of patient disease

vs. 0.78; per-vessel, 0.77 vs. 0.73; $P < 0.001$), which indicates improved automatic interpretation of MPI as compared with current quantitative methods.

Another study by Park et al. aimed at developing an automated GFR quantification method based on deep learning approach to the three-dimensional (3D) segmentation of kidney parenchyma in CT acquired in quantitative kidney SPECT/CT studies [153]. Although SPECT/CT images are reproducible and accurate for measurement of GFR, the necessity of manual drawing VOI on the whole renal parenchyma in CT images is very labor-intensive. They trained a CNN to learn end-to-end mapping between the 3D CT volume and manually segmented VOI using a dataset including 315 patients. 3D Unet with leaky ReLU and dropout layers on 3D smoothed CT images was trained to learn the mapping by minimizing the dice similarity coefficient. GFR then was estimated by applying the manual or automatic VOIs to the SPECT images. High dice similarity coefficient was obtained relative to the manual segmentation (mean = 0.89) for the kidneys in CT images. The GFR values derived using manual and automatic segmentation methods were strongly correlated ($R^2 = 0.96$). Figure 17.12 shows the architecture of the network.

17.4 Current Issues and Future Directions

17.4.1 PET Image Characteristics

Generally speaking, PET images have lower resolution than CT or MRI in the order of 3–5 mm, which is further worsened under cardiac or respiratory motion conditions due to longer acquisition periods. Moreover, PET images are susceptible to limited photon count noise. Advances in hardware such as crystal detector technologies [154] and software such as image reconstruction techniques [155] are poised to improve PET images quality and their subsequent use. Deep learning reconstruction methods are also promising to obtain better spatial resolution PET images as discussed in previous sections, which cost much less to realize comparing with the hardware development approach.

17.4.2 Robustness and Stability of Extracted Image Features

It is well recognized that image acquisition protocols may impact the reproducibility of extracted features from PET images, which may consequently impact the robustness and stability of
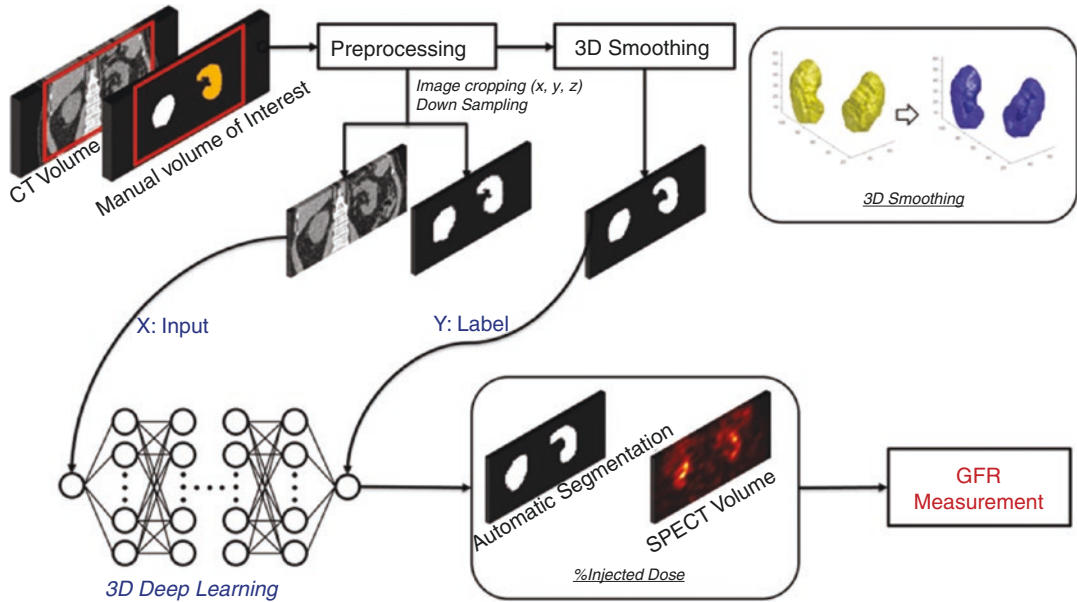
Fig. 17.12 Schematic diagrams of the deep-learning-based renal parenchyma segmentation for the measurement of glomerular filtration rate (GFR) using quantitative single-photon emission computed tomography (SPECT)/computed tomography (CT)

these features for image analysis. This includes static features such as SUV descriptors [156–158] and texture features [159, 160]. Lovat et al. studied 54 patients with type 1 neurofibromatosis with suspicion of malignant transformation and performed 2 sets of PET images at 102 ± 15 min and 252 ± 18 min after 18F-FDG injection [161]. They showed that 25 out of 37 first-order studied parameters, 9 out of 25 second-order, 13 out of 31 higher-order, and 3 out of the 6 fractal features showed a significant change in value between the two uptake times. Image reconstruction and partial volume effects influence the reliability of these features as well.

Larson et al. studied the impact of the reconstruction method on some selected radiomics features, including SUVmax, SUVmean, MTV, CH_{AUC} (what is CH_{AUC}) and some textural features (entropy, correlation, dissimilarity, high-intensity large-area emphasis: HILAE, and ZP) [162]. [CH_{AUC} is area underthe curve of the cumulative histogram (CHAUC)].

Seventy-one tumors in 60 biopsy-proven lung cancer patients with reconstruction using unfiltered point spread function (PSF) with 3 iterations and 21 subsets, PSF-reconstructed images with a 7-mm Gaussian filter (PSF7) filter with 3 iterations and 21 subsets and one OSEM type with 4 iterations and 8 subsets were analyzed. Two delineation methods: a 50% standardized uptake values (SUV) max threshold (SUVmax50%) and fuzzy locally adaptive Bayesian (FLAB) algorithm were used and compared. They found that volumes obtained with SUVmax50% were significantly smaller than FLAB-derived ones, and were significantly smaller in PSF images compared to OSEM and PSF7 images. No significant difference was observed between any of the considered metrics (SUV or heterogeneity features) extracted from OSEM and PSF7 reconstructions.

In a study of multi-cancer site, Hatt et al. reported that changing the discretization from 4 to 256 significantly affected the correlation between MTV and texture features using a dataset of 555 FDG-PET images [163]. Interestingly, texture-based features were shown to have a reproducibility similar to or better than that of simple SUV descriptors [64]. Moreover, textural features from the GLCM seemed to exhibit lower variations

than NGTDM features [159]. Other factors that may impact the stability of these features may include signal-to-noise ratio (SNR), partial volume effect, motion artifacts, resampling size, texture parameters, software being used for feature extraction, and the inherent sensitivity of image biomarkers [39, 160, 164–166]. Denoising methods for mitigation of noise in PET imaging follows their limited photon effects using traditional denoising filtering methods [167, 168], or more advanced methods based on combining wavelet and curvelet transforms characteristics [169] and the recently popular deep learning-based PET image reconstruction [134, 136].

For the reproducibility of PET radiomics features, there are couple of works that implemented a systematic review, which readers can refer to for detailed information [64, 70, 130]. Since no studies on the repeatability of SPECT imaging was found, we will limit ourselves for the PET studies here. Moreover, imaging artifacts may impact the performance of radiomics analysis, though this has been highlighted in the case of CT in head and neck cancers [170], this can further impact attenuation correction in PET imaging, for instance, with detrimental impact on performance.

17.4.3 Standardization of Radiomics Using Image Biomarker Standardization Initiative (IBSI)

Discretization, reconstruction algorithms, ROI delineation, etc. will affect the repeatability and reproducibility of radiomics features. In addition to these factors, reporting the extraction parameters for radiomics features is important for standardization of these features and obtaining a stable model.

Standardization using IBSI was briefly mentioned in the extraction of radiomics features in terms of intensity discretization (fixed bin width and fixed bin number in Sect. 17.2). Except for this, interpolation is usually required in order to make the voxel size isotropic to calculate 3D features. There are several commonly used interpo-

lation algorithms, like nearest neighbor, trilinear, tricubic convolution and tricubic spline interpolation, etc. Another thing to mention is, sometimes, the same feature name might refer to different formula for computation. It is thus crucial to follow a consistent definition of features, like the IBSI for the community to develop usable models. The aggregation method is another parameter that affects the feature calculation. There are 6 types mentioned in the IBSI. (1) Features are computed from 2D directional matrix and averaged over 2D directions and slices; (2) Features are computed from a single matrix after merging 2D directional matrices per slice, and then averaged over slices; (3) Features are computed from a single matrix after merging 2D directional matrices per direction, and then averaged over directions; (4) The feature is computed from a single matrix after merging all 2D directional matrices; (5) Features are computed from each 3D directional matrix and averaged over the 3D directions; (6) The feature is computed from a single matrix after merging all 3D directional matrices. All these extraction parameters (e.g., discretization, aggregation, interpolation, etc.) should be reported in the literature so that the results could be reproduced and compared.

17.4.4 Improved PET-Based Outcome Models

In addition to using appropriate candidate image features for PET-based outcome modeling, "radiomics," a main weakness in using classical logistic regression formalism is that the model's capacity to follow details of the data trends is limited. In addition, for instance, logistic regression model requires the user's feedback to determine whether interaction terms or higher-order terms should be added, making it a trial and error process. A solution to ameliorate this problem is offered by applying machine learning methods [120].

A class of machine learning methods that is particularly powerful, and which we propose to use for image-based outcome prediction, includes

so-called "Kernel-based methods" and their most prominent sub-type, support vector machines (SVMs). These methods have been applied successfully in many diverse areas including outcome prediction [171–175]. Learning is defined in this context as estimating dependencies from data [176]. In the example of outcome prediction (i.e., discrimination between patients who are at low risk versus patients who are at high risk of local failure), the main function of the kernel-based technique would be to separate these two classes with "hyper-planes" that maximize the margin (separation) between the classes in the nonlinear feature space. The objective here is to minimize the bounds on the generalization error of a model on unseen data before rather than minimizing the mean-square error over the training dataset itself (data fitting). Note that the kernel in these cases acts as a similarity function between sample points in the feature space. Moreover, kernels enjoy closure properties, i.e., one can create admissible composite kernels by weighted addition and multiplication of elementary kernels. This flexibility allows for the construction of a neural network by using a combination of sigmoidal kernels. Alternatively, one could choose a logistic regression equivalent kernel by proper choice of the objective function itself.

The conventional feature-based machine learning methods embedded experts' prior knowledge, while the feature selection process is usually blamed to be unstable, especially for high-dimensional feature input. In comparison, neural network methods are able to bypass the feature designing or selection stages, and have shown great potential in clinical image applications, including segmentation, reconstruction, classification, actuary analysis. However, there are several issues restraining its clinical practice, two major ones are the scarcity of data and the difficulty in interpretability. For limit sample size, data augmentation (e.g., affine transformation of the images) during training is commonly adopted. Transfer learning is also a widely used strategy to reduce the difficulty in training, by transferring deep models trained on other datasets (natural images) and then fine-tuning on the target dataset. The structures of the networks can be modified to reduce overfitting as well, such as, adding dropout and batch normalization layers. Dropout randomly deactivates a fraction of the units during training and can be viewed as a regularization technique that adds noise to the hidden units [177]. Batch normalization reduces the internal covariate shift by normalizing for each training mini-batch [178].

For the interpretability, the large number of interacting, nonlinear parts makes it hard to understand deep neural networks [179, 180]. Aiming at improving the interpretability of radiomics for the clinician, graph approaches can be utilized [181], and better visualization tools for deep learning are being developed such as maps highlighting regions of the tumor that impact the prediction of the deep learning classifier are also being proposed. Several groups have developed methods for identifying and visualizing the features in individual test data points that contribute most toward a classifier's output. A well-known method is the Local Interpretable Model-Agnostic Explanations (LIME), which provides explanations of decisions for any machine learning model [182]. Selvaraju et al. proposed a method called Gradient-weighted Class Activation Mapping (Grad-CAM), which uses the gradients of any target concept (say logits for "dog" or even a caption), flowing into the final convolutional layer to produce a coarse localization map highlighting the important regions in the image for predicting the concept [183]. Chattopadhyay et al. further generalized this method into Grad-CAM++ that can explain occurrences of multiple object instances in a single image compared to state-of-the-art [184].

Though evaluation of radiomics in clinical trials is still in its infancy [185], there are 53 clinical trials being reported according to the website clinicaltrials.gov, 9 of them have already been completed. Some examples are given here for the readers. More information can be found from the website above. A registered trial for "Radiomics: A Study of Outcome in Lung Cancer" between the Maastro clinic in the Netherlands, Moffitt Cancer Center from Florida, USA, and Research

Institute Gemelli Hospital Roma, Italy was completed in 2014. A trial named "Radiomics and Clinical Variables Can Differentiate Malignant Nodules and Detect Invasive Adenocarcinoma in Pulmonary Nodules: A Multi-center Study" was completed in 2019 by Maastro clinic, the Affiliated Zhongshan Hospital of Dalian University, the Second Affiliated Hospital of Dalian Medical University, and the Fifth Hospital of Dalian. A trial named "Radiomics for the Prediction of Survival in GBM After Radiotherapy With/Without Temozolomide" was reported by Maastro clinic and completed in 2018.

17.5 Conclusions

Image processing constitutes an indispensable set of tools for analyzing and extracting valuable information from PET and SPECT images. We presented in this chapter an overview of different features that could be extracted from PET and SPECT images and various machine/deep learning methods that could use PET or SPECT images as direct input for different applications including contouring, image quality improving, and response prediction. We have shown that incorporation of different anatomical information from CT and MRI into PET or SPECT is feasible and could yield better results. However, there are challenges still in the use of PET and SPECT with some related to inherited image quality, others related to standardization of image acquisition protocols and reconstruction algorithms, and also some general issues like shortage of data and inadequate interpretability of the models for deep learning approaches that appeared not only in PET or SPECT applications. Nevertheless, advances in hardware and software technologies will further facilitate wider application of advanced image processing and machine learning techniques to PET, SPECT, and hybrid imaging to achieve better clinical results. In particular, the synergy between image analysis and machine learning could provide powerful tools to strengthen and further the utilization of PET and SPECT in clinical practice.

References

1. Verhagen AF, Bootsma GP, Tjan-Heijnen VC, van der Wilt GJ, Cox AL, Brouwer MH, et al. FDG-PET in staging lung cancer: how does it change the algorithm? Lung Cancer. 2004;44:175–81. https://doi.org/10.1016/j.lungcan.2003.11.007.
2. Bradley J, Thorstad WL, Mutic S, Miller TR, Dehdashti F, Siegel BA, et al. Impact of FDG-PET on radiation therapy volume delineation in non-small-cell lung cancer. Int J Radiat Oncol Biol Phys. 2004;59:78–86.
3. Bradley JD, Perez CA, Dehdashti F, Siegel BA. Implementing biologic target volumes in radiation treatment planning for non-small cell lung cancer. J Nucl Med. 2004;45(Suppl 1):96S–101S.
4. Bradley J. Applications for FDG-PET in lung cancer; staging, targeting, and follow-up. Chicago, IL: The Radiological Society of North America; 2004.
5. Erdi YE, Macapinlac H, Rosenzweig KE, Humm JL, Larson SM, Erdi AK, et al. Use of PET to monitor the response of lung cancer to radiation treatment. Eur J Nucl Med. 2000;27:861–6.
6. Mac Manus MP, Hicks RJ. PET scanning in lung cancer: current status and future directions. Semin Surg Oncol. 2003;21:149–55.
7. Mac Manus MP, Hicks RJ, Matthews JP, McKenzie A, Rischin D, Salminen EK, et al. Positron emission tomography is superior to computed tomography scanning for response-assessment after radical radiotherapy or chemoradiotherapy in patients with non-small-cell lung cancer. J Clin Oncol. 2003;21:1285–92.
8. MacManus MR, Hicks R, Fisher R, Rischin D, Michael M, Wirth A, et al. FDG-PET-detected extracranial metastasis in patients with non-small cell lung cancer undergoing staging for surgery or radical radiotherapy—survival correlates with metastatic disease burden. Acta Oncol. 2003;42:48–54.
9. Pandit N, Gonen M, Krug L, Larson SM. Prognostic value of [18F]FDG-PET imaging in small cell lung cancer. Eur J Nucl Med Mol Imaging. 2003;30:78–84.
10. Toloza EM, Harpole L, McCrory DC. Noninvasive staging of non-small cell lung cancer: a review of the current evidence. Chest. 2003;123:137S–46S.
11. Schwartz DL, Ford E, Rajendran J, Yueh B, Coltrera MD, Virgin J, et al. FDG-PET/CT imaging for pre-radiotherapy staging of head-and-neck squamous cell carcinoma. Int J Radiat Oncol Biol Phys. 2005;61:129–36.
12. Suarez Fernandez JP, Maldonado Suarez A, Dominguez Grande ML, Santos Ortega M, Rodriguez Villalba S, Garcia Camanaque L, et al. Positron emission tomography (PET) imaging in head and neck cancer. Acta Otorrinolaringol Esp. 2004;55:303–9.

13. Oyama N, Miller TR, Dehdashti F, Siegel BA, Fischer KC, Michalski JM, et al. 11C-acetate PET imaging of prostate cancer: detection of recurrent disease at PSA relapse. J Nucl Med. 2003;44:549–55.

14. Mutic S, Malyapa RS, Grigsby PW, Dehdashti F, Miller TR, Zoberi I, et al. PET-guided IMRT for cervical carcinoma with positive para-aortic lymph nodes-a dose-escalation treatment planning study. Int J Radiat Oncol Biol Phys. 2003;55:28–35.

15. Miller TR, Grigsby PW. Measurement of tumor volume by PET to evaluate prognosis in patients with advanced cervical cancer treated by radiation therapy. Int J Radiat Oncol Biol Phys. 2002;53:353–9.

16. Ciernik IF. Radiotherapy of rectal cancer. Schweiz Rundsch Med Prax. 2004;93:1441–6.

17. Castellucci P, Zinzani P, Nanni C, Farsad M, Moretti A, Alinari L, et al. 18F-FDG PET early after radiotherapy in lymphoma patients. Cancer Biother Radiopharm. 2004;19:606–12.

18. Spaepen K, Stroobants S, Verhoef G, Mortelmans L. Positron emission tomography with [(18)F]FDG for therapy response monitoring in lymphoma patients. Eur J Nucl Med Mol Imaging. 2003;30(Suppl 1):S97–105.

19. Fogarty GB, Tartaglia CJ, Peters LJ. Primary melanoma of the oesophagus well palliated by radiotherapy. Br J Radiol. 2004;77:1050–2.

20. Biersack HJ, Bender H, Palmedo H. FDG-PET in monitoring therapy of breast cancer. Eur J Nucl Med Mol Imaging. 2004;31(Suppl 1):S112–7.

21. Lind P, Igerc I, Beyer T, Reinprecht P, Hausegger K. Advantages and limitations of FDG PET in the follow-up of breast cancer. Eur J Nucl Med Mol Imaging. 2004;31(Suppl 1):S125–34.

22. Zangheri B, Messa C, Picchio M, Gianolli L, Landoni C, Fazio F. PET/CT and breast cancer. Eur J Nucl Med Mol Imaging. 2004;31(Suppl 1):S135–42.

23. Brun E, Kjellen E, Tennvall J, Ohlsson T, Sandell A, Perfekt R, et al. FDG PET studies during treatment: prediction of therapy outcome in head and neck squamous cell carcinoma. Head Neck. 2002;24:127–35.

24. Hope AJ, Saha P, Grigsby PW. FDG-PET in carcinoma of the uterine cervix with endometrial extension. Cancer. 2006;106:196–200.

25. Kalff V, Duong C, Drummond EG, Matthews JP, Hicks RJ. Findings on 18F-FDG PET scans after neoadjuvant chemoradiation provides prognostic stratification in patients with locally advanced rectal carcinoma subsequently treated by radical surgery. J Nucl Med. 2006;47:14–22.

26. Hicks RJ, Mac Manus MP, Matthews JP, Hogg A, Binns D, Rischin D, et al. Early FDG-PET imaging after radical radiotherapy for non-small-cell lung cancer: inflammatory changes in normal tissues correlate with tumor response and do not confound therapeutic response evaluation. Int J Radiat Oncol Biol Phys. 2004;60:412–8.

27. Grigsby PW, Siegel BA, Dehdashti F, Rader J, Zoberi I. Posttherapy [18F] fluorodeoxyglucose positron emission tomography in carcinoma of the cervix: response and outcome. J Clin Oncol. 2004;22:2167–71.

28. Zaidi H, Alavi A, El Naqa I. Novel quantitative PET techniques for clinical decision support in oncology. Semin Nucl Med. 2018;48:548–64. https://doi.org/10.1053/j.semnuclmed.2018.07.003.

29. Shields AF. Positron emission tomography measurement of tumor metabolism and growth: its expanding role in oncology. Mol Imaging Biol. 2006;8:141–50.

30. Denecke T, Rau B, Hoffmann KT, Hildebrandt B, Ruf J, Gutberlet M, et al. Comparison of CT, MRI and FDG-PET in response prediction of patients with locally advanced rectal cancer after multimodal preoperative therapy: is there a benefit in using functional imaging? Eur Radiol. 2005;15:1658–66.

31. Afshar-Oromieh A, Avtzi E, Giesel FL, Holland-Letz T, Linhart HG, Eder M, et al. The diagnostic value of PET/CT imaging with the (68)Ga-labelled PSMA ligand HBED-CC in the diagnosis of recurrent prostate cancer. Eur J Nucl Med Mol Imaging. 2015;42:197–209. https://doi.org/10.1007/s00259-014-2949-6.

32. Eiber M, Maurer T, Souvatzoglou M, Beer AJ, Ruffani A, Haller B, et al. Evaluation of hybrid 68Ga-PSMA-ligand PET/CT in 248 patients with biochemical recurrence after radical prostatectomy. J Nucl Med. 2015. https://doi.org/10.2967/jnumed.115.154153.

33. Maurer T, Eiber M, Schwaiger M, Gschwend JE. Current use of PSMA-PET in prostate cancer management. Nat Rev Urol. 2016. https://doi.org/10.1038/nrurol.2016.26.

34. Eiber M, Weirich G, Holzapfel K, Souvatzoglou M, Haller B, Rauscher I, et al. Simultaneous Ga-PSMA HBED-CC PET/MRI improves the localization of primary prostate cancer. Eur Urol. 2016;70:829–36. https://doi.org/10.1016/j.eururo.2015.12.053.

35. Benz MR, Allen-Auerbach MS, Eilber FC, Chen HJJ, Dry S, Phelps ME, et al. Combined assessment of metabolic and volumetric changes for assessment of tumor response in patients with soft-tissue sarcomas. J Nucl Med. 2008;49:1579–84. https://doi.org/10.2967/jnumed.108.053694.

36. Yang D-H, Min J-J, Jeong Y, Ahn J-S, Kim Y-K, Cho S-H, et al. The combined evaluation of interim contrast-enhanced computerized tomography (CT) and FDG-PET/CT predicts the clinical outcomes and may impact on the therapeutic plans in patients with aggressive non-Hodgkin's lymphoma. Ann Hematol. 2009;88:425–32.

37. Lambin P, Rios-Velazquez E, Leijenaar R, Carvalho S, van Stiphout RG, Granton P, et al. Radiomics: extracting more information from medical images using advanced feature analysis. Eur J Cancer. 2012;48:441–6. https://doi.org/10.1016/j.ejca.2011.11.036.

38. Kumar V, Gu Y, Basu S, Berglund A, Eschrich SA, Schabath MB, et al. Radiomics: the process and the challenges. Magn Reson Imaging. 2012;30:1234–48. https://doi.org/10.1016/j.mri.2012.06.010.

39. El Naqa I, Grigsby P, Apte A, Kidd E, Donnelly E, Khullar D, et al. Exploring feature-based approaches in PET images for predicting cancer treatment outcomes. Pattern Recogn. 2009;42:1162–71. https://doi.org/10.1016/j.patcog.2008.08.011.

40. Vallieres M, Kay-Rivest E, Perrin LJ, Liem X, Furstoss C, Aerts H, et al. Radiomics strategies for risk assessment of tumour failure in head-and-neck cancer. Sci Rep. 2017;7:10117. https://doi.org/10.1038/s41598-017-10371-5.

41. Kidd EA, El Naqa I, Siegel BA, Dehdashti F, Grigsby PW. FDG-PET-based prognostic nomograms for locally advanced cervical cancer. Gynecol Oncol. 2012;127:136–40. https://doi.org/10.1016/j.ygyno.2012.06.027.

42. Vallieres M, Freeman CR, Skamene SR, El Naqa I. A radiomics model from joint FDG-PET and MRI texture features for the prediction of lung metastases in soft-tissue sarcomas of the extremities. Phys Med Biol. 2015;60:5471–96. https://doi.org/10.1088/0031-9155/60/14/5471.

43. Vaidya M, Creach KM, Frye J, Dehdashti F, Bradley JD, El Naqa I. Combined PET/CT image characteristics for radiotherapy tumor response in lung cancer. Radiother Oncol. 2012;102:239–45. https://doi.org/10.1016/j.radonc.2011.10.014.

44. Wei L, Osman S, Hatt M, El Naqa I. Machine learning for radiomics-based multimodality and multiparametric modeling. Q J Nucl Med Mol Imaging. 2019;63:323–38. https://doi.org/10.23736/S1824-4785.19.03213-8.

45. Sharif MS, Abbod M, Amira A, Zaidi H. Artificial neural network-based system for PET volume segmentation. J Biomed Imaging. 2010;2010:4.

46. Zhao X, Li L, Lu W, Tan S. Tumor co-segmentation in PET/CT using multi-modality fully convolutional neural network. Phys Med Biol. 2018;64:015011.

47. Ypsilantis P-P, Siddique M, Sohn H-M, Davies A, Cook G, Goh V, et al. Predicting response to neoadjuvant chemotherapy with PET imaging using convolutional neural networks. PLoS One. 2015;10:e0137036.

48. Dorbala S, Ananthasubramaniam K, Armstrong IS, Chareonthaitawee P, DePuey EG, Einstein AJ, et al. Single photon emission computed tomography (SPECT) myocardial perfusion imaging guidelines: instrumentation, acquisition, processing, and interpretation. J Nucl Cardiol. 2018;25:1784–846.

49. Arsanjani R, Xu Y, Dey D, Fish M, Dorbala S, Hayes S, et al. Improved accuracy of myocardial perfusion SPECT for the detection of coronary artery disease using a support vector machine algorithm. J Nucl Med. 2013;54:549–55.

50. Betancur J, Otaki Y, Motwani M, Fish MB, Lemley M, Dey D, et al. Prognostic value of combined clinical and myocardial perfusion imaging data using machine learning. JACC Cardiovasc Imaging. 2018;11:1000–9.

51. Betancur J, Hu L-H, Commandeur F, Sharir T, Einstein AJ, Fish MB, et al. Deep learning analysis of upright-supine high-efficiency spect myocardial perfusion imaging for prediction of obstructive coronary artery disease: a multicenter study. J Nucl Med. 2019;60:664–70.

52. Pomper MG, Hammond H, Yu X, Ye Z, Foss CA, Lin DD, et al. Serial imaging of human embryonic stem-cell engraftment and teratoma formation in live mouse models. Cell Res. 2009;19:370.

53. Khalil MM, Tremoleda JL, Bayomy TB, Gsell W. Molecular SPECT imaging: an overview. Int J Mol Imaging. 2011;2011:796025.

54. Umeda T, Koizumi M, Fukai S, Miyaji N, Motegi K, Nakazawa S, et al. Evaluation of bone metastatic burden by bone SPECT/CT in metastatic prostate cancer patients: defining threshold value for total bone uptake and assessment in radium-223 treated patients. Ann Nucl Med. 2018;32:105–13.

55. Fleury V, Ferrer L, Colombié M, Rusu D, Le Thiec M, Kraeber-Bodéré F, et al. Advantages of systematic trunk SPECT/CT to planar bone scan (PBS) in more than 300 patients with breast or prostate cancer. Oncotarget. 2018;9:31744.

56. Ma L, Ma C, Liu Y, Wang X. Thyroid diagnosis from SPECT images using convolutional neural network with optimization. Comput Intell Neurosci. 2019;2019:6212759.

57. Simanek M, Koranda P. SPECT/CT imaging in breast cancer-current status and challenges. In: Biomedical Papers of the Medical Faculty of Palacky University in Olomouc; 2016. p. 160.

58. Serrano-Vicente J, Rayo-Madrid J, Domínguez-Grande M, Infante-Torre J, García-Bernardo L, Moreno-Caballero M, et al. Role of SPECT-CT in breast cancer sentinel node biopsy when internal mammary chain drainage is observed. Clin Transl Oncol. 2016;18:418–25.

59. Wagner T, Buscombe J, Gnanasegaran G, Navalkissoor S. SPECT/CT in sentinel node imaging. Nucl Med Commun. 2013;34:191–202.

60. Thibault G, Angulo J, Meyer F. Advanced statistical matrices for texture characterization: application to cell classification. IEEE Trans Biomed Eng. 2014;61:630–7. https://doi.org/10.1109/tbme.2013.2284600.

61. Zwanenburg A, Vallières M, Abdalah MA, Aerts HJWL, Andrearczyk V, Apte A, et al. The image biomarker standardization initiative: standardized quantitative radiomics for high-throughput image-based phenotyping. Radiology. 2020;295:328–38. https://doi.org/10.1148/radiol.2020191145.

62. van Velden FH, Kramer GM, Frings V, Nissen IA, Mulder ER, de Langen AJ, et al. Repeatability of radiomic features in non-small-cell lung cancer [18 F] FDG-PET/CT studies: impact of reconstruction and delineation. Mol Imaging Biol. 2016;18:788–95.

63. Leijenaar RT, Nalbantov G, Carvalho S, Van Elmpt WJ, Troost EG, Boellaard R, et al. The effect of SUV discretization in quantitative FDG-PET Radiomics: the need for standardized methodology in tumor texture analysis. Sci Rep. 2015;5:11075.

64. Tixier F, Hatt M, Le Rest CC, Le Pogam A, Corcos L, Visvikis D. Reproducibility of tumor uptake heterogeneity characterization through textural feature analysis in 18F-FDG PET. J Nucl Med. 2012;53:693–700.

65. Cook GJ, Azad G, Owczarczyk K, Siddique M, Goh V. Challenges and promises of PET radiomics. Int J Radiat Oncol Biol Phys. 2018;102:1083–9.

66. Hatt M, Le Rest CC, Descourt P, Dekker A, De Ruysscher D, Oellers M, et al. Accurate automatic delineation of heterogeneous functional volumes in positron emission tomography for oncology applications. Int J Radiat Oncol Biol Phys. 2010;77:301–8.

67. Hatt M, Lee JA, Schmidtlein CR, Naqa IE, Caldwell C, De Bernardi E, et al. Classification and evaluation strategies of auto-segmentation approaches for PET: report of AAPM task group no. 211. Med Phys. 2017;44:e1–e42.

68. El Naqa I, Yang D, Apte A, Khullar D, Mutic S, Zheng J, et al. Concurrent multimodality image segmentation by active contours for radiotherapy treatment planning. Med Phys. 2007;34:4738–49.

69. Conti P, Strauss L. The applications of PET in clinical oncology. J Nucl Med. 1991;32:623–48.

70. Lovinfosse P, Visvikis D, Hustinx R, Hatt M. FDG PET radiomics: a review of the methodological aspects. Clin Trans Imaging. 2018;6:379–91.

71. El Naqa I. The role of quantitative PET in predicting cancer treatment outcomes. Clin Trans Imaging. 2014;2:305–20.

72. Strauss LG, Conti PS. The applications of PET in clinical oncology. J Nucl Med. 1991;32:623–48.

73. Larson SM, Erdi Y, Akhurst T, Mazumdar M, Macapinlac HA, Finn RD, et al. Tumor treatment response based on visual and quantitative changes in global tumor glycolysis using PET-FDG imaging. The visual response score and the change in total lesion glycolysis. Clin Positron Imaging. 1999;2:159–71. S1095039799000163 [pii].

74. Jain AK. Fundamentals of digital image processing. Englewood Cliffs, NJ: Prentice Hall; 1989.

75. O'Sullivan F, Roy S, O'Sullivan J, Vernon C, Eary J. Incorporation of tumor shape into an assessment of spatial heterogeneity for human sarcomas imaged with FDG-PET. Biostatistics. 2005;6:293–301. https://doi.org/10.1093/biostatistics/kxi010.

76. O'Sullivan F, Roy S, Eary J. A statistical measure of tissue heterogeneity with application to 3D PET sarcoma data. Biostatistics. 2003;4:433–48. https://doi.org/10.1093/biostatistics/4.3.433.

77. Castleman KR. Digital image processing. Englewood Cliffs, NJ: Prentice Hall; 1996.

78. Haralick R, Shanmugam K, Dinstein I. Texture features for image classification. IEEE Trans Sys Man Cyb SMC. 1973;3:610–21.

79. Zhang J, Tan T. Brief review of invariant texture analysis methods. Pattern Recogn. 2002;35:735–47. https://doi.org/10.1016/S0031-3203(01)00074-7.

80. Castellano G, Bonilha L, Li LM, Cendes F. Texture analysis of medical images. Clin Radiol. 2004;59:1061–9. https://doi.org/10.1016/j.crad.2004.07.008.

81. Chicklore S, Goh V, Siddique M, Roy A, Marsden P, Cook GR. Quantifying tumour heterogeneity in 18F-FDG PET/CT imaging by texture analysis. Eur J Nucl Med Mol Imaging. 2013;40:133–40. https://doi.org/10.1007/s00259-012-2247-0.

82. Galloway MM. Texture analysis using grey level run lengths. NASA STI/Recon Technical Report N. 75; 1974.

83. Thibault G, Fertil B, Navarro C, Pereira S, Cau P, Levy N, et al. Shape and texture indexes application to cell nuclei classification. Int J Pattern Recogn Artif Intell. 2013;27:1357002.

84. Tixier F, Le Rest CC, Hatt M, Albarghach N, Pradier O, Metges J-P, et al. Intratumor heterogeneity characterized by textural features on baseline 18F-FDG PET images predicts response to concomitant radiochemotherapy in esophageal cancer. J Nucl Med. 2011;52:369–78.

85. Cheng N-M, Dean Fang Y-H, Tung-Chieh Chang J, Huang C-G, Tsan D-L, Ng S-H, et al. Textural features of pretreatment 18F-FDG PET/CT images: prognostic significance in patients with advanced T-stage oropharyngeal squamous cell carcinoma. J Nucl Med. 2013;54:1703–9. https://doi.org/10.2967/jnumed.112.119289.

86. Cook GJR, Yip C, Siddique M, Goh V, Chicklore S, Roy A, et al. Are pretreatment 18F-FDG PET tumor textural features in non–small cell lung cancer associated with response and survival after chemoradiotherapy? J Nucl Med. 2013;54:19–26. https://doi.org/10.2967/jnumed.112.107375.

87. Watabe H, Ikoma Y, Kimura Y, Naganawa M, Shidahara M. PET kinetic analysis—compartmental model. Ann Nucl Med. 2006;20:583–8.

88. Graham MM, Peterson LM, Hayward RM. Comparison of simplified quantitative analyses of FDG uptake. Nucl Med Biol. 2000;27:647–55.

89. Patlak CS, Blasberg RG. Graphical evaluation of blood-to-brain transfer constants from multiple-time uptake data. Generalizations. J Cereb Blood Flow Metab. 1985;5:584–90.

90. Choi NC, Fischman AJ, Niemierko A, Ryu JS, Lynch T, Wain J, et al. Dose-response relationship between probability of pathologic tumor control and glucose metabolic rate measured with FDG PET after preoperative chemoradiotherapy in locally advanced non-small-cell lung cancer. Int J Radiat Oncol Biol Phys. 2002;54:1024–35.

91. Thorwarth D, Eschmann S-M, Holzner F, Paulsen F, Alber M. Combined uptake of [18F]FDG and [18F]FMISO correlates with radiation therapy outcome in head-and-neck cancer patients. Radiother Oncol. 2006;80:151–6.

92. Thorwarth D, Eschmann S-M, Paulsen F, Alber M. A model of reoxygenation dynamics of head-and-neck tumors based on serial 18F-Fluoromisonidazole

positron emission tomography investigations. Int J Radiat Oncol Biol Phys. 2007;68:515–21.

93. Turkheimer FE, Aston JA, Asselin MC, Hinz R. Multi-resolution Bayesian regression in PET dynamic studies using wavelets. Neuroimage. 2006;32:111–21. https://doi.org/10.1016/j.neuroimage.2006.03.002.

94. Tibshirani R. Regression shrinkage and selection via the lasso. J R Stat Soc B Methodol. 1996;58:267–88.

95. Wold S, Esbensen K, Geladi P. Principal component analysis. Chemom Intel Lab Syst. 1987;2:37–52.

96. van der Maaten L, Hinton G. Visualizing data using t-SNE. J Mach Learn Res. 2008;9:2579–605.

97. Parmar C, Grossmann P, Bussink J, Lambin P, Aerts HJ. Machine learning methods for quantitative radiomic biomarkers. Sci Rep. 2015;5:13087.

98. Vallières M, Kay-Rivest E, Perrin LJ, Liem X, Furstoss C, Aerts HJ, et al. Radiomics strategies for risk assessment of tumour failure in head-and-neck cancer. Sci Rep. 2017;7:10117.

99. Wu S, Zheng J, Li Y, Wu Z, Shi S, Huang M, et al. Development and validation of an MRI-based radiomics signature for the preoperative prediction of lymph node metastasis in bladder cancer. EBioMedicine. 2018;34:76–84.

100. Zhang Y, Oikonomou A, Wong A, Haider MA, Khalvati F. Radiomics-based prognosis analysis for non-small cell lung cancer. Sci Rep. 2017;7:46349.

101. El Naqa I, Murphy MJ. What is machine learning? Machine Learning in Radiation Oncology. Berlin: Springer; 2015. p. 3–11.

102. Hastie T, Tibshirani R, Friedman J, Franklin J. The elements of statistical learning: data mining, inference and prediction. Math Intell. 2005;27:83–5.

103. Cox DR. Regression models and life-tables. J R Stat Soc B Methodol. 1972;34:187–202.

104. Ishwaran H, Kogalur UB, Blackstone EH, Lauer MS. Random survival forests. Ann Appl Stat. 2008;2:841–60.

105. Van Belle V, Pelckmans K, Van Huffel S, Suykens JA. Support vector methods for survival analysis: a comparison between ranking and regression approaches. Artif Intell Med. 2011;53:107–18.

106. Katzman JL, Shaham U, Cloninger A, Bates J, Jiang T, Kluger Y. DeepSurv: personalized treatment recommender system using a Cox proportional hazards deep neural network. BMC Med Res Methodol. 2018;18:24.

107. Ching T, Zhu X, Garmire LX. Cox-nnet: an artificial neural network method for prognosis prediction of high-throughput omics data. PLoS Comput Biol. 2018;14:e1006076.

108. Joachims T. Transductive inference for text classification using support vector machines: ICML; 1999. p. 200–9.

109. LeCun Y, Bengio Y, Hinton G. Deep learning. Nature. 2015;521:436.

110. Suzuki K. Pixel-based machine learning in medical imaging. J Biomed Imaging. 2012;2012:1.

111. Simonyan K, Zisserman A. Very deep convolutional networks for large-scale image recognition. arXiv preprint arXiv:14091556. 2014.

112. He K, Zhang X, Ren S, Sun J. Deep residual learning for image recognition. In: Proceedings of the IEEE conference on computer vision and pattern recognition; 2016. p. 770–8.

113. Hubel DH, Wiesel TN. Receptive fields and functional architecture of monkey striate cortex. J Physiol. 1968;195:215–43.

114. Hochreiter S, Schmidhuber J. Long short-term memory. Neural Comput. 1997;9:1735–80.

115. Cho K, Van Merriënboer B, Gulcehre C, Bahdanau D, Bougares F, Schwenk H, et al. Learning phrase representations using RNN encoder-decoder for statistical machine translation. arXiv preprint arXiv:14061078. 2014.

116. Kingma DP, Welling M. Auto-encoding variational bayes. arXiv preprint arXiv:13126114. 2013.

117. Li F, Qiao H, Zhang B. Discriminatively boosted image clustering with fully convolutional auto-encoders. Pattern Recogn. 2018;83:161–73.

118. Hinton GE, Salakhutdinov RR. Reducing the dimensionality of data with neural networks. Science. 2006;313:504–7.

119. Kingma DP, Mohamed S, Rezende DJ, Welling M. Semi-supervised learning with deep generative models. In: Advances in neural information processing systems; 2014. p. 3581–9.

120. El Naqa I, Li R, Murphy MJ, editors. Machine learning in radiation oncology: theory and application. 1st ed. Cham: Springer International; 2015.

121. Goodfellow I, Bengio Y, Courville A. Deep learning. Cambridge, MA: MIT Press; 2017.

122. Long J, Shelhamer E, Darrell T. Fully convolutional networks for semantic segmentation. In: Proceedings of the IEEE Computer Society Conference on Computer Vision and Pattern Recognition; 2015. p. 3431–40.

123. Ronneberger O, Fischer P, Brox T. U-net: convolutional networks for biomedical image segmentation. In: International Conference on Medical image computing and computer-assisted intervention. Berlin: Springer; 2015. p. 234–41.

124. Shen D, Wu G, Suk H-I. Deep learning in medical image analysis. Annu Rev Biomed Eng. 2017;19:221–48.

125. Efron B. Bootstrap methods: another look at the jackknife. In: Breakthroughs in statistics. Berlin: Springer; 1992. p. 569–93.

126. Efron B. Better bootstrap confidence intervals. J Am Stat Assoc. 1987;82:171–85.

127. Moons KG, Altman DG, Reitsma JB, Ioannidis JP, Macaskill P, Steyerberg EW, et al. Transparent reporting of a multivariable prediction model for individual prognosis or diagnosis (TRIPOD): explanation and elaboration. Ann Intern Med. 2015;162:W1–W73.

128. Ambroise C, McLachlan GJ. Selection bias in gene extraction on the basis of microarray gene-expression

data. Proc Natl Acad Sci U S A. 2002;99:6562–6. https://doi.org/10.1073/pnas.102102699.

129. Singhi SK, Liu H. Feature subset selection bias for classification learning. In: Proceedings of the 23rd International Conference on machine learning. New York: ACM; 2006. p. 849–56.

130. Zwanenburg A. Radiomics in nuclear medicine: robustness, reproducibility, standardization, and how to avoid data analysis traps and replication crisis. Eur J Nucl Med Mol Imaging. 2019;46(13):2638–55.

131. Wang Y, Zhang P, An L, Ma G, Kang J, Shi F, et al. Predicting standard-dose PET image from low-dose PET and multimodal MR images using mapping-based sparse representation. Phys Med Biol. 2016;61:791.

132. Wang Y, Ma G, An L, Shi F, Zhang P, Lalush DS, et al. Semisupervised tripled dictionary learning for standard-dose PET image prediction using low-dose PET and multimodal MRI. IEEE Trans Biomed Eng. 2016;64:569–79.

133. Wang Y, Yu B, Wang L, Zu C, Lalush DS, Lin W, et al. 3D conditional generative adversarial networks for high-quality PET image estimation at low dose. Neuroimage. 2018;174:550–62.

134. Gong K, Guan J, Kim K, Zhang X, Yang J, Seo Y, et al. Iterative PET image reconstruction using convolutional neural network representation. IEEE Trans Med Imaging. 2019;38:675–85.

135. Ulyanov D, Vedaldi A, Lempitsky V. Deep image prior. Proc IEEE Conf Comput Vis Pattern Recogn. 2018:9446–54.

136. Gong K, Catana C, Qi J, Li Q. PET image reconstruction using deep image prior. IEEE Trans Med Imaging. 2018;38(7):1655–65.

137. Floyd C. An artificial neural network for SPECT image reconstruction. IEEE Trans Med Imaging. 1991;10:485–7.

138. Wong CY, Schmidt J, Bong JS, Chundru S, Kestin L, Yan D, et al. Correlating metabolic and anatomic responses of primary lung cancers to radiotherapy by combined F-18 FDG PET-CT imaging. Radiat Oncol. 2007;2:18. https://doi.org/10.1186/1748-717X-2-18.

139. Coon D, Gokhale AS, Burton SA, Heron DE, Ozhasoglu C, Christie N. Fractionated stereotactic body radiation therapy in the treatment of primary, recurrent, and metastatic lung tumors: the role of positron emission tomography/computed tomography-based treatment planning. Clin Lung Cancer. 2008;9:217–21. https://doi.org/10.3816/CLC.2008.n.032.

140. Steel GG. Basic clinical radiobiology. 3rd ed. London, New York: Arnold; Oxford University Press; 2002.

141. Webb S. The physics of three-dimensional radiation therapy: conformal radiotherapy, radiosurgery, and treatment planning. Bristol, UK; Philadelphia: Institute of Physics; 2001.

142. El Naqa I. Outcomes modeling. In: Starkschall G, Siochi C, editors. Informatics in radiation oncology.

Boca Raton, FL: CRC, Taylor and Francis; 2013. p. 257–75.

143. El Naqa I, Suneja G, Lindsay PE, Hope AJ, Alaly JR, Vicic M, et al. Dose response explorer: an integrated open-source tool for exploring and modelling radiotherapy dose-volume outcome relationships. Phys Med Biol. 2006;51:5719–35.

144. El-Naqa I, Yang Y, Galatsanos NP, Nishikawa RM, Wernick MN. A similarity learning approach to content-based image retrieval: application to digital mammography. IEEE Trans Med Imaging. 2004;23:1233–44. https://doi.org/10.1109/TMI.2004.834601.

145. Lovinfosse P, Janvary ZL, Coucke P, Jodogne S, Bernard C, Hatt M, et al. FDG PET/CT texture analysis for predicting the outcome of lung cancer treated by stereotactic body radiation therapy. Eur J Nucl Med Mol Imaging. 2016;43:1453–60.

146. Yip SS, Kim J, Coroller TP, Parmar C, Velazquez ER, Huynh E, et al. Associations between somatic mutations and metabolic imaging phenotypes in non–small cell lung cancer. J Nucl Med. 2017;58:569–76.

147. Hsu C-Y, Doubrovin M, Hua C-H, Mohammed O, Shulkin BL, Kaste S, et al. Radiomics features differentiate between normal and tumoral high-Fdg uptake. Sci Rep. 2018;8:3913.

148. Budán F, Szigeti K, Weszl M, Horváth I, Balogh E, Kanaan R, et al. Novel radiomics evaluation of bone formation utilizing multimodal (SPECT/X-ray CT) in vivo imaging. PLoS One. 2018;13:e0204423.

149. Rahmim A, Salimpour Y, Jain S, Blinder SA, Klyuzhin IS, Smith GS, et al. Application of texture analysis to DAT SPECT imaging: relationship to clinical assessments. NeuroImage Clin. 2016;12:e1–9.

150. Ashrafinia S, Dalaie P, Yan R, Ghazi P, Marcus C, Taghipour M, et al. Radiomics analysis of clinical myocardial perfusion SPECT to predict coronary artery calcification. J Nucl Med. 2018;59:512.

151. Kawauchi K, Hirata K, Katoh C, Ichikawa S, Manabe O, Kobayashi K, et al. A convolutional neural network-based system to prevent patient misidentification in FDG-PET examinations. Sci Rep. 2019;9:7192.

152. Schwyzer M, Ferraro DA, Muehlematter UJ, Curioni-Fontecedro A, Huellner MW, von Schulthess GK, et al. Automated detection of lung cancer at ultralow dose PET/CT by deep neural networks—initial results. Lung Cancer. 2018;126:170–3.

153. Park J, Bae S, Seo S, Park S, Bang J-I, Han JH, et al. Measurement of glomerular filtration rate using quantitative SPECT/CT and deep-learning-based kidney segmentation. Sci Rep. 2019;9:1–8.

154. Moses WW. Fundamental limits of spatial resolution in PET. Nucl Instrum Meth Phys Res A. 2011;648(Supplement 1):S236–S40. https://doi.org/10.1016/j.nima.2010.11.092.

155. Tong S, Alessio AM, Kinahan PE. Image reconstruction for PET/CT scanners: past achievements and

future challenges. Imaging Med. 2010;2:529–45. https://doi.org/10.2217/iim.10.49.

156. Nahmias C, Wahl LM. Reproducibility of standardized uptake value measurements determined by 18F-FDG PET in malignant tumors. J Nucl Med. 2008;49:1804–8. https://doi.org/10.2967/jnumed.108.054239.

157. Kinahan PE, Fletcher JW. Positron emission tomography-computed tomography standardized uptake values in clinical practice and assessing response to therapy. Semin Ultrasound CT MRI. 2010;31:496–505. https://doi.org/10.1053/j.sult.2010.10.001.

158. Hatt M, Cheze-Le Rest C, Aboagye EO, Kenny LM, Rosso L, Turkheimer FE, et al. Reproducibility of 18F-FDG and 3′-Deoxy-3′-18F-Fluorothymidine PET tumor volume measurements. J Nucl Med. 2010;51:1368–76. https://doi.org/10.2967/jnumed.110.078501.

159. Galavis PE, Hollensen C, Jallow N, Paliwal B, Jeraj R. Variability of textural features in FDG PET images due to different acquisition modes and reconstruction parameters. Acta Oncol. 2010;49:1012–6. https://doi.org/10.3109/0284186X.2010.498437.

160. Cheng NM, Fang YH, Yen TC. The promise and limits of PET texture analysis. Ann Nucl Med. 2013;27:867–9. https://doi.org/10.1007/s12149-013-0759-8.

161. Lovat E, Siddique M, Goh V, Ferner RE, Cook GJ, Warbey VS. The effect of post-injection 18 F-FDG PET scanning time on texture analysis of peripheral nerve sheath tumours in neurofibromatosis-1. EJNMMI Res. 2017;7:35.

162. Lasnon C, Majdoub M, Lavigne B, Do P, Madelaine J, Visvikis D, et al. 18 F-FDG PET/CT heterogeneity quantification through textural features in the era of harmonisation programs: a focus on lung cancer. Eur J Nucl Med Mol Imaging. 2016;43:2324–35.

163. Hatt M, Majdoub M, Vallières M, Tixier F, Le Rest CC, Groheux D, et al. 18F-FDG PET uptake characterization through texture analysis: investigating the complementary nature of heterogeneity and functional tumor volume in a multi–cancer site patient cohort. J Nucl Med. 2015;56:38–44.

164. Lv W, Yuan Q, Wang Q, Ma J, Jiang J, Yang W, et al. Robustness versus disease differentiation when varying parameter settings in radiomics features: application to nasopharyngeal PET/CT. Eur Radiol. 2018;28:3245–54.

165. Foy JJ, Robinson KR, Li H, Giger ML, Al-Hallaq H, Armato SG. Variation in algorithm implementation across radiomics software. J Med Imaging. 2018;5:044505.

166. Traverso A, Wee L, Dekker A, Gillies R. Repeatability and reproducibility of radiomic features: a systematic review. Int J Radiat Oncol Biol Phys. 2018;102:1143–58.

167. El Naqa I, Kawrakow I, Fippel M, Siebers JV, Lindsay PE, Wickerhauser MV, et al. A comparison of Monte Carlo dose calculation denoising techniques. Phys Med Biol. 2005;50:909–22. https://doi.org/10.1088/0031-9155/50/5/014.

168. Zaidi H, Abdoli M, Fuentes CL, El Naqa IM. Comparative methods for PET image segmentation in pharyngolaryngeal squamous cell carcinoma. Eur J Nucl Med Mol Imaging. 2012;39:881–91. https://doi.org/10.1007/s00259-011-2053-0.

169. Le Pogam A, Hanzouli H, Hatt M, Cheze Le Rest C, Visvikis D. Denoising of PET images by combining wavelets and curvelets for improved preservation of resolution and quantitation. Med Image Anal. 17:877–91. https://doi.org/10.1016/j.media.2013.05.005.

170. Wei L, Rosen B, Vallières M, Chotchutipan T, Mierzwa M, Eisbruch A, et al. Automatic recognition and analysis of metal streak artifacts in head and neck computed tomography for radiomics modeling. Phys Imaging Radiat Oncol. 2019;10:49–54.

171. El Naqa I, Bradley J, Deasy J. Machine learning methods for radiobiological outcome modeling. In: Mehta M, Paliwal B, Bentzen S, editors. Physical, chemical, and biological targeting in radiation oncology. Madison, WI: Medical Physics Publishing; 2005.

172. El-Naqa I, Yang Y, Galatsanos NP, Nishikawa RM, Wernick MN. A similarity learning approach to content-based image retrieval: application to digital mammography. IEEE Trans Med Imaging. 2004;23:1233–44.

173. El-Naqa I, Yang Y, Wernick MN, Galatsanos NP, Nishikawa RM. A support vector machine approach for detection of microcalcifications. IEEE Trans Med Imaging. 2002;21:1552–63.

174. Schèolkopf B, Tsuda K, Vert J-P. Kernel methods in computational biology. Cambridge, MA: MIT Press; 2004.

175. Shawe-Taylor J, Cristianini N. Kernel methods for pattern analysis. Cambridge, New York: Cambridge University Press; 2004.

176. Hastie T, Tibshirani R, Friedman JH. The elements of statistical learning: data mining, inference, and prediction: with 200 full-color illustrations. New York: Springer; 2001.

177. Hinton GE, Srivastava N, Krizhevsky A, Sutskever I, Salakhutdinov RR. Improving neural networks by preventing co-adaptation of feature detectors. arXiv preprint arXiv:12070580. 2012.

178. Ioffe S, Szegedy C. Batch normalization: accelerating deep network training by reducing internal covariate shift. arXiv preprint arXiv:150203167. 2015.

179. Yosinski J, Clune J, Nguyen A, Fuchs T, Lipson H. Understanding neural networks through deep visualization. In: arXiv preprint arXiv:150606579; 2015.

180. Sankar V, Kumar D, Clausi DA, Taylor GW, Wong ASISC. End-to-end interpretable discovery Radiomics-driven lung cancer prediction via stacked

interpretable sequencing cells. In: arXiv preprint arXiv:190104641; 2019.

181. Luo Y, McShan D, Ray D, Matuszak M, Jolly S, Lawrence T, et al. Development of a fully cross-validated Bayesian network approach for local control prediction in lung cancer. IEEE Trans Radiat Plasma Med Sci. 2019;3:232–41.

182. Ribeiro MT, Singh S, Guestrin C. Why should i trust you?: explaining the predictions of any classifier. In: Proceedings of the 22nd ACM SIGKDD international conference on knowledge discovery and data mining. New York: ACM; 2016. p. 1135–44.

183. Selvaraju RR, Cogswell M, Das A, Vedantam R, Parikh D, Batra D. Grad-cam: Visual explanations from deep networks via gradient-based localization. In: Proceedings of the IEEE International Conference on Computer Vision; 2017. p. 618–26.

184. Chattopadhay A, Sarkar A, Howlader P, Balasubramanian VN. Grad-cam++: generalized gradient-based visual explanations for deep convolutional networks. 2018 IEEE winter conference on applications of computer vision (WACV). New York: IEEE; 2018. p. 839–47.

185. Nie K, Al-Hallaq H, Li XA, Benedict SH, Sohn JW, Moran JM, et al. NCTN assessment on current applications of radiomics in oncology. Int J Radiat Oncol Biol Phys. 2019;104:302–15. https://doi.org/10.1016/j.ijrobp.2019.01.087.

Quantitative SPECT Imaging

18

Michael Ljungberg

Contents

18.1 Introduction

A scintillation camera is essentially a device that measures two-dimensional (2D) images of a radionuclide distribution in vivo by detecting emitted photons. Due to the construction of the collimator, events in the image obtained from photons emitted from different source depths will be superimposed, and the source depth will not be resolved. The solution is to obtain the three-dimensional (3D) information by measuring projections in different views around the patient and use a reconstruction algorithm. The method is called single-photon emission computed tomography (SPECT). If the activity is not redistributed between organs or tissues over the time of the

M. Ljungberg (✉)
Department of Medical Radiation Physics,
Lund University, Lund, Sweden
e-mail: Michael.Ljungberg@med.lu.se

measurement, then the assumption in any reconstruction method is that there exists an activity distribution for which a corresponding photon emission will result in the projections that are acquired by the system. The goal then, is to determine this distribution in 3D as accurately as possible.

18.2 Factors That Degrade SPECT Imaging

Presently, tomographic image reconstruction in SPECT is often based on iterative methods, such as the maximum likelihood expectation maximisation (ML-EM) and ordered subsets expectation maximisation (OS-EM) methods [1–3]. The approach is to find an activity distribution (described by a set of consecutive 2D tomographic images representing different sections in

the object) that produces the best match to the measured projection data. However, if the measured data suffers from physical effects, such as photon attenuation in the object or unwanted contribution to the projection data from photons scattered in the patient, then the reconstructed solution will not accurately describe the activity distribution. Photon attenuation can actually result in false positive indications, especially in non-homogeneous regions such as the thorax. It is, therefore, important to correct for these effects even if the actual numerical pixel values are of less importance.

The following examples that describe the major factors that degrade SPECT imaging have been created by the use of the Monte Carlo program SIMIND [4, 5] which simulated a cylindrical water phantom and the XCAT anthropomorphic mathematical phantom [6, 7]. The Monte Carlo method allows for the simulation of the photons from their emission from an object to the detection by a scintillation camera. During this process, it is possible to keep track of the interaction history of the photons and observe how the image is formed from these photons. The advantage of categorising each event in the image based on the origin of the photon i.e. primary, scattered, or penetrated photons, is that this makes it possible to study the degradation in detail. The relative activity concentration, defined for the XCAT simulations, were 90, 20, 90, 50, 30, 20 and 1 for the cardiac, the liver, both kidneys, the spleen, gall-bladder, bone and the background, respectively. A simulated perfusion defect with the size of about 10 cm^3 having a 25% uptake relative to the cardiac activity concentration of 90 were also defined.

Different photon energies have been simulated for visualisation, but some of these energies may not be clinically relevant to the simulated radionuclide distribution. A standard Anger-type camera has been simulated with a 3/8-in. crystal thickness and an energy resolution of 9.0% FWHM at 140 keV. Projections were scaled to represent 300 MBq in the XCAT phantom and 30 s acquisition time to define a clinical realistic noise level when applied. Reconstruction were made using an in-house developed filtered back projection algorithm and the IRL iterative reconstruction software, developed by Frey and Tsui at

the Johns Hopkins Medical Center, Baltimore, USA. Included in this package are the ESSE model-based scatter correction [8] and compensation for collimator resolution.

18.2.1 Distance-Dependent Collimator Resolution

The commonly used parallel-hole collimator has the advantage of having a geometrical sensitivity that is independent of the source-to-collimator distance within the field of view (FOV). This means that the conversion factor (cps/MBq) remains constant within the FOV, which greatly simplifies the process of activity quantitation. The spatial resolution, however, depends on the distance to the collimator and the specifications of the holes (diameter, shape, septum thickness and length). In a clinical environment, it is common to have several types of collimators available, which are selected depending on the type of study and energy of the photon. Examples are low-energy high-resolution (LEHR), low-energy general-purpose (LEGP), medium-energy (ME) and high-energy (HE) collimators. Because of the underlying design, even a parallel-hole LEHR collimator will limit the spatial resolution to a best possible value of approximately 10–15 mm for SPECT. This means that although the correct number of counts are acquired by the camera, the position of each event is spread out over a large area (more pixels) if the source is located at a larger distance. This effect can be observed in Fig. 18.1 where profiles through images of three-point sources being located at different distances from the collimator surface are shown for LEGP, LEHR, ME and HE collimators. The profiles show a larger value of the FWHM as the source moves away from the camera. This broadening is less pronounced for the LEHR collimator, but at the expense of a reduction in the measured count rate.

The distance-dependent blurring of an image means that the cps/pixel will not reflect the MBq/ml in a particular voxel. This unwanted effect is called the partial volume effect. The spatial resolution also affects the image contrast and hence the ability to detect small lesions of moderate and low
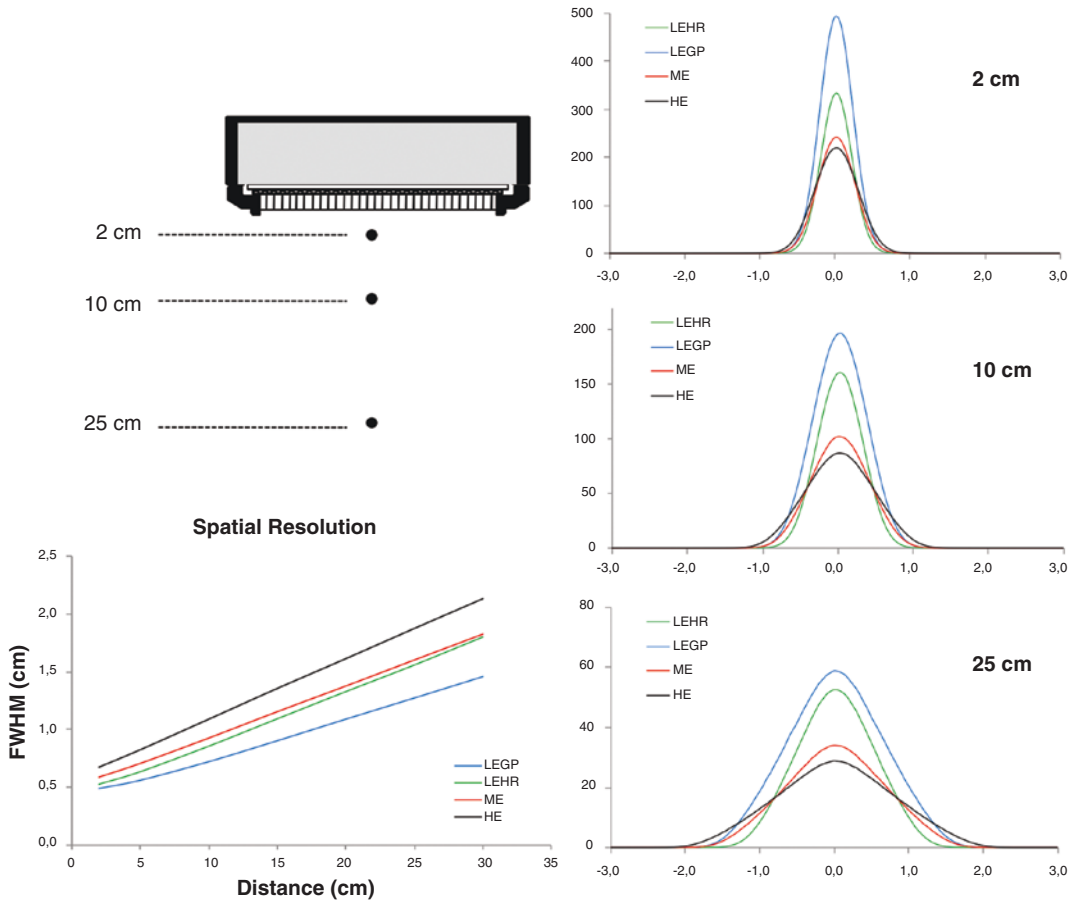
Fig. 18.1 Simulated point-spread function for a ^{99m}Tc point source (140 keV) located at distances of 2, 10 and 25 cm to the lower collimator surface. The images illustrate the importance of always keeping the camera as close as possible to the patient surface. The figure also shows that the magnitude of the degradation in spatial resolution for the four collimators also differs. The activity was the same for all locations and collimators

lesion-to-background activity ratios. In principle, very small lesions can be detected, but the lesion-to-background activity ratios in these cases needs to be very high; however, the smallest volume of a lesion that can be measured should be equal to the order of the spatial resolution of the system.

18.2.2 Photon Attenuation

Some of the photons emitted from the radiopharmaceutical administered to a patient will interact within the patient and therefore not contribute to image formation in the expected way, as can be seen in Fig. 18.2. The basic interaction types for photon energies that are important for nuclear medicine applications are photoabsorption, Compton interaction (photon scattering with energy loss), coherent interaction (photon scattering without energy loss) and pair production (rare since this interaction type can only occur for photons with energies above 1.022 MeV). Consider a rate of photons impinging in a narrow-beam geometry on an object of the thickness d and the density ρ. The number of photons that pass through the object is given by

$$\dot{N} = \dot{N}_0 \cdot e^{-\frac{\mu}{\rho} \cdot \rho \cdot d} \quad (18.1)$$

where $\dot{N}_0$ is the initial narrow-beam photon rate and $\dot{N}$ is the photon rate after passing though the object. The probability of each of the possible interactions can be described by differential cross-section coefficients, and, consequently, the

sum of these coefficients describes the probability of occurrence of any type of interaction. This sum of the coefficients is proportional to the *linear* attenuation coefficient μ.

$$\mu \sim \tau_{photo} + \sigma_{compton} + \sigma_{rayleigh} + \kappa_{pair} \quad (18.2)$$

Photon attenuation depends on the photon energy ($h\nu$), atomic numbers of the composition (Z) and the density (ρ), and values are often tabulated as *mass*-attenuation coefficients, μ/ρ.

In a photo absorption event, the energy of a photon is transferred to an electron in the inter-

acting atom. This electron will, if the photon energy is high enough, liberate itself from the atom and leave the atom with a kinetic energy equal to the incoming photon energy minus the binding energy of the electron. When the vacancy in the electron shell is filled with an outer electron, the binding energy is emitted either as a characteristic X-ray photon or as an Auger electron. The probability for these occurrences depends on the atomic number of the material. Auger electron emission is dominant in low-Z tissue-equivalent materials (Fig. 18.3).
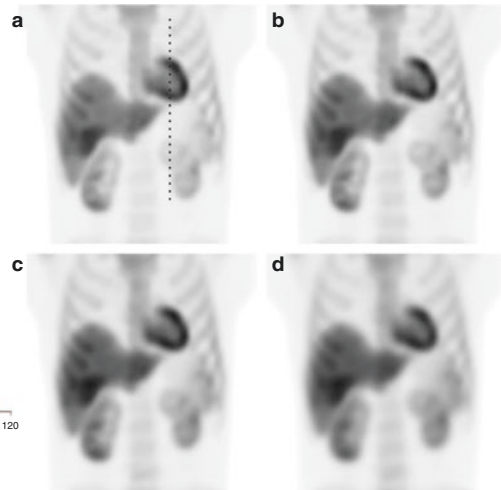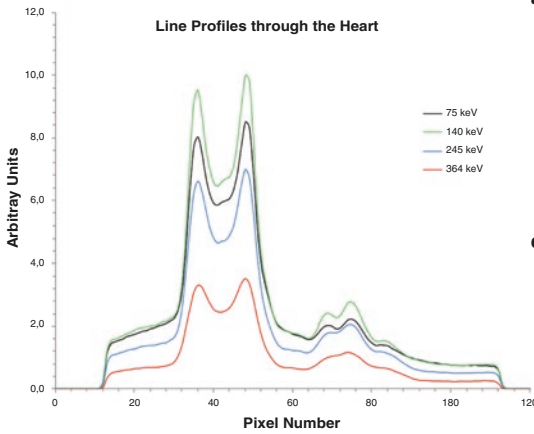
Fig. 18.2 Four frontal projections of the XCAT phantom showing the effect of photon attenuation in the cases of 75 keV (**a**), 140 keV (**b**), 208 keV (**c**) and 364 keV (**d**) photon emission, respectively. Vertical line profiles through the heart and part of the left kidney have been calculated and are compared in the left diagram. The dotted line in projection (**a**) indicates the location of the profiles. Note that these figures were simulated considering photon attenuation alone. For a complete ^{131}I decay, additional counts are added generated by high-energy photons—637 keV (7.12%) and 723 keV (1.78%)—and backscattered from the compartment behind the crystal and by septal penetration
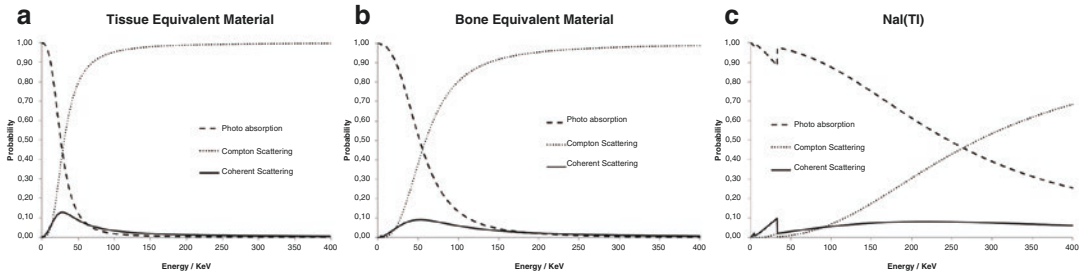
Fig. 18.3 Relative probability for photo-absorptions, Compton scattering and coherent scattering in the energy range up to 400 keV for (**a**) tissue-equivalent material, (**b**) bone-equivalent material and (**c**) NaI(Tl) crystal material. Note the rapid decrease in probability for photo absorption in tissue. Note also that these data are relative, and that the magnitude of the attenuation is much larger for NaI(Tl) as compared to water

18.2.3 Photon Scattering

Photon scatter originates from the limitation of the scintillation camera to accurately measure the energy imparted to the NaI(Tl) crystal. The processes of converting the imparted energy to visible light photons and guiding these photons to the photomultipliers to achieve measurable signals are inherently stochastic. Therefore, the measured signal will have a statistical error even if the imparted energy always remains the same. For new NaI(Tl) crystals, this statistical error is approximately 8–10% (FWHM) for an absorbed energy of 140 keV. This relatively large error implies that an energy discriminator needs to cover about twice this width (16–20%) in order to maintain a reasonable counting statistic. Some of the photons that have been scattered in the patient with a small deflection angle (small loss of energy) may therefore be detected within such a large energy window and thus contribute to the image formation; however, these photons carry wrong spatial information about the location of decay in the object. Such scattered events will result in a degraded image contrast and present a potential problem when trying to quantify regional activity uptakes.

Figure 18.4 shows the true imparted energy in the NaI(Tl) crystal from 140 keV photons (^{99m}Tc), emitted from a point source in centre of a 11 cm radius cylindrical water phantom (18.4a). Note the sharp peak that occurs because the full-absorption from 140 keV photons will be within the same energy channel. Plot 18.4b shows simulated data corresponding to a measured energy spectrum. The peaks are broader due to the poor energy resolution of the camera (9% FWHM at 140 keV). Because of this inaccuracy in the energy measurement, some photons that have been scattered in the phantom are detected within the energy window. Plot 18.4b
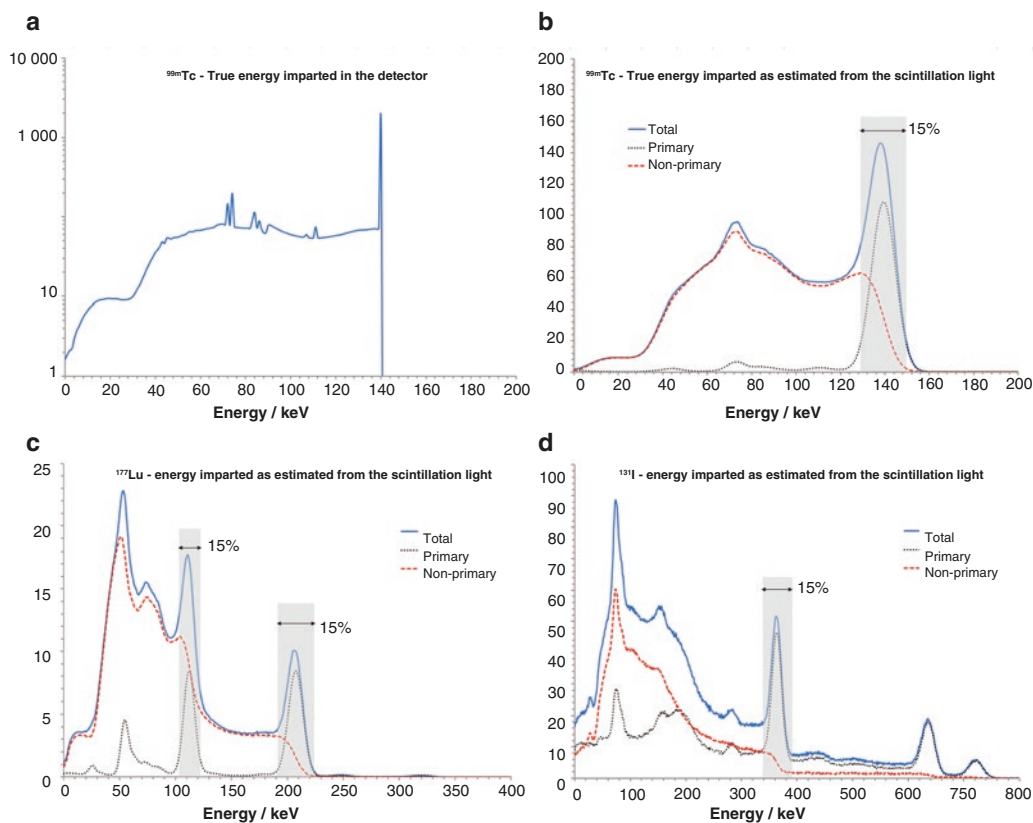
Fig. 18.4 Plot (**a**) shows the true imparted energy in the NaI(Tl) crystal from 140 keV photons (^{99m}Tc) emitted from a point source in centre of a 11 cm diameter cylindrical water phantom. Plot (**b**) displays curves that represent events from primary unattenuated photons and photons scattered in the object. Plots (**c**) and (**d**) show corresponding data for ^{177}Lu and ^{131}I

also displays curves that represent events from primary unattenuated photons and photons scattered in the object. Note that a substantial fraction of scattered photons will contaminate the images acquired within the energy window. In the acquired image, it is not possible to distinguish these events from the primary events. Plots 18.4c and d show corresponding data for ^{177}Lu and ^{131}I.

The energy $h\nu'$ of a scattered photon is directly related to the angle of deflection according to the Compton equation

$$ h\nu' = \frac{h\nu}{1 + \dfrac{h\nu}{m_o c^2}\left(1 - \cos\theta\right)} \qquad (18.3) $$

For higher photon energies, the scattering angles θ tend to peak in the forward direction, but at moderate photon energies (~100 keV) the distribution is relatively symmetrical with a slightly lower probability for scattering angles ±90°. The differential cross-section, as described by the Klein-Nishina relation is given as

$$ d\sigma_{\gamma,\gamma e}^{e} = \frac{r_e^2}{2} \cdot \left(\frac{h\nu'}{h\nu}\right)^2 \cdot \left(\frac{h\nu}{h\nu'} + \frac{h\nu'}{h\nu} - \sin^2\theta\right) \cdot d\Omega $$

$$ (18.4) $$

which determines the probability for a photon being scattered through an angle θ into a solid angle $d\Omega$ relative to the incoming photon trajectory. Eq. (18.4) has been derived based on the assumption that the electron is not bound to the nucleus and in rest. When the photon energy decreases, the binding effect to the nucleus changes the cross-sections slightly.

Since the contribution of scatter in a SPECT projection is a consequence of photon interactions in the object, the amount of scatter (sometimes defined as the scatter-to-total fraction) depends on photon energy, source depth and distribution, and tissue composition in addition to camera-related parameters such as energy resolution and energy window settings. Figure 18.5 shows the variation of the scatter-to-total fraction with these parameters and brings out the different dependences.

From Fig. 18.5a, it can be seen that the scatter-to-total fraction increases with increasing source depth but levels out at or above a moderate source depth (>20 cm). This is because, although the scattering increases with depth, the scattered photons will also be more attenuated compared to the primary photons with higher energies. The degradation in image quality due to Compton scattering is also a function of the energy resolution and thus, the related energy window setting; however, as can be seen from Fig. 18.5b and c, the dependence of these two parameters is quite moderate. Thus, even for new crystals, the scatter-to-total fraction in a scintillation camera image remains quite high (30–50%).

When reviewing tabulated cross-sections for Compton scattering [9], one can see that the relative number of Compton scattering interactions increases with increasing photon energy, as can be seen in Fig. 18.2. It is, therefore, somewhat contradictory that issue of scatter in SPECT is more considerable for photons of low energies (Fig. 18.4d). This happens because a fixed energy window centred on the photo-peak energy is used here. For an initial high photon energy, the relative loss of energy to a secondary electron during a Compton scattering is quite large, which results in a scattered photon of significantly lower energy when compared to using the energy window discriminator in the lower part of the energy distribution. For a lower initial photon energy, the relative loss of energy in a Compton scattering is small, which implies that even for a large scattering angle there is a good chance that a scattered photon in that energy range will be detected within the fixed energy window.

18.2.4 Collimator Septal Penetration

As mentioned above, the purpose of the collimator is to select only those photons emitted in a direction determined by the axial direction of the collimator hole and to reject all other photons. However, because of the exponential characteristics of photon attenuation, there will always be a finite probability for a photon to penetrate the collimator walls (septa) and interact in the crystal
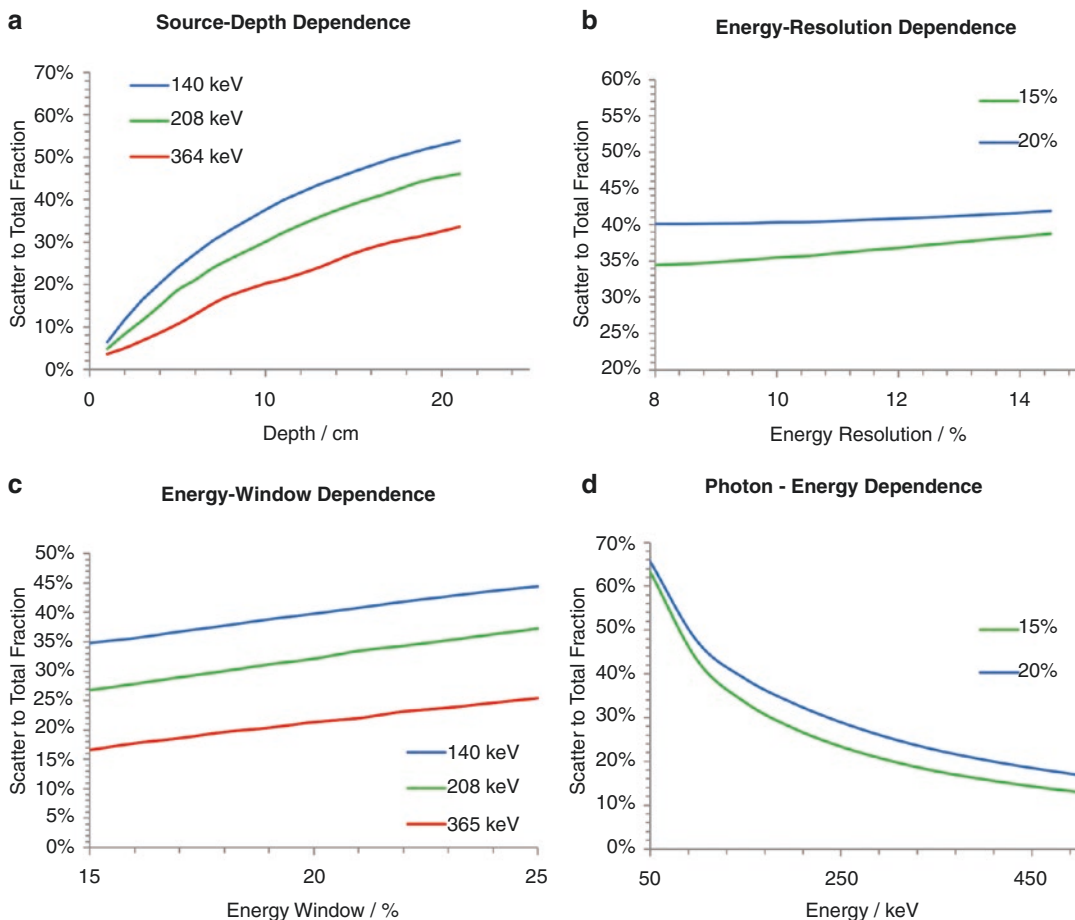
Fig. 18.5 Scatter-to-total dependence on (**a**) source depth, (**b**) energy resolution of the camera, (**c**) energy window setting and (**d**) photon energy. Two energy windows of 15% and 20% have been used when appropriate.

The data have been simulated using a cylindrical water phantom of 15 cm radius and 20 cm length. The point source is located at the centre of the phantom for the results in graph (**b**)–(**d**)

further away from the positions defined by the location of the hole. When constructing a collimator, the selection of wall thickness is, therefore, a compromise among the spatial resolution, system sensitivity and probability of septum penetration.

To illustrate this effect, consider the simulated images shown in Fig. 18.6. The upper row shows three images of a simulation with ^{99m}Tc photons and for LEHR, ME and HE collimator—it can be observed that the image has good quality although the HE collimator provide less spatial resolution. The second row of images shows a simulation with photons of ^{177}Lu for the same set of collimators. Here we see a clear influence of septal pen-

etration for the LEHR collimator, but the other two collimators have sufficient collimator septa thicknesses to minimise the contribution of penetration. The third lower row shows the same simulation for a complete ^{131}I decay. The image for the LEGP collimator is completely deteriorated due to septum penetration and is unusable. Because of the thicker septa of the HE the penetration effects have been reduced and satisfactory image quality has been obtained. Penetration effect can also be seen for the ME collimator. Even when using a HE collimator, penetration will occur since the complete decay of ^{131}I also include the higher photon energies of

637 keV (7.3%) and 723 keV (1.78%). Even though the number of emission per decay of these photons may be low, the high photon energies enables them to penetrate the walls even when an HE collimator is used [10] and these significantly interfere with the image formation.

The unfavourable effects of septum penetration can be reduced either by using a collimator with thicker septa [11] and better attenuating properties, such as tungsten, or the by accounting for the phenomenon using a suitable correction method. If the septum penetration can be modelled, then this effect can be included as a collimator-response function in the forward pro-

Fig. 18.6 The upper row show images photons of ^{99m}Tc impinging on a camera with LEHR, ME and HE collimators. The middle row and lower row show the same simulation but for photons of ^{177}Lu and ^{131}I, respectively. The images are noise-free for a better visualisation of the effects

jection step in an iterative reconstruction method.

To summarise some of these effects, consider the energy spectra displayed in Figs. 18.4b–d and the results in Table 18.1 obtained from these simulations. It can be seen from Table 18.1 that for ^{99m}Tc, there is a significant fraction of non-primary events, mainly due to photon scattering in the object. The penetration fraction is very small, which indicates that the collimator is effective in absorbing photons moving in unwanted directions. For the 208-keV peak energy window of ^{177}Lu, the incidence of non-primary and penetration events is also relatively moderate when using the ME collimator a s compared to, but the fraction of penetration is somewhat larger than for ^{99m}Tc, possibly due to the 321 keV photons in the decay scheme that, despite the low abundance of 0.22%, may contribute to these events due to the increased probability for septal penetration. For the 113 keV peak energy, however, the penetration fraction is low, but the non-primary fraction is very high. This is due to single- and multiple- Compton scatterings of the 208 keV photon which results in photon absorptions detectable in the 113 keV peak energy window.

When using the LEHR collimator for ^{177}Lu imaging, the data in Table 18.1 show that the non-primary fraction is relatively large, and that there is a large fraction of penetration for the 208 keV photons. The cps/MBq is higher, but this results from unwanted counts and hence, does not justify the use of an LEHR collimator. For the simulation of ^{131}I, one can see that the fraction of non-primary events are large mainly due to the

Table 18.1 Count rate per unit activity (cps/MBq) is shown together with the fraction non-primary/total and penetrations/total for three different radionuclides

Radionuclide	Peak energy (keV)	cps/MBq		Non-primary/total		Penetration/total	
		15% window	20% window	15% window	20% window	15% window	20% window
^{99m}Tc (LEHR)	140 (89.1%)	21.5	24.6	39.3%	44.8%	3.2%	3.2%
^{177}Lu (ME)	208 (10.38%)	1.9	2.1	34.0%	39.2%	5.0%	4.9%
	113 (6.2%)	2.6	3.0	65.6%	69.2%	1.3%	1.3%
^{177}Lu (LEHR)	208 (10.38%)	5.2	5.6	76.0%	77.6%	44.2%	43.2%
	113 (6.2%)	2.9	3.5	70.3%	73.7%	10.1%	10.8%
^{131}I (HE)	364 (81.2%)	15.2	17.4	60.2%	64.9%	23.6%	23.5%

large contribution from the penetration of the 636 and 723 keV photons and also the potential contribution from these photons when they backscatter from the material surrounding the NaI(Tl) crystal.

18.2.5 Physiologic and Patient Motions

When acquiring data with a SPECT camera, one should always remember that the acquisition is made using a 'camera shutter' that is open during the entire acquisition time. This means that movement of the patient will result in a degradation of the spatial resolution and in some cases, cause artefacts. Even if the patient is carefully strapped and remains very still, some movements such as respiratory movements and motion of the heart cannot be avoided [12].

Respiratory movements cause spatial changes that depend on the organ. Since the frequency of the breathing is different from the frequency of cardiac motion, respiratory movements will also have an effect on the quality of cardiac imaging even if the gated SPECT is applied. The motion is complicated with translations in the axial or superior/inferior direction causing a blurred image with a potential reduction of counts in the anterior and inferior walls. In tumour detection, the form of the tumour may change to a more elongated or elliptical shape because of breathing and the results may also have a lower image contrast. This has been observed in lung studies with PET and[18]FDG.

18.2.6 Image Noise

Because of the randomness of photon histories, an acquired SPECT image will be affected by statistical errors and related image noise. The noise distribution of the scintillation camera image follows the Poisson distribution where the variance of a measure in a region of interest is the sum of the counts. This implies that in order to get a good image quality, a sufficiently long acquisition time together with a high adminis-

tered activity should be used. Noise in the image also depends on the selected matrix size. Changing from the matrix size of 64×64 to 128×128 will increase the variance in a projection pixel by a factor of four. Note also that reconstruction is usually performed slice by slice, which means that the slice thickness (and consequently the acquired number of counts) is half for a 128×128 matrix as compared to a 64×64 matrix. The mean counts per voxel in a reconstructed SPECT image will, therefore, be reduced by a factor of eight. Thus, it is not always advantageous to increase the matrix size. The time per projection and the number of projections is also of importance. These factors need to be optimised for each study since noise due to improper acquisition parameters can propagate through the reconstruction process and create artefacts in the final image.

18.2.7 Other SPECT Degradation Factors

It is essential that the scintillation camera is well tuned and calibrated. This is especially true for SPECT since deficiencies can result in visible artefacts. For example, non-uniformities in a planar image can be of less importance and sometimes difficult to detect, but when reconstructing data from a SPECT camera with non-uniform regions, artefacts can be seen as distinct rings in the image. The tuning of the centre-of-rotation (COR), that is, the alignment of the electronic centre used in the reconstruction algorithm to the mechanical centre of the camera orbit is also important. A small error in the COR results in the degradation of spatial resolution, and if a larger shift occurs, then also here, a ring artefact may appear. It is also important to calibrate the pixel size carefully when performing the correction for attenuation as well as other quantitative measures. A wrong value can result in either under- or overcorrection due to errors in the parameter x in Eq. (18.1). Other factors that can influence the accuracy in a SPECT study are the selection of acquisition parameters and the related noise. The most important selection here is the number of

Projections

Reconstructions
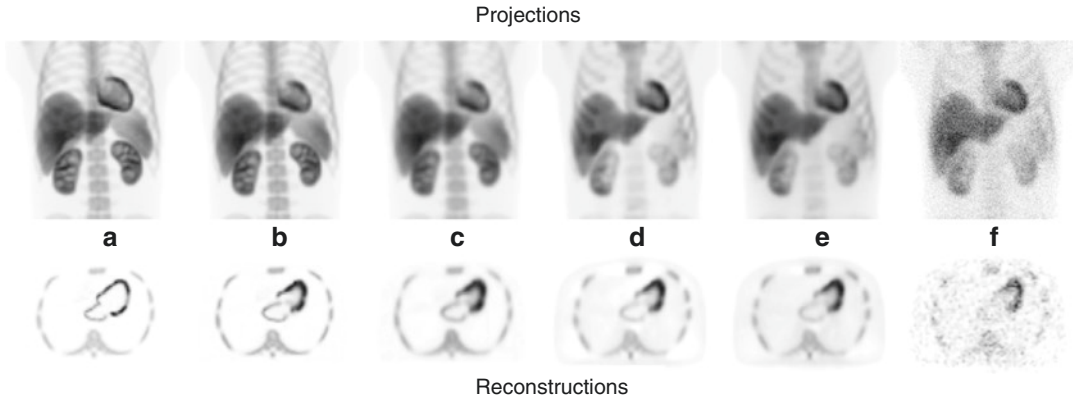
Fig. 18.7 Column (**a**) corresponds to an imaging situation without patient motion and a perfect camera resolution. Column (**b**) includes patient movements (respiration and heart beating). Column (**c**) represents an image with a typical system resolution and patient movements. Column (**d**) also includes photon attenuation. Column (**e**) includes photon attenuation and scatter contribution and column (**f**) is the same as column (**e**) but with noise added

projections and the matrix size. There is a relation between the expected spatial resolution in an image and the number of samples (angles and pixels) as determined by the Nyquist frequency and the number of angular intervals.

Reaching this frequency limit may, in some cases, be difficult depending on the activity administered to the patient and the time required for the acquisition. Generally, there is a trade-off among image quality (the combination of spatial resolution, image contrast and noise level), realistic acquisition times and levels of administered activity. Often, image processing including low-pass filtering are required, although it must be noted that post-acquisition image filtering requires a certain compromise of the spatial resolution. In some investigations where high administered activities are used, limitations in the count rate performance of the camera can result in unexpected results. Dead time problems and pulse pile-up effects can change the system sensitivity (cps/MBq) and calibration factors for scatter correction methods. In addition, significant mispositioning of events due to the unwanted contribution of scintillation light from earlier events may occur because the position of an event is calculated from the centroid of the emitted scintillation light. In this context, it should be remembered that calibrations made for low count rates might thus not be relevant in high count rate imaging.

As data is collected over a relatively long duration, it is important that the patient remains in the same position. Some movements such as cardiac motion and breathing are unavoidable. Cardiac motion can be accounted for using gated SPECT in which the cardiac cycle is divided into a number of separate time-frame acquisitions based on ECG information, especially the R-R interval. It has been standard practice for many years to collect information by this technique and display separately reconstructed images of the different time intervals in a cine-mode display. However, the image quality is most hampered due to noise because of the limited amount of the collected count for 8- or 16-frame gated SPECT. Spatial and temporal filtering is a pre-requisite here for a reasonable image quality. In addition, the number of projections and the number of time frames per cardiac cycle are often reduced in order to increase the time per projection for a given total acquisition time.

Figure 18.7 summarises how the image is degraded by the different factors discussed above. The upper row shows the frontal projections and the lower shows the corresponding reconstructed transversal images selected at a

certain location in the heart. Reconstructions were made with an iterative OS-EM algorithm without any corrections. The simulation was performed using 120-angle projections and a 360° rotation mode. The matrix size was 128×128, and eight iterations and ten subsets were used in the reconstruction. No post-filtering was applied to the reconstructed images. The first set of images (a) represents acquisition with a perfect system in the absence of cardiac or respiratory motion. The reconstructed image still shows some degradation in spatial resolution due to the finite sampling in projection angles, matrix size, and forward projection algorithm. The second column (b) shows the blurring due to respiratory and cardiac motion. When determining the attainable image quality in clinical studies based on phantom experiments, it is important to consider this motion since physical phantoms are most often static. In addition, the third column (c) includes the degradation in spatial resolution caused by the characteristics of the LEHR collimator. The fourth column (d) includes the attenuation of primary photons but no scatter contribution. This mimics a system with perfect energy resolution and a corresponding narrow energy window. The fifth column (e) includes the presence of scatter due to the limited energy resolution. The last column (f) shows the same images as in column (e) but with an added realistic noise level.

18.3 Correction Algorithms

The objective of a reconstruction method is to obtain a source distribution, described as a transversal image that matches the measured projections as accurately as possible. However, if the measured data are affected by photon attenuation, scatter and collimator blurring, the reconstructed images will not be accurate. It is, therefore, important that these physical effects need to be compensated for even if the numerical values in the final image are not very important, in order to obtain a high-quality diagnostic image with better sensitivity and specificity.

18.3.1 Attenuation Correction Methods

When using the filtered back projection method (FBP) to reconstruct images, an attenuation correction need to be applied either prior to or post the reconstruction step. As a pre-processing method, the conjugate-view method can be applied if opposite projection data are available. The main advantage is that the source depth dependence x in Eq. (18.1) becomes cancelled out when the opposite projections are combined by a geometrical-mean operator on a pixel-by-pixel basis. Let P_{ant} and P_{post} be the counts in opposite projections and P_{air} be the counts registered in both cameras without attenuation (assuming a parallel-hole collimator with invariant system sensitivity within the FOV). Then, the geometrical-mean is calculated using

$$\sqrt{P_{ant} \cdot P_{post}} = \sqrt{\left[P_{air} \cdot e^{-\mu \cdot d} \right] \cdot \left[P_{air} \cdot e^{-\mu \cdot (T-d)} \right]}$$
$$= \sqrt{P_{air}^2 \cdot e^{-\mu \cdot T}} = P_{air} \cdot e^{-\mu \cdot T/2}$$

(18.5)

where d is the distance from the source to the surface along the projection line toward the anterior detector and T is the total thickness of the patient's body along the same projection line. The equation is only valid for point-like sources and uniform attenuation. Still, this method is used frequently in planar imaging activity quantitation.

The Chang method [13] is a postprocessing method that is applied to reconstructed SPECT images. The base for this method is the calculation of an attenuation factor averaged for all angles and determined for each voxel location within the boundary of the object. The method can be mathematically described as

$$CF(x,y) = \left[\frac{1}{N} \sum_{I=0}^{N} e^{-\mu \cdot d(x,y,\theta_i)} \right]^{-1}$$
(18.6)

If the information about heterogeneous attenuation, expressed as a map of varying μ values, can be obtained by some type of transmission study (see more about this below), then this informa-

tion can be included in the calculation of the attenuation factor. The method may result in imperfect attenuation compensation and has inferior noise properties.

Today, the most frequently used compensation method for attenuation forms part of an iterative reconstruction method. A common feature of all iterative reconstruction methods is the use of a calculated projection, obtained by forward projecting a first estimate of the activity distribution for the purpose of mimicking the image process. By comparing these calculated projections to match the measured projections using some kind of cost-function, the need for an improvement (often denoted 'an update') of the initial estimated activity distribution can be determined. Photon attenuation can be implemented both in the forward projection step before calculating the final projection bin and in the back projection step. Information about the non-uniform attenuation distribution can be included in the projection steps if appropriate attenuation maps are available either from transmission scans or registered CT images.

18.3.2 Measurement of Photon Attenuation

Properly correcting for attenuation in the thorax region requires a measurement of the distribution of attenuating tissue (an attenuation map) from a transmission measurement using an external radiation source mounted on the opposite side of the patient. For each SPECT projection angle, two measurements are required; one with the patient in situ and another blank study. By calculated the ratio between the two projections on a pixel-by-pixel basis, (*j,j*), line integrals (projections) of the attenuation coefficients can be calculated from the following formula

$$\int \mu_{h\upsilon_{em}}(i,j) = f\left(h\upsilon_{tr}, h\upsilon_{em}\right)\cdot\left[-\ln\left(\frac{P(i,j)_{patient}}{P(i,j)_{blank}}\right)\right]$$

$$(18.7)$$

The function $f(h\upsilon_{tr}, h\upsilon_{em})$ includes normalisation factors and conversion of the μ values from the

photon energy $h\upsilon_{tr}$ (or X-ray spectrum), used for the transmission study to the photon energy $h\upsilon_{em}$ used for the emission study. If the P projections have been obtained from a CT scan, then function f also needs to include a conversion from HU units to a relevant unit (e.g. using a HU-to-mass-density calibration). The actual method for the conversion to linear μ values is vendor-specific. The final μ-projections can then be reconstructed using either FBP or by iterative reconstruction methods.

If a radionuclide is used as a radiation source, it is generally desirable to have properties such that the transmission scan and emission scan can be done simultaneously. This implies that the radionuclide needs to be different from the main radionuclide in order to separate transmission data and have high activity. In earlier days, the most commonly used radionuclide in commercial systems was [153]Gd with a half-life of 242 days and the emission of two major photon energies of 97.5 keV (29.5%) and 103 keV (21.1%), respectively. The method with a radionuclide source suffers from several limitations. First, photons emitted from the main radionuclide (often ^{99m}Tc) that are scattered in the patient were registered in a lower transmission energy window. This led to too-low numerical values of the attenuation coefficients. Second, the source needed to be replaced on an approximately annual basis making the method relatively expensive. Third, the spatial resolution of the camera only resolved the major structures, such as the lungs, and so, the attenuation map could not be used as an anatomical reference map (Fig. 18.8).

The recent developments in combined SPECT/CT systems cancelled out most of the serious issues with radionuclide-based transmission measurements. The resolution and noise characteristics of modern systems are superior and consequently, the quality of the measured attenuation coefficients is, therefore, high. The scaling to other photon energies is relatively accurate despite the fact that the CT images are created from a broad spectrum of bremsstrahlung photon energies. The latest SPECT/CT models include diagnostic CT (spiral) with rapid scanning time and a spatial resolution that meets the requirement for a useful radiological diagnostic modal-

a SPECT camera

b CT detector package

Parallell-beam geometry

Cone-beam geometry

Radionuclide source

X-ray source
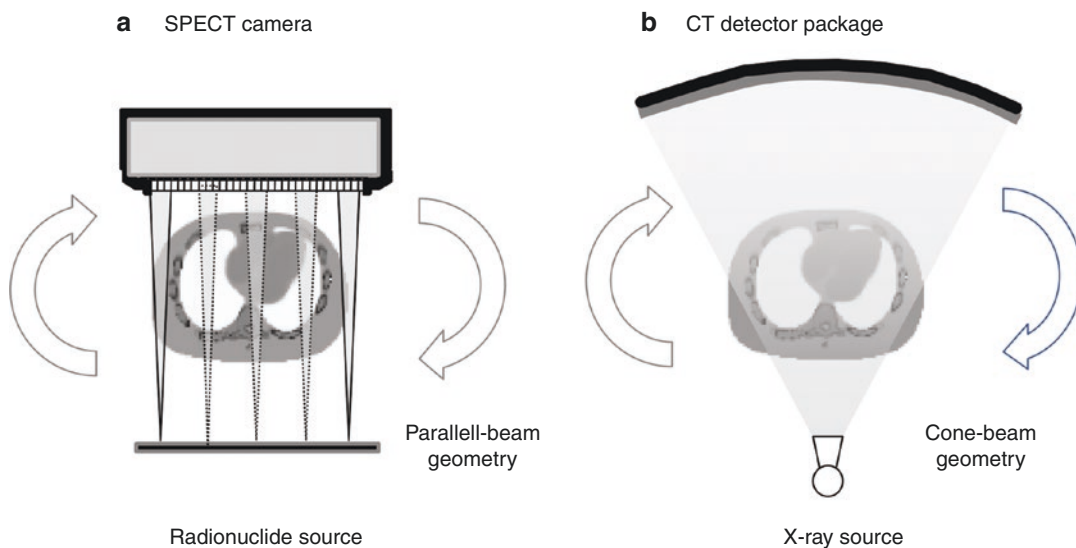
Fig. 18.8 Schematic image of detector principles behind transmission imaging. The the left (**a**), the transmission source was a radionuclide with a proper characteristic and placed on the gantry of the SPECT camera. The the right (**b**), a schematic figure shows the same principles for the CT, but where a ray tube with a cone-beam emission is used. The detector package is also different. In both cases, one also acquires a blank scan without the patient in site

ity in contrast to the first-generation SPECT/CT system that had a spatial resolution of approximately 34 mm. However, it must be noted that CT snapshots do not generally represent the average attenuation caused by the breathing that is 'seen' by the SPECT camera. Artefacts can, therefore, be introduced in an attenuation correction. For more information on the combined SPECT/CT system, see Chap. 14 in this textbook.

18.3.3 Scatter Correction Methods

Correction for scatter is most often made either in the energy domain where scatter in the photo-peak energy window is modelled by collected data in additional energy windows or by using analytical methods that model the scatter directly on photo-peak data directly. One of the early scatter corrections put forth was the dual-energy window method (DEW) proposed by Jaszczak et al. [14]. This method is based on an additional acquisition in a wide lower energy window. Scatter subtraction was applied by assuming that the distribution of counts in this lower energy window is qualitatively equal to the distribution of scatter in the photo-peak window, but only differ quantitatively by a scaling factor k (often set to 0.5 if the width of the scatter window and the main photo-peak window is the same). A scatter-corrected projection is then calculated from

$$P_{\text{primary}} = P_{\text{peak}} - k \cdot P_{2\text{nd}} \qquad (18.8)$$

The main problem with this method is to obtain a proper value of k since this factor essentially is a function of the patient geometry and source distribution. Furthermore, the distribution of scatter in the lower energy window include a larger fraction of events created from multiple-scattered photons with wide angles, which may then cause either over- or under-corrections in specific regions even if the k factor is accurate.

A similar approach is used in the Triple-Energy Window (TEW) method, but this method is based on two narrow adjacently located energy windows around the photo-peak window [15]. By considering the average of the acquired images pixel-by-pixel and scaling by the ratio between the energy window width of the photo-peak window and the scatter windows, a better

scatter estimate will be obtained. A scatter-corrected projection is obtained from

$$P_{\text{primary}} = P_{\text{peak}} - \left[\frac{P_{\text{lower}}}{\Delta E_{\text{lower}}} + \frac{P_{\text{upper}}}{\Delta E_{\text{upper}}} \right] \cdot \frac{\Delta E_{\text{Peak}}}{2}$$

(18.9)

This method does not rely on any scaling factor. However, the main problem here is the noise in the scatter data that mainly results from the narrow energy windows, and scatter images require further processing such as low-pass filtering before subtraction. Nevertheless, this method has been successful not only for [99mTc] studies but also for [131I] studies where the upper scatter window takes into account the down-scatter from the 637 and 723 keV photons which are emitted in the [131I] decay (Fig. 18.9).

Figure 18.10 shows simulated point-spread functions for different point source locations in an 11-cm radius cylindrical water phantom. The unscattered primary component has been separated and is shown as dashed lines. The shape of the scatter component in a point-spread function depends on the source depth to a large extent. For shallow source depths, the probability of multiple scattering is low, and therefore, the shape of the scatter profile is quite narrow. For a large source depth, the distribution becomes wider because of more events from multiple-scattered photons that results in registering a position far away from the decay location.

Frey and Tsui [16] has developed the effective scatter source estimator (ESSE) method, in which the modelling of the scatter is incorporated in an iterative reconstruction method using pre-calculated scatter functions. The method has been proven to be useful for several radionuclides and also efficient in calculating the crosstalk of scatter between two energy windows [17]. However, the method has only limited accuracy in non-homogeneous regions and in cases where an out-of-field-view of the activity becomes important.

The most advanced and potentially accurate methods available today are based on a real-time Monte Carlo scatter calculation. Floyd et al. pioneered studies in this field as early as the mid-

1980s, although the limitations on computational resources prevented the method from maturing for clinical use [18]. However, today it is possible to perform fast and accurate scatter modelling for individual patient geometries and source distributions [19]. In these methods, the activity distribution at various steps in an iterative reconstruction process are linked to an external Monte Carlo-based forward projector that, based on the estimated activity distribution, calculates a projection that fully includes the modelling of scatter in non-uniform regions. The method has been proven clinically useful mainly because of the implementation of fast variance reduction methods especially when modelling the collimator response, and studies have so far been made for [99mTc] [20, 21] and [201Tl] [22]. This method also can include a compensation for septum penetration in the collimator and backscatter for components behind the crystal, and can therefore be useful for studies on [131I] as well [23].

18.3.4 Spatial Resolution Compensation Methods

Compensation for the degradation in spatial resolution due to the collimator-response function (CRF) improves spatial resolution and provides improved quantitative accuracy for small objects. There are two classes of methods: iterative and non-iterative. Non-iterative methods include restoration filters, such as Metz and Wiener filters [24]. These filters are generally applied in the frequency domain to filter image data with a spatially invariant filter that describes the inverse of the PSF function. They will, however, not be as effective at removing spatial variation effects as compared to iterative methods and they tend to have poor noise properties since the inverse filters generally act as a high-pass filter, thereby amplifying noise.

In an iterative reconstruction method, the spatial resolution can be partly compensated for by including a model for distance-dependent blurring in the projector steps (forward and backward). This means that instead of forwarding the data in straight lines along the columns when cal-
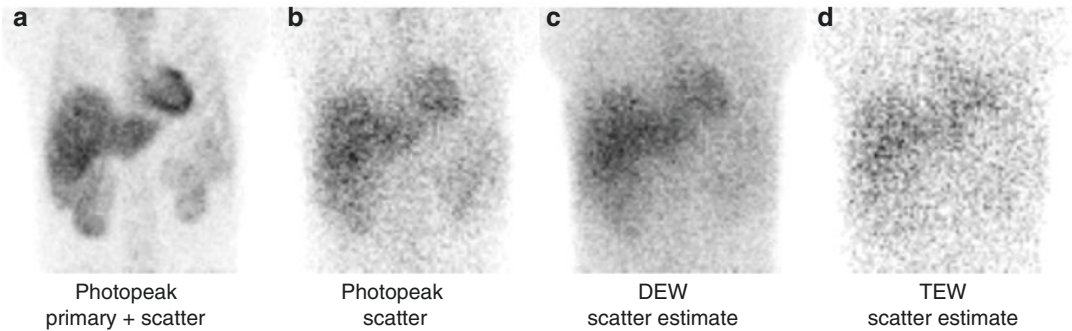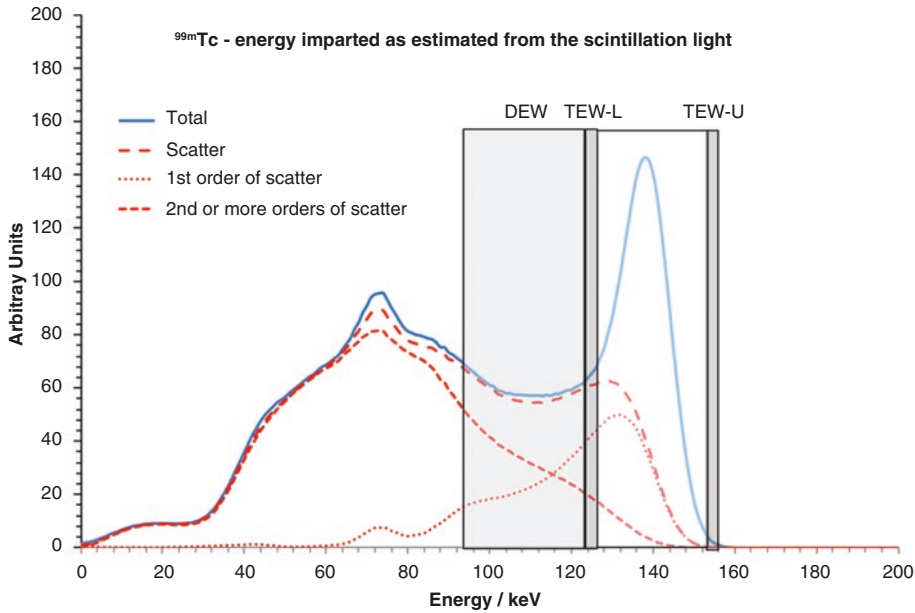
Fig. 18.9 Plot shows the location of the DEW and TEW windows. Image (**a**) shows an image with events from both primary and scattered photons. Image (**b**) shows the true scatter in the photon-peak energy window. Image (**c**) shows the estimation of scatter distribution by a lower wider energy window (DEW method). Image (**d**) show estimation of scatter by TEW method where two narrow energy windows (width 4 keV) is positioned on each side of the main photon-peak window. The simulated spectrum has been divided into total, scatter, first order scatter and second or more orders of scatter. It can be seen that there are two or more orders of scattered events in the DEW region as compared to the photo-peak region. This means that the distribution of scatter will be different in the DEW window, which will result in both over- and under-corrections when subtracting the data from the photo peak window. The difference in distributions can be seen in the images. The problem of noise in the TEW windows due to the narrow energy window size is also evident
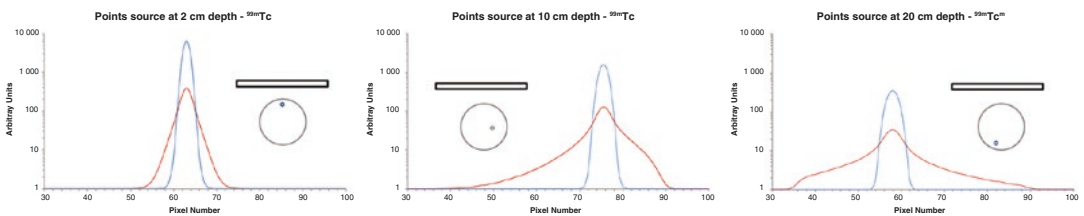
Fig. 18.10 Point-spread functions for three locations inside a cylindrical water phantom. The primary unscattered component is shown as dashed lines. Note the shade in the distribution of the scatter as a function of source depth. Please note the non-symmetry as well

culating the projection value, the projector includes the probability of a photon to pass nearby holes. This spread is often described by a distance-dependent, spatially invariant Gaussian function, but images of the point-spread function can also be explicitly calculated and stored for each distance by Monte Carlo simulation for those cases where septum penetration is important (i.e. imaging with ^{131}I and ^{123}I radiopharmaceuticals). The correction method has an effect similar to low-pass filtering, but it is not perfect in that sense that perfect resolution is not restored since some information about high spatial frequencies is permanently lost. Iterative reconstruction CRF compensation also produces different noise patterns compared to the filtered back projection methods or iterative reconstruction without CRF correction. The correction method tends to increase the noise in the midfrequency range, which may result in a blobby pattern in the reconstructed images, but noise properties can be improved by the accurate modelling of CRF [25]. Some recent software programs have been written to reduce acquisition time by incorporating resolution recovery into the reconstruction process. This helps to improve the resolution properties of the image and hence, signal-to-noise ratios for data acquired with lower count statistics [26].

The degradation of spatial resolution is a function of the distance from the face of the collimator. Thus, a pre-requisite to model the CRF is the information regarding the distance from the COR to the collimator face for every acquisition angle along with the knowledge of the collimator characteristics. For systems that use circular orbits, this information is defined by the radius of rotation. For SPECT system, the distance between the camera and the patient corresponding to each angle can be fine-tuned by sensors on the scintillation camera head. If this method is used, then a CRF correction requires information regarding the variation of organ-to-collimator distances for a particular projection angle. This is the type of information that, however, is not always available from commercial systems or Dicom file headers.

18.3.5　Full Monte Carlo-Based Image Reconstruction

A full Monte Carlo simulation of the radiation transport using a mathematical description of the patient CT and toward the camera has the potential to model all the important physical events that will ultimately affect the formation of a SPECT projection. This means that, if such a model can be included in an iterative reconstruction method, the compensations for physical effects should be more accurate than methods based on approximations such as the DEW and TEW scatter corrections, neglecting scattering in the collimator and related X-ray emissions and backscattering from the surrounding camera housing. Furthermore, since there is a relation between emitted photons (activity) and registered counts for a given source/camera configuration, a reconstructed set of images based on a Monte Carlo model can provide voxel values in terms of the unit of activity (Bq) and thus removing, in principle, the need for separate calibration [27].

A full Monte Carlo simulation of the imaging system can be applied in the forward projection step of an iterative reconstruction procedure. An MC-based back projector step is, however, more difficult to implement and therefore, a dual-matrix OS-EM approach can be adopted using a more simplified model of the radiation transport in the back projection [28–30]. This can be justified since the back projection step more has an effect on the rate of convergence and noise properties [31, 32].

The main limitation of MC simulations is the large computational burden and, consequently, the need for fast computers. It is, therefore, not likely that MC-reconstruction will be a useful tool for routine reconstructions, especially since there might not be a need for it in many cases. However, if the calculation time is not crucial or a 'second opinion' is required, a full Monte Carlo-based image reconstruction may provide more comprehensive information regarding the radionuclide distribution. Full MC-based reconstruction may also be of importance in the imaging of radionuclides with complex decay schemes

such as for ^{131}I [33] and ^{166}Ho [30], or when imaging bremsstrahlung photon emission from β-particle emitting radionuclides such as ^{90}Y [29, 34, 35].

18.3.6 Partial Volume Correction

Reconstructed SPECT images obtained by FBP or iterative reconstruction are degraded by the limited spatial resolution of the collimator system resulting in significant partial volume effects [36]. Because of this effect, spill-in of counts can be significant when evaluating the activity in small regions located in close proximity to neighbouring objects with high activity uptake. In a similar manner, spill-out occurs when quantifying high activity and activity concentrations in small regions. In these cases, it might therefore be of importance to include some kind of partial volume correction (PVC) (Fig. 18.11).

Partial volume effects are of particular interest in clinical applications such as the determination of myocardial wall thickness, in quantitative brain studies where activity concentrations in small structures will be underestimated, and in dosimetry for radionuclide therapy where uptake by small tumours may be important for accurate dose assessment.

The underlying assumption for most PVC methods is that the radioactivity uptake in a specific volume is uniformly distributed, and that the change in counts in this volume can, therefore, be used to develop a correction method. A simple and practical method for partial volume compensation is the use of volume-dependent recovery coefficients which have been determined from either experimental measurements of spheres of various sizes in physical phantoms [37–39] or mathematical simulation. Recovery factor is defined as the ratio between the measured activity in a defined volume and the true activity in the same volume ($RC = A_{meas}/A_{true}$) and is determined for different activity volumes. If the ratio is unity, there is no issue with PV and the correct activity is estimated from the images. However, because of the spatial resolution, this will not be the case for small objects. Figure 18.12 shows an example of the dependence of RC curves on spatial resolution. In practice, the value RC_{vol} that matches the current activity volume and the correct the activity A obtained from the volume with the selected RC ($A' = A/RC_{vol}$) as closely as possible is selected from these RC curves.

The accuracy of RC correction methods is, however, highly dependent on the shape of the object and the background activity of the target structure.
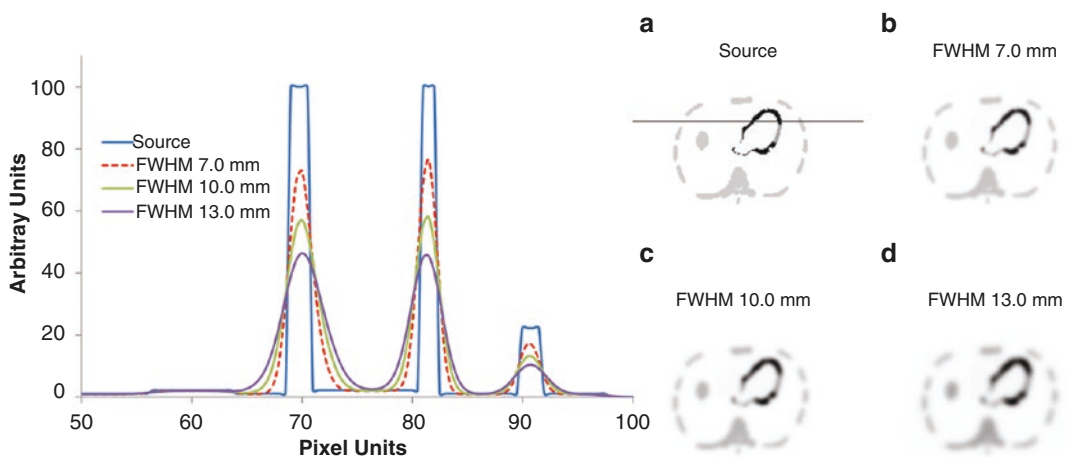
Fig. 18.11 Effect of partial volume. (**a**) shows the activity distribution ('source') and (**b**)–(**d**) shows the image blurred by a Gaussian function that simulates three different spatial resolutions. The profiles through the heart show the 'spill-in' into the left ventricle and 'spill-out' from the myocardial region

Recovery Curves for different spatial resolutions (mm FWHM)
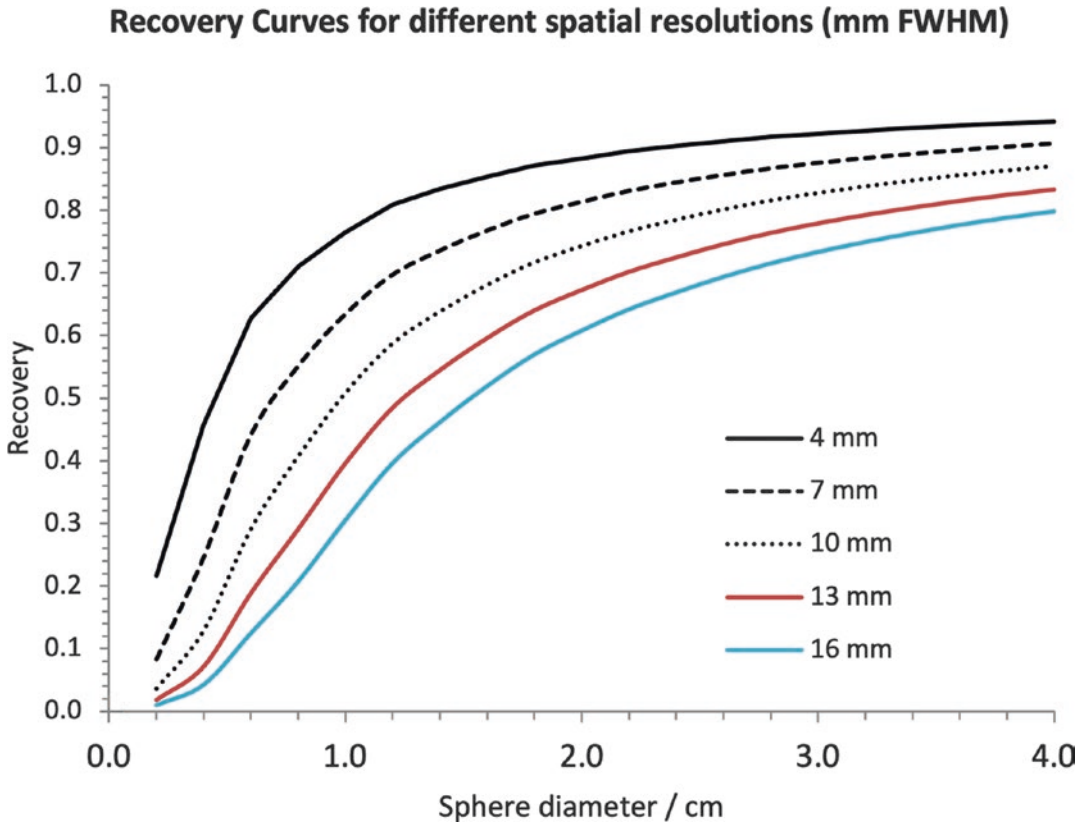
Fig. 18.12 Recovery curves obtained for five different simulated FWHM values of a hypothetic camera system. Initial spherical volumes were created as 3D-images, which were then convolved with a Gaussian function of different standard deviation values (recalculated from the FWHM values according to the relationship FWHM = 2.35 σ). The fraction of counts that appear outside the initial volume after the convolution were then calculated and from these, the displayed RC curves were obtained

A more general approach is to minimise the resolution and penetration effects by implementing a 3D depth-dependent detector response included into the system model of an iterative reconstruction. These implementations have resulted in improved quantification accuracy for higher energy photon emitters such as ^{111}In and [131]I [40–42]. However, these studies show that for small targets and targets within a high background activity, the activity recovery is not complete even when a 3D depth-dependent detector response function is included in the system model.

As dual modality SPECT-CT imaging with good image registration has become available recently, there is much incentive to use the CT based anatomical information to correct for partial volume effects. CT-defined templates have been used for SPECT partial volume correction in myocardial studies [43] in which user-defined templates were mathematically projected to mimic the SPECT process followed by image reconstruction to obtain a pixel-by-pixel PVC for the myocardial region. In more recent SPECT studies, the original template-based PVC was modified to implement a perturbation-based template method, which accounts for the non-linear effects of the iterative reconstruction [42, 44, 45]. Thus, it could be concluded that quantitative accuracy has been demonstrated for SPECT studies with ^{99m}Tc, ^{111}In and [131]I.

18.3.7 Conversion from Counts to Activity

Since a SPECT system measures the number of detected events from photons interacting in the NaI(Tl) crystal and determines a measure of the position for that interaction, an additional step is necessary to obtain an estimate of the activity in the source behind these events. The conversion from the count rate to activity is, therefore, a crucial part of the quantitative procedure. In most cases, a parallel-hole collimator is used in the investigation. In one sense, one can define such a collimator as a number of individual detectors that together determine the final detection of the counts. For a single hole, the probability for detection is determined by the hole-dimension and distance to the source. When considering a single collimator hole, the detection capability of photons passing though this hole depends of the inverse of the square of the distance, but because of the multiple holes, the possibility of a photon to pass through them increases with the square of the distance, resulting in that the total number of detected counts remains the same independent of the distance to the camera. This, however, holds true only for moderate distances from the camera and not very close to the collimator surface. Thus, the number of counts detected will depend on the (a) the collimator design, absorption efficiency of the crystal and (b) size and location of the energy window. The system sensitivity is defined by NEMA (The Association of Electrical Equipment and Medical Imaging Manufacturers) [46] and are measured in a standardised manner by the vendors. Therefore, one can obtain a single conversion factor from cps to MBq. However, the distribution of detected counts depends very much on the source-to-collimator distance so if one want to determine the activity in a ROI (2D) or a VOI (3D) there will be a need to consider the 'spill-out' and 'spill-in' of counts from the ROI/VOI due to the effect of the spatial resolution. The determination of the activity therefore will be dependent of the ROI/VOI that have been defined and therefore, in principle, require a recovery factor for each possible shape we define.

The main purpose of a reconstruction program is to redistribute counts measured along a projection bin back to the origin, from which the photons were emitted that resulted in the detected counts. This means that, for a carefully designed program, the total number of counts in a 3D reconstructed volume should be equal to the number of counts acquired by the camera and if good scatter and attenuation compensation are made, the activity should be possible to be determine from the system sensitivity. Again, this is not the same as saying that the activity in a VOI correct. The quantitation in a VOI can be described by the following eq. [47],

$$A_{\mathrm{VOI}} = \mathrm{cps}_{\mathrm{VOI}} \cdot \frac{1}{\mathrm{RC}_{\mathrm{obj}}} \cdot \frac{1}{\left(\mathrm{cps}/\mathrm{MBq}\right)_{\mathrm{FOV}}}$$

(18.10)

where the activity A_{VOI} in a VOI is determined by the product of (a) the count rate $\mathrm{cps}_{\mathrm{voi}}$ measured in an VOI, (b) the $\mathrm{RC}_{\mathrm{obj}}$ which is the recovery coefficient for an object that best match the dimension of the VOI and (c) the system sensitivity $(\mathrm{cps}/\mathrm{MBq})_{\mathrm{FOV}}$ as have been measured in a FOV of the camera. This assumes that the $\mathrm{cps}_{\mathrm{voi}}$ has been obtained from an image, corrected for scatter and attenuation.

If it is not possible to correct for the entire expected degradation effect and thus apply the above equation, a common procedure is to calibrate the study against an experimental phantom measurement. A phantom and source are selected so that they mimic the patient's geometry and activity distribution as closely as possible and then a SPECT measurement is conducted using the same acquisition- and reconstruction parameters as for the patient measurement. By knowing the activity in the experimental source, one can determine a calibration factor (also in units of cps/MBq) that can be used to determine the activity in the patient-defined VOI. By doing this, it is assumed that the additional effects cancel out because of the calculation procedure. However, one should remember that the calibration factor is, in principle, only valid for the geometry from which it has been derived.

18.4 Influence of Correction Algorithms on Image Quality

Photon attenuation is the single largest factor that degrades the image quality in SPECT. Without proper compensation for attenuation, an absolute estimate of the activity will often be in error by >50%. The magnitude of the effect is higher for low-energy photons and for large parts of the body with high density. Non-uniform attenuation in the head or the thorax can cause undesirable artefacts that impede both visual interpretation and activity quantitation.

Energy window-based scatter correction methods can be applied in two ways; either (a) prior to reconstruction by subtracting the estimated scatter from the projection data prior to reconstruction or (b) incorporating the scatter estimate in an iterative reconstruction method. The disadvantage of the first approach is the fact that subtracting the two noise images results in increasing the noise. This means that some kind of low-pass filtering may need to be applied on the data, resulting in a degradation of the spatial resolution of the image. The second approach of incorporating the measured scatter estimate in the forward projection has shown to have better noise properties and is probably more widely accepted in commercial systems. Accurate scatter correction techniques should improve image contrast and lead to better quantitative accuracy.

The necessary for quantitative SPECT images depends on the application. It is, however, important to understand that even if the actual number in units of MBq or MBq/mL is not important for a particular application, quantification procedures may improve the accuracy and precision in the investigation since compensations correct for the misplacement of counts and thus, provide a better image. On the other hand, if the correction methods used are not properly set up and validated, this can lead to problems. Furthermore, in some cases, image noise can be amplified which is a degrading factor for the image quality despite the theoretical improvement due to a particular compensation.

It is now common to improve the image resolution SPECT by including collimator compensa-tion in the tomographic reconstruction. This can be achieved by modelling the manner in which the photons also pass through the nearby collimator holes. One method to do this during the projector/back projector step is to separate the modelled projection as a function of distance. The different projections are then filtered by a function that describes the PSF for a particular distance (often a Gaussian function). The results of each individual filtering process are then added to a final projection. Addition effects, such as, star-artefacts as a result of septal penetration and collimator scatter can also be included. However, one should be aware of the creation of the edge artefacts as a result of these types of compensations. These artefacts appear as ring-shaped areas of too-low or too-high [36, 48] counts, often close to sharp boundaries (i.e. gradients of counts). This effect does not change the total number of counts in the image if the PSF filters are properly normalised, but it thereby creates a count distribution that does not reflect the actual activity uptake and this can hamper further analysis of, for example, heterogeneity within a volume-of-interest. Figure 18.13 shows an example of these effects.

Despite the many inherent problems with SPECT images the recent advancement in developing correction methods for physical effects, such as photon attenuation, scatter and collimator resolution has made SPECT a quantitative tool for activity measurement. Figure 18.14 shows an example of state of the art reconstruction and activity quantification method including non-uniform attenuation correction, scatter correction using the ESSE method [49] and spatial variant collimator-response correction.

18.5 Applications of SPECT in Dosimetry

One of the areas in nuclear medicine applications that rely on the absolute values of the SPECT images is dosimetry in radionuclide therapy where multiple SPECT acquisitions form the base for therapeutic dose planning. The quantity of the absorbed dose is used to relate the energy

Fig. 18.13 Figure shows the artefacts introduced by the collimator-response compensation. Left image (**a**) shows three spheres reconstructed with scatter and attenuation compensation. Right figure (**b**) shows the same recon-struction including where ´collimator-response compensation (Gaussian) has been included. The hole in the centre of the spheres can clearly be seen
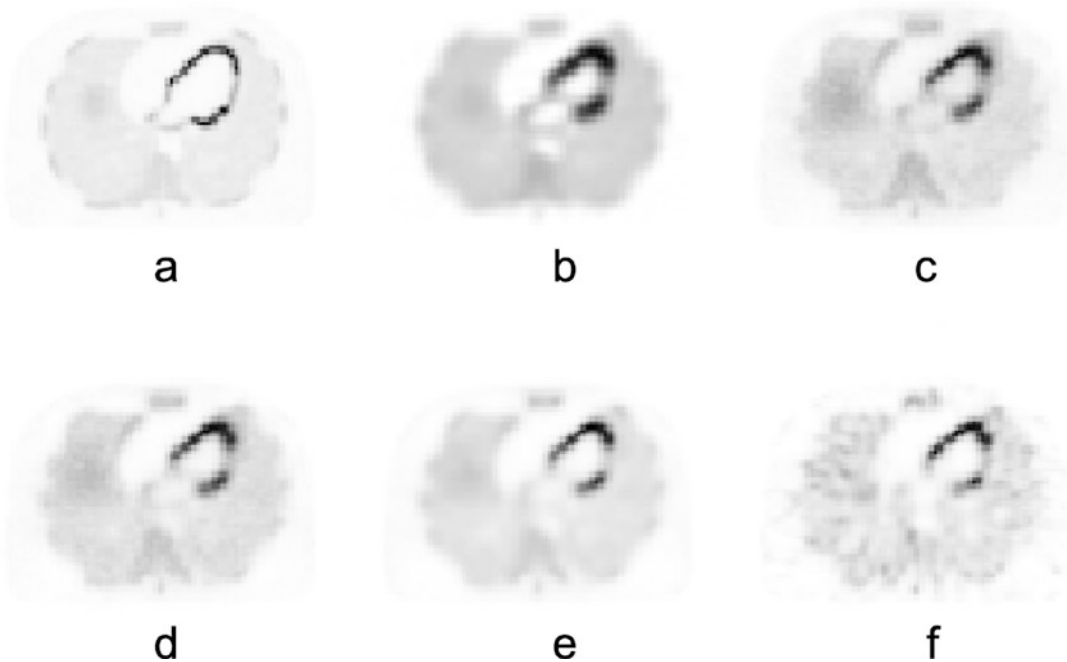
Fig. 18.14 Image (**a**) is reconstructed data mimicking a perfect system without patient movements (the image is equal to Fig. 18.7a). Image (**b**) shows an image of the same data set reconstructed with FBP without corrections. A Butterworth filter with cutoff 0.5 and order 2 was used. Figures (**c–e**) shows images reconstructed with OS-EM (six iterations and ten subsets) using non-homogeneous attenuation correction (**c**), attenuation and scatter correc-tion using the ESSE method (**d**) and scatter and attenua-tion correction together with CRF correction (**e**). Image (**f**) shows an image reconstructed with all correction methods but using a data set with a realistic noise level added

imparted by ionising radiation to a biologic effects and is defined as the mean energy imparted, $d\overline{\varepsilon}$, to the matter in an infinitesimal volume, dV, with mass dm [50, 51], according to

$$D = \frac{d\overline{\varepsilon}}{dm} \qquad (18.11)$$

The SI-unit of the absorbed dose is Gy (1 J/kg) and its value can vary between different parts of an organ or tissue. For cases where there is local difference in the activity uptake and hence the energy delivery, the mean absorbed dose, can be calculated according to

$$D_{\mathrm{T}} = \frac{1}{m_{\mathrm{T}}} \int_{m_{\mathrm{T}}} D \, dm \qquad (18.12)$$

where m_{T} is the mass of a tissue or organ, or some other target volume for which the absorbed dose is determined [52].

18.5.1 The Basic Calculation Scheme

The basic equation for dose calculations has been given by an MIRD publication [53] and is described as

$$D = \frac{1}{m(r_{\mathrm{T}})} \sum_{r_{\mathrm{s}}} \left[\int_{T_1}^{T_2} A(r_{\mathrm{s}}, t) dt \sum_i \Delta_i \cdot \phi(r_{\mathrm{T}} \leftarrow r_{\mathrm{s}}, E_i, t) \right] \qquad (18.13)$$

where n is the number of particles i per disintegration, Δ_i is the average energy emitted for particle i, ϕ is is the absorbed fraction—a geometrical related factor that describe the fraction of energy emitted from a source volume element r_{S} that is absorbed in a target volume element r_{T}. Finally, m is the mass of the target volume element r_{T}. The time integral is the cumulative activity, $\tilde{A}$, and represent the total number of decays between a time interval T_1–T_2. Often this is calculated from the time of injection to infinity. The above equation can be understood as a product of two terms where on term $\tilde{A}$, is proportional to the total number of emitted particles emitted from the source during the time interval and the remaining terms, grouped into a term, called S, describe the radiation transport of energy from this source volume to the target volume, as described by the following

$$D = \sum_{r_{\mathrm{s}}} \tilde{A}(r_{\mathrm{s}}) \cdot S(r_{\mathrm{T}} \leftarrow r_{\mathrm{s}}) \qquad (18.14)$$

where $\tilde{A}$ is a function of the chemical properties of the radiopharmaceutical and the biokinetic distribution while S is a function of the geometry and the physical properties of the radionuclide and the tissue composition. In some cases, $\tilde{A}$ and S represent a population and values can therefore be tabulated but in general both $\tilde{A}$ and S are patient-specific.

In practice, the activity integral $\tilde{A}$ (or the 'area-under-the-curve') is mostly determined by a curve-fitting procedure from a limited number of time-activity values as have been measured by a scintillation camera or SPECT. The cumulative activity then equals the area under the curve and if expressed per unit administered activity is called the residence time.

The estimation of risks for developing cancer due to the usage of radiation is calculated using pre-calculated S values that have been developed by Monte Carlo calculations for the generic mathematical description of a population of interest. This is because such risk estimations are only relevant to a large population of individuals. Therefore, such mathematical descriptions represent a reference male or female i.e. an average of a large population. These S value tables have been compiled in terms of the absorbed dose (Gy) to the target volume per cumulative activity (MBq h) in the source organ. S values are embedded into programs, such as, the OLINDA code [54]. However, the mathematical phantoms have not been developed for individual therapy planning and therefore the dose-conversion factors are not very well representative. To overcome this, one may need to implement the patient's own geometry and biokinetics into a dose calculation Scheme. A principal flowchart showing the steps necessary to consider for 3D patient-specific SPECT (and PET) dosimetry is shown in Fig. 18.15.

Fig. 18.15 Flowchart describing the different steps toward a dosimetry calculation based on quantitative SPECT images
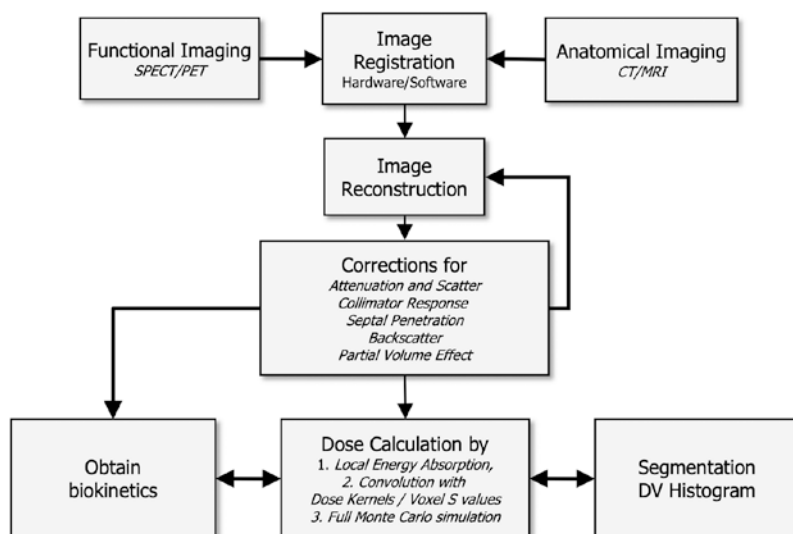
18.5.2 Dose Calculation from Quantitative SPECT Imaging

Most dosimetry studies with scintillation cameras are conducted by planar scintillation camera imaging using the conjugate-view method. As described earlier, this method relies on opposite projections and if taking the geometrical-mean of the opposite projection, the dependence on the source depth is greatly reduced. The attenuation correction then depends only on the thickness of the patient (compared to attenuation correction in PET). The method, however, has several drawbacks. First, the above statement is only valid for a point source. If extended sources are being imaged, (which always is the case in clinical studies) then a correction for the source thickness needs to be made [55]. Second, if over and underlying activities are present then this affect the quantitation since the planar imaging is on a 2D modality and corrections needs to be made [56]. Third, scatter correction and septum penetration may not be accurately modelled and fourthly, the dosimetry needs in most cases to rely on *S*-factors obtained from a mathematical phantom.

SPECT in combination with CT can overcome many of these drawbacks because of the inherent 3D activity determination. The methods, described below, treat each voxel as a source volume and correspondingly, each voxel as a target organ. In practice, one does not store the *S*-factor that corresponds to each combination, but the MIRD equation will remain valid in these cases. The results will be 3D images of absorbed dose distributions useful to obtain, for example, dose-volume histograms and other parameters related to the heterogeneity of imparted energy within the volume of interest.

18.5.3 Energy Locally Absorbed Within a Voxel

In its simplest form, a dose calculation based on quantitative SPECT can assume all kinetic electron energies emitted from the radionuclide as locally absorbed within the voxel volume and disregard the energy distribution from the photons. The absorbed dose is then calculated from the mass of the volume element. This assumption is not as approximate as it sounds because the spatial resolution of a SPECT image used as input is in the same order or larger compared to relevant electron ranges. Thus, the SPECT image may very well show the absorbed dose distribution from electrons. If reviewing the general MIRD equation above, this method corresponds to the case where the target volume equals the source volume ($r_T = r_S$). This type of calculation

may work only on pure β-emitting radionuclides such as ^{90}Y or when the contribution to the absorbed dose from photons can be regarded as negligible.

18.5.4 Convolution Based on Point-Dose Kernels

This method uses a pre-calculated energy distribution in 3D from a point source usually stored as function of the radial distance from the point source normalised to the energy emitted per disintegration. By a mathematical convolution either in the spatial domain or frequency domain, the initial activity image (e.g. a SPECT image) can be converted to absorbed dose images. Berger has published point-dose kernels for both photons [57] and electrons and β particles [58]. Convolution of SPECT images with point-dose kernels should generally be used when the voxel size of the activity matrix is small compared to the path length of the particles. The dose kernels are also generally valid for a uniform material (often water or tissue-equivalent material) and the calculation procedure (often performed in the Fourier domain) is spatially invariant and does not take into account variations either in density or energy distribution due to organ or patient boundaries.

18.5.5 Convolution Based on Voxel *S* Values

Most point-dose kernels are published as the radial distribution of energy from a point-like source. When applying these kernels to a set of voxel-based images, one needs to interpolate these functions to match the different voxel locations—a procedure that sometimes can be very tricky to get right. A more practical approach is to create so-called voxel *S* values where the energy deposition per unit activity in a centre voxel is calculated for each neighbour voxel for a particular voxel grid. Then, only a discrete convolution procedure will be needed. A restriction is that the voxel *S* values must match the voxel size of the

image *A*. The dosimetry at a voxel level has been discussed in MIRD 17 [59] and voxel *S* values have been published by Lanconelli et al. [60] for different voxel sizes. A potential ambiguity with the voxel *S* value approach is the question of whether the source distribution used to calculate the *S* values should be a point source in the middle of a central voxel or if the decay locations should be sampled uniformly within the voxel. The approach selected could result in differences in the result for radionuclides emitting charged particles with a small range. If using a point source, many of the charge-particles may not reach the boundary of the voxel.

18.5.6 Full Monte Carlo Simulated Radiation Transport

The most accurate absorbed dose calculation, but also the most complex and computationally demanding procedure, is a full radiation transport calculation using the Monte Carlo method [61]. The method in this context starts from quantitative accurate SPECT images and registered density images, usually obtained from a patient-specific CT. From this set of images, simulation of individual photon and electron interactions are performed in the 3D density volume by tracing the particles to the end by explicitly simulating all relevant interaction types. The location of a decay corresponds to the apparent voxel location in the Cartesian coordinate system and the number of simulated decays is proportional to the voxel values of the quantitative SPECT images. The imparted energy from each particle is then scored in a matching 3D absorbed energy matrix as the particles are traced through the volume. When all the particles are simulated, the absorbed energy in each voxel per voxel mass gives the absorbed dose. The main advantage of a full Monte Carlo simulation is that it considers the patient geometry and heterogeneities in density and tissue compositions can be included in the absorbed dose calculation.

There are several very competent programs in the public domain which are useful for Monte Carlo absorbed dose calculations. The EGS fam-

ily of programs [62] have been shown to be useful and the simulation of voxel data is relatively straight forward—although it requires some programming skills. In Medical Imaging applications, the GATE Monte Carlo program [63] has attracted much interest due to its flexibility, especially with complex geometries. This program is a layer of the Geant4 program from CERN[1] and can simulate charged particles up to very high energies.

18.5.7 Considerations Related to Absorbed Dose Calculations Based on SPECT/CT Data

The new hybrid systems offer considerable potential for accurate dosimetry both in 2D and 3D. Today, most SPECT/CT systems are based on diagnostic CT acquisition with a spatial resolution of an order of magnitude higher than the SPECT unit. In some systems, the CT unit can be used to obtain useful information also about the attenuation for the planar conjugate-view method by performing a full-length scan (so-called scout measurement). If the scaling between pixel units and density can be determined, then this transmission image will be the correction necessary for planar attenuation correction [64]. The high-quality image obtained from diagnostic CT units makes accurate SPECT quantification possible, and the known limitations with radionuclide-based transmission sources (downscatter, noise and limited spatial resolution) is eliminated by using CT.

Some issues need to be considered when doing absorbed dose calculations based on SPECT data. The most important is the fact that the SPECT images do not show the actual activity distribution. The images are affected by the particular system degradation in spatial resolution and the effect (discussed above in the partial

volume section) is dependent on the source volume.

When calculating the absorbed dose, it is convenient to use CT images if proper scaling to density can be achieved. However, in most modern systems, the spatial resolution of the CT data can be of an order of magnitude better than the SPECT information. When using high-resolution CT as mass images in the voxel-by-voxel absorbed dose calculation, artefacts can be introduced where 'counts' spills out in regions of low densities. In addition, gas in the abdominal parts can result in very high absorbed doses because of the low CT voxel values in combination with blurring due to the limited spatial resolution in SPECT images. One way to overcome this problem is to reduce the spatial resolution of the CT images by convolution with a PSF that match the resolution of the SPECT system.

Most CT units are very fast with respect to image acquisition. This means that a CT image over the thorax may more reflect a particular time segment of the breathing cycle. A SPECT projection is generally acquired over a much longer time meaning that the image reflects a count distribution averaged over the whole respiration cycle. This can thus introduce artefacts during the correction for attenuation and absorbed dose calculations, especially close to the lung boundaries.

Even if SPECT/CT images are accurately registered to each other in a hybrid system, there is a need for image registration when performing multiple SPECT/CT studies in order to obtain voxel-based time-activity curves. Image registration using CT-CT images are preferable here compared to SPECT-SPECT registration as they are more similar. However, if a diagnostic CT is used then the absorbed dose caused by multiple X-ray exposures can be significant. The problem can be reduced if the CT unit can be run in a 'low-dose' mode. The signal-to-noise ratio and spatial resolution may be reduced here, but for attenuation corrections and absorbed dose calculations, this is probably not a serious problem.

---

[1]CERN = European Organization for Nuclear Research, Genève, Switzerland.

18.6　Conclusion

Quantitative SPECT has become a reality today mainly because of the considerable improvements effected in reconstruction algorithms where the corrections for image degradation due to photon attenuation, contribution of events such as the scattering of photons in the patient, collimator and camera housing, and septum penetration can be made in a consistent and natural manner in the forward projector step. The limitations that existed in earlier radionuclide-based transmission measurement methods are eliminated when using high-quality attenuation maps created by CT detectors, which are integrated into the SPECT gantry. Hybrid SPCT/CT systems also provide registered functional and anatomical images, thus reducing the need for software registration methods although registered software may be required when working with multiple SPECT/CT studies. Many scatter correction methods still rely on measurements in the secondary energy window but along with the improvement in computing power, real-time Monte Carlo simulation of scatter may be feasible for clinical use within a few years.

References

1. Shepp LA, Vardi Y. Maximum likelihood reconstruction for emission tomography. IEEE Trans Med Imaging. 1982;1(2):113–22. https://doi.org/10.1109/TMI.1982.4307558.
2. Lange K, Carson R. EM reconstruction algorithms for emission and transmission tomography. J Comput Assist Tomogr. 1984;8(2):306–16. https://www.ncbi.nlm.nih.gov/pubmed/6608535.
3. Hudson HM, Larkin RS. Accelerated image reconstruction using ordered subsets of projection data. IEEE Trans Nucl Sci. 1994;13:601–9.
4. Ljungberg M, Strand SE. A Monte Carlo program simulating scintillation camera imaging. Comp Meth Progr Biomed. 1989;29:257–72.
5. Ljungberg M. The SIMIND Monte Carlo program. In: Ljungberg M, Strand SE, King MA, editors. Monte Carlo calculation in nuclear medicine: applications in diagnostic imaging. Bristol and Philadelphia: IOP Publishing; 1998. p. 145–63.
6. Segars WP, Lalush DS, Tsui BMW. A realistic spline-based dynamic heart phantom. IEEE Trans Nucl Sci. 1999;46(3):503–6.
7. Segars WP. Development of a new dynamic NURBS-based cardiac-torso (NCAT) phantom. Ph.D., University of North Carolina, 2001.
8. Frey EC, Tsui BMW. A new method for modeling the spatially-variant, object-dependent scatter response function in SPECT. In Conference records of the IEEE medical imaging conference, Anaheim, CA, USA, 3–9 Nov 1996.
9. Berger MJ, Hubbell JR. XCOM: photon cross-sections on a personal computer. Washington, DC, . NBSIR 87-3597, -32676.: National Bureau of Standards; 1987.
10. Dewaraja YK, Ljungberg M, Koral KF. Characterization of scatter and penetration using Monte Carlo simulation in 131-I imaging. J Nucl Med. 2000;41(1):123–30. PM:0010647615.
11. Dewaraja YK, Ljungberg M, Koral KF. Accuracy of 131I tumor quantification in radioimmunotherapy using SPECT imaging with an ultra-high-energy collimator: Monte Carlo study. J Nucl Med. 2000;41(10):1760–7. PM:0011038009.
12. Slomka PJ, et al. "Motion-frozen" display and quantification of myocardial perfusion. J Nucl Med. 2004;45(7):1128–34. https://www.ncbi.nlm.nih.gov/pubmed/15235058.
13. Chang LT. A method for attenuation correction in radionuclide computed tomography. IEEE Trans Nucl Sci. 1978;25:638–43.
14. Jaszczak RJ, Greer KL, Floyd CE, Harris CC, Coleman RE. Improved SPECT quantification using compensation for scattered photons. J Nucl Med. 1984;25:893–900.
15. Ogawa K, Harata Y, Ichihara T, Kubo A, Hashimoto S. A practical method for position-dependent Compton-scatter correction in single photon emission CT. IEEE Trans Med Imaging. 1991;10(3):408–12. https://doi.org/10.1109/42.97591.
16. Frey EC, Tsui BMW. A new method for modeling the spatially-variant, object-dependent scatter response function in SPECT. In Conference records of the IEEE medical imaging conference, Anaheim, CA, pp 1082–1082, 1997.
17. Song X, Frey EC, Wang WT, Du Y, Tsui BMW. Validation and evaluation of model-based crosstalk compensation method in simultaneous 99mTc stress and 201Tl rest myocardial perfusion SPECT. IEEE Trans Nucl Sci. 2004;51 Part 1(1):72–9.
18. Floyd CE, Jaszczak RJ, Coleman M. Inverse Monte Carlo: a unified reconstruction algorithm for SPECT. IEEE Trans Nucl Sci. 1985;32:779–85.
19. Beekman FJ, de Jong HW, Slijpen ET. Efficient SPECT scatter calculation in non-uniform media using correlated Monte Carlo simulation. Phys Med Biol. 1999;44(8):N183–92. PM:10473218.
20. Xiao J, de Wit TC, Staelens SG, Beekman FJ. Evaluation of 3D Monte Carlo-based scatter correction for 99mTc cardiac perfusion SPECT. J Nucl Med. 2006;47(10):1662–9. https://www.ncbi.nlm.nih.gov/pubmed/17015903.

21. Liu S, King MA, Brill AB. Accelerated SPECT Monte Carlo simulation using multiple projection sampling and convolution-based forced detection. IEEE Trans Nucl Sci. 2008;55(1):560–8.

22. Xiao J, de Wit TC, Zbijewski W, Staelens SG, Beekman FJ. Evaluation of 3D Monte Carlo-based scatter correction for 201Tl cardiac perfusion SPECT. J Nucl Med. 2007;48(4):637–44. https://doi.org/10.2967/jnumed.106.037259.

23. Shaoying L, King MA, Brill AB, Stabin MG, Farncombe TH. Convolution-based forced detection Monte Carlo simulation incorporating septal penetration modeling. IEEE Trans Nucl Sci. 2008;55(3):967–74.

24. King MA, Schwinger RB, Doherty PW, Penney BC. Two-dimensional filtering of SPECT images using the Metz and Wiener filters. J Nucl Med. 1984;25:1234–40.

25. Beekman FJ, Slijpen ET, de Jong HW, Viergever MA. Estimation of the depth-dependent component of the point spread function of SPECT. Med Phys. 1999;26(11):2311–22. https://doi.org/10.1118/1.598745.

26. Borges-Neto S, et al. Clinical results of a novel wide beam reconstruction method for shortening scan time of Tc-99m cardiac SPECT perfusion studies. J Nucl Cardiol. 2007;14(4):555–65. https://doi.org/10.1016/j.nuclcard.2007.04.022.

27. Gustafsson J, Brolin G, Ljungberg M. Monte Carlo-based SPECT reconstruction within the SIMIND framework. Phys Med Biol. 2018;63(24):245012. https://doi.org/10.1088/1361-6560/aaf0f1.

28. Beekman FJ, de Jong HW, van Geloven S. Efficient fully 3-D iterative SPECT reconstruction with Monte Carlo-based scatter compensation. IEEE Trans Med Imaging. 2002;21(8):867–77. https://doi.org/10.1109/TMI.2002.803130.

29. Elschot M, Lam MG, van den Bosch MA, Viergever MA, de Jong HW. Quantitative Monte Carlo-based ^{90}Y SPECT reconstruction. J Nucl Med. 2013;54(9):1557–63. https://doi.org/10.2967/jnumed.112.119131.

30. Elschot M, et al. Quantitative Monte Carlo-based holmium-166 SPECT reconstruction. Med Phys. 2013;40(11):112502. https://doi.org/10.1118/1.4823788.

31. Zeng GL, Gullberg GT. Frequency domain implementation of the three-dimensional geometric point response correction in SPECT imaging. IEEE Trans Nucl Sci. 1992;39:1444–53.

32. Zeng GL, Gullberg GT. Unmatched projector/back-projector pairs in an iterative reconstruction algorithm. IEEE Trans Med Imaging. 2000;19(5):548–55. https://doi.org/10.1109/42.870265.

33. Dewaraja YK, Ljungberg M, Fessler JA. 3-D Monte Carlo-Based Scatter Compensation in Quantitative I-131 SPECT Reconstruction. IEEE Trans Nucl Sci. 2006;53(1):181. https://doi.org/10.1109/TNS.2005.862956.

34. Dewaraja YK, et al. Improved quantitative (90) Y bremsstrahlung SPECT/CT reconstruction with Monte Carlo scatter modeling. Med Phys. 2017;44(12):6364–76. https://doi.org/10.1002/mp.12597.

35. Lim H, Fessler JA, Wilderman SJ, Brooks AF, Dewaraja YK. Y-90 SPECT ML image reconstruction with a new model for tissue-dependent bremsstrahlung production using CT information: a proof-of-concept study. Phys Med Biol. 2018;63(11):115001. https://doi.org/10.1088/1361-6560/aac1ad.

36. Erlandsson K, Buvat I, Pretorius PH, Thomas BA, Hutton BF. A review of partial volume correction techniques for emission tomography and their applications in neurology, cardiology and oncology. Phys Med Biol. 2012;57(21):R119–59. https://doi.org/10.1088/0031-9155/57/21/R119.

37. Zito F, Gilardi MC, Magnani P, Fazio F. Single-photon emission tomographic quantification in spherical objects: effects of object size and background. Eur J Nucl Med. 1996;23(3):263–71. https://doi.org/10.1007/BF00837624.

38. Koral KF, Dewaraja Y. I-131 SPECT activity recovery coefficients with implicit or triple-energy-window scatter correction. Nucl Instrum Methods Phys Res, Sect A. 1999;422(1–3):688–92.

39. Geworski L, Knoop BO, de Cabrejas ML, Knapp WH, Munz DL. Recovery correction for quantitation in emission tomography: a feasibility study. Eur J Nucl Med. 2000;27(2):161–9. https://doi.org/10.1007/s002590050022.

40. Dewaraja YK, Wilderman SJ, Ljungberg M, Koral KF, Zasadny K, Kaminiski MS. Accurate dosimetry in 131I radionuclide therapy using patient-specific, 3-dimensional methods for SPECT reconstruction and absorbed dose calculation. J Nucl Med. 2005;46(5):840–9. http://jnm.snmjournals.org/cgi/content/abstract/46/5/840.

41. Ljungberg M, Sjogreen K, Liu X, Frey E, Dewaraja Y, Strand SE. A 3-dimensional absorbed dose calculation method based on quantitative SPECT for radionuclide therapy: evaluation for 131-I using Monte Carlo simulation. J Nucl Med. 2002;43(8):1101–9. PM:12163637.

42. He B, Du Y, Song X, Segars WP, Frey EC. A Monte Carlo and physical phantom evaluation of quantitative In-111 SPECT. Phys Med Biol. 2005;50(17):4169–85. https://doi.org/10.1088/0031-9155/50/17/018.

43. Da Silva AJ, Tang HR, Wong KH, Wu MC, Dae MW, Hasegawa BH. Absolute quantification of regional myocardial uptake of 99mTc-sestamibi with SPECT: experimental validation in a porcine model. J Nucl Med. 2001;42(5):772–9. https://www.ncbi.nlm.nih.gov/pubmed/11337575.

44. Yong D, Tsui BMW, Frey EC. Partial volume effect compensation for quantitative brain SPECT imaging. IEEE Trans Med Imaging. 2005;24(8):969–76.

45. Boening G, Pretorius PH, King MA. Study of relative quantification of Tc-99 m with partial volume effect and spillover correction for SPECT oncology imaging. IEEE Trans Nucl Sci. 2006;53(3 Part 2):1205–12.

46. Performance measurements of gamma cameras. In NEMA NU 1-2012, Virginia, 2013.

47. Ljungberg M, et al. MIRD pamphlet no. 26: joint EANM/MIRD guidelines for quantitative 177Lu SPECT applied for dosimetry of radiopharmaceutical therapy. J Nucl Med. 2016;57(1):151–62. https://doi.org/10.2967/jnumed.115.159012.

48. Rahmim A, Qi J, Sossi V. Resolution modeling in PET imaging: theory, practice, benefits, and pitfalls. Med Phys. 2013;40(6):064301. https://doi.org/10.1118/1.4800806.

49. Frey EC, Tsui BMW. Modeling the scatter response function in inhomogeneous scattering media. In Conference records of the IEEE medical imaging conference, 1993, pp 1–1.

50. U. International Commission on Radiation and Measurements. Report 85: fundamental quantities and units for ionizing radiation. J ICRU. 2011;11(1):1–31. https://doi.org/10.1093/jicru/ndr011.

51. Attix FH. Introduction to radiological physics and radiation dosimetry. Hoboken, NJ: John Wiley & Sons, Inc.; 1986.

52. U. International Commission on Radiation and Measurements. Report 86: quantification and reporting of low-dose and other heterogeneous exposures. J ICRU. 2011;11(2):1–77. https://doi.org/10.1093/jicru/ndr028.

53. Loevinger R, Berman M. A revised schema for calculation of the absorbed dose from biologically distributed radionuclides. MIRD Phamplet no. 1, revised. New York: Society of Nuclear Medicine; 1976.

54. Stabin MG, Sparks RB, Crowe E. OLINDA/EXM: the second-generation personal computer software for internal dose assessment in nuclear medicine. J Nucl Med. 2005;46(6):1023–7. https://www.ncbi.nlm.nih.gov/pubmed/15937315.

55. Fleming JS. A technique for the absolute measurement of activity using a gamma camera and computer. Phys Med Biol. 1979;24(1):178–80.

56. Sjogreen K, Ljungberg M, Strand SE. An activity quantification method based on registration of CT and whole-body scintillation camera images, with application to 131I. J Nucl Med. 2002;43(7):972–82. https://www.ncbi.nlm.nih.gov/pubmed/12097471.

57. Berger MJ. Energy deposition in water by photons from point isotropic sources: MIRD pamphlet no. 2. J Nucl Med. 1968;9:15–25.

58. Berger MJ. Distribution of absorbed dose around point sources of electrons and beta particles in water and other media: MIRD pamphlet no. 7. J Nucl Med. 1971;12:5–23.

59. Bolch WE, et al. MIRD pamphlet No. 17: the dosimetry of nonuniform activity distributions—radionuclide S values at the voxel level. Medical Internal Radiation Dose Committee. J Nucl Med. 1999;40(1):11S–36S. https://www.ncbi.nlm.nih.gov/pubmed/9935083.

60. Lanconelli N, et al. A free database of radionuclide voxel S values for the dosimetry of nonuniform activity distributions. Phys Med Biol. 2012;57(2):517–33. https://doi.org/10.1088/0031-9155/57/2/517.

61. Andreo P. Monte Carlo techniques in medical radiation physics. Phys Med Biol. 1991;36(7):861–920. https://doi.org/10.1088/0031-9155/36/7/001.

62. Nelson RF, Hirayama H, Rogers DWO. The EGS4 code system. Stanford, CA: SLAC, SLAC-265; 1985.

63. Jan S, et al. GATE: a simulation toolkit for PET and SPECT. Phys Med Biol. 2004;49(19):4543–61. https://doi.org/10.1088/0031-9155/49/19/007.

64. Minarik D, Sjogreen K, Ljungberg M. A new method to obtain transmission images for planar whole-body activity quantification. Cancer Biother Radiopharm. 2005;20(1):72–6. https://doi.org/10.1089/cbr.2005.20.72.

Quantitation in Nuclear Cardiac Imaging

19

Magdy M. Khalil

Contents

19.1   Introduction

Nuclear cardiac imaging is a typical example that image quantitation has an important role in data interpretation and patient diagnosis. Reproducible and reliable image quantitation relies on robust techniques and well-designed computational algorithms. This in great part related to computer technology and various image-processing tools.

However, the principal motivation for computer analysis is to evaluate an attribute of the image as a metric in an algorithmic manner, independent of observer bias or variability [1].

Tl-201 was one of the radionuclides that received initial attention in cardiac scintigraphy due to its analogous properties to potassium ions. It was commercially available in 1976 and utilized in patients with intermediate likelihood of coronary artery disease (CAD) and after that for risk stratification in patients with known or suspected CAD [2, 3]. Image quantitation in myocardial perfusion imaging has passed through

M. M. Khalil (✉)
Medical Biophysics, Department of Physics, Faculty of Science, Helwan University, Cairo, Egypt

several steps to reach the state-of-the-art quantitation strategies seen today. Planar myocardial thallium-201 scintigraphy was the common mode of data acquisition before the advent of tomographic imaging. In that imaging procedure, a number of planar views were sequentially acquired and were known as stress and redistribution images and acquired at 10-min, 2–4 h, and 6–24 h poststress using mainly three planar views: anterior, 45° and 70° left anterior oblique.

Due to the planar nature of the images and absence of correction techniques for attenuation, scatter, and resolution compensation, images were interpreted with significant loss of spatial and contrast resolution. These degrading factors along with extracardiac tissue activities served to reduce the overall accuracy of the test. While the images were subjectively interpreted for possible myocardial ischemia, this was limited by intra- and interobserver variability, and there was early recognition for automated techniques to reproducibly assist in image quantitation [3–5].

One of the initial approaches devised to quantify the myocardial planar images was based on generating linear intensity profiles of the early and late Tl-201 images providing temporal and spatial representation of the tracer distribution. The method simply relied on coregistering the two data sets and reduction of the 2D images into horizontal count profiles [6]. Another approach was proposed to use a count circumferential profile to quantify the tracer uptake based on radial lines drawn from the center of the heart toward the myocardial walls at certain angular intervals [5]. Both methods are shown in Fig. 19.1.

The advent of tomographic imaging and its introduction in routine nuclear medicine has significantly improved image contrast by removing the underlying and overlying undesired structures. This has made marked improvements in image quality especially, after approval of Tc-99m-based myocardial tracers. The introduction of Tc-99m-labeled compounds and the increase in the number of detector heads have improved the statistical quality of the acquired images. Unlike Tl-201, with Tc-99m-labeled tracers, a longer time between injection and imaging is permitted. In addition, a relatively
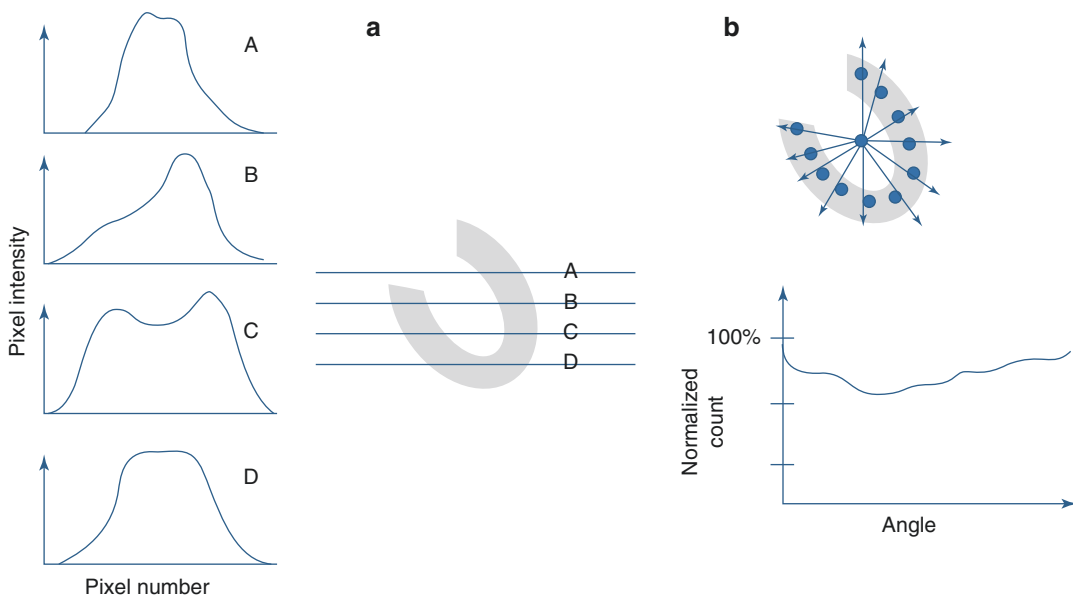
Fig. 19.1 Early methods for image quantitation in myocardial perfusion Tl-201 scintigraphy. (**a**) The quantitation is based on the peak activity determined from a series of linear horizontal profiles drawn over the myocardium while in (**b**) is based on collecting a number of circumferential radial profiles taken from a user-specified center and then constructed into a line profile

large dose can be administered, which is translated into a situation of high count rate resulting in improved signal-to-noise ratio and lesion detectability. Tc-99m-based compounds also allow performing electrocardiograph (ECG)-gating myocardial perfusion with substantial improvement in count statistics and identification of true perfusion defects from those induced by attenuation artifacts [7].

Further improvements to the diagnostic performance of scintigraphic myocardial perfusion images were achieved by adding X-ray computed tomography (CT) to single-photon emission computed tomography (SPECT) imaging in a new hybrid SPECT/CT or PET/CT devices. Anatomically guided perfusion interpretations have opened a new gate for enhancing the diagnostic capability of SPECT imaging in providing more insights as well more information about the stenosed vessels and the affected myocardium.

19.2 Developments and Motivations

SPECT and positron emission tomography (PET) are the two tomographic techniques that provide three-dimensional (3D) or four-dimensional (4D) information about heart perfusion and function/metabolism. A unique attribute that characterizes functional imaging using SPECT or PET tracers over morphological imaging is the capability of deciphering molecular changes and cellular or subcellular dysfunction [8]. Many factors have been associated with the recent development of nuclear cardiac imaging. It can be summarized as follow:

(a) Advances in computer technology, including high-speed processors, storage media, and large-capacity memory chips have facilitated the development of various image-processing tools, providing robust data analysis, reliable data quantitation, and better image display. Another important outcome was the introduction of iterative reconstruction into the clinic, where reconstruction time was a limiting factor due to unavailability of powerful computer systems.

(b) The recognition of image-degrading factors and their impact on image quality and quantitative accuracy have motivated researchers to develop new correction strategies able to enhance the diagnostic performance by reducing or eliminating image-degrading factors.

(c) The practical implementation of resolution recovery has been shown to influence significantly the acquisition time, amount of the injected dose, or both.

(d) New camera designs with or without semiconductor technology dedicated to cardiac imaging are relatively new trend by which better image quality, dose reduction, patient convenience, and comfort as well as scanner throughput can be realized [9, 10].

(e) The relatively recent introduction of SPECT/CT systems has improved the performance of attenuation correction and added a diagnostic value to myocardial perfusion imaging by providing more insights into the anatomy of coronary vessels and degree of stenosis in addition to calcium scoring.

(f) Molecular cardiac imaging has also become an interesting area of research and development and will exploit the potential diagnostic capabilities of radionuclide cardiac SPECT and PET tracers.

(g) PET cardiac imaging is renewed with potential in introducing F18-based tracers in clinical practice.

(h) Machine and deep learning are gaining a growing interest in cardiac imaging with novel approaches at different levels of image recognition, classification, segmentation, and interpretation and this would play a significant role in patient diagnosis, stratification and management.

19.3 Cardiac PET

Myocardial perfusion PET imaging provides several merits including improved spatial and temporal resolution and permits absolute quantitation of myocardial blood flow and coronary flow reserve. It is also able to provide pathophysiologic and

metabolic information of tracer uptake, retention, and kinetics. The tracers ^{15}O-water, ^{13}N-ammonia, and ^{82}Rb are of particular interest due to their physiologic relevance to myocardial blood flow and tissue perfusion [11]. The generic well-established radiotracer Fluorodeoxyglucose (18F-FDG) that is widely used in oncologic imaging can also provide valuable metabolic information of an imaged myocardium. PET can therefore provide a unique opportunity for studying myocardial viability using flow-metabolism imaging protocols. However, the aforementioned tracers are not free from limitations that pushed researchers toward the investigations of new PET compounds.

While SPECT/CT is able to address specific issues related to SPECT MPI, there was an interest in the last decade in reintroducing PET in nuclear cardiology due to a number of features that can impact significantly the diagnostic performance of coronary artery disease.

The uneasy availability and likely cost-related issues were major hurdles in using PET tracers widely in clinical arena. In addition, the short half-lives added some limitation to the investigation procedures. The phenomenon of positron range is another factor that degrades spatial resolution of reconstructed PET images when using some PET tracers (i.e., ^{82}Rb). However, PET cardiac imaging using the conventional ^{15}O, ^{82}Rb, and ^{13}N are relatively faster exploiting the improved count sensitivity of PET scanners in comparison to SPECT-based tracers which also have higher radiation dose to examined patients. However, this high dose was recently mitigated by use of resolution recovery and solid-state scanners permitting one to inject a significantly lower amount of radioactivity or perform the scan in a short time duration [12, 13]. On the other hand, the improved detection capabilities of PET scanners including new scintillation crystals of higher detection efficiency, high light output, and faster response along with compatible electronics have improved PET systems performance. In addition, system point spread function modeling in iterative image reconstruction and improved signal to noise ratio using time of flight have led to improved spatial resolution, image quality, and ultimately improved diagnostic accuracy.

The first-pass extraction fraction for SPECT tracers is generally lower than PET counterparts being approximately 54% for 99mTc-tetrofosmin and 60% for 99mTc-sestamibi. For PET tracers the myocardial extraction is relatively higher being 60% for ^{82}Rb-chloride, 80% for ^{13}N-ammonia, and 94% for ^{18}F-flurpiridaz [14]. These lower retention values of the uptake of SPECT tracers do result in typical underestimation of perfusion defect severity of 20–40% [15].

However, the imaging cutoff values for myocardial blood flow and coronary flow reserve seems not uniform among studies due a number of reasons including the type of radiotracer, kinetic models used in data analysis, variations in software package and other factors [16]. It is noted that extraction of all other PET cardiac tracers is incomplete and decreases in a nonlinear behavior with increasing flow rates. This in turn requires a sort of correction with introduction of noise. Large correction factors are then required with tracers characterized by reduced extraction fraction. Another limitation is that those approaches mainly depend on animal studies to derive model corrections [16–18].

The renewed interest of diagnostic PET imaging in clinical practice of nuclear cardiology is due to a number of factors including availability of PET scanners perhaps combined with an on-site cyclotron, increased availability of ^{82}Rb generators, and the interest to design new 18F-labeled perfusion tracers, which might be an acceptable alternative to an on-site cyclotron and/or expensive generator [19]. Not only the availability of infrastructure was the driving force for the interest but also the accumulating clinical evidence that proved the diagnostic accuracy of PET data specifically in very critical patients with multivessel disease whose blood flow determination could be a strong diagnostic tool [20].

The American Society of Nuclear Cardiology and the Society of Nuclear Medicine and Molecular Imaging have recently recommended the use of myocardial perfusion PET due to sufficient literature indicating its high diagnostic performance [21]. Myocardial perfusion using PET demonstrated a better accuracy than SPECT in assessment of perfusion abnormalities along

Table 19.1 Characteristics of the myocardial perfusion PET tracers

	^{15}O	^{13}NH$_3$	^{82}Rb	^{18}F-Flurpiridaz
Half-life	2.03	9.97 min	1.27	109.8
Production	Cyclotron	Cyclotron	Generator	Cyclotron
Retention fraction at peak stress flow (%)	NA	55–65	25–30	?
Kinetics	Freely diffusible	Trapped in myocardium through metabolism	Trapped in myocardium through metabolism	Trapped in myocardium through metabolism
Positron range (RMS), mm in tissue	1.02	0.57	2.60	0.23
Acquisition mode	Dynamic	Dynamic, static	Dynamic, static	Dynamic, static
Scan duration	6 min	20 min	6 min	20 min
Reconstructed image resolution	8–12	6–10	8–12	4–8
Typical rest dose (3D/2D), mCi	20/30	10/15	30/45	2/3
Typical stress dose (3D/2D), mCi	20/30	10/15	30/45	6/7
Rest-stress total radiation dose, mSv	1.6–2.0	1.5–2.2	1.1–2.2	7–10

Adapted from [11, 30, 37]

with capabilities of estimating myocardial blood flow with high temporal and spatial resolution and tracer concentration down to nanomolar and picomolar concentrations [22]. In terms of effective absorbed dose, one study that comprised 665 laboratories (3067 SPECT studies) and 111 laboratories (532 PET examinations) in the United States yielded an estimate of 3.7 (3.2–4.1) mSv and 12.8 (12.2–14.3) mSv per PET and SPECT study, respectively [23]. The estimates for patient dose due to cardiac PET or SPECT tracers per unit injected activity were 0.14 mSv/MBq for Tl-201, 9.0×10^{-3} mSv/MBq for Tc-99m sestamibi, 8.0×10^{-3} mSv/MBq for Tc-99m tetrofosmin, 1.1×10^{-3} mSv/MBq for Rb-82 and 2.7×10^{-3} mSv/MBq for Ammonia-13 [23]. Physical characteristics and acquisition-related parameters of PET cardiac tracers are summarized in Table 19.1.

cardiac membranes and rapidly equilibrates with tissue compartment without myocardial accumulation. ^{15}O myocardial uptake has a direct linear relationship with blood flow in comparison to other cardiac tracers within SPECT and PET domains, see Fig. 19.2. Its production and fast transfer to the clinical suite might not be easy in many cyclotron-hospital facilities. The good aspect of short half-life permits to perform both stress and rest in less than half an hour providing a tight schedule for the imaging session with an advantage for performing CT angiography [19]. The imaging protocol can be made relatively short so that stress or rest can be performed in 4–5 min dynamic data acquisition with an administered radioactive dose of 24–30 mCi [25]. Other limitations of ^{15}O is the reimbursement issues that may vary from one country to another.

19.3.1 Oxygen-15

Oxygen-15 (^{15}O) is an ideal tracer for tissue blood flow and perfusion but its relatively short half-life (2.06 min) and poor image quality has made it very limited in clinical routine [24, 25], Table 19.1. It exhibits free diffusion across myo-

19.3.2 Ammonia-13

Ammonia-13 (^{13}N) enjoys some good features including longer half-life (9.96 min), relative ease of production and transfer in addition to better image quality when compared to ^{15}O-based examinations. Once taken up by the myocardium

Fig. 19.2 Myocardial tracer uptake versus myocardial blood flow for clinically useful SPECT and PET tracers
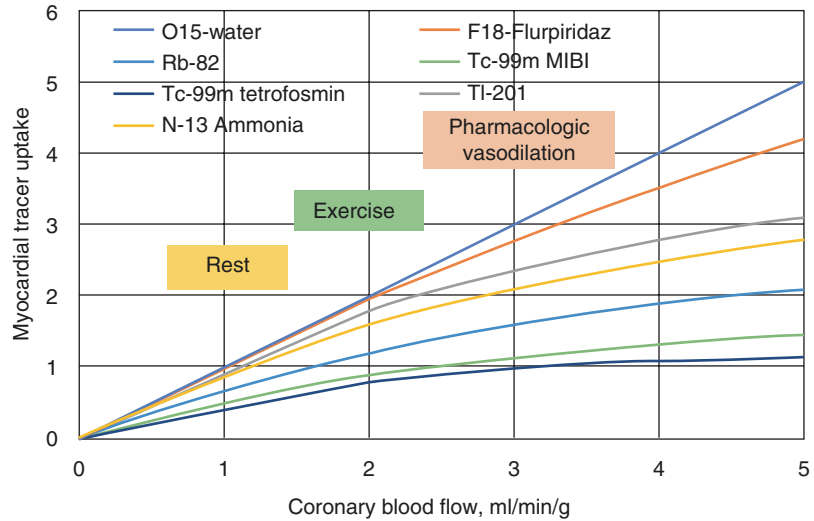
passing through the cell membrane, ammonia equilibrates with its charged form ammonium and converted to glutamine by the effect of gluta-mine synthase. Ammonia-13 is trapped in the myocardial in the form of ^{13}N-gluamine [17, 26]. The extraction fraction of ammonia by myocar-dium is about 80% and thus appear less in linear proportion when compared to ^{15}O as shown in Fig. 19.2. This results in slight inaccurate assess-ment of defect hypoperfusion. The positron range of ^{13}N is 2.53 mm and hence provide image with intermediate quality. A rest-stress protocol is implemented that include an injection of (10–20 mCi) based on system 2D or 3D acquisition mode in both examinations separated by 30 min or even more for pharmacologic stress. Acquisition time may extend to 10 min. The associated effective dose with 20 mCi ammonia-13 injection is low due to relative short half-life and low energy of emitted positrons. As a conse-quence, the urinary bladder is the most critical organ receiving 6 mSv [27].

19.3.3 Rubidium-82

The Rubidium-82 (^{82}Rb) tracer is a generator pro-duced myocardial perfusion PET tracer. It is pro-duced with a strontium-82 (^{82}Sr)/^{82}Rb generator and widely used for diagnosis of coronary artery disease in centers without immediate access to an

on-site cyclotron. It has been widely used in North America in clinical practice [28]. The gen-erator can remain up to 4–6 weeks. The Rb-82 is administered by remote intravenous infusion and the generator can be eluted with >90% yield every 10 min [29]. The US Food and Drug Administration (FDA) has approved ^{82}Rb genera-tors for clinical use in 1989. Its limitation is asso-ciated with relatively high costs which add more budget on the clinic if not met by increased num-ber of referral and patient throughput. Rb-82 is extracted from the arterial blood by all perfused tissues through passive diffusion and active ion transport by the Na-K-ATPase pump [30]. The image quality is not equivalent to other PET trac-ers due to relatively large positron range. The myocardial extraction fraction of Rb-82 is 65% and myocardial uptake decreases nonlinearly with flow [30]. This nonlinearity places addi-tional mathematical corrections on derivation of myocardial blood flow from the rate transporta-tion constant K1. However, determination of myocardial blood flow and coronary flow reserve using Rb-82 has been shown useful in clinical setting [28, 30].

19.3.4 F18 Flurpiridaz

F18 Flurpiridaz is a fluorine-18 (18F) labeled perfusion tracer that has been emerging as prom-

ising PET cardiac tracers. It is a mitochondrial agent that has high myocardial extraction over a wide range of perfusion along with good retention without significant redistribution. It is a structural analogue of pyridaben, a known inhibitor of the NADH:ubiquinone oxidoreductase (i.e., mitochondrial complex-1 (MC-1)) of the electron transport chain [25]. Initial reports of flurpiridaz showed that it has good characteristics as a new myocardial perfusion tracer, such as specific, high myocardial extraction fraction and retention as well as diagnosis and evaluation of coronary artery disease in animal models [31–33]. Moreover, clinical trials showed its superiority to SPECT myocardial perfusion for image quality, diagnostic certainty, and overall diagnosis of coronary artery disease [34]. Further international multicenter clinical trials have been conducted to evaluate diagnostic efficacy of F18-Flurpiridaz in the detection of coronary artery disease [35]. In terms of quantitation of myocardial blood flow, F18-Fluropiridaz was found also feasible over a wide range of cardiac flow in the presence or absence of induced myocardial ischemia [36]. The relatively longer half-life permits also to perform exercise as well as pharmacological stress without lose in image quality or moments of tracer retention.

19.4   Image Acquisition and Processing

While the recent interest in PET was encouraging to renew its utility in clinical practice, SPECT still represents more than 90% of myocardial perfusion imaging. It has been a well-established diagnostic technique in assessment of patients with suspected or known CAD. In cardiac SPECT studies, two data sets are usually acquired: stress and rest images. The former is obtained by exercising the patient using a treadmill or by a pharmacological stress agent. The radiopharmaceutical is injected at peak exercise to be an indicator of occluded vessels when the patient undergoes tomographic scanning. The rest study is performed after injection while the patient in complete resting conditions on the same or a different day.

The imaging protocol differs among institutions such that rest and stress examinations can be performed on the same day using the same radionuclide, such as Tl-201 (stress/redistribution), or Tc-99m-labeled compounds (stress/rest or rest/stress). Another protocol involves performing the stress and rest studies on two different days. The other option is to inject the patient with two different tracers (rest Tl-201/stress Tc-99m); the imaging procedure is performed the same day using an appropriate energy window setting.

Data acquisition is carried out by a rotating gamma camera equipped with one, two, or three detectors encompassing a rotational arc of at least 180°. Data reconstruction is usually performed using the analytical filtered backprojection algorithm or iterative reconstruction, with a smoothing low-pass filter applying an appropriate cutoff frequency and order.

As mentioned, the cardiac images are subjectively interpreted based on visual assessment of tracer distribution within different myocardial segments and depiction of hypoperfusion extent and severity. Although this is the gold standard approach, it remains influenced by interobserver and intraobserver variability along with the expertise of the reading staff. To reduce this variability and standardize the uptake of the tracer by the various segments, a number of software programs have been developed to aid and act as a second observer in the reading session. These methods vary in their theoretical assumptions; geometric modeling of the left ventricle (LV); 2D versus 3D approaches; thresholding and segmentation; valve definition and apical sampling, degree of automation and user intervention; whether count-based or geometric-based; or a combination of these options.

Examples of the commercially available programs are Quantitative Perfusion and Gated SPECT (QPS/QGS, Cedars-Sinai Medical Center, Los Angeles, CA); Emory Cardiac Toolbox (ECTb, Emory University, Atlanta, GA); 4D-MSPECT developed at the University of Michigan Medical Center; Gated SPECT Cardiac Quantification (GSCQ, Yale, New Haven, CT) method; and others. These algorithms have been

evaluated in the literature and some found wide-spread and clinical acceptance among users in quantifying and displaying myocardial perfusion and functional parameters.

There are also some software tools developed to aid in image interpretation or to determine the quality of study interpretation. Some rely on artificial intelligence such as neural networks and case-based approaches to provide increased confidence to the reading physician. Expert systems were also developed to mimic human experts and to rely on a knowledge base of heuristic rules to yield a computer-assisted patient diagnosis. In these approaches, the polar map or the reconstructed images are normally used as inputs for reading and quantifying the myocardial images.

19.5 Quantitative Methods

19.5.1 Quantitative Perfusion/ Gated SPECT

The QGS/QPS method was introduced to sample, analyze, and quantify the myocardium using an ellipsoidal model [38, 39]. Data samples are extracted using equally spaced points in the longitudinal and latitudinal directions. Myocardial sampling is implemented by averaging the wall counts from the endocardial to epicardial borders rather than using the maximal pixel count along the radial profile [40]. By fitting the normal rays on the midmyocardial surface using asymmetric Gaussian functions, the endocardium and epicardium are estimated by certain percentages (i.e., 65%) of the standard deviation (SD) of the Gaussian fit. The peak of the Gaussian function is used to locate the midmyocardial point. For outlining myocardial areas of poor tracer uptake, the SDs are combined with those of each of its four spatial neighboring profiles. Further refinement is then applied by anatomical constraint of constant myocardial volume throughout the cardiac cycle [38]. This approach samples the myocardial points in a 3D ellipsoidal model through equally spaced points, regardless of the heart size; therefore, homologous points can be extracted and pooled to generate normal limit values. Due to

finite sampling, the collected points are scaled to represent the curvature of the myocardium from which they are extracted [38]. This approach was developed by Cedars-Sinai Medical Center in an integrated software package. An output display of the program is shown in Fig. 19.3.

19.5.2 Emory Cardiac Toolbox

The Emory Cardiac Toolbox (ECTb) method works in 3D space and uses the short-axis data set [41, 42]. The ECTb method uses Fourier analysis for wall-thickening estimation and detects a circumferential maximum count profile by applying an anatomically based model accounting for wall thickening to generate theoretical endocardial and epicardial surfaces [41, 43]. The software package integrates myocardial perfusion and function in one application. The program is automated with the possibility to change the short-axis radius and center. Data sampling is performed on the SPECT short-axis slices using a hybrid cylindrical-spherical coordinate system. Cylindrical geometry is used to sample the middle and basal part of the myocardium; the myocardial apex is sampled based on spherical modeling. The center of the coordinate system is the LV long axis, and the search space is limited by the LV radius, apex, and base. The valve plane is defined by two intersecting planes: one perpendicular to the LV long axis in the lateral half of the LV and one angled plane in the septal half of the LV. The program uses eight frames per cardiac cycle in gated myocardial perfusion SPECT studies. In case of contouring a perfusion defect, the algorithm forces the hypoperfused segment to be a smooth connection between adjacent noninfarcted portions of the wall, and because this segment is not thickening, it is pinned to its end diastolic positions [41].

19.5.3 4D-MSPECT

4D-MSPECT (Invia Medical Imaging Solutions, Ann Arbor, MI, USA) is a commercially available algorithm that was developed at the
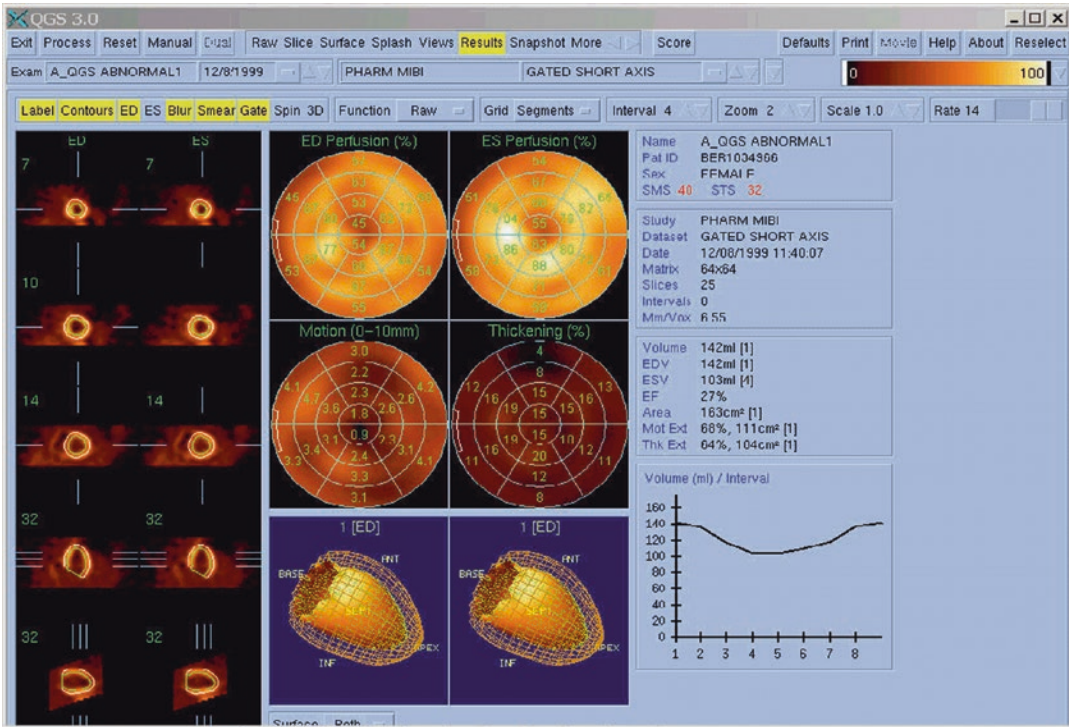
Fig. 19.3 Quantitative perfusion/gated SPECT method (Cedars-Sinai Medical Center, Los Angeles, CA)

University of Michigan Medical Center [44, 45]. The algorithm works to process the data on the basis of a 2D gradient image from which the initial estimates of the ventricle are made. A series of 1D and 2D weighted splines are used to refine the endocardial and epicardial surface estimates. The 4D-MSPECT model also uses a cylindrical-spherical coordinate system for myocardial sampling. The former is used to sample the myocardium from the basal wall to the distal wall, and the latter is used to sample the apex. Weighted spline and data thresholding are used to refine surface estimates, and based on Gaussian fitting, myocardial wall position and thickness are estimated. It has the capability for manual processing when the automatic module fails to accurately delineate the myocardial boundaries. 4D-MSPECT has achieved good correlations with reference techniques in evaluating the myocardial functional parameters [46]. Unlike QGS and ECTb, 4D-MSPECT differs in defining the valve plane in the sense that it permits the mitral

valve plane to move as much as 20 mm inward toward the apex during systole [47]. A snapshot of 4D-MSPECT used in image processing is shown in Fig. 19.4.

19.5.4 pFAST Method

pFAST stands for Perfusion and Functional Analysis for Gated SPECT (pFAST; Sapporo Medical University, Sapporo, Japan) [48, 49]. In this method, the gravity center of each short-axis image is initially determined. A long-axis central line is then identified along all gated long-axis images. Spline curves and a threshold of 30% are used to define the LV base and the epicardial outlines to calculate the maximum circumferential profiles. The epicardial surface is defined as the outer point with 50% of peak activity, which shows a definite viable myocardial mass. Endocardial volume is estimated using a geometric technique. More refinements are performed to
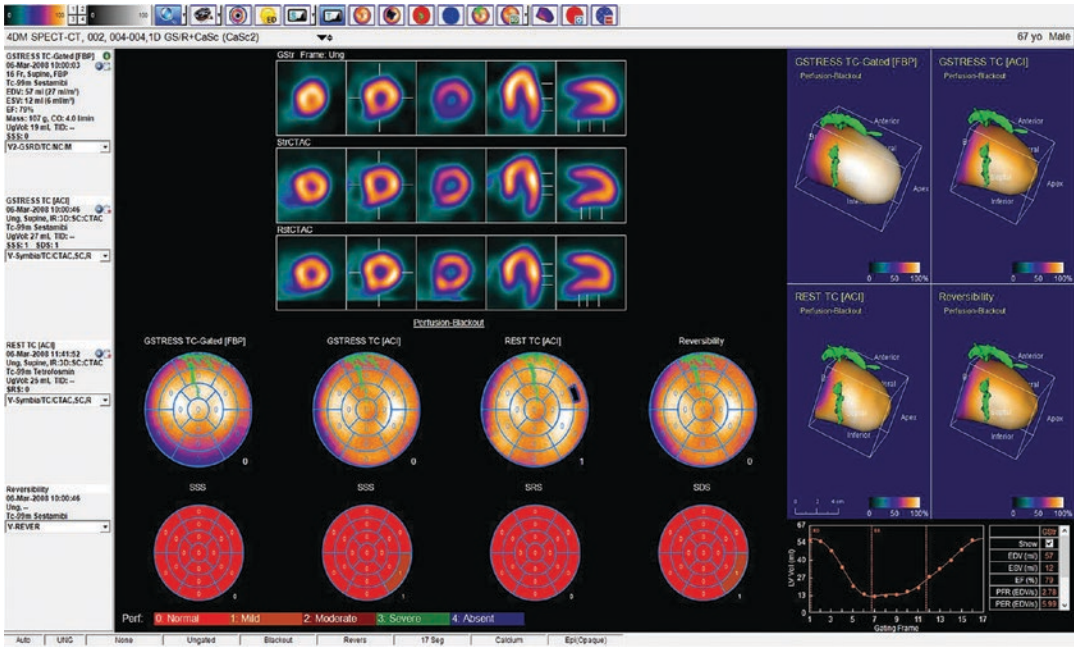
Fig. 19.4 Example of myocardial perfusion and function measurements using 4D-MSPECT. Images are courtesy of INVIA Medical Imaging Solutions, USA

precisely determine the endocardial points using Fourier approximations. Finally, the ejection fraction (EF) is determined from the standard EF formula.

19.5.5 MultiDim

MultiDim (Stanford University Medical School) is a 3D method based on calculating statistical parameters of count distribution moments from the short-axis image volume [50, 51]. The method requires some operator intervention for masking the LV and image thresholding. Masking is performed by manually fitting an ellipsoidal mask around the LV. Thresholding is performed by drawing a region of interest at the base of the LV cavity at end diastole and subtracting the mean value from each pixel [52]. Count sampling is carried out by radial profiles originating from the LV center using equally spaced longitudinal and latitudinal angles across the short-axis images. The endocardial wall is defined as the maxima of the first derivative of the squared activity profiles. Regional wall motion is derived from the phase

and amplitude of the cyclic wave, representing the temporal variation of the first moment of the count distribution. However, the regional thickening is derived from the phase and amplitude of changes in the second moment of the density distribution multiplied by the maximum density. The volumes are calculated from the endocardial surfaces for each time segment [51].

19.5.6 Gated SPECT Cardiac Quantification

Gated SPECT Cardiac Quantification (GSCQ) or Wackers-Liu CQ (Eclipse Systems, Branford, CT, USA) is another method that is based on k-means cluster classification to separate the cardiac region from other extracardiac structures [53]. The myocardial surface boundaries are determined using hybrid count-geometric analysis for the calculation of the LV volumes and EF. The method uses thresholding and the non-gated data to determine a cutoff value that serves to separate the LV volume. More refinements and constraints are carried out to remove the small

remaining volumes within the image and to accurately define and obtain a clean long-axis LV binary image [54]. The long-axis images are resliced to obtain the most apical and basal slices in addition to the myocardial apex. The first apical slice is defined as the first short-axis slice containing the LV cavity, while the position of the last basal slice is defined as the last short-axis slice containing the basal limit of septum plus 10 mm toward the LV base. The algorithm models the apex as a semiellipsoid in 3D space [54].

19.5.7 Left Ventricular Global Thickening Fraction

The left ventricular global thickening fraction (LVGTF) is a count-based method that relies on fractional myocardial thickening to derive the EF, thereby avoiding the step of calculating the LV volumes [55, 56]. It depends on detection of myocardial wall thickening during systolic contraction. The method heavily depends on the partial volume effect, in which the myocardial wall thickness is less than twice the spatial resolution of the imaging system. The pixel counts in end diastolic and end systolic images are used to quantify the myocardial thickening without edge detection or geometric measurements. However, the method uses the systolic and diastolic counts in addition to geometric assumptions to derive a regional thickening fraction and hence to calculate the LV EF [55].

19.5.8 Layer of Maximum Count

Layer of Maximum Count (LMC) method is a different approach that uses the prolate-spheroid geometry to sample the myocardium; it was developed to solve the problem of small hearts [57, 58]. In patients with small hearts, most of the currently available methods tend to underestimate the LV and overestimate the EF. The midmyocardial surface is defined by the LMCs to determine the corresponding EF (i.e., EF_{max}). The LV EF is then calculated by performing a calibration between the EF_{max} and EF estimated from a reference technique, setting the intercept to zero to calculate the regression slope, which is then used to measure the EF in patients with small LVs [58–60]. The method has been evaluated in a population with small hearts versus other quantitative methods using gated blood pool and echocardiography as reference nuclear and nonnuclear techniques, respectively. In the former situation, the LMC outperformed the other methods with moderate correlation and poor interchangeability with gated blood pool studies in patients with small LV. However, in comparison to echocardiography the same method showed a lower correlation but significant in the measurements of EF in patients with normal LV size. A drawback of the method is its dependency on other accurate techniques to derive a calibration factor required to estimate the EF for small LVs.

19.5.9 Cardiac Function Method

The cardiac function method (CAFU; Exini Diagnostics, Sweden) is a nongeometric model-based technique that uses an active shape algorithm [61]. Identification and delineation of the LV is based on a heart-shaped model, and through an iterative process the model is adjusted to optimize the fit with the image data. The algorithm uses 272 landmarks distributed in 17 layers from apex to base with 16 landmarks in each layer [62]. These landmarks are also utilized to give an estimate of myocardial wall motion and thickening. In the former, the normal distance from the landmark to the myocardial surface in both end diastolic and end systolic wall is measured, while thickening calculation is a count ratio for the landmarks in both end diastolic and end systolic frames. The LV volume is calculated using the endocardial surface and the LV valve plane with no constraint placed on basal wall motion [61, 62].

Most of the commercially available quantitative cardiac SPECT methods integrate myocardial perfusion and function in the same software package, and some have more quantitative and display features for multimodality and image fusion using SPECT, PET, and CT images.

Quality assurance tools that allow the user to identify patient motion, artifacts, count density, gating problems, attenuation correction, LV segmentation and identification of myocardial boundaries, and other volumetric problems have also been embedded in these algorithms.

Among those are raw data display, histogramming, valve plane fine-tuning, fusion controls, as well as measures of quality of gated SPECT studies. One of the display features of multimodality imaging is the possibility of aligning the CT vascular coronary tree on the 3D PET or SPECT functional data so that functional perfusion mapping can be visualized, with superimposition of coronary anatomy providing additional diagnostic information.

19.6　Quantification of Perfusion Abnormality

One of the earliest approaches introduced to quantify the distribution of myocardial activity in cardiac tomography was reported more than two decades ago [63]. This approach was based on quantifying the 3D activity distributions within the myocardium into a 2D polar map or "bull's eye." The polar map is constructed through modeling the myocardium into a cylindrical and spherical coordinate system as mentioned in this chapter. Sampling the counts from the cylindrical part is implemented by drawing radial profiles from the center of the short-axis image normal to the myocardial wall (36–60 radial profiles). The maximal pixel count is recorded for each profile and plotted versus the corresponding angle to produce count circumferential curves. The apical portion of the myocardium is sampled by vertical long-axis slices to minimize the effect of partial volume. Sampling the apical portion of the myocardium is illustrated in Fig. 19.5 using different sampling approaches.

The count circumferential profiles are used to construct the polar map, which consists of concentric annuli representing the LV from the apex to the base. Furthermore, a scaling process is performed of the sampled myocardium so that the number of data points remains constant for all patients. However, the polar map distorts the heart shape, size, and geometry [64]. See Fig. 19.5.

To determine the variability and normal limits of the tracer distribution in the myocardium, a
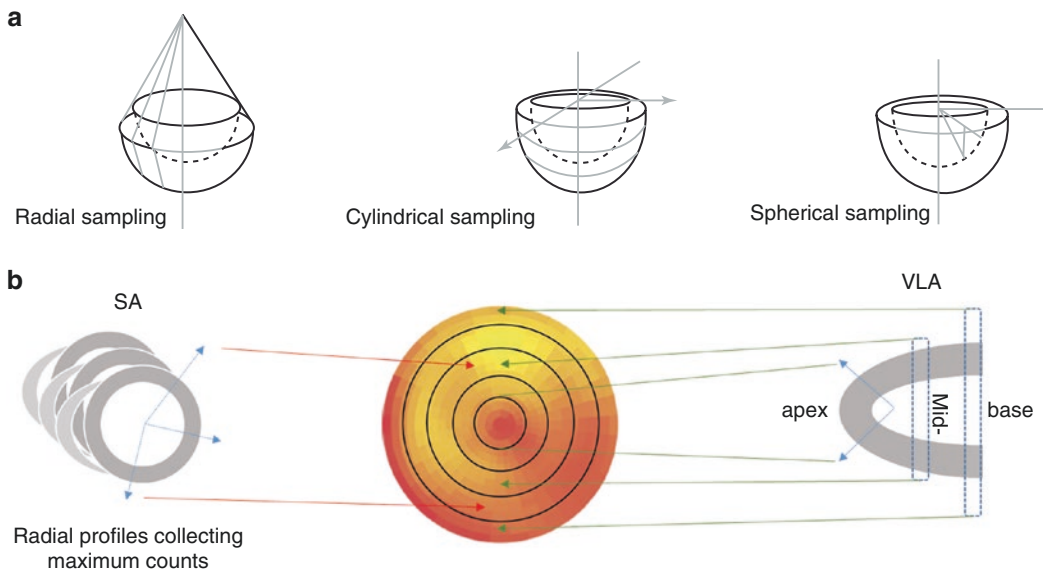
Fig. 19.5 (**a**) Various methods used for sampling of myocardial apex in quantitative cardiac SPECT. (**b**) Mapping of the 3D myocardial count density into a 2D color coded representation called polar map or bull's eye. SA and VLA stand for short and vertical long-axis slices, respectively

normal database is generated based on normal patients or patients with low pretest likelihood (<0.5%) of CAD. The mean value and SD are calculated from the circumferential profile of the normal data set with determination of a threshold value for segmental abnormality.

Polar maps provide quantitative measures of defect extent and severity. In QGS, myocardial sampling is not based on a circumferential profile drawn normally on the LV surface; the entire LV is modeled as a 3D structure with a standard number of equally spaced points regardless of the LV size [40]. In ECTb, the actual defect extent is calculated from the 3D activity distribution rather than from the polar map representation [42]. It is presented as a percentage of the abnormality with respect to the total myocardial volume, individual vascular territories, or actual mass of the hypoperfused myocardium.

To localize the extent of the defect and to pinpoint the location, myocardial segments below a defined threshold are colored black while maintaining the color of the normal ones [65]. Defect severity is expressed in units of SD below the normal mean by a measure called defect severity or total severity score and is displayed in a polar representation referred to as a defect severity map. On this map, severity is scaled by the number of SDs below the normal to a color-coding table so that the most normal region and most abnormal region are differently colored to easily identify the abnormality. Severity score also takes into account the extent and severity of the abnormality and is measured by the number of SDs below the mean of the entire extent of the abnormality [66].

Polar maps have been a simple tool to reduce the whole LV into a 2D image that facilitates the interpretation process by looking at all segments at once (Fig. 19.5b). It also provides a measure of defect reversibility based on normalizing the rest images with respect to the stress images and color-coding scheme. However, volume-weighting and distance-weighting approaches serve to improve one feature over another. The former map tends to distort the defect location but offers an accurate assessment of the defect size. The latter tends to distort the defect size at the cost of improving the accuracy of the defect location. It is therefore recommended not to solely depend on a polar map without paying attention to tomographic slices [67]. Partial and significant reversibility can be determined based on certain percentages of the defect extent. Moreover, measurements of ischemic or scar fractions for a given perfusion defect can be calculated in addition to assessment of myocardial viability [68].

19.6.1 Summed Perfusion Scores

Another semiquantitative approach used to quantify tracer uptake is implemented by dividing the myocardium into 20 segments or the recommended 17 segments [69]. The perfusion of each segment is scored according to a 5-point scoring system: 0–4 (0 = normal, 1 = equivocal reduction, 2 = definite but moderate reduction, 3 = severe reduction of tracer uptake, 4 = absent uptake of radioactivity). The global measure of perfusion is then determined by summing the regional scores of all segments in stress and rest data. This scoring process results in a Summed Stress Score (SSS) and a Summed Rest Score (SRS). The difference between SSS and SRS is the Summed Difference Score (SDS), which is analogous to reversibility. High values for the SSS are an indication of large or severe defects, whereas high values of SDS provide an indication of reversibility and lower values indicate fixed or mostly fixed defects. The SRS is related to the amount of infarcted or hibernating myocardium [70]. The summed score can be used to determine the percentage of myocardium at risk (% of left ventricle) as the ratio of the SSS to the maximum summed value which is considered a severity-weighted estimate of the total defect size [71]. See Table 19.2.

These global perfusion summed scores provide a reported measure for both defect extent and severity, and they can be calculated either visually or by computer-based methods. Reproducibility and diagnostic performance have been reported in a number of studies, including those automated and conducted by human

observers [72]. The SSS is employed to stratify patients into different risk groups according to the following: Individuals with SSS < 4 are considered normal or nearly normal, those with scores of 4–8 are mildly abnormal, those with scores of 9–13 are moderately abnormal, and those with SSS > 13 are severely abnormal.

Table 19.2 Summary of perfusion scores and percent abnormal myocardium in 17 and 20 segment model

Perfusion index	Definition	Significance
Summed stress score (SSS)	Total segmental scores of stress images	Amount of infracted, ischemic, or jeopardized myocardium
Summed rest score (SRS)	Total segmental scores of rest images	Amount of infracted or hibernating myocardium
Summed difference score (SDS)	Difference between SSS and SRS	Amount of ischemic or jeopardized myocardium
	20 segment model	17 segment model
Percent total	SSS × 100/80	SSS × 100/68
Percent ischemic	SDS × 100/80	SDS × 100/68
Percent fixed	SRS × 100/80	SRS × 100/68

Adapted from Fuster V, O'Rourke RA, Walsh RA, Poole-Wilson P. "Hurst's The Heart," 12th edn. 2007

19.6.2 Percent Abnormality

Another global measure of perfusion abnormalities is calculated by normalizing the summed scores to the maximal possible score. In case of the 17-segment model and 5-point scoring system, the maximal possible score is $17 \times 4 = 68$ whereas for the 20-segment model it can be calculated as $20 \times 4 = 80$ (Table 19.2). This percentage measure is called the percentage abnormal myocardium and is applicable to other scoring systems and different myocardial segments. For example, a patient with summed scores of 17 in the 17-segment model will have a percentage abnormality of $17/68 = 40\%$, which bears diagnostic and prognostic information similar to a patient with summed scores of 20 in the 20-segment model ($20/80 = 40\%$) [73]. Expressing the amount of ischemia as percentage myocardium by this approach provides intuitive implications that are not possible with the perfusion scoring system and is applicable to other segmental models and other methods that calculate the percentage of abnormal myocardium [74]. Figure 19.6 shows a comparison between the 17- and 20-segment models and Fig. 19.7 identifies myocardial segments based on the former model.

For risk stratification using the reversibility score, an SDS of 0–2 is considered as low risk
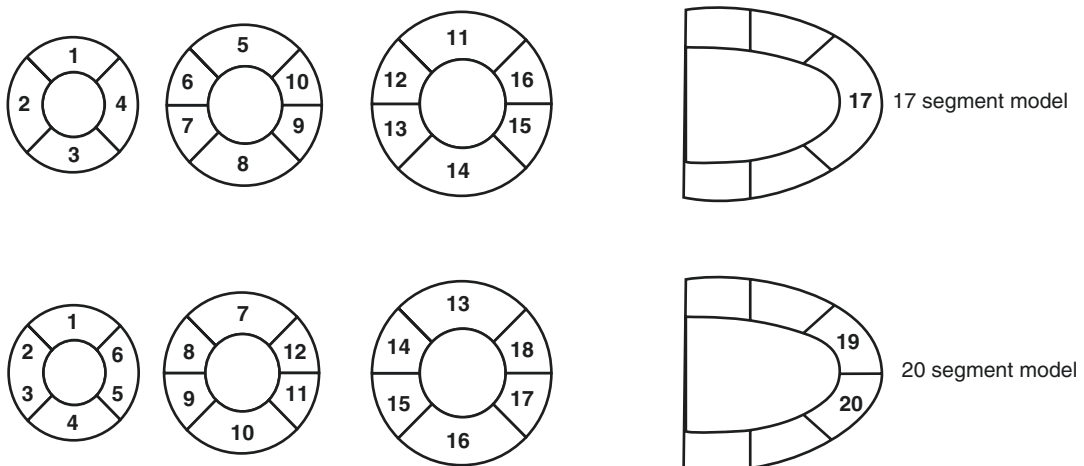
Fig. 19.6 A comparison between 17 and 20 segment models

Fig. 19.7 Myocardial segment identification based on the 17-segment model
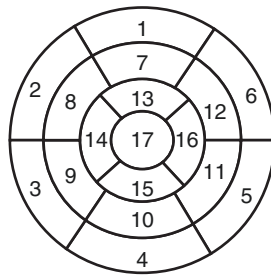
	Basal		Mid-		Apical
1	Basal anterior	7	Mid anterior	13	Apical anterior
2	Basal anteroseptal	8	Mid anteroseptal	14	Apical septal
3	Basal Inferoseptal	9	Mid inferoseptal	15	Apical inferior
4	Basal Inferior	10	Mid inferior	16	Apical lateral
5	Basal Inferolateral	11	Mid inferolateral	17	apex
6	Basal Anterolateral	12	Mid anterolateral		

whereas a range of 3–7 is denoted as intermediate and high risk when greater than 7. Further utilization of the SDS was made by referring to the percentage of the SDS to the maximum possible total score (68 in 17 segment model) as the ischemic burden. As highlighted by Garcia et al. [71] influential research studies have demonstrated that a cutoff of 10% LV ischemic burden could be able to differentiate those patients who would receive revascularization in comparison to patients who would get benefit from medical therapy alone [74, 75].

19.6.3 Generation of Normal Limits

Different schemes were developed to generate normal databases to distinguish abnormal from normal patients in the quantification approaches mentioned. Some of these provide user-specified generation tools for normal limits that are incorporated in the software program with several options for myocardial radiotracer, patient gender, imaging protocol, processing parameters, and so on.

The Emory method is based on collecting a number of patients with a low likelihood of CAD (<0.5%) and deriving a composite pool to extract the mean and SD of the normal limits. Then, a patient study is compared to the normal database to examine and assess the perfusion defects. This approach goes through a number of steps to optimize the threshold value, which is then used to quantify perfusion abnormality in a given patient study. It has specific inherent characteristics, making it dependent on the injected radiopharmaceutical, acquisition protocol, processing parameters, and population studied. It needs a number of normal patients [20–30] or low likelihood of CAD from both genders, another group of patients with significant variation in perfusion location and severity "pilot population," and a validation group of patients to assess the performance of the algorithm in both genders with reported coronary angiography [76, 77]. Thus, approximately 150 patients are required to establish a normal database.

The group at Cedars-Sinai (Los Angeles, CA) developed quantification techniques that are based on various assumptions. One requires a number of normal patients along with another group of patients with a wide range of perfusion abnormalities. The threshold of abnormality is determined by an optimization step in which the computer-generated scores are maximized with the visual scores to obtain an individual segmental threshold. Because of the large number of patients needed to represent a large data set of

segmental hypoperfusion in addition to another group of those with normal or low likelihood of the disease makes it relatively difficult to generate on-site-specific normal limits [39].

Further investigations have revealed another global assessment that combines perfusion defect extent and severity into a continuous measure referred to as the total perfusion deficit (TPD). It provides an overall assessment of hypoperfusion either by vascular territory or for the entire myocardium. In this approach, a reduction in the number of patients required for generation of normal limits is accomplished by obviating those patients with an abnormality. Furthermore, no optimization step is required to derive a segmental threshold, and the technique is based on patients with a low likelihood of the disease [78].

The methods mentioned do not permit aligning the stress with the rest images in a specific geometric orientation, and comparison of a patient study is carried out for the stress and rest separately. This perhaps limits the quantitation algorithm to precisely determine the spatial location of ischemia in stress and rest images. Furthermore, a comparison with database normal values does not account for intrapatient perfusion changes. Faber et al. have shown that by accurate image alignment, changes of 10% and 15% could be detected with false-positive rates of 15% and 10%, respectively, concluding that the mean uptake values can show a statistical significance if the difference is 10% or more in single perfusion studies of single patients [79]. On the other hand, a new measure of ischemia was developed by Slomka et al. [80] to coregister the stress and rest data. The rest images are iteratively reoriented, resized, and normalized to provide the best fit with the stress scans. They have used a new normalization technique based on 10-parameter search criteria and allows determination of the amount of ischemia in stress and rest images without a normal database.

A note from this discussion that developers vary in their representation for the defect extent and severity and differ in their definition and optimization for the threshold value on which segmental abnormality is determined [81, 82]. This has been examined by some comparative

studies conducted to look at the variations that exist among the quantitative cardiac SPECT methods and to investigate their diagnostic performance versus reference techniques. These reports included evaluation for the degree of automation, summed scores (SSS, SDS, SRS), regional and total defect extent using receiver operating characteristic curves and appropriate correlation and agreement statistical tests. Some studies were also performed in comparison to coronary angiography; hence, the sensitivity, specificity, accuracy, and normalcy rates for detection of CAD were estimated for the algorithms. The absence of institutional normal limits as a cause for those variations was also investigated by some researchers if institution-specific normal databases were used. The results, however, demonstrated that significant differences among the various methods do exist in estimating the myocardial perfusion parameters [81–83].

19.7 Quantification of Myocardial Function

19.7.1 Gated Myocardial Perfusion SPECT

The introduction of ECG-gating to myocardial perfusion SPECT imaging has potentially improved the diagnostic and prognostic information in assessing patients with suspected or known CAD [84]. The improvement of count statistics by use of Tc-99m-based tracers, multiple detector systems, advances in computer technology and development of automated quantitative methods has allowed simultaneous acquisition of myocardial perfusion combined with ECG-gated imaging in a feasible manner. As a result, assessment of patient global and regional LV function together with perfusion quantification can be carried out on a routine basis. This in turn has led to a tremendous amount of clinically relevant and valuable information for decision-making in patients with CAD [85]. Figure 19.8 summarizes the steps involved in the calculation of myocardial perfusion and functional parameters.
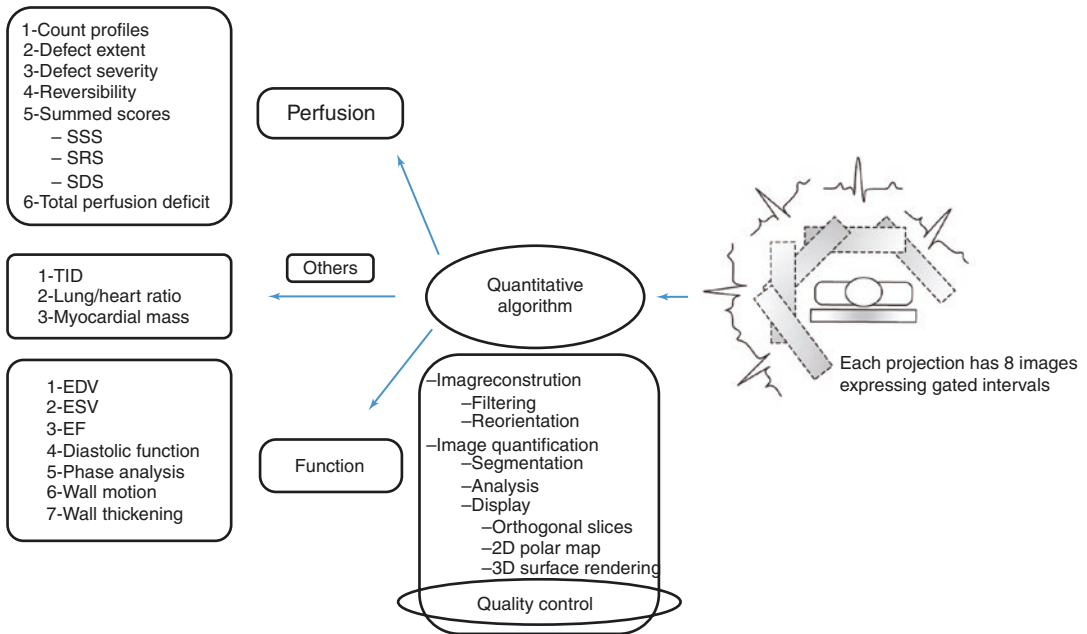
Fig. 19.8 Steps involved in acquiring, processing, and quantifying myocardial perfusion-gated SPECT studies using the quantitative algorithms

Further diagnostic information can be obtained by coregistering data obtained from CT angiography and the metabolic/perfusion images using hybrid SPECT/CT or PET/CT systems. This allows for integrating a large amount of information that was not possible to obtain in a single imaging session. Global functional measures such as end diastolic volume (EDV), end systolic volume (ESV), and EF, in addition to the regional parameters such as regional wall motion and wall thickening, can be evaluated by most of the commercially available quantitative gated SPECT methods.

19.7.2 Acquisition and Processing

Myocardial perfusion-gated SPECT imaging is carried out using three ECG leads placed on the patient's chest and connected to an ECG trigger device. This helps the computer system identify the beginning of the cardiac cycle (the R-R interval) and thereby it can divide the temporal changes of the heart contraction into small time intervals determined by the number of frames/

cycle selected during acquisition setup. The number 8 or 16 frames per cardiac cycle is often chosen since the former provides better count statistics while the latter provides better temporal resolution. Figure 19.9 shows an acquisition for eight frames per cycle. It is also possible to use 32 frames per cardiac cycle to determine the diastolic function. However, this occurs with significant reduction of counts collected over the cardiac frames given the same acquisition time.

The commercial methods provide several tools to process gated and ungated projection data to extract perfusion as well as functional information from gated myocardial perfusion SPECT studies. Functional information obtained from the reconstructed images are LV volumes (EDV and ESV), regional and global EF, myocardial wall motion, and wall thickening.

19.7.3 Volumes and EF Estimation

The underlying notion of ECG-gating myocardial perfusion SPECT studies is to obtain several pictures of the heart during the periodic contrac-

This diagram shows the R-R interval for one heart cycle and the corresponding change in the blood volume. ECG-gating provides a mean for recording the volume change over the heart cycle. This happens by dividing the cycle into gates or frames (e.g., eight frames) or even higher 16 or 32
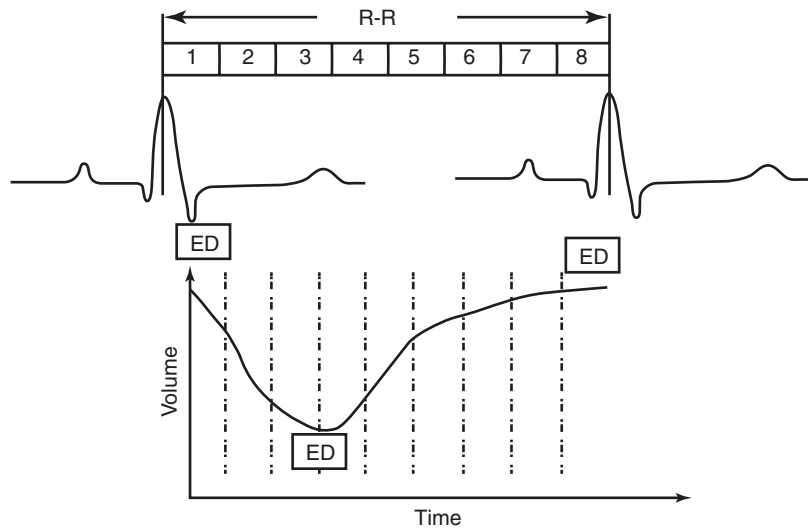
tion. The higher the accuracy in modeling and outlining the LV in these different phases, the better is the reliability of the quantitative results. As mentioned, methods vary in their assumptions for LV geometry. Some are based on an ellipsoidal, cylindrical-spherical, or prolate-spheroidal model, and others are purely count-based techniques. One common step is the segmentation process, by which the LV should be identified and separated from other structures. Methods also vary in their segmentation for the LV as the inclusion of extracardiac tissues can confound the quantitative results [86].

Once the LV has been segmented and the valve plane defined together with determination of myocardial base and apex, outlining of myocardial boundaries can then be estimated. Different approaches have been suggested and implemented to identify endocardial and epicardial boarders as well as myocardial base and apex. Automated modes are often used to delineate the myocardial boundaries; however, in case of contouring errors, operator intervention could be helpful. This also depends on user expertise in addition to interobserver variability. Automated quality control approaches were also developed to judge the quality of the LV shape segmentation as well as valve plane definition in some software programs [87]. These quality control algorithms could provide high accuracy in identifying failure

cases of LV segmentation, leading to an improvement in perfusion quantitation.

Volume-based techniques calculate the ventricular volumes by constructing a time-volume curve using either 8 or 16 frames/cycle. The maximum and minimum points on the volume curve correspond to EDV and ESV, respectively. The EF can then be calculated as a percentage:

$$EF = (EDV - ESV)/EDV * 100$$

Figure 19.10 shows the output display of the ECTb for stress and rest studies together with EDV, ESV, and EF calculations.

19.7.4 Regional Function

Assessment of regional myocardial function has incremental diagnostic and prognostic information over myocardial perfusion parameters alone [88]. Myocardial wall motion and thickening are relatively not uniform as compared to myocardial perfusion. Wall motion is the excursion of the endocardium from end diastole to end systole. A 6-point scoring system is generally used to assess motion abnormality: 0 = normal, 1 = mildly hypokinetic, 2 = moderately hypokinetic, 3 = severely hypokinetic, 4 = akinetic, 5 = dyskinetic. Visual assessment of wall thickening is
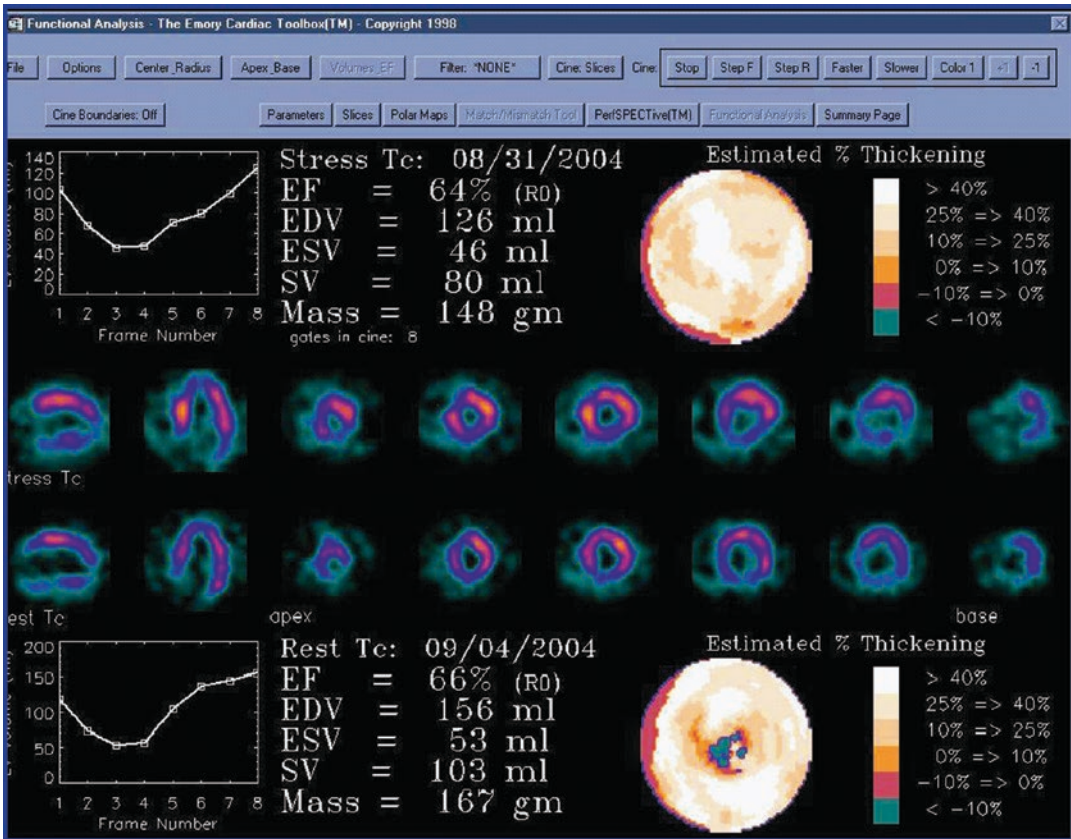
Fig. 19.10 Emory cardiac toolbox display for stress and rest studies where *left* ventricular volumes and EF in addition to wall thickening polar map are shown

often based on the partial volume phenomenon, in which the intensity of the myocardial wall is proportional to the size or degree of wall thickening during cardiac contraction. A 4-point scoring system is used to assess wall thickening: 0 = normal, 1 = mildly reduced, 2 = moderately to severely reduced, 3 = no thickening.

Computer scoring for wall motion and thickening was also developed to reduce observer variability. It calculates the regional function on a segment-by-segment basis in a similar way to calculation of myocardial perfusion. In QGS, regional motion is measured as the distance (in millimeters) between a given endocardial point at end diastole and end systole perpendicular to the average midmyocardial surface between end diastole and end systole [89].

Myocardial thickening is calculated as the percentage increase in myocardial thickness and can be quantified by geometric-based, count-based, or combined methods using geometric count-based techniques [90]. The first detects the spatial position of endocardial and epicardial surfaces to calculate the myocardial thickness in both end diastole and end systole. However, count-based techniques rely on the partial volume effect. Average myocardial thickening of approximately more than 40% at the apex and more than 25% in the rest of the myocardium is considered normal [71]. It should be noted that normal wall motion and thickening are not always concomitant since in some pathological conditions a discordance can take place resulting in abnormal wall motion and preserved thickening or vice versa [91]. A relatively recent progress on myocardial wall motion and thickening algorithms was reported. It showed that detection of the angiographically significant disease by

automated determination of wall motion and thinking scoring was better than or equivalent to expert readers scoring [92].

19.7.5 Diastolic Function

In addition to the determination of the systolic function by myocardial perfusion gated SPECT, myocardial diastolic function can also be estimated which is a useful clinical indicator of LV function and precedes systolic dysfunction in many cardiac diseases. It is advisable that early diagnosis and an appropriate therapy be performed before further progression to diastolic heart failure and cardiac death [93]. Diastolic function can be evaluated by nuclear methods and with other radiographic techniques [94]. Parameters of diastolic function are peak to filling rate (PFR), which is a clinically useful parameter describing the greatest filling rate in early diastole; time to peak filling rate (TTFR); and the mean filling fraction (MFR/3), which is the mean filling rate over the first third of diastole. PFR refers to the peak value of the first derivative of the diastolic portion of the gated frame curve and often reported in terms of EDV.

Parameters of diastolic function require a significantly larger number of gating intervals than often are used. This higher temporal resolution is needed to accurately determine volume changes over a short period of time. The derivatives of the time-volume curve yield information about the rates of emptying and filling. Fourier fitting with three or four harmonics is often used to smooth the time–activity and derivative curves to reduce the statistical fluctuations of the acquired data.

Peak rates and average rates are usually measured in units of end diastolic volumes per second (EDV/s). Per cardiac cycle, a number of 12, 16, or 32 frames may be employed; however, better estimation can be achieved with the highest possible framing rate. One study compared the diastolic and systolic functions using 32 frames versus 8 and 16 frames/cycle taking the gated blood pool as a reference [95]. Accurate assessment of the diastolic as well systolic function was obtained when 32 frames/cycle was applied.

Furthermore, lower systematic errors for both measures were found with the highest temporal sampling. In a population of 90 patients, Akincioglu et al. derived the normal limits for PFR and TTFR as 2.62 ± 0.46 EDV/s and 164.6 ± 21.7 ms, respectively, with abnormality thresholds of PFR < 1.71 EDV/s and TTFR >216.7 ms, respectively, applying 16 frames/cycle, and measurements were performed using the QGS software program [96].

19.7.6 Phase Analysis

Assessment of cardiac mechanical dyssynchrony is an important step for patients scheduled to undergo or who have undergone cardiac resynchronization therapy (CRT) [97]. CRT is used to improve heart function by restoring the heart rhythm contraction in patients with an irregular heartbeat, called LV dyssynchrony. Chen et al. [98] developed a tool for measuring the onset of mechanical contraction based on phase analysis of the cardiac cycle in gated myocardial SPECT imaging using Fourier transform. A phase array is extracted from the 3D count distribution in the eight bins of the gated short-axis slices.

This phase array conveys information about the regional mechanical contraction in a 3D fashion, and a number of quantitative indices are derived from the phase array histogram, such as the peak of the histogram, SD of phase distribution, and phase histogram bandwidth (95% confidence interval). Phase histogram skewness and kurtosis can also be calculated, which indicate the symmetry and peakedness of the distribution, respectively. These measures correspond to specific attributes of the histogram curve and in turn should have clinical relevance in the overall assessment [42, 98].

In a prospective study, 455 patients were analyzed using a commercial software package [99]. A number of 150 corresponded to the control group (i.e., normal subjects) and 305 corresponded to patients with cardiac diseases (including different combinations of mechanical and/or conduction cardiac disease) were identified. A cutoff of SD greater than 18.4 and bandwidth

greater than 51 were the most sensitive parameters (75.7% and 78.7%, respectively). A cutoff value of skewness less than or equal to 3.2 and kurtosis less than or equal to 9.3 were the most specific parameters (92% and 94%, respectively) between control group and patients. A cutoff values of SD >26.1, bandwidth >70, skewness ≤2.89 and kurtosis ≤10.2 were reported for patients with conduction versus mechanical cardiac disease. Furthermore, values of SD >40.2, bandwidth >132, skewness ≤2.3, kurtosis <4.6 were the cutoff values between patients with and without resynchronization therapy criteria [99].

19.7.7 Tomographic ECG-Gating in Equilibrium Radionuclide Angiocardiography (ERNA)

In planar gated blood pool imaging, the anatomical geometry of the cardiac chambers limits a clear separation between right ventricle (RV) and LV. The overlapping atrial and ventricular structures obscure an accurate outlining of the RV. However, tomographic equilibrium radionuclide angiocardiography (ERNA) should be able to estimate the RV parameters more accurately than planar imaging. Adding the tomographic option to the planar gated blood pool imaging allows for better visualization of cardiac chambers and depiction of contractile motion. In this instance, SPECT data can provide better separation of the LV and RV together with information about the contractile function. ERNA can also provide an estimate of the LV and RV volumes and EF in addition to ventricular filling and emptying parameters [100]. A number of research studies were conducted to measure the normal limits for global and regional parameters of diastolic and systolic function using gated blood pool tomographic imaging [101, 102]. Figure 19.11 shows many functional parameters that can be obtained from tomographic ERNA.

A comparison between four different methods (QBS, BP-SPECT, QUBE, and 4D-MSPECT) [103–106] revealed that all methods tended to underestimate the LV volumes (EDV and ESV)

with a trend of greater underestimation as the volume of the LV increased; different trends were observed among algorithms to estimate the RV volumes [107]. In LV EF estimation, most algorithms showed good correlation with the reference values with no significant trends observed across the range of EFs studied. However, all methods showed greater overestimation with an increase of the RV EF [107]. These results were found in consistence with others [108]. It is generally noted that the algorithmic assumptions as well as contour detection vary among methods, which can be fixed count threshold, derivative or gradient-based edge detection, knowledge-based boundary detection, watershed voxel clustering, or neural network-based segmentation [109]. Other patient-related factors such as definition of pulmonary outflow tract, enlarged ventricles, and difficulty of the RV geometry could variably contribute to suboptimal results of volume and EF estimation. Moreover, other technical and processing parameters are yet to be determined and practically optimized [110].

19.7.8 Transient Ischemic Dilation

Transient ischemic dilation (TID) of the LV is measured as a ratio of the LV cavity in the stress images and the LV cavity in rest images. This index has its clinical significance in multivessel stenosis and increased risk of adverse outcomes [111]. It can be calculated from both gated and ungated data sets. The normal limits are constrained by the protocol used since in some circumstances the LV chamber appears different in size, especially when different radionuclides are used (Tc-99m- vs. Tl-201-based images) or patient-detector distance varied greatly in both studies. The myocardial walls in the Tl-201 images appear thicker than in the Tc-99m images, resulting in a smaller cavity size in Tl-201 images. This should be accounted for in interpreting the results of TID. Normal limits and values of TID vary in the literature (1.012–1.40), and sources of this variability are perhaps different radionuclides (Tc-99m, Tl-201, or both), type
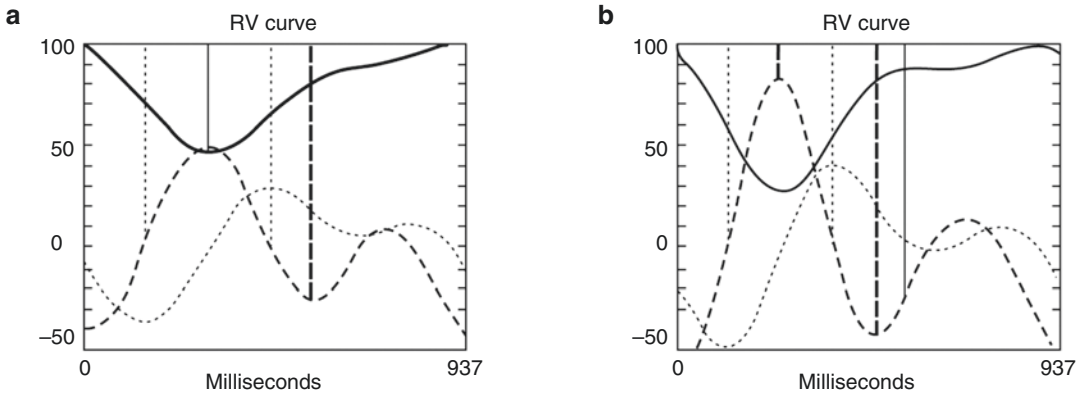
RVEF = 55%	LVEF = 63%
RVEDV = 120 mL	LVEDV = 109 mL
RVESV = 54	LVESV = 40 mL
RV avg_hr = 64 bpm	LV avg_hr = 64 bpm
RV ES_ERF = 244 ms	LV ES_ERF = 244 ms
RV peak er = −2.4 EDV/s	LV peak er = −3.2 EDV/s
RV peak fr = −1.9 EDV/s	LV peak fr = −2.8 EDV/s
RV peak fr time = 144 ms	LV peak fr time = 126 ms

Fig. 19.11 Calculation of regional and global systolic and diastolic myocardial functional parameters for both RV and LV in gated blood pool SPECT using a count-based method. (From [101] with permission from Springer)

of stress (exercise vs. other pharmacological stressors), imaging protocol (single- or 2-day protocol), time of imaging, or other factors [112]. TID can add a diagnostic benefit for detection of severe CAD when combined with perfusion parameters.

In a large international multicenter registry, non-attenuation-corrected, imaging system, radiopharmaceutical, and stress protocol-specific TID limits in supine position were derived from 97.5th percentile and mean ± standard deviations (SD). Reference limits were compared for different solid-state cameras (D-SPECT vs. Discovery), radiotracers (sestamibi vs. tetrofosmin), different types of stress (exercise vs. four different vasodilator-based protocols) as well as different vasodilator-based protocols.

The limits of TID ranged from 1.18 to 1.52 (97.5th percentile) and 1.18 to 1.39 (mean ± 2SD). No statistical difference was found between D-SPECT and Discovery while differences between exercise and vasodilator-based protocols (adenosine, regadenoson, or regadenoson-walk) were observed [113].

Similar to TID is the measurements of myocardial mass. It is estimated from myocardial volume measurements when epicardial and endocardial surfaces are determined even in presence or absence of myocardial gating. High interobserver reproducibility measurements were found in mass measurements in poststress imaging data. However, interchangeability with measurements obtained from CT seems not to be feasible [114].

19.8   Hybrid Cardiac Imaging

There is no doubt that the advent of SPECT/CT and PET/CT has made a significant improvement to myocardial perfusion imaging. Attenuation correction was one the remarkable achievement obtained from the CT portion of the hybrid scanners. A significant reduction of transmission time as well image noise was obtained. Calcium scoring was an additional quantitative metric revealed from CT data set. CT coronary angiography is also a significant addition to myocardial perfusion SPECT merging function with anatomy in a one single session. Cardiac MRI has potential imaging characteristics as when combined with nuclear PET imaging would add enormous amount of anato-molecular information of cardiovascular abnormalities. Cardiac MRI has been used as standard of reference in functional estimation of left and right ventricular volumes and ejection fraction, regional and global wall motion, in addition to its capabilities in determination of tissue characteristics as well as valve function [115].

19.9   Factors Affecting Gated SPECT

Many variables were found to influence the performance of the quantitative gated SPECT methods in estimating the LV volumes and EF. These variables can be classified into acquisition, processing, and patient-related factors.

Selection of the matrix size, zooming factor, count density, framing rate (8 or 16 frames/cycle), and angular resolution (number of projections) and rotation arc (180° vs. 360°), collimators, radionuclide used (Tc-99m vs. Tl), and other factors were found to influence the performance of the estimation task [116–124]. Processing parameters such as reconstruction algorithm (FBP vs. iterative reconstruction), photon attenuation, scatter, resolution recovery, filtering, cutoff value, and zooming during reconstruction were also reported [125–128]. Some other factors are related to the patient and have been studied in the literature, such as irregular heart rate, gating errors (e.g., T-wave elevation), patient motion,

severe perfusion defects and difficulty in outlining the myocardial boundaries, small hearts (underestimation of volumes and overestimation of EF), and high extracardiac [60, 129–131]. Nevertheless, a well-defined acquisition and processing protocol could serve to optimize the results of gated studies. Moreover, quality control software tools as well as visual assessment of patient raw data are also helpful in depicting count variation and patient motion and detecting rejected heart beats.

The variations shown by the quantitative perfusion software programs were also evident in estimating the LV volumes and EF [46, 132, 133]. Relatively large agreement limits were found among methods in addition to systematic and random errors. As a result, the users should be aware of the underlying assumptions of the method used in clinical practice as well as understanding of the sources of error and technical pitfalls. Although most of the methods showed good correlations in comparison to accurate techniques in cardiac imaging achieving acceptable accuracy and reproducibility, interchangeability of values would be of limited clinical outcome, and patient monitoring must be performed in adherence to a single software program.

19.10   Machine Learning

Like other imaging modalities, nuclear cardiac imaging received considerable interest in using machine and deep learning methods in improving diagnostic performance and test accuracy as well as tackling technical challenges associated with image processing, segmentation and data analysis. Investigators were able to show that integration of quantitative myocardial perfusion and functional variables using the support vector machine (SVM) method has significantly improved the diagnostic accuracy of myocardial perfusion and can be superior to expert reader assessment based on ROC analysis [134]. Machine learning with SVM was also shown to provide automatic and accurate valve plane localization minimizing or obviating the need of user intervention in SPECT myocardial perfusion

imaging [135]. Another study was conducted investigating the diagnostic performance of deep learning in detection of obstructive coronary disease in comparison to measurements of TPD in a multicenter study covering nine different sites using new generation solid-state scanners [136]. The study concluded that deep learning has a potential to outperform automatic interpretation of myocardial perfusion imaging in comparison to current standards. A deep convolutional neural network to estimate patient specific attenuation map derived from emission data was also reported [137]. The method is capable of generating attenuation maps to facilitate attenuation correction in SPECT systems installed without or absence of X-ray CT component. The cardiovascular imaging using nuclear techniques is foreseen to be significantly affected by these new technologies and seems that new beginnings are shining on the horizon.

19.11 Conclusions

Cardiac PET has a renewed interest and efforts are being made to make it a daily routine in many nuclear cardiac laboratories. Availability of the old radiotracers like 82Rb and introduction of new F18-labeled compounds, improvement of PET/CT performance characteristics and image reconstruction would interplay to encourage many stakeholders and practitioners to incorporate PET in their diagnostic scheme. Cardiac SPECT and PET imaging provide a tremendous amount of information about myocardial perfusion and function. Many factors are key and still contributing to the development of cardiac scintigraphy, such as radiopharmaceuticals, instrumentation, computational algorithms, and computer technology. Software packages developed to provide such quantitative indices are helpful in patient diagnosis and have become important tools in nuclear cardiology laboratories. The quantitative parameters provided by those programs together with their automated features are unique among other cardiac imaging modalities, and to a considerable extent this has

made nuclear cardiac imaging a well-established diagnostic imaging modality. Further investigations are warranted to explore the qualitative and quantitative capability of cardiac SPECT with use of hybrid imaging techniques.

A number of points should be taken into consideration when using the myocardial perfusion quantitation methods in clinical practice:

- These algorithms assist as a second observer in the reading session, and the visual assessment by an experienced reading physician must be at the forefront. Even with fully automated methods, careful inspection should be followed to check and verify the results of contour generation.
- Quantitative cardiac SPECT methods were shown to differ significantly in their performance along with the degree of automation.
- Normal limits for myocardial perfusion and function were also shown to differ among algorithms and tended to be gender specific.
- Interchangeability of these algorithms is clinically limited to use in patient monitoring or in a decision-making process.
- Quantitative perfusion methods were designed to quantify the myocardial tracer uptake in a relative sense and do not provide an absolute measure of tracer distribution. Furthermore, they do not account for image-degrading factors such as photon attenuation, scatter, and resolution effects.
- New approaches developed to evaluate perfusion defect abnormality should be extensively validated and assessed under a wide range of patient conditions with the available acquisition and processing protocols used in daily practice. Furthermore, validation studies should include not only phantom experiments but also patient data and should be compared to well-established and accurate techniques.
- For proper implementation of the quantitative methods in clinical practice and for better data interpretation, users should be aware of the basic assumptions and concepts underlying those algorithms.

- Machine and deep learning are emerging with special interest on several aspects of myocardial perfusion imaging using SPECT and PET as well other imaging modalities. This would have a direct impact on the practice and management of patients with cardiovascular disease.

References

1. Goris M, Zhu H, Robinson T. A critical discussion of computer analysis in medical imaging. Proc Am Thorac Soc. 2007;4(4):347–9.
2. Beller GA. Myocardial perfusion imaging with thallium-201. J Nucl Med. 1994;35(4):674–80.
3. Beller GA, Gibson RS, Watson DD. Radionuclide methods of identifying patients who may require coronary artery bypass surgery. Circulation. 1985;72(6 Pt 2):V9–22.
4. Ragosta M, Beller GA, Watson DD, Kaul S, Gimple LW. Quantitative planar rest-redistribution 201Tl imaging in detection of myocardial viability and prediction of improvement in left ventricular function after coronary bypass surgery in patients with severely depressed left ventricular function. Circulation. 1993;87(5):1630–41.
5. Garcia E, Maddahi J, Berman D, Waxman A. Space/time quantitation of thallium-201 myocardial scintigraphy. J Nucl Med. 1981;22(4):309–17.
6. Watson DD, Campbell NP, Read EK, Gibson RS, Teates CD, Beller GA. Spatial and temporal quantitation of plane thallium myocardial images. J Nucl Med. 1981;22(7):577–84.
7. Choi JY, Lee KH, Kim SJ, Kim SE, Kim BT, Lee SH, et al. Gating provides improved accuracy for differentiating artifacts from true lesions in equivocal fixed defects on technetium 99m tetrofosmin perfusion SPECT. J Nucl Cardiol. 1998;5(4):395–401.
8. Sogbein OO, Pelletier-Galarneau M, Schindler TH, Wei L, Wells RG, Ruddy TD. New SPECT and PET radiopharmaceuticals for imaging cardiovascular disease. Biomed Res Int. 2014;2014:942960.
9. Slomka P, Hung GU, Germano G, Berman DS. Novel SPECT technologies and approaches in cardiac imaging. Cardiovasc Innov Appl. 2017;2(1):31–46.
10. Slomka PJ, Baum RP. Multimodality image registration with software: state-of-the-art. Eur J Nucl Med Mol Imaging. 2009;36(Suppl 1):S44–55.
11. Driessen RS, Raijmakers PG, Stuijfzand WJ, Knaapen P. Myocardial perfusion imaging with PET. Int J Cardiovasc Imaging. 2017;33(7):1021–31.
12. Partington SL, Valente AM, Bruyere J Jr., Rosica D, Shafer KM, Landzberg MJ, et al. Reducing radiation dose from myocardial perfusion imaging in subjects with complex congenital heart disease. J Nucl Cardiol. 2019. https://doi.org/10.1007/s12350-019-01811-y.
13. Perrin M, Djaballah W, Moulin F, Claudin M, Veran N, Imbert L, et al. Stress-first protocol for myocardial perfusion SPECT imaging with semiconductor cameras: high diagnostic performances with significant reduction in patient radiation doses. Eur J Nucl Med Mol Imaging. 2015;42(7):1004–11.
14. Maddahi J, Packard RRS. PET should replace SPECT in cardiac imaging for diagnosis and risk assessment of patients with known or suspected CAD: pro. J Nucl Cardiol. 2017;24(6):1955–9.
15. deKemp RA, Renaud JM, Klein R, Beanlands RS. Radionuclide tracers for myocardial perfusion imaging and blood flow quantification. Cardiol Clin. 2015;34(1):37–46.
16. Danad I, Raijmakers PG, Knaapen P. Diagnosing coronary artery disease with hybrid PET/CT: it takes two to tango. J Nucl Cardiol. 2013;20(5):874–90.
17. Choi Y, Huang SC, Hawkins RA, Kim JY, Kim BT, Hoh CK, et al. Quantification of myocardial blood flow using 13N-ammonia and PET: comparison of tracer models. J Nucl Med. 1999;40(6):1045–55.
18. Muzik O, Beanlands RS, Hutchins GD, Mangner TJ, Nguyen N, Schwaiger M. Validation of nitrogen-13-ammonia tracer kinetic model for quantification of myocardial blood flow using PET. J Nucl Med. 1993;34(1):83–91.
19. Sciagra R, Passeri A, Bucerius J, Verberne HJ, Slart RH, Lindner O, et al. Clinical use of quantitative cardiac perfusion PET: rationale, modalities and possible indications. Position paper of the Cardiovascular Committee of the European Association of Nuclear Medicine (EANM). Eur J Nucl Med Mol Imaging. 2016;43(8):1530–45.
20. Dorbala S, Di Carli MF. Cardiac PET perfusion: prognosis, risk stratification, and clinical management. Semin Nucl Med. 2014;44(5):344–57.
21. Bateman TM, Dilsizian V, Beanlands RS, DePuey EG, Heller GV, Wolinsky DA. American Society of Nuclear Cardiology and Society of Nuclear Medicine and Molecular Imaging Joint Position Statement on the clinical indications for myocardial perfusion PET. J Nucl Cardiol. 2016;23(5):1227–31.
22. Iskandrian AE, Garcia EV, editors. Nuclear cardiac imaging. 5th ed. New York: Oxford University Press; 2016.
23. Desiderio MC, Lundbye JB, Baker WL, Farrell MB, Jerome SD, Heller GV. Current status of patient radiation exposure of cardiac positron emission tomography and single-photon emission computed tomographic myocardial perfusion imaging. Circ Cardiovasc Imaging. 2018;11(12):e007565.
24. Bergmann SR, Fox KA, Rand AL, McElvany KD, Welch MJ, Markham J, et al. Quantification of regional myocardial blood flow in vivo with H215O. Circulation. 1984;70(4):724–33.
25. Maddahi J, Packard RR. Cardiac PET perfusion tracers: current status and future directions. Semin Nucl Med. 2014;44(5):333–43.

26. Hutchins GD. Quantitative evaluation of myocardial blood flow with [13N]ammonia. Cardiology. 1997;88(1):106–15.

27. Dilsizian V, Bacharach SL, Beanlands RS, Bergmann SR, Delbeke D, Dorbala S, et al. ASNC imaging guidelines/SNMMI procedure standard for positron emission tomography (PET) nuclear cardiology procedures. J Nucl Cardiol. 2016;23(5):1187–226.

28. Yoshinaga K, Klein R, Tamaki N. Generator-produced rubidium-82 positron emission tomography myocardial perfusion imaging-from basic aspects to clinical applications. J Cardiol. 2010;55(2):163–73.

29. Arumugam P, Tout D, Tonge C. Myocardial perfusion scintigraphy using rubidium-82 positron emission tomography. Br Med Bull. 2013;107:87–100.

30. Klein R, Beanlands RS, deKemp RA. Quantification of myocardial blood flow and flow reserve: technical aspects. J Nucl Cardiol. 2010;17(4):555–70.

31. Higuchi T, Nekolla SG, Huisman MM, Reder S, Poethko T, Yu M, et al. A new 18F-labeled myocardial PET tracer: myocardial uptake after permanent and transient coronary occlusion in rats. J Nucl Med. 2008;49(10):1715–22.

32. Yalamanchili P, Wexler E, Hayes M, Yu M, Bozek J, Kagan M, et al. Mechanism of uptake and retention of F-18 BMS-747158-02 in cardiomyocytes: a novel PET myocardial imaging agent. J Nucl Cardiol. 2007;14(6):782–8.

33. Maddahi J, Czernin J, Lazewatsky J, Huang SC, Dahlbom M, Schelbert H, et al. Phase I, first-in-human study of BMS747158, a novel 18F-labeled tracer for myocardial perfusion PET: dosimetry, biodistribution, safety, and imaging characteristics after a single injection at rest. J Nucl Med. 2011;52(9):1490–8.

34. Berman DS, Maddahi J, Tamarappoo BK, Czernin J, Taillefer R, Udelson JE, et al. Phase II safety and clinical comparison with single-photon emission computed tomography myocardial perfusion imaging for detection of coronary artery disease: flurpiridaz F 18 positron emission tomography. J Am Coll Cardiol. 2012;61(4):469–77.

35. Stickel JR, Qi J, Cherry SR. Fabrication and characterization of a 0.5-mm lutetium oxyorthosilicate detector array for high-resolution PET applications. J Nucl Med. 2007;48(1):115–21.

36. Packard RR, Huang SC, Dahlbom M, Czernin J, Maddahi J. Absolute quantitation of myocardial blood flow in human subjects with or without myocardial ischemia using dynamic flurpiridaz F 18 PET. J Nucl Med. 2014;55(9):1438–44.

37. Murthy VL, Bateman TM, Beanlands RS, Berman DS, Borges-Neto S, Chareonthaitawee P, et al. Clinical quantification of myocardial blood flow using PET: joint position paper of the SNMMI cardiovascular council and the ASNC. J Nucl Med. 2017;59(2):273–93.

38. Germano G, Kavanagh PB, Waechter P, Areeda J, Van Kriekinge S, Sharir T, et al. A new algorithm for the quantitation of myocardial perfusion SPECT. I: technical principles and reproducibility. J Nucl Med. 2000;41(4):712–9.

39. Sharir T, Germano G, Waechter PB, Kavanagh PB, Areeda JS, Gerlach J, et al. A new algorithm for the quantitation of myocardial perfusion SPECT. II: validation and diagnostic yield. J Nucl Med. 2000;41(4):720–7.

40. Germano G, Kavanagh PB, Slomka PJ, Van Kriekinge SD, Pollard G, Berman DS. Quantitation in gated perfusion SPECT imaging: the cedars-sinai approach. J Nucl Cardiol. 2007;14(4):433–54.

41. Faber TL, Cooke CD, Folks RD, Vansant JP, Nichols KJ, DePuey EG, et al. Left ventricular function and perfusion from gated SPECT perfusion images: an integrated method. J Nucl Med. 1999;40(4):650–9.

42. Garcia EV, Faber TL, Cooke CD, Folks RD, Chen J, Santana C. The increasing role of quantification in clinical nuclear cardiology: the Emory approach. J Nucl Cardiol. 2007;14(4):420–32.

43. Cooke CD, Garcia EV, Cullom SJ, Faber TL, Pettigrew RI. Determining the accuracy of calculating systolic wall thickening using a fast Fourier transform approximation: a simulation study based on canine and patient data. J Nucl Med. 1994;35(7):1185–92.

44. Ficaro E, Quaife R, Kritzman J, Corbett J. Accuracy and reproducibility of 3D MSPECT for estimating left ventricular ejection fraction in patients with severe perfusion abnormalities. Circulation. 1999;100(Suppl):I26.

45. Ficaro EP, Lee BC, Kritzman JN, Corbett JR. Corridor4DM: the Michigan method for quantitative nuclear cardiology. J Nucl Cardiol. 2007;14(4):455–65.

46. Schaefer WM, Lipke CS, Standke D, Kuhl HP, Nowak B, Kaiser HJ, et al. Quantification of left ventricular volumes and ejection fraction from gated 99mTc-MIBI SPECT: MRI validation and comparison of the Emory Cardiac Tool Box with QGS and 4D-MSPECT. J Nucl Med. 2005;46(8):1256–63.

47. Ficaro E, Kritzman J, Corbett J. Effect of valve plane constraint on LV ejection fractions from gated perfusion SPECT [abstract]. J Nucl Cardiol. 2003;10:S23.

48. Nakata T, Katagiri Y, Odawara Y, Eguchi M, Kuroda M, Tsuchihashi K, et al. Two- and three-dimensional assessments of myocardial perfusion and function by using technetium-99m sestamibi gated SPECT with a combination of count- and image-based techniques. J Nucl Cardiol. 2000;7(6):623–32.

49. Hashimoto A, Nakata T, Wakabayashi T, Kyuma M, Takahashi T, Tsuchihashi K, et al. Validation of quantitative gated single photon emission computed tomography and an automated scoring system for the assessment of regional left ventricular systolic function. Nucl Med Commun. 2002;23(9):887–98.

50. Goris ML, Thompson C, Malone LJ, Franken PR. Modelling the integration of myocardial regional perfusion and function. Nucl Med Commun. 1994;15(1):9–20.

51. Everaert H, Franken PR, Flamen P, Goris M, Momen A, Bossuyt A. Left ventricular ejection fraction from gated SPET myocardial perfusion studies: a method based on the radial distribution of count rate density across the myocardial wall. Eur J Nucl Med. 1996;23(12):1628–33.

52. Everaert H, Bossuyt A, Franken PR. Left ventricular ejection fraction and volumes from gated single photon emission tomographic myocardial perfusion images: comparison between two algorithms working in three-dimensional space. J Nucl Cardiol. 1997;4(6):472–6.

53. Liu YH, Sinusas AJ, Khaimov D, Gebuza BI, Wackers FJ. New hybrid count- and geometry-based method for quantification of left ventricular volumes and ejection fraction from ECG-gated SPECT: methodology and validation. J Nucl Cardiol. 2005;12(1):55–65.

54. Liu YH. Quantification of nuclear cardiac images: the Yale approach. J Nucl Cardiol. 2007;14(4):483–91.

55. Smith WH, Kastner RJ, Calnon DA, Segalla D, Beller GA, Watson DD. Quantitative gated single photon emission computed tomography imaging: a counts-based method for display and measurement of regional and global ventricular systolic function. J Nucl Cardiol. 1997;4(6):451–63.

56. Calnon DA, Kastner RJ, Smith WH, Segalla D, Beller GA, Watson DD. Validation of a new counts-based gated single photon emission computed tomography method for quantifying left ventricular systolic function: comparison with equilibrium radionuclide angiography. J Nucl Cardiol. 1997;4(6):464–71.

57. Feng B, Sitek A, Gulberg G. The prolate spheroidal transform for gated SPECT. IEEE Trans Nucl Sci. 2001;48:872–5.

58. Feng B, Sitek A, Gullberg GT. Calculation of the left ventricular ejection fraction without edge detection: application to small hearts. J Nucl Med. 2002;43(6):786–94.

59. Khalil MM, Attia A, Ali M, Ziada G, Omar A, Elgazzar A. Echocardiographic validation of the layer of maximum count method in the estimation of the left ventricular EF using gated myocardial perfusion SPECT: correlation with QGS, ECTb, and LVGTF. Nucl Med Commun. 2009;30(8):622–8.

60. Khalil MM, Elgazzar A, Khalil W, Omar A, Ziada G. Assessment of left ventricular ejection fraction by four different methods using 99mTc tetrofosmin gated SPECT in patients with small hearts: correlation with gated blood pool. Nucl Med Commun. 2005;26(10):885–93.

61. Lomsky M, Richter J, Johansson L, El-Ali H, Astrom K, Ljungberg M, et al. A new automated method for analysis of gated-SPECT images based on a three-dimensional heart shaped model. Clin Physiol Funct Imaging. 2005;25(4):234–40.

62. Lomsky M, Richter J, Johansson L, Hoilund-Carlsen PF, Edenbrandt L. Validation of a new automated method for analysis of gated-SPECT images. Clin Physiol Funct Imaging. 2006;26(3):139–45.

63. Garcia EV, Van Train K, Maddahi J, Prigent F, Friedman J, Areeda J, et al. Quantification of rotational thallium-201 myocardial tomography. J Nucl Med. 1985;26(1):17–26.

64. Ficaro EP, Corbett JR. Advances in quantitative perfusion SPECT imaging. J Nucl Cardiol. 2004;11(1):62–70.

65. Klein JL, Garcia EV, DePuey EG, Campbell J, Taylor AT, Pettigrew RI, et al. Reversibility bull's-eye: a new polar bull's-eye map to quantify reversibility of stress-induced SPECT thallium-201 myocardial perfusion defects. J Nucl Med. 1990;31(7):1240–6.

66. DePuey EG, Roubin GS, DePasquale EE, Nody AC, Garcia EV, King SB, et al. Sequential multivessel coronary angioplasty assessed by thallium-201 tomography. Catheter Cardiovasc Diagn. 1989;18(4):213–21.

67. Hesse B, Lindhardt TB, Acampa W, Anagnostopoulos C, Ballinger J, Bax JJ, et al. EANM/ESC guidelines for radionuclide imaging of cardiac function. Eur J Nucl Med Mol Imaging. 2008;35(4):851–85.

68. Gibbons RJ, Miller TD, Christian TF. Infarct size measured by single photon emission computed tomographic imaging with (99m)Tc-sestamibi: a measure of the efficacy of therapy in acute myocardial infarction. Circulation. 2000;101(1):101–8.

69. Cerqueira MD, Weissman NJ, Dilsizian V, Jacobs AK, Kaul S, Laskey WK, et al. Standardized myocardial segmentation and nomenclature for tomographic imaging of the heart. A statement for healthcare professionals from the Cardiac Imaging Committee of the Council on Clinical Cardiology of the American Heart Association. Int J Cardiovasc Imaging. 2002;18(1):539–42.

70. Hachamovitch R, Berman DS, Kiat H, Cohen I, Cabico JA, Friedman J, et al. Exercise myocardial perfusion SPECT in patients without known coronary artery disease: incremental prognostic value and use in risk stratification. Circulation. 1996;93(5):905–14.

71. Garcia EV, Slomka P, Moody JB, Germano G, Ficaro EP. Quantitative clinical nuclear cardiology, part 1: established applications. J Nucl Med. 2019;60(11):1507–16.

72. Hsu CC, Chen YW, Hao CL, Chong JT, Lee CI, Tan HT, et al. Comparison of automated 4D-MSPECT and visual analysis for evaluating myocardial perfusion in coronary artery disease. Kaohsiung J Med Sci. 2008;24(9):445–52.

73. Germano G. Quantitative analysis in myocardial SPECT imaging. In: Zaidi H, editor. Quantitative analysis in nuclear medicine imaging. New York: Springer; 2006.

74. Hachamovitch R, Hayes SW, Friedman JD, Cohen I, Berman DS. Comparison of the short-term survival benefit associated with revascularization compared with medical therapy in patients with no prior coronary artery disease undergoing stress myocardial perfusion single photon emission computed tomography. Circulation. 2003;107(23):2900–7.

75. Hachamovitch R, Rozanski A, Shaw LJ, Stone GW, Thomson LE, Friedman JD, et al. Impact of ischaemia and scar on the therapeutic benefit derived from myocardial revascularization vs. medical therapy among patients undergoing stress-rest myocardial perfusion scintigraphy. Eur Heart J. 2011;32(8):1012–24.

76. Van Train KF, Areeda J, Garcia EV, Cooke CD, Maddahi J, Kiat H, et al. Quantitative same-day rest-stress technetium-99m-sestamibi SPECT: definition and validation of stress normal limits and criteria for abnormality. J Nucl Med. 1993;34(9):1494–502.

77. Van Train KF, Garcia EV, Maddahi J, Areeda J, Cooke CD, Kiat H, et al. Multicenter trial validation for quantitative analysis of same-day rest-stress technetium-99m-sestamibi myocardial tomograms. J Nucl Med. 1994;35(4):609–18.

78. Slomka PJ, Nishina H, Berman DS, Akincioglu C, Abidov A, Friedman JD, et al. Automated quantification of myocardial perfusion SPECT using simplified normal limits. J Nucl Cardiol. 2005;12(1):66–77.

79. Faber TL, Modersitzki J, Folks RD, Garcia EV. Detecting changes in serial myocardial perfusion SPECT: a simulation study. J Nucl Cardiol. 2005;12(3):302–10.

80. Slomka PJ, Nishina H, Berman DS, Kang X, Friedman JD, Hayes SW, et al. Automatic quantification of myocardial perfusion stress-rest change: a new measure of ischemia. J Nucl Med. 2004;45(2):183–91.

81. Wolak A, Slomka PJ, Fish MB, Lorenzo S, Acampa W, Berman DS, et al. Quantitative myocardial-perfusion SPECT: comparison of three state-of-the-art software packages. J Nucl Cardiol. 2008;15(1):27–34.

82. Garcia EV, Santana CA, Faber TL, Cooke CD, Folks RD. Comparison of the diagnostic performance for detection of coronary artery disease (CAD) of their program (QPS) with that of the Emory Cardiac Toolbox (ECTb) for automated quantification of myocardial perfusion. J Nucl Cardiol. 2008;15(3):476; author reply -8.

83. Knollmann D, Knebel I, Koch KC, Gebhard M, Krohn T, Buell U, et al. Comparison of SSS and SRS calculated from normal databases provided by QPS and 4D-MSPECT manufacturers and from identical institutional normals. Eur J Nucl Med Mol Imaging. 2008;35(2):311–8.

84. Shaw LJ, Iskandrian AE. Prognostic value of gated myocardial perfusion SPECT. J Nucl Cardiol. 2004;11(2):171–85.

85. Hachamovitch R, Berman DS. The use of nuclear cardiology in clinical decision making. Semin Nucl Med. 2005;35(1):62–72.

86. Achtert AD, King MA, Dahlberg ST, Pretorius PH, LaCroix KJ, Tsui BM. An investigation of the estimation of ejection fractions and cardiac volumes by a quantitative gated SPECT software package in simulated gated SPECT images. J Nucl Cardiol. 1998;5(2):144–52.

87. Xu Y, Kavanagh P, Fish M, Gerlach J, Ramesh A, Lemley M, et al. Automated quality control for segmentation of myocardial perfusion SPECT. J Nucl Med. 2009;50(9):1418–26.

88. Sharir T, Bacher-Stier C, Dhar S, Lewin HC, Miranda R, Friedman JD, et al. Identification of severe and extensive coronary artery disease by postexercise regional wall motion abnormalities in Tc-99m sestamibi gated single-photon emission computed tomography. Am J Cardiol. 2000;86(11):1171–5.

89. Sharir T, Berman DS, Waechter PB, Areeda J, Kavanagh PB, Gerlach J, et al. Quantitative analysis of regional motion and thickening by gated myocardial perfusion SPECT: normal heterogeneity and criteria for abnormality. J Nucl Med. 2001;42(11):1630–8.

90. Buvat I, Bartlett ML, Kitsiou AN, Dilsizian V, Bacharach SL. A "hybrid" method for measuring myocardial wall thickening from gated PET/SPECT images. J Nucl Med. 1997;38(2):324–9.

91. Berman D, Germano G. Clinical gated cardiac SPECT. 1st ed. Armonk: Futura Publishing Company; 1999.

92. Slomka PJ, Berman DS, Xu Y, Kavanagh P, Hayes SW, Dorbala S, et al. Fully automated wall motion and thickening scoring system for myocardial perfusion SPECT: method development and validation in large population. J Nucl Cardiol. 2012;19(2):291–302.

93. Mandinov L, Eberli FR, Seiler C, Hess OM. Diastolic heart failure. Cardiovasc Res. 2000;45(4):813–25.

94. Villari B, Betocchi S, Pace L, Piscione F, Russolillo E, Ciarmiello A, et al. Assessment of left ventricular diastolic function: comparison of contrast ventriculography and equilibrium radionuclide angiography. J Nucl Med. 1991;32(10):1849–53.

95. Kumita S, Cho K, Nakajo H, Toba M, Uwamori M, Mizumura S, et al. Assessment of left ventricular diastolic function with electrocardiography-gated myocardial perfusion SPECT: comparison with multigated equilibrium radionuclide angiography. J Nucl Cardiol. 2001;8(5):568–74.

96. Akincioglu C, Berman DS, Nishina H, Kavanagh PB, Slomka PJ, Abidov A, et al. Assessment of diastolic function using 16-frame 99mTc-sestamibi gated myocardial perfusion SPECT: normal values. J Nucl Med. 2005;46(7):1102–8.

97. Sciagra R, Giaccardi M, Porciani MC, Colella A, Michelucci A, Pieragnoli P, et al. Myocardial perfusion imaging using gated SPECT in heart failure patients undergoing cardiac resynchronization therapy. J Nucl Med. 2004;45(2):164–8.

98. Chen J, Garcia EV, Folks RD, Cooke CD, Faber TL, Tauxe EL, et al. Onset of left ventricular mechanical contraction as determined by phase analysis of ECG-gated myocardial perfusion SPECT imaging: development of a diagnostic tool for assessment of cardiac mechanical dyssynchrony. J Nucl Cardiol. 2005;12(6):687–95.

99. Romero-Farina G, Aguade-Bruix S, Candell-Riera J, Pizzi MN, Garcia-Dorado D. Cut-off values of myocardial perfusion gated-SPECT phase analysis parameters of normal subjects, and conduction and mechanical cardiac diseases. J Nucl Cardiol. 2015;22(6):1247–58.

100. Corbett JR, Akinboboye OO, Bacharach SL, Borer JS, Botvinick EH, DePuey EG, et al. Equilibrium radionuclide angiocardiography. J Nucl Cardiol. 2006;13(6):e56–79.

101. Nichols KJ, Van Tosh A, De Bondt P, Bergmann SR, Palestro CJ, Reichek N. Normal limits of gated blood pool SPECT count-based regional cardiac function parameters. Int J Cardiovasc Imaging. 2008;24(7):717–25.

102. De Bondt P, Nichols KJ, De Winter O, De Sutter J, Vanderheyden M, Akinboboye OO, et al. Comparison among tomographic radionuclide ventriculography algorithms for computing left and right ventricular normal limits. J Nucl Cardiol. 2006;13(5):675–84.

103. Van Kriekinge SD, Berman DS, Germano G. Automatic quantification of left ventricular ejection fraction from gated blood pool SPECT. J Nucl Cardiol. 1999;6(5):498–506.

104. Vanhove C, Franken PR. Left ventricular ejection fraction and volumes from gated blood pool tomography: comparison between two automatic algorithms that work in three-dimensional space. J Nucl Cardiol. 2001;8(4):466–71.

105. Ficaro E, Quaife R, Kritzman J, Corbett J. Validation of a new fully automatic algorithm for quantification of gated blood pool SPECT: correlations with planar gated blood pool and perfusion SPECT. J Nucl Med. 2002;43(Suppl):97P.

106. Nichols K, Saouaf R, Ababneh AA, Barst RJ, Rosenbaum MS, Groch MW, et al. Validation of SPECT equilibrium radionuclide angiographic right ventricular parameters by cardiac magnetic resonance imaging. J Nucl Cardiol. 2002;9(2):153–60.

107. De Bondt P, Claessens T, Rys B, De Winter O, Vandenberghe S, Segers P, et al. Accuracy of 4 different algorithms for the analysis of tomographic radionuclide ventriculography using a physical, dynamic 4-chamber cardiac phantom. J Nucl Med. 2005;46(1):165–71.

108. Nichols K, Humayun N, De Bondt P, Vandenberghe S, Akinboboye OO, Bergmann SR. Model dependence of gated blood pool SPECT ventricular function measurements. J Nucl Cardiol. 2004;11(3):282–92.

109. Port SC. Tomographic equilibrium radionuclide angiography: has its time arrived? J Nucl Cardiol. 2004;11(3):242–4.

110. Adachi I, Umeda T, Shimomura H, Suwa M, Komori T, Ogura Y, et al. Comparative study of quantitative blood pool SPECT imaging with 180 degrees and 360 degrees acquisition orbits on accuracy of cardiac function. J Nucl Cardiol. 2005;12(2):186–94.

111. Heston TF, Sigg DM. Quantifying transient ischemic dilation using gated SPECT. J Nucl Med. 2005;46(12):1990–6.

112. McLaughlin MG, Danias PG. Transient ischemic dilation: a powerful diagnostic and prognostic finding of stress myocardial perfusion imaging. J Nucl Cardiol. 2002;9(6):663–7.

113. Hu LH, Sharir T, Miller RJH, Einstein AJ, Fish MB, Ruddy TD, et al. Upper reference limits of transient ischemic dilation ratio for different protocols on new-generation cadmium zinc telluride cameras: a report from REFINE SPECT registry. J Nucl Cardiol. 2020;27(4):1180–9.

114. Okwuosa TM, Hampole CV, Ali J, Williams KA. Left ventricular mass from gated SPECT myocardial perfusion imaging: comparison with cardiac computed tomography. J Nucl Cardiol. 2009;16(5):775–83.

115. Nensa F, Bamberg F, Rischpler C, Menezes L, Poeppel TD, la Fougere C, et al. Hybrid cardiac imaging using PET/MRI: a joint position statement by the European Society of Cardiovascular Radiology (ESCR) and the European Association of Nuclear Medicine (EANM). Eur Radiol. 2018;28(10):4086–101.

116. Ficaro E, Kritzman J, Hamilton T, Mitchell T, Corbett J. Effect on attenuation corrected myocardial perfusion SPECT on left ventricular ejection fraction estimates [abstract]. J Nucl Med. 2000;41:166.

117. Groch MW, Takamiya Y, Groch PJ, Erwin WD. Quantitative gated myocardial SPECT: effect of collimation on left-ventricular ejection fraction. J Nucl Med Technol. 2000;28(1):36–40.

118. Hambye AS, Vervaet A, Dobbeleir A. Variability of left ventricular ejection fraction and volumes with quantitative gated SPECT: influence of algorithm, pixel size and reconstruction parameters in small and normal-sized hearts. Eur J Nucl Med Mol Imaging. 2004;31(12):1606–13.

119. Hyun IY, Kwan J, Park KS, Lee WH. Reproducibility of Tl-201 and Tc-99m sestamibi gated myocardial perfusion SPECT measurement of myocardial function. J Nucl Cardiol. 2001;8(2):182–7.

120. Manrique A, Hitzel A, Vera P. Impact of photon energy recovery on the assessment of left ventricular volume using myocardial perfusion SPECT. J Nucl Cardiol. 2004;11(3):312–7.

121. Navare SM, Wackers FJ, Liu YH. Comparison of 16-frame and 8-frame gated SPET imaging for determination of left ventricular volumes and ejection fraction. Eur J Nucl Med Mol Imaging. 2003;30(10):1330–7.

122. Pai M, Yang YJ, Im KC, Hong IK, Yun SC, Kang DH, et al. Factors affecting accuracy of ventricular volume and ejection fraction measured by gated tl-201 myocardial perfusion single photon emission computed tomography. Int J Cardiovasc Imaging. 2006;22(5):671–81.

123. Vallejo E, Dione DP, Bruni WL, Constable RT, Borek PP, Soares JP, et al. Reproducibility and accuracy of gated SPECT for determination of left ventricular volumes and ejection fraction: experimental validation using MRI. J Nucl Med. 2000;41(5):874–82; discussion 83–6.

124. Vanhove C, Franken PR, Defrise M, Bossuyt A. Comparison of 180 degrees and 360 degrees data acquisition for determination of left ventricular function from gated myocardial perfusion tomography and gated blood pool tomography. Eur J Nucl Med Mol Imaging. 2003;30(11):1498–504.

125. Marie PY, Djaballah W, Franken PR, Vanhove C, Muller MA, Boutley H, et al. OSEM reconstruction, associated with temporal Fourier and depth-dependant resolution recovery filtering, enhances results from sestamibi and 201Tl 16-interval gated SPECT. J Nucl Med. 2005;46(11):1789–95.

126. Vera P, Manrique A, Pontvianne V, Hitzel A, Koning R, Cribier A. Thallium-gated SPECT in patients with major myocardial infarction: effect of filtering and zooming in comparison with equilibrium radionuclide imaging and left ventriculography. J Nucl Med. 1999;40(4):513–21.

127. Manrique A, Hitzel A, Gardin I, Dacher JN, Vera P. Impact of Wiener filter in determining the left ventricular volume and ejection fraction using thallium-201 gated SPECT. Nucl Med Commun. 2003;24(8):907–14.

128. Gremillet E, Champailler A, Soler C. Fourier temporal interpolation improves electrocardiograph-gated myocardial perfusion SPECT. J Nucl Med. 2005;46(11):1769–74.

129. Nichols K, Dorbala S, DePuey EG, Yao SS, Sharma A, Rozanski A. Influence of arrhythmias on gated SPECT myocardial perfusion and function quantification. J Nucl Med. 1999;40(6):924–34.

130. Kim DW, Park SA, Kim CG. Gating error because of prominent T waves with ECG-gated myocardial SPECT. Clin Nucl Med. 2008;33(4):278–9.

131. Kasai T, Depuey EG, Shah AA, Merla VC. Impact of gating errors with electrocardiography gated myocardial perfusion SPECT. J Nucl Cardiol. 2003;10(6):709–11.

132. Nakajima K, Higuchi T, Taki J, Kawano M, Tonami N. Accuracy of ventricular volume and ejection fraction measured by gated myocardial SPECT: comparison of 4 software programs. J Nucl Med. 2001;42(10):1571–8.

133. Khalil MM, Elgazzar A, Khalil W. Evaluation of left ventricular ejection fraction by the quantitative algorithms QGS, ECTb, LMC and LVGTF using gated myocardial perfusion SPECT: investigation of relative accuracy. Nucl Med Commun. 2006;27(4):321–32.

134. Arsanjani R, Xu Y, Dey D, Fish M, Dorbala S, Hayes S, et al. Improved accuracy of myocardial perfusion SPECT for the detection of coronary artery disease using a support vector machine algorithm. J Nucl Med. 2013;54(4):549–55.

135. Betancur J, Rubeaux M, Fuchs TA, Otaki Y, Arnson Y, Slipczuk L, et al. Automatic valve plane localization in myocardial perfusion SPECT/CT by machine learning: anatomic and clinical validation. J Nucl Med. 2017;58(6):961–7.

136. Betancur J, Commandeur F, Motlagh M, Sharir T, Einstein AJ, Bokhari S, et al. Deep learning for prediction of obstructive disease from fast myocardial perfusion SPECT: a multicenter study. JACC Cardiovasc Imaging. 2018;11(11):1654–63.

137. Shi L, Onofrey JA, Liu H, Liu YH, Liu C. Deep learning-based attenuation map generation for myocardial perfusion SPECT. Eur J Nucl Med Mol Imaging. 2020;47(10):2383–95.

Tracer Kinetic Modeling: Basics and Concepts

20

Kjell Erlandsson

Contents

20.1   Introduction

In nuclear medicine, all studies are dynamic. Although most studies performed in nuclear medicine departments consist of a single static scan, the temporal dimension plays an important role in terms of the timing of the scan after administration of the tracer as well as its length.

In general, a radiotracer is administered by intravenous injection and clinical information is obtained from the uptake of the tracer in different organs and tissues. The uptake is determined by the delivery, retention and clearance of the tracer [1]. The delivery and clearance rates are dependent on the blood flow and the extraction of the tracer from blood to tissue while the retention is determined by metabolism of the tracer or binding of tracer molecules to specific or unspecific binding sites. All these processes are dynamic which, together with the physical decay of the radionuclide, leads to the tracer uptake chang-

K. Erlandsson (✉)
Institute of Nuclear Medicine, University College London, London, UK
e-mail: k.erlandsson@ucl.ac.uk

ing over time in both concentration and spatial distribution. In order to determine quantitative parameters related to physiological or biochemical processes, it is necessary to determine the time-course of the tracer concentration in different organs and tissues. This can be done with a dynamic data acquisition protocol, consisting of a series of scans performed over a period of time from the administration of the radiotracer. Once sufficient knowledge has been accumulated regarding the kinetic behaviour of a certain tracer, it may be possible to develop simplified study protocols, which can provide relevant clinical information while being more patient friendly [2].

Having performed a dynamic acquisition, quantitative values for physiological or biochemical parameters can be determined by applying various mathematical tools to the data. This procedure is known as "kinetic analysis". Time–activity curves (TACs), representing the time-course of tracer concentration in the image, can be generated from dynamic PET or SPECT data. TACs can be obtained either for volumes of interest (VOIs) or for individual voxels, in the case parametric images are required. Absolute quantification of radioactivity is needed and therefore correction for physical effects such as attenuation, scatter, random coincidences (PET), and dead time are essential. Correction for partial volume effects (PVE) may also be needed. PVE correspond to contribution of information between adjacent image regions due to the limited spatial resolution in PET and SPECT [3]. Also, motion correction is obviously essential.

Kinetic analysis is done using a mathematical model of tracer behaviour [4], usually a compartmental model. In order to use such a model, it is necessary to have information about the tracer delivery in the form of an input function, ideally representing the time-course of tracer concentration in arterial plasma. This type of analysis can be useful within different clinical areas, such as cardiology, oncology and neurology, where tracers such as ^{15}O-H$_2$O, ^{18}F-FDG and ^{123}I-IBZM are used for quantification of blood flow, metabolic rate and neuroreceptor binding, respectively. In this chapter, we will describe the basic mathematical tools and concepts used in tracer kinetic modelling.

20.2 Compartmental Modelling

20.2.1 Definitions and Assumptions

In kinetic modelling theory, the term "steady state" is used for the situation when a certain parameter does not change with time. The term "equilibrium" is used for the situation when all compartments in a model are in steady state.

A series of assumptions are needed to proceed with tracer kinetic modelling. The most important of these are [5]:

1. The physiological processes that affect the measurements (e.g. blood flow) are in a steady state throughout the experiment.
2. The radio-ligands used are administered in tracer concentrations, and therefore do not affect the physiological or biochemical processes being studied.
3. The tracer concentration within a compartment is homogeneous—i.e. instantaneous mixing is assumed.

20.2.2 Compartmental Models

Physiological or biochemical systems are often described using compartmental models, in which a tracer is assumed to be transferred between a number of compartments, which can represent separate regions in space (e.g. vascular, interstitial or intracellular space), or alternatively different chemical states (e.g. parent compound, metabolic products or receptor bound tracer molecules). The rate of transfer from one compartment to another is proportional to the concentration in the compartment of origin and a first-order rate constant. In general, a compartmental model is described by a system of differential equations, where each equation corresponds to the sum of all transfer rates to and from a specific compartment:

$$\frac{\mathrm{d}}{\mathrm{d}t}C_i(t) = \sum_{\substack{j=1,\dots N \\ j \neq i}} \left(k_{ij}C_j(t) - k_{ji}C_i(t) \right); \quad i = 1,\dots N$$

(20.1)

where $C_i(\cdot)$ is the tracer concentration in compartment i, k_{ij} is the rate constant for transfer to

compartment i from compartment j, and N is the number of compartments in the model.

Compartmental models can be either reversible or irreversible. The irreversible models are those which contain at least one compartment that does not have an outflow.

In nuclear medicine, a single-index nomenclature is normally used to denote the rate constants. The rate constants for transfer from blood to tissue and from tissue to blood are called K_1 and k_2, respectively, and additional rate constants in the model are called k_3, k_4, etc. These symbols are sometimes qualified with asterisks or primes when necessary. Traditionally, a capital K is used in K_1, while lower case k:s are used for the other rate constants. This is to reflect a distinction in terms of units. While k_i, $i \geq 2$, are expressed in units of [min^{-1}], K_1 is expressed in same units as blood flow: [mL/min/mL] (mL of blood per minute per mL of tissue).

20.2.3 Solving Compartmental Models: The Laplace Transform

The Laplace transform is a useful tool when it comes to solving systems of linear first order differential equation, such as Eq. (20.1). The Laplace transform is defined as:

$$F(s) = \int_0^\infty e^{-st} f(t) \, dt \qquad (20.2)$$

where s is a complex Laplace-space variable.

Using the properties listed in Table 20.1, it is possible to obtain solutions for complex compartmental systems. In particular, the property relating the transform of the derivative of a function to that of the original function is the key to the solution. After taking the Laplace transform of both sides in each equation, the terms are rearranged into the transform of a simple function, such as a sum of constants and exponential functions, and the inverse Laplace transform can then be found.

In the case of biological systems, the solution can often be expressed as:

Table 20.1 Laplace transform pairs

Time domain	Laplace domain
$f(t)$	$F(s)$
k	k/s
e^{kt}	$1/(s-k)$
$ag(t) + bh(t)$	$aG(s) + bH(s)$
$g'(t)$	$sG(s) - g(0)$
$g(t) \otimes h(t)$	$G(s)H(s)$

k, a and b are constants, t and s are variables, $g(\cdot)$, $G(\cdot)$, $h(\cdot)$ and $H(\cdot)$ are functions, $'$ represents derivative and $\otimes$ convolution

$$C_T(t) = H_N(t) \otimes C_a(t) \qquad (20.3)$$

where $C_a(\cdot)$ and $C_T(\cdot)$ are the input and output functions, respectively, $\otimes$ represents the convolution operation and $H_N(\cdot)$ is the impulse response function (IRF) of the model, which has the following general form [6]:

$$H_N(t) = \sum_{i=1}^N \phi_i e^{-\theta_i t} \qquad (20.4)$$

where ϕ_i and θ_i are functions of the individual rate constants of the model (K_1, k_2...), and N is the number of compartments. Irreversible compartments correspond to terms with $\theta_i = 0$, i.e. a constant. The number of terms in the impulse response function is equal to the number of compartments in the model.

Appendix 1 contains examples of Laplace transform derived solutions for different compartmental models. Sometimes it may be necessary to use the technique of partial fractions expansion [7] to find the individual terms of the impulse response function.

20.3 The 1-Tissue Compartment Model: Blood Flow

From a physiological point of view, the term "blood flow" refers to the volume of blood delivered to an organ per unit of time, often expressed in [mL/min], while "perfusion" refers to blood flow per unit of tissue-volume [mL/min/mL]. In the context of tracer kinetic modelling, the two terms are used interchangeably with the latter definition.

A model for quantifying blood flow was developed around the middle of the last century [8]. It was based on the Fick principle, which states that the rate of change of the tracer concentration in tissue is proportional to blood flow and to the difference in the arterial and venous concentrations:

$$\frac{\mathrm{d}}{\mathrm{d}t}C_{\mathrm{T}}(t) = F\left(C_{\mathrm{a}}(t) - C_{\mathrm{v}}(t)\right) \quad (20.5)$$

where $C_{\mathrm{T}}(\cdot)$, $C_{\mathrm{a}}(\cdot)$ and $C_{\mathrm{v}}(\cdot)$ are the tissue, arterial and venous tracer concentrations, respectively, F is blood flow and t is time.

Assuming that the tracer concentration in tissue is at equilibrium with that in venous blood ($C_{\mathrm{T}}(t)/C_{\mathrm{v}}(t) = V_{\mathrm{D}}$), Eq. (20.5) can be rewritten as follows [9]:

$$\frac{\mathrm{d}}{\mathrm{d}t}C_{\mathrm{T}}(t) = FC_{\mathrm{a}}(t) - \frac{F}{V_{\mathrm{D}}}C_{\mathrm{T}}(t) \quad (20.6)$$

The constant V_{D} is the "distribution volume" or "volume of distribution", representing the volume of tissue in which the tracer can move around freely. It is expressed in the units [mL/mL], i.e. mL per mL of tissue, and has a value in the range [0,1]. It is numerically equal to a quantity known as the partition coefficient.

The Kety–Schmidt model is only valid for tracers that are fully extracted from blood to tissue. This is true for many of the tracers used for measuring blood flow, such as ^{15}O-H_2O, ^{13}N-NH_4 and ^{133}Xe. On the other hand, if the tracer is not fully extracted (as in the case of e.g. ^{82}Rb), this may be taken into account using the extraction fraction, E, defined as the fraction of tracer extracted in a single pass through the capillary bed. The extraction fraction can be calculated using the Renkin–Crone formula [10, 11]:

$$E = 1 - \mathrm{e}^{-\mathrm{PS}/F} \quad (20.7)$$

where PS is the permeability surface area product, expressed in the same unites as F [mL/min/mL]. (NB: E is dependent on F.)

Replacing F by FE in Eq. (20.6) and defining the constants $K_1 = FE$ and $k_2 = K_1/V_{\mathrm{D}}$ leads to:
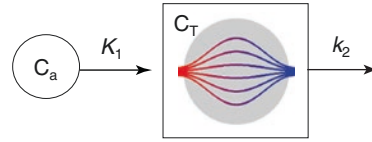
Fig. 20.1 The blood flow model (1-TC). C_{a} and C_{T} are the tracer concentrations in arterial blood and in tissue, respectively, and K_1 and k_2 are rate constants

$$\frac{\mathrm{d}}{\mathrm{d}t}C_{\mathrm{T}}(t) = K_1 C_{\mathrm{a}}(t) - k_2 C_{\mathrm{T}}(t) \quad (20.8)$$

Equation (20.8) can be interpreted as the operational equation for a simple 1-compartment system (Fig. 20.1), and has the solution (see Appendix 1):

$$C_{\mathrm{T}}(t) = K_1 \mathrm{e}^{-k_2 t} \otimes C_{\mathrm{a}}(t) \quad (20.9)$$

The model in Fig. 20.1 has in the past been referred to as a two-compartment model and represented with the arrow corresponding to k_2 directed from the tissue compartment back to blood. This may seem intuitively correct; however, it does not correspond to the actual mathematical relationship between the input and output functions. In practice, the input function is determined separately, and blood is not treated as a compartment in a mathematical sense. For clarity, it may therefore be appropriate to use a nomenclature, in which a model is named after the number of compartments used for describing the tracer distribution in tissue. Hereby, the model in Fig. 20.1 would be called a 1-tissue compartment (1-TC) model.

20.4 Multi-tissue Compartment Models: Neuroreceptor Mapping

Neuroreceptor mapping deals with studies of the systems that control the chemical transmission of neuronal signals across the synapse between two neurons. When an electrical impulse reaches the end of a presynaptic nerve cell, a series of events

are initiated: (1) Neurotransmitter substance is released from vesicles within the presynaptic cell into the synaptic cleft; (2) The neurotransmitter diffuses across to the postsynaptic cell where it binds to a specific type of receptors, triggering a new electrical impulse; (3) The neurotransmitter substance in the synapse is reabsorbed into the presynaptic cell via channels known as transporters, in order to prepare the synapse for the arrival of a new signal. In psychiatric studies, it is of interest to measure the concentration of different types of receptors or transporters in different brain regions. This can be achieved using radiotracers that bind selectively to the receptors or transporters of interest.

20.4.1 In Vitro Quantification

The theory for quantification of neuroreceptor binding in vivo is based on the theory for in vitro binding assays, which involves incubation of a receptor-enriched preparation with a radio-ligand. The basis for this theory is the law of mass action, which states that the ligand binds to receptors (association) at a rate proportional to the concentration of ligand and to the concentration of receptors, and that the resultant ligand-receptor complex breaks down (dissociation) at a rate proportional to the concentration of the complex [12]. This is described in the following equation:

$$\frac{d}{dt}[RL] = k_{on}[R][L] - k_{off}[RL] \quad (20.10)$$

where $[R]$, $[L]$ and $[RL]$ are the concentrations of receptors, ligand and receptor–ligand complex, respectively, and k_{on} and k_{off} are the rate constants for association and dissociation, respectively. Equation (20.10) can be represented as a simple two-compartment model with the rate constants $k_{on}[R]$ and k_{off} (Fig. 20.2). In practice, $k_{on}[R]$ can only be assumed to be constant if $[R] \gg [L]$ (tracer conditions).

During in vitro experiments, a state of equilibrium will be reached after a while, so that the rate of association is equal to the rate of dissociation, and the following relation is obtained:

Fig. 20.2 The in vitro model. L, R and LR represent concentration of ligand, receptors, and ligand–receptor complex, respectively, and k_{on} and k_{off} are constants

$$k_{on}[R][L] = k_{off}[RL] \Leftrightarrow \frac{[R][L]}{[RL]} = \frac{k_{off}}{k_{on}} \equiv K_D \quad (20.11)$$

The constant K_D is known as the equilibrium dissociation constant. Its reciprocal value is known as the affinity of the ligand for the receptor. Thus, a low K_D value corresponds to high affinity.

We now introduce a different set of symbols for free ligand, $F = [L]$, bound ligand, $B = [RL]$, and total receptor concentration, $B_{max} = [R] + [RL]$. With these symbols we can rewrite Eq. (20.11) as follows:

$$B = \frac{B_{max}F}{K_D + F} \quad (20.12)$$

This is known as the Michaelis–Menten equation, and describes the relation between bound and free ligand equilibrium concentrations [13]. If B is plotted as a function of F, this equation corresponds to a saturation curve, which initially rises linearly ($B/F \approx B_{max}/K_D$, $F \ll K_D$) and then gradually plateaus, asymptotically approaching a constant level ($B \approx B_{max}$, $F \gg K_D$). By measuring a series of corresponding B and F values, it is possible to estimate the parameters B_{max} and K_D. A simple solution is obtained using the Scatchard method [14], by plotting (B/F) versus B, which should give a straight line with a slope of ($-1/K_D$) and an intercept of (B_{max}/K_D), as can be seen after rewriting Eq. (20.12) as follows:

$$\frac{B}{F} = \frac{B_{max}}{K_D} - \frac{1}{K_D}B \approx \frac{B_{max}}{K_D} \equiv BP \quad (20.13)$$

The first part of the above equation is valid for any values of B and F, while the second part is an approximation valid only under tracer conditions

$(B \ll B_{\max})$. The constant BP is the "binding potential" [15], which is an important parameter in in vivo neuroreceptor studies. As human in vivo studies are always performed under tracer conditions, in order to avoid pharmacological effects, it is not possible to estimate the values of $B_{\max}$ and K_D separately—only their ratio, BP, can be estimated.

20.4.2 In Vivo Quantification

The in vivo neuroreceptor model is a combination of the two models discussed above; the blood flow model and the in vitro binding assay model. Apart from specific binding to receptors, most tracers will also exhibit so-called nonspecific binding, involving macromolecules such as proteins. Nonspecific binding is not saturable and not displaceable. A general neuroreceptor model therefore requires three tissue compartments (see Fig. 20.3), and can be described as follows:

$$\begin{cases} \dfrac{d}{dt}C_F(t) = K_1 C_p(t) + k_4 C_S(t) + k_6 C_{NS}(t) - \\ \qquad\qquad (k_2 + k_3 + k_5)C_F(t) \\ \dfrac{d}{dt}C_S(t) = k_3 C_F(t) - k_4 C_S(t) \\ \dfrac{d}{dt}C_{NS}(t) = k_5 C_F(t) - k_6 C_{NS}(t) \end{cases}$$

(20.14)

where $C_p(\cdot)$, $C_F(\cdot)$, $C_S(\cdot)$ and $C_{NS}(\cdot)$ are the tracer concentrations in plasma and in the compartments for free, specifically bound and nonspecifically bound tracer, respectively, and K_1, k_2–k_6 are rate constants.

With six free parameters (K_1, k_2–k_6) the 3-TC model is normally too complex to be useful in practical situations. All the parameters may not be identifiable,[1] given the limited amount of information available (one single TAC represents the sum of all tissue compartments) and the presence of noise in the measured data. Therefore, it

---

[1] Parameter identifiability means that a change in the parameter values should always lead to a change in the output function [16].
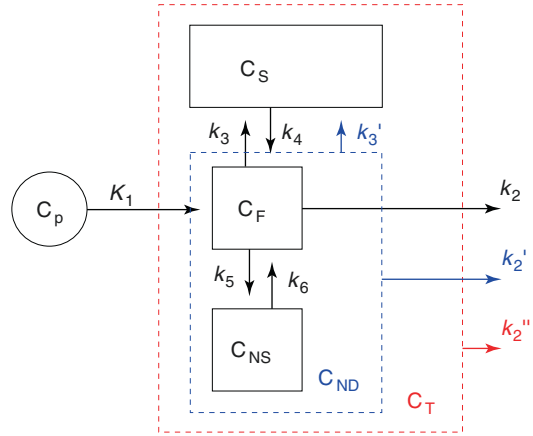
Fig. 20.3 Combined illustration of the 3-TC, 2-TC and 1-TC models for neuroreceptor quantification. C_p is the concentrations of unmetabolised tracer in plasma, C_F, C_{NS} and C_S are the concentrations of free, nonspecifically bound and specifically bound tracer in tissue, respectively, C_{ND} is the concentration of non-displaceable tracer in tissue ($C_{ND} = C_F + C_{NS}$), and C_T is the total concentration of tracer in tissue. The sets of rate constants used in the different models are: $\{K_1,\ k_2{-}k_6\}$ (3-TC), $\{K_1, k_2^{'}, k_3^{'}, k_4\}$ (2-TC) and $\{K_1, k_2^{''}\}$ (1-TC model)

is often necessary to reduce the complexity of the model by reducing the number of compartments. The 3-TC model would thereby be converted to a 2-TC or even a 1-TC model. At this point, it is important to note that when the compartmental structure of a model changes, so does the meaning of the rate constants. It may therefore be appropriate to use different symbols in different models. Hence, in the 2-TC model, k_2 and k_3 become $k_2^{'}$ and $k_3^{'}$, and in the 1-TC model, k_2 becomes $k_2^{''}$ [17]. When dealing with a single model, such distinction may not be necessary, however.

In the 2-TC model (Fig. 20.3, blue components) the free and nonspecific binding compartments are merged into the so-called "non-displaceable" (ND) compartment. The 2-TC model can be described as follows:

$$\begin{cases} \dfrac{d}{dt}C_{ND}(t) = K_1 C_p(t) + k_4 C_S(t) \\ \qquad\qquad -(k_2' + k_3')C_{ND}(t) \\ \dfrac{d}{dt}C_S(t) = k_3' C_{ND}(t) - k_4 C_S(t) \end{cases} \quad (20.15)$$

a

b
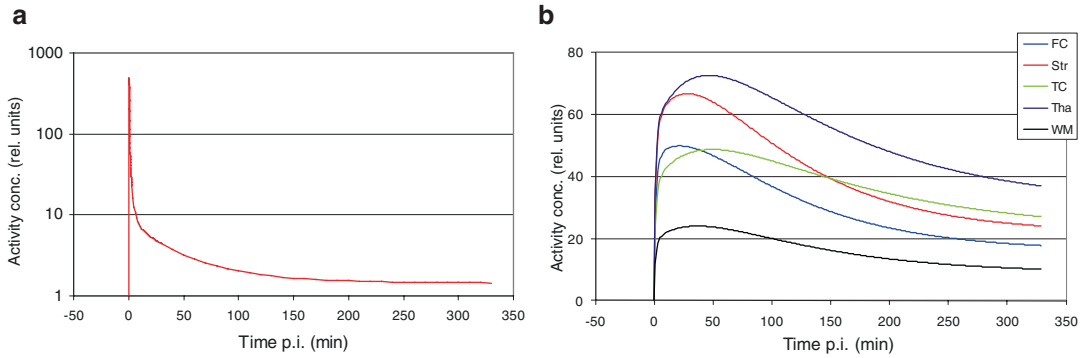
Fig. 20.4 Time–activity curves corresponding to the NMDA receptor SPECT tracer ^{123}I-CNS 1261 with bolus injection; (**a**) arterial plasma input function, (**b**) tissue

curves for various brain regions: Frontal cortex (FC), striatum (Str), temporal cortex (TC), thalamus (Tha) and white matter (WM)

where $C_{\mathrm{ND}}(\cdot)$ is the total tracer concentration in the nondisplaceable compartment, and k_2' and k_3' are rate constants specific to this model.

This simplification implicitly involves the assumption that equilibrium is rapidly established between the F- and NS-compartments, and that the free fraction in tissue, f_{ND}, is constant during the experiment. f_{ND} is defined as:

$$f_{\mathrm{ND}} = \left[\frac{C_{\mathrm{F}}}{C_{\mathrm{F}} + C_{\mathrm{NS}}} \right]_{\mathrm{eq}} = \frac{k_6}{k_5 + k_6} \quad (20.16)$$

The last equality is obtained by setting $\mathrm{d}C_{\mathrm{NS}}(t)/\mathrm{d}t$ in Eq. (20.14) to 0 (equilibrium). The tissue free fraction, f_{ND}, cannot be measured directly. The relationships between the rate constants in the 2-TC and 3-TC models can be derived by equating the transport rates between compartments in the two models, resulting in:

$$k_2' = f_{\mathrm{ND}} k_2; \quad k_3' = f_{\mathrm{ND}} k_3 \qquad (20.17)$$

In the 1-TC model (Fig. 20.3, red components), one single compartment represents non-displaceable and specifically bound tracer in tissue. It can be described by a single differential equation:

$$\frac{\mathrm{d}}{\mathrm{d}t} C_{\mathrm{T}}(t) = K_1 C_{\mathrm{p}}(t) - k_2'' C_{\mathrm{T}}(t) \quad (20.18)$$

where $C_{\mathrm{T}}(\cdot)$ is the total concentration of non-displaceable and specifically bound tracer in tissue, and k_2'' is a rate constants specific to this model. As above we obtain:

$$k_2'' = k_2' \left(\frac{k_4}{k_3' + k_4} \right) = k_2' \left(1 + \frac{k_3'}{k_4} \right)^{-1} \quad (20.19)$$

The 1-TC model for neuroreceptor quantification is mathematically equivalent to the one used for blood flow above (Fig. 20.1). The difference is that, while the main parameter of interest in the case of blood flow measurements is the uptake rate constant, $K_1 = FE$, in the case of neuroreceptor studies, the main parameter of interest is the washout rate constant, k_2'', which reflects the amount of tracer retention in tissue due to receptor binding (sometimes quantified by the parameter $\mathrm{BP}_{\mathrm{ND}} = k_3'/k_4$ (see below)).

Figure 20.4 shows an example of TACs corresponding to a SPECT study using the NMDA receptor tracer [^{123}I]CNS-1261 [18]. The tissue curves were generated with the 2-TC model using averaged rate constants (Table 20.2).

20.5 Input Function

In vivo quantification requires knowledge of the time-course of tracer concentration in arterial plasma, $C_{\mathrm{p}}(t)$, referred to as the arterial input function (AIF). Traditionally, the AIF is obtained by repeated arterial sampling throughout the experiment. The samples first need to be centrifuged, in order to separate plasma and blood cells, and estimate the plasma-to-whole blood concentration ratio (f_{pob}).

Table 20.2 Averaged rate constants for the 2-TC model for the SPECT tracer [^{123}I]CNS-1261

	K_1 (mL/min/mL)	$k_2^{'}$ (min^{-1})	$k_3^{'}$ (min^{-1})	k_4 (min^{-1})
FC	0.172	0.023	0.018	0.036
Str	0.215	0.018	0.016	0.058
TC	0.145	0.019	0.039	0.037
Tha	0.227	0.033	0.106	0.049
WM	0.076	0.025	0.078	0.075

FC frontal cortex, *Str* striatum, *TC* temporal cortex, *Tha* thalamus, *WM* white matter

A factor that complicates the quantification procedure is the presence of radioactive metabolites, produced in peripheral organs (liver, kidneys, lungs, etc.), and released back into the blood stream. If the metabolites can cross the blood–brain barrier (BBB), it would be necessary to use a more complex model with more parameters, resulting in increased variability. This problem can be avoided by appropriate tracer selection. However, radioactive metabolites in the blood stream can in general not be avoided, and metabolite correction of the AIF is therefore needed. For this purpose, high-pressure liquid chromatography (HLPC) can be used to determine the fraction of radioactivity in arterial plasma corresponding to un-metabolised tracer. This "plasma parent fraction" (f_{pp}) starts at 1 for $t = 0$ and decreases with increasing time at a rate that depends on the tracer and on the individual subject. In order to apply a correction, measured data points are fitted with an analytical function, such as e.g. a bi-exponential or the Hill function: $f_{pp}(t) = 1 + (a − 1) \cdot t^b/(c + t^b)$, where a, b and c are parameters to be optimised. For a comprehensive list of functions used for different tracers, see [19].

The measured input function is also affected by nonspecific binding in plasma. Tracer bound to protein molecules is not available for transportation across the BBB. Usually it is assumed that equilibrium is reached quickly between free and protein-bound tracer in plasma, and the free fraction in plasma, f_p, is thereby assumed to be constant during the experiment. It is possible to measure f_p (e.g. by ultrafiltration), but these measurements can have high variability, and this factor is often ignored. The concentration of free parent compound in arterial plasma can thus be obtained as follows:

$$C_{p,F}(t) = f_p C_p(t) = f_p \cdot f_{pp}(t) \cdot f_{pob}(t) \cdot C_a(t)$$
(20.20)

where f_p is the plasma free fraction (assumed constant), $f_{pp}(\cdot)$ the plasma parent fraction, $f_{pob}(\cdot)$ the plasma over whole blood ratio, $C_p(\cdot)$ the total concentration of parent compound in plasma, and $C_a(\cdot)$ the total arterial activity concentration.

Arterial sampling is an invasive and labour-intensive procedure, and it would be a clear advantage if it could be avoided. In some cases, the input function can be obtained directly from the images, if an appropriate blood pool can be identified. This is known as an image derived input function (IDIF) [20]. In thoracic studies, the heart ventricles or the aorta can be used to obtain an IDIF. In brain studies, the carotid arteries can be used but, as they are relatively small, accurate partial volume correction is needed [21]. Also, when using an IDIF, it may be necessary to take a few blood samples for metabolite and plasma-to-whole blood correction, but these samples could be venous samples rather than arterial.

20.6 Outcome Measures

The most fundamental parameters in compartmental modelling are the rate constants (K_1, k_2…). These so-called micro-parameters can usually not be determined with a high degree of precision (apart from K_1), due to noise present in the data (mainly related to limited counting-statistics in the photon detection process). Therefore various so-called macro-parameters are usually determined, by combining two or more micro-parameters, in order to obtain more robust outcome measures. For reversible tracers, the macro-parameters of interest are the total volume of distribution (V_T) and the binding potential (BP), and for irreversible tracers it is the influx rate (K_i).

20.6.1 Total Volume of Distribution

One of the most robust outcome measure is the "total volume of distribution", V_T, defined as the ratio between tracer concentration in tissue and

in plasma at equilibrium. V_T is expressed in units of [mL/mL]. V_T is useful in neuroreceptor studies since it is dependent on the receptor concentration in the target tissue but independent of blood flow (see below). In theory, it corresponds to the integral of the impulse response function of the model [6].

When using compartmental modelling, V_T can be calculated from the rate constants with expressions derived by equilibrium-analysis of the differential equations that describe each model. Thus we obtain the following expressions for the 3-TC, 2-TC and 1-TC models:

$$V_T = \left[\frac{C_T(t)}{C_p(t)}\right]_{eq} = \frac{K_1}{k_2}\left(1 + \frac{k_3}{k_4} + \frac{k_5}{k_6}\right)$$
$$= \frac{K_1}{k_2'}\left(1 + \frac{k_3'}{k_4}\right) = \frac{K_1}{k_2''}$$

$$(20.21)$$

This equation shows that V_T is independent of blood flow: Both K_1 and k_2 depend on blood flow, but their ratio does not, and neither do the rate constants k_3–k_6.

The use of the term "volume of distribution" for quantification of tracer binding may seem a bit confusing. It is used for historical reasons as its calculation is similar to that of the actual distribution volume of a tracer that exhibits neither specific nor nonspecific binding (see blood flow section above). As an afterthought, it may be interpreted as the volume of plasma containing the same total activity as 1 mL of tissue.

20.6.2 Binding Potential

The principal outcome measure in neuroreceptor studies is the binding potential, BP, but in practice it can be difficult to estimate BP according to the definition in Eq. (20.13). In the past several alternative definitions were used, which would sometimes lead to confusion. Therefore, a consensus was reached among researches in the field, and three different types of in vivo binding poten-

tials definitions were proposed: BP_F, BP_p and BP_{ND} [22]. All three are defined in terms of the ratio at equilibrium of the concentration of specifically bound tracer (C_S) vs. a reference concentration. The difference between the three lies in the reference used. For BP_F, it is the free tracer concentration in plasma ($C_{p,F} = f_p C_p$), which at equilibrium is equal to the free concentration in tissue ($C_F = f_{ND}C_{ND}$); for BP_p, it is the total concentration of parent compound in plasma (C_p); and for BP_{ND}, the concentration of nondisplaceable tracer in tissue (C_{ND}).

Another difference with in vitro studies is that in vivo measurements do not reflect the total receptor concentration, B_{max}. Some fraction of the receptors may be occupied by the endogenous transmitter substance (dopamine, serotonin…), by some drug administered to the patient, or by the tracer itself. In vivo studies reflect the concentration of available receptors, B_{avail}.

As in the case of V_T, the various BP-values can be derived from the model parameters. Also, if a brain region exists that is known not to have any specific binding, this can be used as a reference region with the volume of distribution V_{ND}. BP-values can then be derived from V_T and V_{ND} values. This approach usually yields more robust results as compared to estimating the BP-values directly from the rate constants. The relationships between BP, V_T and model parameters is summarised below and illustrated in Fig. 20.5.
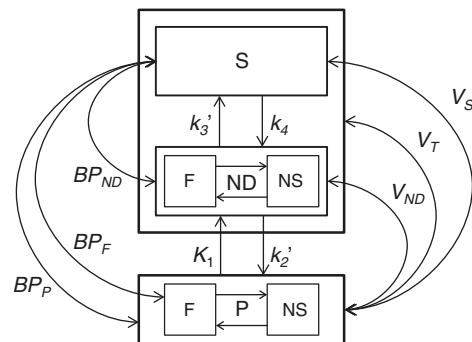
Fig. 20.5 Illustration of the relationships between various binding potentials (BP_X) and volumes of distribution (V_X). (NB: $BP_p = V_S = V_T - V_{ND}$)

$$BP_F \equiv \frac{B_{avail}}{K_D} = \left[\frac{C_S}{C_{p,F}}\right]_{eq} = \left[\frac{C_S}{C_F}\right]_{eq} = \frac{k_3}{k_4}$$

$$BP_p \equiv \left[\frac{C_S}{C_p}\right]_{eq} = f_p \cdot BP_F = \frac{K_1}{k_2'}\frac{k_3'}{k_4} = V_T - V_{ND}$$

$$BP_{ND} \equiv \left[\frac{C_S}{C_{ND}}\right]_{eq} = f_{ND} \cdot BP_F = \frac{k_3'}{k_4} = \frac{V_T - V_{ND}}{V_{ND}}$$

$$\text{(20.22)}$$

Of the three in vivo BP-measures, BP_F is the one that comes closest to the in vitro definition in Eq. (20.13), but it can be difficult to determine in practice. The use of BP_p requires the assumption that f_p is constant between scans or across groups of subjects. BP_{ND} requires the same assumption regarding f_{ND}, but has the advantage that it can be estimated using the reference tissue model, which does not require arterial sampling (see below).

It is generally assumed that a change in BP reflects a change in B_{avail}. Thereby, the fraction of receptors occupied by a drug (occupancy, O) can be estimated by measuring BP before (BP_{base}) and after giving the drug (BP_{drug}) [22]:

$$O \equiv 1 - \frac{B_{avail,drug}}{B_{avail,base}} = 1 - \frac{BP_{drug}}{BP_{base}} \quad \text{(20.23)}$$

where BP in BP_{base} and BP_{drug} can be either BP_F, BP_p or BP_{ND}.

20.7 Parameter Estimation

20.7.1 AIF Models

Once the AIF has been determined and the IRF of the model has been defined, the individual parameters (K_1, k_2...) can be estimated. This is an inverse problem, where an equation of type (Eq. 20.3) represents the forward model, and which can be solved using an iterative procedure, such as the Levenberg–Marquardt algorithm [23]. The goal is to minimise the difference between the measured data (TAC) and the model output function in a least-squares sense. Usually, some kind of weighting scheme is used before combining the data from different time points, to take into account differences in variability due to the changing activity concentration and difference in the length of each timeframe. It is necessary to take into account the fact that a measured tissue TAC will always contain a contribution from blood. This can be done by estimating an extra parameter, representing the blood volume (V_b), or by assuming it is constant (e.g. $V_b = 5\%$). It is important to remember that the total arterial concentration should be used in this term.

The forward model can be implemented using either an analytic solution for the IRF or a numerical calculation based on the differential equations, with e.g. the Runge–Kutta method [24].

20.7.2 Simultaneous Estimation

As an alternative, the input function can be built into the model itself, utilising the fact that different tissue regions have the same AIF. In this case, the AIF is described by an analytical function with a number of parameters, which are estimated simultaneously with those of several tissue TACs [25]. These TACs should be as different from each other as possible. A bonus with this method is that no metabolite correction is needed.

20.7.3 Reference Tissue Models

Another approach, which is often used in brain studies, is the reference tissue model. Here the TAC for a brain region, devoid of specific binding (reference region), is used as an indirect input function. Two alternative models that have been proposed are: The full reference tissue model (FRTM) [26, 27], based on the 2TC-model, and the simplified reference tissue model (SRTM) [28], based on the 1-TC model (see Fig. 20.6). The IRFs for these models are derived in Appendix 2.

In principle FRTM is dependent on the six rate constants: K_1, k_2', k_3', k_4, $^RK_1$ and $^Rk_2'$, where the first four belong to the target region and the latter two to the reference region. However, K_1 and $^RK_1$ only appear in the model equation as a ratio: $R_1 = K_1/^RK_1$. Furthermore, it can be assumed that

the volume of distribution of the non-displaceable compartment (V_{ND}) is the same for both regions: $K_1 / k_2' =^R K_1 /^R k_2' \Leftrightarrow k_2' = R_1^R k_2'$, and thereby the number of model parameters can be reduced to four. SRTM has the following three parameters: R_1, k_2'' and $^R k_2'$. A method for noise-reduction in SRTM has been proposed, taking into account the fact that $^R k_2'$ should be independent of the target region analysed [29].

As an illustration, Fig. 20.7 shows simulated data corresponding to the SPECT tracer ^{123}I-ADAM, which binds to serotonin transporters (presynaptic reuptake channels; 5-HTT), and can be used for measuring occupancy of anti-depressant drugs. The data were generated based on averaged parameters obtained with SRTM [30]. Time–activity curves are shown for the midbrain, which is the region with highest 5-HTT concentration, and for cerebellum, which was the reference region. The parameters used were: $R_1 = 0.85$, $^R k_2' = 0.030 \text{min}^{-1}$ and $BP_{ND} = 1.14$.

20.7.4 Spectral Analysis

From Eqs. (20.3) and (20.4) we obtain:

$$C_T(t) = C_p(t) \otimes \sum_{i=1}^{N} \phi_i e^{-\theta_i t} = \sum_{i=1}^{N} \phi_i \left(C_p(t) \otimes e^{-\theta_i t} \right)$$
$$= \sum_{i=1}^{N} \phi_i \psi_i(t)$$

In the method of spectral analysis [31], a library of basis-functions, $\psi_i(t)$, is first generated for a suitable range of θ_i values. The problem is then solved using a non-negative least-squares fitting algorithm, resulting in a limited number of components, with non-zero coefficients, ϕ_i. The number of non-zero components corresponds to the number of model compartments, which therefore does not need to be fixed beforehand. (Two adjacent non-zero coefficients, ϕ_i and ϕ_{i+1} should in this context be regarded as
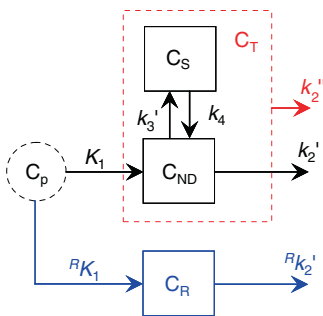
Fig. 20.6 Combined illustration of the full and the simplified reference region models. C_p is the (unknown) concentrations of non-metabolised tracer in plasma, C_{ND} and C_S are the concentrations of non-displaceable and specifically bound tracer in the target tissue, respectively, C_T is the total concentration of tracer in tissue, and C_R is the tracer concentration in the reference region. The sets of rate constants corresponding to the full and simplified models are: $\left\{ K_1, k_2', k_3', k_4,^R K_1,^R k_2' \right\}$ and $\left\{ K_1, k_2'',^R K_1,^R k_2' \right\}$, respectively

Fig. 20.7 Time–activity curves for the 5-HTT SPECT tracer ^{123}I-ADAM. The two curves represent midbrain (MB) and cerebellum (Cer), which was used as a reference region
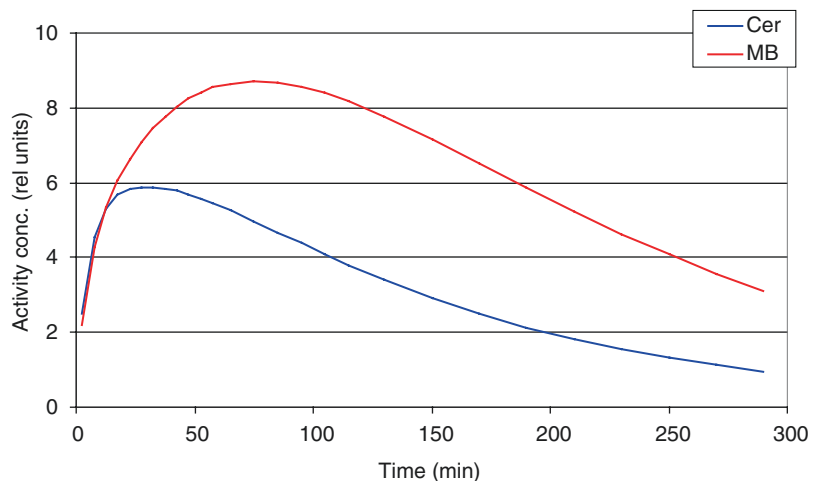
one single component, with a θ value somewhere between θ_i and θ_{i+1}.)

The spectral analysis method is not strictly valid for reference tissue models, where negative components in theory can occur. Therefore a more general method was developed using the basis pursuit technique [32].

20.7.5 Graphical Analysis

An alternative approach to compartmental modelling can be found after integrating the differential equations describing the kinetic models. This yields equations which lend themselves to graphical analysis. The basic idea is that, after an appropriate transformation, the data can be plotted as a graph and a straight line fitted to the points. The slope and intercept of the fitted line will reflect certain characteristics of the tracer uptake or binding. The Logan method [33] was developed specifically for reversible tracers, and

is obtained by plotting $y(t) = \int_0^t C_T(\tau)\,d\tau\,/\,C_T(t)$

vs. $x(t) = \int_0^t C_p(\tau)\,d\tau\,/\,C_T(t)$. After some time

(t^*), a straight line is obtained with a slope equal to V_T. This result is independent of the assumed compartmental structure of the model, as shown in Appendix 3.

This approach is also known as linearisation, since it converts a nonlinear parameter estimation problem into a linear one. For this reason, it is also quite fast, and thereby useful in voxel-based analysis. A limitation of the approach is that it may result in bias with noisy data due to correlation in the noise structure between the dependent and independent variables [34]. A more robust approach has been proposed [35]. A reference region version of the Logan method has also been developed [36].

There is a corresponding method for irreversible tracers, known as the Patlak plot [37]. Here $y(t) = C_T(t)/C_p(t)$ is plotted

vs. $x(t) = \int_0^t C_p(\tau)\,d\tau\,/\,C_p(t)$, and the slope of the
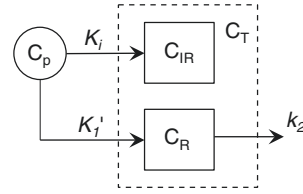
Fig. 20.8 Illustration of the Patlak model. C_p is the concentration of tracer in plasma, C_R and C_{IR} the concentrations of reversible and irreversible tracer uptake, respectively, and C_T is the total concentration of tracer in tissue. The rate constants are: $K_i = K_1 \cdot k_3/(k_2 + k_3)$, $K_1' = K_1 \cdot k_2 / (k_2 + k_3)$ and $k_2' = k_2 + k_3$. The outcome parameters are the irreversible uptake rate, K_i, and the reversible volume of distribution, $V_D = K_1' / k_2'$

linear part of the curve (after equilibrium has been reached) is the influx rate, $K_i = K_1 \cdot k_3/(k_2 + k_3)$. The intercept is the sum of the blood volume, V_b, and the reversible volume of distribution, $V_D = K_1 \cdot k_2/(k_2 + k_3)^2$. The method can be described by an uncoupled 2-TC model with one reversible and one irreversible compartment (Fig. 20.8). This approach is often used for analysis of ^{18}F-FDG data, including the dynamic whole-body imaging technique, based on a multipass, multi-bed acquisition protocol [38].

20.7.6 The Bolus/Infusion Approach

In conventional studies, the tracer is administered with a single injection over a short time period—a so-called "bolus injection". An alternative approach is to use a constant infusion protocol, where tracer is being continuously administered slowly throughout the experiment. The aim is to establish a true equilibrium situation, which allows for direct estimation of V_T as the ratio of tissue and plasma activity concentration, in accordance with the definition (Eq. 20.21) [39]. Equilibrium can be reached more rapidly by using a combination of constant infusion and an initial bolus injection (a "bolus/infusion", B/I, protocol) [40]. This approach is particularly useful in "challenge studies", in which the radiotracer is displaced by a cold competitor. It is also useful in situations when a linear model is not applicable, such as in the case of "multiple ligand concentration receptor assays" [41, 42]. In these

studies, low concentration of the radio-ligand is used in order to estimate B_{max} and K_D separately. A B/I paradigms was also used in order to avoid arterial sampling by replacing it with venous sampling at equilibrium with the SPECT tracer [^{123}I]CNS-1261 [43].

20.7.7 Model Comparison

Choosing a quantification method involves a trade-off between bias, variance and practicality. A model with more parameters will always give a better fit to the data (as judged by the residual sum of squares), but this may be because it is fitting the noise in the data rather than the actual signal. A model with less parameters will lead to less variability in the results, but can also lead to bias, if the model does not properly describe the underlying physiological or biochemical processes. There are various statistical methods for determining the best model, based on the residuals of the fit and on the number of parameters [44–46]. In principle, these methods correspond to application of the old philosophical principle known as "Occam's razor". If two models can describe the data equally well,[2] the best model is the simplest one.

The use of various different models and comparison of the estimated outcome measures is an approach that has been recommended in order to avoid systematic errors related to one particular model. In terms of practicality, it may be appropriate to also consider methods based on simplified data acquisition protocols, such as reference tissue methods, bolus/infusion methods or even single scan protocols. However, these methods should always first be validated versus more complex and accurate ones (see e.g. [47]).

20.8   Applications: Schizophrenia

PET and SPECT studies have been used for many years in psychiatric research. A wide range of tracers have been developed for imaging different

neurotransmitter (especially dopamine and serotonin) systems. These tracers have allowed for studies which aid in the drug development process by providing information on drug delivery, mechanism of action and occupancy levels at targets of interest. Below we present some illustrative examples, based on work from the research career of the late Prof. Lyn S Pilowsky.

Antipsychotic drugs are used for treatment of schizophrenic patients, and their therapeutic effect is believed to be related to blockade of postsynaptic dopamine D_2-receptors. They can be classified into two groups: Typical and atypical (or first and second generation) drugs. The atypical antipsychotics are advantageous in that they produce less Parkinsonian side effects than the typical ones, while preserving high clinical efficacy. Pilowsky et al. [48] used the SPECT tracer ^{123}I-IBZM to compare the atypical drug Clozapine with the typical drug Haloperidol. They showed that Clozapine produced a lower level of D_2/D_3 receptor blockade in the striatum (a central brain structure), which would explain the lower level of Parkinsonian side effects.

Different theories emerged regarding the mechanism of action of atypical drugs, involving either different receptor types or different brain regions. To investigate the importance of blocking serotonin-(5-HT) 2A receptors, Travis et al. [49] used the SPECT tracer ^{123}I-R91150, and found no correlation between clinical efficacy of atypical antipsychotics and 5-HT_{2A} receptor blockade. In order to investigate the extra-striatal D_2 receptor blockade, Pilowsky et al. [50] used ^{123}I-epidepride, a D_2/D_3 receptor tracer with higher affinity than ^{123}I-IBZM. The higher affinity was needed due to the much lower concentration of D_2 receptors outside the striatum. They found that, while typical antipsychotics produce high D_2 receptor occupancy in both striatal and extra-striatal regions (temporal cortex), Clozapine produced high occupancy only in extra-striatal regions. This could explain the clinical efficacy of atypical drugs with low Parkinsonian side-effects. However, this finding remained controversial for some time due to methodological issues, which were eventually solved [51]. The finding was also supported by the results of a

---

[2]No statistically significant difference.

meta-analysis, which pools data from several published PET and SPECT studies [52].

20.9 Conclusions

In this chapter, we have described the basic mathematical tools and concepts used in tracer kinetic modelling for quantification of physiological or biochemical parameters in vivo with PET or SPECT. Summaries of the basic theory discussed here can be found in [53, 54]. The next chapter will describe various methods used in practice for parameter estimation and discuss some examples of practical applications.

Appendix 1: Compartmental Models

Expressions for the impulse response functions for the 1-TC and 2-TC models are derived below. $L\{\cdot\}$ represents the Laplace transform, Laplace domain functions are identified with a tilde, and s is a complex Laplace domain variable.

1-TC Model

$$\frac{\mathrm{d}}{\mathrm{d}t}C_\mathrm{T}(t) = K_1 C_\mathrm{p}(t) - k_2'' C_\mathrm{T}(t)$$

$$\Leftrightarrow$$

$$L\left\{\frac{\mathrm{d}}{\mathrm{d}t}C_\mathrm{T}(t)\right\} = L\left\{K_1 C_\mathrm{p}(t) - k_2'' C_\mathrm{T}(t)\right\}$$

$$\Leftrightarrow$$

$$s\hat{C}_\mathrm{T}(s) - C_\mathrm{T}(0) = K_1 \hat{C}_\mathrm{p}(s) - k_2'' \hat{C}_\mathrm{T}(s)$$

$$\Rightarrow$$

With initial condition, $C_\mathrm{T}(0) = 0$:

$$\hat{C}_\mathrm{T}(s) = \frac{K_1}{s + k_2''}\hat{C}_\mathrm{p}(s)$$

$$\Leftrightarrow \qquad\qquad (20.24)$$

$$C_\mathrm{T}(t) = K_1 \mathrm{e}^{-k_2'' t} \otimes C_\mathrm{p}(t)$$

$$\Leftrightarrow$$

Impulse response function:

$$H_1(t) = K_1 \mathrm{e}^{-k_2'' t} \qquad\qquad (20.25)$$

2-TC Model

$$\frac{\mathrm{d}}{\mathrm{d}t}C_\mathrm{ND}(t) = K_1 C_\mathrm{p}(t) - \left(k_2' + k_3'\right)C_\mathrm{ND}(t) + k_4 C_\mathrm{S}(t)$$

$$\frac{\mathrm{d}}{\mathrm{d}t}C_\mathrm{S}(t) = k_3' C_\mathrm{ND}(t) - k_4 C_\mathrm{S}(t)$$

$$\Leftrightarrow$$

$$\begin{cases} s\hat{C}_\mathrm{ND}(s) - C_\mathrm{ND}(0) = K_1 \hat{C}_\mathrm{p}(s) - \\ \qquad\qquad \left(k_2' + k_3'\right)\hat{C}_\mathrm{ND}(s) + k_4 \hat{C}_\mathrm{S}(s) \\ s\hat{C}_\mathrm{S}(s) - C_\mathrm{S}(0) = k_3' \hat{C}_\mathrm{ND}(s) - k_4 \hat{C}_\mathrm{S}(s) \end{cases}$$

With initial conditions, $C_\mathrm{ND}(0) = C_\mathrm{S}(0) = 0$:

$$\Rightarrow$$

$$\begin{cases} \left(s + k_2' + k_3'\right)\hat{C}_\mathrm{ND}(s) = K_1 \hat{C}_\mathrm{p}(s) + k_4 \hat{C}_\mathrm{S}(s) \\ \left(s + k_4\right)\hat{C}_\mathrm{S}(s) = k_3' \hat{C}_\mathrm{ND}(s) \end{cases}$$

$$\Leftrightarrow$$

$$\begin{cases} \hat{C}_\mathrm{ND}(s) = \left(s + k_2' + k_3' - \dfrac{k_3' k_4}{s + k_4}\right)^{-1} K_1 \hat{C}_\mathrm{p}(s) \\ \hat{C}_\mathrm{S}(s) = \dfrac{k_3'}{s + k_4}\hat{C}_\mathrm{ND}(s) \end{cases}$$

$$\Rightarrow$$

$$\hat{C}_T(s) \equiv \hat{C}_\mathrm{ND}(s) + \hat{C}_\mathrm{S}(s) = \left(1 + \frac{k_3'}{s + k_4}\right)\hat{C}_\mathrm{ND}(s)$$

$$= \left(\frac{s + k_3' + k_4}{s + k_4}\right)\left(\frac{s + k_4}{\left(s + k_2' + k_3'\right)\left(s + k_4\right) - k_3' k_4}\right)$$
$$K_1 \hat{C}_\mathrm{p}(s)$$

$$= \left(\frac{s + k_3' + k_4}{s^2 + \left(k_2' + k_3' + k_4\right)s + k_2' k_4}\right)K_1 \hat{C}_\mathrm{p}(s)$$

$$\widetilde{}$$

$$(20.26)$$

Find poles:

$$s^2 + \left(k_2' + k_3' + k_4\right)s + k_2'k_4 = 0$$

$$\Leftrightarrow$$

$$s = -\frac{1}{2}\left(k_2' + k_3' + k_4 \mp \sqrt{\left(k_2' + k_3' + k_4\right)^2 - 4k_2'k_4}\right)$$

$$\equiv -\theta_{1,2}$$

~~~

Partial fraction expansion:

$$\frac{\phi_1}{s + \theta_1} + \frac{\phi_2}{s + \theta_2} = K_1 \frac{s + k_3' + k_4}{s^2 + \left(k_2' + k_3' + k_4\right)s + k_2'k_4}$$

(20.27)

$$\Leftrightarrow$$

$$\begin{cases} \phi_1 = K_1 \dfrac{k_3' + k_4 - \theta_1}{\theta_2 - \theta_1} \\ \phi_2 = -K_1 \dfrac{k_3' + k_4 - \theta_2}{\theta_2 - \theta_1} \end{cases}$$

~~~

$$(20.26) + (20.27)$$

$$\Rightarrow$$

$$\hat{C}_T(s) = \left(\frac{\phi_1}{s + \theta_1} + \frac{\phi_2}{s + \theta_2}\right)\hat{C}_p(s) \quad (20.28)$$

$$\Leftrightarrow$$

$$C_T(t) = \left(\phi_1 e^{-\theta_1 t} + \phi_2 e^{-\theta_2 t}\right) \otimes C_p(t)$$

$$\Leftrightarrow$$

Impulse response function:

$$H_2(t) = \phi_1 e^{-\theta_1 t} + \phi_2 e^{-\theta_2 t} \quad (20.29)$$

Appendix 2: Reference Tissue Models

1-TC Model

$$\begin{cases} \dfrac{d}{dt}C_T(t) = K_1 C_p(t) - k_2'' C_T(t) \\ \dfrac{d}{dt}C_R(t) = {}^R K_1 C_p(t) - {}^R k_2' C_R(t) \end{cases}$$

$$\Leftrightarrow$$

From Eq. (20.24):

$$\begin{cases} \hat{C}_T(s) = \dfrac{K_1}{s + k_2''}\hat{C}_p(s) \\ \hat{C}_R(s) = \dfrac{{}^R K_1}{s + {}^R k_2'}\hat{C}_p(s) \end{cases}$$

$$\Rightarrow$$

$$\left(\text{with } R_1 = \frac{K_1}{{}^R K_1}\right):$$

$$\hat{C}_T(s) = R_1 \frac{s + {}^R k_2'}{s + k_2''}\hat{C}_R(s)$$

$$= R_1 \hat{C}_R(s) + R_1 \frac{{}^R k_2' - k_2''}{s + k_2''}\hat{C}_R(s)$$

$$\Rightarrow$$

$$C_T(t) = R_1 C_R(t) + R_1 \left({}^R k_2' - k_2''\right)e^{-k_2'' t} \otimes C_R(t)$$

$$\Leftrightarrow$$

Impulse response function:

$$H_{1R}(t) = R_1 \delta(t) + R_1 \left({}^R k_2' - k_2''\right)e^{-k_2'' t}$$

(20.30)

where $\delta(t)$ is the Dirac delta-function.

2-TC model

$$
\begin{cases}
\dfrac{\mathrm{d}}{\mathrm{d}t}C_{\mathrm{ND}}(t) = K_1 C_{\mathrm{p}}(t) - \left(k_2' + k_3'\right)C_{\mathrm{ND}}(t) \\
\qquad\qquad + k_4 C_{\mathrm{S}}(t) \\[2mm]
\dfrac{\mathrm{d}}{\mathrm{d}t}C_{\mathrm{S}}(t) = k_3' C_{\mathrm{ND}}(t) - k_4 C_{\mathrm{S}}(t) \\[2mm]
\dfrac{\mathrm{d}}{\mathrm{d}t}C_{\mathrm{R}}(t) = {}^R K_1 C_{\mathrm{p}}(t) - {}^R k_2' C_{\mathrm{R}}(t)
\end{cases}
$$

From Eqs. (20.24) and (20.28):

$$
\begin{cases}
\hat{C}_{\mathrm{T}}(s) = \left(\dfrac{\phi_1}{s+\theta_1} + \dfrac{\phi_2}{s+\theta_2}\right)\hat{C}_{\mathrm{p}}(s) \\[3mm]
\hat{C}_{\mathrm{R}}(s) = \dfrac{{}^R K_1}{s + {}^R k_2'}\hat{C}_{\mathrm{p}}(s)
\end{cases}
$$
$$
\Rightarrow
$$
$$
\hat{C}_{\mathrm{T}}(s) = \left(\frac{\phi_1}{s+\theta_1} + \frac{\phi_2}{s+\theta_2}\right)\frac{s + {}^R k_2'}{{}^R K_1}\hat{C}_{\mathrm{R}}(s)
$$
$$
\Leftrightarrow
$$

$$
\left(\text{with}\, R_1 = \frac{K_1}{{}^R K_1}\right):
$$

$$
\hat{C}_{\mathrm{T}}(s) = \frac{R_1}{\theta_2 - \theta_1}\left(\frac{\dfrac{k_3' + k_4 - \theta_1}{s+\theta_1} -}{\dfrac{k_3' + k_4 - \theta_2}{s+\theta_2}}\right)\left(s + {}^R k_2'\right)\hat{C}_{\mathrm{R}}(s)
$$

$$
= \frac{R_1}{\theta_2 - \theta_1}
$$
$$
\left(\frac{\left(k_3' + k_4 - \theta_1\right)\left(1 + \dfrac{{}^R k_2' - \theta_1}{s+\theta_1}\right) -}{\left(k_3' + k_4 - \theta_2\right)\left(1 + \dfrac{{}^R k_2' - \theta_2}{s+\theta_2}\right)}\right)\hat{C}_{\mathrm{R}}(s)
$$

$$
= R_1 \hat{C}_{\mathrm{R}}(s) + \frac{R_1}{\theta_2 - \theta_1}
$$
$$
\left(\frac{\dfrac{\left(k_3' + k_4 - \theta_1\right)\left({}^R k_2' - \theta_1\right)}{s+\theta_1} -}{\dfrac{\left(k_3' + k_4 - \theta_2\right)\left({}^R k_2' - \theta_2\right)}{s+\theta_2}}\right)\hat{C}_{\mathrm{R}}(s)
$$
$$
\Leftrightarrow
$$

$$
\hat{C}_{\mathrm{T}}(s) = R_1 \hat{C}_{\mathrm{R}}(s) + \left(\frac{\rho_1}{s+\theta_1} + \frac{\rho_2}{s+\theta_2}\right)\hat{C}_{\mathrm{R}}(s)
$$
$$
(20.31)
$$

where

$$
\begin{cases}
\rho_1 = R_1 \dfrac{\left(k_3' + k_4 - \theta_1\right)\left({}^R k_2' - \theta_1\right)}{\theta_2 - \theta_1} \\[3mm]
\rho_2 = -R_1 \dfrac{\left(k_3' + k_4 - \theta_2\right)\left({}^R k_2' - \theta_2\right)}{\theta_2 - \theta_1}
\end{cases}
$$

$$
\sim\sim\sim
$$
$$
(20.31)
$$
$$
\Rightarrow
$$
$$
C_{\mathrm{T}}(t) = R_1 C_{\mathrm{R}}(t) + \left(\rho_1 \mathrm{e}^{-\theta_1 t} + \rho_2 \mathrm{e}^{-\theta_2 t}\right) \otimes C_{\mathrm{R}}(t)
$$
$$
\Leftrightarrow
$$

Impulse response function:

$$
H_{2\mathrm{R}}(t) = R_1 \delta(t) + \rho_1 \mathrm{e}^{-\theta_1 t} + \rho_2 \mathrm{e}^{-\theta_2 t}
$$
$$
(20.32)
$$

Appendix 3: Logan Graphical Analysis

1-TC Model

$$
\frac{\mathrm{d}}{\mathrm{d}t}C_{\mathrm{T}}(t) = K_1 C_{\mathrm{p}}(t) - k_2'' C_{\mathrm{T}}(t)
$$
$$
\Leftrightarrow
$$
$$
C_{\mathrm{T}}(t) - C_{\mathrm{T}}(0) = K_1 \int_0^t C_{\mathrm{p}}(\tau)\mathrm{d}\tau - k_2'' \int_0^t C_{\mathrm{T}}(\tau)\mathrm{d}\tau
$$

with $C_{\mathrm{T}}(0) = 0$:

$$
\Leftrightarrow
$$
$$
\frac{\int_0^t C_{\mathrm{T}}(\tau)\mathrm{d}\tau}{C_{\mathrm{T}}(t)} = \frac{K_1}{k_2''}\frac{\int_0^t C_{\mathrm{p}}(\tau)\mathrm{d}\tau}{C_{\mathrm{T}}(t)} - \frac{1}{k_2''}
$$
$$
\Rightarrow
$$

$$\frac{\int_0^t C_{\mathrm{T}}(\tau)\mathrm{d}\tau}{C_{\mathrm{T}}(t)} = V_{\mathrm{T}}\frac{\int_0^t C_{\mathrm{p}}(\tau)\mathrm{d}\tau}{C_{\mathrm{T}}(t)} + \mathrm{const.}$$

$$(20.33)$$

2-TC Model

$$\begin{cases}\dfrac{\mathrm{d}}{\mathrm{d}t}C_{\mathrm{ND}}(t) = K_1 C_{\mathrm{p}}(t) - \\ \qquad\qquad \left(k_2' + k_3'\right)C_{\mathrm{ND}}(t) + k_4 C_{\mathrm{S}}(t) \\ \dfrac{\mathrm{d}}{\mathrm{d}t}C_{\mathrm{S}}(t) = k_3' C_{\mathrm{ND}}(t) - k_4 C_{\mathrm{S}}(t)\end{cases}$$

$$\Leftrightarrow$$

$$\begin{cases}C_{\mathrm{ND}}(t) - C_{\mathrm{ND}}(0) = \\ K_1\displaystyle\int_0^t C_{\mathrm{p}}(\tau)\mathrm{d}\tau - \left(k_2' + k_3'\right)\int_0^t C_{\mathrm{ND}}(\tau)\,d\tau \\ + k_4\displaystyle\int_0^t C_{\mathrm{S}}(\tau)\,d\tau \\ C_{\mathrm{S}}(t) - C_{\mathrm{S}}(0) = k_3'\displaystyle\int_0^t C_{\mathrm{ND}}(t)\mathrm{d}\tau - k_4\int_0^t C_{\mathrm{S}}(\tau)\mathrm{d}\tau\end{cases}$$

with $C_{\mathrm{ND}}(0) = C_{\mathrm{S}}(0) = 0$:

$$\Leftrightarrow$$

$$\begin{cases}C_{\mathrm{T}}(t) = K_1\displaystyle\int_0^t C_{\mathrm{p}}(\tau)\mathrm{d}\tau - k_2'\int_0^t C_{\mathrm{ND}}(\tau)\mathrm{d}\tau \\ C_{\mathrm{S}}(t) = k_3'\displaystyle\int_0^t C_{\mathrm{ND}}(\tau)\mathrm{d}\tau - k_4\int_0^t C_{\mathrm{S}}(\tau)\mathrm{d}\tau\end{cases}$$

$$\Leftrightarrow$$

$$\begin{cases}\dfrac{\int_0^t C_{\mathrm{ND}}(\tau)\mathrm{d}\tau}{C_{\mathrm{T}}(t)} = \dfrac{K_1}{k_2'}\dfrac{\int_0^t C_{\mathrm{P}}(\tau)\mathrm{d}\tau}{C_{\mathrm{T}}(t)} - \dfrac{1}{k_2'} \\ \dfrac{\int_0^t C_{\mathrm{S}}(\tau)\mathrm{d}\tau}{C_{\mathrm{T}}(t)} = \dfrac{k_3'}{k_4}\dfrac{\int_0^t C_{\mathrm{ND}}(\tau)\mathrm{d}\tau}{C_{\mathrm{T}}(t)} - \dfrac{1}{k_4}\dfrac{C_{\mathrm{S}}(t)}{C_{\mathrm{T}}(t)}\end{cases}$$

$$\Rightarrow$$

$$\frac{\int_0^t C_{\mathrm{T}}(\tau)\mathrm{d}\tau}{C_{\mathrm{T}}(t)} \equiv \frac{\int_0^t C_{\mathrm{ND}}(\tau) + C_{\mathrm{S}}(\tau)\mathrm{d}\tau}{C_{\mathrm{T}}(t)}$$

$$= \frac{K_1}{k_2'}\frac{\int_0^t C_{\mathrm{P}}(\tau)\mathrm{d}\tau}{C_{\mathrm{T}}(t)} - \frac{1}{k_2'}$$

$$+ \frac{k_3'}{k_4}\left(\frac{K_1}{k_2'}\frac{\int_0^t C_{\mathrm{P}}(\tau)\mathrm{d}\tau}{C_{\mathrm{T}}(t)} - \frac{1}{k_2'}\right) - \frac{1}{k_4}\frac{C_{\mathrm{S}}(t)}{C_{\mathrm{T}}(t)}$$

$$= \frac{K_1}{k_2'}\left(1 + \frac{k_3'}{k_4}\right)\frac{\int_0^t C_{\mathrm{P}}(\tau)\mathrm{d}\tau}{C_{\mathrm{T}}(t)}$$

$$- \frac{1}{k_2'}\left(1 + \frac{k_3'}{k_4}\right) - \frac{1}{k_4}\frac{C_{\mathrm{S}}(t)}{C_{\mathrm{T}}(t)}$$

$$\Leftrightarrow$$

$$\frac{\int_0^t C_{\mathrm{T}}(\tau)\mathrm{d}\tau}{C_{\mathrm{T}}(t)} = V_{\mathrm{T}}\frac{\int_0^t C_{\mathrm{P}}(\tau)\mathrm{d}\tau}{C_{\mathrm{T}}(t)} - \frac{1}{k_2''} - \frac{1}{k_4}\frac{C_{\mathrm{S}}(t)}{C_{\mathrm{T}}(t)}$$

$$\Rightarrow$$

with $C_{\mathrm{S}}(t)/C_{\mathrm{T}}(t) = $ constant (pseudo-equilibrium):

$$\frac{\int_0^t C_{\mathrm{T}}(\tau)\mathrm{d}\tau}{C_{\mathrm{T}}(t)} = V_{\mathrm{T}}\frac{\int_0^t C_{\mathrm{P}}(\tau)\mathrm{d}\tau}{C_{\mathrm{T}}(t)} + \mathrm{const.}$$

$$(20.34)$$

References

1. Cunningham VJ, Gunn RN, Matthews JC. Quantification in positron emission tomography for research in pharmacology and drug development. Nucl Med Commun. 2004;25:643–6.
2. Laruelle M. The role of model-based methods in the development of single scan techniques. Nucl Med Biol. 2000;27:637–42.
3. Erlandsson K, Buvat I, Pretorius PH, Thomas BA, Hutton BF. A review of partial volume correction techniques for emission tomography and their applications in neurology, cardiology and oncology. Phys Med Biol. 2012;57:R119–59.

4. Carson RE. The development and application of mathematical models in nuclear medicine. J Nucl Med. 1991;32:2206–8.

5. Carson RE. Tracer kinetic modelling in PET. In: Valk PE, Bailey DL, Townsend DW, Maisey MN, editors. Positron emission tomography: basic science and clinical practice. London: Springer-Verlag; 2003. p. 147–79.

6. Gunn RN, Gunn SR, Cunningham VJ. Positron emission tomography compartmental models. J Cereb Blood Flow Metab. 2001;21:635–52.

7. Arfken G. Mathematical methods for physicists. San Diego: Academic; 1985.

8. Kety SS, Schmidt CF. The nitrous oxide method for the quantitative determination of cerebral blood flow in man: theory, procedure and normal values. J Clin Invest. 1948;27:476–83.

9. Kety SS. The theory and applications of the exchange of inert gas at the lungs and tissues. Pharmacol Rev. 1951;3:1–41.

10. Renkin EM. Transport of potassium-42 from blood to tissue in isolated mammalian skeletal muscles. Am J Phys. 1959;197:1205–10.

11. Crone C. The permeability of capillaries in various organs as determined by use of the 'indicator diffusion' method. Acta Physiol Scand. 1963;58:292–305.

12. Kerwin RW, Pilowsky LS. Traditional receptor theory and its application to neuroreceptor measurements in functional imaging. Eur J Nucl Med. 1995;22:699–710.

13. Michaelis L, Menten ML. Die kinetik der invertinwirkung. Biochem Z. 1913;49:1333.

14. Scatchard G. The attractions of proteins for small molecules and ions. Ann N Y Acad Sci. 1949;51:660–5.

15. Mintun MA, Raichle ME, Kilbourn MR, Wooten GF, Welch MJ. A quantitative model for the in vivo assessment of drug binding sites with positron emission tomography. Ann Neurol. 1984;15:217–27.

16. Scheibe PO. Identifiability analysis of second-order systems. Nucl Med Biol. 2003;30:827–32.

17. Koeppe RA, Holthoff VA, Frey KA, Kilbourn MR, Kuhl DE. Compartmental analysis of [11C]flumazenil kinetics for the estimation of ligand transport rate and receptor distribution using positron emission tomography. J Cereb Blood Flow Metab. 1991;11:735–44.

18. Erlandsson K, Bressan RA, Mulligan RS, Gunn RN, Cunningham VJ, Owens J, Wyper D, Ell PJ, Pilowsky LS. Kinetic modelling of [123I]-CNS 1261—a novel SPET tracer for the NMDA receptor. Nucl Med Biol. 2003;30:441–54.

19. Tonietto M, Rizzo G, Veronese M, Fujita M, Zoghbi SS, Zanotti-Fregonara P, Bertoldo A. Plasma radiometabolite correction in dynamic PET studies: insights on the available modeling approaches. J Cereb Blood Flow Metab. 2016;36:326–39.

20. Zanotti-Fregonara P, Fadaili EM, Maroy R, Comtat C, Souloumiac A, Jan S, Ribeiro M-J, Gaura V, Bar-Hen A, Trebossen R. Comparison of eight methods for the estimation of the image-derived input function in dynamic [18F]-FDG PET human brain studies. J Cereb Blood Flow Metab. 2009;29:1825–35.

21. Sari H, Erlandsson K, Law I, Larsson HB, Ourselin S, Arridge S, Atkinson D, Hutton BF. Estimation of an image derived input function with MR-defined carotid arteries in FDG-PET human studies using a novel partial volume correction method. J Cereb Blood Flow Metab. 2017;37:1398–409.

22. Innis RB, Cunningham VJ, Delforge J, Fujita M, Gjedde A, Gunn RN, Holden J, Houle S, Huang SC, Ichise M, Iida H, Ito H, Kimura Y, Koeppe RA, Knudsen GM, Knuuti J, Lammertsma AA, Laruelle M, Logan J, Maguire RP, Mintun MA, Morris ED, Parsey R, Price JC, Slifstein M, Sossi V, Suhara T, Votaw JR, Wong DF, Carson RE. Consensus nomenclature for in vivo imaging of reversibly binding radioligands. J Cereb Blood Flow Metab. 2007;27:1533–9.

23. Marquardt DW. An algorithm for least-squares estimation of nonlinear parameters. J Soc Ind Appl Math. 1963;11:431–41.

24. Press WH, Teukolsky SA, Vetterling WT, Flannery BP. Numerical recipies in C: the art of scientific computing. Cambridge: Cambridge University Press; 1992.

25. Feng D, Wong K-P, Wu C-M, Siu W-C. A technique for extracting physiological parameters and the required input function simultaneously from PET image measurements: theory and simulation study. IEEE Trans Inform Technol Biomed. 1997;1:243–54.

26. Cunningham VJ, Hume SP, Price GR, Ahier RG, Cremer JE, Jones AK. Compartmental analysis of diprenorphine binding to opiate receptors in the rat in vivo and its comparison with equilibrium data in vitro. J Cereb Blood Flow Metab. 1991;11:1–9.

27. Lammertsma AA, Bench CJ, Hume SP, Osman S, Gunn K, Brooks DJ, Frackowiak RS. Comparison of methods for analysis of clinical [11C]raclopride studies. J Cereb Blood Flow Metab. 1996;16:42–52.

28. Lammertsma AA, Hume SP. Simplified reference tissue model for PET receptor studies. NeuroImage. 1996;4:153–8.

29. Wu Y, Carson RE. Noise reduction in the simplified reference tissue model for neuroreceptor functional imaging. J Cereb Blood Flow Metab. 2002;22:1440–52.

30. Erlandsson K, Sivananthan T, Lui D, Spezzi A, Townsend CE, Mu S, Lucas R, Warrington S, Ell PJ. Measuring SSRI occupancy of SERT using the novel tracer [123I]ADAM: a SPECT validation study. Eur J Nucl Med Mol Imaging. 2005;32:1329–36.

31. Cunningham VJ, Jones T. Spectral analysis of dynamic PET studies. J Cereb Blood Flow Metab. 1993;13:15–23.

32. Gunn RN, Gunn SR, Turkheimer FE, Aston JAD, Cunningham VJ. Positron emission tomography compartmental models: a basis pursuit strategy for kinetic modelling. J Cereb Blood Flow Metab. 2002;22:1425–39.

33. Logan J, Fowler JS, Volkow ND, Wolf AP, Dewey SL, Schlyer DJ, MacGregor RR, Hitzemann R, Bendriem

B, Gatley SJ, et al. Graphical analysis of reversible radioligand binding from time-activity measurements applied to [N-^{11}C-methyl]-(−)-cocaine PET studies in human subjects. J Cereb Blood Flow Metab. 1990;10:740–7.

34. Slifstein M, Laruelle M. Effects of statistical noise on graphic analysis of PET neuroreceptor studies. J Nucl Med. 2000;41:2083–8.

35. Ogden RT. Estimation of kinetic parameters in graphical analysis of PET imaging data. Stat Med. 2003;22:3557–68.

36. Logan J, Fowler JS, Volkow ND, Wang GJ, Ding YS, Alexoff DL. Distribution volume ratios without blood sampling from graphical analysis of PET data. J Cereb Blood Flow Metab. 1996;16:834–40.

37. Patlak CS, Blasberg RG, Fenstermacher JD. Graphical evaluation of blood-to-brain transfer constants from multiple-time uptake data. J Cereb Blood Flow Metab. 1983;3:1–7.

38. Rahmim A, Lodge MA, Karakatsanis NA, Panin VY, Zhou Y, McMillan A, Cho S, Zaidi H, Casey ME, Wahl RL. Dynamic whole-body PET imaging: principles, potentials and applications. Eur J Nucl Med Mol Imaging. 2019;46:501–18.

39. Carson RE. PET physiological measurements using constant infusion. Nucl Med Biol. 2000;27:657–60.

40. Carson RE, Channing MA, Blasberg RG, Dunn BB, Cohen RM, Rice KC, Herscovitch P. Comparison of bolus and infusion methods for receptor quantitation: application to [18F]cyclofoxy and positron emission tomography. J Cereb Blood Flow Metab. 1993;13:24–42.

41. Kawai R, Carson RE, Dunn B, Newman AH, Rice KC, Blasberg RG. Regional brain measurement of Bmax and KD with the opiate antagonist cyclofoxy: equilibrium studies in the conscious rat. J Cereb Blood Flow Metab. 1991;11:529–44.

42. Holden JE, Jivan S, Ruth TJ, Doudet DJ. In vivo receptor assay with multiple ligand concentrations: an equilibrium approach. J Cereb Blood Flow Metab. 2002;22:1132–41.

43. Bressan RA, Erlandsson K, Mulligan RS, Gunn RN, Cunningham VJ, Owens J, Cullum ID, Ell PJ, Pilowsky LS. A bolus/infusion paradigm for the novel NMDA receptor SPET tracer [123I]CNS 1261. Nucl Med Biol. 2004;31:155–64.

44. Akaike H. A new look at the statistical model identification. IEEE Trans Automat Contr. 1974;19:716–23.

45. Cunningham VJ. Non-linear regression techniques in data analysis. Med Inf (Lond). 1985;10:137–42.

46. Schwarz G. Estimating the dimension of a model. Ann Stat. 1978;6:461–4.

47. Ogden RT, Ojha A, Erlandsson K, Oquendo MA, Mann JJ, Parsey RV. In vivo quantification of serotonin transporters using [11C]DASB and positron emission tomography in humans: modeling considerations. J Cereb Blood Flow Metab. 2007;27:205–17.

48. Pilowsky LS, Costa DC, Ell PJ, Murray RM, Verhoeff NP, Kerwin RW. Clozapine, single photon emission tomography, and the D2 dopamine receptor blockade hypothesis of schizophrenia. Lancet. 1992;340:199–202.

49. Travis MJ, Busatto GF, Pilowsky LS, Mulligan R, Acton PD, Gacinovic S, Mertens J, Terriere D, Costa DC, Ell PJ, Kerwin RW. 5-HT2A receptor blockade in patients with schizophrenia treated with risperidone or clozapine. A SPET study using the novel 5-HT2A ligand ^{123}I-5-I-R-91150. Br J Psychiatry. 1998;173:236–41.

50. Pilowsky LS, Mulligan RS, Acton PD, Ell PJ, Costa DC, Kerwin RW. Limbic selectivity of clozapine. Lancet. 1997;350:490–1.

51. Erlandsson K, Bressan RA, Mulligan RS, Ell PJ, Cunningham VJ, Pilowsky LS. Analysis of D2 dopamine receptor occupancy with quantitative SPET using the high-affinity ligand [123I]epidepride: resolving conflicting findings. NeuroImage. 2003;19:1205–14.

52. Stone JM, Davis JM, Leucht S, Pilowsky LS. Cortical dopamine D2/D3 receptors are a common site of action for antipsychotic drugs--an original patient data meta-analysis of the SPECT and PET in vivo receptor imaging literature. Schizophr Bull. 2009;35(4):789–97.

53. Ichise M, Meyer JH, Yonekura Y. An introduction to PET and SPECT neuroreceptor quantification models. J Nucl Med. 2001;42:755–63.

54. Slifstein M, Laruelle M. Models and methods for derivation of in vivo neuroreceptor parameters with PET and SPECT reversible radiotracers. Nucl Med Biol. 2001;28:595–608.

Quantitative Analysis in PET Imaging

21

M'hamed Bentourkia

Contents

21.1 Introduction

Positron emission tomography (PET) imaging allows measurements of not only a disease for diagnosis or for follow-up and staging, but it is also used to study medication effect, cerebral cognition, behavior, etc. Because of the use of radioactive molecules in PET imaging, which are harmful to the patients, the injected activity (or dose) of the radiotracer is limited to some 3 mCi (111 MBq) for radiotracers with high contrast and long physical half-life such as ^{18}F-FDG, and 10 mCi (370 MBq) for radiotracers like water ($H_2^{15}O$). The use of 3 and 10 mCi are not a limit

for these tracers, they are provided here for illustrative purposes only, however, the doses with the promising new scanners were reported to be less than usual due to the evolvement of the technology.

The new scanners allow measurements of coincident photons fast and with high efficiency. These scanners use sensitive scintillators directly coupled to silicon photomultipliers (SiPM) without light sharing and position decoding (digital photon counting) [1]. Such scanners provide other advantages like energy resolution (11%) which helps refining scatter correction for a better quantification and contrast in the images. In terms of time of photons detection, the best time resolution achieved is actually 210 ps with the Biograph Vision [2]. For example, if a time resolution of 10 ps is reached, the uncertainty on the position of positron annihilation between the two coincident detectors would be around 1.5 mm,

M. Bentourkia (✉)
Faculty of Medicine and Health Sciences,
Department of Nuclear Medicine and Radiobiology,
University of Sherbrooke, Sherbrooke, QC, Canada
e-mail: Mhamed.Bentourkia@USherbrooke.ca

this implies that these positions are sufficient to generate the images and no more need to image reconstruction algorithms [3]. Other scanners for total body are making their way to the clinic. These scanners allow at once to scan a whole body (194 cm axial length) which are highly sensitive and efficient to scan in dynamic mode [4].

Nevertheless, the radiotracer activity to be injected to subjects is always formally limited by the ethics committee of the university or a national agency in accordance with the Declaration of Helsinki [5]. Accordingly, the dose to patients has been specifically studied for almost all developed radiotracers. In average, a low-dose computed tomography (CT) imaging combined with a 370 MBq of ^{18}F-FDG-PET imaging induce an effective dose of about 15 mSv, and CT accounts for more than 54% of the total effective dose [6]. When using a diagnostic CT, the dose is increased. As a reference, the dose to the patient is generally included in the image header of the scans. Several agencies and reports recommend guidelines for a safe imaging with patients and optimization of imaging methodologies [7, 8]. In research, the dose can be high especially for targeted radiotherapy [9], and repetitive scans as for brain activation, cardiac rest-stress imaging, or multi-tracer imaging.

Unfortunately, for some radiotracers, based on their behavior in the body, the injected activity even very high does not improve the contrast like imaging with $H_2{}^{15}O$. Taking again the example of ^{18}F-FDG and $H_2{}^{15}O$, the first has a half-life of 109 min, and it accumulates in the cells after being phosphorylated, thus providing high contrast images. The second has a half-life of 2 min and it is freely diffusible in the cells, meaning no retention of the radiotracer and consequently the images have very low contrast (Fig. 21.1).

Depending on the predefined imaging protocol, several factors have to be considered in PET measurements. Optimally, the images are expected to be of good enough spatial resolution, of good enough contrast and of low statistical noise. The expression "good enough" is here very subjective. It can be translated into the statistical significance of differences between a measured object like a tumor and its background by means

of statistical tests. In other words, an imaging protocol should be optimal for successful imaging parameters. These parameters include the activity of the radiotracer to be injected as a bolus or infusion, the timing of the acquisition as a delayed single scan or in dynamic mode where the scan is initiated some 30 s before radiotracer injection, the duration of the measurement, image correction for subject or organ movement and for partial volume effect (PVE), and image fusion or coregistration.

Coupling imaging modalities provides complementary information other than the anatomical localization. The low spatial resolution of PET is due to its detectors made large enough to intercept the limited number of emitted photons by the radiotracer. The limited spatial resolution is complicated by other factors such as positron range, acollinearity of the annihilation photons, image reconstruction, and again patient and organ motion during the measurement. The most limiting factor in PET imaging are the rejected photons scattering in the subject and having energies lower than approximately 400 keV. With the advances in computing and data handling and storing, the PET scanners are subject to major changes like the acquisition of total body at once to increase scanner sensitivity instead of moving the subject in the scanner to acquire several bed positions [4, 10]. This opportunity will have another major impact which consists in dynamic imaging of the total body which is very profitable for pharmacokinetic modeling.

The combination of magnetic resonance imaging (MRI) with PET allows better spatial resolution and contrast in tissue with a reduced radioactive dose to the patient in comparison to the combined PET/CT [11], although, for some pathologies like lung metastases, PET/CT is the preferred [12]. PET scanners for human imaging are made of crystals or blocks of crystals coupled to a few photomultiplier tubes (PMT). Because the PMT first converts the emitted annihilation photons to electrons which are subsequently accelerated and multiplied in the dynodes of the PMT to provide an amplified signal, the vicinity of the MRI strong magnetic field drastically affects the trajectories of the electrons in the
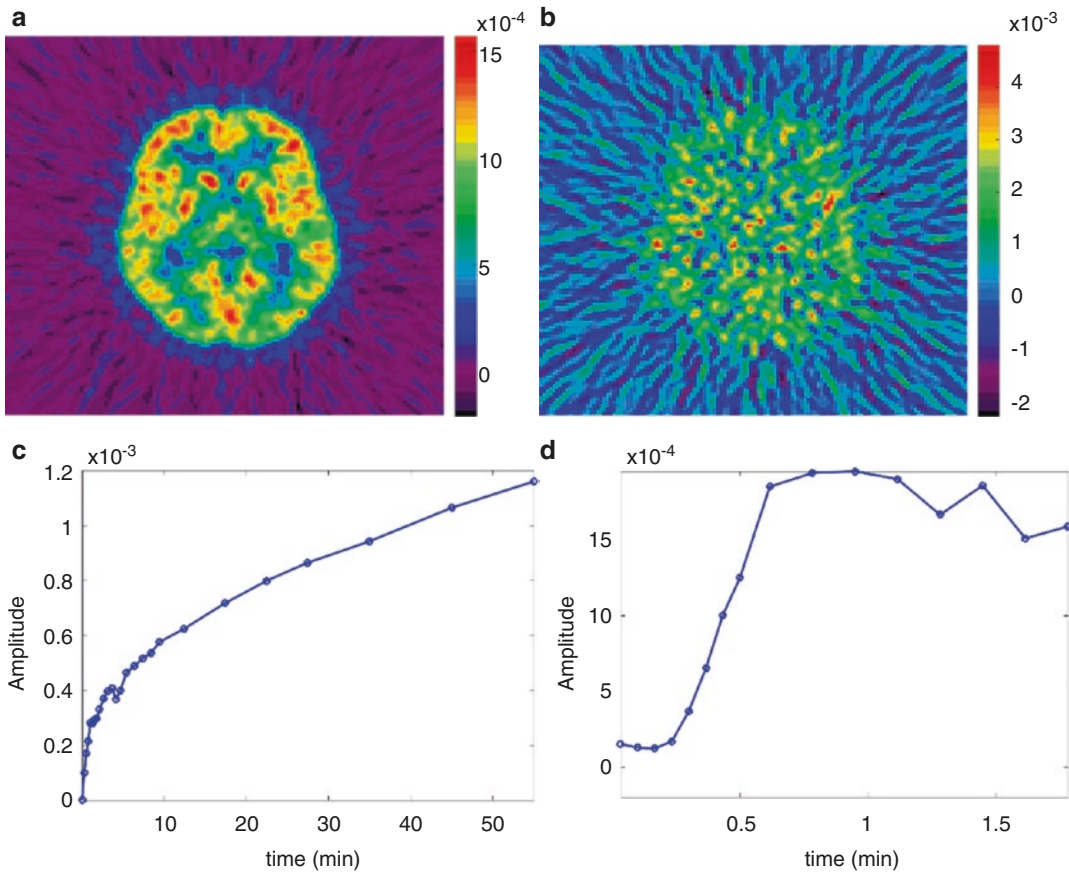
Fig. 21.1 (**a**) Image with ^{18}F-FDG and (**b**) image with $H_2^{15}O$ in the same brain slice of the same young and healthy subject during the same PET imaging session. The images were reconstructed with filtered back projection generating strikes and negative pixel intensity. (**c**) Time– activity curve from the ^{18}F-FDG image in a region of interest placed on the right frontal. (**d**) Although the image with $H_2^{15}O$ appears very noisy, the time–activity curve from the same region as for ^{18}F-FDG is enough accurate to be fitted with a kinetic model

PMT, thus interfering with the signal to be detected. An avenue to avoid this situation was the replacement of PMTs with avalanche photodiodes (APDs) or SiPMs which are not affected by MRI magnetic field [11, 13], or, for some other designers, by active shielding of the PMTs [14], or using optical fibers [11]. Scanners based on SiPMs are very promising. The path of charge carriers in these devices are so short to be unaffected by MRI magnetic field [11]. APDs were used in small animal PET imaging for decades [15–20]. They are more suited to small animal scanners because each crystal is coupled to an APD, and since the number of detectors per ring and the number of rings are not numerous, they can be cabled individually. Till now, this was not

the case for the larger whole-body PET scanners, meanwhile, with the new generation of digital PET scanners individually coupling crystals with SiPMs, the performance of PET will be drastically enhanced [1, 21]. Actually, The hindrance of PET/MRI is the uncertainty in the attenuation correction of PET images based on MRI images where the density of bones is not properly assessed when using MRI [13].

21.2 Image Enhancement

The quality of PET images depends on several factors, but the main requirements in the clinic are the contrast, the spatial resolution, and the

noise. The contrast depends on the technology (hardware and software) and on the physiology e.g., the pharmacokinetic of the radiotracer in the body as discussed above for the case of $H_2^{15}O$. For the other two factors, there is the dependence of the scanner itself on its detectors' sensitivity and architecture which affect the statistical noise and the spatial resolution. The more a scanner has a larger number of detectors with small size to generate high resolution images, the less they intercept photons, and this leads to statistical noise in the images where objects are not well defined and lack some homogeneity (Fig. 21.2). Image correction for noise is well documented where most of the modern algorithms attempt to reduce the noise without reducing the spatial resolution [22, 23]. The spatial resolution and the statistical noise are interdependent. The pixels intensity due to noise has high variability even in a homogeneous tissue. This high variability appears at the high frequencies when transforming the image from spatial domain to Fourier space (frequency domain). To illustrate the dependence between the spatial resolution and the noise, the Gaussian noise added to the brain image in Fig. 21.3b
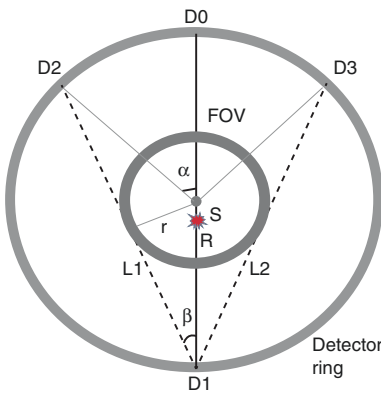
Fig. 21.2 Diagram of a PET detector ring. Detector D1 can be in coincidence with any detector located between D2 and D3 for any point source placed in the field of view (FOV). The number of detectors in coincidence with D1 can be calculated based on detector size, scanner radius (*R*), and FOV radius (*r*). The more the number of detectors per ring is large, the more the images have high resolution. Unfortunately, a large number of detectors per ring means small detectors' size, and consequently, small detectors' size implies less photons detected and hence the images are noisy

was used to be filtered with a Butterworth flat low-pass filter of a frequency cut-off $f_c = 20$ and an order $n = 4$ as in the equation: $B(f) = 1/\sqrt{1 + (f/f_c)^{2n}}$ where f is the frequency. This filter gently reduces the noise at high frequency as depicted in Fig. 21.3f. The low frequency signal in the image to be filtered remains intact as it is multiplied by 1 by the filter (frequencies around 0). The filtered image appears less noisy, but it does not retrieve the original non-added noise image in Fig. 21.3a. The horizontal profiles from the images in Fig. 21.3a and f are plotted in Fig. 21.3g. In this figure, the oscillations disappeared as the filtered image becomes less noisy but also it becomes smooth losing some of its spatial resolution. The effect of noise reduction on spatial resolution is better appreciated on images from line sources where the images show a single sharp peak (Fig. 21.3h). The filtering with Butterworth filter was also used here for the line source and the profiles through the line source images before and after filtering are shown in Fig. 21.3i. The filtered profile becomes wider. The spatial resolution of the line source in the two images as calculated with a Gaussian fit to the profiles at the full width at half maximum were found as 2.43 pixels and 3.94 pixels. At the final, the classical filtering for noise reduction deteriorates the spatial resolution (smooths the image, expands the object image beyond its natural size, and reduces pixels intensity).

Beyond the hardware, most scanners actually include time-of-flight calculation during image reconstruction which helps in refining the spatial resolution, sensitivity, and signal to noise [10, 24]. Basically, if the time of detection of the annihilation photons at the coincident detectors can be measured with precision, there would be no need to image reconstruction since the image can be obtained by incrementing the photon counts at the position of emission. In reality, the detectors need some time to transform the deposited photon energy into counts by collecting, for example, the scintillations in the crystals, then their conversion and amplification in the photomultiplier tube followed by amplification of the signal and match-
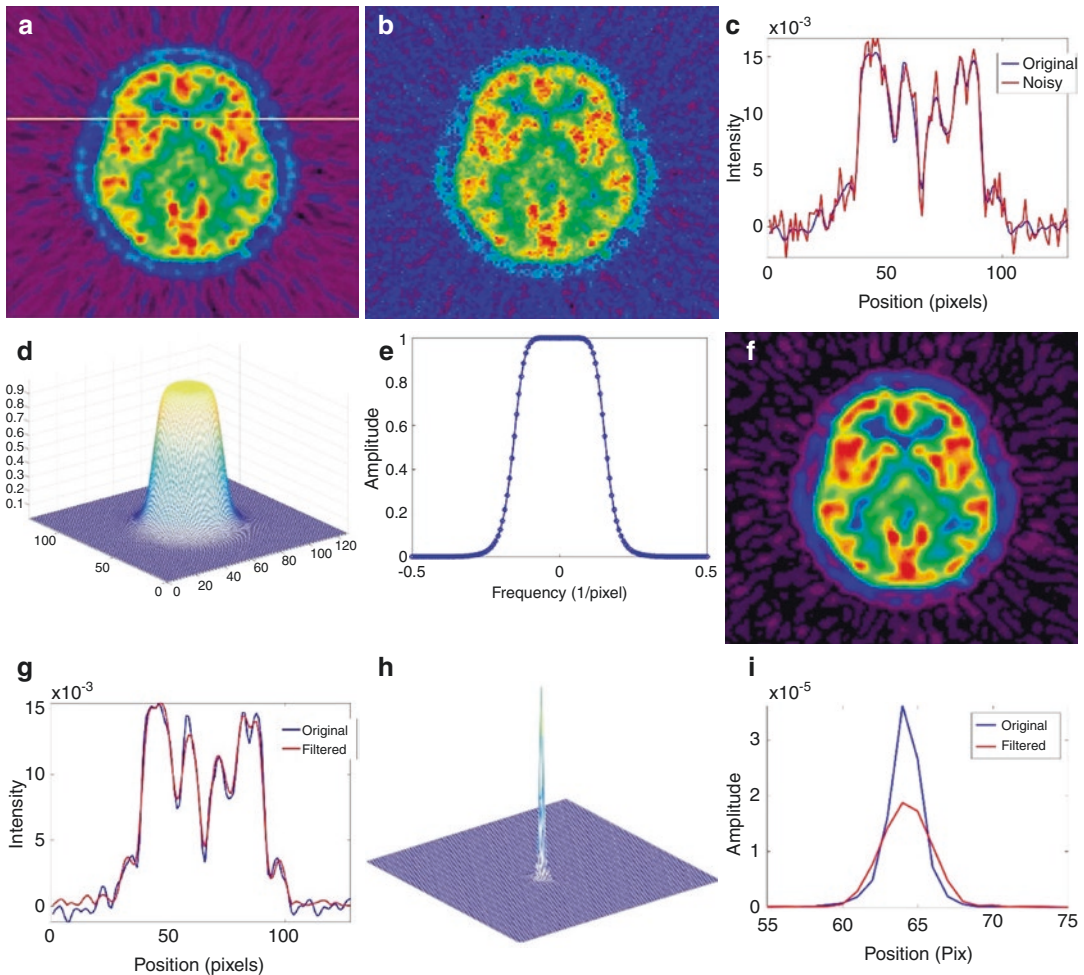
Fig. 21.3 Effect of filtering image noise with a Butterworth filter on image spatial resolution. (**a**) Original brain image from a healthy young volunteer measured with ^{18}F-FDG. The line through the image indicates the position of the profiles plotted in (**c**, **g**). (**b**) Original image added a Gaussian noise. (**c**) Profiles from images in (**a**) and (**b**) depicting the added noise. (**d**) 3D display of a Butterworth filter with a frequency cutoff of 20 and an order of 4. (**e**) A single filter from (**d**) showing its shape and frequency. (**f**) Image in (**b**) with noise filtered with the Butterworth filter. (**g**) Profiles from the images in (**a**, **f**). The filtering effectively reduced the noise, but it did not accurately retrieve the original image. (**h**) Image of a line source. (**i**) Filtering of a line source image resulted in a spread out of the image provoking a deterioration of the spatial resolution

ing the coincidences. This time of detection induces an imprecision on the position of photons emission. Meanwhile, the imprecision on the position was exploited to provide an interval of distance Δx containing the position of the emission along the line of coincidence (source at S on the D0 − D1 coincidence in Fig. 21.2). Note that the faster is the detection, the shorter is Δx. Suppose that the emission source is placed at S as in Fig. 21.2. The time taken by the annihilation photons to travel from S to the coincident detectors D0 and D1 is respectively t_0 and t_1, and $\Delta x = c\Delta t/2$ with $\Delta t = |t_0 - t_1|$ with c is the speed of light (c varies in air and body) [3, 24, 25].

With Philips Gemini TF PET scanners based on LYSO crystals among the first scanners which took advantage of time-of-flight correction [26], the timing resolution was about 500 ps [25]. At this resolution time, the position of positron annihilation can be located at an estimated distance of

7.5 cm on the line of detector coincidence. It has been reported that LaBr3:Ce crystals coupled to SiPMs can reach a timing resolution of 100 ps providing a positioning resolution of 15 mm [27]. Briefly, the implementation of time-of-flight correction is made during image reconstruction by affecting the position of the detected coincidence photons, based on their times of detection, at a confined interval of image bins Δx, instead of to be located on the whole line of response in the field of view. Note that correction for time-of-flight helps in detecting small structures such as small tumors or blood vessels, but it allows also to remove false positive signals in the images (see Fig. 21.7 in [28]).

Several corrections are already included in image reconstruction like radioactivity decay, correction for attenuation, scatter, random, and normalization. The other important factor which is not implicitly considered during image reconstruction is PVE. PVE manifests by expanding the intensity of small size objects, comparable to the scanner spatial resolution or less, beyond their real size. The spill-out (from the object) and spill-in (into the object) introduce errors on object size and intensity. Another factor with comparable consequences as PVE is organ movement. The heart beats force myocardium tissue to be at the position of the ventricular blood pool and vice-versa. This reciprocal contamination results in additional counts in tissue at early frame times and in blood at later frame times in dynamic acquisition (Fig. 21.4). Organ movement like imaging the heart or the lungs can be corrected by recording electric signals by means of electrodes placed on the chest of the patient. Based on the times of these signals, the PET raw data can be reassembled to generate image frames corresponding to a set of time intervals [29]. Figure 21.5 shows an example of a rat heart gated images in 16 frames of 16 ms from a total of 30 min acquisition.
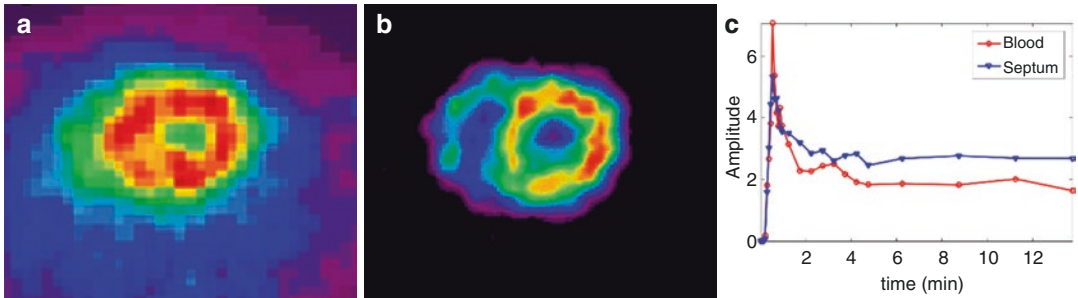
Fig. 21.4 (**a**) A frame image of a rat heart from a dynamic image sequence. (**b**) Image of a rat heart synchronized on heart beats. In (**a**) the reciprocal contamination of tissue and blood blurred the image, and in (**b**) the myocardium tissue appears thin and even the right ventricle is discriminated. (Recent small animal scanners provide better spatial resolution images than these ones but the effect of the mutual contamination remains serious). (**c**) Time–activity curves obtained from the septum and the blood pool in the image in (**a**) showing the blood peak in the septal curve and the high activity at later time points in the blood curve

Fig. 21.5 Rat heart gated images in 16 frames of 16 ms each. Here only eight images are shown
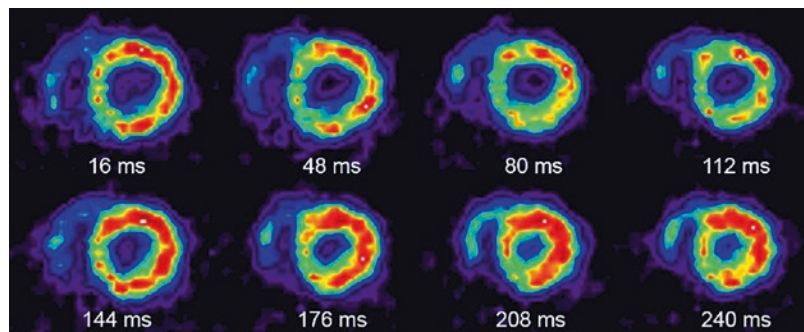
The other movement which might occur during PET imaging is patient movement. In dynamic mode acquisition where the frames are usually short especially early after radiotracer injection, by plotting the time–activity curve of a tissue, it is possible to detect, based on the shape of the curve, the time of the movement. A correction can be made on the curve itself. This procedure is not always simple. The movement can introduce more drastic errors in a single scan acquisition where, due to patient movements, tissue images can overlap, and a tissue can be identified wider than its actual size. Since most PET scanners currently generate events detection in list mode, the best way is to reposition the photon coincidences to their right place with several approaches. The right place of the coincidences is obtained by measuring the movement of the patient as translations and rotations. In the past, these movements were assessed by dense markers for CT imaging and filled with radioactivity for PET imaging. With recent approaches, no markers and no patient manipulation are needed for such tasks, only video cameras take a movie of the patient during the scans, and based on the morphology of the patient, the movements can be retrieved from the video, and these movements serve to correct the PET raw data. This procedure is very useful in brain imaging [30] and other approaches are used for the thorax and abdomen [31].

Since we are talking about brain, let us add another correction which is for brain structure atrophy. Mainly with age, some brain structures become reduced in their volume, and on the images with PET, they appear with low intensity [32].

21.3 Multimodal Imaging

Correction for photons attenuation in PET images is mandatory especially in large bodies like in humans. Monte Carlo simulations demonstrated that only around 9% of the photons are not scattered, 10% of the photons have a single scattering of one of the annihilation photons, and the rest have more than a single scattering for both annihilation photons [33] (Fig. 21.6). Without attenuation and scatter corrections, the images are noisy, having extended background and low intensity, and internal structures in the patient appear with low intensity than the structures on the periphery of the body, thus drastically affecting the contrast.

To correct for photons attenuation, the number of photons detected in a coincidence, the position of photons emission and the medium through which they travel should be known. The first and second are known based on the few transmitted photons recorded in the image. The third is known by measuring the density (in fact density and atomic number) of the medium traversed by the photon. With the early PET scanners, a rotating line source with a long half-life (e.g., ^{68}Germanium [34]) was placed near the scanner detector rings which detected one of the annihilation photons, and the other photon was detected after being transmitted through the patient. The source was rotating around the PET field of view without the patient in the scanner to give a blank scan, then with the patient to give a transmission scan, and finally the line source was retracted and hidden in a box of a dense metal like lead before
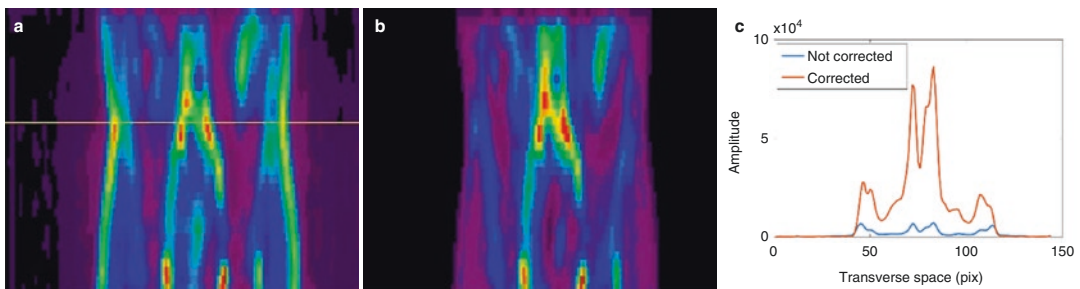
Fig. 21.6 Whole-body image not corrected (**a**) and corrected (**b**) for attenuation and scatter. The images show the aorta and the bifurcating iliac arteries. (**c**) Profiles through the iliac arteries from both images. The profile from the non-corrected image accounts for 12.5% of the counts from the corrected one
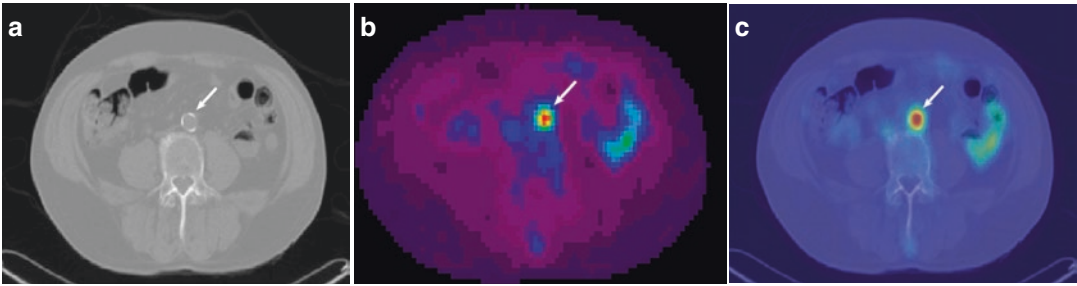
Fig. 21.7 (**a**) CT image showing aorta calcification. (**b**) Corresponding PET image obtained with ^{18}F-FDG. (**c**) Fused CT and PET images

imaging the patient. The blank scan without the patient served to measure the N_0 emitted photons in each coincident detectors, then with the patient in the field of view, the detectors measured the N transmitted photons ($N = N_0 \exp(-\mu x)$), from which the attenuation coefficient μ at each pixel of the image was calculated. The correction for attenuation was then processed for each detector coincidence as $C_{\text{corrected}} = C_{\text{detected}} * \exp \sum_i (\mu_i * \text{pixel width})$ [18]. The attenuation map obtained with such procedures was very noisy. Later, when PET was combined with CT, the rotating source was abandoned and more precise attenuation maps were obtained from CT images directly providing images of attenuation coefficients, but at low energies, which need some corrections to be used for the 511 keV annihilation photons [35]. Attenuation correction with CT is fast in acquisition, has high spatial resolution and less noise. If the scatter correction approach is not efficient, the N detected scattered photons in the patient or in the detectors can be counted as primary photons and used for attenuation correction, even though a scatter discrimination energy window is used and the photons are registered with their energies.

The contribution of CT to PET imaging has not only its importance to correct for attenuation or in its ability to display anatomical structure to allow locating active region in PET imaging either by image fusion or by image coregistration, CT, on its own side can do more, like detecting neoplasms in the whole body or calcifications in arteries, and its unavoidable use in treatment planning in radiotherapy. Its weakness is mainly its reduced contrast in soft tissue (e.g., at low dose, inability to discriminate brain gray and

white matter) and its radiation dose to the patient (Figs. 21.7 and 21.8).

Brain images are excellent with MRI for both spatial resolution and contrast in tissue (Fig. 21.9). MRI is a multiparametric imaging with the capability to measure perfusion, metabolism, cell density and connectivity, and tissue organization. Another advantage of PET/MRI is that they can be used simultaneously spatially and temporally providing complementary information correlated in time [19, 36]. MRI, like CT, can help to correct for PVE, but MRI can do more, for example, to correct PET images for patient motion, respiratory and heart movements [37, 38]. Technically, the PET scanner is inserted in the MR scanner and the front electronic of PET is shielded or is located at a distance [36]. The radiofrequency coils of MRI are inserted inside the PET scanner. They, of course, attenuate the annihilation photons and thus they have to be taken into account in PET attenuation correction [19, 36]. The inconvenient with MRI in this context is its lengthy acquisition to be added to that of PET especially in dynamic mode which can exceed 60 min for both acquisitions [39].

21.4 Specific Imaging Protocols

Some imaging protocols with PET are straight forward like imaging a tumor in the neck with ^{18}F-FDG, i.e., ask the patient to fast for at least 6 h with free access to water, and not to practice hard physical works. Before the scan, the radiotracer is injected in the patient, a waiting time of some 30 till 60 min for its uptake, then the scan is acquired. The patient should be comfortable and
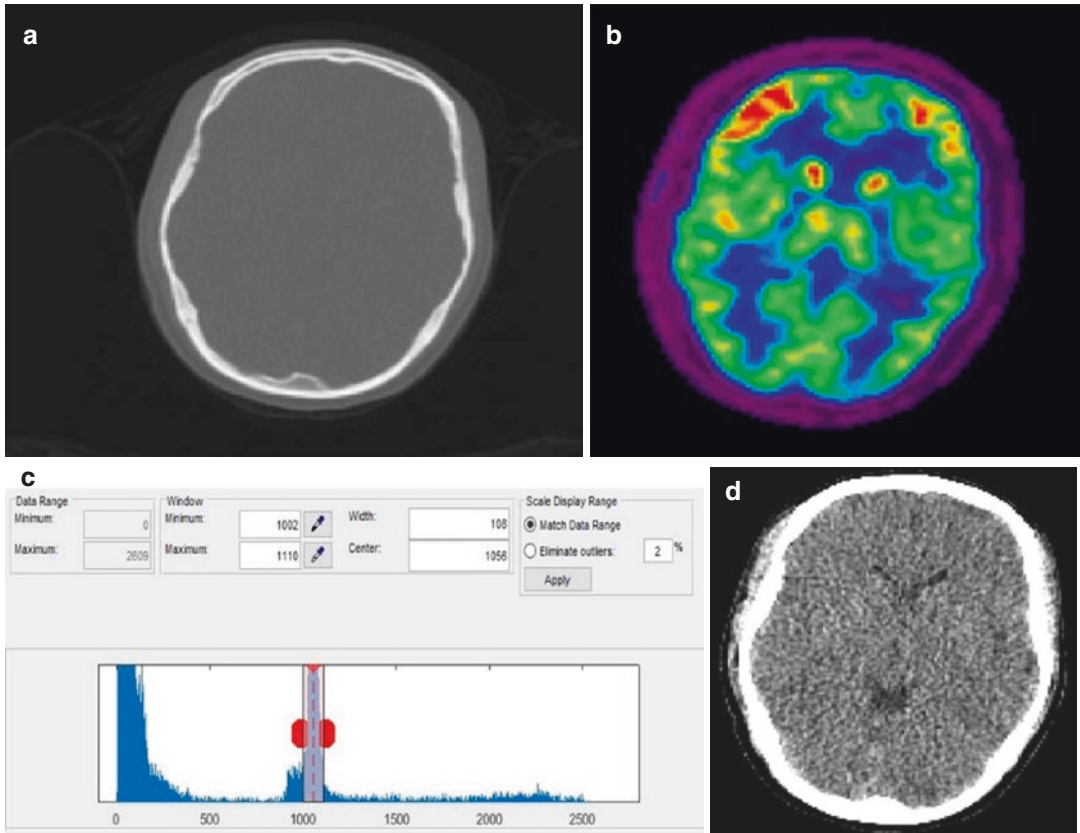
Fig. 21.8 (a) Low-dose CT image of the brain. No brain structure can be identified on this image. (b) Corresponding PET image with ^{18}F-FDG in the same subject. (c) Histogram of image in (a) with a threshold window of 1002–1110 on image intensity to show up some structures in image in (d)
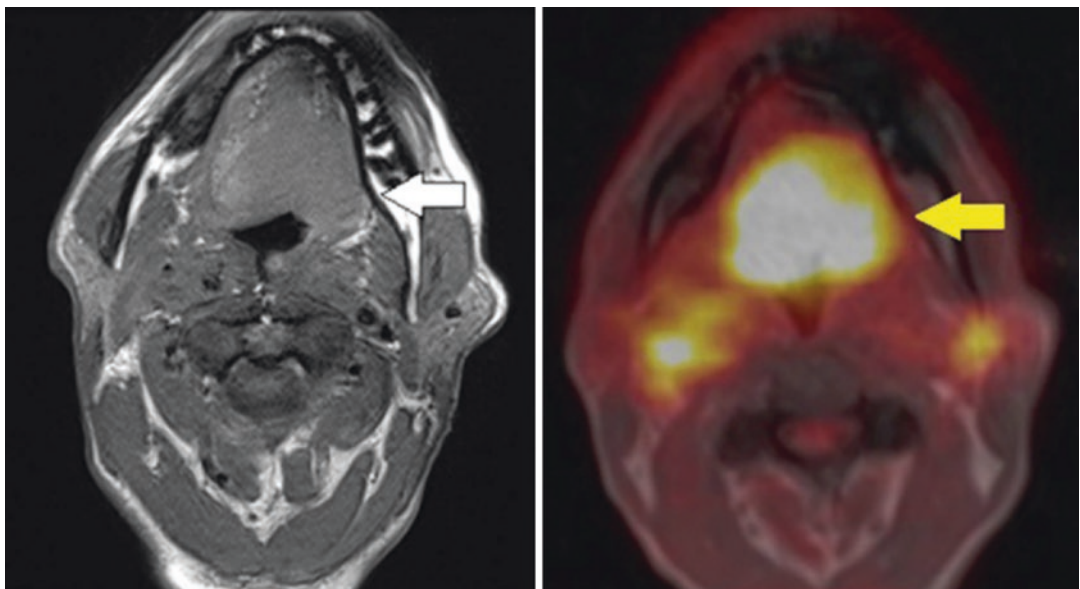

Fig. 21.9 MRI (left) and fused MRI with PET (right) showing abnormality in the tongue of a patient. (Figure extracted from [12] with permission from Elsevier)

in room temperature. However, imaging the heart with ^{18}F-FDG, or a more complicated task like imaging the coronary arteries, necessitates more preparations. This is because the heart can use other substrates than glucose. In fact, the myocardium uses fatty acids in 70% of the cases for its function. It can also use glucose, lactate, and ketone bodies [40]. The option to utilize one substrate or the other depends on the state of the heart as being under stress or affected by a disease like diabetes, even though glucose necessitates less oxygen than fatty acids to be metabolized.

Imaging heart metabolism with ^{18}F-FDG requires the assurance that the heart is ready to use glucose instead of other substrates. To be successful, the imaging has to be preceded with some manipulations called glucose clamp technique. At the beginning, the clamp technique was proposed to test tissue utilization of glucose and its sensitivity to insulin [41]. Two types of clamps can be used: the hyperglycemic and the hyperinsulinemic clamps. They both consist in supplying high levels of glucose or insulin, respectively, with perfusion or infusion. Recall that a high level of blood glucose is lowered by infusion of insulin.

Two common approaches are used in PET imaging with ^{18}F-FDG: the hyperglycemic (HG) and the hyperinsulinemic euglycemic (HIE) techniques. In HG, and after fasting for some 6 h, the patient is given glucose loads based on the fasting plasma glucose. Vitale et al. administered glucose and insulin according to the concentration of glucose in the plasma: (1) if fasting plasma glucose level <7 mmol/L, 25 g of glucose solution is orally taken; (2) if fasting plasma glucose is between 7 and 11 mmol/L, 5 IU of intravenous insulin is given; if fasting plasma glucose is above 11 mmol/L, 10 IU of intravenous insulin is given. Imaging with ^{18}F-FDG starts 1 h later [42]. For HIE which consists in dosing with insulin and maintaining glucose level constant (euglycemic), infusion of 40mU/min/m^2 of body surface area is given then glucose infusion is progressively supplied in order to maintain the plasma glucose level constant when 3 glucose plasma samples obtained at intervals of 5 min do not dif-
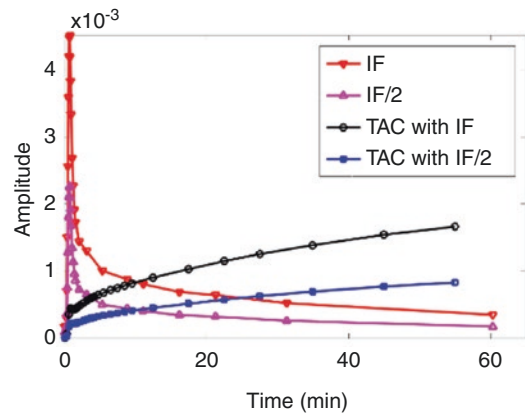
Fig. 21.10 Effect of lowering plasma time–activity curve on tissue uptake of ^{18}F-FDG. IF/2 was obtained by dividing IF by 2. Keeping the same rate constants and blood volume but replacing IF with IF/2 resulted in a tissue TAC which is half of the TAC obtained with IF. In fact, the mathematical demonstration is trivial: TAC = Model $\otimes$ IF, and TAC/2 = Model $\otimes$ IF/2 which is same as TAC/2 = 1/2(Model $\otimes$ IF), i.e. TAC/2 = 1/2(TAC), with the symbol $\otimes$ for convolution operation

fer by 5%, at that stage, the steady state can be considered achieved and the ^{18}F-FDG scan is initiated [42]. Body surface area can be obtained with these two formulas [43, 44]: BSA[m^2] = $w^{0.425}$[kg] × height$^{0.725}$[cm] × 0.007184 and BSA [m^2] = [w[kg] × height[cm]/3600]$^{1/2}$. The unit of insulin infusion is U, which means unit, and it accounts for approximately 34.8 µg of pure crystalline insulin depending on its origin [45, 46].

Lowering plasma ^{18}F-FDG has an impact on tissue uptake of this tracer, but it has no effect on tissue kinetic parameters. As illustration, Fig. 21.10 depicts plasma time–activity curve and a time–activity curve in the putamen of a normal subject imaged with ^{18}F-FDG. When dividing the plasma time–activity curve by 2 then calculating tissue uptake without changing the rate constants and the blood volume fraction, the new time–activity curve was found as the half of the previous one. These calculations are just mathematics, but Carson et al. demonstrated that this is what happens if the plasma glucose is lowered by hyperinsulinemic euglycemic clamp [47]. These authors compared in the same group of individuals the Patlak plot slope from a brain region with and without the clamp, and they
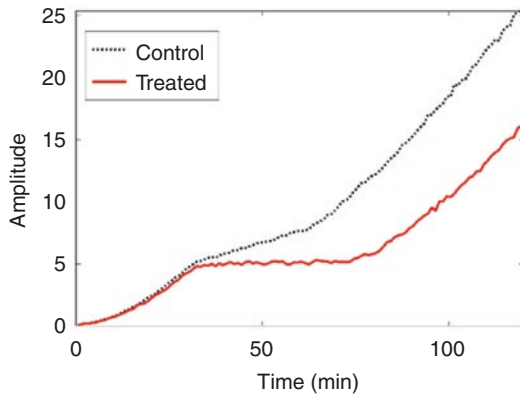
Fig. 21.11 Control and treated rat tumors. Twenty four hours before PET-^{18}F-FDG imaging for 2 h, the rat was injected by an infusion of ZnPcS2. At the time of PET imaging, the light was focused on the tumor to be treated for 30 min, 30 min after ^{18}F-FDG injection and scan initiation. The combination of the light with ZnPcS2 depressed ^{18}F-FDG uptake in the treated tumor, but marginally affected the control tumor which was hidden from the light [49]

observed that the plasma curve of ^{18}F-FDG was lowered by the clamp and consequently the brain region time–activity curve was also lowered, but the Patlak plot slope did not change. From this example, one can note that not all parts of the imaged body are equally supplied by the same quantity of radiotracer in blood, but there should be the same radiotraceur concentration [48]. This is not the case if a perturbation is locally applied to the blood supply or to a tumor itself as shown in Fig. 21.11. In Fig. 21.11, a rat bearing two tumors on the flank, one as a control and the other to be treated, was administered a photodynamic therapy product (ZnPcS2) which is recognized to act on the tumor [49]. The treatment of the tumor consisted in the illumination for a duration of 30 min with a laser light of 670 nm at 30 min after ^{18}F-FDG injection, and the PET scan was carried out for 120 min in dynamic frames of 1 min each. The perturbation with the light affected the time course of tumor uptake of ^{18}F-FDG.

This reasoning includes the most common physical aspect distorting the input function (IF) when extracted from the images. It is well known that PVE affects IF derived from the images not only by pulling down the function as a whole

(i.e., reducing its amplitude), but the decrease of its amplitude occurs early after the injection when the radiotracer activity is mainly contained in blood (spill-out), and there is an increase of amplitude later when the radiotracer has been accumulated in the neighboring tissues where IF is defined (spill-in). Since PVE affects IF not only by a weighting factor as explained above, but by distorting its shape, hence a correction with a geometrical recovery factor to a time–activity curve appears to be not appropriate [50–52]. In fact, each frame image should be specifically corrected. Note that correction for spill-in and spill-out in moving tissues like the heart can be included in the kinetic modeling [53]. Definition of regions-of-interest (ROI) on images either for tissue assessment or for IF definition from heart chambers or from arteries has to be carefully conducted. It has been shown that IF from images is trustable and that from the descending aorta is more accurate as this artery is enough large (25 mm [54, 55]) in comparison to PET scanners spatial resolution [56, 57]. For brain imaging, in average, the actual size of the common carotid artery is greater than 6 mm in men and women, in comparison to the transaxial and axial spatial resolution (full width at half maximum) of a typical scanner which are respectively 5.1 and 4.8 mm [58]. Apart from the size of the tissues to be analyzed, the radiotracer has its role in spill-in and spill-out regions. For example, imaging with $H_2^{15}O$, which is freely diffusible will impact very marginally the arteries when defining IF. Same is the case of imaging with ^{18}F-FMISO which accumulates in hypoxic tissues (not well perfused and lacking oxygen), thus having a lesser effect on IF definition. On the contrary, a necrosed central part of a tumor can appear falsely active due to the spill-in from the high uptake of the radiotracer in the tumor.

With most radiotracers, PET images are usually acquired following a bolus injection of the radiotracer. In some instances, the radiotracer can be administered by infusion like $H_2^{15}O$ or by inhalation when it is in a gas form like $^{11}_6CO_2$, $C^{15}O_2$, $^{15}_8O_2$ [59, 60]. Infusion of a radiotracer is to compensate for its short half-life and clearance from an ROI, and its flow can be determined at

equilibrium [48]. In brain studies with activation paradigms using a bolus injection of $H_2^{15}O$, the time window of changes in cerebral blood flow to allow the detection of the activation is about 20 s. By using a radiotracer infusion, this window is widened which can accommodate more complex activation routines or repeated short activations for a better estimation of cerebral blood flow [61]. It has been reported that a continuous infusion can serve to assess receptor binding parameters at baseline and during a stimulus instead of two bolus injections [47, 62]. In these references, it was suggested to combine bolus and infusion injections in receptor binding studies, and by taking several short scans helps to determine when the constant radioactivity in tissue is reached. Finally, radiotracer infusion is more appropriate to appraise an intervention during the online PET imaging (Fig. 21.11) [49].

21.5   Image Assessment

In the clinic, imaging is mostly processed in a single scan sometime after radiotracer injection. This is advantageous to scan more patients. Recently, simple or semiquantitative analyses were implemented in the scanners to help for a better visualization and also to provide quantitative parameters like the standard uptake value (SUV). It is time consuming to proceed quantitative measurements in the clinic and there is a need to specialists in image analysis to work nearly side by side with the clinicians since there is actually no methods fully validated and implemented to be autonomously used by the clinicians. Several corrections should be implemented by the scanner manufacturers, at least for cancer imaging with ^{18}F-FDG, like PVE correction, patient and organ motion, image reconstruction at the spatial resolution of CT or MRI, noise reduction, etc. Apparently, machine learning and deep learning will be implemented in the clinic before the implementation of pharmacokinetic modeling (the latter could never happen in its present form mainly because of its time consuming!).

In research, many techniques have been reported in the literature on image measurements

and analyses and there is an appreciable ease in the development of radiotracers. There are even more, like the establishment of patient research partners associations which directly consolidate the research in several ways such as recruitment of subjects, improvement of the participation, collaboration and protection of the subjects, long-term follow-up of subjects, establishing links between the researchers and the population [63]. Some such associations are located on site in hospitals and universities.

Not all imaging protocols can be routinely carried out, some diseases and some organs to image are intrinsically challenging. For example, PET imaging of cancer in the lung is affected by lung movement, and imaging of atherosclerosis with any radiotracer is difficult because of artery movement, thin artery wall, and presence of blood in the artery. Lung movement effect in images can be reduced by gating lung motion during the measurement which reduces tumor volume by around 28% and enhances its SUV by some 56% [64]. For the second example, in atherosclerosis, imaging with ^{18}F-FDG is expected to detect the inflammation within artery wall, and this inflammation could be the initiation of the disease, i.e. formation of the atherosclerotic plaque (atheromatous plaque), or the plaque is being inflamed because it is about to detach. When the vulnerable inflamed plaque detaches, it is transported in blood till small blood vessels where it obstructs the vessel. If this happens in the brain, there would be a stroke. The rest of this section is a discussion on published studies of atherosclerosis involving several imaging and image assessment techniques.

Atherosclerosis is among the leading causes of mortality and morbidity worldwide and is the main cause of cardiovascular diseases, including heart failure, stroke, and myocardial infraction. Artery endothelial cells are normally resistant to blood flow and to cell adhesion like leukocytes. However, genetic predisposition, hypertension, insulin resistance, aging, obesity, high saturated fat diet, and smoking contribute to the expression of endothelial adhesion molecule such as P-selectin and vascular cell adhesion molecule-1 (VCAM-1) which recruit adhesion of monocytes
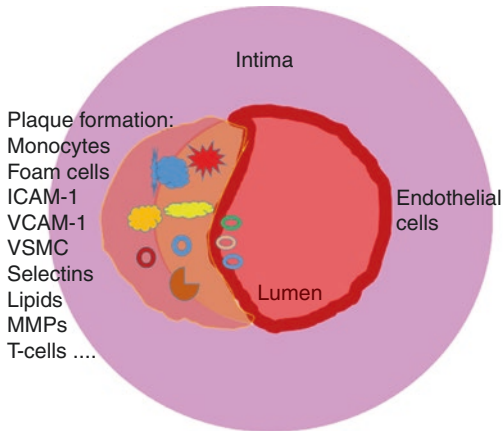
Fig. 21.12 Diagram of a cross section of an artery with a plaque containing an aggregate of several types of cells

and lymphocytes [65]. The atheromatous plaque is originally provoked by an inflammation of the arterial wall, intima, followed by an accumulation of vascular smooth muscle cells, blood-derived inflammatory cells and lipid deposit among other aggregates (Fig. 21.12) [65, 66]. With time, often over many years, the lipid rich plaque evolves to fibrotic and then to calcification [67]. When calcified, the plaque hardens and can remain stable the whole life of the individual [67, 68]. Another study showed that even healthy aged individuals have calcified artery segments (23% of analyzed artery segments were calcified) [69]. Notwithstanding, in a study on 95 months conducted by Ohya et al., the authors reported that in 70 patients with large aortic area of calcification and 67 patients with smaller area, that 67% and 37% deaths occurred in the former and latter groups, respectively, and that cardiovascular deaths were 51.4% in first group and 14.9% in second group [70].

The complications resulting from the plaque are when its volume increases, its cap becomes thin, and then it becomes more inflamed and prone to rupture. The challenge is then how to detect a vulnerable plaque. Generally, atherosclerosis develops silently till the appearance of some complications. The actual test for atheromatous inflammation is with C-reactive protein (CRP) [65]. Tumor necrosis factor-α (TNF-α) is a cytokine (i.e., a protein produced by cells for com-munication between cells) produced by macrophages, endothelial cells and smooth muscle cells which are all present in the plaque. TNF-α stimulates interleukin-6 (IL-6) production by the smooth muscle cells, and IL-6 stimulates the production of CRP in the liver [71]. However, CRP is not specific to vulnerable atheromatous plaques if this protein is produced consequently to other inflammations. It cannot locate the origin of the inflammation, thus, imaging of atherosclerosis is the best avenue to diagnose, locate, and estimate the vulnerability of the plaque. About plaque inflammation treatment, the only available drugs are the statins. They are produced under several names (atorvastatin, pravastatin, fluvastatin, lovastatin, rosuvastatin, and simvastatin) [71, 72]. There are other therapies like reducing meal fat, alcohol, and tobacco, and practicing regular physical activities.

21.5.1 Imaging of Atherosclerosis

The primary goal of atherosclerosis imaging is to detect and locate the artery inflammation which is a precursor to its rupture. There have been several attempts to measure plaque vulnerability with diverse techniques, among them CT, MRI, intravascular ultrasound (IVUS), CT coronary angiography (CTA), PET, single photon emission computed tomography (SPECT), and other techniques [73–78]. Most of these techniques allow the determination of the volume of the plaque and its constituents based on their density and other physical parameters, but till now none of them is able to detect the vulnerability of the plaque. Some of these imaging modalities are invasive like IVUS where a transluminal catheter having a transducer of size around 1 mm is inserted in the artery, and it provides images with 80–200 µm of spatial resolution of soft, fibrous, or calcified plaques. CTA is also invasive. It consists in the insertion of a catheter through the radial or femoral artery till reaching the coronary artery where a contrast agent is injected followed with X-ray imaging.

Inflammation can be seen as cells metabolic activity, and the most appropriate imaging tech-
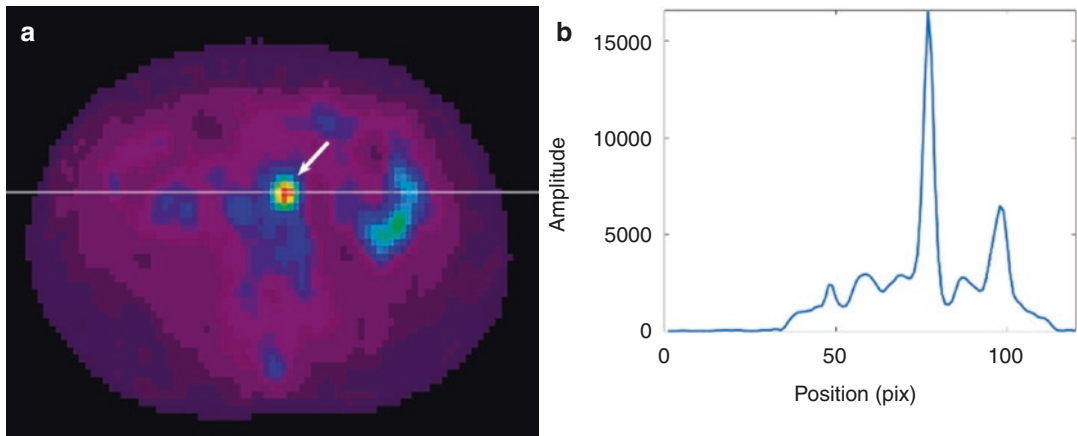
Fig. 21.13 (**a**) PET-^{18}F-FDG transaxial image through the aorta (arrow), and (**b**) profile through the aorta (white line in **a**)). Although this artery slice has calcification, the profile shows a single Gaussian-like peak of the artery

nology for metabolism is PET imaging with appropriate radiotracers. It is not necessary to have a high spatial resolution to locate the artery plaque, its presence at some 5 cm of precision is sufficient enough. If CRP is not specific to artery inflammation neither it can locate the inflammation, PET imaging is too expensive and less available to be used for screening patients to diagnose atherosclerosis. Still, this disease actually remains not faithfully diagnosed. The other hindrance with PET imaging is its difficulty to image the plaque and the artery wall in the presence of the radiotracer in blood which constitutes most of the signal. Figure 21.7 shows images of an artery calcification imaged with CT and uptake of ^{18}F-FDG with PET in the same artery slice. In this CT image, the calcification appears totally surrounding the artery lumen. Of course, on the PET image, there is no distinction between the artery tissue, the calcification and the blood as depicted in Fig. 21.13 where a profile was horizontally extracted from the PET image through the artery, showing a form of Gaussian even at later image frames.

Imaging atherosclerosis with CT allows to clearly locate the calcifications, and even to count the number of calcifications, their intensity and volume [79]. It is known that ^{18}F-FDG has the potential to detect active cells and inflammation, but there are technical hindrances in analyzing the images because of the movement and the thinness of artery walls. The state of the artery being calcified is expected to not uptake ^{18}F-FDG as in the inflammation. On the contrary, when no calcifications are apparent on CT images, there could be an initiation of inflammation which could be detected with PET-^{18}F-FDG. In healthy arteries, there could be also an uptake of ^{18}F-FDG as the arteries are continuously working muscles (media layer). Then, is-it possible to discriminate the calcified, the inflamed and the healthy artery segments in a patient with ^{18}F-FDG? Based on the publications, it seems no clear discrimination between these three artery states was reported. The research was then oriented toward labeling other molecules to specifically target molecules or cells properly involved in atherosclerosis. Several radiotracers have been used in PET like ^{18}F-NaF for bones and artery microcalcifications [80], ^{18}F-mannose [81], 11C-acetate [80], and in SPECT like 99mTc-radiolabeled low-density lipoprotein, and 99mTc and 111In labeled antibodies [82]. Other radiotracers were also reported in the literature [73, 83]. There is actually a consensus that ^{18}F-NaF can image parts of the arteries not being calcified, which means ^{18}F-NaF and CT images provide complementary information, and that ^{18}F-NaF images could be able to locate the building plaque, which does not implicitly mean it can detect the vulnerable plaque [21, 84, 85].

21.5.2 Quantification of Atherosclerosis Imaging

Several studies reported in the literature have their data retrospectively extracted from images of patients who have been scanned for cancer. Such patients could have been taking medication. Very few images were dynamically acquired and analyzed with kinetic modeling which is the most precise approach. Most of the analyses were done with SUV and tissue-to-background or to blood ratio (TBR), and finally, PVE correction was not generally taken into account [86].

The calcifications on CT images were in most publications classified following Agatston et al. scores [87], where each calcification of area greater than 1 mm^2 and of density more than 130 Hounsfield units (HU) was attributed a level as: 1 for density between 130 and 199 HU, 2 for 200–299 HU, 3 for 300–399 HU, and 4 for >400 HU.

Another quantification based on calcification extent was suggested by Derlin et al. [80]. The calcification extent in each artery segment was scaled based on its extent with respect the circumference of the artery wall: 0 means no calcification, 1 means the calcification occupies less than 25% of artery circumference, 2 for 25–50%, 3 for 50–75%, and 4 for calcification extent occupying more than 75% of artery wall. While it is difficult to assess the extent of calcifications, it is more practical to use their areas. Area of artery and areas of calcifications in the same artery can be easily defined by image segmentation. This approach is more precise as the calcification is not unique within an artery segment, in fact, it can occupy different non-adjacent areas [70, 79].

Both of calcification density scores and area levels are independently processed on CT images. For PET image analysis, when the images are acquired in dynamic mode, the sum of the early images can help locating the arteries and veins on each image slice. CT images can also be used to locate the arteries and veins and a CT atlas can be of great help. It is preferable the images be segmented by automatic tools like active contours as these provide reproducible results. An important feature in this type of analysis is image coregistration. Usually PET images are interpolated to match CT images which are of high spatial resolution, and of importance by detecting the calcifications, or by locating stenoses in case of using CT with contrast agents. PET and CT images are different in pixel size which includes number of pixels in the image, the slice sampling and the total number of slices. A PET image is generally made of 144 × 144 pixels depending on scanner architecture. CT images are generally of 512 × 512 pixels. Slice thickness for PET is of 4 mm, while that of CT is of 2 or 4 mm (these numbers are given as indication only). The coregistration of CT and PET images, by any method, will undoubtedly introduce uncertainties, if not, inaccuracies. The coregistration is made in the transaxial and axial views to match the 512 × 512 CT image pixels. The drawback of the coregistration is that it dilutes the data during the mathematical operations. As an example, if a calcification is present on one slice but not on the neighboring slices, by image transformation, the intensity and localization of this calcification would be distributed even on the slices where it does not really exist. In some publications, the authors reported the drawing of an ROI on the arterial wall on the coregistered PET/CT images [88]. Since the PET image of the artery appears like a Gaussian even on the last image frames (Fig. 21.13b), its transformation by coregistration to CT image does not change its shape, and it is not a priori possible to discriminate the arterial wall. Thus, the ROI drawn on the artery wall accounts for the Gaussian flank of the mostly blood signal. The same complication holds when using other radiotracers than ^{18}F-FDG as there is a circulating radioactivity in blood which dominates that in the artery wall.

With dynamic image acquisition, for both SUV and TBR, the time of evaluation should be well defined where the exchange of the radiotracer between blood and tissue reaches a plateau. In static image acquisition, the imaging time is dictated by an appropriate imaging protocol. The images should be corrected for PVE, at least with recovery factors which amplify the image mean values based on the size of the artery images. For dynamic image acquisition, each image frame has to be corrected for PVE in case full PVE

correction is processed, i.e. by including spill-in and spill-out, since spill-in and spill-out vary with time depending on the radiotracer uptake in tissues neighboring the artery or vein images. If SUV is related to the injected activity A[Bq] as defined in SUV = C_{PET}[Bq. kg^{-1}] × w[kg]/A[Bq], the variability becomes minimized since A is not estimated from the images. For TBR, it is defined as TBR = ROI$_{artery}$/ROI$_{vein}$ [89], or, in some publications, ROI$_{vein}$ is replaced by ROI$_{blood}$ where a small ROI is drawn within the artery lumen to potentially exclude artery tissue [88]. TBR can also be obtained by the ratio SUV$_{artery}$/SUV$_{blood}$ [80]. Obviously, it seems these values are the results of blood image manipulation which dominate arterial tissue. There is a certain conflict in ROI determination on arteries. The same ROI on an artery is used as: (1) input function like in brain or tumor studies, and (2) artery studies itself like in atherosclerosis. There are those authors who assume that artery tissue is negligible in artery images, and thus an ROI on an artery like the aorta or the carotid can generate the input function for PET image analysis in other tissues than in arteries, and there are those who use the same ROI on the artery to evidence tissue parameters like SUV and TBR in atherosclerosis imaging. If tissue image in an artery is considered marginal even in the presence of a thrombus or an inflamed plaque, then this artery can serve for an IF.

21.5.3 Dynamic Imaging of Atherosclerosis

Dynamic imaging offers the opportunity to accurately analyze the images by several avenues. The cost for such protocols is the lengthy time, more than 30 min for long half-life radiotracers, which is not profitable for the clinic and not suitable for the patients who are obliged to remain for a long time within the scanner, and sometimes with the arms extended behind the head to avoid both the presence of the cannulated arm in the field of view of the scanner and the additional photon attenuation through the arms.

Dynamic imaging allows to accurately calculate the desired parameters even SUV and TBR. The time–activity curves are exploited to assess the equilibrium or steady state between the blood and tissue, to define blood in the early frames and tissue in the later frames, but above all, the time course of the radiotracer behaves differently in blood than in tissue, and this difference allows to decompose the images into blood and tissue images. The images acquired with ^{18}F-FDG which accumulates in tissue are a good example of blood and tissue separation (Fig. 21.14). By decomposing the images, the same ROI on an artery image generates time–activity curves of blood and tissue from which SUV and TBR can be accurately calculated. It remains how this decomposition is trustable. Several methods have been reported in the literature demonstrating that IF extracted from blood image component is similar to that obtained with blood sampling [50, 57, 90, 91].

If image decomposition is validated and accepted like for ^{18}F-FDG, the subsequent analyses become easier. There is even no need to determine a separate IF. With a slight modification of the pharmacokinetic model for the given radiotracer, the rate constants can be extracted. For example, for ^{18}F-FDG model, and using the macroparameters A_i and B_i instead of k_i for simplification, the model equation can be written as [92]:

$$C_{PET}(t) = \left(A_1 \exp(-B_1 t) + A_2 \exp(-B_2 t)\right) \otimes IF(t) + TBV \times C_{blood}(t) \tag{21.1}$$

where $C_{PET}(t)$ is the time–activity curve obtained from a pixel or an ROI on a given tissue, $C_{blood}(t)$ is the concentration of the radiotracer in whole blood, and TBV × $C_{blood}(t)$ is the concentration of the whole blood radiotracer in that pixel or ROI

which is usually called tissue blood volume. IF(t) can be derived from the whole blood activity $C_{blood}(t)$ as described in [92] and others with a ratio $r(t)$: IF(t) = $r(t) \times C_{blood}(t)$. Finally, the equation of the model becomes:
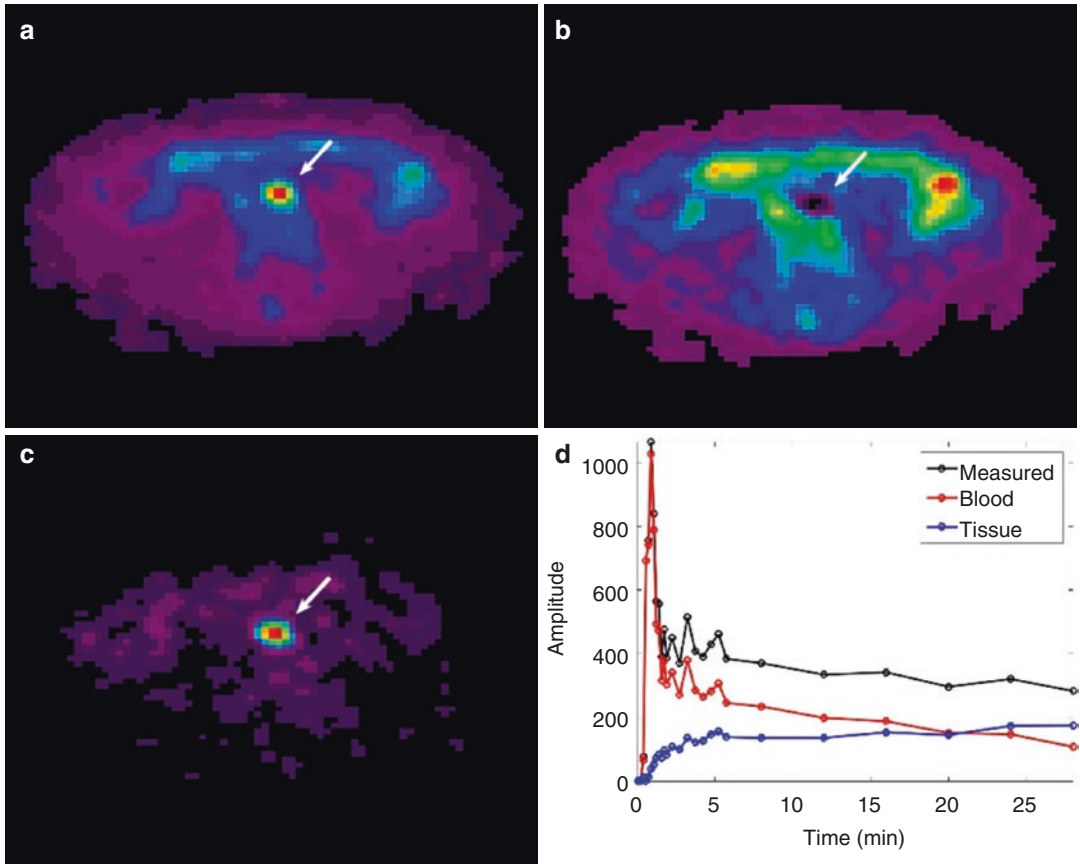
Fig. 21.14 PET-^{18}F-FDG dynamic images (**a**) decomposed with factor analysis into tissue (**b**) and blood (**c**) components and the time–activity curves of the two components obtained with a region of interest on the aorta artery (**d**). The time–activity curves were corrected for PVE with a common recovery factor of 2.7 to the whole artery, which does not correct for spill-in, nor it does correct arterial wall for PVE independently from blood

$$C_{PET}(t) = \left(A_1 \exp(-B_1 t) + A_2 \exp(-B_2 t)\right) \otimes r(t) \times C_{blood}(t) + TBV \times C_{blood}(t) \qquad (21.2)$$

By image decomposition with factor analysis, independent component analysis or by any other means, the quantity of blood volume $TBV \times C_{blood}(t)$ becomes known which can be called $C_{roi-blood}(t) = TBV \times C_{blood}(t)$, and $C_{blood}(t) = C_{roi-blood}(t)/TBV$ which, when inserted in Eq. (21.2) gives:

$$C_{PET}(t) = \left(A_1 \exp(-B_1 t) + A_2 \exp(-B_2 t)\right) \otimes r(t) \times C_{roi-blood}(t)/TBV + C_{roi-blood}(t) \qquad (21.3)$$

In case of the activity in whole blood equals the activity in plasma, $r(t) = 1$. For ^{18}F-FDG, $r(t)$ can be deduced from [92] or from recent references. In essence, the first equation (Eq. 21.1) of the model uses IF and TBV, the derived equation (Eq. 21.3) uses blood volume as defined with image decomposition and the inverse of TBV. This method has been introduced by Bentourkia [93] and applied to atherosclerosis imaging [94].

This approach has another strength. Since blood volume ($C_{\text{roi} - \text{blood}}(t)$) is defined in the same ROI as the tissue to analyze ($C_{\text{PET}}(t)$), by having the same depreciation factor due to PVE, this factor cancels out and there is no need to correct for PVE. From the derived equation (Eq. 21.3), it is possible to use tissue component as $C_{\text{PET}}(t)$ and, in that case, the last term $C_{\text{roi} - \text{blood}}(t)$ can be dropped.

Because the image decomposition in two or more components might assign noise generally to tissue components, it is recommended to use the measured time–activity curve for $C_{\text{PET}}(t)$, not the tissue component, and to keep the equation with $C_{\text{roi} - \text{blood}}(t)$.

21.6 Conclusion

Quantitative PET image analysis is still very challenging, and it is until now not practical in the clinic. The images should be self-sufficient for biological and physiological parameter calculations. The recent combination of PET/CT and PET/MRI will instigate new avenues toward total quantitative imaging, prior to the advent of deep learning for total automated imaging.

References

1. Zhang J, Maniawski P, Knopp MV. Performance evaluation of the next generation solid-state digital photon counting PET/CT system. EJNMMI Res. 2018;8:97.
2. van Sluis J, de Jong J, Schaar J, Noordzij W, van Snick P, Dierckx R, Borra R, Willemsen A, Boellaard R. Performance characteristics of the digital biograph vision PET/CT system. J Nucl Med. 2019;60:1031–6.
3. Lecoq P. Pushing the limits in time-of-flight PET imaging. IEEE Trans Radiat Plasma Med Sci. 2017;1:473–85.
4. Badawi RD, Shi H, Hu P, Chen S, Xu T, Price PM, Ding Y, Spencer BA, Nardo L, Liu W, Bao J, Jones T, Li H, Cherry SR. First human imaging studies with the EXPLORER total-body PET scanner. J Nucl Med. 2019;60:299–303.
5. Declaration of Helsinki. World Medical Association Declaration of Helsinki: ethical principles for medical research involving human subjects. JAMA. 2013;310:2191–4.
6. Huang B, Law MW, Khong PL. Whole-body PET/CT scanning: estimation of radiation dose and cancer risk. Radiology. 2009;251:166–74.
7. ICRP. The 2007 recommendations of the International Commission on Radiological Protection. ICRP publication 103. Ann ICRP. 2007;37:1–332.
8. N.S.P.N. 2-2018. Performance measurements of positron emission tomographs (PETS). Rosslyn: National Electrical Manufacturers Association; 2018.
9. Li T, Ao ECI, Lambert B, Brans B, Vandenberghe S, Mok GSP. Quantitative imaging for targeted radionuclide therapy dosimetry - technical review. Theranostics. 2017;7:4551–65.
10. Cherry SR, Jones T, Karp JS, Qi J, Moses WW, Badawi RD. Total-body PET: maximizing sensitivity to create new opportunities for clinical research and patient care. J Nucl Med. 2018;59:3–12.
11. Vandenberghe S, Marsden PK. PET-MRI: a review of challenges and solutions in the development of integrated multimodality imaging. Phys Med Biol. 2015;60:R115–54.
12. Szyszko TA, Cook GJR. PET/CT and PET/MRI in head and neck malignancy. Clin Radiol. 2018;73:60–9.
13. Nensa F, Beiderwellen K, Heusch P, Wetter A. Clinical applications of PET/MRI: current status and future perspectives. Diagn Interv Radiol. 2014;20:438–47.
14. Zaidi H, Ojha N, Morich M, Griesmer J, Hu Z, Maniawski P, Ratib O, Izquierdo-Garcia D, Fayad ZA, Shao L. Design and performance evaluation of a whole-body ingenuity TF PET-MRI system. Phys Med Biol. 2011;56:3091–106.
15. Petrillo GA, McIntyre RJ, Lecomte R, Lamoureux G, Schmitt D. Scintillation detection with large-area reach-through avalanche photodiodes. IEEE Trans Nucl Sci. 1984;31:417–23.
16. Lecomte R, Cadorette J, Rodrigue S, Lapointe D, Rouleau D, Bentourkia M, Yao R, Msaki P. Initial results from the Sherbrooke avalanche photodiode positron tomograph. IEEE Trans Nucl Sci. 1996;43:1952–7.
17. Fontaine R, Belanger F, Viscogliosi N, Semmaoui H, Tetrault M, Michaud J, Pepin C, Cadorette J, Lecomte R. The hardware and signal processing architecture of LabPET™, a small animal APD-based digital PET scanner. IEEE Trans Nucl Sci. 2009;56:3–9.
18. Jones T, Townsend D. History and future technical innovation in positron emission tomography. J Med Imaging (Bellingham). 2017;4:011013.
19. Cabello J, Ziegler SI. Advances in PET/MR instrumentation and image reconstruction. Br J Radiol. 2018;91:20160363.
20. Pichler B, Swann B, Rochelle J, Nutt R, Cherry S, Siegel S. Lutetium oxyorthosilicate block detector readout by avalanche photodiode arrays for high resolution animal PET. Phys Med Biol. 2004;49:4305–19.
21. Hsu DFC, Ilan E, Peterson WT, Uribe J, Lubberink M, Levin CS. Studies of a next-generation silicon-photomultiplier-based time-of-flight PET/CT system. J Nucl Med. 2017;58:1511–8.

22. Liu H, Wang K, Tian J. Postreconstruction filtering of 3D PET images by using weighted higher-order singular value decomposition. Biomed Eng Online. 2016;15:102.

23. Kim JH, Ahn IJ, Nam WH, Ra JB. An effective post-filtering framework for 3-D PET image denoising based on noise and sensitivity characteristics. IEEE Trans Nucl Sci. 2015;62:137–47.

24. Surti S. Update on time-of-flight PET imaging. J Nucl Med. 2015;56:98–105.

25. Vandenberghe S, Mikhaylova E, D'Hoe E, Mollet P, Karp JS. Recent developments in time-of-flight PET. EJNMMI Phys. 2016;3:3.

26. Surti S, Kuhn A, Werner ME, Perkins AE, Kolthammer J, Karp JS. Performance of Philips Gemini TF PET/CT scanner with special consideration for its time-of-flight imaging capabilities. J Nucl Med. 2007;48:471–80.

27. Schaart DR, Seifert S, Vinke R, van Dam HT, Dendooven P, Löhner H, Beekman FJ. LaBr3:Ce and SiPMs for time-of-flight PET: achieving 100 ps coincidence resolving time. Phys Med Biol. 2010;55:N179–89.

28. Lois C, Jakoby BW, Long MJ, Hubner KF, Barker DW, Casey ME, Conti M, Panin VY, Kadrmas DJ, Townsend DW. An assessment of the impact of incorporating time-of-flight information into clinical PET/CT imaging. J Nucl Med. 2010;51:237–45.

29. Lang N, Dawood M, Büther F, Schober O, Schäfers M, Schäfers K. Organ movement reduction in PET/CT using dual-gated Listmode acquisition. Z Med Phys. 2006;16:93–100.

30. Olesen OV, Sullivan JM, Mulnix T, Paulsen RR, Hojgaard L, Roed B, Carson RE, Morris ED, Larsen R. List-mode PET motion correction using markerless head tracking: proof-of-concept with scans of human subject. IEEE Trans Med Imaging. 2013;32:200–9.

31. Pépin A, Daouk J, Bailly P, Hapdey S, Meyer M-E. Management of respiratory motion in PET/computed tomography: the state of the art. Nucl Med Commun. 2014;35:113.

32. Sintini I, Schwarz CG, Martin PR, Graff-Radford J, Machulda MM, Senjem ML, Reid RI, Spychalla AJ, Drubach DA, Lowe VJ, Jack CR Jr, Josephs KA, Whitwell JL. Regional multimodal relationships between tau, hypometabolism, atrophy, and fractional anisotropy in atypical Alzheimer's disease. Hum Brain Mapp. 2019;40:1618–31.

33. Bentourkia M, Laribi M, Lakinsky E, Cadorette J. Scatter restoration in PET imaging. In: 2002 IEEE nuclear science symposium conference record, vol.1072, 2002. p. 1075–9.

34. Nakamoto Y, Osman M, Cohade C, Marshall LT, Links JM, Kohlmyer S, Wahl RL. PET/CT: comparison of quantitative tracer uptake between germanium and CT transmission attenuation-corrected images. J Nucl Med. 2002;43:1137–43.

35. van Dalen JA, Visser EP, Vogel WV, Corstens FHM, Oyen WJG. Impact of Ge-68/Ga-68-based versus CT-based attenuation correction on PET. Med Phys. 2007;34:889–97.

36. Disselhorst JA, Bezrukov I, Kolb A, Parl C, Pichler BJ. Principles of PET/MR imaging. J Nucl Med. 2014;55:2s–10s.

37. Polycarpou I, Tsoumpas C, King AP, Marsden PK. Impact of respiratory motion correction and spatial resolution on lesion detection in PET: a simulation study based on real MR dynamic data. Phys Med Biol. 2014;59:697–713.

38. Tsoumpas C, Mackewn JE, Halsted P, King AP, Buerger C, Totman JJ, Schaeffter T, Marsden PK. Simultaneous PET–MR acquisition and MR-derived motion fields for correction of non-rigid motion in PET. Ann Nucl Med. 2010;24:745–50.

39. Robson PM, Dweck MR, Trivieri MG, Abgral R, Karakatsanis NA, Contreras J, Gidwani U, Narula JP, Fuster V, Kovacic JC, Fayad ZA. Coronary artery PET/MR imaging: feasibility, limitations, and solutions. JACC Cardiovasc Imaging. 2017;10(10):1103–12.

40. Jensen MD, Ekberg K, Landau BR. Lipid metabolism during fasting. Am J Physiol Endocrinol Metab. 2001;281:E789–93.

41. DeFronzo RA, Tobin JD, Andres R. Glucose clamp technique: a method for quantifying insulin secretion and resistance. Am J Phys. 1979;237:E214–23.

42. Vitale GD, deKemp RA, Ruddy TD, Williams K, Beanlands RSB. Myocardial glucose utilization and optimization of 18F-FDG PET imaging in patients with non–insulin-dependent diabetes mellitus, coronary artery disease, and left ventricular dysfunction. J Nucl Med. 2001;42:1730–6.

43. Kim CK, Gupta NC, Chandramouli B, Alavi A. Standardized uptake values of FDG: body surface area correction is preferable to body weight correction. J Nucl Med. 1994;35:164–7.

44. Verbraecken J, Van de Heyning P, De Backer W, Van Gaal L. Body surface area in normal-weight, overweight, and obese adults. A comparison study. Metabolism. 2006;55:515–24.

45. Lacey AH. The unit of insulin. Diabetes. 1967;16:198–200.

46. Takayama M, Yamauchi K, Aizawa T. Quantification of insulin. Diabet Med. 2014;31:375–6.

47. Carson R. Tracer kinetic modeling in PET. In: Positron emission tomography. London: Springer; 2006. p. 127–59.

48. Huang SC, Phelps ME, Hoffman EJ, Kuhl DE. A theoretical study of quantitative flow measurements with constant infusion of short-lived isotopes. Phys Med Biol. 1979;24:1151–61.

49. Boubacar P, Sarrhini O, Lecomte R, van Lier JE, Bentourkia M. A real-time follow-up of photodynamic therapy during PET imaging. Photodiagn Photodyn Ther. 2015;12:428–35.

50. Zanotti-Fregonara P, Chen K, Liow J-S, Fujita M, Innis RB. Image-derived input function for brain PET studies: many challenges and few opportunities. J Cereb Blood Flow Metab. 2011;31:1986–98.

51. Harri M, Mika T, Jussi H, Nevalainen OS, Jarmo H. Evaluation of partial volume effect correction methods for brain positron emission tomography: quantification and reproducibility. J Med Phys. 2007;32:108–17.

52. Soret M, Bacharach SL, Buvat I. Partial-volume effect in PET tumor imaging. J Nucl Med. 2007;48:932–45.

53. Du Y, Madar I, Stumpf M, Rong X, Fung GSK, Frey E. Compensation for spill-in and spill-out partial volume effects in cardiac PET imaging. J Nucl Cardiol. 2013;20(1):84–98.

54. Erbel R, Eggebrecht H. Aortic dimensions and the risk of dissection. Heart. 2006;92:137–42.

55. McComb BL, Munden RF, Duan F, Jain AA, Tuite C, Chiles C. Normative reference values of thoracic aortic diameter in American College of Radiology Imaging Network (ACRIN 6654) arm of National Lung Screening Trial. Clin Imaging. 2016;40:936–43.

56. van der Weerdt AP, Klein LJ, Boellaard R, Visser CA, Visser FC, Lammertsma AA. Image-derived input functions for determination of MRGlu in cardiac 18F-FDG PET scans. J Nucl Med. 2001;42:1622–9.

57. de Geus-Oei LF, Visser EP, Krabbe PF, van Hoorn BA, Koenders EB, Willemsen AT, Pruim J, Corstens FH, Oyen WJ. Comparison of image-derived and arterial input functions for estimating the rate of glucose metabolism in therapy-monitoring 18F-FDG PET studies. J Nucl Med. 2006;47:945–9.

58. Kemp BJ, Kim C, Williams JJ, Ganin A, Lowe VJ. NEMA NU 2-2001 performance measurements of an LYSO-based PET/CT system in 2D and 3D acquisition modes. J Nucl Med. 2006;47:1960–7.

59. Saleem A, Price PM. Early tumor drug pharmacokinetics is influenced by tumor perfusion but not plasma drug exposure. Clin Cancer Res. 2008;14:8184–90.

60. Muzik O, Mangner TJ, Leonard WR, Kumar A, Janisse J, Granneman JG. 15O PET measurement of blood flow and oxygen consumption in cold-activated human brown fat. J Nucl Med. 2013;54:523–31.

61. Beason-Held LL, Desmond RE, Herscovitch P, Carson RE. Bolus injection versus slow infusion of [15O] water for positron emission tomography activation studies. J Cereb Blood Flow Metab. 2016;19:843–52.

62. Carson RE. PET physiological measurements using constant infusion. Nucl Med Biol. 2000;27:657–60.

63. de Wit M, Abma T, Koelewijn-van Loon M, Collins S, Kirwan J. Involving patient research partners has a significant impact on outcomes research: a responsive evaluation of the international OMERACT conferences. BMJ Open. 2013;3:e002241.

64. Nehmeh SA, Erdi YE, Ling CC, Rosenzweig KE, Squire OD, Braban LE, Ford E, Sidhu K, Mageras GS, Larson SM, Humm JL. Effect of respiratory gating on reducing lung motion artifacts in PET imaging of lung cancer. Med Phys. 2002;29:366–71.

65. Packard RRS, Libby P. Inflammation in atherosclerosis: from vascular biology to biomarker discovery and risk prediction. Clin Chem. 2008;54:24–38.

66. Lee S-J, Park S-H. Arterial ageing. Korean Circ J. 2013;43:73.

67. Pugliese G, Iacobini C, Fantauzzi CB, Menini S. The dark and bright side of atherosclerotic calcification. Atherosclerosis. 2015;238:220–30.

68. Nandalur KR, Baskurt E, Hagspiel KD, Phillips CD, Kramer CM. Calcified carotid atherosclerotic plaque is associated less with ischemic symptoms than is noncalcified plaque on MDCT. AJR Am J Roentgenol. 2005;184:295–8.

69. Orellana MR, Bentourkia M, Sarrhini O, Fulop T, Paquet N, Lavallee E, Turcotte E, Khalil A. Assessment of inflammation in large arteries with 18F-FDG-PET in elderly. Comput Med Imaging Graph. 2013;37:459–65.

70. Ohya M, Otani H, Kimura K, Saika Y, Fujii R, Yukawa S, Shigematsu T. Vascular calcification estimated by aortic calcification area index is a significant predictive parameter of cardiovascular mortality in hemodialysis patients. Clin Exp Nephrol. 2011;15:877–83.

71. Blake GJ, Ridker PM. Novel clinical markers of vascular wall inflammation. Circ Res. 2001;89:763–71.

72. Darwish IA, Al-Obaid AR, Al-Malaq HA. Generation of polyclonal antibody with high avidity to rosuvastatin and its use in development of highly sensitive ELISA for determination of rosuvastatin in plasma. Chem Cent J. 2011;5:38.

73. Gaemperli O, Shalhoub J, Owen DRJ, Lamare F, Johansson S, Fouladi N, Davies AH, Rimoldi OE, Camici PG. Imaging intraplaque inflammation in carotid atherosclerosis with 11C-PK11195 positron emission tomography/computed tomography. Eur Heart J. 2011;33:1902–10.

74. Cai J-M, Hatsukami TS, Ferguson MS, Small R, Polissar NL, Yuan C. Classification of human carotid atherosclerotic lesions with in vivo multi-contrast magnetic resonance imaging. Circulation. 2002;106:1368–73.

75. Andrews JPM, Fayad ZA, Dweck MR. New methods to image unstable atherosclerotic plaques. Atherosclerosis. 2018;272:118–28.

76. Revkin JH, Shear CL, Pouleur HG, Ryder SW, Orloff DG. Biomarkers in the prevention and treatment of atherosclerosis: need, validation, and future. Pharmacol Rev. 2007;59:40–53.

77. Vallabhajosula S, Fuster V. Atherosclerosis: imaging techniques and the evolving role of nuclear medicine. J Nucl Med. 1997;38:1788–96.

78. Achenbach S, Raggi P. Imaging of coronary atherosclerosis by computed tomography. Eur Heart J. 2010;31:1442–8.

79. Al-Enezi MS, Abdo RA, Mokeddem MY, Slimani FAA, Khalil A, Fulop T, Turcotte E, Bentourkia M. Assessment of artery calcification in atherosclerosis with dynamic 18F-FDG-PET/CT imaging in elderly subjects. Int J Cardiovasc Imaging. 2019;35:947–54.

80. Derlin T, Habermann CR, Lengyel Z, Busch JD, Wisotzki C, Mester J, Pavics L. Feasibility of 11C-acetate PET/CT for imaging of fatty acid synthesis in the atherosclerotic vessel wall. J Nucl Med. 2011;52:1848–54.

81. Tahara N, Mukherjee J, de Haas HJ, Petrov AD, Tawakol A, Haider N, Tahara A, Constantinescu CC, Zhou J, Boersma HH, Imaizumi T, Nakano M, Finn A, Fayad Z, Virmani R, Fuster V, Bosca L, Narula J. 2-deoxy-2-[18F]fluoro-d-mannose positron emission tomography imaging in atherosclerosis. Nat Med. 2014;20:215–9.

82. Elkhawad M, Rudd JHF. Radiotracer imaging of atherosclerotic plaque biology. Cardiol Clin. 2009;27:345–54.

83. Nahrendorf M, Zhang H, Hembrador S, Panizzi P, Sosnovik DE, Aikawa E, Libby P, Swirski FK, Weissleder R. Nanoparticle PET-CT imaging of macrophages in inflammatory atherosclerosis. Circulation. 2008;117:379–87.

84. Oliveira-Santos Md, Castelo-Branco M, Silva R, Gomes A, Chichorro N, Abrunhosa A, Donato P, Pedroso de Lima J, Pego M, Gonçalves L, Ferreira MJ. Atherosclerotic plaque metabolism in high cardiovascular risk subjects—a subclinical atherosclerosis imaging study with 18 F-NaF PET-CT. Atherosclerosis. 2017;260:41–6.

85. Kitagawa T, Yamamoto H, Nakamoto Y, Sasaki K, Toshimitsu S, Tatsugami F, Awai K, Hirokawa Y, Kihara Y. Predictive value of 18F-sodium fluoride positron emission tomography in detecting high-risk coronary artery disease in combination with computed tomography. J Am Heart Assoc. 2018;7(20):e010224.

86. Izquierdo-Garcia D, Davies JR, Graves MJ, Rudd JHF, Gillard JH, Weissberg PL, Fryer TD, Warburton EA. Comparison of methods for magnetic resonance-guided [18-F]fluorodeoxyglucose positron emission tomography in human carotid arteries. Stroke. 2009;40:86–93.

87. Agatston AS, Janowitz WR, Hildner FJ, Zusmer NR, Viamonte M Jr, Detrano R. Quantification of coronary artery calcium using ultrafast computed tomography. J Am Coll Cardiol. 1990;15:827–32.

88. Janssen T, Bannas P, Herrmann J, Veldhoen S, Busch JD, Treszl A, Münster S, Mester J, Derlin T. Association of linear 18F-sodium fluoride accumulation in femoral arteries as a measure of diffuse calcification with cardiovascular risk factors: a PET/CT study. J Nucl Cardiol. 2013;20:569–77.

89. Kim TN, Kim S, Yang SJ, Yoo HJ, Seo JA, Kim SG, Kim NH, Baik SH, Choi DS, Choi KM. Vascular inflammation in patients with impaired glucose tolerance and type 2 diabetes. Circ Cardiovasc Imaging. 2010;3:142–8.

90. Ahn JY, Lee DS, Lee JS, Kim SK, Cheon GJ, Yeo JS, Shin SA, Chung JK, Lee MC. Quantification of regional myocardial blood flow using dynamic H2(15)O PET and factor analysis. J Nucl Med. 2001;42:782–7.

91. Moussaoui S, Carteret C, Brie D, Mohammad-Djafari A. Bayesian analysis of spectral mixture data using Markov chain Monte Carlo methods. Chemom Intell Lab Syst. 2006;81:137–48.

92. Phelps ME, Huang SC, Hoffman EJ, Selin C, Sokoloff L, Kuhl DE. Tomographic measurement of local cerebral glucose metabolic rate in humans with (F-18)2-fluoro-2-deoxy-D-glucose: validation of method. Ann Neurol. 1979;6:371–88.

93. Bentourkia M. Kinetic modeling of PET data without blood sampling. IEEE Trans Nucl Sci. 2005;52:697–702.

94. Al-enezi MS, Bentourkia M. Kinetic modeling of dynamic PET-18F-FDG atherosclerosis without blood sampling. IEEE Trans Radiat Plasma Med Sci. 2020;1–6.